GEOPHYSICAL MONOGRAPH SERIES

Submarine Landslides

AGU 100
ADVANCING EARTH AND SPACE SCIENCE

Subaqueous Mass Transport Deposits from Outcrops to Seismic Profiles



Editors
Kei Ogata
Andrea Festa
Gian Andrea Pini

WILEY

Geophysical Monograph Series

196 **Extreme Events and Natural Hazards: The Complexity Perspective** *A. Surjalal Sharma, Armin Bunde, Vijay P. Dimri, and Daniel N. Baker (Eds.)*
197 **Auroral Phenomenology and Magnetospheric Processes: Earth and Other Planets** *Andreas Keiling, Eric Donovan, Fran Bagenal, and Tomas Karlsson (Eds.)*
198 **Climates, Landscapes, and Civilizations** *Liviu Giosan, Dorian Q. Fuller, Kathleen Nicoll, Rowan K. Flad, and Peter D. Clift (Eds.)*
199 **Dynamics of the Earth's Radiation Belts and Inner Magnetosphere** *Danny Summers, Ian R. Mann, Daniel N. Baker, and Michael Schulz (Eds.)*
200 **Lagrangian Modeling of the Atmosphere** *John Lin (Ed.)*
201 **Modeling the Ionosphere-Thermosphere** *Jospeh D. Huba, Robert W. Schunk, and George V. Khazanov (Eds.)*
202 **The Mediterranean Sea: Temporal Variability and Spatial Patterns** *Gian Luca Eusebi Borzelli, Miroslav Gacic, Piero Lionello, and Paola Malanotte-Rizzoli (Eds.)*
203 **Future Earth – Advancing Civic Understanding of the Anthropocene** *Diana Dalbotten, Gillian Roehrig, and Patrick Hamilton (Eds.)*
204 **The Galápagos: A Natural Laboratory for the Earth Sciences** *Karen S. Harpp, Eric Mittelstaedt, Noemi d'Ozouville, and David W. Graham (Eds.)*
205 **Modeling Atmospheric and Oceanic Flows: Insightsfrom Laboratory Experiments and Numerical Simulations** *Thomas von Larcher and Paul D. Williams (Eds.)*
206 **Remote Sensing of the Terrestrial Water Cycle** *Venkat Lakshmi (Ed.)*
207 **Magnetotails in the Solar System** *Andreas Keiling, Caitriona Jackman, and Peter Delamere (Eds.)*
208 **Hawaiian Volcanoes: From Source to Surface Rebecca** *Carey, Valerie Cayol, Michael Poland, and Dominique Weis (Eds.)*
209 **Sea Ice: Physics, Mechanics, and Remote Sensing** *Mohammed Shokr and Nirmal Sinha (Eds.)*
210 **Fluid Dynamics in Complex Fractured-Porous Systems** *Boris Faybishenko, Sally M. Benson, and John E. Gale (Eds.)*
211 **Subduction Dynamics: From Mantle Flow to Mega Disasters** *Gabriele Morra, David A. Yuen, Scott King, Sang Mook Lee, and Seth Stein (Eds.)*
212 **The Early Earth: Accretion and Differentiation** *James Badro and Michael Walter (Eds.)*
213 **Global Vegetation Dynamics: Concepts and Applications in the MC1 Model** *Dominique Bachelet and David Turner (Eds.)*
214 **Extreme Events: Observations, Modeling and Economics** *Mario Chavez, Michael Ghil, and Jaime Urrutia-Fucugauchi (Eds.)*
215 **Auroral Dynamics and Space Weather** *Yongliang Zhang and Larry Paxton (Eds.)*
216 **Low-Frequency Waves in Space Plasmas** *Andreas Keiling, Dong-Hun Lee, and Valery Nakariakov (Eds.)*
217 **Deep Earth: Physics and Chemistry of the Lower Mantle and Core** *Hidenori Terasaki and Rebecca A. Fischer (Eds.)*
218 **Integrated Imaging of the Earth: Theory and Applications** *Max Moorkamp, Peter G. Lelievre, Niklas Linde, and Amir Khan (Eds.)*
219 **Plate Boundaries and Natural Hazards** *Joao Duarte and Wouter Schellart (Eds.)*
220 **Ionospheric Space Weather: Longitude and Hemispheric Dependences and Lower Atmosphere Forcing Timothy Fuller-Rowell,** *Endawoke Yizengaw, Patricia H. Doherty, and Sunanda Basu (Eds.)*
221 **Terrestrial Water Cycle and Climate Change Natural and Human-Induced Impacts** *Qiuhong Tang and Taikan Oki (Eds.)*
222 **Magnetosphere-Ionosphere Coupling in the Solar System** *Charles R. Chappell, Robert W. Schunk, Peter M. Banks, James L. Burch, and Richard M. Thorne (Eds.)*
223 **Natural Hazard Uncertainty Assessment: Modeling and Decision Support** *Karin Riley, Peter Webley, and Matthew Thompson (Eds.)*
224 **Hydrodynamics of Time-Periodic Groundwater Flow: Diffusion Waves in Porous Media** *Joe S. Depner and Todd C. Rasmussen (Auth.)*
225 **Active Global Seismology** *Ibrahim Cemen and Yucel Yilmaz (Eds.)*
226 **Climate Extremes** *Simon Wang (Ed.)*
227 **Fault Zone Dynamic Processes** *Marion Thomas (Ed.)*
228 **Flood Damage Survey and Assessment: New Insights from Research and Practice** *Daniela Molinari, Scira Menoni, and Francesco Ballio (Eds.)*
229 **Water-Energy-Food Nexus – Principles and Practices** *P. Abdul Salam, Sangam Shrestha, Vishnu Prasad Pandey, and Anil K Anal (Eds.)*
230 **Dawn–Dusk Asymmetries in Planetary Plasma Environments** *Stein Haaland, Andrei Rounov, and Colin Forsyth (Eds.)*
231 **Bioenergy and Land Use Change** *Zhangcai Qin, Umakant Mishra, and Astley Hastings (Eds.)*
232 **Microstructural Geochronology: Planetary Records Down to Atom Scale** *Desmond Moser, Fernando Corfu, James Darling, Steven Reddy, and Kimberly Tait (Eds.)*
233 **Global Flood Hazard: Applications in Modeling, Mapping and Forecasting** *Guy Schumann, Paul D. Bates, Giuseppe T. Aronica, and Heiko Apel (Eds.)*
234 **Pre-Earthquake Processes: A Multidisciplinary Approach to Earthquake Prediction Studies** *Dimitar Ouzounov, Sergey Pulinets, Katsumi Hattori, and Patrick Taylor (Eds.)*
235 **Electric Currents in Geospace and Beyond** *Andreas Keiling, Octav Marghitu, and Michael Wheatland (Eds.)*
236 **Quantifying Uncertainty in Subsurface Systems** *Celine Scheidt, Lewis Li, and Jef Caers (Eds.)*
237 **Petroleum Engineering** *Moshood Sanni (Ed.)*
238 **Geological Carbon Storage: Subsurface Seals and Caprock Integrity** *Stephanie Vialle, Jonathan Ajo-Franklin, and J. William Carey (Eds.)*
239 **Lithospheric Discontinuities** *Huaiyu Yuan and Barbara Romanowicz (Eds.)*
240 **Chemostratigraphy Across Major Chronological Eras** *Alcides N.Sial, Claudio Gaucher, Muthuvairavasamy Ramkumar, and Valderez Pinto Ferreira (Eds.)*
241 **Mathematical Geoenergy:Discovery, Depletion, and Renewal** *Paul Pukite, Dennis Coyne, and Daniel Challou (Eds.)*
242 **Ore Deposits: Origin, Exploration, and Exploitation** *Sophie Decree and Laurence Robb (Eds.)*
243 **Kuroshio Current: Physical, Biogeochemical and Ecosystem Dynamics** *Takeyoshi Nagai, Hiroaki Saito, Koji Suzuki, and Motomitsu Takahashi (Eds.)*
244 **Geomagnetically Induced Currents from the Sun to the Power Grid** *Jennifer L. Gannon, Andrei Swidinsky, and Zhonghua Xu (Eds.)*
245 **Shale: Subsurface Science and Engineering** *Thomas Dewers, Jason Heath, and Marcelo Sánchez (Eds.)*

Geophysical Monograph 246

Submarine Landslides

Subaqueous Mass Transport Deposits from Outcrops to Seismic Profiles

Kei Ogata
Andrea Festa
Gian Andrea Pini
Editors

This Work is a co-publication of the American Geophysical Union and John Wiley and Sons, Inc.

AGU 100
ADVANCING EARTH AND SPACE SCIENCE

WILEY

This Work is a co-publication between the American Geophysical Union and John Wiley & Sons, Inc.

This edition first published 2020 by John Wiley & Sons, Inc., 111 River Street, Hoboken, NJ 07030, USA and the American Geophysical Union, 2000 Florida Avenue, N.W., Washington, D.C. 20009

© 2020 American Geophysical Union

All rights reserved. No part of this publication may be reproduced, stored in a retrieval system, or transmitted, in any form or by any means, electronic, mechanical, photocopying, recording, or otherwise, except as permitted by law. Advice on how to obtain permission to reuse material from this title is available at http://www.wiley.com/go/permissions

Published under the aegis of the AGU Publications Committee

Brooks Hanson, Executive Vice President, Science
Lisa Tauxe, Chair, Publications Committee
For details about the American Geophysical Union visit us at www.agu.org.

Wiley Global Headquarters
111 River Street, Hoboken, NJ 07030, USA

For details of our global editorial offices, customer services, and more information about Wiley products visit us at www.wiley.com.

Limit of Liability/Disclaimer of Warranty
While the publisher and authors have used their best efforts in preparing this work, they make no representations or warranties with respect to the accuracy or completeness of the contents of this work and specifically disclaim all warranties, including without limitation any implied warranties of merchantability or fitness for a particular purpose. No warranty may be created or extended by sales representatives, written sales materials, or promotional statements for this work. The fact that an organization, website, or product is referred to in this work as a citation and/or potential source of further information does not mean that the publisher and authors endorse the information or services the organization, website, or product may provide or recommendations it may make. This work is sold with the understanding that the publisher is not engaged in rendering professional services. The advice and strategies contained herein may not be suitable for your situation. You should consult with a specialist where appropriate. Neither the publisher nor authors shall be liable for any loss of profit or any other commercial damages, including but not limited to special, incidental, consequential, or other damages. Further, readers should be aware that websites listed in this work may have changed or disappeared between when this work was written and when it is read.

Library of Congress Cataloging-in-Publication Data

Hardback: 9781119500582

Cover Design: Wiley
Cover Image: Conglomerate rock located at Point Reyes, California, deposited by a submarine landslide (licensed under CC BY-SA)

Set in 10/12pt Times New Roman by SPi Global, Pondicherry, India

10 9 8 7 6 5 4 3 2 1

Dedicated to Nello Luciani and Giuliana Barbieri, who keep lighting the darkness

CONTENTS

List of Contributors ..... **ix**

Preface ..... **xiii**

Acknowledgments ..... **xv**

Part I: Submarine Landslide Deposits in Orogenic Belts

1. **Submarine Landslide Deposits in Orogenic Belts: Olistostromes and Sedimentary Mélanges**
   Kei Ogata, Andrea Festa, Gian Andrea Pini, and Juan Luis Alonso 3
2. **Mass-Transport Deposits in the Foredeep Basin of the Miocene Cervarola Sandstones Formation (Northern Apennines, Italy)**
   Alberto Piazza and Roberto Tinterri 27
3. **Late Miocene Olistostrome in the Makran Accretionary Wedge (Baluchistan, SE Iran): A Short Review**
   Jean-Pierre Burg 45
4. **Spatial Distribution of Mass-Transport Deposits Deduced From High-Resolution Stratigraphy: The Pleistocene Forearc Basin (Boso Peninsula, Central Japan)**
   Masayuki Utsunomiya and Yuzuru Yamamoto 57
5. **Mass-Transport Deposits as Markers of Local Tectonism in Extensional Basins**
   Tiago M. Alves and Davide Gamboa 71
6. **Block Generation, Deformation, and Interaction of Mass-Transport Deposits With the Seafloor: An Outcrop-Based Study of the Carboniferous Paganzo Basin (Cerro Bola, NW Argentina)**
   Matheus S. Sobiesiak, Victoria Valdez Buso, Ben Kneller, G. Ian Alsop, and Juan Pablo Milana 91
7. **The Carboniferous MTD Complex at La Peña Canyon, Paganzo Basin (San Juan, Argentina)**
   Victoria Valdez Buso, Juan Pablo Milana, Matheus S. Sobiesiak, and Ben Kneller 105
8. **Mass-Transport Complexes of the Marnoso-arenacea Foredeep Turbidite System (Northern Apennines, Italy): A Reappraisal After Twenty-Years**
   Gian Andrea Pini, Claudio Corrado Lucente, Sonia Venturi, and Kei Ogata 117
9. **Fold and Thrust Systems in Mass-Transport Deposits Around the Dead Sea Basin**
   G.Ian Alsop, Rami Weinberger, Shmuel Marco, and Tsafrir Levi 139
10. **Eocene Mass-Transport Deposits in the Basque Basin (Western Pyrenees, Spain): Insights Into Mass-Flow Transformation and Bulldozing Processes**
    Aitor Payros and Victoriano Pujalte 155
11. **Neogene and Quaternary Mass-Transport Deposits From the Northern Taranaki Basin (North Island, New Zealand): Morphologies, Transportation Processes, and Depositional Controls**
    Suzanne Bull, Malcolm Arnot, Greg Browne, Martin Crundwell, Andy Nicol, and Lorna Strachan 171

Part II: Submarine Landslide Deposits in Current Active and Passive Margins

12. Modern Submarine Landslide Complexes: A Short Review
Katrin Huhn, Marcos Arroyo, Antonio Cattaneo, Mike A. Clare, Eulàlia Gràcia, Carl B. Harbitz, Sebastian Krastel, Achim Kopf, Finn Løvholt, Marzia Rovere, Michael Strasser, Peter J. Talling, and Roger Urgeles 183

13. An Atlas of Mass-Transport Deposits in Lakes
Maddalena Sammartini, Jasper Moernaut, Flavio S. Anselmetti, Michael Hilbe, Katja Lindhorst, Nore Praet, and Michael Strasser.....201

14. Style and Morphometry of Mass-Transport Deposits Across the Espírito Santo Basin (Offshore SE Brazil)
Davide Gamboa, Tiago M. Alves, and Kamaldeen Olakunle Omosanya 227

15. Submarine Landslides on the Nankai Trough Accretionary Prism (Offshore Central Japan)
Gregory F. Moore, Jason K. Lackey, Michael Strasser, and Mikiya Yamashita 247

16. Seismic Examples of Composite Slope Failures (Offshore North West Shelf, Australia)
Nicola Scarselli, Ken McClay, and Chris Elders 261

17. Submarine Landslides Around Volcanic Islands: A Review of What Can Be Learned From the Lesser Antilles Arc
Anne Le Friant, Elodie Lebas, Morgane Brunet, Sara Lafuerza, Matt Hornbach, Maya Coussens, Sebastian Watt, Michael Cassidy, Peter J. Talling, and IODP 340 Expedition Science Party.....277

18. Submarine Landslides in an Upwelling System: Climatically Controlled Preconditioning of the Cap Blanc Slide Complex (Offshore NW Africa)
Morelia Urlaub, Sebastian Krastel, and Tilmann Schwenk 299

19. Submarine Landslides Along the Mixed Siliciclastic-Carbonate Margin of the Great Barrier Reef (Offshore Australia)
Ángel Puga-Bernabéu, Jody Michael Webster, Robin Jordan Beaman, Amanda Thran, Javier López-Cabrera, Gustavo Hinestrosa, and James Daniell.....313

20. Submarine Landslides on the Seafloor: Hints on Subaqueous Mass-Transport Processes From the Italian Continental Margins (Adriatic and Tyrrhenian Seas, Offshore Italy)
Fabiano Gamberi, Giacomo Dalla Valle, Federica Foglini, Marzia Rovere, and Fabio Trincardi.....339

Index.....357

See electronic version for color representation of the figures in this book.

LIST OF CONTRIBUTORS

Juan Luis Alonso
Department of Geology, University of Oviedo, Oviedo, Spain

G. Ian Alsop
Department of Geology and Petroleum Geology, School of Geosciences, University of Aberdeen, Aberdeen, United Kingdom

Tiago M. Alves
3D Seismic Lab, School of Earth and Ocean Sciences, Cardiff University, Cardiff, United Kingdom

Flavio S. Anselmetti
Institute of Geological Sciences and Oeschger Centre for Climate Change Research, University of Bern, Bern, Switzerland

Malcolm Arnot
Department of Petroleum Geoscience, GNS Science, Lower Hutt, New Zealand

Marcos Arroyo
Polytechnic University of Catalunya, Barcelona, Spain

Robin Jordan Beaman
College of Science and Engineering, James Cook University, Cairns, Queensland, Australia

Greg Browne
Department of Petroleum Geoscience, GNS Science, Lower Hutt, New Zealand

Morgane Brunet
University of Bremen, Bremen, Germany

Suzanne Bull
Department of Petroleum Geoscience, GNS Science, Lower Hutt, New Zealand

Jean-Pierre Burg
Department of Earth Sciences, ETH- and University Zurich, Zurich, Switzerland

Victoria Valdez Buso
Department of Geology and Petroleum Geology, School of Geosciences, University of Aberdeen, Aberdeen, United Kingdom

Michael Cassidy
Department of Earth Sciences, University of Oxford, Oxford, United Kingdom

Antonio Cattaneo
IFREMER, Géosciences Marines, Brest, France

Mike A. Clare
National Oceanography Centre, University of Southampton Waterfront Campus, Southampton, United Kingdom

Maya Coussens
University of Southampton, Southampton, United Kingdom

Martin Crundwell
Department of Petroleum Geoscience, GNS Science, Lower Hutt, New Zealand

Giacomo Dalla Valle
Institute for Marine Sciences (ISMAR), National Council of Research (CNR), Bologna, Italy

James Daniell
College of Science and Engineering, James Cook University, Cairns, Queensland, Australia

Chris Elders
Department of Applied Geology, Curtin University, Perth, Western Australia, Australia

Andrea Festa
Department of Earth Sciences, University of Turin, Turin, Italy

Federica Foglini
Institute for Marine Sciences (ISMAR), National Council of Research (CNR), Bologna, Italy

Fabiano Gamberi
Institute for Marine Sciences (ISMAR), National Council of Research (CNR), Bologna, Italy

Davide Gamboa
Portuguese Institute for the Sea and the Atmosphere (IPMA, I.P.), Lisbon, Portugal

Eulàlia Gràcia
B-CSI, Institute of Marine Sciences (CSIC), Barcelona, Spain

Carl B. Harbitz
Norwegian Geotechnical Institute, Oslo, Norway

Michael Hilbe
Institute of Geological Sciences and Oeschger Centre for Climate Change Research, University of Bern, Bern, Switzerland

Gustavo Hinestrosa
School of Geosciences, Geocoastal Research Group, University of Sydney, Sydney, New South Wales, Australia

Matt Hornbach
SMU Dedman College, Dallas, Texas, United States

Katrin Huhn
MARUM – Center for Marine Environmental Sciences, University of Bremen, Bremen, Germany

Ben Kneller
Department of Geology and Petroleum Geology, School of Geosciences, University of Aberdeen, Aberdeen, United Kingdom

Achim Kopf
MARUM – Center for Marine Environmental Sciences, University of Bremen, Bremen, Germany

Sebastian Krastel
Institute of Geosciences, Christian-Albrechts-University, Kiel, Germany

Jason K. Lackey
Department of Earth Sciences, University of Hawaii, Honolulu, Hawaii, United States

Sara Lafuerza
Sorbonne University, Paris, France

Anne Le Friant
CNRS, Paris Institute of Earth Physics, University of Paris, Paris, France

Elodie Lebas
Christian-Albrechts-University of Kiel, Kiel, Germany

Tsafrir Levi
Geological Survey of Israel, Jerusalem, Israel

Katja Lindhorst
Institute of Geoscience, University of Kiel, Kiel, Germany

Javier López-Cabrera
Irish Centre for Research in Applied Geosciences, University College Dublin, Dublin, Ireland

Finn Løvholt
Norwegian Geotechnical Institute, Oslo, Norway

Claudio Corrado Lucente
Agency for Territorial Safety and Civil Protection, Emilia-Romagna Region, Rimini, Italy

Shmuel Marco
Department of Geophysics, Tel Aviv University, Tel Aviv-Yafo, Israel

Ken McClay
Fault Dynamics Research Group, Department of Earth Sciences, Royal Holloway University of London, Egham, United Kingdom

Juan Pablo Milana
CONICET and Institute of Geology, National University of San Juan, San Juan, Argentina

Jasper Moernaut
Institute of Geology, University of Innsbruck, Innsbruck, Austria

Gregory F. Moore
Department of Earth Sciences, University of Hawaii, Honolulu, Hawaii, United States

Andy Nicol
Department of Geological Sciences, University of Canterbury, Christchurch, New Zealand

Kei Ogata
Faculty of Science, Department of Earth Sciences, Free University of Amsterdam, Amsterdam, The Netherlands

Kamaldeen Olakunle Omosanya
Timelapsegeo AS, Trondheim, Norway

Aitor Payros
Department of Stratigraphy and Paleontology, University of the Basque Country (UPV/EHU), Bilbao, Spain

Alberto Piazza
Department of Chemistry, Life Sciences and Environmental Sustainability, Earth Sciences Unit, University of Parma, Parma, Italy

Gian Andrea Pini
Department of Mathematics and Geosciences, University of Trieste, Trieste, Italy

Victoriano Pujalte
Department of Stratigraphy and Paleontology, University of the Basque Country (UPV/EHU), Bilbao, Spain

Nore Praet
Renard Centre of Marine Geology, Ghent University, Ghent, Belgium

Ángel Puga-Bernabéu
Department of Stratigraphy and Paleontology, University of Granada, Granada, Spain; *and*
School of Geosciences, Geocoastal Research Group, University of Sydney, Sydney, New South Wales, Australia

Marzia Rovere
Institute for Marine Sciences (ISMAR), National Council of Research (CNR), Bologna, Italy

Maddalena Sammartini
Institute of Geology, University of Innsbruck, Innsbruck, Austria

Nicola Scarselli
Fault Dynamics Research Group, Department of Earth Sciences, Royal Holloway University of London, Egham, United Kingdom

Tilmann Schwenk
Faculty of Geosciences, MARUM-Center for Marine Environmental Sciences, University of Bremen, Bremen, Germany

Matheus S. Sobiesiak
Postgraduate Program in Geology, University of the Sinos Valley, São Leopoldo, Rio Grande do Sul, Brazil

Lorna Strachan
School of Environment, University of Auckland, Auckland, New Zealand

Michael Strasser
Institute of Geology, University of Innsbruck, Innsbruck, Austria

Peter J. Talling
Departments of Earth Sciences and Geography, University of Durham, Durham, United Kingdom

Amanda Thran
School of Geosciences, EarthByte Group, University of Sydney, Sydney, New South Wales, Australia

Roberto Tinterri
Department of Chemistry, Life Sciences and Environmental Sustainability, Earth Sciences Unit, University of Parma, Parma, Italy

Fabio Trincardi
Institute for Marine Sciences (ISMAR), National Council of Research (CNR), Bologna, Italy

Roger Urgeles
B-CSI, Institute of Marine Sciences (CSIC), Barcelona, Spain

Morelia Urlaub
GEOMAR Helmholtz Centre for Ocean Research Kiel, Kiel, Germany

Masayuki Utsunomiya
Research Institute of Geology and Geoinformation, Geological Survey of Japan, AIST, Tsukuba, Japan

Sonia Venturi
Ecosistema s.c.r.l., Imola, Italy

Sebastian Watt
University of Birmingham, Birmingham, United Kingdom

Jody Michael Webster
School of Geosciences, Geocoastal Research Group, University of Sydney, Sydney, New South Wales, Australia

Rami Weinberger
Geological Survey of Israel, Jerusalem, Israel; and Department of Geological and Environmental Sciences, Ben Gurion University of the Negev, Beer Sheva, Israel

Yuzuru Yamamoto
Department of Mathematical Science and Advanced Technology, Japan Agency for Marine-Earth Science and Technology (JAMSTEC), Yokohama Institute for Earth Sciences, Yokohama, Japan

Mikiya Yamashita
Japan Agency for Marine-Earth Science and Technology (JAMSTEC), Yokohama, Japan

PREFACE

Giant (>1 km^3) submarine landslides are common in every subaqueous geodynamic context (from passive and active continental margins to oceanic and continental intraplate settings) and are among the most threatening geohazard in offshore and coastal areas, due to their recurrence times (about 50 years), dimensions (thousands of cubic kilometers), long traveled distances (hundreds of kilometers), terminal velocity (up to 20 m/s), and proven ability to generate tsunamis, whose destructive potential equals that of large earthquakes. Moreover, such submarine landslides also play fundamental role in changing geological fluxes, as they critically impact the hydrosphere, atmosphere, cryosphere, lithosphere, and biosphere in several ways, with strong synergic autocyclic (local to intraregional) and allocyclic (interregional to global) interactions and interplay of causes and effects (e.g., seismic shocks, liquefaction/fluidization, gas hydrate dissociation, etc.).

The vast amount of geophysical data acquired from modern active and passive margins show that submarine landslide deposits systematically occur at various scales, varying in abundance, morphology, and other characteristics depending on the mode, nature, and interplay of different geological processes in their depositional setting. These geological units, called mass-transport deposits (MTDs) and complexes (MTCs), represent the products of either single depositional event or composite bodies originating from superposed, multiple events, respectively, and may involve sediments with different degrees of consolidation/lithification and grain sizes (from clay to silt to sand to gravel size). Their volume can range from tens of cubic meters to up to hundreds of thousands of cubic kilometers, extending over areas up to millions of square kilometers and showing long runout distance (more than 500 km, considering the associated, forerunning turbulent flows) over very low-angled (0.05°) slopes. In summary these units can occur in every type of geologic setting, and for different causes, their upper scale threshold is sometimes transitional with gravitational and tectonically transported nappes (differing mainly in terms of velocity of processes), and the amounts of transferred material in a single, large-scale mass-transport event may overcome the cumulative, yearly sediment discharge of all the major modern river systems combined. Such bodies are commonly characterized by great internal heterogeneity and deformation, resulting in acoustic artifacts and transparent zones in 2D and 3D seismic imagery, and thus usually overlooked in terms of internal anatomy.

The ancient "fossil" counterparts of these MTDs and MTCs are widely represented in orogenic belts and in exhumed subduction-accretion complexes, being known in the classic literature as "olistostromes" and "sedimentary mélanges." These units represent optimal submarine landslide deposits' analogues that can be studied directly in the field instead of using geophysical tools. Olistostromes in fact provide insights from the micro- to the mesoscale (2D or 3D) not only within the thickness of the whole deposit but also within the underlying and overlying units, with a resolution unresolvable by modern geophysical means. In this framework, detailed studies combining high-resolution marine geophysical data, well core analysis, and outcrop-based surveys show a partition of internal structural arrangement into discrete deformation domains, suggesting (i) differential movement of discrete bodies of mass during translation and emplacement, (ii) episodic pulses during the same depositional event(s), and (iii) interplay of different, synchronous mass-transport processes.

The practical implications of submarine landslide studies *sensu lato* are timely and of high importance. Natural disasters directly or indirectly caused by submarine landslides in near shore, coastal, and offshore areas could potentially result in huge socioeconomic losses; therefore it is reasonable to understand that the broadband study of mass-transport processes and the robust linking of cause-effect relationships are crucial for a sustainable civil development and need to be considered as an integral part of both "pure" and "applied" scientific research.

Despite the important scientific repercussions (e.g., sediment delivery processes, changes in global to local geological cycles) and socioeconomic implications (e.g., destabilization of coastal/offshore infrastructures, submarine cables ruptures, etc.), our understanding of the controlling mechanisms remains severely limited. This is especially due to the lack of in-depth, shared knowledge between marine and field geologists. In fact, the products of these submarine landslide events are generally well preserved in the ancient to recent geological record, from mountain belts to present-day continental margins, and they have been intensively studied at different scales and detail and for different purposes, leading to the production of an overwhelming amount of data and interpretations, which usually remain confined within the boundaries of specific field of specialization. As consequence, important, combined information coming from the study of these geological units is still basically

"undigested" and underappreciated by the scientific community at whole.

In this framework, the actual challenge is to gather all the available data into a broadband, synoptic outline of the different types of MTDs, with a combined approach that illustrates the main common features of the different case studies in an immediate, reader-friendly way, allowing cross-disciplinary and multiscale observations and (re)interpretations. In this book we emphasize this integrated and intuitive approach presenting updated and comparable on- and offshore case studies collected in exhumed orogenic bets and modern active and passive margins worldwide to provide a tuned-up, timely overview of large-scale, heterogeneous sedimentary mass-transport processes and products, with an exhaustive and comprehensive perspective.

This book gathers original and review contributions to showcase submarine landslide deposits from both field-based and geophysical studies, and it is organized in two main parts: Part I dedicated to outcrop case studies from exhumed orogenic belts and Part II dedicated to the seismic-acoustic (and core) examples studied in marine geology surveys of continental margins. Each section is introduced by a review chapter that briefly outlines the state of the art and the way further in that specific discipline.

The book format is designed to provide:

1. an updated and integrated knowledge about the different types of large-scale subaqueous MTDs and their generating processes, through the integrated and comparative analysis of outcrop-based and geophysical case studies from ancient and modern continental margins worldwide;
2. an updated, comprehensive set of information about submarine landslide products and processes and related geohazard implications; and
3. a readily available, easy reading, and standardized reference guide to the study of sedimentary MTDs in general, with a seamless conceptual continuity from outcrops and cores to seismic profiles.

Kei Ogata
Free University of Amsterdam, The Netherlands

Andrea Festa
University of Turin, Italy

Gian Andrea Pini
University of Trieste, Italy

ACKNOWLEDGMENTS

The following reviewers are thankfully acknowledged (in alphabetical order): Juan Luis Alonso, Christian Beck, Hannah Brooks, Sebastian Cardona, Daniele Casalbore, Paolo Conti, Luis Pedro Fernández, Joana Gafeira Goncalves, Michael Garcia, Aggeliki Georgiopoulou, Jan Golonka, Andrew N. Green, Shun-Kun Hsu, Kijiro Kawamura, Mattia Marini, Massimo Moretti, Vittorio Maselli, Lilian Navarro, Odonne Francis, Yujiro Ogawa, Luca Pandofi, Loren A. Raymond, Francesca Remitti, Claudia Romagnoli, Jonas B. Ruh, Jara Schnyder, Maria Rosaria Senatore, Glenn Sharman, Luis Somoza, Lorna Strachan, Enrico Tavarnelli, Roberto Tinterri, Roger Urgeles, Morelia Urlaub, Gustavo Villarosa, Geoff Wadge, Sally Watson, Marek Wendorff, and Yuzuru Yamamoto.

Part I
Submarine Landslide Deposits in Orogenic Belts

1

Submarine Landslide Deposits in Orogenic Belts: Olistostromes and Sedimentary Mélanges

Kei Ogata[1], Andrea Festa[2], Gian Andrea Pini[3], and Juan Luis Alonso[4]

ABSTRACT

Olistostrome and sedimentary mélange are two synonymous genetic terms referring to the "fossil" products of ancient submarine mass-transport processes exhumed in orogenic belts. Lithology, stratigraphy, lithification degree, and structural anatomy of these units reflect the synergic and combined action of different mass-transport processes leading to composite deposits developed through multistage deformation phases. The general depositional physiography, tectonic setting, and the type, scale, and rate of slide mass transformation mechanisms during the downslope motion and emplacement and postdepositional processes are the main factors controlling the final internal anatomy of olistostromes and sedimentary mélanges. These features are commonly progressively reworked by subsequent burial, diapiric, and tectonic processes and may be eventually almost completely obliterated by metamorphic processes during orogenic belt and/or subduction complex evolution. The correct recognition of olistostromal units and their intrinsic features in different orogenic belts needs extensive and careful fieldwork and ultimately provides excellent proxies for the timing of various tectonic-sedimentary events interacting during the Wilson cycle. The basic concepts of structural geology, sedimentology, stratigraphy, and basin analysis should be jointly applied in studying the internal structure, lithological arrangement, and formation-deformation mechanisms of olistostromes and sedimentary mélanges.

1.1. INTRODUCTION

Major sedimentary accumulations (basin wide) originated from large-scale submarine landslides and slope failures crop out widely within the sedimentary record of mountain belts throughout the world (Figure 1.1). These ancient "fossil" counterparts of the mass-transport deposits (MTDs) and mass-transport complexes (MTCs), which are commonly observed in the geophysical profiles of present-day continental margins (see, e.g., Hampton et al., 1996; Weimer & Shipp, 2004, and further discussed in Part II), are also known by the synonymous names "olistostrome" or "sedimentary mélange." Such units are invaluable tools for the study of the internal anatomy of submarine landslide deposits across different scales (Lucente & Pini, 2008; Ogata et al., 2012a; Festa et al., 2016).

Present-day MTDs are commonly characterized by great internal heterogeneity and deformation, resulting in two-dimensional (2D) and three-dimensional (3D) seismic imagery characterized by acoustic artifacts and transparent zones. For this reason, apart from some exceptions (see, e.g., Gamboa et al., 2010; Strasser et al., 2012; Ogata et al., 2014a; Alves, 2015), including the most representative ones discussed in this book, the complex internal structure of MTDs usually has been overlooked.

[1] *Faculty of Science, Department of Earth Sciences, Free University of Amsterdam, Amsterdam, The Netherlands*

[2] *Department of Earth Sciences, University of Turin, Turin, Italy*

[3] *Department of Mathematics and Geosciences, University of Trieste, Trieste, Italy*

[4] *Department of Geology, University of Oviedo, Oviedo, Spain*

Submarine Landslides: Subaqueous Mass Transport Deposits from Outcrops to Seismic Profiles, Geophysical Monograph 246, First Edition. Edited by Kei Ogata, Andrea Festa, and Gian Andrea Pini.
© 2020 American Geophysical Union. Published 2020 by John Wiley & Sons, Inc.



Figure 1.1 (a) Geographical distribution of major olistostromes and sedimentary mélanges and some examples (Source: Modified from Festa et al. (2016)). (b) Oligocene-Miocene Val Tiepido-Canossa olistostrome, Northern Apennines, Italy. (c) Athalassa member olistostrome in the Pliocene Nicosia Formation, Cyprus. (d) Eocene Fanlo unit olistostrome, south central Pyrenees, Spain. (e) Detail of intrabasinal blocks enclosed in the Paleogene megabeds of the Friuli-Julian Basin, NE Italy. (f) Basalt slide block in one of the Miocene Taranaki Basin olistostromes, New Zealand. (g) Fluid escape structure cutting a carbonate slide block in the Eocene Hecho Group "megaturbidites," Pyrenees, Spain. (h) Folded slide blocks in one of the Miocene Rudeis Formation olistostromes, Sinai, Egypt. (i) Plio-Pleistocene Chikura Group olistostrome, Japan. (j) Eastern Argentine Precordillera sedimentary mélange(s) in the Silurian La Rinconada Formation, San Juan Province, Argentina. Dashed lines indicate bedding (e.g., crude lamination, subunit boundaries, base and roof contacts). Circled person(s) for scale.

Detailed studies combining high-resolution marine geophysical data, outcrop-based surveys, and core analysis show systematic partitions of the internal structural arrangement of MTDs and MTCs into discrete deformation domains, suggesting (i) differential movement of discrete bodies of mass during translation and emplacement, (ii) episodic pulses during the same depositional event(s), and (iii) interplay of different synchronous mass-transport processes (King et al., 2011; Vanneste et al., 2011; Ogata et al., 2012a, 2014b; Omosanya & Alves, 2012; Joanne et al., 2013).

From the point of view of the internal structures and kinematics, both the lower detachment surface and the shear zones separating the individual masses inside the body are characterized by features reflecting different mechanisms of movement (e.g., Pini et al., 2010a, 2010b, 2012). Among these mechanisms are the dispersive forces due to the grain-to-grain acoustic resonance interactions (Melosh, 1987) and the interstitial fluid overpressure in a matrix with the characteristics of a hyperconcentrated suspension (Mutti, 1992; Mutti et al., 1999, 2006; Ogata et al., 2012a, 2012b).

Recent outcrop-based studies, such as those discussed in Part I, document that fluid overpressure can enable slide-flow transformation from discrete coherent movement to uniform cohesive flow, along with progressive disruption of sediment blocks and seafloor (e.g., Ogata et al., 2012a, 2014b). These studies confirm the concept of evolution of mass-transport processes, from sliding slumping to blocky flow, debris flow, and eventually turbidity flow and deposition (Mutti et al., 2006; Festa et al., 2016).

Field-based studies are still extremely valuable, as they provide important insights on the internal evolution of a submarine landslide from the microscale to the mesoscale (2D or 3D) within the thickness of the whole deposit, and they also reveal the relationships with the underlying and overlying sedimentary units. Thus, field studies provide a resolution of tails unresolvable by modern geophysical means of investigations.

1.2. HISTORICAL OUTLINE

"Olistostrome" derives from the Greek "olistomai" (to slide) and "stroma" (accumulation) and is a term first introduced by Flores (1955) to define mappable sedimentary deposits included within normally bedded geological sequences, characterized by lithologically and/or petrographically heterogeneous and mixed materials, emplaced by a semifluid mass (Flores, 1955, 1956). The original definition specifies the internal "chaotic" anatomy of these bodies, which is characterized by various degrees of bedding disruption. Nonetheless, olistostromes can be systematically differentiated into a matrix component ("binder"), which consists of fine-grained heterogeneous material, a block component with discrete elements from the size of pebbles to boulders and up to several cubic kilometers in volume ("bodies of harder rocks"). Over time, the term acquired more specific subdivisions, such as "allolistostrome" for bodies containing both native (i.e., intraformational) and exotic (i.e., extraformational) blocks and "endolistostrome" for olistostromes containing only native blocks (Elter & Raggi, 1965). Additionally, since the reintroduction of the term *mélange* (Bailey & McCallien, 1950; Hsü, 1968; Gansser, 1974), recognition of the wide distribution of mélanges, and the consequent debate on the tectonic versus sedimentary origin of block-in-matrix bodies, the terms "sedimentary mélange" and "olistostromal mélange" have been adapted and (re) used to identify polymictic "chaotic" units bounded by depositional contacts and commonly thought to represent deposits deriving from submarine landsliding (see, e.g., Berkland et al., 1972; Cowan, 1974; Hsü, 1974; Moore et al., 1976; Silver & Beutner, 1980; Raymond, 1984; Bettelli & Panini, 1985; Cowan, 1985; Cowan & Pini, 2001; Şengör, 2003; Medialdea et al., 2004; Camerlenghi & Pini, 2009; Festa et al., 2010a, 2012b, 2015b; Dilek et al., 2012). It is worthy to note that a considerable number of authors have been using other popular terms such as "megabreccia" or "sedimentary breccia" (e.g., Kolasa & Ślączka, 1985; Wendorff, 2005a). Tectonic and sedimentary *mélanges* can coexist, especially within accretionary wedges and collisional belts, and their distinction in many cases is a challenge (Festa et al., 2010a, 2010b, 2012a).

In most orogenic belts and exhumed subduction-accretion complexes, a strong morphological convergence exists between the meso- to map-scale elements of the block-in-matrix fabric both in large to basin-wide olistostromes and in tectonic mélanges. This still fuels the long-lasting debate on the nature and mode of geological processes leading to the formation of "chaotic" rock assemblages, particularly in areas of well-preserved exhumed subduction-accretion complexes (see, e.g., Berkland et al., 1972; Aalto, 1981, 2014; Cloos, 1982, 1984; Raymond, 1984; Cowan, 1985; Brandon, 1989; Okamura, 1991; Ukar, 2012; Wakabayashi, 2012, 2015; Ogawa et al., 2014; Platt, 2015; Raymond & Bero, 2015; Ukar & Cloos, 2015, 2016; Raymond, 2017).

Within the context of the debate, the concept of "precursory olistostrome" introduced by Elter and Trevisan (1973) and later reemphasized by Vollmer and Bosworth (1984), for instance, emphasizes the crucial role of submarine landsliding in the formation and evolution of collisional orogenic belts, highlighting the interplay between tectonic and depositional processes in accretionary complexes and fold and thrust belts. This idea derives from the Alpine *wildflysch* concept

(see Mutti et al. (2009) for a complete review), which stressed the occurrence of "chaotic" deposits that result from gravitational reworking of the deformational front of advancing tectonic nappes.

1.3. SUBMARINE LANDSLIDE STUDIES: AN INTEGRATED APPROACH

The large amount of data coming from geophysical surveys of modern continental margins strongly enhanced our understanding of the overall morphology of submarine landslides, commonly referred to as mass-transport deposits (MTDs). These studies provide a detailed outline of the external geometries, vertical/lateral extension, and surface/basal attitude of these deposits (e.g., Prior et al., 1984, 1987; Huvenne et al., 2002; Canals et al., 2004; Yamamoto et al., 2009). Nonetheless, such data reveal only partial information about the internal anatomy of these bodies, mainly because of the resolution limit of the geophysical method, the ambiguity of interpretation (e.g., Gardner et al., 1999; Lee et al., 2004), and the common presence of transparent zones (Coleman & Prior, 1988).

In contrast to remote geophysical analyses, in the field, it is often difficult to appreciate the whole geometry and external morphology of submarine landslide deposits, generally because of exposure and preservation limits (Woodcock, 1979; Macdonald et al., 1993; Shanmugam, 2015). Good outcrops, however, generally permit detailed observations on the emplacement mechanisms and in particular observations on micro- and mesoscale structures and their vertical/lateral stratigraphic relationships over short to medium distances (see, among many others, Woodcock, 1979; Gawthorpe & Clemmey, 1985; Sherba, 1989; Alonso et al., 2006, 2015; Delteil et al., 2006; Burg et al., 2008; Callot et al., 2008; Lucente & Pini, 2008; Yamamoto et al., 2009; Codegone et al., 2012a; Ogata et al., 2012a; Festa et al., 2016).

In classic *mélanges*, the mesoscale block-in-matrix fabric commonly characterizes the vast majority of MTDs. In both MTDs and tectonic *mélanges*, this kind of fabric is thought to be primarily achieved through progressive disruption (fragmentation) of stratified sequences of sediments through the operation of several interacting or overlapping mechanisms. That yield a broad spectrum of products, constrained between two end members represented by undeformed successions and block-in-matrix rocks (see Festa et al. (2016)). In this framework, processes related to sedimentary mass transport, commonly involving non-lithified to poorly lithified material, are efficient mechanisms of stratal disruption, which can be achieved both inside (e.g., partial disaggregation of still stratified blocks) and outside the slide body (e.g., within the uppermost portion of the overridden substrate) during its downslope motion (Strachan, 2002; Lucente & Pini, 2003; Mutti et al., 2009; Pini et al., 2010a, 2010b; Odonne et al., 2011). At the outcrop scale, this kind of deformation yields a broad spectrum of sedimentary MTD products ranging from almost undeformed lithologies (e.g., slide block facies), through folded and boudinaged successions (e.g., slump-slide facies), to block-in-matrix bodies (e.g., blocky and debris-flow facies), characterized by the occurrence of a strongly mixed, liquidized (in the sense of Allen (1982)) matrix (Mutti et al., 2006; Ogata et al., 2012a; Figure 1.2).

The other necessary prerequisite for *mélange* formation is lithologic mixing (Hsü, 1968). The inclusion of "exotic" blocks (Hsü, 1968; Berkland et al., 1972; Cloos, 1982; Avé Lallemant & Guth, 1990; Ernst, 2016) is achieved by sedimentary mass transport and slope tectonics only where deformation leads to the uplift and the subsequent reworking of various rocks. Exotic blocks are extraformational (i.e., extrabasinal and extradepocentral) and often belong to different structural units and/or paleogeographic domains of the intrabasinal sediments, being alien/foreign with respect to the final depositional environment. Compression-, extension-, and strike-slip-related growth structures and mud-serpentine diapiric phenomena are thought to develop marginal and intrabasinal bathymetric highs and/or steep slopes (scarps) exposing rocks, which may become involved as "exotics" in gravity-related processes. In exposed collisional belts, this kind of sedimentary mixing is clearly represented by the so-called precursory olistostromes (Elter & Trevisan, 1973), recognizable in ancient foredeep successions, and epi-nappe MTDs, typical of wedge-top basins (see Festa et al. (2010a, 2012b)).

1.4. ANATOMY OF SUBMARINE LANDSLIDES FROM OUTCROP PERSPECTIVE: PROCESSES AND PRODUCTS

A wide range of mesoscale structures can be recognized in olistostromes and sedimentary mélanges, testifying to different deformation mechanisms that facilitate the downslope mobility of a slide mass. The correct identification and interpretation of such structures are crucial to a better understanding of the factors controlling the origin, preservation, and significance of these units in the evolution of orogenic belts.

Mechanisms supporting the extraordinary downslope mobility of olistostromes and sedimentary *mélanges* can be inferred by applying advanced structural geology tools to fold and fault data and statistics, in addition to application of the standard sedimentological ones (Woodcock, 1979; Bradley & Hanson, 1998; Strachan, 2002; Strachan & Alsop, 2006; Ogata, 2010; Ogata et al., 2012a, 2012b).

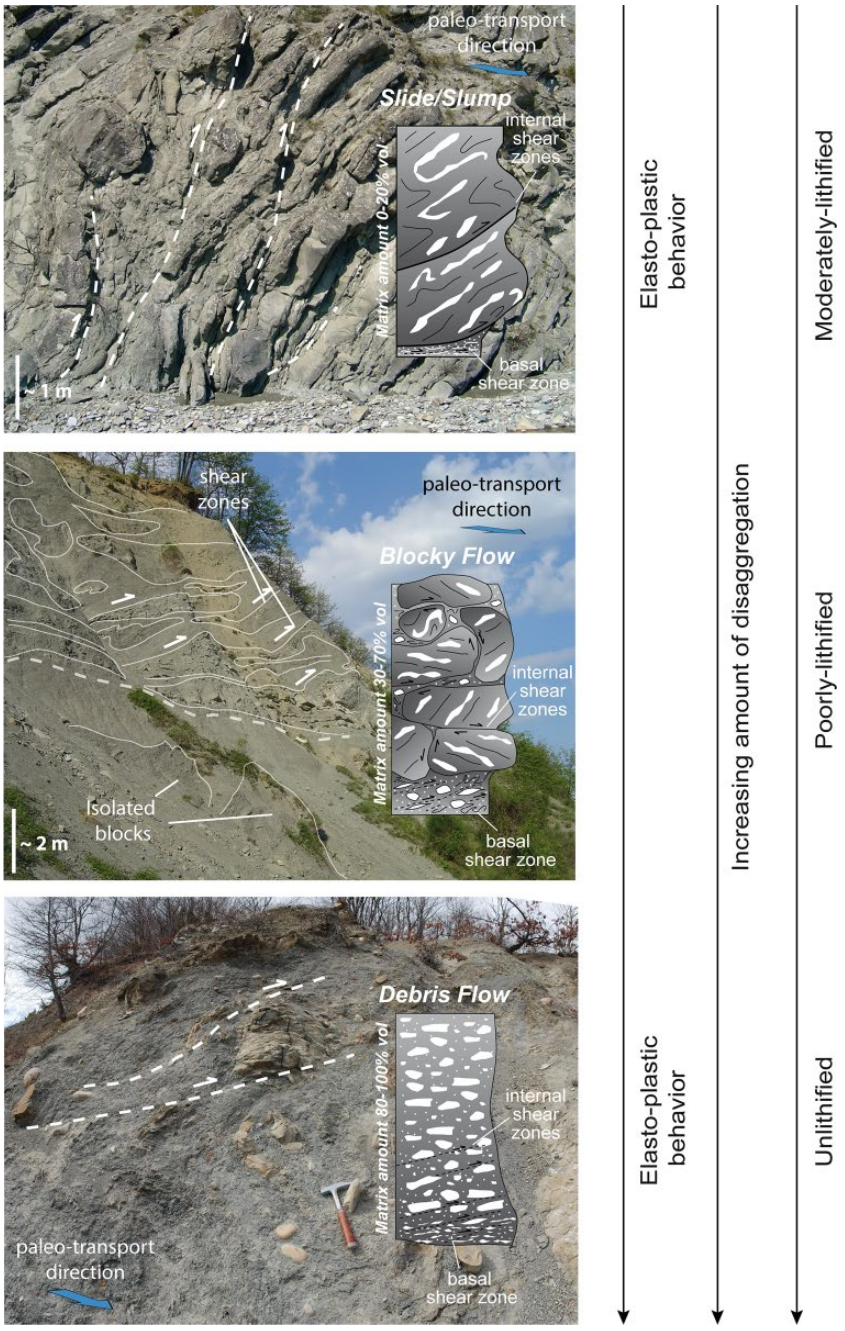


Figure 1.2 Principal mass-transport facies types recognizable in olistostromes and sedimentary mélanges. Source: Modified from Festa et al. (2016).

Mixed pure and simple shear mechanisms due to the coupled cyclic action of dynamic/static loading and differential movements of a slide mass and its internal components produce a variety of asymmetrical structures ranging from microscopic- to outcrop-/map-scale structures. These include boudinage, pseudo-sigma and SC structures, duplexes, and intrafolial folds (Ogata et al., 2016). All these structures can be interpreted to be products of soft-sediment deformation developed at low confining pressures (i.e., surficial conditions) involving undrained, water-saturated, poorly to unconsolidated sediments. The sediments both failed on slopes and eroded from the overridden seafloor, as indicated by microscopic analyses highlighting independent particulate flow with minor or no grain breakage (see, e.g., Ogata et al., 2014b). Close morphological similarities with

ductile (and brittle-ductile) structures documented in structurally deeper rocks (up to metamorphic) allow us to adopt some of the descriptive, nongenetic terminology classically used in structural geology (e.g., Passchier & Trouw, 2005) as proposed by Ogata et al. (2016).

Accordingly, the shape, spatial arrangement, and geometric relationships of structures can be used as stand-alone kinematic indicators to record local differential movements between the internal slide parts or in combination for a robust interpretation of the general paleo-transport directions (e.g., Lucente & Pini, 2003; Strachan & Alsop, 2006; Ogata et al., 2014b). Moreover, these structures appear specifically and systematically distributed within slide bodies, allowing application of detailed strain-partitioning models to the slide anatomy (Ogata et al., 2016). In summary, the identification of various structures in outcrops helps us better interpret the general and local slide kinematics of olistostromes and sedimentary mélanges, and recognition of these structures complements the data sets of small-scale features provided by drill cores, borehole logging, and geophysical imaging.

At larger scales, the systematic examination of basin-wide olistostromes and sedimentary *mélanges* reveals common types of mass-transport facies associations, defining composite bodies in their depocentral areas (Figure 1.3). The inferred provenances suggest unusually long runout distances (tens to hundreds of kilometers) and thus high mobility of thick (200–300 m), shale-dominated cohesive units, as also confirmed by observations on modern examples (see below). Olistostromes and sedimentary *mélanges* created by cohesive muddy debris flow (see, e.g., Pini et al., 2012) are expected to be deposited by relatively slow moving slide masses, in which the internal deformation is achieved through "viscous" shear zones in a clay-dominated matrix. Field observations backed up by experimental setups have shown, however, that the emplacement of such clay-rich debris flows might actually be characterized by fast-paced processes when sustained by a thin (up to a meter in thickness) and continuous basal shear zone. Such debris flows are therefore capable of carrying material for long distances. In such clay-rich debris flows, most of the deformation takes place along the basal shear zone composed of a mixture of water and loose sediments, which represents a "lubricating carpet" created by hydroplaning, shear-wetting, and liquefaction/fluidization processes (e.g., Pini et al., 2012; Ogata et al., 2014b). This model of flow and deformation is in line with observations from both modern and ancient submarine landslides and from laboratory experiments (e.g., De Blasio et al., 2006 and reference therein). For example, the so-called "autoacephalation" (i.e., progressive separation and detachment of the flow head from the body) mechanism proposed for slide masses undergoing hydroplaning can explain the occurrence of isolated slide blocks and detached parts of cohesive debris flows that are usually referred to as forerunner and outrunner blocks (Parker, 2000; Harbitz et al., 2003).

In the Northern Apennines, where olistostromes and sedimentary *mélanges* occur discontinuously over areas about 300 km long and tens of kilometers wide, they have brecciated intervals of substratum material (centimeters and up to meters in thickness), with soft-sediment intraclasts at the base (Festa et al., 2015a, 2015b). The internal structural-stratigraphic relationships suggest a poorly consolidated to loose state of the underlying sediments (i.e., overridden substratum) during motion and immediately after the emplacement. Clastic matrix formation is spatially and temporally associated with millimeter- to centimeter-thick sedimentary injections, representing the deformation products driven by fluid overpressure and consequent liquidization of the substratum as a result of the dynamic loading of the moving slide mass. Centimeter- to meter-thick, ductile "mylonite-like" shear zones occur at the base and within these units, displaying pervasive deformation fabrics in both soft and hard microclasts and clasts, that define a constriction plus flattening-type (i.e., prolate plus oblate) strain ellipsoid, with a prevailing component of stretching along the direction of flow and a minor component of planar flattening due to vertical compaction. The shear zones represent the loci of concentrated viscous deformation, which acted either in combination with basal "carpet" processes or in isolation, after dissipation of the basal fluid overpressure during the syn-emplacement and early post-emplacement phases of a slide mass (see also Ogata et al., 2014a). Hydroplaning, shear-wetting, and liquidization processes during downslope translation of submarine landslides are effective mechanisms to explain occurrence of basin-wide olistostromes, sedimentary *mélanges*, and "gravitational nappes" (e.g., Debelmas & Kerchkove, 1973) characterized by long runout distances achieved in relatively short time spans. These mechanisms also provide an explanation for the great mobility of slide blocks and olistoliths up to hundred cubic meters in volume, comparable to the outrunner blocks imaged on the present-day seafloor and its subsurface. This type of isolated outsized slide blocks and olistoliths also occurs in front of large olistostromes and sedimentary *mélanges* ascribed to nappe sheets (e.g., in the External Ligurian units of the Northern Apennines; Marroni & Pandolfi, 2001; Marroni et al., 2010), or, at their bases, due to their subsequent downslope translation (e.g., central Appalachians [see Codegone et al., 2012a], Porma mélange [see Alonso et al., 2006, 2015]). Such elements may also originate during rapid deceleration of a submarine landslide front, as the inertia of over-consolidated blocks with high momentum enhances their inherited motions (e.g., De Blasio et al., 2006), as

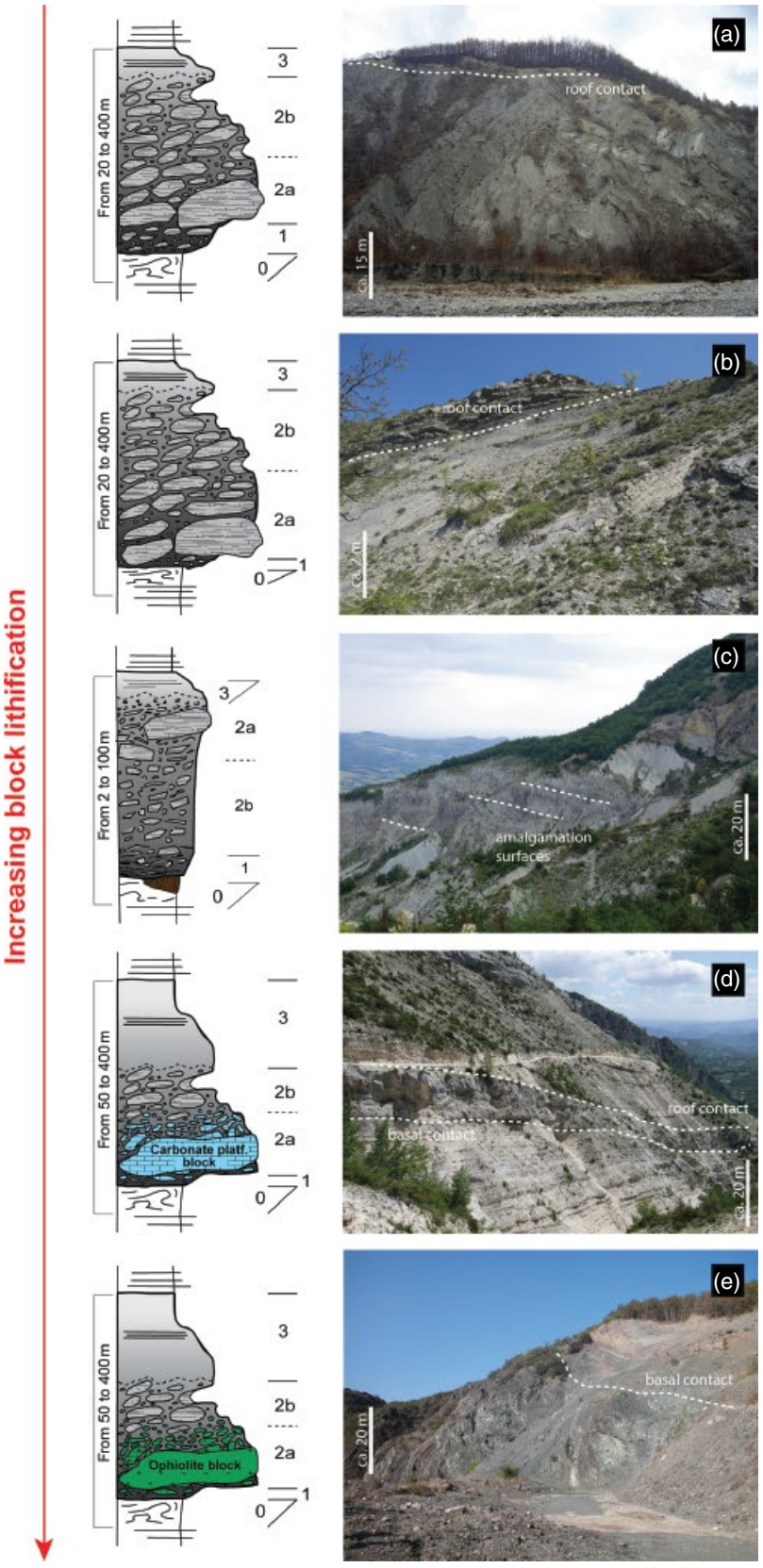


Figure 1.3 Composite bodies and mass-transport facies associations in olistostromes and sedimentary mélanges (Source: Modified from Festa et al. (2016)) and representative examples from the Northern Apennines in Italy. Internal subdivisions: (0) slide/slump-type, in situ deformation; (1) blocky/debris-flow-type, mixed intra/extrabasinal material; (2a) slide/slump-type, extrabasinal material dominant; (2b) blocky/debris-flow-type, intrabasinal material dominant; (3) debris/grain to turbulent flow-type, mixed intra/extrabasinal material. (a) Early Oligocene Specchio unit. (b) Miocene Marnoso-arenacea Casaglia-Monte della Colonna unit. (c) Amalgamated Cretaceous to Eocene Ligurian-type olistostromes. (d) Cretaceous-Eocene Scaglia Formation "megabreccia." (e) Ophiolite slide blocks in the late Cretaceous Casanova unit of the Basal Ligurian Complexes (succession is overturned).

observed ahead of the front of modern submarine landslides characterized by tens of kilometers of runout distance, that developed on less than one degree average slopes (e.g., Prior et al., 1987; Nissen et al., 1999; Canals et al., 2004; Nielsen & Kuijpers, 2004).

1.5. DISTRIBUTION OF OLISTOSTROMES AND SEDIMENTARY MÉLANGES

According to the classic Wilson cycle, the earliest phases involve passive margin tectonic development. Olistostromes and sedimentary *mélanges* bear evidence of this early cycle context. Extensional tectonics and rifting-related geological processes commonly lead to the formation of various types of submarine landslide deposits at different scales during rift-drift suite evolution.

In passive margin and other similar extensional settings, olistostromes develop at (i) thinned continental margins, (ii) at carbonate platform margins, (iii) at ocean-continent transition (OCT) zones, and (iv) along oceanic core complexes (see Camerlenghi & Pini, 2009; Festa et al., 2010b, 2016; Figure 1.4).

In such settings, debris flows, debris avalanches, and block fall/slides create megabreccias, isolated olistoliths, and olistolith fields, commonly characterized by angular clasts and blocks (decimeters to several tens of meters in size) and subordinate, smaller, sometimes rounded clasts, older than the enclosing fine-grained matrix. This material is sourced from elevated rift shoulders, intrabasinal topographic highs (e.g., horsts), and active footwall scarps, sometimes representing basin to depocenter margin faults. Steep slopes of carbonate platforms developed along rifted continental edges or intrabasinal highs generate similar processes and products. In this latter case, the matrix is predominantly pelagic limestone. Among the best examples of this type of deposits are exhumed masses in the Southern and Northern Calcareous Alps (e.g., Castellarin, 1972; Channell et al., 1992; Böhm et al., 1995; Bosellini, 1998; Ortner, 2001; Amerman et al., 2009), the Apennines (e.g., Bernoulli, 2001; Graziano, 2001), Western Hellenides (Naylor & Hale, 1976; Ghikas et al., 2010), the Appalachians (e.g., Rast & Kohles, 1986; Bailey et al., 1989; Rast & Horton, 1989), and the rifting phase of the Neoproterozoic Lufilian Arc, Central Africa (Wendorff, 2005a, 2005b).

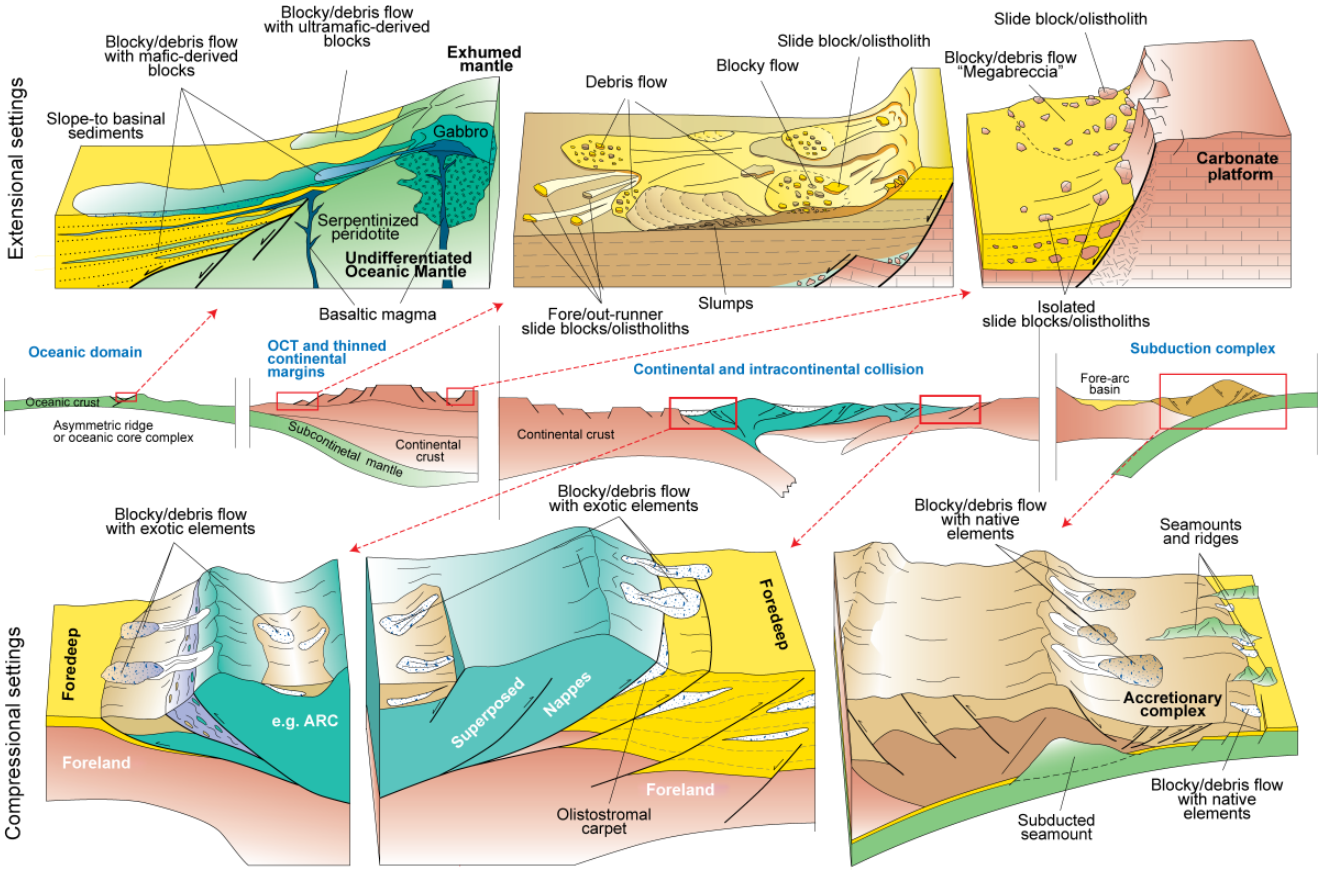


Figure 1.4 Conceptual representation of the distribution of in olistostromes and sedimentary mélanges in the different geologic settings. Source: Modified from Festa et al. (2016).

Olistostrome and sedimentary *mélanges* developed at OCTs are usually poorly sorted, with blocks of fine-grained carbonates, siliciclastic turbidites, and/or brecciated (matrix-supported) masses. These units can be either monomictic (i.e., dominated by native, intrabasinal clasts) when formed adjacent to rifted passive margins or polymictic (i.e., with mixing of exotic, extrabasinal clasts and matrix material consisting of mixed deep-sea sediments) when developed close to the oceanic domain. Slide blocks and olistoliths may reach several kilometers in size. Hydroplastic to pseudo-brittle deformation of blocks and clasts and soft-sediment deformation to liquefaction/fluidization of the matrix (e.g., fluidal features, in situ folding, boudinage, lithological and grain size mixing, etc.) indicate that sediments were non-lithified to poorly lithified at the time of emplacement. Olistostromes and sedimentary *mélanges* formed in paleo-OCTs are widely documented in the circum-Mediterranean region (e.g., Apennines [see De Libero, 1998; Pini et al., 2004], Hellenides-Albanides [see Smith et al., 1979; Shallo, 1990; Shallo & Dilek, 2003], Taurides [see Dilek & Rowland, 1993]), the central Appalachians (e.g., Jacobi & Mitchell, 2002; Wise & Ganis, 2009; Codegone et al., 2012a), and the Argentine Precordillera (Banchig, 1995; Keller, 1999; Alonso et al., 2008).

In an oceanic realm, collapse of intrabasinal paleobathymetric highs of serpentinized peridotites, related to mid-oceanic ridge and seamount settings (and associated lithologies), results primarily in debris-flow formation (e.g., Gansser, 1974; Lagabrielle et al., 1986; Dilek & Rowland, 1993; Sarifakioglu et al., 2014; Liu et al., 2015). Such debris flows commonly consist of clast- to matrix-supported angular clasts of mafic to ultramafic rocks, embedded in a matrix composed mainly of pelagic limestone and/or medium- to coarse-grained sandstone with ophiolite-derived detrital material. Isolated ophiolitic slide blocks and olistoliths swarms/fields, related to block fall/sliding and debris avalanches, also usually occur. Well-documented examples of these types of deposits are recognized in the Western Alps and Pyrenees (e.g., Lagabrielle et al., 1984; Lagabrielle, 1994; Lagabrielle & Lemoine, 1997; Clerc et al., 2012; Balestro et al., 2014, 2015a, 2015b; Festa et al., 2015a; Tartarotti et al., 2017), in the Apennines (e.g., Abbate et al., 1970; Decandia & Elter, 1972; Bortolotti et al., 2001), and in the Western U.S. Cordillera (e.g., Saleeby, 1979).

In addition to development of olistostromes and sedimentary *mélanges* in the early stages of the Wilson cycle, the later phases, represented by convergent margin and subduction zone settings, are characterized by MTD units involving variable degrees of stratal disruption related to both the consolidation state at the time of the slope failure and the final runout distance of slide masses. Slide material includes deformed sediments and/or extrabasinal rocks generally older and more consolidated than intrabasinal components, coming from the accretionary wedge front and/or wedge-top basins. Extrabasinal clasts and blocks comprise bed fragments or entire bedsets, locally displaying their original subduction-related tectonic fabric elements. In this case, the sedimentary matrix usually varies from shale and generally fine-grained sediments to medium- to coarse-grained sandstones. Boudinage-related pinch-and-swell structures, intrafolial folds, detached (rootless) slump folds, and soft-sediment "ball-and-pillows" are most commonly found within the matrix. Diffused and pervasive occurrence of mesoscale contractional and extensional duplexes, imbricated elements, isoclinal and drag folding, and other shear zone kinematic indicators are also widely documented (e.g., Taira et al., 1992; Yamamoto et al., 2009; Ogata et al., 2016). The inferred genetic processes that are reflected by these facies are debris flows, debris avalanches, and sliding and slumping, together characterized by complex interacting and overlapping relationships.

Among the possible trigger mechanisms classically preferred for the formation of olistostromes and sedimentary *mélanges* in such settings, the most invoked is tectonic oversteepening, due to the slope instability expected at accretionary wedge fronts and retro-wedge fronts of doubly verging accretionary wedges. This structural configuration is controlled by the temporal and spatial variations of processes that include "basal" and "frontal tectonic erosion" (*sensu* von Huene & Lallemand, 1990; Clift & Vannucchi, 2004; Rowe et al., 2013), subduction erosion, seamount and ridge subduction (Collot et al., 2001; Lewis et al., 2004; Hühnerbach et al., 2005; Anma et al., 2011; Kawamura et al., 2011), and thrust faulting and folding (see Martinez-Catalan et al., 1997; Marroni & Pandolfi, 2001; von Huene et al., 2004; Ruh, 2016). Migration of overpressurized fluids and diagenetic boundaries represent possible additional contributors (e.g., Barber et al., 1986; Lash, 1987; Codegone et al., 2012b; Barber, 2013; Festa et al., 2013, 2015b).

Important examples of oceanic subduction- and suprasubduction-related olistostromes and sedimentary *mélanges* occur in the circum-Mediterranean orogenic belts, such as the Apennines (see Abbate et al., 1970; Elter & Trevisan, 1973; Naylor, 1982; Bertotti et al., 1986; Elter et al., 1991; Pini, 1999; Marroni & Pandolfi, 2001), the Corsican and Western Alps (see Polino, 1984; Durand-Delga, 1986; Deville et al., 1992; Balestro et al., 2015a), Oman (e.g., Michard et al., 1991), Albanides (e.g., Bortolotti et al., 1996; Dilek et al., 2005), Hellenides (e.g., Jones & Robertson, 1991; Bortolotti et al., 2003; Ghikas et al., 2010), the Anatolian range (see Yilmaz & Maxwell, 1984; Parlak & Robertson, 2004; Dangerfield et al., 2011; Okay et al., 2012; Sarifakioglu et al., 2012, 2014), and Cyprus (see Swarbick & Naylor, 1980). Other

classical examples are exhumed in the Appalachians (see, e.g., Lash, 1985, 1987; Wise & Ganis, 2009; Codegone et al., 2012a) and in the circum-Pacific orogenic belts, such as the Western U.S. Cordillera (see, e.g., Aalto, 1981, 2014; Hitz & Wakabayashi, 2012; Raymond & Bero, 2015; Wakabayashi, 2015; Raymond, 2017), the Caribbean (see, e.g., Hernaiz Huerta et al., 2012; Escuder-Viruete et al., 2015), New Zealand (see, e.g., Chanier & Ferrière, 1991; Delteil et al., 2006; Lamarche et al., 2008), and Japan (see, e.g., Aoya et al., 2006; Yamamoto et al., 2009; Osozawa et al., 2011). Some of the best examples occur in the Al Hajar Mountains (Oman) (e.g., Michard et al., 1991), Albanides (e.g., Bortolotti et al., 1996; Dilek et al., 2005), the Hellenides (e.g., Jones & Robertson, 1991; Bortolotti et al., 2003, 2013; Ghikas et al., 2010), the western Anatolides (e.g., Sarifakioglu et al., 2012, 2014), and coastal New Zealand (Delteil et al., 2006).

Olistostromes and sedimentary *mélanges* developed in collisional and intra-collisional settings directly relate to the early phases of mountain-building processes and can be subdivided into sub-nappe, intra-nappe, and epi-nappe ones based on their relative location with respect to the allochthonous units (Camerlenghi & Pini, 2009; Festa et al., 2010a, 2012b, 2016). Sub-nappe olistostromes comprise precursory olistostromes and olistostromal carpet. The precursory olistostromes (*sensu* Elter & Trevisan, 1973) consist of classic olistostromes (and/or wildflysch; e.g., Mutti et al., 2009) with a block-in-matrix fabric, emplaced by cohesive debris flows and/or block avalanches in migrating foredeep basins (e.g., Bird, 1963; Root & MacLachlan, 1978; Behr et al., 1982; Frisch, 1984; Pini, 1999; Lucente & Pini, 2003, 2008; Masson et al., 2008; Festa et al., 2010b, 2012b; Vezzani et al., 2010; González Clavijo et al., 2016). They represent the so-called closure facies commonly resting atop foredeep units and predating the thrust-related deformation and subsequent incorporation into a collisional belt. Among the most representative examples are the Aveto and Macigno formations of the Northern Apennines (e.g., Lucente & Pini, 2003, 2008) and the Tarakli Flysch in Turkey (e.g., Catanzariti et al., 2013).

On the other hand, olistostromal carpets (Pini et al., 2004) comprise coalescing and overlapping aprons of debris flow and avalanche lobes in front of advancing nappes. These deposits are tectonically overridden by allochthonous nappes, which are also the source of discrete slide elements, whereas loose to poorly consolidated sediments comprising the matrix likely originate from thrust-top basins and slope sediments deposited atop the nappe front (e.g., Alonso et al., 2006). In such a context, the superposition of tectonic shearing on the primary (gravitational) fabric elements typically complicates the final products. Some of the best examples of such units have been documented at the base of the Taconic thrust front in the Appalachians (see, e.g., Vollmer & Bosworth, 1984; Lash, 1987; Bosworth, 1989; Codegone et al., 2012a; Festa et al., 2012a), in the Central Alps (Kempf & Pfiffner, 2004), at the base of the Ligurian units in the Apennines of Italy (e.g., Mattioni et al., 2006; Lucente & Pini, 2008; Festa et al., 2010b; Vezzani et al., 2010; Ogata et al., 2012a; Festa et al., 2013), in the Anatolide-Tauride orogenic belts (e.g., Bailey & McCallien, 1950, 1953; Dilek & Delaloye, 1992; Dilek, 2006; Sarifakioglu et al., 2012), in the Othris mountains in Greece (Smith et al., 1979), in Taiwan (Page & Suppe, 1981), and along thrust fronts in the Neoproterozoic Lufilian Arc (Wendorff, 2005b).

Intra-nappe olistostromes and sedimentary *mélanges* mainly consist of blocks of intrabasinal origin, parts of older sedimentary successions, or both enclosed within a lithologically similar matrix. Breccias, megabreccias, and outsized isolated olistoliths can be produced by rockfall and gravity flow processes. In this framework, large-scale intra-nappe shear zones related to out-of-sequence thrusting (e.g., megathrust splays) may form olistostromal carpet-like units (Festa et al., 2010a and reference therein).

Epi-nappe olistostromes and sedimentary *mélanges* form by gravitational instability along the margins of piggyback, thrust- and wedge-top, episutural, and satellite basins. Both blocks and the matrix in these units are sourced from tectonically dismembered and imbricated sedimentary successions, usually arranged in thrust stacks (e.g., Papani, 1963; Bettelli & Panini, 1989; Bettelli et al., 1989, 1994; Pini, 1999; Panini et al., 2002; Ferrière et al., 2004; Festa et al., 2005, 2015b, 2015c; Remitti et al., 2011; Ogata et al., 2012a, 2014b; Martín-Merino et al., 2014; Barbero et al., 2017). In such environments, the typical triggering mechanisms speculated for mass flows are seismic shocks. Nonetheless, climatic control could also play a significant role, mainly by varying the sedimentation rates and relative sea level.

1.6. GETTING OVER THE "SIZE" AND "PRESERVATION" PARADOXES

In contrast to modern tectonic settings, in which the vast majority of MTDs occur in passive margin settings (e.g., Macdonald et al., 1993; Mienert et al., 2003; Camerlenghi & Pini, 2009), olistostromes and sedimentary *mélanges* that form along active margins are more commonly represented in exhumed subduction-accretion complexes. Additionally, MTDs and MTCs observed in modern continental margins appear to be several orders of magnitude larger than their "fossil" counterparts (e.g., Woodcock, 1979).

This "paradox" can be solved taking into consideration that such deposits may represent either the product of a single depositional event (i.e., MTD) or composite bodies (i.e., MTC), created by multiple superposed

events (Heck & Speed, 1987; Macdonald et al., 1993; Lucente & Pini, 2003; Ogata et al., 2012a, 2012b, 2014a; Pini et al., 2012).

There are three main factors inferred to strongly influence the preservation of olistostromes and sedimentary *mélanges* in orogenic belts (Festa et al., 2016): (i) slide-flow transformation during transfer and emplacement, (ii) volume of the involved failed material, and (iii) the type and magnitude of the overprinting tectonic deformation during subsequent orogenic stages.

1.6.1. Slide to Flow Transformation

Olistostrome and sedimentary *mélange* formation involves the whole continuum of mass-transport processes (Lucente & Pini, 2003; Ogata et al., 2012a; Festa et al., 2016). The deposits are usually expressed as composite units made up of discrete subunits. These can be subdivided on the basis of composition, structures, and sense of movement, and are interpreted to be either products of discrete slide masses that moved differentially within the same depositional event or subunits formed by multiple overlapping events closely spaced in space and time (Strachan, 2002; Lucente & Pini, 2003; Ogata et al., 2012a, 2012b, 2014b).

Therefore, in an ideal situation, the final anatomy of the slide body depends on the amount of segregation/separation of the different structural-stratigraphic facies associations along with the downslope movement (i.e., frontally confined vs. frontally emergent; see Figure 1.5a). This is conceptually similar to the "flow efficiency" criterion introduced by Mutti et al. (1999) for turbidite deposits: highly efficient olistostromes and sedimentary mélanges, for example, are characterized by well-separated facies populations forming deposits with laterally varying facies associations and marked boundaries and relatively homogeneous vertical stratigraphy. Similar deposits are expected to develop mainly in passive margins, where continental slopes show smoother physiography and constant gradients (i.e., graded profiles; Prather, 2003).

On the contrary, low-efficiency olistostromes and sedimentary *mélanges* have more heterogeneous internal stratigraphy, characterized by strong lateral/vertical variations, horizontal heterotopy, and interfingering of different facies associations over short distances, testifying to incomplete/partial segregation. The lateral and vertical internal strain partitioning is controlled by the local seafloor morphology (e.g., laterally confined vs. unconfined; see Figure 1.5b). These deposits are expected in depositional settings showing complex physiographies with structurally confined depocenters and intrabasinal highs (e.g., above-grade profiles; Prather, 2003) representing local morphological barriers that favor local flow transformations (e.g., Ogata et al., 2014b).

The olistostromes and sedimentary *mélanges* of the Northern Apennines consist of two main end-member structural associations: (i) mud-dominated deposits including centimeter- to meter-sized lithic blocks enclosed in a brecciated detrital matrix, which also sustain bedded rafts tens of meters and up to kilometers in size, and (ii) sand-dominated deposits, rich in clastic matrix made

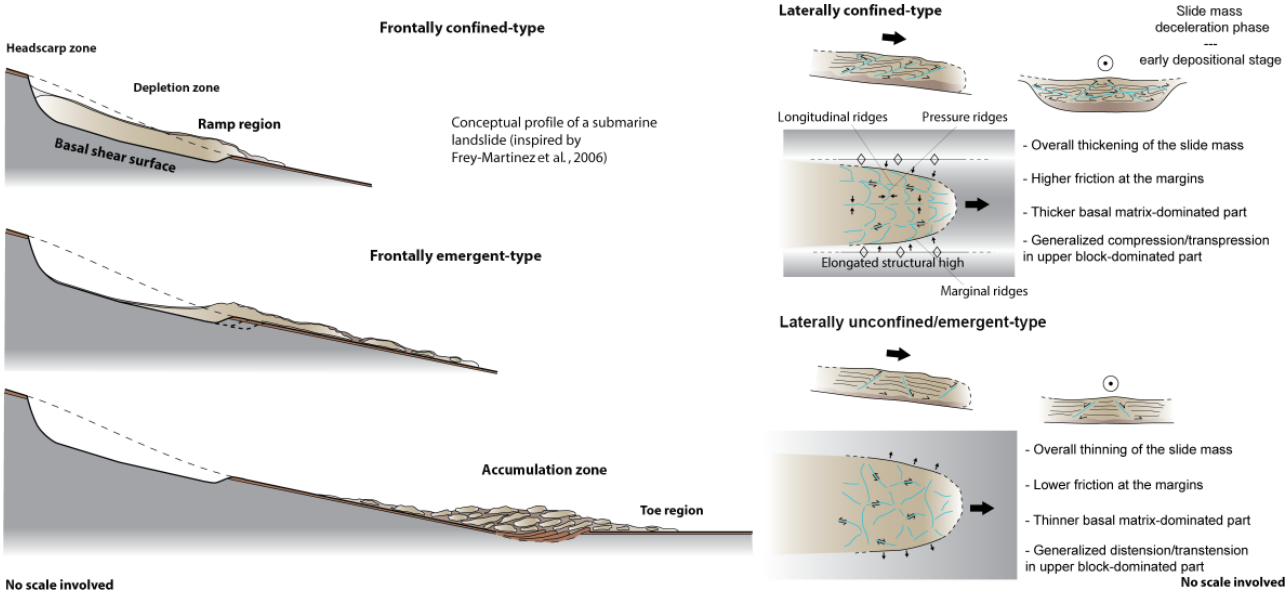


Figure 1.5 Cartoons depicting the concept of structural control on slide-flow transformation. Source: Modified from Ogata (2010).

up by an unsorted mixture of different grain size populations. The matrices of these two types of deposits usually show the typical features of a hyperconcentrated suspension (*sensu* Mutti, 1992; Ogata et al., 2012b, 2014a) and are commonly arranged as bipartite bodies with a block-dominated portion overlying a matrix-dominated one. This arrangement is inferred to record a complex debris flow carrying coherent blocks (meters to hundreds of meters wide) embedded as isolated slump-like folds (e.g., blocky-flow deposits *sensu* Mutti et al., 2006). Other units commonly associated with olistostromes and sedimentary *mélanges* in this setting are slump-slide-like deposits, mainly developed in sandy sediments (e.g., foredeep turbidites), in which deformation is accommodated by discrete shear zones that allow differential movement of individual coherent slide elements of different dimensions, with limited entrainment of extrabasinal material and lithological mixing.

All these types of deposits are characterized by multiscale ductile shear zones ranging from microscopic "films" of silt and deformation/disaggregation bands to seismically measurable large, inverse polarity reflectors that testify to local excess pore pressure (e.g., Ogata et al., 2014a). The Miocene Casaglia-Monte della Colonna body of the Marnoso-arenacea Formation (>350 km^2 and up to 300 m thick; see Lucente & Pini, 2003, 2008; Pini et al., this volume), the Oligocene Specchio unit of the Epiligurian succession (about 1500 km^2 and average thickness of 100 m; see Ogata et al., 2012a, 2012b), the late Oligocene to early Miocene Val Tiepido-Canossa argillaceous breccias (about 300 km^2 and up to 300 m thick; see Bettelli & Panini, 1985; Panini et al., 2002; Remitti et al., 2011; Festa et al., 2015b) in the Northern Apennines, the Paleogene carbonate "megabreccia" (23 megabeds up to 1500 km^2 and up to 260 m thick each) of the Julian-Slovenian Basin in the Southern Alps (e.g., Tunis & Venturini, 1992; Ogata et al., 2014b; Ogata et al., this volume), and the Eocene foredeep carbonate megabreccias in the south central Pyrenees (Payros et al., 1999; Ogata et al., 2012b) are among the best examples of this type of basin-wide olistostrome and sedimentary *mélange*.

1.6.2. The Slide Volume

The size dichotomy between submarine landslide deposits observed in outcrops and those identified in modern continental margins has been debated since the early 1980s (see, e.g., Woodcock, 1979; Macdonald et al., 1993; Lucente & Pini, 2003; Camerlenghi & Pini, 2009; Pini et al., 2012; Ogata et al., 2014b). In fact, the latter appear to be, on average, several orders of magnitude larger in cross-sectional area than their inferred ancient counterparts, as consequence of outcrop exposure conditions and/or actual changes in the magnitude of processes responsible for their formation (see Woodcock, 1979; Macdonald et al., 1993; Pini et al., 2012).

A first-order solution to this issue is the (re)interpretation of olistostromes and sedimentary *mélanges* as MTCs (Pini et al., 2012). This solution reveals substantial similarities in size, distribution, recurrence/frequency, and runout distance between ancient and some modern submarine slide complexes in different tectonic environments (e.g., Camerlenghi & Pini, 2009; Festa et al., 2010a; Pini et al., 2012; Ogata et al., 2014a; Calvès et al., 2015).

A showcase example of a large ancient deposit is the Miocene Makran olistostrome in Iran, associated with an accretionary complex, representing one of the largest and best preserved examples of large-scale sedimentary mélange ever documented (about 42,000 and 10,000 km^2 distributed over an area of 72,000 km^2; Burg, this volume). Other examples include the Cretaceous basal complex and the Oligocene wedge-top basins of the Northern Apennines (e.g., Bertotti et al., 1986; Bettelli et al., 1989; Elter et al., 1991; Pini, 1999; Remitti et al., 2011; Pini et al., 2012; Ogata et al., 2012a, 2014a; Festa et al., 2015b), the late Carboniferous Porma mélange and other units of the Cantabrian Zone (Alonso et al., 2006, 2015), the Ordovician sedimentary *mélanges* of the Argentine Precordillera (Banchig, 1995; von Gosen et al., 1995; Alonso et al., 2008; Sobiesiak et al., 2016), and the Paleogene carbonate megabreccia units in NW Italy and Slovenia (Ogata et al., 2014b).

1.6.3. Tectonic Reworking

Olistostromes and sedimentary *mélanges* in ancient orogenic belts and exhumed subduction-accretion complexes typically record multiple tectonic deformational events. Therefore, the original fabrics are commonly overprinted and significantly reworked, complicating their distinction from tectonic *mélanges* (e.g., Raymond, 1984; Raymond & Terranova, 1984; Cowan, 1985; Pini, 1999; Festa et al., 2013; and reference therein). This is particularly evident in the olistostromal carpets formed at the base of intracollisional nappes and in olistostromes involved in thrust faulting and tectonic shearing in subduction zones and accretionary complexes. Exotic blocks supplied by mass-transport events at the front of a nappe, for instance, can be easily misinterpreted as blocks incorporated through tectonic slicing and shearing, and also the other way around, given the convergence in appearance of block-in-matrix fabrics in the two end-member products (i.e., olistostromes overprinted by tectonic deformational features and tectonic *mélanges* bearing those features). This morphological convergence of deformation products is at the base of a long-lasting debate, especially in the Western U.S. Cordillera (e.g., Berkland et al., 1972; Silver & Beutner, 1980; Cloos, 1982; Raymond, 1984; Cowan,

1985; Brandon, 1989; Platt, 2015; Raymond & Bero, 2015; Ukar & Cloos, 2015; Wakabayashi, 2015; and reference therein) and in all exhumed subduction-accretion complexes worldwide (e.g., Pini, 1999; Alonso et al., 2006, 2008, 2015; Şengör, 2003; Festa et al., 2010a, 2012b; Balestro et al., 2015b; Wakita, 2015; Barbero et al., 2017; Tartarotti et al., 2017).

The matrix composition, however, provides crucial information for this distinction as documented, for example, in the Franciscan Complex by Aalto (1981, 2014), Erickson (2011), and Raymond and Bero (2015)). For example, olistostromes and sedimentary *mélanges* with bedded slide blocks (e.g., rafts, floaters), such as those composed of specific turbidite facies and grain-flow deposits and enclosed in a sandstone matrix, are stratigraphically and sedimentologically consistent with parts of lower slope base-of-slope sedimentary successions, therefore pointing against the flow mélange origin (Raymond & Bero, 2015; Wakabayashi, 2015). Therefore, the compositional attributes of matrix and blocks may provide significant clues for better understanding the evolution of subduction complexes and accretionary wedges.

1.7. OLISTOSTROMES AND SEDIMENTARY *MÉLANGES* AS MARKERS OF GEOLOGIC EVENTS

The discontinuous distribution of olistostromes and sedimentary *mélanges* in space and time within ancient orogenic belts and subduction-accretion complexes may reflect significant physical and mechanical changes in their depositional settings of formation. Tectonic events commonly show a strong correspondence with transgressive-regressive sedimentation cycles, which are, in turn, in agreement with the local and global sea level variations (see, e.g., Vail & Mitchum, 1980; Haq et al., 1987; Haq & Schutter, 2008; Snedden & Liu, 2010). Eustatic sea level fluctuations commonly result in the formation of large-scale unconformities at stratigraphic sequence boundaries, and therefore, with the exception of local cases controlled by autogenic forcing, the length of each time interval incorporating olistostrome and sedimentary *mélange* deposition appears to correspond to a single tectono-sedimentary cycle. In active margins, these cycles can be defined, for example, by the time span between the nappe emplacement and the related subsidence initiation favoring the accumulation of regressive sedimentary sequences that could, in turn, facilitate mass-transport processes in frontal parts of advancing nappe sheets (e.g., Scherba, 1989; Lucente & Pini, 2008; Festa et al., 2015b).

In all orogenic belts, the temporal and spatial distribution of different types of olistostromes and sedimentary *mélanges* commonly records different tectonic stages within the Wilson cycle of evolution of ocean basins, from the early rift-drift stages to later subduction, collision, and orogenic exhumation phases (e.g., Dilek, 2003; Dilek & Newcomb, 2003; Wendorff, 2005a, 2005b; Salamon & Königshof, 2010; Festa et al., 2016 for a complete review). For instance, different types of olistostrome and sedimentary *mélange* have been well documented to be associated with the late Jurassic rifting stage during the opening of the Alpine Tethys (e.g., Elter & Trevisan, 1973; De Libero, 1998; Cieszkowski et al., 2012; Clerc et al., 2012; Balestro et al., 2015a; Festa et al., 2015a; Tartarotti et al., 2017), the late Jurassic to early Cretaceous collapse of passive margin carbonate platforms (e.g., Castellarin, 1972; Cecca et al., 1981; Fazzuoli et al., 1985; Bernoulli, 2001; Graziano, 2001; Ślączka et al., 2012), the late Cretaceous to early Paleogene subduction stages (e.g., Elter & Trevisan, 1973; Marroni & Pandolfi, 2001), and the Eocene to Miocene collisional and intra-collisional stages (e.g., Abbate et al., 1970; Bettelli et al., 1989; Pini, 1999; Panini et al., 2002; Lucente & Pini, 2003, 2008; Camerlenghi and Pini, 2009; Festa et al., 2010b, 2015b; Remitti et al., 2011; Codegone et al., 2012b; Ogata et al., 2012a, 2014a; Barbero et al., 2017), or rifting of the Rodinia supercontinent and Gondwana assembly documented in the Neoproterozoic pan-African Lufilian Arc of Central Africa (Wendorff, 2005b, 2011). Interestingly, the frontal thrust of the Carpathians in Poland overrides and partly deforms an olistostrome of salt rocks deposited in the Miocene foredeep of the Western Carpathians (Kolasa & Ślączka, 1985).

The recurrence time of the generating events thus appears to be directly related to the temporal frequency of sudden orogenic phases, their magnitude, and their control on depositional cycles. The apparent discontinuous distribution of olistostromes and sedimentary *mélanges* within different ages of rock and in different tectonic settings actually define a specific "family" of tectonic events, with primary triggering mechanisms and resulting slide bodies, within the overall continuum of deformation events recognized in the evolution of orogenic belts (see Camerlenghi & Pini, 2009; Festa et al., 2016). Therefore, olistostromes and sedimentary *mélanges*, when reasonably characterized and understood, can be used as spatial-temporal markers of geologic events, and their study can provide a powerful tool for basin analysis at various scales, as well as for geohazard prediction and mitigation.

The recurrence time interval of olistostromes in the ancient geological record may be revealed with varying degrees of accuracy, depending on the resolution of the constrained timing of emplacement and the subsequent tectonic deformation and burial history (e.g., as constrained by reaching or not reaching metamorphic conditions). Although the emplacement of each single slide body is a geologically instantaneous event, their

episodic emplacement frequency may vary from thousands of years to several millions of years (e.g., Scherba, 1989; Delteil et al., 2006; Graziano, 2001; Wise & Ganis, 2009; Camerlenghi & Pini, 2009; Festa et al., 2015c, 2016). This time range is ultimately controlled by the duration of each tectonic phase on a regional scale, or more specifically, by the interplay with climatically forced processes (e.g., sedimentary transgressive-regressive cycles, global climate changes, gas hydrate dissociations; see, e.g., Nisbet & Piper, 1998).

1.8. CONCLUSIONS AND THE WAY FORWARD

In this brief review, we have examined the internal anatomy of different types of olistostrome and sedimentary *mélange* in various orogenic belts and in exhumed subduction complexes. These units represent the ancient "fossil" counterparts of MTDs and MTCs observed in every present-day active and passive margin. In addressing the long-debated "olistostrome versus tectonic *mélange*" problem, we emphasize that the different types of olistostrome and sedimentary *mélange* show characteristic features closely related to the specific depositional settings. We show that the systematic and updated documentation of their structural-stratigraphic architecture, texture, and fabric and the nature and composition of their internal discrete elements and their matrix provide critical information on different types of deformation processes, with important practical implications, for instance, in our understanding of submarine-landslide-related geohazards (Figure 1.6).

In particular, their lithological makeup presents key evidence for determining the internal architecture of exhumed subduction complexes. Variations in sediment delivery mechanisms and the types and volumes of material fed into accretionary wedges and subduction channels may change significantly during discrete evolutionary phases and in specific parts of an accretionary wedge.

Olistostromes and sedimentary *mélanges* are typically composite bodies, consisting of different parts, not exclusively the products of single depositional events. Their internal structure, in fact, may reflect close superposition

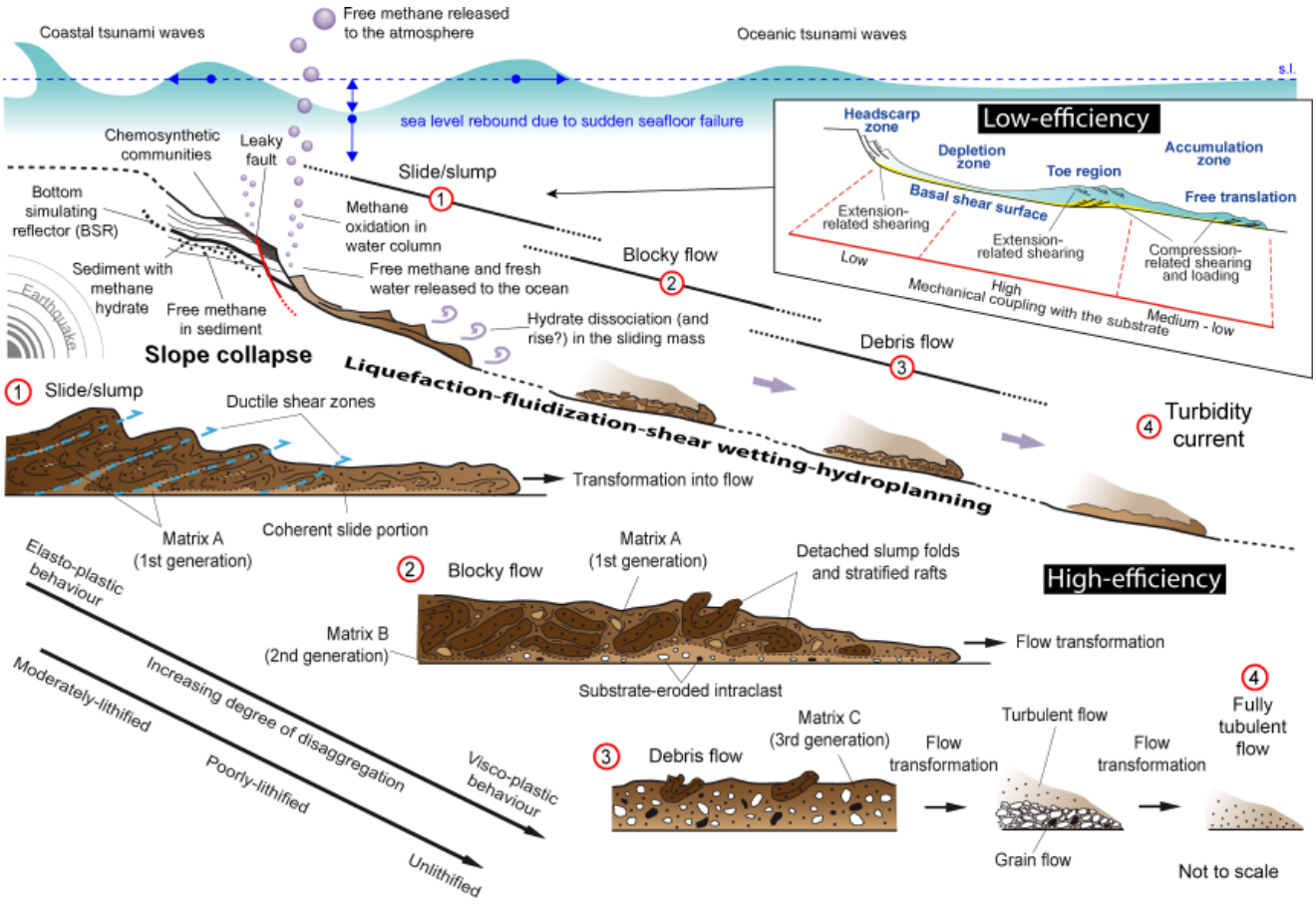


Figure 1.6 Summary cartoon illustrating the different mass-transport processes, main causes, and consequences characterizing olistostromes and sedimentary mélange emplacement. Source: Modified from Festa et al. (2016).

in space and time of different events and/or pulses within the same depositional event, resulting in MTCs that are comparable to those observed in modern submarine settings. Slide masses may reach extraordinary long runout distances (tens to hundreds of kilometers) from the source area that may not be evident from their internal fabric and composition. This large runout may be due to the combination of hydroplaning, shear-wetting, and liquidization mechanisms, occurring during downslope translation at the base of and inside the gravitational body, respectively. Additionally, in contrast to the current geophysical observations suggesting that submarine landslides are mainly associated with gravitational slope instability of passive margins, olistostromes and sedimentary *mélanges* are widely represented in the ancient geological record of active margin settings. This widespread occurrence is made possible by (i) downslope slide-flow transformation of materials, (ii) the composition and degree of lithification, and (iii) the physiography of the depositional setting.

The detailed characterization of these units in outcrop can be effectively achieved through the implementation of classic sedimentological and structural geology techniques, which can help in bridging the data gap between observations of exposed ancient olistostromes/sedimentary *mélanges* and analyses of modern MTDs (limited by the resolution of the geophysical methods). In this framework, a multi-scale structural analysis, supported by sedimentological and stratigraphic observations, carried on continuous 3D exhumed rock assemblages, is deemed necessary to thoroughly document the strain partitioning caused by differential movements within a slide mass.

Olistostromes and sedimentary *mélanges* are thus fundamental geological bodies to be carefully examined in studying orogenic belts and exhumed subduction complexes. They represent excellent markers for tectonic and climatic events, and their ages and structures can be effectively used to enhance the quality of basin analysis and modeling outputs.

ACKNOWLEDGMENTS

We are deeply indebted to Emiliano Mutti, who keeps teaching us all what a real geologist is and what geology actually means. This research has been supported by research grants from the Italian Ministry of University and Research (PRIN 2010/2011 "GEOPROB (Geodynamic Processes of Oceanic Basins)" n. 2010AZR98L_002 to G. A. Pini), the Università di Trieste (FRA 2013; Italy to G. A. Pini), and Università di Torino (Ricerca Locale "ex 60%" 2014–2016 to A. Festa). Two anonymous reviewers are gratefully acknowledged for having greatly improved the overall quality of the manuscript.

REFERENCES

Aalto, K. R. (1981). Multistage mélange formation in the Franciscan Complex, northernmost California. *Geology*, *9*, 602–607.

Aalto, K. R. (2014). Examples of Franciscan Complex *mélanges* in northernmost California Coast Ranges, a retrospective. *International Geology Review*, *56*(5), 555–570.

Abbate, E., Bortolotti, V., & Passerini, P. (1970). Olistostromes and olistoliths. In G. Sestini (Ed.), *Development of the Northern Apennines Geosyncline, Sedimentary Geology* (Vol. 4, 3/4, pp. 521–557). Amsterdam, The Netherlands: Elsevier.

Allen, J. R. L. (1982). *Sedimentary structures: Their character and physical basis* (Vol. 657 II). Amsterdam, The Netherlands: Elsevier.

Alonso, J. L., Gallastegui, J., García-Sansegundo, J., Farias, P., Rodrìguez Fernández, L. R., & Ramos, V. A. (2008). Extensional tectonics and gravitational collapse in an Ordovician passive margin: The Western Argentine Precordillera. *Gondwana Research*, *13*, 204–215.

Alonso, J. L., Marcos, A., & Suàrez, A. (2006). Structure and organization of the Porma mélange: Progressive denudation of a submarine nappe toe by gravitational collapse. *American Journal of Science*, *306*, 32–65.

Alonso, J. L., Marcos, A., Villa, E., Suarez, A., Merino-Tomé, O. A., & Fernandez, L. P. (2015). *Mélanges* and other types of block-in-matrix formations in the Cantabrian Zone (Variscan Orogen, northwest Spain): Origin and significance. *International Geology Review*, *57*(5–8), 563–580.

Alves, T. (2015). Submarine slide blocks and associated soft-sediment deformation in deep-water basins: A review. *Marine and Petroleum Geology*, *67*, 262–285. https://doi.org/10.1016/j.marpetgeo.2015.05.010

Amerman, R., Trudgill, B., Nelson, E. P., & Pyles, D. R. (2009). 4-D distribution of deepwater mass-transport deposits (Late Cretaceous Gosau Subgroup, Muttekopg Area, Northern Calcareous Alps, Austria): Implications for syndepositional structural reconstruction. AAPG Datapages. Search and Discovery Article #30108.

Anma, R., Ogawa, Y., Moore, G., Kawamura, K., Sasaki, T., Kawakami, S., et al. (2011). Structural profile and development of accretionary complex in the Nankai trough, off Kii peninsula, Southwest Japan: Results of submersible studies. In Y. Ogawa, R. Anma, & Y. Dilek (Eds.), *Accretionary prisms and convergent margin tectonics in the northwest Pacific Basin* (pp. 169–190). Dordrecht, The Netherlands: Springer Science. https://doi.org/10.1007/978-90-481-8885-7_8

Aoya, M., Tsuboi, M., & Wallis, S. R. (2006). Origin of eclogitic metagabbro mass in the Sambagawa belt: Geological and geochemical constraints. *Lithos*, *89*, 107–134.

Avé Lallemant, H. G., & Guth, L. R. (1990). Role of extensional tectonics in exhumation of eclogites and blueschists in an oblique subduction setting: Northeast Venezuela. *Geology*, *18*, 950–953.

Bailey, E. B., & McCallien, W. J. (1950). The Ankara mélange and the Anatolian thrust. *Nature*, *166*, 938–940.

Bailey, E. B., & McCallien, W. J. (1953). *Serpentine lavas, the Ankara mélange and the Anatolian thrust, Transactions of the Royal Society of Edinburgh* (Vol. 62, no. 11, pp. 403–442). Edinburgh, London: Oliver & Boyd.

Bailey, R. H., Skehan, J. W., Dreier, R. B., & Webster, M. J. (1989). Olistostromes of the Avalonian terrane of southeastern New England. In J. W. Horton, Jr. & N. Rast (Eds.), *Mélanges and olistostromes of the Appalachians, Geological Society of America Special Paper* (Vol. 228, pp. 93–112). Boulder, CO: Geological Society of America.

Balestro, G., Festa, A., Dilek, Y., & Tartarotti, P. (2015a). Prealpine extensional tectonics of a Peridotite-localized oceanic Core complex in the late Jurassic, high-pressure Monviso ophiolite (Western Alps). *Episodes*, *38*(4), 266–282. https://doi.org/10.18814/epiiugs/2015/v38i4/82421

Balestro, G., Festa, A., & Tartarotti, P. (2015b). Tectonic significance of different block-in-matrix structures in exhumed convergent plate margins: Examples from oceanic and continental HP rocks in inner Western Alps (Northwest Italy). *International Geology Review*, *57*(5–8), 581–605.

Balestro, G., Lombardo, B., Vaggelli, G., Borghi, A., Festa, A., & Gattiglio, M. (2014). Tectonostratigraphy of the northern Monviso meta-ophiolite complex (Western Alps). *Italian Journal of Geosciences*, *133*(3), 409–426. https://doi.org/10.3301/IJG.2014.13

Banchig, A. L. (1995). Evolución del margin continental Cámbrico-Ordovícico de la Sierra del Tontal entre el río San Juan y Los Sombreros, San Juan (Unpublished PhD thesis), 202 pp. Argentina: Universidad Nacional de San Juan.

Barber, A. J. (2013). The origin of mélanges: Cautionary tales from Indonesia. *Journal of Asian Earth Sciences*, *76*, 428–438.

Barber, A. J., Tjokrosapoetro, S., & Charlton, T. R. (1986). Mud volcanoes, shale diapirs, wrench faults and *mélanges* in accretionary complexes, Eastern Indonesia. *American Association of Petroleum Geologists Bulletin*, *70*, 1729–1741.

Barbero, E., Festa, A., Fioraso, G., & Catanzariti, E. (2017). Geology of the Curone and Staffora Valleys (NW Italy): Field constraints for the Late Cretaceous – Pliocene tectonostratigraphic evolution of Northern Apennines. *Journal of Maps*, *13*(2), 879–891.

Behr, H. J., Engel, W., & Franke, W. (1982). Varisican wildflysch and nappe tectonics in the Saxothuringian zone (Northeast Bavaria, West Germany). *American Journal of Science*, *282*, 1438–1470.

Berkland, J. O., Raymond, L. A., Kramer, J. C., Moores, E. M., & O'Day, M. (1972). What is Franciscan? *American Association of Petroleum Geologists Bulletin*, *56*, 2295–2302.

Bernoulli, D. (2001). Mesozoic-Tertiary carbonate platforms, slope and basins of the external Apennines and Sicily. In G. B. Vai & I. P. Martini (Eds.), *Anatomy of an orogen: The Apennines and adjacent Mediterranean basins* (pp. 307–325). Dordrecht, The Netherlands: Kluwer Academic.

Bertotti, G., Elter, P., Marroni, M., Meccheri, M., & Santi, R. (1986). Le argilliti a blocchi di M. Veri: Considerazioni sulla evoluzione tettonica del Bacino Ligure nel Cretaceo superiore. *Ofioliti*, *11*(3), 193–220.

Bettelli, G., Bonazzi, U., Fazzini, P., & Panini, F. (1989). Schema introduttivo alla geologia delle Epiliguridi dell'Appennino modenese e delle aree limitrofe. *Memorie Della Società Geologica Italiana*, *39*, 215–244.

Bettelli, G., Conti, S., & Panini, F. (1994). Brecce poligeniche a matrice argillosa alla base della successione Epiligure della Coltre della Val Marecchia (Appennino tosco-marchigiano): Implicazioni tettoniche. *Atti Ticinesi di Scienze della Terra*, *37*, 111–131.

Bettelli, G., & Panini, F. (1985). Il mélange sedimentario della Val Tiepido (Appennino modenese)- composizione litologica, distribuzione areale e posizione stratigrafica. *Atti della Società dei Naturalisti e Matematici di Modena*, *115*, 91–106.

Bettelli, G., & Panini, F. (1989). I *mélanges* dell'Appennino Settentrionale dal T. Tersinaro al T. Sillaro. *Memorie della Societa Geologica Italiana*, *39*, 187–214.

Bird, J. M. (Ed.) (1963). Sedimentary structures in the Taconic sequence rocks of the southern Taconic region. In *Stratigraphy, structure, sedimentation and paleontology of the southern Taconic region, eastern New York: Guidebook for field trip three, 1963 annual meet-in New York City, Geological Society of America* (pp. 5–21). Albany, NY: GSA.

Böhm, F., Dommergues, J.-L., & Meister, C. (1995). Breccias of the Adnet Formation: Indicators of a Mid-Liassic tectonic event in the Northern Calcareous Alps (Salzburg/Austria). *Geologische Rundschau*, *84*, 272–286.

Bortolotti, V., Carras, N., Chiari, M., Fazzuoli, M., Marcucci, M., Photiades, A., & Principi, G. (2003). The Argolis Peninsula in the paleogeographic and geodynamic frame of the Hellenides. *Ofioliti*, *28*, 79–94.

Bortolotti, V., Chiari, M., Marroni, M., Pandolfi, L., Principi, G., & Saccani, E. (2013). Geodynamic evolution of ophiolites from Albania and Greece (Dinaric-Hellenic belt): One, two, or more oceanic basins? *International Journal of Earth Sciences*, *102*, 783–811.

Bortolotti, V., Kodra, A., Marroni, M., Mustafa, F., Pandolfi, L., Principi, G., & Saccani, E. (1996). Geology and petrology of the ophiolitic sequences in the Mirdita region, northern Albania. *Ofioliti*, *21*, 3–20.

Bortolotti, V., Principi, G., & Treves, B. (2001). Ophiolites, Ligurides and the tectonic evolution from spreading to convergence of a Mesozoic Western Tethys segment. In G. B. Vai & I. P. Martini (Eds.), *Anatomy of an orogen: The Apennines and adjacent Mediterranean basins* (pp. 151–164). Dordrecht, The Netherlands: Kluwer Academic.

Bosellini, A. (1998). Scalloped versus faulted carbonate margins and the origin of basinal megabreccias. *Memorie della Società Geologica Italiana*, *53*, 63–74.

Bosworth, W. (1989). Mélange fabrics in the unmetamorphosed external terranes of the northern Appalachians. In J. W. Horton, Jr. & N. Rast (Eds.), *Mélanges and olistostromes of the Appalachians, Geological Society of America Special Papers* (Vol. 228, pp. 65–91). Boulder, CO: GSA.

Bradley, D., & Hanson, L. (1998). Paleoslope analysis of slump folds in the Devonian Flysch of Maine. *Journal of Geology*, *106*, 305–318.

Brandon, M. T. (1989). Deformational styles in a sequence of olistostromal mélanges, Pacific Rim Complex, western Vancouver Island, Canada. *Geological Society of America Bulletin*, *101*, 1520–1542.

Burg, J.-P. (this volume). Late Miocene olistostrome in the Makran accretionary wedge: Short review. In K. Ogata, A. Festa, & G. A. Pini (Eds.), *Submarine landslides: Subaqueous mass transport deposits from outcrops to seismic profiles* (pp. 45–56). Hoboken, NJ/Washington, DC: Wiley/American Geophysical Union.

Burg, J. P., Bernoulli, D., Smit, J., Dolati, A., & Bahroudi, A. (2008). A giant catastrophic mud and debris flow in the Miocene Makran. *Terra Nova*, *20*, 181–193.

Callot, P., Sempere, T., Odonne, F., & Robert, E. (2008). Giant submarine collapse of a carbonate platform at the Turonian-Coniacian transition: The Ayabacas Formation, southern Peru. *Basin Research*, *20*, 333–357.

Calvès, G., Huuse, M., Clift, P. D., & Brusset, S. (2015). Giant fossil mass wasting off the coast of West India: The Nataraja submarine slide. *Earth and Planetary Science Letters*, *432*, 265–272.

Camerlenghi, A., & Pini, G. A. (2009). Mud volcanoes, olistostromes and Argille scagliose in the Mediterranean region. *Sedimentology*, *56*, 319–365.

Canals, M., Lastras, G., Urgeles, R., Casamor, J. L., Mienert, J., Cattaneo, A., et al. (2004). Slope failure dynamics and impacts from seafloor and shallow sub-seafloor geophysical data: An overview. *Marine Geology*, *213*, 9–72.

Castellarin, A. (1972). Evoluzione paleotettonica sin-sedimentaria del limite tra "piattaforma veneta" e "bacino lombardo", a Nord di Riva del Garda. *Giornale di Geologia*, *2*(38), 11–212.

Catanzariti, R., Ellero, A., Cöncüoglu, M. C., Marroni, M., Ottria, M., & Pandolfi, L. (2013). The Tarakli Flysch in the Boyali area (Sakarya Terrane, northern Turkey): Implications for the tectonic history of the IntraPontide suture zone. *Comptes Rendus Geoscience*, *345*, 454–461.

Cecca, F., Cresta, S., Giovagnoli, M. C., Manni, R., Mariotti, N., Nicosia, U., & Santantonio, M. (1981). Tithonian 'Ammonitico Rosso' near Bolognola (Marche-Central Apennines): A shallow nodular limestone. In A. Farinacei & S. Elmi (Eds.), *Rosso ammonitico symposium proceedings* (pp. 91–112). Roma: Edizioni Tecnoscienza.

Chanier, F., & Ferrière, J. (1991). From a passive margin to an active margin: Tectonic and sedimentary processes linked to the birth of an accretionary prism (Hikurangi margin, New Zealand). *Bulletin Société Géologique de la France*, *162*, 649–660.

Channell, J. E. T., Brandner, R., Spieler, A., & Stoner, J. S. (1992). Paleomagnetism and paleogeography of the Northern Calcareous Alps (Austria). *Tectonics*, *11*, 792–810.

Cieszkowski, M., Golonka, J., Ślączka, A., & Waskowska, A. (2012). Role of the olistostromes and olistoliths in tectonostratigraphic evolution of the Silesian Basin in Outer West Carpathians. *Tectonophysics*, *568–569*, 248–265.

Clerc, C., Lagabrielle, Y., Neumaier, M., Reynaud, J.-Y., & de Saint Blanquat, M. (2012). Exhumation of subcontinental mantle rocks: Evidence from ultramafic-bearing clastic deposits nearby the Lherz peridotite body, French Pyrenees. *Bulletin de la Societè Géologique de France*, *183*(5), 443–459.

Clift, P., & Vannucchi, P. (2004). Controls on tectonic accretion versus erosion in subduction zones: Implications for the origin and recycling of the continental crust. *Reviews of Geophysics*, *42*(2), RG2001. https://doi.org/10.1029/2003RG000127

Cloos, M. (1982). Flow melanges: Numerical modeling and geologic constraints on their origin in the Franciscan subduction complex, California. *Geological Society of America Bulletin*, *93*, 330–345.

Cloos, M. (1984). Flow *mélanges* and the structural evolution of accretionary wedges. In L. A. Raymond (Ed.), *Mélanges: Their nature, origin, and significance, Special Paper* (Vol. 198, pp. 71–79). Boulder, CO: Geological Society of America.

Codegone, G., Festa, A., & Dilek, Y. (2012b). Formation of Taconic *Mélanges* and broken formations in the Hamburg Klippe, Central Appalachian Orogenic Belt, Eastern Pennsylvania. *Tectonophysics*, *568–569*, 215–229.

Codegone, G., Festa, A., Dilek, Y., & Pini, G. A. (2012a). Small-scale polygenetic *mélanges* in the Ligurian accretionary complex, northern Apennines, Italy, and the role of shale diapirism in superposed mélange evolution in orogenic belts. *Tectonophysics*, *568–569*, 170–184.

Coleman, J. M., & Prior, D. B. (1988). Mass wasting on continental margins. *Annual Review of Earth and Planetary Sciences*, *16*, 101–119.

Collot, J.-Y., Lewis, K., Lamarche, G., & Lallemand, S. (2001). The giant Ruatoria debris avalanche on the northern Hikurangi margin, New Zealand: Result of oblique seamount subduction. *Journal of Geophysical Research*, *106*(9), 19271–19297.

Cowan, D. S. (1974). Deformation and metamorphism of the Franciscan Subduction Zone Complex north–west of Pacheco Pass, California. *Geological Society of America Bulletin*, *85*, 1623–1634.

Cowan, D. S. (1985). Structural styles in Mesozoic and Cenozoic *mélanges* in the western Cordillera of North America. *Geological Society of America Bulletin*, *96*, 451–462.

Cowan, D. S., & Pini, G. A. (2001). Disrupted and chaotic rock units in the Apennines. In G. B. Vai & I. P. Martini (Eds.), *Anatomy of a mountain belt: The Apennines and adjacent Mediterranean Basins* (pp. 165–176). Dordrecht, The Netherlands: Kluwer Academic.

Dangerfield, A., Harris, R., Sarifakioglu, E., & Dilek, Y. (2011). Tectonic evolution of the Ankara Mélange and associated Eldivan ophiolite near Hançili, central Turkey. In J. Wakabayashi & Y. Dilek (Eds.), *Melanges: Processes of formation and societal significance, Special Paper* (Vol. 480, pp. 143–169). Boulder, CO: Geological Society of America. https://doi.org/10.1130/2011.2480(06)

De Blasio, F. V., Elverhøi, A., Engvik, L. E., Issler, D., Gauer, P., & Harbitz, C. (2006). Under-standing the high mobility of subaqueous debris flows. *Norwegian Journal of Geology*, *86*, 275–284.

De Libero, C. M. (1998). Sedimentary vs. tectonic deformation in the "Argille Scagliose" of Mt. Modino (Northern Apennines). *Giornale di Geologia*, *56*, 143–166.

Debelmas, J., & Kerchkove, C. (1973). Large gravity nappes in the French-Italian and French-Swiss Alps. In K. A. DeJong & R. Scholten (Eds.), *Gravity and tectonics* (pp. 189–200). New York, NY: Wiley.

Decandia, F. A., & Elter, P. (1972). La "zona" ofiolitifera del Bracco nel settore compreso fra Levanto e la Val Graveglia (Appennino Ligure). *Memorie della Societa Geologica Italiana*, *11*, 503–530.

Delteil, J., Mercier De Lepinay, B., Morgans, H. E. G., & Field, B. D. (2006). Olistostromes marking tectonic events, East Coast, New Zealand. *New Zealand Journal of Geology and Geophysics*, *49*, 517–531.

Deville, E., Fudral, S., Lagabrielle, I., Marthaler, M., & Sartori, M. (1992). From oceanic closure to continental collision:

A synthesis of the "Schistes lustrés" metamorphic complex of the Western Alps. *Geological Society of America Bulletin*, *104*, 127–139.

Dilek, Y. (2003). Ophiolites, plumes and orogeny. In Y. Dilek & P. T. Robinson (Eds.), *Ophiolites in Earth history, Special Publication* (Vol. 218, pp. 9–19). London, UK: Geological Society of London.

Dilek, Y. (2006). Collision tectonics of the Eastern Mediterranean region: Causes and consequences. *Geological Society of America Special Papers*, *409*, 1–13.

Dilek, Y., & Delaloye, M. (1992). Structure of the Kizildag ophiolite, a slow-spread Cretaceous ridge segment north of the Arabian promontory. *Geology*, *20*, 19–22. https://doi.org/10.1130/0091-7613(1992)020

Dilek, Y., Festa, A., Ogawa, Y., & Pini, G. A. (2012). Chaos and geodynamics: Mélanges, Mélange-forming processes and their significance in the geological record. *Tectonophysics*, *568–569*, 1–6. https://doi.org/10.1016/j.tecto.2012.08.002

Dilek, Y., & Newcomb, S. (2003). *Ophiolite concept and the evolution of geological thought, Geological Society of America Special Paper* (Vol. 373, 504 p.). Boulder, CO: The Geological Society of America.

Dilek, Y., & Rowland, J. C. (1993). Evolution of a conjugate passive margin pair in Mesozoic southern Turkey. *Tectonics*, *12*, 954–970. https://doi.org/10.1029/93TC01060

Dilek, Y., Shallo, M., & Furnes, H. (2005). Rift-drift, seafloor spreading, and subduction zone tectonics of Albanian ophiolites. *International Geology Review*, *47*, 147–176. https://doi.org/10.2747/0020-6814.47.2.147

Durand-Delga, M. (1986). Principaux traits de la Corse Alpine et correlations avec les Alpes Ligures. *Memorie della Societa Geologica Italiana*, *28*, 285–329.

Elter, P., Marroni, M., Molli, G., & Pandolfi, L. (1991). Le caratteristiche stratigraphiche del Complesso di M. Penna/Casanova (Alta Val di Trebbia, Appennino Settentrionale). *Atti Ticinensi di Scienze della Terra*, *34*, 97–106.

Elter, P., & Raggi, G. (1965). Contributo alia conoscenza dell'Appennino ligure: I. Osservazioni preliminari sulla posizione delle ofioliti nella zona di Zignago (La Spezia); 2. Considerazioni sul problema degli olistostromi. *Bollettino Della Società Geologica Italiana*, *84*(3), 303–322.

Elter, P., & Trevisan, L. (1973). Olistostromes in the tectonic evolution of the Northern Apennines. In K. A. De Jong & R. Scholten (Eds.), *Gravity and tectonics* (pp. 175–188). New York, NY: Wiley.

Erickson, R. (2011). Petrology of a Franciscan olistostrome with a massive sandstone matrix: The King Ridge Road mélange at Cazadero, California. In J. Wakabayashi & Y. Dilek (Eds.), *Mélanges: Processes of formation and societal significance, GSA Special Papers* (Vol. 480, pp. 171–188). Boulder, CO: Geological Society of America. https://doi.org/10.1130/2011.2480(07)

Ernst, W. G. (2016). Franciscan mélanges: Coherent blocks in a low-density, ductile matrix. *International Geology Review*, *58*(5), 626–642. https://doi.org/10.1080/00206814.2015.1108879

Escuder-Viruete, J., Suárez-Rodríguez, A., Gabites, J., & Pérez-Estaún, A. (2015). The Imbert Formation of northern Hispaniola: A tectono-sedimentary record of arc-continent collision and ophiolite emplacement in the northern Caribbean subduction-accretionary prism. *Solid Earth Discussions*, *7*, 1827–1876.

Fazzuoli, M., Ferrini, G., Pandeli, E., & Sguazzoni, G. (1985). Le formazioni giurassico-mioceniche della falda toscana a nord dell'Arno: Considerazioni sull'evoluzione sedimentaria. *Memorie della Societa Geologica Italiana*, *30*, 159–201.

Ferrière, J., Reynaud, J.-Y., Pavlopoulos, A., Bonneau, M., Migiros, G., Chanier, F., et al. (2004). Geologic evolution and geodynamic controls of the Tertiary intramontane piggyback Meso-Hellenic basin, Greece. *Bulletin de la Société Géologiques de France*, *175*(4), 361–381.

Festa, A., Balestro, G., Dilek, Y., & Tartarotti, P. (2015a). A Jurassic oceanic core complex in the high-pressure Monviso ophiolite (western Alps, NW Italy). *Lithosphere*, *7*, 646–652. https://doi.org/10.1130/L458.1

Festa, A., Codegone, G., & Pini, G. A. (2012a). Polygenetic mélanges: The interplay of tectonic, sedimentary and diapiric processes in exhumed accretionary wedges. *Rendiconti Online della Società Geologica Italiana*, *22*, 86–89.

Festa, A., Dilek, Y., Codegone, G., Cavagna, S., & Pini, G. A. (2013). Structural anatomy of the Ligurian accretionary wedge (Monferrato, NW Italy), and evolution of superposed mélanges. *Geological Society of America Bulletin*, *125*(9–10), 1580–1598. https://doi.org/10.1130/B30847.1

Festa, A., Dilek, Y., Pini, G. A., Codegone, G., & Ogata, K. (2012b). Mechanisms and processes of stratal disruption and mixing in the development of *mélanges* and broken formations: Redefining and classifying mélanges. *Tectonophysics*, *568–569*, 7–24. https://doi.org/10.1016/j.tecto.2012.05.021

Festa, A., Fioraso, G., Bissacca, E., & Petrizzo, M. R. (2015b). Geology of the Villalvernia-Varzi line between Scrivia and Curone valleys (NW Italy). *Journal of Maps*, *11*(1), 39–55.

Festa, A., Ogata, K., Pini, G. A., Dilek, Y., & Alonso, J. L. (2016). Origin and significance of olistostromes in the evolution of orogenic belts: A global synthesis. *Gondwana Research*, *39*, 180–203. https://doi.org/10.1016/j.gr.2016.08.002

Festa, A., Ogata, K., Pini, G. A., Dilek, Y., & Codegone, G. (2015c). Late Oligocene–early Miocene olistostromes (sedimentary mélanges) as tectono-stratigraphic constraints to the geodynamic evolution of the exhumed Ligurian accretionary complex (Northern Apennines, NW Italy). *International Geology Review*, *57*(5–8), 540–562.

Festa, A., Piana, F., Dela Pierre, F., Malusà, M. G., Mosca, P., & Polino, R. (2005). Oligocene-Neogene kinematic constraints in the retroforeland basin of the Northwestern Alps. *Rendiconti online della Società Geologica Italiana (nuova serie)*, *1*, 107–108.

Festa, A., Pini, G. A., Dilek, Y., & Codegone, G. (2010a). *Mélanges* and mélange-forming processes: A historical overview and new concepts. *International Geology Review*, *52*(10–12), 1040–1105. https://doi.org/10.1080/00206810903557704

Festa, A., Pini, G. A., Dilek, Y., Codegone, G., Vezzani, L., Ghisetti, F., et al. (2010b). Peri-Adriatic *mélanges* and their evolution in the Tethyan realm. *International Geology Review*, *52*(4–6), 369–406. https://doi.org/10.1080/00206810902949886

Flores, G. (1955). *Les résultats des études pour les recherches pétrolifères en Sicile: Discussion*. Proceedings of the 4th World Petroleum Congress, Rome, Casa Editrice Carlo Colombo, Section 1/A/2, 121–122.

Flores, G. (1956). The results of the studies on petroleum exploration in Sicily: Discussion. *Bollettino del Servizio Geologico d'Italia*, *78*, 46–47 (English translation of the 1955 paper).

Frey-Martínez, J., Cartwright, J., & James, D. (2006). Frontally confined versus frontally emergent submarine landslides: A 3D seismic characterisation. *Marine and Petroleum Geology*, *23*, 585–604. https://doi.org/10.1016/j.marpetgeo.2006.04.002

Frisch, W. (1984). Sedimentological response to late Mesozoic subduction in the Penninic windows of the eastern Alps. *Geologische Rundschau*, *73*, 33–45.

Gamboa, D., Alves, T., Cartwright, J., & Terrinha, P. (2010). MTD distribution on a 'passive' continental margin: The Espírito Santo Basin (SE Brazil) during the Palaeogene. *Marine and Petroleum Geology*, *27*, 1311–1324. https://doi.org/10.1016/j.marpetgeo.2010.05.008

Gansser, A. (1974). The ophiolite mélange: A world-wide problem on Tethyan examples. *Eclogae Geologicae Helvetiae*, *67*, 479–507.

Gardner, J. V., Prior, D. B., & Field, M. E. (1999). Humboldt slide: A large shear-dominated retrogressive slope failure. *Marine Geology*, *154*/*1*, 323–338.

Gawthorpe, R. L., & Clemmey, H. (1985). Geometry of submarine slides in the Bowland Basin (Dinantian) and their relation to debris flows. *Journal of the Geological Society of London*, *142*, 555–565.

Ghikas, A. C., Dilek, Y., & Rassios, A. E. (2010). Structure and tectonics of sub-ophiolitic mélanges in the Western Hellenides (Greece) and implications for Ophiolite emplacement tectonics. *International Geology Review*, *52*, 423–453.

González Clavijo, E., Dias da Silva, I. F., Gutiérrez-Alonso, G., & Díez Montes, A. (2016). U/Pb age of a large dacitic block locked in an Early Carboniferous synorogenic mélange in the Parautochthon of NW Iberia: New insights on the structure/sedimentation Variscan interplay. *Tectonophysics*. https://doi.org/10.1016/j.tecto.2016.01.001

Graziano, R. (2001). The cretaceous megabreccias of the Gargano Promontory (Apulia, southern Italy): Their stratigraphic and genetic meaning in the evolutionary framework of the Apulia Carbonate Platform. *Terra Nova*, *13*, 110–116.

Hampton, M. A., Lee, H. J., & Locat, J. (1996). Submarine landslides. *Reviews of Geophysics*, *34*, 33–59.

Haq, B. U., Hardenbol, J., & Vail, P. R. (1987). Chronology of fluctuating sea levels since the Triassic (250 million years ago to present). *Science*, *235*, 1156–1167.

Haq, B. U., & Schutter, S. R. (2008). A chronology of Paleozoic Sea-level changes. *Science*, *322*, 64–68.

Harbitz, C. B., Parker, G., Elverhøi, A., Marr, J. G., Mohrig, D., & Harff, P. A. (2003). Hydroplaning of subaqueous debris flows and glide blocks: Analytical solutions and discussions. *Journal of Geophysical Research*, *108*(B7), 2349. https://doi.org/10.1029/2001JB001454

Heck, F. R., & Speed, R. C. (1987). Triassic olistostrome and shelf-basin transition on the western Great Basin: Paleogeographic implications. *Geological Society of America Bulletin*, *99*, 539–551.

Hernaiz Huerta, P. P., Pérez-Valera, F., Abad, M., Monthel, J., & Diaz de Neira, A. (2012). *Mélanges* and olistostromes in the Puerto Plata area (northern Dominican Republic) as a record of subduction and collisional processes between the Caribbean and North-American plates. *Tectonophysics*, *568–569*, 266–281.

Hitz, B., & Wakabayashi, J. (2012). Unmetamorphosed sedimentary mélange with high-pressure metamorphic blocks in a nascent forearc basin setting. *Tectonophysics*, *568–569*, 124–134.

Hsü, K. J. (1968). Principles of *mélanges* and their bearing on the Franciscan-Knoxville paradox. *Geological Society of America Bulletin*, *79*, 1063–1074.

Hsü, K. J. (1974). Melanges and their distinction from olistostromes. In R. H. Dott, Jr. & R. H. Shaver (Eds.), *Modern and ancient geosynclinal sedimentation, SEPM Special Publication* (Vol. 19, pp. 321–333). Tulsa, OK: SEPM.

Hühnerbach, V., Massonì, D. G., Bohrmann, G., Bull, J. M., & Weinrebe, W. (2005). Deformation and submarine landsliding caused by seamount subduction beneath the Costa Rica continental margin: New insights from high-resolution sidescan sonar data. *Geological Society, London, Special Publications*, *244*, 195–205.

Huvenne, V. A. I., Croker, P. F., & Henriet, J. P. (2002). A refreshing 3D view of an ancient collapse and slope failure. *Terra Nova*, *14*, 33–40.

Jacobi, R. D., & Mitchell, C. E. (2002). Geodynamical interpretation of a major unconformity in the Taconic Foredeep: Slide scar or onlap unconformity? *Physics and Chemistry of the Earth*, *27*, 169–201.

Joanne, C., Lamarche, G., & Collot, J.-Y. (2013). Dynamics of giant mass transport in deep submarine environments: The Matakaoa Debris Flow, New Zealand. *Basin Research*, *25*, 1–18. https://doi.org/10.1111/bre.12006

Jones, G., & Robertson, A. H. F. (1991). Tectonostratigraphy and evolution of the Mesozoic Pindos ophiolite and related units, northwestern Greece. *Journal of the Geological Society of London*, *148*, 267–288.

Kawamura, K., Ogawa, Y., Hara, H., Anma, R., Dilek, Y., Kawakami, S., et al. (2011). Rapid exhumation of metamorphosed sediment with gravitational collapse in an active eastern Nankai accretionary prism, Japan. In Y. Ogawa, R. Anma, & Y. Dilek (Eds.), *Accretionary prisms and convergent margin tectonics in the Northwest Pacific Basin*. Dordrecht, The Netherlands: Springer Science. https://doi.org/10.1007/978-90-481-8885-7_10

Keller, M. (1999). *Argentine Precordillera: Sedimentary and plate tectonic history of a Laurentian crustal fragment in South America, The Geological Society of America, Special Paper* (Vol. 341, 131 pp.). Boulder, CO: Geological Society of America.

Kempf, O., & Pfiffner, A. (2004). Early tertiary evolution of the North Alpine Foreland Basin of the Swiss Alps and adjoining areas. *Basin Research*, *16*, 549–567.

King, P. R., Ilg, B. R., Arnot, M., Browne, G. H., Strachan, L. J., Crundwell, M., & Helle, K. (2011). Outcrop and seismic examples of MTDs, Taranaki Basin, New Zealand. In R. C. Shipp, P. Weimer, & H. W. Posamentier (Eds.), *Mass-transport deposits in deepwater settings* (Vol. 96, pp. 311–348). SEPM Special Publication. https://doi.org/10.2110/sepmsp.096.311

Kolasa, K., & Ślączka, A. (1985). Sedimentary salt megabreccias exposed in the Wieliczka mine, Fore-Carpathian depression. *Acta Geologica Polonica*, *35*, 221–241.

Lagabrielle, Y. (1994). Ophiolites of the southwestern Alps and the structure of the Tethyan oceanic lithosphere. *Ofioliti*, *19*, 413–434.

Lagabrielle, Y., & Lemoine, M. (1997). Alpine, Corsican and Apennine ophiolites: The slow-spreading ridge model. *Comptes Rendus de l'Académie des Sciences*, *325*, 909–920.

Lagabrielle, Y., Polino, R., Auzende, J. M., Blanchet, R., Caby, R., Fudral, S., et al. (1984). Les temoins d'une tectonique intraoceanique dans le domaine Tethysien: Analyse des rapports entre les ophiolites et leurs couvertures metasedimentaires dans la zone Piemontaise des Alpes Franco-Italiennes. *Ofioliti*, *9*(1), 67–88.

Lagabrielle, Y., Whitechurch, H., Marcoux, J., Juteau, T., Reuber, I., Guillocheau, F., & Capan, U. (1986). Obduction-related ophiolitic polymict breccias covering the ophiolites of Antalya (southwestern Turkey). *Geology*, *14*, 734–737.

Lamarche, G., Joanne, C., & Collot, J.-Y. (2008). Successive, large mass-transport deposits in the south Kermadec fore-arc basin, New Zealand: The Matakaoa submarine instability complex. *Geochemistry, Geophysics, Geosystems*, *9*(4), Q04001. https://doi.org/10.1029/2007GC001843

Lash, G. G. (1985). Accretion-related deformation of an ancient (early Paleozoic) trench-fill deposit, central Appalachian orogen. *Geological Society of America Bulletin*, *96*, 1167–1178.

Lash, G. G. (1987). Diverse melanges of an ancient subduction complex. *Geology*, *15*, 652–655.

Lee, H. J., Normark, W. R., Fisher, M. A., Greene, H. G., Edwards, B. D., & Locat, J. (2004). *Timing and extent of submarine landslides in Southern California*. Offshore Technology Conference, Houston; paper no. 16744.

Lewis, K. B., Lallemand, S., & Carter, L. (2004). Collapse in a Quaternary shelf basin off East Cape, New Zealand: Evidence for the passage of a subducted seamount inboard of the Ruatoria giant avalanche. *New Zealand Journal of Geology and Geophysics*, *47*, 415–429.

Liu, F., Yang, J.-S., Dilek, Y., Xu, X.-Z., Xu, X.-Z., Liang, F.-H., et al. (2015). Geochronology and geochemistry of the basaltic lavas in the Dongbo and Purang ophiolites of the Yarlung-Zangbo Suture zone: Plume-influenced continental margin-type oceanic lithosphere in southern Tibet. *Gondwana Research*, *27*, 701–718. https://doi.org/10.1016/j.gr.2013.08.002

Lucente, C. C., & Pini, G. A. (2003). Anatomy and emplacement mechanism of a large submarine slide within the Miocene foredeep in the Northern Apennines, Italy: A field perspective. *American Journal of Science*, *303*, 565–602.

Lucente, C. C., & Pini, G. A. (2008). Basin-wide mass-wasting complexes as markers of the Oligo-Miocene foredeep-accretionary wedge evolution in the Northern Apennines, Italy. *Basin Research*, *20*, 49–71.

Macdonald, D. I. M., Moncrieff, A. C. M., & Butterworth, P. J. (1993). Giant slide deposits from a Mesozoic fore-arc basin, Alexander Island, Antarctica. *Geology*, *21*(11), 1047–1050.

Marroni, M., Meneghini, F., & Pandolfi, L. (2010). Anatomy of the Ligure-Piemontese subduction system: Evidence from Late Cretaceous–Middle Eocene convergent margin deposits in the Northern Apennines, Italy. *International Geology Review*, *52*, 1160–1192. https://doi.org/10.1080/00206810903545493

Marroni, M., & Pandolfi, L. (2001). Debris flow and slide deposits at the top of the Internal Liguride ophiolitic sequence, Northern Apennines, Italy: A record of frontal tectonic erosion in a fossil accretionary wedge. *Island Arc*, *10*, 9–21.

Martinez-Catalan, J., Arenas, R., Diaz Garcia, F., & Abati, J. (1997). Varisican accretionary complex of Northwest Iberia: Terrane correlation and succession of tectonothermal events. *Geology*, *25*, 1103–1106.

Martín-Merino, G., Fernández, L. P., Colmenero, J. R., & Bahamonde, J. R. (2014). Mass-transport deposits in a Variscan wedge-top foreland basin (Pisuerga area, Cantabrian Zone, NW Spain). *Marine Geology*, *356*, 71–87.

Masson, H., Bussy, F., Eichenberger, M., Giroud, N., Meilhac, C., & Presniakov, S. (2008). Early Carboniferous age of the Versoyen ophiolites and consequences: Non-existence of a 'Valais ocean' (Lower Penninic, Western Alps). *Bulletin de la Société Géologiques de France*, *179*(4), 337–355.

Mattioni, L., Tondi, E., Shiner, P., Renda, P., Vitale, S., & Cello, G. (2006). The Argille Varicolori unit in Lucania (Italy): A record of tectonic offscraping and gravity sliding in the Mesozoic-Tertiary Lagonegro Basin, southern Apennines. In G. Moratti & A. Chalouan (Eds.), *Tectonics of the Western Mediterranean and North Africa, Special Publications* (Vol. 262, pp. 277–288). London, UK: Geological Society.

Medialdea, T., Vegas, R., Somoza, L., Vázquez, J. T., Maldonado, A., Díaz-del-Río, V., et al. (2004). Structure and evolution of the "Olistostrome" complex of the Gibraltar Arc in the Gulf of Cádiz (eastern Central Atlantic): Evidence from two long seismic cross-sections. *Marine Geology*, *209*, 173–198.

Melosh, J. H. (1987). The mechanics of large rock avalanches. *GSA Reviews in Engineering Geology*, *7*, 41–49.

Michard, A., Chopin, C., & Goffé, B. (1991). Obduction versus subduction and collision in the Oman case and in the other Tethyan setting. In T. J. Peters, A. Nicolas, & R. G. Coleman (Eds.), *Ophiolite genesis and evolution of the oceanic lithosphere, Petroleum Structural Geology* (Vol. 5, pp. 447–467). Dordrecht, The Netherlands: Springer.

Mienert, J., Berndt, C., Laberg, J. S., & Vorren, T. (2003). Slope instability of continental margins. In G. Wefer, D. Billet, D. Hebbeln, B. B. Jørgensen, M. Schlüter, & T. van Weering (Eds.), *Ocean margin systems* (pp. 179–193). Berlin, Germany: Springer.

Moore, D. G., Curray, J. R., & Emmel, F. J. (1976). Large submarine slide (olistostrome) associated with Sunda Arc subduction zone, northeast Indian Ocean. *Marine Geology*, *21*, 211–226.

Mutti, E. (1992). *Turbidite sandstones* (275 pp.). San Donato Milanese, Italy: Agip-Istituto di Geologia, Università di Parma.

Mutti, E., Bernoulli, D., Ricci Lucchi, F., & Tinterri, R. (2009). Turbidities and turbidity currents from Alpine 'flysch' to the exploration of continental margins. *Sedimentology*, *56*, 267–318.

Mutti, E., Carminatti, M., Moreira, J. L. P., & Grassi, A. A. (2006). Chaotic Deposits: Examples from the Brazilian offshore and, from outcrop studies in the Spanish Pyrenees and Northern Apennines, Italy. American Association Petroleum Geologists Annual Meeting, Houston, TX.

Mutti, E., Tinterri, R., Remacha, E., Mavilla, N., Angella, S., & Fava, L. (1999). *An introduction to the analysis of ancient turbidite basins from an outcrop perspective, AAPG Course Note*

(Vol. 39, pp. 93). Tulsa, OK: American Association of Petroleum Geologists.

Naylor, M. A. (1982). The Casanova Complex of the Northern Apennines: A mélange formed on a distal passive continental margin. *Journal of Structural Geology*, *4*, 1–18.

Naylor, M. A., & Hale, T. (1976). Palaeogeographic significance of rocks and structures beneath the Vourinos ophiolite, northern Greece. *Journal of the Geological Society, London*, *132*, 667–676.

Nielsen, T., & Kuijpers, A. (2004). Geohazard studies offshore the Faroe Islands: Slope instability, bottom currents and subseabed sediment mobilisation. *Geological Survey of Denmark and Greenland Bulletin*, *4*, 57–60.

Nisbet, E. G., & Piper, D. J. W. (1998). Gian submarine landslides. *Nature*, *392*, 329–330.

Nissen, S. E., Haskell, N. L., Steiner, C. T., & Coterill, K. L. (1999). Debris flow outrunner blocks, glide tracks, and pressure ridges identified on the Nigerian continental slope using 3-D seismic coherency. *The Leading Edge*, *18*, 550–561.

Odonne, F., Callot, P., Debroas, E.-J., Sempere, T., Hoareau, G., & Maillard, A. (2011). Soft-sediment deformation from submarine sliding: Favourable conditions and triggering mechanisms in examples from the Eocene Sobrarbe delta (Ainsa, Spanish Pyrenees) and the mid-Cretaceous Ayabacas Formation (Andes of Peru). *Sedimentary Geology*, *235*, 234–248.

Ogata, K. (2010). Mass transport complexes in structurally-controlled basins: The Epiligurian Specchio Unit (Northern Apennines, Italy) (Unpublished PhD thesis). University of Parma.

Ogata, K., Mountjoy, J. J., Pini, G. A., Festa, A., & Tinterri, E. (2014a). Shear zone liquefaction in mass transport deposit emplacement: A multi-scale integration of seismic reflection and outcrop data. *Marine Geology*, *356*, 50–64. https://doi.org/10.1016/j.margeo.2014.05.00

Ogata, K., Pini, G. A., Festa, A., Pogačnik, Ž., & Lucente, C. C. (2016). Meso-scale kinematic indicators in exhumed mass transport deposits: Definitions and implications. In G. Lamarche, J. Mountjoy, S. Bull, T. Hubble, S. Krastel, E. Lane, et al. (Eds.), *Submarine mass movements and their consequences, Advances in Natural and Technological Hazards Research* (Vol. 41, pp. 461–468). Dordrecht, The Netherlands: Springer International.

Ogata, K., Pogačnik, Ž., Pini, G. A., Tunis, G., Festa, A., Camerlenghi, A., & Rebesco, M. (2014b). The carbonate mass transport deposits of the Paleogene Julian-Slovenian Basin (Italy/Slovenia): Internal anatomy and inferred genetic processes. *Marine Geology*, *356*, 88–110.

Ogata, K., Tinterri, R., Pini, G. A., & Mutti, E. (2012a). Mass transport-related stratal disruption within sedimentary mélanges: Examples from the northern Apennines (Italy) and south-central Pyrenees (Spain). *Tectonophysics*, *568–569*, 185–199.

Ogata, K., Tinterri, R., Pini, G. A., & Mutti, E. (2012b). The Specchio Unit (Northern Apennines, Italy): An ancient mass transport complex originated from near-coastal areas in an intra-slope setting. In Y. Yamada, et al. (Eds.), *Submarine mass movements and their consequences: Advances in natural and technological hazards research* (Vol. 31, pp. 595–605). Dordrecht, The Netherlands: Springer International.

Ogata, K., Festa, A., Pini, G. A., & Alonso, J. L. (this volume). Ancient submarine landslide complexes: A short review. In K. Ogata, A. Festa, & G. A. Pini (Eds.), *Submarine landslides: Subaqueous mass transport deposits from outcrops to seismic profiles* (pp. 3–26). Hoboken, NJ/Washington, WC: Wiley/American Geophysical Union.

Ogawa, Y., Mori, R., Tsunogae, T., Dilek, Y., & Harris, R. (2014). New interpretation of the Franciscan Mélange at San Simeon coast, California: Tectonic intrusion into an accretionary prism. *International Geology Review*. https://doi.org/10.1080/00206814.2014.968813

Okamura, Y. (1991). Large-scale melange formation due to seamount Subduction: An example from the Mesozoic accretionary complex in central Japan. *The Journal of Geology*, *99*(5), 661–674.

Okay, A. I., İşintek, I., Altıner, D., Özkan-Altıner, S., & Okay, N. (2012). An olistostrome–mélange belt formed along a suture: Bornova Flysch zone, western Turkey. *Tectonophysics*, *568–569*, 282–295. https://doi.org/10.1016/j.tecto.2012.01.007

Omosanya, K. O., & Alves, T. M. (2012). A 3-dimensional seismic method to assess the provenance of Mass-Transport Deposits (MTDs) on salt-rich continental slopes (Espírito Santo Basin, SE Brazil). *Marine and Petroleum Geology*, *44*, 223–239. https://doi.org/10.1016/j.marpetgeo.2013.02.006

Ortner, H. (2001). Growing folds and sedimentation of the Gosau Group, Muttekopf, Northern Calcareous Alps, Austria. *International Journal of Earth Sciences*, *90*, 727–739.

Osozawa, S., Pavlis, T., & Flowers, M. F. J. (2011). Sedimentary block-in-matrix fabric affected by tectonic shear, Miocene Nabae complex, Japan. In J. Wakabayashi & Y. Dilek (Eds.), *Mélanges: Processes of formation and societal significance, Geological Society of America Special Papers* (Vol. 480, pp. 189–206). Boulder, CO: GSA. https://doi.org/10.1130/2011.2480(08)

Page, B. M., & Suppe, J. (1981). The Pliocene Lichi melange of Taiwan: Its plate-tectonic and olistostromal origin. *American Journal of Science*, *281*, 193–227.

Panini, F., Fioroni, C., Fregni, P., & Bonacci, M. (2002). Le rocce caotiche dell'Oltrepo Pavese: Note illustrative della Carta Geologica dell'Appennino vogherese tra Borgo Priolo e Ruino. *Atti Ticinensi di Scienze della Terra*, *43*, 83–109.

Papani, G. (1963). Su un olistostroma di 'Argille Scagliose' intercalato nella serie oligo-miocenica del subappennino reggiano (nota preliminare). *Bollettino della Societa Geologica Italiana*, *82*(3), 195–202.

Parker, G. (2000). Hydroplaning outrunner blocks from autoacephalated subaqueous debris flows and landslides. *Eos, Transactions of the American Geophysical Union*, *81*(48), Fall Meet. Suppl., Abstract OS51D-08

Parlak, O., & Robertson, A. (2004). The ophiolite-related Mersin Melange, southern Turkey: Its role in the tectonic-sedimentary setting of Tethys in the Eastern Mediterranean region. *Geological Magazine*, *141*(3), 257–286.

Passchier, C. W., & Trouw, R. A. (2005). *Microtectonics* (365 pp.). Berlin/Heidelberg, Germany and New York, NY: Springer.

Payros, A., Pujalte, V., & Orue-Etxebarria, X. (1999). The South Pyrenean Eocene carbonate megabreccias revisited: New interpretation based on evidence from the Pamplona Basin. *Sedimentary Geology*, *125*, 165–194.

Pini, G. A. (1999). *Tectonosomes and olistostromes in the Argille Scagliose of the Northern Apennines, Italy, Special Papers* (Vol. 335, 73 pp.). Boulder, CO: Geological Society of America.

Pini, G. A., Camerlenghi, A., Ogata, K., Cowan, D. S., & Urgeles, R. (2010a). Olistostromes and olistoliths: A historical review and modern perspectives. *Geologica Balcanica*, *39*(1–2), 309–310.

Pini, G. A., Camerlenghi, A., Ogata, K., Festa, A., Codegone, G., Lucente, C. C., & Urgeles, R. (2010b). Olistostromes, *mélanges* and mass-transport deposits. *Rendiconti Online della Società Geologica Italiana*, *11*, 445–446.

Pini, G. A., Lucente, C. C., Cowan, D. S., De Libero, C. M., Dellisanti, F., Landuzzi, A., et al. (2004). The role of olistostromes and argille scagliose in the structural evolution of the Northern Apennines. In L. Guerrieri, I. Rischia, & L. Serva (Eds.), *Field trip guidebooks, 32nd IGC Florence 20–28 August 2004, Memorie Descrittive della Carta Geologica d'Italia* (Vol. 63, pp. 1–40). Firenze, Italy: Litoterrazzi S.p.A.

Pini, G. A., Ogata, K., Camerlenghi, A., Festa, A., Lucente, C. C., & Codegone, G. (2012). Sedimentary *mélanges* and fossil mass-transport complexes: A key for better understanding submarine mass movements? In Y. Yamada, et al. (Eds.), *Submarine mass movements and their consequences, Advances in Natural and Technological Hazards Research* (Vol. 31, pp. 585–594). Dordrecht, The Netherlands: Springer Science+Business Media B.V.

Pini, G. A., Venturi, S., Lucente, C. C., & Ogata, K. (this volume). Mass transport complexes of the Marnoso-arenacea foredeep turbidites system, Northern Apennine of Italy: A twenty-year after reappraisal. In K. Ogata, A. Festa, & G. A. Pini (Eds.), *Submarine landslides: Subaqueous mass transport deposits from outcrops to seismic profiles* (pp. 117–137). Hoboken, NJ/Washington, WC: Wiley/American Geophysical Union.

Platt, J. P. (2015). Origin of Franciscan blueschist-bearing mélange at San Simeon, central California coast. *International Geology Review*, *57*(5–8), 843–868.

Polino, R. (1984). Les seriés océaniques du haut Val de Suse (Alpes Cottiennes): Analyse des couvertures sédimentaires. *Ofioliti*, *9*(3), 547–554.

Prather, B. E. (2003). Controls on reservoir distribution, architecture and stratigraphic trapping in slope settings. *Marine and Petroleum Geology*, *20*(6), 529–545. https://doi.org/10.1016/j.marpetgeo.2003.03.009

Prior, D. B., Bornhold, B. D., & Johns, M. W. (1984). Depositional characteristics of a submarine debris flow. *Journal of Geology*, *92*, 707–727.

Prior, D. B., Doyle, E. H., & Neurauter, T. (1987). The Currituck slide, Mid-Atlantic continental slope-revisited. *Marine Geology*, *73*, 25–45.

Rast, N., & Horton, J. W., Jr. (1989). Melanges and olistostromes in the Appalachians of the United States and mainland Canada: An assessment. In J. W. Horton, Jr. & N. Rast (Eds.), *Mélanges and olistostromes of the Appalachians, Special Papers* (Vol. 228, pp. 1–16). Boulder, CO: Geological Society of America.

Rast, N., & Kohles, K. M. (1986). The origin of the Ocoee Supergroup. *American Journal of Science*, *286*, 593–616.

Raymond, L. A. (1984). Classification of melanges. In L. A. Raymond (Ed.), *Melanges: Their nature, origin and significance, Special Papers* (Vol. 198, pp. 7–20). Boulder, CO: Geological Society of America.

Raymond, L. A. (2017). What is Franciscan? Revisited. International Geology Review. Online version. https://doi.org/10.1080/00206814.2017.1396933.

Raymond, L. A., & Bero, D. (2015). Sandstone-matrix mélanges, architectural subdivision, and geologic history of accretionary complexes: A sedimentological and structural perspective from the Franciscan Complex of Sonoma and Marin counties, California, USA. *Geosphere*, *11*(4), 1–34. https://doi.org/10.1130/GES01137.1

Raymond, L. A., & Terranova, T. (1984). *The melange problem: A review, Geological Society of America Special Paper* (Vol. 198, pp. 1–3). Boulder, CO: Geological Society of America.

Remitti, F., Vannucchi, P., Bettelli, G., Fantoni, L., Panini, F., & Vescovi, P. (2011). Tectonic and sedimentary evolution of the frontal part of an ancient subduction complex at the transition from accretion to erosion: The case of the Ligurian wedge of the northern Apennines, Italy. *Geological Society of America Bulletin*, *123*, 51–70.

Root, S. I., & MacLachlan, D. B. (1978). Western limit of Taconic allochthons in Pennsylvania. *Geological Society of America Bulletin*, *89*, 1515–1528.

Rowe, C. D., Moore, J. C., Remitti, F., & the IODP (International Ocean Discovery Program) Expedition 343/343T Scientists (2013). The thickness of subduction plate boundary faults from the seafloor into the seismogenic zone. *Geology*, *41*, 991–994. https://doi.org/10.1130/G34556.1

Ruh, J. B. (2016). Submarine landslides caused by seamounts entering accretionary wedge systems. *Terra Nova*. https://doi.org/10.1111/ter.12204

Salamon, M., & Königshof, P. (2010). Middle Devonian olistostromes in the Rheno-Hercynian zone (Rheinisches Schiefergebirge): An indication of back arc rifting on the southern shelf of Laurussia. *Gondwana Research*, *17*, 281–291.

Saleeby, J. (1979). Kaweah serpentinite mélange, Southwest Sierra Nevada foothills, California. *Geological Society of America Bulletin*, *90*, 29–46.

Sarifakioglu, E., Dilek, Y., & Sevin, M. (2014). Jurassic–Paleogene intra-oceanic magmatic evolution of the Ankara Mélange, North Central Anatolia, Turkey. *Solid Earth Discussions*, *5*, 77–108. https://doi.org/10.5194/se-5-77-2014

Sarifakioglu, E., Dilek, Y., & Winchester, J. A. (2012). Late Cretaceous subduction initiation and Paleocene–Eocene slab breakoff magmatism in South-Central Anatolia, Turkey. *International Geology Review*, *55*, 66–87. https://doi.org/10.1080/00206814.2012.727566

Scherba, I. G. (1989). Stage and phases of formation of Cenozoic olistostromes in the Alpine Fold Belt. In G. Y. Leonov & V. E. Khain (Eds.), *Global correlation of tectonic movements* (pp. 49–82). New York, NY: Wiley.

Şengör, A. M. C. (2003). The repeated rediscovery of *mélanges* and its implication for the possibility and the role of objective evidence in the scientific enterprise. In Y. Dilek & S. Newcomb (Eds.), *Ophiolite concept and the evolution of geological thought, Special Papers* (Vol. 373, pp. 385–445). Boulder, CO: Geological Society of America.

Shallo, M. (1990). Ophiolitic mélange and flyschoidal sediments of the Tithonian–Lower Cretaceous in Albania. *Terra Nova*, *2*, 476–483.

Shallo, M., & Dilek, Y. (2003). Development of the ideas on the origin of Albanian ophiolites. *Geological Society of America Special Papers*, *373*, 351–364.

Shanmugam, G. (2015). The landslide problem. *Journal of Palaeogeography*, *4*(2), 109–166. https://doi.org/10.3724/SP.J.1261.2015.00071

Silver, E. A., & Beutner, E. C. (1980). Melanges. *Geology*, *8*, 32–34.

Ślączka, A., Renda, P., Cieszkowski, M., Golonka, J., & Nigro, F. (2012). Sedimentary basin evolution and olistoliths formation: The case of Carpathian and Sicilian regions. *Tectonophysics*, *568–569*, 306–319.

Smith, A. G., Woodcock, N. H., & Naylor, M. A. (1979). The structural evolution of a Mesozoic continental margin, Othris Mountains, Greece. *Journal of the Geological Society of London*, *136*, 589–601.

Snedden, J. W., & Liu, C. (2010). A compilation of Phanerozoic sea-level change, coastal onlaps and recommended sequence designations. AAPG Search and discovery article #40594.

Sobiesiak, M. S., Kneller, B., Alsop, G. I., & Milana, J. P. (2016). Inclusion on substrate blocks within a mass transport deposit: A case study from Cerro Bola, Argentina. In G. Lamarche, J. Mountjoy, S. Bull, T. Hubble, S. Krastel, E. Lane, et al. (Eds.), *Submarine mass movements and their consequences, Advances in Natural and Technological Hazards Research* (Vol. 41, pp. 487–496). Dordrecht, The Netherlands: Springer.

Strachan, L. J. (2002). Slump-initiated and controlled syndepositional sandstone remobilization: An example from the Namurian of County Clare, Ireland. *Sedimentology*, *49*, 25–41.

Strachan, L. J., & Alsop, G. I. (2006). Slump folds as estimators of paleoslope: A case study from the Fisherstreet Slump of County Clare, Ireland. *Basin Research*, *18*, 451–470.

Strasser, M., Henry, P., Kanamatsu, T., Thu, M. K., Moore, G. F., & IODP Expedition 333 Scientists (2012). Scientific drilling of mass-transport deposits in the Nankai accretionary wedge: First results from IODP Expedition 333. In Y. Yamada, et al. (Eds.), *Submarine mass movements and their consequences, Advances in Natural and Technological Hazards Research* (Vol. 31, pp. 671–681). Springer Science+Business Media B.V. https://doi.org/10.1007/978-94-007-2162-3_60

Swarbick, R. E., & Naylor, M. A. (1980). The Kathikas melange, SW Cyprus: Late Cretaceous submarine debris flows. *Sedimentology*, *27*, 63–78.

Taira, A., Byrne, T., & Ashi, J. (1992). *Photographic atlas of an accretionary prism: Geological structures of the Shimanto Belt, Japan* (124 pp.). Tokyo, Japan: Springer-Verlag and University of Tokyo Press.

Tartarotti, P., Festa, A., Benciolini, L., & Balestro, G. (2017). Record of Jurassic mass transport processes through the orogenic cycle: Understanding chaotic rock units in the high-pressure Zermatt-Saas ophiolite (Western Alps). *Lithosphere*, *9*(3), 399–407.

Tunis, G., & Venturini, S. (1992). Evolution of the southern margin of the Julian Basin with emphasis on the megabeds and turbidities sequence of the southern Julian Alps (NE Italy). *Geologia Croatica*, *45*, 127–150.

Ukar, E. (2012). Tectonic significance of low-temperature blueschist blocks in the Franciscan mélange at San Simeon, California. *Tectonophysics*, *568-569*, 154–169.

Ukar, E., & Cloos, M. (2015). Magmatic origin of low-T mafic blueschist and greenstone blocks from the Franciscan mélange, San Simeon, California. *Lithos*, *230*, 17–29.

Ukar, E., & Cloos, M. (2016). Graphite-schist blocks in the Franciscan Mélange, San Simeon, California: Evidence of high-P metamorphism. *Journal of Metamorphic Geology*, *34*, 191–208.

Vail, P. R., & Mitchum, R. M. (1980). *Global cycles of sea-level change and their role in exploration*. Proceedings of the 10th World Petroleum Congress, Bucharest, Romania (pp. 95–104).

Vanneste, M., Harbitz, C. B., De Blasio, F. V., Glimsdal, S., Mienert, J., & Elverhøi, A. (2011). Hinlopen-Yermak Landslide, Arctic Ocean: Geomorphology, landslide dynamics and tsunami simulations. In R. C. Shipp, P. Weimer, & H. W. Posamentier (Eds.), *Mass-transport deposits in deep-water settings* (Vol. 96, pp. 509–527). SEPM Special Publication. https://doi.org/10.2110/sepmsp.096.509

Vezzani, L., Festa, A., & Ghisetti, F. (2010). *Geology and tectonic evolution of the Central-Southern Apennines, Italy, Geological Society of America, Special Paper* (Vol. 469, 58 pp.). Boulder, CO: Geological Society of America, accompanying by a CD-ROM including the "Geological-Structural Map of the Central-Southern Apennines (Italy)" at 1:250.000 scale, Sheets 1 and 2, doi:https://doi.org/10.1130/2010.2469

Vollmer, F. W., & Bosworth, W. (1984). Formation of melange in a foreland basin overthrust setting: Example from Taconic Orogen. In L. A. Raymond (Ed.), *Melanges: Their nature, origin, and significance, Geological Society of America, Special Papers* (Vol. 198, pp. 53–70). Boulder, CO: Geological Society of America.

von Gosen, W., Buggishs, W., & Lehnert, O. (1995). Evolution of the early Paleozoic mélange at the eastern margin of the Argentine Precordillera. *Journal of South America Earth Sciences*, *8*, 405–424.

von Huene, R., & Lallemand, S. (1990). Tectonic erosion along the Japan and Peru convergent margin. *Geological Society of America Bulletin*, *102*, 704–720.

von Huene, R., Ranero, C. R., & Vannucchi, P. (2004). Generic model of subduction erosion. *Geology*, *32*, 913–916.

Wakabayashi, J. (2012). Subducted sedimentary serpentinite mélanges: Record of multiple burial-exhumation cycles and subduction erosion. *Tectonophysics*, *568–569*, 230–247.

Wakabayashi, J. (2015). Anatomy of a subduction complex: Architecture of the Franciscan Complex, California, at multiple length and time scales. *International Geology Review*, *57*, 669–743.

Wakita, K. (2015). OPS mélange: A new term for *mélanges* of convergent margins of the world. *International Geology Review*, *57*(5–8), 529–539.

Weimer, P., & Shipp, C. (2004). *Mass transport complexes: Musing on past uses and suggestions for future directions*. Offshore technology conference, Paper 16752, Houston, 3–6 May 2004.

Wendorff, M. (2005a). Lithostratigraphy of Neoproterozoic syn-rift sedimentary megabreccia from Mwambashi, Copperbelt of Zambia, and correlation with olistostrome succession from Mufulira. *South African Journal of Geology*, *108*, 505–524.

Wendorff, M. (2005b). Evolution of Neoproterozoic-lower Palaeozoic Lufilian arc, Central Africa: A new model based

on syntectonic conglomerates. *Journal of the Geological Society of London*, *162*, 5–8.

Wendorff, M. (2011). Tectonosedimentary expressions of the evolution of the Fungurume foreland basin in the Lufilian arc, Neoproterozoic-lower Palaeozoic, Central Africa. In D. van Hinsbergen, S. J. H. Buiter, T. H. Torsvik, C. H. Gaina, & S. J. Webb (Eds.), *Out of Africa: A synopsis of 3.8 Ga of Earth history* (pp. 69–83). London, UK: The Geological Society.

Wise, D. U., & Ganis, G. R. (2009). Taconic Orogeny in Pennsylvania: A 15–20 m.y. Apennine-style Ordovician event viewed from its Martic hinterland. *Journal of Structural Geology*, *31*, 887–899.

Woodcock, N. H. (1979). The use of slump structures as palaeoslope orientation estimators. *Sedimentology*, *26*(1), 83–99.

Yamamoto, Y., Nidaira, M., Ohta, Y., & Ogawa, Y. (2009). Formation of chaotic rock units during primary accretion processes: Examples from the Miura-Boso accretionary complex, Central Japan. *Island Arc*, *18*, 496–512.

Yilmaz, P. O., & Maxwell, J. C. (1984). An example of an obduction melange: The Alakir Çay unit, Antalya complex, southwest Turkey. In L. A. Raymond (Ed.), *Melanges: Their nature, origin, and significance, Special Paper* (Vol. 198, pp. 139–152). Boulder, CO: Geological Society of America.

2

Mass-Transport Deposits in the Foredeep Basin of the Miocene Cervarola Sandstones Formation (Northern Apennines, Italy)

Alberto Piazza and Roberto Tinterri

ABSTRACT

In this chapter, we discuss different types of mass-transport deposits that characterize foredeep basins. In particular, we have focused on the Cervarola Sandstones Formation, Aquitanian-Burdigalian in age, which was deposited in a northwest-southeast elongate foredeep basin forming at the front of the growing Northern Apennine orogenic wedge. Within the turbiditic succession, three types of mass-transport deposits can be observed: (i) extrabasinal basin wide olistostromes that mark the base and the top of the turbiditic succession and are related to the allochthonous unit advancement, (ii) intrabasinal slumps related to the activity of tectonic structures internal to the basin, and (iii) particular megabeds, six in number, characterizing the turbiditic succession. We have described each type of mass-transport deposit in detail, giving an interpretation of the related depositional processes and introducing a facies model for megaturbidites. Finally, a paleogeographic model has been proposed, which describes the meaning of each mass-transport deposit type in the foredeep basin framework.

2.1. INTRODUCTION

Foredeeps are complex basins developed at the front of accretionary prisms where sedimentary and tectonic processes are strongly related. As a consequence, the stratigraphic successions deposited in these basins are characterized by a wide spectrum of melange-type rocks frequently reworked by postdepositional tectonic process (Camerlenghi & Pini, 2009). This work focuses on different types of mass-transport deposits (MTDs) recognized within the foredeep turbidites of the Aquitanian to Burdigalian Cervarola Sandstones Formation (CSF) cropping out in the Northern Apennines. This formation is one of the most important turbidite basins marking the main evolutionary stages of the Apennine foredeep (Figure 2.1). Each one of the recognized MTD types is characterized by specific facies and composition that record different origins. The study of these MTDs has been possible thanks to the high-resolution physical stratigraphy of the CSF recently performed by Tinterri and Piazza (2019) (see also Piazza, 2016; Figure 2.1c). This detailed stratigraphic framework is essential to (i) estimate the real extension of the MTDs and their lateral facies changes; (ii) discriminate, on the basis of their characteristics, the primary origin of these deposits, that is, whether they have a sedimentary or tectonic origin (in the latter case, the MTDs can be used as markers to define the tectonic events affecting the turbiditic basin and the adjacent areas); and (iii) define the influence of these MTDs in the shaping of the basin morphology and their effects on "normal" turbiditic deposition.

Department of Chemistry, Life Sciences and Environmental Sustainability, Earth Sciences Unit, University of Parma, Parma, Italy

Submarine Landslides: Subaqueous Mass Transport Deposits from Outcrops to Seismic Profiles, Geophysical Monograph 246, First Edition. Edited by Kei Ogata, Andrea Festa, and Gian Andrea Pini.
© 2020 American Geophysical Union. Published 2020 by John Wiley & Sons, Inc.

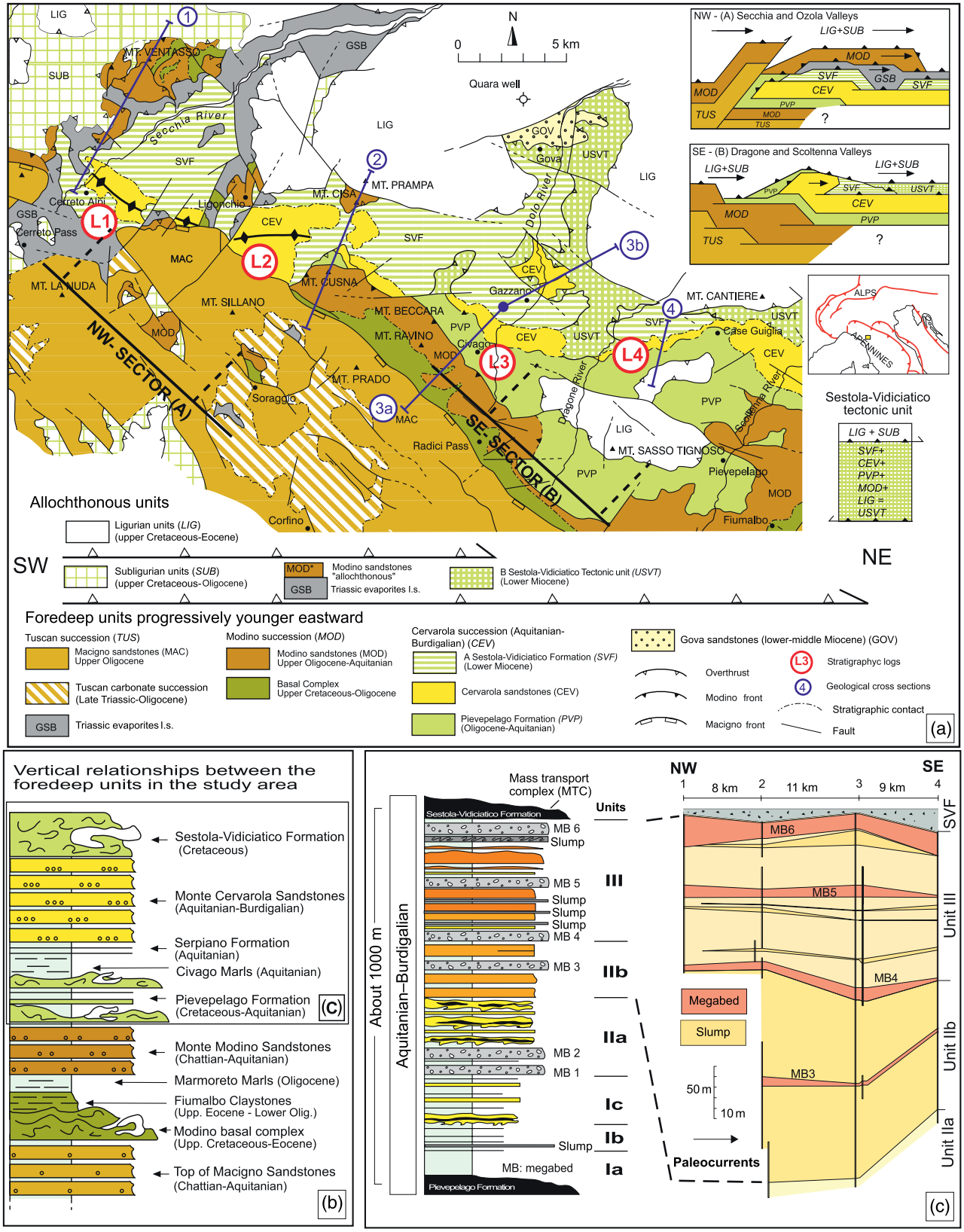


Figure 2.1 (a) Geological map of the study area (Source: Modified from Vescovi (2005)), in which structural schemes of the northwestern (A) and southeastern (B) sectors are shown. The paleogeographic position of the Modino succession is still being debated (Chicchi & Plesi, 1991a). (b) Schematic section illustrating the stratigraphic relationships between the foredeep units in the study area (Source: Modified from Gunther and Reutter (1985)). (c) Schematic stratigraphic section of the Cervarola Sandstones Formation with a detail that shows a stratigraphic cross section in which the distribution of slumps and megabeds can be observed. Source: Modified from Tinterri and Piazza (2019).

2.2. GEOLOGICAL SETTING

The Northern Apennine foredeep is characterized by NW-SE elongate turbidite basins progressively migrating eastward, since upper Oligocene, in response to thrust propagation and allochthonous Ligurian unit advancement in the same direction (Ricci Lucchi, 1986; di Biase & Mutti, 2002). The foredeep sediments have a main north/northwestern Alpine provenance even if minor lateral and southern (carbonatic) supplies are present (Gandolfi et al., 1983; Ricci Lucchi, 1986; Andreozzi & Di Giulio, 1994; Botti et al., 2002; Valloni et al., 2002).

The turbiditic foredeep deposits are represented, from the innermost (southwestern and oldest) to the outermost (northeastern and youngest), by the Macigno-Monte Modino (upper Oligocene-Aquitanian), Monte Cervarola (Aquitanian-Burdigalian) and Marnoso-arenacea (Langhian-Tortonian) successions (Dallan Nardi & Nardi, 1974; Ricci Lucchi, 1986; Argnani & Ricci Lucchi, 2001; Lucente & Pini, 2008). During the migration processes, the foredeep units became themselves part of the orogenic wedge, and today, they crop out, deeply deformed by the NE-vergent postdepositional tectonic, in the axial portion of the mountain chain (Figure 2.1a) (Boccaletti et al., 1990).

Before focusing on the foredeep Cervarola Sandstones succession, we need to take a look at the complex geology of the studied segment of the Northern Apennines, located between the Secchia and Scoltenna valleys (Figure 2.1). In order to show the general structural features of the area, four geological cross sections have been constructed on the basis of the official geological map at a 1 : 10,000 scale (Apat-Regione Emilia Romagna, 2002), supplemented with new field data (Figure 2.2). The general structural architecture is characterized by the superposition of the allochthonous Ligurian units, represented here by the cretaceous Monte Caio Helminthoid Flysch and the Poggio Mezzature turbiditic sandstones (Figure 2.2) (Plesi et al., 2002a), above the para-autochthonous foredeep units (Macigno, Modino, and Cervarola succession) belonging to the Adria Microplate (Elter et al., 2003) (Figure 2.1a). In between them, there is a relatively thin stack of tectonic units (Subligurian units, Triassic evaporites l.s., and Sestola-Vidiciatico tectonic unit; Figure 2.1a).

2.2.1. The Foredeep Units: Geometrical Relationships and Previous Interpretations

The foredeep units appear deeply affected by a NW-SE trending fold and thrust belt type deformation with a northeastward vergence that produced overturned anticlines characterized by extensive overturned limb (i.e., geologic cross sections 2 and 3a in Figure 2.2). As it can be observed in cross section 3a (Figure 2.2), each foredeep turbiditic succession is separated by "chaotic" units or "chaotic complexes" that contain mixed gravitationally and tectonically reworked material and make the geological setting even more complex. The original geometrical relationships between the different turbiditic successions before the folding processes can be reconstructed for the studied area as shown in Figure 2.1b; nevertheless, the literature reports a long-standing debate on palinspastic position of each turbiditic succession, depending on the interpretation of the "chaotic complexes" and the nature of their contacts (tectonic vs. stratigraphic point of view).

The upper Oligocene Macigno Sandstones succession, having a thickness ranging between 2 and 3 km, is the only one that has a defined stratigraphic position as it is placed at the top of the Tuscan carbonatic succession (Ghibaudo, 1980; Ciarapica & Passeri, 1998; Plesi et al., 2002a); in the studied area, the Macigno Sandstones appear folded in an overturned anticline and lowered by a normal fault with respect to the terrains outcropping northeastward (cross sections 2 and 3a in Figure 2.2; Chicchi & Plesi, 1991b).

The lowermost "chaotic complex" characterizes the base of the Modino turbiditic succession and divides it from the underlying Macigno Sandstones (Figure 2.1b). It comprises portions with Ligurian affinity composed by destroyed block-in-matrix cretaceous argillaceous breccias (AVP in Figure 2.2) containing cretaceous Helminthoid Flysch blocks (Abetina Reale Flysch, ABT in Figure 2.2), which pass upward into wedge front and slope related Eocene-Oligocene shales and marls (Fiumalbo Shales and Marmoreto Marls) (Figure 2.1b). The interpretation of this chaotic "complex" and the consequent nature of the contact between the Macigno and Modino successions remain controversial and have been interpreted in two different ways by various authors:

1. The Modino succession is stratigraphically linked to the underling Macigno succession, and it would represent the prosecution of deposition after the emplacement in the Macigno foredeep of an MTD (the Modino basal complex) generated by the destabilization of the front of the allochthonous Ligurian prism (Merla, 1951; Dallan Nardi & Nardi, 1974, Gunther & Reutter, 1985; Abbate & Bruni, 1989; Pandeli et al., 1994; Lucente & Pini, 2008).

2. The Modino succession represents an inner sub-basin of the Macigno foredeep. It was deposited on the toe of the Ligurian wedge (the Modino basal complex), and, in the meanwhile, it was progressively overthrusting, toward NE, the Macigno foredeep deposits (Reutter, 1969; Bettelli et al., 1989; Chicchi & Plesi, 1991a; De Libero, 1998; Marchi et al., 2017; Cornamusini et al., 2018).

A second "chaotic complex" divides the Modino succession from the overlying Aquitanian-Burdigalian Cervarola turbiditic succession, and it is called Pievepelago Formation (Nardi & Tongiorgi, 1962; Nardi, 1965; Reutter, 1969; Bettelli et al., 1989; Lucente & Pini, 2008)

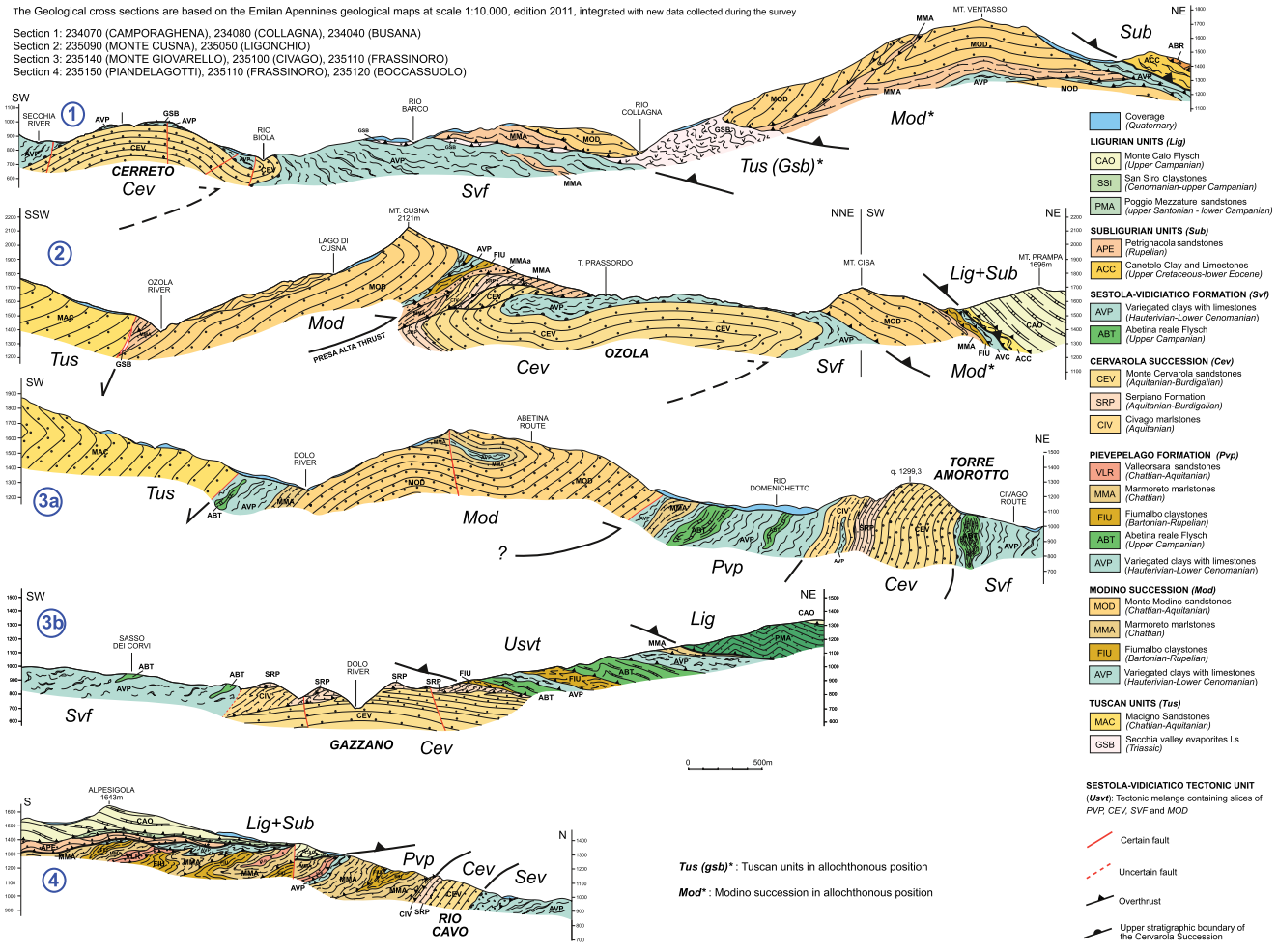


Figure 2.2 Geological cross section of the studied area. The cross sections are based on the Emilian Apennine geological maps at scale 1 : 10,000, edition 2011, supplemented with new data collected during the survey. The numbers of the maps sheet are reported in the picture. Trace of section in Figure 2.1.

(Figure 2.1b). The Pievepelago Formation contains (i) destroyed block-in-matrix cretaceous deposits and outsized blocks with Ligurian affinity (Abetina Reale Flysch), (ii) Priabonian-Rupelian clay lithologies (Fiumalbo Claystones), (iii) Chattian-Aquitanian marlstones (Marmoreto Marls) and fine-grained sandstones (Valleorsara Sandstones) (Figures 2.1b and 2.2). This lithologic association appears deeply affected by the postdepositional tectonic and exposes variable thickness from 200 to 400 m (Nardi, 1964a; Reutter, 1969). The Pievepelago Formation is draped by the Aquitanian Civago Marlstones that represent the basal portion of the Cervarola turbiditic succession (Figure 2.1b). Also for the Pievepelago Formation, different interpretations have been suggested by different authors. Nardi (1964a, 1964b), Fazzini (1966), Reutter and Schlüter (1968), Reutter (1969), Bettelli et al. (1989), and Camerlenghi and Pini (2009) interpreted it as an alternation of MTDs (lithologies "i" and "ii") that testify the destabilization of the toe of the Ligurian prism and the "normal" deposition characterized by the Chattian-Aquitanian marlstones and sandstones (lithology iii). Conversely, Chicchi and Plesi (1991b), Plesi et al. (2000), Plesi et al. (2002b), and Remitti et al. (2007) include all the lithologies belonging to the Pievepelago Formation, together with the Modino succession, within a tectonic subunit called Modino-Pievepelago that would represent the front of the embryonic accretionary prism. In spite of the different interpretations, the various authors agree that the Pievepelago units would represent, at the time of the Cervarola Sandstones deposition, the inner southwestern slope of the foredeep, draped by the deposition of marly and silty deposits (Civago Marlstone) as confirmed by the sedimentological studies (Tinterri & Piazza, 2019).

In this chapter, the name "Sestola-Vidiciatico Formation" (SVF in Figures 2.1 and 2.2) identifies the uppermost "chaotic complex" that marks the top of the Cervarola succession (Figure 2.1c), where it is composed by destroyed bock-in-matrix Cretaceous argillaceous deposits (AVP in Figure 2.2 and in Plesi et al. (2002a, 2002b)) containing cretaceous Helminthoid Flysch blocks (Abetina Reale Flysch, ABT in Figure 2.2 and in Plesi et al. (2002a, 2002b)) and isolated ophiolite blocks. Also for this chaotic complex, different interpretations have been given by several authors, but, in this regard, the situation is even more complex because the Sestola-Vidiciatico Formation is not followed at the top by others foredeep turbiditic deposits, but it appears overthrust by allochthonous units. Some authors interpreted it as a sedimentary melanges (olistostromes) produced by the destabilization of the front of the Ligurian accretionary prism progressively advancing on the foredeep (Baldacci et al., 1967; Krampe, 1969; Reutter, 1969; Gunther & Reutter, 1985; Camerlenghi & Pini, 2009; Tinterri & Piazza, 2018), whereas others insert these terrains within a tectonic unit, called Sestola-Vidiciatico (Modino-Ventasso subunit for Plesi et al. (2002a, 2002b)), developed at the shear zone between the allochthonous Ligurian units and para-autochthonous foredeep ones; consequently, they interpret the basal contact with the Cervarola Sandstones always as tectonic (Chicchi & Plesi, 1991b; Plesi et al., 2002a; Remitti et al., 2007; Cornamusini et al., 2018). As discussed herein, we think that both units are present, the olistostromes (SVF in Figure 2.1) and the tectonic unit (USVT in Figure 2.1), but they should be distinguished since they have different genetic meaning and composition.

2.2.2. Tectonic Remarks

As briefly illustrated above, the shear zone developed between the allochthonous Ligurian units and the Oligo-Miocene foredeep is characterized by tectonic units classically known as Subligurian units l.s. (Elter et al., 2003). These units can be interpreted as a tectonic mélange that shows different features to the NW and SE of the Secchia Valley (Figure 2.1a): to the NW, it consists of Subligurian units *sensu stricto* (Plesi, 1975; Montanari & Rossi, 1982), whereas, to the SE, it is characterized by the Sestola-Vidiciatico tectonic unit, that is, a tectonic mélange fed both by the upper Ligurian units and by the lower units belonging to the foredeep successions (Remitti et al., 2007; Vannucchi et al., 2012; see USVT in Figure 2.1a and cross section 3b in Figure 2.2). Close to the Secchia Valley, this shear zone is characterized by the presence of Triassic evaporites l.s. (GSB in Figures 2.1 and 2.2) (Andreozzi et al., 1987; Vescovi, 2005; Scaglie del Secchia in Plesi et al. (2002a, 2002b)) and slivers of Modino foredeep succession (MOD* in Figures 2.1 and 2.2) (Ventasso subunit in Plesi et al. (2002a); Vescovi, 2005), which have been dragged over the Cervarola succession and Sestola-Vidiciatico Formation by the Ligurian unit advancement. The latter situation is shown quite well in the Monte Ventasso and Monte Cisa outcrops (see cross sections 1 and 2 in Figure 2.2). The lateral variability in the structural shaping is a peculiar feature of the Northern Apennine units (Ghelardoni, 1965; Piazza et al., 2016), as well as of the Cervarola succession that shows, in the study area, two different deformation patterns in the northwestern (A) and southeastern (B) sectors (Figure 2.1a).

A. NW sector: In this area, the Cervarola succession crops out in tectonic windows shaped as a recumbent anticline facing toward NE and with a general NW-SE or E-W axial trend (Cerreto and Ozola windows in cross sections 1 and 2 of Figure 2.2) (Chicchi & Plesi, 1991c). The southern margin of the Ozola window is characterized by an overturned syncline probably linked to the overthrusting of the Modino succession and associated Pievepelago Formation (Presa alta thrust in cross section 2 of Figure 2.2).

B. SE sector: In this sector, the Cervarola succession that crops out in the southern margin of the studied area is completely verticalized, or northeastward overturned, together with the underlying and overlaying Pievepelago and Sestola-Vidiciatico Formations (Torre Amorotto and Rio Cavo successions in cross sections 3a and 4 of Figure 2.2). In the map of Figure 2.1, this set of verticalized terrains, cropping out from Mt. Beccara to Case Guiglia, appears like a W-E elongated band (Civago-Guiglia band in Reutter (1969)) that shows an amount of northeastward movement increasing from NW to SE and reaches a maximum, of at least 5 km, in the Case Guiglia area where it gains a "Subligurian" position. Conversely, in the external northeastern areas, the foredeep deposits (Cervarola succession according to Plesi et al. (2002a)) crop out in the Gazzano tectonic window (cross section 3b), shaped as a gently anticline and tectonically overthrust by the Sestola-Vidiciatico tectonic unit.

2.3. STRATIGRAPHY AND FACIES ANALYSIS OF THE CERVAROLA SANDSTONES FORMATION (CSF)

The stratigraphic studies made on the CSF by Andreozzi (1989, 1991) and Andreozzi et al. (1995) have shown that the CSF is characterized by at least three turbidite systems, which, from northwest to southeast, are Torre dell'Amorotto, Scoltenna, and Fellicarolo-Dardagna. This work focuses on the proximal portion of the Cervarola basin, that is, the Torre dell'Amorotto system, which has been studied in four main areas (from L1 to L4) between the Secchia and Scoltenna valleys (see Tinterri & Piazza, 2019; Figure 2.1a, c).

In particular, the Torre dell'Amorotto system shows a total thickness, measured from base to top, in LOG 3 (Figure 2.1a) of about 1000 m, and it is composed of different lithotypes showing complex lateral/vertical relationships (Plesi et al., 2002a, 2002b; Tinterri & Piazza, 2018): Civago Marlstone, Serpiano Formation (fine-grained sandstones in thin beds), and Cervarola Sandstones *sensu stricto* (Figure 2.1b). In the recent work by Tinterri and Piazza (2019), the relationships between these lithotypes have been clarified through detailed bed-by-bed physical correlation and facies analysis (Figure 2.1c). The fine-grained and thin facies (Civago Marlstone and Serpiano Formation) are deposited by the more turbulent and diluted portion of the turbidity currents and essentially characterize the morphological highs within the basin, which, in their turn, are induced by (i) growth of syn-depositional compressive tectonic structures both parallel and transversal to the basin elongation and (ii) the emplacement of huge MTDs such as the Pievepelago Formation. These morphologic highs work, within the basin, like barriers that can produce turbidite flows reflections and ponding phenomena that are recorded by well-determined types of facies and variations in the paleocurrent directions (Tinterri & Piazza, 2019). Conversely, the coarse-grained and thick facies (Cervarola Sandstones *sensu stricto*) essentially characterize depocentral areas and are deposited by the basal dense portion of turbidite flows. The vertical distribution of facies in the Cervarola turbiditic succession shows a progressive thickening and coarsening upward trend, which testifies a compensation of the morphology created by the basal Pievepelago MTD and the progressive narrowing and closure of the foredeep basin related to the northeastward propagation of the orogen (Tinterri & Piazza, 2019). In this setting, the Cervarola basin can be considered a complex foredeep (*sensu* Ricci Lucchi, 1986), that is, a basin characterized by evident syn-depositional tectonic activity able to produce important structural highs and depocenters.

2.4. MASS-TRANSPORT DEPOSITS WITHIN THE CERVAROLA SANDSTONES SUCCESSION

The Cervarola succession is characterized by the occurrence of deposits that cannot be described as classical turbidites. In particular, intercalated within the turbiditic succession, we can find 5 slumps and 6 megabeds that are 3–28 m thick, show a basinal extension, and have been used as key beds for stratigraphic correlations (Andreozzi, 1991; Tinterri & Piazza, 2019). These types of deposits, together with the Pievepelago and Sestola-Vidiciatico "chaotic" formations characterizing the base and top of the turbiditic succession, are the three types of MTDs that can be found in the Cervarola succession. The detailed description in the following section will show that these three types of deposits actually have different composition, facies, and provenance testifying that each one of them has a different meaning in the foredeep evolution.

2.4.1. Extrabasinal Chaotic Units: Pievepelago and Sestola-Vidiciatico Formations

2.4.1.1. Description

Extrabasinal "chaotic" units characterize the base and the top of the Cervarola turbiditic succession (Figures 2.1b and 2.3a, b).

The base of the succession crops out in the Torre Amorotto section close to the incision produced by the Dolo River (LOG 3 in Figure 2.1a, cross section 3a in Figure 2.2). It consists of destroyed, block-in-matrix, cretaceous deposits characterized by an argillaceous dark matrix with brecciated fabric and marly-calcareous blocks from centimeters to meters in size (Figure 2.3b). This lithological association is draped by the Civago Marlstones, and it returns twice,

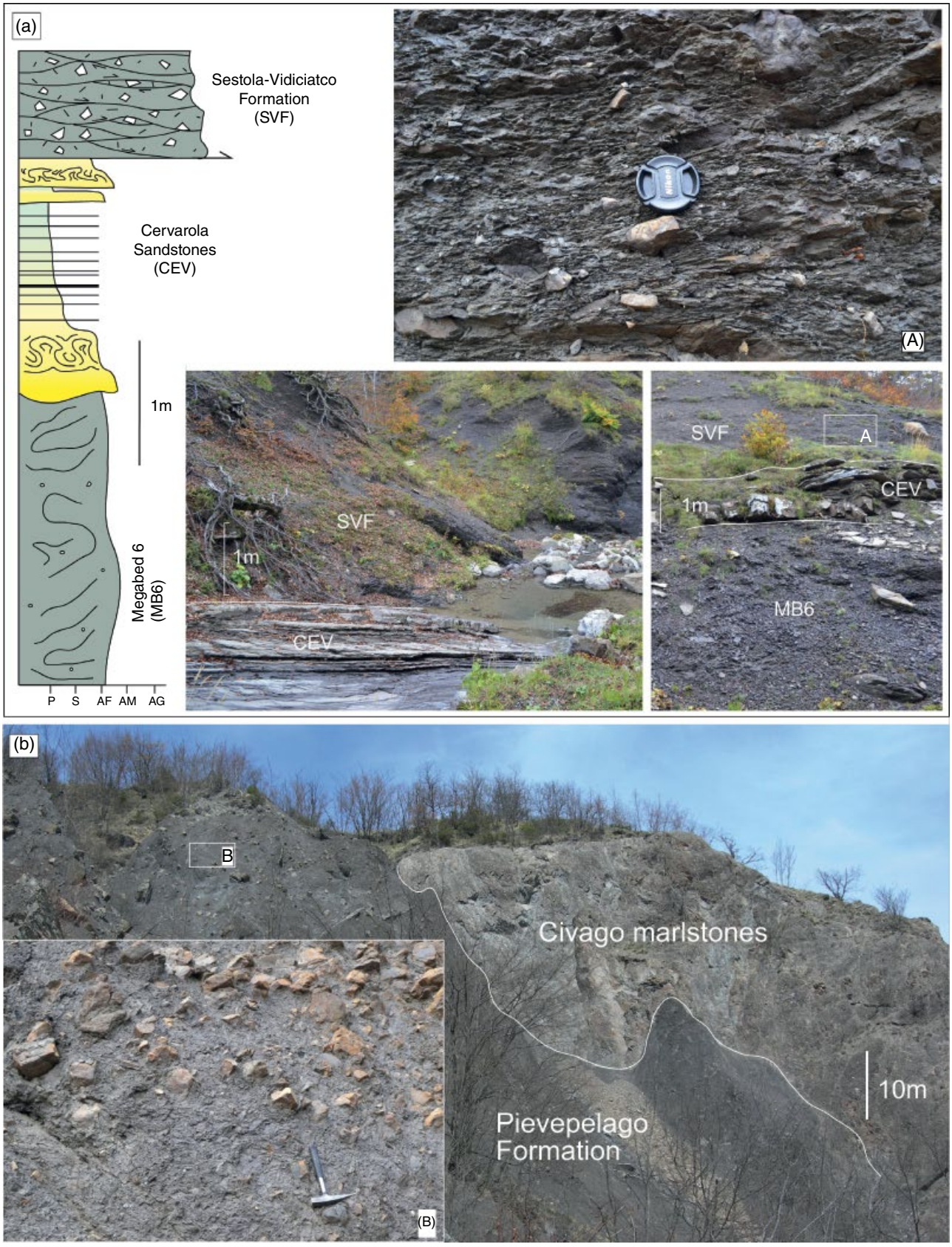


Figure 2.3 (a) The upper contact of the Cervarola Sandstones with the overlying Sestola-Vidiciatico Formation (Log 2 in Figure 2.1a, latitude 44.299668, longitude 10.379833). Image (A) shows a detail on the typical block-in-matrix brecciated fabric. (b) The basal contact between the Civago Marlstones (member of the Cervarola turbiditic succession) and the Pievepelago Formation (Log 3 in Figure 2.1a, latitude 44.257309, longitude 10.485450′). In (B), a detail on the block-in-matrix fabric of the Pievepelago Formation.

always intercalated within the Civago Marlstones (Andreozzi, 1991; Tinterri & Piazza, 2019).

Also, the upper boundary of the Cervarola turbiditic succession (Figure 2.3a) is well preserved, and it always shows the same features in all the studied stratigraphic sections: the turbiditic succession terminates with megabed 6 (see the description in Section 2.4.3), overlaid by at least 1.5 m of fine-grained thin turbiditic beds, in their turn covered by destroyed cretaceous deposits with a block-in-matrix fabric characterized by an argillaceous dark matrix and marly-calcareous blocks from centimeters to meters in size (Figure 2.3a). In this case, the block-in-matrix fabric shows a specific cleavage that, although pervasive, does not mask the brecciated fabric of the clayey matrix (Figure 2.3a).

2.4.1.2. Interpretation

The two described "chaotic" deposits show the same facies that are typical of the MTDs or olistostromes (*sensu* Camerlenghi & Pini, 2009): sedimentary mélanges. The composition of these MTD (olistostromes) is extrabasinal with a clear Ligurian affinity testifying that they derive from the destabilization of the toe of the Ligurian prism moving progressively toward the northeast. According to Nardi (1964a, 1964b), Fazzini (1966), Reutter (1969), Gunther and Reutter (1985), Bettelli et al. (1989), Andreozzi (1991), Lucente and Pini (2008), and Camerlenghi and Pini (2009), we insert the olistostromes cropping out at the base of the Cervarola succession within the Pievepelago Formation. Conversely, in Plesi et al. (2002a, 2002b), while being interpreted as olistostromes, they are identified as a member of the Civago Marlstones (Brecce del Rio Rumale), only in Cornamusini et al. (2018) the existence of these olistostromes at the base of the Cervarola succession is denied without any explanation.

As described in Section 2.2, the Pievepelago Formation facies association is typical of the inner slope of the foredeep basin. The emplacement of the 100 meter thick MTDs generates, within the basin, morphological highs that can be reached only by the turbulent portion of the bipartite turbidite flows whose basal dense parts tend to move in more external depocentral areas. As a consequence, the "normal" turbiditic sedimentation above the MTDs is essentially characterized by fine-grained facies, as well as documented in the basal portion of the Cervarola turbiditic succession characterized by 200 m of marlstone (Civago Marlstones) draping the Pievepelago Formation (Figure 2.3b).

The olistostrome occurring at the top the Cervarola succession is here defined as Sestola-Vidiciatico Formation with the meaning already given in the geological setting. Since, in some recent literature, this olistostrome is interpreted as a tectonic mélange and, consequently, the basal contact with the Cervarola Sandstones as tectonic, this issue is exhaustively dealt with in the discussion. For now, we just observe that the cleavage shown by the Sestola-Vidiciatico Formation can be simply explained as a compaction cleavage that may occur locally close and parallel to the basal contact of olistostromes, if induced by sediment flows, or elsewhere if induced by postdepositional compaction and tectonics (Camerlenghi & Pini, 2009).

2.4.2. Slumps

This term indicates MTDs essentially consisting of folded and fractured intraformational fine-grained facies (thin silty beds) with evidence of soft-sediment deformations that sometimes suggest transport directions toward the NE (Figure 2.4a, b, b'). They show important lateral thickness variation, from 40–50 cm to 14 m, and limited extension within the basin as they disappear in the proximal Log 1 (see Figure 2.1c). The stratigraphic succession is characterized by five slumps; four of them are concentrated at the top of the turbiditic succession, in the upper unit III, whereas another one is located in the basal fine-grained portion of the stratigraphic succession (Figure 2.1c). Tinterri and Piazza (2019) documented that the emplacement of these slumps, even though they are characterized by reduced thicknesses, could generate subtle morphologies able to influence the turbidite facies distribution. In particular, the top of the slumps is generally sealed by fine-grained and thin-bedded facies (Figure 2.4b) that gradually compensate the slump morphology.

2.4.2.1. Interpretation

Based on the type of deformation and composition, these deposits can be interpreted as slumps related to the destabilization of the fine-grained sediments deposited on the structurally controlled morphological highs (Tinterri & Piazza, 2019). The progressive growth of the highs induced by tectonic activity can indeed generate gravitative instabilities affecting the turbiditic deposits that are consequently forced to slump down from the highs toward the depocentral areas. The compensation processes occurring above the slumps suggest that the morphology they create is able to influence the turbidity currents.

2.4.3. Megabeds

The studied stratigraphic succession is characterized by six megabeds that are a specific characteristic of the Cervarola turbiditic succession (Andreozzi, 1991) and have been fundamental to correlate the different stratigraphic logs (MB from 1 to 6 in Figure 2.1c). They mainly consist of very thick matrix-supported conglomerates (F2 facies by Mutti et al. (2003)) showing thickness variations from 3 to 28 m with basinal extension and lateral facies variations on short distances (Figures 2.5 and 2.6). These megabeds

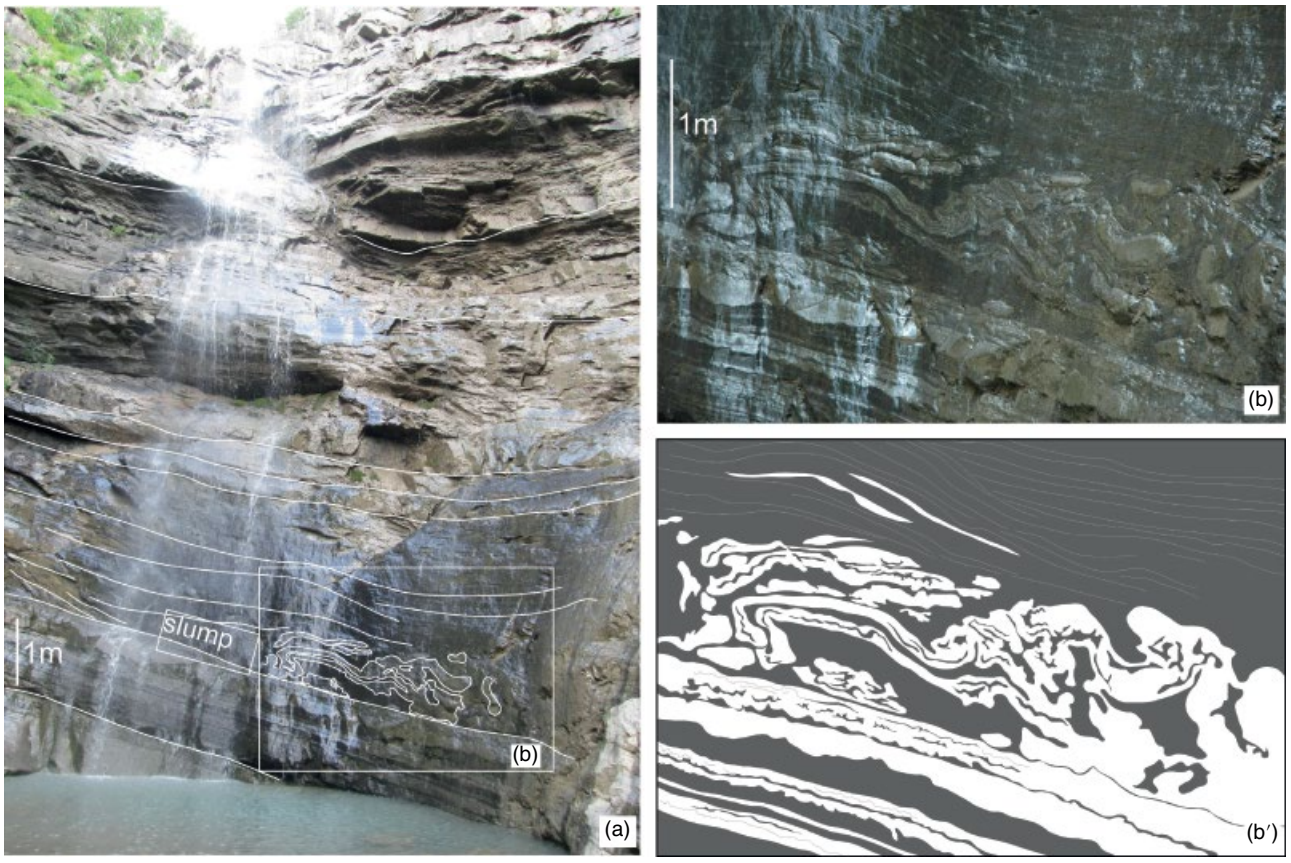


Figure 2.4 (a) Panoramic view on the turbiditic succession cropping out at the Lavacchiello waterfall (Log 2 in Figure 2.1, latitude 44.294443, 1 longitude 10.3668887) characterized by a slump deposit at the base of the cliff. (b and b′) Detail on the twisted slumped beds.

consist of three main facies (see also Tinterri & Piazza, 2019) that, from base to top, are as follows:

1. Facies consisting of completely deformed turbidite beds eroded from the substratum in which the muddy sandstone matrix is essentially absent (Figure 2.5c). This facies characterizes especially the morphological highs (Figure 2.6a–c) and, in some cases, is very similar to the blocky-flow deposits by Mutti et al. (2006) (see also Ogata et al., 2012, 2014).

2. Matrix-supported conglomerate characterized by pebbles, cobbles, and boulders (from 2 mm to 70 cm) and a muddy sandstone matrix that can be interpreted as a F2 facies (*sensu* Mutti et al., 1999, 2003) (Figure 2.5a, b). In general, the paraconglomerate can show a rough normal gradation with a basal part where folded turbidite beds can be common (facies 2a) and an upper part characterized by a classic paraconglomerate composed of large amount of fine-grained muddy-silty sediment in which round-shaped silty boulders with an alteration-related yellowish color can be present (see facies 2b in Figures 2.5a, b and 2.6a, b). The analysis of the lateral facies distribution, based on detailed stratigraphic cross sections, points out that this facies, unlike the blocky-flow facies 1, tends to characterize the more depocentral areas (see Figure 2.6a, b).

3. These megabeds are always draped by a medium- to fine-grained normally graded and laminated sandstone bed with strongly lenticular geometries characterized by flow impact basal mudstone breccia and diffuse convolute lamination (Figure 2.5a, d). The lenticular geometry is essentially related to the irregular top of the underlying F2 facies.

2.4.3.1. Interpretation

This facies sequence is very similar to that of megaturbidites described by Labaume et al. (1987), Mutti et al. (1999), or Kleverlaan (1987) and can be seen as the product of different flow processes that changed in time and space, reflecting various types of flow transformation. In particular, these megaturbidites can be interpreted as deposited by bipartite flows characterized by a basal dense or hyperconcentrated flow able to deposit facies 1 and 2 and an upper turbulent flow able to deposit facies 3 (see Figure 2.6a–c). Specifically, the leading edges of basal dense flows, characterized by considerable erosive

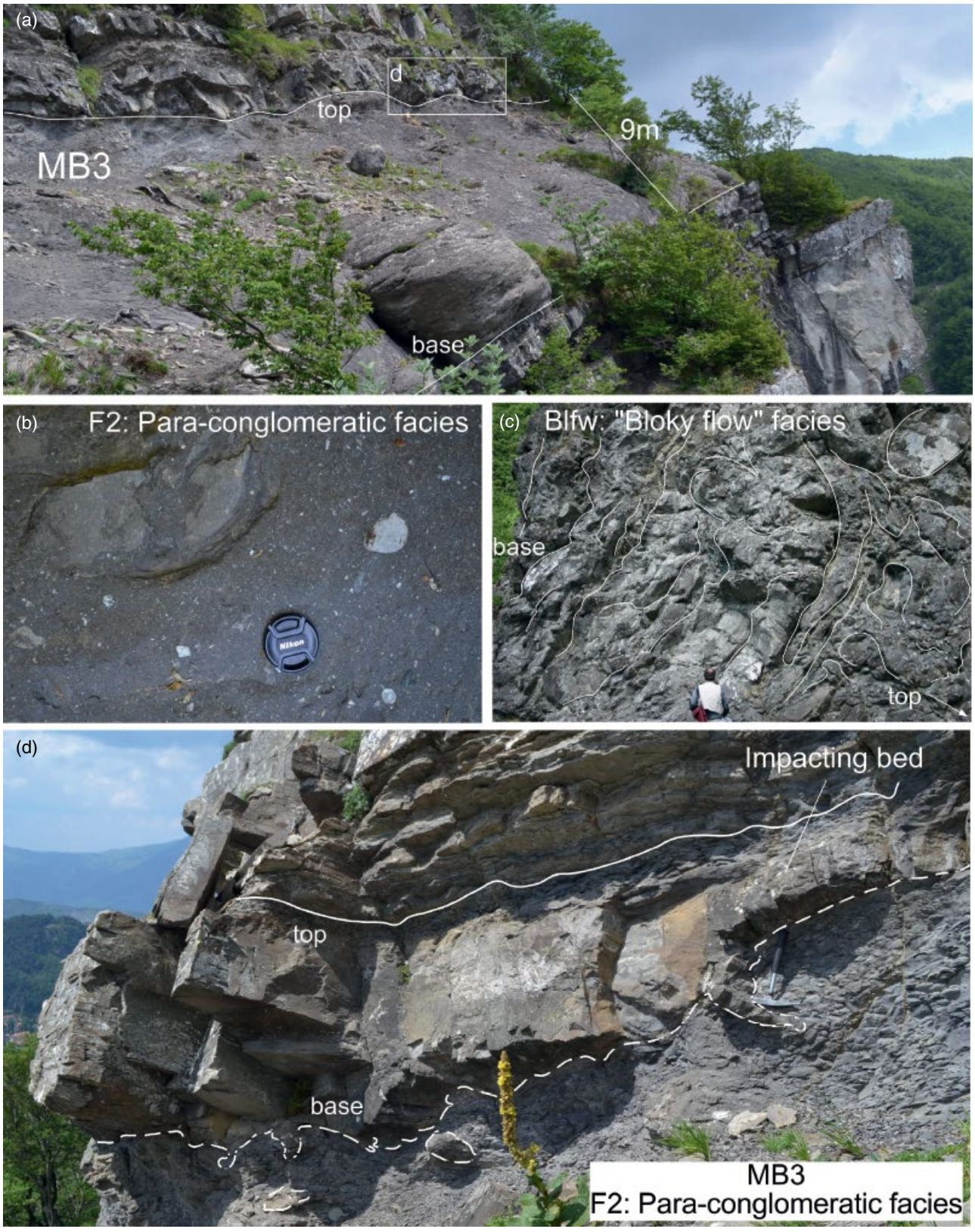


Figure 2.5 (a) Panoramic overview on the megabed MB 3 in Log 2 (Figure 2.1a, latitude 44.309574, longitude 10.358890). (b) Detail on the paraconglomeratic facies F2 characterizing the megabeds. (c) Example of a blocky-flow deposit (Blfw) in MB 6 (Log 3) mainly composed of folded turbidite beds. (d) Detail showing the upper affiliated turbidite bed associated to MB 3; see (a) for the location of this bed.

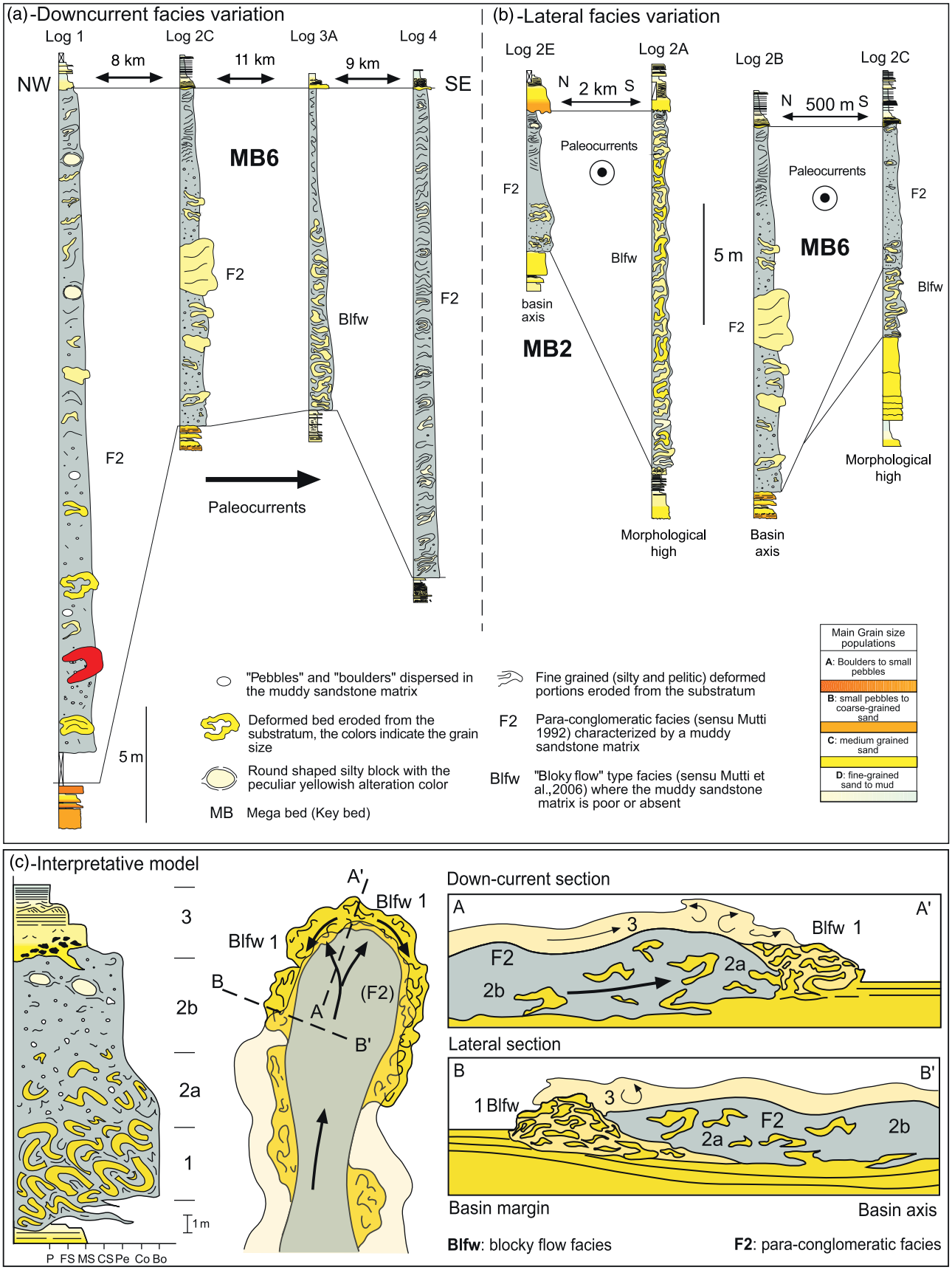


Figure 2.6 (a) Detailed stratigraphic cross section describing the downcurrent evolution of megabed MB6. (b) Stratigraphic cross sections describing megabeds MB2 and MB6 in a transect perpendicular to the paleocurrents. (c) Depositional model explaining the relationships between paraconglomerates deposited by hyperconcentrated flows and blocky-flow facies (Blfw).

capacity, can operate like a bulldozer on the underlying turbidite deposits (Mutti et al., 1999; Butler & McCaffrey, 2010; Eggenhuisen et al. 2011; Ogata et al., 2012; Fonnesu et al., 2016). However, if the dense flow is not able to entirely incorporate all the eroded material, the latter tends to accumulate at its flow front producing, in some cases, a "blocky-flow" facies (Figure 2.6c), that is, a complex deposit made of oversized folded turbidite slide blocks in which the muddy sandstone matrix, typical of hypercontracted or debris flows, is poor or absent (see Mutti et al., 2006; Ogata et al., 2012). In this process, erosion can occur through delaminations of the basal dense flow (*sensu* Fonnesu et al., 2016) favoring overpressured sand injections and bulking of entire blocks of turbidite succession that can be successively folded and fractured by the bulldozer effect of the flow leading edge (Figure 2.6c).

These types of flows and processes can also justify facies 2a, that is, a F2 facies characterized by large folded turbidite beds, which essentially records a transitional deposit between the blocky-flow facies 1 and facies 2b composed of a classic paraconglomerate F2. From this point of view, facies 2a and 2b can be interpreted as deposited by the leading and trailing edges of a basal dense flow, respectively. The fact that these morphologic highs can favor impact and delamination processes of dense flow fronts can explain the evidence that "blocky-flow" facies tend to characterize morphological highs (such as the southern inner margin of the basin), whereas F2 facies tend to characterize the axial depocentral areas (see Figure 2.6a, b).

Conversely, the sandstone beds at the top of the basal paraconglomerate are another typical characteristic of the megaturbidites and can be interpreted as the deposit of affiliated turbidity currents (*sensu* Mohrig & Marr, 2003) resulting from the head transformation of the underlying dense flows able to deposits the paraconglomeratic facies (see Figure 2.6c).

Finally, the provenance and the trigger mechanisms of these debris flows are a problem still unsolved. Although a detailed petrographic analysis would be necessary, in the foredeep segment studied in this work, their basinal extension suggests an apical provenance from the more proximal portion of the foredeep.

2.5. DISCUSSION

The three types of MTDs characterizing the Cervarola foredeep basin have different meanings, and their emplacement records important regional events affecting the basin evolution. In Figure 2.7, their meaning has been schematically reconstructed.

The extrabasinal MTDs (type 1 in Figure 2.7) derive from the destabilization of the allochthonous Ligurian prism during important advancement phases and can be defined as precursory olistostromes (Elter & Trevisan, 1973; Dallan Nardi & Nardi, 1974; Camerlenghi & Pini, 2009; Cornamusini et al., 2017). Since they are the precursors of the Ligurian nappe emplacement, these MTDs are a typical characteristic of the Northern Apennine Oligo-Miocene foredeep. The basal olistostrome (i.e., the Pievepelago Formation) is not immediately followed by the Ligurian nappe, and, consequently, the turbiditic deposition in the foredeep continues with the deposition of the Cervarola succession, even if it appears strongly influenced by the morphology induced by the emplacement of the MTD (Tinterri & Piazza, 2019). Conversely, the upper olistostrome (i.e., the Sestola-Vidiciatico Formation) is directly followed by the emplacement of the Ligurian nappe, and it marks, in the study area, the ending of the turbiditic deposition in the foredeep. This peculiar position at the top of the foredeep succession has generated some confusion over time. After being introduced by Reutter (1969) to define the sedimentary olistostrome at the top of the Cervarola succession, the term "Sestola-Vidiciatico" has been used in the literature to indicate all the units that directly overlie the foredeep successions in the area between the Secchia (to the NW) and Sillaro (to the SE) valleys. As a result, the same name has been used to indicate the tectonic mélange, the Sestola-Vidiciatico tectonic unit (USVT in Figures 2.1, 2.2, and 2.7), developed in the shear zone between the allochthonous Ligurian units and the "autochthonous" foredeep ones (Remitti et al., 2007, 2010; Vannucchi et al., 2012; Mittempergher et al., 2018). The Sestola-Vidiciatico tectonic mélanges, indeed, occur through a tectonic contact at the top of the foredeep deposits in more external northeastern areas than those studied in this work (e.g., the Gazzano tectonic window, cross section 3b in Figure 2.2).

The aspect of the upper boundary of the Cervarola succession stimulates discussion of some problems. Chicchi and Plesi (1991a) and Plesi et al. (2002b) in a tectonic point of view suggest that the top of the Cervarola succession is always characterized by an overthrust with a "ramp and flat" geometry: (i) the ramps could be identified, for examples, in the Presa alta thrust (cross section 2 in Figure 2.2) and at the top of the Gazzano window (cross section 3b in Figure 2.2) where the turbiditic succession appears truncated by the overthrusting and slices of fine-grained turbidites (Civago Marlstones and Serpiano Formation) result, in turn, detached and northeastward displaced; (ii) to the contrary, the "flats" should characterize the top of the turbiditic succession where it does not appear truncated (e.g., in Cerreto and the Ozola anticlines; Figure 2.2). If there are no doubts in the individuation of the ramps, conversely, we believe that many arguments suggest that the flats by Chicchi and Plesi

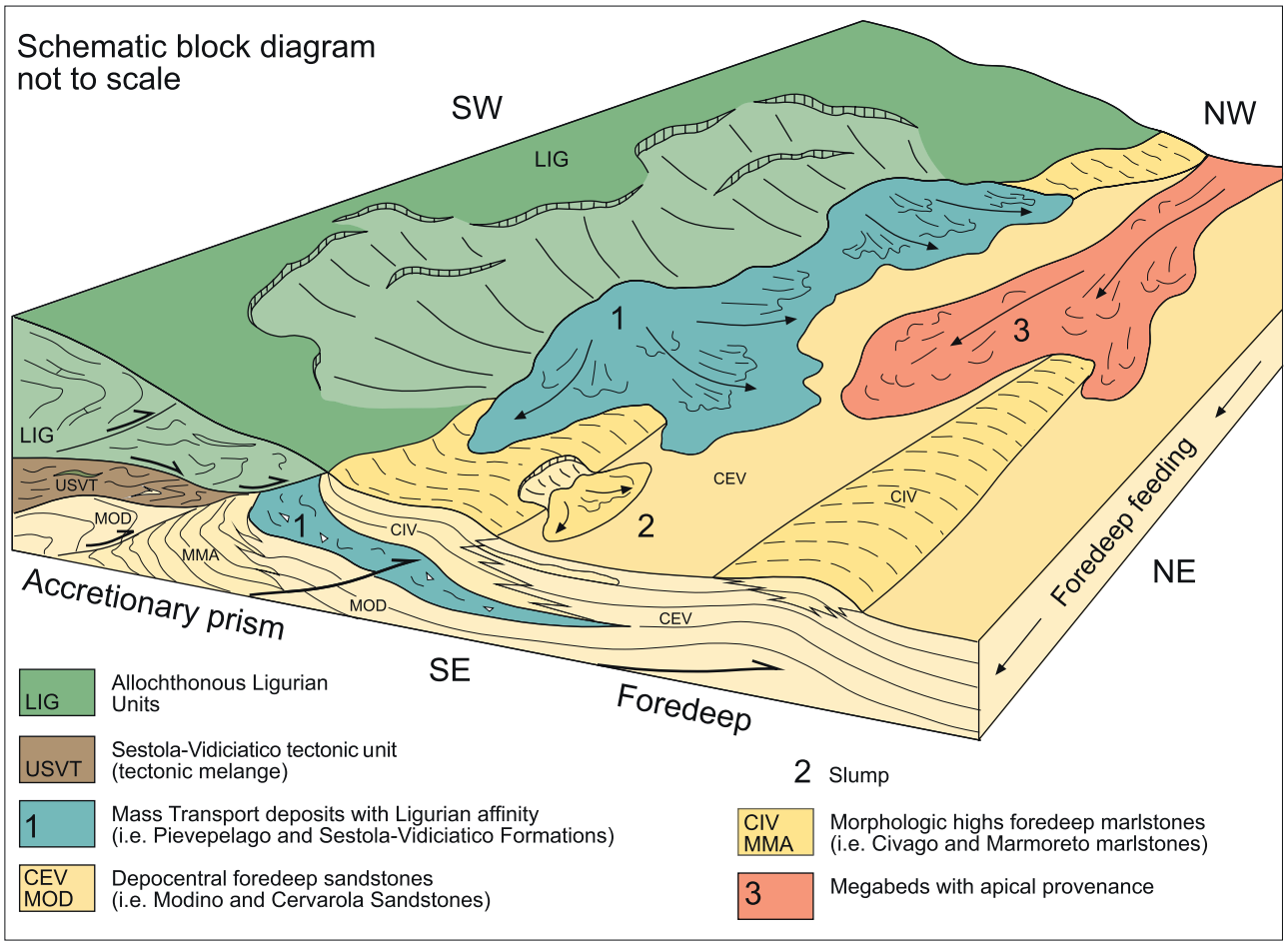


Figure 2.7 Schematic block diagram illustrating the northern Apennine foredeep at the time of the Cervarola Sandstones deposition (lower Miocene). The picture shows the tree type of mass-transport deposits occurring in the Cervarola succession.

(1991b) are actually the upper stratigraphic boundary of the Cervarola succession:

1. The "flats" of Plesi et al. (2002a, 2002b) are characterized by a hanging wall block always consisting of olistostromic facies (AVP in Plesi et al., 2002a, and in Figure 2.2). If the ramp and flat surfaces were related to the same thrust sheet, they should be characterized, in the hanging wall, by the same units; conversely, in the "flat," we never find the detached slices of fine-grained Cervarola succession that always characterize the ramp.

2. In all the studied stratigraphic succession, for 30 km downcurrent, the upper contact of the Cervarola succession with the olistostromic facies (SVF in Figure 2.1) shows the same features (Figure 2.1c; Andreozzi, 1991; Tinterri & Piazza, 2019), that is, the turbidite succession always finishes with megabed MB 6 overlain by about 1.5 m of thin and fine-grained sandstone beds before the MTD emplacement (Figure 2.2a). This type of contact is not consistent with a tectonic-type contact, which cuts the turbiditic succession, placing the roof contact at different stratigraphic level.

As a consequence, the listed argumentations allows us to suggest that, in the studied stratigraphic sections, the upper boundary of the Cervarola succession is preserved and characterized by the emplacement of the Sestola-Vidiciatico olistostrome. The prosecution of the internal ramps (e.g., Presa alta thrust in cross section 2 of Figure 2.2) should be searched for within and/or at the top of the Sestola-Vidiciatico olistostrome and not at the boundary with the underlying Cervarola succession.

In this setting, it is quite surprising that a gravity mass-transport complex having the magnitude of the Sestola-Vidiciatico Formation, which has a wide and regional extension, did not heavily erode down into the turbiditic succession, as found in other similar situations at the base of huge MTDs (see Lucente & Pini, 2003; Camerlenghi &

Pini, 2009; Tagliaferri & Tinterri, 2016). Two hypothesis can be made: (i) the Sestola-Vidiciatico olistrostrome, which can reach thickness of hundreds of meters, is not the result of a single huge event, but it is the sum of numerous debris flows with limited erosive capacity; (ii) it records the deposition of one big MTD that moved on an overpressure carpet preventing the substratum erosion; and (iii) the observed sections are in a distal sector of the MTD depositional area, where it is characterized by limited erosional capability as described for the Casaglia MTDs in the Marnoso-arenacea Formation (Lucente & Pini, 2008; Tagliaferri & Tinterri, 2016).

Another aspect worthy of discussion is the particular distribution of the intraformational slumps (type 2 MTDs in Figure 2.7) that are concentrated at the top of the turbiditic succession in the upper unit 3 (Figure 2.1c; Tinterri & Piazza, 2019). Their emplacement has been interpreted as related to the activity of the tectonic structure that confined the internal southwestern margin of the basin (Tinterri & Piazza, 2019). The particular distribution of the slumps at the top of the succession suggests a link between the increase in the tectonic activity of the internal structure and the Ligurian unit advancement to the NE. In this setting, the slumps can be considered as the premonitory events of the incipient closing of the foredeep basin operated by advancement and collapse of the allochthonous Ligurian prism, recorded by the Sestola-Vidiciatico Formation emplacement. This upward increase in slumps heralding the closure of the foredeep basin can be also observed in other foredeeps, such as that of the Marnoso-arenacea Formation (Tinterri & Muzzi Magalhaes, 2011; Tinterri & Tagliaferri, 2015) and Macigno Formation (Ghibaudo, 1980).

The last point of discussion concerns the specific megabeds that characterize the Cervarola turbiditic succession and show the typical facies sequence of many megaturbidites described in other foredeep basins (Figures 2.1c, 2.5, and 2.6). Not only have the detailed physical stratigraphy and facies analysis allowed a depositional model to be proposed, but also hypothesis to be made about the meaning of the facies distribution in relation to the structural highs and depocenters. Indeed, the megaturbidites can be interpreted as deposited by a bipartite flow composed of an upper turbulent flow and a basal debris flow whose leading edge is able to produce blocky-flow facies against the structural highs that favor impact and delamination processes (Figure 2.6c). The transformation of the front of this basal debris flow due to the shear stress derived from the water displacement produces an affiliate turbidity current that can drape the irregular top of the basal paraconglomerate deposited by the debris flow (Figure 2.6c). Furthermore, these megaturbidites seem to have random distribution within the turbiditic succession, and, as described in the previous chapters, they have a basinal distribution suggesting an apical northwestern provenance. As a consequence, it is not possible to directly link the emplacement of these megabeds to tectonic events affecting the studied segment of the foredeep. Nevertheless, it can be supposed that their genesis is related to sediment failure in more proximal area probably induced by tectonic events, such as growth of syndepositional structures or seismic shocks.

2.6. CONCLUSIONS

This chapter discusses the meaning of three types of MTDs characterizing the Cervarola foredeep basin (Figure 2.7). The first ones are the extrabasinal basin wide olistostromes, represented by the Pievepelago and Sestola-Vidiciatico formations. They mark the base and top of the turbiditic succession and are related to the allochthonous unit advancement. The second ones are the intrabasinal slumps related to the activity of tectonic structures internal to the basin; they tend to be concentrated in the upper part of the Cervarola stratigraphic succession because they herald the tectonic phase producing the closure of the foredeep basin through the emplacement of the upper Sestola-Vidiciatico MTD. Finally, in the CSF, there is a third type of MTD that is represented by six megaturbidites. They are characterized by a well-defined facies sequence made of three main facies: (i) a basal blocky-flow deposit (*sensu* Mutti et al., 2006; Ogata et al., 2012), (ii) a paraconglomerate F2 facies characterized in its basal part by large blocks of turbidite beds, and (iii) a massive to laminated normal graded bed characterized by lenticular geometries that tend to compensate the irregular top of the underlying facies 2. This facies sequence is interpreted as deposited by a bipartite flow composed of a basal debris flow able to deposit facies 1 and 2 and an affiliated upper turbidity current produced by the head transformation of the basal debris-flow leading edge (*sensu* Mohrig & Marr, 2003) able to deposit the upper facies 3. The lateral distribution of the facies, highlighted by detailed stratigraphic cross sections (see Figure 2.5a, b), has also allowed a depositional model to be proposed explaining the lateral facies distribution in relation to the basin morphology (see Figure 2.5c). This lateral facies distribution has also lead to the understanding that the development of the blocky-flow facies 1 is related to the impact processes of the basal dense flow against the structural highs (see Figure 2.5).

In conclusion, these three types of MTDs that are typical characteristics of the Cervarola Sandstones succession can represent a reference example on the types of MTDs that can be found in a foredeep.

ACKNOWLEDGMENTS

The authors want to thank Maurizio Andreozzi, Andrea Artoni, Paolo Vescovi, Kei Ogata, Alessio Tagliaferri, Andrea Civa, and Michele Laporta for discussions and advice. The authors are also grateful to editors Kei Ogata and Gian Andrea Pini and two anonymous reviewers for their helpful comments and suggestions. The authors also want to express their sincere thanks to Petrobras S.A. (Petróleo Brasileiro S.A.) and, in particular, to Pierre Muzzi Magalhaes and Mário Carminatti for funding this work.

REFERENCES

Abbate, E., & Bruni, P. (1989). Modino-Cervarola o Modino e Cervarola? Torbiditi oligo-mioceniche ed evoluzione del margine Nord-appenninico. *Memorie Società Geologica Italiana*, *39*(1987), 19–33.

Andreozzi, M. (1989) Stratigrafia fisica delle Arenarie del Cervarola (settore NW–Appennino Settentrionale) e relative osservazioni biostratigrafiche basate sui nannofossili calcarei (Unpublished Phd thesis). Università degli studi di Parma, academic year 1988–1989, II cycle, IT.

Andreozzi, M. (1991). Stratigrafia fisica delle Arenarie di M. Cervarola nel settore nord-occidentale dell'Appennino Settentrionale tra la Val Secchia (RE) e la Val Panaro (MO). *Memorie Descrittive della Carta Geologica d'Italia*, *46*, 269–285.

Andreozzi, M., Casanova, S., Chicchi, S., Ferrari, S., Patterlini, P. E., Pesci, M., & Zanzucchi, G. (1987). Riflessione sulle evaporiti triassiche dell'alta val Secchia (RE). *Memorie Società Geologica Italiana*, *39*, 69–75.

Andreozzi, M., & Di Giulio, A. (1994). Stratigraphy and petrography of the Mt. Cervarola sandstones in the type area, Modena province. *Memorie Società Geologica Italiana*, *48*, 351–360.

Andreozzi, M., Dinelli, E., & Tateo, F. (1995). Volcaniclastic key beds and megaturbidites in an early-Miocene turbidite system, Mt. Cervarola Fm. (northern Apennines). *Giornale di Geologia*, *57*(1–2), 159–178.

Apat-Regione Emilia (2002). Emilian Apennines geological maps at scale 1.10.000, edition 2011.

Argnani, A., & Ricci Lucchi, F. (2001). Tertiary silicoclastic turbidite systems of Northern Apennines. In G. B. Vai & I. P. Martini (Eds.), *Anatomy of an Orogen: the Appenines and the Adjiacent Mediterranean Basins* (pp. 327–350). London, UK: Kluwer Academic Publishers.

Baldacci, F., Brandi, P. G., Nardi, R., Squarci, P., & Taffi, L. (1967). Sulla giacitura dei calcari cavernosi e dei gessi di Sassalbo, del passo del Cerreto e della Val di secchia (Appennino Tosco-Emiliano). *Memorie Società Geologica Italiana*, *6*, 199–211.

Bettelli, G., Bonazzi, U., Fazzini, P., & Gelmini, R. (1989). I flysch terziari del crinale appenninico (Macigno, Modino, Cervarola). *Memorie Società Geologica Italiana*, *39*, 1–17.

Boccaletti, M., Calamita, F., Deiana, G., Gelati, R., Massari, F., Moratti, G., & Ricci Lucchi, F. (1990). Migrating foredeep-thrust belt systems in the northern Apennines and southern Alps. *laeogeography, Palaeoclimatology, Palaeoecology*, *77*, 3–14. https://doi.org/10.1016/0031-0182(90)90095-O

Botti, F., Palandri, S., & Plesi, G. (2002). The Mt. Cervarola Sandstones in the T. Fellicarolo and T. Dardagna Valleys (Northern Apennines): Petrographic and biostratigraphic features, regional correlations. *Bollettino-Societa Geologica Italiana*, *1*, 305–317.

Butler, R. W. H., & McCaffrey, W. D. (2010). Structural evolution and sediment entrainment in mass-transport complexes: Outcrop studies from Italy. *Journal of the Geological Society*, *167*, 617–631.

Camerlenghi, A., & Pini, G. A. (2009). Mud volcanoes, olistostromes and Argille scagliose in the Mediterranean region. *Sedimentology*, *56*, 319–365.

Chicchi, S., & Plesi, G. (1991a). Il Complesso di M. Modino-M. Cervarola nell'alto Appennino emiliano (tra il Passo di Lagastrello e il M. Cimone) e i suoi rapporti con la Falda toscana, l'Unità di Canetolo e le Liguridi. *Memorie Descrittive della Carta Geologica d'Italia*, *46*, 139–163.

Chicchi, S., & Plesi, G. (1991b). Sovrascorrimenti e strutture associate dell'Alto Appennino emiliano fra il Passo del Lagastrello ed il Monte Cimone. *Studi Geologici Camerti*, *1990*, 99–108.

Chicchi, S., & Plesi, G. (1991c). Sedimentary and tectonic lineations as markers of a regional deformation: An example from the oligo-miocene arenaceous flysch of the Northern Apennines. *Bollettino della Società Geologica Italiana*, *110*, 601–616.

Ciarapica, G., & Passeri, L. (1998). Evoluzione paleogeografica degli Appennini. *Atti Ticinesi -Scienze della Terra*, *40*, 233–290.

Cornamusini, G., Conti, P., & Bambini, A. M. (2018). The Late Oligocene to Early Miocene foredeep basin system evolution of the Northern Apennines (Emilia-Tuscany, Italy): Review and new litho-biostratigraphic data. *Italian Journal of Geosciences*, *137*, 396–419.

Cornamusini, G., Conti, P., Bonciani, F., Callegari, I., & Martelli, L. (2017). Geology of the "Coltre della Val Marecchia" (Romagna-Marche Northern Apennines, Italy). *Journal of Maps*, *13*(2), 207–218.

Dallan Nardi, L., & Nardi, R. (1974). Schema stratigrafico-strutturale dell'Appennino Settentrionale. *Memorie della Accademia lunigianese di scienze G. Cappellini*, *42*, 1–212.

De Libero, C. M. (1998). Sedimentary vs. tectonic deformation in the "Argille Scagiose" of Mt. Modino (Northern Apennines). *Giornale di Geologia*, *56*, 143–166.

Di Biase, D., & Mutti, E. (2002). The "proto Adriatic basin". In E. Mutti, F. R. Lucchi, & M. Roveri (Eds.), *Revisiting turbidites of the Marnoso-arenacea Formation and their basin-margin equivalents: Problems with classic models: Excursion guidebook: Parma, Italy 21–22 May 2002* (120 pp.). Parma, Italy: Copy Press.

Eggenhuisen, J. T., McCaffrey, W. D., Haughton, P. D. W., & Butler, R. W. H. (2011). Shallow erosion beneath turbidity currents and its impact on the architectural development of turbidite sheet systems. *Sedimentology*, *58*, 936–959.

Elter, P., Grasso, M., Parrotto, M., & Vezzani, L. (2003). Structural setting of the Apennine-Maghrebian thrust belt. *Episodes*, *26*, 205–211.

Elter, P., & Trevisan, L. (1973). Olistostromes in the tectonic evolution of the Northern Apennines. In K. A. de jong & R. Scholten (Eds.), *Gravity and tectonics* (pp. 175–188). New York, NY: Wiley.

Fazzini, P. (1966). La geologia dell'alta Val Dolo. *Bollettino della Società Geologica Italiana*, *84*(6), 213–238.

Fonnesu, M., Patacci, M., Haughton, P. D. H., Felletti, F., & McCaffrey, W. D. (2016). Hybrid event beds generated by local substrate delamination on a confined-basin floor. *Journal of Sedimentary Research*, *86*, 929–943.

Gandolfi, G., Paganelli, L., & Zuffa, G. G. (1983). Petrology and dispersal pattern in the Marnoso-arenacea Formation (Miocene, Northern Apennines). *Journal of Sedimentary Petrology*, *53*, 493–507.

Ghelardoni, R. (1965). Osservazioni sulla tettonica trasversale dell'Appennino settentrionale. *Bollettino della Societa Geologica Italiana*, *84*, 277–290.

Ghibaudo, G. (1980). Deep-sea fan deposits in the Macigno Formation (Middle-Upper Oligocene) of the Gordana valley, Northern Apennines, Italy. *Journal of Sedimentary Research*, *50*, 723–742.

Gunther, K., & Reutter, K. J. (1985). Il significato dell'Unità di M. Modino-M. Cervarola tra il Passo delle Radici ed il Monte Falterona in relazione alla tettonica dell'Appennino settentrionale. *Giornale di Geologia*, *47*, 15–34.

Kleverlaan, K. (1987). Gordo megabed: a possible seismite in a Tortonian submarine fan, Tabernas basin, Province Almeria, southeast Spain. *Sedimentary Geology*, *51*, 165–180.

Krampe, K. D. (1969). Sulla posizione dei terreni preliassici nell'Appennino tosco-emiliano fra Sassalbo e Busana (Massa-Carrara, Reggio Emilia). *L'Ateneo Parmense- Acta Naturalia*, *1*, 11–136.

Labaume, P., Mutti, E., & Seguret, M. (1987). Megaturbidites: A depositional model from the Eocene of the SW-Pyrenean Foreland Basin, Spain. *Geo-Marine Letters*, *7*, 91–101.

Lucente, C. C., & Pini, G. A. (2003). Anatomy and emplacement mechanism of a large submarine slide within the Miocene foredeep in the Northern Apennines, Italy: A field perspective. *American Journal of Science*, *303*, 565–602.

Lucente, C. C., & Pini, G. A. (2008). Basin-wide mass-wasting complexes as markers of the Olio-Miocene foredeep-accretionary wedge evolution in the Northern Apennines, Italy. *Basin Research*, *20*, 49–71.

Marchi, A., Catanzariti, R., & Pandolfi, L. (2017). Calcareous nannofossil biostratigraphy: a tool for understanding the stratigraphic evolution of the Mt. Modino unit (Northern Apennines, Italy). *Italian Journal of Geosciences*, *136*(2), 171–185.

Merla, G. (1951). Geologia dell'Appennino settentrionale. *Bollettino della Società Geologica Italiana*, *70*, 95–382.

Mittempergher, S., Cerchiari, A., Remitti, F., & Festa, A. (2018). From soft sediment deformation to fluid assisted faulting in the shallow part of a subduction megathrust analogue: The Sestola-Vidiciatico tectonic Unit (Northern Apennines, Italy). *Geological Magazine*, *155*, 438–450.

Mohrig, D., & Marr, J. G. (2003). Constraining the efficiency of turbidity-current generation from submarine slides, slumps and debris flow using laboratory experiments. *Marine and Petroleum Geology*, *20*, 883–899.

Montanari, L., & Rossi, M. (1982). Evoluzione delle unità stratigrafico-strutturali terziarie del nordappennino: l'Unità di Canetolo. *Bollettino della Società Geologica Italiana*, *101*, 257–289.

Mutti, E., Carminatti, M., Moreira, J. L. P., & Grassi, A. A. (2006). *Chaotic deposits: Examples from the Brazilian offshore and from outcrop studies in the Spanish Pyrenees and Northern Apennines, Italy*. AAPG Annual Meeting, April 9–12, Houston, TX.

Mutti, E., Tinterri, R., Benevelli, G., di Biase, D., & Cavanna, G. (2003). Deltaic, mixed and turbidite sedimentation of ancient foreland basins. *Marine and Petroleum Geology*, *20*, 733–755.

Mutti, E., Tinterri, R., Remacha, E., Mavilla, N., Angella, S., & Fava, L. (1999). *An introduction to the analysis of ancient turbidite basins from an outcrop perspective, AAPG Course Notes* (Vol. 39, 93 pp.). Tulsa, OK: American Association of Petroleum Geologists.

Nardi, R. (1964a). Contributo alla geologia dell'Appennino Tosco-emiliano 3- I rapporti tra le arenarie del Monte Cervarola e il Macigno lungo la valle dello Scoltenna (prov. di Modena). *Bollettino della Società Geologica Italiana*, *83*(2), 361–372.

Nardi, R. (1964b). Contributo alla geologia dell'Appennino Tosco-emiliano 4 – La geologia della valle dello Scoltenna tra Pievepelago e Montecreto (Appennino modenese). *Bollettino della Società Geologica Italiana*, *83*(4), 353–400.

Nardi, R. (1965). Schema geologico dell'Appennino tosco-emiliano tra M. Cusna e M. Cimone e considerazione sulle unità tettoniche. *Bollettino della Società Geologica Italiana*, *81*(3), 1–76.

Nardi, R., & Tongiorgi, M. (1962). Contributo alla geologia dell'Appennino tosco-emiliano 1 –Stratigrafia e tettonica dei dintorni di Pievepelago (Appennino Modenese). *Bollettino-Societa Geologica Italiana*, *81*(3), 1–76.

Ogata, K., Mountjoy, J. J., Pini, G. A., Festa, A., & Tinterri, R. (2014). Shear zone liquefaction in mass transport deposit emplacement: A multi-scale integration of seismic reflection and outcrop data. *Marine Geology*, *356*, 50–64.

Ogata, K., Tinterri, R., Pini, G. A., & Mutti, E. (2012). The Specchio Unit (Northern Apennines, Italy): An ancient mass transport originated from near-coastal areas in an intraslope setting. In Y. Yamada, K. Kawamura, K. Ikehara, Y. Ogawa, R. Urgeles, D. Mosher, et al. (Eds.), *Submarine mass movements and their consequences, Advances in Natural and Technological Hazards Research* (Vol. 31, pp. 595–605). Dordrecht, The Netherlands: Springer Science+Business Media B.V.

Pandeli, F., Ferrini, G., & Lazzari, D. (1994). Lithofacies and petrography of the macigno Formation from the Abetone to the Monti del Chianti areas (Northern Apennines). *Memorie Società Geologica Italiana*, *48*(1), 321–329.

Piazza, A. (2016). Stratigrafia fisica ed analisi di facies dei depositi torbiditici della Formazione delle Arenarie del Monte Cervarola tra la Val Secchia e la Val Scoltenna (Aquitaniano-Burdigaliano, Appennino Settentrionale) (Phd thesis). XXVIII cycle, Università degli Studi di Parma.

Piazza, A., Artoni, A., & Ogata, K. (2016). The Epiligurian wedge-top succession in the Enza Valley (Northern Apennines):

Evidence of a syn-depositional transpressive system. *Swiss Journal of Geosciences*, *109*, 17–36.

Plesi, G. (1975). La Nappe de Canetolo. *Bulletin de la Société géologique de France*, *6*, 979–983.

Plesi, G., Chicchi, S., Daniele, G., & Palandri, S. (2000). La struttura dell'alto Appennino reggiano-parmense, fra Valditacca, il Passo di Pradarena e il Monte Ventasso. *Bollettino della Società Geologica Italiana*, *119*, 267–296.

Plesi, G., Daniele, G., Chicchi, S., Bettelli, G., Catanzariti, R., Cerrina Feroni, A., et al. (2002a). Carta geologica d'Italia alla scala 1:50.000, foglio 235, Pievepelago, S.EL.CA. Firenze, Servizio Geologico d'Italia – Regione Emilia Romagna.

Plesi, G., Daniele, G., Chicchi, S., Bettelli, G., Catanzariti, R., Cerrina Feroni, A., et al. (2002b). Note illustrative della Carta geologica d'Italia alla scala 1:50.000, foglio 235, Pievepelago, S.EL.CA. Firenze, Servizio Geologico d'Italia – Regione Emilia Romagna.

Remitti, F., Bettelli, G., & Vannucchi, P. (2007). Internal structure and tectonic evolution of an underthrust tectonic mélange: The Sestola-Vidiciatico tectonic unit of the Northern Apennines, Italy. *Geodinamica Acta*, *20*(1–2), 37–51.

Remitti, F., Vannucchi, P., Bettelli, G., Fantoni, L., Panini, F., & Vescovi, P. (2010). Tectonic and sedimentary evolution of the frontal part of an ancient subduction complex at the transition from accretion to erosion: The case of the Ligurian wedge of the northern Apennines, Italy. *Geological Society of America Bulletin*, *123*, 51–70.

Reutter, K. J. (1969). La Geologia dell'alto Appennino Modenese tra Civago e Fanano e considerazioni geotettoniche sulla unità di M. Modino-M. Cervarola. L'Ateneo Parmense. *Acta Naturalia*, *5*(2), 1–88.

Reutter, K. J., & Schlüter, H. U. (1968). La struttura delle arenarie dell'Unità di M. Modino-M. Cervarola nella zona di Bobbio (Piacenza) e nell'Appennino modenese. *Ateneo Parmense-Acta Naturalia*, *II*(fasc. 2), 1–23.

Ricci Lucchi, F. (1986). The Oligocene to recent foreland basins of the northern Apennines. In P. Allen & P. Homewood (Eds.), *Foreland basins, Special Publication of the International Association of Sedimentologists* (Vol. 8, pp. 105–139). Oxford, UK: Blackwell Scientific.

Tagliaferri, A., & Tinterri, R. (2016). The tectonically-confined Firenzuola turbidite system (Marnoso-arenacea Formation, northern Apennines, Italy). *Italian Journal of Geosciences*, *135*, 425–443.

Tinterri, R., & Muzzi Magalhaes, P. (2011). Synsedimentary structural control on foredeep turbidites: An example from Miocene Marnoso-arenacea Formation, Northern Apennines, Italy. *Marine and Petroleum Geology*, *28*, 628–657.

Tinterri, R., & Piazza, A. (2019). Turbidites facies response to the morphological confinement of a foredeep (Cervarola Sandstones Formation, Miocene, northern Apennines, Italy). *Sedimentology*, *66*(2), 636–674.

Tinterri, R., & Tagliaferri, A. (2015). The syntectonic evolution of foredeep turbidites related to basin segmentation: Facies response to the increase in tectonic confinement (Marnoso-arenacea Formation, Miocene, Northern Apennines, Italy). *Marine and Petroleum Geology*, *67*, 81–110.

Valloni, R., Cipriani, N., & Morelli, C. (2002). Petrostratigraphic record of the Apennine Foredeep Basins, Italy. *Bollettino della Società Geologica Italiana*, *1*(2002), 455–465.

Vannucchi, P., Remitti, F., & Bettelli, G. (2012). Lateral variability of the erosive plate boundary in the Northern Apennines, Italy. *Italian Journal of Geosciences*, *13*(2), 215–227.

Vescovi, P. (2005). The Middle Miocene Mt. Ventasso – Mt. Cimone arcuate structure of the Emilia Apennines. *Bollettino della Società Geologica Italiana*, *124*, 53–67.

3

Late Miocene Olistostrome in the Makran Accretionary Wedge (Baluchistan, SE Iran): A Short Review

Jean-Pierre Burg

ABSTRACT

This chapter describes and interprets a chaotic sedimentary unit of exotic blocks and pebbly mudstones set in a muddy matrix. This unit is regionally distributed in the onshore Makran accretionary wedge in southeast Iran. Formerly named "colored mélange," it is interpreted as a huge submarine mass flow deposit formed in Tortonian-Messinian times (between 11.8 and 9.6 Ma). Internal structures and contact with previously folded wedge sequences favor fast-rated (e.g., high-density turbidites, cohesive debris flows) rather than slow-rated (e.g., slump, creep) dominant processes. South-southwestward flow directions determined from sense-of-shear criteria indicate that the source area was an either submarine or subaerial paleo-high located to the north of the outcrops. This interpretation is consistent with the lithology of the exotic blocks. The large olistostrome represents a major sediment failure that occurred shortly after the beginning of a regional folding event. An external trigger mechanism, such as earthquakes, may have triggered the mass-wasting process.

3.1. INTRODUCTION: GEOLOGICAL SETTING

Geologists prospecting oil potential were impressed by the complexity of dismembered units in southeast Iran, where the expression "colored mélange" was coined (Gansser, 1955). Later work on the Makran (Baluchistan) geology recognized that this descriptive terminology confusingly encompassed both tectonic imbrications of fault-bounded blocks and sedimentary "wildflyschs" of exotic blocks in a shale-dominated matrix (Delaloye & Desmons, 1980; McCall, 1983). This is the case in the Iranian Makran, where the tectonic imbrication of ophiolitic, metamorphic, magmatic, and sedimentary rocks delineates the north dipping thrust between the North Makran backstop and the sedimentary accretionary wedge (Figure 3.1, Burg et al., 2013). This tectonic imbrication is interpreted as a trench "mélange" formed in a north dipping subduction zone during latest Cretaceous/Paleocene times (McCall & Kidd, 1982). In turn, the "wildflysch" (sedimentary mélange) is part of the onshore Makran accretionary wedge exposed in southeast Iran. This wedge is composed of three major, east/west oriented zones, namely, from north to south, that is, from the structural top to bottom, the Inner, Outer, and Coastal Makran. These three zones are separated by major north dipping thrust contacts (Figure 3.1, Burg et al., 2013). The Inner and Outer Makran pinch out to the west, but they extend eastward into Pakistan where structural trends are more cylindrical than in the Iranian part. This difference in structural grain is readily seen on satellite images (e.g., https://www.google.com/earth, Figure 3.2) and is largely due to the geomorphological expression of the "sedimentary mélange" outcrops in southeast Iran, which are absent in the Pakistani Makran, to the east (Figure 3.2, Hunting Survey Corporation, 1960; Burg et al., 2008). The sedimentary successions in the Inner, Outer, and Coastal Makran are dominated by

Department of Earth Sciences, ETH- and University Zurich, Zurich, Switzerland

Submarine Landslides: Subaqueous Mass Transport Deposits from Outcrops to Seismic Profiles, Geophysical Monograph 246, First Edition. Edited by Kei Ogata, Andrea Festa, and Gian Andrea Pini.
© 2020 American Geophysical Union. Published 2020 by John Wiley & Sons, Inc.

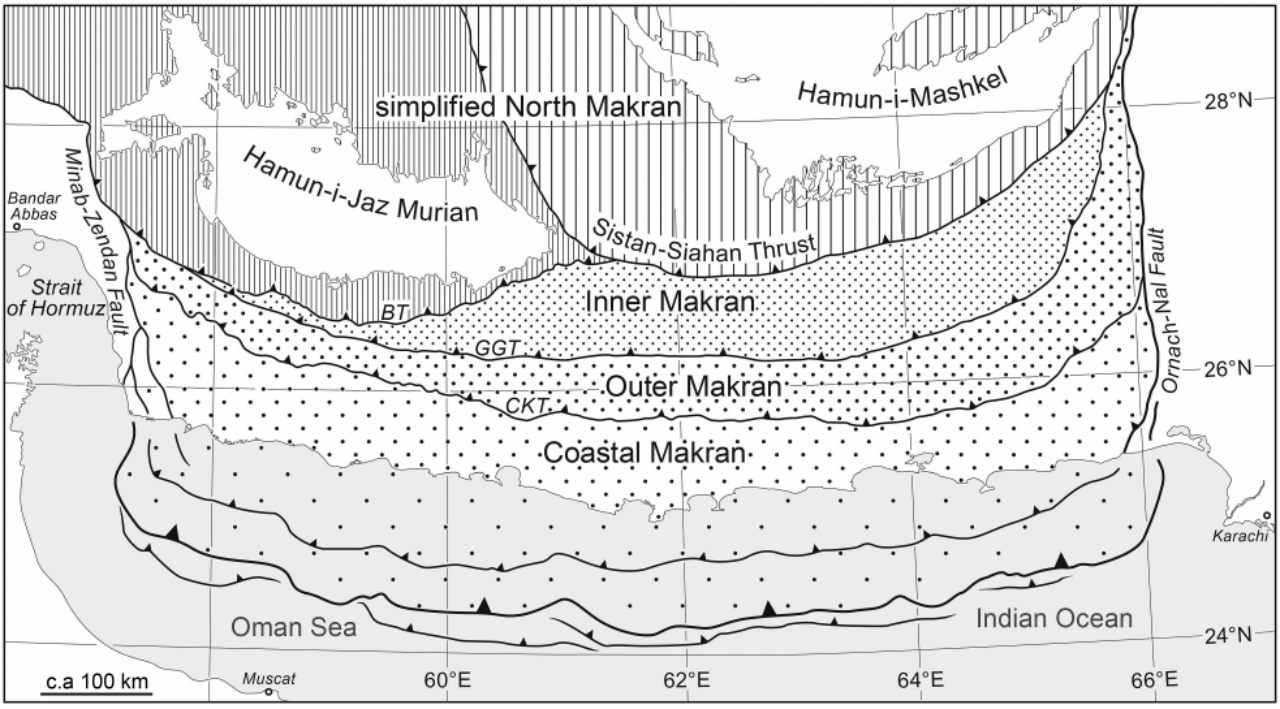


Figure 3.1 General setting and simplified map of the tectono-stratigraphic zones forming Makran accretionary wedge. BT, Bashakerd Thrust; GGT, Ghasr Ghand Thrust; CKT, Chah Khan Thrust. Source: Offshore structures from Ellouz-Zimmermann et al. (2007b), Grando and McClay (2007), and the National Iranian Oil Company (unpublished).

Eocene, Oligocene, and Miocene deposits, respectively (Dolati, 2010). Early Eocene mudstones and radiolaritic shales interlayered with thin-bedded sandstones and ash layers (pelagic/hemipelagic outer fan lobe systems in the scheme of Mutti and Ricci-Lucchi (1978)) grade upward into late Eocene-Oligocene shales with progressively coarser and thicker-bedded turbiditic sandstones, including conglomeratic channels (outer fan followed by inner fan). This evolution indicates progradation of a submarine fan in a deep marine environment (e.g., Mohammadi et al., 2016). Late Oligocene to early Miocene sequences are channelized sandstone-dominated turbidites with abundant sole marks, slumps, and cross-stratification indicating strong and erosive currents during sediment transport (delta slope and inner to supra fan environments). In the late Miocene, coarse cross-bedding, symmetrical ripples, and herringbone structures document the local influence of waves and tidal currents. Well-preserved plant fossils (leaves and wood) suggest deposition near land. Intercalated and patchy coral algal limestones (McCall, 1985a; McCall et al., 1994), typically with a muddy matrix, document deposition in the photic zone on a dominantly siliciclastic shelf. The occurrence of ubiquitous secondary gypsum points to primary deposition in a basin with restricted water circulation under arid conditions. The upper Miocene is usually marl dominated, which suggests high sedimentation rates and possibly dysoxic conditions for the black levels (Dolati, 2010; Burg et al., 2013). Mollusc shells, in particular marine gastropods, indicate a shallow shelf depositional environment. Channelized sandstone and conglomerates with pebble imbrication may be foreshore deposits. Pliocene-Pleistocene layers of oyster shells and shell fragments, bioturbation, vertical burrows, and bidirectional cross-bedding in poorly consolidated sandstones indicate, along with thick conglomerate layers, a very shallow water and intertidal depositional environment (McCall, 1985b). Late Pleistocene coarse-grained conglomerates, sandstones, and siltstones without sedimentary structure or component indicating a marine environment cover with a small angular unconformity the Miocene-Pleistocene sequences. The sedimentary facies is consistent with continental river deposition. In summary, the successive sedimentary facies record the general filling and shallowing of an oceanic basin with the southward (oceanward) migration of a foredeep, leading to the development of a late Miocene wedge-top basin. The "sedimentary mélange" described in this chapter forms part of the upper Miocene in all three zones, albeit with different structural and sedimentary contacts described

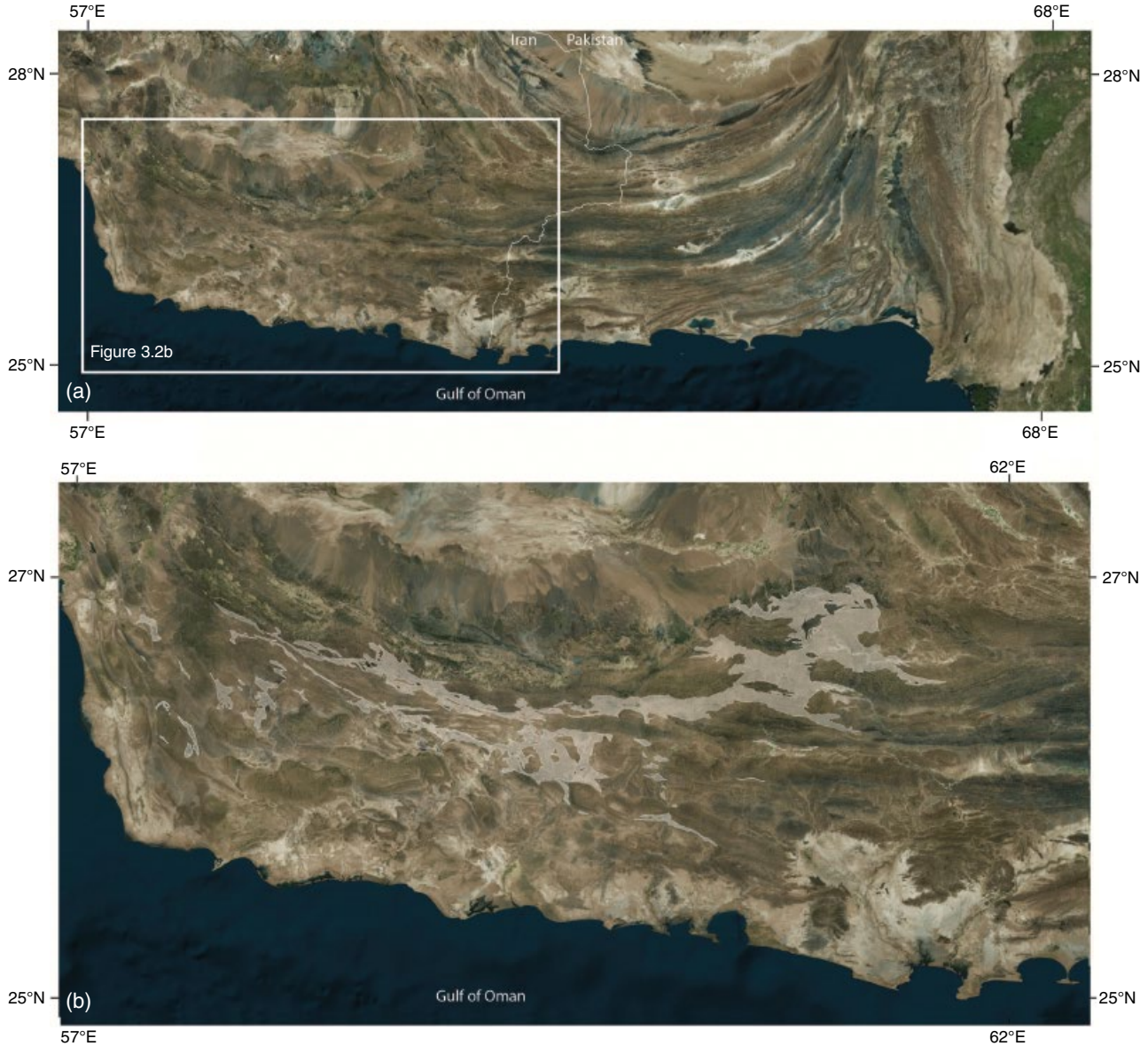


Figure 3.2 (a) Satellite image of the onshore accretionary wedge. Compare the variable terrain morphology between regular fold trends in the east (Pakistan side) and blurred trends in the west (Iran side). (b) Simplified map of the olistostrome (whitened) in the Iranian Makran. Same background image as in Figure 3.2a. Source: SASPlanet. (*See electronic version for color representation of this figure*)

in a following paragraph. This "mélange," initially ascribed to within accretionary wedge deformation and diapiric processes (McCall, 1983), was reinterpreted as a matrix-supported olistostrome based on the chaotic scattering of exotic elements of various sizes, shapes, and lithology in a muddy, shaly matrix with soft-sediment deformation structures (Burg et al., 2008). The olistostrome nature of the mélange is further confirmed by mixing of neritic, benthic, and pelagic foraminifera species (Burg et al., 2008). Its age is constrained by the under- and overlying rock units. The youngest substrate on which it rests unconformably consists of mid-Miocene sediments in Outer Makran. The oldest possible early Tortonian (c. 11.6 Ma; Burg et al., 2008) age is given by the youngest pelagic fossils found in the matrix (Burg et al., 2008). The youngest possible age of 9.6 Ma is inferred from nannofossils of the overlying marls (zone NN10; Dolati, 2010).

The present-day location of the Makran accretionary wedge reflects a southward (oceanward) migration of the subduction trench which is located offshore, to the south (White, 1982). GPS measurements document

approximately north-south convergence at a rate of c. 20 mm/a between the Arabian and Eurasian plates at the longitude of the Gulf of Oman (Masson et al., 2007). Current motions recalculated from seafloor spreading rates and fault azimuths for the major plates account for convergence rates increasing from 35.5–36.5 mm/a in the western Makran to 40–42 mm/a in the east (DeMets et al., 2010). This is consistent with an anticlockwise rotation of the rigid Arabian plate with respect to Eurasia around a pole located in Kurdistan (Hatzfeld & Molnar, 2010).

The topic of this contribution is to review field characteristics that classify the "sedimentary mélange" as an olistostrome.

3.2. GEOMETRY AND INTERNAL STRUCTURE

The "sedimentary mélange" of onshore Makran is a chaotic, non-metamorphic unit with a greenish muddy, shaly matrix without any recognizable internal stratigraphy or bedding and containing randomly mixed clasts of various age, composition (limestone, sandstone and shales, conglomerates, chert, schist, pillowed and non-pillowed lavas, gabbro, and serpentinite), shapes (rounded to angular), and sizes (from millimeter up to a few kilometer across). The "mélange" is mainly matrix supported with a matrix of pebbly mudstone (Figure 3.3). Although this formation locally shows drag folds and a distinct fissility due tectonic overprint, in particular next to faults and within regional

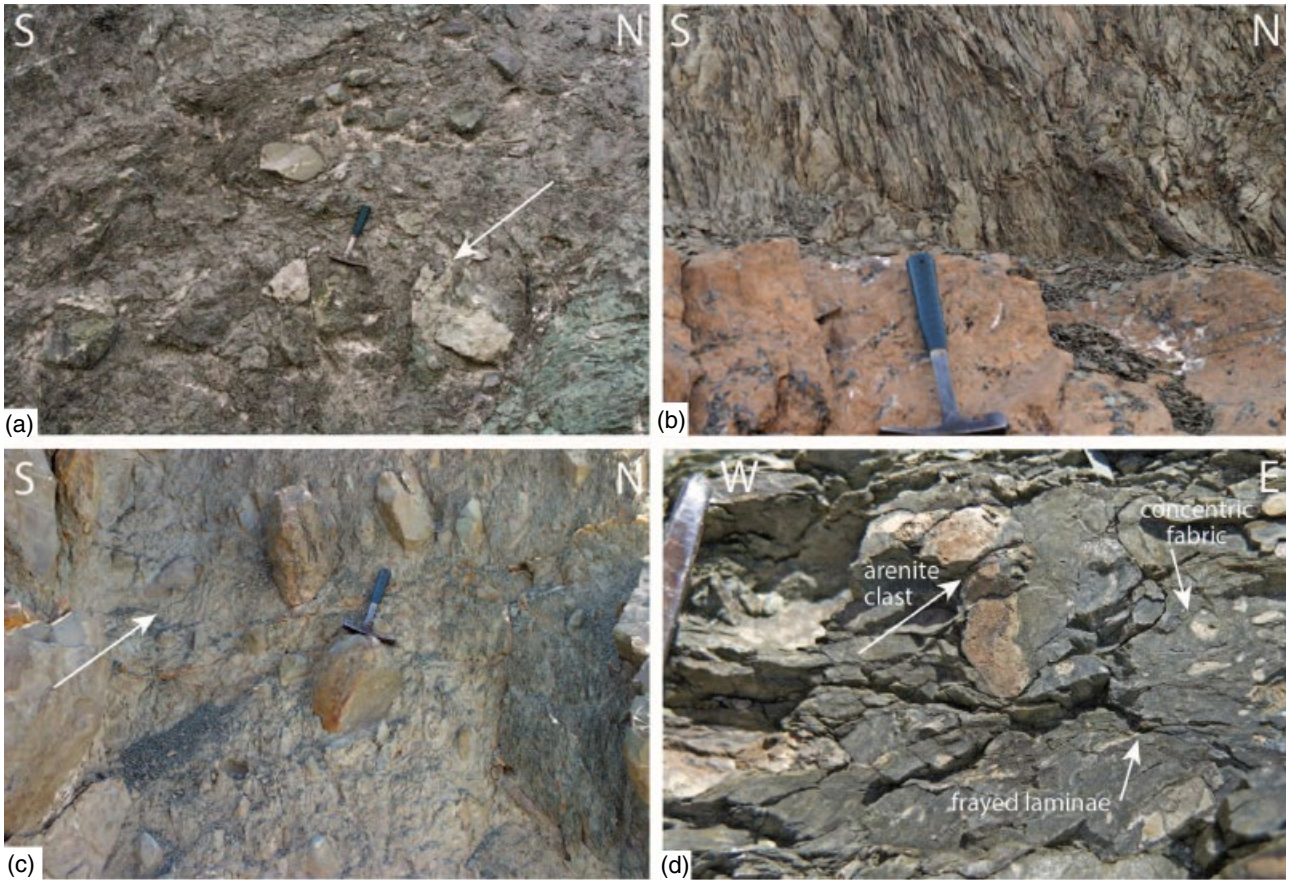


Figure 3.3 Sedimentary characteristics of the Makran olistostrome. (a) Pebbly mudstones typical of the non-foliated matrix texture. Outcrop at 26°21′24.4″N; 060°05′10.2″E; arrow: folded tail in matrix attributed to rolling (top to the south of the pink limestone clast, below). (b) Subvertical scaly fabric of the mud matrix (top part of the picture) abutting against a pink limestone clast (bottom, supporting hammer); outcrop at 26°41′55.9″N; 061°08′58.1″E). (c) Pebbly mudstones with slightly oriented matrix fabric; arrow and hammer: randomly oriented pebbly clasts of sandstone without strain shadow; outcrop at 26°41′38.3″N; 060°28′54.6″E. (d) Dark muddy matrix (outcrop at 26°28′45.6″N; 061°14′39.6″E) showing fluidal soft-sediment deformation without any tectonic overprint (concentric matrix orientation around clast and frayed laminae, arrowed). Note folded arenitic clasts, suggesting that arenite was not fully lithified at the time of redeposition. Hammer pick on the left for scale. (*See electronic version for color representation of this figure*)

east-west trending fold-hinge zones, most outcrops display structural and sedimentary criteria of an olistostrome (Flores, 1955), that is, a submarine mass flow (e.g., Festa et al., 2010). We separately describe in more details the matrix and the clasts to justify this interpretation.

3.2.1. Matrix Features

The regionally distributed, weak scaly fabric of the bedding-less matrix is, in general, a wavy, phacoidal to anastomosing spaced cleavage, without stretching lineation and independent from mapped fold axes. This matrix cleavage does not prominently wrap around the hard clasts (Figure 3.3b) as would be expected for a tectonically induced foliation. The fabric of the matrix is too weak to represent a deformation pervasive and penetrative enough to have caused the hefty scattering of clasts of any size and, more importantly, with various lithologies along strike: if clasts were due to tectonic boudinage, they would be more regular in shape, size, and spacing, and interboudins would display neck structures (e.g., Weiss, 1972) that are inexistent. In addition, the original stratigraphy would be preserved to a variable extent by boudinage processes (e.g., pp. 405–433 in Price & Cosgrove, 1990). The scaly, heterogeneous fabric may have been emphasized by later low compaction/deformation, as indicated by minor deflection against hard clasts of any size (Figures 3.3c and 3.4). However, the cleavage planes show no sign of shear or strain, for example, any linear fabric element, in particular where the matrix displays only soft-sediment structures (Figure 3.3d).

In places, the cleavage merges into isolated and locally anastomosing high-strain zones and planes identified from the more intense fabric (Figure 3.4b), occasionally glossy cleavage planes, ridge-and-groove striations, and slickensides.

3.2.2. Clastic Elements

Gravel-size grains up to several hundred meters big blocks (macroliths in the classification of Terry and Goff (2014)) are randomly distributed in the matrix. These clasts consist of ophiolitic (peridotite, gabbro, pillow lava, and massive basalt) and pelagic sedimentary rocks (radiolarian silts and cherts, biomicritic limestones) partly derived from North Makran (Figure 3.1), which also delivered marbles, rare blueschists, and andesites, together with reworked chunks of the underlying Eocene to Early Miocene turbidites (sandstone and shale; Burg et al., 2008). Some of these exotic "bodies of harder rocks" (olistoliths as described since Flores (1955)) have preserved their internal coherence. The original sedimentary facies can still be identified, in particular in limestone and turbidite blocks and slabs, sometimes in pillow lavas with their attached radiolarite cover. Globotruncana limestones are common clasts. Nummulitic limestones represent an Eocene shallow-water carbonate shelf in the source area. The youngest olistoliths found so far are Miocene wackes

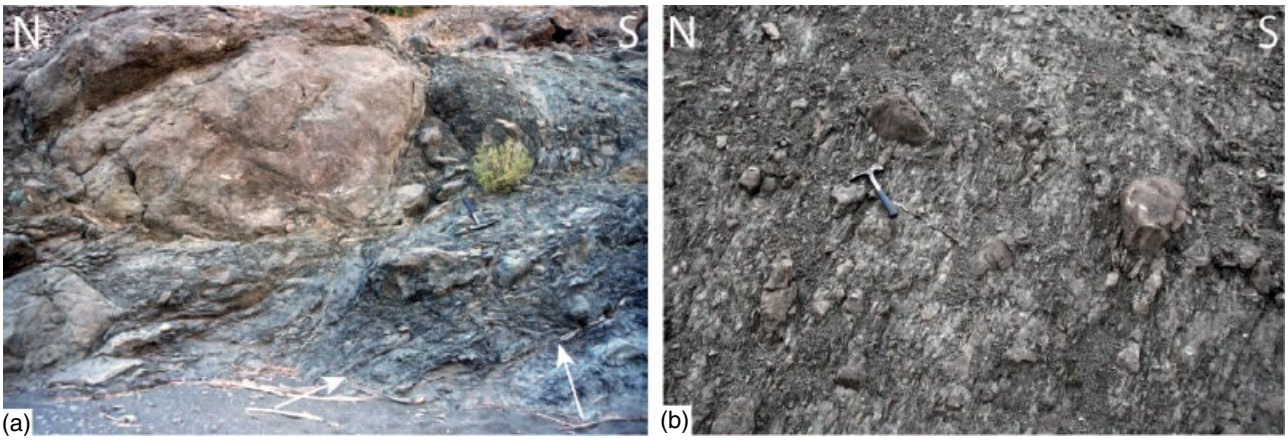


Figure 3.4 Scaly fabric of the olistostrome matrix. (a) Globotruncana-bearing pink limestone in a matrix whose spaced cleavage does not delimit pressure shadows but instead wraps around the largest block (vertical fabric in front of the block, on the right hand side, flat below); bottom right corner: the fabric intensifies into high-strain zones and planes (arrowed) with ridge-and-groove striations, slickensides, and calcite fibers. The background fabric is therefore interpreted as the flow fabric developed, while the visco-plastic matrix and the blocks were being transported together; brittle planes may be late-stage deposition or later faults; outcrop at 26°27′51.1″N; 060°01′12.2″E. Sigmoidal shapes in the matrix indicate a bulk top to the south sense of shear. (b) Scaly fabric in a shear zone or possibly emphasized by later compaction of the shaly matrix as indicated by minor deflection, yet abutments against hard sandstone pebbles of various sizes; outcrop at 26°47′31.7″N; 061°35′47.9″E. (*See electronic version for color representation of this figure*)

and limestones with benthonic and planktonic microfossils' microfauna (McCall, 1983; Dolati, 2010).

The size and lithology of the exotic blocks change from north to south with kilometer-size blocks of lavas, radiolarian cherts, and Cretaceous pelagic and Eocene-Oligocene shallow-water limestones being more abundant to the north, where outcrops are most impressive (Figure 3.5). To the south, toward the toe of the sedimentary mélange, such relatively old exotic blocks are rare and generally smaller in size. Lithologically, clasts are more monotonous; most blocks are sandstones similar to those of the underlying turbidites. This geographical gradation in the lithological and size distribution of the blocks is consistent with the bulk southward flow pattern deduced from soft-sediment structures in the shaly matrix and around the exotic blocks.

3.2.3. Clast/Matrix Relationships: Flow Direction

Some clast/matrix contacts are faulted (expectably, late tectonic faulting will be concentrated between strong blocks and weak matrix); yet, many contacts contain matrix structures such as distorted and sheared, dissociated laminae typical of soft-sediment deformation (Figures 3.3d and 3.4). Structures such as open to isoclinal folds of disrupted sandy beds floating in the nonfolded matrix (Figure 3.3a, d), ball-and-pillow structures, and contorted and frayed laminae point also to soft-sediment deformation (Figure 3.3a). Such structural relationships are taken as evidence for incorporation of exotic rocks of various lithologies and sizes within a muddy matrix (olistoliths in olistostrome). Widespread zones of pebbly mudstones (Figure 3.3a, c) are regarded as evidence for the mobile, water-saturated nature of the olistostrome matrix. The scaly fabric is interpreted as the flow fabric developed during transport of both the ductile matrix and the incorporated clasts. The different morphologies of the matrix fabric and associated higher-strain zones and planes can be related to rheological variations mirroring variations in water content and fluid migration patterns as reported from deformation experiments in variably water-saturated argillaceous rocks (Arch et al., 1988; Arch & Maltman, 1990; Dehandschutter et al., 2005). Coexistence of shear zones with a ductile fabric and undeformed zones is indeed common in a subaqueous mass and debris flows (Hampton, 1972). In view of their proximity (Figure 3.4a), some of the high-strain zones may represent kinematic effects due the adjacent and more rigid olistolith (e.g., Allen, 1982; Mills, 1983). Strain and dewatering localization into shear zones may reflect a change in bulk rheology of the matrix from a fluid suspension to a more visco-plastic material (e.g., Maciel et al., 2009; Kameda & Morisaki, 2017), as can be expected from the loss of water, while the mass flow decelerated before it was brought to a standstill. Such a rheological evolution has been argued for translation to deposition of sediment gravity flows (e.g., Postma, 1986; Ogata et al., 2012) and is the most plausible account for the most ductile shear zones identified from the lined up orientation of the matrix cleavage only (Figure 3.4b). This interpretation is more disputable for the more brittle, striated, and often calcite-fiber-bearing shear zones (Figure 3.4a), which may be either late depositional features once the general flow of a dewatered matrix has come to a halt, or postdepositional fault planes due to reactivation of pre-olistostrome thrusts (Smit et al., 2010), or simply late faults since faulting continued until the present (Dolati & Burg, 2013). Brittle zones have been discarded to sort out the bulk flow direction. The latter was inferred from displacement features (offset markers, shear bands) and local structural asymmetry (rootless



Figure 3.5 Panoramic (a) and close-ups (b and c) views of the olistostrome from 26°06′52.8″N; 059°46′58.0″E. Note the gradual change in size and composition of clasts from north to south: (b) dominantly sandstone, smaller in the south than in the north (c) where various lithologies are limestone (white-colored) radiolarites (red) and lavas (black). (*See electronic version for color representation of this figure*)

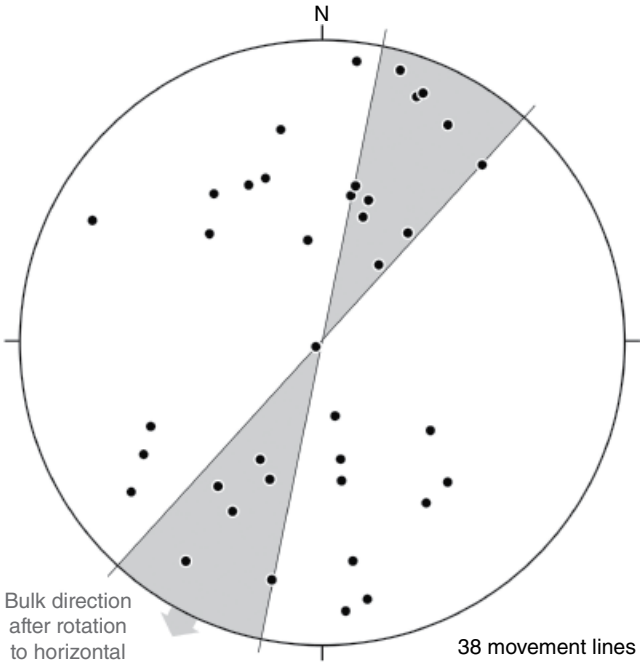


Figure 3.6 Lower hemisphere stereoplot of movement directions inferred from non-brittle structures within the olistostrome shaly matrix. Scattering is attributed to local variations in bulk southeastward flow direction and post-olistostrome folding. Plunge correction made by rotation around the local strike of the line-bearing plane.

drag and slump folds, sigmoidal scaly fabric, and indicators of clast rotation in non-lithified matrix; Figures 3.3 and 3.4). Owing to the lack of linear features, the inferred directions (orthogonal to fold axes and sigmoidal shapes, rotation direction) are scattered, but deliver a bulk southward direction (Figure 3.6).

3.3. RELATIONSHIP WITH THE HOST SEDIMENTARY SUCCESSION

The Makran olistostrome overlies Paleocene to Oligocene turbidites in the north and lower to upper mid-Miocene turbidites farther south (McCall, 1983; Dolati, 2010).

Its unconformable base is exposed in many places, whereas in others, faulted contacts represent later thrusts and faults. The erosional character of the base, with truncation of the underlying turbidites, is accompanied by the presence of intraformational clasts comparable to the underlying deposits (Figure 3.7a). Such clasts were obviously incorporated in a mobile mass flow. On a map scale, the unconformity truncates folds developed in the underlying Eocene-mid-Miocene turbidites, as readily seen on published geological maps at 1/250,000 scale (McCall & Eftekhar Nezhad, 1993), and also seals thrust zones (Burg et al., 2013).

Mostly in the south, the base is nearly parallel to the bedding of the underlying Miocene turbidites and slope deposits with apparently limited or no erosion. The contact plane is locally faulted but does not display prominent slickensides evidencing the lack of friction; however, the olistostrome muddy matrix presents a strong, but soft-sediment scaly fabric (Figure 3.7b). Altogether, the basal contact of the olistostrome reflects deep-reaching abrasion and mechanical erosion of its substratum, which was already involved in thin-skin tectonics.

In general, block-containing shales are directly covered by secondary-gypsum-rich upper Miocene marls (Figure 3.8). A coarse-grained sandstone, which is interpreted to be penecontemporaneous with the olistostrome and emplaced in a single depositional event, locally caps the olistostrome.

Neither previous studies (McCall, 1985b) nor more recent investigations (Burg et al., 2008) were able to define separate episodes of mass flow in the "sedimentary mélange." However, present-day structural and stratigraphical data do not permit deciding whether there was a single, sudden or a slower, creeping motion.

3.4. APPROXIMATE VOLUME AND COVERED AREA

The protuberant blocks of various lithologies and sizes impel to the landscape a peculiar morphology (Figure 3.6) and facilitate mapping of the sedimentary mélange with the help of high-resolution satellite images. Outcrops are found over a strike length of c. 420 km from the so-called Minab-Zendan fault zone, the western boundary of the Makran accretionary wedge, to near the Iran-Pakistan border, and over a maximum north-south width of c. 150 km, although the frontal (southern) limit, covered by younger sediments, is unknown (Figure 3.2b). That would make an area of at least 63,000 km^2. However, outcrops are patchy, and since the olistostrome rests over a folded substratum exposing older (Eocene) sequences in the north than in the south, it is likely that this submarine mass flow expanded in paleo-valleys around and between paleo-highs, so it originally did not cover the entire region. The maximum estimated thickness is 600 m in the north, pinching out toward the south. This thickness is in a paleo-canyon incised in a syncline of Oligocene sandstone-dominated turbidites. Assuming a regional average thickness of 200 m, it would make a volume of <13,000 km^3. This figure is not extraordinary for submarine mass movements (e.g., Mills, 1983; Hjelstuen et al., 2007; Festa et al., 2016), being much smaller than the dimensions of the giant olistostrome associated with the Gibraltar accretionary wedge (at least 50,000 km^3, Torelli et al., 1997).

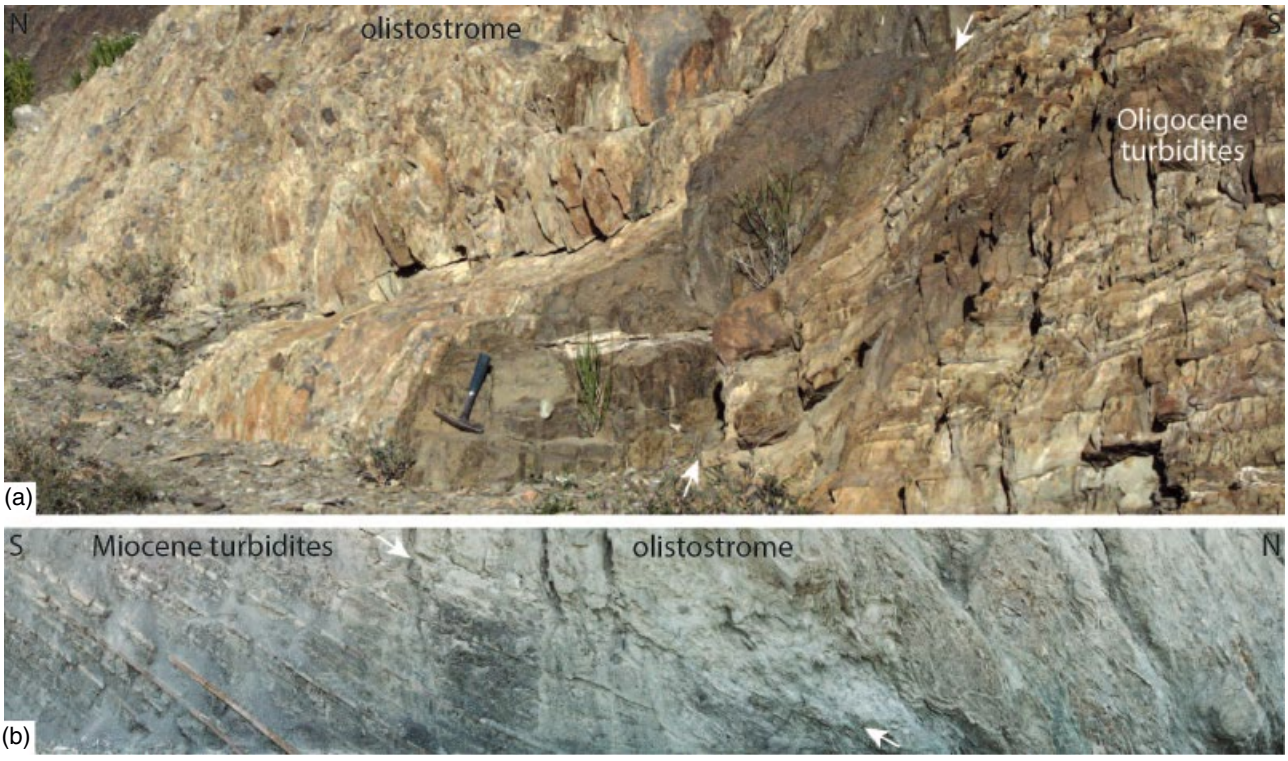


Figure 3.7 Basal contacts of the olistostrome (white arrows). (a) Unconformity on folded and foliated Oligocene turbidites with shallowly north dipping layers; the dark color of the unconformable shales on which the hammer is placed is due to weathering; outcrop at 26°28′17.2″N; 060°42′59.2″E. (b) Abrasion sheared zone at the base of the olistostrome resting on Langhian (NN5) turbidites; outcrop at 25°54′04.8″N; 060°37′00.3″E. (*See electronic version for color representation of this figure*)



Figure 3.8 Panoramic view of the top of the olistostrome from GPS point 25°55′33.7″N; 059°50′39.0″E; the geologist stands on the contact with the overlying marls. Source: Courtesy A. Dolati. (*See electronic version for color representation of this figure*)

3.5. UPDATED INTERPRETATIONS

Like the chaotic body of the Gibraltar Arc accretionary wedge, the Makran olistostrome is intercalated within the sedimentary sequence of the wedge. Although the Gibraltar Arc olistostrome has been overprinted by later deformation, its deposition along a seaward dipping surface is attributed to downslope gravitational transport in a submarine setting (Medialdea et al., 2004). The same interpretation applies to the Makran olistostrome, whose structural and textural features show that it formed by southward (trenchward) movement of a fluid to visco-plastic submarine mass flow. Contrasting to the Gibraltar Arc, the Makran

olistostrome does not overlie an undisturbed succession, but a previously folded and eroded substratum of variable ages. The olistostrome and its substratum were later folded and thrusted.

Geologists have found no field evidence for multiphase folding (McCall, 1996; Burg et al., 2013). From relationships to the regional tectonics, it has been concluded that a single phase of folding reached its climax in the Tortonian throughout the entire Makran. This tectonic instability would have triggered the mass flow.

The chaotic shaly matrix containing sandstone clasts derived from the underlying turbidites suggests that the Makran mass flow was water rich and may have been further liquefied and progressively disintegrated during its transport downslope. Hard rock elements of all sizes and shapes apparently traveled passively in the mud-rich flow, whose strength allowed for the preservation of the original internal structuring of some exotics. Clasts from blocks down to pebbles and clasts of carbonate rocks derived from the disintegration of a large platform originally involved in the sliding mass. Blocks of ultramafic and mafic igneous rocks and deep-sea radiolarites may derive from the older "colored mélange" or could be seafloor elements that were progressively incorporated into the sliding mass during its transport. Other blocks are likely derived from the slope and from older carbonate platforms incorporated into the flow. Matrix structures, in particular around blocks and near the bottom boundary, record deformational fabrics generated during transport. The process was apparently fast enough to prevent the formation of any sort of internal organization. It is impossible to determine whether the olistostrome was formed through successive sliding events or from a single massive event. Burg et al. (2008) argued that it was emplaced during one catastrophic event because they were not able to separate different episodes of mass movement nor found any undisturbed sedimentary layers between individual mass flows.

Remobilization and injection of clastic material, soft-sediment deformation, and the inclusion of coherent blocks are part of the processes involved in the downslope motion. The large lateral extent of the olistostrome and its preservation in synclines and outliers on older turbidites argue against spreading out from mud diapirs and mud volcanoes as inferred by McCall and Kidd (1982). The clear polarity from proximal to distal with an erosional base in the north evolving into a paraconformity in the south and a southward reduction in block size is another criterion against mud diapirism. Instead, the Makran olistostrome was transported for c. 150 km, which is not a disturbing magnitude since mass flows are known to travel hundreds of kilometers on the seafloor, even along very gently dipping slopes (e.g., Bugge et al., 1987; Masson et al., 1998).

3.6. CONCLUSION

Much of the "colored mélange" in the Iranian Makran is an olistostrome emplaced as a huge submarine mass flow during Tortonian-Messinian times (between 11.8 and 9.6 Ma). The matrix-supported olistostrome consists of exotic blocks and pebbly mudstones chaotically distributed within a muddy matrix which in places displays a weak scaly fabric and includes soft-sediment deformation features. Internal structures and contact with previously folded wedge sequences favor fast-rated (e.g., high-density turbidites, cohesive debris flows) rather than slow-rated (e.g., slump, creep) dominant processes. The source area for the olistostrome was an either submarine or subaerial paleo-high located to the north of the outcrops at the time of the motion of the mass flow. The prominent olistostrome records a major sediment failure that occurred shortly after the beginning of a regional folding event. This event may reflect the initiation of a new tectonic regime along the Arabia-Eurasia collision zone. An external mechanism, such as earthquakes, may have triggered the mass-wasting process.

ACKNOWLEDGMENTS

This work has been supported by the Swiss National Fond projects 2-77 634-05 and 2-77644-09, the ETH Zurich project 0-20481-08, the Geological Survey of Iran, and the National Iranian Oil Company. Two anonymous reviews have been very useful to sharpen descriptions and make interpretations more understandable.

REFERENCES

Allen, J. R. L. (1982). *Sedimentary structures: Their character and physical basis*. Amsterdam, The Netherlands: Elsevier.

Arch, J., & Maltman, A. (1990). Anisotropic permeability and tortuosity in deformed wet sediments. *Journal of Geophysical Research*, *95*, 9035–9045.

Arch, J., Maltman, A. J., & Knipe, R. J. (1988). Shear-zone geometries in experimentally deformed clays: The influence of water content, strain rate and primary fabric. *Journal of Structural Geology*, *10*, 91–99.

Bugge, T., Befring, S., Belderson, R. H., Eidvin, T., Jansen, E., Kenyon, N. H., et al. (1987). A giant three-stage submarine slide off Norway. *Geo-Marine Letters*, *7*, 191–198.

Burg, J.-P., Bernoulli, D., Smit, J., Dolati, A., & Bahroudi, A. (2008). A giant catastrophic mud-and-debris flow in the Miocene Makran. *Terra Nova*, *20*, 188–193.

Burg, J.-P., Dolati, A., Bernoulli, D., & Smit, J. (2013). Structural style of the Makran Tertiary accretionary complex in SE-Iran. In K. Al Hosani, F. Roure, R. Ellison, & S. Lokier (Eds.), *Lithosphere dynamics and sedimentary basins: The Arabian Plate and analogues* (pp. 239–259). Heidelberg, Germany: Springer Verlag.

Dehandschutter, B., Vandycke, S., Sintubin, M., Vandenberghe, N., & Wouters, L. (2005). Brittle fractures and ductile shear bands in argillaceous sediments: Inferences from Oligocene Boom Clay (Belgium). *Journal of Structural Geology*, *27*, 1095–1112.

Delaloye, M., & Desmons, J. (1980). Ophiolites and melange terranes in Iran: A geochronological study and its paleotectonic implications. *Tectonophysics*, *68*, 83–111.

DeMets, C., Gordon, R. G., & Argus, D. F. (2010). Geologically current plate motions. *Geophysical Journal International*, *181*, 1–80.

Dolati, A. 2010. Stratigraphy, structure geology and low-temperature thermochronology across the Makran accretionary wedge in Iran. In *Department of Earth sciences*, eds. ETH, 168. Zürich, Switzerland: ETH.

Dolati, A., & Burg, J.-P. (2013). Preliminary fault analysis and paleostress evolution in the Makran Fold-and-Thrust Belt in Iran. In K. Al Hosani, F. Roure, R. Ellison, & S. Lokier (Eds.), *Lithosphere dynamics and sedimentary basins: The Arabian Plate and analogues* (pp. 261–277). Heidelberg, Germany: Springer Verlag.

Ellouz-Zimmermann, N., Lallemant, S. J., Castilla, R., Mouchot, N., Leturmy, P., Battani, A., et al. (2007b). Offshore frontal part of the Makran Accretionary Prism (Pakistan): The Chamak Survey. In O. Lacombe, J. Lavé, F. Roure, & J. Vergès (Eds.), *Thrust belts and foreland basins: From fold kinematics to hydrocarbon systems* (pp. 349–364). Berlin, Germany: Springer.

Festa, A., Ogata, K., Pini, G. A., Dilek, Y., & Alonso, J. L. (2016). Origin and significance of olistostromes in the evolution of orogenic belts: A global synthesis. *Gondwana Research*, *39*, 180–203.

Festa, A., Pini, G. A., Dilek, Y., & Codegone, G. (2010). Mélanges and mélange-forming processes: A historical overview and new concepts. *International Geology Review*, *52*, 1040–1105.

Flores, G. (1955). *Les résultats des études pour les recherches pétrolifères en Sicile: Discussion*. Paper presented at 4th World Petroleum Congress: Rome, Casa Editrice Carlo Colombo Section 1/A/2 (pp. 121–122).

Gansser, A. (1955). *New aspects of the geology in Central Iran*. Paper presented at 4th World Petroleum Congress, Roma (pp. 279–300).

Grando, G., & McClay, K. (2007). Morphotectonics domains and structural styles in the Makran accretionary prism, offshore Iran. *Sedimentary Geology*, *196*, 157–179.

Hampton, M. A. (1972). The role of subaqueous debris flow in generating turbidity currents. *Journal of Sedimentary Research (SEPM)*, *42*, 775–793.

Hatzfeld, D., & Molnar, P. (2010). Comparisons of the kinematics and deep structures of the Zagros and Himalaya and of the Iranian and Tibetan plateaus and geodynamic implications. *Reviews of Geophysics*, *48*(2), RG2005.

Hjelstuen, B. O., Eldholm, O., & Faleide, J. I. (2007). Recurrent Pleistocene mega-failures on the SW Barents Sea margin. *Earth and Planetary Science Letters*, *258*, 605–618.

Hunting Survey Corporation, L. (1960). *Reconnaissance geology of part of West Pakistan: A report*. Toronto, Canada: Government of Canada for Government of Pakistan.

Kameda, J., & Morisaki, T. (2017). Sensitivity of clay suspension rheological properties to pH, temperature, salinity, and smectite-quartz ratio. *Geophysical Research Letters*, *44*, 9615–9621.

Maciel, G. F., Santos, H. K., & Ferreira, F. O. (2009). Rheological analysis of water clay compositions in order to investigate mudflows developing in canals. *Journal of the Brazilian Society of Mechanical Sciences and Engineering*, *31*, 64–74.

Masson, D. G., Canals, M., Alonso, B., Urgeles, R., & Hunerbach, V. (1998). The Canary Debris Flow: Source area morphology and failure mechanism. *Sedimentology*, *45*, 411–432.

Masson, F., Anvari, M., Djamour, Y., Walpersdorf, A., Tavakoli, F., Daignières, M., et al. (2007). Large-scale velocity field and strain tensor in Iran inferred from GPS measurements: New insight for the present-day deformation pattern within NE Iran. *Geophysical Journal International*, *170*, 436–440.

McCall, G. J. H. (1983). Mélanges of the Makran, southeastern Iran. In G. J. H. McCall (Ed.), *Ophiolitic and related mélanges* (pp. 292–299). Stroudsburg, PA: Hutchinson Ross.

McCall, G. J. H. (1985a). *Explanatory text of the Fannuj quadrangle map 1:250,000*. Tehran, Iran: Geological Survey of Iran.

McCall, G. J. H. (1985b). *Area report: East Iran Project-Area no: 1 (North Makran & South Baluchestan)*. Tehran, Iran: Heidary.

McCall, G. J. H. (1996). The inner Mesozoic to Eocene Ocean of south and central Iran and associated microcontinents. *Geotectonics*, *29*, 490–499.

McCall, G. J. H., & Eftekhar Nezhad, J. (1993). *Explanatory text of the Nikshahr quadrangle map: 1:250,000*. Tehran, Iran: Geological Survey of Iran.

McCall, G. J. H., & Kidd, R. G. W. (1982). The Makran, Southeastern Iran: The anatomy of a convergent plate margin active from Cretaceous to Present. In J. K. Leggett (Ed.), *Trench – Fore-arc geology: Sedimentation and tectonics of modern and ancient plate margins* (pp. 387–397). London, UK: Geological Society.

McCall, J., Rosen, B., & Darrell, J. (1994). Carbonate deposition in accretionary prism settings: Early Miocene coral limestones and corals of the Makran Mountain Range in Southern Iran. *Facies*, *31*, 141–178.

Medialdea, T., Vegas, R., Somoza, L., Vázquez, J. T., Maldonado, A., Díaz-del-Río, V., et al. (2004). Structure and evolution of the "Olistostrome" complex of the Gibraltar Arc in the Gulf of Cádiz (eastern Central Atlantic): Evidence from two long seismic cross-sections. *Marine Geology*, *209*, 173–198.

Mills, P. C. (1983). Genesis and diagnostic value of soft-sediment deformation structures: A review. *Sedimentary Geology*, *35*, 83–104.

Mohammadi, A., Burg, J.-P., Winkler, W., Ruh, J., & von Quadt, A. (2016). Detrital zircon and provenance analysis of Late Cretaceous–Miocene onshore Iranian Makran strata: Implications for the tectonic setting. *Geological Society of America Bulletin*, *128*(9–10), 1481–1499.

Mutti, E., & Ricci-Lucchi, F. (1978). Turbidites of the northern Apennines: Introduction to facies analysis. *International Geology Review*, *20*, 125–166.

Ogata, K., Mutti, E., Pini, G. A., & Tinterri, R. (2012). Mass transport-related stratal disruption within sedimentary

mélanges: Examples from the northern Apennines (Italy) and south-central Pyrenees (Spain). *Tectonophysics*, *568–569*, 185–199.

Postma, G. (1986). Classification for sediment gravity-flow deposits based on flow conditions during sedimentation. *Geology*, *14*, 291–294.

Price, N. J., & Cosgrove, J. W. (1990). *Analysis of geological structures*. Cambridge, UK: Cambridge University Press.

Smit, J., Burg, J.-P., Dolati, A., & Sokoutis, D. (2010). Effects of mass waste events on thrust wedges: Analogue experiments and application to the Makran accretionary wedge. *Tectonics*, *29*, 11.

Terry, J. P., & Goff, J. (2014). Megaclasts: Proposed revised nomenclature at the coarse end of the Udden-Wentworth grain-size scale for sedimentary particles. *Journal of Sedimentary Research*, *84*, 192–197.

Torelli, L., Sartori, R., & Zitellini, N. (1997). The giant chaotic body in the Atlantic Ocean off Gibraltar: New results from a deep seismic reflection survey. *Marine and Petroleum Geology*, *14*, 125–138.

Weiss, L. E. (1972). *The minor structures of deformed rocks: A photographic atlas*. Berlin, Germany: Springer Verlag.

White, R. S. (1982). Deformation of the Makran accretionary sediment prism in the Gulf of Oman (north-west Indian Ocean). In J. K. Leggett (Ed.), *Trench and fore-arc geology: Sedimentation and tectonics on modern and ancient active plate margins* (pp. 357–372). London, UK: Geological Society.

4

Spatial Distribution of Mass-Transport Deposits Deduced From High-Resolution Stratigraphy: The Pleistocene Forearc Basin (Boso Peninsula, Central Japan)

Masayuki Utsunomiya[1] and Yuzuru Yamamoto[2]

ABSTRACT

A well-established stratigraphy, based on abundant tephra marker beds, has revealed the spatial distributions and origins of basin-wide (>10 km) mass-transport deposits (MTDs) within the Pleistocene forearc basin fill that is exposed in central Japan (i.e., the Kazusa Group). Ten map-scale MTDs in the Kazusa Group were classified as either type I or III based on their lithofacies and internal structures. The type I MTDs were intercalated with alternating sandstone and siltstone and typically occur as 5–20 m thick layers of debrites consisting of blocks and rounded gravels within a muddy sand matrix. The type II MTDs were intercalated with siltstone-dominated strata and reach 100 m in thickness and consist of large (>10 m) blocks of alternating sandstone and siltstone. Index fossils, combined with the marker beds, reveal that these blocks in the type II MTDs originated from deeper strata (>60 m below the seafloor). Type III is characterized by a ramp-flat structure and repeated imbricate thrusts, identified at the map scale. The formation of the MTDs was apparently associated with rapid sedimentation and consequent generation of excess fluid pressure. These findings were based on high-resolution stratigraphy, which confirms that taking a stratigraphic perspective can contribute to a more comprehensive understanding of subaqueous mass-transport processes.

4.1. INTRODUCTION

Submarine landslides and the resulting downslope deposits (mass-transport deposits [MTDs]) develop on active continental margins (e.g., Hampton et al., 1996). These deposits have received a great deal of attention because they are associated with large amounts of sediment flux to the deep sea (Posamentier & Walker, 2006) and geohazards such as tsunamis and have the potential to destroy near-shore infrastructure, leading to major impacts on human life (Masson et al., 2006). In particular, basin-scale MTDs pose a significant hazard potential, and their preconditioning factors, such as sedimentation rate, relative sea-level change, and slope inclination, are key factors that must be considered when assessing the likelihood of failure. These factors are reflected in the long-term (at least 10–100 ky) evolution of a sedimentary basin (e.g., the development of submarine fans and tectonic uplift/subsidence).

Seismic profiles, especially offshore profiles, provide a cross section of geological structures and are useful for examining the large-scale geometry of MTDs (see the geophysical chapters). A combination of horizon picking, tectonic restoration, and chronology may enable us to study the relationship between MTD generation and long-term tectonics. On the other hand, outcrop- or core-scale observations have other advantages that allow us to examine

[1] *Research Institute of Geology and Geoinformation, Geological Survey of Japan, AIST, Tsukuba, Japan*

[2] *Department of Mathematical Science and Advanced Technology, Japan Agency for Marine-Earth Science and Technology (JAMSTEC), Yokohama Institute for Earth Sciences, Yokohama, Japan*

Submarine Landslides: Subaqueous Mass Transport Deposits from Outcrops to Seismic Profiles, Geophysical Monograph 246, First Edition. Edited by Kei Ogata, Andrea Festa, and Gian Andrea Pini.
© 2020 American Geophysical Union. Published 2020 by John Wiley & Sons, Inc.

their lithological variations, mode of deformation, and the mechanisms that trigger submarine slope failure. The integration of these two approaches and their respective advantages would lead to a better understanding of MTDs from the macroscale to the microscale. There are two ways to integrate these approaches: (i) analyses of seismic profiles along with high-resolution core sampling and (ii) field-based studies of MTDs, including the lateral distribution of each lithological unit and stratigraphic markers. In this chapter, we introduce the latter approach.

Slides, slumps, and debris flows are major mass-wasting processes. Slide is a shear failure along discrete shear planes with little internal deformation, while slump is accompanied by rotation along shear surfaces (Stow, 1986). Slumps show pervasive deformation, representing asymmetric or recumbent folds and associated thrusting (e.g., Lucente & Pini, 2003; Stow, 2005). Debris flows are flowing aggregates with non-Newtonian systems with a plastic-like yield strength, resulting in deposits with poor sorting, less internal structures, and the absence of original bedding (Leeder, 2011).

The Pleistocene Kazusa Group is exposed on the Boso Peninsula, central Japan, and has been assigned to the lower-middle Pleistocene stratotype section of the NW Pacific region because it is characterized by high sedimentation rates, abundant tephra marker beds, and planktonic microfossils that enable high-resolution stratigraphic correlations (Kazaoka et al., 2015). These correlations provide clues to the distribution, basin-scale lateral variations in texture, and detailed kinematic and mechanical characteristics of the MTDs. Such stratigraphic markers can be used to constrain the spatial extent and age of emplacement of the MTDs, and recent advances have also shown that they can be used to determine the origins of the constituent blocks and estimate the excavated volume and geometries of the MTDs. This information would help to improve our understanding of the nature of MTDs in sedimentary basins.

4.2. GEOTECTONIC BACKGROUND

The Miura and Boso areas of central Japan are located to the west of the world's only known "trench-trench-*trench*" triple junction, where the Philippine Sea Plate subducts beneath the North American Plate and the Pacific Plate subducts beneath both of the other plates (Figure 4.1a). In this unique tectonic setting, the Izu-Bonin arc on the Philippine Sea Plate is colliding with the Honshu arc on the North American Plate. Deformation processes related to the relative motions of these three plates and the arc-arc collision are recorded in the structural and paleomagnetic signatures from this area (Yoshida et al., 1984; Kotake et al., 1995; Yamamoto & Kawakami, 2005; Kanamatsu & Herrero-Bervera, 2006).

The Mineoka ophiolite complex divides the geology of the Miura and Boso peninsulas into two broad parts. To the south of the complex are two accretionary complexes and trench-slope cover sediments (Saito, 1992; Yamamoto & Kawakami, 2005; Yamamoto et al., 2005, 2017, 2018; Kawakami & Shishikura, 2006; Yamamoto, 2006). To the north of the complex lies a post-middle-Miocene forearc basin (Mitsunashi et al., 1979; Nakajima et al., 1981; Suzuki et al., 1995; Nakajima & Watanabe, 2005) composed of the middle Miocene to upper Pliocene Miura (Awa) Group in its southern part and the Pleistocene Kazusa Group and the overlying Pleistocene Shimosa Group in its northern part (Nakajima & Watanabe, 2005).

4.2.1. Kazusa Group on the Boso Peninsula

The Pleistocene Kazusa Group is composed of a shallow- to deep-marine succession that is ~3 km thick (e.g., Ito & Katsura, 1992; Suzuki et al., 1995) in the middle of the Boso Peninsula (Figure 4.1b). The Kazusa Group is divided into 13 formations based on lithofacies and stratigraphic positions (Figure 4.1b, c). The lower and middle Kazusa Group generally consists of deep-sea (submarine fan and basin plain), upper slope, and outer shelf deposits, whereas the upper Kazusa Group comprises shallow-marine deposits (Katsura, 1984; Ito & Katsura, 1992). The Kazusa Group abuts against the older forearc basin fill of the Miura Group, resulting in the lower part of the Kazusa Group being exposed only on the eastern side of the Boso Peninsula. Immediately above the contact is the basal sandstone and conglomerate succession (the Kurotaki Formation), which is thought to be contemporaneous with the laterally adjacent turbidite successions of the lower part of the Kazusa Group (i.e., the Katsuura, Namihana, Ohara, and the lower Kiwada formations) on the eastern Boso Peninsula and the Tomiya and lower Kiwada formations on the western side of the peninsula (Mitsunashi & Suda, 1980; Nakajima & Watanabe, 2005). The paleoslope dips southeastward in the lower Kazusa Group and northeastward in the middle and upper Kazusa Group, as inferred from paleocurrent analyses of turbidites (Hirayama & Nakajima, 1977; Tokuhashi, 1992).

4.2.2. High-Resolution Stratigraphic Framework

The Kazusa Group contains numerous tephra marker beds and abundant microfossils, which have facilitated lateral stratigraphic correlations and the reliable determination of depositional ages. The Kazusa Group contains >500 tephra beds of which ~150 are local tephra marker beds that are numbered in descending stratigraphic order and prefixed with an abbreviation that indicates the formation (e.g., "Kd" indicates the Kiwada Formation; Mitsunashi et al., 1959). In cases where the number is assigned to a set of several tephra layers, the layers are

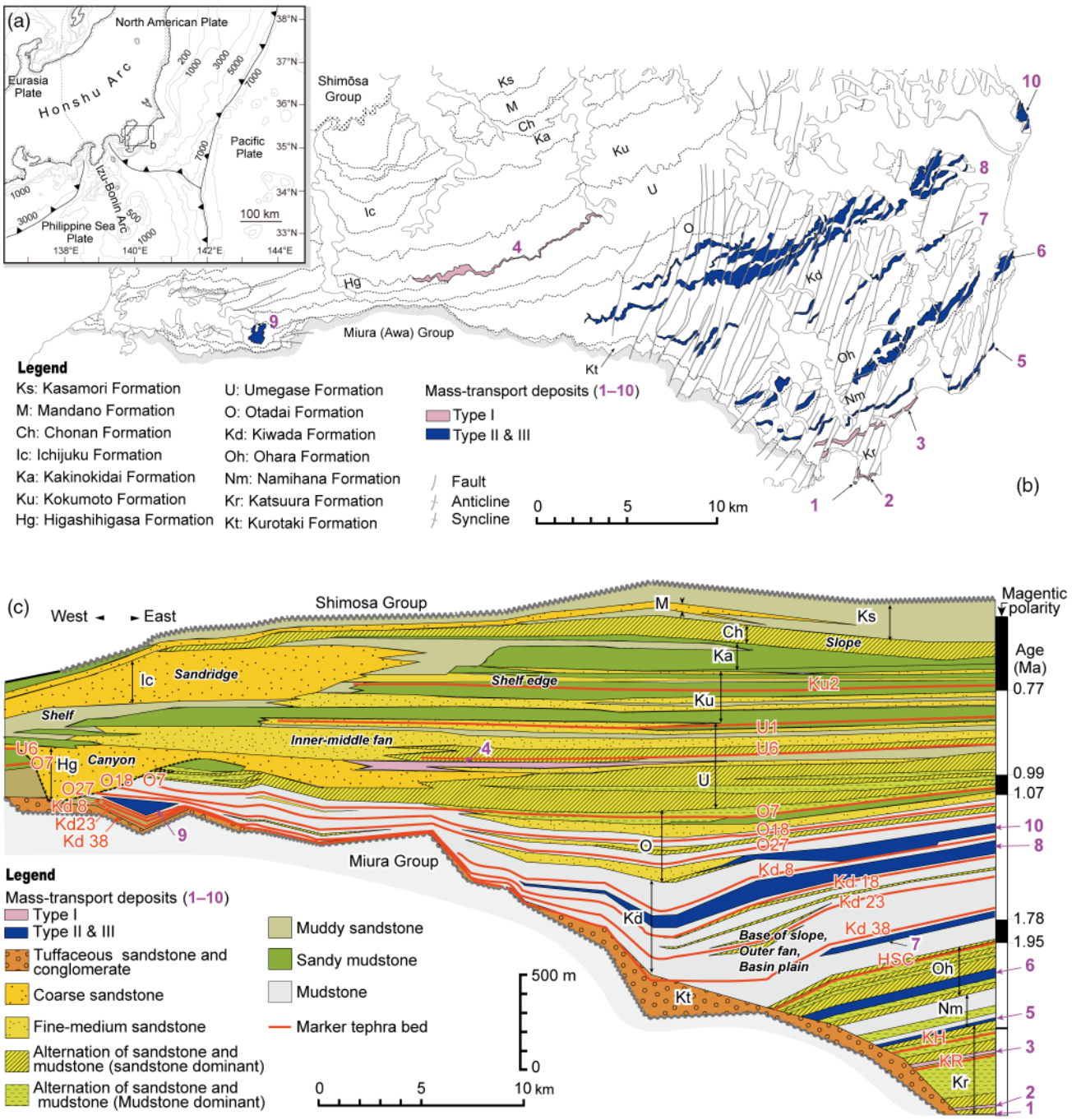


Figure 4.1 Geotectonic background of MTDs in forearc basin fill, Kazusa Group, on the Boso Peninsula, central Japan. (a) Present-day plate configuration showing the tectonic setting of central Japan. (b) Geological map of the Pleistocene Kazusa Group showing the distribution of MTDs. The base geological map is from this study (eastern part of the map), Mitsunashi et al. (1962; central part), and Nakajima and Watanabe (2005; western part). MTDs described in this chapter are numbered 1–10 in ascending stratigraphic order. (c) Stratigraphic east-west cross section and background sedimentary facies indicative of the sedimentary environment of the Kazusa Group on the Boso Peninsula. Lithology is based on this study (eastern part of the cross section), Suzuki et al. (1995; central part), and Nakajima and Watanabe (2005; western part). Magnetostratigraphy is after Niitsuma (1976), Tsuji et al. (2005), and Suganuma et al. (2015). Sedimentary environments are after Katsura (1984) and Ito and Katsura (1992).

distinguished using letters at the end of the code, in descending stratigraphic order (e.g., Kd8A, Kd8B; Satoguchi, 1995). These tephra beds include regionally widespread tephra beds that have been correlated with other major Pleistocene sedimentary basins across the Japanese islands (Satoguchi & Nagahashi, 2012; Ito et al., 2016; Tamura et al., 2019).

Tracing the tephra marker beds enables the creation of continuous composite sections, and, consequently, there have been numerous stratigraphic studies of the Kazusa Group based on sequence stratigraphy (Ito & Katsura, 1992), microbiostratigraphy (Oda, 1977; Sato & Takayama, 1988; Sato et al., 1988; Utsunomiya et al., 2017), magnetostratigraphy (Niitsuma, 1976; Okada & Niitsuma, 1989; Kusu et al., 2014, 2016; Suganuma et al., 2015), and oxygen isotope stratigraphy (Okada & Niitsuma, 1989; Pickering et al., 1999; Tsuji et al., 2005; Nozaki et al., 2014). The depositional age of the Kazusa Group on the Boso Peninsula is estimated to be 2.4–0.45 Ma (Ito et al., 1992; Nakazato & Sato, 2001). The sedimentation rates, without considering consolidation, are 0.5 m/ky for the lower Kazusa Group and 2–3 m/ky for the middle and the upper Kazusa Group (Kazaoka et al., 2015).

This stratigraphic framework has been used to constrain the stratigraphic positions and lateral extent of sedimentary units. For example, the individual turbidite layers in the middle Otadai Formation have been traced laterally for more than 38 km based on the correlation of tephra beds (Hirayama & Nakajima, 1977). In addition, MTDs in the Kiwada and Umegase formations have been traced laterally for more than several kilometers (Koike, 1955; Mitsunashi et al., 1962; Ogiwara & Ito, 2011).

4.3. DISTRIBUTION AND CHARACTERISTICS OF MTDS IN THE KAZUSA GROUP

The high-resolution stratigraphy from the study area also enables correlation of the sporadically exposed MTDs, which makes it possible to examine the lateral distribution of each MTD. Identification of marker beds in the coherent layers just above or below the MTDs indicates whether the MTDs developed in the same time interval or during different intervals. Similar approaches have also been reported from accretionary prism and trench-slope sediments (Yamamoto et al., 2009; Yamamoto & Kawakami, 2014). Using this approach, we identified at least 10 large-scale MTDs distributed laterally over more than 10 km (Figure 4.1b, c) in the Kazusa Group. Table 4.1 lists the stratigraphic positions in which the MTDs developed. Basin-scale MTDs are restricted to the slope and deeper marine sequences of the lower and middle parts of the Kazusa Group (Figure 4.1b, c). The east-west cross section in Figure 4.1c shows the lateral distribution and stratigraphic position of the MTDs. In this chapter, the MTDs are divided into three types based on the lithological composition of the constituent blocks and surrounding matrix.

4.3.1. Type I

The type I MTDs in the Kazusa Group are characterized by debrite showing block-in-matrix texture (Figure 4.3a–c). They are intercalated within the Katsuura and Umegase formations (Figure 4.1b, c). The type I MTDs are typically represented by a layered body, 5–20 m thick, in which the matrix consists of muddy sand or sandy mud with a wide variation in mud content. Abundant rounded gravels (granule-pebble in size) and bioclasts are scattered throughout the matrix (Figure 4.3b, c). The gravels are composed of chert, volcanic and plutonic rocks, and metamorphic rocks (e.g., hornfels; Koike, 1955). The bioclasts are composed mainly of mollusks (e.g., oysters) and echinoids that were probably derived from a shallow-marine environment, and all had been affected by dissolution, fragmentation, and abrasion. Rounded gravel clasts were not observed in the background strata. The blocks are less than 10 m long (long axis) and consist of siltstone, sandstone, and alternating beds of sandstone and siltstone (Figure 4.3a–c). Rolled-up sandstone blocks were observed in the sand-rich intervals (Figure 4.2a). The MTDs are overlain by turbidities with a lens-like geometry that seem to have filled depressions in the highly irregular upper surfaces of the MTDs (e.g., Yamamoto et al., 2007, 2009).

The MTDs in the Katsuura Formation, which were first investigated by Koike (1955), correspond to the type I MTDs as defined in this chapter. The MTDs can be traced laterally for more than 12 km in the same stratigraphic positions, and their distribution extends to the eastern offshore area. Other type I MTDs in the Umegase Formation can also be traced laterally for 12 km along the overlying tephra marker bed U6 (Mitsunashi et al., 1962; Figure 4.1b, c).

4.3.2. Type II

The type II MTDs consist of folded blocks that range from tens of centimeters to more than tens of meters in width and thickness, in a sandy mud matrix commonly containing volcaniclastics (e.g., pumice grains and euhedral crystals). The type II MTDs are intercalated within the Ohara and Kiwada formations (Figure 4.1b, c). Based on the lateral correlation of the tephra marker beds, this type of MTD can be traced laterally for more than several tens of kilometers (Figure 4.1b, c). The overall thickness of these MTDs ranges from ~20 to 100 m. They contain blocks characterized by folding, internal minor faulting, different attitude of bedding planes from the general trend, and occasionally overturn (Figure 4.3f, g; Utsunomiya, 2018).

Table 4.1 MTDs in the Kazusa Group on the Boso Peninsula

MTD No.	Stratigraphic Level	Age (Ma)	Lateral Distribution (km)	Thickness (m)	Facies Type	References	Figures and the Locality (Latitude, Longitude)
1	Lowermost Katsuura Formation	2.3–2.4	>0.1	5	Type I	Kamiya et al. (2018)	Figure 4.3a: Cape Hachiman (35°08′06″N, 140°18′37″E)
2	Katsuura Formation	2.3–2.4	>1.5	10	Type I	Koike (1955)	Figures 4.2a and 4.3b: Sea cliff near the Katsuura lighthouse (35°08′19″N, 140°18′57″E)
3	Katsuura Formation	2.2–2.3	>12	20	Type I	Koike (1955) and Kamiya et al. (2018)	Figure 4.3c: Sea cliff at Hebara (35°10′15″N, 140°20′28″E)
4	Umegase Formation	1.0	12	Tens of meters in total	Type I	Mitsunashi et al. (1962) and Mitsunashi and Kakimi (1964)	–
5	Lowermost Namihana Formation	2.1	>15	10	Type II	Koike (1955) and Kamiya et al. (2018)	Figure 4.3d and e: Misone, Isumi City (35°12′09″N, 140°23′36″E)
6	Ohara Formation	2.0	>20	50–100	Type II	Kamiya et al. (2018)	–
7	Between Kd39-Kd38 tephra beds middle Kiwada Formation	1.76–1.75	>20	~10	Type II	–	–
8	Between Kd18-Kd8 tephra beds middle Kiwada Formation	1.3	>20	30–100	Type II	Utsunomiya (2018)	Figure 4.3f: Ohno, Isumi City (35°15′06 N″, 140°17′37″E) Figure 4.3g, h: Ohno, Isumi City (35°15′04 N″, 140°17′41″E)
9	Between Kd8-O27 tephra beds uppermost Kiwada Formation	1.2	2	Up to 120	Type II	Kishi and Masuda (1991), Nakajima and Watanabe (2005), and Ogiwara and Ito (2011)	–
10	Between Kd8-O27 tephra beds uppermost Kiwada Formation	1.2	>20	40 (Cape Taito), 70 (Otaki)	Type III (slide)	Yamauchi (1969), Fukuda et al. (2015), and Utsunomiya et al. (2018)	Figure 4.2b, Cape Taito (35°18′43″N, 140°24′48″E) Figure 4.2i, Otaki Town (35°14′35″N, 140°15′04″E)



Figure 4.2 Outcrops where different types of MTDs are typically exposed. (a) An ~10 m thick MTD consisting of a muddy sand and sandy mud matrix with rounded gravels and rolled-up sandstone blocks (MTD-2: type I). (b) Flat-ramp geometry in the slide body (MTD-10: type III). The block slid to the north and was duplicated by imbricate thrusts.

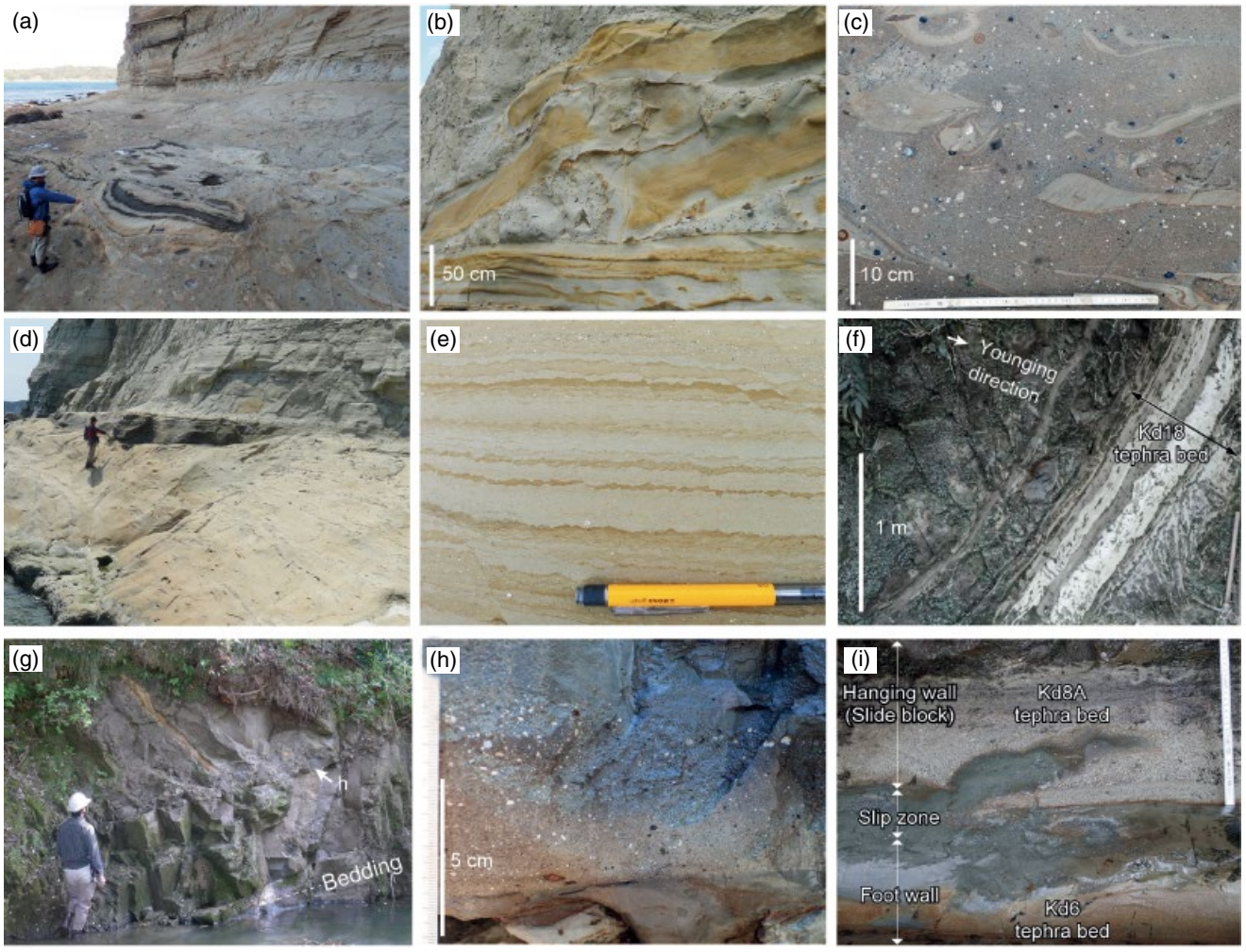


Figure 4.3 Outcrops where MTDs of each type are typically exposed. (a) An ~5 m thick MTD consisting of clastic blocks and a muddy sand and sandy mud matrix associated with well-rounded gravels (granule to pebble in size) and bioclasts (e.g., molluscan fossils; MTD-1: type I). The person is pointing at a block of alternating sandstone and mudstone in the matrix that is a few meters long. (b) Close-up photograph showing the basal part of a type I MTD. Location is shown by white arrow in Figure 4.2a. The matrix components (muddy sand and sandy mud including rounded gravels) were emplaced under the sandstone blocks (MTD-2: type I). (c) Mud clasts showing cohesive deformation and rounded gravels (MTD-3: type I). (d) Person pointing at lenticular-shaped turbidite filling depressions in the highly irregular upper surface of MTD-5 (type II). (e) Example of blocks representing sheared texture in MTDs. Laminated siltstone cut by numerous R′ shear bands with 2–10 mm displacement (MTD-5: type II). (f) Photograph of an overturned siltstone block containing the tephra bed Kd18 in MTD-8 (type II). (g) Photograph of the base of an MTD that appears to be bedding parallel to the underlying strata (MTD-8: type II). Note the oblique contact between the tephra bed in the block and the underlying strata. (h) Close-up photograph of (g), showing the basal slip zone composed of poorly sorted particles of silt and volcaniclastic material (mainly pumice grains). The location is shown by the white arrow in (g). (i) Basal slip plane of the slide block immediately above tephra bed Kd6 in the background strata and overlying tephra bed Kd8A in the slide block (MTD-10: type III). Note the sedimentary dykes injected into the basal part of the slide block. (*See electronic version for color representation of this figure*)

Their pervasive deformations indicate they are classified as slumps (Figure 4.3d–g). The basal slip zone is composed of poorly sorted particles of silt and volcaniclastic material (mainly pumice grains; Figure 4.3h). As with the type I MTDs, the tops of the slump deposits are overlain by turbidite sandstone layers (Figure 4.3d), and the siltstone blocks commonly show pervasive internal shearing (Figure 4.3d, e). The base of each slump is typically parallel to the underlying strata (Figure 4.3g).

Many tephra beds are intercalated within the larger blocks (>10 m), and this enabled us to identify the stratigraphic origins of the component blocks. For example, MTD-8 contains abundant tephra marker beds. Some of the tephra beds in the blocks show unique lithology, shapes of glass shards, and mineral compositions and so can be correlated with the underlying (i.e., older) Kd32, Kd31, Kd23, and Kd18 tephras (Figure 4.3f). In addition, the calcareous nannofossil *Gephyrocapsa* spp. in the underlying strata shows an upward increase in maximum size, from <3.5 to >6 μm (Figure 4.4, after Utsunomiya (2018)). Although the MTDs are intercalated in the horizon characterized by the large (>5.5 μm) *Gephyrocapsa* spp. zone, the blocks contain *Gephyrocapsa* spp. showing a wide variety of maximum sizes (<4 to >6 μm), as well as the extinct species *Calcidiscus macintyrei*. These calcareous nannofossil assemblages are consistent with the occurrence of the older marker beds in the large blocks. Based on this evidence, Utsunomiya (2018) concluded that the components of MTD-8 were remobilized from more than 60 m below the pre-MTD seafloor, leading to deeply excavated slope failure (Figure 4.5b).

4.3.3. Type III

We were able to trace MTD-10 laterally along the stratigraphic interval between the tephra marker beds Kd8A and O27. Its lateral distribution exceeds 20 km, and it extends to the offshore area east of the peninsula. This MTD was characterized by a flat-ramp structure and folded strata with little internal deformation above the basal slip zone (Figure 4.2b). Therefore, this MTD was generated by a submarine landslide associated with a localized basal shear plane.

The mode of deformation of MTD-10 can be clearly observed along the sea cliff exposure at Cape Taito (Figure 4.2b) and has been already described by Yamauchi (1969) and Fukuda et al. (2015). According to Fukuda et al. (2015), MTD-10 exposed at Cape Taito has a run-out length of ~5 km and 3×10^7 m^3 in volume, and the slope gradient of the original outer fan is estimated to be between 0.31° and 0.46°. The lateral extension of the MTD, around 15 km west of Cape Taito, has been described as the Otaki MTD (Utsunomiya et al., 2018). The geometry of the basal imbricate thrust indicates that the sliding direction was to the north. Although oblique to the paleoflow from turbidites of the Otadai Formation (Hirayama & Nakajima, 1977), this direction is consistent with the overall migration of the depocenter (Mitsunashi & Yamauchi, 1988).

The slide plane was located within different horizons at the two sites described above, that is, immediately

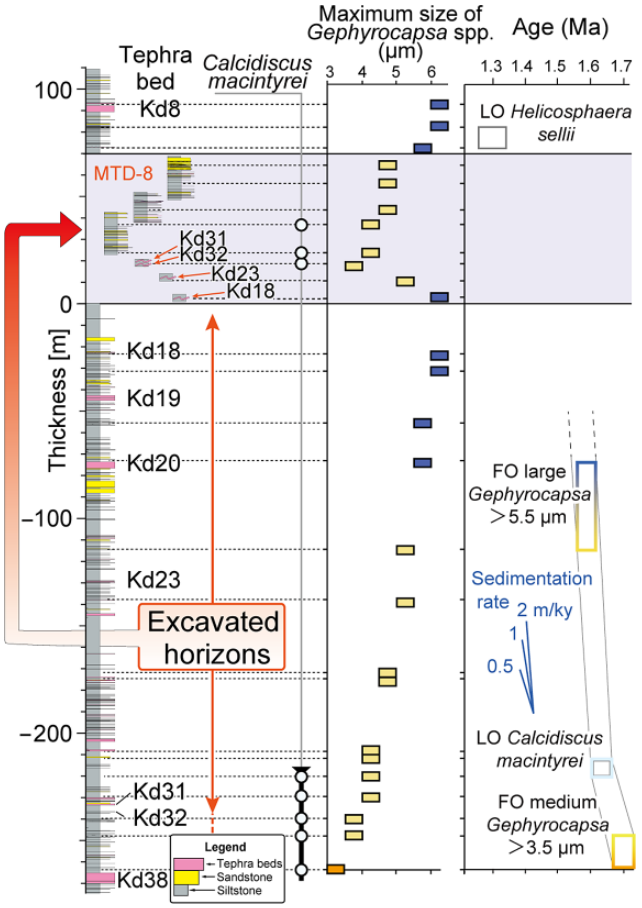


Figure 4.4 Stratigraphy of MTD-8 and model of the cause of submarine slope failure, edrawn from Utsunomiya (2018). Also shown is an integrated lithological column including calcareous nannofossil biostratigraphic data. In the strata underlying MTD-8, *Gephyrocapsa* spp. shows a gradual increase in maximum length to >6 μm, and *C. macintyrei* disappears. Tephra beds and calcareous nannofossil assemblages in blocks in the MTD indicate the locations of the original horizons (excavated horizons). Astronomically tuned ages of nannofossil biohorizons are after Raffi et al. (2006). FO and LO indicate the first and last occurrence datum, respectively.

below tephra marker bed Kd8A in the westernmost outcrop and 20 m above Kd8A at Cape Taito, where it exhibits a staircase-like geometry (Figure 4.5c). At both sites, the slide planes are located immediately below pumice-rich coarse-ash and lapilli tephra beds (Fukuda et al., 2015; Utsunomiya et al., 2018), suggesting that the lithological boundaries between the coarse-ash to lapilli tephra beds and underlying silt acted as slide planes in preference to other horizons. Sedimentary dykes intruded the slide blocks from the slip zone (Figure 4.3i), which

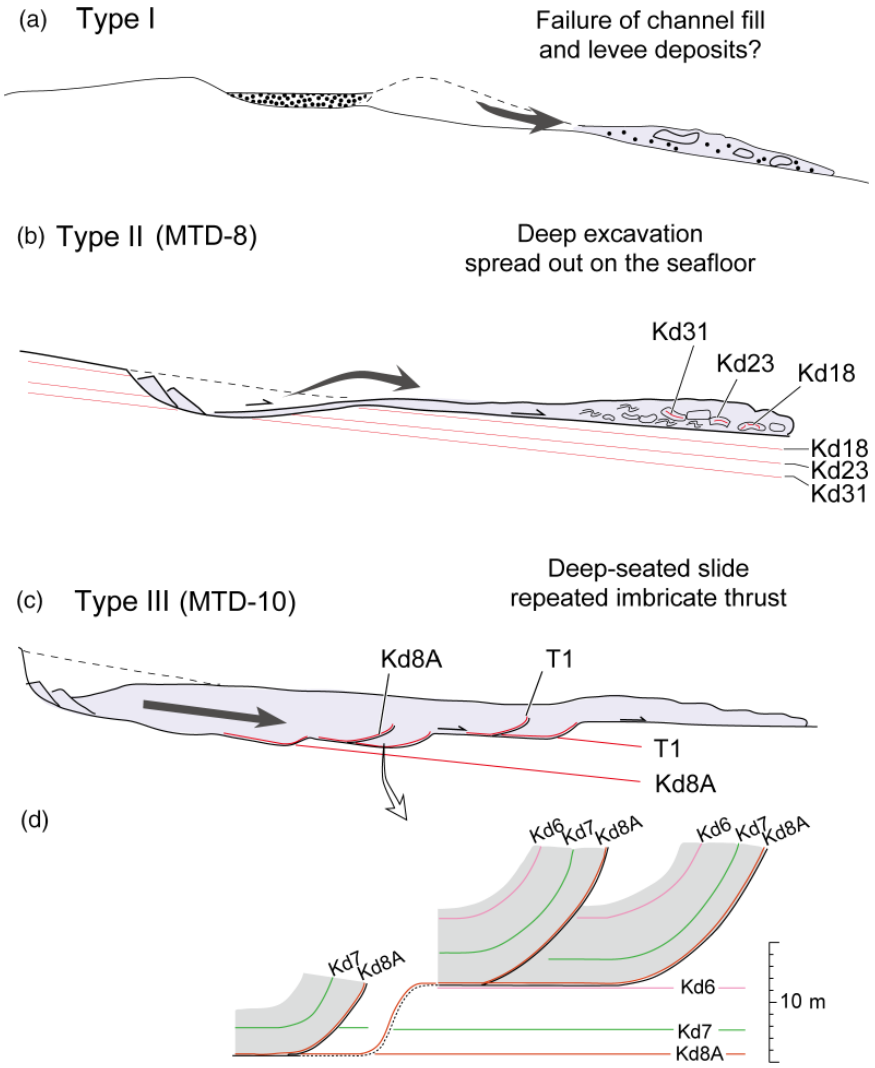


Figure 4.5 Schematic models of the submarine landslides that produced the MTDs in the Kazusa Group. (a) Type I model showing the failure of channel-fill and channel-wall deposits, based on the assumption that the rounded gravel clasts were derived from channel-fill deposits. (b) Schematic representation of a deep-excavated slope failure that resulted in MTD-8, a type II MTD. (c, d) Model describing the formation process of MTD-10, a type III MTD (slide). T1 represents tephra bed 1 described by Fukuda et al. (2015).

indicates pore pressure within the slip zone (Utsunomiya et al., 2018).

4.4. SUMMARY AND DISCUSSION

High-resolution stratigraphy based on tracing many stratigraphic markers in the Pleistocene Kazusa Group (forearc basin) enabled us to laterally trace MTDs and analyze the origins of their component blocks. This provides useful information regarding the scale, geometry, failure mechanism, and transport process of the MTDs. The stratigraphic distribution of the three types of MTDs clearly reflects the background sedimentary facies.

The type I MTDs are characterized by a pebble-bearing, muddy sand matrix intercalated with sand-rich layers. The rounded granules and pebbles that characterize type I MTDs were not observed in the background strata, suggesting they originated from a submarine slope failure in pebble-rich sediment (probably channel fill; Figure 4.5a). A muddy debris flow possibly prevented the segregation and settling of the gravels during transport, owing to mixing with unconsolidated silty sediments entrained from the substrate (Crowell, 1957).

The type II MTDs are commonly intercalated within siltstone-dominated horizons (Figure 4.1b, c). The sedimentation rate of the strata below MTD-8 (type II), where these MTDs are most numerous, ranges between 0.7 and 2.7 m/ky without considering consolidation (Utsunomiya, 2018). The biostratigraphy indicates a constant sedimentation rate in the coherent layers. In addition, a near-complete tephra marker sequence was identified in MTD-8, suggesting continuous sedimentation in the excavation area until the slope failure occurred. Consolidation tests and the physical properties of the lower Kazusa Group provide evidence of excess fluid pressure, which is thought to be related to the formation of large-scale MTDs (Kamiya et al., 2018). Therefore, the rapid deposition of such fine-grained sediment and the consequent generation of excess fluid pressure apparently contributed to the formation of the deeply excavated submarine slope failure. Type II could be a distal equivalent of type III. That is, type II initiated movement as a slide and moved over a sufficiency long distance to mix and deform, leading to formation of slump texture.

The type III MTD (a slide) represented by MTD-10 is intercalated with the uppermost siltstone-dominated horizon (Figures 4.1b, c and 4.2b). Lateral correlation of coherent strata underlying MTD-10 revealed that slide planes were preferentially formed below two different coarse ashes to lapilli tephra beds, resulting in the staircase-like geometry (Figure 4.5c). High-shear-strength tephra beds would have contributed to translational mobilization of the siltstone-dominated strata. Similar flat-ramp structures, although at a different scale, are generally recognized in offshore slides characterized by a very gentle slope (e.g., Frey-Martínez et al., 2006; Morita et al., 2011, 2012). Morita et al. (2011, 2012) reported vertical parallel dykes formed by fluid escape from the basal slide plane. The sedimentary dykes were also observed in MTD-10 (Figure 4.3i), suggesting excess pore pressure within the slip zone. Therefore, MTD-10 represents a useful analogue for this kind of MTD.

This chapter has demonstrated that a high-resolution stratigraphic study of the Kazusa Group can reveal the spatial distribution of MTDs. Recently, outcrop studies of excellent exposures in cliffs (e.g., Macdonald et al., 1993; Dykstra et al., 2011), together with seismic reflection profiles from the vicinity of the outcrop (e.g., King et al., 2011), have made a significant contribution to linking geophysical data to outcrop studies. In addition to these studies, construction of a detailed stratigraphy based on marker beds represents a powerful approach to improving our understanding of the dynamics of basin-scale submarine slope failures. Recent advances in the study of MTDs within the Kazusa Group have shown that index fossils and key beds are valuable tools for identifying the stratigraphic origins of constituent blocks. Although few studies have reconstructed the biostratigraphy of blocks in MTDs (Ingram et al., 2011; Utsunomiya, 2018), this approach has great potential in terms of identifying the transport processes based on the distribution and arrangement of blocks from different depths below the seafloor. The study of MTDs from a stratigraphic perspective can contribute to a more comprehensive understanding of subaqueous mass-transport processes.

ACKNOWLEDGMENTS

We thank Kei Ogata for his great efforts in editing this book. Two anonymous reviewers are appreciated for their critical reviews and constructive comments. We thank Terumasa Nakajima for providing unpublished geological data and Ryuta Shukuwa for being kind enough to take a photograph of the sea cliff using a UAV. This study was supported by a JSPS Grant-in-Aid for Scientific Research (No. 17K18415).

REFERENCES

Crowell, J. C. (1957). Origin of pebbly mudstones. *Bulletin of the Geological Society of America*, *68*, 993–1010.

Dykstra, M., Garyfalou, K., Kertznus, A., Kneller, B., Milana, J. P., Molinaro, M., et al. (2011). Mass-transport deposits: Combining outcrop studies and seismic forward modeling to understand lithofacies distributions, deformation, and their seismic stratigraphic expression. In R. C. Shipp, P. Weimer, & H. W. Posamentier (Eds.), *Mass transport deposits in deepwater settings, Special Publication* (Vol. 96, pp. 293–310). Tulsa, OK: SEPM (Society for Sedimentary Geology).

Frey-Martínez, J., Cartwright, J., & James, D. (2006). Frontally confined versus frontally emergent submarine landslides: A 3D seismic characterization. *Marine and Petroleum Geology*, *23*, 585–604.

Fukuda, K., Suzuki, M., & Ito, M. (2015). The origin and internal structures of submarine-slide deposits in a lower Pleistocene outer-fan succession in the Kazusa forearc basin on the Boso Peninsula of Japan. *Sedimentary Geology*, *321*, 70–85. https://doi.org/10.1016/j.sedgeo.2015.03.009

Hampton, M. A., Lee, H. J., & Locat, J. (1996). Submarine landslides. *Reviews of Geophysics*, *34*, 33–59. https://doi.org/10.1029/95RG03287

Hirayama, J., & Nakajima, T. (1977). Analytical study of turbidites, Otadai Formation, Boso Peninsula, Japan. *Sedimentology*, *24*, 747–779. https://doi.org/10.1111/j.1365-3091.1977.tb01914.x

Ingram, W.C., Mosher, D.C., and Wise Jr., S.W. (2011), Biostratigraphy of an Upper Miocene mass-transport deposit on Demerara Rise, northern South American margin. In R. C. Shipp, P. Weimer & H. W. Posamentier (Eds.) *Mass transport deposits in deepwater settings, SEPM (Society for Sedimentary Geology) Special Publication. 96*, 293–310, SEPM, Tulsa, OK.

Ito, M., Kameo, K., Satoguchi, Y., Masuda, F., Hiroki, Y., Takano, O., et al. (2016). Neogene−Quaternary sedimentary successions. In T. Moreno, S. Wallis, T. Kojima, & W. Gibbons (Eds.), *The geology of Japan* (pp. 309–337). London, UK: Geological Society.

Ito, M., & Katsura, Y. (1992). Inferred glacio-eustatic control for high-frequency depositional sequences of the Plio-Pleistocene Kazusa Group, a forearc basin fill in Boso Peninsula, Japan. *Sedimentary Geology*, *80*, 67–75. https://doi.org/10.1016/0037-0738(92)90032-M

Ito, M., Kawabe, T., & Ohara, S. (1992). Sequence stratigraphic analysis of the Pliocene Kurotaki Formation, Boso Peninsula, Japan (in Japanese with English abstract). *Journal of the Sedimentological Society of Japan*, *36*, 9–17. https://doi.org/10.14860/jssj1972.36.9

Kamiya, N., Utsunomiya, M., Yamamoto, Y., Fukuoka, J., Zhang, F., & Lin, W. (2018). Formation of excess fluid pressure, sediment fluidization and mass-transport deposits in the Plio-Pleistocene Boso forearc basin, central Japan. In G. Lintern, D. C. Mosher, L. G. Moscardelli, P. T. Bobrowsky, C. Campbell, J. D. Chaytor, et al. (Eds.), *Subaqueous mass movements and their consequences: Assessing geohazards, environmental implications and economic significance of subaqueous landslides* (pp. 477). London, UK: Geological Society. https://doi.org/10.1144/SP477.20

Kanamatsu, T., & Herrero-Bervera, E. (2006). Anisotropy of magnetic susceptibility and paleomagnetic studies in relation to the tectonic evolution of the Miocene–Pleistocene accretionary sequence in the Boso and Miura Peninsulas, central Japan. *Tectonophysics*, *418*, 131–144. https://doi.org/10.1016/j.tecto.2005.12.017

Katsura, Y. (1984). Depositional environments of the Plio-Pleistocene Kazusa Group, Boso Peninsula, Japan. *Science reports of the Institute of Geoscience, University of Tsukuba, Section B: Geological Sciences*, *5*, 69–104.

Kawakami, S., & Shishikura, M. (2006). *Geology of the Tateyama district, Quadrangle Series, 1: 50,000* (pp. 82). Tsukuba, Japan: Geological Survey of Japan, AIST.

Kazaoka, O., Suganuma, Y., Okada, M., Kameo, K., Head, M. J., Yoshida, T., et al. (2015). Stratigraphy of the Kazusa Group, Boso Peninsula: An expanded and highly-resolved marine sedimentary record from the Lower and Middle Pleistocene of central Japan. *Quaternary International*, *383*, 116–135. https://doi.org/10.1016/j.quaint.2015.02.065

King, P. R., Ilg, B. R., Arnot, M., Browne, G. H., Strachan, L. J., Crundwell, M., & Helle, K. (2011). Outcrop and seismic examples of mass-transport deposits from a late Miocene deep-water succession, Taranaki Basin, New Zealand. In R. C. Shipp, P. Weimer, & H. W. Posamentier (Eds.), *Mass transport deposits in deepwater settings, SEPM (Society for Sedimentary Geology) Special Publication* (Vol. 96, pp. 311–348). Tulsa, OK: SEPM.

Kishi, M., & Masuda, F. (1991). Slump deposits of the Otsukayama Formation, Kazusa Group, Chiba (in Japanese with English abstract). *Journal of the Sedimentological Society of Japan*, *34*, 71–74. https://doi.org/10.14860/jssj1972.34.71

Koike, K. (1955). Geo-historical significance of inter-formational disturbances (in Japanese with English abstract). *The Journal of the Geological Society of Japan*, *61*, 566–582. https://doi.org/10.5575/geosoc.61.566

Kotake, N., Koyama, M., & Kameo, K. (1995). Magnetostratigraphy and biostratigraphy of the Plio-Pleistocene Chikura and Toyofusa groups, southernmost part of the Boso Peninsula, central Japan (in Japanese with English abstract). *The Journal of the Geological Society of Japan*, *101*, 515–531. https://doi.org/10.5575/geosoc.101.515

Kusu, C., Nozaki, A., Okada, M., Wada, H., & Majima, R. (2014). Lithology and upper boundary of the Olduvai Subchronozone in a core recovered from the middle Kazusa Group (Lower Pleistocene) on the Miura Peninsula, Pacific side of central Japan (in Japanese with English abstract). *The Journal of the Geological Society of Japan*, *120*, 53–70. https://doi.org/10.5575/geosoc.2014.0002

Kusu, C., Okada, M., Nozaki, A., Majima, R., & Wada, H. (2016). A record of the upper Olduvai geomagnetic polarity transition from a sediment core in southern Yokohama City, Pacific side of central Japan. *Progress in Earth and Planetary Science*, *3*, 26. https://doi.org/10.1186/s40645-016-0104-7

Leeder, M. (2011). *Sedimentology and sedimentary basins: From turbulence to tectonics* (768 pp.) (2nd ed.). Oxford, UK: Wiley-Blackwell.

Lucente, C. C., & Pini, G. A. (2003). Anatomy and emplacement mechanism of a large submarine slide within the Miocene foredeep in the Northern Apennines, Italy: A field perspective. *American Journal of Science*, *303*, 565–602. https://doi.org/10.2475/ajs.303.7.565

Macdonald, D. I. M., Moncrieff, A. C., & Butterworth, P. J. (1993). Giant slide deposits from Mesozoic fore-arc basin, Alexander Island, Antarctica. *Geology*, *21*, 1047–1050. https://doi.org/10.1130/0091-7613(1993)021<1047:GSDFAM>2.3.CO;2

Masson, D. G., Harbitz, C. B., Wynn, R. B., Pedersen, G., & Løvholt, F. (2006). Submarine landslides: Processes, triggers and hazard prediction. *Philosophical Transactions of the Royal Society of London*, *364*, 2009–2039. https://doi.org/10.1098/rsta.2006.1810

Mitsunashi, T., & Kakimi, T. (1964). On the intra-formational disturbances (in Japanese, title translated). *GSJ Chishitsu News*, *117*, 8–14.

Mitsunashi, T., Kikuchi, T., Suzuki, Y., Hirayama, J., Nakajima, T., Oka, S., et al. (1979). Surface geology. In T. Mitsunashi (Ed.), *Explanatory text of the geological map of Tokyo Bay and adjacent areas, Miscellaneous Map Series, Scale 1:100,000*. Kawasaki, Japan: The Geological Survey of Japan.

Mitsunashi, T., & Suda, Y. (1980). *The geological map of Japan, Otaki, Scale 1:200 000, 1 Sheet*. Tsukuba, Japan: Geological Survey of Japan.

Mitsunashi, T., & Yamauchi, S. (1988). Tectonic evolution of the sedimentary basin of the Kazusa Group, Kanto District, Japan. *Memoir of the Geological Society of Japan*, *2*, 29–32. (in Japanese with English abstract)

Mitsunashi, T., Yasukuni, N., & Shinada, Y. (1959). Stratigraphical section of the Kazusa Group along the shores of the Rivers Yoro and Obitsu (in Japanese with English abstract). *Bulletin of the Geological Survey of Japan*, *10*, 83–98.

Mitsunashi, T., Yazaki, K., Kageyama, K., Shimada, T., Ono, E., Yasukuni, N. et al. (1962), *Geological maps of the oil and gas field of Japan*. No. 4, Futtsu-Otaki, Scale 1:50 000, 1 sheet. Kawasaki, Japan: Geological Survey of Japan.

Morita, S., Nakajima, T., & Hanamura, Y. (2011). Submarine slump sediments and related dewatering structures: Observations of 3D seismic data obtained for the continental slope off Shimokita Peninsula, NE Japan. *Journal of Geological Society of Japan*, *117*, 95–98. (in Japanese with English abstract)

Morita, S., Nakajima, T., & Hanamura, Y. (2012). Possible ground instability factor implied by slumping and dewatering structures in high-methane-flux continental slope. In Y. Yamada, K. Kawamura, K. Ikehara, Y. Ogawa, R. Urgeles, D. C. Mosher, et al. (Eds.), *Submarine mass movement and their consequence, Advances in Natural and Technological Hazards Research* (Vol. 31, pp. 311–320). Dordrecht, The Netherlands: Springer.

Nakajima, T., Makimoto, H., Hirayama, J., & Tokuhashi, S. (1981). *Geology of the Kamogawa district, Quadrangle Series, 1: 50,000* (pp. 48). Tsukuba, Japan: Geological Survey of Japan.

Nakajima, T., & Watanabe, M. (2005). *Geology of Futtsu district, Quadrangle Series, 1: 50,000* (102 pp.). Tsukuba, Japan: Geological Survey of Japan, AIST.

Nakazato, H., & Sato, H. (2001). Chronology of the Shimosa Group and movement of the "Kashima" uplift zone, central Japan. *The Quaternary Research (Daiyonki-Kenkyu)*, *40*(3), 251–257. https://doi.org/10.4116/jaqua.40.251

Niitsuma, N. (1976). Magnetic stratigraphy in the Boso Peninsula (in Japanese with English abstract). *The Journal of the Geological Society of Japan*, *82*, 163–181. https://doi.org/10.5575/geosoc.82.163

Nozaki, A., Majima, R., Kameo, K., Sakai, S., Kouda, A., Kawagata, S., et al. (2014). Geology and age model of the Lower Pleistocene Nojima, Ofuna, and Koshiba formations of the middle Kazusa Group, a forearc basin-fill sequence on the Miura Peninsula, the Pacific side of central Japan. *Island Arc*, *23*, 157–179.

Oda, M. (1977). Planktonic foraminiferal biostratigraphy of the Late Cenozoic sedimentary sequences, central Honshu, Japan. *Science Reports of Tohoku University, 2nd Series (Geology)*, *48*, 1–72.

Ogiwara, H., & Ito, M. (2011). Origin and internal organization of widespread composite soft-sediment deformation units in a deep-water forearc basin: The lower Pleistocene Kazusa Group on the Boso Peninsula, Japan. *Sedimentary Geology*, *237*, 209–221. https://doi.org/10.1016/j.sedgeo.2011.03.003

Okada, M., & Niitsuma, N. (1989). Detailed paleomagnetic records during the Brunhes–Matuyama geomagnetic reversal, and a direct determination of depth lag for magnetization in marine sediments. *Physics of the Earth and Planetary Interiors*, *56*, 133–150. https://doi.org/10.1016/0031-9201(89)90043-5

Pickering, K. T., Souter, C., Oba, T., Taira, A., Schaaf, M., & Platzman, E. (1999). Glacio-eustatic control on deep-marine clastic forearc sedimentation, Pliocene−mid-Pleistocene (c. 1180−600 ka) Kazusa Group, SE Japan. *Journal of Geological Society*, *156*, 125–136. https://doi.org/10.1144/gsjgs.156.1.0125

Posamentier, H. W., & Walker, R. G. (2006). Deep-water turbidites and submarine fans. In H. W. Posamentier & R. G. Walker (Eds.), *Facies models revisited, Special Publication* (Vol. 84, pp. 397–520). Tulsa, OK: SEPM (Society for Sedimentary Geology).

Raffi, I., Backman, J., Fornaciari, E., Pälike, H., Rio, D., Lourens, L., & Hilgen, F. (2006). A review of calcareous nannofossil astrobiochronology encompassing the past 25 million years. *Quaternary Science Reviews*, *25*, 3113–3137.

Saito, S. (1992). Stratigraphy of Cenozoic strata in the southern terminus area of Boso Peninsula, Central Japan (in Japanese). *Contribution of Institute of Geology and Paleontology, Tohoku University*, *93*, 1–37.

Sato, T., & Takayama, T. (1988). Calcareous nannofossil zones of the Quaternary (in Japanese with English abstract). *The Memoir of the Geological Society of Japan*, *30*, 205–217.

Sato, T., Takayama, T., Kato, M., Kudo, T., & Kameo, K. (1988). Calcareous microfossil biostratigraphy of the uppermost Cenozoic formations distributed in the coast of the Japan Sea, part 4: Conclusion (in Japanese with English abstract). *Journal of the Japanese Association for Petroleum Technology*, *53*(6), 474–491. https://doi.org/10.3720/japt.53.475

Satoguchi, Y. (1995). Tephrostratigraphy in the lower to middle Kazusa Group in the Boso Peninsula, Japan (in Japanese with English abstract). *Journal of Geological Society of Japan*, *101*, 767–782. https://doi.org/10.5575/geosoc.101.767

Satoguchi, Y., & Nagahashi, Y. (2012). Tephrostratigraphy of the Pliocene to Middle Pleistocene series in Honshu and Kyushu Islands, Japan. *Island Arc*, *21*, 149–169. https://doi.org/10.1111/j.1440-1738.2012.00816.x

Stow, D. A. V. (1986). Deep clastic seas. In H. G. Reading (Ed.), *Sedimentary environment and facies* (2nd ed., pp. 399–444). Oxford, UK: Blackwell Scientific.

Stow, D. A. V. (2005). *Sedimentary rocks in the field*. London, UK: Manson Publishing.

Suganuma, Y., Okada, M., Horie, K., Kaiden, H., Takehara, M., Senda, R., et al. (2015). Age of Matuyama-Brunhes boundary constrained by U-Pb zircon dating of a widespread tephra. *Geology*, *43*, 491–494. https://doi.org/10.1130/G36625.1

Suzuki, Y., Kodama, K., Mitsunashi, T., Oka, S., Urabe, A., Endo, T. et al. (1995), *Geology of the Tokyo Bay and adjacent areas, Miscellaneous Map Series 20*, Scale 1:100 000, 2 sheets, 109 p. Geological Survey of Japan, Tsukuba, Japan (in Japanese with English abstract).

Tamura, I., Mizuno, K., Utsunomiya, M., Nakajima, T., & Yamazaki, H. (2019). Widespread tephra of the Kazusa Group distributed in the Boso Peninsula, Chiba Prefecture, Japan: Especially, tephrostratigraphy and tephra correlation of the lower part of the Kazusa Group (in Japanese with English abstract). *Journal of the Geological Society of Japan*, *125*, 23–39.

Tokuhashi, S. (1992). Paleocurrent of the turbidite sandstones in the Upper Pliocene Katsuura Formation of the lowermost Kazusa Group, Boso Peninsula, central Japan (in Japanese with English abstract). *The Journal of Geological Society of Japan*, *98*, 943–952. https://doi.org/10.5575/geosoc.98.943

Tsuji, T., Miyata, Y., Okada, M., Mita, I., Nakagawa, H., Sato, Y., & Nakamizu, M. (2005). High-resolution chronology of the lower Pleistocene Otadai and Umegase Formations of the Kazusa Group, Boso Peninsula, central Japan - Chronostratigraphy of the JNOC TR-3 cores based on oxygen isotope, magnetostratigraphy and calcareous nannofossil. *Journal of Geological Society of Japan*, *111*, 1–20.

Utsunomiya, M. (2018). Distribution, age, and origin of a submarine landslide deposit in the Pleistocene Kiwada Formation, forearc basin fill on the Boso Peninsula, east-central Japan: Constraints from tephro- and biostratigraphy. *Island Arc*, *27*, e12254. https://doi.org/10.1111/iar.12254

Utsunomiya, M., Kusu, C., Majima, R., Tanaka, Y., & Okada, M. (2017). Chronostratigraphy of the Pliocene–Pleistocene boundary in forearc basin fill on the Pacific side of central Japan: Constraints on the spatial distribution of an unconformity resulting from a widespread tectonic event. *Quaternary International*, *456*, 125–137. https://doi.org/10.1016/j.quaint.2017.05.034

Utsunomiya, M., Noda, A., & Otsubo, M. (2018). Preferential formation of a slide plane of translational submarine landslide deposits in the Pleistocene forearc basin fill exposed on central Japan. In G. Lintern, D. C. Mosher, L. G. Moscardelli, P. T. Bobrowsky, C. Campbell, J. D. Chaytor, et al. (Eds.), *Subaqueous mass movements and their consequences: Assessing geohazards, environmental implications and economic significance of subaqueous landslides, Special Publications* (pp. 477). London, UK: Geological Society. https://doi.org/10.1144/SP477.3

Yamamoto, Y. (2006). Systematic variation of shear-induced physical properties and fabrics in the Miura-Boso accretionary prism: The earliest processes during off scraping. *Earth and Planetary Science Letters*, *244*, 270–284. https://doi.org/10.1016/j.epsl.2006.01.049

Yamamoto, Y., Hamada, Y., Chiyonobu, S., Kamiya, N., Ojima, T., & Saito, S. (2017). Geothermal structure of the Miura-Boso Plate subduction margin, central Japan. *Tectonophysics*, *710–711*, 81–87. https://doi.org/10.1016/j.tecto.2016.11.004

Yamamoto, Y., Kameda, J., Fukuyama, M., & Yamaguchi, H. (2018). Initiation of tectonic mélange formation associated with the smectite–illite transition at 2–4 km depth in a subduction zone: Hota accretionary complex, central Japan. In T. Byrne, M. B. Underwood, III, D. Fisher, L. McNeill, D. Saffer, K. Ujiie, & A. Yamaguchi (Eds.), *Geology and tectonics of subduction zones: A tribute to Gaku Kimura, Geological Society of America, Special Papers* (Vol. 534, pp. 115–127). Boulder, CO: Geological Society of America. https://doi.org/10.1130/2018.2534

Yamamoto, Y., & Kawakami, S. (2005). Rapid tectonics of the late Miocene Boso accretionary prism related to the Izu-Bonin arc collision. *The Island Arc*, *14*, 178–198.

Yamamoto, Y., & Kawakami, S. (2014). Along-strike migration of intermittent submarine slope failures at subduction margins: Geological evidence from the Chikura Group, central Japan. In S. Krastel, J.-H. Behrmann, D. Völker, M. Stipp, C. Berndt, R. Urgeles, et al. (Eds.), *Submarine mass movements and their consequences, Advances in Natural and Technological Hazards Research Series* (Vol. 37, pp. 551–560). Cham, Switzerland: Springer International. https://doi.org/10.1007/978-3-319-00972-8_49

Yamamoto, Y., Mukoyoshi, H., & Ogawa, Y. (2005). Structural characteristics of shallowly buried accretionary prism: Rapidly uplifted Neogene accreted sediments on the Miura-Boso Peninsula, central Japan. *Tectonics*, *24*, TC5008. https://doi.org/10.1029/2005TC001823

Yamamoto, Y., Nidaira, M., Ohta, Y., & Ogawa, Y. (2009). Formation of chaotic rock-units during primary accretion processes: Examples from the Miura–Boso accretionary complex, Central Japan. *Island Arc*, *18*, 496–512. https://doi.org/10.1111/j.1440-1738.2009.00676.x

Yamamoto, Y., Ogawa, Y., Uchino, T., Muraoka, S., & Chiba, T. (2007). Large-scale chaotically mixed sedimentary body within the Late Pliocene to Pleistocene Chikura Group, Central Japan. *Island Arc*, *16*, 505–507. https://doi.org/10.1111/j.1440-1738.2007.00587.x

Yamauchi, S. (1969). Structural analysis of the intraformational disturbances (in Japanese with English abstract). *Journal of the Geological Society of Japan*, *75*, 293–302. https://doi.org/10.5575/geosoc.75.293

Yoshida, S., Shibuya, H., Torii, M., & Sasajima, S. (1984). Post-Miocene clockwise rotation of the Miura Peninsula and its adjacent area. *Journal of Geomagnetism and Geoelectricity*, *36*, 579–584. https://doi.org/10.5636/jgg.36.579

5

Mass-Transport Deposits as Markers of Local Tectonism in Extensional Basins

Tiago M. Alves[1] and Davide Gamboa[2]

ABSTRACT

Outcrop data from SE Crete and a high-quality seismic volume from SE Brazil are used to characterize five types of mass-transport deposits that are clear markers of tectonism in extensional basins. They include (1) carbonate blocks and breccia-conglomerates showing limited gravitational collapse; (2) disrupted blocks, carbonate megabreccias, and boulder conglomerates on tectonically active slopes; (3) blocks and debris-flow deposits accumulated distally from exposed fault scarps; (4) chaotic volumes of turbidites, chalk, and evaporites; and (5) continental/shallow-marine debris cones derived from fault scarps. At outcrop, submarine slide blocks are observed on the slopes of tectonically active basin shoulder highs. The slide blocks occur together with sandy mass-transport deposits that reflect the remobilization of "background" slope sediment (types 3 and 4). Soft-sediment deformation styles document important shearing within blocks and their basal shear zones. On 3D seismic data, early-stage mass-transport deposits reveal important faulting and the generation of a thick basal shear zone. Mass-transport deposits of types 1 and 2 alternate in space with type 4 intervals. We propose that the classification of mass-transport deposits in this work can be used to recognize syn-rift units accumulated in extensional settings throughout the world, particularly when tectonic subsidence outpaces sedimentation to hinder the deposition of "typical" syn-rift growth geometries.

5.1. INTRODUCTION

Stratigraphic intervals comprising recurrent mass-wasting deposits are accumulated in extensional basins during periods of significant tectonic activity (Kvalstad et al., 2005; Buttler & Tavarnelli, 2006; Deptuck et al., 2007; Jenner et al., 2007; Moore & Strasser, 2016; Ortiz-Karpf et al., 2018). This is also the case of Crete, where undeformed strata alternate with large, rafted slide blocks of meter to kilometer scales and associated mass-transport deposits (MTDs). These syn-rift strata were deposited during a period of intense tectonic activity associated with the onset of slab rollback under the Aegean Arc, a phenomenon that led to extensional fragmentation and rifting in what is, at present, the Aegean Sea (Brun & Sokoutis, 2010; Reilinger et al., 2010). Such syn-rift strata are now exposed because of the significant tectonic uplift recorded on Crete during the late Pliocene-Quaternary. In fact, the island of Crete comprised four distinct fault-bounded islands during late Miocene extension, and multiple outcrop and offshore locations show upper Miocene-Holocene MTDs accumulated close to active normal faults (Huson & Fortuin, 1985; Alves et al., 2007; Strozyk et al., 2010; Alves & Cupkovic, 2018).

As syn-rift strata comprise mass-wasting intervals sourced from tectonically active topography and associated fault-bounded scarps (Stewart & Hancock, 1988; Borgomano, 2000; McNeill et al., 2005; Brothers et al.,

[1] *3D Seismic Lab, School of Earth and Ocean Sciences, Cardiff University, Cardiff, United Kingdom*

[2] *Portuguese Institute for the Sea and the Atmosphere (IPMA, I.P.), Lisbon, Portugal*

Submarine Landslides: Subaqueous Mass Transport Deposits from Outcrops to Seismic Profiles, Geophysical Monograph 246, First Edition. Edited by Kei Ogata, Andrea Festa, and Gian Andrea Pini.
© 2020 American Geophysical Union. Published 2020 by John Wiley & Sons, Inc.

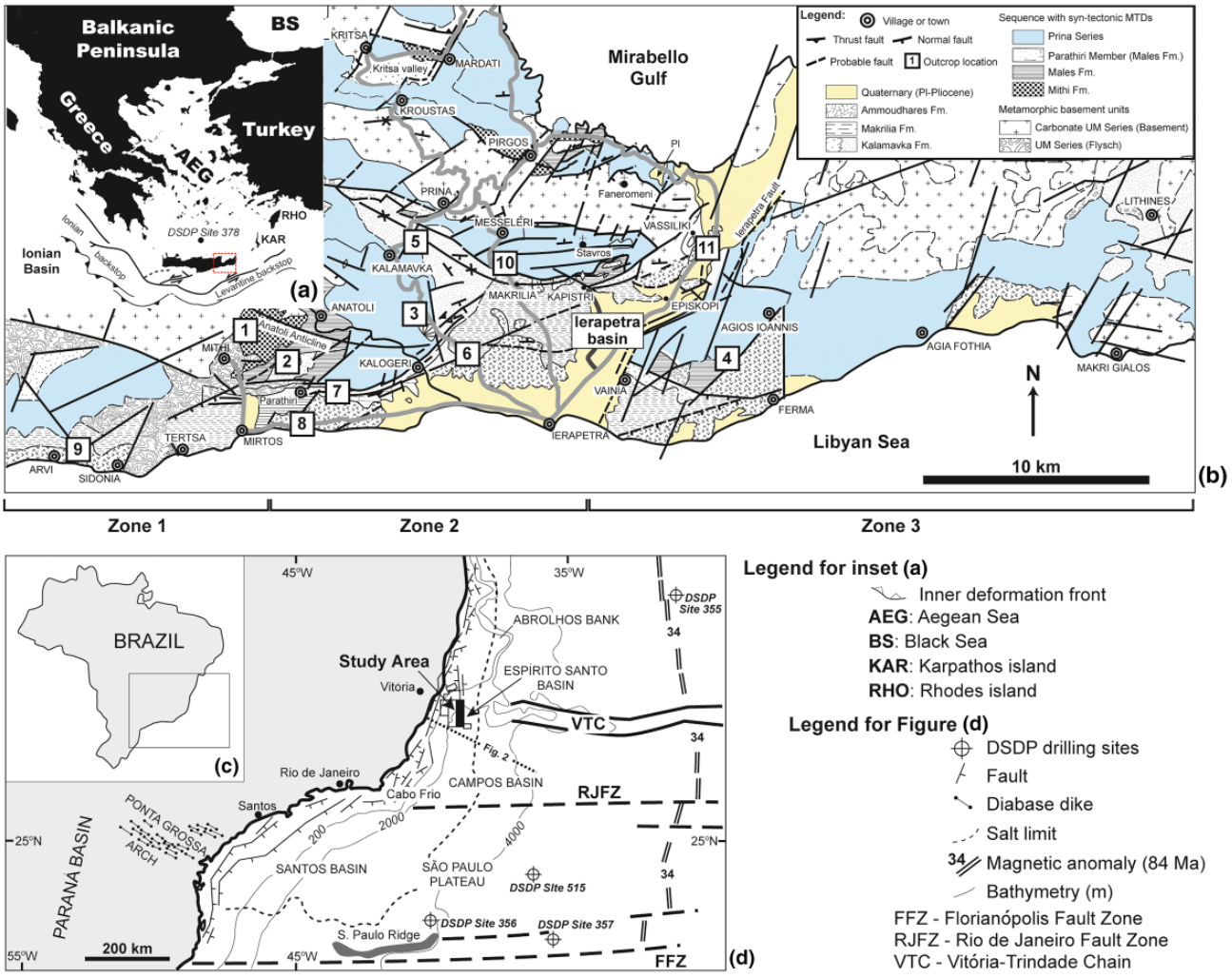


Figure 5.1 (a) Regional geological map of the southern Cretan margin highlighting the relative location of Crete in relation to the Aegean Sea, Greek and Turkish landmasses. Source: Modified from Alves and Cupkovic (2018). (b) Geological maps of SE Crete in which the study area is located. Source: Modified from Alves and Cupkovic (2018) after Postma et al. (1993). Note the location of outcrops 1–11 referred to in the text. (c) Inset showing the relative location of the SE Brazil continental margin, in which the Espírito Santo Basin is included. (d) Location map of the study area in the Espírito Santo Basin, SE Brazil. Source: Modified from Alves and Lourenço (2010).

2017), this chapter characterizes five types of MTDs in SE Crete and assesses their importance as markers of local tectonism in extensional basins. First, we document different types of MTDs accumulated in an extensional basin exposed in SE Crete; the Ierapetra Basin (Figure 5.1a, b). On Crete, we recognize the presence of thick mass-transport intervals in deepwater stratigraphic successions whenever tectonic-driven changes in slope morphology (i.e., *oversteepening*) are capable of disrupting slope strata to a greater degree, often destabilizing sediment at depths that are significantly below the paleoseafloor (see Kvalstad et al., 2005; Dunlap et al., 2010; Alves, 2015; Gamboa & Alves, 2015). This setting is particularly recorded in subsiding, sediment-starved basins during the main stages of syn-rift tectonics (e.g., Wilson et al., 2001). Later, a seismic-based example of a blocky MTD in their initial development stages is imaged on the margins of a subsiding salt withdrawal basin in SE Brazil (Figure 5.1c, d). An MTD was documented here due to the high-quality seismic data that images it; distinct blocks in this deposit have been disrupted very moderately and a well-developed basal shear zone is imaged on seismic data. The seismic example thus provides key insights on the original geometry of blocky MTDs and their basal shear zones.

Following the definition by Alves (2015), the terms "submarine slide block" and "block" refer in this work to large volumes (generally >1000 m^3 when blocks are

imaged on seismic data) of undeformed to moderately deformed strata generated in submarine environments (e.g., Ravnås et al., 1997; McLeod & Underhill, 1999; De Blasio et al., 2006). Blocks, or megaclasts, are defined as being larger than boulders (>4.1 m) and show characteristic features in deep-marine basins around the world (Blair & McPherson, 1999). In fact, blocks in deep-marine settings are often a constituent part of strata remobilized during slope instability events, called mass-transport deposits (MTDs) and mass-transport complexes (MTCs) on seismic data, or olistostromes when referring to the outcrop successions in which they are included (Dimitrijević & Dimitrijević, 1973; Buttler & Tavarnelli, 2006; Ogata et al., 2012; Okay et al., 2012; Festa et al., 2014). Accordingly, the term mass-transport deposit (MTD) refers in this chapter to a distinct volume of sediment at outcrop or seismic data that is associated with a discrete instability event (Pickering & Hiscott, 2015). MTCs correspond to recurrent instability events and occur as stacked successions of MTDs in sedimentary basins.

5.2. DATA SET AND METHODS

Two distinct data sets are analyzed in this chapter so that outcrop information can be compared and contrasted to high-quality three-dimensional (3D) seismic data. Outcrop data from late Miocene paleoslopes in SE Crete document structures and strata that are seldom observed in seismic data (Figure 5.1). Outcrop data were acquired in the Kalogeri-Myrtos-Kalamavka area, NW of Ierapetra, into Agia Fotia and Makry Gialos to the east of Ierapetra (Figure 5.1a). The approach was to map in detail any morphological features with evidence for gravitational collapse within the Prina Series and the Males, Kalamavka, Makrilia, and Ammoudhares formations (Figure 5.2a). Army maps of scale 1 : 50,000 (Hellenic Mapping and Cadastral Organization) were used for the field mapping. The relative dating of the investigated units was based on Fortuin (1977, 1978), Meulenkamp (1979), Postma and Drinia (1993), Postma et al. (1993), Ten Veen and Postma (1999), and van Hinsbergen and Meleunkamp (2006).

The evaporite-rich Ammoudhares Formation was used as a regional marker below which extensional basins were developing in the late Miocene (Figure 5.2a). Through five successive field seasons (2009–2013), we mapped exposed carbonate blocks and slumped strata with more than 25 m^2 in surface area (see Alves & Lourenço, 2010; Alves, 2015). After 2013, in annual field campaigns leading to 2018, we mapped slumped strata in siliciclastic intervals that are part of the Kalamavka, Makrilia, and Ammoudhares formations (Alves & Cupkovic, 2018) (Figure 5.2a). In total, we collected sedimentological data, outcrop logs, and photomosaics from more than 100 field sites. The nomenclature of Spence and Tucker (1997) used to characterize megabreccia successions is adopted throughout this work.

Later in this chapter, 3D seismic data from the upper continental slope of Espírito Santo (SE Brazil) are interpreted to illustrate the first stages of block formation and associated glide zone geometries (Figures 5.1 and 5.2). The seismic volume from SE Brazil has a bin spacing of 12.5 m, a 2 ms vertical sampling window, and was acquired with a 6×5700 m array of streamers. Data processing included resampling, spherical divergence corrections and zero-phase conversions undertaken prior to stacking, 3D pre-stack time migration using the Stolt algorithm, and one-pass 3D migration. Seismic velocity data from Deep Sea Drilling Program (DSDP) Sites 356 (Kumar et al., 1976) and 515/516 (Barker, 1983; Barker et al., 1983; Gambôa et al., 1983) were used to depth convert the seismic data (see Figures 5.1d and 5.2b). Stratigraphic information in Fiduk et al. (2004) and França et al. (2007) were used to identify and date the seismic-stratigraphic units that comprise submarine slide blocks offshore Espírito Santo. Based on the dominant frequency of the interpreted seismic volume (40 Hz), vertical seismic resolution varies between 10 and 18 m in block-laden strata.

In order to describe the MTDs from SE Brazil, we mapped their base and tops to extract a series of seismic attribute maps. Seismic attributes used in our analysis include root-mean-square (RMS) amplitude slices and isochron maps to visualize the geometry of remnant and rafted blocks. RMS amplitude maps depict average squared-amplitude values from individual samples within a defined interval (Brown, 2004; Marfurt & Alves, 2015). Block height was measured directly on vertical seismic profiles after converting these for true depths using borehole information in Barker et al. (1983) and França et al. (2007).

5.3. GEOLOGICAL SETTING

On Crete, basement units of pre-Miocene age include carbonate strata accumulated on two ancient microcontinents (Apulia-Adria) and in a failed rift arm of Permian age (Thomson et al., 1998, 1999; Stampfli, 2005). These basement units are usually grouped as part of a Lower Sequence that includes, at its base, a phyllite-quartzite unit, and a Carboniferous to Middle Triassic, largely clastic, partly carbonaceous, sedimentary sequence (Krahl et al., 1983). Younger shallow-water carbonate strata in the Gavrovo and Plattenkalk units are also part of the Lower Sequence on the island of Crete (Creutzburg et al., 1977). In the study area, basement rocks of pre-Miocene age are chiefly part of the Plattenkalk unit, a Permian to Eocene

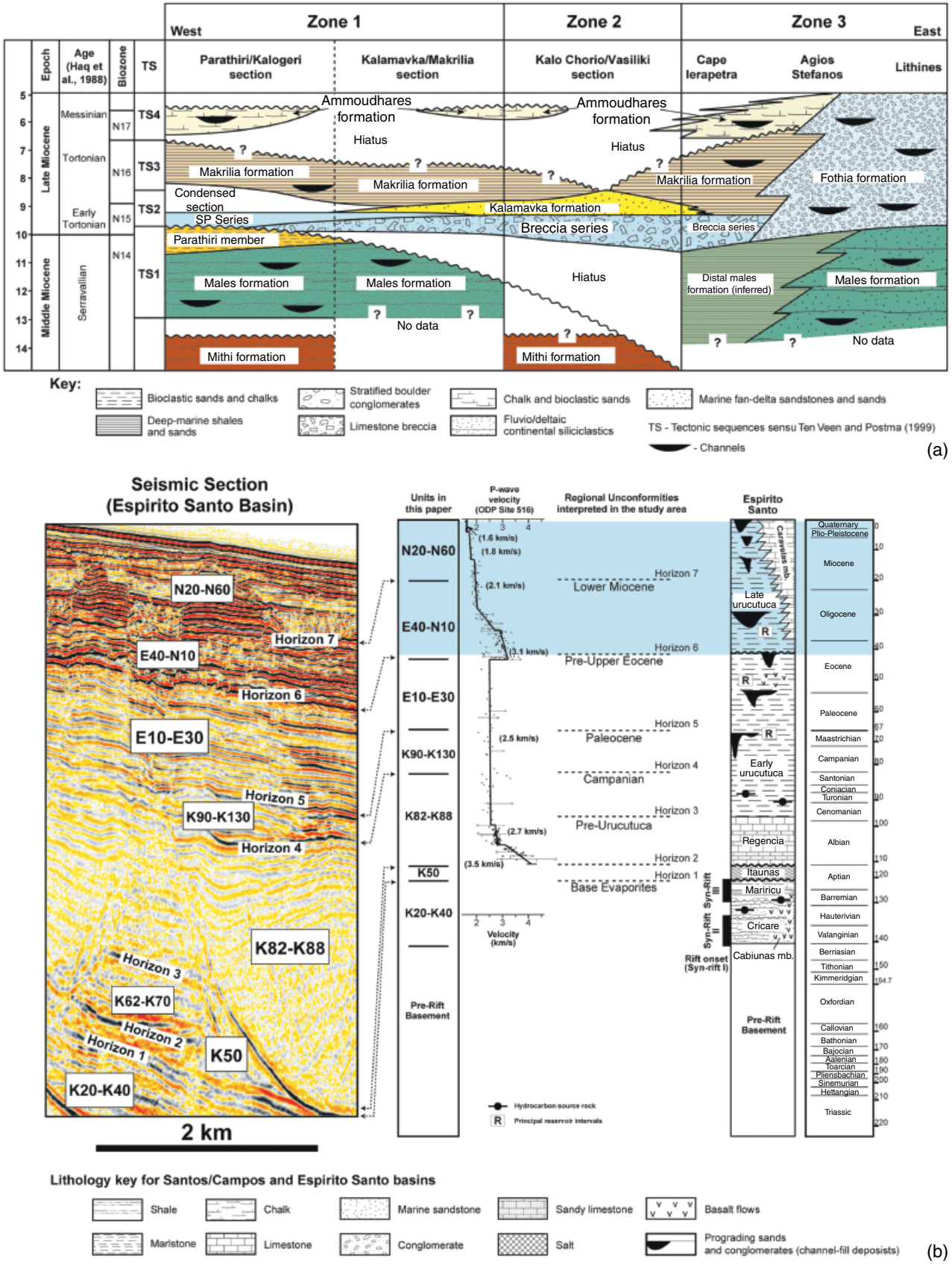


Figure 5.2 Schematic diagrams illustrating the tectono-sedimentary evolution of Crete and SE Brazil in the Late Cenozoic. (a) Principal lithological units in the Ierapetra region and southern Crete. This diagram, based on Postma and Drinia (1993), is compared in this figure with their counterparts to the east of Ierapetra (Zone 3) and with the Tectonic Sequences of Ten Veen and Postma (1999). (b) Seismic stratigraphy of the Espírito Santo Basin, SE Brazil. In both figures (a) and (b), the shaded areas in blue highlight the stratigraphic intervals in which mass wasting is frequently observed. SP Series, Stratified Prina Series.

carbonate interval initially representing shallow-water environments, but transitioning toward deepwater carbonates and cherts. Eocene to Oligocene calcareous flysch occurs on the top of the Plattenkalk unit (Seidel et al., 1982; Bonneau, 1984; Thomson et al., 1999).

Above the Plattenkalk unit occur lower-grade metamorphic rocks (Tripolitza Unit in SE Crete) and other Neogene supradetachment strata deposited above an extensional detachment formed in the first stages of extensional collapse of the Aegean Sea (e.g., *Cretan Detachment*, Ring & Reischmann, 2002; Seidel et al., 2007). In these same supradetachment units are observed blocks within mixed carbonate-siliciclastic successions accumulated over tectonically active submarine slopes (Fortuin, 1977; Postma et al., 1993; Ten Veen & Postma, 1999; Zachariasse et al., 2008; Alves & Lourenço, 2010). The Tripolitza and Neogene units are usually eroded on top of footwall highs and extensional *klippen*, but can be >1500 m thick in extensional basins surrounding these latter highs. Offshore South Crete, tectonic troughs comprise a minimum of 1200 ms two-way time (~1500 m) of Neogene strata (Alves et al., 2007). Comprehensive reviews of the Neogene stratigraphy of SE Crete are given in Postma and Drinia (1993), Ten Veen and Postma (1999), and Alves and Cupkovic (2018).

5.3.1. Ierapetra Basin, SE Crete

In the study area of SE Crete were generated, during the Serravalian-Tortonian, multiple paleoslopes flanking a half-graben representing the Ierapetra Basin (Figure 5.1a). The Ierapetra Basin is composed of up to 1400 m of strata accumulated from the Langhian(?)-Serravalian (Miocene) to the Quaternary (Postma & Drinia, 1993).

At the base of the stratigraphic succession filling the Ierapetra Basin is the Mithi Formation (>100 m thick), a continental unit composed of immature breccias, red sands and mudstones fed from varied basement units, although clasts are predominantly igneous in the interior of this unit (Ten Veen & Postma, 1999; Figure 5.2a). This formation represents deposition in alluvial fans and comprises lignitic clays (Fortuin & Peters, 1984). The Mithi Formation is suggestively Langhian in age, equivalent to marine sediments interpreted at the base of the Strabo Trench, to the south of the island (Ryan et al., 1973 in Postma et al. (1993)). It represents the first evidence for erosion of a broad Aegean landmass.

The Males Formation (>500 m thick), an upper Serravalian alluvial unit that gradually becomes marine toward its top, overlies the Mithi Formation to feed a large part of siliciclastic blocks and proximal fluvial/deltaic deposits to the younger Prina Series (Figure 5.2a). In contrast to the Mithi Formation, the Males unit represents mature fluvial drainage systems reflecting deposition from east to west. The presence of thick (50–100 m) fluvial channels is a key character of the Males Formation, which was putatively deposited at the southern edge of a wide Aegean landmass (Fortuin & Peters, 1984).

Lower Tortonian limestone-rich breccia-conglomerates, blocks, and MTDs, overlie the Males Formation (Postma & Drinia, 1993; Figure 5.2a). This distinct interval, the Prina Series (~500 m thick), is divided into a breccia series at its base and a stratified series at its top (Postma & Drinia, 1993). A pronounced deepening event is associated with the deposition of the Prina Series (Ten Veen & Postma, 1999; Alves & Lourenço, 2010; Alves & Cupkovic, 2018). Such an event reflects the onset of tectonic extension in the Southern Aegean Sea, with important transtension and tilt-block rotation accompanying the fragmentation of the Aegean landmass (Fortuin & Peters, 1984). Late Tortonian tectonics in the Ierapetra Basin is thus marked by the fragmentation of breccia-conglomerate blocks (originally part of the Prina Series) above and within deep-marine deposits of the Kalamavka and Makrilia formations (Figures 5.2a and 5.3).

The Kalamavka Formation (~600 m thick) comprises stream-dominated alluvial fan deposits that transition toward the south and southwest into marine fine-grained sandstones (Figure 5.2a). The succession is light colored and contains large and small blocks, which are erosive over "background" slope strata. These "background" slope units reflect the accumulation of submarine fan intervals composed of calcareous sandstones, coarse-grained channel-fill deposits interfingering with blocky and breccia-conglomeratic material in the Prina Complex.

In contrast to the Kalamavka unit, the Makrilia Formation (>400 m thick) is mostly composed of fine-grained siliciclastic sediment (silt and clay) interrupted by intervals of sandy turbidites and MTDs, which are chiefly silty-sandy and devoid of carbonate blocks (Figure 5.2a). Nevertheless, a few blocks are visible in the Makrilia Formation as pointed out by Alves and Cupkovic (2018). The Makrilia Formation represents the complete establishment of marine basins in the area occupied by the island of Crete.

5.3.2. Espírito Santo Basin, SE Brazil

The Espírito Santo Basin (ESB) of SE Brazil records two distinct Late Cretaceous-Cenozoic tectonic phases: transitional and late drift (Ojeda, 1982; Fiduk et al., 2004; Figure 5.2b). The late Aptian transitional phase saw the deposition of thick evaporites in a restricted basin (Mohriak, 2003; Fiduk et al., 2004; Davison, 2007). Upper Cretaceous to Cenozoic open marine sequences later draped the Aptian evaporites during the opening of the southern Atlantic Ocean (drift phase). An early drift phase in SE Brazil correlates with a marine transgressive

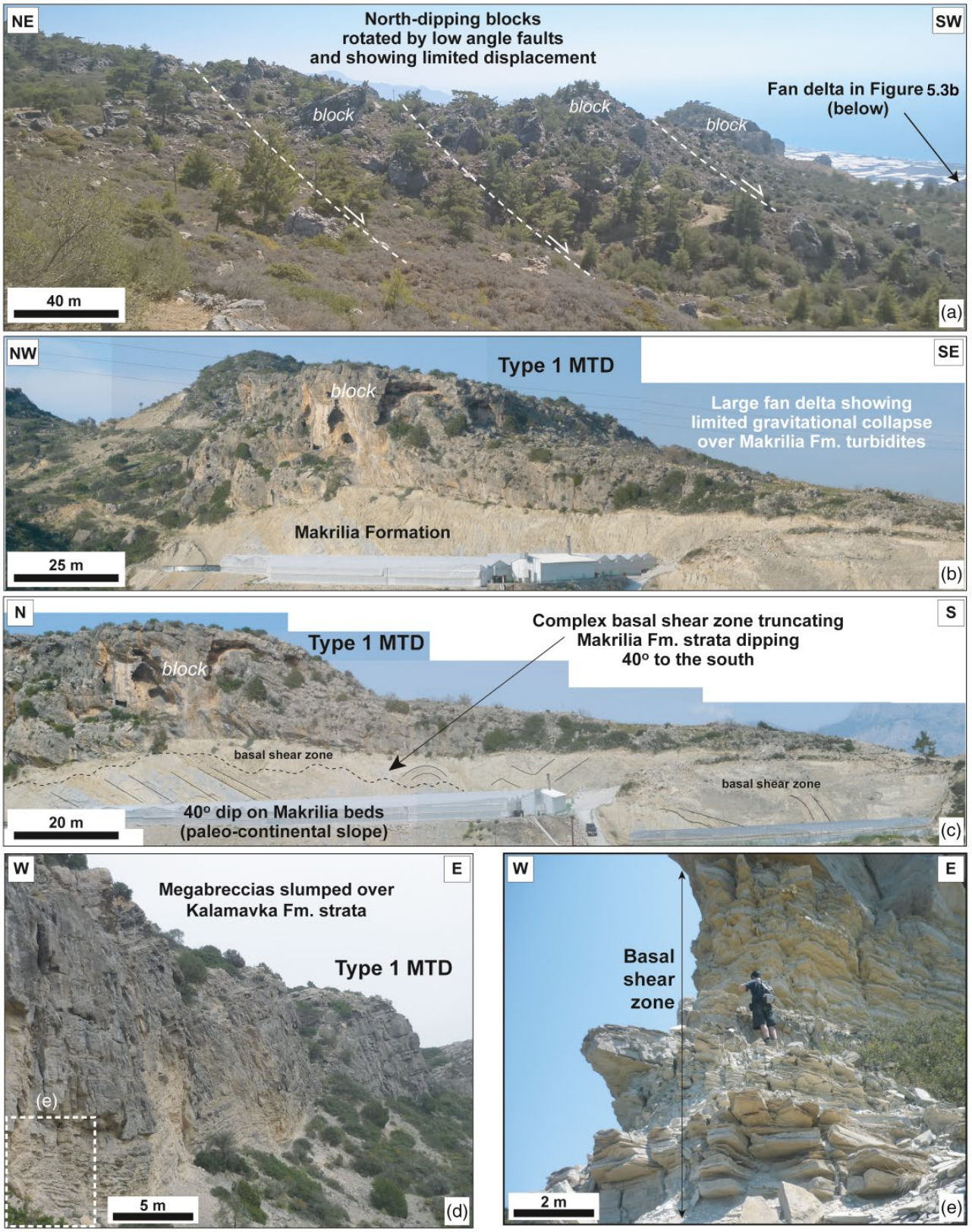


Figure 5.3 Outcrop examples of type 1 MTDs as documented in SE Crete. (a) Proximal type 1 MTDs at location 1 near Anatoli, NW of Ierapetra (Figure 5.1b). Here low-angle rotational faults tilted a series of fan deltas and blocks to the north, accompanying the late Serravalian-Tortonian extension in SE Crete. The blocks are included (and in some places, buried) under upper slope facies of the Kalamavka Formation. (b) Type 1 MTD in Ammoudhares (location 2; Figure 5.1b) showing a very moderately disrupted fan delta over unconformable marine strata of the Makrilia Formation. (c) The same type 1 MTD presents here a complex basal shear zone within the Makrilia Formation. (d) Detail of laterally spread blocks (type 1 MTD) at Agios Dimitrios, location 3 (Figure 5.1b). (e) The basal shear zone of these same blocks is shown here as a highly deformed interval reaching >10 m in thickness (location 3; Figure 5.1b).

megasequence that includes Albian shallow-water carbonates (Demercian et al., 1993; França et al., 2007; Figure 5.2b). These platform carbonates were covered by Upper Cretaceous-Paleocene mudstones deposited during a deepening phase (Mohriak, 2003; Davison, 2007). In the lower Eocene, the onset of a marine regressive megasequence became associated with the development of a prograding continental slope. This prograding sequence was able to transport sediment from hinterland sources to the west, and from the Abrolhos Bank, onto the continental rise and abyssal plain off Espírito Santo (Mohriak, 2003; Fiduk et al., 2004; Figure 5.1d).

Salt diapirs occur in the mid-slope region of the ESB, transitioning into allochthonous salt walls and canopies toward the lower continental slope (Demercian et al., 1993; Mohriak, 1995; Fiduk et al., 2004; Davison, 2007). In such a setting, multiple Cenozoic mass-wasting events occurred in the ESB during regressive and transgressive cycles (Moreira & Carminatti, 2004), slope progradation (Gamboa et al., 2010), and salt tectonics (Gamboa et al., 2011; Omosanya & Alves, 2013, 2014; Gamboa & Alves, 2016; Gamboa et al., 2018).

5.4. TYPES OF SYN-TECTONIC MASS-TRANSPORT DEPOSITS (MTDS)

Late Serravalian-Tortonian extensional tectonics in SE Crete resulted in the sliding of mass-transport blocks over the paleoslopes bounding the Ierapetra Basin to the east and west (Postma & Drinia, 1993; Alves & Lourenço, 2010; Figures 5.3 and 5.4). Blocks are embedded in marine slope strata, over which they were transported and later covered with; although the strata within the blocks were first deposited in shallow-shelf environments prior to being disrupted on fault-bounded slopes (Fortuin, 1977). The late Miocene paleoslopes of SE Crete are now exposed due to tectonic uplift, which started in the late Pliocene and continues to the present day (Peters & Troelstra, 1984; Postma & Drinia, 1993; Zachariasse et al., 2008; Gallen et al., 2014).

5.4.1. Type 1: Carbonate Blocks and Breccia-Conglomerates Showing Limited Gravitational Collapse

Type 1 MTDs comprise autochthonous carbonate blocks and boulder conglomerates that show moderate weathering and minor collapse features (Figure 5.3a, b). They relate to fault-bounded footwall blocks and other syn-rift highs formed in the late Miocene and were very moderately displaced on marine slopes. Very moderate lateral spreading of boulder conglomerate units is therefore interpreted in the field (Alves & Lourenço, 2010). Ravines and chasms up to 30 m wide can be observed splitting the largest carbonate blocks. Part of these ravines were generated in the late Miocene, with subsequent tectonic uplift and emersion of Crete contributing to the preferential erosion of fractured portions of the carbonate megabreccias, fan deltas, and cones (Figure 5.3b). Sandy blocks sourced from the Males Formation also occur in this type, with wedges of coarse-grained sand outcropping adjacently to carbonate megabreccias (Figure 5.3b, e).

5.4.2. Type 2: Disrupted Blocks, Carbonate Megabreccias, and Boulder Conglomerates on Tectonically Active Slopes

Boulder conglomerates and megabreccias are unconformable over continental to shallow-marine siliciclastic strata of the Males and Kalamavka formations (Figure 5.4a–c). Locally, in a relatively proximal position of the Ierapetra paleoslope, multiple carbonate blocks alternate spatially with boulder conglomerates, channel fill, and submarine fan deposits, some of which are also disrupted. As pointed out by Alves and Lourenço (2010), type 2 MTDs reveal greater disaggregation in comparison to type 1, with marked post-depositional disaggregation of carbonate blocks, sandy blocks sourced from the Males Formation, and adjacent slope siliciclastic intervals (Figure 5.4a–c). Structural deformation shows more pronounced spreading of megablocks in type 2 MTDs when compared to type 1.

5.4.3. Type 3: Blocks and Debris-Flow Deposits (Boulder Conglomerates) Accumulated Distally From Exposed Fault Scarps

In type 3 MTDs, a large proportion of disaggregated carbonate blocks occurs above (or within) marine strata of the Kalamavka Formation (Figure 5.4d, e). Significant slumping is also observed close to the limit between the Makrilia and Ammoudhares formations (and within this latter unit), west of Myrtos (in the Tertsa-Arvi region), and south of the Anatoli anticline (Fortuin, 1978; Figure 5.1b).

The basal contacts of blocks with the Kalamavka Formation are usually erosional, particularly under isolated blocks that were embedded in, or rafted over, marine siliciclastic sediment (Figure 5.5a). Outcropping blocks are also part of larger carbonate bodies buried underneath slope strata (Figure 5.5).

Structural deformation is chiefly concentrated at the base of rafted blocks (Figure 5.4e), as exemplified by recumbent and sheath folds, imbricated faults, and injection features intruding vertical fractures in blocks (see Gamboa & Alves, 2015). Such deformation features tend to occur in sand-bearing strata and in thicker basal intervals intercalated with mud-prone beds (Figure 5.4e). Kinematic interpretations from the basal

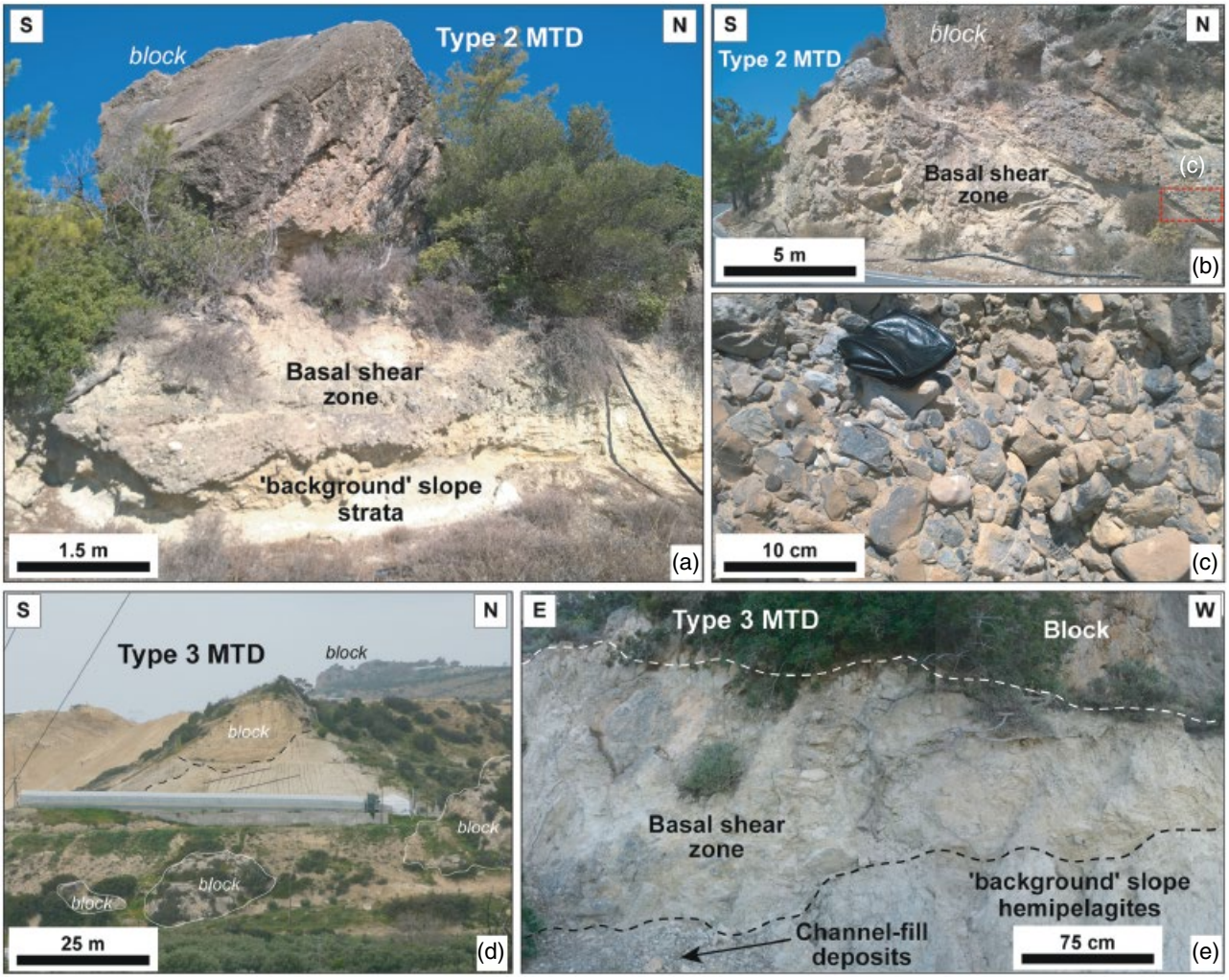


Figure 5.4 (a) Collapsed block over a basal shear zone composed of breccia-conglomerates and remobilized siliciclastic slope strata (location 4; Figure 5.1b), classified as a type 2 MTD. The "background" slope strata in this location belong to the Kalamavka Formation. (b) A similar example of a type 2 MTD from near the village of Kalamavka (location 5; Figure 5.1b), comprising a ~10 m basal shear zone with complex folds and convoluted bedding. The block above was transported over slope strata in the Kalamavka Formation. (c) Detail of a conglomerate interval observed below the rafted block in location 5 (Figure 5.1b). In contrast with breccia-conglomerates occurring within slide blocks, which comprise a fine-grained carbonate cement, the conglomerates in the photo are loosely bound by a siliciclastic matrix. In other locations, breccia-conglomerates in basal shear zones also show similar siliciclastic matrices, a character revealing some degree of entrainment in "background" slope sediment. (d) Example of isolated blocks from the area west of Gra Ligia (location 6; Figure 5.1b), showing some degree of entrainment (and sinking) in slope strata (type 3 MTD). (e) Moderate entrainment observed under a rafted block part of a type 3 MTD in location 2 (Figure 5.1b).

deformation in the basal shear intervals are consistent with the direction of movement of the large rafted blocks (Gamboa & Alves, 2016).

5.4.4. Type 4: Chaotic Volumes of Turbidites, Chalk, and Evaporites

Turbidite sands, marls, and clays in the Makrilia Formation comprise a ≤450 m deep-marine unit of Tortonian age (Fortuin & Peters, 1984; Postma & Drinia, 1993). The Makrilia Formation drapes the blocks and interfingers laterally with the Kalamavka Formation (Alves & Lourenço, 2010).

Examples of localized siliciclastic deposits lacking rafted blocks include bed-parallel MTDs transported over sandy, mobile, detachment zones (Figure 5.6a, b). The MTDs in Figure 5.6a, b reveal the typical complex geometry of such deposits, with internal folds in chalky

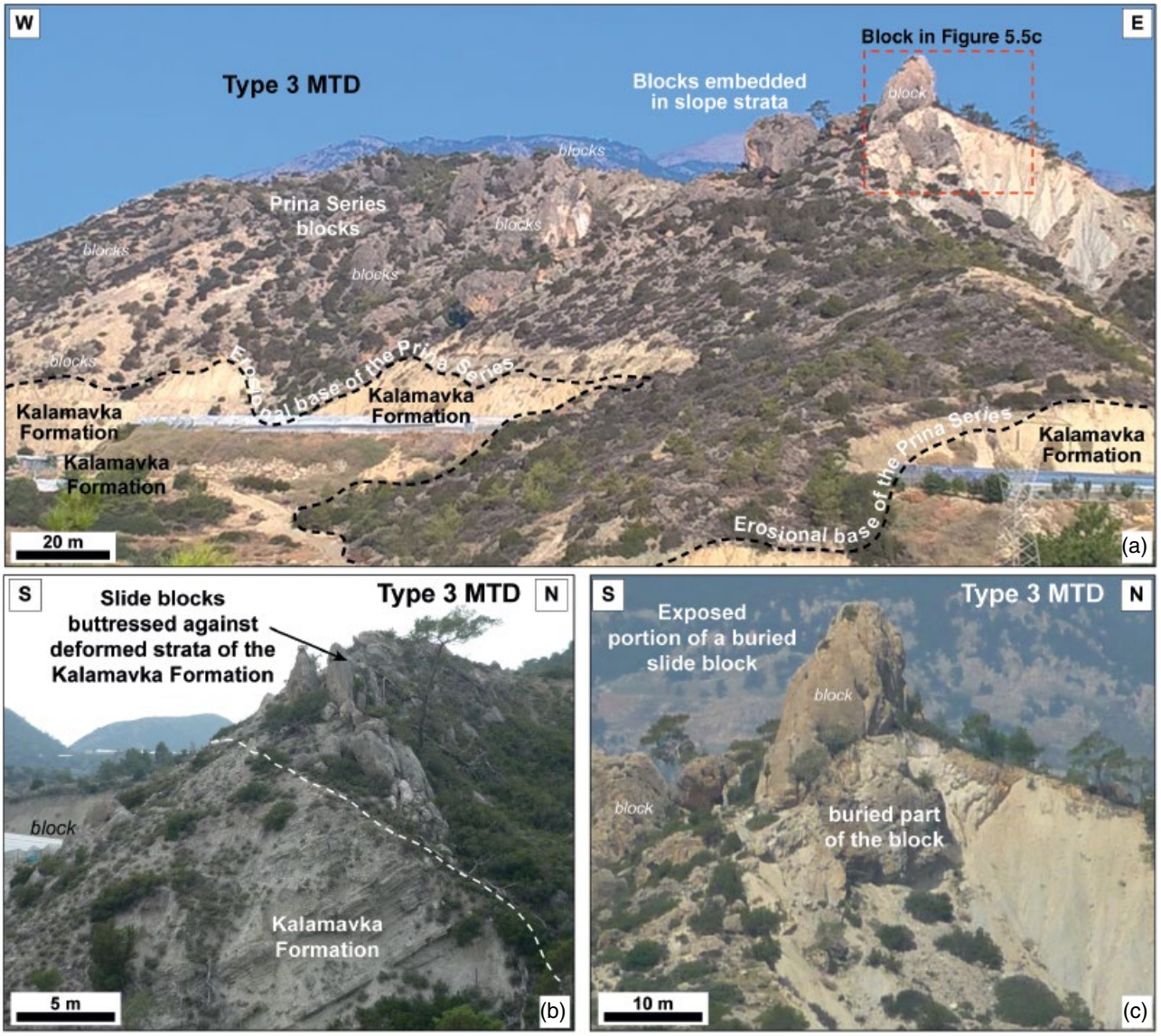


Figure 5.5 (a) Example of significant entrainment in slope strata (type 3 MTD) around Ammoudhares (location 7; Figure 5.1b). Here, the Prina Series is highly erosional and shows blocks either sunken into siliciclastic slope strata or eroding it. (b) In this example, blocks in the Prina Series were dislodged and buttressed against south dipping slope strata (type 3 MTD), also in location 7 (Figure 5.1b). (c) Inset from Figure 5.5a, showing an isolated block in more detail. The block is embedded into mudstone-dominated strata. The block was disrupted and then sank into a ductile, malleable sea floor.

(Figure 5.6a) and muddy (Figure 5.6b) strata being intercalated with chaotic masses of contorted sediment with a clear basal surface. In the MTD in Figure 5.6a, chalky and carbonate boulders alternate with evaporite (gypsum) clasts. In the two examples above, the basal surface in the type 4 MTDs is formed of immature and poorly sorted sands and very fine pebbles. Other meter-scale MTDs comprise deformed strata confined by a bed-parallel, sandy glide plane; these MTDs do not entrain into slope strata (Laberg et al., 2017). In these cases, the basal glide plane becomes a low-angle truncation surface laterally denoting very moderate erosion of seafloor strata during MTD deposition (Figure 5.6b).

5.4.5. Type 5: Steep Debris on the Foot of Large Fault Scarps

Observed rockfalls from fractured carbonate blocks are mainly post-Tortonian features (Peters & Troelstra, 1984), but are interpreted here to have also occurred during the

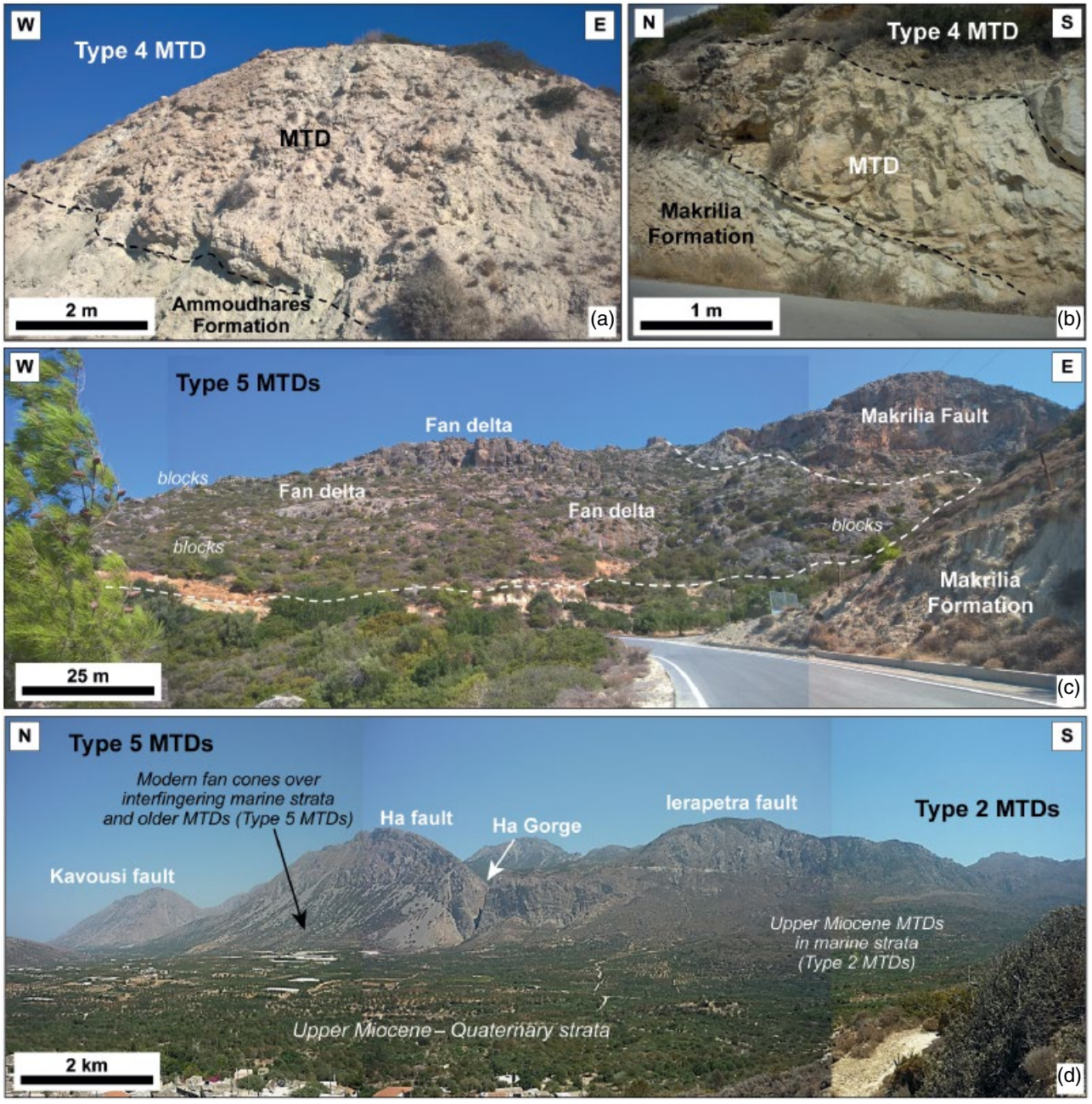


Figure 5.6 Examples of type 4 and type 5 MTDs in which slumped and slide strata occur in a siliciclastic sequence and are bounded by sharp basal shear zones, denoting little entrainment. (a) Type 4 MTD at Nea Myrtos (location 8; Figure 5.1b). Here the imaged interval comprises a remobilized chalky MTD with calcareous and evaporitic clasts, part of the Ammoudhares Formation (Messinian). Cavernous gypsum occurs stratigraphically above this outcrop location. The base of the MTD is highlighted by the dashed line in the photo. (b) Type 4 MTD near Arvi (location 9; Figure 5.1b) revealing episodic destabilization of strata within the Makrilia Formation. At coastal outcrops, slumping and sliding of siliciclastic blocks is common toward the top of the Makrilia Formation. The base and top of the MTD are highlighted in the photo by the dashed lines. The sense of movement in the MTD is from north to south. (c) Series of breccia-conglomerate fan deltas (type 5 MTDs) near the village of Makrilia (location 10; Figure 5.1b). These coarse-grained footwall degradation complexes (see Alves & Cupkovic, 2018) were sourced from footwall scarps exposed at (or near) the surface. (d) Panoramic view of type 2 and 5 MTDs near the Ierapetra Fault Zone (location 11; Figure 5.1b). Type 5 MTDs comprise fan cones that interfinger with marine strata and older MTDs near the Kavousi and Ha fault segments. The Ierapetra Fault shows older, upper Miocene degradation complexes (type 2 MTDs) in its immediate hanging wall, embedded in marine strata.

late Miocene collapse of the studied (marine) paleoslope (Figure 5.6c, d). They are chiefly observed against exposed footwall blocks (Figure 5.6c, d). Fallen blocks reach 20 m in length, being in average <10 m in diameter. This style is mostly subaerial, except for fallen blocks embedded in the Kalamavka, Makrilia, and Ammoudhares formations that are part of debris fans and interfingering turbidites (Figure 5.6c).

Two examples of type 5 MTDs are provided in this chapter; one example associated with the erosion of multiple faults segments at Makrilia (Figure 5.6c) and a second example associated with fault segments of the Ierapetra Fault Zone (Figure 5.6d), whose evolution was diachronous from south to north. In Figure 5.6c are shown a series of megabreccia fan deltas that are part of a larger degradation complex (see Alves & Cupkovic, 2018). This degradation complex is deposited among strata belonging to the Makrilia Formation, whose stratotype was defined 200 m from the photo, at the village of Makrilia (Fortuin, 1977). The second example in Figure 5.6d shows type 2 MTDs deposited on the hanging-wall block of the Ierapetra Fault, embedded in marine strata. Type 5 MTDs predominate in the presently active (and presumably younger) Ha and Kavousi fault segments (Figure 5.6d). Here, the fan deltas and cones imaged in Figure 5.6d are deposited over shallow-marine strata of the Ammoudhares and Makrilia formations.

5.5. KEY MARKERS OF TECTONIC ACTIVITY

An important aspect of multiple basins across the world is that slide blocks are ubiquitous in tectonically active settings. This is particularly the case of peri-Alpine successions of Southern Europe and New Zealand that were uplifted during the Cenozoic (Jiao et al., 2017; Keller, 2017). Slide blocks and MTDs are also present in ancient passive-margin systems within slope deposits as old as the Neoproterozoic Isaac Formation (Windermere Supergroup) in the southern Canadian Cordillera (Arnott et al., 2011; Navarro & Arnott, 2018). The presence of these rather old blocks hints at important tectonism in the Neoproterozoic. Outcrop analogues of a younger age include the Friuli Basin in NE Italy and Slovenia (Ogata et al., 2014), the Italian Dolomites (Brandner et al., 1991), upper Paleogene and Holocene successions in NW Italy (Migeon et al., 2011; Perotti et al., 2012), the Gorgoglione Flysch Basin of the Italian Southern Apennines (Buttler & Tavarnelli, 2006), the Schistes-à-Blocs Unit in SE France (Kerckhove & Antoine, 1964; Kerckhove, 1974; Campredon et al., 1977; Pêcher et al., 1992; Dumont et al., 2011), Sumba Island in Indonesia (Roep & Fortuin, 1996), and parts of New Zealand (Collot & Davy, 1998; Collot et al., 2001; Lamarche et al., 2008; Goff et al., 2010). These and other outcrop regions document similar structural styles to SE Crete and SE Brazil.

5.5.1. Thickening and Deepening of Marine Facies Toward Basin Depocenters

The Ierapetra Basin was filled by a minimum of 1400 m of sediments in the late Miocene-early Pliocene (Fortuin, 1977). A key characteristic of fault activity in this basin is the presence of abrupt thickness variations, with evidence for syn-tectonic erosion and deposition in shoulder areas to the NW and E. The basin is dominated by distal marine facies in its central part, and, conversely, its two shoulders record important mass wasting with large-scale megabreccia blocks dominating the successions deposited there (Figures 5.3–5.6). In these two shoulder areas, boulder conglomerate and megabreccia blocks overlie continental to shallow-marine siliciclastic units of the Males and Kalamavka formations (Figures 5.3–5.5). This setting is particularly well documented on the western part of the Ierapetra Basin, whereas a combination of fault scarps and displaced megabreccia blocks is observed toward its eastern shoulder (see figure 14 in Alves and Cupkovic (2018)). Sediment progradation toward the SE, and also from the eastern basin shoulder toward Ierapetra, is well documented at outcrop (Figures 5.3 and 5.6d). As a result of fault-controlled subsidence during the late Serravalian-Tortonian, the Males Formation is found a few meters below the surface in the Anatoli region (NW Ierapetra; Figure 5.1b), whereas aquifers in the Males Formation are buried ~650 m under Ierapetra (N. Lagoudakis, Pers. Comm.), i. e., underneath a thick succession of Makrilia Formation sands and muds. Similar variations in the thickness of upper Serravalian-Tortonian strata are also clear when comparing the study area with outcrop data from the islands of Gavdos and Koufonissi (Fortuin & Peters, 1984).

5.5.2. Slumping and Folding of Strata on Oversteepened Slopes

Lower-mid-Tortonian strata in the Kalamavka Formation contain gray-blue marls and sands with abundant marine fauna, over which extensive MTDs and rafted blocks were transported downslope (see figures 2 and 3 in Alves and Lourenço (2010)). Blocks are spread through an area of more than 12 km^2 on the western shoulder of the Ierapetra Basin. Similar deposits occur along the western shoulder of the Ierapetra Basin and along the southern coast of Crete.

Reflecting a distal position relative to the Kalamavka Formation, the Makrilia Formation is composed of deep-marine turbidite sands, marls, and clays with a

Tortonian age (Fortuin & Peters, 1984; Postma & Drinia, 1993). The Makrilia Formation drapes the blocks and interfingers laterally with the Kalamavka Formation (Alves & Lourenço, 2010). Non-entraining MTDs are observed in the Kalamavka, Makrilia, and Ammoudhares formations, away from slide blocks (Figure 5.6a, b). They include bed-parallel MTDs transported over sandy or chalky, mobile, detachment layers.

A certain degree of entrainment is nevertheless found at the base of the Prina Series, a large mass-transport unit consisting of upper Serravalian-Tortonian strata (Figure 5.5a). Here, the base of the Prina Series comprises an irregular erosive surface that is overlain by coarse-grained sands and conglomerates transported downslope in multiple events. Isolated blocks and boulders of distinct sizes occur 2–20 m above the base of the Prina Series.

The MTDs in Figure 5.3b–e show moderately collapsed blocks above basal glide zones with a complex geometry, including internal folds in muddy strata interrupted by the injection of sandy material from the basal surface. The basal surface is, in itself, a local unconformity formed of immature and poorly sorted sands and very fine pebbles. In contrast, the MTDs in Figure 5.6a, b comprise deformed strata confined by bed-parallel glide planes. In both non-entrained MTDs, the basal glide plane becomes a low-angle truncation surface laterally in the succession, denoting very moderate erosion of seafloor strata during slope instability.

Other styles of failure associated with tectonic oversteepening are identified at outcrop. Figure 5.4d, e shows examples of collapsed slide blocks, ~20 m in height, denoting a limited amount of entrainment in slope strata. In other example (Figure 5.4b, c), slide blocks show fractured breccia-conglomerates at their base, suggesting the remobilization (and rolling) of the larger blocks over a siliciclastic substrate. The presence of basal sandy and conglomeratic layers of distinct thickness in Figure 5.4b, e is associated with the formation of complex glide zones, which are clearly stratified and accommodate the movement of blocks at different rates, at different depths (see Alves, 2015).

From the above, it is documented that both sand and mud layers may form glide planes that can be restricted to specific intervals, and examples of both entrained and non-entrained relationships have been found in Crete.

5.5.3. Kinematic Indicators of Syn-tectonic Deformation

In SE Crete, blocks present kinematic indicators that are of interest to understanding the physics and directions of ancient mass movements. Most of the kinematic structures documented at outcrop reflect transport styles such as (i) gliding; (ii) block drag and skipping; (iii) toppling; (iv) free fall; and (v) translation over high-density megabreccia flows. We assume, in the tectonically active setting of Crete, that block movement was associated with earthquake activity, sediment liquefaction, and block sinking into background slope strata. Other structures represent post-depositional tectonic deformation and block remobilization on a tectonically oversteepened slope, as pointed out in Section 5.5.2.

Figure 5.4a, b shows basal glide zones below submarine blocks. In Figure 5.4a, ~2 m of strata were remobilized below a discrete block. In Figure 5.4b, ~10 m of strata belonging to the Kalamavka Formation were deformed underneath a collapsed fan delta block. The region of deformed basal strata abruptly changes into an undeformed stratified succession 10 m below the base of the collapsed block. Detailed analysis of basal structures under the two blocks denotes the presence of contorted successions of foliated sediment alternating with folded intervals and truncated horizons (see Alves et al., 2015). Importantly, the breccia-conglomerates observed at the base of these blocks have a poorly consolidated sandy/muddy matrix, demonstrating a certain degree of entrainment of these dense breccia-conglomerate flows in slope strata (Figure 5.4c). Most of the truncation (and foliation) observed at outcrop is tectonic in origin and results from the putative slow downslope movement of blocks on the paleoslopes of SE Crete (Figure 5.5b, c).

The presence of a basal conglomerate package is observed below rafted blocks in several other locations. Highly fractured breccia-conglomerate deposits accumulated at the base of an 8.3 m high block in Figure 5.4e. The presence of a faulted basal sandy layer 1–2 m below the base of the collapsed block is noticed here. This sandy layer shows evidence of extensional collapse (and faulting) of the sea floor (see figure 11a, b in Alves and Lourenço (2010)) due to increased loading imposed on the sea floor by the block.

5.6. DISCUSSION

MTDs are common features occurring on the flanks of salt structures in SE Brazil. The internal character of such MTDs is often influenced by nearby structures through faulting of pre-collapse strata, which can facilitate the creation of blocks, or by creating topographic relief that influence the deposit runout and, consequently, deformation within the blocks. The relationship between growing salt structures and nearby MTDs can provide reliable indicators for the timing of halokinesis (Gamboa & Alves, 2016). In parallel, the presence of deformed strata packages from discrete MTDs can be related to particular slope instability events, provided that the

source area is along the salt structure, i. e., the degree of deformation is often an indicator of the extent of remobilization. The geometry and thickness of the basal intervals of MTDs in SE Brazil is also influenced by these factors. Thus, MTDs occurring in SE Brazil have been shown to have complex, stepped basal intervals when occurring in the vicinity of faults that are linked to salt structures (Gamboa et al., 2012), in areas with laterally heterogeneous (paleo)-seafloor competence (Omosanya & Alves, 2013), or when interacting with preexisting channel systems (Gamboa et al., this volume). In the opposite spectrum, basal shear zones observed at seismic scales can be barely distinguished from surrounding (in situ) strata (Gamboa & Alves, 2016); yet significant deformation occurs within them. Importantly, the relationship between the basal surfaces and nearby faults is a timing proxy for fault reactivation, especially if these are linked to deep salt structures (Omosanya & Alves, 2014; Gamboa & Alves, 2016; Gamboa et al., this volume).

5.6.1. MTDs as Markers of Tectonic Movements From Seismic to Outcrop Scales

Figure 5.7 depicts strata flanking a salt ridge in SE Brazil where multiple MTDs are observed. The majority of the deposits are represented by fairly thin strata packages with moderate amplitude, mottled reflections underlain by an irregular, locally stepped basal seismic reflection. However a relatively thick (~100–200 m thick) high-amplitude MTD X, linked to the flanks of salt diapir B and showing numerous internal faults, stands out from adjacent strata (Figure 5.7). Of relevance is the presence of a complex basal surface that contrasts from that of other MTDs. The base of the intra-MTD X faults serves as a proxy for the lowermost coherent strata in the deposit. However, evidence of deformation exists along a basal shear interval expressed by lateral changes in thickness, shape, and amplitude of reflections overlying the interpreted basal horizon (Figure. 5.7b, c).

Considering its proximity to the source area and relatively small remobilization distance, MTD X likely shows features that are characteristic of the syn-tectonic type I MTDs recognized in SE Crete, with similarities between the two cases being clear when considering the fault geometries and structural complexity of the basal shear interval. MTD X was very moderately disrupted, it is highly faulted, and shows a well-developed basal shear zone that can be mapped. West of MTD X, the seismic character abruptly shifts to a low-amplitude, chaotic package likely to represent a distinct type 2 syn-tectonic slope failure event associated with a nearby salt structure to the west, or even a deposit sourced from elsewhere. Alternatively, it could represent a distal portion of MTD X marked by an abrupt increase of deformation, effectively documenting a sharp transition from a type 1 to a type 2 syn-tectonic MTD (Figure 5.7b, c). One key aspect is that the complexity and thickness of the type 2 basal shear interval will be generally smaller compared to type 1 deposits, based on the 3D seismic data interpreted in this work, and there may be a lower deformation contrast between the basal intervals and the bulk of the remobilized deposit (see Figure 5.7c). In addition, type 1 and 4 MTDs occur, respectively, above and below MTD X in the seismic profile in Figure 5.7c.

The identification of distinct types of syn-tectonic MTDs is relevant for MTD genesis (e.g., Moscardelli & Wood, 2016). Where multiple deposits are present, and are potentially sourced from distinct points, the recognition of different MTD types can help discerning between slope failure events occurring at identical stratigraphic intervals, which often share common detachment levels at seismic scales (e.g., Gamboa & Alves, 2016), and those with no timing relationships in terms of their onset and subsequent emplacement. If two or more distinct types are associated with a single MTD, a likely situation in those mass-wasting deposits with longer runout distances, the recognition of distinct MTD types will provide a proxy for the degree and style of deformation expected at progressively higher distances from their source areas.

5.6.2. Relationship Among Block Size, Thickness of Basal Shear Zone, and the Physical Scale of Mass-Wasting Events

Buried and near-seafloor submarine landslides have ubiquitous basal shear zones on top of which failed strata are remobilized (Alves & Lourenço, 2010; Alves, 2015; Sun et al., 2017, 2018) or seismically resolved surfaces (Huvenne et al., 2002; Sultan et al., 2007; Bull et al., 2009). Physical models of debris-flow deposits and associated outrunner blocks have so far stressed the importance of hydroplaning in the translational movement of cohesive strata (Ilstad et al., 2004). Hence, scale relationships between the size of displaced blocks, basal glide zones, and landslide volume(s) are important data to help characterizing past landslides and therefore predict future ones. An example provided in the literature is that of hydroplaning zones in ancient landslides, with the intrusion of a water layer at the base of debris-flow masses favoring downslope movement and the eventual detachment of parts of the landslide (outrunner blocks) from the original failed body. Examples of water intrusion have been documented at the base of modern submarine slides offshore the Canary islands (Masson et al., 2006) and may have occurred in the rock record (see, for instance, Callot et al., 2008; Alves & Cartwright, 2009).

In the recent past statistical data from SE Crete, compared with information from high-resolution seismic data from 60 published case studies on various continental

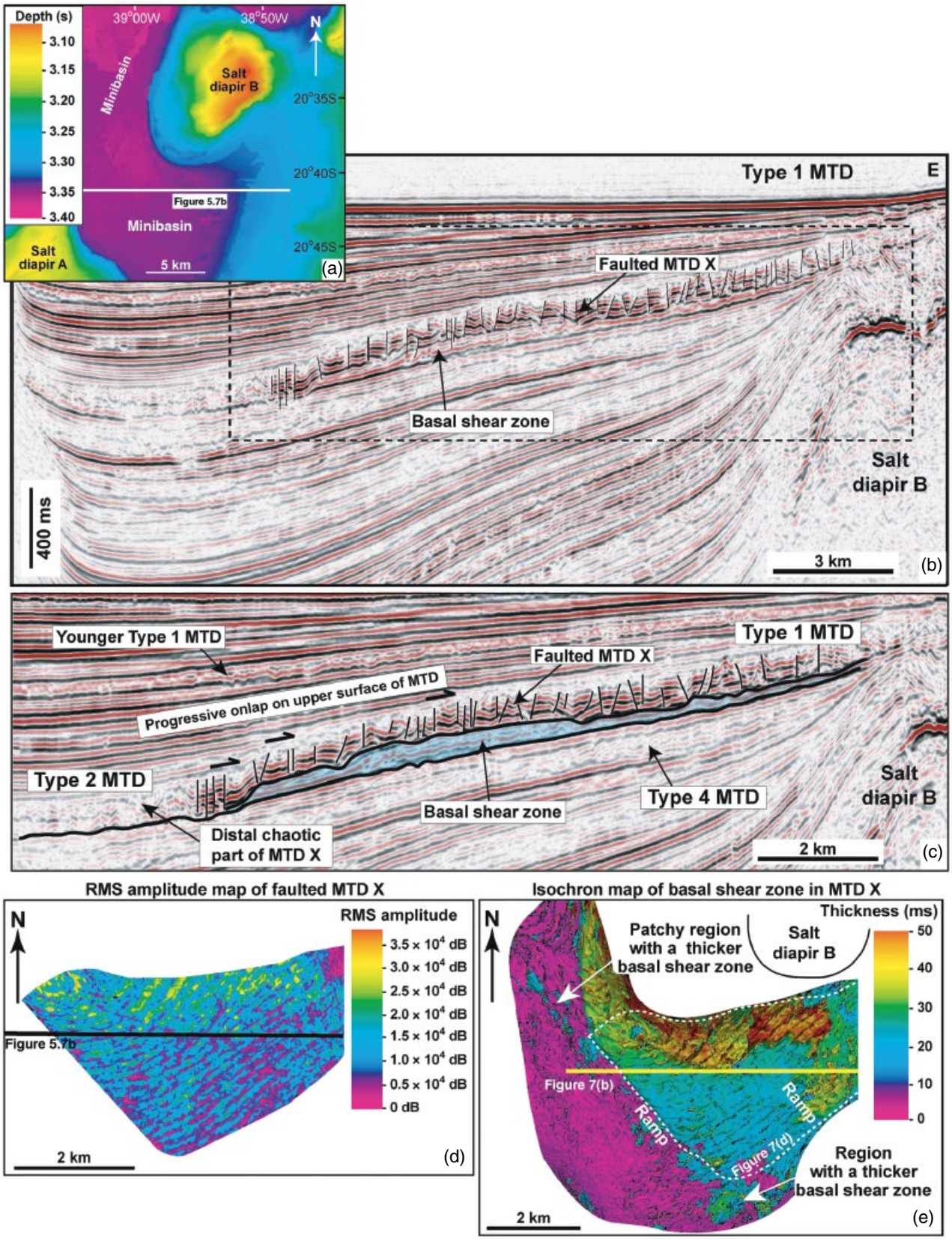


Figure 5.7 (a) Location map of the seismic line in Figure 5.7b. (b) Detail of a basal shear zone from SE Brazil (type 1 MTD) revealing distinct thickness and structural deformation on seismic data. MTD X was remobilized on the southern flank of a growing salt structure (salt diapir B). Note the transparent zone of ~50 ms separating the rotated blocks from the continuous surface usually mapped as a basal glide plane. This basal shear zone is highly deformed. (c) Zoomed section into MTD X, revealing in detail the thickness of its basal shear zone and the sharp transition from a type 1 to a type 2 MTD toward the west, that is, away from the flanks of salt diapir B. (d) RMS amplitude map of MTD X in Figure 5.7b. (e) Isochron map of the basal shear zone of the MTD X shown above in Figure 5.7b, c.

margins, allowed the establishment of scale relationships between the thickness of failed blocks and the corresponding thickness of deformed basal strata. Figure 5.8a, b shows the graphs published in Alves and Lourenço (2010), illustrating the relationship between the thickness of failed strata and the thickness of basal shear zones for (i) upper Miocene MTDs in SE Crete and (ii) Holocene submarine landslides documented by seismic and core data on multiple continental margins. Significant is the difference between the average thickness of basal shear surfaces observed in SE Crete (3.1 m on average) and those below Holocene submarine landslides (12.8 m on average, reaching a maximum of 65 m). The thickness values for failed strata and basal surfaces are also substantially larger in the Holocene examples (Figure 5.8a, b). However, both modern and ancient examples show failed strata to be 2.0–20 times thicker than the underlying basal shear surface.

Average ratios between failed strata and their corresponding basal shear surfaces reach 5 : 1 for the outcrop examples from SE Crete and 9 : 1 for Holocene submarine landslides (Figure 5.4b). Hence, the ratio between the thickness of failed strata and the corresponding thickness of deformed strata at the base (R) is in the order of $5 < R < 10$. Such a variation in the ratio R can be explained if the interpreted basal surface is a basal shear zone rather than a simple surface (e.g., Alves & Lourenço, 2010; Ogata et al., 2014; Sobiesiak et al., 2018). Geological phenomena capable of altering the value of R within the proposed limits include the following: (i) recurrent landslides that accumulate as multiple masses of failed material may show ratios (R) below the average; (ii) variations in the stiffness of substrate strata may cause variations in the thickness of basal shear zones; (iii) the relative density and/or thickness (therefore, weight) as well as the mode of transport (debris flows, turbidite flows, frontally confined vs. frontally emergent slides) may alter the inertia of the landslide mass, thus causing significant variations in the depth of subsurface strata deformed during failure (i.e., entrainment); and (iv) variations in seafloor topography leading to distinct levels of entrainment in slope strata.

5.7. CONCLUSIONS

MTDs in SE Crete mark sudden events of slope instability associated with extensional (syn-rift) tectonism. These comprise distinct types and are located in varied parts of late Miocene extensional basins. The results in this work can be summarized as follows:

1. Five types of MTDs reflect tectonic activity in extensional basins. These MTDs comprise carbonates, cemented siliciclastics, and other hardened lithologies in finer-grained slope successions and are deposited adjacently to large-scale tectonic structures. The five types of mass-transport include (1) carbonate blocks and breccia-conglomerates showing limited gravitational collapse; (2) disrupted blocks, carbonate megabreccias, and boulder conglomerates on tectonically active slopes; (3) blocks and debris-flow deposits accumulated distally from exposed fault scarps; (4) chaotic volumes of turbidites, chalk, and evaporites; (5) continental/shallowmarine debris cones derived from the largest fault scarps.

2. Common characteristics in submarine slide blocks include the presence of kinematic indicators at the base and within the larger blocks. These kinematic indicators are associated with structural deformation or strata remobilization and can form preferential areas for the accumulation or percolation of fluids in subsurface MTDs.

3. Soft-sediment kinematic indicators are varied and complex. They include complex folding, with pinch-and-swell structures, dilational jogs, stretched clasts, and imbricated clasts comprising the most reliable indicators (see Alves, 2015).

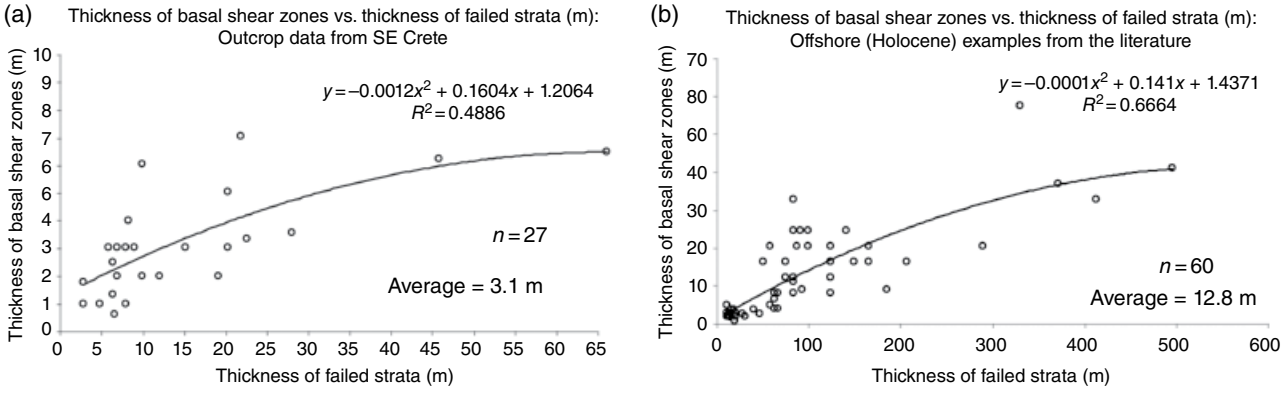


Figure 5.8 Graphs showing scale relationships between the thickness of basal shear surfaces and associated failed strata above. Source: Modified from Alves and Lourenço (2010). (a) Thickness of basal shear zones vs. height of blocks from the outcrop examples in SE Crete. (b) Thickness of basal shear zones vs. thickness of failed strata for offshore (Holocene) examples documented in the literature.

4. Specific remobilization styles are observed at outcrop, such as the alternation in space of autochthonous blocks, in situ breccia-conglomerates, and disrupted deepwater blocks that are laterally spread. These blocks can form important compaction-related structural traps in overlying strata if buried at significant depths.

As a corollary of this work, we reassess the ratio (R) between the thickness of blocks (and presumably of MTDs) and corresponding thickness of their basal glide zones as varying between 5 and 10. This ratio confirms the existence of important basal sediment deformation in all MTDs investigated in this chapter. We postulate that such an observation has important implications in terms of geohazard modeling and the recognition of overpressures (and fluid accumulations) on the base of such type(s) of deposits.

ACKNOWLEDGMENTS

This work was developed under research grants from the Royal Society, Geological Society of London, TEPA-Total Angola, and Husky Energy. The Geological and Mining Institute (IGME) in Greece is acknowledged for the fieldwork permission awarded to both T. Alves and D. Gamboa. D. Gamboa thanks the Sêr Cymru National Research Network for Low Carbon Energy and Economy for research support and publishes with the permission of the Executive Director, British Geological Survey. We thank G.A. Pini and E. Tavarnelli for their constructive comments to an early draft of this chapter.

REFERENCES

Alves, T. M. (2015). Submarine slide blocks and associated soft-sediment deformation in deep-water basins: A review. *Marine and Petroleum Geology*, *67*, 262–285.

Alves, T. M., & Cartwright, J. A. (2009). Volume balance of a submarine landslide in the Espírito Santo Basin, offshore Brazil: Quantifying seafloor erosion, sediment accumulation and depletion. *Earth and Planetary Science Letters*, *288*, 572–580.

Alves, T. M., & Cupkovic, T. (2018). Footwall degradation styles and associated sedimentary facies distribution in SE Crete: Insights into tilt-block extensional basins on continental margins. *Sedimentary Geology*, *367*, 1–19.

Alves, T. M., & Lourenço, S. D. N. (2010). Geomorphologic features related to gravitational collapse: Submarine landsliding to lateral spreading on a late Miocene–Quaternary slope (SE Crete, eastern Mediterranean). *Geomorphology*, *123*, 13–33.

Alves, T. M., Lykousis, V., Sakellariou, D., Alexandri, S., & Nomikou, P. (2007). Constraining the origin and evolution of confined turbidite systems: Southern Cretan margin, Eastern Mediterranean Sea (34°30–36°N). *Geo-Marine Letters*, *27*, 41–61.

Alves, T. M., Omosanya, K., & Gowling, P. (2015). Volume rendering of enigmatic high-amplitude anomalies in southeast Brazil: A workflow to distinguish lithologic features from fluid accumulations. *Interpretation*, *3*(2), A1–A14. https://doi.org/10.1190/INT-2014-0106.1

Arnott, R. W. C., Wallace, K., & Laurin, J. (2011). Stratal architecture and temporal evolution of a passive margin mass-transport deposit, Neoproterozoic Isaac Formation, Cariboo Mountains, British Columbia, Canada. In R. C. Shipp, P. Weimer, & H. W. Posamentier (Eds.), *Mass transport deposits in deep water settings, Special Publication (SEPM (Society for Sedimentary Geology))* (Vol. 96, pp. 221–234). Tulsa, OK: SEPM (Society for Sedimentary Geology).

Barker, P. F. (1983). Tectonic evolution and subsidence history of the Rio-Grande Rise. In P. F. Barker, R. L. Carlson, & D. A. Hohnson (Eds.), *Initial reports of the Deep Sea Drilling Program* (Vol. 72, pp. 953–976). Washington, DC: Government Printing Office.

Barker, P. F., Buffler, R. T., & Gambôa, L. A. (1983). A seismic reflection study of the Rio Grande Rise. In P. F. Barker, R. L. Carlson, & D. A. Hohnson (Eds.), *Initial reports of the Deep Sea Drilling Program* (Vol. 72, pp. 499–517). Washington, DC: Government Printing Office.

Blair, T. C., & McPherson, J. G. (1999). Grain-size and textural classification of coarse sedimentary particles. *Journal of Sedimentary Research*, *69*, 6–19.

Bonneau, M. (1984). Correlation of the Hellenide nappes in the south-east Aegean and their tectonic reconstruction. *Geological Society, London, Special Publications*, *17*, 517–527.

Borgomano, J. (2000). The Upper Cretaceous carbonates of the Gargano-Murge region, southern Italy: A model of platform-to-basin transition. *AAPG Bulletin*, *84*, 1561–1588.

Brandner, R., Flügel, E., & Senowbari-Daryan, B. (1991). Microfacies of carbonate slope boulders: Indicator of the source area (Middle Triassic: Mahlknecht Cliff, Western Dolomites). *Facies*, *25*, 279–295.

Brothers, D. S., Maier, K. L., Kliesener, J. W., Conrad, J. E., & Chaytor, J. D. (2017). The Santa Cruz Basin seubmarine landslide complex, Southern California: Repeated failure of uplifted basins sediment. In *From the mountains to the Abyss: The California Borderland as an archive of Southern California geologic evolution, SEPM Special Publication* (Vol. 110). Tulsa, OK: SEPM. https://doi.org/10.2110/sepmsp.110.0

Brown, A. R. (2004). *Interpretation of three-dimensional seismic data* (6th ed., 665 pp.). Tulsa, OK: American Association of Petroleum Geologists.

Brun, J.-P., & Sokoutis, D. (2010). 45 m.y. of Aegean crust and mantle flow driven by trench retreat. *Geology*, *38*, 815–818.

Bull, S., Cartwright, J., & Huuse, M. (2009). A review of kinematic indicators from mass-transport complexes using 3D seismic data. *Marine and Petroleum Geology*, *26*, 1132–1151.

Buttler, R. W. H., & Tavarnelli, E. (2006). The structure and kinematics of substrate entrainment into high-concentration sandy turbidites: A field example from the Gorgoglione 'flysch' of southern Italy. *Sedimentology*, *53*, 655–670.

Callot, P., Odonne, F., & Sempere, T. (2008). Liquification and soft-sediment deformation in a limestone megabreccia: The Ayabacas giant collapse, Cretaceous, southern Peru.

Sedimentary Geology, *212*, 49–69. https://doi.org/10.1016/j.sedgeo.2008.10.006

Campredon, R., Franco, M., Giannerini, G., Gigot, P., Irr, F., Lanteaume, M., et al. (1977). Les déformations de conglomérats pliocènes de l'arc de Nice (chaînes subalpines méridionales). *Compte Rendu. Sommaire des Séances. Société Géologique de France*, *2*, 75–77.

Collot, J. Y., & Davy, B. (1998). Forearc structures and tectonic regimes at the oblique subduction zone between the Hikurangi Plateau and the southern Kermadec margin. *Journal of Geophysical Research: Solid Earth*, *103*, 623–650.

Collot, J. Y., Lewis, K., Lamarche, G., & Lallemand, S. (2001). The giant Ruatoria debris avalanche on the northern Hikurangi margin, New Zealand: Result of oblique seamount subduction. *Journal of Geophysical Research: Solid Earth*, *106*, 19271–19297.

Creutzburg, N., Drooger, C. W., Meulenkamp, J. E., Papastamatiou, J., Seidel, E., & Tataris, A. (1977). *Geological map of Crete (1:200.000)*. Athens, Greece: Institute of Geology and Mineral Exploration (IGME).

Davison, I. (2007). Geology and tectonics of the South Atlantic Brazilian salt basins. In A. C. Ries, R. W. H. Butler, & R. H. Graham (Eds.), *Deformation of the continental crust: The legacy of Mike Coward* (Vol. 272, pp. 345–359). London, UK: Geological Society, Special Publications.

De Blasio, F. V., Engvik, L. E., & Elverhøi, A. (2006). Sliding of outrunner blocks from submarine landslides. *Geophysical Research Letters*, *33*. https://doi.org/10.1029/2005GL025165

Demercian, S., Szatmari, P., & Cobbold, P. R. (1993). Style and pattern of salt diapirs due to thin-skinned gravitational gliding, Campos and Santos basins, offshore Brazil. *Tectonophysics*, *228*, 393–433.

Deptuck, M. E., Mosher, D. C., Campbell, D. C., Hughes-Clarke, J. E., & Noseworthy, D. (2007). Along slope variations in mass failures and relationships to major Plio-Pleistocene morphological elements, SW Labrador Sea. In V. Lykousis, D. Sakellariou, & J. Locat (Eds.), *Submarine mass movements and their consequences* (pp. 37–45). Berlin, Germany: Springer.

Dimitrijević, M., & Dimitrijević, M. (1973). Olistostrome mélange in the Yugoslavian Dinarides and late Mesozoic plate tectonics. *The Journal of Geology*, *81*, 328–340.

Dumont, T., Simon-Labric, T., Authemayou, C., & Heymes, T. (2011). Lateral termination of the north-directed Alpine orogeny and onset of westward escape in the Western Alpine arc: Structural and sedimentary evidence from the external zone. *Tectonics*, *30*. https://doi.org/10.1029/2010TC002836

Dunlap, D. B., Wood, L. J., Weisenberger, C., & Jabour, H. (2010). Seismic geomorphology of offshore Morocco's east margin, Safi Haute Mer area. *Bulletin of the American Association of Petroleum Geologists*, *94*, 615–642.

Festa, A., Dilek, Y., Gawlick, H.-J., & Missoni, S. (2014). Mass-transport deposits, olistostromes and soft-sediment deformation in modern and ancient continental margins, and associated natural hazards. *Marine Geology*, *356*, 1–4.

Fiduk, J. C., Brush, E. R., Anderson, L. E., Gibbs, P. B., & Rowan, M. G. (2004). Salt deformation, magmatism, and hydrocarbon prospectivity in the Espirito Santo Basin, offshore Brazil. In P. J. Post, D. L. Olson, K. T. Lyons, S. L. Palmes, P. F. Harison, & N. C. Rosen (Eds.), *Salt-sediment interactions and hydrocarbon prospectivity: Concepts, applications, and case studies for the 21st century. GCSSEPM 24th annual research conference, Houston, Texas* (pp. 370–392). Houston, TX: GCSSEPM.

Fortuin, A.R., 1977. Stratigraphy and sedimentary history of the Neogene deposits in the Ierapetra region, Eastern Crete, GUA Papers in Geology Series (Vol. 1, 164 pp.) (PhD thesis). University of Utrecht.

Fortuin, A. R. (1978). Late Cenozoic history of Eastern Crete and implications for the geology and dynamics of the Southern Aegean area. *Geologie en Mijnbouw*, *57*, 461–464.

Fortuin, A. R., & Peters, J. M. (1984). The Prina Complex in eastern Crete and its relationship to possible Miocene strike-slip tectonics. *Journal of Structural Geology*, *6*, 459–476.

França, R. L., Del Rey, A. C., Tagliari, C. V., Brandão, J. R., & Fontanelli, P. R. (2007). Bacia de Espírito Santo. *Boletim de Geociencias da Petrobras*, *15*, 501–509.

Gallen, S. F., Wegmann, K. W., Bohnenstiehl, D. R., Pazzaglia, F. J., Brandon, M. T., & Fassoulas, C. (2014). Active simultaneous uplift and margin-normal extension in a forearc high, Crete, Greece. *Earth and Planetary Science Letters*, *398*, 11–24.

Gamboa, D., Alves, T., & Cartwright, J. (2011). Distribution and characterization of failed (mega) blocks along salt ridges, southeast Brazil: Implications for vertical fluid flow on continental margins. *Journal of Geophysical Research*, *116*, B08103.

Gamboa, D., Alves, T., Cartwright, J., & Terrinha, P. (2010). MTD distribution on a 'passive' continental margin: The Espírito Santo Basin (SE Brazil) during the Palaeogene. *Marine and Petroleum Geology*, *27*, 1311–1324.

Gamboa, D., Alves, T., & Omosanya, K. (this volume). Style and morphometry of mass-transport deposits across the Espírito Santo Basin, SE Brazil. In K. Ogata, A. Festa, & G. A. Pini (Eds.), *Submarine landslides: Subaqueous mass transport deposits from outcrops to seismic profiles* (pp. 227–246). Washington, DC/Hoboken, NJ: American Geophysical Union/Wiley.

Gamboa, D., & Alves, T. M. (2015). Three-dimensional fault meshes and multi-layer shear in mass-transport blocks: Implications for fluid flow on continental margins. *Tectonophysics*, *647*, 21–32.

Gamboa, D., & Alves, T. M. (2016). Bi-modal deformation styles in confined mass-transport deposits: Examples from a salt minibasin in SE Brazil. *Marine Geology*, *379*, 176–193.

Gamboa, D., Alves, T. M., & Cartwright, J. (2012). Seismic-scale rafted and remnant blocks over salt ridges in the Espírito Santo Basin, Brazil. In Y. Yamada, K. Kawamura, K. Ikehara, Y. Ogawa, R. Urgeles, D. C. Mosher, et al. (Eds.), *Submarine mass movements and their consequences* (pp. 629–638). Berlin, Germany: Springer.

Gambôa, L. A., Buffler, R. T., & Barker, P. F. (1983). Seismic stratigraphy and geologic history of the Rio-Grande Gap and Southern Brazil Basin. In P. F. Barker, R. L. Carlson, & D. A. Hohnson (Eds.), *Initial reports of the Deep Sea Drilling Project* (Vol. 72, pp. 481–497). Washington, DC: U.S. Printing Office.

Goff, J., Nichol, S., Chagué-Goff, C., Horrocks, M., McFadgen, B., & Cisternas, M. (2010). Predecessor to New Zealand's

largest historic trans-South Pacific tsunami of 1868 AD. *Marine Geology*, *275*, 155–165.

Haq, B. U., Hardenbol, J., & Vail, P. R. (1988). Mesozoic and Cenozoic chronostratigraphy and cycles of sea-level change. In C. K. Wilgus, B. S. Hastings, C. G. S. C. Kendall, C. A. Ross, & J. C. Van Wagoner (Eds.), *Sea-level changes: An integrated approach, SEPM Special Publication* (Vol. 42, pp. 7–108). Tulsa, OK, SEPM.

Huson, W. J., & Fortuin, A. R. (1985). The Lithinon slide: A large submarine slide in the South Cretan Trough, Eastern Mediterranean. *Marine Geology*, *65*, 103–111.

Huvenne, V. A., Croker, P. F., & Henriet, J.-P. (2002). A refreshing 3D view of an ancient sediment collapse and slope failure. *Terra Nova*, *14*, 33–40.

Ilstad, T., De Blasio, F. V., Elverhøi, A., Harbitz, C. B., Engvik, L., Longva, O., & Marr, J. G. (2004). On the frontal dynamics and morphology of submarine debris flows. *Marine Geology*, *213*, 481–497.

Jenner, K. A., Piper, D. J., Campbell, D. C., & Mosher, D. C. (2007). Lithofacies and origin of late Quaternary mass transport deposits in submarine canyons, central Scotian Slope, Canada. *Sedimentology*, *54*, 19–38.

Jiao, R., Herman, F., & Seward, D. (2017). Late Cenozoic exhumation model of New Zealand: Impacts from tectonics and climate. *Earth-Science Reviews*, *166*, 286–298.

Keller, B. (2017). Massive rock slope failure in Central Switzerland: History, geologic–geomorphological predisposition, types and triggers, and resulting risks. *Landslides*, *14*, 1633–1653.

Kerckhove, C. (1974). *Notice explicative de la Carte géologique de France au 1/50000è*, feuille Barcelonnette (895), Bureau de Recherches Géologiques et Minières, Orléans.

Kerckhove, C., & Antoine, P. (1964). Sur l'existence de failles de décrochement dans le massif des Bauges. *Trav. Lab. Géol. Fac. Sci. Univ. Grenoble*, *40*, 81–89.

Krahl, J., Kauffmann, G., Kozur, H., Richter, D., Förster, O., & Heinritz, F. (1983). Neue Daten zur Biostratigraphie und zur tektonischen Lagerung der Phyllit-Gruppe und der Trypali-Gruppe auf der Insel Kreta (Griechenland). *Geologische Rundschau*, *72*, 1147–1166.

Kumar, N., Gambôa, L., & Supko, P. (1976). Evolution of marginal plateau – DSDP data from Site 356 on the São-Paulo Plateau (Brazilian continental margin). *Bulletin of the American Association of Petroleum Geologists*, *60*(4), 690–690.

Kvalstad, T. J., Andresen, L., Forsberg, C. F., Berg, K., Bryn, P., & Wangen, M. (2005). The Storegga slide: Evaluation of triggering sources and slide mechanics. *Marine and Petroleum Geology*, *22*, 245–256.

Laberg, J. S., Strasser, M., Alves, T. M., Gao, S., Kawamura, K., Kopf, A., & Moore, G. F. (2017). Internal deformation of a muddy gravity flow and its interaction with the seafloor (site C0018 of IODP Expedition 333, Nankai Trough, SE Japan). *Landslides*, *14*, 849–860.

Lamarche, G., Joanne, C., & Collot, J. Y. (2008). Successive, large mass-transport deposits in the south Kermadec fore-arc basin, New Zealand: The Matakaoa Submarine Instability Complex. *Geochemistry, Geophysics, Geosystems*, *9*(4). https://doi.org/10.1029/2007GC001843

Marfurt, K. J., & Alves, T. M. (2015). Pitfalls and limitations in seismic attribute interpretation of tectonic features. *Interpretation*, *3*(1), SB5–SB15. https://doi.org/10.1190/INT-2014-0122.1

Masson, D., Harbitz, C., Wynn, R., Pedersen, G., & Løvholt, F. (2006). Submarine landslides: Processes, triggers and hazard prediction. *Philosophical Transactions of the Royal Society of London A: Mathematical, Physical and Engineering Sciences*, *364*, 2009–2039.

McLeod, A. E., & Underhill, J. R. (1999). Processes and products of footwall degradation, northern Brent Field, Northern North Sea. In A. J. Fleet & S. A. R. Boldy (Eds.), *Petroleum geology of northwest Europe: Proceedings of the 5th conference* (pp. 91–106). London, UK: Geological Society.

McNeill, L. C., Collier, R. E. L., De Martini, P. M., Pantosti, D., & D'Addezio, G. (2005). Recent history of the Eastern Eliki Fault, Gulf of Corinth: Geomorphology, palaeoseismology and impact on palaeoenvironments. *Geophysical Journal International*, *161*, 154–166.

Meulenkamp, J. E. (1979). Field guide to the Neogene of Crete. In N. Symeonidis, D. Papanikolaou, & M. Dermitzakis (Eds.), *Field guide to the Neogene of Crete, Series A* (Vol. 32, pp. 1–32). Athens, Greece: Department of Geology and Paleontology of the University of Athens.

Migeon, S., Cattaneo, A., Hassoun, V., Larroque, C., Corradi, N., Fanucci, F., et al. (2011). Morphology, distribution and origin of recent submarine landslides of the Ligurian Margin (North-western Mediterranean): Some insights into geohazard assessment. *Marine Geophysical Research*, *32*, 225–243.

Mohriak, W. U. (1995). Salt tectonics structural styles: Contrasts and similarities between the South Atlantic and the Gulf of Mexico. In C. J. Travis, H. Harrison, M. R. Hudec, B. C. Vendeville, F. J. Peel, & B. E. Perkins (Eds.), *Salt, sediment and hydrocarbons, Gulf Coast Section of the Society of Economic Paleontologists and Mineralogists (GCSSEPM Foundation), 16th annual research conference* (pp. 177–191). Houston, TX: Society of Economic Paleontologists and Mineralogists (GCSSEPM Foundation).

Mohriak, W. U. (2003). Bacias sedimentares da margem continental Brasileira. In L. A. Bizzi, C. Schobbenhaus, R. M. Vidotti, & J. H. Goncalves (Eds.), *Geologia, Tectonica e Recursos Minerais do Brasil* (pp. 87–165). Brasilia: CPRM.

Moore, G. F., & Strasser, M. (2016). *Large mass transport deposits in Kumano Basin, Nankai Trough, Japan, Submarine Mass Movements and their Consequences* (pp. 371–379). Berlin, Germany: Springer.

Moreira, J. L. P., & Carminatti, M. (2004). Sistemas deposicionais de talude e de bacia no Eoceno da Bacia de Santos. *Boletim de Geociencias da Petrobras*, *12*, 73–87.

Moscardelli, L., & Wood, L. J. (2016). Morphometry of mass-transport deposits as a predictive tool. *Bulletin of the Geological Society of America*, *128*, 47–80.

Navarro, L., & Arnott, R. W. C. (2018). Stratal architecture and evolution of a slope mass-transport complex, Isaac Formation, Neoproterozoic Windermere Supergroup, southern Canadian Cordillera, British Columbia, Canada. In D. G. Lintern, D. C. Mosher, L. G. Moscardelli, P. T. Bobrowsky, C. Campbell, J. D. Chaytor, et al. (Eds.), *SP477 subaqueous mass movements and their consequences: Assessing geohazards, environmental*

implications and economic significance of subaqueous landslides (Vol. 477). London, UK: Geological Society of London. https://doi.org/10.1144/SP477.24

Ogata, K., Mutti, E., Pini, G. A., & Tinterri, R. (2012). Mass transport-related stratal disruption within sedimentary mélanges: Examples from the northern Apennines (Italy) and south-central Pyrenees (Spain). *Tectonophysics*, *568*, 185–199.

Ogata, K., Pogačnik, Ž., Pini, G. A., Tunis, G., Festa, A., Camerlenghi, A., & Rebesco, M. (2014). The carbonate mass transport deposits of the Paleogene Friuli Basin (Italy/Slovenia): Internal anatomy and inferred genetic processes. *Marine Geology*, *356*, 88–110. https://doi.org/10.1016/j.margeo.2014.06.014

Ojeda, H. A. O. (1982). Structural framework, stratigraphy, and evolution of Brazilian marginal basins. *Bulletin of the American Association of Petroleum Geologists*, *66*, 732–749.

Okay, A. I., İşintek, İ., Altıner, D., Özkan-Altıner, S., & Okay, N. (2012). An olistostrome–mélange belt formed along a suture: Bornova Flysch zone, western Turkey. *Tectonophysics*, *568*, 282–295.

Omosanya, K. O., & Alves, T. M. (2013). Ramps and flats of mass-transport deposits (MTDs) as markers of seafloor strain on the flanks of rising diapirs (Espírito Santo Basin, SE Brazil). *Marine Geology*, *340*, 82–97.

Omosanya, K. O., & Alves, T. M. (2014). Mass-transport deposits controlling fault propagation, reactivation and structural decoupling on continental margins (Espírito Santo Basin, SE Brazil). *Tectonophysics*, *628*, 158–171.

Ortiz-Karpf, A., Hodgson, D. M., Jackson, C. A. L., & McCaffrey, W. D. (2018). Mass-transport complexes as markers of deep-water fold-and-thrust belt evolution: Insights from the southern Magdalena fan, offshore Colombia. *Basin Research*, *30*, 65–88.

Pêcher, A., Barféty, J., & Gidon, M. (1992). Structures est-ouest anténummulitiques à la bordure orientale du massif des Ecrins-Pelvoux (Alpes françaises). *Géologie Alpine, Grenoble, Série spéciale Résumés*, *1*, 72–73.

Perotti, E., Bertok, C., d'Atri, A., Martire, L., Piana, F., & Catanzariti, R. (2012). A tectonically-induced Eocene sedimentary mélange in the West Ligurian Alps, Italy. *Tectonophysics*, *568*, 200–214.

Peters, J. M., & Troelstra, S. R. (1984). Early Pliocene sedimentation in the Cretan region: Implications for the timing and amount of vertical motion along the south Hellenic Arc (Eastern Mediterranean). *Marine Geology*, *56*, 335–344.

Pickering, K., & Hiscott, R. (2015). *Deep marine systems: Processes, deposits, environments, tectonic and sedimentation* (776 pp.). Chichester, UK: Wiley.

Postma, G., & Drinia, H. (1993). Architecture and sedimentary facies evolution of a marine, expanding outer-arc half-graben (Crete, late Miocene). *Basin Research*, *5*, 103–124.

Postma, G., Fortuin, A. R., & van Wamel, W. A. (1993). Basin-fill patterns controlled by tectonics and climate: The Neogene 'fore-arc' basins of eastern Crete as a case history. *Special Publication of the International Association of Sedimentologists*, *20*, 335–362.

Ravnås, R., Bondevik, K., Helland-Hansen, W., Lømo, L., Ryseth, A., & Steel, R. J. (1997). Sedimentation history as an indicator of rift initiation and development: The late Bajocian-Bathonian evolution of the Oseberg-Brage area, northern North Sea. *Norsk Geologisk Tidsskrift*, *77*, 205–232.

Reilinger, R., McClusky, S., Paradissis, D., Ergintav, S., & Vernant, P. (2010). Geodetic constraints on the tectonic evolution of the Aegean region and strain accumulation along the Hellenic subduction zone. *Tectonophysics*, *488*, 22–30.

Ring, U., & Reischmann, T. (2002). The weak and superfast Cretan detachment, Greece: Exhumation at subduction rates in extruding wedges. *Journal of the Geological Society*, *159*, 225–228.

Roep, T. B., & Fortuin, A. R. (1996). A submarine slide scar and channel filled with slide blocks and megarippled Globigerina sands of possible contourite origin from the Pliocene of Sumba, Indonesia. *Sedimentary Geology*, *103*, 145–160.

Ryan, W. B. F., Hsü, K. J., Cita, M. B., Dumitrica, P., Lort, J. M., Mayne, W., et al. (1973). *Initial reports of the Deep Sea Drilling Project 13 (sire report 10)* (pp. 323–353). Washington, DC: US Government Printing Office.

Seidel, E., Kreuzer, H., & Harre, W. (1982). A late Oligocene/early Miocene high pressure belt in the External Hellenides. *Geologisches Jahrbuch*, E23, 165–206.

Seidel, M., Seidel, E., & Stöckhert, B. (2007). Tectono-sedimentary evolution of lower to middle Miocene half-graben basins related to an extensional detachment fault (western Crete, Greece). *Terra Nova*, *19*, 39–47.

Sobiesiak, M. S., Kneller, B., Alsop, G. I., & Milana, J. P. (2018). Styles of basal interaction beneath mass transport deposits. *Marine and Petroleum Geology*, *98*, 629–639.

Spence, G. H., & Tucker, M. E. (1997). Genesis of limestone megabreccias and their significance in carbonate sequence stratigraphic models: A review. *Sedimentary Geology*, *112*, 163–193.

Stampfli, G. M. (2005). Plate tectonics of the Apulia-Adria microcontinents. In I. R. Finetti (Ed.), *CROP PROJECT: Deep seismic exploration of the central Mediterranean and Italy* (pp. 747–766). Amsterdam, The Netherlands: Elsevier.

Stewart, I. S., & Hancock, P. L. (1988). Normal fault zone evolution and fault scarp degradation in the Aegean region. *Basin Research*, *1*, 139–153.

Strozyk, F., Strasser, M., Förster, A., Kopf, A., & Huhn, K. (2010). Slope failure repetition in active margin environments: Constraints from submarine landslides in the Hellenic fore arc, eastern Mediterranean. *Journal of Geophysical Research: Solid Earth*, *115*, B8. https://doi.org/10.1029/2009JB006841

Sultan, N., Voisset, M., Marsset, B., Marsset, T., Cauquil, E., & Colliat, J.-L. (2007). Potential role of compressional structures in generating submarine slope failures in the Niger Delta. *Marine Geology*, *237*, 169–190.

Sun, Q., Alves, T., Lu, X., Chen, C., & Xie, X. (2018). True volumes of slope failure estimated from a Quaternary mass-transport deposit in the northern South China Sea. *Geophysical Research Letters*, *45*, 2642–2651.

Sun, Q., Alves, T., Xie, X., He, J., Li, W., & Ni, X. (2017). Free gas accumulations in basal shear zones of mass-transport deposits (Pearl River Mouth Basin, South China Sea): An important geohazard on continental slope basins. *Marine and Petroleum Geology*, *81*, 17–32.

Ten Veen, J. H., & Postma, G. (1999). Neogene tectonics and basin fill patterns in the Hellenic outer-arc (Crete, Greece). *Basin Research*, *11*, 223–241.

Thomson, S. N., Stöckhert, B., & Brix, M. R. (1998). Thermochronology of the high-pressure metamorphic rocks of Crete, Greece: Implications for the speed of tectonic processes. *Geology*, *26*, 259–262.

Thomson, S. N., Stöckhert, B., & Brix, M. R. (1999). Miocene high-pressure metamorphic rocks of Crete, Greece, rapid exhumation by buoyant escape. In U. Ring, M. T. Brandon, G. S. Lister, & S. D. Willett (Eds.), *Exhumation processes, normal faulting, ductile flow and erosion, Special Publications* (Vol. 154, pp. 87–107). London, UK: Geological Society of London.

van Hinsbergen, D. J. J., & Meleunkamp, J. E. (2006). Neogene supradetachment basin development on Crete (Greece) during exhumation of the South Aegean core complex. *Basin Research*, *18*, 103–124.

Wilson, R. C. L., Manatschal, G., & Wise, S. (2001). Rifting along non-volcanic passive margins: Stratigraphic and seismic evidence from the Mesozoic successions of the Alps and western Iberia. *Geological Society of London, Special Publication*, *187*, 429–452.

Zachariasse, W. J., van Hinsbergen, D. J. J., & Fortuin, A. R. (2008). Mass wasting and uplift on Crete and Karpathos during the early Pliocene related to initiation of south Aegean left-lateral, strike-slip tectonics. *Bulletin of the Geological Society of America*, *120*, 976–993.

6

Block Generation, Deformation, and Interaction of Mass-Transport Deposits With the Seafloor: An Outcrop-Based Study of the Carboniferous Paganzo Basin (Cerro Bola, NW Argentina)

Matheus S. Sobiesiak[1], Victoria Valdez Buso[2], Ben Kneller[2], G. Ian Alsop[2], and Juan Pablo Milana[3]

ABSTRACT

Mass-transport processes are notorious for their ability to carry large blocks or megaclasts, to deform sediments, and to interact with the seafloor through deformation and/or erosion of the substrate. These processes, together with their influence on slope sedimentation, are themes we address via direct field observation of three Carboniferous-aged mass-transport deposits (MTDs) (labeled I, II, and III) from Cerro Bola, NW Argentina. Internal deformation can be observed in all three MTDs, although it is best developed in MTD II, a 180 m thick vertically zoned MTD with deformation evolving upward from a simple shear dominated base to a pure shear middle zone and finally back into a simple shear dominated topmost zone. The contact between MTDs I and II and their underlying sandstone substrates are also locally deformed, with plastic deformation affecting up to ~20 m of substrate below the MTD base. Conversely, the basal contact between MTD II and the substrate is also in part erosional, marked by scours and grooves that truncate the bedding in the topmost layers of the substrate. Additionally, the presence of large blocks composed of diverse lithologies embedded within the MTDs, together with the sedimentological description of the MTD's matrix and the aforementioned interaction with the seafloor, suggests at least two processes accountable for block generation within MTDs.

6.1. INTRODUCTION

Mass-transport deposits (MTDs) are described from both seismic and outcrop data sets in terms of internal structures (e.g., Farrell, 1984; Ogata et al., 2014a; Sobiesiak et al., 2016b; Alsop et al., 2017), basal interaction (e.g., Draganits et al., 2008; Laberg et al., 2016; Sobiesiak et al., 2018), creation of accommodation space (e.g., Fairweather, 2015; Kneller et al., 2016), and the presence of blocks (e.g., Macdonald et al., 1993; Dykstra et al., 2011; Alves, 2015; Sobiesiak et al., 2016b). The internal structures of MTDs are usually described in relation to stress/strain fields, with compressional fields associated with thrust planes, reverse faults, slump folds, and shear planes (e.g., Farrell, 1984; Alsop et al., 2017; Sobiesiak et al., 2017), while extensional strains are expressed as normal faults, boudinage, mullions, and pull-aparts, among others (e.g., Dykstra et al., 2011; Alsop & Marco, 2014; Alves, 2015).

When an MTD moves downslope, it translates over a detachment surface termed a basal shear surface (BSS) or basal glide plane. This surface is developed due to progressive shear failure and defines the lower limit of the MTD, thus separating deformed sediment above from undeformed strata below (e.g., Hampton et al., 1996; Frey-Martínez et al., 2006; Bull et al., 2009; Omosanya & Alves, 2013). The

[1] *Postgraduate Program in Geology, University of the Sinos Valley, São Leopoldo, Rio Grande do Sul, Brazil*

[2] *Department of Geology and Geophysics, School of Geosciences, University of Aberdeen, Aberdeen, United Kingdom*

[3] *CONICET and Institute of Geology, National University of San Juan, San Juan, Argentina*

Submarine Landslides: Subaqueous Mass Transport Deposits from Outcrops to Seismic Profiles, Geophysical Monograph 246, First Edition. Edited by Kei Ogata, Andrea Festa, and Gian Andrea Pini.
© 2020 American Geophysical Union. Published 2020 by John Wiley & Sons, Inc.

interaction between the BSS and the substrate has been widely documented both from seismic data (e.g., McGilvery & Cook, 2003; Gee et al., 2005; Moscardelli et al., 2006; Posamentier et al., 2011; Alves et al., 2014) and more rarely from outcrop data (e.g., Gawthorpe & Clemmey, 1985; Lucente & Pini, 2003; Butler & Tavarnelli, 2006; Dykstra et al., 2011; Ogata et al., 2012; Dakin et al., 2013; Sobiesiak et al., 2016b, 2018). The nature of these interactions is usually described as erosional, creating features such as scours (Nissen et al., 1999; Posamentier & Kolla, 2003), grooves (Posamentier & Kolla, 2003; Bull et al., 2009), striations (Gee et al., 2005; Bull et al., 2009), and monkey fingers (McGilvery & Cook, 2003). However, new studies have revealed that the interaction between an MTD and the seafloor can be deformational, resulting in the development of soft-sediment deformational structures within the upper part of sediment pile that is below the detachment surface in the case of frontally confined MTDs (Frey-Martínez et al., 2006) or immediately beneath the seafloor in frontally emergent MTDs (e.g., Alves & Lourenço, 2010; Laberg et al., 2016; Sobiesiak et al., 2018) and lacking sediment incorporation into the flow.

In addition, blocky MTDs are increasingly recognized as a consequence of slope failure and instability (e.g., Macdonald et al., 1993; Alves, 2015), with blocks being defined by Alves (2015) as anything larger than boulder size (>4.1 m) (Blair & McPherson, 1999). From seismic data, blocks have been subdivided into rafted, remnant, and outrunner blocks (e.g., Prior et al., 1984; Nissen et al., 1999; Bull et al., 2009). However, the above distinctions are made difficult in outcrop, due to scale and limits of exposure, among other factors. On the other hand, lithological differences between blocks and their surrounding strata are easily identified at outcrop.

The main aim of this chapter is to provide a summary of published data and a comprehensive overview of three MTDs (MTD I, MTD II, and MTD III) cropping out in superbly exposed sections at Cerro Bola in La Rioja Province, NW Argentina.

In detail, we consider the following:

1. What is the nature of the interaction between MTDs and the seafloor, and how deep can this interaction penetrate?

2. How does deformation affect the MTD sediments themselves, and how is it distributed throughout the deposit?

3. What types of blocks occur within the MTDs, what do they represent, and what processes are capable of creating them?

6.2. GEOLOGICAL SETTING

Paganzo is an epicratonic basin resulting from the accretion of three crustal blocks (Famatina, Cuyania, and Chilenia) along the western margin of the Gondwana craton during the Ordovician and Early Carboniferous (Limarino et al., 2002, 2006; Desjardins et al., 2009). The basin is located in northwestern Argentina (Figure 6.1) extending over an area of 30,000 km^2 and containing up to ~4500 m of sediments (Paganzo Group) (Ramos, 1988). The basin is bound to the north by the Alto de La Puna and to the south and east by the Pampean and Pie de Palo highs (Limarino & Spalletti, 2006). To the west, the basin is limited by the Precordillera, separating Paganzo from the western basins of Calingasta-Uspallata and Rio Blanco.

Fernandez-Seveso and Tankard (1995) and Azcuy et al. (1999) subdivided the Paganzo Group into three formations: Guandacol, Tupe, and Patquia. The Guandacol Formation was affected by the late Paleozoic glaciation and records at least three glacial-deglacial cycles, resulting in a glacially derived package overlain by thick proglacial and postglacial marine packages, including deltaic sediments, black shales, turbidites and MTDs suggesting a periglacial environment (Fernandez-Seveso & Tankard, 1995; Limarino et al., 2002; Milana et al., 2010; Valdez Buso, 2015). The Tupe Formation is characterized by sediments deposited in fluvial, lacustrine, and marginal marine environments, and the Patquia Formation consists of a red bed succession comprising alluvial fan, fluvial, and playa lake lithofacies encroaching on a marginal to shallow marine environment.

Cerro Bola is a mountain located at the border between La Rioja and San Juan provinces, near the town of Villa Unión (~30 km SW) (Figures 6.1 and 6.2). Structurally, the mountain consists of a large north-south trending west-vergent periclinal anticline that forms the hanging wall to a thrust system that dips eastward at ~24° (Milana et al., 2010).The thrust system is related to the Neogene to Quaternary Pampean Range orogenic deformation (Zapata & Allmendinger, 1996). The sedimentary succession at Cerro Bola was deposited on the western margin of Paganzo Basin, exposing Carboniferous sediments from the Guandacol Formation to Permian red beds of the Patquia (Milana et al., 2010). The Guandacol Formation is related to glaciogenic lithostratigraphy (Valdez et al., 2015), and in the Cerro Bola area, the relation of this formation with Tupe and Patquia formations is to date still poorly understood (Valdez et al., 2015). At least three major glacial-deglacial cycles are recorded in Cerro Bola (e.g., Milana et al., 2010; Dykstra et al., 2011; Valdez et al., 2015; Fallgatter et al., 2017).

The Guandacol stratigraphy preserved at Cerro Bola encompasses roughly ten units that can be traced confidently across the mountain side (from base to top): a fluvio-deltaic sequence (FD I); an MTD (MTD I) that contains sandstone blocks; another fluvio-deltaic unit (FD II) displaying an eroded top; an MTD (MTD II) that also contains sandstone blocks; ponded turbidite sandstones; black shales (maximum flooding zone); turbidite sandstones package; fluvio-deltaic sequence

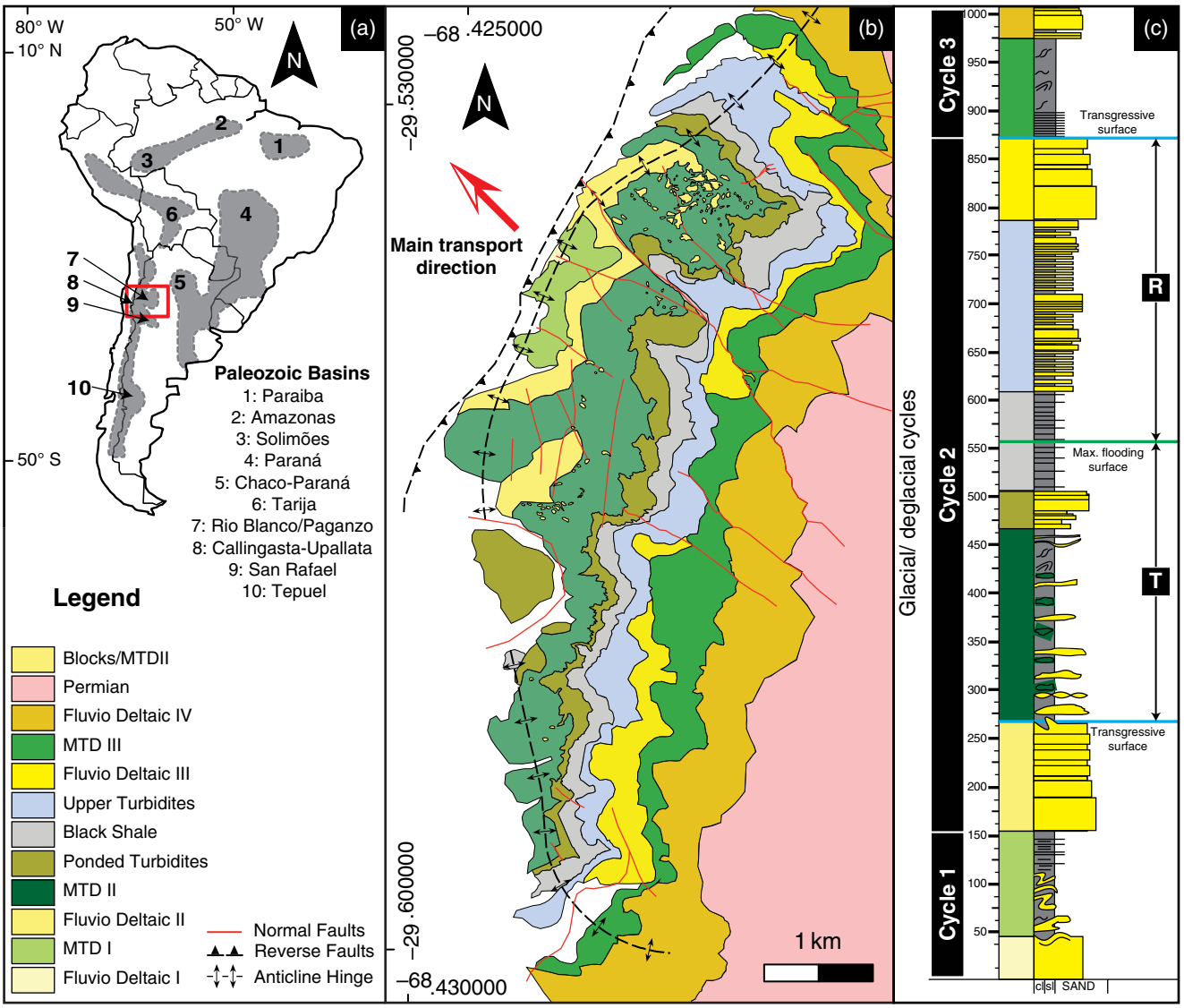


Figure 6.1 (a) Outline map of South America highlighting the late Paleozoic sedimentary basins. Red rectangle locates the study area. Source: Modified from Gulbranson et al. (2010). (b) Geological map of Cerro Bola. Source: Modified from Dykstra et al. (2011). Red arrow indicates the main transport direction (NW). (c) Stratigraphic column from Cerro Bola. (*See electronic version for color representation of this figure*)

(FD III); an MTD (MTD III); and a fluvio-deltaic sequence (FD IV). Then everything is capped by Permian red beds (Pataquia Formation) (Milana et al., 2010) (Figures 6.1 and 6.2). In total, the stratigraphic thickness cropping out in Cerro Bola exceeds 1 km (Milana et al., 2010; Dykstra et al., 2011) (Figures 6.1 and 6.2).

6.3. MASS-TRANSPORT DEPOSITS AT CERRO BOLA

Cerro Bola is a strike section through part of the Paganzo Basin, with a ~1200 m thick stratigraphic succession exposed at outcrop that extends for 10 km in length with excellent two- and three-dimensional exposure (Figure 6.2). At Cerro Bola, we describe three MTDs exposed along the mountain side: The first two MTDs (MTD I and MTD II) are the most accessible, and both possess outsized sandstone and siltstone blocks, internal deformational structures, and signs of interaction with the underlying substrate (Dykstra et al., 2011; Valdez et al., 2015; Fallgatter et al., 2017; Sobiesiak et al., 2016a, 2016b, 2018). The third, MTD III, differs from the older two and displays a deeply incised basal surface that cuts into the upper surface of the underlying sandstone deposit (Milana et al., 2010; Valdez et al., 2015).

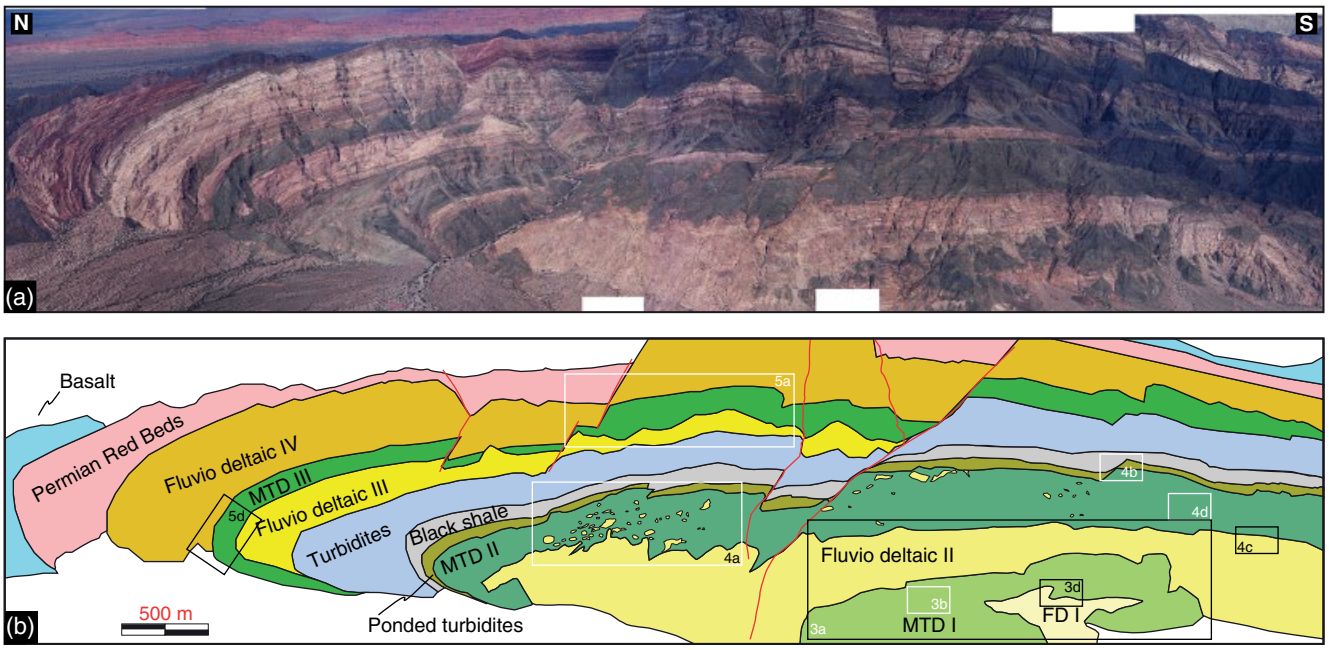


Figure 6.2 (a) Oblique photomosaic looking east toward Cerro Bola. (b) Line drawing showing the interpretation for the whole Cerro Bola stratigraphy. Note local contacts (erosive and/or pinching) between MTDs II and III and their respective substrate: the Fluvio-Deltaic II and III. Location for Figures 6.3, 6.4, and 6.5 is shown. The legend is the same as Figure 6.1.

6.3.1. MTD I

MTD I is the oldest exposed at Cerro Bola and only outcrops in the core of the anticline (Figures 6.2 and 6.3a). The deposit, which is ~115 m thick and outcrops for ~1.5 km along depositional strike, consists of a massive green-colored silty matrix (Figure 6.3a, b) with pebbles, cobbles, and boulders of coarse-grained granitoid and metamorphic rocks originating from the Precambrian basement (Valdez et al., 2015). The MTD contains blocks of sandstone (Figure 6.3b) that range in size from ~3 to 5 m in diameter. These light orange sandstone blocks are composed of massive medium- to coarse-grained sandstone. Additionally, blocks of green-colored, undeformed to moderately deformed bedded siltstone can be found throughout the MTD (Figure 6.3c). The deposit matrix possesses no real markers, making internal soft-sediment deformation difficult to recognize (Valdez et al., 2015).

However, we do record a ~14 m thick zone showing intense ductile deformation in the upper zone of the fluvio-deltaic sediments (FDI) directly below MTD I (Figure 6.3d), which we infer to have occurred while the sediment was unlithified. The deformation includes highly deformed sediments that contain pinch-and-swell structures, along with various scales of folding and sheared matrix. According to Valdez et al. (2015), the deformation style resembles ductile structures described in metamorphic rocks. The majority of sandstone blocks within MTD I occur near the base.

Valdez et al. (2015) described MTD I from Cerro Bola and Sierra de Maz, a locality ~10 km northwest of Cerro Bola that exposes the same glacially influenced stratigraphy. Here they were able to identify a 20 m thick turbidite package composed of dark brown, medium- to coarse-grained sandstone capped by black shale deposited atop MTD I. These turbidites are locally developed in Sierra de Maz and are interpreted as deposits restricted by MTD topography, termed ponded turbidites. Equivalent ponded turbidites are not found above MTD I in Cerro Bola.

6.3.1.1. Interpretation

MTD I is interpreted to be produced from the failure of accumulations of ice-rafted debris, or "aquatill," where basement clasts contained within the matrix are interpreted to be remobilized dropstones. Stratified siltstone blocks are considered to be coherent remnants of the original sediments that were more rigid and survived the flow deformation. This interpretation is based on the similarities between the average composition of the siltstone blocks and the MTD matrix. The sandstone blocks may originate from the erosion of the substrate or from sandstones within a heterogeneous MTD protolith. It is impossible to distinguish between these alternative models due to the lack of directly supporting data

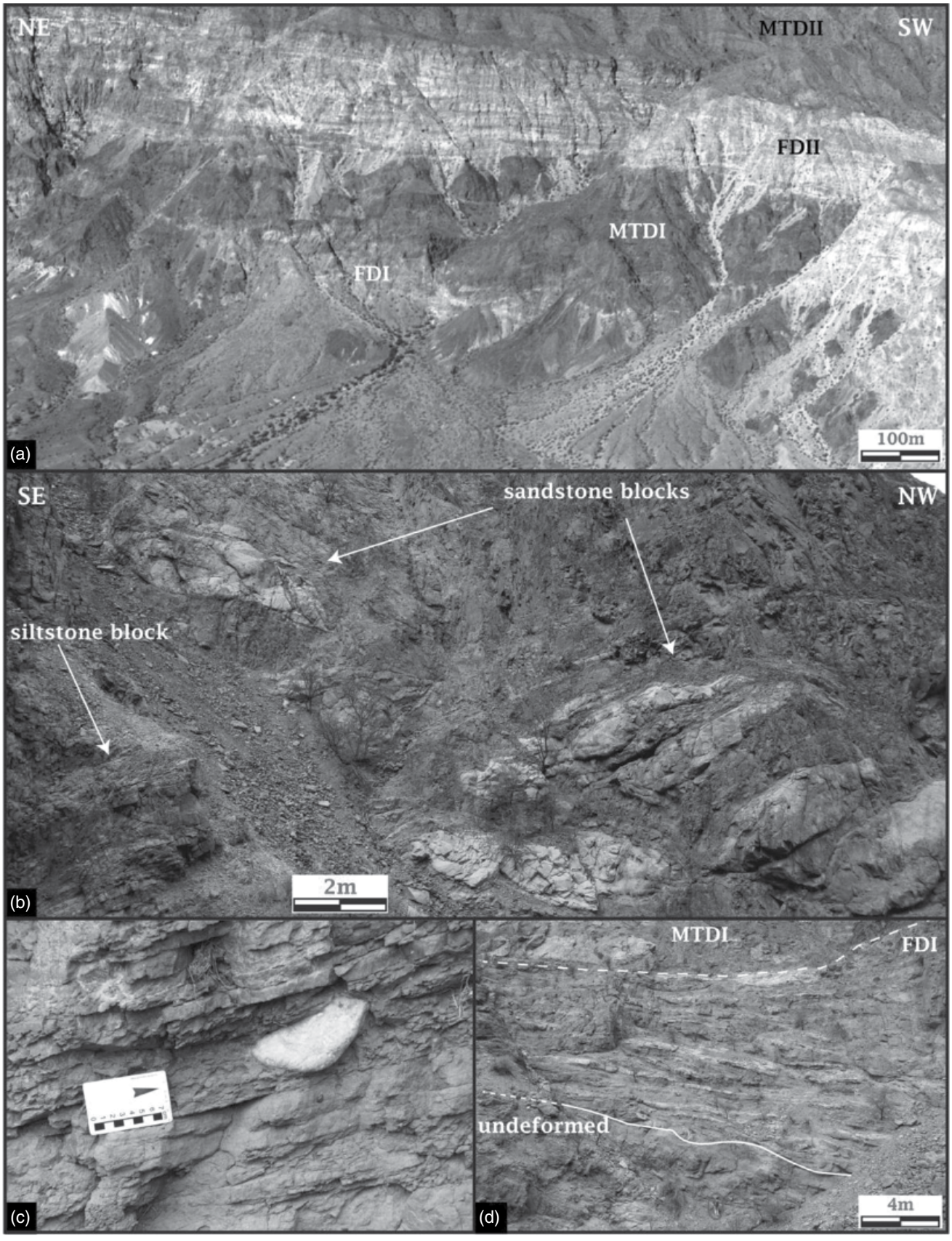


Figure 6.3 (a) Oblique aerial photograph looking southeast toward Cerro Bola. (b) General photograph showing MTD I with its green matrix and the presence of sandstone and siltstone blocks embedded in MTD I. (c) Moderately deformed, bedded siltstone block with a dropstone. (d) Deformational zone developed at the upper zone of the Fluvio-Deltaic I, commencing directly below MTD I. Note the highly deformed sediments in the deformation zone and the presence of small sandstone blocks within MTD I.

(e.g., evidence for basal erosion), and the sandstone blocks may in fact originate from a combination of both substrate erosion and disintegration of a heterogeneous protolith.

The flow is considered to be dominated by pure shear deformation due to the boudinage of sandstone and siltstone blocks. Regardless of whether the MTD as a whole is dominated by pure shear, there must have been a significant component of simple shear operating at least along the lower boundary, as shown by the ~14 m thick deformational zone recorded at the contact between the MTD and the sandy substrate. Valdez et al. (2015) suggest that sandstone blocks may owe their origin to substrate deformation and shearing, followed by their consequent incorporation into the translating flow.

6.3.2. MTD II

MTD II is up to ~180 m thick and crops out for over ~8 km along strike (Milana et al., 2010; Dykstra et al., 2011; Sobiesiak et al., 2016a, 2016b, 2018; Fallgatter et al., 2017) (Figure 6.2). Moreover, it is the most accessible, best exposed, and therefore the most studied of Cerro Bola's MTDs.

In general, MTD II is very similar to MTD I, consisting of green, fine-grained, silty sediments that are remobilized and highly sheared (Figure 6.4a). The matrix contains granule- to boulder-sized clasts of Precambrian granitoid and metamorphic basement rocks, sandstone and siltstone blocks (Figure 6.4a), and ball-shaped concretions (which give the name "Bola" to the mountain). MTD II has irregular boundaries, with the upper boundary displaying onlap of overlying sediments, together with local slumping away from regions of higher surface topography (e.g., Fairweather, 2015; Kneller et al., 2016) (Figure 6.4b). The lower boundary is marked by two styles of basal interaction (Sobiesiak et al., 2018). The first consists of basal scours that cut into and "pluck" parts of the underlying fluvio-deltaic sandstone (Dykstra et al., 2011; Sobiesiak et al., 2016b, 2018) (Figures 6.2 and 6.4a). The second type of basal interaction is where ductile shear of unlithified sediment is developed directly below the base of the MTD (Sobiesiak et al., 2016a, 2018) (Figure 6.4c). Additionally, MTD II is vertically zoned and can be stratigraphically divided into three distinct lower, middle, and upper units with transitional boundaries according to variations in texture and structures (Dykstra et al., 2011; Sobiesiak et al., 2016b) (Figure 6.4a).

Sandstone and siltstone blocks are present throughout the whole of MTD II. In general, whitish to orange sandstone blocks comprise medium- to coarse-grained, moderately sorted arkosic sandstone (Figure 6.4a, d, e). The blocks are highly fractured, generally with no discernible internal structure, but locally primary features such as large-scale trough cross-stratification, ripples, and climbing ripples are recorded (Garyfalou, 2015; Sobiesiak et al., 2016b) (Figure 6.4d, e). Usually, the margins of sandstone blocks display interaction with the MTD, marked by the shearing and/or deformation of the surrounding matrix (Milana et al., 2010; Dykstra et al., 2011; Sobiesiak et al., 2016b). Light to dark green siltstone blocks (Dykstra et al., 2011) are composed of sandstone, siltstone, and dark mudstone layers, with each layer ranging in thickness from millimeters up to 10 cm (Sobiesiak et al., 2016b). Random granule- to boulder-sized clasts are preserved within siltstone blocks, where the layers below and above are deflected around these clasts. Siltstone blocks display only weak internal ductile deformation, but are highly fractured. A full description of sandstone and siltstone blocks from MTD II can be found in Sobiesiak et al. (2016b).

The lower zone of MTD II ranges from 40 up to 60 m in thickness (Sobiesiak et al., 2016b) and is characterized by the occurrence of sandstone blocks within a variably sand-rich matrix and sand streak lithology. Sandstone blocks locally comprise ~30% of the MTD exposure ranging from a few meters up to ~90 m long and up to ~15 m thick (Sobiesiak et al., 2016b) (Figure 6.4a). Additionally, there is a vertical distribution of blocks, with larger and more irregular blocks found near the base of MTD II (Sobiesiak et al., 2016a). Sand streak lithology is similar to the sandstone blocks and the underlying substrate (Garyfalou, 2015), with sand streaks being very abundant near sandstone blocks and close to the contact with the substrate. Sand streaks record complex deformation with superimposed strain histories (Dykstra et al., 2011; Sobiesiak et al., 2016b). The sand-rich matrix is present throughout the whole lower zone of MTD II, although the amount of sand entrained within the matrix decreases vertically through the deposit.

The contact between the lower and middle zones of MTD II is transitional over ~15 m and marked by the vertical decrease and eventual disappearance of sand entrained into the silty matrix (Sobiesiak et al., 2016b). The middle zone is itself characterized by the presence of siltstone blocks within a silty matrix and ranges in thickness from 50 up to 90 m (Sobiesiak et al., 2016b). The matrix to the middle zone is composed of highly sheared and fractured green siltstone, containing granitoid and metamorphic clasts. Sandstone blocks are still present, but are less frequent and generally smaller when compared with those in the lower zone. Large-scale folding and boudinage of sandstone blocks is observed in the middle zone.

The contact between the middle and the upper zone of MTD II is transitional and is marked by the presence of a thick folded and fractured turbidite sandstone bed including a meter-thick mud cap (megabed), intermittently

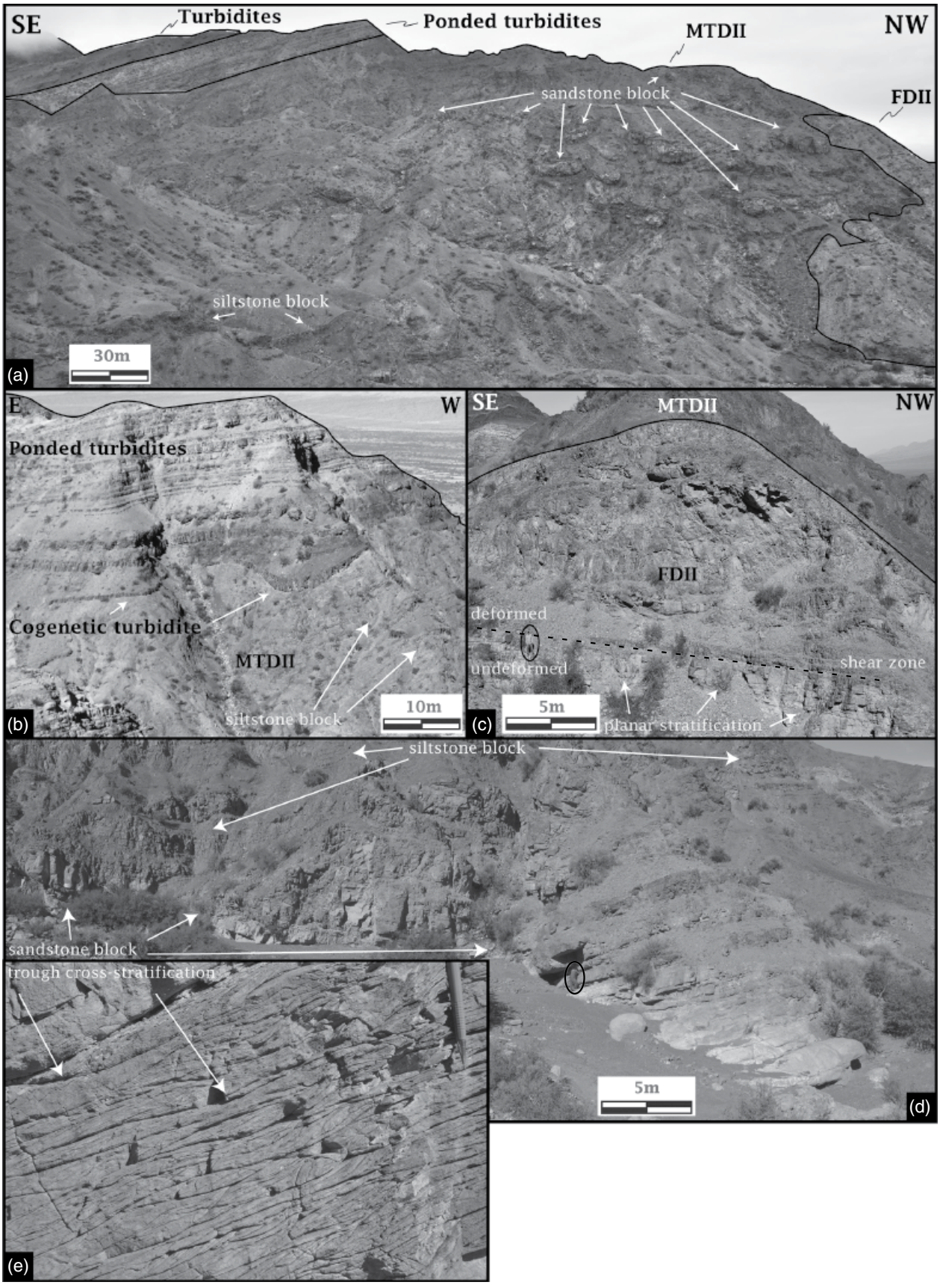


Figure 6.4 (a) Mosaic parallel to the inferred transport direction showing MTD II stratigraphy and sandstone block distribution. (b) Photo showing the presence of co-genetic turbidites, followed by ponded turbidites deposited on top of the MTD. Note that the co-genetic turbidites thicken and thin as they drape the topographic lows and highs. (c) Photograph showing the deformation zone between MTD II and Fluvio-Deltaic II, where the zone is bounded at the top by MTD II and the base by a shear zone that separates deformed from undeformed sandstone. (d) Example of a large bedded sandstone block inside MTD II. (e) Example of original bedding preserved within a block, with cross-stratification from the block at Figure 6.4d.

distributed along the lower portion of the upper zone. The upper zone is 40–60 m thick (Sobiesiak et al., 2016b), with the green siltstone matrix containing basement clasts. Sandstone and siltstone blocks are less frequent and much smaller than those from the underlying zones. The upper zone is marked by the occurrence of thrust zones, large-scale folding, and thrust fault imbrication (Dykstra et al., 2011; Sobiesiak et al., 2016b).

Soft-sediment deformation can be found throughout the whole of MTD II, with folds and faults being the most commonly observed structures. The lower zone contains the greatest concentration of structures, although this might simply reflect the presence of distinct sandy markers within the matrix that readily record and highlight the deformation. Other structures such as mullions, boudins, shear lozenge, pull-aparts, sheath folds, bookshelf (dominoes) faulting, and flame structures are observed throughout the MTD (Sobiesiak et al., 2016b).

The lower boundary of MTD II is extremely irregular where erosional features cut into the underlying sandstone to create scours, gouges, and/or grooves (Dykstra et al., 2011; Sobiesiak et al., 2016b) (Figure 6.2). These erosional depressions range in size from couple of meters up to ~100s of meters in length and up to ~20 m deep (Sobiesiak et al., 2016b). Additionally, soft-sediment deformation affects the uppermost ~20 m of the underlying sandstone sequence (Sobiesiak et al., 2018) (Figure 6.4c). Deformation of the substrate starts at the contact with MTD II and continues downward until a sharp shear surface defines the boundary between the deformed and undeformed substrate (Sobiesiak et al., 2018). Deformation of the substrate is recorded in a series of soft-sediment structures such as recumbent, overturned, parasitic (S and Z) fold types, boulder rotation, boudins, pinch-and-swell structures, mullion structures, bed attenuation, and the formation of proto-block-shaped structures (Sobiesiak et al., 2018).

The upper boundary of MTD II is recorded by a succession of turbidites that show interaction with the topographic top surface of the MTD at different scales (Fairweather, 2015; Kneller et al., 2016) (Figure 6.4a, b). The turbidites vary from 0 to ~60 m thick and have been subdivided into five stratigraphic units according to their style of topographic filling (Fairweather, 2015). In general, they consist of massive to rippled and normally graded beds of coarse- to fine-grained light yellow sandstone that are capped by siltstone and mudstone. Sitting directly on top of the MTD is a single green turbidite that drapes the topography and is interpreted as being co-genetic to MTD II (Dykstra et al., 2011; Kneller et al., 2016; Sobiesiak et al., 2016b; Fallgatter et al., 2017) (Figure 6.4b). The first units occur as isolated lenses that onlap topographic highs on the upper surface of MTD II and locally slump off it. The topographic irregularities are interpreted as isolated basins that are progressively filled and buried over time, namely, first those at a small scale (few meters in amplitude, meters in wavelength), then into intermediate scale (tens of meters in amplitude, 500–1000 m in wavelength), and finally into large length scales (6500 m, with amplitudes of the order of 100 m), which affect only the upper and more extensive units (Fairweather, 2015; Kneller et al., 2016).

6.3.2.1. Interpretation

MTD II has similar characteristics to MTD I, such as the presence of sandstone and siltstone blocks, basal deformation, basement clasts, and greenish silty matrix. Consequently, MTD II is interpreted to be the result of glacially influenced sediments (ice-rafted debris) having undergone remobilization. Crystalline clasts embedded in the matrix are interpreted as dropstones, siltstone blocks as the least deformed end member of the MTD protolith (Dykstra et al., 2011; Sobiesiak et al., 2016b), and sandstone blocks as derived from seafloor erosion. The interpretation of seafloor erosion and subsequent incorporation of sandstone blocks into MTD II is supported by field observations such as erosional surfaces cutting into the underlying sandstone, petrographic resemblance between sandstone blocks and substrate sandstone (Garyfalou, 2015), and even a block apparently arrested in the process of entrainment into the MTD (Sobiesiak et al., 2016a, 2016b). The broad zonation of MTD II is interpreted to be due to different deformational styles affecting each of the zones. The lower zone is considered to be dominated by simple shear, leading to sand streaks, while the middle zone comprises a greater component of pure shear leading to boudinage. The upper zone is associated with simple shear deformation resulting in fold and thrust systems. Additionally, the ~20 m thick zone of deformation below MTD II is interpreted to reflect shear of underlying sediments created as the MTD moved downslope. When grouped together with erosional scours, this indicates a complex morphology and behavior of the BSS, as well as variations in flow and substrate properties. Turbidites deposited on top of MTD II are interpreted as ponded turbidites, as they markedly onlap the topographic relief created during MTD movement (Dykstra et al., 2011; Valdez et al., 2015; Sobiesiak et al., 2016a, 2016b).

6.3.3. MTD III

MTD III is up to ~120 m thick and crops out for ~10 km along depositional strike. It is the most difficult of the Cerro Bola MTDs to access due to its high stratigraphic position on the mountain. In general, the MTD consists dominantly of a dark green colored siltstone that can be broadly subdivided into two zones (lower and upper) according to its internal deformation and stratification

(Figure 6.5a–c). At the northern and southern areas of Cerro Bola, the lower zone comprises about ~50 m of the deposit and displays coherently bedded sediments (Figure 6.5a–c), only locally deformed. It consists of thin (~10s of centimeters thick) sand beds with abundant rippled surfaces and convolute bedding, including clasts (dropstones) with deflected layers above and below, interbedded with mudstone and more rarely shales. The upper zone of the deposit is extensively deformed, composed of folded and/or disrupted sandstone beds in a silty rich matrix. Additionally, scattered pebbles, cobbles, and boulders of crystalline basement rocks are also present. In the central part of the inlier, however, the whole of MTD III (lower and upper zone) is deformed and displays soft-sediment deformation features such as slump folds (Valdez et al., 2015).

The base of MTD III is marked by the occurrence of an E-W trending erosional surface (Figure 6.5a, b) that is clearly exposed for at least 1.5 km and forms a truncation surface that cuts into the underlying sandstone beds (Fluvio-Deltaic III) (Valdez et al., 2015). The underlying sandstones are sharply cut by this surface causing up to ~150 m of sandstones to be excised and locally reaching almost complete removal (Figure 6.5b). Additionally, the erosional surface locally displays a polished plane containing striations aligned toward 320–140° (Puigdomenech Negre, 2014). A unit of purplish conglomeratic sandstones that are irregularly distributed in lenticular bodies appears to lie within incisions into this surface. The incised sandstones are stratified and toward the top of the sequence display traction features, such as cross-bedding (Valdez et al., 2015). The upper boundary of the deposit locally displays a succession of turbidite beds that pinch out laterally (Figure 6.5d) and onlap against the MTD top.

6.3.3.1. Interpretation

MTD III consists largely of ice-rafted debris, together with possible turbidite, much of which has been remobilized and transported downslope as an MTD. The erosion surface might be interpreted as the slide scar of a mass movement (Valdez et al., 2015). Alternatively, the erosional surface locally displays a U-shaped morphology (see figure 10b in Valdez et al. (2015)) which taken together with the polished striated surfaces described by Puigdomenech Negre (2014) could be interpreted as the product of glacial movement. Finally, the surface may represent an incised valley in the top of the delta. The lower zone of MTD III, where it is coherently bedded and relatively undeformed, may represent large coherent slide blocks or MTD protolith still in its original position. Lastly, the turbidites deposited on top of the MTD are interpreted as ponded turbidites, denoting confinement by the interaction of these flows with the rugged MTD topographic surface.

6.4. DISCUSSION

6.4.1. Seafloor Interaction

Studies of the interaction of MTDs with the seafloor have recently been undertaken using both outcrop and seismic data (e.g., Prior et al., 1984; Gee et al., 2005; Moscardelli et al., 2006; Alves & Lourenço, 2010; Laberg et al., 2016; Sobiesiak et al., 2018). The documented interaction is considered to occur in two styles, erosional and deformational, which are not mutually exclusive. The erosional power of MTDs at Cerro Bola can be recognized from MTD II and MTD III, with the former displaying basal irregularities interpreted as scours and/or grooves cutting down into the underlying sandstone (Figure 6.2) and the latter displaying a ~150 m incision into substrate (Figure 6.5a, b). Additionally, MTDs I and II both contain sandstone blocks (Figures 6.3b and 6.4a, d, e), which are similar in composition to the underlying sandstones and may be interpreted as being derived from erosion of the substrate (Garyfalou, 2015; Sobiesiak et al., 2016b).

Laberg et al. (2016) described an MTD from the Nankai Trough, SE Japan, where five sudden indentations were recorded in the BSS. However, this MTD had no seismic-scale blocks, and the indentations were interpreted as slabs detached at different stratigraphic levels during slope failure. Alternatively, Gee et al. (2005) documented linear features scoured in the seafloor, which the authors interpreted as grooves. The process of groove making is described as the dragging of a tool (such as rigid blocks) contained at the base of the flow that would scour the substrate. This would mean that seafloor erosion could also be a consequence of blocks. Moscardelli et al. (2006) also described erosional features from offshore Trinidad, where the main reason for seafloor scouring was due to the erosive power of the flow that transitioned from a confined into a partially confined setting. In summary, a range of factors may influence seafloor erosion, ranging from the presence of large blocks that may create grooves, weak layers within the seafloor sediments, to variations in flow dynamics that lead to wider erosive features.

The other type of MTD interaction relates to deformation of the seafloor. This is well illustrated at Cerro Bola by MTDs I and II, which display a ~14 m (Figure 6.3d) and a ~20 m thick (Figure 6.4c) deformation zone localized in the uppermost layers of the substrate sandstone, respectively. Penetration of the strain profile into the substrate resulted in the development of soft-sediment deformation (folds, boudins, and proto-blocks, among others) spread throughout the whole affected area. The lower contact of the deformed substrate is bounded by a sharp shear zone that clearly separates deformed from undeformed and

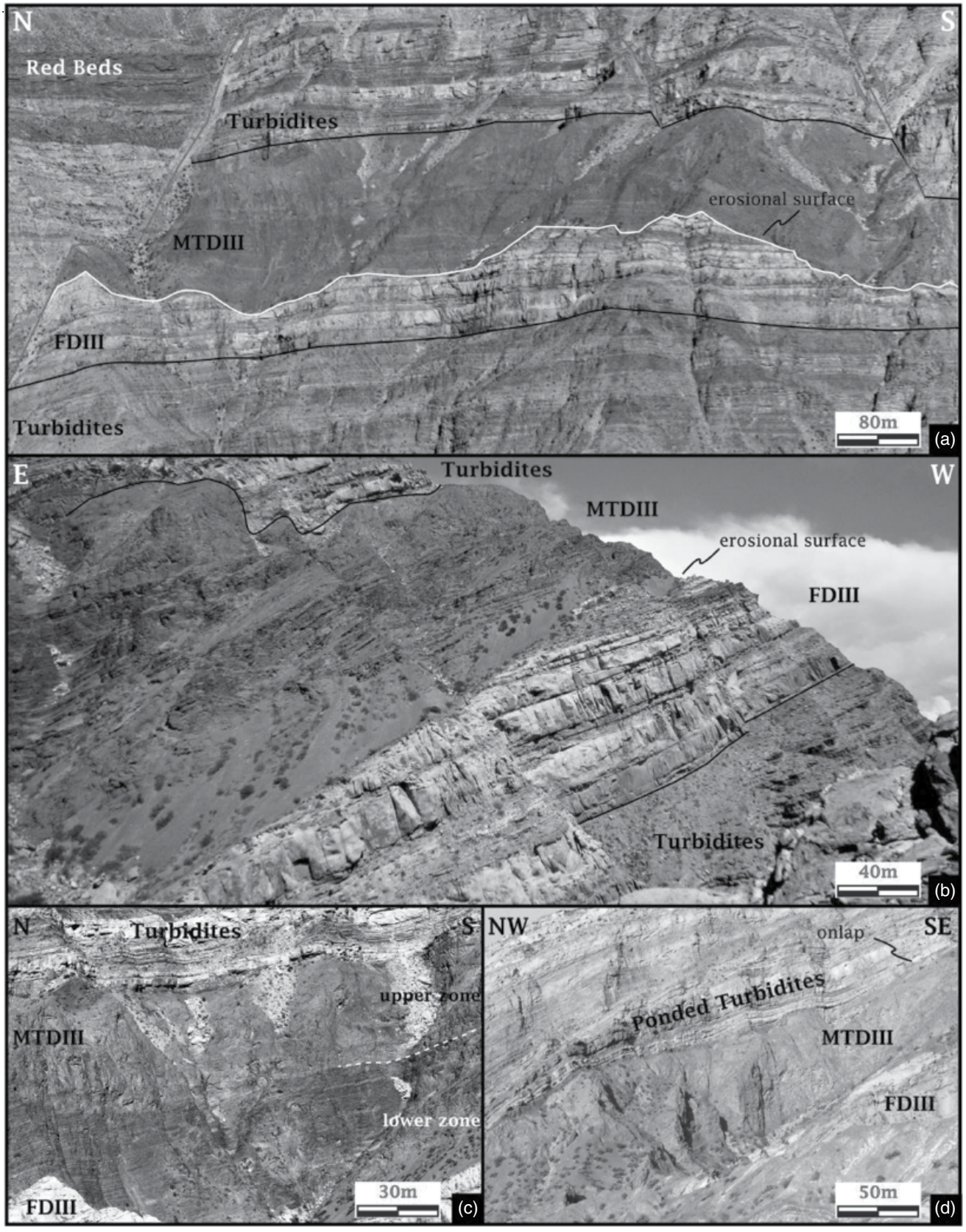


Figure 6.5 (a) Aerial photo showing a section of MTD III and the indented undulating erosional surface between MTD III and Fluvio-Deltaic III. Note that the Fluvio-Deltaic is almost completely removed at the right-hand side of the image. (b) Close-up photo of the erosional surface and MTD III. Deformed and bedded strata within MTD III can be noticed as well as variably dipping bedded blocks. (c) Photomosaic of the northern part of Cerro Bola, displaying the internal divisions of MTD III. Lower zone shows coherently bedded sediments and above the disrupted strata from the upper zone. (d) Turbidite succession (ponded turbidite) that pinches out (toward the right-hand side) and onlaps against the rugged topography of the MTD.

evenly bedded sediments. Such basal deformation has been described by only a few authors from outcrop (Alves & Lourenço, 2010; Butler & McCaffrey, 2010; Valdez et al., 2015; Sobiesiak et al., 2018) and core (Laberg et al., 2016) and more rarely from seismic data (Alves, 2015). We suggest that the stress exerted by the flow is not restricted to its base, but penetrates a considerable distance into the substrate, thus deforming it. Similar observations were made by Alves and Lourenço (2010) and Laberg et al. (2016) where the basal shear zone lies within and deformed the sandy substrate.

Additionally, the depth of penetration of deformation into the substrate in relation to the height of the overlying MTD was calculated by Sobiesiak et al. (2018) using both Carboniferous MTDs I and II from Cerro Bola and, as a comparison, a Neogene MTD from SE Crete described by Alves and Lourenço (2010). From Cerro Bola, the deformation zone of MTD II was ~11% of the total thickness of the overlying MTD, and for MTD I, it was ~12%; however Alves and Lourenço (2010) calculated the deformation as ~15% of the total thickness of the overlying MTD. The observations above support the conclusion that in some cases, the BSS of an MTD can be considered as a zone rather than a discrete surface (Alves & Lourenço, 2010). Unfortunately, the variables that control the formation of these zones are at present poorly known, although it could be conjectured that the significant factors will likely be those that control the shear stress of the MTD (mainly the speed of movement, thickness, and density) and the yield strength and rheology of the substrate (controlled by degree of lithification, fluid pressure, and lithologies).

6.4.2. Toward a Model for Block Generation

Blocks within MTDs are frequently classified into rafted, remnant, and outrunner blocks (e.g., Prior et al., 1984; Bull et al., 2009; Posamentier et al., 2011; Alves, 2015). Outrunners are defined as those blocks that are detached from the leading edge of the MTD and have moved downslope beyond the front of the flow (e.g., Prior et al., 1984; Bull et al., 2009). They are associated with a type of basal erosion called glide tracks, and the blocks themselves are not found embedded within the MTD, but at the end of the glide track (Prior et al., 1984; Nissen et al., 1999). Remnant blocks are defined as "isolated blocks of material that have not experienced failure" (Bull et al., 2009). These blocks are bounded by sets of faults and are vertically connected with underlying non-MTD substrate, thus lacking basal disruption (Alves & Cartwright, 2009; Alves, 2015). Rafted blocks, on the other hand, behave as a "coherent block" transported downslope by the flow and are usually described as "floating within the disaggregated chaotic matrix of the MTD" (Alves, 2015). Rafted blocks are also called "translated" or "intact" blocks (e.g., Masson et al., 1993; Bull et al., 2009). All blocks described from Cerro Bola are classified as rafted blocks.

Analysis of MTDs I and II from Cerro Bola provides an opportunity to differentiate rafted blocks into sandstone and siltstone blocks, according to their lithological differences, and classify them into either "native" (intra-formational) or "exotic" (extra-formational) in respect to their genetic relation to the host and/or encasing lithology (e.g., Masson et al., 1993; Haughton et al., 2003; Lucente & Pini, 2003; Jackson et al., 2009; Ogata et al., 2014b; Festa et al., 2016). The sandstone blocks in general are composed of a whitish to orange sandstone and appear to be derived by erosion of the substrate (Figure 6.4d, e). These sandstone blocks are interpreted as exotic blocks and are thus considered to be coherent fragments of externally sourced material of different lithology from the MTD, potentially displaying distinct rheological behavior from the flow matrix. MTD II shows clear interaction with the underlying sandstone deposit in the form of irregular gouges and/or grooves (described in Section 6.3.2). Additionally, in places, it is possible to see blocks arrested in the process of entrainment by the flow. Such evidence corroborates the interpretation that the blocks originated from the shearing of the underlying unit. A notable observation is that blocks can originate by substrate erosion. However, at the same time, the presence of blocks can produce seafloor erosion through the process of groove making or tooling.

Within MTD II, block size and frequency diminish upward through the deposit (Figure 6.4a). To explain this vertical distribution, a model was proposed by Sobiesiak et al. (2016a) in which large sandstone blocks ascended through the MTD matrix via buoyancy. First, the blocks of varying sizes would be eroded from the underlying substrate and incorporated into the base of the flow. The blocks would rise through the matrix by virtue of their lower density. As they ascend, they would undergo shear stripping, stretching, and/or fragmentation, depending on the behavior of the matrix and the contrast in material properties between block and matrix. This process would reduce the size of blocks as they move up, resulting in smaller blocks higher in comparison with those at the base. Additionally, the accumulation of blocks at the base of the flow can be explained by other factors: (i) it is the closest part of the MTD to their point of origin, and/or (ii) some blocks possess neutral buoyancy, or may be even denser than the matrix, therefore fostering the accumulation of blocks along the basal contact.

Siltstone blocks, on the other hand, are interpreted as native blocks comprising light to dark green layered siltstone (Figure 6.3c) and are considered to be the least deformed remnants of the MTD protolith (Dykstra

et al., 2011; Valdez et al., 2015; Sobiesiak et al., 2016b). The siltstone blocks are interpreted as being derived from the same source material or lithology as the main MTD body. The rheological behavior of siltstone blocks does not differ significantly from the overall flow, and they are more or less evenly distributed throughout the MTD stratigraphy (Sobiesiak et al., 2016b). However, there are places where siltstone blocks are difficult to distinguish from the actual MTD matrix due to their similarity with the matrix and the indistinct bedding that can be confused with matrix fractures. In conclusion, siltstone blocks are interpreted as remnants of the MTD protolith, and because they have a similar rheology and density to the MTD matrix, they would simply be carried passively downslope by the moving flow. Such rafts would get progressively smaller due to their fragmentation during transport, as shown by Alves and Cartwright (2009). Nevertheless, care must be taken when classifying blocks; on some occasions, MTDs may have a heterogeneous origin including a range of lithologies, and the resulting blocks may display a different lithology from the desegregated, mixed, and homogeneous host matrix.

6.5. CONCLUSIONS

We have summarized and discussed the main aspects and structures of three Carboniferous MTDs exposed at Cerro Bola. The main conclusions can be summarized as follows:

1. Two types of basal interaction are developed that demonstrate the erosional and/or deformational power of MTDs. Seafloor deformation is recorded below MTDs I and II and erosion is recorded below MTDs II and III. The character and nature of the interaction between the MTD and the seafloor is complex and poorly understood, though variables that influence MTD's shear stress and the substrate rheology and yield strength are significant factors that would influence the occurrence, style, and thickness of erosion and/or deformation zone.

2. MTD rafted blocks can be generated by two means. First, these blocks can be generated by the disaggregation of the MTD protolith, imparting similar properties to the block as the main MTD body. Therefore, such blocks are more likely to preserve original features or undergo less deformation as they may only "float" within the matrix. Second, they can be generated by the erosion of the seafloor, where the blocks are made of externally sourced material and of different lithology with respect to the MTD matrix, potentially exhibiting mechanical behavior distinctly different from the overall flow. Consequently, these blocks may be reworked by the flow due to their contrast in physical properties.

3. Additionally, the presence of "exotic" blocks within the MTD is not strictly indicative of erosion, since MTDs can have a heterogeneous source composed of multiple lithologies. Also exotic blocks can be the result of seafloor erosion and/or can tool the seafloor and be the agent of erosion.

ACKNOWLEDGMENTS

The research presented here was carried out with support from CNPq-Brazil (National Council for Scientific and Technological Development) in partnership with Shell Brazil. We thank Massimo Moretti and an anonymous reviewer whose constructive comments and criticisms helped to improve the text; their efforts are highly appreciated. Finally, we thank Kei Ogata, Gian Andrea Pini, and Andrea Festa for editing this volume.

REFERENCES

Alsop, G. I., & Marco, S. (2014). Fold and fabric relationships in temporally and spatially evolving slump systems: A multicell flow model. *Journal of Structural Geology*, *63*, 27–49. https://doi.org/10.1016/j.jsg.2014.02.007

Alsop, G. I., Marco, S., Levi, T., & Weinberger, R. (2017). Fold and thrust systems in Mass Transport Deposits. *Journal of Structural Geology*, *94*, 98–115. https://doi.org/10.1016/j.jsg.2016.11.008

Alves, T. M. (2015). Submarine slide blocks and associated soft-sediment deformation in deep-water basins: A review. *Marine and Petroleum Geology*, *67*, 262–285. https://doi.org/10.1016/j.marpetgeo.2015.05.010

Alves, T. M., & Cartwright, J. A. (2009). Volume balance of a submarine landslide in the Espírito Santo Basin, offshore Brazil: Quantifying seafloor erosion, sediment accumulation and depletion. *Earth and Planetary Science Letters*, *288*, 572–580. https://doi.org/10.1016/j.epsl.2009.10.020

Alves, T. M., & Lourenço, S. D. N. N. (2010). Geomorphologic features related to gravitational collapse: Submarine landsliding to lateral spreading on a Late Miocene–Quaternary slope (SE Crete, eastern Mediterranean). *Geomorphology*, *123*, 13–33. https://doi.org/10.1016/j.geomorph.2010.04.030

Alves, T. M., Strasser, M., & Moore, G. F. F. (2014). Erosional features as indicators of thrust fault activity (Nankai Trough, Japan). *Marine Geology*, *356*, 5–18. https://doi.org/10.1016/j.margeo.2013.07.011

Azcuy, C., Carrizo, H. A., & Caminos, R. (1999). Carbonífero y Pérmico de las Sierras Pampeanas, Famatina, Precordillera, Cordillera Frontal y Bloque de San Rafael. *Instituto de Geología y Recursos Minerales Geología Argentina, Anales*, *29*(12), 261–318*, Buenos Aires.*, **251**

Blair, T. C., & McPherson, J. G. (1999). Grain-size and textural classification of coarse sedimentary particles. *Journal of Sedimentary Research*, *69*, 6–19. https://doi.org/10.2110/jsr.69.6

Bull, S., Cartwright, J., & Huuse, M. (2009). A review of kinematic indicators from mass-transport complexes using 3D seismic data. *Marine and Petroleum Geology*, *26*, 1132–1151. https://doi.org/10.1016/j.marpetgeo.2008.09.011

Butler, R. W. H., & McCaffrey, W. D. (2010). Structural evolution and sediment entrainment in mass-transport complexes: Outcrop studies from Italy. *Journal of the Geological Society*, *167*, 617–631. https://doi.org/10.1144/0016-76492009-041

Butler, R. W. H., & Tavarnelli, E. (2006). The structure and kinematics of substrate entrainment into high-concentration sandy turbidites: A field example from the Gorgoglione 'flysch' of southern Italy. *Sedimentology*, *53*, 655–670. https://doi.org/10.1111/j.1365-3091.2006.00789.x

Dakin, N., Pickering, K. T., Mohrig, D., & Bayliss, N. J. (2013). Channel-like features created by erosive submarine debris flows: Field evidence from the Middle Eocene Ainsa Basin, Spanish Pyrenees. *Marine and Petroleum Geology*, *41*, 62–71. https://doi.org/10.1016/j.marpetgeo.2012.07.007

Desjardins, P. R., Buatois, L. A., Limarino, C. O., & Cisterna, G. A. (2009). Latest Carboniferous–earliest Permian transgressive deposits in the Paganzo Basin of western Argentina: Lithofacies and sequence stratigraphy of a coastal-plain to bay succession. *Journal of South American Earth Sciences*, *28*, 40–53. https://doi.org/10.1016/j.jsames.2008.10.003

Draganits, E., Schlaf, J., Grasemann, B., & Argles, T. (2008). Giant submarine landslide grooves in the Neoproterozoic/Lower Cambrian Phe Formation, northwest Himalaya: Mechanisms of formation and palaeogeographic implications. *Sedimentary Geology*, *205*, 126–141. https://doi.org/10.1016/j.sedgeo.2008.02.004

Dykstra, M., Garyfalou, K., Kertznus, V., Kneller, B., Milana, J. P., Molinaro, M., et al. (2011). Mass-transport deposits: Combining outcrop studies and seismic forward modeling to understand lithofacies distributions, deformation, and their seismic expression. *SEPM Special Publication*, *95*, 1–25.

Fairweather, L. (2015). Mechanisms of supra-MTD topography generation and the interaction of turbidity currents with such deposits (Unpublished PhD thesis). University of Aberdeen.

Fallgatter, C., Kneller, B., Paim, P. S., & Milana, J. P. (2017). Transformation, partitioning and flow-deposit interactions during the run-out of megaflows. *Sedimentology*, *64*, 359–387. https://doi.org/10.1111/sed.12307

Farrell, S. (1984). A dislocation model applied to slump structures, Ainsa Basin, South Central Pyrenees. *Journal of Structural Geology*, *73*, 727–736. https://doi.org/http://dx.doi.org/10.1016/0191-8141(84)90012-9

Fernandez-Seveso, F., & Tankard, A. J. (1995). Tectonics and stratigraphy of the late Paleozoic Paganzo Basin of Western Argentina and its regional implications. *Petroleum Basins of South America*, 285–301.

Festa, A., Ogata, K., Pini, G. A., Dilek, Y., & Alonso, J. L. (2016). Origin and significance of olistostromes in the evolution of orogenic belts: A global synthesis. *Gondwana Research*, *39*, 180–203. https://doi.org/10.1016/j.gr.2016.08.002

Frey-Martínez, J., Cartwright, J., & James, D. (2006). Frontally confined versus frontally emergent submarine landslides: A 3D seismic characterisation. *Marine and Petroleum Geology*, *23*, 585–604. https://doi.org/http://dx.doi.org/10.1016/j.marpetgeo.2006.04.002

Garyfalou, K. (2015). Integrated analysis of mass-transport deposits: Outcrop, 3D seismic interpretation and fast Fourier transform (Unpublished PhD thesis). University of Aberdeen.

Gawthorpe, R. L., & Clemmey, H. (1985). Geometry of submarine slides in the Bowland Basin (Dinantian) and their relation to debris flows. *Journal of the Geological Society*, *142*, 555–565. https://doi.org/10.1144/gsjgs.142.3.0555

Gee, M. J. R., Gawthorpe, R. L., & Friedmann, J. S. (2005). Giant striations at the base of a submarine landslide. *Marine Geology*, *214*, 287–294. https://doi.org/10.1016/j.margeo.2004.09.003

Gulbranson, E. L., Montanez, I. P., Schmitz, M. D., Limarino, C. O., Isbell, J. L., Marenssi, S. A., & Crowley, J. L. (2010). High-precision U-Pb calibration of Carboniferous glaciation and climate history, Paganzo Group, NW Argentina. *Geological Society of America Bulletin*, *122*, 1480–1498. https://doi.org/10.1130/B30025.1

Hampton, M. A., Lee, H. J., & Locat, J. (1996). Submarine landslides. *Reviews of Geophysics*, *34*, 33–59. https://doi.org/10.1029/95RG03287

Haughton, P. D. W., Barker, S. P., & McCaffrey, W. D. (2003). 'Linked' debrites in sand-rich turbidite systems: Origin and significance. *Sedimentology*, *50*, 459–482. https://doi.org/10.1046/j.1365-3091.2003.00560.x

Jackson, C. A.-L., Zakaria, A. A., Johnson, H. D., Tongkul, F., & Crevello, P. D. (2009). Sedimentology, stratigraphic occurrence and origin of linked debrites in the West Crocker Formation (Oligo-Miocene), Sabah, NW Borneo. *Marine and Petroleum Geology*, *26*, 1957–1973. https://doi.org/10.1016/j.marpetgeo.2009.02.019

Kneller, B., Dykstra, M., Fairweather, L., & Milana, J. P. (2016). Mass-transport and slope accommodation: Implications for turbidite sandstone reservoirs. *AAPG Bulletin*, *100*, 213–235. https://doi.org/10.1306/09011514210

Laberg, J. S., Strasser, M., Alves, T. M., Gao, S., Kawamura, K., Kopf, A., & Moore, G. F. (2016). Internal deformation of a muddy gravity flow and its interaction with the seafloor (site C0018 of IODP Expedition 333, Nankai Trough, SE Japan). *Landslides*, *14*, 849–860. https://doi.org/10.1007/s10346-016-0766-7

Limarino, C., Tripaldi, A., Marenssi, S., & Fauqué, L. (2006). Tectonic, sea-level, and climatic controls on Late Paleozoic sedimentation in the western basins of Argentina. *Journal of South American Earth Sciences*, *22*, 205–226. https://doi.org/10.1016/j.jsames.2006.09.009

Limarino, C. O., Césari, S. N., Net, L. I., Marenssi, S. A., Gutierrez, R. P., & Tripaldi, A. (2002). The Upper Carboniferous postglacial transgression in the Paganzo and Río Blanco basins (northwestern Argentina): Facies and stratigraphic significance. *Journal of South American Earth Sciences*, *15*, 445–460. https://doi.org/10.1016/S0895-9811(02)00048-2

Limarino, C. O., & Spalletti, L. A. (2006). Paleogeography of the upper Paleozoic basins of southern South America: An overview. *Journal of South American Earth Sciences*, *22*, 134–155. https://doi.org/10.1016/j.jsames.2006.09.011

Lucente, C. C., & Pini, G. A. (2003). Anatomy and emplacement mechanism of a large submarine slide within a Miocene foredeep in the northern Apennines, Italy: A field perspective. *American Journal of Science*, *303*, 565–602.

Macdonald, D. I. M., Moncrieff, A. C. M., & Butterworth, P. J. (1993). Giant slide deposits from a Mesozoic fore-arc basin, Alexander Island, Antarctica. *Geology*, *21*, 1047. https://doi.org/10.1130/0091-7613(1993)021<1047:GSDFAM>2.3.CO;2

Masson, D. G., Huggett, Q. J., & Brunsden, D. (1993). The surface texture of the Saharan Debris Flow deposit and some speculations on submarine debris flow processes. *Sedimentology*,*40*,583–598.https://doi.org/10.1111/j.1365-3091.1993.tb01351.x

McGilvery, T. A. (Mac), & Cook, D. L. (2003). *The influence of local gradients on accommodation space and linked depositional elements across a stepped slope profile, Offshore Brunei*. Paper presented at Shelf Margin Deltas and Linked Down Slope Petroleum Systems: 23rd Annual, Society of Economic Paleontologists and Mineralogists (pp. 387–419). https://doi.org/10.5724/gcs.03.23.0387.

Milana, J. P., Kneller, B., & Dykstra, M. (2010). Mass-transport deposits and turbidites, syn-to-post-Glacial Carboniferous basins of Western Argentina. *ISC 2010 Field Guide*, 01–88.

Moscardelli, L., Wood, L., & Mann, P. (2006). Mass-transport complexes and associated processes in the offshore area of Trinidad and Venezuela. *AAPG Bulletin*, *90*, 1059–1088. https://doi.org/10.1306/02210605052

Nissen, S. E., Haskell, N. L., Steiner, C. T., & Coterill, K. L. (1999). Debris flow outrunner blocks, glide tracks, and pressure ridges identified on the Nigerian continental slope using 3-D seismic coherency. *The Leading Edge*, *18*, 595–599. https://doi.org/10.1190/1.1438343

Ogata, K., Mountjoy, J. J., Pini, G. A., Festa, A., & Tinterri, R. (2014a). Shear zone liquefaction in mass transport deposit emplacement: A multi-scale integration of seismic reflection and outcrop data. *Marine Geology*, *356*, 50–64. https://doi.org/10.1016/j.margeo.2014.05.001

Ogata, K., Mutti, E., Pini, G. A., & Tinterri, R. (2012). Mass transport-related stratal disruption within sedimentary mélanges: Examples from the northern Apennines (Italy) and south-central Pyrenees (Spain). *Tectonophysics*, *568–569*, 185–199. https://doi.org/10.1016/j.tecto.2011.08.021

Ogata, K., Pogačnik, Ž., Pini, G. A., Tunis, G., Festa, A., Camerlenghi, A., & Rebesco, M. (2014b). The carbonate mass transport deposits of the Paleogene Friuli Basin (Italy/Slovenia): Internal anatomy and inferred genetic processes. *Marine Geology*, *356*, 88–110. https://doi.org/10.1016/j.margeo.2014.06.014

Omosanya, K. O., & Alves, T. M. (2013). A 3-dimensional seismic method to assess the provenance of Mass-Transport Deposits (MTDs) on salt-rich continental slopes (Espírito Santo Basin, SE Brazil). *Marine and Petroleum Geology*, *44*, 223–239. https://doi.org/10.1016/j.marpetgeo.2013.02.006

Posamentier, H. W., & Kolla, V. (2003). Seismic geomorphology and stratigraphy of depositional elements in deep-water settings. *Journal of Sedimentary Research*, *73*, 367–388. https://doi.org/10.1306/111302730367

Posamentier, H. W., Martinsen, O. J., & Shipp, R. C. (2011). The character and genesis of submarine mass-transport deposits: Insights from outcrop and 3D seismic data. In *Mass-transport deposits in deepwater settings, Special Publication* (Vol. 96, pp. 7–38). Tulsa, OK: SEPM. https://doi.org/10.2110/sepmsp.096.007

Prior, D. B., Bornhold, B. D., Johns, M. W., Suhayda, J. N., Bornhold, B. D., & Johns, M. W. (1984). Depositional characteristics of a submarine debris flow. *Journal of Geology*, *92*, 707–727. https://doi.org/00221376

Puigdomenech Negre, C. G. (2014). *The Relationship between Deltaic and Turbidite Succession at Cerro Bola (LR - Argentina) and Vidal Ramos (SC - Brazil)*. Universidade do Vale do Rio dos Sinos.

Ramos, V. A. (1988). The tectonics of the Central Andes; 30° to 33°S latitude. In S. P. Clark, J. Suppe, & B. C. Burchfiel (Eds.), *Processes in continental lithospheric deformation, Special Paper* (Vol. 218, pp. 31–54). Boulder, CO: Geological Society of America. https://doi.org/10.1130/SPE218-p31

Sobiesiak, M. S., Alsop, G. I., Kneller, B., & Milana, J. P. (2017). Sub-seismic scale folding and thrusting within an exposed mass transport deposit: A case study from NW Argentina. *Journal of Structural Geology*, *96*, 176–191. https://doi.org/10.1016/j.jsg.2017.01.006

Sobiesiak, M. S., Kneller, B., Alsop, G. I., & Milana, J. P. (2016a). Inclusion of substrate blocks within a mass transport deposit: A case study from Cerro Bola, Argentina. In G. Lamarche & J. Mountjoy (Eds.), *Submarine mass movements and their consequences, Advance in Natural and Technological Hazards Research* (pp. 487–496). Cham, Switzerland: Springer International. https://doi.org/10.1007/978-3-319-20979-1_49

Sobiesiak, M. S., Kneller, B., Alsop, G. I., & Milana, J. P. (2016b). Internal deformation and kinematic indicators within a tripartite mass transport deposit, NW Argentina. *Sedimentary Geology*, *344*, 364–381. https://doi.org/10.1016/j.sedgeo.2016.04.006

Sobiesiak, M. S., Kneller, B. C., Alsop, G. I., & Milana, J. P. (2018). Styles of basal interaction beneath mass transport deposits. *Marine and Petroleum Geology*, *98*, 629–639. https://doi.org/10.1016/j.marpetgeo.2018.08.028

Valdez Buso, V. (2015). The geological record of the late Paleozoic Ice Age in Paganzo (Argentina) and Paraná (Brazil) Basins: Comparison of sedimentary successions and glacial cycles (Unpublished PhD thesis). Universidade do Vale do Rio.

Valdez, V. B., Milana, J. P., & Kneller, B. C. (2015). Megadeslizamientos gravitacionales de la formación guandacol en Cerro Bola y Sierra de Maz y su relación con la glaciación del Paleozoico tardío, La Rioja, Argentina. *Latin American Journal of Sedimentology and Basin Analysis*, *22*, 109–133.

Zapata, T. R., & Allmendinger, R. W. (1996). Thrust-front zone of the Precordillera, Argentina: A thick-skinned triangle zone. *AAPG Bulletin*, *80*, 359–381. https://doi.org/10.1306/64ED87E6-1724-11D7-8645000102C1865D

7

The Carboniferous MTD Complex at La Peña Canyon, Paganzo Basin (San Juan, Argentina)

Victoria Valdez Buso[1], Juan Pablo Milana[2], Matheus S. Sobiesiak[3], and Ben Kneller[1]

ABSTRACT

The La Peña Canyon section (San Juan Province, western Argentina) provides outstanding examples of different varieties of mass-transport deposits (MTDs) and related sediments, showing a wide range of lithologies (from mud to sand dominated), scales and styles of deformation (from imbricate thrusts comprising the entire thickness of the deposit down to meso- and microscale folding), and mechanical responses (ductile, brittle) according to the rheology of the sediment. Specific observations include (i) the amalgamation of MTDs and the recognition of amalgamation surfaces; (ii) the tendency for MTDs to make up a progressively smaller proportion of the succession as the basin fills; (iii) the progressive disaggregation and homogenization of the protolith, from clear boundaries between a muddy matrix and sandy blocks and slabs up to almost complete mixing generating a "holomictite" (*nom, nov*.), via intermediate stages of peperite-like lithologies; (iv) slow deformation contemporaneous with deposition of overlying sediments (progressive slumping), suggesting emplacement or post-emplacement modification by creep; and (v) the tendency to find clean, structureless gravel at the sole of some larger MTDs, suggesting a mechanism for MTD sliding involving a layer of gravel with overpressured pore fluid, combining models of hydroplaning and linked cavity systems.

7.1. INTRODUCTION

Mass-transport deposits (MTDs) are the products of a kind of gravity flow, formed when a coherent mass of material is initially translated downslope above a basal shear surface during submarine slope failure (Hampton et al., 1996; Owen et al., 2007). MTDs are highly complex and comprise the entire spectrum of deposits that were deposited *en masse*, such as creep, slide, slump, debris flow, and multiphase granular flow (e.g., Lucente & Pini, 2003; Posamentier & Martinsen, 2011). They are thus part of a continuum of processes that can evolve with time from one to another. During mass transport, the solid particles generally remain in contact with one another. Some MTDs are believed to form slowly, while others form catastrophically but may continue to creep subsequently (Fairweather 2014; Kneller et al., 2016 and references therein). Once failure initiates, the event may progress by means of a number of mass-movement processes (Martinsen, 1994; Bull et al., 2009). The emplacement of MTDs can occur over a range of time scales. Events triggered tectonically or by fluid overpressure may induce catastrophic and rapid emplacement of an MTD, while others may form sufficiently slowly as they move downslope to allow coeval sedimentation. Single deposits formed by catastrophic emplacement are herein called discrete MTDs. Progressive slumping can be grouped into two main mechanisms: (i) creep, involving

[1] *Department of Geology and Petroleum Geology, School of Geosciences, University of Aberdeen, Aberdeen, United Kingdom*

[2] *CONICET and Institute of Geology, National University of San Juan, San Juan, Argentina*

[3] *Postgraduate Program in Geology, University of the Sinos Valley, São Leopoldo, Rio Grande do Sul, Brazil*

Submarine Landslides: Subaqueous Mass Transport Deposits from Outcrops to Seismic Profiles, Geophysical Monograph 246, First Edition. Edited by Kei Ogata, Andrea Festa, and Gian Andrea Pini.
© 2020 American Geophysical Union. Published 2020 by John Wiley & Sons, Inc.

very slow, constant movement of the whole mass, and (ii) multiple episodes of incremental time-limited movement. The internal composition and stratigraphy of the resultant MTD would be different in each case. Discrete slumping would produce sedimentary bodies with well-defined margins, both laterally and downslope. Progressive slumps may grade into upward undeformed deposits that were accumulating over the same period as MTD emplacement (e.g., Kneller et al., 2016).

The succession of MTDs at La Peña Canyon shows exceptional quality and degree of exposure, of a scale of MTDs that are suitable for comparison with seismic data. This 3.5 km long section includes ~1000 m of stratigraphy that includes a number of large MTDs that can be traced for several kilometers, from a purely depositional area up to the basin margin. Six main MTDs are described in this study, named MTD1 to MTD6 (see geological map, Figure 7.1c), some of which are up to 220 m thick. Some are intercalated with sandstone turbidite intervals, while others appear amalgamated (Figure 7.2a, b). Two of these MTDs (MTD3 and MTD4) are related to deglacial sedimentation, and part of the protolith of these MTDs is formed of proglacial sediments such as ice-rafted debris deposits (massive/stratified diamictites or thin-bedded sandstones and siltstone couplets with dropstones). These are comparable to those reported from Cerro Bola 60 km to the NNW (Milana et al., 2010; Sobiesiak et al., this volume), which are related to three glacial-deglacial cycles (Dykstra et al., 2011; Valdez et al., 2015; Sobiesiak et al., 2016b), each associated with glacio-eustatic/glacio-isostatic fluctuations and each of which coincides with the development of a seismic-scale MTDs. La Peña section provides the opportunity to study also non-glacially related large-scale MTDs and therefore contributes to more general depositional models.

7.2. REGIONAL SETTING

La Peña section is located toward the northeastern margin of the late Paleozoic Paganzo Basin (Fernandez-Seveso & Tankard, 1995; Limarino et al., 2002) in central western Argentina (Figure 7.1a, b). It occupied an area of 140,000 km^2, with up to 4500 m of Carboniferous to

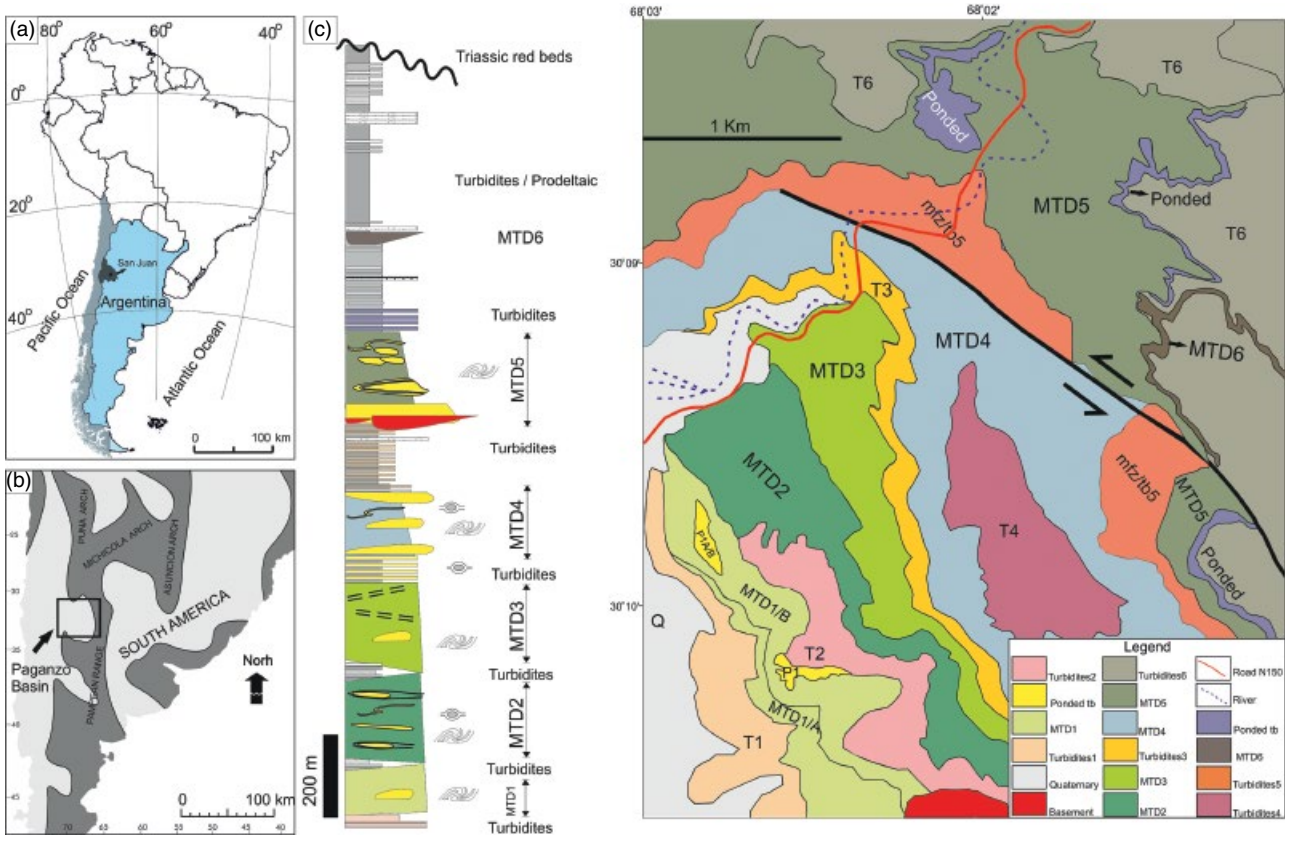


Figure 7.1 (a) Outline map of South America, highlighting Argentina and San Juan province. (b) Paleogeography of South America by the Carboniferous time. The black square shows the location of the Paganzo Basin. (c) Stratigraphic column and geological map of the study area. *"See electronic version for color representation of this figure"*

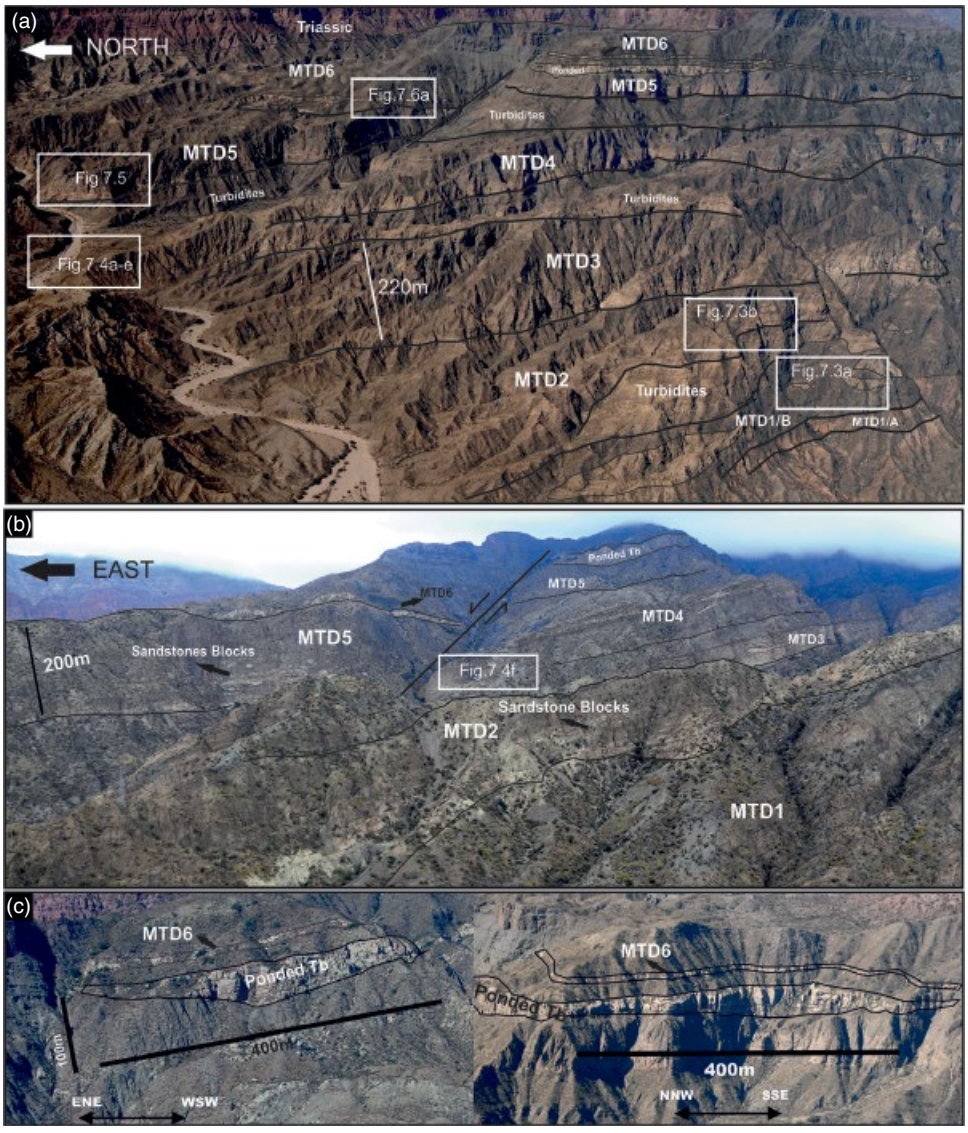


Figure 7.2 (a) Oblique aerial photo interpretation of the different MTDs in La Peña Canyon. Notice the size of some of them. (b) Ground photo interpretation showing the lateral variation of some MTDs, from sandy base like the case of MTD2, MTD3, and MTD5 from rafted blocks. (c) Aerial photo interpretation of the ponded sandstones on top of MTD5. White squares show the location of Figures 7.3–7.6 that appear in the text. (*See electronic version for color representation of this figure*)

Permian sedimentary fill, collectively called the Paganzo Group (Ramos, 1988).

This basin is one of several pericratonic basins that received glacial sediments during and immediately after the middle to late Carboniferous Gondwanan glaciation (Eyles et al., 1995; Limarino et al., 2002, 2013; Caputo et al., 2008; Gulbranson et al., 2010). The Paganzo Basin rests on a strongly compartmentalized basement of Precambrian to Devonian rocks. The tectonic setting remains controversial and has been variously interpreted as a retroarc foreland basin related to the Punta del Agua volcanism to the west (Ramos, 1988; Limarino et al., 2006) or as a strike-slip basin (Fernández-Seveso & Tankard, 1995); parts of it are described as a rift basin (Astini et al., 1995; Milana et al., 2010). Salfity and Gorustovich (1983) noted significant regional differences in the sedimentary fill, so it may not be a single basin, but a series of interconnected basins with slightly different tectonic regimes. Most authors subdivide the Paganzo Group into three formations: Guandacol, Tupe, and Patquía. The Guandacol Formation is up to 1000 m thick sequence of proglacial sediments ranging from distal

turbidites, shales, and MTDs with dropstones; Tupe Formation is a 1300 m thick sequence of fluvial, lacustrine, and marine sediments; and Patquía Formation is a 1000 m thick succession of continental red bed sediments, fluvial facies, and playa lake deposits. Only the Guandacol Formation is exposed at La Peña; it is locally interpreted as a slope system with proglacial influence.

7.3. LOCAL SETTING

La Peña section crops out along a gorge of the same name and is accessible via Ruta Nacional 150 (RN 150) as it crosses the Ischigualasto Range, between the main entrance to Ischigualasto Park and the beginning of Bermejo Valley. La Peña Canyon is incised into the western flank of the Ischigualasto and Caballo Anca ranges, part of a large basement-cored block uplift whose western mountain front is defined by the crustal-scale east dipping Valle Fértil reverse fault. This fault strongly influenced sedimentation from the Paleozoic onward and probably had a normal (down to the ENE) displacement during the Carboniferous. The MTD-dominated succession to the ENE of the fault is over 1000 m thick (Figure 7.1c) and is overlain by 200 m of turbidites and pro-deltaic sediments, irregularly eroded beneath Triassic red beds (Milana et al., 2010). It has been suggested (Milana et al., 2010) that the Carboniferous paleoslope at La Peña had an irregular shape, as kinematic indicators in some MTDs suggest a transport direction toward the NNE while in others infer flow to the WNW. The section thickens dramatically to the NNW, but disappears into the subsurface only a few kilometers north of La Peña gorge.

The deformation within the MTDs of the Guandacol Formation at La Peña was previously interpreted as a tectonic effect of proximity to the nearby Valle Fértil fault. However, our work has shown that the deformation was syn-depositional and partitioned by the boundaries between the well-exposed large-scale MTDs of different types. About 85% of the lower half of the section is composed of MTDs, while in the upper half the proportion of MTDs reduces to about 35% (Figure 7.2a–c), the stratigraphy consisting generally of turbidites with some pro-delta and delta-front sands. Within La Peña Canyon itself, the lower part of the Carboniferous section lies in the subsurface. However, 3 km further to the SSW, older Carboniferous rocks are seen to onlap Precambrian basement (Figure 7.1c) which we interpret as a contemporaneous high.

7.4. THE MTD COMPLEX AT LA PEÑA SECTION

In this contribution, we give an overview and brief description of the six MTDs that crop out in the study area. The oldest unit recognized in this section is a delta-front/pro-deltaic package with subordinate turbidites that locally reaching about 100 m in thickness.

7.4.1. MTD1

This MTD is up to 150 m thick, and can be subdivided into three units, MTD1A, MTD1B, and MTD1C (Figures 7.1c and 7.2a). MTD1A is dominantly sandy and up to 30 m thick, and consists of slightly deformed medium to coarse sandstones with minor mud content, and is recognizable by its lighter beige color. The middle part (MTD1B) has mixed lithologies of sandstones and siltstones and shows a darker color which distinguishes it from the lower unit, and discrete sandstone blocks and rafts are more evident than in the lower part where everything appears homogenized. The upper part (MTD1C) consist of a silty-muddy matrix with sandstone blocks several meters thick (Figure 7.3a) and shows a sharp contact with MTD1B. Above MTD1C, there is a bedded sandstone unit that pinches out to the north, and hence it is not seen along the road section. We interpret this bedded light-colored unit as being ponded in the topographic relief on top of MTD1C. These whitish ponded medium-grained sandstones are quite irregular at their base, but they tend to be flat on the top. On top of these ponded sands, there follows a darker-colored well-bedded turbidite succession up to 80 m thick. This unit also wedges out to the north and completely disappears along the road section (Figures 7.1c and 7.2a), where it appears that MTD1 amalgamates with MTD2 and it is almost impossible to distinguish their boundary. To the south, the sandy part of the lower MTD1A rests directly on the Precambrian basement, suggesting that the basement showed significant relief, rising to the SSW.

7.4.2. MTD2

This MTD is up to 200 m thick and can be traced for several kilometers (Figure 7.2b). It shows similar characteristics to MTD1, and it is also the first one that crops out along the RN 150 road section. This MTD shows significant stratigraphic changes; in its lower part, it is possible to recognize a banded unit consisting of light-colored elongate sand bodies (meters thick and tens of meters long) in a darker fine-grained matrix; the sand bodies shows extensional deformation representing a sort of boudinage (Figure 7.3b). In the middle part of the deposit, massive sandstone blocks, some up to 20 m long by 7 m thick, are distributed through a dark siltstone matrix (Figure 7.3b). The upper part is dominantly dark siltstones. As in MTD1, we do not recognize any evidence of proglacial sedimentation. This is important to mention because the overlying MTD3 and MTD4 clearly show influence of deglacial sedimentation on the mass movement.

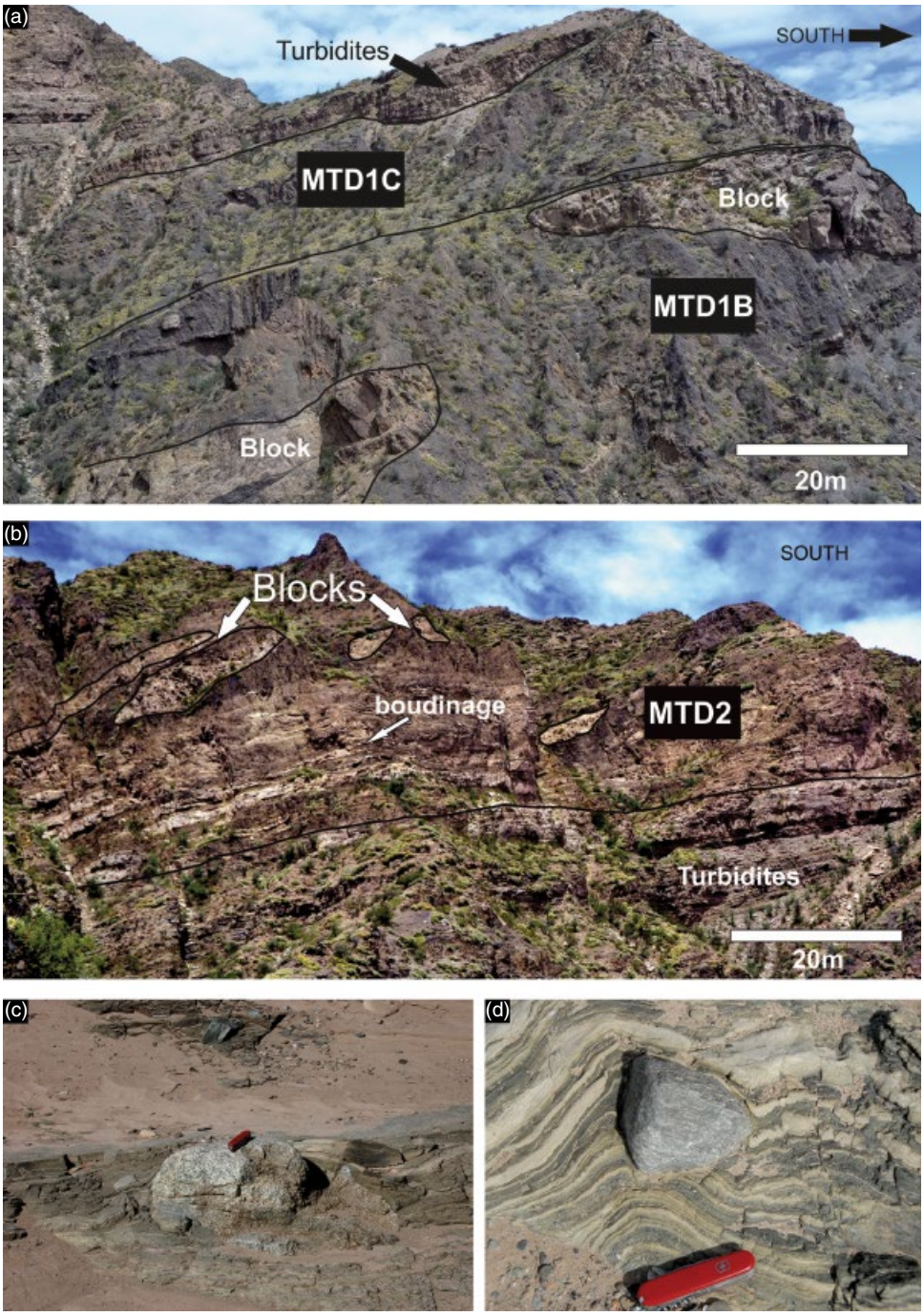


Figure 7.3 (a) Photograph of MTD1 showing sandstones blocks. (b) Base of MTD2 showing the basal deformation and sandstones blocks within the matrix. (c and d) Precambrian dropstones recognized in MTD3.

7.4.3. MTD3

This MTD is up to 220 m thick, starting with a highly sheared sandy lower unit up to 40 m thick, followed by a middle massive green-colored silty diamictite containing sandstone blocks that can be recognized at a distance (Figure 7.2b) and also along the road cuts and gorge sides. The upper part consists of silty diamictite with dispersed clasts of coarse-grained granitoid and metamorphic rocks (Figure 7.3c, d) derived from the Precambrian basement (interpreted as ice-rafted debris), with a few scattered sandstone rafts. The middle unit is separated from the silty upper unit by a clear boundary (Figure 7.2b). MTD3 is capped by a 30 m thick succession of sandy

turbidites and small-scale slumps, interbedded with dark shales. Bedding in these turbidites show clear fanning toward the top of the MTD3 (Kneller et al., 2016) suggesting that the MTD was still deforming while this autochthonous turbidite succession was being deposited. These autochthonous sediments are locally removed by shearing at the base of the overlying MTD4.

7.4.4. MTD4

MTD4, about 200 m thick, is very well exposed along the road and the river section and along an N-S creek that separates it from MTD5. This MTD shows a clear base, marked by a few decimeter thick layer of structureless, poorly sorted, clast-supported gravel (Figure 7.4a). The overlying deposit is composed of a fine-grained silty matrix, containing outsized clasts of granitoid and metamorphic basement rocks which are interpreted as ice-rafted debris or dropstones. Blocks of medium to fine-grained sandstone up to 20 m long and 6 m thick (Figure 7.4b), with occasional sandy gravel layers, are immersed in a silty matrix that rarely permits the recognition of original bedding. Sandstone occurs as isolated streaks or as rounded blebs with sharp margins (Figure 7.4c, d). This texture (which we term "holomictite"; see below) is only observed at the lower and intermediate levels of the MTD4. The intermediate section is composed of moderately folded beds, where some original stratification is visible. The upper section, composed of well-bedded sediments, rests semi-conformably on top of the deformed sediments forming a complex of large (>20 m), coherent, tilted blocks, some with apparently fanning internal bedding (Figure 7.4e). At the top, local soft-sediment deformation, such as compressional microfaults and microfolding, is recorded, and some of the thicker sandy layers appear highly fluidized and deformed.

We suggest that the basal gravel at the base of this MTD is associated with lubrication of the MTD in a way that partially resembles hydroplaning (cf., Mohrig et al., 1998). This will be discussed further in the context of MTD5.

Also, this MTD exhibits an example of what we call here a "holomictite," which shows sedimentary peperite-like texture, and is the result of progressive mixing of different types of sediment, one sand rich and the other silt/mud rich, at a centimeter scale. In some cases, the protolith is disassembled into large blocks that typically remain coherent; sand is sheared into streaks from the margins of these blocks and is progressively mixed at a grain scale into the MTD matrix to be absorbed within it (Dykstra et al., 2011; Garyfalou, 2015; Sobiesiak et al., 2016a). Elsewhere, the sandy component constitutes small blebs or clots with discrete margins, in which the sand and the matrix appear to behave as poorly miscible liquids. These blebs become progressively smaller until a complete homogenization occurs.

This MTD shows a clear differentiation of deformation zones through its almost 200 m thickness; the basal highly deformed layer may have accommodated most movement by plastic deformation, helped by some degree of liquefaction. The degree of deformation decreases upward from strongly deformed and contorted heterolithic beds to progressively less deformed ones. We do not observe any sharp break in the sedimentary succession of this MTD. Taken with the apparent fanning stratigraphy in the blocks of the upper zone, this suggests that the upper unit may have been deposited contemporaneously with continuing deformation of the underlying units.

MTD4 is followed by a thick succession of dark shales and fine-grained distal turbidites that are interpreted as the maximum flooding stage in the section. This unit also shows that glacial conditions were over at that stage.

7.4.5. MTD5

This is the best exposed single MTD in this canyon and a fine example of a non-glacially related MTD. The road tunnel excavated through it exposes excellent examples of this MTD's internal facies. The exposure of MTD5 is continuous for 13 km along strike (Figure 7.2a), displaying a dip section through the deposit from the headwall scar to the basin floor, where, prior to MTD emplacement, black shales were accumulating. A continuous 2 km long depositional strike section is also exposed perpendicular to the presumed northward transport direction. Low regional dips combined with a maximum thickness of MTD5 of up to 200 m produce continuous outcrops of this unit over c. 15 km^2. As at the base of MTD4, there is a conspicuous irregular sheet of clean, rounded, and structureless gravels immediately above the erosional base of the MTD5. Above this, the MTD is vertically quite homogeneous although there is a larger concentration of sandstone blocks in the lower third. This MTD shows different degrees of mixing between the two main lithologic constituents (sand and mud), with particles ranging in size from millimeter to blocks or rafts of sandstone up to 100 m long, with sheared contacts. The blocks within the lower part of MTD5 shown in the Figure 7.5a–c are about 50 m long by 7 m thick and decrease in size upward through the deposit (cf., Sobiesiak et al., 2016a). The main process of sand block disaggregation in the MTD is by "streaking out" of sand from block margins; no examples of clots were observed in this MTD. Overlying sediments are ponded massive turbidite sandstones found within topographic lows on top of the MTD coarse-grained, angular sand and minor gravel, deposited in patches over the MTD, controlled by the MTD's own topography. Almost no mud is observed

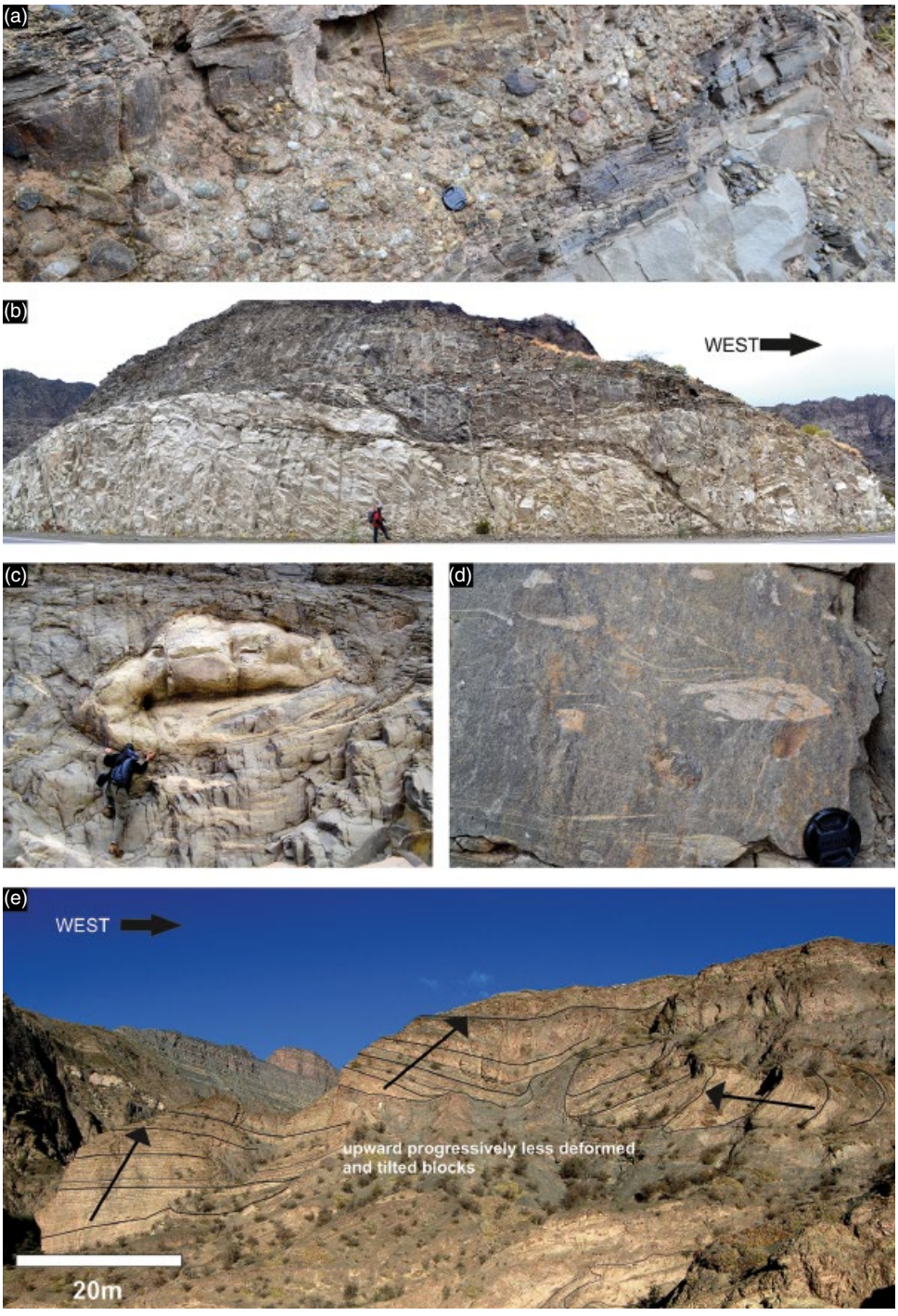


Figure 7.4 (a) Matrix-supported conglomerate at the base of MTD4. (b and c) Sandstone rafted block of diverse sizes immerse in a silty-muddy diamictite. Person for scale. Notice the sandstone streaks around the block mixed with the diamictite. (d) Sandstone blebs (liquefied) and the final product of the progressive mixture here called as a "holomictite." (e) Middle and upper part of MTD4 showing the highly deformed diamictite and the tilted remnant blocks of coherent material. The black arrows show the direction of the rotated blocks. (*See electronic version for color representation of this figure*)

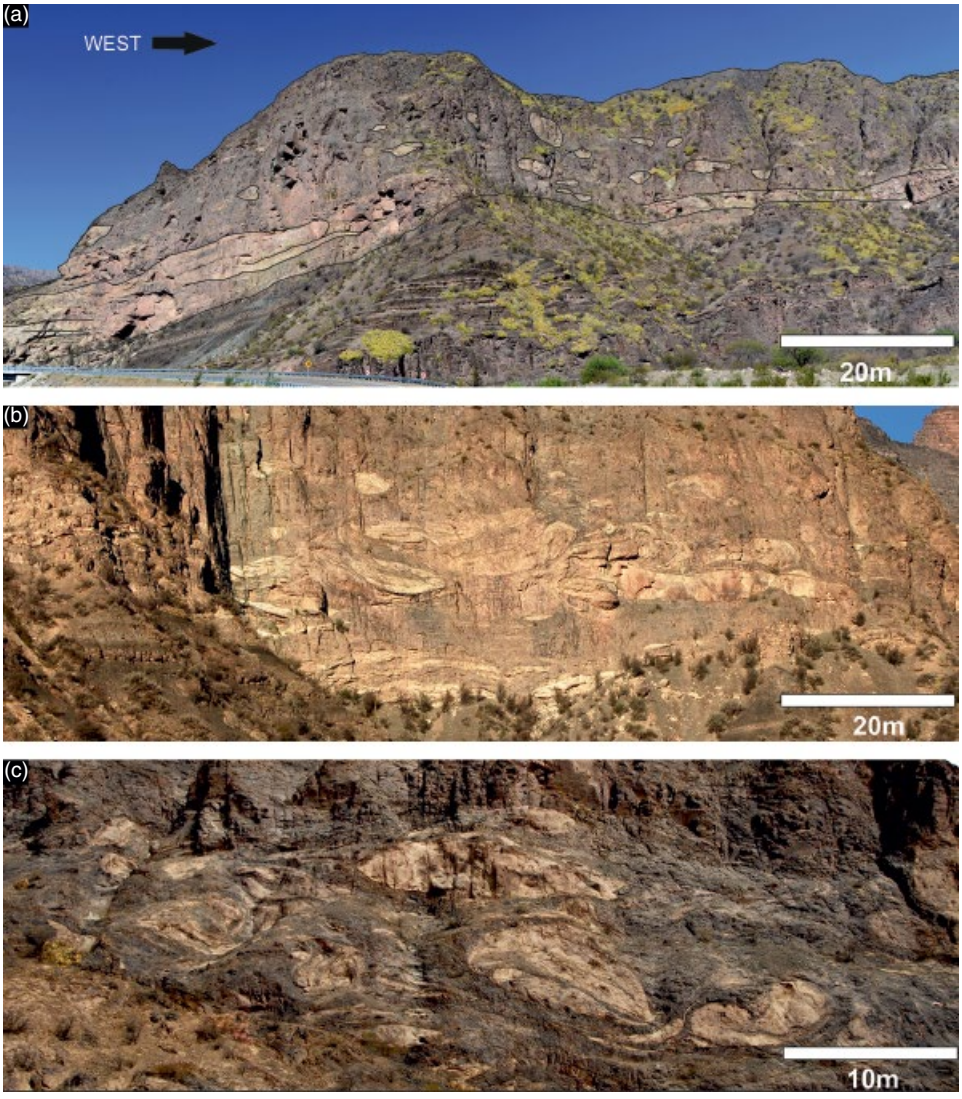


Figure 7.5 (a) The MTD5 along the road N 150 on top of a black silty turbidite package. Notice the different sandstone blocks sized along the entire outcrop. (b and c) Detail photograph of the middle part of this MTD showing the sandstone blocks and sheared contacts.

within this ponded sandstone unit, while mud appears immediately after the topography is filled.

The emplacement of MTD5 coincided with a rejuvenation of the associated non-MTD transport systems; while pre-MTD5 sedimentation on the basin floor was muddy (dark shales), the sedimentation directly above MTD5 switches to coarse-grained, angular sand, with minor associated gravel.

The sheet of gravels found at the base of MTD5 may have played a role in the emplacement of this 200 m thick mass over dark shales and thin-bedded turbidites without significant deformation of the underlying sediments. This implies high mobility and minimal substrate interaction. There is just a 30–50 cm shear zone in the uppermost shales immediately below MTD5, observed over a long distance in La Peña gorge. The gravel layer itself constitutes an easily deformable bed, contributing to the mobility. Additionally, as suggested for MTD4, we believe the gravel may have played a role sustaining an overpressured hydraulic system that acted as lubrication. The trapping of a layer of overpressured water between the mass movement and the seabed has been suggested to explain high mobility of subaqueous debris flows (Mohrig et al., 1998; De Blasio et al., 2004). We suggest that the interconnected pore fluid within the basal gravel provides such a layer. Such a mechanism combines elements of the hydroplaning model and of the linked cavity system model that has been used to explain high mobility of surging glaciers (Kamb, 1987). In linked cavity systems, it has been demonstrated that when the subglacial

tunnel network is disrupted, a series of smaller conduits may develop creating a network in which hydraulic pressure may reach up to 89% of the ice overburden (Kamb, 1987), in accordance with observations of increased water pressure in fast flowing glaciers (Iverson et al., 1995; Clarke, 2005). The large quantity of water required to sustain the linked cavity system where movement is over sediment rather than directly over bedrock (Harrison & Post, 2003) would be readily available in a subaqueous setting.

7.4.6. MTD6

MTD6 is a sand-dominated MTD can be traced for several kilometers (Figure 7.6a), whose main characteristic is its rapid lateral change over a few tens of meters from sets of imbricated sandstone slices (Figure 7.6b) into individual sets of sandstone blocks (Figure 7.6b), both embedded in a debrite. The MTD is composed of heterolithic and pebbly mudstones and sandstone units (from base to top). The heterolithic unit comprises an intercalation of ~15 cm thick sandstone beds with dark mudstone layers. The debrite unit, which accounts for <10% of the body, is a light grey colored pebbly mudstone, consisting of granule to small pebble sized quartz clasts within a muddy matrix and mainly found separating sandstones blocks. Lastly, the sandstone unit is light orange colored, composed of medium- to coarse-grained, structureless sandstone. The MTD was subdivided into imbricate- and block-dominated parts (Figure 7.6b, c) according to the deformational structures recorded in each of the domains, especially by the sandstone beds (Sobiesiak et al., 2017). The imbricate-dominated domain (Figure 7.6b) consists of a "pop-up" block and two sets of thrust faults manifested by the dislocation of sandstone slices. The overall size of this domain is ~8 m thick and ~70 m wide, ending at the beginning of the block-dominated portion of the deposit. The "pop-up" block involves two opposite dipping thrust faults that dislocate the sandstone bed between the thrusts upward. Laterally, the "pop-up" block evolves into the imbricate thrusts, which are made of three coherent sandstone slices separated by two sets of thrust faults that diverge upward from the sole. The sandstone slice at the far end of the deposit possesses a fanlike morphology as it lies buttressed against the block-dominated domain. The contact between the sandstone and the heterolithic mudstone is irregular, showing symmetric flame structures and mud injections along the thrust fault planes. The pebbly mudstone unit occurs in the uppermost portion of the heterolithics, concordant to bedding as thin (~4 cm) discontinuous bodies that thicken and thin laterally.

The block-dominated part consists of individual sandstone blocks (up to 4 m high and ~12 m wide) wrapped usually by a thin mudstone (up to ~30 cm) and embedded within the pebbly mudstone unit. The pebbly mudstone is the matrix in which the sandstone blocks are enclosed; however, below sandstone blocks, the pebbly mudstone occurs as discontinuous lenses of varying thicknesses (Figure 7.6c, d) (up to 30 cm) and is occasionally absent. The pebbly mudstone is usually found close to the contact with the sandstone blocks, but wherever a thicker (up to ~40 cm) heterolithic package occurs in between, the latter display deformational features such as asymmetrical folds and pinch and swell.

Additionally, there is evidence of the pebbly mudstone being injected upward and forming necked areas (Figure 7.6d). As this unit was injected into the sandstone, it ripped off fragments of the sandstone and more rarely of the heterolithic mudstone, resulting in the incorporation of "secondary clasts" (Figure 7.6e) that are typically elongate and range from 5 to 60 cm in size. The sandstone blocks from the imbricate-dominated sandstones possess sets of structures that indicate interaction between the units, such as (i) shallow downward injection of sandstone into the heterolithics, (ii) seams of anastomosing mud injected upward at the sandstone block base, (iii) clusters of mud clasts, and (iv) diapir- and sill-like structures of pebbly mudstone into the heterolithics, among others.

The model proposed to explain the fault-dominated MTD emplacement is first the pebbly mudstone deposited on top of a heterolithic mudstone unit; subsequently, another heterolithic mudstone unit was deposited intercalating mudstone and thin sandstone layers, probably trapping water within the pebbly mudstone, followed by the deposition of a thick sandstone package. An unknown trigger made the whole package fail, having the wet pebbly mudstone as a detachment surface. As material translated downslope, part of the sandstone layer was boudinaged and fragmented by the flow as it sunk into the pebbly mudstone to form the block-dominated sandstone. On the other hand, part of the sandstone translated as a single unit, undergoing limited deformation until it was buttressed, developing thrust fault imbrication and the pop-up block to develop the fault-dominated sandstone.

7.5. DEPOSITIONAL MODEL

Different scales of deformation and varying rheological responses, according to lithology and strain rate, are evident both between and within MTDs (from base to the top) of the La Peña section. Several of the MTDs have a conspicuously sandy unit at the base. Apparently, as the MTD progressively moves down the slope, this sandy unit either breaks apart into blocks or may form a continuous zone of ductile deformation (perhaps by liquefaction) that accommodates much of the basal shear, which will erase most traces of the original stratification. Fine-grained



Figure 7.6 (a) An overview of the length of this MTD. (b) Imbricated sandstone blocks that form part of this MTD. (c) Sandstone blocks embedded within the debrite. (d) Pebbly mudstone injected within the sandstone. (e) Sandstones and mudstones clasts embedded in the debrite.

sand blocks show the most ductile deformation as they disaggregate and mix with the matrix lithology (proglacial diamictites in case of MTD3 and MTD4). On the other hand, the upper part of the MTD may show discrete blocks that retain a high degree of internal integrity (MTD4). Heterolithic blocks seem to behave in a more brittle way compared with the fine sand ones, due to the presence of a cohesive component, breaking apart and rotating as they move, but remaining internally coherent. Finally, some sand blocks progressively disaggregate until they reach the centimeter-size liquid-like clots that may be held together by internal tension forces, whereas others

form schlieren on their sheared margins that disintegrate grain by grain.

In the six examples provided here, at least two show evidence of progressive slumping. Clear fanning of the turbidites on top of MTD3 and progressively decreasing rotations of blocks at the top of MTD4 provide outstanding examples of this process of continued MTD deformation at the basal section. Continuing deposition may take place: either progressively and concurrently with emplacement by continuous creep (in which case the MTD will show diffuse upper boundaries) or on top of the MTD postdating most of the movement (in which case overlying sediments will onlap or downlap a discrete surface).

7.6. DISCUSSION AND CONCLUSIONS

The observations made in La Peña show various features that may shed some light on the processes of MTD development and emplacement:

a. *Progressive slumping* within MTDs: We draw attention to the possibility that an MTD may remain active after the first event of emplacement, thus creating a dynamic substrate for turbidity current deposition. Such a process of progressive slumping is known in many subaerial environments (creep), and we suggest it is also evident in deepwater environments. In such a case, the stratal architecture of the ponded beds will be affected by the continued deformation of the MTD, which may include deformation of the MTD surface, growth strata, or semi-passive translation on top, as well as more complex strain histories within the MTD itself.

b. *Nature of the protolith*: Behavior is partly controlled by original lithology but is also likely to be dependent on factors such as water content and strain rate.

c. *Mixing process at MTDs*: We recognized different styles of mixing between sand and mud, either as streaks sheared off a more coherent block, sometime even containing original sedimentary structures, or as blebs or clots in a mud matrix ("holomictite") that appear to disaggregate progressively. The differences must be related to the rheological contrast between the parent sand body and the surrounding mud, in the case of the block-and-streak texture acting as highly miscible fluids but with strongly contrasting apparent viscosity and in the case of the "holomictite" acting as poorly miscible fluids of similar viscosity. The cause of these differences is not clear but is probably due more to differences in the sand than in the mud and might relate to grain size distribution or water content, the latter a function of the degree of consolidation of the sand prior to incorporation in the MTD.

d. *Distribution of sand*: Sandstone blocks with the MTDs tend to be concentrated near the base. This might either be a consequence of original stratigraphy in the protolith (i.e., an original basal sandy unit), or downward gravitational segregation of blocks that were originally more uniformly distributed, or incorporation of material from a sandy substrate (Sobiesiak et al., 2016a). It also is important to note that in some cases, an MTD could be shaped almost entirely of sand, as the MTD6.

e. *Proximality*: Any aspect of MTD facies that is controlled by time-dependent processes will vary with runout (such as the degree of block assimilation or protolith mixing) in addition to any time-dependent effects on deformation rates (such as thixotropy). It is also related to dominant stress within the MTD and resulting deformation, in the simplest cases extension at proximal reaches and compression at distal reaches.

f. *Hydroplaning*: La Peña provides two good examples of large MTDs (c. 200 m thick) showing an unusual concentration of structureless clean gravel along the sole of the MTD. Also, the level of deformation of the muddy beds immediately below these thick MTDs suggests a mechanism that prevented excessive shearing of the substrate, requiring the existence of a layer of very low strength that facilitated sliding. We propose that MTDs may experience long runouts due to a combination of hydroplaning (Mohrig et al., 1998) and linked cavity system models similar to those of surging glaciers (Kamb, 1987). The pore fluid of the gravel observed in the base of both large MTDs may have provided the high pressure needed to overcome the sediment mass overburden to facilitate fast sliding.

ACKNOWLEDGMENTS

The authors would like to express their gratitude to the reviewers and their suggestions to improve the manuscript and also to thank PRAX-2 Joint Industry Project (PetroChina, Statoil, BP, Aker BP, and VNG) for their financial support.

REFERENCES

Astini, R. A., Benedetto, J. L., & Vaccari, N. E. (1995). The early Paleozoic evolution of the Argentine Precordillera as a Laurentian rifted, drifted, and collided terrane: A geodynamic model. *Geological Society of America Bulletin*, *107*, 253–273.

Bull, S., Cartwright, J., & Huuse, M. (2009). A review of kinematic indicators from mass-transport complexes using 3D seismic data. *Marine and Petroleum Geology*, *26*, 1132–1151.

Caputo, M. V., de Melo, J. H. G., Streel, M., & Isbell, J. L. (2008). Late Devonian and Early Carboniferous glacial records of South America. In C. R. Fielding, T. D. Frank, & J. L. Isbell (Eds.), *Resolving the Late Paleozoic Ice Age in time and space, Geological Society of America Special Publication* (Vol. 441, pp. 161–173). Boulder, CO: Geological Society of America.

Clarke, G. K. (2005). Subglacial processes. *Annual Review of Earth Planetary Sciences*, *33*, 247–276.

De Blasio, F. V., IIstad, T., Elverhøi, A., Issler, D., & Harbitz, C. B. (2004). *High mobility of subaqueous debris flows and the lubricating-layer model*. Paper presented in Offshore Technology Conference. Houston, TX.

Dykstra, M., Garyfalou, K., Kertznus, V., Kneller, B., Milana, J. P., Molinaro, M., et al. (2011). Mass-transport deposits: Combining outcrop studies and seismic forward modeling to understand lithofacies distributions, deformation, and their seismic expression. *SEPM Special Publication*, *95*, 1–25.

Eyles, N., Gonzales Bonorino, G., Eyles, C. H., Franca, A. B., & Lopez Paulsen, O. (1995). Hydrocarbon-bearing late Paleozoic glaciated basins of southern and central South America. In A. J. Tankard (Ed.), *Petroleum basins of South America, American Association of Petroleum Geologists, AAPG Memoir* (Vol. 62, pp. 165–183).

Fairweather, L. (2014). Mechanisms of supra-MTD topography generation and the interaction of turbidity currents with such deposits, (Unpublished PhD thesis). Aberdeen, Scotland: University of Aberdeen.

Fernandez-Seveso, F., & Tankard, A. J. (1995). Tectonics and stratigraphy of the Late Paleozoic Paganzo Basin of Western Argentina and its regional implications. *Petroleum Basins of South America*, *62*, 285–301.

Garyfalou, K. (2015). Integrated analysis of mass-transport deposits: Outcrop, 3D seismic interpretation and fast fourier transform, (Unpublished PhD thesis). Aberdeen, Scotland: University of Aberdeen.

Gulbranson, E. L., Montañez, I. P., Schmitz, M. D., Limarino, C. O., Isbell, J. L., Marenssi, S. A., & Crowley, J. L. (2010). High-precision U-Pb calibration of Carboniferous glaciation and climate history, Paganzo Group, NW Argentina. *Geological Society of America Bulletin*, *122*, 1480–1498.

Hampton, M. A., Lee, H. J., & Locat, J. (1996). Submarine landslides. *Reviews of Geophysics*, *34*, 33.

Harrison, W. D., & Post, A. S. (2003). How much do we really know about glacier surging? *Annals of Glaciology*, *36*, 1–6.

Iverson, N. R., Hanson, B., Hooke, R. L. B., & Jansson, P. (1995). Flow mechanism of glaciers on soft beds. *Science*, *267*, 80–81. https://doi.org/10.1126/science.267.5194.80

Kamb, B. (1987). Glacier surge mechanism based on linked cavity configuration of the basal water conduit system. *Journal of Geophysical Research*, *92*, 9083–9100.

Kneller, B., Dykstra, M., Fairweather, L., & Milana, J. P. (2016). Mass-transport and slope accommodation: Implications for turbidite sandstone reservoirs. *AAPG Bulletin*, *100*, 213–235.

Limarino, C. O., Césari, S. N., Net, L. I., Marenssi, S. A., Gutierrez, R. P., & Tripaldi, A. (2002). The Upper Carboniferous postglacial transgression in the Paganzo and Río Blanco basins (northwestern Argentina): Facies and stratigraphic significance. *Journal of South American Earth Sciences*, *15*, 445–460.

Limarino, C. O., Césari, S. N., Spalletti, L. A., Taboada, A. C., Isbell, J. L., Geuna, S., & Gulbranson, E. L. (2013). A paleoclimatic review of Southern South America during the late Paleozoic: A record from icehouse to extreme greenhouse conditions. *Gondwana Research*, *25*, 1396–1421.

Limarino, C. O., Tripaldi, A., Marenssi, S. A., & Fauqué, L. (2006). Tectonic, sea level, and climatic controls on late Paleozoic sedimentation in the western basins of Argentina. *Journal of South American Earth Sciences*, *33*, 205–226.

Lucente, C. C., & Pini, G. A. (2003). Anatomy and emplacement mechanism of a large submarine slide within a Miocene foredeep in the northern Apennines, Italy: A field perspective. *American Journal of Science*, *303*, 565–602.

Martinsen, O. J. (1994). Mass movements. In A. Maltman (Ed.), *The geological deformation of sediments* (pp. 127–165). London, UK: Chapman and Hall.

Milana, J. P., Kneller, B., & Dykstra, M. (2010). Mass-transport deposits and turbidites, Syn-to-Post-Glacial Carboniferous basins of Western Argentina. *ISC 2010 Field Guide*, 01–88.

Mohrig, D., Whipple, K. X., Hondzo, M., Ellis, C., & Parker, G. (1998). Hydroplaning of subaqueous debris flows. *Geological Society of America Bulletin*, *110*, 387–394.

Owen, M., Day, S., & Maslin, M. (2007). Late Pleistocene submarine mass movements: Occurrence and causes. *Quaternary Science Reviews*, *26*, 958–978.

Posamentier, H.W. & Martinsen, O.O.J., 2011. The character and genesis of submarine mass-transport deposits: Insights from outcrop and 3D seismic data. In Shipp, R.C., Weimer, P., Posamentier, H.W. (Eds.), *Mass-transport deposits in deepwater settings, SEPM (Society for Sedimentary Geology)*, 7–38. Tulsa, OK: SEPM.

Ramos, V. A. (1988). The tectonics of central Andes; 30°–33° S latitude. In S. Clark & D. Burchfiel (Eds.), *Processes in continental lithosphere deformation, Geological Society of America Special Publication* (Vol. 218, pp. 31–54). Boulder, CO: Geological Society of America.

Salfity, J., & Gorustovich, S. A. (1983). Paleogeografía de la cuenca del Grupo Paganzo, Paleozoico superior. *Asociación Geológica Argentina, Revista*, *38*, 437–453.

Sobiesiak, M., Valdez Buso, V., Kneller, B., Alsop, I., & Milana, J. (this volume, pp. 91–104). Block generation, deformation and interaction of mass transport deposits with the seafloor: An outcrop-based study of the Carboniferous at Cerro Bola, NW Argentina. In K. Ogata, A. Festa, & G. A. Pini (Eds.), *Submarine landslides: Subaqueous mass transport deposits from outcrops to seismic profiles*. Hoboken, NJ/Washington, DC: Wiley/AGU.

Sobiesiak, M. S., Alsop, G. I., Kneller, B., & Milana, J. P. (2017). Sub-seismic scale folding and thrusting within an exposed mass transport deposit: A case study from NW Argentina. *Journal of Structural Geology*, *96*, 176–191. https://doi.org/10.1016/j.jsg.2017.01.006

Sobiesiak, M. S., Kneller, B., Alsop, G. I., & Milana, J. P. (2016a). Inclusion of substrate blocks within a mass transport deposit: A case study from Cerro Bola, Argentina. In G. Lamarche, J. Mountjoy, et al. (Eds.), *Submarine mass movements and their consequences, 7th international symposium. Advance in Natural and Technological Hazards Research* (pp. 487–496). Cham, Switzerland: Springer International Publishing. https://doi.org/10.1007/978-3-319-20979-1_49

Sobiesiak, M. S., Kneller, B., Alsop, G. I., & Milana, J. P. (2016b). Internal deformation and kinematic indicators within a tripartite mass transport deposit, NW Argentina. *Sedimentary Geology*, *344*, 364–381. https://doi.org/10.1016/j.sedgeo.2016.04.006

Valdez, V. B., Milana, J. P., & Kneller, B. C. (2015). Megadeslizamientos gravitacionales de la formación guandacol en Cerro Bola y Sierra de Maz y su relación con la glaciación del Paleozoico tardío, La Rioja, Argentina. *Latin American Journal of Sedimentology and Basin Analysis*, *22*, 109–133.

8

Mass-Transport Complexes of the Marnoso-arenacea Foredeep Turbidite System (Northern Apennines, Italy): A Reappraisal After Twenty-Years

Gian Andrea Pini[1], Claudio Corrado Lucente[2], Sonia Venturi[3], and Kei Ogata[4]

ABSTRACT

The Casaglia-Monte della Colonna is one of the best exposed "fossil" mass-transport complex (MTC) cropping out in a foredeep succession exhumed in a mountain chain and represents a unique opportunity to study an internal architecture resulting from the (geologically) simultaneous collapses of an accretionary wedge front, slope, and basin plain deposits. The high variety of internal structures and the different MTC-substratum interactions depend on the geometry of MTC basal contact and the provenance of the remobilized sediments. In the 20 years from our first studies on this MTC, the better condition of some outcrops and the advances in methodological and interpretative tools enable us to provide an update scenario, with more details on the internal structures and a better comprehension of the complex interactions with the substratum.

8.1. INTRODUCTION

Mass-transport deposits (MTDs) represent a common occurrence in exhumed stratigraphic successions in mountain chains worldwide (Alves, 2015; Dykstra, 2005; Shipp et al., 2011; Yamada et al., 2012), and their number further increases considering that several cases of "chaotic" units (sedimentary mélanges or olistostromes) originated from submarine landsliding (Pini, 1999; Alonso et al., 2006; Burg et al., 2008; Camerlenghi & Pini, 2009; Cowan, 1985; Festa et al., 2010a, 2010b, 2012, 2016; Raymond, 1984, 2017; Raymond & Bero, 2015; Wakabayashi, 2011).

MTDs show different internal organization and structures due to sensible changes in composition and consolidation of translated rocks and sediments (Alves, 2015; Dykstra et al., 2011; Pini et al., 2012). An extreme variability exists, therefore, for their morphological aspect, the presence/absence, shape and amount of floaters (large blocks with poorly deformed bed packages), and the style of internal deformations. MTDs may result from multistage and/or multisource depositional events, having a complex internal structure and being made up of different sediments/rocks from various sources (mass-transport complexes [MTCs]; Weimer & Shipp, 2004). Fossil MTCs, especially large-scale and basin-wide ones, are usually complex units involving the entire spectrum of mass-transport processes (Lucente & Pini, 2003; Posamentier & Martinsen, 2011). They often comprise discrete subunits, defined on the base of composition, provenance, structures, and sense of movement. These subunits can represent single mass-transport events, pulses, or discrete masses moving differentially in the same event (Festa et al., 2016; Lucente & Pini, 2003; Ogata et al., 2012b, 2014a; Swarbick and Naylor, 1980). Another key point is the effects that MTDs/MTCs

[1] *Department of Mathematics and Geosciences, University of Trieste, Trieste, Italy*

[2] *Agency for Territorial Safety and Civil Protection, Emilia-Romagna Region, Rimini, Italy*

[3] *Ecosistema s.c.r.l., Imola, Italy*

[4] *Faculty of Science, Department of Earth Sciences, Free University of Amsterdam, Amsterdam, The Netherlands*

Submarine Landslides: Subaqueous Mass Transport Deposits from Outcrops to Seismic Profiles, Geophysical Monograph 246, First Edition. Edited by Kei Ogata, Andrea Festa, and Gian Andrea Pini.
© 2020 American Geophysical Union. Published 2020 by John Wiley & Sons, Inc.

can have on the underlying sediments (substrata) (Alves & Lourenco, 2010; Ogata et al., 2014b; Sobiesiak et al., 2016, 2018; van den Merve et al., 2011).

Pini et al. (2012) distinguished three types of MTDs/MTCs in the Apennines, in which the internal movements and translation/emplacement of bodies take place for (i) shear-dominated viscous flows within a muddy matrix (Type 1), (ii) mud-silt-sandy matrix sustained by fluid overpressure (Type 2), and (iii) concentrated shear zones/surfaces with advection of grains and fluid (overpressured basal carpets) (Type 3). This chapter will show an example of a Type 3 MTC cropping out in the Romagna Apennines of Italy, namely, the Casaglia-Monte della Colonna, aiming to show the kinematic of emplacement, mechanism of internal deformation, and how progressive stratal disruption operates down flow, especially addressing the interaction with the substratum.

We are here presenting an updated review of the knowledge about the Casaglia-Monte della Colonna MTC, based on our previous works (Lucente, 2000, 2002; Lucente & Pini, 1999, 2002, 2003, 2008) integrated by new field observations and interpretations matured in more than 20 years of focused observations. 20 years of time modified the outcrops revealing new details. Furthermore, the advancements of computer software and hardware and of digital photography made easily available the 3D reconstructions of outcrops by close-range photogrammetry starting from an array of multiple viewpoint photographs (see, e.g., Bistacchi et al., 2015). We here better define, therefore, the internal features of key outcrops (Casaglia A and B and SP 477 outcrop) through 3D reconstructions of outcrops. We also illustrate parts of the MTC that were not studied before (Santerno sector) or not easily accessible to an international audience (Isola B, Ciriegiolo B, Rio di Gamogna, and Le Piane outcrops) being part of previous works in Italian language (Lucente, 2000, 2002).

8.2. GEOLOGICAL SETTING

The Northern Apennines of Italy are an arcuate orogenic wedge (Figure 8.1a) built up in different tectonic phases from Cretaceous to Plio-Pleistocene (Carmignani et al., 2004; Castellarin et al., 1992; Cerrina Feroni et al., 2002, 2004; Molli et al., 2010). A still active extensional tectonics characterizes the Tyrrhenian side and the axial part of the chain (Bonini et al., 2016; Carmignani et al., 1994; Collettini et al., 2006; Sani et al., 2009), while a contractional tectonics is still active beneath the Po Plain and the Adriatic Sea (Figure 8.1a) (Boccaletti et al., 2011; Bonini et al., 2014, 2016; Toscani et al., 2009).

The structurally highest and the most far traveled structural units, the Ligurian Nappe, comprises deformed stratigraphic successions and mélanges originated from a Jurassic-Eocene ocean belonging to the Alpine Tethys (Internal Ligurian units) and its southeastward transition to the Adria Microplate (External Ligurian and Subligurian units) (Bortolotti et al., 2001; Cerrina Feroni et al., 2002; Marroni et al., 2017; Marroni & Pandolfi, 2007). The internal structural setting of the Internal Ligurian units largely derives from the southeastward dipping subduction of the oceanic crust in a Cretaceous-Paleogene double-vergent accretionary wedge (Malavieille et al., 2016; Marroni et al., 2010, 2017). The structural setting of the External Ligurian and Subligurian units originates from the northwestward directed subduction of the ocean-continent transition and the thinned continental margin of Adria Microplate beneath the accretionary wedge and the Eurasia/Iberia plates (Marroni et al., 2010, 2017; Molli et al., 2010; Molli & Malavieille, 2010).

The southeastward to northwestward switch in subduction is considered to occur in middle Eocene (Ligurian phase). This scenario is not generally accepted, since the age is debated (Argnani, 2012; Boccaletti et al., 1971, 1980; Doglioni et al., 1998; Marroni et al., 2010; Molli et al. 2010) and the paleo-tectonic reconstructions are complicated by the highly extended and articulated continental margin of the Adria Microplate (see, e.g., Marroni et al., 2017) and a very complex paleogeographic and geodynamic scenario (see, e.g., Argnani, 2002; Stampfli et al., 1998, 2002). Thus, although several authors support a change in subduction direction (subduction flip) involving the subduction of the continental margin of the Adria Microplate (see, e.g., Boccaletti et al., 1971; Doglioni et al., 1998; Marroni et al. 2017; Molli, 2008; Molli et al., 2010; Vignaroli et al., 2008), alternative views have been presented (Argnani, 2002, 2012; Faccenna et al., 2001; Principi & Treves, 1984).

However, apart from these different paleo-tectonic models, severe deformation of continental margin of Adria Microplate took place from Oligocene to Recent time in areas originally placed to the SE of the Subligurian domain. This originates the other structural units of the Northern Apennine accretionary wedge, namely, from W/SW to E/NE, the Tuscan units and the Romagna-Umbria and Po Plain fold and thrust belts (Barchi et al., 2001; Carmignani et al., 2001). The onset of these deformations corresponds to the opening of back-arc basins (Liguro-Provençal-Balearic and Tyrrhenian basins) (Carminati et al., 2012; Dewey et al., 1989; Faccenna et al., 2004; Gueguen et al., 1998; Malinverno & Ryan, 1986), up to the emplacement of back-arc oceanic crust (Carminati et al., 2012; Roca, 2001; Sartori, 1990), and to the coupled counterclockwise rotation of the accretionary wedge and the Corsica-Sardinia continental block (Muttoni et al., 2000; Speranza et al., 1997, 2002). Rotation and protracted extension in the back-arc region is responsible for the east/northeastward migration of the

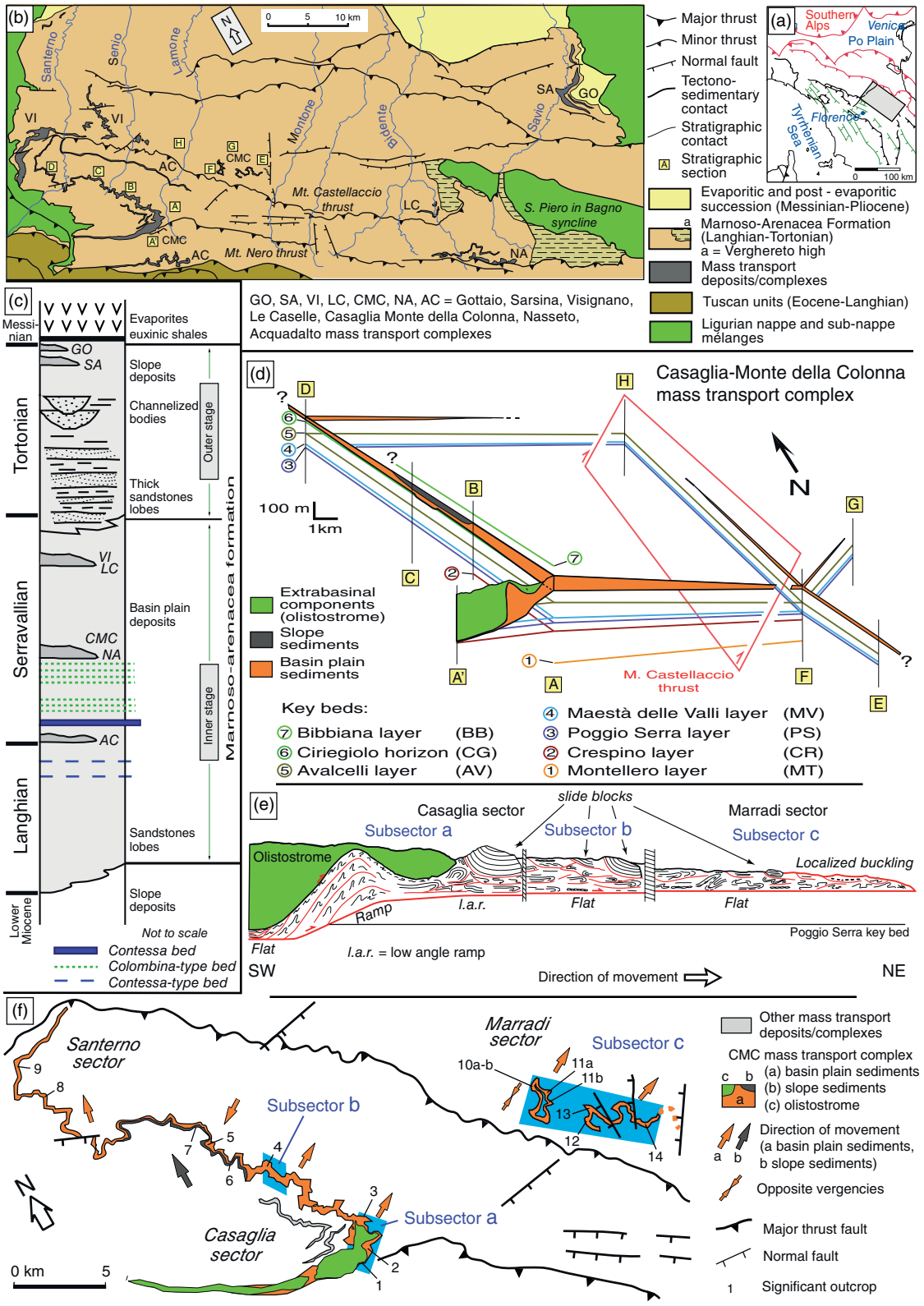


Figure 8.1 (a) Schematic structural map of the Northern Apennines. Key to the tectonic structures: red, thick lines, buried fronts of Northern Apennines and Southern Alps; red, thin lines, buried thrusts; black lines, outcropping structures (thrusts with triangles); green, normal faults. Triangles and barbs indicate hanging wall. Gray box shows the location of (b). Source: Modified from Festa et al. (2010b). (b) Schematic geological map of the Romagna-Tuscan Apennines. (c) Synthetic stratigraphic subdivision of the Miocene succession of the Romagna-Tuscan Apennines focused on the Marnoso-arenacea Formation. (d) Fence diagram illustrating the geometry of Casaglia-Monte della Colonna mass-transport complex with respect to key beds. Locations of stratigraphic sections are shown in (b). (e) Composite transect summarizing the principal structural features observed in the subsectors outlined in (f). (f) Geological map of the Casaglia-Monte della Colonna mass-transport complex, showing its component units, the directions of flow, and the locations of the outcrops described in the text. Source: All the figures are, modified, from Lucente and Pini (2003). (*See electronic version for color representation of this figure*)

accretionary wedge (Boccaletti et al., 1990). Within this framework, the Ligurian Nappe always occupied the highest position in the tectonic stack of the wedge, progressively thrusting over the Tuscan units and the Romagna-Umbria fold and thrust belt. Atop the deforming Ligurian Nappe, slope to shelf, piggyback, satellite basins developed (Epiligurian units; Ricci Lucchi & Ori, 1985).

The Tuscan units and the Romagna-Umbria fold and thrust belt share a common stratigraphy from Permian-Mesozoic continental and marine deposits and Paleogene slope deposits up to Oligocene-Miocene-Pliocene thousands of meter-thick turbiditic successions. The turbiditic successions represent the sedimentary infills of a migrating (and rejuvenating) foredeep complex, which took place onto the flexed Adria continental margin at the front of the Apennine accretionary wedge (Ricci Lucchi, 1986).

The Marnoso-arenacea Formation is the middle to late Miocene infill of this migrating foredeep complex (Boccaletti et al., 1990) exhumed and excellently exposed in the Northern Apennine chain (Ricci Lucchi and Ori, 1985). This formation extends for over 180 km in length and 40 km in width and comprises over 3000 m of deep-water turbidites. The Marnoso-arenacea Formation consists of an older "inner" (Langhian-Serravallian) and a younger "outer" (Tortonian) evolutionary stages (Ricci Lucchi, 1975, 1986). The inner stage represents the phase of maximum subsidence and lateral extent of the basin, with a large development of basin plain turbidites. This stage shows an impressive lateral continuity of individual beds, allowing basin-wide correlations (Amy & Talling, 2006; Ricci Lucchi & Valmori, 1980; Talling et al., 2007; Tinterri et al., 2012).

The sediment dispersal pattern was along the longitudinal axis of a narrow foredeep (Gandolfi et al., 1983; Ricci Lucchi, 1978). Paleocurrent data show a southeast directed transport direction from Alpine sources through multiple entry points. A carbonate platform at the southeastern edge of the basin supplied carbonate turbidites, the so-called "colombine" layers, the calcareous composition of which is easily recognizable in field. Minor and sporadic sources located along the accretionary wedge front at the southwest margin of the basin supplied hybrid megabeds (Contessa and Contessa-like beds; Ricci Lucchi & Valmori, 1980).

Paleocurrent data and bed-by-bed correlation, also across different thrust units, point out an original flat paleo-topography of the basin except for the Verghereto area where a well-documented intrabasinal high developed subsequently to synsedimentary tectonic activity (Amy & Talling, 2006; Lucente, 2004). However, at a closer scale, sedimentary features suggest local topographic control on sedimentation through gentle high (see ponded foredeep of Mutti et al. (2003)). This physiographic framework caused ponding and flow reflection-deflection of turbidity currents and MTDs/MTCs, resulting in changes in sedimentary facies and in lateral thickness of both bed packages and individual layers (Lucente, 2004; Roveri et al., 2002; Tinterri & Muzzi Magalhaes, 2011; Tinterri & Tagliaferri, 2015).

Several MTDs/MTCs characterize the basin plain and the inner slope, involving sediments of various origin and state of consolidation. Frequency peaks in slide distribution occurred in the early Serravallian and late Tortonian, representing phases of enhanced basin-scale instability (Landuzzi, 2005; Lucente & Pini, 2002, 2008).

From a tectonic point of view, the Marnoso-arenacea Formation is a consistent part of the sedimentary succession involved in the lowest and northeasternmost (external) structural unit of the Northern Apennine mountain chain and the Romagna-Umbria fold and thrust belt. The thrust faults and fault-related folds strike out from NW to SE, parallel to the main direction of the Apennine structures (e.g., Capozzi et al., 1991; de Jager, 1979) (Figure 8.1b). This results in broad asymmetric synclines separated by narrow anticlines. Following De Donatis and Mazzoli (1994), the fold geometries are consistent with detachment folds, deformed by breakthrough faults in the hinges and forelimbs, that often evolved in regional-scale thrusts (Figure 8.1b). These structures enucleate during the sedimentation (Bonini, 2006; De Donatis & Mazzoli, 1994; de Jager, 1979), so anticlines originated the intrabasinal highs mentioned earlier (Lucente, 2004; Lucente & Pini, 2003, 2008; Roveri et al., 2002; Tinterri & Muzzi Magalhaes, 2011). Changes in bed thickness occur from the anticlinal hinges to limbs (Panieri et al., 2009; Tinterri & Tagliaferri, 2015; Tagliaferri et al., 2018) with the stratigraphic succession assuming a classic fan-type shape (grow successions; Bonini, 2006; Tinterri and Tagliaferri, 2015).

8.3. CASAGLIA-MONTE DELLA COLONNA MTC: PHYSIOGRAPHY AND INTERNAL STRUCTURES

Recognized as originated by mass-transport processes since Renzi (1967), the Casaglia-Monte della Colonna body (shortened in CMC) occurs in the Serravallian Marnoso-arenacea Formation of the inner stage, in the westernmost sector of the Romagna-Tuscan Apennines (Figure 8.1b). Its position in the stratigraphy (Figure 8.1c) is above the Contessa key bed, in an interval characterized by basin plain turbidites, mainly corresponding to facies D_1, D_2, D_3, and G of Mutti and Ricci Lucchi (1972, 1975). An impressive continuity of beds and very distinctive turbidites from different sources (alpine sourced siliciclastic, carbonate "colombine," and southwest sourced hybrid turbidites) define either basin-wide or local key beds. It has been

possible, therefore, to outline the 3D stratigraphic relationships of the MTC with the underlying beds (substratum) (Figures. 8.1d) (Lucente 2000; Lucente & Pini, 2003).

Compositionally tripartite, the MTC comprises (i) deformed basin plain deposits, (ii) deformed fine-grained slope deposits, and (iii) extrabasinal material coming from the paleo-Apennine wedge front (Figure 8.1d–f). The extrabasinal component, defined in literature as "olistostrome" (Lucente & Pini, 2003), comprises hectometer- to kilometer-scale, heterogeneous blocks (olistoliths) sourced from the Subligurian units of the Ligurian Nappe (calcarenites and shales, middle Eocene), the Epiligurian slope basin (shales, cherty shales, and volcanoclastic layers, early Miocene), and the "closure" deposits of the Tuscan foredeep turbidites (shales and sporadic sandstone beds, early to middle Miocene) (see Lucente, 2000; Lucente & Pini, 2008). Each block maintains the original bedding and internal tectonic structures (folds, faults, cleavage, and boudinage). They are, therefore, not only extrabasinal but also belong to different structural units and have different composition, ages, and fabric with respect to the Marnoso-arenacea intrabasinal components; thus they can be considered as exotic (Festa et al., 2010a, 2010b, 2012). Nonetheless, a typical element of classic olistostromes (see Flores (1955); Type A of Lucente and Pini (2003)), the fine-grained matrix bounding the blocks, is lacking (see Type C olistostromes of Lucente and Pini (2003)).

A kinematically coherent association of slump horizons and slide blocks causes the remobilization of the intrabasinal component (basin plain and slope deposits) (Type 3 MTCs of Pini et al. (2012)) (Figure 8.1e). The differential movement of individual detached bed packages of different dimensions is incrementally achieved along shear zones and surfaces. Beds are laterally continuous and block-in-matrix intervals (debrites) are not common, being present only locally at the top (co-genetic debris flow). Meters to ten of meter-thick zones of intense stratal disruption (up to block-in-matrix fabric) develop less frequently within and at the base of the MTC due to severe folding and boudinage of beds (Lucente & Pini, 2003).

In this chapter, we will focus on the intrabasinal components, referring to Lucente and Pini (2003, 2008) for the extrabasinal one. A southwest to northeast transport is recorded in the basin plain and extrabasinal components in the southeasternmost area of Casaglia and the Marradi sectors (Figure 8.1f), while in the northwestern area, the basin plain component displays a southward to northward sense of movement (Santerno sector; Figure 8.1f) (Lucente, 2000; Lucente & Pini, 2003). Two superposed sub-bodies characterize the central part of the Casaglia sector with northeast to southwest transported basin plain deposits underlying S- to N-translated slope deposits.

8.3.1. The Southwest to Northeast Directed Basin Plain Deposits: Casaglia Sector

This is the most distinctive part of the CMC body, where its bottom surface depicts a staircase trajectory. The changes in the basal angle with respect to the substratum beds, shown in Figure 8.1d and e, correspond, from SW to NE, to:

1. an almost layer-parallel translation zone (lower flat, stratigraphic section A′);
2. an extrusion zone cutting the stratigraphic column for over 200 m (ramp, between stratigraphic sections A′ and A, with a cutoff angle of 8°);
3. a low-angle ramp (northeast and north of section A until the subsector b with a cutoff angle of less than 1°); and
4. an upper flat above the Ciriegiolo key bed (subsector b, stratigraphic section B).

The distribution and style of structures change in the diverse part of the MTC as summarized in Figure 8.1e (Lucente & Pini, 2003).

The best exposure of the translation zone crops out in a road cut (Figure 8.2a) close to Casaglia Village (Casaglia "A," outcrop 1 in Figure 8.1f). Thrusting of bed packages occur along discrete listric shear surfaces, which change down flow from layer parallel (flat) to a low-angle ramp. Thinner beds develop recumbent folds bounded by shear surfaces and with curved hinge lines (sheathlike folds). Lucente and Pini (2003) inferred the direction of movement, here and in the other CMC sectors, from fold axis distribution and vergence, using the separation arc method (Hansen, 1971; Woodcock, 1979).

A debrite composed of blocks of sandstones dispersed in a silty-clayey matrix characterizes the upper part of the outcrop beneath the olistostromes. The Marnoso-arenacea Formation below the debrite is thin-bedded, fine-grained, and intensely deformed up to a complete stratal disruption with isolated boudins and rootless slump folds.

The Casaglia "B" outcrop (2 in Figure 8.1f) shows a large section of basin plain deposits and subordinate slope facies arranged in large-scale anticlines and stacked by thrusting (see also Lucente and Taviani (2005)) (Figure 8.2b). This stacking causes thrust surfaces to be folded and uprighted. Folds share a common northeastward vergence with a single counter-verging fold. This zone corresponds to the steepest part of the ramp.

The Bibbiana-Monte della Colonna outcrop (outcrop 3 in Figure 8.1f), at the edge of the ramp, shows hectometer-scale outsized blocks (slide blocks) bounded by belts of metric-scale folds (Figures 8.2c and 8.3a–c). In these belts, folds change from close to isoclinal toward NE with their axial planes following the attitude of the belt, changing from steeply inclined to recumbent with a predominant

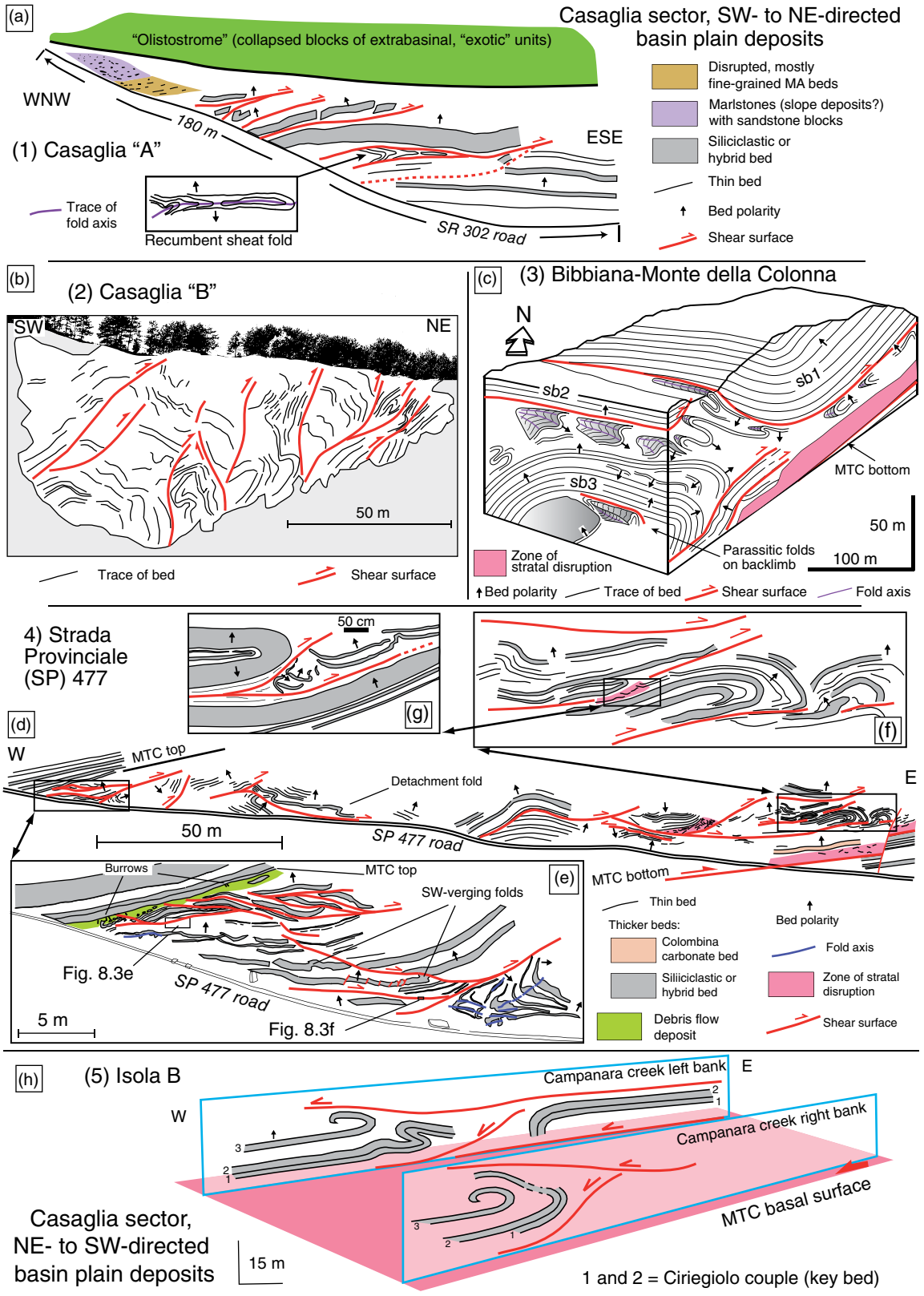


Figure 8.2 Line drawings of key outcrops in the Casaglia sector of the Casaglia-Monte della Colonna mass-transport complex. All the figures refer to the northeast directed basin plain deposits, except (h) illustrating the basal structures of the southwest directed part of the mass-transport complex. Numbers before the outcrop names refer to the locations in Figure 8.1f. (c) and (g) are from Lucente and Pini (2003), modified. (h) is from Lucente (2000), modified.

upside-down bed attitude. The contact between slide blocks and fold belts are abrupt, marked by millimeter-thick shear zones. Folds in slide blocks show a southwest to northeast transition, from a steeply inclined close fold (slide block 3) with associated parasitic folds (Figure 8.3c, d) to gentle folds (slide block 1) originated from accommodation of bed packages above listric normal faults. An interval of increasing stratal disruption with boudins and disrupted folds characterizes the basal part and accommodate the largest strain (Figure 8.2c).

The outcrop along the SP 477 road (outcrop 4, formerly known as SS 477 outcrop; Lucente & Pini, 2003) develops onto the upper flat. Normal faults already recognized in Lucente and Pini (2003) extend also in deeper parts of the MTC and have a down-flow continuation in faults parallel to beds and basal contact (flats) and in low-angle thrust cutting upsection (spoon-shaped faults; van der Merwe et al., 2011) (Figure 8.2d, e). Detachment folds develop above the flats and become recumbent, close to isoclinal folds in the thrust (Figure 8.2d, f, g).

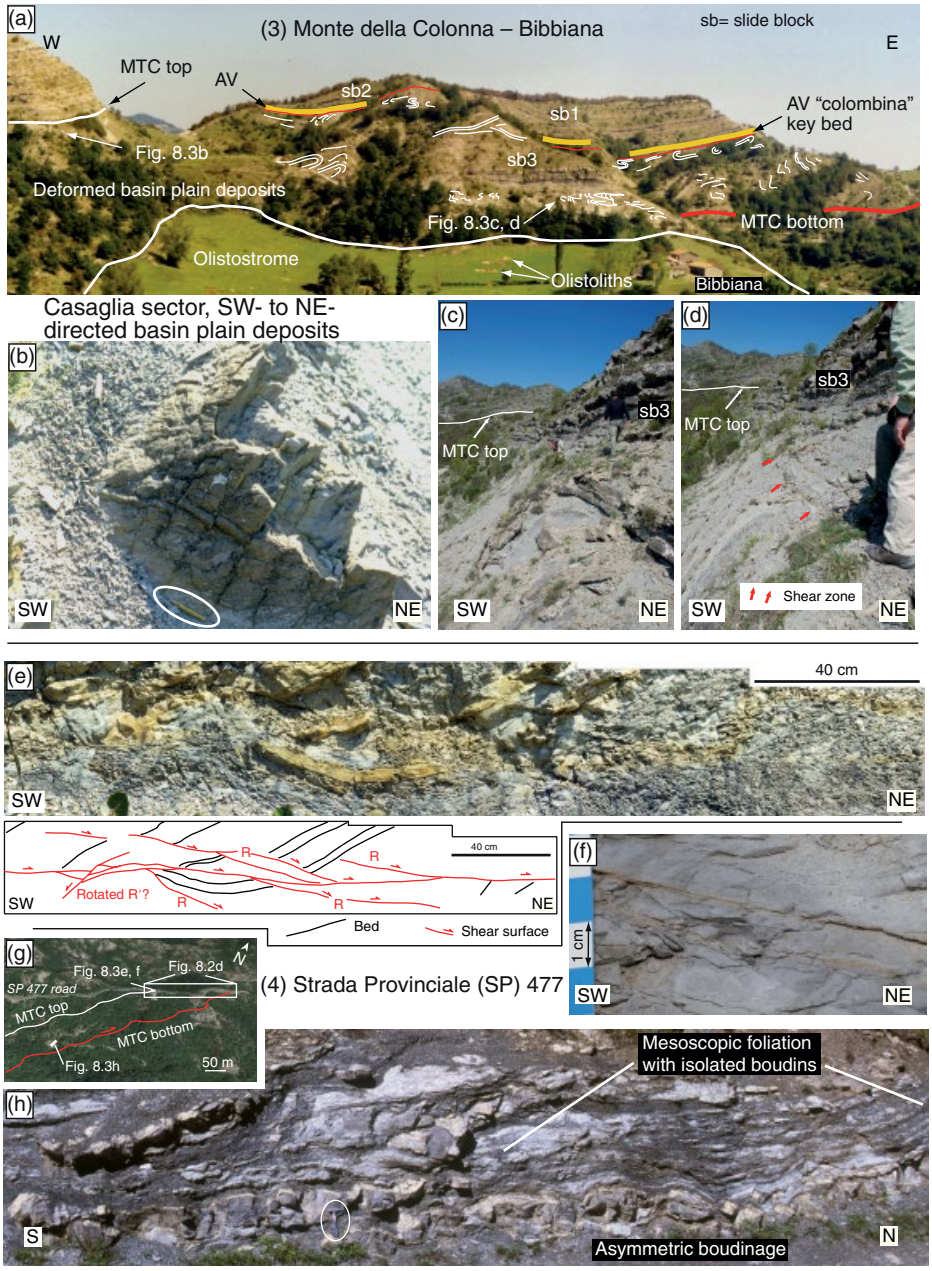


Figure 8.3 Photographs illustrating some key features of the deformed basin plain deposits of the Casaglia sector. Numbers before the outcrop names refer to the locations in Figure 8.1f. Line drawing in (a) is from Lucente and Pini (2003) modified. (c) and (d) show the parasitic folds on the backlimb of the upright fold constituting slide block 3.

Stratal disruption occurs when faults cut up the stratigraphic succession (Figure. 8.2g). Slide blocks are smaller than in the Bibbiana-Monte della Colonna outcrop, and some of them are upside down (Figure 8.2d). As already shown in Lucente and Pini (2003), the upper part of the MTC displays an array of horses (extensional duplex), which overlies a system of listric normal faults (Figure 8.2e). The normal faults crosscut an interval characterized by isolated slump folds and boudins dispersed in a finer-grained matrix (debrite), which corresponds to the last stage of MTC deposition (co-genetic debris flow). This suggests that the activity of normal faults extended after the CMC emplacement. Normal faults cut previous contractional features, such as asymmetric folds, testifying a first phase of southwestward translation (Figure 8.2e). Asymmetric domino-type boudinage (Etchecopar, 1977; Rodrigues & Pamplona, 2018) occurs in the lowest part of the MTC and laterally evolves in block-in-matrix features, showing clear mesoscopic foliation due to stretching of finer-grained beds (Figure 8.3h). Domino-type boudinage suggests a top to the NE movement in predominant simple shear regime, which is also coherent with the clockwise rotation and sigma-like structures affecting the separated boudins (Figure 8.3h).

8.3.2. The Southwest to Northeast Directed Basin Plain Deposits: Marradi Sector

Basin plain turbidites and hemipelagic beds prevail in the Marradi sector. Beds are thinner than in the Casaglia sector, often lacking the "b" interval (D_2 and D_3 of Mutti and Ricci Lucchi (1972, 1975)), which may suggest a provenance from more marginal (southwesterly?) position of the basin plain (Lucente, 2000). In the sector, the basal contact shows a constant flat attitude and corresponds to the more distal, spilling-over zone of the CMC, which reaches here its minimum thickness (20–10 m). The different outcrops share strong deformation caused by folding and symmetric, flattening-type, or asymmetric boudinage. Folds are developed at meters to tens of centimeters scale (Figures 8.4a–e, and 8.5a–g, l).

A general planar bed attitude, almost parallel to the basal contact, characterizes the Val del Calvo outcrops (10a-b in Figure 8.1f). Recumbent folds with limbs pinched and swelled in either symmetric or asymmetric (shear band type) style, deform the overall bedding (Figure 8.4a, b). Internal deformation (layer-parallel extension?) can increase, locally developing isolated boudins and rootless slump folds (Figure 8.4c). Although the general fold vergence is toward NE, counter-verging (southwest facing) folds systematically occur (Figure 8.4a, b). Low-angle normal faults cause bedding rotation and cleavage (Figure 8.4b).

In the Tramanzo outcrops (11a-b in Figure 8.1f), a complex system of superposed recumbent and often refolded folds, with contorted hinges and associated parasitic folds, dominate in the upper part of the body (Figure 8.5a, c). In the lower part, beds tend to be subparallel and appear deformed by small detachment folds (box folds and counter-vergent folds; Figures 8.4e and 8.5b). Fold limbs are thinned, but continuous, with few examples of flattening-type, pinch-and-swell boudinage and few isolated oblate boudins. Hinge zone thickening is observed in the largest majority of cases.

The Pian di Lorino outcrop (12 in Figure 8.1f) shows a peculiar style of progressive deformation of the bedding, implying a layer-parallel, flattening-type boudinage (pinch and swell), subsequently reworked into a stacking of blocks (Figure 8.5d, f), and a last folding stage (Figure 8.5d, e). Folds occur at a different scale (meter to tens of meters scale), with moderate to gently inclined axes (overfolds) and vergence toward NE (Figure 8.5d). Low-angle thrusts are also present (Figure 8.5d).

Listric faults (Figure 8.5g) characterizes the Rio Gamogna outcrop (13 in Figure 8.1f). They are characterized by cumulative displacement achieved by incremental movement along millimeter-thick shear zones (Figure 8.5k) and evolve down flow from normal faults to layer-parallel faults (detachments). This creates detachment folds in the hanging wall, cleavage, and pinch-and-swell, flattening-type boudinage of thin sandstone/siltstone beds (Figure 8.5g, h). Thicker beds are characterized by asymmetric domino-type boudinage (Figure 8.5i), suggesting a general simple shear deformation. Meter-scale undeformed blocks of thin-bedded turbidites occur at the top of the MTC (Figure 8.5g).

The Le Piane outcrops (14 in Figure 8.1f) displays large-scale, close to recumbent folds in the upper part, deforming both fine-grained and thick, coarse beds (Figure 8.5l). A clear axial plane cleavage occurs in thicker beds. Other similar beds in the same deformed bed packages appear involved in folds as isolated symmetric lenses due to layer-parallel boudinage.

8.3.3. Casaglia Sector, Central Zone: The North Verging Slope Deposits

Slope deposits are the exclusive component of the upper CMC body and show higher deformation than their basin plain counterpart show. The overall structural attitude is dominated by systems of gently dipping to recumbent folds, shear surfaces acting as normal faults, and pinch-and-swell, constriction-type boudinage of the coarser beds (Tc-e turbidites). Coarser beds (Tc-e, Td-e) appear deformed into strongly flattened, isolated folds, often coaxially refolded by progressive shear deformation (Farrell & Eaton, 1987). This produced non-cylindrical folds (true sheath folds have not observed) and spiral-like,

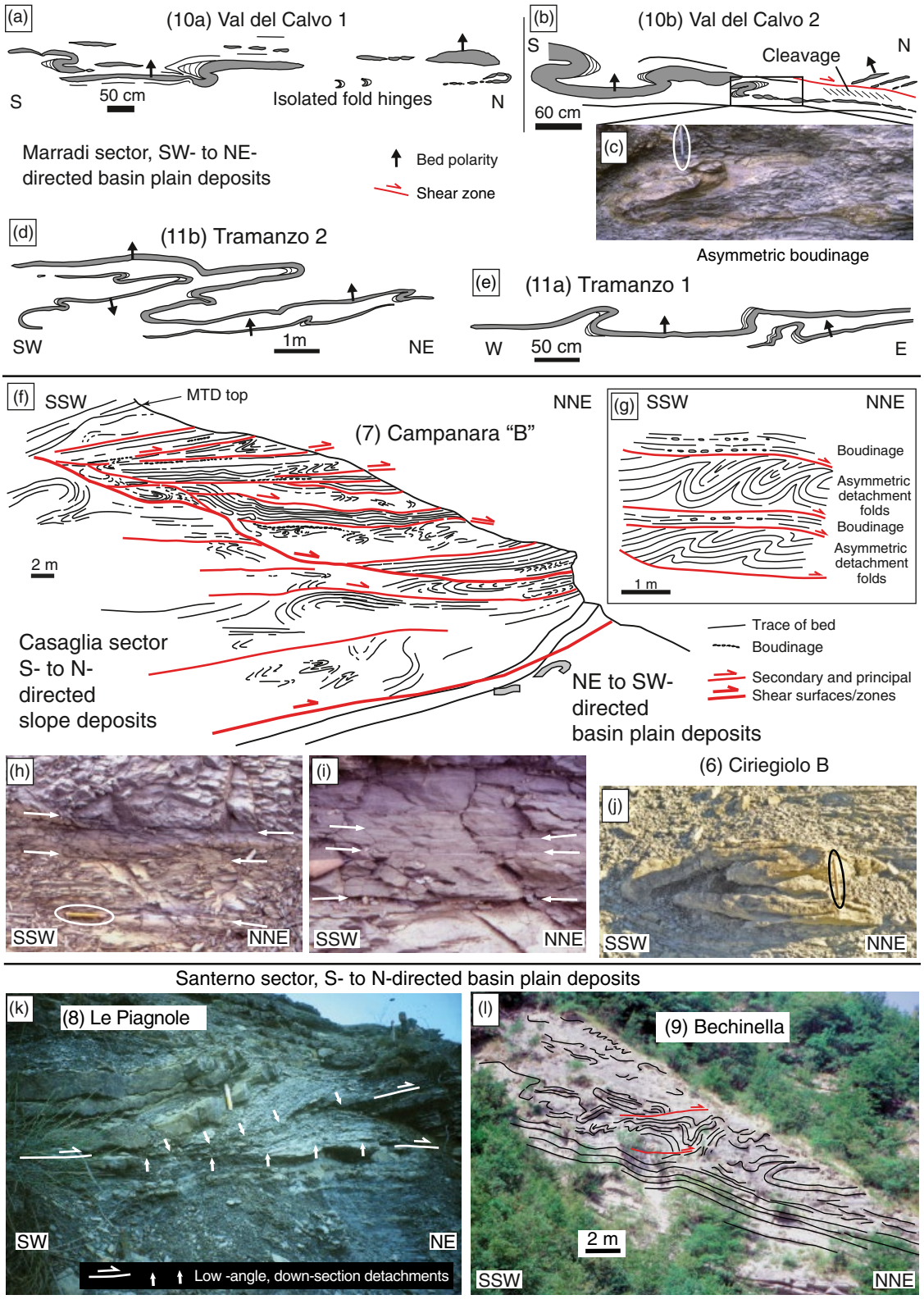


Figure 8.4 Photographs and line drawings showing key features of the deformed basin plain deposits in the Marradi sector (a–e), the deformed slope deposits in the Casaglia sector (f–j), and the deformed basin plain deposits in the Santerno sector (k and l). White arrows in (h) and (i) point out the shear surfaces associated with the listric principal shear zone of (f). Pen and pencils are for scale in (c, h, and J): pencil tip is for scale in (i). Numbers before the outcrop names refer to the locations in Figure 8.1f. (d–g) are from Lucente and Pini (2003), modified. (a) and (b) are from Lucente (2000), modified.

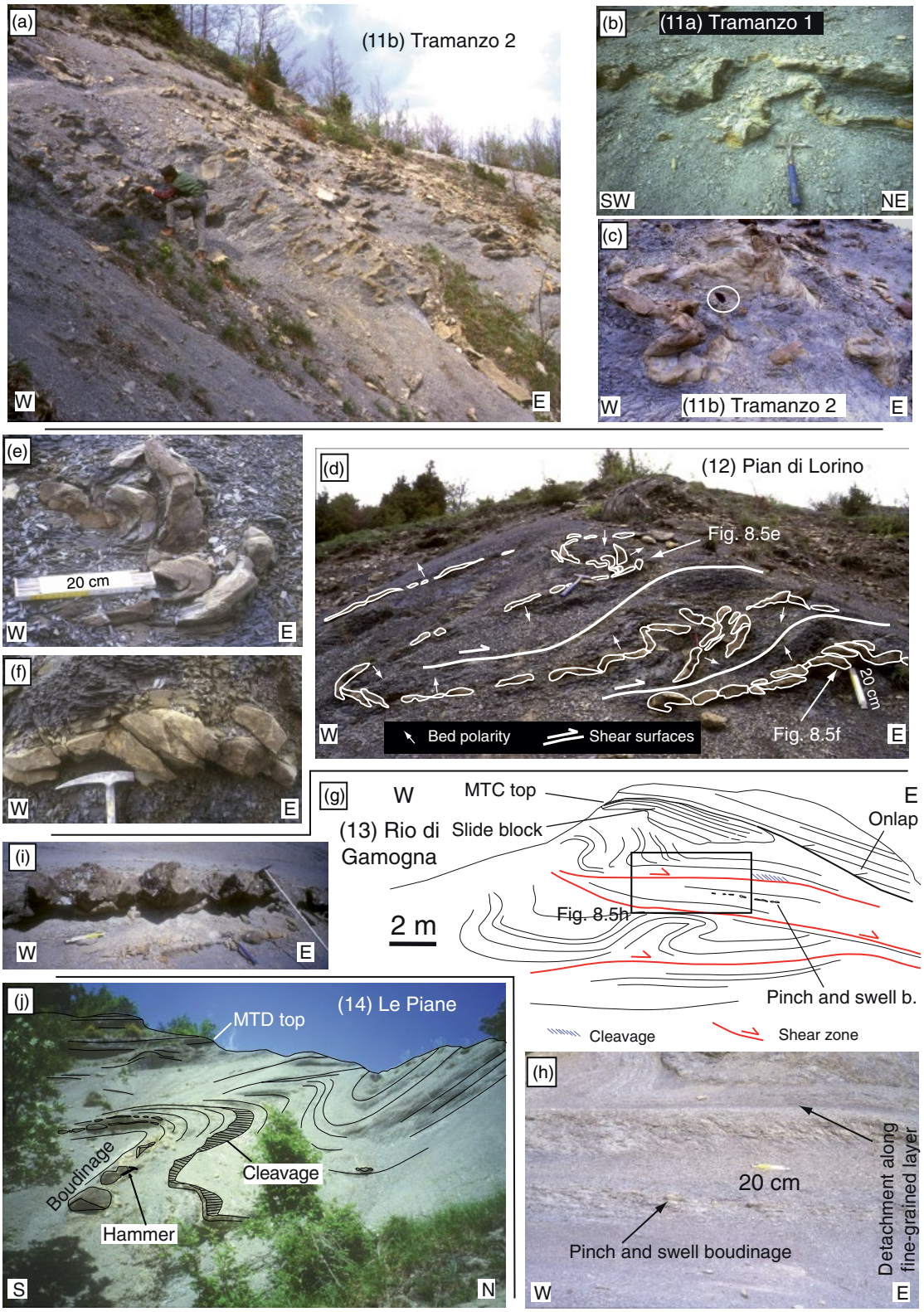


Figure 8.5 Photographs and line drawings showing key features of the northeast directed basin plain deposits of the Marradi sector. Numbers before the outcrop names refer to the locations in Figure 8.1f. Lens cap (6 cm in diameter) is for scale in (c). (g) and the line drawing on (j) are from Lucente (2000), modified.

axially refolded folds (Figure 8.4j) (Alsop & Marco, 2013). Strong layer-parallel extension often occurs as suggested by isolated boudins and rootless slump folds. The occurrence of reverse faults, triangle zones, and buckle folding of boudin trains also suggests local compression (Lucente, 2000).

The best exposed outcrop, the Campanara outcrop (outcrop 7 in Figure 8.1f; see Figure 8.4f), allows observations on a notably continuous shear surface arranged as a normal, listric major (master) fault, which connects smaller low-angle listric normal faults in the hanging wall (Figure 8.4f, g). These faults appear as shear surfaces/bands, systematically associated with trains of prolate-shaped boudins and asymmetric detachment folds, the axial surface of which is progressively rotated down flow (Figure 8.4f, g). In the footwall, shear surfaces/bands are less continuous and clear, the continuity of the beds is no greater than a few meters, and deformation is higher due to severe flattening-type (oblate) boudinage, asymmetric folds, and stacking of boudins. The deformation seems prevailingly associated with a certain amount of simple shear, which become greater in some parts of the body, causing dispersion of isolated boudins and fold hinges in a sand-silt matrix.

8.3.4. Casaglia Sector, Central Zone: The Southwest Verging Basin Plain Deposits

In this zone, the lower body of the CMC comprises basin plain deposits similar to the ones described before for the easternmost zone (mainly D_1, D_2, and D_3 of Mutti and Ricci Lucchi (1972, 75)). Sense of transport constantly shows a northeast to southwest direction, and the general organization of the body, from bottom to top, implies three to four meters of concentrated deformation with asymmetric domino-like boudinage and isolated fold hinges, followed by meter-scale recumbent folds with thinned and disrupted overturned limbs.

The strong basal interaction with the substratum in this area is testified by a scour ripping up the Ciriegiolo key beds (west of section B in Figure 8.1f). The Isola outcrop displays the down-flow, layer-parallel displacement of a 10 m thick bed package comprising the Ciriegiolo key beds (beds 1 and 2 in Figure 8.2h) along a weaker, thin-bedded, and fine-grained interval (see, e.g., Butler & McCaffrey, 2010). Two detachment folds occur above the layer-parallel detachment surface exposed along the left bank of the creek. The shearing related to the mass transport above caused spiral-like (re)folding of the detached beds (Figure 8.2h).

8.3.5. Santerno Sector: The North Verging Basin Plain Deposits

A low-angle ramp characterizes this zone showing an average cutoff angle of less than 1°. In the Le Piagnole locality, the top part of the MTC shows shear surfaces displacing beds in a downsection direction (Figure 8.4k), transitioning down flow in spoon-shaped faults. Pinch-and-swell, constriction-type boudinage and cleavage occur near fault surfaces. Isolated boudins made up of thinner beds occur when strain increases and are locally subject to north verging stacking. Meter-scale folds deform beds that have been previously boudinaged as described for the other outcrops.

The Bechinella outcrop shows gently dipping overfolded to recumbent synclines, with strongly flattened anticlinal counterparts (Figure 8.4l), representing detachment folds originated from the main basal contact and two shear surfaces (thrusts). Folds become progressively more asymmetric down flow and recumbent to isoclinal in the median part of the outcrop. Basal contact has a staircase shape, with a low-angle ramp overlaid by ripped up and stacked chunks of beds. Trains of smaller-scale recumbent folds characterize the middle-upper part, depicting a progressive decrease in bed continuity upward and down flow.

8.4. SHEAR ZONES

Discrete shear zone or surfaces accommodate differential movements of slide blocks and detached bed packages, displacement along listric normal faults, thrust, and at the base of detachment fold trains. They do not show brittle/frictional features such as striations, mineral recrystallizations (slikenfibers), or mesoscopic evidence of cataclasis, showing instead the following features:

1. Thin (around 1–5 cm thick) silty-clayey beds represent the décollement surfaces that enable the onset of detachment folds, as evidenced in the displaced slope deposits of the Casaglia sector (Figure 8.5h);

2. Mechanical discontinuities (e.g., fault surfaces) cutting and offsetting beds and bed packages (Figures 8.3e, f and 8.4h), which can be outlined either by a thin (<1 mm) layer of less cemented silt, finer than the host rocks (Figure 8.4i), or by sand grains coarser than the host rocks (Figure 8.3f). The latter are usually dispersed along fault surfaces according to the sense of movement, but clearly originate from disaggregated sandstone beds.

These fault surfaces never occur as isolated features; smaller subsidiary surfaces usually branch/splay out from the larger one. A typical example is the normal faults of the extensional duplex system exposed in the SP 477 outcrop (Figure 8.3e), which are locally complicated by secondary fault surfaces corresponding to R planes (low-angle, synthetic Riedel planes of Riedel (1929)). Both R and P planes (P or thrust planes; see Skempton, 1966) characterize other outcrops of the CMC, such as the Campanara one (see Section 8.3.3).

Mesoscopic ductile faults are common structures related to shallow level deformation in accretionary prisms and slides (see Hanamura & Ogawa, 1993; Maltman, 1988; Yamamoto et al., 2005, 2009) and have been related to a mechanism of independent granular flow, with rotation and translation of grain, enabled by low effective confining stress and fluid overpressure (Ogata et al., 2014a). A similar mechanism may be sustained here, as suggested by dedicated preliminary study performed on oriented samples of fault surfaces collected in the Bibbiana area (Dykstra, 2005).

These mesoscopic ductile faults represent the surfaces along which the differential movement of the slide blocks took place. A direct linkage with detachment and recumbent folds, boudinage (see the examples of the Campanara outcrop), and boudin stacking is clear. These features appear to be contemporaneous with all the phases of internal deformation and do not seem to characterize just the later stages as suggested by Martinsen and Bakken (1990).

8.5. DOMAINS OF INTERNAL DEFORMATION

The geometric attitude of the basal contact strongly influences the internal structures, since the distribution of zones with a similar deformation style (deformational domains [DD]; Figure 8.6a) follows local changes in the basal contact angle. The high-angle ramp in the Casaglia area corresponds to the DD-8 (Figure 8.6a), characterized by stacking and folding of thrust sheets originated in the lower flat (translation zone, DD-9), and to the development of secondary fold trains. Lucente and Pini (2003) highlighted the role of the emplacement of the extrabasinal component (olistostromes) in further remobilizing, dragging, and (re)accumulating the intrabasinal component, which is in turn arranged into folded by the antiformal thrust stack. High local compression originated here an intense fluid expulsion and elutriation and the onset of chemosynthetic communities after the CMC emplacement (Lucente & Taviani, 2005).

The edge of the extrusion zone, represented by the transition from ramp to low-angle ramp, corresponds to a change in structural style from a system of upright folds (DD-7) to spoon-shaped listric faults associated with gently inclined to recumbent folds (DD-6) (Figure 8.6b). Folds are organized in a continuous belt bounded by slide blocks with their axial surfaces following the belt boundaries (Figures 8.2c and 8.6b). Folds often have their forelimbs more extended or are completely overturned (label d in Figure 8.6b). Due to their geometry, folds can originate from (a) entire fold trains translated from deeper zones (ramp zone), (b) parasitic fold detached from bedded slide blocks along shear zones (see Figure 8.3c–d), and (c) erosion by shear of the base of slide blocks during their down-flow movement (see a, b, and c labels in Figure 8.6b).

The upper flat above the Ciriegiolo horizon (subsector b in Figure 8.1b) shows again undeformed slide blocks separated by shear zones and spoon-shaped faults, which make up the thickest part of the MTC, having only a thin shear zone (up to some meters thick) at the base (DD-5). In comparison with the Bibbiana-Monte della Colonna area (DD-6), however, the thickness of bedded slide blocks and fault-bounded bed packages is reduced; thus the number of faults inside the body is higher and the fold belt is lacking. Typically, faults are associated with intense stratal deformation, with the development of sigmoidal structures, asymmetric domino-type boudinage (Figure 8.2e), and detachment folds. The axial surfaces of such folds are progressively rotated to horizontal (recumbent folds) at the fault tips or at the ramps. Here the forelimbs are subject to strong flattening and elisions. In places (Figure 8.6c), recumbent folds become isoclinal due to the loading exerted by overlying slide blocks (Figures 8.2f–g). Zones of localized stratal disruption occur at the front of advancing isoclinal folds (Figure 8.2g) with development of parasitic folding, boudinage, and boudin stacking (Lucente & Pini, 2003).

The basal zone of concentrated deformation is evident between Bibbiana-Monte della Colonna (outcrop 3 in Figure 8.1f and DD-6 in Figure 8.6a) and SP 477 outcrop (outcrop 4 and DD-5). It is related to prevailing simple shear deformation recorded by pervasive isoclinal folding and asymmetric boudinage of either domino or shear band types, causing stretching of less competent beds and separation of blocks (isolated boudins) (Etchecopar, 1977; Rodrigues & Pamplona, 2018; Swanson, 1992).

In the domain DD-3, the deformation is severely partitioned in the slope sediments, as in the emblematic case of the Campanara (outcrop 7 in Figure 8.1f; see Figure 8.4a–c). Here a normal listric fault bounds a more organized upper limb (hanging wall), with normal faults separating folded bed packages, and a more stratally disrupted and generally deformed footwall. Extension prevails in the hanging wall, while the footwall shows evidence of a prevailing simple shear related deformation, with greater stratal disruption due to severe boudinage, folding, and stacking of blocks. The marked difference between the hanging wall and footwall suggests that the main listric fault represents the boundary and gliding plane between a translated slide block (floater) and the more deformed and mobile substrate.

DD-4 domain displays an internal strain partitioning similar to the other parts of the CMC that moved above the upper flat onto the Ciriegiolo key bed (DD-5) and the more internal low-angle ramp (DD-6). Meter-scale folds deforming prevailingly continuous beds overlap a basal shear zone of concentrated stratal disruption. The main difference stands in the direction of movement, opposed to the main body of CMC, and the presence of a kilometer-sized scour ripping up the Ciriegiolo key beds.

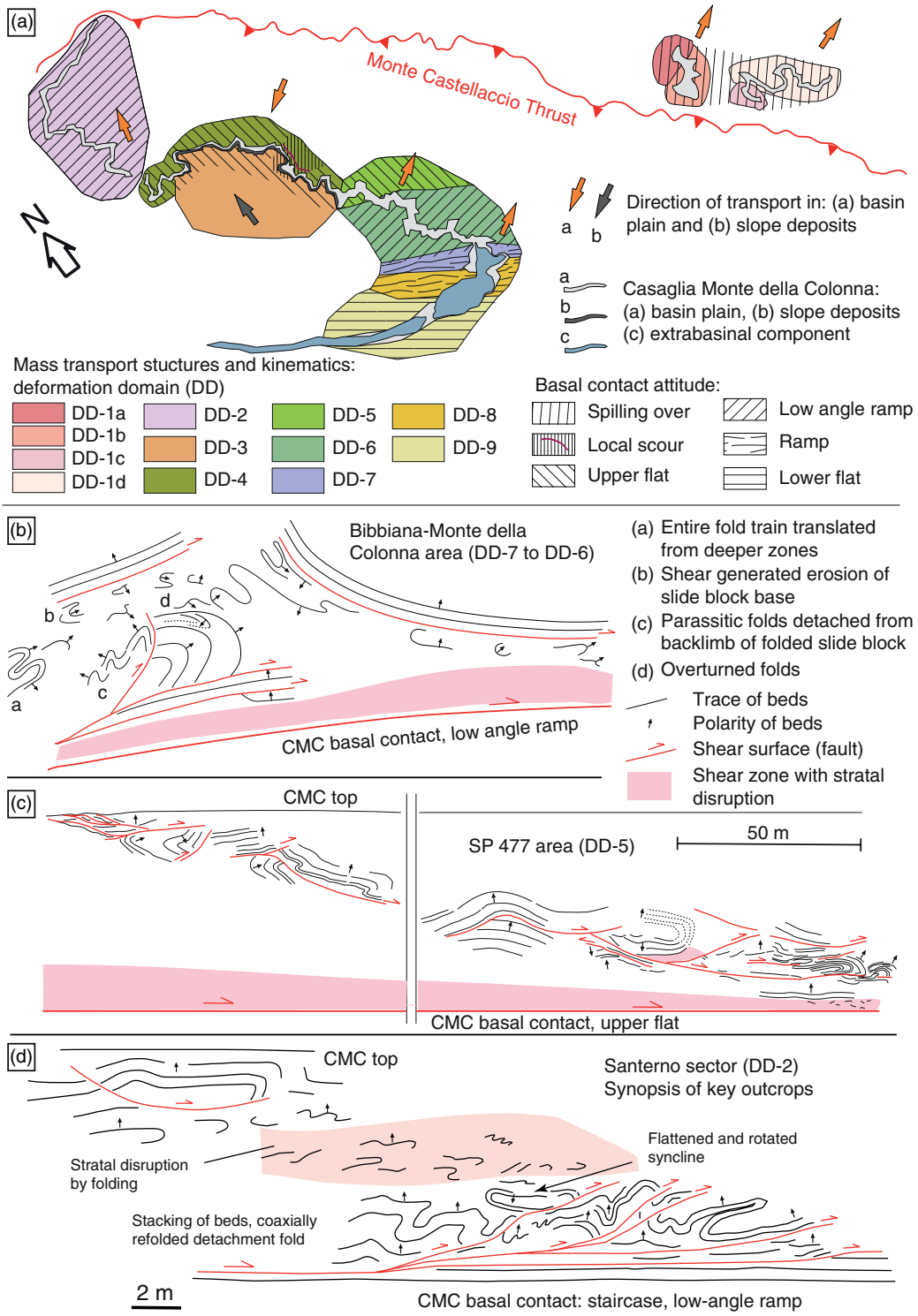


Figure 8.6 (a) Distribution of the domains characterized by similar deformation style and features versus attitude of basal contact in the Casaglia-Monte della Colonna mass-transport complex. (b–d) interpretative, synoptic diagrams based on key outcrops.

The deformation scenario in the Santerno sector (DD-2; Figure 8.6d) differs from the two previous zones, since detachment folds originated from the basal contact and stacking of ripped up beds (Figure 8.4f) replaces the stratally disrupted shear zone. Close and upright detachment folds evolve down flow into gently inclined, asymmetric tight folds. A progressive flattening and disruption of fold limbs occurs upsection, causing the development of recumbent isoclinal folds, isolated or arranged in smaller systems. Spoonlike faults and undeformed, bedded slide blocks characterize the upper part. Bed packages bounded by spoonlike faults and slide blocks are thinner than the other isopic zones.

Trains of recumbent folds with planar curvilinear axes deform the thinner beds of Marradi sector (DD-1a, DD-1b, DD-1c, DD-1d) in association with curved shear zones and cleavage. A generalized stretching of fold limbs couples with a pronounced thickening of hinges. The upper part of the body hosts meter-scale slide blocks (floaters) deformed by listric normal faults and meter-scale folds acting on either undeformed or symmetrically boudinaged beds

Style of deformation changes according to the different subdomains: in DD-1a (exemplified by outcrops 10a-b), stretching of fold limbs often results in symmetric and asymmetric pinch-and-swell boudinage, reaching extreme extension within narrow belts of aligned isolated boudins and rootless slump folds. Boudinage style suggests both pure (flattening of beds) and simple shear (sub-simple shear; Fossen & Cavalcante, 2017). Subdomain DD1b (outcrops 11a-b) shows a lower part with packages of almost continuous beds, relatively poorly deformed by small-scale detachment folds (Figure 8.5e), which dip at low angle to the basal surface of CMC. The upper part shows a more complex system of stacked recumbent folds with contorted hinges and limbs (Figure 8.5b–d). The latter are much more continuous than in DD-1a. Meter-scale, close to tight asymmetric folds deforming stacked boudins characterize the subdomain DD-1c (outcrop 12). This suggests a regime of protracted, progressive deformation in which simple shear dominated flow overprints flattening-type extension (oblate pinch-and-swell boudinage), causing subsequent stacking of boudins and, then, folding.

Counter-verging (southwestward) folds and box folds are common features in these subdomains, being particularly abundant in subdomain DD-1b. They have been tentatively interpreted as related to a frontal confinement due to intrabasinal highs or deceleration of the leading edge of MTC due to deposition-emplacement (see Lucente & Pini, 2003).

The subdomain DD-1d (outcrops 13 and 14) represents the upper part of the MTC, hosting slide blocks of undeformed bedded sequences bounded by and meter-scale folds deforming both continuous and symmetrically boudinaged beds. Listric normal faults are responsible for slide block movement.

Deformation in subdomains DD-1a to DD-1d originates by flattening and simple shear acting concomitantly (sub-simple shear), and often in superposition, throughout the MTC. Although more evident in subdomain DD-1c, this alternation of extension and compression is documented in all the subdomains, as already described by Lucente and Pini (2002). Internal pulses or "waves" of differential decreasing/increasing translation velocity may explain this behavior.

Flattening structures (pure shear) together with simple shear suggest a certain amount of lateral spreading, compatible with a condition of spilling/spreading of remobilized sediments over the basin floor. In the same way, strong bed extension developed in more continuous beds (from DD-1b to DD-1a) may represent local increase in lateral spreading. This interpretation is supported by the position of these extended zones, fitting well with the flat basal surface and the distal position, but is not completely compatible with the coexisting buckling effects (box folds and counter-vergencies) observed in subdomains DD-1a, DD-1b, and DD-1c. Spreading might represent a stage of free extension of the remobilized sediments, overprinted and/or alternated with generalized simple shearing due to faster/slower advance of the upper part of the MTC. Buckling might originate during the last stages of deceleration and emplacement of the CMC slide mass.

Poorly deformed, detached bed packages and coherent, meters to ten of meter-scale folds are present atop the MTC in the more easterly, distal subdomain (DD-1d). They occur above the most deformed parts representing the most external slide blocks.

8.6. ORIGIN OF THE DISPLACED INTRABASINAL SEDIMENTS AND MECHANISM OF TRANSLATION

The intrabasinal beds involved in the Casaglia-Monte della Colonna MTC are the same found in the underlying stratigraphic section (substratum). The displaced sediments in the deformation domains from DD-8 to DD-5 derive from the stratigraphic succession below the CMC basal contact, as directly suggested by the presence of AV and MV key beds in more MTC outcrops (Lucente, 2000) (see, e.g., Figure 8.3a). Here the translation of the MTC materials occurs by extrusion from the ramp and confined spilling over with prolate-type extension. Simple shear is present and overprint (or alternate) with extension, in an overall progressive fashion. Prevalence of simple shear on extension characterizes the lowest part of the body (the always present basal shear zone) or fold belts, and stratal disruption zones originated by the

relative movement of large slide blocks. The differential independent movement of slide blocks and detached bed packages along spoon-shaped shear surfaces enables a flow-type mobility for the largest part of the MTC. Internal deformation progressively increases in slide blocks and detached bed packages down flow (compare Bibbiana-Monte della Colonna and SP 477 outcrops), causing a more diffuse folding and the onset of systems of internal faults (Figures 8.2d, f, g, and 8.6c). This ultimately causes the decrease in size of slide blocks and bed packages. Folds progressively tightened in recumbent isoclinal folds.

A source of the counter-verging basin plain deposits above the upper flat (DD-4) cannot be directly recognized, since the likely related ramp has been eroded. Sediments involved in this branch of CMC are basin plain deposits very similar to those exposed below the MTC. A direct provenance form the local substratum with a short transport and the in situ deformation of the substratum is observable in the scour zone, but the style of deformation in the rest of the CMC recalls the ones observed in the other northeasterly sectors (DD-8–DD-5), suggesting a protracted translation and a more distal provenance.

An unsolved point is the nature of the contact between the northeast and southwest moving masses (DD-5 and DD-4) above the same layer (Ciriegiolo key bed), particularly because of the unfavorable outcrop conditions in this key area.

Concerning the slope sediments of domain DD-3, the deflection due to the already spilled-over, northeast moving basin plain sediments (DD-7–DD-5) can be the reason for the northward direction of movement. The preserved continuity of beds and the strong internal organization of listric normal fault systems inside the large slide block in the upper part of the MTC are possibly inherited structures associated with the initial stage of slope failure. This hypothesis may explain the strong contrast with the much more deformed and disrupted lower part, which is a more common style of internal deformation in the CMC, and the marked difference between this slide block and the other ones observed.

In the Marradi sector, the CMC shows internal beds similar to the underlying section, but the flat attitude of substratum and the flattening-type extension associated with simple shear seem to favor the hypothesis of lateral and frontal spreading in a non-confined spilling-over zone. Such beds cannot derive from the ramp zones because the sedimentary facies does not correspond. A provenance from a more proximal area located southward of the translation-extrusion zone is also not plausible because the obstacle of the masses extruded from the ramp. In this framework, they might derive from an intermediate part, now not preserved because of the shortening exerted by the Monte Castellaccio thrust and subsequent erosion. These deposits should have been dragged by northeastward movement of basin plain deposits. The stacked, poorly deformed beds at the base of MTC in DD-1c may correspond to eroded portion of substratum related to this mechanism and translated down flow.

The Santerno sector represents a low-angle ramp with the basal contact progressively rising from the Ciriegiolo key beds up to 10 m above. The basal contact shows a staircase attitude with longer flat zones alternated to small ramp that cut, translate, and stack few beds (Figure 8.6d). Composition and facies of involved basin plain sediments correspond to those of the Casaglia sector and the ones in the same Santerno sector. The style of folds and their upward progressive disruption upward support a mechanism of inclusion of substrate for the lower part, while the upper component (bed packages involved in folds and spoonlike faults) can originate from more southerly or southwesterly areas. Following this hypothesis, the direction of movement can be compatible with a provenance from failures southwest of the Casaglia sector and the deflection of the displaced sediments along the direction of the basin due to the obstacle of the masses already extruded (paleo-bathymetry) in the Casaglia-Bibbiana area (see Lucente & Pini, 2003). A provenience from a closer, independent southwesterly source, thus placed northwestward of Casaglia sector, is an alternative hypothesis (Lucente, 2004).

It is worthy to note that the internal style of the CMC in the Santerno sector recalls the general organization observed in the Marradi sector, with bed packages detached from substratum and passing upward to trains of folds and higher disruption of beds, and the absence of the consistent basal shear zone typical of other sectors. Movement along faults is important in the slope deposits and in the Bibbiana to SS 477 outcrops, being less important in the Marradi and Santerno sectors where slump-like structure dominate. This similitude is not striking, however, since Santerno sector CMC lacks the flattening-type boudinage and shows the unique feature of detachment folds ripped up from the substratum (Figure 8.6d). This sector is more compatible with a depositionally confined type of MTC and not a spilling-over one (Ogata et al., 2012a).

8.7. CONCLUDING REMARKS

The Casaglia-Monte della Colonna body represents one of the best and continuously exposed "fossil" MTC in foredeep succession exhumed in a mountain chain. This allows the unique opportunity to study the internal

architecture of a submarine landslide complex resulting from the (geologically) simultaneous collapses of the accretionary wedge front (Ligurian Nappe derived extrabasinal), slope, and basin plain deposits (see Lucente & Pini, 2008). The different angles of the basal contact on the substratum cause changes in flow mechanics, internal structures, and deformational regime (stretching vs. flattening vs. simple shear).

After 20 years from the pioneering work of Lucente (2000), we better understood the internal structures and substrate-MTC interactions in the lower flat and in the ramp of the Casaglia zone (Casaglia A and B outcrops) and in the Santerno sector. The latter was not interpreted in detail before. We also presented materials that were not easily available to an international audience (Lucente, 2000, 2002), as in the case of the southwest translated basin plain deposits of the Isola sector. We also propose a new interpretative scheme according to the areal distribution of the internal deformation features linked to geometry of the MTC base.

Nonetheless, some open problems remain, for instance, the characterization of the mechanisms preconditioning and triggering the wedge-slop-basin plain failure. In previous work, we suggested the onset and failure of a temporary slope (following Ricci Lucchi (1978)) and the contemporaneous collapse of the slope and front of the wedge due to retrogressive failure. The CMC and the other bodies containing Ligurian Nappe derived materials, slope, and basin plain deposits (Visignano, Nasseto and Le Caselle MTCs, Landuzzi, 2005; Lucente, 2004; Lucente & Pini, 2003) suggest that the instability of the entire frontal system of the wedge-slope-basin plain repeatedly occurred in the inner stage of Marnoso-arenacea foredeep. The Nasseto and CMC units pertain to the same stratigraphic horizon, being constrained by the same regional-scale key beds (Lucente, 2000, 2004; Lucente & Pini, 2003), suggesting that basin-wide instability occurred.

ACKNOWLEDGMENTS

We are indebted to Franco Ricci Lucchi, who has been the co-supervisor of the C.C. Lucente PhD thesis, from which all this initiated. The comments and observations of Yujiro Ogawa and Yuzuru Yamamoto greatly improved the manuscript. This work has been realized with the support by research grants from the Italian Ministry of University and Research (PRIN 2003 n. 2003040755_006, PRIN 2010/2011 "GEOPROB [Geodynamic Processes of Oceanic Basins]," n. 2010AZR98L_002), the Università di Bologna (RFO 2007-2012 and "ex60%" 1998–2006), and the Università di Trieste (FRA 2013).

REFERENCES

Alonso, J. L., Marcos, A., & Suárez, A. (2006). Structure and organization of the Porma mélange: progressive denudation of a submarine nappe toe by gravitational collapse. *American Journal of Science*, *306*, 32–65. https://doi.org/10.2475/ajs.306.1.32

Alsop, G. I., & Marco, S. (2013). Seismogenic slump folds formed by gravity-driven tectonics down a negligible subaqueous slope. *Tectonophysics*, *605*, 48–69. https://doi.org/10.1016/j.tecto.2013.04.004

Alves, T. M. (2015). Submarine slide blocks and associated soft-sediment deformation in deep-water basins: A review. *Marine and Petroleum Geology*, *67*, 262–285. https://doi.org/10.1016/j.marpetgeo.2015.05.010

Alves, T. M., & Lourenço, S. D. N. (2010). Geomorphologic features related to gravitational collapse: Submarine landsliding to lateral spreading on a Late Miocene–Quaternary slope (SE Crete, eastern Mediterranean). *Geomorphology*, *123*, 13–33. https://doi.org/10.1016/j.geomorph.2010.04.030

Amy, L. A., & Talling, P. J. (2006). Anatomy of turbidites and linked debrites based on long distance (120-30 km) bed correlation, Marnoso-arenacea Formation, Northern Apennines, Italy. *Sedimentology*, *53*, 161–212. https://doi.org/10.1111/j.1365-3091.2005.00756.x

Argnani, A. (2002). The Northern Apennines and the kinematics of Africa–Europe convergence. *Bollettino della Società Geologica Italiana*, Vol. Speciale n. 1, 47–60.

Argnani, A. (2012). Plate motion and the evolution of Alpine Corsica and Northern Apennines. *Tectonophysics*, *579*, 207–219. https://doi.org/10.1016/j.tecto.2012.06.010

Barchi, M., Landuzzi, A., Minelli, G., & Pialli, G. (2001). Outer northern Apennines. In G. B. Vai & I. P. Martini (Eds.), *Anatomy of an Orogen: The Apennines and adjacent Mediterranean basins* (pp. 215–254). Dordrecht, The Netherlands: Kluwer Academic. https://doi.org/10.1007/978-94-015-9829-3_15

Bistacchi, A., Balsamo, F., Storti, F., Mozafari, M., Swennen, R., Solum, J., et al. (2015). Photogrammetric digital outcrop reconstruction, visualization with textured surfaces, and three-dimensional structural analysis and modeling: Innovative methodologies applied to fault-related dolomitization (Vajont Limestone, Southern Alps, Italy). *Geosphere*, *11*(6), 2031–2048. https://doi.org/10.1130/GES01005.1

Boccaletti, M., Ciaranfi, N., Cosentino, D., Deiana, G., Gelati, R., Lentini, F., et al. (1990). Palinspastic restoration and paleogeographic reconstruction of the peri-Tyrrhenian area during the Neogene. *Palaeogeography, Palaeoclimatology, Palaeoecology*, *77*(1), 41–50. https://doi.org/10.1016/0031-0182(90)90097-Q

Boccaletti, M., Coli, M., Decandia, F. A., Giannini, E., & Lazzarotto, A. (1980). *Evoluzione dell'Appennino settentrionale secondo un nuovo modello strutturale* (Vol. 21, pp. 359–373). *Memorie della Società Geologica Italiana*.

Boccaletti, M., Corti, G., & Martelli, L. (2011). Recent and active tectonics of the external zone of the Northern Apennines (Italy). *International Journal of Earth Sciences*, *100*(6), 1331–1348. https://doi.org/10.1007/s00531-010-0545-y

Boccaletti, M., Elter, P., & Guazzone, G. (1971). Plate tectonic models for the development of the Western Alps and Northern Apennines. *Nature Physical Sciences*, *234*(49), 108–111. https://doi.org/10.1038/physci234108a0

Bonini, L., Toscani, G., & Seno, S. (2014). Three-dimensional segmentation and different rupture behaviour during the 2012 Emilia seismic sequence (Northern Italy). *Tectonophysics*, *630*, 33–42. https://doi.org/10.1016/j.tecto.2014.05.006

Bonini, M. (2006). Detachment folding–related Miocene submarine slope instability in the Romagna Apennines (Italy). *Journal of Geophysical Research*, *111*, B01404. https://doi.org/10.1029/2004JB003552

Bonini, M., Corti, G., Delle Donne, D., Sani, F., Piccardi, L., Vannucci, G., et al. (2016). Seismic sources and stress transfer interaction among axial normal faults and external thrust fronts in the Northern Apennines (Italy): A working hypothesis based on the 1916–1920 time–space cluster of earthquakes. *Tectonophysics*, *680*, 67–89. https://doi.org/10.1016/j.tecto.2016.04.045

Bortolotti, V., Principi, G., & Treves, B. (2001). Ophiolites, Ligurides and the tectonic evolution from spreading to convergence of a Mesozoic Western Tethys segment. In G. B. Vai & I. P. Martini (Eds.), *Anatomy of an Orogen: The Apennines and adjacent Mediterranean basins* (pp. 151–164). Dordrecht, The Netherlands: Kluwer Academic. https://doi.org/10.1007/978-94-015-9829-3_11

Burg, J.-P., Bernoulli, D., Smit, J., Dolati, A., & Bahroudi, A. (2008). A giant catastrophic mud-and-debris flow in the Miocene Makran. *Terra Nova*, *20*, 188–193. https://doi.org/10.1111/j.1365-3121.2008.00804.x

Butler, R. W. H., & McCaffrey, W. D. (2010). Structural evolution and sediment entrainment in mass-transport complexes: outcrop studies from Italy. *Journal of the Geological Society*, *167*, 617–631. https://doi.org/10.1144/0016-76492009-041

Camerlenghi, A., & Pini, G. A. (2009). Mud volcanoes, olistostromes and Argille scagliose in the Mediterranean region. *Sedimentology*, *56*, 319–365. https://doi.org/10.1111/j.1365-3091.2008.01016.x

Capozzi, R., Landuzzi, A., Negri, A., & Vai, G. B. (1991). Stili deformativi ed evoluzione tettonica della successione Neogenica Romagnola. In G. Pialli, M. Barchi, & M. Menichetti (Eds.), *Studi preliminari all'acquisizione dati del profilo CROP 03, Punta Ala-Gabicce, Studi Geologici Camerti* (Vol. 1991/1, pp. 261–278). Camerino: Università degli Studi di Camerino.

Carmignani, L., Conti, P., Cornamusini, G., & Meccheri, M. (2004). The internal Northern Apennines, the Northern Tyrrhenian Sea and the Sardinia-Corsica block. In U. Crescenti, S. D'offizi, S. Merlino, & L. Sacchi (Eds.), *Geology of Italy: Special volume of the Italian Geological Society for the IGC 32 Florence-2004* (pp. 59–77). Roma: Società Geologica Italiana.

Carmignani, L., Decandia, F. A., Disperati, L., Fantozzi, P. L., Kligfield, R., Lazzarotto, A., et al. (2001). Inner Northern Apennines. In G. B. Vai & I. P. Martini (Eds.), *Anatomy of an Orogen: The Apennines and adjacent Mediterranean basins* (pp. 197–214). Dordrecht, The Netherlands: Kluwer Academic. https://doi.org/10.1007/978-94-015-9829-3_14

Carmignani, L., Decandia, F. A., Fantozzi, P. L., Lazzarotto, A., Liotta, D., & Meccheri, M. (1994). Tertiary extensional tectonics in Tuscany (Northern Apennines, Italy). *Tectonophysics*, *238*, 295–315. https://doi.org/10.1016/0040-1951(94)90061-2

Carminati, E., Doglioni, C., Gelabert, G., Panza, G. F., Raykova, R. B., Roca, E., et al. (2012). Evolution of the Western Mediterranean. In D. G. Roberts & A. W. Bally (Eds.), *Regional geology and tectonics: Phanerozoic passive margins, cratonic basins and global tectonic maps* (pp. 436–470). Amsterdam, The Netherlands: Elsevier Science. https://doi.org/10.1016/C2010-0-67672-3

Castellarin, A., Cantelli, L., Fesce, A. M., Mercier, J. P., Picotti, V., Pini, G. A., et al. (1992). Alpine compressional tectonics in the Southern Alps. Relations with the N-Apennines. *Annales Tectonicae*, *6*, 62–94.

Cerrina Feroni, A., Ottria, G., & Ellero, A. (2004). The Northern Apennine, Italy: Geological structure and transpressive evolution. In U. Crescenti, S. D'offizi, S. Merlino, & L. Sacchi (Eds.), *Geology of Italy: Special volume of the Italian Geological Society for the IGC 32 Florence-2004* (pp. 15–32). Roma: Società Geologica Italiana.

Cerrina Feroni, A., Ottria, G., Martinelli, P., & Martelli, L. (2002). *Structural geological map of the Emilia-Romagna Apennines,1:250,000 scale map and explanatory notes*. Firenze: SELCA.

Collettini, C., De Paola, N., Holdsworth, R. E., & Barchi, M. R. (2006). The development and behaviour of low-angle normal faults during Cenozoic asymmetric extension in the Northern Apennines, Italy. *Journal of Structural Geology*, *28*(2), 333–352. https://doi.org/10.1016/j.jsg.2005.10.003

Cowan, D. S. (1985). Structural styles in Mesozoic and Cenozoic mélanges in the western Cordillera of North America. *Geological Society of America Bulletin*, *96*, 451–462. https://doi.org/10.1130/0016-7606(1985)96<451:SSIMAC>2.0.CO;2

De Donatis, M., & Mazzoli, S. (1994). Kinematic evolution of thrust-related structures in the Umbro-Romagnolo Parautochthon (Northern Apennines, Italy). *Terra Nova*, *6*, 563–574. https://doi.org/10.1111/j.1365-3121.1994.tb00523.x

de Jager, J. (1979). The relation between tectonics and sedimentation along the "Sillaro line" (northern Apennines, Italy). *Geologica Ultraiectina*, *19*, 1–98.

Dewey, J. F., Helman, M. L., Turco, E., Hutton, D. H. W., & Knott, S. D. (1989). Kinematics of the western Mediterranean. In M. P. Coward & D. Dietrich (Eds.), *Alpine tectonics, Geological Society, London, Special Publication* (Vol. 45, pp. 265–283). London, UK: Geological Society. https://doi.org/10.1144/GSL.SP.1989.045.01.15

Doglioni, C., Mongelli, F., & Pialli, G. (1998). Boudinage of the Alpine Belt in the Apenninic back-arc. *Memorie della Società Geologica Italiana*, *52*, 457–468.

Dykstra M. (2005). Dynamics of Sediment Mass-Transport from the Shelf to the Deep Seas (Doctoral dissertation). Retrieved from Researchgate. (https://www.researchgate.net/publication/253302343). Santa Barbara: University of California.

Dykstra, M., Garyfalou, K., Kertznus, V., Kneller, B., Milana, J. P., Milinaro, M., et al. (2011). Mass-transport deposits: Combining

outcrop studies and seismic forward modeling to understand lithofacies distributions, deformation, and their seismic expression. In R. C. Shipp, P. Weimer, & H. W. Posamentier (Eds.), *Mass-transport deposits in deepwater settings, SEPM Special Publication* (Vol. 96, pp. 293–310). Broken Arrow, OK: SEPM (Society for Sedimentary Geology).

Etchecopar, A. (1977). A plane kinematic model of progressive deformation in a polycrystalline aggregate. *Tectonophysics*, *39*, 121–139.

Faccenna, C., Becker, T. W., Lucente, F. P., Jolivet, L., & Rossetti, F. (2001). History of subduction and back-arc extension in the Central Mediterranean. *Geophysical Journal International*, *145*(3), 809–820. https://doi.org/10.1046/j.0956-540x.2001.01435.x

Faccenna, C., Piromallo, C., Crespo-Blanc, A., Jolivet, L., & Rossetti, F. (2004). Lateral slab deformation and the origin of the western Mediterranean arcs. *Tectonics*, *23*, TC1012. https://doi.org/10.1029/2002TC001488

Farrell, S. G., & Eaton, S. (1987). *Slump strain in the Tertiary of Cyprus and the Spanish Pyrenees. Definition of palaeo-slopes and models of soft-sediment deformation, Geological Society, London, Special Publication* (Vol. 29, pp. 181–196). London, UK: Geological Society. https://doi.org/10.1144/GSL.SP.1987.029.01.15

Festa, A., Dilek, Y., Pini, G. A., Codegone, G., & Ogata, K. (2012). Mechanisms and processes of stratal disruption and mixing in the development of mélanges and broken formations: Redefining and classifying mélanges. *Tectonophysics*, *568–569*, 7–24. https://doi.org/10.1016/j.tecto.2012.05.021

Festa, A., Ogata, K., Pini, G. A., Dilek, Y., & Alonso, J. L. (2016). Origin and significance of olistostromes in the evolution of orogenic belts: A global synthesis. *Gondwana Research*, *39*, 180–203. https://doi.org/10.1016/j.gr.2016.08.002

Festa, A., Pini, G. A., Dilek, Y., & Codegone, G. (2010a). Mélanges and mélange-forming processes: A historical overview and new concepts. In Y. Dilek (Ed.), *Alpine concept in geology, International Geology Review* (Vol. 52(10–12), pp. 1040–1105). London, UK: Taylor & Francis. https://doi.org/10.1080/00206810903557704

Festa, A., Pini, G. A., Dilek, Y., Codegone, G., Vezzani, L., Ghisetti, F., et al. (2010b). Peri-Adriatic mélanges and their evolution in the Tethyan realm. *International Geology Review*, *52*, 369–403. https://doi.org/10.1080/00206810902949886

Flores, G. (1955). Les résultates des études pour la recherche pétrolifère en Sicilie, Discussion: Rome. Paper Presented at Proceedings, Fourth World Petroleum Congress, Section 1/A/2 (pp. 121–122).

Fossen, H., & Cavalcante, G. C. G. (2017). Shear zones: A review. *Earth-Science Reviews*, *171*, 434–455. http://dx.doi.org/10.1016/j.earscirev.2017.05.002

Gandolfi, G., Paganelli, L., & Zuffa, G. G. (1983). Petrology and dispersal pattern (Miocene, Northern Apennines). *Journal of Sedimentary Petrology*, *53*, 493–507. https://doi.org/10.1306/212F8215-2B24-11D7-8648000102C1865D

Gueguen, E., Doglioni, C., & Fernandez, M. (1998). On the post-25 Ma geodynamic evolution of the western Mediterranean. *Tectonophysics*, *298*(1–3), 259–269. https://doi.org/10.1016/S0040-1951(98)00189-9

Hanamura, Y., & Ogawa, Y. (1993). Layer-parallel faults, duplexes, imbricate thrust and vein structures of the Miura Group. Keys to understanding the Izu fore-arc sediments accretion to the Honsu fore-arc. *The Island Arc*, *3*, 126–161. https://doi.org/10.1111/j.1440-1738.1993.tb00081.x

Hansen, E. (1971). *Strain facies*. New York, NY: Springer-Verlag.

Landuzzi, A. (2005). Sin-depositional emplacement of the Liguride allochthon in the Miocene foredeep of the Western Romagna Apennines (Italy). In G. Pasquarè, C. Venturini, & G. Groppelli (Eds.), *Mapping Geology in Italy, ISPRA, Servizio Geologico* (pp. 219–226). Roma: Istituto Poligrafico dello Stato.

Lucente, C. C. (2000). Orizzonti di frana sottomarina nella F.ne marnoso-arenacea (Appennino tosco romagnolo): organizzazione interna e implicazioni paleogeografiche (Doctoral dissertation). Bologna: Alma Mater Studiorum Università di Bologna.

Lucente, C. C. (2002). Geometry and emplacement of an extensive submarine slide body (Marnoso-arenacea Fm, northern Apennines, Italy). *Bollettino della Società Geologica Italiana*, *Volume Speciale 1-2002*, 385–392.

Lucente, C. C. (2004). Topography and paleogeographic evolution of a middle Miocene foredeep basin plain (Northern Apennines, Italy). *Sedimentary Geology*, *170*(3–4), 107–134. https://doi.org/10.1016/j.sedgeo.2004.06.002

Lucente, C. C., & Pini, G. A. (1999). Stratigraphic correlation and some submarine slide bodies in the lower Serravallian Marnoso-arenacea Formation, northern Apennines: Preliminary analysis. *Giornale di Geologia*, (ser. 3), *61*, 99–106, Bologna

Lucente, C. C., & Pini, G. A. (2002). Mechanisms of emplacement and significance of chaotic bodies embedded in turbidite successions of the northern Apennines. In E. Mutti, F. Ricci Lucchi, & M. Roveri (Eds.), *Revisiting turbidites of the Marnoso-arenacea formation and their basin-margin equivalents: problems with classic models. Excursion Guidebook. Università di Parma and Eni-Agip Division, 64th EAGE Conference and Exhibition, Florence (Italy)* (Vol. III, pp. 16–26). Parma: Copy & Press S.r.l. Editrice Campus.

Lucente, C. C., & Pini, G. A. (2003). Anatomy and emplacement mechanism of a large submarine slide within the Miocene foredeep in the Northern Apennines, Italy: A field perspective. *American Journal of Science*, *303*(7), 565–602. https://doi.org/10.2475/ajs.303.7.565

Lucente, C. C., & Pini, G. A. (2008). Basin-wide mass-wasting complexes as markers of the Oligo-Miocene foredeep-accretionary wedge evolution in the Northern Apennines, Italy. *Basin Research*, *20*(1), 49–71. https://doi.org/10.1111/j.1365-2117.2007.00344.x

Lucente, C. C., & Taviani, M. (2005). Chemosynthetic communities as fingerprints of submarine sliding-linked hydrocarbon seepage, Miocene deep-sea strata of the Tuscan-Romagna Apennines, Italy. *Paleogeography, Paleoclimatology, Paeloecology*, *227*(1-3), 176–190. https://doi.org/10.1016/j.palaeo.2005.04.025

Malavieille, J., Molli, G., Genti, M., Dominguez, S., Beyssa, O., Taboada, A., et al. (2016). Formation of ophiolite-bearing tectono-sedimentary mélanges in accretionary wedges by

gravity driven submarine erosion: Insights from analogue models and case studies. *Journal of Geodynamics*, *100*, 87–103. http://dx.doi.org/10.1016/j.jog.2016.05.008

Malinverno, A., & Ryan, W. (1986). Extension in the Tyrrhenian Sea and shortening in the Apennines as result of arc migration driven by sinking of the lithosphere. *Tectonics*, *5*(2), 227–245. https://doi.org/10.1029/TC005i002p00227

Maltman, A. (1988). The importance of shear zones in naturally deformed wet sediments. *Tectonophysics*, *145*(1–2), 163–175. https://doi.org/10.1016/0040-1951(88)90324-1

Marroni, M., Meneghini, F., & Pandolfi, L. (2010). Anatomy of the Ligure-Piemontese subduction system: Evidence from Late Cretaceous–middle Eocene convergent margin deposits in the Northern Apennines, Italy. *International Geology Review*, *52*(10–12), 1160–1192. https://doi.org/10.1080/00206810903545493

Marroni, M., Meneghini, F., & Pandolfi, L. (2017). A revised subduction inception model to explain the Late Cretaceous, double-vergent orogen in the precollisional western Tethys: Evidence from the Northern Apennines. *Tectonics*, *36*(10), 2227–2249. https://doi.org/10.1002/2017TC004627

Marroni, M., & Pandolfi, L. (2007). The architecture of an incipient oceanic basin: A tentative reconstruction of the Jurassic Liguria-Piemonte basin along the Northern Apennine–Alpine Corsica transect. *International Journal of Earth Science*, *96*(6), 1059–1078. https://doi.org/10.1007/s00531-006-0163-x

Martinsen, O. J., & Bakken, B. (1990). Extensional and compressional zones in slumps and slides in the Namurian of County Clare, Ireland. *Journal of Geological Society of London*, *147*, 153–164. https://doi.org/10.1144/gsjgs.147.1.0153

Molli, G. (2008). Northern Apennine-Corsica orogenic system: An updated overview. *Geological Society London Special Publications*, *298*(1), 413–442. London: Geological Society. https://doi.org/10.1144/SP298.19

Molli, G., Crispini, L., Malusà, G. M., Mosca, P., Piana, F., & Federico, L. (2010). Geology of the western Alps–Northern Apennines junction area: A regional review. In M. Beltrando, A. Peccerillo, M. Mattei, S. Conticelli, & C. Doglioni (Eds.), *The Geology of Italy: tectonics and life along plate margins, Journal of Virtual Explorer* (Vol. 36, pp. 1–49). https://doi.org/10.3809/jvirtex.2010.00215

Molli, G., & Malavieille, J. (2010). Orogenic processes and the Alps/Apennines geodynamic evolution: insights from Taiwan. *International Journal of Earth Sciences*, *100*(5), 1207–1224. http://dx.doi.org/. doi:10.1007/s00531-010-0598-y

Mutti, E., & Ricci Lucchi, F. (1972). Le torbiditi dell'Appennino settentrionale: Introduzione all'analisi di facies. *Memorie della Società Geologica Italiana*, *11*, 161–199.

Mutti, E., & Ricci Lucchi, F. (1975). Turbidite facies and facies associations. In E. Mutti, G. C. Parea, F. R. Lucchi, M. Sagri, G. Zanzucchi, G. Ghibaudo, & S. Jaccarino (Eds.), *Examples of Turbidite Facies and Facies Associations from Selected Formations of the Northern Apennines*. *X International Congress of Sedimentology, Nice-1975,* Field Trip A 11 (pp. 21–36). Modena: S.T.E.M. Mucchi.

Mutti, E., Tinterri, R., Benevelli, G., di Biase, D., & Cavanna, G. (2003). Deltaic, mixed and turbidite sedimentation of ancient foreland basins. *Marine and Petroleum Geology*, *20*(6–8), 733–755. https://doi.org/10.1016/j.marpetgeo.2003.09.001

Muttoni, G., Lanci, L., Argnani, A., Hirt, A. M., Cibin, U., Abrahamsen, N., et al. (2000). Paleomagnetic evidence for a Neogene two-phase counterclockwise tectonic rotation in the Northern Apennines (Italy). *Tectonophysics*, *326*, 241–253. https://doi.org/10.1016/S0040-1951(00)00140-2

Ogata, K., Mountjoy, J. J., Pini, G. A., Festa, A., & Tinterri, R. (2014a). Shear zone liquefaction in mass transport deposit emplacement: a multi-scale integration of seismic reflection and outcrop data. *Marine Geology*, *356*, 50–64. https://doi.org/10.1016/j.margeo.2014.05.001

Ogata, K., Mutti, E., Tinterri, R., & Pini, G. A. (2012a). Mass transport-related stratal disruption within sedimentary mélange: Examples from the northern Apennines (Italy) and south-central Pyrenees (Spain). *Tectonophysics*, *568–569*, 185–199. https://doi.org/10.1016/j.tecto.2011.08.021

Ogata, K., Pogačnik, Ž., Pini, G. A., Tunis, G., Festa, A., Camerlenghi, A., et al. (2014b). The carbonate mass transport deposits of the Paleogene Julian-Slovenian Basin (Italy/Slovenia): internal anatomy and inferred genetic processes. *Marine Geology*, *356*, 88–110. https://doi.org/10.1016/j.margeo.2014.06.014

Ogata, K., Tinterri, R., Pini, G. A., & Mutti, E. (2012b). The Specchio Unit (Northern Apennines, Italy): An ancient mass transport complex originated from near-coastal areas in an intra-slope setting. In Y. Yamada, K. Kawamura, K. Ikehara, Y. Ogawa, R. Urgeles, D. Mosher, et al. (Eds.), *Submarine mass movements and their consequences, Advances in Natural and Technological Hazards Research* (Vol. 31, pp. 595–605). Dordrecht, The Netherlands: Springer Science+Business Media B.V. https://doi.org/10.1007/978-94-007-2162-3_53

Panieri, G., Camerlenghi, A., Conti, S., Pini, G. A., & Cacho, I. (2009). Methane seepages recorded in benthic foraminifera from Miocene seep carbonates, Northern Apennines (Italy). *Palaeogeography, Palaeoclimatology, Palaeoecology*, *284*(3–4), 271–282. https://doi.org/10.1016/j.palaeo.2009.10.006

Pini, G. A. (1999). *Tectosomes and olistostromes in the Argille scagliose of Northern Apennines, Geological Society of America Special Paper* (Vol. 335, pp. 1–70). Boulder: Geological Society of America. https://doi.org/10.1130/0-8137-2335-3.1

Pini, G. A., Ogata, K., Camerlenghi, A., Festa, A., Lucente, C. C., & Codegone, G. (2012). Sedimentary mélanges and fossil mass-transport complexes: a key for better understanding submarine mass movements? In Y. Yamada, K. Kawamura, K. Ikehara, Y. Ogawa, R. Urgeles, D. Mosher, et al. (Eds.), *Submarine mass movements and their consequences, Advances in Natural and Technological Hazards Research* (Vol. 31, pp. 585–594). Dordrecht, The Netherlands: Springer Science+Business Media B.V. https://doi.org/10.1007/978-94-007-2162-3_52

Posamentier, H. W., & Martinsen, O. J. (2011). The character and genesis of submarine mass-transport deposits: insights from outcrop and 3D seismic data. In R. C. Shipp, P. Weimer, & H. W. Posamentier (Eds.), *Mass-transport deposits in deepwater settings, SEPM Special Publication* (Vol. 96, pp. 1–32). Broken Arrow, OK: SEPM (Society for Sedimentary Geology).

Principi, G., & Treves, B. (1984). Il sistema corso-appenninico come prisma d'accrezione. Riflessi sul problema generale del limite Alpi-Appennino. *Memorie della Società Geologica Italiana*, *28*, 549–576.

Raymond, A. L. (Ed.) (1984). *Melanges: Their nature, origin, and significance, Geological Society of America Special Paper* (Vol. 198). Boulder: Geological Society of America. https://doi.org/10.1130/SPE198

Raymond, A. L. (2017). What is Franciscan?: revisited. *International Geology Review*, *60*(16), 1968–2030. https://doi.org/10.1080/00206814.2017.1396933

Raymond, A. L., & Bero, D. A. (2015). Sandstone-matrix mélanges, architectural subdivision, and geologic history of accretionary complexes: A sedimentological and structural perspective from the Franciscan Complex of Sonoma and Marin counties, California, USA. *Geosphere*, *11*(4), 1–34. https://doi.org/10.1130/GES01137.1

Renzi, G. (1967). Sui livelli franati e i "calcari a Lucina" nella Formazione Marnoso-arenacea delle Alte Valli del Lamone e del Senio. *Studi Romagnoli*, *17*, 155–162.

Ricci Lucchi, F. (1975). Miocene paleogeography and basin analysis in the Periadriatic Apennines. In C. Squyres (Ed.), *Geology of Italy* (Vol. 2, pp. 129–236). Castelfranco Veneto-Tripoli: P.E.S.L.

Ricci Lucchi, F. (1978). Turbidite dispersal in a Miocene deep-sea plain. *Geologie en Mijnbouw*, *57*, 559–576.

Ricci Lucchi, F. (1986). The Oligocene to recent foreland basins of the northern Apennines. In P. A. Allen & P. Homewood (Eds.), *Foreland basins, IAS Special Publication* (Vol. 8, pp. 105–139). Oxford, UK: Blackwell Scientific. https://doi.org/10.1002/9781444303810.ch6

Ricci Lucchi, F., & Ori, G. G. (1985). Field excursion D: Syn-orogenic deposits of a migrating basin system in the NW Adriatic foreland. In P. Allen (Ed.), *Foreland basins, excursion guidebook* (pp. 137–176). Fribourg: International Association of Sedimentologists.

Ricci Lucchi, F., & Valmori, E. (1980). Basin-wide turbidites in Miocene, over-supplied deep-sea plain: a geometrical analysis. *Sedimentology*, *27*(3), 241–270. https://doi.org/10.1111/j.1365-3091.1980.tb01177.x

Riedel, W. (1929). Zur Mechanik Geologischer Brucherscheinungen. Ein Beitrag zum Problem der "Fiederspalten". *Centralblatt für Mineralogie, Geologie und Paleontologie B*, *8*, 354–368.

Roca, E. (2001). The Northwest Mediterranean Basin (Valencia trough, Gulf of Lions and Liguro-Provençal basins): Structure and geodynamic evolution. In P. A. Ziegler, W. Cavazza, A. H. F. Robertson, & S. Crasquin-Soleau (Eds.), *Peri-Tethys memoir 6: Peri-tethyan rift/wrench basins and passive margins, IGCP 369, Mémoires du Muséum d'histoire naturelle. Paris* (Vol. 186, pp. 671–706). Paris, France: Muséum d'Histoire naturelle.

Rodrigues, B. C., & Pamplona, J. (2018). Boudinage and shear-band boudins: A meso to micro-scale tool in structural analysis. *Journal of Structural Geology*, *114*, 280–287. https://doi.org/10.1016/j.jsg.2017.11.019

Roveri, M., Ricci Lucchi, F., Lucente, C. C., Manzi, V., & Mutti, E. (2002). Stratigraphy, facies and basin fill history of the Marnoso-arenacea Formation. In E. Mutti, F. Ricci Lucchi, & M. Roveri (Eds.), *Revisiting turbidites of the Marnoso-arenacea formation and their basin-margin equivalents: Problems with classic models. Excursion Guidebook. Università di Parma and Eni-Agip Division, 64th EAGE Conference and Exhibition, Florence (Italy)* (Vol. III, pp. 1–15). Parma: Copy & Press S.r.l. Editrice Campus.

Sani, F., Bonini, M., Piccardi, L., Vannucci, G., Delle Donne, D., Benvenuti, M., et al. (2009). Late Pliocene–Quaternary evolution of outermost hinterland basins of the Northern Apennines (Italy), and their relevance to active tectonics. *Tectonophysics*, *476*, 336–356. https://doi.org/10.1016/j.tecto.2008.12.012

Sartori, R. (1990). The main results of ODP Leg 107 in the frame of Neogene to recent geology of Perityrrhenian areas. In K. A. Kastens, J. Mascle, C. Auroux, E. Bonatti, C. Broglia, J. Channell, et al. (Eds.), *Proceedings of the ocean drilling program, Scientific Results* (Vol. 107, pp. 715–730). College Station, TX: Ocean Drilling Program. https://doi.org/10.2973/odp.proc.sr.107.183.1990

Shipp, R. C., Weimer, P., & Posamentier, H. W. (Eds.) (2011). *Mass-transport deposits in deepwater settings, SEPM Special Publication* (Vol. 96). Broken Arrow, OK: SEPM (Society for Sedimentary Geology). https://doi.org/10.2110/sepmsp.096

Skempton, A.W. (1966). Some observation of tectonic shear zones. In: *Proceedings of the 1st Congress International Society of Rock Mechanics*, Lisbon 1, 329–335

Sobiesiak, M. S., Kneller, B., Alsop, G. I., & Milana, J. P. (2016). Internal deformation and kinematic indicators within a tripartite mass transport deposit, NW Argentina. *Sedimentary Geology*, *344*, 364–381. https://doi.org/10.1016/j.sedgeo.2016.04.006

Sobiesiak, M. S., Kneller, B., Alsop, G. I., & Milana, J. P. (2018). Styles of basal interaction beneath mass transport deposits. *Marine and Petroleum Geology*, *98*, 629–639. https://doi.org/10.1016/j.marpetgeo.2018.08.028

Speranza, F., Sagnotti, L., & Mattei, M. (1997). Tectonics of the Umbria–Marche–Romagna arc (central-northern Apennines, Italy): New paleomagnetic constraints. *Journal of Geophysical Research*, *102*, 3153–3166. https://doi.org/10.1029/96JB03116

Speranza, F., Villa, I. M., Sagnotti, L., Florindo, F., Cosentino, D., Cipollari, P., et al. (2002). Age of the Corsica and Sardinia rotation and Liguro-Provencal Basin spreading: New paleomagnetic and Ar/Ar evidences. *Tectonophysics*, *347*(4), 231–251. https://doi.org/10.1016/S0040-1951(02)00031-8

Stampfli, G. M., Borel, G. D., Marchant, R., & Mosar, J. (2002). Western Alps geological constraints on western Tethyan reconstructions. In G. Rosenbaum & G. S. Lister (Eds.), *Reconstruction of the evolution of the Alpine-Himalayan Orogen. Journal of the Virtual Explorer* (Vol. 7, pp. 75–104). https://doi.org/10.3809/jvirtex.2002.00057

Stampfli, G. M., Mosar, J., Marquer, D., Marchant, R., Baudin, T., & Borel, G. (1998). Subduction and obduction processes in the Swiss Alps. *Tectonophysics*, *296*(1–2), 159–204. https://doi.org/10.1016/S0040-1951(98)00142-5

Swanson, M. T. (1992). Late Acadian-Alleghenian transpressional deformation: Evidence from asymmetric boudinage in the Casco Bay area, coastal Maine. *Journal of Structural Geology*, *14*, 323–341. https://doi.org/10.1016/0191-8141(92)90090-J

Swarbick, R. E., & Naylor, M. A. (1980). The Kathikas melange,SW Cyprus: Late Cretaceous submarine debris flows. *Sedimentology*, *27*(1), 63–78. https://doi.org/10.1111/j.1365-3091.1980.tb01158.x

Tagliaferri, A., Tinterri, R., Pontiggia, M., Da Pra, A., Davoli, G., & Bonamini, E. (2018). Basin-scale, high-resolution three-

dimensional facies modeling of tectonically confined turbidites: An example from the Firenzuola system (Marnoso-arenacea Formation, northern Apennines, Italy). *AAPG Bulletin*, *102*(8), 1601–1626. https://doi.org/10.1306/12081716521

Talling, P. J., Amy, L. A., Wynn, R. B., Blackbourn, G., & Gibson, O. (2007). Evolution of turbidity currents deduced from extensive thin turbidites: Marnoso Arenacea Formation (Miocene), Italian Apennines. *Journal of Sedimentary Research*, *77*(3), 172–196. https://doi.org/10.2110/jsr.2007.018

Tinterri, R., & Muzzi Magalhaes, P. (2011). Synsedimentary structural control on foredeep turbidites: An example from Miocene Marnoso-arenacea Formation, Northern Apennines, Italy. *Marine and Petroleum Geology*, *28*, 629–657. https://doi.org/10.1016/j.marpetgeo.2010.07.007

Tinterri, R., Muzzi Magalhaes, P., & Tagliaferri, A. (2012). Foredeep turbidites of the Miocene Marnoso-arencea Formation (Northern Apennines, Italy). *Geological Field Trips (ISPRA e Società Geologica Italiana)*, *4*(2.1), 1–132. https://doi.org/10.3301/GFT.2012

Tinterri, R., & Tagliaferri, A. (2015). The syntectonic evolution of foredeep turbidites related to basin segmentation: Facies response to the increase in tectonic confinement (Marnoso-arenacea Formation, Miocene, Northern Apennines, Italy). *Marine and Petroleum Geology*, *67*, 81–110. https://doi.org/10.1016/j.marpetgeo.2015.04.006

Toscani, G., Burrato, P., Di Bucci, D., Seno, S., & Valensise, G. (2009). Plio-Quaternary tectonic evolution of the Northern Apennines thrust fronts (Bologna-Ferrara section, Italy): Seismotectonic implications. *Italian Journal of Geosciences*, *128*(2), 605–613. https://doi.org/10.3301/IJG.2009.128.2.605

van den Merwe, W. C., Hodgson, D. M., & Flint, S. S. (2011). Origin and terminal architecture of a submarine slide: A case study from the Permian Vischkuil Formation, Karoo Basin, South Africa. *Sedimentology*, *58*(7), 2012–2038. https://doi.org/10.1111/j.1365-3091.2011.01249.x

Vignaroli, G., Faccenna, C., Jolivet, L., Piromallo, C., & Rossetti, F. (2008). Subduction polarity reversal at the junction between the Western Alps and the Northern Apennines, Italy. *Tectonophysics*, *450*(1–4), 34–50. https://doi.org/10.1016/j.tecto.2007.12.012

Wakabayashi, J. (2011). Mélanges of the Franciscan complex, California: Diverse structural settings, evidence for sedimentary mixing, and their connection to subduction processes. In J. Wakabayashi & Y. Dilek (Eds.), *Mélanges: Processes of formation and societal significance, Geological Society of America Special Paper* (Vol. 480, pp. 117–141). Boulder: Geological Society of America. https://doi.org/10.1130/2011.2480(05)

Weimer, P., & Shipp, C. (2004). Mass transport complexes: Musing on past uses and suggestions for future directions. In *Offshore technology conference, Houston, 3–6 May 2004,* Paper 16752. Houston TX: Offshore Technology Conference. https://doi.org/10.4043/16752-MS

Woodcock, N. H. (1979). The use of slump structures as paleoslope orientation estimators. *Sedimentology*, *26*(1), 83–99. https://doi.org/10.1111/j.1365-3091.1979.tb00339.x

Yamada, Y., Kawamura, K., Ikehara, K., Ogawa, Y., Urgeles, R., Mosher, D., et al. (Eds.) (2012). *Submarine Mass Movements and their consequences, Advances in Natural and Technological Hazards Research* (Vol. 31). Dordrecht, The Netherlands: Springer Science+Business Media B.V. https://doi.org/10.1007/978-94-007-2162-3

Yamamoto, Y., Mukoyoshi, H., & Ogawa, Y. (2005). Structural characteristics of shallowly buried accretionary prism: Rapidly uplifted Neogene accreted sediments on the Miura-Boso Peninsula, central Japan. *Tectonics*, *24*, TC5008. https://doi.org/10.1029/2005TC001823

Yamamoto, Y., Nidaira, M., Ohta, Y., & Ogawa, Y. (2009). Formation of chaotic rock units during primary accretion processes: Examples from the Miura–Boso accretionary complex, central Japan. *The Island Arc*, *18*(3), 496–512. https://doi.org/10.1111/j.1440-1738.2009.00676.x

9

Fold and Thrust Systems in Mass-Transport Deposits Around the Dead Sea Basin

G. Ian Alsop[1], Rami Weinberger[2,3], Shmuel Marco[4], and Tsafrir Levi[2]

ABSTRACT

The late Pleistocene Lisan Formation outcropping around the Dead Sea preserves exceptional 3D exposures of fold and fault systems generated during soft-sediment slumping associated with mass-transport deposits (MTDs). Vergence of slump folds outcropping to the west of the Dead Sea is generally (>90%) toward the east and consistent with depocenter-directed movement of MTDs. On a regional scale, the direction of slumping inferred from the fold and thrust geometries systematically varies along the entire ~100 km length of the western Dead Sea Basin. The fold and thrust systems are interpreted to form part of a large-scale radial system of MTDs directed toward the basin's depocenter and to be triggered by earthquakes generated along the Dead Sea Fault. The progressive evolution of MTDs is broadly categorized into initiation, translation, cessation, relaxation, and compaction phases. Deformation may become most evolved where slope failure initiates and MTD movement commences. Consequently, many MTDs display the greatest deformation in their central area, and this diminishes toward the leading edge where MTD displacement was still initiating. Thrust packages may define piggyback sequences during MTD translation, while in other cases, overstep thrust sequences are formed, leading to a range of crosscutting and overprinting relationships. The recognition that MTDs may be reworked by younger seismically triggered events suggests that in some cases, the seismic recurrence interval may be shorter than anticipated. Our observations of heterogeneous lateral compaction, together with upright folding that represents an early phase of layer-parallel shortening, may help explain why some contraction is apparently missing from seismic sections across large-scale MTDs. In addition, conjugate normal faults that strike parallel to the dip of the paleoslope indicate a component of non-plane strain deformation associated with "out-of-plane" movement. MTDs in the Dead Sea Basin are best described as having open-ended toes (a variant of frontally confined toes) in which further movement is impeded by downslope strata that form a "soft" buttress. Observations that contraction and extension may overprint one another at any position within an MTD suggest that second-order flow cells may locally interact with one another and are linked to "pockets" of "surging" or "slackening" flow during overall downslope translation of the MTD. The spacing of thrust ramps within MTDs are linearly related to the thickness of the section to define an approximate 5 : 1 ratio across a range of scales. In summary, the MTDs in the Lisan Formation exposed around the Dead Sea Basin are triggered by seismic events, may be facilitated by mechanical heterogeneity linked to detrital-rich horizons, and are ultimately controlled by the paleoslope orientation.

[1] *Department of Geology and Geophysics, School of Geosciences, University of Aberdeen, Aberdeen, United Kingdom*

[2] *Geological Survey of Israel, Jerusalem, Israel*

[3] *Department of Geological and Environmental Sciences, Ben Gurion University of the Negev, Beer Sheva, Israel*

[4] *Department of Geophysics, Tel Aviv University, Tel Aviv-Yafo, Israel*

9.1. INTRODUCTION AND REGIONAL SETTING OF MTDS IN THE DEAD SEA BASIN

The Dead Sea Basin is a pull-apart basin formed between two sinistral and left-stepping fault strands that comprise the Dead Sea Fault (Figure 9.1a) (e.g., Garfunkel,

Submarine Landslides: Subaqueous Mass Transport Deposits from Outcrops to Seismic Profiles, Geophysical Monograph 246, First Edition. Edited by Kei Ogata, Andrea Festa, and Gian Andrea Pini.
© 2020 American Geophysical Union. Published 2020 by John Wiley & Sons, Inc.

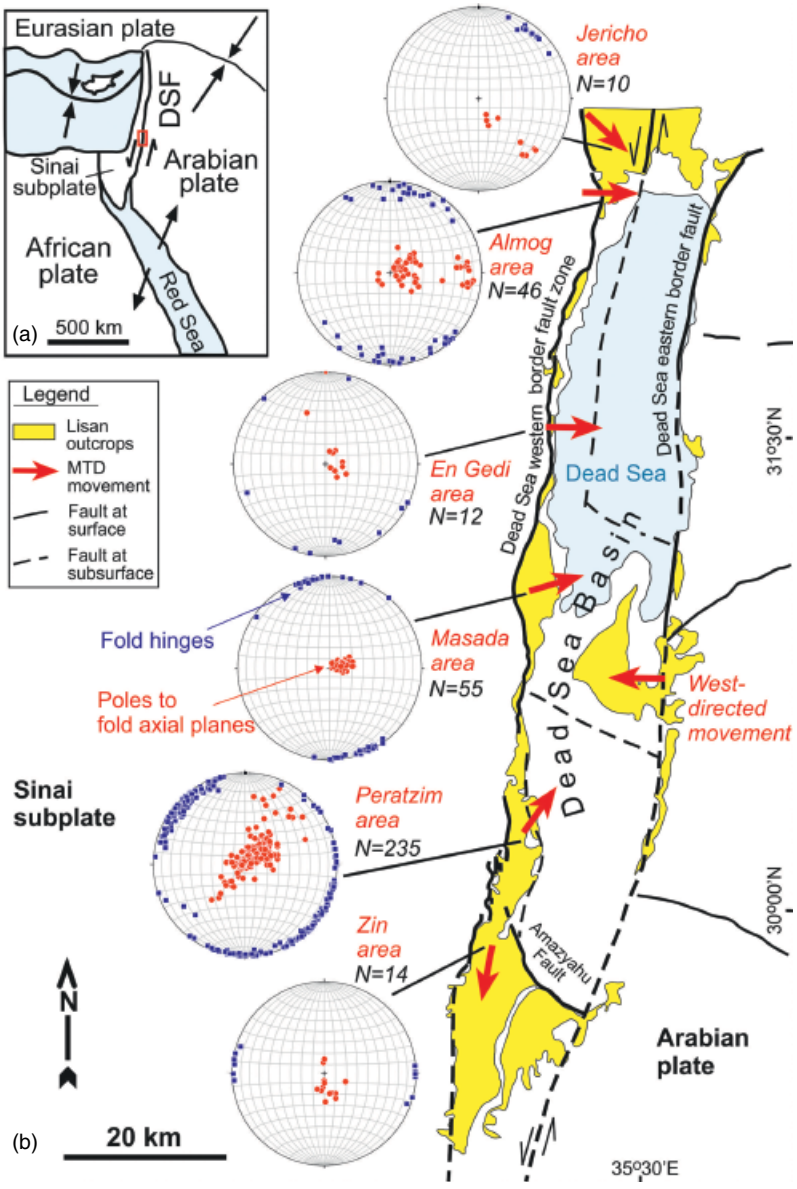


Figure 9.1 (a) General tectonic map of the Middle East showing the location of study area (red box) along the Dead Sea Fault (DSF). The DSF transfers the opening motion in the Red Sea to the Taurus-Zagros collision zone. (b) Map of the Dead Sea showing the position of localities referred to in the text and the extent of the Lisan Formation outcrops. Stereonets show fold hinges (blue squares) and poles to axial planes (red circles) that have been measured from slump folds within MTDs of the Lisan Formation. The red arrows represent the inferred direction of MTD movement within the Lisan Formation and form a semi-radial pattern centered around the Dead Sea Basin. Westerly directed movement along the eastern margin of the basin is based on El-Isa and Mustafa (1986). (*See electronic version for color representation of this figure*)

1981, 2014; Sneh and Weinberger, 2014). The Dead Sea Fault forms a transform boundary that has been active since the early to middle Miocene (e.g., Nuriel et al., 2017), including during the late Pleistocene when the Lisan Formation was deposited between 70 and 15 ka in a precursor lake to the Dead Sea (Haase-Schramm et al., 2004). Numerous earthquakes have been triggered by the Dead Sea Fault, resulting in coseismic deformation (e.g., Agnon et al., 2006; Weinberger et al., 2016), together with soft-sediment deformation and mass-transport deposits (MTDs) in the Lisan Formation (El-Isa and Mustafa, 1986; Marco et al., 1996; Alsop and Marco, 2011). It is these MTDs that are exceptionally well exposed in outcrops of the Lisan Formation around the Dead Sea

Basin that form the focus of this study (Marco et al., 1996; Alsop et al. 2016). The MTDs that we describe are generally no more than a few meters thick, with constraints of continuous exposure limiting our ability to trace them along strike for ~500 m, and downslope for a few kilometers, suggesting overall volumes for individual MTDs of <0.5 km^3. However, larger MTDs exist, as significant numbers of deformed horizons have been recovered from cores through the Lisan Formation in the depocenter of the Dead Sea Basin (Lu et al., 2017; Kagan et al. 2018).

Coseismic slip along bedding planes in the Lisan Formation results in horizontal offset of vertical clastic dikes and is created by seismic waves generated by earthquakes passing through the sediment (Weinberger et al., 2016). Such seismic events are also thought to trigger older MTDs within the Lisan Formation, where topography created in the hanging wall of normal faults is infilled by breccia formed during the same seismic event (e.g., El-Isa and Mustafa, 1986; Marco et al., 1996; Alsop and Marco, 2011). A recent discussion of the seismic origin of MTDs within the Lisan Formation is provided by Lu et al. (2017). Following the initial seismic event that triggers slope failure, MTDs then undergo gravity-driven downslope movement toward the depocenter of the basin (Alsop and Marco, 2012a). Multiple MTDs that are transported into the center of the basin have resulted in a threefold thickening of the Lisan Formation where penetrated by drill cores (Lu et al., 2017; Kagan et al., 2018). Thus, although slope failure is triggered by an earthquake which perhaps lasts in the order of seconds (e.g., see Shani-Kadmiel et al., 2014), subsequent downslope movement of MTDs generates the observed fold and thrust systems and is gravity driven. This downslope movement of MTDs is completed prior to deposition of an overlying sedimentary "cap" that settles out of suspension, potentially "in a matter of just hours or days" (Alsop et al., 2016, p. 80).

The Lisan Formation comprises a sequence of alternating aragonite-rich and detrital-rich laminae on a submillimeter scale. Aragonite-rich laminae are considered to precipitate from hypersaline waters in hot dry summers, while winter floods wash detrital sediment into the lake to create annual varve-like cycles (Begin et al., 1974). Detrital laminae within the varved aragonite-rich Lisan Formation consist of quartz and calcite grains with minor feldspar, and clays (illite-smectite), and display grain sizes of ~8–10 μm (silt), while the thicker detrital-rich units are classified as very fine sands (60–70 μm) (Haliva-Cohen et al., 2012). The sedimentation rate of the Lisan Formation is estimated from varve counting combined with isotopic dating and is thought to average ~1 mm/year (Prasad et al., 2009). These exceptional layer-cake stratigraphies, developed on a centimeter scale within the lacustrine environment, potentially provide numerous easy-slip horizons to facilitate translation of the MTDs.

The Lisan Formation was deposited on very gentle slopes of <1° (Alsop and Marco, 2013). MTDs that move down very low angle slopes are frequently reported in the literature (e.g., Lewis, 1971; Almagor and Garfunkel, 1979; Gibert et al., 2005; Garcia-Tortosa et al., 2011; Gladkov et al., 2016), with modern failures recorded on gradients as low as 0.25° (e.g., Wells et al., 1980; Field et al., 1982). Hence, the very gentle slopes developed in the Lisan Formation should not be considered too low or insufficient to drive downslope movement, as supported by analogue experiments that demonstrate that such low gradients are capable of driving sediment deformation (e.g., Owen, 1996). Within the Lisan Formation, failure and translation of MTDs on very gentle slopes (<1°) may be facilitated by pore fluid pressure (e.g., Arkin & Michaeli, 1986) that is increased during seismicity and also loading associated with translation of MTDs themselves (Alsop et al., 2018).

This study aims to review a number of factors pertaining to MTDs around the Dead Sea Basin, which may also have more general relevance:

1. Analyzing regional patterns of MTD movement around the Dead Sea Basin
2. Analyzing structural sequences during internal evolution of MTDs
3. Analyzing reworking triggered by multiple seismic events within MTDs
4. Analyzing contractional structures that are hidden on seismic images
5. Analyzing the external geometry of MTDs around the Dead Sea Basin

9.2. ANALYZING REGIONAL PATTERNS OF MTD MOVEMENT AROUND THE DEAD SEA BASIN

The careful measurement of slump fold orientation has long been used to infer the direction of paleoslopes (e.g., Woodcock, 1976a, 1976b, 1979; Korneva et al., 2016; Jablonska et al., 2018). Detailed fieldwork along a >100 km transect down the western margin of the Dead Sea Basin allowed Alsop and Marco (2012a) and Alsop et al. (2018) to objectively test if the orientation and geometry of slump folds within MTDs accurately reflects the orientations of paleoslopes over a regional scale. To achieve this aim, Alsop and Marco (2012a) used five different methods of slump transport analysis that provided consistent results and are typically within 15° of one another at each site. Excavation reveals the 3D geometry of slump structures, with fold hinges displaying an arc of orientations consistent with east directed movement, while thrusts display pronounced basinward vergence. Alsop and Marco (2012a) recognized that >90% of fold

hinges verge broadly toward the east, while associated axial planes generally (>90%) dip toward the west. In detail, southeast directed slumping of MTDs is recognized in the north, easterly directed transport of MTDs in the central portion, and northeast directed MTD movement at the southern end of the Dead Sea at the Peratzim locality (Figure 9.1b). The folds are typically inferred to initiate at high angles to paleoslope and verge in the flow direction. These consistent relationships support flow perturbation models in which transport-normal fold hinges are generated by layer-parallel shearing during broadly east directed slumping (Alsop and Marco, 2011, 2012a, 2012b; Alsop et al., 2016).

These studies (Alsop and Marco, 2012a; Alsop et al., 2018) form a rare regional analysis of fold data sets developed in MTDs over a regional scale and permit the recognition of a large-scale radial MTD system directed toward the depocenter of the Dead Sea. This is also supported by the studies of El-Isa and Mustafa (1986) who recognized westerly directed movement of MTDs within the Lisan Formation on the eastern margin of the basin. This radial pattern demonstrates not only the reliability of techniques to determine MTD transport but also the >90° variability of slope failure directions along the c. 100 km western margin of the Dead Sea Basin. The depositional dips (<1°) of the Lisan Formation demonstrate that local tectonics has not significantly affected the MTD transport directions with time, apart from at the Zin locality where the south-southwest directed transport is interpreted to reflect large-scale "block" tilting adjacent to the transverse Amazyahu Fault (Figure 9.1b) (Weinberger et al., 2017; Alsop et al., 2018). Thus, although MTDs within the Lisan Formation may be of slightly different (late Pleistocene) ages along the length of the Dead Sea Basin, they portray an overall coherent radial movement pattern because of the general absence of local tectonics and tilting. The gross pattern proves that the shape, and in particular the vergence, of deformed layers is governed by paleoslopes linked to MTD movement (Alsop and Marco, 2012a). The general pattern of movement is corroborated by anisotropy of magnetic susceptibility (AMS) fabrics that have been sampled from MTDs down the western margin of the Dead Sea and also display a radial pattern that mirrors the structural studies (Weinberger et al., 2017).

9.3. ANALYZING STRUCTURAL SEQUENCES DURING INTERNAL EVOLUTION OF MTDS

9.3.1. Distinguishing General Structural Sequences

A range of fold patterns and thrust geometries created during the structural evolution of MTDs can be determined from seismic sections (e.g., Frey-Martinez et al., 2005; Jolly et al., 2016; Reis et al., 2016; Cruciani et al., 2017) and outcrop studies (e.g., Lucente and Pini, 2003; Sharman et al., 2015; Ortner and Kilian, 2016; Basilone, 2017; Sobiesiak et al., 2017). Alsop and Marco (2011) recognized that the progressive evolution of folding within MTDs may be broadly categorized into initiation, translation, cessation, relaxation, and compaction phases. Folding which initiates as upright "billows" within MTDs may be progressively modified with increasing downslope directed simple shear to create asymmetric folds that develop into overturned folds, which are themselves eventually cut by downslope verging thrust systems (Alsop and Marco, 2011; Alsop et al., 2019a) (Figure 9.2a). It should be noted that the initial weak upright folds may form beyond the tip of the underlying detachment and that these early upright folds, which may partially be amplified by density variations (e.g., Alsop and Marco, 2011), are sheared over with ongoing downslope translation (Alsop et al., 2016) (Figure 9.2a–c). Meanwhile, upright folds continue to initiate at the new leading edge of the downslope propagating MTD. Therefore, the greatest deformation and most evolved structures may develop in the center of MTDs where deformation has been most protracted, rather than at downslope toes as commonly assumed (see Alsop et al., 2016).

9.3.2. Distinguishing Detailed Thrust Sequences

A range of different thrust sequences can be interpreted from both orogenic belts (e.g., Dahlstrom, 1970; Boyer and Elliot, 1982; Morley, 1988; Boyer 1992) and MTDs (e.g., de Vera et al., 2010; Ireland et al., 2011; Scarselli et al., 2016). In piggyback thrusting, new thrusts develop in the footwall of existing thrusts, potentially resulting in a back-steepening and rotation of the older thrust and an overall forward propagating system of thrusts down the slope (Figures 9.2d, 9.3a–d, and 9.4a). Some thrusts are back-rotated through the vertical so that hanging wall sequences become inverted. Examples of piggyback thrusting have been observed and interpreted from MTDs within the Peratzim study area of the Dead Sea Basin (Alsop et al., 2017a) (Figure 9.2d–f).

In an overstep (or "breakback") sequence of thrusts, new thrusts form in the hanging wall of existing thrusts, resulting in a backward propagating system of thrusts (i.e., upslope in the opposite direction to thrust transport) (Alsop et al., 2018) (Figure 9.3b–f). In addition, new thrusts may cut through existing thrusts in their footwall, resulting in re-imbrication of the sequence in an overall upslope direction. Examples of overstep thrusting have been observed and interpreted from MTDs within the Zin study area of the Dead Sea Basin (Alsop et al., 2018) (Figures 9.1b and 9.4b). Synchronous thrusting develops where more than one thrust moves at the same time and

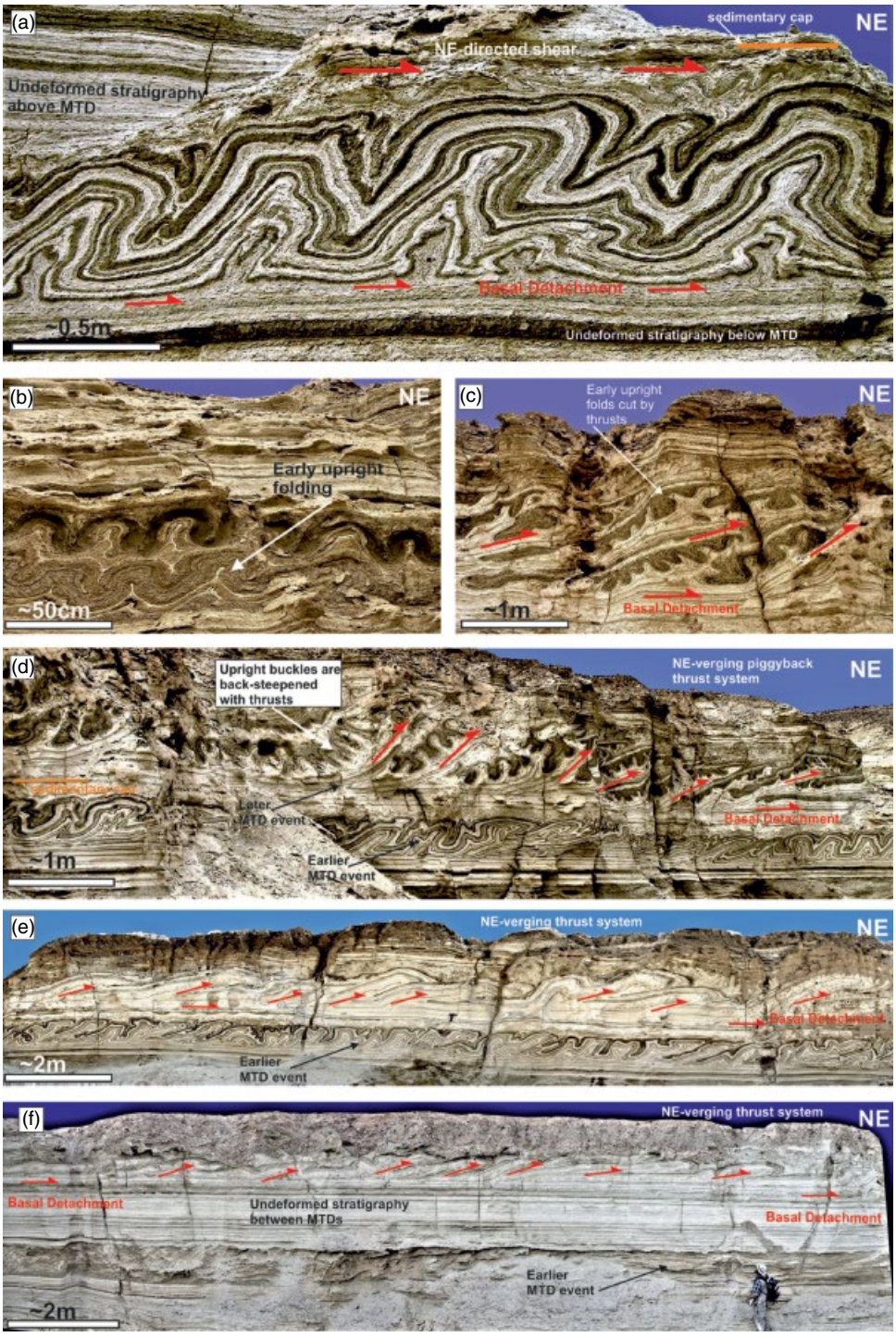


Figure 9.2 Photographs of folds and thrusts developed within MTDs of the Lisan Formation at Peratzim (N31°0449.6 E35°2104.2) (see Figure 9.1b for location). (a) Upright folds above a basal detachment that display northeast directed vergence and shear toward the basin. (b) Early upright "billow" folds that are subsequently carried on northeast verging thrusts (c). (d) Piggyback thrust sequence results in older thrusts (and the "billow" folds they carry) being progressively back-steepened. (e) Earlier (lower) MTD event dominated by folding, overlain by a northeast verging thrust system within a younger MTD. (f) Distinct northeast verging thrust system above a basal detachment that separates the MTD from undeformed stratigraphy below.

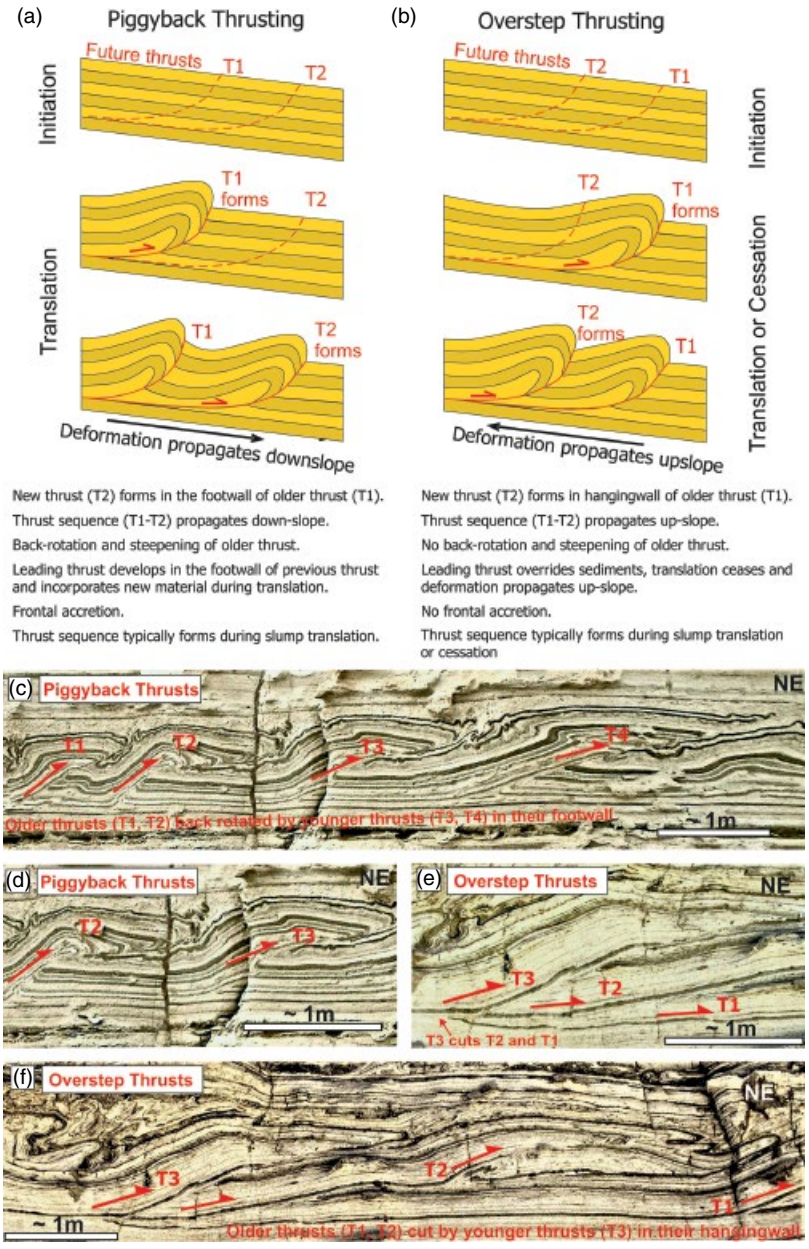


Figure 9.3 Summary cartoons of (a) piggyback thrust sequences versus (b) overstep thrust sequences. The schematic drawings show where future thrusts (T) may form during MTD initiation and their subsequent development in the translation and cessation phases of MTD movement. Text highlights the main differences between the two sequences and the direction of thrust propagation. (c) Example of piggyback thrusting from Peratzim, with (d) showing enlarged detail, where older thrusts (T1, T2) are back-steepened by younger thrusts (T3, T4) forming beneath them. (e) Example of overstep thrusting from Peratzim, with (f) showing enlarged detail, where older thrusts (T1, T2) are cut by younger thrusts (T3) forming above them.

may be supported by (a) systematic increases in displacement across older imbricates in the thrust system, whereby older thrusts continue to move and therefore accumulate the greatest displacement, and (b) bridging "shortcut" faults that develop below folded detachments (Alsop et al., 2018). Backthrusts that are truncated by forethrusts become immediately inactive and therefore display less displacement during synchronous thrusting (Figure 9.4b). In addition, oversteepened back thrusts indicate that basinward directed movement continued upslope of the backthrusts, and this suggests synchronous movement (e.g., Alsop et al., 2017b). Based on modeling, Liu and Dixon (1995, p. 885) note that "early formed thrusts continue to accumulate displacement even while new ones are

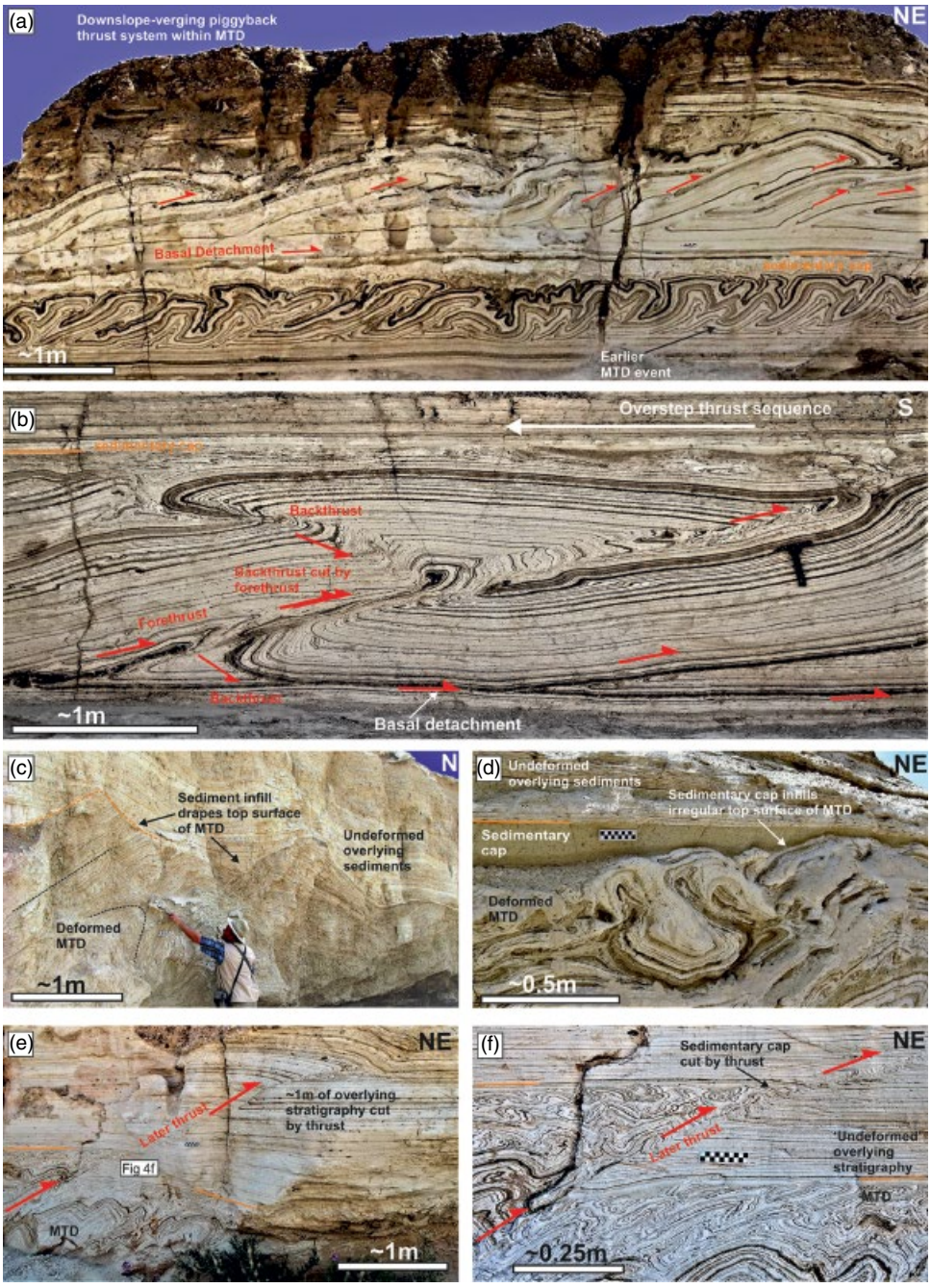


Figure 9.4 Photographs of folds and thrusts developed within MTDs of the Lisan Formation. (a) Earlier MTD event dominated by folding, overlain by a northeast verging piggyback thrust system within a younger MTD at Peratzim (refer to Figure 9.2e). (b) Southerly directed forethrust that cuts an older, underlying backthrust to define an overstep thrust sequence at Zin (N31.00615, E35.26342) (see Figure 9.1b for location). (c) Example of infilling of MTD top surface topography by later sedimentation at Almog (N31°4751.8 E35°2715.3) (see Figure 9.1b for location). (d) Sedimentary "cap" that infills the irregular top surface of the underlying and folded MTD at Peratzim. (e, f) Later thrust that cuts an MTD, together with ~1 m of overlying stratigraphy at Peratzim. The close-up photograph (f) clearly shows the younger thrust displacing the sedimentary cap, demonstrating that it represents a later "event" associated with reworking of the MTD.

nucleating." Thus, strict piggyback or overstep sequences are not necessarily supported by modeling studies, and a more relaxed approach to thrust sequencing may be required.

Analysis of larger-scale MTDs is generally based on seismic analysis, with Jolly et al. (2016, p. 74) describing a 40 km transect from the deepwater Niger delta and noting that "there is no evidence for simple forward-propagating (or piggyback) thrusting as is often predicted for fold and thrust belts." This corroborates earlier work by Corredor et al. (2005) from the same area who used stratigraphic relationships to suggest that forward propagation (piggyback), backward propagation, and coeval thrusting could all develop.

If thrusts develop during translation of the MTDs, then both piggyback and overstep sequences may form (Figure 9.3a, b). The development of piggyback thrust sequences during the translation of the MTD is different to previous models, which suggested that thrusts were generated much later during cessation of movement (e.g., Farrell, 1984; Strachan, 2008) and involve an overstep sequence as contraction propagates back upslope through the MTD (Alsop and Marco, 2011). Conversely, thrusting which forms during cessation of downslope movement generates contractional strain that propagates back up the slope from the toe and will therefore only generate overstep or out-of-sequence thrusts that will still typically verge downslope toward the basin (Alsop et al., 2018).

9.4. ANALYZING REWORKING TRIGGERED BY MULTIPLE SEISMIC EVENTS WITHIN INDIVIDUAL MTDS

A number of separate MTD horizons are observed within the Lisan Formation indicating several discrete failure "events." This deformation is considered to be triggered by earthquakes associated with seismicity along the Dead Sea Fault. Each individual MTD horizon within the Dead Sea Basin is overlain by a sedimentary "cap" deposited out of suspension following the seismically triggered failure event (Figure 9.4c, d). These "mixed" detrital and aragonite units, which may be up to 30 cm thick, comprise mud, silt, sand, and millimeter-scale fragments that infill irregularities along the top surface of the underlying MTD (Alsop et al., 2019) (Figure 9.4d). They immediately postdate the failure event that created the MTD and therefore form a natural "bounding surface" that separate the deformed sediments below from overlying non-deformed horizons. Sedimentary caps are not therefore deformed by the underlying MTD event that created them.

However, sedimentary caps may be reworked by later deformation associated with subsequent seismic events, suggesting that individual MTDs may hide more than one seismic event (Alsop et al., 2016). In some cases within the Lisan Formation, later thrusts cut the cap, and together with a further ~1 m of overlying stratigraphy, comprising aragonite-rich laminae that are deposited at a rate of ~1 mm/year (Prasad et al., 2009) (Figure 9.4e, f). New deformation that significantly postdates the underlying MTD cannot be directly associated with aftershocks or "settling" linked to the original earthquake and therefore represent multiple failure events within the individual MTD. Furthermore, MTDs that have previously been shown to be created by a double seismic event are generally thicker and marked by a greater downslope translation, compared to the immediately overlying and underlying MTDs (Alsop et al., 2016). Thus, some MTDs may conceal more than one seismic event, meaning that simple counting of deformed intervals may significantly underestimate seismic recurrence intervals. The recognition that up to 10% of MTDs may be reworked by younger seismically triggered events suggests that in some cases, the seismic recurrence interval may be shorter than previously estimated (Alsop and Marco, 2011).

9.5. ANALYZING CONTRACTIONAL STRUCTURES THAT ARE HIDDEN ON SEISMIC IMAGES

Theoretically, the amount of shortening in the downslope contractional portions of MTDs should be equivalent to, and balance, the degree of extension recorded in the upslope domain (e.g., Farrell, 1984). However, seismic sections across gravity-driven fold and thrust belts forming offshore MTDs frequently do not balance, with the amount of shortening being up to 40% less than extension measured in the upslope domain (e.g., Butler and Paton, 2010). There are a number of reasons why contraction and extension may not balance within MTD systems.

Firstly, although 40% shortening is recorded within fold and thrust systems at Peratzim, there is a 10% reduction in the amount of shortening taken up by folding and thrusting along individual thrusts (Alsop et al., 2017a). This led Alsop et al. (2017a) to suggest that heterogeneous lateral compaction increases toward the surface by ~10% and is in accord with similar estimates made by Butler and Paton (2010). This may reflect the fact that sediment toward the top of the depositional pile is more susceptible to horizontal shortening and lateral compaction during MTD movement, as it originally suffered less compaction and dewatering during limited overburden loading close to the surface.

Secondly, upright folding is interpreted to be rotated along back-steepened thrusts, indicating that it represents an early phase of layer-parallel shortening that predates thrusting (Alsop and Marco, 2011; Alsop et al. 2016) (Figure 9.2c, d). These relatively small-scale contractional

structures, with amplitudes of <2 m, may be difficult to identify on seismic sections as they are below the limits of seismic resolution.

Thirdly, estimates of upslope extension may be inaccurate due to variation in the nature and lithology of sediments being deformed closer to the upslope margin. Within Peratzim, there is an increasing detrital input toward the upslope margin, due to sediment sourced from wadi flood events. It has been suggested that extension associated with MTD translation may be partially hidden within these detrital-rich units by ductile thinning and attenuation (Alsop et al., 2016).

Fourthly, normal faults within MTDs define conjugate systems that strike parallel to the dip of the paleoslope (Alsop and Marco, 2011). Such conjugate faults indicate a component of non-plane strain deformation associated with transport-normal extension. Such "out-of-plane" movement will clearly complicate (if not negate) efforts to "balance" contraction and extension along an assumed transport-parallel section. Collectively, these observations of layer-parallel compaction, early small-scale folding, variable mechanical stratigraphy, and out-of-plane movement may provide an explanation as to why some seismic sections across basin-scale MTDs fail to balance.

9.6. ANALYZING THE EXTERNAL GEOMETRY OF MTDS AROUND THE DEAD SEA BASIN

9.6.1. Do Frontally Confined or Frontally Emergent Models Best Constrain the Bulk Geometry of MTDs?

MTDs may be divided into two categories: frontally emergent, where they translate downslope over undeformed stratigraphy and typically terminate with a distinct (emergent) thrust to form surface topography, or frontally confined, where they do not overrun downslope stratigraphy and therefore fail to create significant topographic relief (Frey-Martinez et al., 2006). Within the Dead Sea Basin, the downslope toes of MTDs do not overrun undeformed strata and are not therefore frontally emergent (Alsop et al., 2016, 2018). In detail, the toes of MTDs within the Lisan Formation are marked by upright fold trains that diminish in amplitude downslope before passing directly into undeformed beds (Alsop et al., 2016) (Figure 9.5a–c). As such, they are best described as open-ended toes (a variant of frontally confined systems) in which the apparently undeformed strata form a "soft" buttress that impedes further downslope movement (Alsop et al., 2016, 2018). Given that MTDs in the Dead Sea Basin do not terminate downslope with a distinct (emergent) thrust, but rather with upright folds in a more diffuse boundary, then significant contraction and lateral compaction could be potentially missed from analysis of seismic sections through offshore MTDs.

9.6.2. Do Critical Taper Models Constrain the Bulk Geometry of MTDs?

The "critical taper" model (e.g., Davis et al., 1983; Dahlen, 1990; Koyi, 1995) is generally applied to orogenic belts, where wedges of material are driven up a gentle underlying detachment by compression acting behind a buttress during collisional tectonics. Such modeling of critical tapers has also been applied to other settings such as accretionary complexes, and its potential role in MTDs is debated (e.g., see Bilotti and Shaw, 2005; Frey-Martinez et al., 2006; Morley, 2007; Morley et al., 2011; Alsop et al., 2018). Thrusts terminate at the same upper level in MTDs of the Lisan Formation, meaning that they generally lack surface topography and do not define a critical taper. In detail, MTDs in the Lisan Formation may be traced downslope for ~500 m where they display negligible thickness variations and taper angles of just 0.19–0.38° (Alsop et al., 2016, 2017a) (Figure 9.5b). This is an order of magnitude less than angles of ~4° typically observed in accretionary complexes (e.g., Yang et al., 2016) and is considered a consequence of weak saturated sediments translating along low-friction basal detachments marked by high fluid pressures (Alsop et al., 2016, 2017a, 2017b, 2018). This pronounced weakness also results in extreme ratios of MTD thickness compared to their downslope extent, with these ratios being significantly larger than in typical accretionary complexes (Alsop et al., 2017a). In summary, the critical taper model does not adequately explain the bulk MTD geometries developed around the Dead Sea Basin.

9.6.3. Do Dislocation Models Constrain the Bulk Geometry of MTDs?

Traditional dislocation models developed by Farrell (1984), where extension (E) is focused at the head and contraction (C) in the lower toe of an MTD, although broadly applicable in many situations (e.g., Martinsen and Bakken, 1990), are perhaps a gross simplification (Figure 9.6a). If cessation of MTD movement occurred first at the upslope head, then a late extensional strain wave (E2) propagates downslope (Figure 9.6b), whereas if cessation initiates at the downslope toe, then a contractional strain wave (C2) migrates upslope (Figure 9.6c). Within the Lisan Formation, contractional folds and extensional fractures and shears are developed in close proximity and overprint one another (Alsop and Marco, 2014) (Figure 9.5d–f). These spatial and temporal interrelationships between contractional and extensional structures led Alsop and Marco (2014) to propose that individual MTDs are composed of a series of second-order dislocation or "flow" cells that allow pockets of extension and contraction to develop anywhere in the MTD (Figure 9.6d, e). This "multi-cell flow model" involves coeval second-order

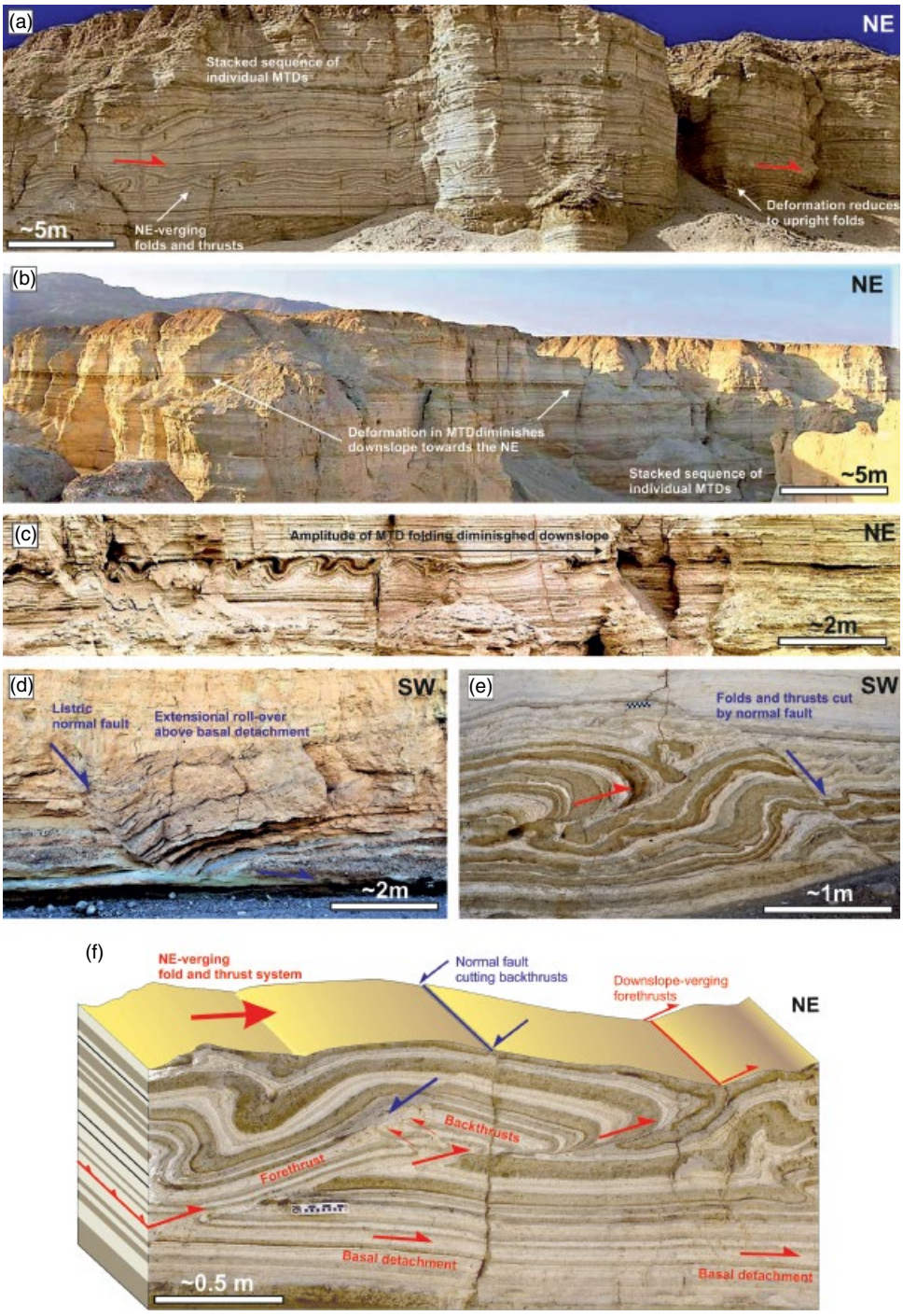


Figure 9.5 Photographs of MTDs within the Lisan Formation at Peratzim. (a, b) MTDs dying out downslope toward the NE, where we observe undeformed beds at the same stratigraphic interval. (c) Close-up photograph of inclined folds within an MTD, which diminish downslope into upright folds and eventually into relatively undeformed beds. (d) Listric fault that detaches on sands and muds within the Lisan Formation and results in extension of several meters. (e) Extensional normal fault cutting contractional folds and thrusts within a northeast translating MTD. (f) Photograph and interpreted top surface showing normal faults cutting contractional folds and thrusts.

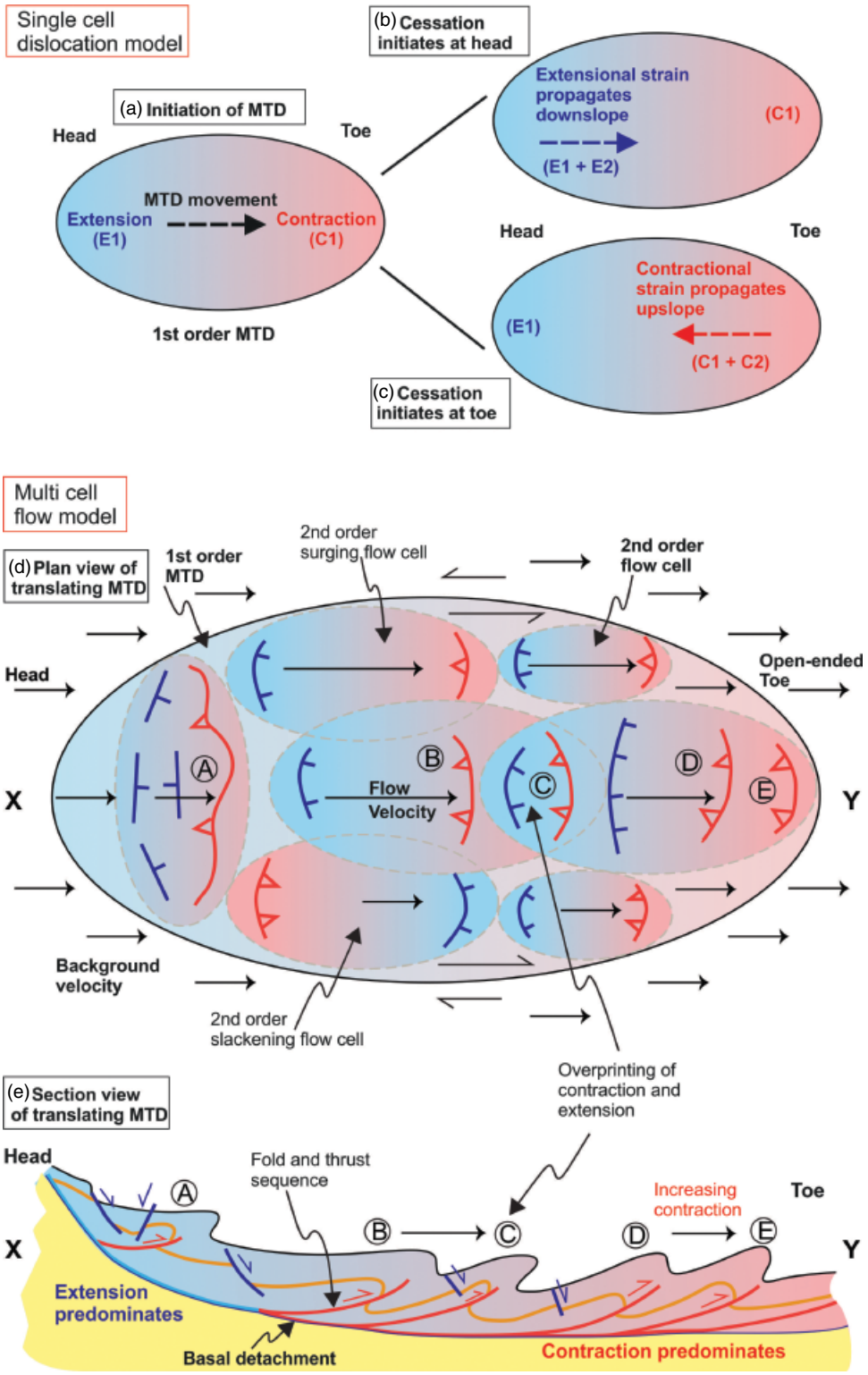


Figure 9.6 Schematic cartoon illustrating (a) the single-cell dislocation model of Farrell (1984) applied across an MTD (Source: Modified from Alsop and Marco (2014)). (a) During initiation of MTD movement, extension (E1) is concentrated at the head and contraction (C1) toward the toe of the MTD. (b) If subsequent cessation of MTD movement commences at the head, then additional extensional strain (E2) propagates downslope (broken arrow), whereas in (c), cessation initiates at the toe, resulting in additional contractional strain (C2) propagating back upslope. (d) Schematic plan view and (e) associated section view of the multi-cell flow model generated during translation of the MTD. Pockets of "surging" and "slackening" flow create second-order flow cells that interact with one another to create a range of extensional and contractional overprinting scenarios.

flow cells that interact with neighboring cells during translation of the MTD, resulting in extensional shears potentially overprinting folds (and vice versa) (Figure 9.6d, e). While the traditional single-cell dislocation model (e.g., Farrell, 1984) concentrates on structures generated during the initiation and cessation of the first-order MTD (Figure 9.6a–c), the multi-cell flow model focuses on second-order structures created during actual translation of the MTD (Figure 9.6d, e). Variations in "surging" or "slackening" flow within the MTD as it translates downslope may interact, resulting in extensional and contractional structures that are superimposed on one another in any order and in any position within the overall MTD. The strict spatial (toe and head) division of structures created during initiation and cessation of movement within traditional single-cell dislocation models is in general too simplistic and inadequate when compared to the reality observed at the outcrop scale in MTDs.

9.6.4. Do Models of Thrust Ramp Spacing Constrain the Bulk Geometry of MTDs?

The spacing between thrust ramps is defined by Liu and Dixon (1995) as the bed length between adjacent thrust ramps, when measured parallel to transport. This distance may be compared with the thickness of the stratigraphic section cut by the thrust, with Liu and Dixon (1995) noting that the spacing of thrust ramps is linearly related to the thickness of the section. Alsop et al. (2017a) noted that thicker thrust sequences are in general associated with larger thrust displacements in MTDs around the Dead Sea Basin. In detail, the average spacing of thrust ramps and the thickness of the thrust sequence in MTDs around the Dead Sea Basin display an approximate 5 : 1 ratio across a range of scales and also from piggyback sequences (e.g., Alsop et al., 2017a) and overstep sequences (e.g., Alsop et al., 2018).

These ratios are similar to those recorded in other MTDs (e.g., Gibert et al., 2005), offshore fold and thrust belts (e.g., Zalan, 2005; Butler and Paton, 2010), accretionary complexes, and orogenic belts (e.g., Morley et al., 2017). The frontally confined MTDs of the Dead Sea Basin may therefore be best interpreted using models of open-ended toes, which involve dislocation cells marked by multi-cell flow and regular thrust ramp spacing linked to bulk thickness of the MTD.

9.7. CONCLUSIONS

9.7.1. Analyzing Regional Patterns of MTD Movement Around the Dead Sea Basin

The Dead Sea Basin provides an ideal "controlled" case study where direct observations can be made at −425 m below global sea level to test the robustness of slump fold analysis to determine MTD transport directions. We have recognized a large-scale radial system of MTD movement centered on the Dead Sea depocenter. MTD transport directions vary by >90° along the ~100 km western shoreline of the Dead Sea, from southeast directed movement in the north to more northeast directed translation in the south (Figure 9.1b). This permits a better understanding of the variability that may develop in MTD movement around a modern basin. It also allows a greater appreciation of the potential complexities generated in ancient basins, where uncertainties in the paleogeographic context, together with possible later tectonics, may hide original relationships.

9.7.2. Analyzing Structural Sequences During Internal Evolution of MTDs

The progressive evolution of MTDs may be categorized into initiation, translation, cessation, relaxation, and compaction phases of deformation. Deformation may become most evolved where slope failure initiates and MTD movement commences. The implication is that many MTDs display the greatest deformation in the central area, and this diminishes toward the leading edge where MTD displacement may still be initiating. A variety of structural sequences may be observed, ranging from piggyback thrust sequences, where younger thrusts form sequentially downslope, to overstep thrust sequences, where newer thrusts propagate in an upslope direction (Figure 9.3a, b and 9.4a, b). Both of these broad sequences may themselves display aspects of synchronous thrusting, where older thrusts continue to move and therefore accrue larger displacements, while new thrusts develop. This overall variation in displacement across imbricates during synchronous thrusting may be resolvable in seismic sections and therefore represents a potential test of synchronous thrusting within large-scale MTDs.

9.7.3. Analyzing Reworking Triggered by Multiple Seismic Events Within MTDs

Individual MTDs are directly overlain by thin (up to 30 cm) sedimentary caps that are deposited out of suspension and infill relief on the MTD surface following the slope failure event. Where such sedimentary caps are themselves folded and displaced by thrusts, then subsequent deformation must have occurred (Figure 9.5e, f). Such later thrusts may also cut up to ~1 m of overlying, otherwise undeformed stratigraphy, indicating that this "event" was ~1000 years later and unrelated to aftershocks from the original failure event. Thus, outcrop studies around the Dead Sea Basin have provided detailed observations and criteria that MTDs may be reworked by

younger seismic events, meaning that in some ~10% cases, earthquake "events" may have been miscounted and the seismic recurrence interval may be shorter than realized.

9.7.4. Analyzing Contractional Structures That Are Hidden on Seismic Images

In a number of cases, contractional strain is typically found to be "missing" when attempts are made to balance large-scale structures in gravity-driven MTDs. An increase in heterogeneous lateral compaction toward water-rich sediments near the sediment surface together with upright folding that represents an early phase of layer-parallel shortening (e.g., Figure 9.2b–d) may help explain some of this contraction that is apparently not observed in seismic sections. In addition, conjugate normal faults that strike parallel to the dip of the paleoslope indicate a component of non-plane strain deformation associated with "out-of-plane" movement. This clearly complicates balancing and may help account for some of the "hidden" shortening.

9.7.5. Analyzing the External Geometry of MTDs Around the Dead Sea Basin

MTDs in the Dead Sea Basin are best described as having open-ended toes (a variant of frontally confined) in which further downslope movement is impeded by apparently undeformed strata that forms a "soft" buttress. Thrusts typically terminate at the same upper level in these MTDs, meaning that they generally lack surface topography and do not define pronounced critical tapers. As such, critical taper angles in MTDs may be an order of magnitude less than those in accretionary complexes, and the critical taper model does not therefore adequately explain the bulk MTD geometries developed around the Dead Sea Basin. Traditional dislocation models, where extension is focused at the head and contraction in the lower toe of an MTD, are a gross simplification and also not directly applicable to the Dead Sea Basin. Observations that contraction and extension may overprint one another at any positon within an MTD suggest that second-order flow cells may locally interact with one another and are linked to "pockets" of "surging" or "slackening" flow during overall downslope translation of the MTD (Figure 9.6d, e). Thrust sequences within MTDs follow established patterns, with the spacing of thrust ramps linearly related to the thickness of the section to define an approximate 5 : 1 ratio across a range of scales. In summary, the MTDs in the Lisan Formation around the Dead Sea Basin are triggered by seismic events, may be facilitated by mechanical heterogeneity linked to detrital-rich horizons, and are ultimately controlled by the paleoslope orientation.

ACKNOWLEDGMENTS

RW was supported by the Israel Science Foundation (ISF grant no. 868/17). SM acknowledges the Israel Science Foundation (ISF grant no. 1645/19). TL acknowledges the Israeli government GSI DS project 40706. We would like to thank the two anonymous reviewers and the editors for their constructive comments.

REFERENCES

Agnon, A., Migowski, C., & Marco, S. (2006). Intraclast breccia layers in laminated sequences: recorders of paleo-earthquakes. In Y. Enzel, A. Agnon, & M. Stein (Eds.), *New frontiers in Dead Sea paleoenvironmental research, Geological Society of America Special Publication* (pp. 195–214). Boulder, CO: Geological Society of America.

Almagor, G., & Garfunkel, Z. (1979). Submarine slumping in continental margin of Israel and Northern Sinai. *American Association of Petroleum Geologists Bulletin*, *63*, 324–340.

Alsop, G. I., & Marco, S. (2011). Soft-sediment deformation within seismogenic slumps of the Dead Sea Basin. *Journal of Structural Geology*, *33*, 433–457.

Alsop, G. I., & Marco, S. (2012a). A large-scale radial pattern of seismogenic slumping towards the Dead Sea Basin. *Journal of the Geological Society*, *169*, 99–110.

Alsop, G. I., & Marco, S. (2012b). Tsunami and seiche-triggered deformation within offshore sediments. *Sedimentary Geology*, *261*, 90–107.

Alsop, G. I., & Marco, S. (2013). Seismogenic slump folds formed by gravity-driven tectonics down a negligible subaqueous slope. *Tectonophysics*, *605*, 48–69.

Alsop, G. I., & Marco, S. (2014). Fold and fabric relationships in temporally and spatially evolving slump systems: A multicell flow model. *Journal of Structural Geology*, *63*, 27–49.

Alsop, G. I., Marco, S., Levi, T., & Weinberger, R. (2017a). Fold and thrust systems in Mass Transport Deposits. *Journal of Structural Geology*, *94*, 98–115.

Alsop, G. I., Marco, S., Weinberger, R., & Levi, T. (2016). Sedimentary and structural controls on seismogenic slumping within Mass Transport Deposits from the Dead Sea Basin. *Sedimentary Geology*, *344*, 71–90.

Alsop, G. I., Marco, S., Weinberger, R., & Levi, T. (2017b). Upslope-verging back thrusts developed during downslope-directed slumping of mass transport deposits. *Journal of Structural Geology*, *100*, 45–61.

Alsop, G. I., Weinberger, R., & Marco, S. (2018). Distinguishing thrust sequences in gravity-driven fold and thrust belts. *Journal of Structural Geology*, *109*, 99–119.

Alsop, G. I., Weinberger, R., Marco, S., & Levi, T. (2019). Identifying soft-sediment deformation in rocks. *Journal of Structural Geology*, 125, 248–255. https://doi.org/10.1016/j.jsg.2017.09.001

Alsop, G.I., Weinberger, R., Marco, S., Levi, T. (2019a). Folding during soft-sediment deformation. Geological Society Special Publication, Bond, C.E. and Lebit, H.D. (Editors) Folding

and fracturing of rocks: 50 years since the seminal text book of J.G. Ramsay. doi.org/10.1144/SP487.1.

Arkin, Y., & Michaeli, L. (1986). The significance of shear strength in the deformation of laminated sediments in the Dead Sea area. *Israel Journal of Earth Sciences*, *35*, 61–72.

Basilone, L. (2017). Seismogenic rotational slumps and translational glides in pelagic deep-water carbonates. Upper Tithonian-Berriasian of Southern Tethyan margin (W Sicily, Italy). *Sedimentary Geology*, *356*, 1–14.

Begin, Z. B., Ehrlich, A., & Nathan, Y. (1974). *Lake Lisan, the Pleistocene precursor of the Dead Sea, Geological Survey of Israel Bulletin* (Vol. 63, pp. 30). Jerusalem, Israel: Geological Survey of Israel.

Bilotti, F., & Shaw, J. H. (2005). Deep-water Niger Delta fold and thrust belt modeled as a critical taper wedge: The influence of elevated basal fluid pressure on structural styles. *American Association of Petroleum Geologists Bulletin*, *89*, 1475–1491.

Boyer, S. E. (1992). Geometric evidence for synchronous thrusting in the southern Alberta and northwest Montana thrust belts. In K. McClay (Ed.), *Thrust tectonics* (pp. 377–390). London: Chapman and Hall.

Boyer, S. E., & Elliot, D. (1982). Thrust systems. *American Association of Petroleum Geologists Bulletin*, *66*, 1196–1230.

Butler, R. W. H., & Paton, D. A. (2010). Evaluating lateral compaction in deepwater fold and thrust belts: How much are we missing from "nature's sandbox"? *GSA Today*, *20*, 4–10. https://doi.org/10.1130/GSATG77A.1

Corredor, F., Shaw, J. H., & Bilotti, F. (2005). Structural styles in the deep-water fold and thrust belts of the Niger Delta. *American Association of Petroleum Geologists Bulletin*, *89*, 753–780.

Cruciani, F., Barchi, M. R., Koyi, H. A., & Porreca, M. (2017). Kinematic evolution of a regional-scale gravity-driven deep-water fold-and-thrust belt: The Lamu Basin case-history (East Africa). *Tectonophysics*, *712–713*, 30–44.

Dahlen, F. A. (1990). Critical taper model of fold- and thrust-belts and accretionary wedges. *Annual Reviews Earth Planetary Science*, *18*, 55–99.

Dahlstrom, C. D. A. (1970). Structural geology in the eastern margin of the Canadian Rocky Mountains. *Bulletin of Canadian Petroleum Geology*, *18*, 332–406.

Davis, D., Suppe, J., & Dahlen, F. A. (1983). Mechanics of fold-and-thrust belts and accretionary wedges. *Journal of Geophysical Research*, *88*(B2), 1153–1172.

de Vera, J., Granado, P., & McClay, K. (2010). Structural evolution of the Orange Basin gravity-driven system, offshore Namibia. *Marine and Petroleum Geology*, *27*, 223–237.

El-Isa, Z. H., & Mustafa, H. (1986). Earthquake deformations in the Lisan deposits and seismotectonic implications. *Geophysical Journal of the Royal Astronomical Society*, *86*, 413–424.

Farrell, S. G. (1984). A dislocation model applied to slump structures. *Ainsa Basin, South Central Pyrenees, Journal of Structural Geology*, *6*, 727–736.

Field, M. E., Gardner, J. V., Jennings, A. E., & Edwards, B. D. (1982). Earthquake-induced sediment failures on a 0.25° slope, Klamath River delta, California. *Geology*, *10*, 542–546.

Frey-Martinez, J., Cartwright, J., & Hall, B. (2005). 3D seismic interpretation of slump complexes: examples from the continental margin of Israel. *Basin Research*, *17*, 83–108.

Frey-Martinez, J., Cartwright, J., & James, D. (2006). Frontally confined versus frontally emergent submarine landslides: A 3D seismic characterisation. *Marine and Petroleum Geology*, *23*, 585–604.

Garcia-Tortosa, F. J., Alfaro, P., Gibert, L., & Scott, G. (2011). Seismically induced slump on an extremely gentle slope (<1°) of the Pleistocene Tecopa paleolake (California). *Geology*, *39*, 1055–1058.

Garfunkel, Z. (1981). Internal structure of the Dead Sea leaky transform (rift) in relation to plate kinematics. *Tectonophysics*, *80*, 81–108.

Garfunkel, Z. (2014). Lateral motion and deformation along the Dead Sea Transform. In Z. Garfunkel, Z. Ben-Avraham, & E. Kagan (Eds.), *Dead Sea transform fault system: Reviews* (pp. 109–150). Dordrecht, The Netherlands: Springer. https://doi.org/10.1007/978-94-017-8872-4

Gibert, L., Sanz de Galdeano, C., Alfaro, P., Scott, G., & Lopez Garrido, A. C. (2005). Seismic-induced slump in Early Pleistocene deltaic deposits of the Baza Basin (SE Spain). *Sedimentary Geology*, *179*, 279–294.

Gladkov, A. S., Lobova, E. U., Deev, E. V., Korzhenkov, A. M., Mazeika, J. V., Abdieva, S. V., et al. (2016). Earthquake-induced soft-sediment deformation structures in Late Pleistocene lacustrine deposits of Issyk-Kul lake (Kyrgyzstan). *Sedimentary Geology*, *344*, 112–122.

Haase-Schramm, A., Goldstein, S. L., & Stein, M. (2004). U-Th dating of Lake Lisan aragonite (late Pleistocene Dead Sea) and implications for glacial East Mediterranean climate change. *Geochimica et Cosmochimica Acta*, *68*, 985–1005.

Haliva-Cohen, A., Stein, M., Goldstein, S. L., Sandler, A., & Starinsky, A. (2012). Sources and transport routes of fine detritus material to the Late Quaternary Dead Sea Basin. *Quaternary Science Reviews*, *50*, 55–70.

Ireland, M. T., Davies, R. J., Goulty, N. R., & Moy, D. J. (2011). Thick slides dominated by regular-wavelength folds and thrusts in biosiliceous sediments on the Vema Dome offshore of Norway. *Marine Geology*, *289*, 34–45.

Jablonska, D., Di Celma, C., Tondi, E., & Alsop, G. I. (2018). Internal architecture of mass-transport deposits in basinal carbonates: A case study from southern Italy. *Sedimentology*, *65*, 1246–1276. https://doi.org/10.1111/sed.12420

Jolly, B. A., Lonergan, L., & Whittaker, A. C. (2016). Growth history of fault-related folds and interaction with seabed channels in the toe-thrust region of the deep-water Niger delta. *Marine and Petroleum Geology*, *70*, 58–76.

Kagan, E., Stein, M., & Marco, S. (2018). Integrated palaeoseismic chronology of the last glacial Lake Lisan: From lake-margin seismites to deep-lake mass transport deposits. *Journal of Geophysical Research: Solid Earth*, *123*, 2806–2824. https://doi.org/10.1002/2017jB014117

Korneva, I., Tondi, E., Jablonska, D., Di Celma, C., Alsop, I., & Agosta, F. (2016). Distinguishing tectonically- and gravity-driven synsedimentary deformation structures along the Apulian platform margin (Gargano Promontory, southern Italy). *Marine and Petroleum Geology*, *73*, 479–491.

Koyi, H. (1995). Mode of internal deformation in sand wedges. *Journal of Structural Geology*, *17*, 293–300.

Lewis, K. B. (1971). Slumping on a continental slope inclined at 1-4°. *Sedimentology*, *16*, 97–110.

Liu, S., & Dixon, J. M. (1995). Localization of duplex thrust-ramps by buckling: Analog and numerical modelling. *Journal of Structural Geology*, *17*, 875–886.

Lu, Y., Waldmann, N., Alsop, G. I., & Marco, S. (2017). Interpreting soft sediment deformation and mass transport deposits as seismites in the Dead Sea depocentre. *Journal of Geophysical Research: Solid Earth*, *122*(10), 8305–8325. https://doi.org/10.1002/2017JB014342

Lucente, C. C., & Pini, G. A. (2003). Anatomy and emplacement mechanism of a large submarine slide within a Miocene foredeep in the northern Appenines, Italy: A field perspective. *American Journal of Science*, *303*, 565–602.

Marco, S., Stein, M., Agnon, A., & Ron, H. (1996). Long term earthquake clustering: a 50,000 year paleoseismic record in the Dead Sea Graben. *Journal of Geophysical Research*, *101*, 6179–6192.

Martinsen, O. J., & Bakken, B. (1990). Extensional and compressional zones in slumps and slides in the Namurian of County Claire, Eire. *Journal of the Geological Society, London*, *147*, 153–164.

Morley, C. K. (1988). Out-of-sequence thrusts. *Tectonics*, *7*, 539–561.

Morley, C. K. (2007). Interaction between critical wedge geometry and sediment supply in a deepwater fold belt, NW Borneo. *Geology*, *35*, 139–142.

Morley, C. K., King, R., Hillis, R., Tingay, M., & Backe, G. (2011). Deepwater fold and thrust belt classification, tectonics, structure and hydrocarbon prospectivity: A review. *Earth Science Reviews*, *104*, 41–91.

Morley, C. K., von Hagke, C., Hansberry, R. L., Collins, A. S., Kanitpanyacharoen, W., & King, R. (2017). Review of major shale-dominated detachment and thrust characteristics in the diagenetic zone: Part I, meso- and macro-scopic scale. *Earth-Science Reviews*, *173*, 168–228.

Nuriel, P., Weinberger, R., Kylander-Clark, A. R. C., Hacker, B. R., & Cradock, J. P. (2017). The onset of the Dead Sea transform based on calcite age-strain analyses. *Geology*, *45*, 587–590.

Ortner, H., & Kilian, S. (2016). Sediment creep on slopes in pelagic limestones: Upper Jurassic of Northern Calcareous Alps, Austria. *Sedimentary Geology*, *344*, 350–363.

Owen, G. (1996). Experimental soft-sediment deformation: Structures formed by the liquefaction of unconsolidated sands and some ancient examples. *Sedimentology*, *43*, 279–293.

Prasad, S., Negendank, J. F. W., & Stein, M. (2009). Varve counting reveals high resolution radiocarbon reservoir age variations in palaeolake Lisan. *Journal of Quaternary Science*, *24*, 690–696.

Reis, A. T., Araújo, E., Silva, C. G., Cruz, A. M., Gorini, C., Droz, L., et al. (2016). Effects of a regional décollement level for gravity tectonics on late Neogene to recent large-scale slope instabilities in the Foz do Amazonas Basin, Brazil. *Marine and Petroleum Geology*, *75*, 29–52.

Scarselli, N., McClay, K., & Elders, C. (2016). Seismic geomorphology of Cretaceous megaslides offshore Namibia (Orange Basin): Insights into segmentation and degradation of gravity-driven linked systems. *Marine and Petroleum Geology*, *75*, 151–180.

Shani-Kadmiel, S., Tsesarsky, M., Louie, J. N., & Gvirtzman, Z. (2014). Geometrical focusing as a mechanism for significant amplification of ground motion in sedimentary basins: Analytical and numerical study. *Bulletin of Earthquake Engineering*, *12*, 607–625.

Sharman, G. R., Graham, S. A., Masalimova, L. U., Shumaker, L. E., & King, P. R. (2015). Spatial patterns of deformation and palaeoslope estimation within the marginal and central portions of a basin-floor mass-transport deposit, Taranaki Basin, New Zealand. *Geosphere*, *11*, 266–306.

Sneh, A., & Weinberger, R. (2014). *Major structures of Israel and Environs, Scale 1:50,000*. Jerusalem, Israel: Israel Geological Survey.

Sobiesiak, M., Alsop, G. I., Kneller, B. C., & Milana, J. P. (2017). Sub-seismic scale folding and thrusting within an exposed mass transport deposit: A case study from NW Argentina. *Journal of Structural Geology*, *96*, 176–191.

Strachan, L. J. (2008). Flow transformations in slumps: A case study from the Waitemata Basin, New Zealand. *Sedimentology*, *55*, 1311–1332.

Weinberger, R., Levi, T., Alsop, G. I., & Eyal, Y. (2016). Coseismic horizontal slip revealed by sheared clastic dikes in the Dead Sea basin. *Geological Society of America Bulletin*, *128*, 1193–1206.

Weinberger, R., Levi, T., Alsop, G. I., & Marco, S. (2017). Kinematics of Mass Transport Deposits revealed by magnetic fabrics. *Geophysical Research Letters*, *44*, 7743–7749.

Wells, J. T., Prior, D. B., & Coleman, J. M. (1980). Flowslides in muds on extremely low angle tidal flats, northeastern South America. *Geology*, *8*, 272–275.

Woodcock, N. H. (1976a). Ludlow Series slumps and turbidites and the form of the Montgomery Trough, Powys, Wales. *Proceedings of the Geologists Association*, *87*, 169–182.

Woodcock, N. H. (1976b). Structural style in slump sheets: Ludlow Series, Powys, Wales. *Journal of the Geological Society, London*, *132*, 399–415.

Woodcock, N. H. (1979). The use of slump structures as palaeoslope orientation estimators. *Sedimentology*, *26*, 83–99.

Yang, C. M., Dong, J. J., Hsieh, Y. L., Liu, H. H., & Liu, C. L. (2016). Non-linear critical taper model and determination of accretionary wedge strength. *Tectonophysics*, *692*, 213–226.

Zalan, P. V. (2005). End members of gravitational fold and thrust belts (GFTBs) in the deep waters of Brazil. In J. H. Shaw, C. Connors, & J. Suppe (Eds.), *Seismic interpretation of contractional fault-related folds. American Association of Petroleum Geologists, Seismic Atlas, AAPG Studies in Geology* (Vol. 53, pp. 147–156). Tulsa, OK: The American Association of Petroleum Geologists.

10

Eocene Mass-Transport Deposits in the Basque Basin (Western Pyrenees, Spain): Insights Into Mass-Flow Transformation and Bulldozing Processes

Aitor Payros and Victoriano Pujalte

ABSTRACT

Subaqueous mass-flow transformation has been considered to involve a series of steps (slide, slump, debris flow, and turbidity current). Recent studies have shown that other processes, such as reconcentration of turbidity currents and substrate entrainment (bulldozing), can interfere this evolution. To date, exactly how bulldozing operates has not been extensively studied. This paper aims to address this gap using as reference Eocene mass-transport deposits (MTDs). Mass-wasting processes destabilized shelfal and slope deposits, thus creating bipartite sediment gravity flows that moved toward the SE. The individual thickness of the MTDs ranges from 10 to 33 m, with an estimated minimum extent of 1.5×10^6 m^2 and average volume of 24×10^6 m^3. Four different types of MTDs have been identified, which allowed a facies model to be conceived. This model shows that the characteristics of the sedimentary processes switched from slides to slumps, which in turn eventually became debris flows. However, it shows that the transformation did not occur en masse and was not linear: bulldozing processes contributed to maintaining flow heterogeneity and even produced retrograde mass-flow transformation. The potential effects of these processes should be taken into account when determining the proximal or distal nature of other MTDs.

10.1. INTRODUCTION

Of the processes which can transport sediment into the deep sea, submarine mass flows are one of the most significant and can cause tsunamis and other threats to seafloor infrastructures (Talling et al., 2014; Moscardelli & Wood, 2016). Consequently, significant research has been carried out into the processes that trigger submarine mass flows and their downslope evolution. Given the intrinsic difficulties in monitoring submarine mass flows in situ, part of the research is based on deposits preserved on both the present-day seafloor and the geological record (e.g., Mutti et al., 1984; Mulder & Cochonat, 1996; Payros et al., 1999; Lucente & Pini, 2003; Wynn & Masson, 2003; Bull et al., 2009; Masson et al., 2010; Dykstra et al., 2011; Ogata et al., 2014; Tinterri & Tagliaferri, 2015).

Submarine mass flows (and consequent deposits) are generally regarded as part of a sequential process, including en masse transformation from slide to slump, from slump to debris flows, and eventually from debris flow to turbidity current (Hampton, 1972; Varnes, 1978; Mulder & Cochonat, 1996; Mohring & Marr, 2003; Strachan, 2008). However, this pattern can be affected by the reconcentration of turbidity currents, which creates debris flows (Talling et al., 2004; Pierce et al., 2018), or by extensive substrate entrainment (bulldozing), which causes an increase in mass-flow volume and density (Jackson, 2011; Van der Merwe et al., 2011; Hodgson et al., 2018).

Department of Stratigraphy and Paleontology, University of the Basque Country (UPV/EHU), Bilbao, Spain

Submarine Landslides: Subaqueous Mass Transport Deposits from Outcrops to Seismic Profiles, Geophysical Monograph 246, First Edition. Edited by Kei Ogata, Andrea Festa, and Gian Andrea Pini.
© 2020 American Geophysical Union. Published 2020 by John Wiley & Sons, Inc.

There is a notable lack of information about how bulldozing occurs, how it affects downslope mass-flow transformation, and how it contributes to mass-flow heterogeneity. The aim of this study is to partially fill the gap by analyzing Eocene mass-transport deposits (MTDs) exposed in coastal outcrops of the western Pyrenean Basque Basin (Figure 10.1). Although the quality of these Eocene outcrops has been known since the early 20th century (see review in Payros et al. (2016)), sedimentological studies of the interbedded MTDs were not undertaken until the late 1990s (e.g., Pujalte et al., 1997). Furthermore, many issues regarding these deposits, such as their variations over space and time and their relationship with potential source areas, have not been addressed to date.

10.2. GEOLOGICAL SETTING

The Pyrenees is a collision mountain belt formed by the N-S convergence of the European and Iberian plates in Santonian-Miocene times (Muñoz, 2002). This orogenic

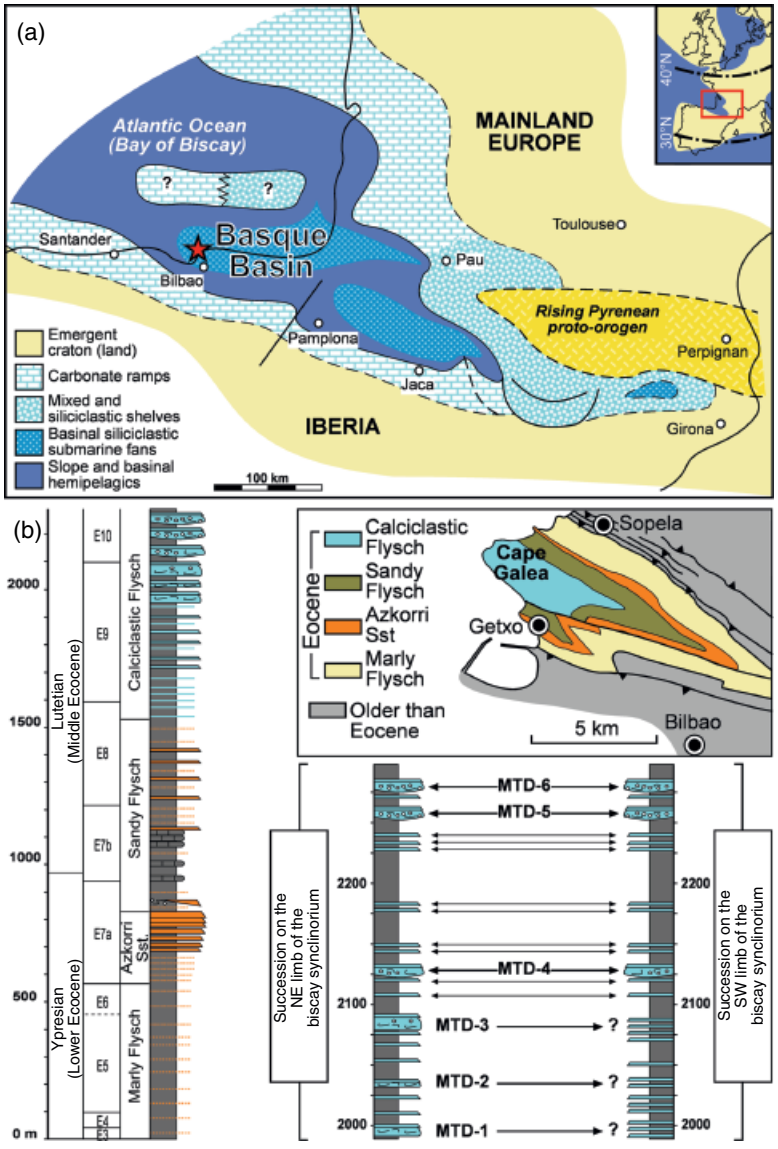


Figure 10.1 (a) Simplified paleogeographic maps of the Pyrenean area, showing the location of the study area (star). (b) Inset, geological map of the study area at the northwestern tip of the Biscay synclinorium in the Cape Galea area. Left, lithological log of the Eocene succession exposed on coastal outcrops of the northeastern limb of the Biscay synclinorium, showing chronostratigraphy (planktonic foraminiferal E scale refers to Wade et al. (2011)) and lithostratigraphy. Lower right, lithological logs of the upper part of the Calciclastic Flysch exposed on the northern and southern limbs of the Biscay synclinorium, showing the stratigraphic position and correlation of the six large-scale MTDs studied herein and other smaller-scale MTDs.

belt consists largely of a series of SE-NW trending fold-and-thrust systems. Superimposed on this general structural trend are some N-S folds and NE-SW faults, which influenced its fold-and-thrust development locally.

In Late Cretaceous and Paleogene times, Iberia was a microplate located between the larger African and European plates (Figure 10.1a). The Iberian plate progressively rotated anticlockwise and encroached on the southwestern margin of the European plate, resulting in a N-S collision and the uplift of the Pyrenean orogen (Muñoz, 2002). Tectonic uplift started in the northeastern part of the Iberian plate, creating a narrow interplate marine gulf which opened northwestward into the Atlantic Ocean at approximately 30–35°N paleolatitude (Pujalte et al., 2002).

The Basque Basin was located in the westernmost part of the Pyrenean gulf, where a large-scale siliciclastic submarine fan was sourced from the north and northeast (Pujalte et al., 2002; Payros et al., 2006; Hodgson & Wild, 2007). The studied early-middle Eocene succession is exposed in the western part of the province of Biscay, 15 km to the northwest of Bilbao, along both northern and southern limbs of a SE-NW trending synclinorium (Figure 10.1b). Inland exposures are generally poor, but the succession is well exposed on coastal cliffs, approximately 60 m high. The early-middle Eocene succession (>2300 m thick) is mostly made up of hemipelagic limestones and marls with intercalations of turbidites and other sediment gravity-flow deposits, which accumulated at approximately 1000–1500 m water depth (Payros et al., 2006). The MTDs analyzed in this study are included in the youngest stratigraphic unit, the so-called Calciclastic Flysch (Figure 10.1b). The Calciclastic Flysch is approximately 800 m thick on the northern limb of the synclinorium (Payros et al., 2006), but only the uppermost 350 m is continuously exposed on the southern limb due to the occurrence of several faults. The MTDs are restricted to the upper 550 m of the Calciclastic Flysch. According to available biostratigraphic information (Orue-Etxebarria et al., 1984), these deposits accumulated during planktonic foraminiferal biozones *Globigerinatheka subconglobata* and *Morozovella lehneri* (earliest part), equivalent to standard zones E9 and E10 (Wade et al., 2011). The planktonic/benthonic foraminiferal ratio varies between 70 and 92% (Orue-Etxebarria et al., 1984), which suggests accumulation at approximately 1000 m water depth (Payros et al., 2006).

10.3. SEDIMENTOLOGY OF THE CALCICLASTIC FLYSCH AND INTERCALATED MTDS

The Calciclastic Flysch is composed of thin-bedded hemipelagic marls and limestones with abundant intercalations of calciclastic sediment gravity-flow deposits. Most of the latter correspond to mixed sandy-bioclastic turbidites with individual thicknesses ranging from just a few centimeters to up to 2 m. Most of the turbidites show divisions T(a)-b-c of the Bouma sequence (Bouma, 1962), but some are massive, all generally being capped by a homogeneous marl layer (divisions Td-e of the Bouma sequence). They most commonly show plane-parallel geometry, but some display erosive bases. Turbidite amalgamation is rare, with no evidence of large-scale vertical arrangement of facies observed. Paleocurrent indicators (mainly sole marks and cross-lamination) are scarce, with ambiguity in few directed toward the southeast (average, 120°; range, 75–180°; N, 14).

Intercalated throughout the turbidite succession are abundant MTDs (Figure 10.1b). A minimum of 26 packages from the southern limb of the Biscay synclinorium and 21 packages from the northern limb can be classified as MTDs. On average MTD packages are between 2 and 5 m thick and show a tripartite internal organization. This tripartite structure can be divided into (i) a basal interval composed of contorted and fragmented strata embedded in a marly matrix with variable amounts of limestone and marl clasts; (ii) graded, mixed sandy-bioclastic layers which in some cases show Bouma divisions a, b, and c; and (iii) a cap of marl attributable to Bouma's divisions d and e. These characteristics suggest that downslope moving mass flows (debris flows and/or slumps) were overridden by high-density turbidity currents (Hampton, 1972; Mulder & Cochonat, 1996; Mohring & Marr, 2003).

Six of the MTDs exposed on the northern limb of the synclinorium are notable due to their significantly greater thickness (in excess of 10 m) and constitute the basis for this study. The youngest three large-scale MTDs, along with the smaller-scale MTDs and turbidites interbedded in the upper part of the stratigraphic succession, can also be identified on the southern limb of the synclinorium, providing the opportunity to analyze their lateral variations (Figure 10.1b). However, the three large-scale MTDs identified in the lower succession of the northern limb cannot be conclusively correlated with specific layers of the southern limb, due to the presence of numerous MTDs. The basal intervals of the large-scale MTDs show different sedimentological characteristics according to their position in the stratigraphic succession. This suggests that the large-scale MTDs may have been accumulated by different mechanisms or under different circumstances.

10.3.1. MTD-1 and MTD-2

10.3.1.1. Description

These two MTDs, 10 and 12 m thick, respectively, show a similar internal structure on the northern limb of the Biscay synclinorium, with open folds and generally laterally continuous internal beds. They are separated by a

50 m thick succession which is mainly composed of plane-parallel, thin-bedded limestones, marls, and turbidites, but also includes two small-scale MTDs (Figure 10.1b). It was not possible to determine which, if any, of the small-scale MTDs found in the equivalent stratigraphic interval of the southern limb correspond to MTD-1 and MTD-2. In addition, MTD-2 is not physically accessible on the northern limb of the synclinorium, with exposure restricted to the upper cliff section. Conversely, MTD-1 is well exposed both on the cliff and the wave-cut platform (Figure 10.2). Consequently, the following description is mainly based on the features displayed by MTD-1.

The main body of MTD-1 is composed of laterally continuous beds, similar to those in the background deposits of the Calciclastic Flysch, which are folded and faulted locally (Figure 10.2). The area with the greatest evidence of internal deformation is located in the wave-cut platform. In the central part of the exposure, the beds describe a very gentle syncline, approximately 30 m wide along strike. To the northwest, this syncline turns into a west verging, small-scale, low-angle blind thrust, the throw of which decreases upsection. This attenuation results in the transformation of the thrust into an overturned anticline in the middle part of the deformed sediment mass and a disharmonic, close to upright anticline in the uppermost part. The top of this anticline is partly truncated at the upper surface of MTD-1, which is flat. Further to the NW, the low-angle blind thrust and overlying anticline progressively smooth and turn into mostly flat-lying beds. To the southeast of the central syncline, the main body of MTD-1 is characterized by a stack of several SE verging low-angle thrusts which, in some cases, transform laterally into disharmonic anticlines (Figure 10.2). Oblique aerial views show that the stacked thrust sheets pass further to the SE (in the cliff outcrop)

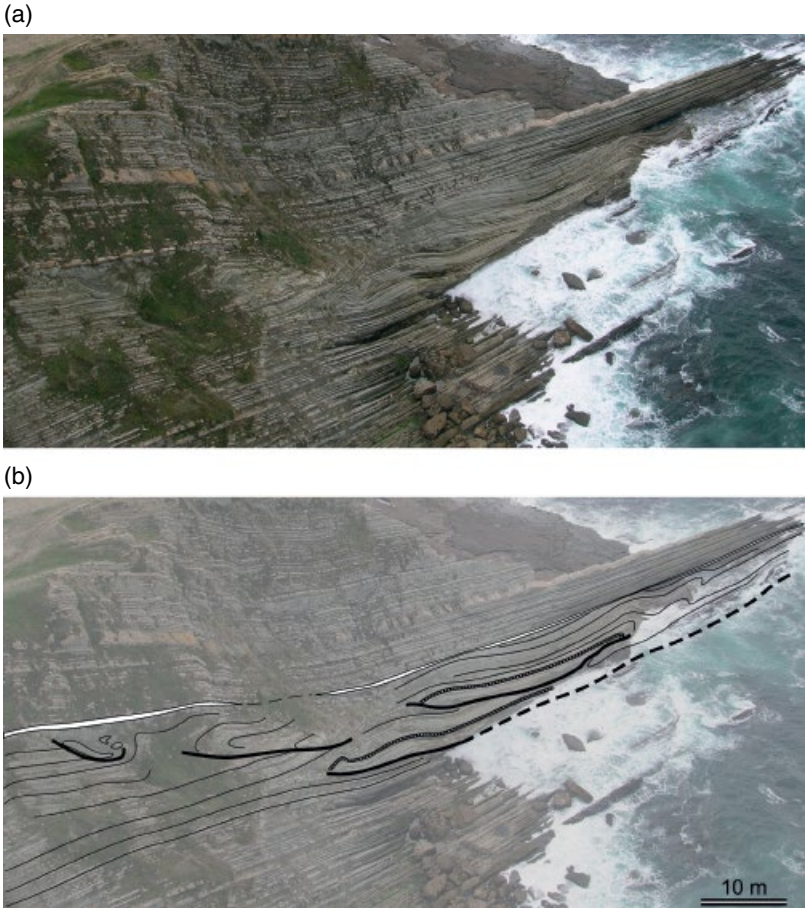


Figure 10.2 (a) Oblique aerial view of the succession containing MTD-1 on the northern limb of the Biscay synclinorium. Bedding strike is SE-NW (from lower left to upper right) and bed younging upward. (b) Interpreted sketch of MTD-1, showing distribution of key beds (patterned lines) and faults (thick solid lines); the top white bed is its capping turbidite. Beds included in MTD-1 are gently folded and turn into flat-lying beds laterally. Note that thrust-and-fold vergence is toward the SE on the left but toward the NW on the right.

into packages of beds that are parallel to general bedding. The lateral transition from thrust to undeformed beds occurs at different positions depending on the stratigraphic level within the MTD, the transition zone being located progressively more to the southeast upsection.

The upper part of MTD-1 corresponds to a calcarenite-marl couplet, the thickness of the calcarenite varying laterally between less than 10 and 50 cm. It is an erosive-based, normally graded, sandy-bioclastic layer with abundant larger foraminifera (e.g., *Nummulites*, orthophragminids, etc.) and some marly clasts in its lower part. The calcarenite is gradually overlain by a homogenous marl bed.

10.3.1.2. Interpretation

MTD-1 and MTD-2 show evidence of relatively mild internal deformation, as most component beds are just gently folded. However, deformation was more intense locally and resulted in the formation of low-angle blind thrusts and associated anticlines. The distribution of these structures in MTD-1 shows that the shear stress exerted during the downslope movement was laterally heterogeneous (Van der Merwe et al., 2011). Furthermore, the geometry of the SE verging structures suggests the influence of outward propagating compressional forces (Figure 10.2). Thus, the area affected by the deformation progressively increased upward, as the lowermost SE verging thrusts pass laterally into undeformed deposits. This allows definition of a complex but generally concave-up basal shear zone across slope (Varnes, 1978; Bull et al., 2009). Overall, the main body of MTD-1 is interpreted as the deposit of either a slide or an incipient slump (Mulder & Cochonat, 1996).

The thrust on the NW segment of the exposure is west verging, whereas those found on the SE segment are SE verging (Figure 10.2). Two scenarios can explain the occurrence of opposing vergences within the same MTD. On the one hand, it is well known that MTDs typically display a curved, lobate frontal margin as a consequence of velocity differences in the central and marginal portions of the mass flow (Lucente & Pini, 2003; Frey-Martinez et al., 2006; Sawyer et al., 2012). Downslope expansion of the curved frontal margin of MTD-1 could have resulted in divergent compressional forces and formation of opposed-verging thrusts (Frey-Martinez et al., 2006; Bull et al., 2009; Alves, 2015). Alternatively, the opposing thrusts observed in MTD-1 could be marginal rather than forward directed structures. Laterally directed compression structures in the form of low-angle thrusts on the lateral margins of MTDs have previously been reported from seismic lines (Posamentier & Martinsen, 2011). In either scenario, the exposure of MTD-1 would be oblique to the true mass movement, implying that the prevalent downslope movement was toward the SSE.

The capping calcarenite-marl couplet was formed by a turbidity current (Bouma, 1962). The composition of the calcarenite suggests that the turbidity current was originally constituted of particles derived from shallow-water carbonate ramps (Payros et al., 1999, 2007, 2010) but was also capable of eroding and entraining marly material (both clasts and disaggregated) as it moved downslope. The overlying marl represents late-stage decantation from the diluted turbulent wake developed above the turbidity current (Bouma, 1962). The truncation of the anticlines in the MTD below the turbiditic deposit suggests that the activity of the mass flow and the turbidity current must have been virtually simultaneous. The turbidity current must have been energetic and voluminous, but the thickness of the resulting turbidite was comparatively reduced. This suggests that some of the sediment load was transported further downslope.

10.3.2. MTD-3

10.3.2.1. Description

MTD-3 was identified on the northern limb of the Biscay synclinorium (Figure 10.3). Several small-scale MTDs occur in the equivalent stratigraphic interval of the southern limb, but it cannot be stated which, if any, corresponds to MTD-3 (Figure 10.1b). Consequently, the following description is based exclusively on the features observed on the northern limb.

The main body of MTD-3 is 8.5 m thick and is composed of packages of folded and faulted strata (Figure 10.3). Three main thrusts can be identified, which dip toward the NW after tectonic restoration. The throw of the thrusts is small in the lower part of MTD-3, where the component strata are only slightly deformed. However, both the throw and deformation increase upward, the hanging-wall strata being greatly disaggregated in the upper part of the sediment mass. In addition to the main thrusts, some minor thrusts and antithetic normal faults also occur.

The three main thrusts delimit four different blocks in the sediment mass. Each block is characterized by the occurrence of a syncline and an anticline. These folds are well defined in the lower and middle part of the sediment mass, where the majority of the beds are thicker on the hinges than on the limbs, but the component strata are greatly disaggregated in the upper part (Figure 10.3). Most folds are overturned, but recumbent structures also occur, primarily in the lower part of the blocks. Although the continuity of successive folds is interrupted by thrusts and normal faults, reconstruction calculations show that fold wavelength is approximately 15 m and amplitude ranges from 4 to 5 m. After restoration for tectonic tilting, the axial planes dip toward the NW, indicating that prevalent fold vergence was toward the SE.

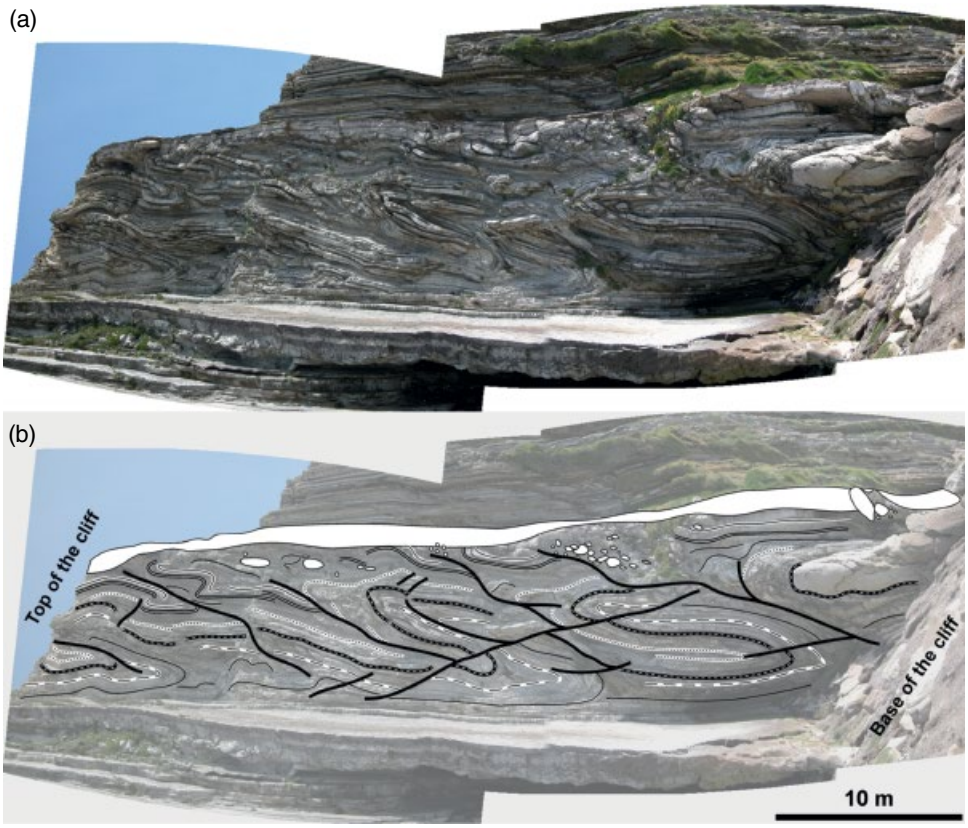


Figure 10.3 (a) Photomosaic of MTD-3 on the northern limb of the Biscay synclinorium. Note that the photograph has been rotated (beds dip toward the southwest). (b) Interpreted sketch of MTD-3, showing the distribution of key beds (patterned lines) and faults (thick solid lines); the top white bed is the capping turbidite. The main slump interval is composed of overturned synclines and anticlines separated by thrusts, all of which show vergence toward the SE. Bed fragmentation is greater in the upper part of the slump deposit, especially at the culmination of strata uplifted along thrusts.

The uppermost part of MTD-3 is an irregular-based and flat-topped calcarenite layer, the thickness of which varies laterally from 2.2 m to 50 cm (Figure 10.3). Locally, the lower part of the calcarenite layer contains pockets of dispersed, heterometric, angular to subrounded mudstone clasts, the largest of which almost reach the top of the bed and show imbrication toward the SE. The calcarenite is gradually overlain by a marl layer, approximately 0.5 m thick.

10.3.2.2. Interpretation

The mass of folded and faulted strata can be classified as a semi-coherent slump (Alsop & Marco, 2013). The bed thickening exhibited on many fold hinges and the thinning on the limbs are typical in slump-related structures (Jablonska et al., 2018). Slumps are generally characterized by beds that can be traced reliably along well-defined folds formed during weak-moderate deformation within coherent portions of the sediment mass. However, deformation can be more intense locally, resulting in semi-coherent slumps characterized by beds that become increasingly disrupted by discontinuities associated with thrusts and detachments within strongly deformed semi-coherent portions of the mass flow (Alsop & Marco, 2013). The dip of both thrusts and overturned axial planes in MTD-3 shows that the slump movement was toward the SE.

Variations in the intensity of deformation within MTD-3 were likely related to zones of variable shearing, which were in turn produced by different velocities within the mass flow, perhaps caused by local variations in slope gradient (Strachan, 2008; Jablonska et al., 2018). Local slump deceleration may have caused an upslope propagating compressional strain wave that resulted in progressive folding and thrusting. Synclines may have been associated with zones of slackening flow, whereas anticlines resulted from locally surging flow regimens. Subsequent flow deceleration may have resulted in increased compression and shear strain on the back limbs of the slump anticlines, which caused the formation of the main thrusts.

The occurrence of zones of relative acceleration and zones of slackening flow contributed to local disarticulation

of some beds within the slump. Internal deformation and bed disarticulation generally increased from the base to the top of the slump sheet (Figure 10.3). This arrangement indicates that intra-slump shear stress increased upward as flow velocity became faster (Allen, 1997). However, maximum disarticulation was concentrated at the culminations of the strata uplifted along thrust planes, suggesting that they were affected by maximum stretching and shearing at the top of the slump. This process may also have caused the imbrication observed in some of the clasts. These features confirm that the thrusts were not formed during slump cessation (e.g., Strachan, 2008) but during the active phase of the mass transport. An additional factor that controlled the intensity of bed disarticulation was the composition of the slumped strata. Multilayered heterogenous materials, which show different mechanical properties depending on the coherency of their components, are more easily disarticulated. The strata in the lower part of the MTD-3 slump sheet are mostly limestones, all of which were characterized by similar mechanical properties, thus hampering disarticulation. Conversely, the beds in the upper part of the slump sheet are composed of alternating limestones and marls, the contrast of which resulted in increased disarticulation. Bed fragmentation in the upper part of the slump could also have resulted from its dilution and transformation into a more fluidal flow type as a consequence of mixing with the overlying seawater (Strachan, 2008). The small antithetic normal faults in the slump mass were most likely created by extensional relaxation after the emplacement of the slump.

The overlying calcarenitic and marly layers capping MTD-3 are interpreted as turbiditic deposits (Bouma, 1962). Variations in the thickness of the calcarenite layer show that the distribution of the turbidity current was affected by the slump-related topography.

10.3.3. MTD-4

10.3.3.1. Description

The exposure of this MTD on the northern limb of the synclinorium (Figure 10.4) constituted the main basis for the preliminary sedimentological study carried out by Pujalte et al. (1997). The lowermost 12 m of MTD-4 (interval S1 of Pujalte et al. (1997)) consists of well-stratified, plane-parallel thin layers of limestones, marls, and turbidites, which show similar characteristics to those found throughout the Calciclastic Flysch (Figure 10.4). In the approximately ENE-WSW cliff section, the internal deformation of interval S1 is unclear, with all beds seemingly parallel to the general bedding. However, when seen in the NW-SE wave-cut platform, interval S1 is shown to be affected by a system of imbricated overlapping thrusts, suggesting duplex-style compression (Figure 10.4a). The horizontal distance between successive thrusts ranges from 3 to 6 m. Each thrust-bounded imbricated horse is composed of a 4 m thick succession that contains a 1 m thick marly bed at the base. This marly bed, which acted as the main detachment layer, corresponded to the Te interval of an underlying 4 m thick MTD. Following on from the observations in the wave-cut platform, a closer inspection of the cliff outcrop using high-resolution photographs showed that the apparently undeformed interval S1 is composed of a characteristic set of strata that is repeated at least five times in the vertical succession, each set being bounded at its base and top by thrusts that lie almost parallel to bedding (Figure 10.4c). When the tilted succession found in interval S1 is restored to its original horizontal position, its internal thrusts display surfaces that on average dip 32° toward the northwest (328°), therefore indicating synsedimentary compressive forces directed toward the southeast (148°).

The main body of MTD-4 is composed of a heterogeneous breccia, 15.6 m thick on the northern limb of the synclinorium and 23.4 m thick on the southern limb. Observations from the northern limb of the synclinorium (Pujalte et al., 1997) suggest that the breccia consists of two parts, the thicknesses of which vary laterally (Figure 10.4b). The lower breccia (interval S2 of Pujalte et al. (1997)) is characterized by heterometric clasts ranging from just a few centimeters to tens of meters. The smallest clasts in interval S2 are composed of both mudstones and calcarenites, which respectively resemble the hemipelagic and turbidite layers found throughout the Calciclastic Flysch, suggesting that the clasts were probably ripped up from there. The largest boulders are generally contorted and imbricated fragments of strata, most of which are composed of mudstones. However, the largest imbricated slab, which extends for 11 m upward from the base of interval S2 over a lateral distance of 32 m, is coherent and 2.8 m in thickness, comprising layers of all the lithologies found in the Calciclastic Flysch (calcarenitic turbidites and hemipelagic marls and limestones). This slab shows internal thrusts and is loosely coiled around an originally horizontal axis in the upper part of interval S2 (Figure 10.4b). At its lowermost end, this slab is rooted to, and overturned from, the 2.8 m thick succession of undeformed deposits underlying interval S2. A notable 40 cm thick marly bed below this 2.8 m thick succession constituted the detachment layer that allowed the partial removal of the coherent set of strata and its incorporation into the breccia. Therefore, the lower boundary of interval S2 is erosive, its relief reaching 3.8 m in the studied outcrop. When MTD-4 is restored to its original horizontal position, both the inclination of the erosive base of the breccia and its internal imbrication and thrusts show apparent dips toward the NW. This suggests that the deposit was affected by synsedimentary compressional forces with a component vector directed toward the SE.

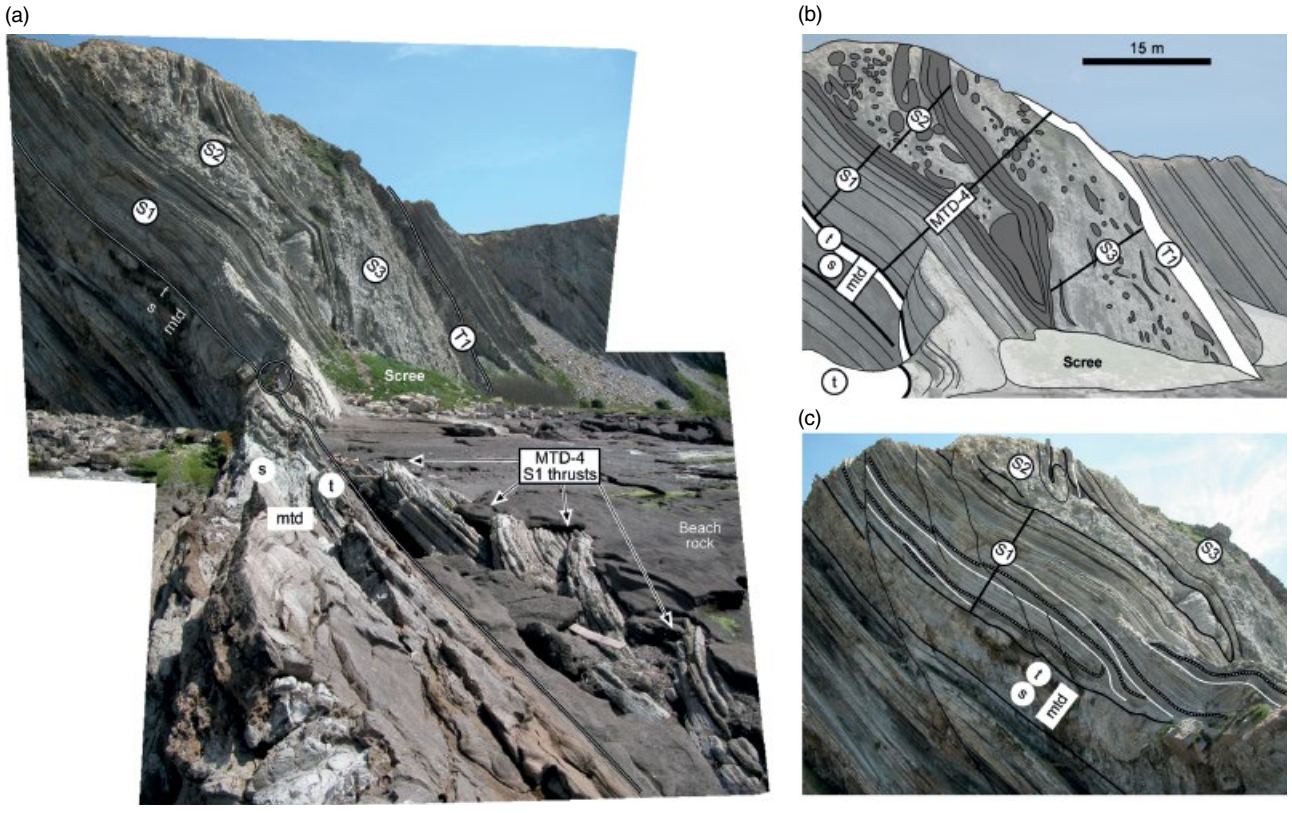


Figure 10.4 (a) Photomosaic of MTD-4 on the northern limb of the Biscay synclinorium (encircled people provide the scale; beds dip toward the southwest), showing the distribution of internal divisions S1, S2, S3, and T1 explained in the text (mtd refers to an underlying small-scale MTD composed of a basal "s" slump and an upper "t" turbidite). (b) Interpreted sketch of MTD-4 on the cliff section, showing that the uppermost beds of interval S1 (gray) were uplifted, overturned, and curled. (c) Interval S1 exposed at the cliff, showing the distribution of key beds (patterned lines) which reveal the occurrence of easily missed thrusts (white lines). However, the S1 thrusts are more clearly visible on the practically orthogonal wave-cut platform exposure (a).

The upper part of the MTD-4 breccia (interval S3 of Pujalte et al. (1997)) is matrix-supported with some randomly dispersed meter-sized boulders and fragments of contorted strata, which are mainly composed of mudstones similar to those in the hemipelagic limestone layers of the Calciclastic Flysch (Figure 10.4). However, the bulk of the S3 breccia is constituted of a marly matrix with centimeter-decimeter-sized clasts, including mudstones and calcarenites. Rhodoliths and *Nummulites* tests up to 3 cm in diameter also occur in the uppermost 6 m of the S3 breccia. In some cases, the *Nummulites* tests are concentrated on the surface of well-rounded mudstone clasts, which can therefore be classified as armored mud balls. Overall, a crude fining upward arrangement can be observed in the S3 breccia of MTD-4.

MTD-4 is capped by 2 m of a normally graded and crudely laminated calcarenitic layer (rudstone-packstone; division T1 of Pujalte et al. (1997)) and 3.4 m of homogeneous marls (division T2 of Pujalte et al. (1997)). The calcarenitic layer is almost exclusively constituted of *Nummulites* tests in the middle zone but can include marly soft clasts in the lower zone. Its base is sharp and slightly irregular. The correlative intervals on the southern limb of the synclinorium show very similar characteristics.

10.3.3.2. Interpretation

The imbricated thrusts in the duplex system of the S1 interval indicate displacement toward the SE under compressional forces (Figure 10.4a). Displacement of each of the imbricated horses in interval S1 was relatively short, and their internal deformation was mild, suggesting that compression and shear stress were relatively weak. It can be concluded that the thrusts of the S1 interval were created by the overload and shear stress of the downslope moving mass flow on the seabed (Van der Merwe et al., 2009, 2011; Watt et al., 2012). The shear stress reached a potential detachment layer located several meters below the seabed, thus triggering repetitive thrusting processes. The detachment layer was an especially thick plastic marl layer that corresponded to the Te interval capping a small-scale MTD. Whether the

significant thickness of this marl layer was sufficient to allow repetitive thrusting or whether the material had specific rheological characteristics that increased its ductility cannot be determined with the available data.

The orientation of the imbricated slabs in interval S2 coincides with that of the imbricated thrusts in interval S1, strongly suggesting that the same forces were responsible for all the compressional structures found within MTD-4. The lowermost part of the largest imbricated slab in interval S2 is attached to the underlying S1 succession (Figure 10.4b), showing that the slab was partially lifted from the substrate as a consequence of the shear stress exerted by the mass flow on the seabed. This process may have been facilitated by the occurrence of a relatively thick plastic marl layer in the underlying succession (Van der Merwe et al., 2011). Once the upstream tip of the slab was detached from the seabed and incorporated into the mass flow, the slab was pushed forward and upward, it was subsequently turned over, and it eventually acquired its characteristic imbrication. Furthermore, the upper part of the overturned and imbricated slab also became loosely coiled around an originally horizontal axis (Figure 10.4b), resembling the curls that are formed when a knife is pulled over a stick of butter. This shows that the sediment layers within the slab were cohesive but not fully lithified. The rolling of the upper part of the slab was a result of intra-flow rotational deformation, which in all likelihood was driven by the combined action of simultaneous vertical forces (gravity pulling downward) and horizontal forces (shearing as a consequence of a faster moving upper part of the flow) (Allen, 1997). Regardless of the flow dynamics, the fact that the overturned, imbricated, and partly folded slab in MTD-4 is attached to the underlying substrate allows interpretation of interval S2 as a coherent slump with evidence of incipient, partial transformation into debris flow. The orientation of all the compressional features produced by the shear stress of the flow demonstrates that mass-transport direction was toward the SE.

The matrix-supported S3 breccia represents a debris-flow deposit. The intraformational composition of most clasts (mainly hemipelagic mudstones) indicates that the debris flow was derived from the slope. However, the occurrence of bioclasts in the uppermost part of the S3 breccia strongly suggests that some mixing occurred between the debris flow and the overlying T1 calcarenitic layer. Furthermore, the finding of armored mud balls coated with *Nummulites* within the S3 breccia shows that the transport and accumulation of both the breccia and the calcarenite were partly simultaneous. Armored mud balls are formed when clay chunks are broken from the substrate and rolled downcurrent, acquiring "armor" as coarser particles are pressed into their soft exterior (Bandyopadhyay & Gupta, 1990; Chun et al., 2002). Therefore, the armored mud balls in MTD-4 were transported for some time and distance at the interface between the S3 debris flow and the overlying T1 calcarenite, where they became rounded and coated with *Nummulites*. Subsequently, the mud balls sank at least 6 m into the underlying muddy breccia. This gravity-driven process could have occurred either when the mass flow was still moving or after it froze. However, sinking during the active phase seems more plausible, as the downward displacement of the clasts would have been facilitated by shearing within and on top of the debris flow. The entrainment of sediment and water into the upper part of the debris flow resulted in relatively reduced viscosity and sediment strength, thus creating the conditions for gravity-driven vertical segregation of clasts according to their size (Mohrig et al., 1998; Payros et al., 1999; Strachan, 2008). These characteristics suggest that the S3 breccia underwent relatively prolonged downslope transport.

The T1 and T2 divisions of MTD-4 resemble the calcarenitic and marly layers capping older MTDs and are interpreted as turbiditic deposits (Bouma, 1962; Pujalte et al., 1997).

10.3.4. MTD-5 and MTD-6

10.3.4.1. Description

MTD-5 and MTD-6 are exposed at the core of the Biscay synclinorium, being separated from each other by 10 m of plane-parallel, thin-bedded limestones, marls, and turbidites (Figure 10.5a, b). Both MTDs show a similar internal structure, their main bodies being composed of heterogeneous breccias, approximately 13 m thick in MTD-5 and 15 m thick in MTD-6. Internally, both breccias were subdivided into two divisions by Pujalte et al. (1997). The lower division of the breccias (referred to as S2 by Pujalte et al. (1997)) is characterized by meter-sized boulders and fragments of contorted and imbricated strata (Figure 10.5c, d). The upper division (referred to as interval S3) consists of fining upward intraformational breccias, including centimeter-decimeter-sized clasts of mudstones and calcarenites, alongside loose specimens of rhodoliths and *Nummulites* tests. However, oblique aerial views of the outcrops demonstrate that both breccia intervals, despite overlapping locally, are in general separated along strike, thus defining lateral facies changes in the breccia deposits. On the northern limb of the synclinorium, the MTD-5 breccia is composed exclusively of S3 deposits in the NW but changes completely into S2 deposits in less than 50 m toward the SE (Figure 10.5a, b). The lateral transition between the MTD-5 S2 and S3 deposits corresponds to an oblique zone that originally dipped toward the NW. A similar arrangement can be observed in the MTD-6 breccia exposed on the southern limb of the synclinorium (Figure 10.5d–f). Here, a S3-only breccia in the NW

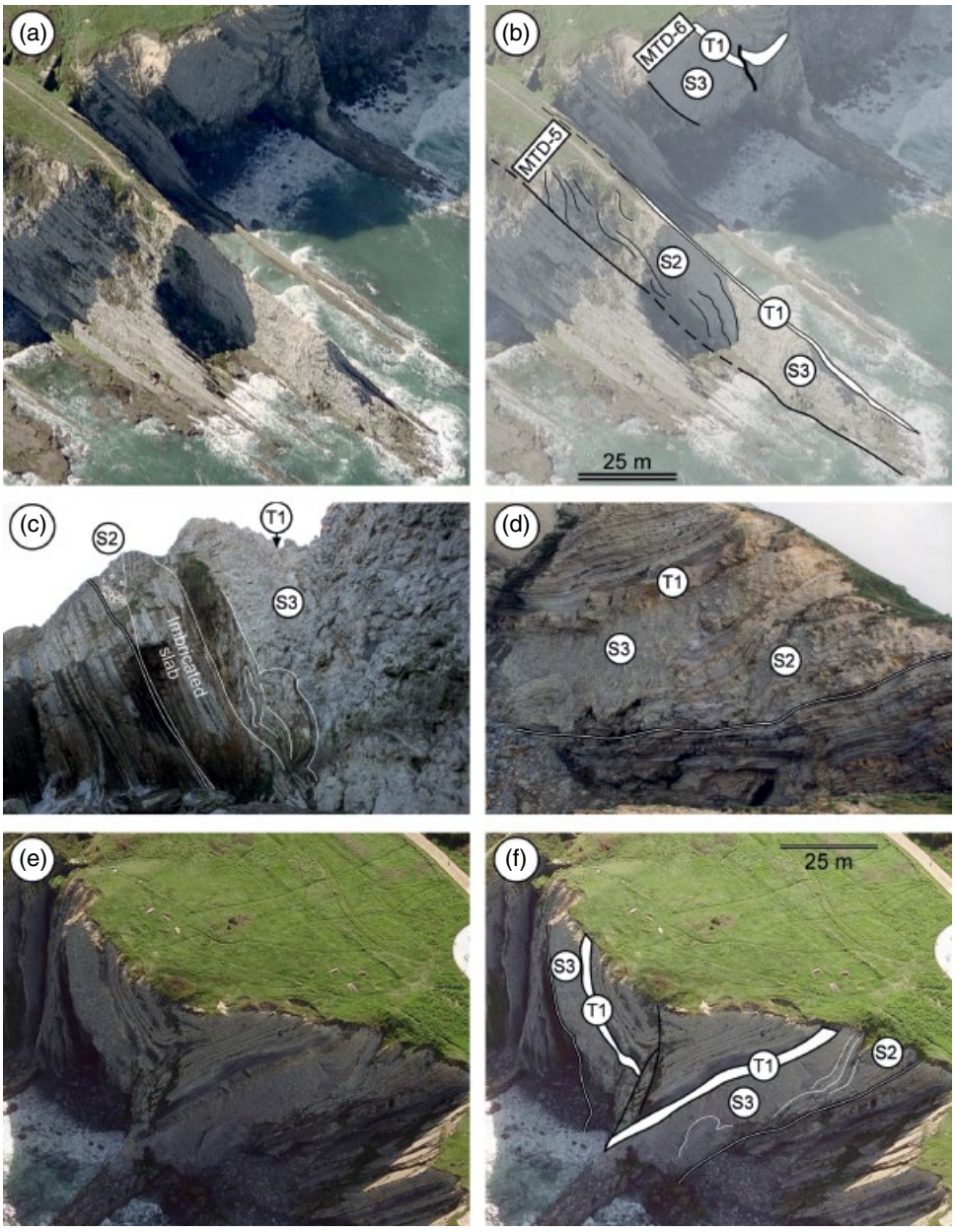


Figure 10.5 (a) Oblique aerial view of the succession containing MTD-5 and MTD-6 on the northern limb of the Biscay synclinorium. Bedding strike is SE-NW (from upper left to lower right) and bed younging upward. (b) Interpreted sketch of MTD-5, showing the distribution of its internal divisions S2, S3, and T1 as explained in the text. (c) Field view of MTD-5 on the northern limb of the Biscay synclinorium. (d) Field view of MTD-6 on the southern limb of the Biscay synclinorium, showing distribution of internal divisions S2, S3, and T1 explained in the text. (e, f) Oblique aerial view and interpreted sketch of MTD-6 at the core of the Biscay Synclinorium.

turns into a practically S2-only breccia in the SE in less than 40 m. Similar to MTD-5, the lateral change in the facies of the MTD-6 breccia occurs through an inclined transitional zone dipping toward the NW. In both MTD-5 and MTD-6, the inclination of the S2–S3 lateral transitional zone coincides with that of the imbricated slabs found within their S2 breccias.

MTD-5 and MTD-6 are overlain by erosive-based, normally graded, sandy-bioclastic layers (~0.8 m thick in MTD-5 and 1.3 m thick in MTD-6) with abundant larger foraminifera (e.g., *Nummulites*, orthophragminids, etc.) and some marly clasts in their lower parts (interval T1 of Pujalte et al. (1997)). These calcarenite layers gradually change upward into homogenous marl beds (interval T2

of Pujalte et al. (1997)), approximately 1 m thick in MTD-5 and 1.3 m thick in MTD-6.

10.3.4.2. Interpretation

The two types of basal breccias (S2 and S3) in MTD-5 and MTD-6 represent laterally transitional, and partly overlapping, debris-flow deposits. The S3 breccias show similar facies characteristics to the equivalent interval in MTD-4, and their interpretation is therefore the same. The coarser-grained S2 breccias of MTD-5 and MTD-6 also share some characteristics with the equivalent interval in MTD-4, such as the occurrence of imbricated slabs dipping toward the NW, but there are some significant differences. The largest imbricated slab in MTD-4 is attached to the underlying succession, whereas slabs in MTD-5 and MTD-6 are detached clasts, independent from each other. The S2 breccias of MTD-5 and MTD-6 are systematically located to the SE of the S3 breccias, the oblique transitional zone between both facies being inclined toward the NW (Figure 10.5). These characteristics suggest that the overall depositional architecture of the S2 and S3 breccias was a result of the shear stress beneath and within the debris flow (Dykstra et al., 2011; Jackson, 2011). It can be concluded that the shear stress exerted by the downslope moving S3 debris flow on the seabed ripped up fragments of cohesive, though not fully lithified, layers from the underlying deposits, which were incorporated into the lower and frontal parts of the debris flow and formed the S2 breccia (Hodgson et al., 2018). This reveals the great erosive power of the debris flows. In addition, the relative position of the S2 and S3 debrites suggests that sediment transport was in general toward the SE. This is confirmed by the inclination of both the S2 slabs and the S3–S2 lateral transition zone toward the SE, which was caused by intra-flow shearing driven by vertical variations in the speed of the debris flow (slower at the bottom, faster at the top; Allen, 1997).

The graded sandy calcarenite (T1) and the overlying marl layer (T2) represent sedimentation from voluminous turbidity currents (Bouma, 1962; Pujalte et al., 1997; Payros et al., 1999). Interval T2 represents late-stage decantation from the diluted turbulent wake developed above the turbidity current.

10.4. DISCUSSION

10.4.1. Facies Model

All the Eocene large-scale MTDs in the Biscay synclinorium were created by the displacement of sediment masses along a submarine slope facing toward the SE (150°). The degree of their internal deformation, which increases progressively upsection (Figure 10.1b), allows the identification of four different types of MTDs which are stratigraphically ordered. Their differences cannot be attributed to variations in rheological properties, as the material in all MTDs is similar. Consequently, the stratigraphic arrangement suggests that each type of MTD represents a snapshot of a continuum of processes (and consequent deposits) that occurred during downslope mass flow. The oldest MTDs, which exhibit the mildest internal deformation, represent mass flows that did not evolve significantly, suggesting short runout distance. Conversely, the youngest MTDs show the most intense internal deformation as a consequence of prolonged downslope transport. Accordingly, a facies model composed of four facies belts (1–4, from proximal to distal) has been conceived (Figure 10.6).

Facies belt 1 (characterized by MTD-1 and MTD-2) represents the area where mass-flow processes were initiated. Local destabilization of the slope deposits resulted in mass failure and sliding along a concave-up, spoon-shaped, complex basal zone (Varnes, 1978; Bull et al., 2009). Shear stress was intense at the base of the mass flow, which resulted in the formation of low-angle thrusts, but rapidly decreased upward, which resulted in gently folded strata (Figure 10.6). However, the pressure and shear stress exerted by the sliding mass on adjacent deposits caused the progressive lateral expansion of the destabilized deposits (Posamentier & Martinsen, 2011).

Facies belt 2 (characterized by MTD-3) represents the increase in internal deformation of the mass flow as it moved downslope. Variable velocities within the mass flow, perhaps caused by local variations in slope gradient, produced different shear intensity within the mass flow. Local deceleration caused an upslope propagating compressional strain wave that resulted in progressive folding and thrusting. Consequently, the sliding mass flow transformed into a semi-coherent slump (Figure 10.6). Intra-slump shear stress increased upward as flow velocity became faster (Allen, 1997), causing local disarticulation of the slumped strata. This process had the greatest effect at the culminations of the strata uplifted along thrust planes. Bed fragmentation and progressive dilution in the upper part of the slump eventually resulted in the local transformation of the slump into a more fluid debris flow.

As a consequence of increased internal shear, the downslope moving slump transformed into a debris flow in facies belt 3 (characterized by the S3 interval of MTD-4). Turbulent mixing between the upper surface of the downslope moving debris flow and ambient water resulted in relatively reduced viscosity and sediment strength (Payros et al., 1999; Strachan, 2008), thus creating the conditions for gravity-driven vertical segregation of clasts according to their size (Figure 10.6). At the same time, the shear stress exerted by the debris flow on the seabed resulted in the partial uplifting, overturning,

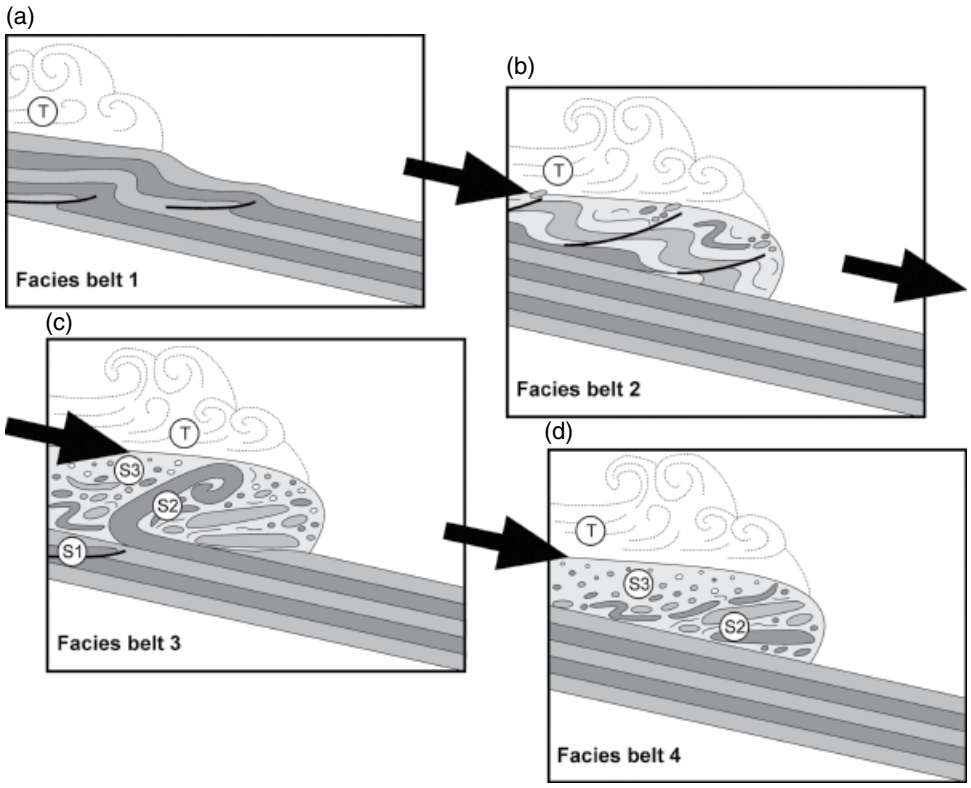


Figure 10.6 Facies model of the Eocene large-scale MTDs studied in the Basque Basin (see text for further explanation). (a) Initial sliding in facies belt 1. (b) Transformation of the mass flow into a slump in facies belt 2. (c) Formation of a debris flow (S3) in facies belt 3, which caused thrusting and sliding of deeply buried strata (S1) and local retrograde transformation into a slump through partial uplifting, overturning, and rolling of the seabed strata (S2). (d) Definitive transformation into a debris flow in facies belt 4. A turbidity current (T) surrounded the mass flow throughout its downslope displacement.

and rolling of the cohesive but not fully lithified strata (Van der Merwe et al., 2011; Hodgson et al., 2018). This bulldozing process implies that some portions of fully developed debris flow transformed back into slumps through the incorporation of underlying strata into the mass flow (characterized by the S2 interval in MTD-4). Consequently, areas with different speed and shear (greater in the debris flow than in the slump) occurred within the same mass flow. Furthermore, the shear stress exerted by the debris flow on the seabed also resulted in the sliding of deeply buried strata along imbricated thrusts (characterized by the S1 interval in MTD-4). It is reasonable to suggest that if the shear stress had continued further, the thrust blocks would eventually have been incorporated into the mass flow.

Finally, facies belt 4 (characterized by MTD-5 and MTD-6) represents the definitive transformation of the heterogeneous mass flow into a debris flow (Figure 10.6). The transformation implies that the strata uplifted and overturned from the seabed were eventually broken apart, became detached from their roots, and were transported downslope as isolated, imbricated slabs. Extensive substrate entrainment led to an increase in flow volume. The process also contributed to maintaining flow heterogeneity, as two types of sediment masses (coarse-grained S2 and finer-grained S3 intervals) coexisted within the same debris flow, which in all likelihood entailed different velocities. However, it seems reasonable to assume that increasing internal shear along downslope transport would most likely result in disaggregation of the largest slabs and formation of a more homogeneous debris flow.

A turbidity current (characterized by intervals T1 and T2 of Pujalte et al. (1997)) surrounded the mass flow throughout its downslope displacement (Figure 10.6). As the mass flow evolved and transformed into a debris flow, some mixing with the upper turbidity current occurred, as evidenced by the occurrence of bioclasts in the uppermost part of the debrites and mud clasts within the turbidites. However, both flows generally remained separate, which implies that considerable shear stress existed at the interface. The low-viscosity turbidity current probably outran the underlying debris flow and reached further into the basin. Consequently, an additional zone located

beyond facies belt 4, which would be characterized exclusively by a thick bedded turbidite, can also be envisaged (for a similar distal evolution in other MTDs, see Payros et al., 1999).

Taking everything into account, it can be concluded that the spectrum of deposits produced by mass-wasting processes in the Eocene Basque Basin is well represented in the vertical arrangement of facies found in MTD-4 (Figure 10.4). Its basal S1 interval can be taken as equivalent of incipient sliding and thrusting in facies belt 1. Interval S2 represents complex slumping processes further downslope along facies belts 2 and 3. Interval S3 is the representation of fully evolved debris flows in facies belt 4. Finally, intervals T1 and T2 are probably similar to turbidites accumulated beyond facies belt 4.

10.4.2. Dimensions

10.4.2.1. Extent and Volume of MTDs

MTD-4 is the oldest large-scale MTD that can be identified reliably on the northern and southern limbs of the synclinorium (Figure 10.1b). Minimum estimates of its original extent and volume were calculated on the basis of its current geographic position on both limbs of the synclinorium. The length of MTD-4 is greater than 532 m in the direction of paleocurrents (150°). Its width, once the limbs of the synclinorium are unfolded, can be estimated to be greater than 720 m. Given that the internal characteristics of MTD-4 are similar throughout its exposure, these values provide the minimum extent of facies belt 3. If the average composite thickness of the basal breccias (intervals S2 and S3) and capping turbidite (intervals T1 and T2) on both limbs is considered, MTD-4 has a volume in excess of $9 \times 10^6\,m^3$. However, if the 12 m thick S1 interval is also included, as it was pushed and thrust by the shear stress exerted by the mass flow on the seabed, MTD-4 has a volume greater than $14 \times 10^6\,m^3$.

If the oldest MTD-1 found on the northern limb of the synclinorium were represented by one of the small-scale MTDs from the lower part of the succession on the southern limb (Figure 10.1b), its extent would reach almost 1700 m parallel to paleocurrent direction and 1200 m across. Estimation of its volume is more difficult due to the significant lateral variations in thickness.

The values above are minimum estimates. The total downslope extent of the MTDs, from their most proximal sites (characterized by facies belt 1) to the most distal areas (characterized by facies belt 4) and beyond (characterized by hypothetic turbidite deposits lacking basal breccias), cannot be determined due to outcrop constraints. However, some assumptions can be made in order to gain further insight into dimensional aspects of the MTDs (Moscardelli & Wood, 2016). If each of the four characteristic facies belts in the MTD model extended over the $532 \times 720 m^2$ estimated above for facies belt 3 using MTD-4 data, an ideal MTD would cover an area of at least $1.5 \times 10^6\,m^2$ (up to $8 \times 10^6\,m^2$ if the potential extent of MTD-1 is considered for each of the facies belts). Taking into account the average thickness of 16 m derived from all MTDs, the sediment volume within an ideal MTD would be in excess of $24 \times 10^6\,m^3$ (potentially, up to $130 \times 10^6\,m^3$).

10.4.2.2. Topographic Relief of MTDs

The thickness of the MTD-4 breccia increased downcurrent from 15.6 on the northern limb of the synclinorium to 23.4 m on the southern limb. The difference of 7.8 m can be partly attributed to erosion of the seabed and incorporation of ripped up clasts into the breccia. However, the overlying deposits suggest that the downcurrent increase in the thickness of MTD-4 cannot be exclusively attributed to basal erosion, but increasing topographic relief must also be considered. The first layer above MTD-4 that can be clearly identified on both limbs of the synclinorium is a 15 cm thick turbidite. Upsection from this key turbidite, all beds can be readily correlated between both limbs, but none can be correlated between the top of MTD-4 and the key turbidite. This key turbidite lies 10.3 m above MTD-4 on the northern limb but only 8.5 m above MTD-4 on the southern limb. This suggests that the top of MTD-4 may have caused a topographic relief of 1.8 m on the seabed. This topography diverted subsequent turbidity currents toward lower areas, until the relief was eventually compensated, the seabed became flat again, and extensive sedimentation of turbidites resumed throughout the area.

10.4.3. Triggering Mechanism

Several processes have been suggested as being capable of triggering submarine mass-wasting processes which result in large-scale MTDs overlain by turbidites (e.g., Mulder & Cochonat, 1996; Masson et al., 2010). In some case studies, the shear stress exerted by large-scale turbidity currents derived from shelfal areas on the underlying slope sediments triggered the destabilization of the latter, leading to the formation of MTDs overlain by turbidites (Talling et al., 2004; Pierce et al., 2018). In other cases, initial mass wasting is known to have affected only the slope deposits, which are intrinsically prone to failure. Subsequently, overlying co-genetic turbidity currents were generated either by the shear of ambient water on the mass-flow surface or by upward elutriation of fluidized sediment through the mass flow (e.g., Hampton, 1972; Mohrig et al., 1998; Mohring & Marr, 2003; Strachan, 2008; Sawyer et al., 2012). In both cases, the sediment composition of the turbidity current is comparable to that of the parental mass flow. Alternatively, in some cases, the mass failure of slope sediments is believed to have triggered tsunamis, which eventually

stirred up shelfal clastic sediments causing their downslope displacement as turbidity currents (Wynn & Masson, 2003; Gisler et al., 2010).

In the present case study, all MTDs are systematically overlain by turbidites, indicating that there may have been a genetic relationship between mass flows and turbidity currents. This is supported by the fact that some mixing between the mass flow and the overlying turbidity current also occurred. However, several lines of evidence explained below suggest that the turbidites capping the MTDs were not generated as by-products of the mass flows, neither did the MTDs result from the shear exerted by turbidity currents on the seabed. The fact that the composition of the turbidites (mainly shelfal bioclastic components) is different to that of the underlying MTDs (mainly slope-derived contorted and fragmented strata) shows that the turbidity currents were not formed as by-products of parental mass flows. In addition, the fact that turbidites cover the oldest MTDs (1 and 2, which involved little downslope displacement and were therefore unlikely to generate tsunamis) suggests that the destabilization of shelfal sediments was triggered independently. Finally, the volume of the MTDs systematically surpasses that of the overlying turbidite, rendering it unlikely that the shear stress exerted by an initial turbidity current on the seabed triggered large-scale destabilization of slope deposits. Taking everything into account, it can be concluded that both the mass flow and the overlying turbidity currents were triggered by a process that affected and destabilized the slope and shelfal sediments simultaneously. Given that the force required would be considerable, earthquakes are the most likely cause (Mutti et al., 1984; Seguret et al., 1984; Alsop & Marco, 2013; Tinterri & Tagliaferri, 2015).

10.4.4. Source Area

Sedimentary structures from both the large-scale MTDs and the thinner-bedded calciturbidites of the Calciclastic Flysch show that prevalent gravity-driven downslope sediment transport was toward the SE (150°). This suggests that a shallow-water carbonate source area was located to the NW of the study area. According to paleogeographic reconstructions of the Pyrenean area in Eocene times (Pujalte et al., 2002), in which the main shallow-water ramps were located to the south (Figure 10.1a), two alternative scenarios are possible. On the one hand, an uplifted area could have existed in the middle of the 1000–1500 m deep basin, which has not been identified in the oceanic and seismic surveys carried out in the Bay of Biscay to date (Roca et al., 2011). On the other hand, a northward protruding salient could have existed in the southern margin of the basin. Such a situation has been described in the Pamplona area, where the geometry and behavior of the carbonate ramp was influenced by the synsedimentary activity of the Pamplona fault (Figure 10.1a; Payros et al., 2007, 2010). This is a NE trending deep fracture that in Eocene time caused rapid subsidence of the eastern fault block, whereas the western block remained uplifted and under shallow-marine waters. Consequently, a hinge zone developed on top of the Pamplona fault and produced a NE trending local slope facing eastward, which efficiently funneled carbonate sediment gravity flows in that direction. Similarly, Eocene calciturbidites found in the Oyambre section, to the west of the present study area, were also directed eastward (Payros et al., 2015), suggesting that another northward salient of the southern carbonate ramp may also have existed there.

The evolution of the source area of the studied large-scale MTDs can be reconstructed using their stratigraphic arrangement. The fact that the most proximal MTDs are the oldest (MTD-1 and MTD-2 from facies belt 1) and the most distal MTDs are the youngest (MTD-5 and MTD-6 from facies belt 4) suggests a progressive backstepping of the source area. This evolution is in line with that previously described for the source areas of other South Pyrenean Eocene MTDs (Payros et al., 1999).

10.5. CONCLUSIONS

The submarine mass-wasting processes that created the Basque MTDs were most likely triggered by earthquakes that destabilized backstepping shelfal and slope deposits simultaneously, thus creating bipartite sediment gravity flows that moved downslope toward the SE. A facies model composed of four facies belts (1–4, from proximal to distal) has been conceived. The characteristics of the sedimentary processes (and consequent deposits) changed downslope. The proximal facies belt 1 is mainly characterized by sliding processes. Downslope, facies belt 2 is typified by slump deposits. These slumps evolve into debris flows in facies belt 3, but bulldozing processes are capable of thrusting, uplifting, overturning, and rolling up underlying seabed strata, meaning that some portions of fully developed debris flows can transform back into slumps. In facies belt 4, the heterogeneous mass flow is definitively transformed into a debris flow when the uplifted and overturned strata are eventually broken apart and transported downslope as isolated, imbricated slabs. An independent but simultaneous turbidity current was sourced from shelfal areas and surrounded the mass flow throughout its downslope displacement. Some mixing between the top of the debris flow and the overriding turbidity current occurred, but both flows generally remained separate. A hypothetical zone located beyond facies belt 4 would be characterized exclusively by a thick bedded turbidite.

This facies model illustrates how extensive substrate entrainment can lead to an increase downslope in mass-flow

volume and contribute to maintaining flow heterogeneity. Furthermore, the model shows that downslope mass-flow transformation is not linear (en masse transformation from slide to slump and from slump to debris flows), but rather retrograde transformation may also occur. The potential effects of these processes should be taken into account when determining the proximal or distal nature of other MTDs.

ACKNOWLEDGMENTS

This research was funded by the Spanish government project CGL2015-65404-R (MINECO/FEDER, EU) and by the Basque government research group IT-930-16. We are grateful to the editor Kei Ogata for the invitation to participate in this volume. Thanks are due to Carl Sheaver for his language corrections and to two AGU reviewers (Roberto Tinterri and anonymous) for their comments.

REFERENCES

Allen, P. A. (1997). *Earth surface processes*, (404 pp.). Oxford, UK: Blackwell.

Alsop, G. I., & Marco, S. (2013). Seismogenic slump folds formed by gravity-driven tectonics down a negligible subaqueous slope. *Tectonophysycs*, *605*, 48–69.

Alves, T. M. (2015). Submarine slide blocks and associated soft-sediment deformation in deep-water basins: A review. *Marine and Petroleum Geology*, *67*, 262–285.

Bandyopadhyay, B. K., & Gupta, A. (1990). Submarine debris-flow deposits from the Ordovician Mane Ting Formation in Tethyan Black Mountain Basin, Central Bhutan. *Journal of the Geological Society of India*, *36*, 277–289.

Bouma, A. (1962). *Sedimentology of some flysch deposits: A graphic approach to facies interpretation*, (168 pp.). Amsterdam, The Netherlands: Elsevier.

Bull, S., Cartwright, J., & Huuse, M. (2009). A review of kinematic indicators from mass-transport complexes using 3D seismic data. *Marine and Petroleum Geology*, *26*, 1132–1151.

Chun, S. S., Choe, M. Y., & Chough, S. K. (2002). Armored mudstone boulders in submarine debris-flow deposits, the Hunh-hae Formation, Pohang Basin: An evidence for the large-scale slumping of adjacent area of a submarine channel or scar wall. *Geosciences Journal*, *6*, 215–225.

Dykstra, M., Garyfalou, K., Kertznus, V., Kneller, B., Milana, J., Molinaro, M., et al. (2011). Mass-transport deposits: Combining outcrop studies and seismic forward modeling to understand litofacies distributions, deformation, and their seismic stratigraphic expression. In R. C. Shipp, P. Weimer, & H. W. Posamentier (Eds.), *Mass-transport deposits in deep-water settings, SEPM Special Publications* (Vol. *96*, pp. 293–310). Tulsa, OK: Society for Sedimentary Geology.

Frey-Martinez, J., Cartwright, J., & James, D. (2006). Frontally confined versus frontally emergent submarine landslides: A 3D seismic characterisation. *Marine and Petroleum Geology*, *23*, 585–604.

Gisler, G., Weaver, R. P., & Gittings, M. L. (2010). Calculations of tsunamis from submarine landslides. In D. C. Mosher, R. C. Shipp, L. Moscardelli, J. D. Chaytor, C. D. P. Baxter, H. J. Lee, & R. Urgeles (Eds.), *Submarine mass movements and their consequences, Series in Advances in Natural and Technological Hazards Research* (Vol. *28*, pp. 695–704). Dordrecht, The Netherlands: Springer.

Hampton, M. A. (1972). The role of subaqueous debris flow in generating turbidity currents. *Journal of Sedimentary Petrology*, *42*, 245–275.

Hodgson, D. M., & Wild, R. (2007). Facies and architecture of the Lezonabar Member, Higuer-Guetaria Formation, Errentzun Zabal, Spain. In T. H. Nilsen, R. D. Shew, G. S. Steffens, & J. R. J. Studlick (Eds.), *Atlas of deep-water outcrops, AAPG Studies in Geology Series* (Vol. *56*, pp. 348–350). Tulsa, OK: American Association of Petroleum Geologists & Shell Exploration and Production.

Hodgson, D. M., Brooks, H. L., Ortiz-Karpf, A., Spychala, Y., Lee, D. R., & Jackson, C. A. L. (2018). Entrainment and abrasion of megaclasts during submarine landsliding and their impact on flow behaviour. In D. G. Lintern, D. C. Mosher, L. G. Moscardelli, P. T. Bobrowsky, C. Campbell, J. D. Chaytor, et al. (Eds.), *Subaqueous mass movements and their consequences: Assessing geohazards, environmental implications and economic significance of subaqueous landslides, Special Publications of the Geological Society, London* (Vol. *477*). London, UK: Geological Society. https://doi.org/10.1144/SP477.26

Jablonska, D., Di Celma, C. N., Tondi, E., & Alsop, G. I. (2018). Internal architecture of mass-transport deposits in basinal carbonates: A case study from southern Italy. *Sedimentology*, *65*, 1246–1276.

Jackson, C. A. L. (2011). Three-dimensional seismic analysis of megaclast deformation within a mass transport deposit; implications for debris flow kinematics. *Geology*, *39*, 203–206.

Lucente, C. C., & Pini, G. A. (2003). Anatomy and emplacement mechanism of a large submarine slide within a Miocene foredeep in the Northern Apennines, Italy: A field perspective. *American Journal of Science*, *303*, 565–602.

Masson, D. G., Wynn, R. B., & Talling, P. J. (2010). Large landslides on passive continental margins: Processes, hypotheses and outstanding questions. In D. C. Mosher, R. C. Shipp, L. Moscardelli, J. D. Chaytor, C. D. P. Baxter, H. J. Lee, & R. Urgeles (Eds.), *Submarine mass movements and their consequences, Series in Advances in Natural and Technological Hazards Research* (Vol. *28*, pp. 153–165). Dordrecht, The Netherlands: Springer.

Mohring, D., & Marr, J. G. (2003). Constraining the efficiency of turbidity current generation from submarine debris flows and slides using laboratory experiments. *Marine and Petroleum Geology*, *20*, 883–899.

Mohrig, D., Whipple, K. X., Hondzon, M., Ellis, C., & Parker, G. (1998). Hydroplaning of subaqueous debris flows. *Geological Society of America Bulletin*, *110*, 387–394.

Moscardelli, L., & Wood, L. (2016). Morphometry of mass-transport deposits as a predictive tool. *Geological Society of America Bulletin*, *128*, 47–80.

Mulder, T., & Cochonat, P. (1996). Classification of offshore mass movements. *Journal of Sedimentary Research*, *A66*, 43–57.

Muñoz, J. A. (2002). Alpine tectonics I: The Alpine system north of the Betic Cordillera; the Pyrenees. In W. Gibbons &

T. Moreno (Eds.), *The geology of Spain* (pp. 370–385). London, UK: The Geological Society.

Mutti, E., Ricci Lucchi, F., Seguret, M., & Zanzucchi, G. (1984). Seismoturbidites: A new group of resedimented deposits. *Marine Geology*, *55*, 103–116.

Ogata, K., Pogacnik, Z., Pini, G. A., Tunis, G., Festa, A., Camerlenghi, A., & Rebesco, M. (2014). The carbonate mass transport deposits of the Paleogene Friuli Basin (Italy/Slovenia): Internal anatomy and inferred genetic processes. *Marine Geology*, *356*, 88–110.

Orue-Etxebarria, X., Lamolda, M., & Apellaniz, E. (1984). Bioestratigrafía del Eoceno Vizcaino por medio de los foraminíferos planctónicos. *Revista Española de Micropaleontología*, *16*, 241–263.

Payros, A., Dinarès-Turell, J., Monechi, S., Orue-Etxebarria, X., Ortiz, S., Apellaniz, E., & Martinez-Braceras, N. (2015). The Lutetian/Bartonian transition (middle Eocene) at the Oyambre section (northern Spain): Implications for standard chronostratigraphy. *Palaeogeography, Palaeoclimatolology, Palaeoecology*, *440*, 234–248.

Payros, A., Orue-Etxebarria, X., & Pujalte, V. (2006). Covarying sedimentary and biotic fluctuations in Lower-Middle Eocene Pyrenean deep-sea deposits: Palaeoenvironmental implications. *Palaeogeography, Palaeoclimatolology, Palaeoecology*, *234*, 258–276.

Payros, A., Pujalte, V., & Orue-Etxebarria, X. (1999). The South Pyrenean Eocene carbonate megabreccias revisited: New interpretation based on evidence from the Pamplona Basin. *Sedimentary Geology*, *125*, 165–194.

Payros, A., Pujalte, V., & Orue-Etxebarria, X. (2007). A point-sourced calciclastic submarine fan complex (Eocene Anotz Formation, western Pyrenees): Facies architecture, evolution and controlling factors. *Sedimentology*, *54*, 137–168.

Payros, A., Pujalte, V., Orue-Etxebarria, X., Apellaniz, E., Bernaola, G., Baceta, J. I., et al. (2016). The relevance of Iberian sedimentary successions for Paleogene stratigraphy and timescales. In M. Montenari (Ed.), *Stratigraphy and Timescales* (Vol. *1*, pp. 393–489). Amsterdam, The Netherlands: Academic Press, Elsevier.

Payros, A., Pujalte, V., Tosquella, J., & Orue-Etxebarria, X. (2010). The Eocene storm-dominated foralgal ramp of the western Pyrenees (Urbasa–Andia Formation): An analogue of future shallow-marine carbonate systems? *Sedimentary Geology*, *228*, 184–204.

Pierce, C. S., Haughton, P. D. W., Shannon, P. M., Pulham, A. J., Barker, S. P., & Martinses, O. J. (2018). Variable character and diverse origin of hybrid event beds in a sandy submarine fan system, Pennsylvanian Ross Sandstone Formation, western Ireland. *Sedimentology*, *65*, 952–992.

Posamentier, H. W., & Martinsen, O. (2011). The character and genesis of submarine mass-transport deposits: Insight from outcrop and 3D seismic data. In R. C. Shipp, P. Weimer, & H. W. Posamentier (Eds.), *Mass-transport deposits in deepwater settings, SEPM Special Publications* (Vol. *96*, pp. 7–38). Tulsa, OK: Society for Sedimentary Geology.

Pujalte, V., Baceta, J. I., & Payros, A. (2002). Tertiary: Western Pyrenees and Basque-Cantabrian region. In W. Gibbons & T. Moreno (Eds.), *The geology of Spain* (pp. 293–301). London, UK: Geological Society.

Pujalte, V., Payros, A., Orue-Etxebarria, X., & Baceta, J. I. (1997). Secuencia evolutiva de los epósitos resedimentados eocenos de Punta Galea, Bizkaia: Relevancia para la determinación del sentido de transporte de laminas de slump. *Geogaceta*, *22*, 169–172.

Roca, E., Muñoz, J. A., Ferrer, O., & Ellouz, N. (2011). The role of the Bay of Biscay Mesozoic extensional structure in the configuration of the Pyrenean orogen: Constraints from the MARCONI deep seismic reflection survey. *Tectonics*, *30*, TC2001.

Sawyer, D. E., Flemings, P. B., Buttles, J., & Mohrig, D. (2012). Mudflow transport behavior and deposit morphology: Role of shear stress to yield strength ratio in subaqueous experiments. *Marine Geology*, *307*, 28–39.

Seguret, M., Labaume, P., & Madariaga, R. (1984). Eocene seismicity in the Pyrenees from megaturbidites of the South Pyrenean Basin (Spain). *Marine Geology*, *55*, 117–131.

Strachan, L. J. (2008). Flow transformation in slumps: A case study from the Waitemata Basin, New Zealand. *Sedimentology*, *55*, 1311–1332.

Talling, P. J., Amy, L. A., Wynn, R. B., Peakall, J., & Robinson, M. (2004). Beds comprising debrite sandwiched within co-genetic turbidite: Origin and widespread occurrence in distal depositional environments. *Sedimentology*, *51*, 163–194.

Talling, P. J., Clare, M., Urlaub, M., Pope, E., Junt, J. E., & Watt, S. F. L. (2014). Large submarine landslides on continental slopes: Geohazards, methane release, and climate change. *Oceanography*, *27*, 32–45.

Tinterri, R., & Tagliaferri, A. (2015). The syntectonic evolution of foredeep turbidites related to basin segmentation: Facies response to the increase in tectonic confinement (Marnoso-arenacea Formation, Miocene, Northern Apennines, Italy). *Marine and Petroleum Geology*, *67*, 81–110.

Van der Merwe, W. C., Hodgson, D. M., & Flint, S. S. (2009). Widespread synsedimentary deformation on a muddy deep-water basin-floor: The Vischkuil Formation (Permian), Karoo Basin, South Africa. *Basin Research*, *21*, 389–406.

Van der Merwe, W. C., Hodgson, D. M., & Flint, S. S. (2011). Origin and terminal architecture of a submarine slide: A case study from the Permian Vischkuil Formation, Karoo Basin, South Africa. *Sedimentology*, *58*, 2012–2038.

Varnes, D. J. (1978). Slope movement types and processes. In R. L. Schuster & R. J. Krizek (Eds.), *Landslides: Analysis and control, Special Report* (Vol. *176*, pp. 11–33). Washington, DC: National Academy of Sciences.

Wade, B. S., Pearson, P. N., Berggren, W. A., & Palike, H. (2011). Review and revision of Cenozoic tropical planktonic foraminiferal biostratigraphy and calibration to the geomagnetic polarity and astronomical time scale. *Earth-Science Reviews*, *104*, 111–142.

Watt, S. F. L., Talling, P. J., Vardy, M. E., Heller, V., Hühnerbach, V., Urlaub, M., et al. (2012). Combinations of volcanic-flank and seafloor-sediment failure offshore Montserrat, and their implications for tsunami generation. *Earth and Planetary Science Letters*, *319*, 228–240.

Wynn, R. B., & Masson, D. G. (2003). Canary islands landslides and tsunami generation: Can we use turbidite deposits to interpret landslide processes? In J. Locat, J. Mienert, & L. Boisvert (Eds.), *Submarine mass movements and their consequences, Series in Advances in Natural and Technological Hazards Research* (Vol. *19*, pp. 325–332). Dordrecht, The Netherlands: Springer.

11

Neogene and Quaternary Mass-Transport Deposits From the Northern Taranaki Basin (North Island, New Zealand): Morphologies, Transportation Processes, and Depositional Controls

Suzanne Bull[1], Malcolm Arnot[1], Greg Browne[1], Martin Crundwell[1], Andy Nicol[2], and Lorna Strachan[3]

ABSTRACT

Mass-transport deposits (MTDs) from outcrop and seismic data in northern Taranaki, New Zealand, are used to illustrate the wide variety of morphologies present and their stratigraphic architecture. The MTDs may have formed by multiple generative precursors including active fault movement and volcanism, a narrow shelf flanking the eastern basin margin, and high sedimentation rates produced by regional uplift of hinterland areas, together with sea level changes over time. We outline sedimentary and structural features and biostratigraphy from base to top within two MTDs in outcrop examples. The biostratigraphy at the Tongaporutu site indicates the MTD originated in shallower outer shelf and upper slope settings and traveled down the slope into bathyal settings where it was deposited. In the Rapanui example, we have observed crude clast sorting formed during this transport. At Rapanui, the upper surface of the MTD was passively draped by subsequent turbidite mass flows, while at Tongaporutu, a period of hemipelagic mudstone deposition separates the top of the MTD from the overlying sandstone-mudstone sediments. Using 2D and 3D seismic data, we observe distinct zones within an individual MTD characterized by varying levels of internal disaggregation, suggesting changing flow processes with basal surface scouring, indicating high levels of substrate erosion during MTD emplacement.

11.1. INTRODUCTION

Mass-transport deposits (MTDs) are a ubiquitous feature of Neogene and Quaternary deepwater marine successions in the northern part of the Taranaki Basin, New Zealand (Figure 11.1). They represent the products of mass wasting derived from the eastern margin of the basin that were transported into deeper water settings (lower bathyal) during periods of high sedimentation and slope progradation. Here we present outcrop and subsurface examples of these MTD deposits and illustrate the wide variety of MTD morphologies, internal stratigraphy and lithologies, and biostratigraphic features. Mechanisms which may have initiated the mass wasting are suggested, along with how the outcrop and seismic examples contribute to our understanding of their flow behavior and final deposition.

Aspects of the MTD succession have been described elsewhere (e.g., Strachan, 2002; King et al., 2011; Omeru, 2014; Sharman et al., 2015). This study focuses on specific examples, two outcrop examples which are easily accessible and illustrate morphologic features, transportation processes, and depositional controls that are similar to other MTDs along the coastal section. The seismic example is a much larger-scale feature than the outcrop examples.

[1] *Department of Petroleum Geoscience, GNS Science, Lower Hutt, New Zealand*

[2] *Department of Geological Sciences, University of Canterbury, Christchurch, New Zealand*

[3] *School of Environment, University of Auckland, Auckland, New Zealand*

Submarine Landslides: Subaqueous Mass Transport Deposits from Outcrops to Seismic Profiles, Geophysical Monograph 246, First Edition. Edited by Kei Ogata, Andrea Festa, and Gian Andrea Pini.
© 2020 American Geophysical Union. Published 2020 by John Wiley & Sons, Inc.

The Taranaki Basin MTDs are unique globally, in that the same succession of ancient MTD deposits (though not necessarily stratigraphically equivalent MTDs) can be studied at a range of scales both in superbly exposed outcrop sections and in the subsurface using seismic reflection data.

11.2. GEOLOGIC SETTING OF THE NORTH TARANAKI MARGIN

The Taranaki Basin on the western side of North Island, New Zealand, represents a back-arc rift depocenter, which has experienced both extensional tectonics and back-arc volcanism in the Neogene-Recent (King & Thrasher, 1996; Giba et al., 2010). High sedimentation rates characterize the Neogene and Quaternary sedimentary succession immediately west of the eastern basin-bounding Taranaki Fault, a reverse fault structure active particularly in Oligocene and Miocene time (Stagpoole & Nicol, 2008). High sedimentation rates are likely to have been an important preconditioning factor to slope failure, with estimates varying between 30 cm/kyr (King et al., 1993), 45 cm/kyr (ARCO Petroleum NZ Inc., 1992), and 2 m/kyr (Maier et al., 2016), and can be as high as 240 m/kyr for the most rapidly deposited parts of the progradational slope succession (Crundwell, 2016). Sediment feeding the basin was derived from the tectonically active hinterland of the central North Island and northern South Island to the east and south of the basin. Rapid deposition and migration of the shelf wedge is attributed to increased sediment supply from Pliocene-Recent times, which is related to uplift of the ancestral Southern Alps in response to increasing convergence along the plate boundary to the south of Taranaki Basin (Strachan, 2002; Kamp et al., 2004; Hansen & Kamp, 2006).

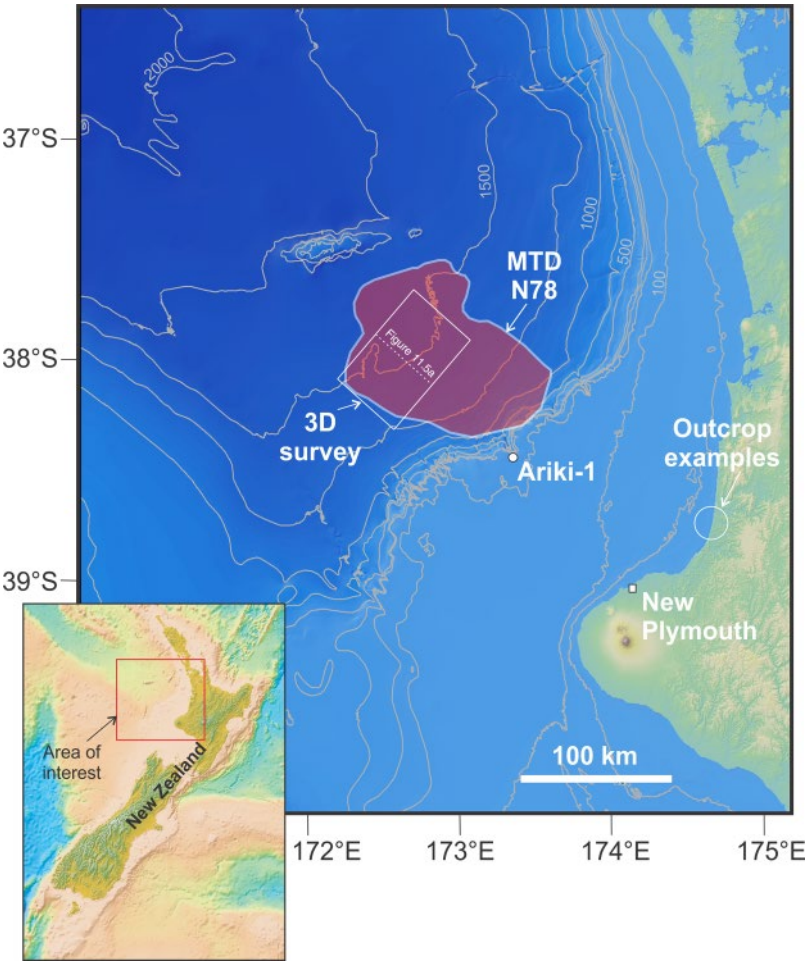


Figure 11.1 Location map of the northern Taranaki study area west of the North Island, New Zealand. The outcrops used in this study and the location of the offshore MTD N78 are indicated. The bathymetry (in meters) is displayed for the offshore area. Inset map shows the general location of the study area.

Table 11.1 Summarized Geometric and Lithological Data for Outcrop and Seismic Examples of MTDs in Northern Taranaki

	Rapanui Stream	Tongaporutu Beach	Seismic example N78
Location	−38.7997; 174.5892	−38.8161; 174.5897	−38.0480; 173.0155
Age	Late Miocene	Late Miocene	Late Pliocene to early Pleistocene
MTD thickness or TWT interval	~10 m	~10 m	0–210 ms TWT
MTD extent	>600 m wide (outcrop extent)	>150 m wide (outcrop extent)	Area: 10,130 km^2; estimated volume of 960 km^3 (Omeru, 2014)
Internal stratal features	Large heterolithic blocks (up to 5 m diameter) at base, with disseminated sandstone and siltstone more common toward top	Three stratigraphic units: (1) folded interval (at base), (2) laminated mudstone, and (3) highly calcareous mudstone with interbedded tuff beds	Three zones: (1) low reflection continuity (moderate to high disaggregation), (2) partially disaggregated intact blocks, and (3) transparent and structureless (high disaggregation)
Bottom/top contact features of MTD	Sharp planar base with irregular, undulose top	Base not exposed with planar but locally irregular top. Adjacent outcrops indicate meter-scale relief at top of feature	Top varies between low relief/rugosity to high relief/rugosity. Bottom is generally planar but varies from rough and heavily scoured to relatively smooth
Biostratigraphic comments		Faunas from sediments below the MTD represent lower bathyal water depths of 1000–1500 m	
Paleowater depth (from foraminifera)		Faunas within the lower portion of the MTD indicate uppermost slope in water depths of 200–400 m. Samples from the upper portion of the MTD represent lower bathyal water depths c. 1000 m	
Average transport direction	Toward the NW	Toward the NW	Toward the WNW

Location data are given in latitude and longitude (WGS84) coordinates.

11.3. OUTCROP EXAMPLES

Two outcrop localities, Rapanui Stream and Tongaporutu Beach (Table 11.1 and Figure 11.1), are described in this study. At both localities, the MTDs occur within otherwise stratigraphically conformable successions of interbedded sandstones, mudstones, and minor tuff beds of the Late Miocene Mount Messenger Formation (Browne et al., 2007; King et al., 2007, 2011).

11.3.1. Rapanui Stream

The outcrop at Rapanui Stream (38.7997S; 174.5892E) comprises a ~10 m thick MTD over an outcrop distance of 600 m, bounded at its northern extent by a fault, and dipping beneath the level of the beach in its southern extent. The basal contact is sharp and planar, while the upper contact is sharp but undulose with up to 80 cm of relief (Figure 11.2a–d). Internally, the fill of the MTD comprises variable proportions of five main lithotypes:

1. Sandstone and mudstone blocks: Large (up to 5 m diameter) blocks of coherent sandstone (Figure 11.2b) occur with similarly large (up to 8 m diameter) mudstone blocks (Figure 11.2c), both of which are similar to the underlying and overlying Mount Messenger Formation lithologies. The sandstone blocks are generally equant to slightly elongate in shape with rounded margins, whereas the mudstone blocks typically are more elongate, locally very long, and thin with tapered ends and maybe inclined relative to the regional bedding orientation (Figure 11.2d).

2. Interbedded sandstone and mudstone: Moderately well to well sorted, fine to very fine grained sandstone interbedded with mudstone which form clasts or packages within the MTD, commonly displaying folded (Figure 11.2e) and brittle fracture deformation.

3. Sandstone: Well sorted fine to very fine grained sandstone that forms a matrix lithology throughout the MTD.

4. Mudstone: Very fine grained sandy mudstone that forms a matrix lithology throughout the MTD and may contain scattered molluscan fragments in discrete layers.

5. Concretions: Isolated cemented calcareous concretions up to 30 cm in diameter occur scattered throughout the MTD.

Well-exposed coastal cliffs typically show larger blocks toward the basal portion of the MTD with finer-grained

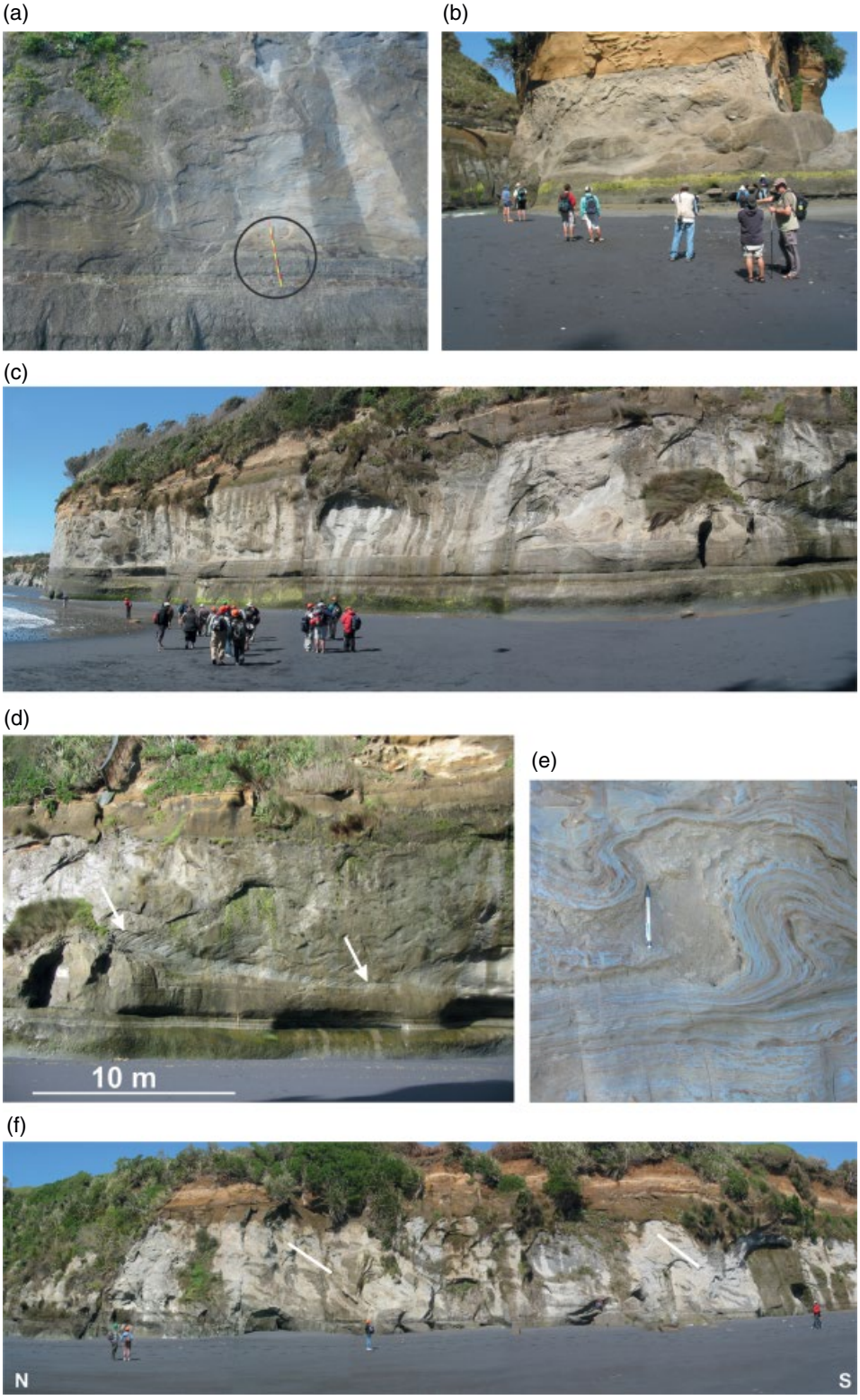


Figure 11.2 Rapanui Stream outcrop. (a) Sharp planar basal contact of the MTD (1 m scale bar circled). (b) Large blocks of sandstone (darker colored) within the lower part of the MTD. The top of the MTD is marked by the tan/buff/brown-colored sandstone and mudstone. (c) General outcrop view of the MTD south of Rapanui Stream. The MTD is represented by the generally lighter-colored interval in the middle of the image, with darker-colored turbidite sandstones below and above. Note the sharp planar basal contact, overlain by large light-colored blocks of siltstone and darker-colored sandstone. (d) Large tapered block of light-colored siltstone (arrowed) within the MTD. (e) Soft-sediment deformation within interbedded sandstone and siltstone (pencil for scale). (f) General view of the MTD north of Rapanui Stream showing the general south dipping fabric (white lines) associated with the darker-colored sandstone and lighter-colored siltstone blocks within the MTD. The base of the MTD is marked by darker-colored sandstones at bottom left, while the top is marked by the base of the brown/tan-colored sandstones forming the upper portion of the cliff. (*See electronic version for color representation of this figure*)

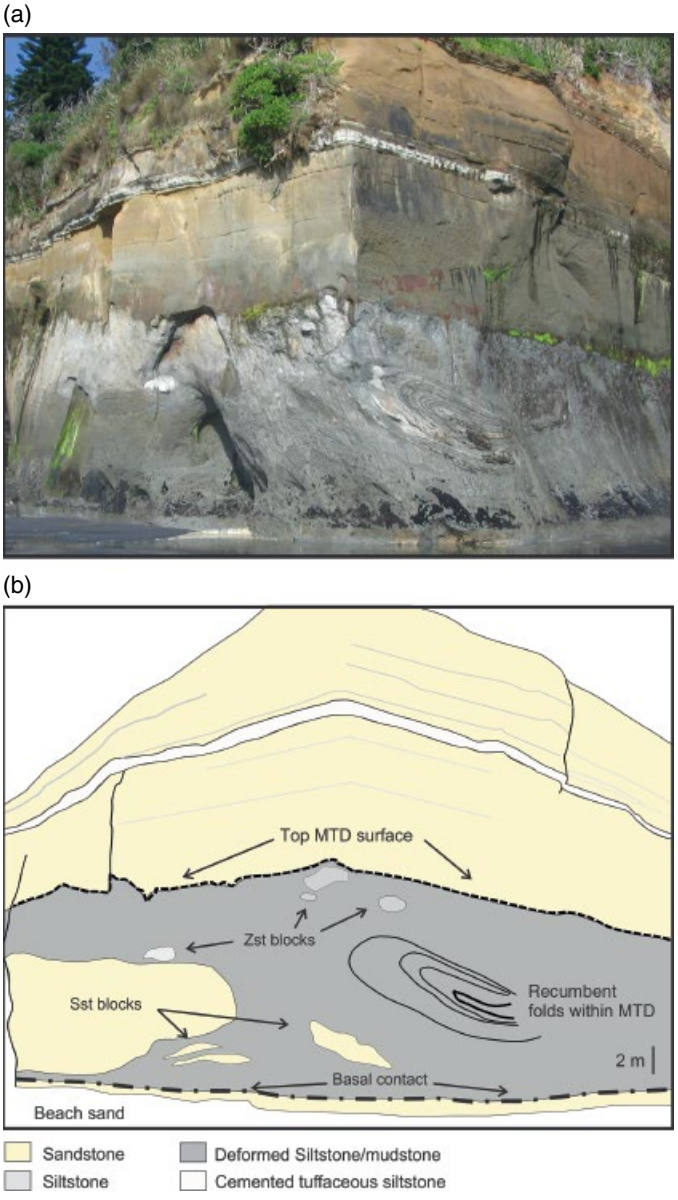


Figure 11.3 Photo and interpretive sketch of the upper portion of the MTD at Rapanui. Features to note are the predominance of sandstone blocks toward the base of the MTD, with mudstone above, and the irregular upper contact of the MTD with the overlying sandstone.

lithologies toward the top. In places the upper ~2 m is predominantly fine-grained mudstone (Figures 11.2b and 11.3). Locally at Rapanui Beach, southerly dipping preferential alignment of elongate blocks, clasts, and fold axes within the MTD trending approximately east-west indicates a clear northerly vergence fabric (Figure 11.2f). The basal contact at Rapanui is characterized by mudstone within the MTD overlying underformed sandstone beds from the Mount Messenger Formation (Figure 11.2b, c). Although there are larger sandstone blocks in the basal part of this MTD, the slide plane appears to be related to movement on basal mudstone.

11.3.2. Tongaporutu Beach

The MTD at Tongaporutu Beach (38.8161S, 174.5897E; Figure 11.4) is ~10 m thick and is exposed for ~150 m along the Tongaporutu River. Although poorly exposed, the basal contact, where observed, appears sharp and planar. Stratigraphically above this contact, three lithological units are identified, with the lower two (Units 1 and 2) comprising the MTD (Figure 11.4a, d, e).

Unit 1 is stratigraphically the lowermost unit comprising deformed medium to thin interbedded alternating sandstone and slightly calcareous mudstone (8.5 m thick), with

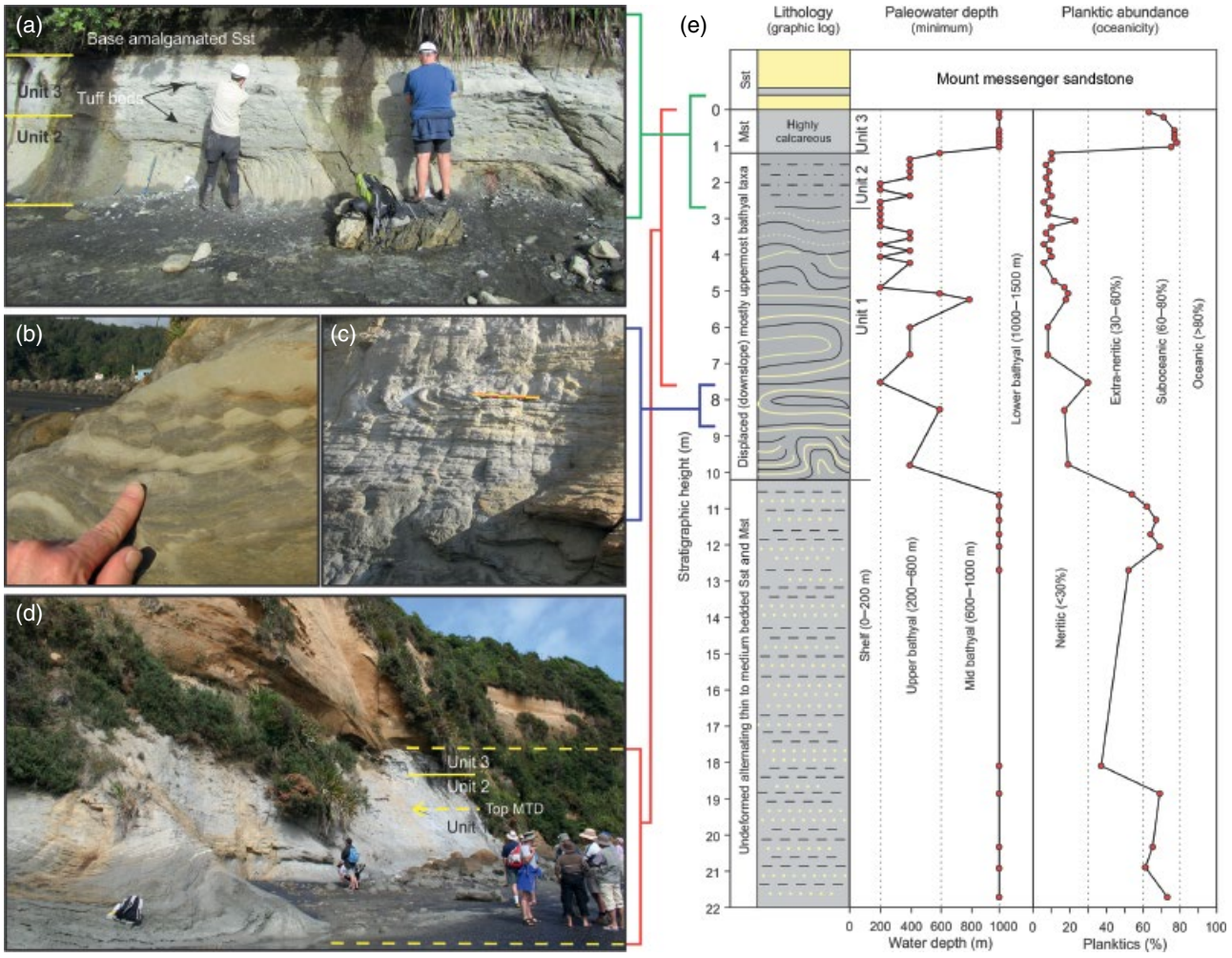


Figure 11.4 Tongaporutu Beach outcrop. (a) Units 2 and 3 with two tuff beds (arrowed). Unit 2 comprises laminated slightly calcareous mudstone, and Unit 3 is a highly calcareous hemipelagic mudstone. The top of Unit 3 is a sharp planar surface, overlain by brown-colored sandstone of the Mount Messenger Formation. (b) Normal faults within alternating sandstone and mudstone within Unit 1 near the base of the MTD. (c) Recumbent fold within Unit 1 comprising alternating sandstone and mudstone toward the base of the MTD. Scale bar in the fold axis is 50 cm with 10 cm divisions. (d) Units 1–3, showing the transition from the MTD in Unit 1 into the overlying lighter-colored poorly bedded mudstone with tuff (units 2 and 3). Folds are evident in the lower left of Unit 1. Brown-colored units in the upper part of the image are sandstones of the overlying Mount Messenger Formation. (e) Stratigraphic section through the MTD showing general lithologies, paleowater depth and oceanicity data from foraminiferal assemblages, and stratigraphic units mentioned in the text. (*See electronic version for color representation of this figure*)

thicker more deformed beds toward the base. Open to tight recumbent folds with subhorizontal axial planes are common (Figure 11.4c), and where there is a greater abundance of alternating sandstone and mudstone, decimeter-scale extensional normal faults are common (Figure 11.4b). Some of these are axial plane normal faults formed during folding. The majority of the tight folding occurs in the lower half of this unit, and more open folds increase in abundance upward through this unit (Figure 11.4d, e).

Unit 2 is the upper unit of laminated slightly calcareous mudstone (1.6 m thick) (Figure 11.4a, d).

Unit 3 comprises the uppermost unit of massive to bedded, bioturbated, highly calcareous sparsely fossiliferous hemipelagic mudstone (1.3 m thick) with very thin interbedded tuffs and tuffaceous sandstones (Figure 11.4a). These deposits are interpreted to be the hemipelagic sediments deposited on top of the MTD after it was emplaced.

Foraminiferal faunas from sediments underlying the MTD suggests deposition in lower bathyal water depths (1000–1500 m), under an extra-neritic to suboceanic water mass, in slightly hypoxic conditions. Sediments

within the MTD predominantly contain an upper to mid bathyal taxa, including hypoxic-tolerant species, and have neritic planktic abundances (Figure 11.4e; Crundwell, 2004). These faunas indicate the sediments of the MTD were largely sourced from the uppermost slope in water depths of 200–400 m, from a site closer to land. Additionally, some sediment from the upper and mid slope (400–1000 m) was incorporated into the MTD as it traveled downslope. The hemipelagic mudstone of Unit 3 above the MTD was deposited in lower bathyal water depths c. 1000 m, under extra-neritic to suboceanic conditions (Figure 11.4e), and is interpreted to represent a period of slope stability prior to the onset of rapid slope progradation out over the site.

At this location, the basal failure plane, although poorly exposed, appears to be related to mudstone beds at the base of Unit 1. This is similar to that observed at the Rapanui location where it appears that mudstone at the base of the MTD acted as the basal failure plane. This is also consistent with other MTD outcrop sections to the south of Tongaporutu Beach.

11.4. SEISMIC EXAMPLE

The MTD identified from 2D and 3D seismic reflection data is located close to the contemporaneous slope, occurring within late Pliocene to early Pleistocene (3.33–2.17 Ma) mudstones and minor mudstones of northern Taranaki Basin (Figure 11.5a). The MTD is part of a succession of six large stacked MTDs recognized by Bull and Arnot (2013) and Omeru (2014). The MTD, here termed "MTD N78" (Figure 11.5a), covers an area of

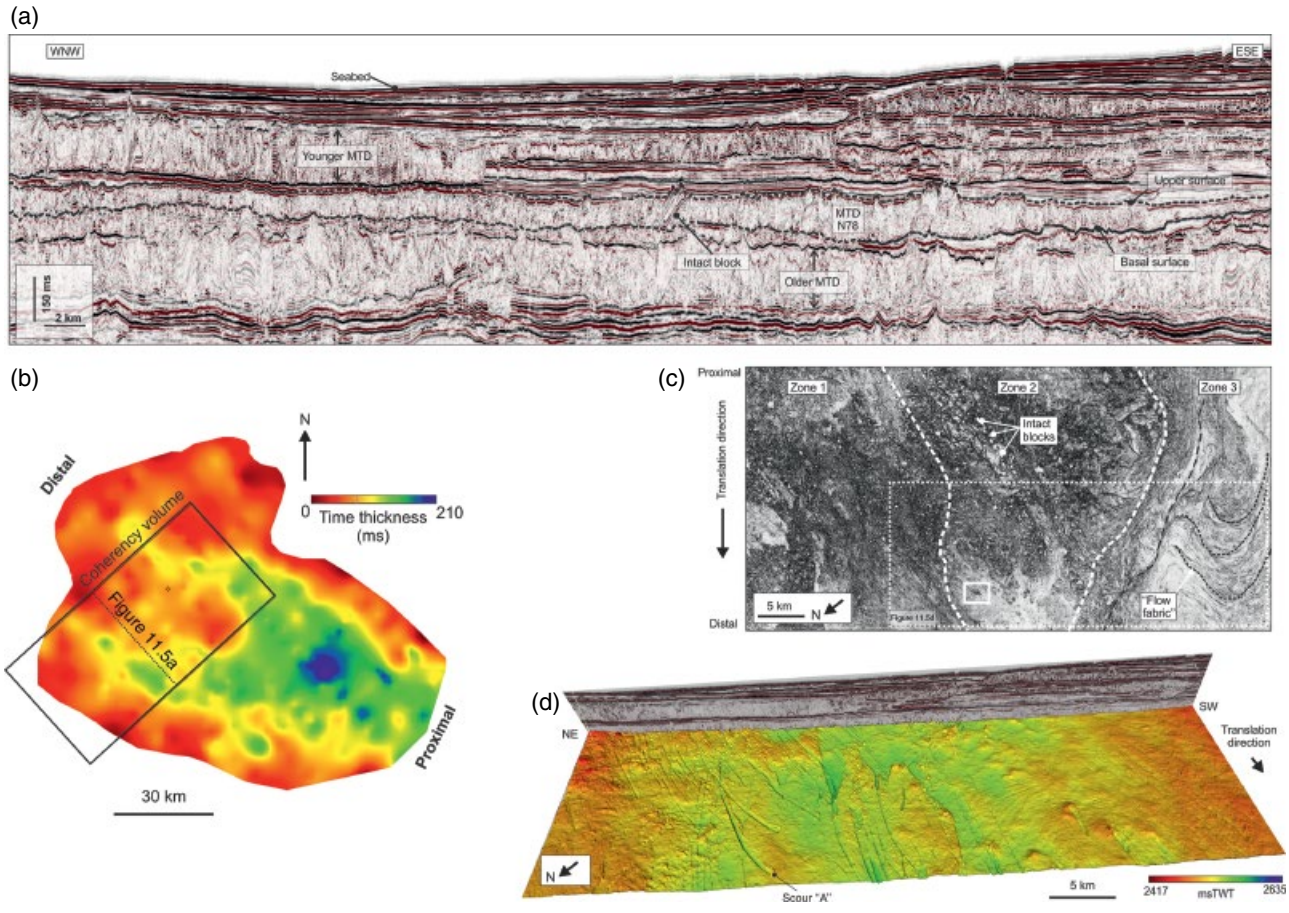


Figure 11.5 MTD N78 imaged using 2D and 3D seismic data. (a) 3D seismic dip line showing upper and lower surfaces and internal character of MTD N78 (labeled). Location shown in Figures 11.1 and 11.5b. (b) Isochron (time thickness) map of MTD N78 based on interpretation of 2D seismic data. (c) Slice through coherency volume flattened on the basal surface of MTD N78 (white, coherent, dark, less coherent) showing distinct lateral zones of internal character. White rectangle indicates intact block associated with the terminus of the basal surface scour "A" (labeled in Figure 11.5d). Location of coherency volume shown in Figures 11.1 and 11.5b. (d) 3D perspective view of an inset area of the basal surface of MTD N78. Location shown in Figure 11.5b. (*See electronic version for color representation of this figure*)

~10,130 km^2 and has an estimated volume of 960 km^3 (Omeru, 2014). Interpretation of 2D seismic reflection profiles shows that the MTD is roughly paddle shaped in plan view and reaches a maximum thickness of 210 ms TWT (Figure 11.5b). The thickest areas correspond to mounded upper surface topography and discrete zones of stacked, continuous internal reflections, interpreted to represent a concentration of partially disaggregated intact blocks of relatively competent material close to the source area (Figure 11.5a, c). The MTD pinches out laterally and distally and therefore appears to have spread freely across the contemporaneous seafloor (i.e., "unconfined-type" MTD after Frey-Martinez et al., 2006). Based on the orientation of lateral and distal margins and of basal surface scours (see below), an overall transport direction to the WNW is interpreted. An inset area of the MTD imaged by a 3D seismic survey (Figures 11.1 and 11.5c) reveals three distinct lateral zones identified using the combined character of the upper and lower bounding surfaces and the internal anatomy of the MTD.

Zone 1 features an upper surface which exhibits moderate rugosity; internally, the MTD shows low reflection continuity indicating a high level of disaggregation (Figure 11.5c). The basal surface is generally planar, but in places appears rough, and features numerous slightly curved scours which have "V"-shaped cross sections and are up to 10 m deep and <100 m across (Figure 11.5d). Scours are typically attributed to the erosional action of intact blocks of material being transported at the base of debris-like flow (Posamentier & Kolla, 2003; Gee et al., 2005, 2007). Zone 2 (Figure 11.5c) has an upper surface which exhibits a high level of relief and rugosity (Figure 11.5a) along with relatively high reflectivity internally, with zones of stacked, continuous reflections interpreted as partially disaggregated intact blocks. These blocks are up to 1 km wide and 125 m high (Figure 11.5a). The basal surface in Zone 2 is also affected by narrow V-shaped scours (Figure 11.5d). In addition, there are scours that are curved and become wider and deeper downslope, with relatively flat bases and terminating at an intact block, for example, scour labeled "Scour A" in Figure 11.5d, which is associated with the intact block indicated by the white rectangle on Figure 11.5c. At least two of these scours cross, an unusual phenomenon previously interpreted to result from the rotation of intact blocks as they are translated within a debris-like flow (Draganits et al., 2008). Zone 3 (Figure 11.5c) is characterized by a low-relief, low-rugosity upper surface, transparent and structureless internal seismic character, and a relatively smooth basal surface which features linear, narrow V-shaped scours (Figure 11.5a, d). This part of the MTD is the thinnest area imaged by the 3D survey with an average thickness of 60 m. The coherency slice through the MTD shows that Zone 3 exhibits a series of concave-downslope banding forming a "flow fabric" (Figure 11.5c), which along with the apparent very high levels of internal disaggregation, are interpreted here to be the product of ductile deformation.

It is noted that Zones 1 and 2, which feature the heaviest scouring, occur where MTD N78 directly overlies an older MTD deposit and increases the rugosity of the basal surface (compared to Zone 3 which overlies a subparallel, highly continuous package interpreted as undeformed background sedimentation). Therefore, the degree of scouring sustained by the basal surface may be determined by both the dominant slope failure process of the translating mass and the nature of the underlying substrate. The erosive nature of the basal surface suggests that MTD N78 may have significantly increased its mass through entrainment of the underlying substrate, which appears to have been an important process for all six of the Plio-Pleistocene MTDs described by Omeru (2014).

11.5. DISCUSSION

All the MTDs described either in outcrop or seismic display a wide range of morphologies and internal fabrics. These examples demonstrate considerable complexity and individuality in each of the MTDs, but they also demonstrate several attributes or features which are common to all the examples. Table 11.1 presents a summary of observations for each of the MTD examples.

For all of the MTDs, the basal contact, interpreted as a failure plane along which the MTD traveled, is generally sharp, planar, and largely conformable with underlying strata although local erosion is evident. In the case of the two outcrop examples, the failure plane appears to be related to mudstone beds at the base of the MTD units. However, given the inferred translation of the MTDs from upper slope to bathyal water depths, we do not know whether the initial plane of weakness was also a mudstone interval. The upper contact in contrast is either sharp and planar (as in the Tongaporutu example) or sharp and irregular with decimeter relief as in the Rapanui example or up to 70 ms or ~70 m relief as in Zone 2 of MTD N78. The irregular upper surfaces reflect depositional topography at the top of the MTD. It appears that at Rapanui, the overlying sandstone passively draped this upper contact and that there might have been some soft-sediment deformation (fluidization) contributing to the irregular nature of the contact, which may also have occurred in the case of MTD N78. Both outcrop examples have been interpreted as having translated to the NW, while MTD N78 is interpreted to have been translated to the WNW.

Outcrop examples show a range of lithological and fabric variations down to a millimeter scale and demonstrate the high vertical variability of MTDs. The observed size

sorting at Rapanui Stream, with larger blocks near the base and finer-grained lithologies toward the top, is interpreted to be a crude sorting within the flow. Similarly, the crude southerly dipping clast fabric seen at Rapanui is taken to reflect layer-parallel shear within the flow. Due to friction, the basal portion of the flow moved slower than the upper portion of the flow, resulting in an imbricated fabric with the long axis of clasts dipping toward the source area of the MTD (Figure 11.2f). At Tongaporutu, the uppermost hemipelagic interval (Unit 3; Figure 11.4d) marks a post–MTD emplacement period of background sedimentation where foraminiferal faunas show a change in water depth from uppermost slope (200–400 m) in samples from the basal portion of the MTD (Units 1 and 2) to lower bathyal water depths (c. 1000 m) in Unit 3 at the top of the MTD.

In contrast, while the resolution of the seismic data is restricted to a maximum of c. 10 m vertically, the scale and extensive data coverage of MTD N78 enables examination of depositional geometries over distances of tens of kilometers. In particular, the observations from MTD N78 highlight the highly variable nature of lateral deformation found within individual MTDs, which can occur as distinct but closely juxtaposed zones. Such variation is commonly linked to (i) progressive and nonuniform flow transformation from initial "slide" type behavior of relatively coherent material close to the source area into more mobile debris-flow behavior in the more distal areas, with a concomitant progressive thinning and decrease in upper surface relief downslope; (ii) the paleo-topography below and adjacent to the flow; (iii) localized variation in flow velocity and/or multiple phases of movement (Masson et al., 1993; Strachan, 2002, 2008; Gee et al., 2005); and (iv) depositional heterogeneity, in terms of variations in bed thickness and also lateral and vertical changes in the lithology (e.g., sandstone vs. mudstone). Sharman et al. (2015) noted that lithology variation had a strong influence on internal MTD architecture.

The MTDs described here, likely formed by multiple mechanisms and a number of factors, could have influenced preconditioning of the slope and possible triggering mechanisms. These factors include an active tectonic margin flanked by a relatively narrow shelf margin and high sedimentation rates produced by regional uplift of hinterland areas to the east and south. For the outcrop examples, foraminiferal faunas and biostratigraphic dating suggest the MTDs are largely sourced from the uppermost slope in water depths of 200–400 m, during periods of very rapid sedimentation and slope progradation out into the basin (Crundwell, 2016). However, it is difficult to determine the relative contribution of these mechanisms. In addition, other factors such as cyclic relative sea level fluctuations could have contributed to the initiation of MTDs as well as changes in accommodation space and sediment supply through time. The significance of these relative sea level changes was greater in shallower upper slope and shelf settings. Such changes possibly contributed to inducing MTD failure in outer shelf and upper slope settings and their emplacement into deeper water settings.

The seismic and outcrop examples presented here provide insights at very different scales of observation. The outcrop examples have the advantage in that they enable the lithologies within and adjacent to the MTDs to be examined and sampled and vertical and lateral changes albeit over a limited lateral extent to be characterized. However, the 2D nature of these particular outcrops and the limited outcrop extent (hundreds of meters) does not allow the larger geometry of the MTDs to be examined. In contrast, the seismic example has the advantage of enabling the large-scale internal variation to be mapped over significant distances (tens of kilometers). However, for the seismic example, there are no data available on lithologies within and adjacent to MTD N78 and small-scale features.

11.6. CONCLUSIONS

Superb coastal exposures together with an extensive subsurface data set allow the description of both outcrop and seismically imaged examples of MTDs of comparable age from the northern Taranaki Basin, New Zealand. Analysis of the various examples using different methods of investigation and over differing scales reveals the broad variation in vertical and lateral deformation found within individual MTDs, along with similarities in gross architecture and internal features, including the basal and upper contact geometries, presence of translated blocks of intact material, and evidence of ductile deformation.

ACKNOWLEDGMENTS

Seismic interpretation was undertaken using Paradigm software. We appreciate the technical reviews by Mark Lawrence and Tusar Sahoo (GNS Science) and very useful comments provided in reviews by Glenn Sharman, Morelia Urlaub, and Andrea Festa. Funding for this work came from the New Zealand Government Strategic Science Investment Fund to GNS Science under the Sedimentary Basin Research Programme.

REFERENCES

ARCO Petroleum NZ Inc. (1992). Arawa-1 Final Well Report PPL38436. *Ministry of Commerce New Zealand unpublished Petroleum Report PR 1824*.

Browne, G. H., King, P. R., Arnot, M. J., & Helle, K. (2007). A complete middle to inner basin floor-fan cycle, Mount Messenger Formation, Tongaporutu, New Zealand. In *Atlas*

of deep-water outcrops, AAPG Studies in Geology (Vol. 56, pp. 245–248). American Association of Petroleum Geologists. https://doi.org/10.1306/1240947St563

Bull, S., & Arnot, M. J. (2013). *Repeated large-scale slope failures associated with a rapidly prograding shelf margin from the Plio-Pleistocene of the Deepwater Taranaki Basin, New Zealand*. Paper presented at 6th International Symposium on Submarine Mass Movements and Their Consequences, Monday 23 September 2013 to Wednesday 25 September 2013, GEOMAR East shore: book of abstracts. GEOMAR.

Crundwell, M. P. (2004). New Zealand Late Miocene biostratigraphy and biochronology: Studies of planktic foraminifers and bolboforms at oceanic sites 593 and 1123, and selected onland sections (Unpublished PhD thesis). New Zealand: University of Waikato.

Crundwell, M. P. (2016). A new method for interpolating ages between calibrated control points based on foraminiferal concentrations. *Journal of Sedimentary Research*, *86*, 438–447.

Draganits, E., Schlaf, J., Grasemann, B., & Argles, T. (2008). Giant submarine landslide grooves in the Neoproterozoic/Lower Cambrian Phe Formation, northwest Himalaya: Mechanisms of formation and palaeogeographic implications. *Sedimentary Geology*, *205*, 126–141.

Frey-Martinez, J., Cartwright, J., & James, D. (2006). Frontally confined versus frontally emergent submarine landslides: A 3D seismic characterisation. *Marine and Petroleum Geology*, *23*, 585–604.

Gee, M. J. R., Gawthorpe, R. L., & Friedmann, J. S. (2005). Giant striations on the base of submarine landslide. *Marine Geology*, *214*, 287–294.

Gee, M. J. R., Uy, H. S., Warren, J., Morley, C. K., & Lambiase, J. J. (2007). The Brunei slide: A giant submarine landslide on the northwest Borneo Margin revealed by 3D seismic data. *Marine Geology*, *246*, 9–23.

Giba, M., Nicol, A., & Walsh, J. J. (2010). Evolution of faulting and volcanism in a backarc basin and its implications for subduction processes. *Tectonics*, *29*, TC4020. https://doi.org/10.1029/2009TC002634

Hansen, R. J., & Kamp, P. J. J. (2006). New insights into the condensed nature and stratigraphic significance of the Late Neogene Ariki Formation, Taranaki Basin. Paper presented at 2008 New Zealand Petroleum Conference, Auckland, New Zealand.

Kamp, P. J. J., Vonk, A. J., Bland, K. J., Hansen, R. J., Hendy, A. J. W., McIntyre, A. P., et al. (2004). Neogene stratigraphic architecture and tectonic evolution of Wanganui, King Country, and eastern Taranaki Basins, New Zealand. *New Zealand Journal of Geology and Geophysics*, *47*, 625–644. https://doi.org/10.1080/00288306.2004.9515080

King, P. R., Browne, G. H., Arnot, M. J., & Crundwell, M. P. (2007). A 2-D oblique-dip outcrop transect through a 3rd-order, progradational, deep-water clastic succession, Urenui-Mount Messenger Formations, New Zealand. In *Atlas of deep-water outcrops, AAPG Studies in Geology* (Vol. 56). Tulsa, OK: The American Association of Petroleum Geologists.

King, P. R., Ilg, B. R., Arnot, M., Browne, G. H., Strachan, L. J., Crundwell, M., & Helle, K. (2011). Outcrop and seismic examples of mass-transport deposits from a Late Miocene deep-water succession, Taranaki Basin, New Zealand. In R. C. Shipp, P. Weimer, & H. W. Posamentier (Eds.), *Mass-transport deposits in deepwater settings, Society for Sedimentary Geology (SEPM) Special Publication* (Vol. 96, pp. 311–348). Tulsa, OK: SEPM.

King, P. R., Scott, G. H., & Robinson, P. H. (1993). *Description, correlation and depositional history of Miocene sediments outcropping along north Taranaki coast, Institute of Geological & Nuclear Sciences Monograph* (Vol. 5). Lower Hutt, New Zealand: Institute of Geological & Nuclear Sciences.

King, P. R., & Thrasher, G. P. (1996). *Cretaceous-Cenozoic geology and petroleum systems of the Taranaki Basin, New Zealand, Institute of Geological & Nuclear Sciences Monograph* (Vol. 13). Lower Hutt, New Zealand: Institute of Geological & Nuclear Sciences.

Maier, K. L., Crundwell, M. P., Coble, M. A., King, P. R., & Graham, S. A. (2016). Refined depositional history and dating of the Tongaporutuan reference section, north Taranaki, New Zealand: New volcanic ash U–Pb zircon ages, biostratigraphy and sedimentation rates. *New Zealand Journal of Geology and Geophysics*, *59*, 313–329.

Masson, D. G., Hugget, Q. J., & Brunsden, D. (1993). The surface texture of the Saharan debris flow deposit and some speculation on submarine debris flow processes. *Sedimentology*, *40*, 583–598.

Omeru, T. (2014). Mass transport deposits: implications for reservoir seals (Unpublished PhD thesis). Cardiff, UK: University of Wales.

Posamentier, H. W., & Kolla, V. (2003). Seismic geomorphology and stratigraphy of depositional elements in deep-water settings. *Journal of Sedimentary Research*, *73*, 367–388.

Sharman, G. R., Graham, S. A., Masalimova, L. U., Shumaker, L. E., & King, P. R. (2015). Spatial patterns of deformation and paleoslope estimation within the marginal and central portions of a basin-floor mass-transport deposit, Taranaki Basin, New Zealand. *Geosphere*, *11*, 266–306. https://doi.org/10.1130/GES01126.1

Stagpoole, V. M., & Nicol, A. (2008). Regional structure and kinematic history of a large subduction back thrust: Taranaki Fault, New Zealand. *Journal of Geophysical Research. Solid Earth*, *113*, B01403. https://doi.org/10.1029/2007JB005170

Strachan, L. (2008). Flow transformations in slumps: A case study from the Waitemata Basin, New Zealand. *Sedimentology*, *55*, 1311–1332.

Strachan, L. J. (2002). Geometry to genesis: a comparative field study of slump deposits and their modes of formation (Unpublished PhD thesis). Cardiff, UK: University of Wales.

Part II
Submarine Landslide Deposits in Current Active and Passive Margins

12

Modern Submarine Landslide Complexes: A Short Review

Katrin Huhn[1], Marcos Arroyo[2], Antonio Cattaneo[3], Mike A. Clare[4], Eulàlia Gràcia[5], Carl B. Harbitz[6], Sebastian Krastel[7], Achim Kopf[1], Finn Løvholt[6], Marzia Rovere[8], Michael Strasser[9], Peter J. Talling[10], and Roger Urgeles[5]

ABSTRACT

Submarine landslides have been identified in almost all ocean basins worldwide. The largest submarine landslides occur on very shallow slopes and can be far larger than any terrestrial landslide. Submarine landslides can produce tsunami whose far-reaching effects can rival those produced by earthquake-tsunamis and threaten increasingly populated coastlines. Even small landslides can damage very expensive and critically important offshore infrastructure, such as pipelines used for oil and gas recovery, and telecommunication cables that now carry over 95% of digital data traffic. A better understanding of submarine landslide processes, including triggering mechanisms, preconditioning factors, timing, and frequency as well as dynamics of submarine landslide, and their consequences are of clear societal and economic importance. Despite their importance, many fundamental submarine landslide processes are still poorly understood. We currently have many studies that have mapped and sampled submarine landslide deposits; however, in order to fill outstanding but key knowledge gaps, future studies may have to go beyond this in order to unravel processes governing submarine landslides with even more interdisciplinary approaches. This chapter provides a very short review about submarine landslide studies, with emphasis on the emerging needs in future landslide research.

12.1. GENERAL CHARACTERISTICS AND PECULIARITIES

Submarine landslides occur on virtually all ocean slopes worldwide. They cover a wide range of settings, from passive to active continental margins, river-fed pro-deltas, and submarine fans, on the flanks of volcanic islands as well as glaciated and sediment-starved margins (e.g., Hampton et al., 1996; Hühnerbach et al., 2004; Masson et al., 2006; Twichell et al., 2009; among many others; e.g., Figure 12.1a). It is apparent that submarine landslide deposits form a significant proportion of the sedimentary succession of all continental margins, both active and passive (Hampton et al., 1996; Boyd et al., 2010; Giles et al., 2010). For example, the surface expression of mass-wasting deposits covers a large percentage of the Mediterranean Sea (18%) and of the Gulf of Mexico (27%) (McAdoo et al., 2000; Urgeles & Camerlenghi, 2013).

[1] *MARUM – Center for Marine Environmental Sciences, University of Bremen, Bremen, Germany*
[2] *Polytechnic University of Catalunya, Barcelona, Spain*
[3] *IFREMER, Géosciences Marines, Brest, France*
[4] *National Oceanography Centre, University of Southampton Waterfront Campus, Southampton, United Kingdom*
[5] *B-CSI, Institute of Marine Sciences (CSIC), Barcelona, Spain*
[6] *Norwegian Geotechnical Institute, Oslo, Norway*
[7] *Institute of Geosciences, Christian-Albrechts-University, Kiel, Germany*
[8] *Institute for Marine Sciences (ISMAR), National Council of Research (CNR), Bologna, Italy*
[9] *Institute of Geology, University of Innsbruck, Innsbruck, Austria*
[10] *Departments of Earth Sciences and Geography, University of Durham, Durham, United Kingdom*

Submarine Landslides: Subaqueous Mass Transport Deposits from Outcrops to Seismic Profiles, Geophysical Monograph 246, First Edition. Edited by Kei Ogata, Andrea Festa, and Gian Andrea Pini.
© 2020 American Geophysical Union. Published 2020 by John Wiley & Sons, Inc.

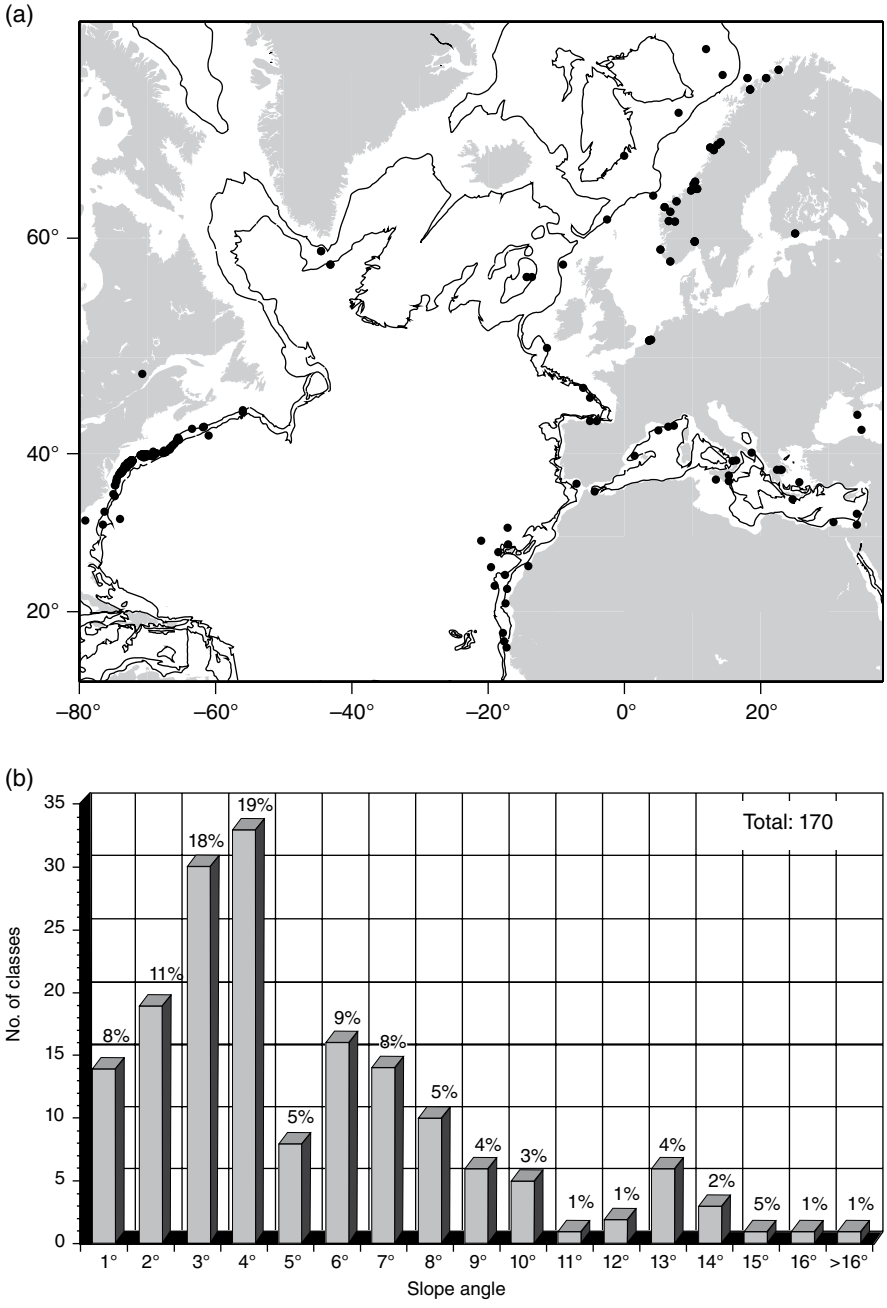


Figure 12.1 (a) Exemplarily mapped slope failures in the western and eastern North Atlantic including adjacent seas (Mediterranean Sea, Black Sea, Baltic Sea), fjords of Norway and eastern Canada, and failures in other limited/confined areas. Each point represents a single failure or slope failure complex. Source: From Hühnerbach et al. (2004). (b) Frequency distribution of empirical compiled data from modern examples of submarine landslides with increasing slope angle along the U.S. Atlantic continental slope. Source: After Shanmugam (2015).

The largest submarine landslides can affect more than 10,000 km^2 of the seafloor and involve >1000 km^3 of sediments. Some well-known, extremely large examples include the Storegga Slide (e.g., Bryn et al., 2003; Haflidason et al., 2004), the Trænadjupet Slide (e.g., Laberg & Vorren, 2000), the Hinlopen Slide (e.g., Vanneste et al., 2006; Winkelmann et al., 2008), and the Sahara Slide Complex (e.g., Embley, 1980; Georgiopoulou et al., 2010). These failed materials can move downslope for hundreds of kilometers (e.g., Masson, 1994). Landslides transforming into turbidity currents can flow even longer distances, and their deposits are capable to cover large parts of ocean basins (e.g., Masson, 1994; Talling et al., 2007; Hsu et al., 2008). Thus, submarine landslides can be several orders of

magnitudes larger than their terrestrial counterparts. Perhaps even more remarkably, submarine landslides can occur on exceptionally low gradient slopes (<1°; Figure 12.1b), which are almost always stable on land (Field et al., 1982).

As summarized by Urgeles and Camerlenghi (2013), submarine landslides have unique peculiarities compared to their much better studied onshore equivalents: (a) specific sediment types, which allow (i) failure to occur on very low slope gradient (Figure 12.1b) and potentially (ii) exhibit a high degree of remolding (e.g., Tanaka & Locat, 1999; Volpi et al., 2003; Løvholt et al., 2017); (b) the common presence of fully saturated sediments, which may be charged with dissolved gas and thus might cause hazardous effects in case of unloading (Tréhu et al., 2004; Vanoudheusden et al., 2004; Sultan et al., 2008); and (c) the ambient seawater, which might cause long failure runout due to hydroplaning at their flow front (Mohrig et al., 1998; Harbitz et al., 2003; De Blasio et al., 2006). Furthermore, the environmental stresses imposed on the seafloor (e.g., water hydrostatic pressure and currents resulting from tides, waves, and internal waves) create additional unique conditions for submarine landslides. Therefore, although the physical behavior of submarine landslides builds on understanding of terrestrial soils (e.g., Lambe & Whitman, 1969), boundary conditions for the material involved in submarine landslides are significantly different, and similarities between the morphologies of emerged and submerged slope failures may belie totally different processes.

The continental margin architecture and slope stratigraphy, in particular the stacking of layers with different physical properties or permeabilities, play an important role where failure surfaces are localized in the sediment stratigraphy. The concept of mechanically weaker layers of lower shear strength, which serve as preferred failure and glide planes of submarine landslides, is today widely accepted (e.g., Masson et al., 2010; Locat et al., 2014; see below for details in Section 12.3). Nevertheless, the interplays between a variety of physical processes and parameters (e.g., sediment composition and texture, grain interlocking, grain breakage, transient pore pressure fluctuations) are still not fully understood and have therefore become the focus of numerous recent research projects. In addition to so-called preconditioning factors, there are a number of short-term triggers that may reduce submarine slope stability (e.g., Masson et al., 2006; Locat & Lee, 2009). Among the processes, most crucial to slope stability are (i) seismic loading (i.e., earthquakes), (ii) storm wave loading, (iii) rapid sedimentation (in deltas, through mass wasting, etc.), (iv) gas hydrate dissociation, (v) deep-seated fluid generation and upward migration and seepage, (vi) oversteepening, (vii) cyclic loading by tides, (viii) gas charging, (ix) groundwater charging, and (x) base-of-slope erosion. Both long-term preconditioning factors and short-term triggers are discussed more detail in Section 12.3.

Due to their size, long runout distances, and high transport velocities (up to 20 m/s; Hsu et al., 2008), submarine landslides can be very hazardous because of their potential to generate harmful tsunamis at an ocean-wide scale (ten Brink et al., 2009; Løvholt et al., 2015; Urgeles et al., 2018) as well as their potential to damage critical offshore infrastructure. For instance, underwater telecommunication cables, which transport more than 95% of all digital data traffic, are vulnerable to damage by submarine landslides and their runout (Carter et al., 2009; Cattaneo et al., 2012; Pope et al., 2017). A first well-documented example for cable breaks was the earthquake-triggered Grand Banks landslide and turbidity currents, which occurred offshore Newfoundland in 1929 (Piper & Aksu, 1987). More recently, 11 telecommunication cable breaks were caused by the earthquake-triggered submarine landslides and turbidity currents in the Kaoping Canyon offshore SW Taiwan (Hsu et al., 2008). Thus, a deeper understanding of the timing and frequency of submarine landslides is important and timely.

12.2. DISTRIBUTION AND CLASSIFICATION

Numerous studies of the modern seafloor have revealed that large landslides occur preferentially along passive margins, whereas small-scale but more frequent events occur along active margins. For example, only ~7 and 3% of the tectonically active California and Oregon margin seafloors, respectively, are occupied by mass-wasting deposits (McAdoo et al., 2000) in comparison to the 27% at passive margins mentioned above. At first glance, this may contradict observations that (i) the majority of ancient landslides are associated with seismically active zones (e.g., Pini, 1999; Camerlenghi & Pini, 2009) and (ii) earthquakes are identified in many studies as the most common trigger mechanisms of submarine landslides (e.g., Locat, 2001; Sultan et al., 2004a; Haeussler et al., 2014). However, the low occurrence of landslides on active margins has been explained by (i) a lack of available sediments (Tappin et al., 2007) and/or (ii) an increase of sediment shear strength caused by earthquake shaking (Lee et al., 2004; Strozyk et al., 2010; ten Brink et al., 2016). At sites of low sedimentation rate and with frequent earthquakes, the excess pore pressures generated by sedimentation may have time to dissipate, such that normal consolidation prevails, or the sediment may become over-consolidated (Sawyer & DeVore, 2015; ten Brink et al., 2016). In addition, there is still a lack of completeness of marine surveys. As most landslide morphologies tend to be draped and preserved, the number of small to midsized landslides may even increase in line

with the increasing high and ultrahigh resolution of geophysical mapping cruises (Lee, 2005; Casas et al., 2016).

Extensive statistical studies investigating magnitudes of modern terrestrial landslides, in terms of both area and volume, showed that landslides exhibit a power law scaling behavior distribution (Stark & Hovius, 2001 and references herein; Figure 12.2a). This observation has been confirmed using numerous submarine landslide complexes within different tectonic settings (e.g., Chaytor et al., 2009; Moernaut & De Batist, 2011; Urgeles & Camerlenghi, 2013). The rollover points observed in power law scaling of submarine landslides point to incomplete catalogues for the smaller failure sizes (<1 km^3). The number of such events will increase with improvement of offshore technology and higher-resolution mapping of the *sub*-seafloor, including the ability to identify not only buried landslide deposits but also buried landslide scars (Posamentier et al., 2007). Several studies have already shown that there are 3.5 times more landslides of 1 km^3 than landslides of 10 km^3 and ~12 times more than landslides of 100 km^3 (Urgeles & Camerlenghi, 2013; Figure 12.2b). Data from the Mediterranean Sea suggest that this ocean basin experiences ~1.5 times slope failures >10^{-3} km^3 every year and one slope failure in excess of 10 km^3 every ~1000 years (Urgeles & Camerlenghi, 2013).

It is challenging to conduct robust statistical and/or comparative analyses of landslide distributions (size, volume, etc.) as the term "slide" is not always consistently used; rather many authors use "submarine landslides" as superordinate term for all types of deposits resulting from gravity-driven sediment transport. The definition and measurement of morphometric parameters are not always performed in a consistent manner between studies or disciplines (e.g., Clare et al., 2018). However, submarine landslides are typically distinguished from other mass-wasting events (e.g., debris flows) as a coherent translational block on a planar glide plane (shear surface), without internal deformation (e.g., Nardin et al., 1979; Mulder & Cochonat, 1996; Moscardelli & Wood, 2008; Figure 12.3). After initial slope destabilization, a slide may transformed into a slump, which represents a coherent rotational mass transport. Upon addition of fluid during downslope motion, slumped material may transform into a debris flow (Shanmugam, 2015). These flows can then grow dramatically in size and pick up speed, entraining material from the substrate and margin, but the mechanism of its growth is still unclear (Iverson et al., 2011). Even if a landslide shows a well-developed seafloor expression, it cannot be identified with a single event; rather it is a sequence or composite of events.

Mass-transport complexes (MTCs) are the sedimentary expression of stacked or adjacent mass-transport deposits (MTD) with internal facies variably consisting of rotated, translated blocks or thrusted blocks, as well as

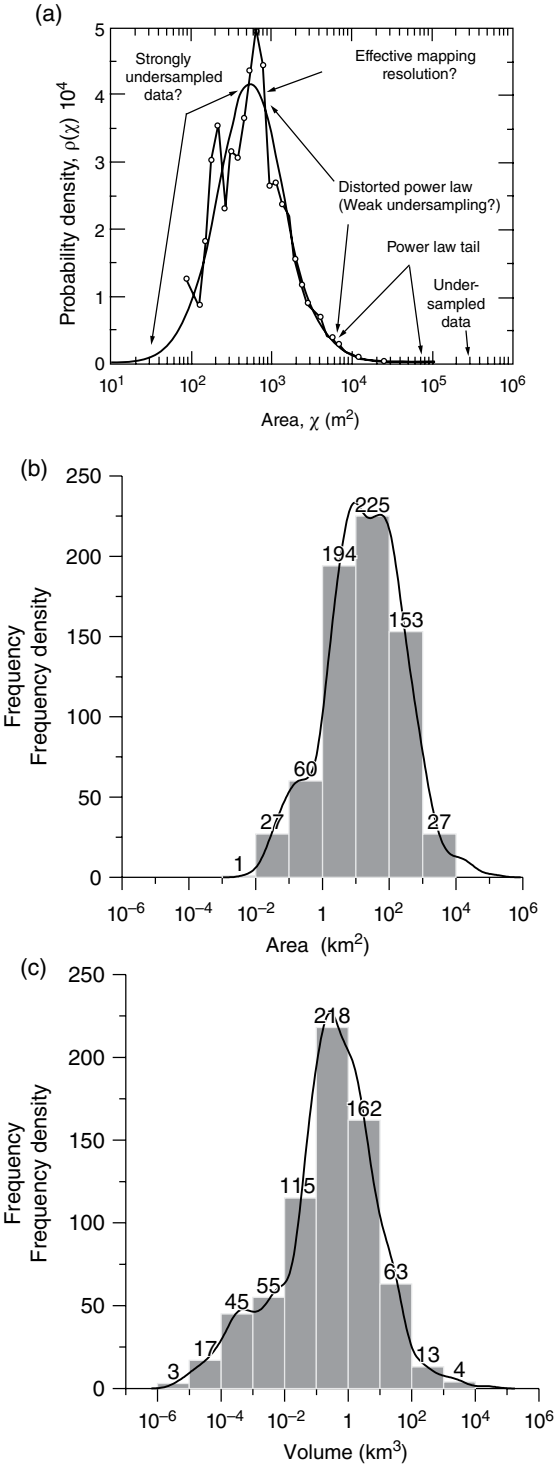


Figure 12.2 (a) An example of landslide size distribution, from the Central Range of Taiwan, plotted as a probability function. Source: From Stark and Hovius (2001). (b) and (c) Magnitude indicators of submarine landslides in the Mediterranean Sea whereby (b) shows the area (log scale) versus frequency and kernel density function and (c) the volume (log scale) versus frequency and kernel density function. Source: After Urgeles and Camerlenghi (2013).

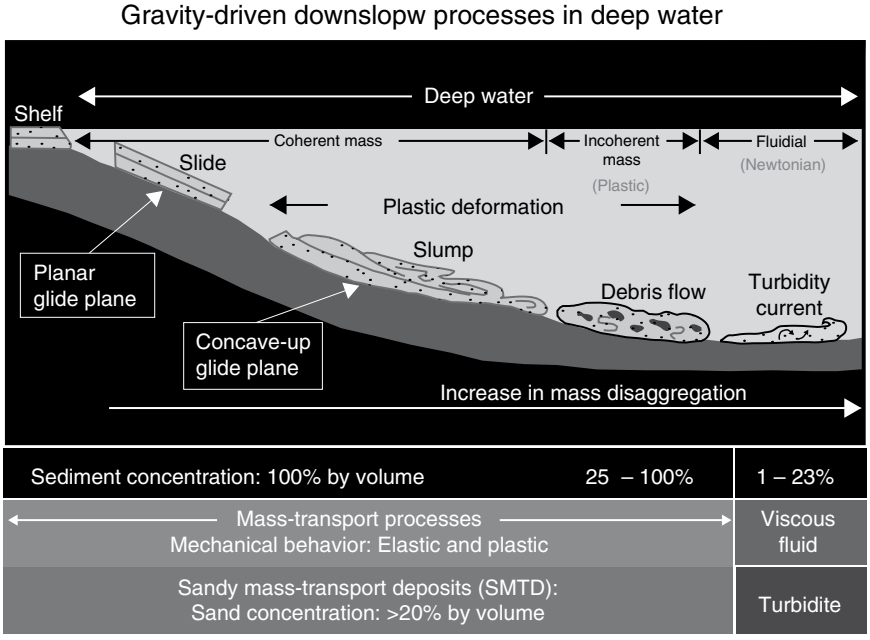


Figure 12.3 Schematic diagram showing four common types of gravity-driven downslope processes that transport sediment into deep marine environments: slides that may be transformed into a slump, which represents a coherent rotational mass transport of a block or strata on a concave-up glide plane with internal deformation. Upon addition of fluid during downslope movement, slumped material may transform into a debris flow that transports sediment as an incoherent mass in which intergranular movements predominate over shear-surface movements. As fluid content increases in debris flow, the flow may evolve into a Newtonian turbidity current. Not all turbidity currents, however, evolve from debris flows. Some turbidity currents may evolve directly from sediment failures. Turbidity currents can develop near the shelf edge, on the slope, or in distal basinal settings. Source: After Shanmugam (2015).

chaotic facies. MTCs are characterized by great lateral extent, and individual events within the MTCs have the ability to flow across gentle slopes and to transport intact blocks with dimensions of tens or even hundreds of meters (Shanmugam, 2015). MTCs have been increasingly recognized along several continental margin settings worldwide, through enhanced resolution bathymetric maps (Lastras et al., 2002, 2004; Gamberi et al., 2011; Rovere et al., 2014) and 3D seismic data (Moscardelli et al., 2006; Dalla Valle et al., 2013), and, by combining diverse data sets, across different scales and resolutions (Georgiopoulou et al., 2018).

In addition, slope failures causing submarine landslides may also progress in a staged fashion, such as retrogressive failures where the unloading from downslope failures sequentially imposes new failures upslope. The best known example of a retrogressive slope failure is the Storegga Slide (Kvalstad et al., 2005), although other large landslides, such as the Trænadjupet Slide, exhibit retrogressive failure too (Løvholt et al., 2017). In these cases, enhanced morphometric analyses contribute largely to the understanding of mass-wasting processes, provided that bathymetric data are of sufficient high resolution (Micallef et al., 2007).

12.3. TRIGGERS AND PRECONDITIONING FACTORS

Submarine landslides occur if the applied shear stresses, such as due to gravity, seismic shaking, and wave loading, exceed the shear strength (τ) of the slope sediments (e.g., Løseth, 1999; Sultan et al., 2004a). Applied gravity forces increase if slope angle increases as a consequence of, for example, tectonic movements referred as oversteepening. However, tectonic oversteepening is regarded more as an important precursor prior to slope failure rather than a trigger mechanism. Moreover, it is widely accepted that landslides are initiated when the shear strength of the slope material decreases in a short time (e.g., Løseth, 1999). The most efficient way to decrease the shear strength is a transient increase of pore pressure (Δu), because the effective stress is the overburden stress σ_n (primarily caused by the sediment weight) acting normal to a failure plane, minus the pore pressure (u) such that $\tau = \mu(\sigma_n - \Delta u)$ (e.g., Pestana et al., 2000; Talling et al., 2014; Figure 12.4). Here μ is the coefficient of friction. In general, the most common mechanisms that increase the pore pressure, and hence decrease the effective stress in the sediment, include rapid sedimentation

(>mm/yr) and/or tectonic loading, earthquakes, tidal variations, mineral dehydration, gas charging, and gas hydrate dissociation and dissolution processes (e.g., Hampton et al., 1996; Sultan et al., 2004b; Locat & Lee, 2009; Dugan & Sheahan, 2012; Urgeles & Camerlenghi, 2013; Hsu et al., 2018; Figure 12.4c).

Most conceptual models for slope failure based on the assumption of the presence of mechanically weak layers, which have intrinsically lower shear strength, are embedded in the slope stratigraphic architecture (e.g., Masson et al., 2010). Particularly, the sequencing of layers with different physical properties, especially permeabilities, plays an important role on where failure surfaces are localized. In many submarine landslide studies, it has been hypothesized that soft clays (e.g., Kvalstad et al., 2005; Dan et al., 2007), loose granular silts and sands (e.g., L'Heureux et al., 2012), high-porous ash layers (e.g., Kuhlmann et al., 2016), or altered volcanic deposits with high liquefaction potential (Miramontes et al., 2018) could act as weak layers, thereby serving as potential basal failure planes of submarine landslides. The physical understanding is based on the assumption that, for example, the high-porous ash-layer matrix would collapse during cyclic loading, generating transient high pore pressure (e.g., Wiemer & Kopf, 2017). A similar process is also hypothesized for diatom-ooze-rich sediments, which are susceptible to building up excess pore fluid during burial due to their high compressibility and water content (e.g., Volpi et al., 2003; Urlaub et al., 2018a). Although such layers are prone to generate transient high pore pressures, an overlaying low-permeable layer is required as a barrier to upward drainage (e.g., Dugan & Sheahan, 2012). Overpressure is most likely to be found where low-permeability ($<10^{-16}$ m^2) layers have inhibited pore fluid escape or there have been large forcing mechanisms (e.g., rapid sedimentation, tectonic stressing, heating, and volume-creating reactions; Dugan & Sheahan, 2012). The genesis and magnitude of overpressure can be controlled by physical processes (e.g., rapid sedimentation, tectonic loading, and lateral fluid transfer), as well as thermal and chemical processes

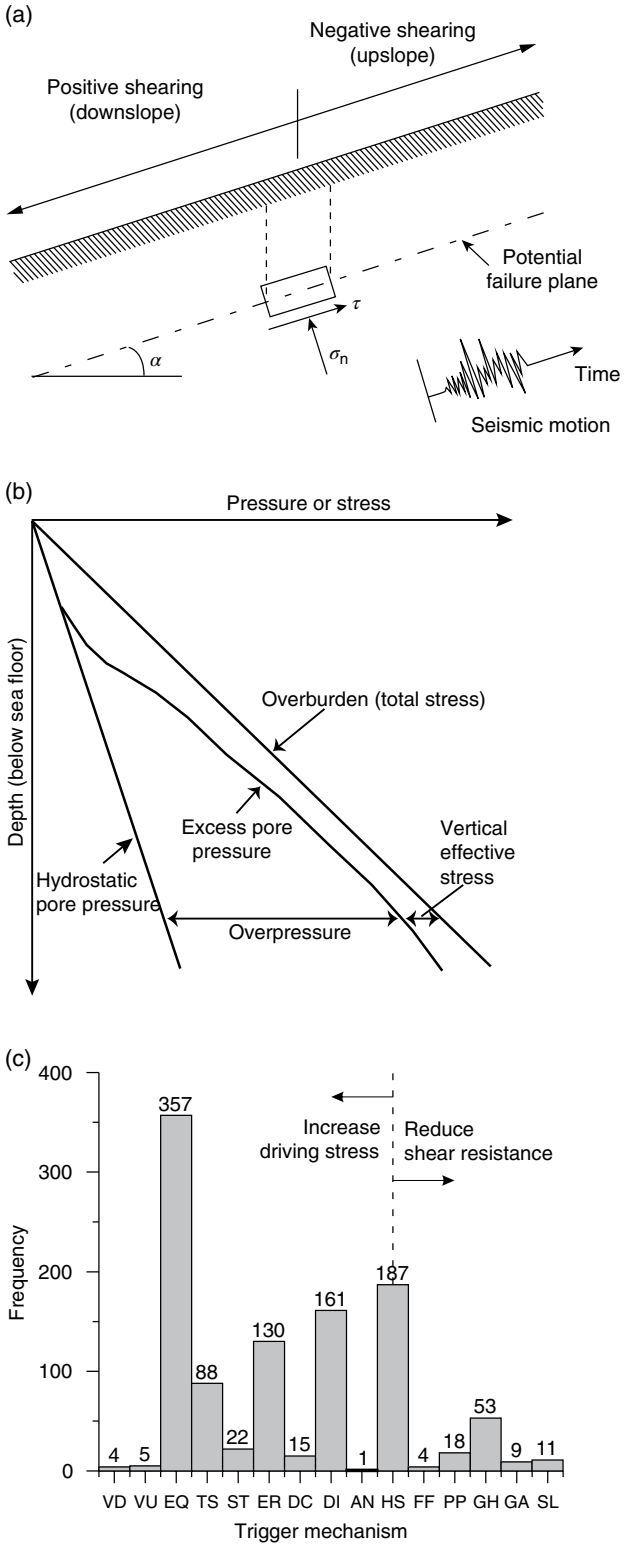


Figure 12.4 (a) Relationship between overburden (total stress; σ_n) and excess pore pressure (u) acting normal to a failure plane, and shear strength (τ) along the failure plane. Source: From Pestana et al. (2000). (b) Generalized example of change in overburden, hydrostatic pore pressure, excess pore pressure, and vertical effective stress with depth below the seafloor. Source: Modified from Talling et al. (2014). (c) Major factors cited to be involved in triggering slope failure offshore (separated according to those that increase the driving stress and those that reduce the shear strength [VD, volcano development; VU, volcano uplift; EQ, earthquake; TS, tectonic steepening; ST, steepening; ER, erosion; DC, differential compaction; DI, diapirism; AN, anthropic; HS, high sedimentation rates; FF, fluid flow; PP, pore pressure; GH, gas hydrates; GA, gas; SL, sea level]). Source: After Urgeles and Camerlenghi (2013).

(e.g., aquathermal expansion, hydrocarbon generation, mineral diagenesis, and organic maturation; Dugan & Sheahan, 2012). Thus, a stratigraphic sequence of embedded high-permeability sediments between low-permeability layers could be an essential preconditioning factor for submarine landslides, although it is still unknown where the failure plane is located: in the weak layer, in the covering layer, or along the interface (e.g., Kuhlmann et al., 2016; Urlaub et al., 2018a). Moreover, further uncertainties remain, as, for example, volcanic ash itself and diatoms exhibit high shear strength, and more importantly, shear strength even increases with increasing diatom content due to particle interlocking (e.g., Wiemer & Kopf, 2017). On the other hand, the concept of seismic strengthening also needs to be considered. Although it has been proposed that numerous submarine landslides are ultimately triggered by earthquakes (i.e., cyclic loading driven by seismic shaking; Figure 12.4c), repeated, non-failure seismic events can actually strengthen the sediment through development of excess pore pressure during earthquakes and subsequent drainage, resulting in a densification during intervening periods (ten Brink et al., 2016). This in turn is in agreement with the observation that most modern giant landslides are observed at passive margins rather than at active margins. More research is needed on the mechanics of weak layers to gain a deeper insight into the geo-mechanical behavior of submarine slope sediments. This is no trivial task, as weak layers are mostly destroyed by landslide masses, such that the sediment of which the weak layer consisted has vanished with the landslide.

Another widely debated aspect of submarine landslide initiation is the impact of climate change (see also next paragraphs). It has been repeatedly hypothesized that deepwater warming may have triggered gas hydrate dissociation in the past, thus contributing to global greenhouse gas levels and possibly to the catastrophic collapse of submarine continental slopes (Kennett et al., 2003). For example, in the last decade, deep Eastern Mediterranean water masses have undergone a temperature increase in excess of 0.5 °C (Della Vedova et al., 2003). Gas hydrates, solid "icelike" compounds of methane and water present in the pore spaces of marine sediments at continental margins, are sensitive to small changes in ambient pressure and temperature (Brewer et al., 1998). Dissociation of only a small amount of gas hydrate can substantially weaken slope sediments (Grozic, 2010). Recent studies suggested that cracking of the seafloor induced by gas hydrate dissociation might be ongoing in areas of the North Atlantic (Driscoll et al., 2000) and the Arctic Ocean (Mienert, 2009). Natural environmental changes, such as those associated with glacial/interglacial climate changes, are capable of generating free gas from hydrates, subsequent expansion of pore fluids, and pore pressure buildup, thus weakening sediment strength (Lee, 2009). Westbrook et al. (2009) and Phrampus and Hornbach (2012) report data and thermal models suggesting that changes in the Gulf Stream are rapidly destabilizing methane hydrates along the North American and Arctic continental margins. In addition, a few submarine landslides occur in areas that presently or previously contained gas hydrates (e.g., Hornbach et al., 2007; Mountjoy et al., 2014; Pecher et al., 2017; Chen et al., 2018; Kuhlmann et al., 2018). Nevertheless, the involved mechanisms, both for past and modern events, are still poorly understood, and there is no clear evidence of the interplay between gas hydrate dissociation and subsequent slope failure. Although new mechanisms for gas hydrate dissociation such as variations in pore water salinity were recently proposed (Riboulot et al., 2018), there is still a clear lack in knowledge on how gas hydrates relate to sediment stability.

Other peculiar factors that may favor mechanical weakness are sediment compaction and diagenesis (i.e., chemical changes occurring in sediments after their deposition; e.g., Volpi et al., 2003; Davies & Clark, 2006), sudden loss of strength during compaction of marine mud (destructuring), or the influence of groundwater systems on pore water distribution in nearshore marine sediments, such as in the case of the Nice margin failure in the Western Mediterranean (Dan et al., 2007). Here it has been realized that interstitial fluid flow in continental margin sediments plays a fundamental role in submarine landslide initiation (e.g., Stegmann et al., 2011; see also Figure 12.4c).

In recent years, it has also been proposed that the intrinsic sedimentary characteristics of contourites (sediments deposited under the action of oceanic bottom currents) may favor seafloor instability and failure (Laberg & Camerlenghi, 2008; Verdicchio & Trincardi, 2008; Miramontes et al., 2016). Hence, also continental margin stratigraphic architecture may control localization of excess pore pressures that build up at depth and determine a decrease in sediment shear strength that can lead to slope failure (Dugan & Flemings, 2000).

At this point, it has to be mentioned that a deeper insight into the key role of preconditioning factors or individual trigger mechanisms, for example, specific earthquake events, requires solid age dating, which is shown being one of the big challenges in recent submarine landslide studies.

12.4. AGE DATING: CAPABILITIES AND LIMITATIONS

Precise age dating of the timing of slope failure is still a very challenging task (Vizcaino et al., 2006; Gràcia et al., 2010; Urlaub et al., 2013; Clare et al., 2014). In a recent study based on 68 large and well-studied landslides

worldwide, Urlaub et al. (2013) stated that uncertainties in ages are significant for a large part of the database and dating is often of poor quality. Various uncertainties still exist regarding an accurate age dating of the landslide event, which typically rise from both the availability of samples and the used method. The most used method is radiocarbon dating. However, this dating is problematic for marine sediments because of the freshwater reservoir effect (Philippsen, 2013) which always falsifies an accurate age determination. In addition, radiocarbon dating is limited to date sediments younger than 45,000 years. However, submarine landslides are in many cases much older, and such age dating is needed to accurately estimate frequencies and recurrence rates of submarine landslides over long periods or to link these to specific triggers, for example, sea level variations. In order to enable this, other methodical approaches are used, such as correlation of oxygen isotope curves and/or tephrochronology, but these techniques enable rather rough estimation than an accurate dating. Therefore, in most studies, the reliability of the individual age data is given for each deposit. Maslin et al. (2004) established a qualitative age reliability index for ages of MTD. They stressed that this is not an attempt to grade the research, but rather that it is a measure of the difficulties encountered when dating each individual deposit. The age reliability index is ranked as "excellent" (1) if reliable and reproducible radiocarbon dates at least above and below the deposit and in some cases within the deposit are available. In contrast, a "poor" (5) qualification indicates that either no radiocarbon dates are available and that ages were inferred by correlation to adjacent dated sediment cores or that there has been significant erosion of sediments overlying the MTD.

12.5. CLIMATE CONTROL AND INTERPLAY

Numerous studies have hypothesized that climate conditions, particularly their impact on sea level fluctuations and sedimentation rate, may control timing and frequency of submarine landslides (Maslin et al., 2004; Lebreiro et al., 2009; Lee, 2009). This may be supported by the view that most landslides occur in areas of highest sediment accumulation rates and/or during periods of rapid sedimentation. An example is given by Hanebuth and Henrich (2009) for the Cap Timiris Canyon offshore NW Africa, where turbidites were frequently triggered by large dust influx events. In addition, stratigraphic analysis of marine sequences in high-latitude continental margins and hydrogeological modeling efforts suggest that ice loading of continental shelves during glacial maxima had a major role in focusing of fluids, pore pressure development, and onset of slope failure producing climatically controlled deposition of submarine landslides (Llopart et al., 2015, 2019). Furthermore, it is well known that significant seismicity develops during deglaciation of these margins due to isostatic rebound, which aids in producing the stresses needed to trigger slope failure in high-latitude continental margins (Hampel et al., 2009; Brothers et al., 2013). Finally, Berndt et al. (2009) propose that global warming followed by increased seismicity around the edge of the present-day ice sheets (in particular Greenland) may trigger slope instability. Increased global temperatures may also influence slope stability from changes to the seasonality, frequency, and intensity of extreme weather events (storminess and rainfall) and from rises in global sea level (BGS, 2009).

However, other recent studies, which tried to integrate as many data sets as possible from the various regions worldwide, could not substantiate the concept that climate conditions, particularly that changes in sea level and sedimentation rate, may control timing and frequency of submarine landslides on a global scale (e.g., Korup et al., 2012; Urgeles & Camerlenghi, 2013; Urlaub et al., 2013; Pope et al., 2015; Figure 12.5). An alternative hypothesis is therefore that submarine landslides are near to random in time (Clare et al., 2014; Pope et al., 2017). Moreover, some statistical analyses have shown that there is no evidence for an immediate influence of rapid sedimentation on slope stability as failures tend to occur several thousand years after periods of high sedimentation rates (Urlaub et al., 2013; Figure 12.5). Such delays, perhaps of variable duration, will also act to decouple landslide timing from driving climate forces. At the same time, however, the various studies have also shown that the role of different controlling factors may vary between different geological settings, for example, river deltas and fans clearly respond to rapid sedimentation by multiple slope collapses, and their role might get lost in global data set, or the uncertainties are too great to identify an underlying correlation. Perhaps most importantly, the statistical analysis shows that we need to date a larger number of landslides, more precisely, to be able to determine whether landslides are random or nonrandom in time (Pope et al., 2017). So the proposed hypothesis that future climatic change may increase the frequency of submarine landslides cannot be fully answered nor neglected. Rather, this hypothesis is still to be tested rigorously.

12.6. GEOHAZARD POTENTIAL AND TSUNAMIS

Submarine landslides can be by far larger than any terrestrial landslide. They may produce tsunamis whose far-reaching effects can rival those produced by earthquake-tsunamis and thus threaten increasingly populated coastlines worldwide (Figure 12.6a; e.g., Camerlenghi et al., 2007; Lo Iacono et al., 2012; Harbitz et al., 2014). The most critical parameters for tsunami generation are

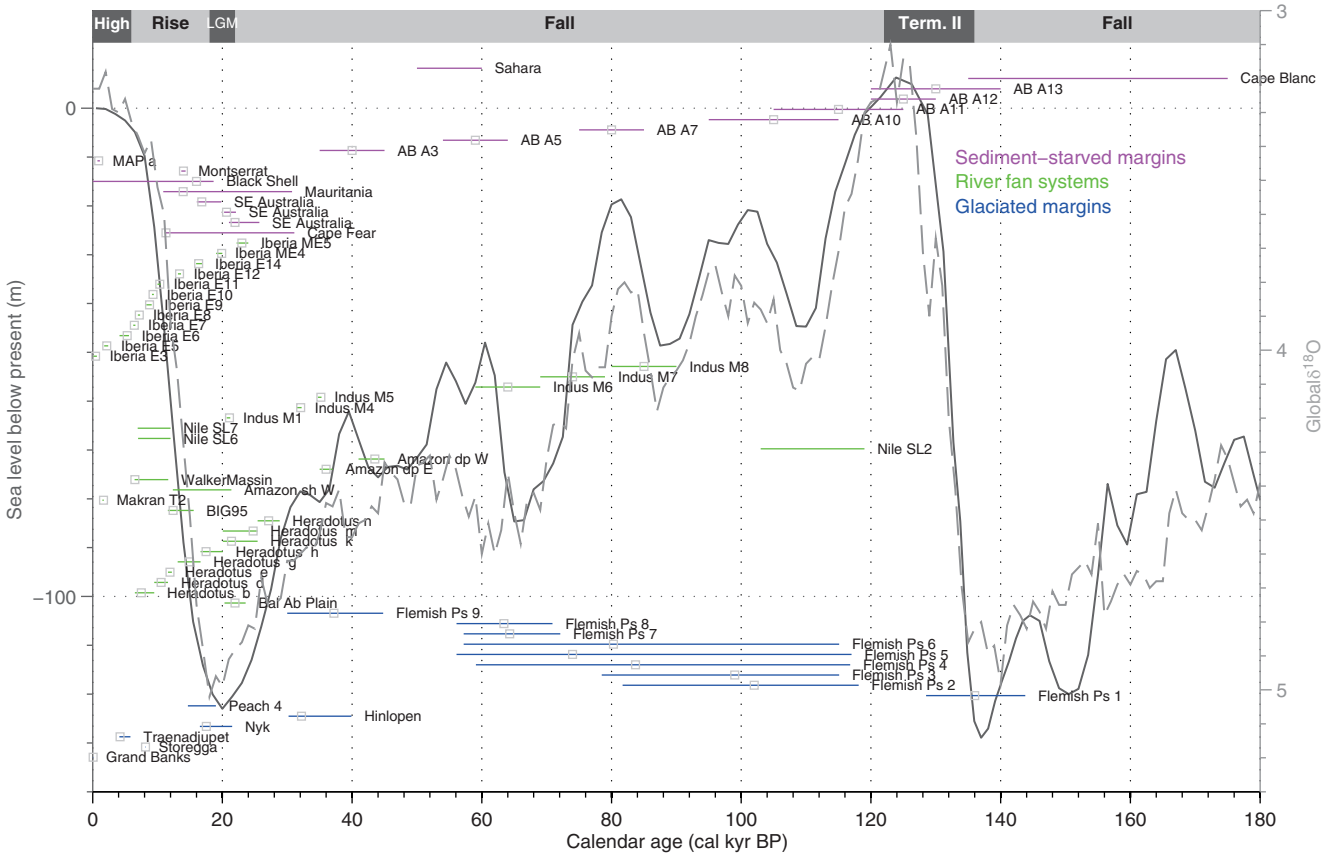


Figure 12.5 Global mean sea level (dark gray curve; Waelbroeck et al., 2002) and global stack of benthic d18O records (light gray curve; Lisiecki & Raymo, 2005) plotted with all submarine landslides including their individual uncertainty intervals. If available, the age with highest probability is shown by a gray square. The color of the uncertainty line indicates the sedimentary environment (river fan systems with high terrestrial input, glaciated margins, and sediment-starved margins). The gray timeline on the upper part of the figure indicates the sea level patterns: Sea level fall and lowstand from 180 to 136 ka BP, sea level rise and highstand during Termination II (136e122 ka BP), sea level fall (122e22 ka BP), the Last Glacial Maximum (LGM) from 22 to 18 ka BP followed by a sea level rise (18e6 ka BP), and the modern sea level highstand (6e0 ka BP). (For interpretation of the references to color in this figure legend, the reader is referred to the web version of this article). Source: After Urlaub et al. (2013). (*See electronic version for color representation of this figure*)

the failed volume, the water depth, the landslide velocity, and the landslide acceleration in different tectonic settings. In addition, the location of landslide source and the release mechanism have a strong control on the scale of the tsunami. For example, the landslide tsunami generation is most efficient when slope failure occurs in relatively shallow waters because the buildup of the resulting wave is much more efficient (e.g., Harbitz et al., 2006; Løvholt et al., 2015). Furthermore, for the same unit volume, a landslide originating on the submerged flanks of a volcanic island will produce a smaller tsunami than a landslide comprising the subaerial volcanic edifice (Watt et al., 2012). In addition, tsunami magnitude is also critically dependent on whether failure occurs in one stage or in successive separate stages. Failure in a series of stages separated by a few tens of seconds or minutes can substantially reduce the resulting tsunami magnitude (e.g., Haugen et al., 2005). It has been shown that such staged failure can involve failure of more blocks at a time (e.g., Gauer et al., 2005). If the cascading failures are efficiently conveyed into a large debris flow, the tsunami generation can yet become pronounced (Løvholt et al., 2017). With a certain time gap between the individual stages, the landward tsunami can be even higher than for a one-stage event (Løvholt et al., 2005).

Historically, the first evidence of a truly massive landslide-induced tsunami was due to the 1929 Grand Banks Slide with a slide volume larger than 150 km^3 (e.g., Piper et al., 1999), possibly caused by a combination of a large slump and translational landslide that later evolved into a turbidity current (Løvholt et al., 2018). A well-known prehistorical event is the Storegga submarine landslide

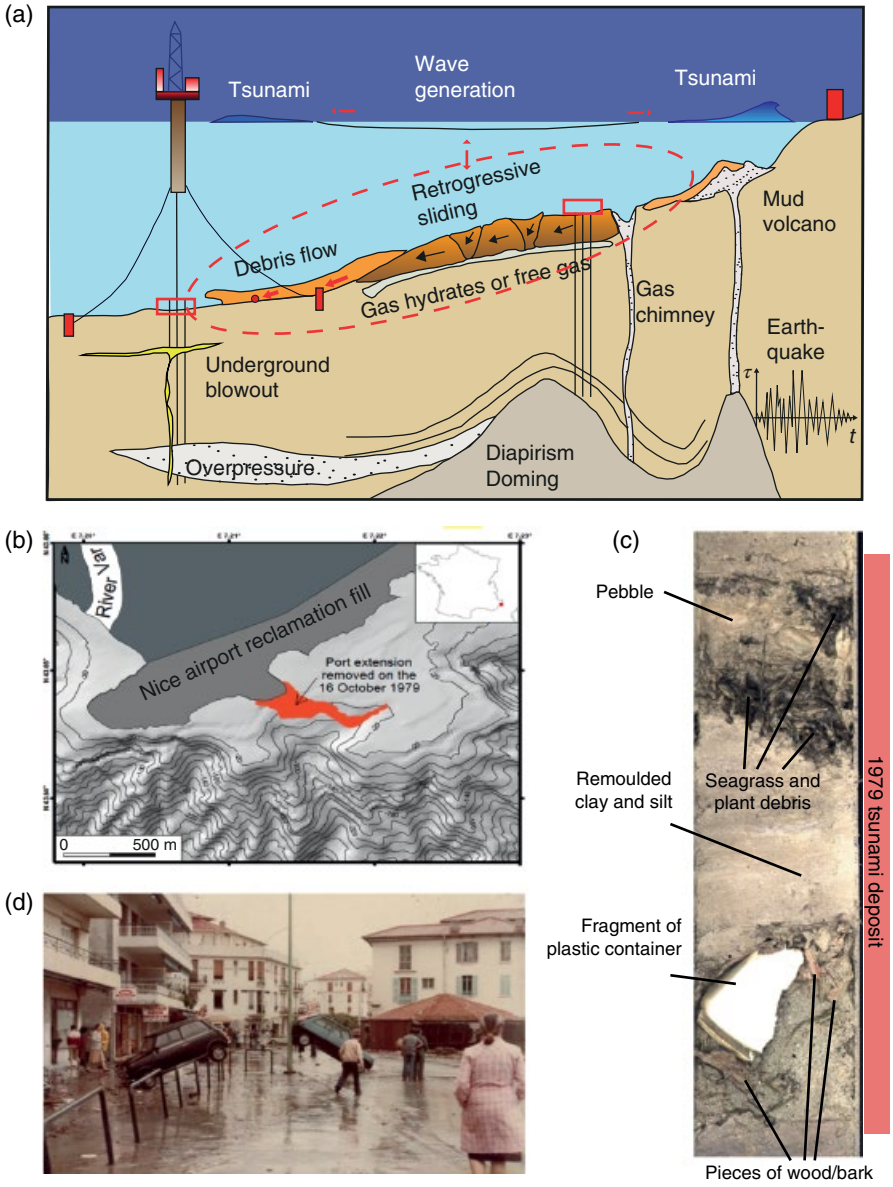


Figure 12.6 (a) Offshore geohazards. Submarine slides generated by human activity are recognized as submarine geohazards for first party (seabed structures) and for third party (population) because of their potential to generate tsunamis. Source: After Camerlenghi et al. (2007). Submarine slides are known to occur also as a consequence of the natural evolution of continental margins. (b) Map of the Nice Airport Slide that occurred on 16 October 1979. Red contour shows collapsed pier construction that caused the landslide and 2–3 m high tsunami; inset shows map of France. Source: After Kopf et al. (2016). (c) Photograph of dislocated cars and flooded streets in the village of Antibes west of the Nice landslide. Source: https://www.nicematin.com/faits-divers/il-y-a-39-ans-un-tsunami-faisait-onze-morts-sur-la-cote-dazur-267342. (d) Photograph of core (detail) taken north of the Nice landslide scar that shows the tsunamite deposited after the 1979 event; note the plastic and wood/bark pieces and remolded nature of the deposit. Source: After Kopf et al. (2016). (*See electronic version for color representation of this figure*)

that occurred 8200 years ago offshore Norway and involved >3000 km^3 of sediment. It generated a tsunami that ran up to heights of up to 20 m around surrounding European coasts (Bondevik et al., 2005). Yet high mobility dynamics is integral for generating a large tsunami, and a slower evolution and more gradual mass release is hypothesized to be the reason for the clear lack of tsunami evidence from the giant Trænadjupet Slide (with a volume of about 500 km^3) just north of the Storegga Slide (Løvholt et al., 2017).

However, even small landslides, such as the ~4 km^3 1998 Papua New Guinea landslide, can cause tsunami

run-up exceeding 10 m (Synolakis et al., 2002; Tappin et al., 2008), illustrating that moderately large submarine landslides can damage important seafloor and coastal constructions. Similarly, the well-studied 1979 Nice Airport landslide mobilized ~0.0022 km^3 near the airport of Nice and ~0.0062 km^3 in the mid-slope and displaced sufficient water to generate a tsunami wave of 2–3 m along the French Riviera (Dan et al., 2007; Kopf et al., 2016; Figure 12.6b).

Submarine landslides and associated tsunamis are an international challenge, crossing national and oceanographic boundaries. Although landslide-tsunamis may be just as large as earthquake-triggered tsunamis, it is more difficult to provide warning for landslide-triggered tsunamis compared to earthquake-triggered tsunamis, because earthquakes are recorded on global seismological networks serving as precursors (Løvholt et al., 2015). However, current efforts are trying to mitigate offshore geohazards by implementing global monitoring systems, such as tsunami detection and early warning systems recently installed in the Pacific Ocean. Additionally, an array of in situ instruments has been connected to the EMSO seafloor cabled network offshore Nice, France. These EMSO-connected systems have proven powerful in unraveling the governing factors that lower effective stress in sediments and hence impose significant landslide risk to densely populated areas (e.g., Stegmann et al., 2011). Nevertheless, much more is needed to unravel processes governing hazards such as submarine landslides over time.

12.7. LONG-TERM MONITORING

Although long-term monitoring is valuable for continental slopes threatened by recurring destabilization and those which are heavily used by various infrastructure, direct monitoring is still in its infancy. The reasons for that are (i) challenging environments and remote settings, which were previously prohibitively costly (Talling et al., 2013; Kelley et al., 2014); (ii) technological issues related to positioning accuracy, data resolution, and communications (Hughes Clarke, 2012); (iii) equipment limitations in measuring key parameters (e.g., measuring fast and/or high-concentration flows with acoustic instruments; Hughes Clarke, 2016); and (iv) the often destructive nature of the events that may damage the monitoring devices (Khripounoff et al., 2003). Perhaps the most difficult problem to solve is knowing which location on a continental slope will fail next and then whether such failure occurs over short enough time scales (two to five years) of most science projects. Landslide monitoring may thus be restricted to locations (e.g., delta fronts; Hughes Clarke, 2016) where failure occurs very frequently and such landslides tend to be small in volume. Nevertheless, geotechnical monitoring of offshore sites is becoming more commonplace, such as the deployment of in situ piezometers and tiltmeters to understand slope stability issues at specific locations (Figure 12.7; e.g., Strout & Tjelta, 2005; Stegmann et al., 2012; Clare et al., 2017). Besides, repeated seafloor surveys using high-resolution multibeam systems revealed not just the scale but also the frequency of submarine landslides in several systems worldwide (e.g., along the Nice slope (Kelner et al., 2014); at active pro-deltas (Hughes Clarke, 2016; Obelcz et al., 2017); in deepwater submarine canyons (Mountjoy et al., 2018; Smith et al., 2007)). Such measurements have proven to be suitable particularly in areas with large displacements and shallow-water conditions. For instance, annual seafloor surveys at the submarine delta of the Ogooué River, Gabon, between 2004 and 2009 revealed slope failures (up to 2.5 million m^3) that occur on at least annual basis (Biscara et al., 2012).

Beyond morphologic changes, monitoring with instruments such as broadband ocean bottom seismometers (OBS) can provide information on the timing and nature of slope failure. In the southern Tyrrhenian Sea, OBS monitoring revealed not only earthquake-related seismicity but also low-frequency seismicity events related to volcanic degassing and its relationship with submarine landsliding (Sgroi et al., 2014). Similar interpretations have been made from multiple moored hydrophones offshore West Mata volcano in the Lau Basin near Tonga (Caplan-Auerbach et al., 2014) where velocities of submarine landslides were estimated from triangulation. Even shore-based monitoring may provide insights into submarine landslide activity. For instance, offshore landslides have been detected in the Kaoping Canyon, offshore Taiwan, using terrestrial broadband seismic networks (Lin et al., 2010). Furthermore, most recently, advances in seafloor geodetic monitoring have enabled monitoring of the slow displacement of the volcanic flank offshore Mount Etna, thus providing the first detailed, direct quantification on conditions prior to, and during, large-scale slope instability (Urlaub et al., 2018b). Following this excellent example, further volcanic flanks and continental slopes, which are characterized by landslides, should be monitored with geodetic tools in the future in order to obtain comparable data sets to gain a deeper insight into displacement rates at different geological settings.

Other major recent advances have been made through directly measuring turbidity currents (e.g., Xu et al., 2004; Azpiroz-Zabala et al., 2017; Paull et al., 2018). Indeed, it could be argued that the most compelling future need is to monitor conditions before and during submarine landslides. Without such direct measurements of events, it may be challenging to make major advances or test models. However, monitoring large submarine landslides may be more challenging than for turbidity

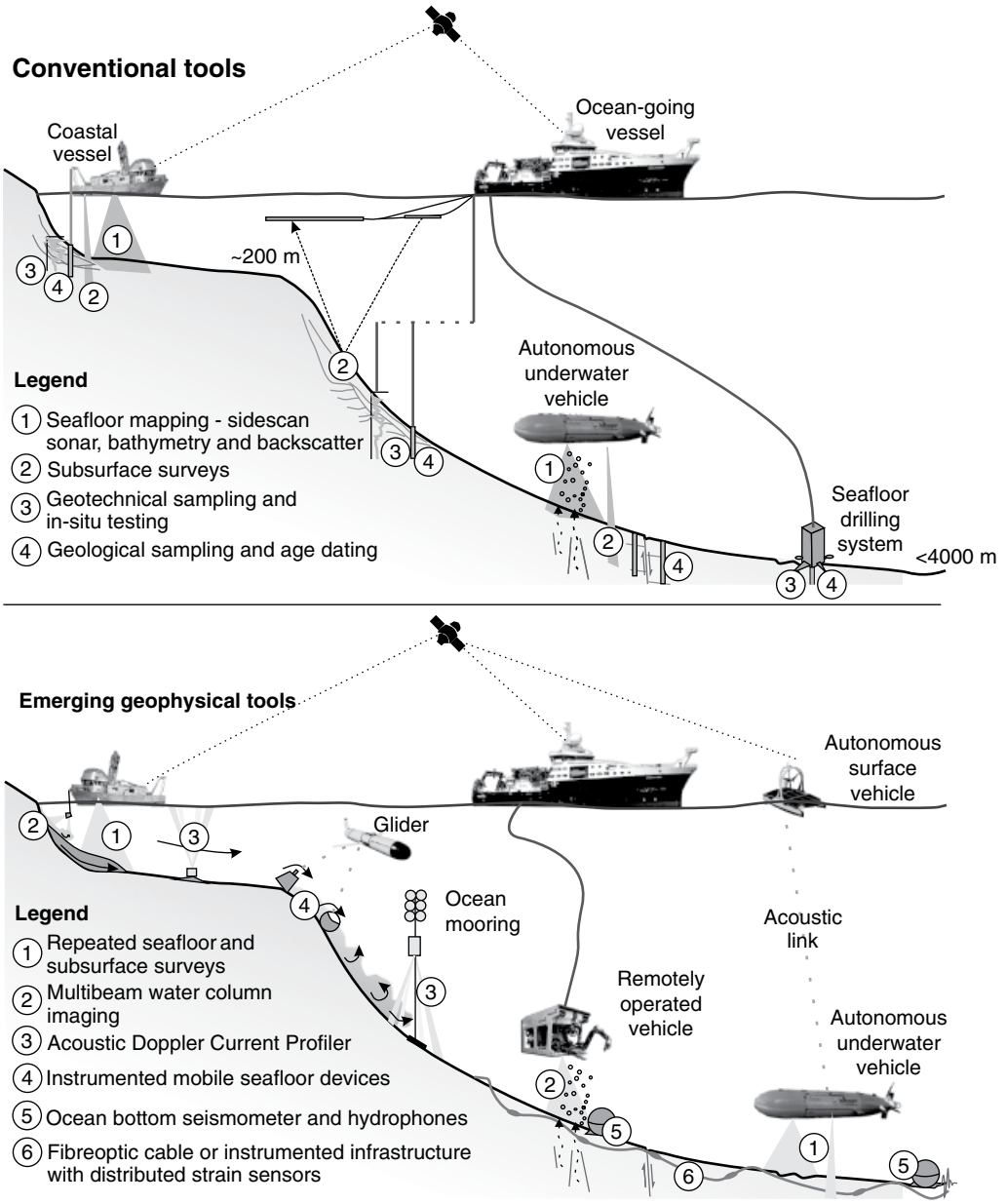


Figure 12.7 Conventional and emerging geophysical tools for monitoring offshore geohazards discussed in this paper. ROV image from neptunems.com. ASV image from asvglobal.com. Source: After Clare et al. (2017).

currents, as it is unclear where the next landslide will occur and some have recurrence intervals (>100–1000s of years) that are too long for most research (<5-year) projects. Perhaps monitoring will only ever be possible in locations where landslides are frequent, such as on prograding deltas (Hughes Clarke, 2016; Obelcz et al., 2017).

Initial monitoring work has provide new results such as that (presumably landslide-triggered) submarine flows can occur without an obvious external trigger (earthquake, storm wave loading, etc.; Paull et al., 2018) and not all submarine landslides trigger long runout flows (Hizzett et al., 2017). Such work suggests that slopes may be preconditioned and remain close to failure for long periods.

We currently have many studies and excellent data sets that investigate landslides from different perspectives; however, in order to fill outstanding but key knowledge gaps, future studies should become even more interdisciplinary, bringing more expertise together, and perhaps utilize new technologies.

12.8. SUMMARY

This chapter provides a very short review of submarine landslide studies, with some emphasis on the emerging needs in future landslide research. The wealth of publications, and the limited space for this article, ensures that it is not complete. However, we emphasize that, despite the wealth of studies over the past decades, much is still unknown or at least uncertain. There are many open questions and technological challenges that the next generation of researchers and the joint European Training Network (ETN) SLATE, whose members have contributed toward this chapter, have to address.

ACKNOWLEDGMENTS

This manuscript benefited from the critical review of Aggeliki Georgiopoulou and a second unknown reviewer. We want to thank them for their thoughtful work and insightful comments. We also thank the European Union for funding the ETN SLATE in the EU Framework Programme for Research and Innovation Horizon 2020 (grant agreement no. 721403).

REFERENCES

Azpiroz-Zabala, M., Cartigny, M. J., Talling, P. J., Parsons, D. R., Sumner, E. J., Clare, M. A., et al. (2017). Newly recognized turbidity current structure can explain prolonged flushing of submarine canyons. *Science Advances*, *3*(10), e1700200.

Berndt, C., Brune, S., Nisbet, E., Zschau, J., & Sobolev, S. V. (2009). Tsunami modeling of a submarine landslide in the Fram Strait. *Geochemistry, Geophysics, Geosystems*, *10*, Q04009. https://doi.org/10.1029/2008GC002292

BGS (2009) *TRANSFER project deliverable D3.1–D3.5: An examination of non-seismic sources of tsunamis and their impacts on European coastlines – WP3 of EU project TRANSFER* http://www.transferproject.eu

Biscara, L., Hanquiez, V., Leynaud, D., Marieu, V., Mulder, T., Gallissaires, J. M., et al. (2012). Submarine slide initiation and evolution offshore Pointe Odden, Gabon: Analysis from annual bathymetric data (2004–2009). *Marine Geology*, *299*, 43–50.

Bondevik, S., Løvholt, F., Harbitz, C., Mangerud, J., Dawson, A., & Svendsen, J. I. (2005). The Storegga Slide tsunami: Comparing field observations with numerical observations. *Marine and Petroleum Geology*, *22*, 195–208.

Boyd, R., Keene, J., Hubble, T., Gardnr, J, Glenn, K., Ruming, K., Exon, N. (2010) Southeast Australia a Cenozoic continental margin dominated by mass transport. pp 1–18, in *Submarine mass movements and their consequences, Advances in Natural and Technological Hazard Research*. D.C. Mosher, C. Shipp, L. Moscardelli, J. Chaytor, C. Baxter, H. Lee, et al. eds, vol. 28, Springer, Dordrecht, The Netherlands.

Brewer, P. G., Orr, F. M., Friederich, G., Kvenvolden, K. A., & Orange, D. L. (1998). Gas hydrate formation in the deep sea: In situ experiments with controlled release of methane, natural gas and carbon dioxide. *Energy & Fuels*, *12*, 183–188.

Brothers, D. S., Luttrell, K. M., & Chaytor, J. D. (2013). Sea-level–induced seismicity and submarine landslide occurrence. *Geology*, *41*, 979–982. https://doi.org/10.1130/G34410.1

Bryn, P., Solheim, A., Berg, K., Lien, R., Forsberg, C. F., Haflidason, H., et al. (2003). The storegga slide complex: Repeated large scale sliding in response to climatic cyclicity. In J. Locat & J. Mienert (Eds.), *Submarine mass movements and their consequences, Advances in Natural and Technological Hazards Research* (Vol. 19, pp. 215–222). Dordrecht, The Netherlands: Kluwer Academic.

Camerlenghi, A., & Pini, G. A. (2009). Mud volcanoes, olistostromes, and argille scagliose in the Mediterranean Region. *Sedimentology*, *56*, 319–365. https://doi.org/10.1111/j.1365-3091.2008.01016.x

Camerlenghi, A., Urgeles, R., Ercilla, G., & Brückman, W. (2007). Scientific ocean drilling behind the assessment of geohazards from submarine slides. *Scientific Drilling*, *4*, 45–47.

Caplan-Auerbach, J., Dziak, R. P., Bohnenstiehl, D. R., Chadwick, W. W., & Lau, T. K. (2014). Hydroacoustic investigation of submarine landslides at West Mata volcano, Lau Basin. *Geophysical Research Letters*, *41*(16), 5927–5934.

Carter, L., Burnett, D., Drew, S., Hagadorn, L., Marle, G., Bartlett-McNeil, D., & Irvine, N. (2009). *Submarine cables and the oceans: Connecting the world, UNEP-WCMC Biodiversity Series* (Vol. 31). Cambridge, UK: ICPC/UNEP/UNEP-WCMC.

Casas, D., Chiocci, F., Casalbore, D., Ercilla, G., & de Urbina, J. O. (2016). Magnitude-frequency distribution of submarine landslides in the Gioia Basin (southern Tyrrhenian Sea). *Geo-Marine Letters*, *36*, 405–414.

Cattaneo, A., Babonneau, N., Ratzov, G., Dan-Unterseh, G., Yelles, K., Bracène, R., et al. (2012). Searching for the seafloor signature of the 21 May 2003 Boumerdès earthquake offshore central Algeria. *Natural Hazards and Earth System Sciences*, *12*, 2159–2172.

Chaytor, J. D., ten Brink, U. S., Solow, A. R., & Andrews, B. D. (2009). Size distribution of submarine landslides along the U.S. Atlantic margin. *Marine Geology*, *264*, 16–27. https://doi.org/10.1016/j.margeo.2008.08.007

Chen, S.-C., Tsai, C.-H., Hsu, S.-K., Yeh, Y.-C., Liu, C.-S., Chung, S.-H., & Wei, C.-Y. (2018). Fangliao Slide – A large slope failure in the upper Kaoping Slope off southwest Taiwan. *Terrestrial, Atmospheric and Oceanic Sciences*, *29*, 17–30.

Clare, M., Chaytor, J., Dabson, O., Gamboa, D., Georgiopoulou, A., Eady, H., et al. (2018). A consistent global approach for the morphometric characterization of subaqueous landslides. *Geological Society, London, Special Publications*, *477*. https://doi.org/10.1144/SP477.15

Clare, M., Vardy, M. E., Cartigny, M. J. B., Talling, P. J., Himsworth, M. D., Dix, J. K., et al. (2017). Direct monitoring of active geohazards: Emerging geophysical tools for deep-water assessments. *Near Surface Geophysics*, *15*, 427–444. https://doi.org/10.3997/1873-0604.2017033

Clare, M. A., Talling, P. J., Challenor, P., Malgesini, G., & Hunt, J. (2014). Distal turbidites reveal a common distribution for large (>0.1 km^3) submarine landslides recurrence. *Geology*, *42*(3), 263–266. https://doi.org/10.1130/G35160.1

Dalla Valle, G., Gamberi, F., Rocchini, P., Minisini, D., Errera, A., Baglioni, L., & Trincardi, F. (2013). 3D seismic geomorphology of mass transport complexes in a foredeep basin: Examples from the Pleistocene of the Central Adriatic Basin (Mediterranean Sea). *Sedimentary Geology*, *294*, 127–141. https://doi.org/10.1016/j.sedgeo.2013.05.012

Dan, G., Sultan, N., & Savoye, B. (2007). The 1979 Nice harbour catastrophe revisited: Trigger mechanism inferred from geotechnical measurements and numerical modelling. *Marine Geology*, *245*, 40–64.

Davies, R. J., & Clark, I. R. (2006). Submarine slope failure primed and triggered by silica and its diagenesis. *Basin Research*,*18*(3),339–350.https://doi.org/10.1111/j.1365-2117.2006.00297.x

De Blasio, F. V., Elverhøi, A., Engvik, L., Issler, D., Gauer, P., & Harbitz, C. (2006). Understanding the high mobility of subaqueous debris flows. *Norwegian Journal of Geology*, *86*, 275–284.

Della Vedova, B., Pellis, G., Camerlenghi, A., Foucher, J. P., & Harmegnies, F. (2003). Thermal history of deep-sea sediments as a record of recent changes in the deep circulation of the eastern Mediterranean. *Journal of Geophysical Research*, *108*(C9), 8110. https://doi.org/10.1029/2002JC001402

Driscoll, N. W., Weissel, J. K., & Goff, J. A. (2000). Potential for large-scale submarine slope failure and tsunami generation along the U.S. mid-Atlantic coast. *Geology*, *28*, 407–410.

Dugan, B., & Flemings, P. B. (2000). Overpressure and fluid flow in the New Jersey continental slope: Implications for slope failure and cold seeps. *Science*, *289*, 288–291.

Dugan, B., & Sheahan, T. C. (2012). Offshore sediment overpressures of passive margins: Mechanisms, measurement, and models. *Reviews of Geophysics*, *50*, RG3001. https://doi.org/10.1029/2011RG000379

Embley, R. W. (1980). The role of mass transport in the distribution and character of deep-ocean sediments with special reference to the North Atlantic. *Marine Geology*, *38*, 23–50. https://doi.org/10.1016/0025-3227(80)90050-X

Field, M. E., Gardner, J. V., Jennings, A. E., & Edwards, B. D. (1982). Earthquake-induced sediment failures on a 0.25° slope, Klamath River delta, California. *Geology*, *10*, 542–546.

Gamberi, F., Rovere, M., & Marani, M. (2011). Mass-transport complex evolution in a tectonically active margin (Gioia Basin, Southeastern Tyrrhenian Sea). *Marine Geology*, *279*(1–4), 98–110. https://doi.org/10.1016/j.margeo.2010.10.015

Gauer, P., Kvalstad, T. J., Forsberg, C. F., Bryn, P., & Berg, K. (2005). The last phase of the Storegga slide: Simulation of retrogressive slide dynamics and comparison with slide scar morphology. *Marine and Petroleum Geology*, *22*, 311–218. https://doi.org/10.1016/j.marpetgeo.2004.10.004

Georgiopoulou, A., Krastel, S., Finch, N., Zehn, K., McCarron, S., Huvenne, V., et al. (2018). On the timing and nature of the multiple phases of slope instability on eastern Rockall Bank, Northeast Atlantic. *Geochemistry, Geophysics, Geosystems*. https://doi.org/10.31223/osf.io/cyuwn

Georgiopoulou, A., Masson, D. G., Wynn, R. B., & Krastel, S. (2010). Sahara Slide: Age, initiation, and processes of a giant submarine slide. *Geochemistry, Geophysics, Geosystems*, *11*(7). https://doi.org/10.1029/2010GC003066

Giles, P., Nichols, G., & Wilford, D. (2010). Alluvial Fans: From reconstructing past environments to identifying contemporary hazards. *Geomorphology*, *118*(1–2), 224.

Gràcia, E., Vizcaino, A., Escutia, C., Asioli, A., Rodés, A., Pallàs, R., et al. (2010). Holocene earthquake record offshore Portugal (SW Iberia): Testing turbidite paleoseismology in a slow-convergence margin. *Quaternary Science Reviews*, *29*, 1156–1172.

Grozic, J.L.H. 2010. Interplay between gas hydrates and submarine slope failure. Pp. 11–30 in *Submarine mass movements and their consequences, Advances in Natural and Technological Hazard Research*. D.C. Mosher, C. Shipp, L. Moscardelli, J. Chaytor, C. Baxter, H. Lee et al. eds, vol. 28, Springer, Dordrecht, The Netherlands.

Haeussler, P. J., Parsons, T., Finlayson, D. P., Hart, P., Chaytor, J. D., Ryan, H., & Liberty, L. (2014). New imaging of submarine landslides from the 1964 earthquake near Whittier, Alaska, and a comparison to failures in other Alaskan fjords. In S. Krastel, J.-H. Behrmann, D. Völker, M. Stipp, C. Berndt, R. Urgeles, et al. (Eds.), *Submarine mass movements and their consequences* (Vol. 37, pp. 361–370). Cham, The Netherlands: Springer. https://doi.org/10.1109/DATE.2004.1269268

Haflidason, H., Sejrup, H. P., Nygard, A., Mienert, J., Bryn, P., Lien, R., et al. (2004). The Storegga Slide: Architecture, geometry and slide development. *Marine Geology*, *213*, 201–234. https://doi.org/10.1016/j.marpetgeo.2004.10.008

Hampel, A., Hetzel, R., Maniatis, G., & Karow, T. (2009). Three-dimensional numerical modeling of slip rate variations on normal and thrust fault arrays during ice cap growth and melting. *Journal of Geophysical Research*, *114*. https://doi.org/10.1029/2008JB006113

Hampton, M. A., Lee, H. J., & Locat, J. (1996). Submarine landslides. *Reviews of Geophysics*, *34*, 33. https://doi.org/10.1029/95RG03287

Hanebuth, T. J. J., & Henrich, R. (2009). Recurrent decadal-scale dust events over Holocene western Africa and their control on canyon turbidite activity (Mauritania). *Quaternary Science Reviews*, *28*(3-4), 261–270. https://doi.org/10.1016/j.quascirev.2008.09.024

Harbitz, C. B., Løvholt, F., & Bungum, H. (2014). Submarine landslide tsunamis: How extreme and how likely? *Natural Hazards*, *72*(3), 1341–1374. https://doi.org/10.1007/s11069-013-0681-3

Harbitz, C. B., Løvholt, F., Pedersen, G., & Masson, D. G. (2006). Mechanisms of tsunami generation by submarine landslides. *Norwegian Journal of Geology*, *86*, 255.

Harbitz, C. B., Parker, G., Elverhøi, A., Marr, J. G., Mohrig, D., & Harff, P. A. (2003). Hydroplaning of subaqueous debris flows and glide blocks: Analytical solutions and discussion. *Journal of Geophysical Research*, *108*(B7), 2349. https://doi.org/10.1029/2001JB001454

Haugen, K. B., Løvholt, F., & Harbitz, C. B. (2005). Fundamental mechanisms for tsunami generation by submarine mass flows in idealized geometries. *Marine and Petroleum Geology*, *22*, 209–218.

Hizzett, J., Hughes Clarke, J. E., Sumner, E. J., Cartigny, M. J. B., Talling, P. J., & Clare, M. (2017). Which triggers produce the most erosive, frequent and longest runout turbidity currents on deltas? *Geophysical Research Letters*, *45*, 855–863.

Hornbach, M. J., Lavier, L. L., & Ruppel, C. D. (2007). Triggering mechanism and tsunamogenic potential of the Cape Fear Slide complex, U.S. Atlantic margin. *Geochemistry, Geophysics, Geosystems*, *8*, Q12008. https://doi.org/10.1029/2007GC001722

Hsu, S.-K., Kuo, J., Lo, C.-L., Tsai, C.-H., Doo, W.-B., Ku, C.-Y., & Sibuet, J.-C. (2008). Turbidity currents, submarine landslides and the 2006 Pingtung earthquake off SW Taiwan. *Terrestrial, Atmospheric and Oceanic Sciences*, *19*(6), 767–772.

Hsu, S.-K., Lin, S.-S., Wang, S.-Y., Tsai, C.-H., Doo, W.-B., Chen, S.-C., et al. (2018). Seabed gas emissions and submarine land- slides off SW Taiwan. *Terrestrial, Atmospheric and Oceanic Sciences*, *29*, 7–15.

Hughes Clarke, J. E. (2012). Optimal use of multibeam technology in the study of shelf morphodynamics. *International Association of Sedimentologists. Special Publication*, *44*, 3–28.

Hughes Clarke, J. E. (2016). First wide-angle view of channelized turbidity currents links migrating cyclic steps to flow characteristics. *Nature Communications*, *7*, 11896.

Hühnerbach, V., Masson, D. G., & Partners of the COSTA project (2004). Landslides in the North Atlantic and its adjacent seas: An analysis of their morphology, setting and behaviour. *Marine Geology*, *213*, 343–362. https://doi.org/10.1016/j.margeo.2004.10.013

Iverson, R. M., Reid, M. E., Logan, M., LaHusen, R. G., Godt, J. W., & Griswold, J. P. (2011). Positive feedback and momentum growth during debris-flow entrainment of wet bed sediment. *Nature Geoscience*, *4*, 116–121.

Kelley, D. S., Delaney, J. R., & Juniper, S. K. (2014). Establishing a new era of submarine volcanic observatories: Cabling axial seamount and the endeavour segment of the Juan de Fuca Ridge. *Marine Geology*, *352*, 426–450.

Kelner, M., Sebastien, M., Tric, E., Courboulex, F., Dano, A., Trebourg, T., et al. (2014). Recent morphological changes of the nice continental slope. *Engineering Geology for Society and Territory*, *4*, 221–225.

Kennett, J. P., Cannariato, K. G., Hendy, I. L., & Behl, R. (2003). *Methane hydrates in Quaternary climate change: The clathrate gun hypothesis* (216 pp.). Washington, DC: AGU.

Khripounoff, A., Vangriesheim, A., Babonneau, N., Crassous, P., Dennielou, B., & Savoye, B. (2003). Direct observation of intense turbidity current activity in the Zaire submarine valley at 4000 m water depth. *Marine Geology*, *194*(3–4), 151–158. https://doi.org/10.1016/S0025-3227(02)00677-1

Kopf, A., Stegmann, S., Garziglia, S., Sultan, N., Henry, P., Dennielou, B., et al. (2016). Soft sediment deformation in the shallow submarine slope off Nice (France) as a result of a variably charged Pliocene aquifer and mass wasting processes. *Sedimentary Geology*, *344*, 290–309. https://doi.org/10.1016/j.sedgeo.2016.05.014

Korup, O., Görüm, T., & Hayakawa, Y. (2012). Without power? Landslide inventories in the face of climate change. *Earth Surface Processes and Landforms*, *37*, 92–99. https://doi.org/10.1002/esp.2248

Kuhlmann, J., Huhn, K., & Ikari, M. J. (2016). Do embedded volcanoclastic layers serve as potential glide planes? An integrated analysis from the Gela Basin offshore southern Sicily. In G. Lamarche, J. Mountjoy, S. Bull, T. Hubble, S. Krastel, E. Lane, et al. (Eds.), *Submarine mass movements and their consequences, Advances in Natural and Technological Hazards Research* (Vol. 41, pp. 273–280). Cham, Switzerland: Springer International.

Kuhlmann, J., Orpin, A. R., Mountjoy, J. J., Crutchley, G. J., Henrys, S., Lunenburg, R., & Huhn, K. (2018). Seismic and lithofacies characterization of a gravity core transect down the submarine Tuaheni Landslide Complex, NE New Zealand. *Geological Society of London, Special Publication*, *477*. https://doi.org/10.1144/SP477.37

Kvalstad, T. J., Andresen, L., Forsberg, C. F., Berg, K., Bryn, P., & Wangen, M. (2005). The Storegga Slide: Evaluation of triggering sources and slide mechanics. *Marine and Petroleum Geology*, *22*, 245–256. https://doi.org/10.1016/j.marpetgeo.200410.1019

Laberg, J. S., & Camerlenghi, A. (2008). The significance of contourites for submarine slope stability. In M. Rebesco & A. Camerlenghi (Eds.), *Contourites, Developments in Sedimentology* (Vol. 60, pp. 537–556). Amsterdam, The Netherlands: Elsevier.

Laberg, J. S., & Vorren, T. O. (2000). The Trænadjupet Slide, offshore Norway: Morphology, evacuation and triggering mechanisms. *Marine Geology*, *171*, 95–114. https://doi.org/10.1016/S0025-3227(00)00112-2

Lambe, T. W., & Whitman, R. V. (1969). *Soil mechanics* (Vol. 53). New York, NY: Wiley.

Lastras, G., Canals, M., Hughes-Clarke, J. E., Moreno, A., Batist, M. D., Masson, D. G., & Cochonat, P. (2002). Seafloor imagery from the BIG'95 debris flow, western Mediterranean. *Geology*, *30*, 871–874. https://doi.org/10.1130/0091-7613

Lastras, G., Canals, M., Urgeles, R., Hughes-Clarke, J. E., & Acosta, J. (2004). Shallow slides and pockmark swarms in the Eivissa Channel, western Mediterranean Sea: Shallow slides and pockmark swarms. *Sedimentology*, *51*, 837–850. https://doi.org/10.1111/j.1365-3091.2004.00654.x

Lebreiiro, S. M., Voelker, A. H. L., Vizcaino, A., Abrantes, F. G., Alt-Epping, U., Jung, S., et al. (2009). Sediment instability on the Portuguese continental margin under abrupt glacial climate changes (last 60 kyr). *Quaternary Science Reviews*, *28*, 3211–3223.

Lee, H. J. (2005). Undersea landslides: Extent and significance in the Pacific Ocean, an update. *Natural Hazards and Earth System Sciences*, *5*(6), 877–892. https://doi.org/10.5194/nhess-5-877-2005

Lee, H. J. (2009). Timing of occurrence of large submarine landslides on the Atlantic Ocean margin. *Marine Geology*, *264*, 53–64. https://doi.org/10.1016/j.margeo.2008.09.009

Lee, H. J., Orzech, K., Locat, J., Boulanger, E., & Konrad, J.-M. (2004). *Seismic strengthening, a conditioning factor influencing submarine landslide development*. Paper presented at 57th Canadian Geotechnical Conference (Session 7G), Québec, Canadian Geotechnical Society (pp. 8–14).

L'Heureux, J. S., Longva, O., Steiner, A., Hansen, L., Vardy, M. E., Vanneste, M., et al. (2012). Identification of weak layers and their role for the stability of slopes at Finneidfjord, northern Norway. In Y. Yamada, K. Kawamura, K. Ikehara, Y. Ogawa, R. Urgeles, D. Mosher, et al. (Eds.), *Submarine mass movements and their consequences, Advances in Natural*

and Technological Hazards Research (Vol. 29, pp. 321–330). Dordrecht, The Netherlands: Springer.

Lin, C. H., Kumagai, H., Ando, M., & Shin, T. C. (2010). Detection of landslides and submarine slumps using broadband seismic networks. *Geophysical Research Letters*, *37*(22), L22309.

Lisiecki, L. E., & Raymo, M. E. (2005). A Pliocene-Pleistocene stack of 57 globally distributed benthic δ18O records. *Paleoceanography*, *20*(1), PA1003–PA1010.

Llopart, J., Urgeles, R., Camerlenghi, A., Lucchi, R. G., Rebesco, M., & De Mol, B. (2015). Late Quaternary development of the Storfjorden and Kveithola Trough Mouth Fans, northwestern Barents Sea. *Quaternary Science Reviews*, *129*, 68–84. https://doi.org/10.1016/j.quascirev.2015.10.002

Llopart, J., Urgeles, R., Forsberg, C. F., Camerlenghi, A., Vanneste, M., Rebesco, M., et al. (2019). Fluid flow and pore pressure development throughout the evolution of a trough mouth fan, western Barents Sea. *Basin Research*, *31*(3), 487–513.

Lo Iacono, C., Gràcia, E., Zaniboni, F., Pagnoni, G., Tinti, S., Bartolomé, R., et al. (2012). Large, deep water slope failures: Implications for landslide-generated tsunamis. *Geology*, *40*(10), 931–934. https://doi.org/10.1130/G33446.1

Locat, J. (2001). Instabilities along ocean margins: A geomorphological and geotechnical perspective. *Marine and Petroleum Geology*, *18*, 503–512. https://doi.org/10.1016/S0264-8172(00)00076-3

Locat, J., & Lee, H. J. (2009). Submarine landslides: Advances and challenges. *Canadian Geotechnical Journal*, *39*, 193–212. https://doi.org/10.1139/t01-089

Locat, J., Leroueil, S., Ariane Locat, A., & Lee, H. J. (2014). Weak layers: Their definition and classification from a geotechnical perspective. In S. Krastel, J.-H. Behrmann, D. Völker, M. Stipp, C. Berndt, R. Urgeles, et al. (Eds.), *Submarine mass movements and their consequences, Advances in Natural and Technological Hazards Research* (Vol. 37, pp. 3–11). Cham, Switzerland: Springer. https://doi.org/10.1007/978-3-319-00972-8_39

Løseth, T. M. (1999). *Submarine massflow sedimentation*. Berlin, Germany: Springer Verlag.

Løvholt, F., Bondevik, S., Laberg, J. S., Kim, J., & Boylan, N. (2017). Some giant submarine landslides do not produce large tsunamis. *Geophysical Research Letters*, *44*. https://doi.org/10.1002/2017GL074062

Løvholt, F., Harbitz, C. B., & Haugen, K. B. (2005). A parametric study of tsunamis generated by submarine slides in the Ormen Lange/Storegga area off western Norway. *Marine and Petroleum Geology*, *22*, 219–231. https://doi.org/10.1016/j.marpetgeo.2004.10.017

Løvholt, F., Pedersen, G., Harbitz, C. B., Glimsdahl, S., & Kim, J. (2015). On the characteristics of landslide tsunamis. *Philosophical Transactions of the Royal Society A*, *373*, 20140376. https://doi.org/10.1098/rsta.2014.0376

Løvholt, F., Schulten, I., Mosher, D., Harbitz, C. B., & Krastel, S. (2018). Modelling the 1929 Grand Banks slump and landslide tsunami. *Geological Society of London, Special Publication*. https://doi.org/10.1144/SP477.28

Maslin, M., Owen, M., Day, S., & Long, D. (2004). Linking continental slope failures and climate change: Testing the clathrate gun hypothesis. *Geology*, *32*, 53–56. https://doi.org/10.1130/G20114.1

Masson, D. G. (1994). Late Quaternary turbidity current pathways to the Madeira Abyssal Plain and some constraints on turbidity current mechanisms. *Basin Research*, *6*, 17–33. https://doi.org/10.1111/j.1365-2117.1994.tb00072.x

Masson, D. G., Harbitz, C. B., Wynn, R. B., Pedersen, G., & Løvholt, F. (2006). Submarine landslides: Processes, triggers and hazard prediction. *Philosophical Transactions of the Royal Society A*, *364*, 2009–2039.

Masson, D. G., Wynn, R. B., Talling, P. J., Mosher, D., Moscardelli, L., Baxter, C. D. P., et al. (2010). Large landslides on passive continental margins: Processes, hypotheses and outstanding questions. In D. Mosher, C. Shipp, L. Moscardelli, J. Chaytor, & C. D. P. Baxter (Eds.), *Submarine mass movements and their consequences, Advances in Natural and Technological Hazards Research* (Vol. 28, pp. 153–165). Dordrecht, The Netherlands: Springer.

McAdoo, B. G., Pratson, L. F., & Orange, D. L. (2000). Submarine landslide geomorphology, US continental slope. *Marine Geology*, *169*, 103–136. https://doi.org/10.1016/S0025-3227(00)00050-5

Micallef, A., Berndt, C., Masson, D. G., & Stow, D. A. V. (2007). A technique for the morphological characterization of submarine landscapes as exemplified by debris flows of the Storegga Slide. *Journal of Geophysical Research*, *112*, F02001. https://doi.org/10.1029/2006JF000505

Mienert, J. (2009). *Methane hydrate and submarine slides, Encyclopedia of Ocean Sciences*. Elsevier. https://doi.org/10.1016/B978-012374473-9.0704-9

Miramontes, E., Cattaneo, A., Jouet, G., Théreau, E., Thomas, Y., Rovere, M., et al. (2016). The Pianosa contourite depositional system (northern Tyrrhenian Sea): Drift morphology and Plio-Quaternary stratigraphic evolution. *Marine Geology*, *378*, 20–42. https://doi.org/10.1016/j.margeo.2015.11.004

Miramontes, E., Sultan, N., Garziglia, S., Jouet, G., Pelleter, E., & Cattaneo, A. (2018). Altered volcanic deposits as basal failure surfaces of submarine landslides. *Geology*, *46*(7), 663–666.

Moernaut, J., & De Batist, M. (2011). Frontal emplacement and mobility of sublacustrine landslides: Results from morphometric and seismostratigraphic analysis. *Marine Geology*, *285*(1), 29–45.

Mohrig, D., Whipple, K. X., Hondzo, M., Ellis, C., & Parker, G. (1998). Hydroplaning of subaqueous debris flow. *Geological Society of America Bulletin*, *110*, 387–394. https://doi.org/10.1130/0016-7606(1998)110<0387:HOSDF>2.3.CO;2

Moscardelli, L., & Wood, L. (2008). New classification system for mass transport complexes in offshore Trinidad. *Basin Research*, *20*(1), 73–98. https://doi.org/10.1111/j.1365-2117.2007.00340.x

Moscardelli, L., Wood, L., & Mann, P. (2006). Mass-transport complexes and associated processes in the offshore area of Trinidad and Venezuela. *AAPG Bulletin*, *90*(7), 1059–1088. https://doi.org/10.1306/02210605052

Mountjoy, J. J., Howarth, J. D., Orpin, A. R., Barnes, P. M., Bowden, D. A., Rowden, A. A., & Patton, J. R. (2018). Earthquakes drive large-scale submarine canyon development and sediment supply to deep-ocean basins. *Science Advances*, *4*(3), eaar3748.

Mountjoy, J. J., Pecher, I., Henrys, S., Crutchley, G., Barnes, P. M., & Plaza-Faverola, A. (2014). Shallow methane hydrate system controls ongoing, downslope sediment transport in a low-velocity active submarine landslide complex, Hikurangi Margin, New Zealand. *Geochemistry, Geophysics, Geosystems*, *15*(11), 4137–4156. https://doi.org/10.1002/2014GC005379

Mulder, T., & Cochonat, P. (1996). Classification of offshore mass movements. *Journal of Sedimentary Research*, *66*, 43–57. https://doi.org/10.1306/D42682AC-2B26-11D7-8648000102C1865D

Nardin, T. R., Hein, F. J., Gorsline, D. S., & Edwards, B. D. (1979). A review of mass movement processes and acoustic characteristics, and contrasts in slope and base-of-slope systems versus canyon-fan-basin floor systems. In L. J. Doyle & O. H. Pilkey (Eds.), *Geology of continental slopes, SEPM Special Publication* (Vol. 27, pp. 61–73). Tulsa, OK: Society of Economic Paleontologists and Mineralogists.

Obelcz, J., Xu, K., Georgiou, I. Y., Maloney, J., Bentley, S. J., & Miner, M. D. (2017). Sub-decadal submarine landslides are important drivers of deltaic sediment flux: Insights from the Mississippi River Delta Front. *Geology*, *45*(8), 703–706.

Paull, C. K., Talling, P. J., Maier, K., Parsons, D., Xu, J., Caress, D., et al. (2018). Powerful turbidity currents driven by dense basal layers. *Nature Communications*. https://doi.org/10.1038/s41467-018-06254-6

Pecher, I. A., Villinger, H., Kaul, N., Crutchley, G. J., Mountjoy, J. J., Huhn, K., et al. (2017). A fluid pulse on the Hikurangi subduction margin: Evidence from a heat flux transect across the upper limit of gas hydrate stability. *Geophysical Research Letters*, *44*(24), 12385–12395. https://doi.org/10.1002/2017GL076368

Pestana, J. M., Biscontin, G., Nadim, F., & Andersen, K. (2000). Modeling cyclic behavior of lightly overconsolidated clays in simple shear. *Soil Dynamics and Earthquake Engineering*, *19*(7), 501–519.

Philippsen, B. (2013). The freshwater reservoir effect in radiocarbon dating. *Heritage Science*, *1*, 24. https://doi.org/10.1186/2050-7445-1-24

Phrampus, B., & Hornbach, M. (2012). Recent changes to the Gulf Stream causing widespread gas hydrate destabilization. *Nature*, *490*, 527–530. https://doi.org/10.1038/nature11528

Pini, G. A. (1999). Tectonosomes and olistostromes in the Argille Scagliose of the Northern Apennines, Italy. *Geological Society of America Special Papers*, *335*, 1–70. https://doi.org/10.1130/0-8137-2335-3.1

Piper, D. J. W., & Aksu, A. E. (1987). The source and origin of the 1929 Grand Banks turbidity current inferred from sediment budgets. *Geo-Marine Letters*, *7*(4), 177–182.

Piper, D. J. W., Cochonat, P., & Morrison, M. L. (1999). The sequence of events around the epicenter of the 1929 Grand Banks earthquake: Initiation of the debris flows and turbidity current inferred from side scan sonar. *Sedimentology*, *46*, 79–97. https://doi.org/10.1046/j.13653091.1999.00204.x

Pope, E., Talling, P. J., Urlaub, M., Hunt, J. E., Clare, M. A., & Challenor, P. (2015). Are large submarine landslides temporally random or do uncertainties in available age constraints make it impossible to tell? *Marine Geology*, *369*, 19–33. https://doi.org/10.1016/j.margeo.2015.07.002

Pope, E. L., Talling, P. J., & Carter, L. (2017). Which earthquakes trigger damaging submarine mass movements: Insights from a global record of submarine cable breaks? *Marine Geology*, *384*, 131–146. https://doi.org/10.1016/j.margeo.2016.01.009

Posamentier, H. W., Davies, R. J., Cartwright, J., & Wood, L. J. (2007). Seismic geomorphology: An overview. In R. J. Davies, H. W. Posamentier, L. J. Wood, & J. A. Cartwright (Eds.), *Seismic geomorphology: Applications to hydrocarbon exploration and production, Special Publications* (Vol. 277, pp. 1–14). London, UK: Geological Society.

Riboulot, V., Ker, S., Sultan, N., Thomas, Y., Marsset, B., Scalabrin, C., et al. (2018). Freshwater lake to salt-water sea causing widespread hydrate dissociation in the Black Sea. *Nature Communications*, *9*(117), 1–8.

Rovere, M., Gamberi, F., Mercorella, A., & Leidi, E. (2014). Geomorphometry of a submarine mass-transport complex and relationships with active faults in a rapidly uplifting margin (Gioia Basin, NE Sicily margin). *Marine Geology*, *356*, 31–43. https://doi.org/10.1016/j.margeo.2013.06.003

Sawyer, D. E., & DeVore, J. R. (2015). Elevated shear strength of sediments on active margins: Evidence for seismic strengthening. *Geophysical Research Letters*, *42*, 10,216–10,221. https://doi.org/10.1002/2015GL066603

Sgroi, T., Monna, S., Embriaco, D., Giovanetti, G., Marinaro, G., & Favali, P. (2014). Geohazards in the Western Ionian Sea. *Oceanography*, *27*(2), 154.

Shanmugam, G. (2015). The landslide problem. *Journal of Palaeogeography*, *4*(2), 109–166. https://doi.org/10.3724/SP.J.1261.2015.00071

Smith, D. P., Kvitek, R., Iampietro, P. J., & Wong, K. (2007). Twenty-nine months of geomorphic change in upper Monterey Canyon (2002–2005). *Marine Geology*, *236*(1–2), 79–94.

Stark, C. P., & Hovius, N. (2001). The characterization of landslide size distributions. *Geophysical Research Letters*, *28*, 1091–1094. https://doi.org/10.1029/2000GL008527

Stegmann, S., Sultan, N., Kopf, A., Approoual, R., & Pelleau, P. (2011). Hydrogeology and its effect on slope stability along the coastal aquifer of Nice, Franc. *Marine Geology*, *280*, 168–181.

Stegmann, S., Sultan, N., Pelleau, P., Apprioual, R., Garziglia, S., Kopf, A., & Zabel, M. (2012). *A long-term monitoring array for landslide precursors*. A case study at the Ligurian Slope. OTC Proceedings, Houston April 2012, paper number OTC-23271-PP.

Strout, J. M., & Tjelta, T. I. (2005). In situ pore pressure: What is their significance and how can they be reliably measured? Marine Petrol. *Geology*, *22*, 275–285.

Strozyk, F., Strasser, M., Förster, A., Kopf, A., & Huhn, K. (2010). Slope failure repetition in active margin environments: Constraints from submarine landslides in the Hellenic forearc, eastern Mediterranean. *Journal of Geophysical Research*, *115*, B08103. https://doi.org/10.1029/2009JB006841

Sultan, N., Cattaneo, A., Urgeles, R., Lee, H., Locat, J., Trincardi, F., et al. (2008). A geomechanical approach for the genesis of sediment undulations on the Adriatic Shelf. *Geochemistry, Geophysics, Geosystems*, *9*, Q04R03.

Sultan, N., Cochonat, P., Canals, M., Cattaneo, A., Dennielou, B., Haflidason, H., et al. (2004a). Triggering mechanisms of slope instability processes and sediment failures on continental margins: A geotechnical approach. *Marine Geology*, *213*(2004), 291–321. https://doi.org/10.1016/j.margeo.2004.10.011

Sultan, N., Cochonat, P., Foucher, J. P., & Mienert, J. (2004b). Effect of gas hydrate melting on seafloor slope stability. *Marine Geology*, *231*, 379–401. https://doi.org/10.1016/j.margeo.2004.10.015

Synolakis, C. E., Jean-Pierre, B., Borrero, J. C., Davies, H. L., Okal, E. A., Silver, E. A., et al. (2002). The slump origin of the 1998 Papua New Guinea Tsunami. *Proceedings: Mathematical, Physical and Engineering Sciences*, *458*(2020). https://doi.org/10.1098/rspa.2001.0915

Talling, P. J., Clare, M., Urlaub, M., Pope, E., Hunt, J. E., & Watt, S. F. L. (2014). Large submarine landslides on continental slopes: Geohazards, methane release, and climate change. *Oceanography*, *27*(2), 32–45. https://doi.org/10.5670/oceanog.2014.38

Talling, P. J., Paull, C. K., & Piper, D. J. (2013). How are subaqueous sediment density flows triggered, what is their internal structure and how does it evolve? Direct observations from monitoring of active flows. *Earth-Science Reviews*, *125*, 244–287.

Talling, P. J., Wynn, R. B., Masson, D. G., Frenz, M., Cronin, B. T., Schiebel, R., et al. (2007). Onset of submarine debris flow deposition far from original giant landslide. *Nature*, *450*, 541–544.

Tanaka, H., & Locat, J. (1999). A microstructural investigation of Osaka Bay clay. *Canadian Geotechnical Journal*, *36*, 493–508.

Tappin, D., McNeil, L., Henstock, T., and Mosher, D., 2007, Mass wasting processes offshore Sumatra, in Lykousis, V., Sakellariou D., Locat J. et al., eds., *Submarine mass movements and their consequences*: Amsterdam, The Netherlands, Springer, p. 327–336, doi:https://doi.org/10.1007/978-1-4020-6512-5_34.

Tappin, D. R., Watts, P., & Grilli, S. T. (2008). The Papua New Guinea tsunami of 17 July 1998: Anatomy of a catastrophic event. *Natural Hazards and Earth System Sciences*, *8*, 243–266.

ten Brink, U. S., Andrews, B. D., & Miller, N. C. (2016). Seismicity and sedimentation rate effects on submarine slope stability. *Geology*, *44*, 563–566.

ten Brink, U. S., Barkan, R., Andrews, B. D., & Chaytor, J. D. (2009). Size distributions and failure initiation of submarine and subaerial landslides, Earth Planet. *Science Letters*, *287*, 31–42.

Tréhu, A. M., Flemings, P. B., Bangs, N. L., Chevallier, J., Gràcia, E., Johnson, J. E., et al. (2004). Feeding methane vents and gas hydrate deposits at south Hydrate Ridge. *Geophysical Research Letters*, *31*, L23310.

Twichell, D. C., Chaytor, J. D., ten Brink, U. S., & Buczkowski, B. (2009). Morphology of late Quaternary submarine landslides along the U.S. Atlantic continental margin. *Marine Geology*, *264*, 4–15. https://doi.org/10.1016/j.margeo.2009.01.2009

Urgeles, R., Bahk, J.-J., Lee, S.-H., Horozal, S., Cukur, D., Kim, S.-P., et al. (2018). Tsunami hazard from submarine landslides: Scenario-based assessment in the Ulleung Basin, East Sea (Japan Sea). *Geosciences Journal*. https://doi.org/10.1007/s12303-018-0044-x

Urgeles, R., & Camerlenghi, A. (2013). Submarine landslides of the Mediterranean Sea: Trigger mechanisms, dynamics, and frequency-magnitude distribution. *Journal of Geophysical Research, Earth Surface*, *118*, 2013JF002720. https://doi.org/10.1002/2013JF002720

Urlaub, M., Geersen, J., Krastel, S., & Schwenk, T. (2018a). *Diatom ooze: Crucial for the generation of submarine megaslides? Geology*, *46*(4), 331–334. https://doi.org/10.1130/G39892.1

Urlaub, M., Petersen, F., Gross, F., Bonforte, A., Puglisi, G., Guglielmino, F., et al. (2018b). *Gravitational collapse of Mount Etna's southeastern flank*. *Science Advances*, *4*(10), eaat9700. https://doi.org/10.1126/sciadv.aat9700

Urlaub, M., Talling, P. J., & Masson, D. G. (2013). Timing and frequency of large submarine landslides: Implications for understanding triggers and future geohazard. *Quaternary Science Reviews*, *72*, 63–82. https://doi.org/10.1016/j.quascirev.2013.04.020

Vanneste, M., Mienert, J., & Buenz, S. (2006). The Hinlopen Slide: A giant, submarine slope failure on the northern Svalbard margin, Arctic Ocean. *Earth and Planetary Science Letters*, *245*(1–2), 373–388. https://doi.org/10.1016/j.epsl.2006.02.045

Vanoudheusden, E., Sultan, N., & Cochonat, P. (2004). Mechanical behaviour of unsaturated marine sediments: Experimental and theoretical approaches. *Marine Geology*, *213*, 323–342.

Verdicchio, G., & Trincardi, F. (2008). Mediterranean shelf-edge muddy contourites: Examples from the Gela and South Adriatic basins. *Geo-Marine Letters*, *28*(3), 137–151. https://doi.org/10.1007/s00367-007-0096-9

Vizcaino, A., Gràcia, E., Pallàs, R., Garcia-Orellana, J., Escutia, C., Casas, D., et al. (2006). Sedimentology, physical properties and ages of mass-transport deposits associated to the Marquês de Pombal Fault, Southwest Portuguese Margin. *Norwegian Journal of Geology*, *86*, 173–182.

Volpi, V., Camerlenghi, A., Hillenbrand, C.-D., Rebesco, M., & Ivaldi, R. (2003). Effects of biogenic silica on sediment compaction and slope stability on the Pacific margin of the Antarctic Peninsula. *Basin Research*, *15*, 339–363.

Waelbroeck, C., Labeyrie, L., Michel, E., Duplessy, J., McManus, J., Lambeck, K., et al. (2002). Sea-level and deep water temperature changes derived from benthic foraminifera isotopic records. *Quaternary Science Reviews*, *21*(1–3), 295–305.

Watt, S. F. L., Talling, P. J., Vardy, M. E., Heller, V., Hühnerbach, V., Urlaub, M., et al. (2012). Emplacement dynamics and tsunami hazards from volcanic island flank collapses and adjacent seafloor sediment failures. *Earth and Planetary Science Letters*, *319–320*, 228–240.

Westbrook, G. K., Thatcher, K., Rohling, E. J., Piotrowski, A. M., Pälike, H., Osborne, A., et al. (2009). Escape of methane gas from the seabed along the West Spitsbergen continental margin. *Geophysical Research Letters*, *36*, L15608. http://dx.doi.org/abs/10.1029/2009GL039191

Wiemer, G., & Kopf, A. J. (2017). On the role of volcanic ash deposits as preferential submarine slope failure planes. *Landslides*, *14*(1), 223–232. https://doi.org/10.1007/s10346-016-0706-6

Winkelmann, D., Geissler, W., Schneider, J., & Stein, R. (2008). Dynamics and timing of the Hinlopen/Yermak Megaslide north of Spitsbergen, Arctic Ocean. *Marine Geology*, *250*, 34–50.

Xu, J. P., Noble, M. A., & Rosenfeld, L. K. (2004). In-situ measurements of velocity structure within turbidity currents. *Geophysical Research Letters*, *31*(9). https://doi.org/10.1029/2004GL019718

13

An Atlas of Mass-Transport Deposits in Lakes

Maddalena Sammartini[1], Jasper Moernaut[1], Flavio S. Anselmetti[2], Michael Hilbe[2], Katja Lindhorst[3], Nore Praet[4], and Michael Strasser[1]

ABSTRACT

Mass-transport deposits (MTDs) and related turbidites are common features in lacustrine environments and are intercalated within uniform lacustrine background sedimentation. Evidence of MTDs has been described worldwide in many lakes of different origin. They have been reported to result from various types of mass-movement processes, which can affect the subaquatic slopes but also the shoreline and basin. Based on bibliographic research on sublacustrine-landslide-related studies, we identified four different types of mass movements that occur independently from the type of lake, but differ in source area, type of failure initiation, transport mechanism, and resulting MTDs. These are (i) lateral slope landslides, (ii) margin collapses, (iii) delta collapses, and (iv) rockfalls. This study aims to illustrate variabilities and commonalities of lacustrine MTDs resulting from these four different mass-movement processes by presenting type examples of published multi-method investigations on lacustrine MTDs. Furthermore, this study provides a perspective on the wide range of applications of MTD research in lakes, due to their well-constrained boundaries, smaller size, continuity in sedimentation, and the possibility to be surveyed on a complete basin-wide scale.

13.1. INTRODUCTION

Similar to advanced geophysical imaging, geotechnical testing, and geological sampling of mass-transport deposits (MTDs) and slope sequences in the oceanic realm, the understanding of subaquatic mass-movement processes has also advanced through numerous investigations in lakes (e.g., Chapron et al., 1999; Girardclos et al., 2007; Moernaut & De Batist, 2011; Moernaut et al., 2017; Schnellmann et al., 2002; Strasser & Anselmetti, 2008; Wiemer et al., 2015). Such limnogeological, process-oriented research on causes and consequences of mass movements in lakes have revealed that general characteristics of MTDs, as well as their underlying transport and initiation processes (e.g., slope preconditioning and landslide-triggering factors) are often comparable to those described in the classical submarine landslide literatures (Hampton et al., 1996; Lamarche et al., 2016; Locat & Lee, 2002; Masson et al., 2006; Talling et al., 2015). Given that lakes have well-constrained boundary conditions and smaller sizes and offer the possibility to be investigated on a complete basin-wide scale, studying mass movements in lacustrine environments offers a series of advantages that make lake studies vital to improving our knowledge on marine processes as well. In particular, hydroacoustic surveying in lakes typically uses higher frequencies and takes place in shallower water depths, leading to a higher signal-to-noise ratio and higher vertical resolution for bathymetric and subsurface structures than in many marine campaigns. Sub-bottom profiling in lakes often uses 3.5 kHz seismic sources, which result in a theoretical decimeter-scale vertical resolution.

[1] *Institute of Geology, University of Innsbruck, Innsbruck, Austria*

[2] *Institute of Geological Sciences and Oeschger Centre for Climate Change Research, University of Bern, Bern, Switzerland*

[3] *Institute of Geoscience, University of Kiel, Kiel, Germany*

[4] *Renard Centre of Marine Geology, Ghent University, Ghent, Belgium*

Submarine Landslides: Subaqueous Mass Transport Deposits from Outcrops to Seismic Profiles, Geophysical Monograph 246, First Edition. Edited by Kei Ogata, Andrea Festa, and Gian Andrea Pini.
© 2020 American Geophysical Union. Published 2020 by John Wiley & Sons, Inc.

Furthermore, smaller water depths in lakes result in smaller spatial footprints of the geophysical signal and thus higher horizontal resolution. Due to the smaller scale of landslide features and, in many cases, limited sediment thickness overlying the bedrock, conventional coring from mobile platforms at comparably low logistical costs often reaches down to critical depths, crossing gliding surfaces. This allows a complete sampling and characterization of MTDs and the (intact) stratigraphic sequences adjacent to subaqueous slope failures.

Bibliographic research using keyword searches (in English) and citation analyses in different online research platforms, such as Web of Science, Google Scholar, and ResearchGate, provides evidence of mass movements described in 172 lakes worldwide (Figure 13.1 and Table 13.1). This compilation may not be complete because some MTD descriptions in various lake publications have likely been missed due to differences in terminology and due to the fact that domestic scientific literature, in respective languages, has not been considered. Nevertheless, this compilation shows that mass movements occur in all types of lakes of different origins, such as glacigenic lakes (119 descriptions), tectonic lakes (23 descriptions), crater lakes (11 descriptions), dammed lakes (11 descriptions), karstic lakes (5 descriptions), meteorite-impact lakes (2 descriptions), and fluvial lakes (1 description) (Table 13.1).

Among all surveyed literature, 38 publications present a comprehensive sublacustrine-landslide-related study that maps and characterizes at least one or more MTD in detail within the investigated lake. Other studies typically focus on other themes (e.g., paleoclimate or paleoenvironment) but describe or infer MTDs in either core or reflection seismic data. Abovementioned distribution of MTD occurrences and lake types is certainly biased by the fact that various studies have different investigation foci and methodological approaches. Thus, the bibliographic data set cannot be statistically analyzed for process-based interpretations. However, we will start to categorize different generic types of mass movements in lakes, independently of the type of lakes in which they occur. In the following, we distinguish four main mass-movement types, based on their source areas, mode of failure initiation, transport mechanism, and resulting MTD:

1. Lateral slope landslides occur on non-deltaic sublacustrine slopes characterized by hemipelagic draping sedimentation and consist in a translational or rotational movement of coherent lake internal sediments along a distinct basal shear surface. The lateral slope landslides are usually facilitated by the presence of a weak layer and triggered by external mechanisms, such as an earthquake or anthropogenic loading along the shoreline (e.g., Beigt et al., 2016; Lowag et al., 2012; Normandeau et al., 2016; Schnellmann et al., 2002; Simonneau et al., 2013).

2. Margin collapses are typically larger in extent and show complex multistage failures, which affect the entire sublacustrine slope and (possibly) the shore. These, usually deep-seated failures, are controlled by local tectonic structures crosscutting lake morphology and are able to remobilize a great amount of different sediments and rocks (e.g., Chassiot et al., 2016; Gardner et al., 2000; Lindhorst et al., 2015).

3. Delta collapses are subaquatic slope failures on prograding river delta fans beyond the gravitational sediment transport processes related to hydrodynamics and sediment flux of the river itself. Depending on size and volume, they show various failure modes initiated by either an external mechanism, such as an earthquake or a rockfall (e.g., Kremer et al., 2015; Praet et al., 2017; Van Daele et al., 2015), or they can occur spontaneously due to high sedimentation loading (Girardclos et al., 2007; Hilbe & Anselmetti, 2014; Vogel et al., 2015).

4. Rockfalls refer to a vertical or near-vertical fall of blocks and/or fragments of rocks from a very steep rock cliff. They can have both subaquatic and subaerial origin, the latter being common in lakes in mountainous settings with steep rock cliffs surrounding the lake's shoreline (Bozzano et al., 2009; Karlin et al., 2004; Schnellmann et al., 2006).

All these mechanisms of failure can evolve downslope in sediment density flows, which can further be distinguished by their sediment concentration, nature and size of clasts, and flow rheology into debris flows or turbidity currents (Ito, 2008; Talling, 2013; Talling et al., 2015), resulting in various different types of deposits. However, this study of MTDs in lakes mainly presents geophysical data that cannot distinguish between these various flow types. Thus, adopting Dott's classification (1963), we refer to MTDs as all types of mass-movement deposits with the exception for deposits generated by turbidity currents combined with potentially related tsunami and seiche waves (Schnellmann et al., 2005; Shanmugan and Wang, 2015). For the latter, we use the term turbidite, which indicates water-entrained and/or resuspended sediment transported in a turbulent flow that can cover the terminal depocenter of lacustrine basins with a typical ponding geometry. Whenever these units appear as mappable, homogeneous to transparent seismic facies in reflection data, we refer to them as megaturbidites (according to the initial description by Bouma (1987) and definition in lakes by Schnellmann et al. (2006)).

This chapter presents MTDs and their co-genetic turbidites resulting from the four abovementioned types of mass movements in lakes. We will present selected examples of published lacustrine MTD studies, reviewing and describing their characteristic features as observed in the different limnogeological data sets, and briefly discuss their underlying generic processes, also with respect to

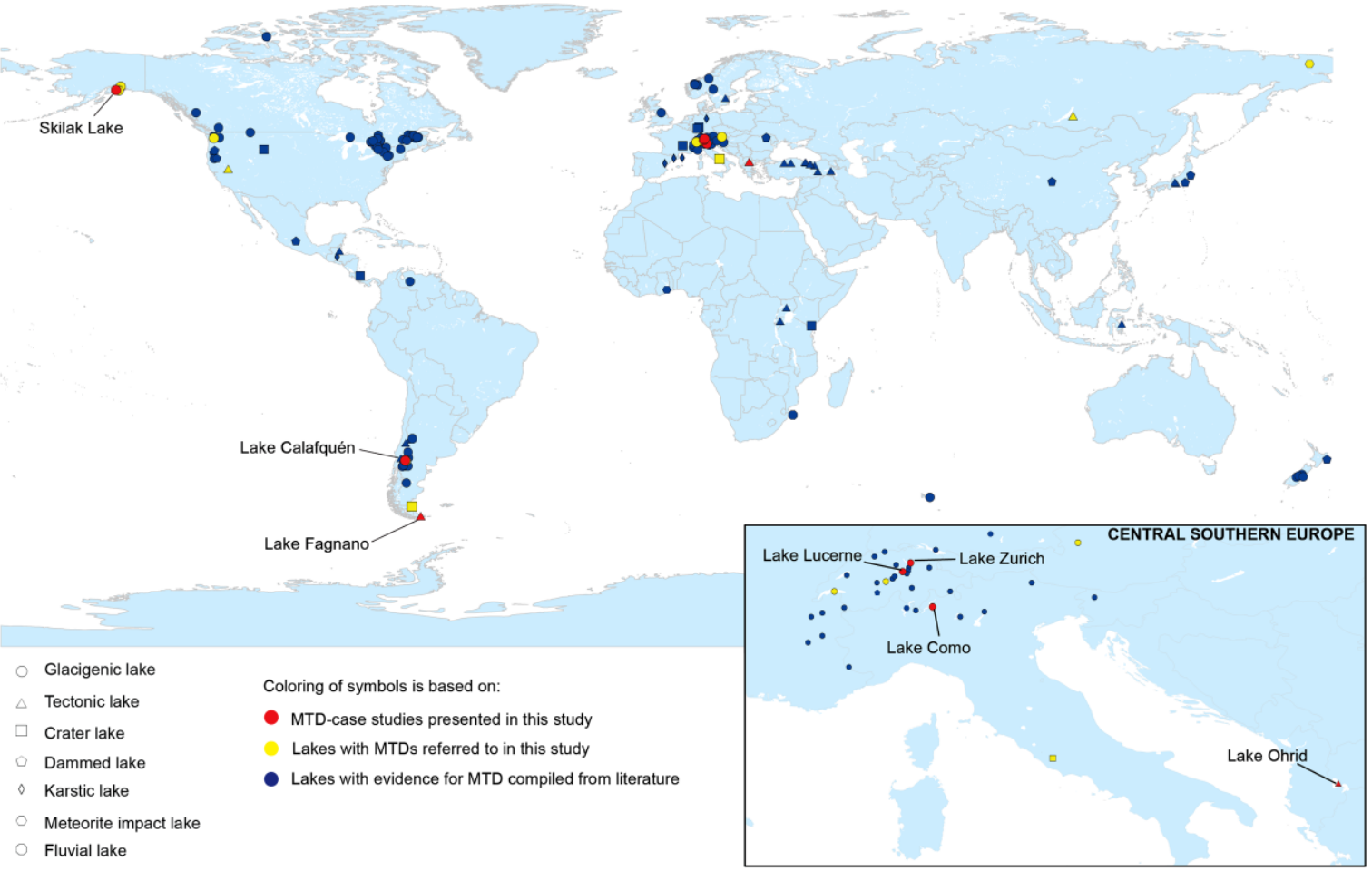


Figure 13.1 Results of bibliographic research of MTDs in lakes. (a) World map with locations of the 172 lakes, with evidences of MTDs, found among all surveyed literature. Different symbols are used to mark lakes of different origin. The coloring of symbols is based on following: seven lakes which provide case studies for this work are highlighted with red. Lakes referred to in this study are marked in yellow. All other lakes are marked in blue (Table 13.1). (b) Zoom-in on central southern Europe. (*See electronic version for color representation of this figure*)

Table 13.1 Results of Bibliographic Research: Complete List of Lakes, and Relative References, which Show Evidences of Mass Movements

Continent	State	Lake	Origin	X	Y	References
Africa	Uganda/Congo	Albert	Tectonic lake	30.884347	1.630893	Zhang (2014)
	Ghana	Bosumtwi	Meteorite-impact lake	−1.411160	6.503118	Zhang (2014)
	Kenya/Tanzania	Challa	Crater lake	37.699714	−3.318075	Moernaut (2010), Moernaut and De Batist (2011), and Van Daele et al. (2017)
	Rwanda/Congo	Kivu	Tectonic lake	29.189661	−1.996564	Zhang et al. (2014)
	South Africa	Sibaya	Fluvial lake	32.683924	−27.353425	Miller (1998)
Asia	Russia	Baikal	Tectonic lake	108.171387	53.465161	Solovyeva et al. (2016)
	Japan	Biwa	Tectonic lake	136.115799	35.289488	Shiki et al. (2000)
	Russia	El'gygytgyn	Meteorite-impact lake	172.088555	67.485405	Juschus et al. (2009) and Sauerbrey et al. (2013)
	Japan	Inawashiro	Dammed lake	140.092417	37.472901	Yamasaki et al. (2017)
	China	Mengda	Dammed lake	102.674927	35.791375	Wang et al. (2014)
	Japan	Motosu	Dammed lake	138.583946	35.463676	Lamair et al. (2018)
	Japan	Suigetsu	Tectonic lake	135.883001	35.585148	Schlolaut et al. (2014)
	Indonesia	Towuti	Tectonic lake	121.501236	−2.722211	Vogel et al. (2015)
Australia	New Zealand	Ellery	Glaciogenic lake	168.658192	−44.054135	Howarth et al. (2016)
	New Zealand	Mapourika	Glaciogenic lake	170.201744	−43.315778	Howarth et al. (2014)
	New Zealand	Paringa	Glaciogenic lake	169.407763	−43.718605	Howarth et al. (2014)
	New Zealand	Tekapo	Glaciogenic lake	170.531664	−43.872311	Upton and Osterberg (2007)
	New Zealand	Tutira	Dammed lake	176.893036	−39.223018	Eden and Froggatt (1996) and Eden and Page (1998)
Europe	Switzerland	Aegeri	Glaciogenic lake	8.623066	47.121892	Kremer et al. (2017)
	Italy	Albano	Crater lake	12.670069	41.746726	Bozzano et al. (2009)
	Germany	Ammersee	Glaciogenic lake	11.119747	48.003253	Czymzik et al. (2010)
	France	Annecy	Glaciogenic lake	6.181355	45.846619	Beck (2009)
	France	Anterne	Glaciogenic lake	6.798005	45.991043	Arnaud et al. (2002) and Beck (2009)
	Turkey	Asagitepecik	Tectonic lake	38.588203	40.038753	Boës et al. (2010)
	Switzerland	Baldegg	Glaciogenic lake	8.261777	47.198446	Becker et al. (2005), Kremer et al. (2017), and Monecke et al. (2004)
	Spain	Banyoles	Karstic lake	2.754747	42.125066	Morellón et al. (2014)
	Germany	Bergsee	Glaciogenic lake	7.935082	47.571356	Becker et al. (2005)
	Slovenia	Bohinj	Glaciogenic lake	13.857800	46.283974	Rapuc et al. (2018)
	Romania	Bolatau	Dammed lake	25.430116	47.622246	Mîndrescu et al. (2013)
	Turkey	Boraboy	Tectonic lake	36.153416	40.803828	Boës et al. (2010)
	Norway	Botn	Glaciogenic lake	9.975287	63.577343	L'Heureux et al. (2012)
	France	Bramant	Glaciogenic lake	6.175668	45.199594	Guyard et al. (2007)
	Switzerland	Brienz	Glaciogenic lake	7.964883	46.724371	Girardclos et al. (2007)
	Switzerland	Cadagno	Glaciogenic lake	8.711389	46.549722	Wirth (2013)
	France	Chauvet	Crater lake	2.830942	45.459764	Chapron et al. (2012)
	Italy	Como	Glaciogenic lake	9.265594	46.016039	Fanetti et al. (2008)
	Switzerland	Constance	Glaciogenic lake	9.375587	47.621792	Schwestermann (2016)

Spain	Estanya	Karstic lake	0.528781	42.028665	Morellón et al. (2009)
Switzerland	Geneva	Glaciogenic lake	6.513519	46.449922	Kremer et al. (2015) and Kremer et al. (2017)
Italy	Ghirla	Glaciogenic lake	8.822210	45.917008	Wirth (2013)
Turkey	Gollukoy	Tectonic lake	37.467177	40.377552	Avşar et al. (2014b, 2015) and Boës et al. (2010)
Germany	Hämel	Karstic lake	9.310587	52.759386	Merkt and Müller (1999)
Turkey	Hazar	Tectonic lake	39.400584	38.486118	Hage et al. (2017)
Germany	Holzmaar	Crater lake	6.878268	50.119050	Kienel and Vos (2007)
Romania	Iezerul Sadovei	Dammed lake	25.447824	47.603319	Florescu et al. (2017) and Mîndrescu et al. (2013)
Italy	Iseo	Glaciogenic lake	10.071373	45.730869	Lauterbach et al. (2012)
Germany	Laacher See	Crater lake	7.270045	50.412440	Goepel et al. (2015)
Turkey	Ladik	Tectonic lake	36.011226	40.907904	Boës et al. (2010)
France	Laffrey	Glaciogenic lake	5.777071	45.010812	Nomade et al. (2005)
Switzerland	Lauerz	Glaciogenic lake	8.600759	47.034121	Bussmann and Anselmetti (2010)
France	Le Bourget	Glaciogenic lake	5.866013	45.732187	Beck et al. (2009), Chapron et al. (1999), Moernaut (2010), Moernaut and De Batist (2011), and Van Rensbergen et al. (1999)
Italy	Ledro	Glaciogenic lake	10.750551	45.878059	Simonneau et al. (2013) and Wirth (2013)
Norway	Lovatnet	Glaciogenic lake	6.950828	61.826720	Hansen et al. (2016)
Switzerland	Lucerne	Glaciogenic lake	8.434990	47.013968	Hilbe and Anselmetti (2014, 2015), Hilbe et al. (2011), Kremer et al. (2017), Schnellmann (2004), Schnellmann et al. (2002, 2005, 2006), Siegenthaler and Sturm (1991), Strasser (2008), and Strasser et al. (2006, 2007, 2011)
Switzerland	Lungern	Glaciogenic lake	8.161791	46.800932	Becker et al. (2005), Kremer et al. (2017), and Monecke et al. (2004)
Italy	Maggiore	Glaciogenic lake	8.643735	45.957743	Kämpf et al. (2012)
Norway	Medvatnet	Glaciogenic lake	6.044933	62.030821	Bøe et al. (2004)
Germany	Meerfelder Maar	Crater lake	6.757112	50.101057	Brauer et al. (1999)
Norway	Mjøsa	Glaciogenic lake	11.043332	60.692705	Bøe et al. (2004) and Forsberg et al. (2016)
Austria	Mondsee	Glaciogenic lake	13.380141	47.820546	Daxer (2017) and Daxer et al. (in press)
France	Montcineyre	Crater lake	2.896329	45.458693	Chapron et al. (2012)
Norway	Nedstevatnet	Glaciogenic lake	6.048390	62.037701	Bøe et al. (2004)
Switzerland	Neuchâtel	Glaciogenic lake	6.869964	46.912111	Kremer et al. (2017) and Reusch (2016)
Switzerland	Oeschinen	Dammed lake	7.726746	46.498243	Knapp et al. (2018)
Macedonia/ Albania	Ohrid	Tectonic lake	20.716438	41.030420	Lindhorst et al. (2012, 2014, 2015) and Wagner et al. (2012)
France	Pavin	Crater lake	2.887795	45.495443	Chapron et al. (2012) and Chassiot et al. (2016)
Italy	Prag (Braies)	Glaciogenic lake	12.085370	46.694200	Irmler et al. (2006) and Thielemann et al. (2007)
Norway	Rotevatnet	Glaciogenic lake	6.112222	62.140545	Bøe et al. (2004)

(Continued)

Table 13.1 (Continued)

Continent	State	Lake	Origin	X	Y	References
	Turkey	Sapanca	Tectonic lake	30.256571	40.717929	Leroy et al. (2010)
	Switzerland	Sarnen	Glaciogenic lake	8.218264	46.868130	Becker et al. (2005) and Monecke et al. (2004)
	Switzerland	Seelisberg	Glaciogenic lake	8.571668	46.958520	Becker et al. (2005), Kremer et al. (2017), and Monecke et al. (2004)
	Switzerland	Seewen	Glaciogenic lake/ former lake	7.646078	47.431396	Becker et al. (2005)
	Switzerland	Silvaplana	Glaciogenic lake	9.789848	46.446965	Bellwald (2012) and Kremer et al. (2017)
	Norway	Storsætervatnet	Glaciogenic lake	6.140754	61.943097	Bøe et al. (2004)
	Spain	Taravilla	Karstic lake	−1.974468	40.651063	Garcés et al. (2008)
	Switzerland	Thun	Glaciogenic lake	7.715342	46.690246	Kremer et al. (2017), Reusch (2016), and Wirth (2008)
	Turkey	Van	Tectonic lake	42.935837	38.620052	Cukur et al. (2013)
	Sweden	Vättern	Tectonic lake	14.458459	58.297375	Jakobsson et al. (2014)
	France	Vens	Glaciogenic lake	6.931750	44.310785	Petersen et al. (2014)
	Switzerland	Walen	Glaciogenic lake	9.201050	47.123293	Kremer et al. (2017)
	UK	Windermere	Glaciogenic lake	−2.932697	54.370922	Lowag et al. (2012) and Vardy et al. (2010)
	Turkey	Yenigaga	Tectonic lake	32.026213	40.780418	Avşar et al. (2014a) and Boës et al. (2010)
	Turkey	Zinav	Tectonic lake	37.272972	40.448196	Boës et al. (2010)
	Switzerland	Zurich	Glaciogenic lake	8.654473	47.255703	Kelts and Hsü (1980), Kremer et al. (2017); Strasser (2008); Strasser and Anselmetti (2008), Strasser et al. (2006, 2008, 2013), Strupler (2017), and Strupler et al. (2017, 2018a, 2018b)
North America	Canada	A Jacques	Glaciogenic lake	−69.703382	48.247999	Ouellet (1997)
	Canada	Au Basque	Glaciogenic lake	−69.830471	48.017854	Ouellet (1997)
	Canada	Au Porc-Epic	Glaciogenic lake	−70.587410	47.928205	Ouellet (1997)
	Canada	Barley	Glaciogenic lake	−70.657945	47.805174	Ouellet (1997)
	Canada	Bays	Glaciogenic lake	−79.056587	45.233075	Doughty et al. (2014)
	USA	Bolan	Glaciogenic lake	−123.459167	42.021944	Morey et al. (2013)
	Canada	Buteux	Glaciogenic lake	−69.926233	48.048540	Ouellet (1997)
	Canada	Cape Bounty East High Artic	Glaciogenic lake	−109.531803	74.889965	Normandeau et al. (2016)
	Canada	Cape Bounty West High Artic	Glaciogenic lake	−109.592743	74.891710	Normandeau et al. (2016)
	USA/Canada	Champlain	Glaciogenic lake	−73.342432	44.533333	Manley and Manley (2009)
	Guatemala	Chichój	Karstic lake	−90.476317	15.360591	Brocard et al. (2014)
	USA	Crescent	Glaciogenic lake	−123.818065	48.058517	Pollen (2016)
	Canada	Dasserat	Glaciogenic lake	−79.405034	48.245625	Brooks (2016)
	Canada	Des Martres	Glaciogenic lake	−70.634830	47.833454	Ouellet (1997)
	Canada	Des Sables	Glaciogenic lake	−69.674262	48.300076	Ouellet (1997)
	Alaska	Eklutna	Glaciogenic lake	−149.041901	61.379127	Praet et al. (2017)
	Canada	Éternité	Glaciogenic lake	−70.535266	48.236256	Locat et al. (2016)
	Canada	Fairbanks	Glaciogenic lake	−81.425385	46.465236	Doughty et al. (2014)

Canada	Gull	Glaciogenic lake	−78.776608	44.853313	Doughty et al. (2014)
Canada	Ha Ha	Glaciogenic lake	−70.844788	48.039284	Ouellet (1997)
Canada	Jacques Cartier	Glaciogenic lake	−71.224424	47.587400	Ouellet (1997)
Canada	Joseph	Glaciogenic lake	−79.756279	45.209376	Doughty et al. (2014)
Alaska	Kenai	Glaciogenic lake	−149.573333	60.392222	Praet et al. (2017)
Canada	Kenogami	Glaciogenic lake	−71.372276	48.318188	Ouellet (1997)
Canada	Kipawa	Glaciogenic lake	−78.853512	46.851269	Doughty et al. (2014)
Costa Rica	Laguna Caliente	Crater lake	−84.230852	10.197810	Rouwet et al. (2011)
Canada	Lakelse	Glaciogenic lake	−128.558873	54.379166	Geertsema et al. (2018)
Canada	Lillooet	Glaciogenic lake	−122.511099	50.252367	Heideman et al. (2015)
USA	Loon	Dammed lake	−123.838856	43.587438	Richardson et al. (2018)
Canada	Mazinaw	Glaciogenic lake	−77.195263	44.910116	Doughty et al. (2014)
Canada	Mekinac	Glaciogenic lake	−72.675959	47.054536	Ouellet (1997)
Canada	Muskoka	Glaciogenic lake	−79.443169	45.024281	Doughty et al. (2014)
Canada	Nipissing	Glaciogenic lake	−79.766235	46.274834	Doughty et al. (2014)
Canada	Ontario	Glaciogenic lake	−77.874527	43.647007	Doughty et al. (2014)
USA	Owasco	Glaciogenic lake	−76.510170	42.825405	Curtin et al. (2015) and Mullins and Halfman (2001)
Canada	Parry Sound	Glaciogenic lake	−80.113335	45.351180	Doughty et al. (2014)
Mexico	Patzcuaro	Dammed lake	−101.642285	19.616456	Garduño-Monroy et al. (2011)
Guatemala	Petén Itzá	Tectonic lake	−89.815043	16.993861	Mueller et al. (2010)
Canada	Petit Malbaie	Glaciogenic lake	−70.659490	47.773230	Ouellet (1997)
Canada	Pohenegamook	Glaciogenic lake	−69.266871	47.489206	Ouellet (1997)
USA	Quinault	Glaciogenic lake	−123.870510	47.473411	Leithold et al. (2018)
Canada	Rousseau	Glaciogenic lake	−79.611139	45.159951	Doughty et al. (2014)
USA	Sanger	Glaciogenic lake	−123.647341	41.901730	Morey et al. (2013)
Canada	Seminaire (1)	Glaciogenic lake	−69.817064	48.005521	Ouellet (1997)
Canada	Seminaire (2)	Glaciogenic lake	−69.825122	47.993244	Ouellet (1997)
USA	Seneca	Glaciogenic lake	−76.897716	42.632829	Curtin et al. (2015)
Canada	Simcoe	Glaciogenic lake	−79.372101	44.432064	Doughty et al. (2014)
Alaska	Skilak	Glaciogenic lake	−150.333889	60.416389	Praet et al. (2017)
Canada	Squatec	Glaciogenic lake	−68.575511	47.675684	Ouellet (1997)
Canada	St. Joseph	Glaciogenic lake	−71.637078	46.909790	Ouellet (1997)
Canada/USA	Superior	Glaciogenic lake	−86.968072	47.737173	Voytek (2010)
Canada	Tadoussac	Glaciogenic lake	−69.672246	48.222528	Doig (1990) and Ouellet (1997)
USA	Tahoe	Tectonic lake	−120.031246	39.092185	Gardner et al. (2000), Maloney et al. (2013), and Smith et al. (2013)
Canada	Témiscouata	Glaciogenic lake	−68.827200	47.670589	Lajeunesse et al. (2017) and Ouellet (1997)
Canada	Timiskaming	Glaciogenic lake	−79.586849	47.453166	Doughty et al. (2013) and Doughty et al. (2014)
USA	Triangle	Dammed lake	−123.574305	44.173217	Morey et al. (2013)
USA	Upper Squaw	Dammed lake	−123.015139	42.031691	Morey et al. (2013)

(Continued)

Table 13.1 (Continued)

Continent	State	Lake	Origin	X	Y	References
	Canada	Vermilion	Glaciogenic lake	−81.402340	46.523084	Doughty et al. (2014)
	Canada	Wanapitei	Glaciogenic lake	−80.740242	46.739743	Doughty et al. (2014)
	USA	Washington	Glaciogenic lake	−122.261244	47.622203	Karlin et al. (2004)
	Canada/USA	Waterton	Glaciogenic lake	−113.902418	49.037400	Eyles et al. (2000)
	USA	Yellowstone	Crater lake	−110.329877	44.433956	Morgan et al. (2003)
South America	Chile	Aculeo	Tectonic lake	−70.915278	−33.846389	Van Daele et al. (2015)
	Chile	Budi	Tectonic lake	−73.287048	−38.884152	Wallner (2008)
	Chile	Calafquén	Glaciogenic lake	−72.155457	−39.520992	Moernaut et al. (2009, 2014, 2017) and Van Daele et al. (2014, 2015)
	Chile	Castor	Glaciogenic lake	−71.787071	−45.599807	Van Daele et al. (2016)
	Chile/Argentina	Fagnano	Tectonic lake	−67.968292	−54.575047	Waldmann et al. (2008, 2011)
	Argentina	Frias	Glaciogenic lake	−71.799166	−41.062840	Chapron et al. (2006)
	Chile	Icalma	Glaciogenic lake	−71.282129	−38.794701	Bertrand et al. (2008) and Moernaut (2010)
	Argentina	Laguna Potrok Aike	Crater lake	−70.379444	−51.963056	Anselmetti et al. (2009)
	Chile	Laja	Glaciogenic lake	−71.291656	−37.318503	Van Daele et al. (2015)
	Chile	Llanquihue	Glaciogenic lake	−72.825279	−41.146862	Van Daele et al. (2015)
	Chile	Lo Encanado	Glaciogenic lake	−70.133328	−33.671497	Van Daele et al. (2015)
	Chile	Maihue	Glaciogenic lake	−72.025166	−40.282014	Van Daele et al. (2015)
	Venezuela	Mucubají	Glaciogenic lake	−70.828773	8.797230	Carrillo et al. (2008)
	Argentina	Nahuel Huapi	Glaciogenic lake	−71.335556	−41.090278	Chapron et al. (2006) and Beigt et al. (2016)
	Chile	Negra	Glaciogenic lake	−70.122814	−33.642063	Van Daele et al. (2015)
	Chile	Neltume	Glaciogenic lake	−71.981049	−39.792578	Van Daele et al. (2015)
	Chile	Panguipulli	Glaciogenic lake	−72.240257	−39.699527	Moernaut et al. (2017) and Van Daele et al. (2015)
	Chile	Pellaifa	Glaciogenic lake	−71.955643	−39.599075	Van Daele et al. (2015)
	Chile	Pullinque	Glaciogenic lake	−72.145500	−39.564941	Van Daele et al. (2015)
	Chile	Puyehue	Glaciogenic lake	−72.481270	−40.671004	Chapron et al. (2006), Moernaut et al. (2007), and Van Daele et al. (2015)
	Chile	Ranco	Glaciogenic lake	−72.354584	−40.203264	Van Daele et al. (2015)
	Chile	Riñihue	Glaciogenic lake	−72.298622	−39.839123	Moernaut et al. (2014, 2017) and Van Daele et al. (2015)
	Chile	Rupanco	Glaciogenic lake	−72.502213	−40.813809	Van Daele et al. (2015)
	Chile	Vichuquen	Tectonic lake	−72.045937	−34.820075	Van Daele et al. (2015)
	Chile	Villarrica	Glaciogenic lake	−72.095718	−39.248739	Moernaut (2010), Moernaut et al. (2009, 2014, 2017), and Van Daele et al. (2014, 2015)
Antarctica	France	d'Armor	Glaciogenic lake	69.707292	−49.458729	Heirman et al. (2012)

other global examples. This aims at (i) illustrating the variability and similarities of lacustrine MTDs resulting from different mass-movement processes and (ii) providing views and perspectives of the wide range of fundamental to applied science applications of MTD research in lakes and beyond.

13.2. SELECTED CASE STUDIES OF LACUSTRINE MTDs RESULTING FROM DIFFERENT MASS-MOVEMENT PROCESSES

13.2.1. MTDs Generated From Lateral Slope Landslides

As selected case study, we present the neighboring Horgen and Oberrieden slides in Lake Zurich, Switzerland (Figure 13.2), compiled after the original studies by Kelts and Hsü (1980), Strasser et al. (2013), and Strupler et al. (2017, 2018a). Perialpine Lake Zurich (47°15′N; 8°41′E; 135 m deep) is located in northern Switzerland and occupies a glacially overdeepened trough. The southern slope of the central part of the main basin shows evidence of several subaqueous lateral slope landslides, which generated MTDs and turbidites that can be traced within the central basin (Strasser & Anselmetti, 2008). The 1875 CE Horgen Slide and the 1918 CE Oberrieden Slide represent two prominent examples of translational slides, in which the lacustrine sedimentary drape covering the slope has failed along a basal surface of glacial deposits due to human activity in the nearshore area (Figure 13.2a). Even if they are only 1 km apart, the two resulting MTDs show different frontal emplacement styles. They are classified (following the classification scheme by Frey-Martinez et al. (2006)) as a frontally emergent landslide (1875 CE Horgen Slide) and a frontally confined landslide (1918 CE Oberrieden Slide) (Strupler, 2017). The difference lies in the ability of the sliding mass to ramp up from its basal shear surface and travel downslope over layers of undisturbed sediments.

The 1875 CE Horgen Slide represents a multiple-phase event (Kelts & Hsü, 1980) and is characterized by an irregular erosional surface of 0.33 km^2, with terraces and gullies. The depositional zone starts at the base of the slope and expands toward the central basin for ~630 m. The presence of several blocks with dimensions up to 20 m allows differentiating the MTD from the lake bottom in multibeam bathymetry data (Figure 13.2b). In seismic data, the MTD is characterized by a transparent-to-chaotic facies. The MTD reaches its maximum thickness, which is ~6.6 m, at the base of the slope. The deposit thins toward the basin until it appears as a wedge that pinches out within parallel-stratified undisturbed sediments. A frontal ramp structure in the proximal part of the frontally emergent landslide (highlighted with a black solid line in Figure 13.2d) marks the point in which the landslide was able to ramp up from the original basal shear surface and move downslope over undisturbed sediments. Turbidite deposits, in the deep basin, have been described in sediment cores by Kelts and Hsü (1980). Their longitudinal distribution along the axis of the deep basin suggests that turbidity currents generated by the sliding events were deflected by the opposite steep slope.

The single-phase 1918 CE Oberrieden Slide covers a translational area of 0.16 km^2, with a clear scarp and the presence of various gullies on the steepest slope. The depositional zone consists of a rough surface with radially parallel frontal bulges ("a" white arrow in Figure 13.2c). The bulges occur at the toe of the deposit, forming a ~250 m wide zone within the frontal compressional regime during MTD emplacement. Such frontally confined MTDs are not able to ramp up from the basal surface. Therefore, they undergo a restricted downslope translation with consequent plowing of downslope adjacent sediments. As result of the frontal thrusts, the toe area is protruding from the lake bottom by ~3.5 m. The MTD is visible in seismic data as a transparent-to-chaotic unit with a maximum thickness that is larger in the distal part of the landslide body, where it reaches ~15 m. This area shows frontal thrust structures, which separate blocks of tilted and/or folded sediment sections (Figure 13.2e).

According to Moernaut and De Batist (2011), the frontal emplacement of a slide is mainly controlled by the height of the center of gravity, which is determined, in turn, by the relative height drop between headscarp and frontal ramp and subsurface depth of the basal shear surface (i.e., the initial thickness of the sliding mass). A big height drop and a shallow basal shear surface result in a greater landslide's ability to ramp out and evolve in a frontally emergent landslide. Furthermore, frontally emergent landslides usually show a higher mobility of the sliding deposits that are free to move outward for long distances. In agreement with Moernaut and De Batist (2011), the frontally emergent Horgen Slide shows a higher value of height drop and a smaller value of initial thickness of the sliding mass, that is, 130 and 4 m against 83 and 11.5 m of the Oberrieden confined landslide. The emergent Horgen Slide is also characterized by a higher runout distance (1180 vs. 865 m).

Evidence of mass movements occurred in draped lateral slopes, and comparable MTDs with either frontally emergent or frontally confined emplacement processes are found in lakes of different origin worldwide. For instance, Anselmetti et al. (2009), who investigated the crater lake of Laguna Potrok Aike in Argentina, highlighted the presence of eight event horizons, with mass movements originated from the lateral slopes, in the last 8600 cal yr BP. These instability events were more frequent during periods of high sedimentation and lowering

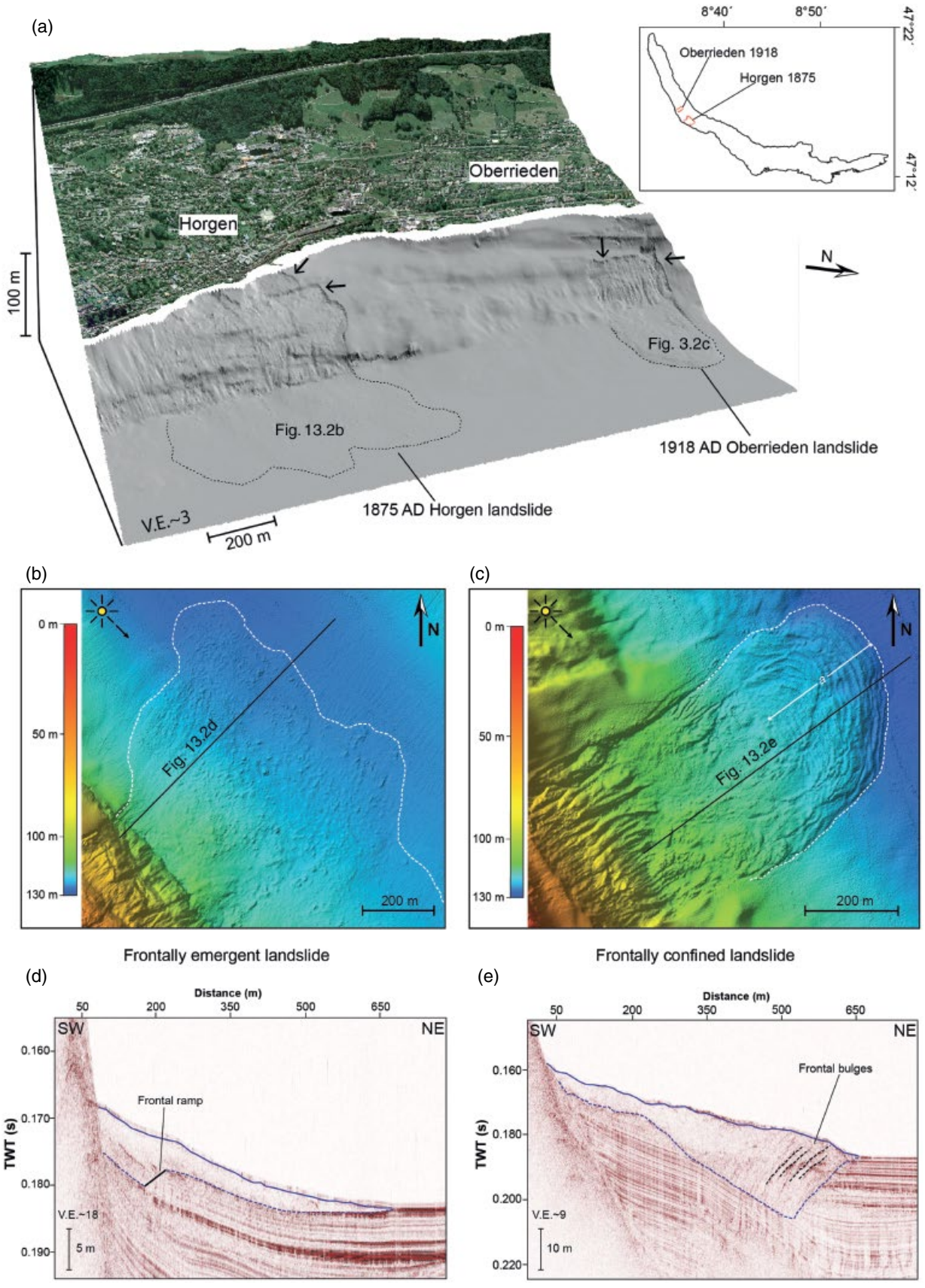


Figure 13.2 Lateral slope MTD case study, Lake Zurich (Switzerland). (a) Location of the 1875 CE Horgen and the 1918 CE Oberrieden landslides in Lake Zurich. Black arrows: slide scarps; dotted black lines: deposit area. (b) Multibeam bathymetry data of the 1875 CE Horgen MTD. The deposit area is highlighted by the presence of several blocks. (c) Multibeam bathymetry data of the 1918 CE Oberrieden MTD. Parallel frontal bulges (marked with "*a*" white arrow) outline the deposit extension. 3.5 kHz seismic profiles along the frontally emergent Horgen MTD (d) and the frontally confined Oberrieden MTD (e). Blue line and dashed blue line mark the top and the base of the deposits, respectively. Location of profiles in Figure 13.2b, c. Source: Modified after Strupler et al. (2017). © 2017 Springer Nature. (*See electronic version for color representation of this figure*)

of the lake's water level. Lateral slope instabilities occurred also in Lake Baikal, the oldest and deepest lake on Earth, as documented in seismic data by several lens-shaped bodies with chaotic seismic facies (Solovyeva et al., 2016). These MTDs are separated in time, indicating repeated instability events from the same slope, most likely related to activity of the tectonic movements in the Baikal rift system.

Sauerbrey et al. (2013) identified and classified different types of Quaternary MTDs in meteorite-impact Lake El'gygytgyn. About 16% of the total sediment thickness accumulated in this 3.6 Myr old Siberian lake is composed of MTDs from lateral slope landslides, which took place along a weak sediment layer, mobilizing and disintegrating packages of lacustrine sediments overlying it.

13.2.2. MTDs Generated From Margin Collapses

Here we present the Udenisht Slide Complex (USC) in Lake Ohrid (Albania/Macedonia; Figure 13.3) as an example of this complex mass-failure process (Lindhorst et al., 2012, 2015; Wagner et al., 2012). Lake Ohrid (41°05′N; 20°45′E; maximum water depth 293 m) was formed between 3 and 5 Ma BP, representing one of the oldest lakes in Europe. It occupies ~360 km^2 of an active graben on the Balkan Peninsula. The USC is located in the southwestern part of the lake and represents the largest mass-wasting event found within the basin (Figure 13.3a). It involved ~0.11 km^3 of sediments of the southwestern margin, which traveled northeast for up to 10 km, covering almost 10% of the entire basin and reaching a maximum thickness of 50 m. Age estimations based on the thickness of the post-failure sediment drape suggest that the USC is most likely younger than 1500 yr (Lindhorst et al., 2012).

The USC has been surveyed and described in detail with multibeam bathymetry and multichannel seismic and high-resolution parasound data. Bathymetric data show that the failure zone is bounded by ~25 m high sidewalls. In the upper part, the zone is characterized by steep slope angles of up to 10° and in the lower part by an irregular topography (Figure 13.3b, c), which is related to the presence of massive isolated blocks with dimensions up to 50 by 10 m. In 100 and 180 m of water depth, two parallel north-south striking morphological steps delineate tectonic faults (marked with black dashed lines in Figure 13.3c), which likely played an important role in the instability occurrence and deposit distribution, as inferred from the geometrical relation between the USC sidewall and fault lineament. No clear headscarp is visible in the bathymetry data. This suggests a shallow (nearshore) initiation of the failure that involved the entire margin slope. The occurrence of two other slides, pockmark structures and a prominent fault-related structure north of the USC slide area, hint toward a relationship between active tectonics, focused fluid flow, and landslide initiation (Figure 13.3b). The deposition area of the USC starts at ~150 m of water depth, where the slope angle is ~4°, and continues for up to 10 km into the deep basin, until it reaches an area with slope angle of <1.5°. The proximal part of the deposit is characterized by a hummocky top surface that stands out among the overall smooth topography. Moving toward the central basin, the top of the USC MTD becomes smoother and, therefore, hardly discernible from the general lake floor.

The multichannel seismic data show that the USC represents just the most recent of several MTDs that occurred in the same area (Figure 13.3d). These deposits, which are visible as a chaotic-to-transparent seismic facies, intercalate conformable subparallel reflections. The northern sidewall of the USC landslide is visible as an abrupt 25 m high step in morphology. The thickness of the MTD increases gradually eastward toward the central basin, where bright spot amplitude anomalies, possibly related to fluid migration, are imaged (marked with circles in Figure 13.3d).

A more detailed description of the USC features is obtained from 10 kHz parasound data (Figure 13.3e). These data show that part of the transported mass has been trapped on the slope by several massive isolated blocks imaged on multibeam bathymetry. The MTD area is divided in three sections based on surface morphology, internal structure, and thickness (Lindhorst et al., 2012). The upper section (I in Figure 13.3e) shows a very rough topography and high-amplitude reflections within the deposit. The limited thickness of the deposit in this area allows identifying the base of the MTD, indicated by a high-amplitude seismic horizon (marked with a dashed line in Figure 13.3e). The middle section (II) corresponds with the main slide body. Here the MTD is characterized by a maximum 50 m thick chaotic-to-transparent seismic facies with internal high-amplitude reflections. The high reflectivity of the lake floor prevents deeper penetration of the seismic signal, which is not reaching the base of the deposit. An abrupt decrease of the deposit thickness in combination with a frontal ramp structure within the deep basin separates section II from section III. The distal section (III) shows an irregular and discontinuous lake-floor reflection, indicating a high roughness of the top surface. Below and in front of the slide toe, parallel layers of undisturbed sediments are imaged. The collapse of the southwestern margin of Lake Ohrid occurred in at least two phases in a retrogressive pattern, and it was most likely triggered by an earthquake (Lindhorst et al., 2012).

A big margin collapse has also been described in the tectonic Lake Tahoe (United States) (Gardner et al., 2000) and relates, most likely, to the activity of the faults that border

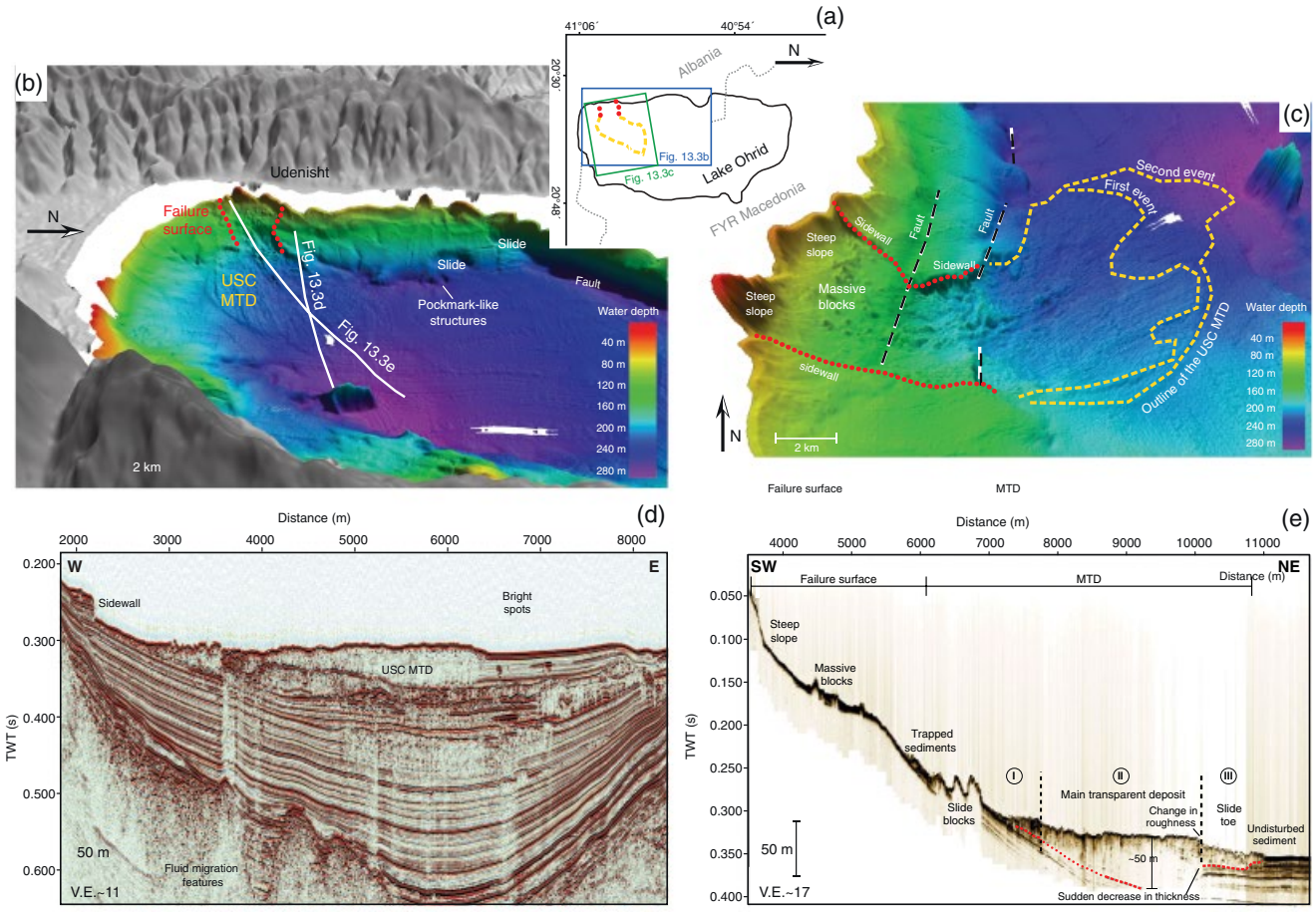


Figure 13.3 Margin collapse MTD case study, Lake Ohrid (Albania/Macedonia). (a) Location map of Lake Ohrid and margin collapse MTD. Blue and green boxes indicate positions of 3D perspective view and zoomed-in image shown as figures. (b) 3D perspective view of the southern area of Lake Ohrid. Red dotted line indicates the failure surface of the USC, and yellow dashed line the MTD extension. Two smaller MTD, a fault and pockmark-like structures, are marked north of the USC. (c) 3D image of the USC area with interpretation of the most prominent morphological features described in the text. (d) Multichannel seismic profile across the USC. Several MTDs, visible as chaotic-to-transparent facies among the normal subparallel reflections, are identified. The USC MTD is marked on top by a yellow line and at the base by a yellow dashed line. Older MTDs are marked with green lines. The sidewall of the margin collapse landslide and fluid migration-related features are marked in the figure. (e) Parasound profile cutting the USC failure surface and MTD with interpretation of the main instability-related features. The MTD is divided in three sections (I, II, III), described in the text. A dashed red line marks the base of the MTD. Source: Modified after Lindhorst et al. (2012). © 2012 Springer Nature. (*See electronic version for color representation of this figure*)

the lake basin, converging at a zone within McKinney Bay. Around ~60 ka BP (Smith et al., 2013), the entire northwestern margin of the lake failed, generating a major mass movement that traveled toward the eastern margin. The failure brought to a change in the lake morphology, with the creation of the present-day McKinney Bay, a 12 km long embayment in the lake's shoreline. The respective MTD is imaged in reflection seismic data as chaotic deposit with up to 40 m thickness across the deep basin, including big blocks up to 1000 m long and 80 m high, which are also prominently visible in bathymetric data.

13.2.3. MTDs Generated From Delta Collapses

The Muota delta collapse in Lake Lucerne (Switzerland) is presented to illustrate MTDs resulting from delta slope failures (Figure 13.4) (Hilbe & Anselmetti, 2014; Siegenthaler & Sturm, 1991). This event occurred in 1687 CE and is historically documented as a 5 m high tsunami that took place during fair-weather and no-wind conditions (Billeter, 1923; Bünti and Wyrsch, 1973; Dietrich, 1689). The Treib Basin and Lake Uri are two of the seven sub-basins of perialpine Lake Lucerne, a glacigenic lake in

Central Switzerland (47°N, 8.4°E) (Figure 13.4a). They have elongated shapes bounded by steep slopes and reach maximum depths of 123 and 199 m for the Treib and Lake Uri basins, respectively. Both basins preserved evidence of the big subaqueous instability on the Muota delta in 1687 CE (Hilbe & Anselmetti, 2014).

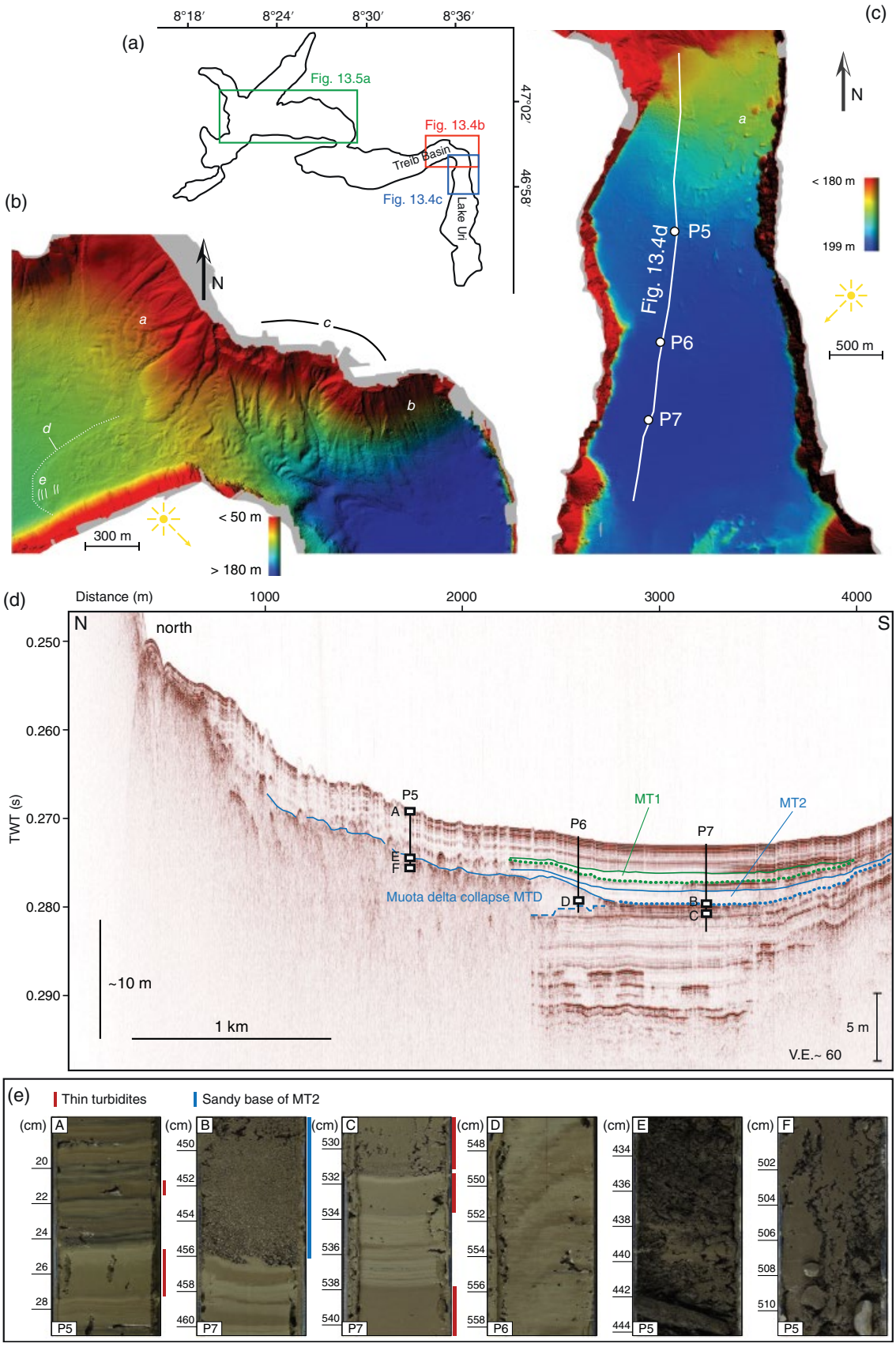
The prograding delta of Muota River shows a complex morphological structure with lateral scarps and channels running from the central depositional fan to the deeper basins (Figure 13.4b). In the western part, toward the Treib Basin, the slopes are characterized by low slope angles and smooth surfaces ("a" in Figure 13.4b), whereas the eastern part shows steeper slopes with constant angles of about 20–25° ("b" in Figure 13.4b), which descend to Lake Uri. The headscarp of the 1687 CE delta collapse, which is not clearly detectable in this area, was most likely located within the currently active fan and is overprinted by the rapid deposition of post-event deltaic sediments (indicated with "c" black line in Figure 13.4b). The Muota delta collapse evolved in two directions, forming MTDs with distinct characteristic features in both Treib Basin and Lake Uri (Hilbe & Anselmetti, 2014). The main part of the failed sediments descended toward Lake Uri, generating a MTD at the base of the slope and an associated turbidite, whereas westward it induced deformation of the basin sediment of Treib Basin. Here, at the toe of Muota delta, a 300 m wide lobe structure extends for 800 m toward the basin and is delineated by an external bulge of 1–2 m height (marked with "d" in Figure 13.4b). Smaller parallel bulges, protruding just a few decimeters, are present within the lobe ("e" in Figure 13.4b). Toward the base of the slope, they are replaced by a more hummocky topography.

The MTD in Lake Uri extends southward of the delta slope for 1.5 km, asymmetrically covering the entire basin in east-west direction, with thicknesses of 10 m in the east and 2–6 m in the west. In the northeastern part, the MTD shows a hummocky upper surface, with irregularities up to 30 m wide and 4 m high ("a" in Figure 13.4c), which become less pronounced toward the southwest.

The seismic penetration is very low near the delta due to the presence of free gas in the sediments. The signal reaches 15 m depth in the central basin, revealing chaotic-to-transparent facies within the generally well-stratified sediments (Figure 13.4d). Sediment cores show that the latter is mainly characterized by gray to brown muddy layers with intercalated thin turbidites, not resolvable in seismic data (Figure 13.4e-A, core P5; Figure 13.4e-C, core P7). On the seismic profiles, two major megaturbidites, with thicknesses of 1 and 1.5 m, are identified (MT1 and MT2 in Figure 13.4d), both showing a ponding geometry. This basin-focused depositional pattern is most likely the result of seiches following the mass movement. These periodic oscillations of water level may move coarser sediments back and forth on the lake floor and keep the fine sediments in suspension for a longer period of time. This generates a focused and symmetrical deposition of sediments in the central basins (Beck, 2009; Hilbe & Anselmetti, 2014). In the cores, the corresponding turbidites usually have a sandy base, which creates a sharp contrast with the underlying undisturbed muddy layers (Figure 13.4e-B, core P7).

The lower megaturbidite (MT2) is related to the Muota delta collapse and is overlaying the associated MTD, which shows an irregular, southward dipping top surface and ends with a 2 m high and 200 m wide tapering wedge that comprises layers of deformed laminated mud (Figure 13.4e-D, core P6). Core P5 revealed in the uppermost meter of the MTD the presence of plants remains, mainly grass and some wood fragments, along with gravel and mud clasts (Figure 13.4e-E, core P5), which are covering a sequence between almost homogeneous mud and mud-rich gravel with rounded pebbles (Figure 13.4e-F, core P5). The total volume of the deposit is $\sim 1 \times 10^6\,m^3$, but a considerable part is not coming from the source area, as intact or weakly deformed blocks of sediments were entrained within the mass movement (Hilbe & Anselmetti, 2014).

Prograding delta fans are more susceptible to instability than non-deltaic draped lateral slopes, due to the high amount of clastic sediment input leading to oversteepening and possible development of pore water overpressure. Therefore, mass movements in delta fans, with different size and triggering mechanisms, are common features in many lakes worldwide. For instance, a delta slope failure was identified in Lake Quinault (United States) based on the presence of an MTD and megaturbidite in the deep basin and can possibly be linked to the giant ($M_w \sim 9$) 1700 CE Cascadia earthquake (Leithold et al., 2018). Megathrust earthquakes are also interpreted as a trigger for delta-collapse-related MTDs occurring at correlative stratigraphic levels across three south central Alaskan proglacial lakes (Praet et al., 2017). Delta and alluvial fan failure deposits, related to the 1964 CE Alaska earthquake, represent 95% of the total landslide volume in Kenai Lake, 33–39% in Eklutna Lake, and 15% in Skilak Lake. A spontaneous delta collapse occurred in spring 1996 CE in Lake Brienz (Switzerland). The event was detected by a series of events (i.e., seiches, turbidity increase, and low oxygen concentrations in deep waters) and created a large megaturbidite deposit, which is covering the flat lake basin (Girardclos et al., 2007). In Lake Geneva, a large delta collapse in 523 CE, resulting in a prominent MTD and megaturbidite deposit, was triggered by a subaerial rockfall loading and mobilizing the water-saturated delta plain (Kremer et al., 2015).


(a)
8°18′
8°24′
8°30′
8°36′
47°02′
46°58′
Fig. 13.5a
Fig. 13.4b
Fig. 13.4c
Treib Basin
Lake Uri
(b)
N
a
b
c
d
e
300 m
< 50 m
> 180 m
(c)
N
a
Fig. 13.4d
P5
P6
P7
< 180 m
199 m
500 m
(d)
Distance (m)
1000
2000
3000
4000
N
north
S
TWT (s)
0.250
0.260
0.270
0.280
0.290
P5
A
E
F
P6
D
P7
B
C
MT1
MT2
Muota delta collapse MTD
~10 m
1 km
5 m
V.E.~ 60
(e)
Thin turbidites
Sandy base of MT2
(cm)
A
P5
B
P7
C
P7
D
P6
E
P5
F
P5

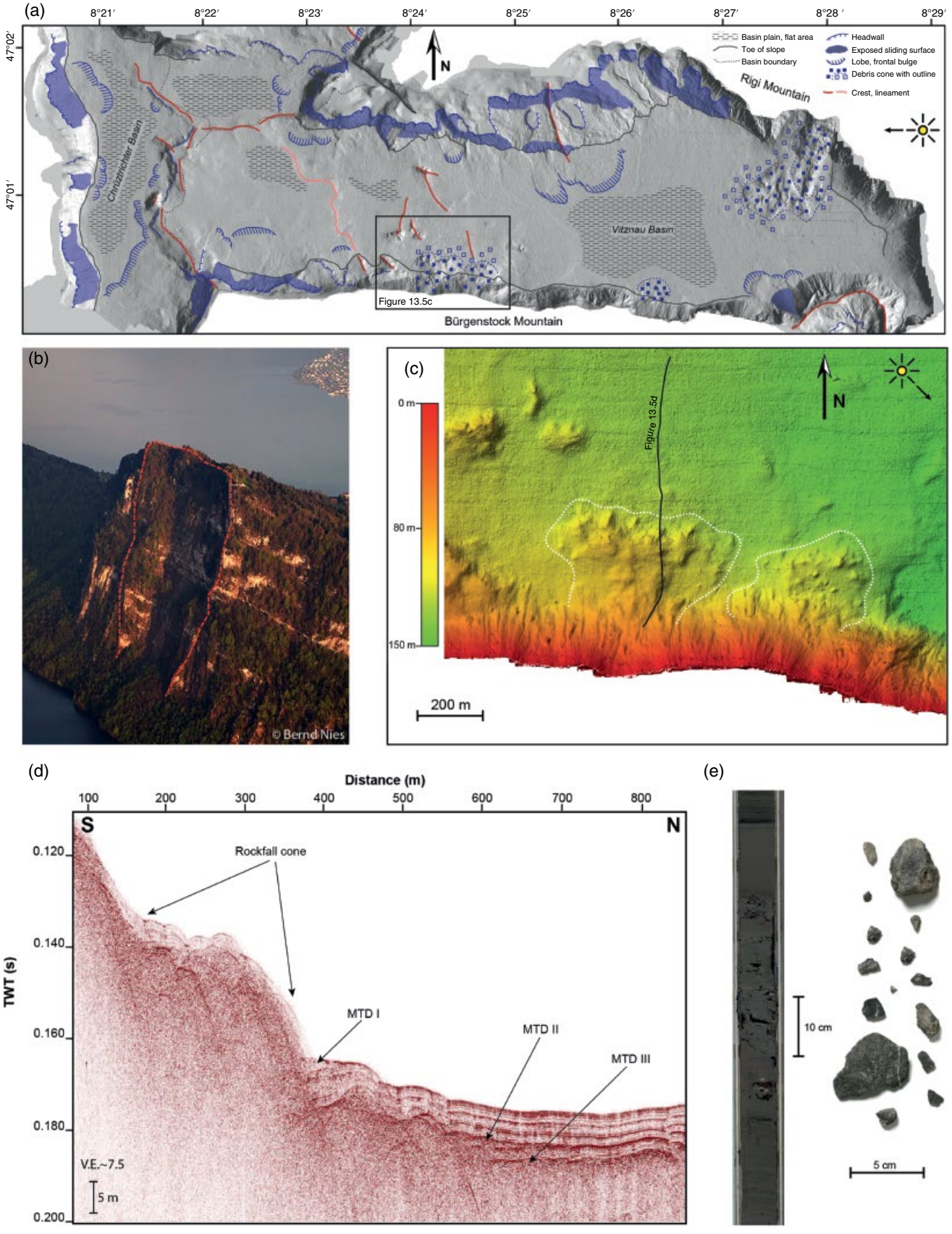
13.2.4. MTDs Generated From Rockfalls

Repeated rockfall activity from the steep cliff of Bürgenstock Mountain, on Lake Lucerne (Switzerland), offers a representative case study for MTDs related to this type of gravitational mass movement (Figure 13.5) (Hilbe et al., 2011; Schnellmann et al., 2006). The Vitznau Basin is one of the three distal basins of Lake Lucerne, Central Switzerland (47°N, 8.4°E), and is located at the Alpine Front. The basin is surrounded to the south by the steep limestone cliffs of Bürgenstock Mountain and to the north by the conglomerate slopes of Rigi Mountain, which show a more gentle topography. Rockfall deposits and rockfall-evolved MTDs are abundant in the Vitznau Basin, and they are present at the base of the slopes in the form of debris cones (Figure 13.5a). These generally triangular-shaped deposits show hummocky, irregular topography and positive relief on bathymetric maps. The bathymetric data of the Vitznau Basin highlight the presence of a major event at the base of Rigi Mountain, as well as several repeated events at the toe of the Bürgenstock cliffs (Figure 13.5a). In this area, rockfalls originate from the steep slopes above lakeshores, as highlighted by the presence of subaerial scarps (Figure 13.5b).

Schnellmann et al. (2006) report at least 6 rockfall events that occurred in the Bürgenstock cliff area during the last 12000 yr, with the latest correlated to a strong regional earthquake in 1601 CE. On the bathymetry data, this area shows two distinct rockfall cones, both characterized by hummocky surfaces with only large-scale irregularities (Figure 13.5c). Small-scale irregularities, most likely associated with isolated blocks, which have been smoothed out by post-failure sedimentation. The larger cone, located to the west, covers an area of ~0.2 km^2 and extends for 320 m north to the base of the slope. On seismic data, it appears as a chaotic seismic facies with some discontinuous high-amplitude reflections and an irregular upper surface (Figure 13.5d). This irregular surface and the likely presence of isolated blocks lead to a low penetration of the seismic signal. At the foot of the rockfall cone, three MTDs are identified at different stratigraphic levels (marked with I, II, and III in Figure 13.5d). They are likely to be rockfall-evolved deposits, and, therefore, their presence confirms a repeated rockfall activity in this area. These wedge-shaped units, of which the thickness is decreasing toward the basin, are characterized by a chaotic seismic facies with high-amplitude reflections. This common feature for rockfall-evolved deposits is most likely related to the presence of rock fragments in a muddy matrix, as shown in the core of Figure 13.5e. The core in Figure 13.5d represents the sedimentary succession through a rockfall-evolved deposit and highlight the presence of limestone fragments up to 5 cm within the deposit. The deposit overlies laminated layers of undeformed sediments and is, in turn, overlain by a 10 cm thick turbidite.

Rockfalls are common events in subaerial steep slopes and can generate water waves and secondary instabilities on the subaquatic slopes, leaving significant imprints in the lacustrine record. The 1960 CE Great Chilean Earthquake (M_w 9.5) triggered several rockfalls along the slopes bordering Lake Pellaifa. Several of these rockfalls surged into the lake leading to a reported tsunami and subsequent seiche, which resulted in the deposition of a 2 m thick megaturbidite in the deep basin (Van Daele et al., 2015). Daxer et al. (2018) reports the occurrence of repeated rockfall activity from the southern shore of Lake Mondsee (Austria), based on morphological evidence and seismic and core data. The infrequent but repeated rockfalls originated from a steep and weathered cliff, shaping the present-day morphology of the shore. Even if the volumes of these events are not comparable with the ones in Lake Lucerne, the instabilities have led to

Figure 13.4 Delta collapse MTD case study, Lake Lucerne (Switzerland). (a) Location of the Treib and Lake Uri basins in Lake Lucerne. Red and blue boxes indicate positions of detailed bathymetric maps shown as figures. (b) Multibeam bathymetric data of Muota delta and the easternmost part of Treib Basin. Features described in the text are labeled: "*a*" slope with low slope angles and smooth surfaces; "*b*" slope with steep angles; "*c*" currently active fan; "*d*" external bulge of collapse-related lobe; and "e" small parallel bulges within the deposit. (c) Multibeam bathymetric data of the northern part of Lake Uri showing a hummocky surface at the toe of the Muota delta ("*a*"). (d) 3.5 kHz seismic profile along the northern part of Lake Uri (see Figure 13.4c for location). The 1687 CE Muota delta collapse MTD is marked with blue line on top and blue dashed line at the base. The related megaturbidite and a younger megaturbidite are outlined (top, solid line; base, dotted line) and labeled (MT2 and MT1). Vertical black lines show the position of sediment core, and white boxes with black outline show the detailed location of images presented in Figure 13.4e. (e) Photographs of split core surfaces showing typical lithologies from Lake Uri: (A) laminated muddy layers with turbidites, (B) sandy base of collapse-related megaturbidite (MT2), (C) laminated muddy layers with turbidites, (D) deformed laminated mud in frontal wedge of Muota delta collapse MTD, (E) accumulation of plants remains, and (F) muddy gravel with rounded pebbles. Red and blue lateral lines indicate turbidite layers and the sandy base of MT2, respectively. Source: Modified after Hilbe and Anselmetti (2014). © 2014 John Wiley and Sons. (*See electronic version for color representation of this figure*)


(a)
8°21′
8°22′
8°23′
8°24′
8°25′
8°26′
8°27′
8°28′
8°29′
47°02′
47°01′
N
Basin plain, flat area
Toe of slope
Basin boundary
Headwall
Exposed sliding surface
Lobe, frontal bulge
Debris cone with outline
Crest, lineament
Rigi Mountain
Chrüzitrichter Basin
Vitznau Basin
Figure 13.5c
Bürgenstock Mountain
(b)
© Bernd Nies
(c)
0 m
80 m
150 m
Figure 13.5d
N
200 m
(d)
Distance (m)
100
200
300
400
500
600
700
800
S
N
0.120
0.140
0.160
0.180
0.200
TWT (s)
Rockfall cone
MTD I
MTD II
MTD III
V.E.~7.5
5 m
(e)
10 cm
5 cm

various sedimentological imprints in the nearshore area, as indicated by cores and seismic data.

Rockfall deposits are the most frequent instability events in Lake Albano, Italy, as reported by Bozzano et al. (2009). All these deposits are related to combined subaerial-subaqueous instability events, as suggested by the presence of subaerial scarps along the shoreline and of subaquatic deposits, such as "block fields" and isolated blocks of up to 100 m^2 wide that are visible on the lake floor.

13.3. VERTICAL SUCCESSION OF INTERCALATED MTDs IN BASIN-FILL SEQUENCES

As already mentioned in several of the examples presented above, MTDs originating from different types of instability are often intercalated within the lacustrine normal background sedimentation, representing a distinct MTD stratigraphy. MTDs often appear to be deposited in a vertical succession, suggesting a repeated destabilization of the same slope area through time. In the sedimentary sequence, these deposits are generally separated by layers of undisturbed sediments, of which the thickness depends on the background sedimentation rate and on the frequency of mass movements.

In the following, we will present 4 examples of vertical succession of intercalated MTDs visualized on 3.5 kHz pinger seismic data from four different lakes worldwide (Figure 13.6). We briefly showcase how identification and dating of MTDs stratigraphy extends the historic event catalogue to prehistoric times, unraveling geological information about the long-term instability occurrence linked to either long-term preconditioning or short-term trigger factors as they may relate to past climate, environment, and/or seismotectonic conditions.

13.3.1. Skilak Lake

Skilak Lake is a glacigenic lake on the Kenai Peninsula, in south central Alaska (60°24′N; 150°20′W). The lake basin consists of two sub-basins: a deep proximal basin with maximum depth of 194 m that gradually transitions into a shallower distal basin, which reaches 140 m depth. Based on seismic-stratigraphic interpretations, Praet et al. (2017) map several MTDs intercalated between the uniform background sedimentation and their related megaturbidites in the central part of the deep basin. Seven event horizons are identified, each of them comprising multiple coeval MTDs widespread over the lake basins (Figure 13.6a). Instabilities, which comprise mostly lateral slope landslides, occurred on both northern and southern slopes, as indicated by the stratigraphically correlated MTDs at the base of the opposite slopes. These failures can also generate megaturbidites, which were deposited in the deepest part of the lake and which are characterized by the typical ponding geometry. Seismic data show that the northern MTDs are usually larger than the southern ones. This is interpreted as a consequence of the larger amount of sediments on the more gentle northern slopes, compared to the steeper southern ones. The youngest event corresponds to the 1964 CE (M_w 9.2) earthquake in this area. This earthquake triggered a total of 23 mass movements in Skilak Lake with a total volume of $9.9 \times 107\ m^3$. The related megaturbidite has an estimated total volume of $2.7 \times 106\ m^3$. Synchronous failure of different lacustrine slopes hints at regional trigger mechanism, such as a strong earthquake. Thus, prehistoric stratigraphic levels with coeval landslides can be used to infer the occurrence of strong earthquakes (Praet et al., 2017).

13.3.2. Lake Como

Lake Como (46°10′N; 09°16′E) is located in the Italian Alps and has depths of up to 425 m. It has a glacial origin enhanced by tectonic preconditioning and therefore has a complex shape with three lake branches. The deepest part of the lake (Argegno Basin) is situated in the southwestern branch, which is separated from the other branches by a submerged plateau (Bellagio Plateau). Two prominent MTDs and their associated megaturbidites are identified from reflection seismic data in the Argegno Basin (Figure 13.6b) (Fanetti et al., 2008). The two MTDs are located at the foot of the plateau at ~5 and 8 m subsurface

Figure 13.5 Rockfall MTD case study, Lake Lucerne (Switzerland). (a) Bathymetric map of Chrüztrichter and Vitznau basins in Lake Lucerne with interpretation of the main observed morphologies, including rockfall cones. See Figure 13.4a for location. Source: Modified after Hilbe et al. (2011). © 2011 Springer Nature. (b) Aerial photograph of the steep slope of Bürgenstock Mountain. A dashed red line marks the rockfall scarp. Photograph by Bernd Nies. (c) Detailed bathymetric data of two rockfall cones, marked with white dashed line, at the toe of Bürgenstock Mountain (see Figure 13.5a for location). (d) 3.5 kHz seismic profile across a major rockfall cone. At the foot of the rockfall cone, three rockfall-evolved MTDs are identified at different stratigraphic levels, suggesting a repeated rockfall activity from the Bürgenstock cliffs. See Figure 13.5c for location. Source: Modified after Schnellmann et al. (2006). © 2006 Springer Nature. (e) Example of sediment core through rockfall-evolved MTD and photograph of rock fragments. Source: Modified after Schnellmann et al. (2006). © 2006 Springer Nature.

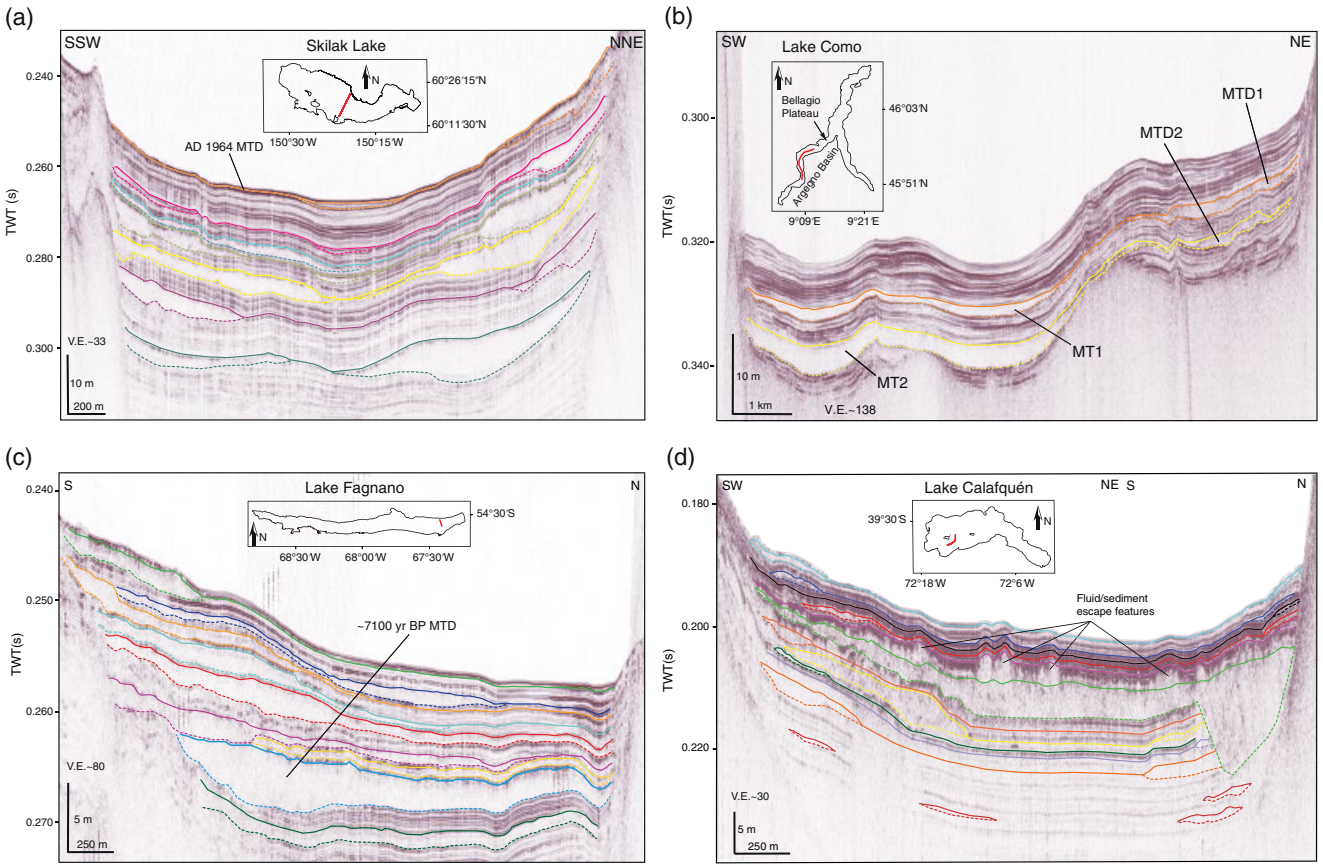


Figure 13.6 Examples of vertical succession of intercalated MTDs. MTDs are marked on top by solid line and at the base by dashed line. (a) 3.5 kHz seismic profile in Skilak Lake (Alaska). Seven event horizons are identified, each comprising coeval MTDs. The youngest event, in orange, corresponds to the 1964 CE (M_w 9.2) earthquake in Alaska. Source: Modified after Praet et al. (2017). © 2017 Elsevier. (b) 3.5 kHz seismic profile in Lake Como (Italy). Two prominent MTDs, labeled with "MTD1" and "MTD2," and their related megaturbidites (top, solid line; base, dotted line) are identified at the toe of Bellagio Plateau. Source: Modified after Fanetti et al. (2008). © 2017 Elsevier. (c) 3.5 kHz seismic profile in Lake Fagnano (Argentina/Chile). Several MTDs are identified at different stratigraphic levels. The asymmetry of the most prominent event, highlighted in light blue, leads to an inclined post-failure stratigraphy. Source: Modified after Waldmann et al. (2011). © 2017 John Wiley and Sons. (d) 3.5 kHz seismic profile in Lake Calafquén (Chile). Several frontally emergent MTDs are identified at the base of the slopes. The largest deposit, highlighted in green, is the result of three simultaneous failures along different slopes. Above this horizon, fluid/sediment escape features, possibly related to earthquake-induced liquefaction and fluidization of buried MTD soft sediments, are marked. Source: Modified after Moernaut et al. (2017). © 2017 Elsevier. (*See electronic version for color representation of this figure*)

depth. The basinward (southward) thinning, wedge-shaped MTD bodies, with irregular and locally erosive basal and hummocky top surfaces, have similar chaotic-to-transparent reflectivity patterns, which is in clear contrast to the high-amplitude and continuous reflections of undisturbed sediments, above, between, and below. The MTDs are the result of large slides that occurred on the steep slopes of the plateau. A morphological sill, which divides the upper and deepest part of the basin, defines the distal limits of the MTDs and most likely has played an important role in the evolution of the mass flows into turbidity currents. The correlative megaturbidites are prominently imaged as an acoustically transparent seismic facies and sharp, high-amplitude upper and lower reflections between the horizontally stratified background sediments. They show a ponding geometry onlapping on the basin edges, and they extend over the entire basin length (~5 km), reaching maximum thicknesses of 1.5 m (MT1) and 3 m (MT2). As these megaturbidites are not yet cored, Fanetti et al. (2008) estimated the ages from near-surface radionuclide (cesium-137) dating and extrapolation of sedimentation rates and suggest that the events occurred in the twelfth (MT1) and sixth centuries (MT2). Since there is historical evidence for a strong

regional earthquake in the twelfth century, Fanetti et al. (2008) further speculated that the observed mass movements in Lake Como could have triggered by seismic shaking of the sediment-overloaded steep slope of the Bellagio Plateau.

13.3.3. Lake Fagnano

Lake Fagnano (54°32′S; 67°59′W) is located on the main island of Tierra del Fuego (Argentina/Chile), in a pull-apart basin that was further shaped by glaciers. It is divided in a western basin and a smaller eastern basin with maximum depths of 110 and 210 m, respectively. The seismic data in the eastern basin allow identifying several event horizons of synchronous MTDs and related megaturbidites within well-stratified sediments (Figure 13.6c) (Waldmann et al., 2011). The chaotic seismic facies of MTDs are located at the base of the southern slope and are getting thinner toward the center of the basin. The MTDs generally have smooth upper surfaces, but show irregular bases, which are locally eroding and deforming the overridden basin sediments. In the deep basin, related megaturbidites are identified as seismically transparent facies with ponding geometry. The most prominent event was dated ~7100 yr BP taking into consideration one regionally documented tephra layer, radiocarbon ages, and modeled sedimentation rates. This MTD is lens shaped and fills the basin in an asymmetric way, leading to an inclined post-failure basin stratigraphy. This inclination is further enhanced by the repeated occurrence of mass movements from the southern slope and is clearly preserved in the actual lake bottom morphology.

The simultaneous occurrence of different mass movements suggests an external trigger mechanism, most likely earthquakes along the active Magallanes-Fagnano transform fault, which were able to mobilize the sedimentary drape of the southern slope. The northern slope is too steep to permit sediment accumulation.

13.3.4. Lake Calafquén

Lake Calafquén (39°31′S; 72°08′W) is a glacigenic lake at the foot of the south central sector of the Andes. It consists of a main large basin with depths up to 215 m and a smaller basin to the southwest. The studied southwest basin is characterized by numerous coeval MTDs at different stratigraphic layers (Figure 13.6d). The MTDs are located at the base of the slopes and are classified as frontally emergent landslides, as shown by the presence of frontal ramps in the seismic data (Moernaut, 2010).

The largest deposit covers the entire southwestern basin and is the result of three simultaneous failures along different slope segments. The mass movement has deeply deformed the sediments at the base of the slope, which become therefore included in the chaotic-to-transparent facies of the deposit. Vertical acoustic wipeouts and intercalated upward-concave zones of up to 80 m wide and 1.9 m thick with low-amplitude reflections are identified above the deposit and have been related to fluid migration activity. Moernaut et al. (2009) suggests that these features have been created by earthquake-induced liquefaction and fluidization of the soft sediments of the buried MTD, resulting in sediment extrusions at the contemporaneous lake bottom, forming sediment volcanoes.

The presence of multiple MTDs in all the stratigraphic event horizons suggests that the occurrence of instabilities is strictly related to the seismic activity of the area, which is dominated by the megathrust earthquake cycle of the Chilean subduction zone (Moernaut et al., 2014, 2017). The youngest event corresponds to the giant 1960 CE (M_w 9.5) earthquake, which generated instabilities along the steep flanks of the lake. It comprises seven MTDs located at the base of the slope and a 5 cm thick turbidite, which cannot be identified on seismic data, but which was confirmed by cores (Moernaut et al., 2017).

13.4. DISCUSSION/CONCLUSION

Bibliographic research highlights that mass movements are common processes in all types of lacustrine environments and can be classified based on the source area, initiation and transport mechanisms, and resulting MTDs and megaturbidites. In particular, we focused on four different instability mechanisms and their related deposits. The reported examples highlight that in reflection seismic data, MTDs often show similar features, even when related to different mass-movement processes. These common features include their geometries (wedge-shaped bodies), internal seismic facies (typically characterized by chaotic-to-transparent facies), the irregularity of the upper surface, and the presence of related megaturbidites toward the basin. Nevertheless, the use of multi-method investigations on lake-basin-wide scales brings complementary information about the erosional and depositional area, allowing to differentiate between different mass-movement mechanisms.

In the last decades, the study of sublacustrine instabilities became increasingly important in different research fields, for example, paleoclimate, paleoseismology, and natural hazard assessment. Due to their small size, well-constrained boundaries, and spatial and temporal continuity in sedimentation, lakes provide well-datable sedimentary archives of the past environmental and climatic changes of the lake and its surrounding. Furthermore, high-energy natural events such as earthquakes, floods, and

shore and delta collapses have been shown to leave important fingerprints in the lacustrine sedimentation, allowing to extend the historic event catalogue to prehistoric times. Single MTDs with large correlative megaturbidites can be caused by, for example, spontaneous delta collapse, for which no external trigger is needed (e.g., Girardclos et al., 2007), while strong earthquakes have been proven to be able to generate synchronous basin-wide mass movements and resuspend large amounts of sediments (Schnellmann et al., 2002). The resulting coeval multiple MTDs and related megaturbidites form distinct and characteristic fingerprints of past earthquakes in the sedimentary record (Kremer et al., 2017; Praet et al., 2017). The identification and dating of these synchronous instability events allow reconstructing frequency and seismic mechanisms of paleo-earthquakes in the area (Doughty et al., 2014; Howarth et al., 2014). When the studied lake and geophysical imaging reveals vertical succession of intercalated MTDs, which can be cored to date the event horizons, the earthquake recurrence pattern can be analyzed. Furthermore, integration of these data with other data set allows for rough estimates of the magnitude of causing earthquake (Becker et al., 2005; Boës et al., 2010; Kremer et al., 2017; Lauterbach et al., 2012; Strasser et al., 2006, 2013). Thus, studies of historic and prehistoric instabilities and their deposits are essential for natural hazard assessment, which also includes slope stability analysis and tsunami modeling (Lindhorst et al., 2014; Strasser et al., 2011; Strupler et al., 2017, 2018a, 2018b).

One key question in the current research of landslide is whether the lacustrine landslides can be scaled up to the much larger marine landslide. If lakes could be considered as small-scale model of marine environment, the study of lacustrine mass movement would become even more significant, improving our understanding of marine instability events with the details and advantages of lacustrine investigations.

ACKNOWLEDGMENTS

This work is supported by the European Training Network SLATE (Submarine Landslides and their impact on European continental margins), in the frame of the Marie Skłodowska-Curie program.

The authors would like to thank Marc De Batist, Nicolas Waldmann, and Sebastian Krastel for sharing their data and Bernd Nies for kindly allowing the use of his aerial photograph.

IHS Markit is acknowledged for their educational grant program providing the Kingdom seismic interpretation software.

We thank editor Andrea Festa and two anonymous reviewers for handling and constructive comments on the manuscript.

REFERENCES

Anselmetti, F. S., Ariztegui, D., De Batist, M., Catalina Gebhardt, A., Haberzettl, T., Niessen, F., et al. (2009). Environmental history of southern Patagonia unravelled by the seismic stratigraphy of Laguna Potrok Aike. *Sedimentology*, *56*(4), 873–892.

Arnaud, F., Lignier, V., Revel, M., Desmet, M., Beck, C., Pourchet, M., et al. (2002). Flood and earthquake disturbance of 210Pb geochronology (Lake Anterne, NW Alps). *Terra Nova*, *14*(4), 225–232.

Avşar, U., Hubert-Ferrari, A., Batist, M. D., & Fagel, N. (2014a). A 3400 year lacustrine paleoseismic record from the North Anatolian Fault, Turkey: Implications for bimodal recurrence behavior. *Geophysical Research Letters*, *41*(2), 377–384.

Avşar, U., Hubert-Ferrari, A., De Batist, M., Lepoint, G., Schmidt, S., & Fagel, N. (2014b). Seismically-triggered organic-rich layers in recent sediments from Göllüköy Lake (North Anatolian Fault, Turkey). *Quaternary Science Reviews*, *103*, 67–80.

Avşar, U., Hubert-Ferrari, A., De Batist, M., Schmidt, S., & Fagel, N. (2015). Sedimentary records of past earthquakes in Boraboy Lake during the last ca 600 years (North Anatolian Fault, Turkey). *Palaeogeography, Palaeoclimatology, Palaeoecology*, *433*, 1–9.

Beck, C. (2009). Late Quaternary lacustrine paleo-seismic archives in north-western Alps: Examples of earthquake-origin assessment of sedimentary disturbances. *Earth-Science Reviews*, *96*(4), 327–344.

Becker, A., Ferry, M., Monecke, K., Schnellmann, M., & Giardini, D. (2005). Multiarchive paleoseismic record of late Pleistocene and Holocene strong earthquakes in Switzerland. *Tectonophysics*, *400*(1–4), 153–177.

Beigt, D., Villarosa, G., Gómez, E. A., & Manzoni, C. (2016). Subaqueous landslides at the distal basin of Lago Nahuel Huapi (Argentina): Towards a tsunami hazard evaluation in Northern Patagonian lakes. *Geomorphology*, *268*, 197–206.

Bellwald, B. (2012). Paleoseismological implications of the sediment stratigraphy in Lake Silvaplana (Engadine, Eastern Switzerland) (Master dissertation). Zurich, Switzerland: ETH.

Bertrand, S., Charlet, F., Chapron, E., Fagel, N., & De Batist, M. (2008). Reconstruction of the Holocene seismotectonic activity of the Southern Andes from seismites recorded in Lago Icalma, Chile, 39 S. *Palaeogeography, Palaeoclimatology, Palaeoecology*, *259*(2–3), 301–322.

Billeter, J. (1923). Pfarrer Jakob Billeter von Aegeri und seine Chronik. Heimat-Klänge, Sonntags-Beilage zu den "Zuger Nachrichten". *Jahrgang*, *4*, 28.

Bøe, R., Longva, O., Lepland, A., Blikra, L. H., Sønstegaard, E., Haflidason, H., et al. (2004). Postglacial mass movements and their causes in fjords and lakes in western Norway. *Norwegian Journal of Geology/Norsk Geologisk Forening*, *84*(1), 35–55.

Boës, X., Moran, S. B., King, J., Cağatay, M. N., & Hubert-Ferrari, A. (2010). Records of large earthquakes in lake sediments along the North Anatolian Fault, Turkey. *Journal of Paleolimnology*, *43*(4), 901–920.

Bouma, A. H. (1987). Megaturbidite: An acceptable term? *Geo-Marine Letters*, *7*(2), 63–67.

Bozzano, F., Mazzanti, P., Anzidei, M., Esposito, C., Floris, M., Fasani, G. B., & Esposito, A. (2009). Slope dynamics of Lake Albano (Rome, Italy): Insights from high resolution bathymetry. *Earth Surface Processes and Landforms*, *34*(11), 1469–1486.

Brauer, A., Endres, C., & Negendank, J. F. (1999). Lateglacial calendar year chronology based on annually laminated sediments from Lake Meerfelder Maar, Germany. *Quaternary International*, *61*(1), 17–25.

Brocard, G., Adatte, T., Magand, O., Pfeifer, H. R., Bettini, A., Arnaud, F., et al. (2014). The recording of floods and earthquakes in Lake Chichój, Guatemala during the twentieth century. *Journal of Paleolimnology*, *52*(3), 155–169.

Brooks, G. R. (2016). Evidence of late glacial paleoseismicity from submarine landslide deposits within Lac Dasserat, northwestern Quebec, Canada. *Quaternary Research*, *86*(2), 184–199.

Bünti, J. L., & Wyrsch, J. (1973). *Chronik des Johann Laurentz Buenti, Landammann 1661–1736*. Stans, Switzerland: Historischer Verein Nidwalden.

Bussmann, F., & Anselmetti, F. S. (2010). Rossberg landslide history and flood chronology as recorded in Lake Lauerz sediments (Central Switzerland). *Swiss Journal of Geosciences*, *103*(1), 43–59.

Carrillo, E., Beck, C., Audemard, F. A., Moreno, E., & Ollarves, R. (2008). Disentangling late Quaternary climatic and seismo-tectonic controls on Lake Mucubají sedimentation (Mérida andes, Venezuela). *Palaeogeography, Palaeoclimatology, Palaeoecology*, *259*(2–3), 284–300.

Chapron, E., Ariztegui, D., Mulsow, S., Villarosa, G., Pino, M., Outes, V., et al. (2006). Impact of the 1960 major subduction earthquake in Northern Patagonia (Chile, Argentina). *Quaternary International*, *158*(1), 58–71.

Chapron, E., Beck, C., Pourchet, M., & Deconinck, J. F. (1999). 1822 earthquake-triggered homogenite in Lake Le Bourget (NW Alps). *Terra Nova*, *11*(2–3), 86–92.

Chapron, E., Ledoux, G., Simonneau, A., Albéric, P., St-Onge, G., Lajeunesse, P., et al. (2012). New evidence of Holocene mass wasting events in recent volcanic lakes from the French Massif Central (lakes Pavin, Montcineyre and Chauvet) and implications for natural hazards. In Y. Yamada, K. Kawamura, K. Ikehara, Y. Ogawa, R. Urgeles, D. Mosher, et al. (Eds.), *Submarine mass movements and their consequences* (pp. 255–264). Dordrecht, The Netherlands: Springer.

Chassiot, L., Chapron, E., Di Giovanni, C., Albéric, P., Lajeunesse, P., Lehours, A. C., & Meybeck, M. (2016). Extreme events in the sedimentary record of maar Lake Pavin: Implications for natural hazards assessment in the French Massif Central. *Quaternary Science Reviews*, *141*, 9–25.

Cukur, D., Krastel, S., Demirel-Schlüter, F., Demirbağ, E., Imren, C., Niessen, F., et al. (2013). Sedimentary evolution of Lake Van (Eastern Turkey) reconstructed from high-resolution seismic investigations. *International Journal of Earth Sciences*, *102*(2), 571–585.

Curtin, T., Crocker, M. L., & Wheatley, G. (2015). *Magnetic fabrics preserved by lacustrine sediment in two New York Finger Lakes (USA) revealed evidence for deformation during coring and changes in paleoenvironmental conditions [abstract]*. Paper presented at 6th International Limnogeology Congress (ILIC 2015), Reno, Nevada.

Czymzik, M., Dulski, P., Plessen, B., Von Grafenstein, U., Naumann, R., & Brauer, A. (2010). A 450 year record of spring-summer flood layers in annually laminated sediments from Lake Ammersee (southern Germany). *Water Resources Research*, *46*(11), W11528.

Daxer, C. (2017). Postglacial sedimentary infill of Lake Mondsee (Eastern Alps, Austria) and rockfall activity revealed by reflection seismics and sediment-core analysis (Master dissertation). Innsbruck, Austria: University of Innsbruck.

Daxer, C., Moernaut, J., Taylor, T., Haas, J. N., & Strasser, M. (2018). Late glacial and Holocene sedimentary infill of Lake Mondsee (Eastern Alps, Austria) and historical rockfall activity revealed by reflection seismics and sediment-core analysis. *Austrian Journal of Earth Science*, *111*(1), 111–134.

Dietrich, J. (1689). Diarium von P. Josep Dietrich von Einsiedeln (1645–1704). Klosterarichiv Einsiedeln.

Doig, R. (1990). 2300 yr history of seismicity from silting events, in Lake Tadoussac, Charlevoix, Quebec. *Geology*, *18*(9), 820–823.

Dott, R. H., Jr. (1963). Dynamics of subaqueous gravity depositional processes. *AAPG Bulletin*, *47*(1), 104–128.

Doughty, M., Eyles, N., & Eyles, C. (2013). High-resolution seismic reflection profiling of neotectonic faults in Lake Timiskaming, Timiskaming Graben, Ontario-Quebec, Canada. *Sedimentology*, *60*(4), 983–1006.

Doughty, M., Eyles, N., Eyles, C. H., Wallace, K., & Boyce, J. I. (2014). Lake sediments as natural seismographs: Earthquake-related deformations (seismites) in central Canadian lakes. *Sedimentary Geology*, *313*, 45–67.

Eden, D. N., & Froggatt, P. C. (1996). A 6500-year-old history of tephra deposition recorded in the sediments of Lake Tutira, eastern North Island, New Zealand. *Quaternary International*, *34*, 55–64.

Eden, D. N., & Page, M. J. (1998). Palaeoclimatic implications of a storm erosion record from late Holocene lake sediments, North Island, New Zealand. *Palaeogeography, Palaeoclimatology, Palaeoecology*, *139*(1), 37–58.

Eyles, N., Boyce, J. I., Halfman, J. D., & Koseoglu, B. (2000). Seismic stratigraphy of Waterton Lake, a sediment-starved glaciated basin in the Rocky Mountains of Alberta, Canada and Montana, USA. *Sedimentary Geology*, *130*(3–4), 283–311.

Fanetti, D., Anselmetti, F. S., Chapron, E., Sturm, M., & Vezzoli, L. (2008). Megaturbidite deposits in the Holocene basin fill of Lake Como (southern Alps, Italy). *Palaeogeography, Palaeoclimatology, Palaeoecology*, *259*(2–3), 323–340.

Florescu, G., Hutchinson, S. M., Kern, Z., Mindrescu, M., Cristea, I. A., Mihăilă, D., et al. (2017). Last 1000 years of environmental history in Southern Bucovina, Romania: A high resolution multi-proxy lacustrine archive. *Palaeogeography, Palaeoclimatology, Palaeoecology*, *473*, 26–40.

Forsberg, C. F., Heyerdahl, H., & Solheim, A. (2016). Underwater mass movements in lake Mjøsa, Norway. In

Submarine mass movements and their consequences (pp. 191–199). Cham, Switzerland: Springer.

Frey-Martínez, J., Cartwright, J., & James, D. (2006). Frontally confined versus frontally emergent submarine landslides: A 3D seismic characterisation. *Marine and Petroleum Geology*, *23*(5), 585–604.

Garcés, B. V., Moreno, A., Navas, A., Mata, P., Machín, J., Huertas, A. D., et al. (2008). The Taravilla lake and tufa deposits (Central Iberian Range, Spain) as palaeohydrological and palaeoclimatic indicators. *Palaeogeography, Palaeoclimatology, Palaeoecology*, *259*(2–3), 136–156.

Gardner, J. V., Mayer, L. A., & Hughs Clarke, J. E. (2000). Morphology and processes in lake Tahoe (California-Nevada). *Geological Society of America Bulletin*, *112*(5), 736–746.

Garduño-Monroy, V. H., Soria-Caballero, D. C., Israde-Alcántara, I., Hernández Madrigal, V. M., Rodríguez-Ramírez, A., Ostroumov, M., et al. (2011). Evidence of tsunami events in the Paleolimnological record of Lake Pátzcuaro, Michoacán, Mexico. *Geofísica Internacional*, *50*(2), 147–161.

Geertsema, M., Blais-Stevens, A., Kwoll, E., Menounos, B., Venditti, J. G., Grenier, A., & Wiebe, K. (2018). Sensitive clay landslide detection and characterization in and around Lakelse Lake, British Columbia, Canada. *Sedimentary Geology*, *364*, 217–227.

Girardclos, S., Schmidt, O. T., Sturm, M., Ariztegui, D., Pugin, A., & Anselmetti, F. S. (2007). The 1996 AD delta collapse and large turbidite in Lake Brienz. *Marine Geology*, *241*(1–4), 137–154.

Goepel, A., Lonschinski, M., Viereck, L., Büchel, G., & Kukowski, N. (2015). Volcano-tectonic structures and CO 2-degassing patterns in the Laacher See basin, Germany. *International Journal of Earth Sciences*, *104*(5), 1483–1495.

Guyard, H., Chapron, E., St-Onge, G., Anselmetti, F. S., Arnaud, F., Magand, O., et al. (2007). High-altitude varve records of abrupt environmental changes and mining activity over the last 4000 years in the Western French Alps (Lake Bramant, Grandes Rousses Massif). *Quaternary Science Reviews*, *26*(19–21), 2644–2660.

Hage, S., Hubert-Ferrari, A., Lamair, L., Avşar, U., El Ouahabi, M., Van Daele, M., et al. (2017). Flow dynamics at the origin of thin clayey sand lacustrine turbidites: Examples from Lake Hazar, Turkey. *Sedimentology*, *64*(7), 1929–1956.

Hampton, M. A., Lee, H. J., & Locat, J. (1996). Submarine landslides. *Reviews of Geophysics*, *34*(1), 33–59.

Hansen, L., Waldmann, N., Storms, J. E., Eilertsen, R. S., Ariztegui, D., Chapron, E., & Nesje, A. (2016). Morphological signatures of mass wasting and delta processes in a fjord-lake system: Insights from Lovatnet, western Norway. *Norwegian Journal of Geology*, *96*(3), 1–21.

Heideman, M., Menounos, B., & Clague, J. J. (2015). An 825-year long varve record from Lillooet Lake, British Columbia, and its potential as a flood proxy. *Quaternary Science Reviews*, *126*, 158–174.

Heirman, K., De Batist, M., Arnaud, F., & De Beaulieu, J. L. (2012). Seismic stratigraphy of the late Quaternary sedimentary infill of Lac d'Armor (Kerguelen archipelago): A record of glacier retreat, sedimentary mass wasting and southern Westerly intensification. *Antarctic Science*, *24*(6), 608–618.

Hilbe, M., & Anselmetti, F. S. (2014). Signatures of slope failures and river-delta collapses in a perialpine lake (Lake Lucerne, Switzerland). *Sedimentology*, *61*(7), 1883–1907.

Hilbe, M., & Anselmetti, F. S. (2015). Mass movement-induced tsunami hazard on perialpine Lake Lucerne (Switzerland): Scenarios and numerical experiments. *Pure and Applied Geophysics*, *172*(2), 545–568.

Hilbe, M., Anselmetti, F. S., Eilertsen, R. S., Hansen, L., & Wildi, W. (2011). Subaqueous morphology of Lake Lucerne (Central Switzerland): Implications for mass movements and glacial history. *Swiss Journal of Geosciences*, *104*(3), 425–443.

Howarth, J. D., Fitzsimons, S. J., Norris, R. J., & Jacobsen, G. E. (2014). Lake sediments record high intensity shaking that provides insight into the location and rupture length of large earthquakes on the Alpine Fault, New Zealand. *Earth and Planetary Science Letters*, *403*, 340–351.

Howarth, J. D., Fitzsimons, S. J., Norris, R. J., Langridge, R., & Vandergoes, M. J. (2016). A 2000 yr rupture history for the Alpine fault derived from Lake Ellery, South Island, New Zealand. *Bulletin*, *128*(3–4), 627–643.

Irmler, R., Daut, G., & Mäusbacher, R. (2006). A debris flow calendar derived from sediments of lake Lago di Braies (N. Italy). *Geomorphology*, *77*(1–2), 69–78.

Ito, M. (2008). Downfan transformation from turbidity currents to debris flows at a channel-to-lobe transitional zone: The lower Pleistocene Otadai Formation, Boso Peninsula, Japan. *Journal of Sedimentary Research*, *78*(10), 668–682.

Jakobsson, M., Björck, S., O'Regan, M., Flodén, T., Greenwood, S. L., Swärd, H., et al. (2014). Major earthquake at the Pleistocene-Holocene transition in Lake Vättern, southern Sweden. *Geology*, *42*(5), 379–382.

Juschus, O., Melles, M., Gebhardt, A. C., & Niessen, F. (2009). Late Quaternary mass movement events in Lake El′gygytgyn, North-eastern Siberia. *Sedimentology*, *56*(7), 2155–2174.

Kämpf, L., Brauer, A., Dulski, P., Lami, A., Marchetto, A., Gerli, S., et al. (2012). Detrital layers marking flood events in recent sediments of Lago Maggiore (N. Italy) and their comparison with instrumental data. *Freshwater Biology*, *57*(10), 2076–2090.

Karlin, R. E., Holmes, M., Abella, S. E. B., & Sylwester, R. (2004). Holocene landslides and a 3500-year record of Pacific Northwest earthquakes from sediments in Lake Washington. *GSA Bulletin*, *116*(1–2), 94–108.

Kelts, K., & Hsü, K. J. (1980). Resedimented facies of 1875 Horgen slumps in Lake Zurich and a process model of longitudinal transport of turbidity currents. *Eclogae Geologicae Helvetiae*, *73*(1), 271–281.

Kienel, U., & Vos, H. (2007). *Turbidite sedimentation in Lake Holzmaar (Germany) – rare events generated by climate modulated Poisson Process [abstract]*. Paper presented at 4th International Limnogeology Congress (ILIC 2007), Barcelona, Spain.

Knapp, S., Gilli, A., Anselmetti, F. S., Krautblatter, M., & Hajdas, I. (2018). Multistage rock-slope failures revealed in lake sediments in a seismically active Alpine region (Lake Oeschinen, Switzerland). *Journal of Geophysical Research. Earth Surface*, *123*(4), 658–677.

Kremer, K., Hilbe, M., Simpson, G., Decrouy, L., Wildi, W., & Girardclos, S. (2015). Reconstructing 4000 years of mass

movement and tsunami history in a deep peri-Alpine lake (Lake Geneva, France-Switzerland). *Sedimentology*, *62*(5), 1305–1327.

Kremer, K., Wirth, S. B., Reusch, A., Fäh, D., Bellwald, B., Anselmetti, F. S., et al. (2017). Lake-sediment based paleoseismology: Limitations and perspectives from the Swiss Alps. *Quaternary Science Reviews*, *168*, 1–18.

Lajeunesse, P., Sinkunas, B., Morissette, A., Normandeau, A., Joyal, G., St-Onge, G., & Locat, J. (2017). Large-scale seismically-induced mass-movements in a former glacial lake basin: Lake Témiscouata, northeastern Appalachians (eastern Canada). *Marine Geology*, *384*, 120–130.

Lamair, L., Hubert-Ferrari, A., Yamamoto, S., El Ouahabi, M., Vander Auwera, J., Obrochta, S., et al. (2018). Volcanic influence of Mt. Fuji on the watershed of Lake Motosu and its impact on the lacustrine sedimentary record. *Sedimentary Geology*, *363*, 200–220.

Lamarche, G., Mountjoy, J., Bull, S., Hubble, T., Krastel, S., Lane, E., et al. (Eds.) (2016). *Submarine mass movements and their consequences: 7th international symposium* (Vol. 41). Cham, Switzerland: Springer.

Lauterbach, S., Chapron, E., Brauer, A., Hüls, M., Gilli, A., Arnaud, F., et al. (2012). A sedimentary record of Holocene surface runoff events and earthquake activity from Lake Iseo (Southern Alps, Italy). *The Holocene*, *22*(7), 749–760.

Leithold, E. L., Wegmann, K. W., Bohnenstiehl, D. R., Smith, S. G., Noren, A., & O'Grady, R. (2018). Slope failures within and upstream of Lake Quinault, Washington, as uneven responses to Holocene earthquakes along the Cascadia subduction zone. *Quaternary Research*, *89*(1), 178–200.

Leroy, S. A., Schwab, M. J., & Costa, P. J. (2010). Seismic influence on the last 1500-year infill history of Lake Sapanca (North Anatolian Fault, NW Turkey). *Tectonophysics*, *486*(1–4), 15–27.

L'Heureux, J. S., Eilertsen, R. S., Glimsdal, S., Issler, D., Solberg, I. L., & Harbitz, C. B. (2012). The 1978 quick clay landslide at Rissa, mid Norway: Subaqueous morphology and tsunami simulations. In *Submarine mass movements and their consequences* (pp. 507–516). Dordrecht, the Netherlands: Springer.

Lindhorst, K., Gruen, M., Krastel, S., & Schwenk, T. (2012). Hydroacoustic analysis of mass wasting deposits in Lake Ohrid (FYR Macedonia/Albania). In Y. Yamada, K. Kawamura, K. Ikehara, Y. Ogawa, & R. Urgeles (Eds.), *Submarine mass movements and their consequences* (pp. 245–253). Dordrecht, The Netherlands: Springer.

Lindhorst, K., Krastel, S., Papenberg, C., & Heidarzadeh, M. (2014). Modeling submarine landslide-generated waves in Lake Ohrid, Macedonia/Albania. In S. Krastel, J.-H. Behrmann, D. Völker, M. Stipp, C. Berndt, R. Urgeles, et al. (Eds.), *Submarine mass movements and their consequences* (pp. 497–506). Cham, Switzerland: Springer.

Lindhorst, K., Krastel, S., Reicherter, K., Stipp, M., Wagner, B., & Schwenk, T. (2015). Sedimentary and tectonic evolution of Lake Ohrid (Macedonia/Albania). *Basin Research*, *27*(1), 84–101.

Locat, J., & Lee, H. J. (2002). Submarine landslides: Advances and challenges. *Canadian Geotechnical Journal*, *39*(1), 193–212.

Locat, J., Turmel, D., Habersetzer, M., Trottier, A. P., Lajeunesse, P., & St-Onge, G. (2016). Earthquake induced landslides in Lake Eternité, Québec, Canada. In G. Lamarche, J. Mountjoy, S. Bull, T. Hubble, S. Krastel, E. Lane, et al. (Eds.), *Submarine mass movements and their consequences* (pp. 361–370). Cham, Switzerland: Springer.

Lowag, J., Bull, J. M., Vardy, M. E., Miller, H., & Pinson, L. J. W. (2012). High-resolution seismic imaging of a Younger Dryas and Holocene mass movement complex in glacial lake Windermere, UK. *Geomorphology*, *171*, 42–57.

Maloney, J. M., Noble, P. J., Driscoll, N. W., Kent, G. M., Smith, S. B., Schmauder, G. C., et al. (2013). Paleoseismic history of the Fallen Leaf segment of the West Tahoe–Dollar Point fault reconstructed from slide deposits in the Lake Tahoe Basin, California-Nevada. *Geosphere*, *9*(4), 1065–1090.

Manley, P. L., & Manley, T. O. (2009). Underwater Surveys of Lake Champlain Vermont–Historical Artifacts. *Bottom Bathymetry and First Observations of Underwater Slumps: Professional Surveyor Magazine* (pp. 18–20).

Masson, D. G., Harbitz, C. B., Wynn, R. B., Pedersen, G., & Løvholt, F. (2006). Submarine landslides: Processes, triggers and hazard prediction. *Philosophical Transactions of the Royal Society of London A: Mathematical, Physical and Engineering Sciences*, *364*(1845), 2009–2039.

Merkt, J., & Müller, H. (1999). Varve chronology and palynology of the Lateglacial in Northwest Germany from lacustrine sediments of Hämelsee in Lower Saxony. *Quaternary International*, *61*(1), 41–59.

Miller, W. R. (1998). The bathymetry, sedimentology and seismic stratigraphy of Lake Sibaya-Northern KwaZulu-Natal (Doctoral dissertation). Durban, South Africa: University of Natal.

Mîndrescu, M., Cristea, A. I., Hutchinson, S. M., Florescu, G., & Feurdean, A. (2013). Interdisciplinary investigations of the first reported laminated lacustrine sediments in Romania. *Quaternary International*, *293*, 219–230.

Moernaut, J. (2010). Sublacustrine landslide processes and their paleoseismological significance: Revealing the recurrence rate of giant earthquakes in South-Central Chile (PhD thesis). Ghent, Belgium: Ghent University.

Moernaut, J., & De Batist, M. (2011). Frontal emplacement and mobility of sublacustrine landslides: Results from morphometric and seismostratigraphic analysis. *Marine Geology*, *285*(1–4), 29–45.

Moernaut, J., De Batist, M., Charlet, F., Heirman, K., Chapron, E., Pino, M., et al. (2007). Giant earthquakes in South-Central Chile revealed by Holocene mass-wasting events in Lake Puyehue. *Sedimentary Geology*, *195*(3–4), 239–256.

Moernaut, J., De Batist, M., Heirman, K., Van Daele, M., Pino, M., Brümmer, R., & Urrutia, R. (2009). Fluidization of buried mass-wasting deposits in lake sediments and its relevance for paleoseismology: Results from a reflection seismic study of lakes Villarrica and Calafquén (South-Central Chile). *Sedimentary Geology*, *213*(3–4), 121–135.

Moernaut, J., Van Daele, M., Heirman, K., Fontijn, K., Strasser, M., Pino, M., et al. (2014). Lacustrine turbidites as a tool for quantitative earthquake reconstruction: New evidence for a variable rupture mode in south central Chile. *Journal of Geophysical Research. Solid Earth*, *119*(3), 1607–1633.

Moernaut, J., Van Daele, M., Strasser, M., Clare, M. A., Heirman, K., Viel, M., et al. (2017). Lacustrine turbidites

produced by surficial slope sediment remobilization: A mechanism for continuous and sensitive turbidite paleoseismic records. *Marine Geology*, *384*, 159–176.

Monecke, K., Anselmetti, F. S., Becker, A., Sturm, M., & Giardini, D. (2004). The record of historic earthquakes in lake sediments of Central Switzerland. *Tectonophysics*, *394*(1–2), 21–40.

Morellón, M., Anselmetti, F. S., Valero-Garcés, B., Giralt, S., Ariztegui, D., Sáez, A., et al. (2014). The influence of subaquatic springs in lacustrine sedimentation: Origin and paleoenvironmental significance of homogenites in karstic Lake Banyoles (NE Spain). *Sedimentary Geology*, *311*, 96–111.

Morellón, M., Valero-Garces, B. L. A. S., Anselmetti, F., Ariztegui, D., Schnellmann, M., Moreno, A. N. A., et al. (2009). Late Quaternary deposition and facies model for karstic Lake Estanya (North-eastern Spain). *Sedimentology*, *56*(5), 1505–1534.

Morey, A. E., Goldfinger, C., Briles, C. E., Gavin, D. G., Colombaroli, D., & Kusler, J. E. (2013). Are great Cascadia earthquakes recorded in the sedimentary records from small forearc lakes? *Natural Hazards and Earth System Sciences*, *13*(10), 2441.

Morgan, L. A., Shanks, W. C., III, Lovalvo, D. A., Johnson, S. Y., Stephenson, W. J., Pierce, K. L., et al. (2003). Exploration and discovery in Yellowstone Lake: Results from high-resolution sonar imaging, seismic reflection profiling, and submersible studies. *Journal of Volcanology and Geothermal Research*, *122*(3–4), 221–242.

Mueller, A. D., Anselmetti, F. S., Ariztegui, D., Brenner, M., Hodell, D. A., Curtis, J. H., et al. (2010). Late Quaternary palaeoenvironment of northern Guatemala: Eevidence from deep drill cores and seismic stratigraphy of Lake Petén Itzá. *Sedimentology*, *57*(5), 1220–1245.

Mullins, H. T., & Halfman, J. D. (2001). High-resolution seismic reflection evidence for middle Holocene environmental change, Owasco Lake, New York. *Quaternary Research*, *55*(3), 322–331.

Nomade, J., Chapron, E., Desmet, M., Reyss, J. L., Arnaud, F., & Lignier, V. (2005). Reconstructing historical seismicity from lake sediments (Lake Laffrey, western Alps, France). *Terra Nova*, *17*(4), 350–357.

Normandeau, A., Lamoureux, S. F., Lajeunesse, P., & Francus, P. (2016). Sediment dynamics in paired High Arctic lakes revealed from high-resolution swath bathymetry and acoustic stratigraphy surveys. *Journal of Geophysical Research. Earth Surface*, *121*(9), 1676–1696.

Ouellet, M. (1997). Lake sediments and Holocene seismic hazard assessment within the St. Lawrence Valley, Québec. *Geological Society of America Bulletin*, *109*(6), 631–642.

Petersen, J., Wilhelm, B., Revel, M., Rolland, Y., Crouzet, C., Arnaud, F., et al. (2014). Sediments of Lake Vens (SW European Alps, France) record large-magnitude earthquake events. *Journal of Paleolimnology*, *51*(3), 343–355.

Pollen, A. F. (2016). The sedimentary record of past earthquakes identified in holocene sediments of lake crescent, Washington (Master's thesis). Raleigh, NC: North Carolina State University.

Praet, N., Moernaut, J., Van Daele, M., Boes, E., Haeussler, P. J., Strupler, M., et al. (2017). Paleoseismic potential of sublacustrine landslide records in a high-seismicity setting (south-central Alaska). *Marine Geology*, *384*, 103–119.

Rapuc, W., Sabatier, P., Andrič, M., Crouzet, C., Arnaud, F., Chapron, E., et al. (2018). 6600 years of earthquake record in the Julian Alps (Lake Bohinj, Slovenia). *Sedimentology*, *65*(5), 1777–1799.

Reusch, A. M. (2016). Sublacustrine paleoseismology and fluid flow in the Western Swiss Molasse Basin: New constraints from the sedimentary archive of Lake Neuchâtel-Mass-transport deposits, subsurface sediment mobilization and geomorphology (Doctoral dissertation Nr. 23131). Zurich, Switzerland: ETH.

Richardson, K. N. D., Hatten, J. A., & Wheatcroft, R. A. (2018). 1500 years of lake sedimentation due to fire, earthquakes, floods and land clearance in the Oregon Coast Range: Geomorphic sensitivity to floods during timber harvest period. *Earth Surface Processes and Landforms*, *43*(7), 1496–1517.

Rouwet, D., González, G., Mora-Amador, R.,& Ramírez, C. (2011). Past activity of Laguna Caliente crater lake (Poás Volcano, Costa Rica) based on paleolacustrine deposits: A preliminary study [abstract]. Paper presented at 5th International Limnogeology Congress (ILIC 2011), Konstanz, Germany.

Sauerbrey, M. A., Juschus, O., Gebhardt, A. C., Wennrich, V., Nowaczyk, N. R., & Melles, M. (2013). Mass movement deposits in the 3.6 Ma sediment record of Lake El'gygytgyn, Far East Russian Arctic. *Climate of the Past*, *9*(4), 1949–1967.

Schlolaut, G., Brauer, A., Marshall, M. H., Nakagawa, T., Staff, R. A., Ramsey, C. B., et al. (2014). Event layers in the Japanese Lake Suigetsu 'SG06'sediment core: Description, interpretation and climatic implications. *Quaternary Science Reviews*, *83*, 157–170.

Schnellmann, M., Anselmetti, F. S., Giardini, D., & McKenzie, J. A. (2005). Mass movement-induced fold-and-thrust belt structures in unconsolidated sediments in Lake Lucerne (Switzerland). *Sedimentology*, *52*(2), 271–289.

Schnellmann, M., Anselmetti, F. S., Giardini, D., & Mckenzie, J. A. (2006). 15,000 Years of mass-movement history in Lake Lucerne: Implications for seismic and tsunami hazards. *Eclogae Geologicae Helvetiae*, *99*(3), 409–428.

Schnellmann, M., Anselmetti, F. S., Giardini, D., McKenzie, J. A., & Ward, S. N. (2002). Prehistoric earthquake history revealed by lacustrine slump deposits. *Geology*, *30*(12), 1131–1134.

Schnellmann, M. P. (2004). Late quaternary mass-movements in a perialpine lake (Lake Lucerne, Switzerland) (Doctoral dissertation Nr. 15533). Zurich, Switzerland: ETH.

Schwestermann, T. (2016). Mass-movement event stratigraphy in lake constance (Master dissertation). Zurich, Switzerland: ETH.

Shanmugam, G., & Wang, Y. (2015). The landslide problem. *Journal of Palaeogeography*, *4*(2), 109–166.

Shiki, T., Kumon, F., Inouchi, Y., Kontani, Y., Sakamoto, T., Tateishi, M., et al. (2000). Sedimentary features of the seismo-turbidites, Lake Biwa, Japan. *Sedimentary Geology*, *135*(1–4), 37–50.

Siegenthaler, C., & Sturm, M. (1991). Slump induced surges and sediment transport in Lake Uri, Switzerland.

Internationale Vereinigung für theoretische und angewandte Limnologie: Verhandlungen, *24*(2), 955–958.

Simonneau, A., Chapron, E., Vannière, B., Wirth, S. B., Gilli, A., Di-Giovanni, C., et al. (2013). Mass-movement and flood-induced deposits in Lake Ledro, southern Alps, Italy: Implications for Holocene palaeohydrology and natural hazards. *Climate of the Past*, *9*, 825–840.

Smith, S. B., Karlin, R. E., Kent, G. M., Seitz, G. G., & Driscoll, N. W. (2013). Holocene subaqueous paleoseismology of Lake Tahoe. *Bulletin*, *125*(5–6), 691–708.

Solovyeva, M. A., Starovoytov, A. V., Akhmanov, G. G., Khlystov, O. M., Khabuev, A. V., Tokarev, M. Y., & Chensky, D. A. (2016). The evolution of slump-induced destruction of Kukuy Griva slope (Lake Baikal) revealed on the base of the data of seismic and acoustic surveys. *Moscow University Geology Bulletin*, *71*(6), 416–428.

Strasser, M. (2008). *Quantifying late Quaternary natural hazards in Swiss lakes: Subaquatic landslides, slope stability assessments, paleoseismic reconstructions and lake outbursts, Beiträge zur Geologie der Schweiz., Geotechnische Serie* (Vol. 95). Zurich, Switzerland: ETH.

Strasser, M., & Anselmetti, F. (2008). Mass-movement event stratigraphy in Lake Zurich; A record of varying seismic and environmental impacts. *Beiträge zur Geologie der Schweiz, Geotechnische Serie*, *95*, 23–41.

Strasser, M., Anselmetti, F. S., Fäh, D., Giardini, D., & Schnellmann, M. (2006). Magnitudes and source areas of large prehistoric northern Alpine earthquakes revealed by slope failures in lakes. *Geology*, *34*(12), 1005–1008.

Strasser, M., Hilbe, M., & Anselmetti, F. S. (2011). Mapping basin-wide subaquatic slope failure susceptibility as a tool to assess regional seismic and tsunami hazards. *Marine Geophysical Research*, *32*(1–2), 331–347.

Strasser, M., Monecke, K., Schnellmann, M., & Anselmetti, F. S. (2013). Lake sediments as natural seismographs: A compiled record of Late Quaternary earthquakes in Central Switzerland and its implication for Alpine deformation. *Sedimentology*, *60*(1), 319–341.

Strasser, M., Schindler, C., & Anselmetti, F. S. (2008). Late Pleistocene earthquake-triggered moraine dam failure and outburst of Lake Zurich, Switzerland. *Journal of Geophysical Research. Earth Surface*, *113*(F2), F02003.

Strasser, M., Stegmann, S., Bussmann, F., Anselmetti, F. S., Rick, B., & Kopf, A. (2007). Quantifying subaqueous slope stability during seismic shaking: Lake Lucerne as model for ocean margins. *Marine Geology*, *240*(1–4), 77–97.

Strupler, M. (2017). Basin-wide assessment of the earthquake-triggered landslide-and tsunami hazard (Doctoral dissertation Nr. 24407). Zurich, Switzerland:ETH.

Strupler, M., Danciu, L., Hilbe, M., Kremer, K., Anselmetti, F. S., Strasser, M., & Wiemer, S. (2018a). A subaqueous hazard map for earthquake-triggered landslides in Lake Zurich, Switzerland. *Natural Hazards*, *90*(1), 51–78.

Strupler, M., Hilbe, M., Anselmetti, F. S., Kopf, A. J., Fleischmann, T., & Strasser, M. (2017). Probabilistic stability evaluation and seismic triggering scenarios of submerged slopes in Lake Zurich (Switzerland). *Geo-Marine Letters*, *37*(3), 241–258.

Strupler, M., Hilbe, M., Kremer, K., Danciu, L., Anselmetti, F. S., Strasser, M., & Wiemer, S. (2018b). Subaqueous landslide-triggered tsunami hazard for Lake Zurich, Switzerland. *Swiss Journal of Geosciences*, *111*(1–2), 1–19.

Talling, P. J. (2013). Hybrid submarine flows comprising turbidity current and cohesive debris flow: Deposits, theoretical and experimental analyses, and generalized models. *Geosphere*, *9*(3), 460–488.

Talling, P. J., Allin, J., Armitage, D. A., Arnott, R. W., Cartigny, M. J., Clare, M. A., et al. (2015). Key future directions for research on turbidity currents and their deposits. *Journal of Sedimentary Research*, *85*(2), 153–169.

Thielemann, A., Daut, G., & Mäusbacher, R. (2007). Sedimentological and chronological investigations of debris flow events and the associated sediment dynamic of the alpine lake Pragser Wildsee (Lago di Braies) [abstract]. *Geophysical Research Abstracts*, *9*. EGU 2007, Vienna, Austria

Upton, P., & Osterberg, E. C. (2007). Paleoseismicity and mass movements interpreted from seismic-reflection data, Lake Tekapo, South Canterbury, New Zealand. *New Zealand Journal of Geology and Geophysics*, *50*(4), 343–356.

Van Daele, M., Bertrand, S., Meyer, I., Moernaut, J., Vandoorne, W., Siani, G., et al. (2016). Late Quaternary evolution of Lago Castor (Chile, 45.6 S): Timing of the deglaciation in northern Patagonia and evolution of the southern westerlies during the last 17 kyr. *Quaternary Science Reviews*, *133*, 130–146.

Van Daele, M., Meyer, I., Moernaut, J., De Decker, S., Verschuren, D., & De Batist, M. (2017). A revised classification and terminology for stacked and amalgamated turbidites in environments dominated by (hemi) pelagic sedimentation. *Sedimentary Geology*, *357*, 72–82.

Van Daele, M., Moernaut, J., Doom, L., Boes, E., Fontijn, K., Heirman, K., et al. (2015). A comparison of the sedimentary records of the 1960 and 2010 great Chilean earthquakes in 17 lakes: Implications for quantitative lacustrine palaeoseismology. *Sedimentology*, *62*(5), 1466–1496.

Van Daele, M., Moernaut, J., Silversmit, G., Schmidt, S., Fontijn, K., Heirman, K., et al. (2014). The 600 yr eruptive history of Villarrica Volcano (Chile) revealed by annually laminated lake sediments. *Bulletin*, *126*(3–4), 481–498.

Van Rensbergen, P., De Batist, M., Beck, C., & Chapron, E. (1999). High-resolution seismic stratigraphy of glacial to interglacial fill of a deep glacigenic lake: Lake Le Bourget, Northwestern Alps, France. *Sedimentary Geology*, *128*(1–2), 99–129.

Vardy, M. E., Pinson, L. J., Bull, J. M., Dix, J. K., Henstock, T. J., Davis, J. W., & Gutowski, M. (2010). 3D seismic imaging of buried Younger Dryas mass movement flows: Lake Windermere, UK. *Geomorphology*, *118*(1–2), 176–187.

Vogel, H., Russell, J. M., Cahyarini, S. Y., Bijaksana, S., Wattrus, N., Rethemeyer, J., & Melles, M. (2015). Depositional modes and lake-level variability at Lake Towuti, Indonesia, during the past~ 29 kyr BP. *Journal of Paleolimnology*, *54*(4), 359–377.

Voytek, E. B. (2010). Seismic stratigraphy of Thunder Bay and the Isle Royale region of Lake Superior (MS thesis). Duluth, MN: University of Minnesota Duluth.

Wagner, B., Francke, A., Sulpizio, R., Zanchetta, G., Lindhorst, K., Krastel, S., et al. (2012). Possible earthquake trigger for

6th century mass wasting deposit at Lake Ohrid (Macedonia/Albania). *Climate of the Past*, *8*(6), 2069–2078.

Waldmann, N., Anselmetti, F. S., Ariztegui, D., Austin, J. A., Jr., Pirouz, M., Moy, C. M., & Dunbar, R. (2011). Holocene mass-wasting events in Lago Fagnano, Tierra del Fuego (54° S): Implications for paleoseismicity of the Magallanes-Fagnano transform fault. *Basin Research*, *23*(2), 171–190.

Waldmann, N., Ariztegui, D., Anselmetti, F. S., Austin, J. A., Jr., Dunbar, R., Moy, C. M., & Recasens, C. (2008). Seismic stratigraphy of Lago Fagnano sediments (Tierra del Fuego, Argentina)-A potential archive of paleoclimatic change and tectonic activity since the Late Glacial. *Geologica Acta: An International Earth Science Journal*, *6*(1), 101–110.

Wallner, J. (2008). Holozäne Landschaftsentwicklung am Lago Budi, Chile (38, 9°C): Paläolimnologisch/paläoseismische Untersuchungen an Lagunensedimenten (Doctoral dissertation). Jena, Germany: University of Jena.

Wang, Y., Herzschuh, U., Liu, X., Korup, O., & Diekmann, B. (2014). A high-resolution sedimentary archive from landslide-dammed Lake Mengda, north-eastern Tibetan Plateau. *Journal of Paleolimnology*, *51*(2), 303–312.

Wiemer, G., Moernaut, J., Stark, N., Kempf, P., De Batist, M., Pino, M., et al. (2015). The role of sediment composition and behavior under dynamic loading conditions on slope failure initiation: A study of a subaqueous landslide in earthquake-prone South-Central Chile. *International Journal of Earth Sciences*, *104*(5), 1439–1457.

Wirth, S. B. (2008). Lake Thun sediment record: 300 years of human impact, flood events and subaquatic slides (Master dissertation). Zurich, Switzerland: ETH.

Wirth, S. B. (2013). The Holocene flood history of the Central Alps reconstructed from lacustrine sediments (Doctoral dissertation Nr. 20860). Zurich, Switzerland: ETH.

Yamasaki, S., Kataoka K. S., Nagahashi, Y. (2017). *Seismic reflection profiling of lacustrine deposits and discovery of an extremely large sublacustrine landslide in Lake Inawashiro, Fukushima, Japan [abstract]*. Paper presented at JpGU-AGU Joint Meeting 2017, Chiba, Japan.

Zhang, X. (2014). Lacustrine turbidites from tropical African lakes as indicators of hydrologic and climatic changes (Doctoral dissertation). Syracuse University – ALL.182.

Zhang, X., Scholz, C. A., Hecky, R. E., Wood, D. A., Zal, H. J., & Ebinger, C. J. (2014). Climatic control of the late Quaternary turbidite sedimentology of Lake Kivu, East Africa: Implications for deep mixing and geologic hazards. *Geology*, *42*(9), 811–814.

14

Style and Morphometry of Mass-Transport Deposits Across the Espírito Santo Basin (Offshore SE Brazil)

Davide Gamboa[1], Tiago M. Alves[2], and Kamaldeen Olakunle Omosanya[3]

ABSTRACT

This work summarises the research undertaken on mass-transport deposits (MTDs) across the slope of the salt-rich Espírito Santo Basin in SE Brazil. The three stratigraphic units analysed show MTDs with variable characteristics. Paleogene MTDs in Unit 1 have the lowest average area (137 Km^2) and are associated to fractured paleo-highs related to salt structures. Mid-Eocene to Oligocene MTDs in Unit 2 consist of large, southeast-directed flows derived from the northwestern area of the basin, with average areas and volumes of 495 Km^2 and 35 Km^3. Salt control on MTD flow is limited during the early depositional stages of Unit 2, but a clear influence is inferred to occur from the late Eocene-Oligocene. Miocene-Holocene MTDs in Unit 3 are variably confined. In proximal areas confinement is limited and MTDs have southeast-directed flows. In the transitional and distal domains, MTDs are highly confined by salt fairways that force decreases in MTD size and shifts in flow direction. MTDs in Unit 3 are up to 576 Km^2 in proximal areas but do not exceed 42 Km^2 in distal areas. The variability of MTDs offshore the Espírito Santo Basin relates to their flow dynamics and the influence of salt structures.

14.1. INTRODUCTION

Passive continental margins are prone to host large remobilized deposits derived from slope collapse events triggered by multiple mechanisms. These include over-steepening due to sediment accumulation or uplift, hydrate dissociation, fluid overpressure, the presence of weak layers, erosion by bottom currents, sea level changes, earthquakes and volcanism (Coleman & Prior, 1988; Elliott et al., 2010; Hampton et al., 1996; Laberg & Camerlenghi, 2008; Mountjoy et al., 2014; Nisbet & Piper, 1998; Paull et al., 1996; Pickering & Corregidor, 2005; Posamentier & Martinsen, 2011; Tripsanas et al., 2004; Weimer & Shipp, 2004). The deposits resulting from slope failures in subaqueous environments are commonly named as mass-transport deposits (MTDs). They tend to be sourced from the upper slope regions, often associated with large headwall scars, to extend towards the distal basin domain (Bull et al., 2009; Posamentier & Martinsen, 2011).

In salt-rich continental margins such as SE Brazil, West Africa or the Gulf of Mexico the 'passive' character of continental margins is changed by continuous halokinesis and gravitational gliding. Overburden faulting, regional folding and local subsidence, followed by gravitational collapse of strata flanking salt structures result from halokinesis (e.g. Davison et al., 2000; Gamboa & Alves, 2016; Gee et al., 2006; Maselli & Kneller, 2018; Tripsanas et al., 2004). Over growing diapirs, overburden strata is commonly thinned or completely removed by erosional processes, which accumulate the eroded material in peripheral salt withdrawal basins (Giles & Lawton, 2002). The slope instability of domains associated with

[1] *Portuguese Institute for the Sea and the Atmosphere (IPMA, I.P.), Lisbon, Portugal*

[2] *3D Seismic Lab, School of Earth and Ocean Sciences, Cardiff University, Cardiff, United Kingdom*

[3] *Timelapsegeo AS, Trondheim, Norway*

Submarine Landslides: Subaqueous Mass Transport Deposits from Outcrops to Seismic Profiles, Geophysical Monograph 246, First Edition. Edited by Kei Ogata, Andrea Festa, and Gian Andrea Pini.
© 2020 American Geophysical Union. Published 2020 by John Wiley & Sons, Inc.

salt structures promotes the occurrence of MTDs on the proximal slope, and in multiple distal locations adjacent to rising salt diapirs and ridges (Beaubouef & Abreu, 2010; Gamboa & Alves, 2016). In addition, structurally-induced topography leads to (i) the development of sediment fairways and salt mini-basins that influence the route of the mass flows (Fiduk et al., 2004; Love et al., 2005; Ortiz-Karpf et al., 2018; Tripsanas et al., 2004) and (ii) the creation of barriers that can stop or deviate mass flows, influencing the erosional patterns of salt mini-basins (Gamboa et al., 2010; Posamentier and Martinsen, 2011). As a result, MTDs in these settings present a wide range of internal deformation styles expressed by blocky textures, slumps and debrites, each corresponding to a progressive increase in remobilisation distance across the slope (Alves, 2015; Bull et al., 2009; Frey-Martínez et al., 2006; Gafeira et al., 2007; Hampton et al., 1996; O'Leary, 1991; Weimer & Shipp, 2004). However, given the potential for salt structures to induce slope failures at various distances across the slope, low remobilisation MTDs are prone to occur towards distal basin areas (Gamboa & Alves, 2016; Madof et al., 2009; Maia, 2018). These can form point-sourced MTDs derived from the locations affected by the salt diapirs or very wide, short length MTDs resulting from instability on the flanks of long salt ridges.

This work summarises research completed during the last ten years on MTDs of the Espírito Santo Basin (ESB) (Figure 14.1a). We focus on the size, style and distribution of MTDs influenced by salt structures along the three salt tectonic domains (extensional, transitional and compressional) of the ESB slope (Figure 14.1b), and how they fit into established morphometry-based classification schemes. Furthermore, databases of MTD metrics have been devised to record the presence, size and recurrence of slope failures that pose risks for submarine infrastructure or coastal communities (see Clare et al., 2018 and references therein). This dataset contributes to existing databases of MTDs by providing examples applicable to continental margins with recurrent mass-failures.

14.2. GEOLOGICAL SETTING OF THE ESPÍRITO SANTO BASIN

The Espírito Santo Basin is the northernmost of a series of Mesozoic rift basins located in SE Brazil (Davison, 2007; Fiduk et al., 2004). After a transitional stage that led to deposition of thick evaporitic units within a restricted basin, a two-phase drift stage dominated the Late Cretaceous to Cenozoic evolution of SE Brazil (Fiduk et al., 2004; Mohriak, 2003). The early drift stage records the accumulation of Albian carbonate platforms underneath Upper Cretaceous-Paleogene mudstones. The transition to the late drift stage (Lower Eocene) is marked by a marine regressive megasequence that deposited prograding sequences on the entire continental slope of SE Brazil (Demercian et al., 1993; Moreira and Carminatti, 2004). This eustatic event is associated with early/mid Eocene to Oligocene volcanic activity and the development of the Abrolhos Bank (Fainstein & Summerhayes, 1982). The bank is shallow, but shows an abrupt shelf break and narrow slope area (Mohriak, 2003). Erosion in hinterland mountain ranges and ongoing volcanic activity led to a high input of mixed siliciclastic and volcaniclastic sediment to the continental slope. Several erosive episodes took place in the Espírito Santo Basin during the drift stage associated with the incision of the Regência Canyon in the Cretaceous (Bruhn & Walker, 1997) and the Rio Doce Turbidite System submarine channel in the Cenozoic (Fiduk et al., 2004; França et al., 2007). Recurrent mass-wasting events led to the deposition of thick and laterally continuous MTDs in the proximal and mid-slope parts of the Espírito Santo Basin (Gamboa et al., 2010; Omosanya and Alves, 2013b), but laterally equivalent MTD-rich units have been identified in distal regions (Gamboa & Alves, 2016).

Thin-skinned extension occurs in proximal areas of the Espírito Santo Basin, with thin Aptian salt and salt welds connecting the pre- and post-salt units. Here, large salt rafts composed of Cretaceous strata occur in conjunction with large listric faults rooting in salt pillows (Alves, 2012). These features are followed downslope by a wide area with salt diapirs, part of a mid-slope transitional domain (Figure 14.1b). Allochthonous salt walls and canopies linked to thick evaporite successions occur in the distal compressional domain, leading to the development of elongated confined minibasins (Davison, 2007; Fiduk et al., 2004; Mohriak, 1995). Regional tectonic uplift resulting from the emplacement of the Abrolhos Bank led to tilting of the ESB, and subsequent acceleration of gravitational gliding, with consequent deformation of several salt structures during the early Cenozoic (Fiduk et al., 2004). Recent salt growth episodes are recorded by deformation of the modern seafloor in the transitional and compressional domains (Fiduk et al., 2004; Schreiner et al., 2009) (Figures 14.1b and 14.2).

14.2.1. Seismic Stratigraphy of the Espírito Santo Basin

Three main Late Cretaceous-Cenozoic seismic-stratigraphic units are identified in the 3D seismic data (Figure 14.2). The lowermost Unit 1, Late Cretaceous to Mid-Eocene in age, shows low amplitude reflections and local thickening of strata onlapping buried salt structures at depth. These laterally change into sub-parallel seismic reflections with increased amplitude in stratigraphic packages (with minor thickness changes) towards its top.

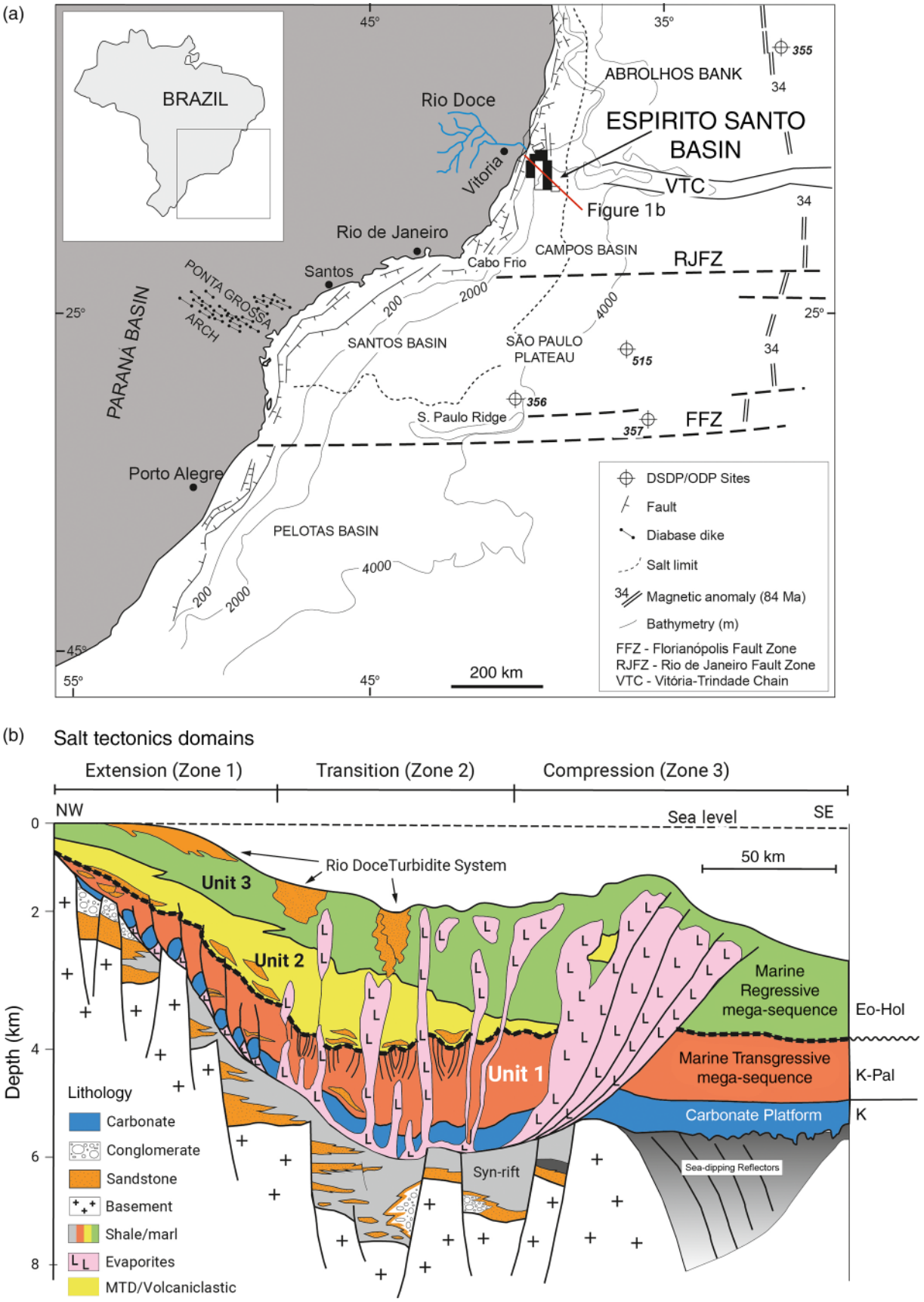


Figure 14.1 (a) Regional map showing the limits of the SE Brazil's offshore basins. The Espírito Santo Basin (ESB) is located toward the north, close to the Abrolhos Bank. (b) Schematic cross section of the ESB illustrating main sequences and the three salt tectonics domains. K, Cretaceous; K-Pal, Cretaceous to Paleogene; Eo-Hol, mid-Eocene to Holocene. Source: Adapted from Fiduk et al. (2004) and Gamboa et al. (2010).

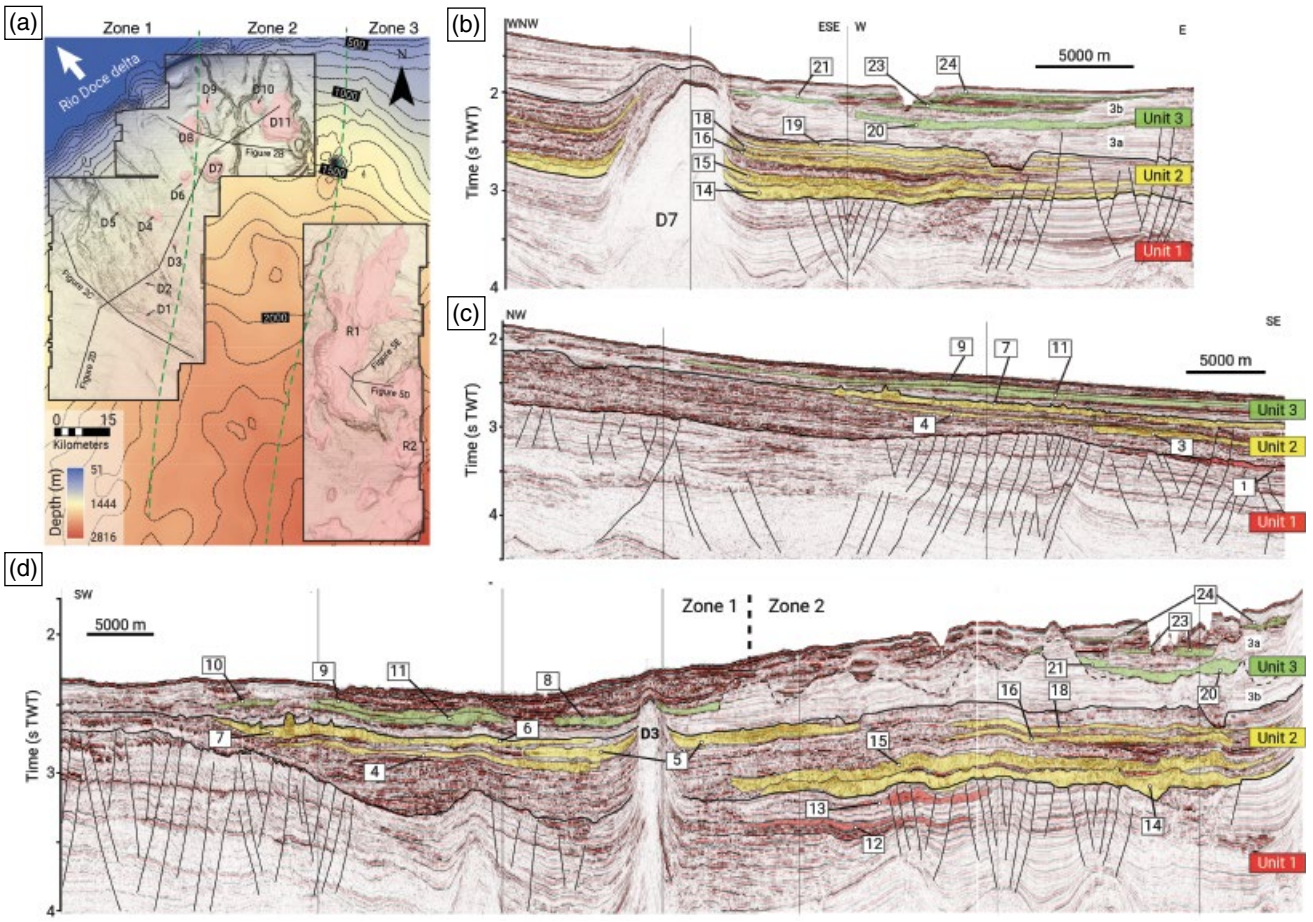


Figure 14.2 (a) Bathymetric map of the Espírito Santo Basin. Detailed sections with outlined seafloor dip morphology mark the limits of the 3D seismic surveys. Three zones with MTDs are identified, correlatable with the salt tectonics domains. Dx highlight the location of salt diapirs in the basin, and Rx the large salt ridges observed in the distal domain. (b, c, and d) Vertical seismic profiles illustrating the character of the three main seismic units and structural features. Interpreted MTDs are highlighted. Numbers in the boxes correspond to the MTD ID. Source: Bathymetry data courtesy of the GEBCO (2014).

Unit 1 shows a change in seismic character across the slope, with various high-amplitude packages associated with turbiditic fans being observed on the proximal domain. These become nearly absent towards the transitional domain where low seismic amplitudes predominate. The rising salt structures are a key control on the presence of the high-amplitude strata towards the distal domains of the basin.

Unit 2 rests on an erosional unconformity of Mid-Eocene age, marked by an abrupt change in seismic amplitude and truncation of numerous crestal faults in Unit 1 (Baudon & Cartwright, 2008; Gamboa et al., 2011). Its top is estimated to be Late Oligocene-Early Miocene, and is coincident with a change from high amplitude mottled seismic reflections to the low amplitude, continuous reflection character of Unit 3. Across the margin, Unit 2 is characterised by very high seismic amplitudes and numerous packages of sub-parallel to chaotic reflections, marking a relative abundance of MTDs. High amplitude sub-parallel reflections alternate with chaotic packages. The high amplitude reflections observed in this unit are, according to Fiduk et al. (2004), due to the supply of siliciclastic sediment from the margin and to the predominance of reflective volcaniclastic material derived from the Abrolhos Bank.

Unit 3 is interpreted to be Miocene to Holocene in age, and shows seismic reflections with good lateral continuity, sub-divided into two sub-units (Gamboa et al., 2012). The lower part, identified as sub-unit 3a, is characterised by low amplitude sub-parallel reflections, interpreted to represented fine-grained deposits. The thickness of this sub-unit is highly variable, being thin to nearly absent towards the proximal domains. Sub-unit 3b is characterised by high to very high seismic amplitudes,

associated with Pliocene to Holocene prograding submarine fan systems, often interrupted by MTDs with chaotic reflections. The distinction between sub-units 3a and 3b is less clear towards the distal domains of the basin, particularly in areas uplifted by compressional salt structures that are less affected by canyon systems (see Gamboa & Alves, 2016).

14.3. DATA AND METHODS

Three 3D seismic volumes (BES100, BES2, BMES1) covering the proximal, transitional and distal domains of the continental slope of the Espírito Santo Basin where used for this study. All shared the same data acquisition geometry, which used a dual airgun array and six 5700 m-long streamers. Seismic signal was sampled at 2 ms and zero-phased migrated with a 12.5 m grid line spacing (inlines and crosslines). The data were zero-phased and in SEG normal polarity. Depth conversions of the time domain seismic data for MTD thickness estimation were based on P-wave velocity data at DSDP Site 516 (Barker et al., 1983). These include seismic velocities of 1500 m/s for the water column, 1800 m/s for the Miocene-Holocene interval, 2100 m/s for the Eocene-Oligocene interval, 3100 m/s for the base of the Mid-Eocene unit and 2500 m/s for the Late Cretaceous/Paleocene interval. These velocities and the dominant frequency of 40 Hz of the seismic volume indicate a vertical resolution of 10 m for the shallower units and 20 m towards the Paleocene-Cretaceous strata.

The interpretation of MTDs was based on the identification of seismic packages with disrupted internal character, bounded by top and basal seismic horizons that can be planar, irregular, marked by steep ramps, or by a combination of these. The MTD upper surface is generally irregular, but this can be modified by subsequent mass-flows (Weimer and Shipp, 2004). The internal character of MTDs can show mottled and chaotic reflections, folded and faulted reflections, or intact segments representing undeformed blocks (Bull et al., 2009). Isochron maps and seismic attributes (RMS (root-mean square) amplitude and variance cubes) were used to complement our morphometric analysis. The RMS amplitude attribute shows the average squared amplitude values within the interval between the top and base MTD surfaces (Brown, 2004). Variance attributes convert a seismic volume of continuity (normal reflections) into a volume of discontinuity, highlighting faults and stratigraphic limits (Brown, 2004).

We measured MTD length as the longest path along its direction of movement, equivalent to deposit length parameter in Clare et al (2018). MTDs were classified following Frey-Martínez et al. (2006), which divide MTDs into frontaly confined if the whole deposit is contained by a frontal ramp, and frontaly emergent if the remobilized mass overcomes the frontal ramp. A combination of these styles can also occur (e.g. Gamboa & Alves, 2016) and frontally unconfined slides must also be considered (Clare et al., 2018). The slope/shelf attachment from Moscardelli and Wood (2016) classifies MTDs according to their relative location. Detached MTDs are controlled by localized instabilities on the slope, or flanks of structures. Attached MTDs are controlled by extrabasinal processes such as sea level fluctuations or tectonics. We also used the binary morphological classification (type 1 and type 2) defined by Gamboa and Alves (2016). This was originally based on the ratio between the headwall scarp and the run-out distance of the MTDs. However, given the lack of defined headwalls for most of the MTDs shown here, we redefined this latter parameter to use a more classic length/width ratio. As our length measurement is equivalent to run-out, the only effective difference is the use of the MTD width, which can be less precise than detailed measurements of the scarp. Thus, type 1 MTDs are defined by length/width ratios larger than 1, resulting in downslope elongated deposits. Type 2 MTDs have length/width ratios lower than 1.

14.4. CHARACTER OF MASS-TRANSPORT DEPOSITS ACROSS THE ESPÍRITO SANTO SLOPE

Here we present an overview of 30 MTDs (see Figures 14.2–14.6) that occur on the continental slope of the ESB, together with a summary of geomorphic parameters in Figure 14.7. The area of occurrence of MTDs is divided into proximal to transitional, transitional and compressional domains, equivalent to the salt tectonics regime at each slope location. These are identified as Zones 1, 2 and 3, respectively.

14.4.1. Zone 1: Proximal to Transitional Domains

Zone 1 includes the proximal region of the slope, covered by the BES100 3D survey, and is considered to include part of the (near) transitional domain given the presence of five salt diapirs towards the east. These proximal diapirs are smaller comparatively to others on the slope, and do not have any marked expression on the seafloor (Figure 14.2a). Salt tectonics and associated structures play a subtle, but important control on the slope depocentres in Zone 1, with relevance for a large anticline toward the south. Post-Paleogene strata over this anticline are very thin compared to other regions of the basin (Figure 14.2c,d). A key stratigraphic reference in the basin is the Mid-Eocene erosional unconformity separating Units 1 and 2. While easily identified elsewhere in the basin (e.g., Alves et al., 2009; Gamboa et al., 2010),

the unconformity is less obvious in the northern and central areas of Zone 1, becoming clearer towards the south where it erodes the faulted Unit 1 (Figure 14.2d). Eleven MTDs (MTD 1 to MTD 11) are shown here as examples of Zone 1. Thickness and amplitudes maps, blended with an intra-MTD variance slice of four deposits in Zone 1, are shown in Figure 14.3, namely MTDs 2, 6, 7 and 8. Attribute maps of the remaining MTDs mapped in Zone 1 are compiled Figure 14.6, although it is not possible to show their features in full detail.

MTD 1 occurs in Unit 1 and is one of the oldest presented here. Its incision is controlled by faults in Unit 1 (Figure 14.2d), which fully confine the lower amplitude MTDs (Figure 14.6a). This suggests a localized origin and possibly short remobilization distance, with relevant internal deformation suggested by low variance patterns. The overlying MTD 2 rests close to the unconformity separating Units 2 and 1. Attribute and thickness maps of MTD2 show internal NW-SE buttressing structures and thickening towards the NE (Figure 14.3a), indicating a NE-directed flow (Figure 14.3a and 14.6a). The length of MTD 2 (6.8 km) is shorter than its width (9 km), suggesting the presence of a high-width type 2 MTD (Gamboa & Alves, 2016). The deposit thins westwards towards the major anticlinal structure (Figure 14.3a), being sourced from its flank, and is interpreted to have a short remobilization distance. The limits of the MTD's toe indicate some frontal confinement partially influenced by pre-existing faults.

MTD 3 overlies MTDs 1 and 2, but occurs within Unit 2. It is larger and is characterized by high seismic amplitudes (Figure 14.2). Its full limits are not known due to the limited extent of the 3D seismic survey, but attribute maps indicate a flow originated from the NW with a deposit (at least) 19 km long and 13 km wide, covering an area of (at least) 166 m^2 (Figure 14.6b). The contrast in flow character between MTD 3 and underlying MTDs reveals a change in Unit 2, with longer runouts, higher area coverage and increased internal heterogeneity. This trend is well represented by MTD 4, which is pierced by two diapirs that influence the mass flow paths. This is inferred from the seismic attribute maps, which show thicker areas with higher amplitudes regions diverting from the area between D1 and D2, but converge towards the SE (Figure 14.6c). MTD 5 is another example of a large deposit in Unit 2 (Figure 14.2d). It covers an area of 578.75 m^2 but its size extends beyond the survey limits. The basal surface of MTD 5 is marked by ramps (Omosanya and Alves, 2013a) which are highlighted by sharp contrasts in thickness (Figure 14.3). MTD 5 is interpreted to result from a SE-directed flow, supported by NW–SE orientated striations and high-amplitude patches. Compressional ridges within thicker, low variance areas of the MTD further support a SE-directed flow (Figure 14.3B). Salt diapirs are likely to have influenced the flow, as suggested by the low thickness promontory south of diapir D3 and by the thickened slumped strata in the gap immediately south of diapirs D4 and D5 (Figure 14.3b). MTD 6 sits south of, and partially overlaps MTD5. MTD 6 is one of the deposits at the top limit to Unit 2. Thickening and strata disaggregation near the diapirs, especially D2, suggests the structures influenced localized increases in deformation of the MTD (Figure 14.6d).

The southern limit of MTD 6 merges with the northeast edge of MTD 7 (Figure 14.2e), possibly the most impressive MTD identified on the ESB margin. It includes very large blocks that protrude as pinnacles up to 400 m above the top of the debritic matrix (Figure 14.2e and 14.3c). The whole MTD covers a length of 44 km, initially flowing eastwards from its proximal domain but shifting southeastward distally. The headwall of MTD 7 is not covered by the 3D seismic data, but is clearly located further south from the source point of the other SE-flowing MTDs in Unit 2 (Figure 14.7b). The bulk of the debritic deformation, represented by high variance patterns, is concentrated in the flow corridor where the geometric blocks occur. MTD 7 gradually thins towards its flanks. Towards the southern flank thinning is due to the structural high that forces its pinchout (Figure 14.2e), although to the north is due to accommodation with adjacent strata (Figure 14.2d). An average thickness of 73 m was calculated for the deposit, but the maximum thickness recorded was over 400 m at the top of the largest block closer to the headwall. Complex flow dynamics are likely to have occurred in MTD 7 given the co-existence of large, variable deformed blocks and the highly disaggregated, thinned debritic matrix (Gamboa & Alves, 2015b). Another striking aspect of MTD7 is the prolonged influence on accommodation space the blocks had after they were formed. This occurred through means of differential compaction (Alves and Cartwright, 2010), and the establishment of sediment transfer routes for turbidites around the tortuous paths created by the block tops (Ward et al., 2018).

The remaining MTDs 8 to 11 occur within the uppermost subdivision of Unit 3 (Figure 14.2), characterized by higher seismic amplitudes associated with prograding, clastic strata of the Late/Post Miocene Rio Doce Canyon System (Fiduk et al., 2004). The four MTDs occur at roughly equivalent positions near the base of sub-unit 3b, with lateral stratigraphical equivalents observed in Zone 2.

As in other deposits analyzed, the extent of MTD 8 is truncated by the 3D survey limits. The MTD comprises high-amplitude internal reflections, and covers an area of (over) 310 km^2. Salt diapirs D3 and D4 influenced MTD emplacement as the thicker, lower variance packages

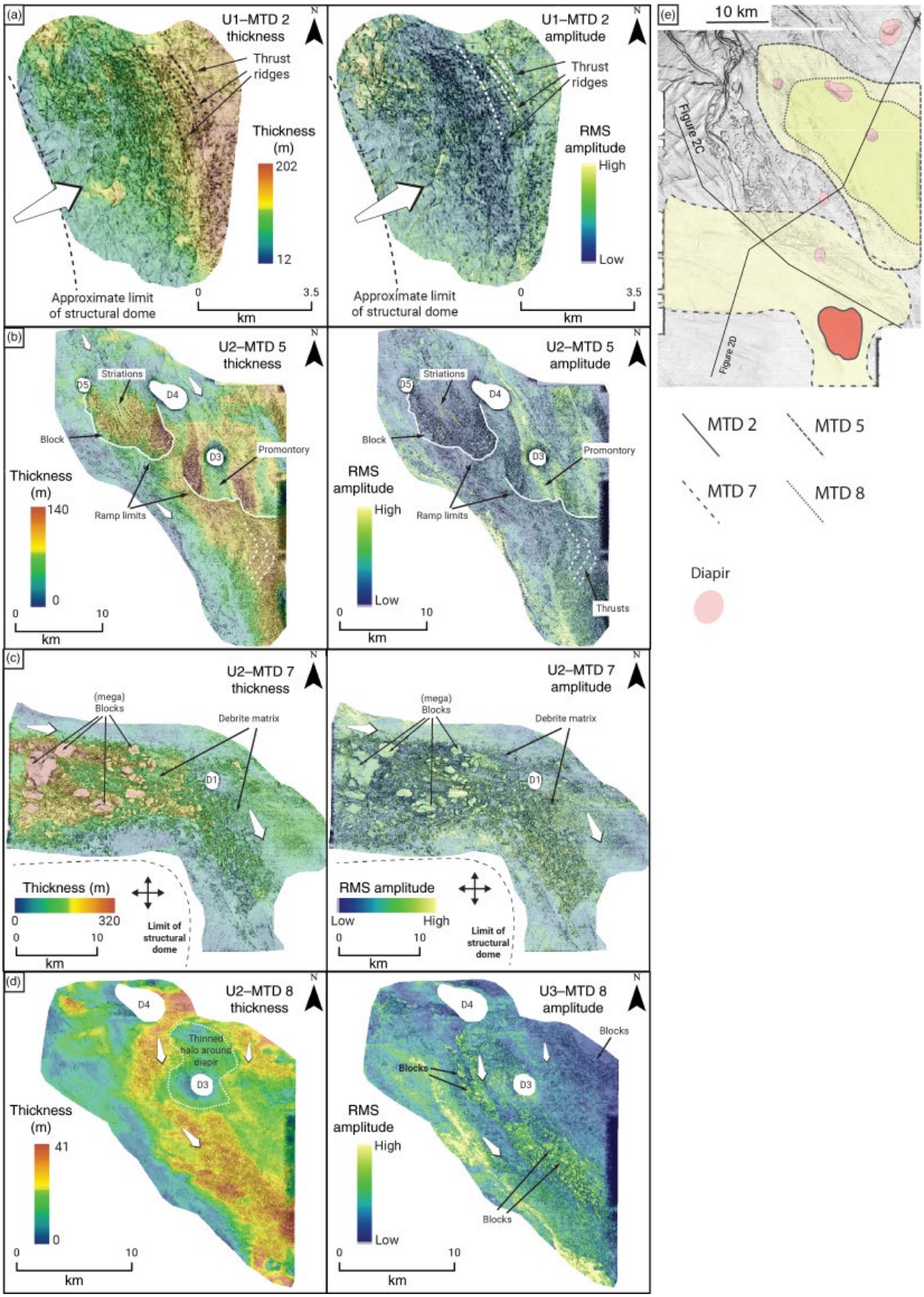


Figure 14.3 (a–d) Attribute maps of four MTDs interpreted in Zone 1. The left-hand panel on each pair shows an attribute blend of thickness (colored) with variance. The right-hand panel shows a blend of RMS amplitude calculated between the top and base of the MTD with variance. High-variance values are shown as dark, mottled patterns on the map. Large arrows indicate general directions of flow. (e) Seafloor dip-map overlain by the limits of MTDs shown in this figure.

occur on the downslope flank of the structures. The thinner halo around diapir D3 suggest that salt-related (positive) topography hindered sediment accumulation in the area (Figure 14.3d). Higher amplitude and thickness areas in this MTD coincide with a corridor containing rafted blocks (Figure 14.3d). MTDs 9, 10 and 11 were sourced from an area southward of MTD8 (Figure 14.7b), coincident with the source of the blocky MTD 7. Judging by the size of blocks in MTD 7, it is possible that the associated headwall carved a major flow path that influenced the sediment input to the slope and the source of Unit 3 MTDs. The three MTDs have relative thicknesses of about 30 to 40 m when compared to those in Units 1 and 2 (Figure 14.7). Despite the widespread coverage, lateral pinchouts toward the rims of MTDs in Unit 3 indicate an influence of stratigraphic confinement, possibly by compensational stacking or by eroding pre-existing channels. This is supported by MTD 10 (Figure 14.6f), which has the higher length/width (L/W) ratio observed in Zone 1. It shows a thicker central path where the bulk of the flow was concentrated, gradually thinning toward the edges.

14.4.2. Zone 2: Transitional Domain

The 3D dataset representing the transitional domain is somewhat limited, yet it shows larger diapirs delimiting NW-SE to N-S oriented sediment fairways (Figure 14.2a) that variably confine MTDs through time (Gamboa et al., 2010). The deeper MTDs 12 and 13 occur in Unit 1 and are located southwest of diapirs D7 and D8 (Figure 14.7a). Strikingly, MTDs or disrupted strata are virtually absent west of diapir D7 and into the transitional domain in Unit 1 (Figure 14.2b,d). MTDs 12 and 13 were influenced by salt-related faults. The attribute maps of MTD12 have thickened, elongated patches of low amplitude and high variance, interpreted as locations were strata were deformed parallel to crestal fault arrays (Figure 14.6h). MTD 13 is comparatively narrower than MTD 12, at 10 km, but extends upslope in a parallel direction to the diapir alignment (Figure 14.4a). We consider the emplacement of these MTDs to be strongly constrained by faults and diapirs deforming Unit 1, as revealed by sharp changes in thickness (Figure 14.4a). The thicker, more deformed MTD 13 occurs between diapirs D6 and D7, suggesting a localized source controlled by nearby structures (see the laterally-equivalent MTDs 1 and 2 in Zone 1).

The overlying Unit 2 has a high proportion of MTDs, constituting 60 to 70% of its strata. Strikingly, the majority of MTDs, and their thicker examples, occur where diapirs and buried salt structures are present (Gamboa et al., 2010). MTD frequency and thickness sharply decrease eastwards, imposed by the presence of diapirs D10 and D11. The lowermost MTD14 has the bulk of its strata adjacent to diapirs D8 and D7, thinning towards its western and eastern limits. This is one of the largest MTDs identified, covering 820 Km^2 and with a volume of 90 Km^3. Many blocks are present within MTD 14, showing a range of deformation from nearly intact and unremobilized to highly tilted or thrusted ones (Gamboa et al., 2011). The limits of MTD 14 expand from those in Gamboa et al. (2011) to include a portion of the MTD located south of diapir D11. Although the deposit is thinner and of lower amplitude in this latter area (Figure 14.4b), the localized high variance patterns within the crestal fault corridor south of diapir D11 supports the interpretation of strata disaggregation and localized collapse over the structural high. MTD 14 has been interpreted as having a complex movement, with central blocks and failed strata symmetrically spread from the collapse of an elongated structural high associated with buried salt structures. Nearby subsidence favored thicker accumulations of strata and the east-directed movement of blocks from the west (Gamboa et al, 2011). The overlying MTD15 is the largest here identified, covering an area of 825 km^2 and showing a volume of 110 km^3. Its eastern limit is clearly identified, pinching-out out towards salt diapirs D10 and D11 (Figure 14.6i) (see also Gamboa et al., 2010), but its toe is not imaged in seismic data. Thus, its length is greater than the measured 30 km. The thicker accumulations of MTD 15, up to circa 290 m, occur within the diapir area but, unlike the underlying deposit, it shows indications of a large SE-directed mass-flow with higher remobilization distances (Figure 14.6i).

The MTDs on the upper half of Unit 2 show a gradual decrease in size. For instance, MTD 16 shows a similar SE-directed flow pattern to MTD 15, but it is smaller and its full width is covered by the 3D seismic (505 Km^2, 24 Km^3 and 26 km wide). The full length extends beyond the data limit, with at least 28 km being observed. The thickness of MTD 16 indicates an eastward shift of the main slope epocenter in Zone 2. Of relevance are the low values of thickness and variance between diapirs D7 and D8, showing a 'cleaner' pattern. This suggests the shielding of erosion by growing topography. MTD 17 contrasts to the style of the remaining deposits. It consists of a SW-directed narrow frontally confined slump with internal thrusts, being 11 km long and 6 wide, covering as area of 28 Km^2 (Figure 14.6k). It occurs near the higher confinement area between diapirs D9 and D10, and its flow direction to the SW indicates an increasing influence of salt diapirs confining the flows toward a sediment fairway. This aspect is further supported by MTDs 18 and 19, which are laterally contained by the same fairway.

Furthermore, arcuate patches in the thickness patterns of both MTDs and thin accumulations on the downslope flanks of diapirs support an increasing influence of rising salt structures on MTD flow (Figure 14.6l). MTD 18 evidences a decreasing trend of overall MTD size towards the top of Unit 2 (Figure 14.2B, 6), covering 358 Km^2 and being 20 km wide but the measured length of 29 km is underestimated. This trend is further supported by MTD 19, which covers 274 km^2. This MTD also spreads into a wide area south of diapir D11, but it is segmented due to erosion by a Miocene submarine canyon (Figure 14.2c and 7m). MTD 19 is laterally equivalent to MTDs 6 and 7 in Zone 1, indicating that widespread mass-failure events occurred in the ESB around the late Oligocene.

Mass-transport deposits in Unit 3 occur, as in zone 1, within the high amplitude sub-unit 3b, associated with strata of the recent Rio Doce Turbidite System. Despite being much thicker in Zone 2 than in Zone 1, the low amplitude sub-unit 3a does not show any evidence of relevant submarine mass-flows along the continental slope (Figure 14.2d). At the base of sub-unit 3b is MTD 20, which flowed to the south and is completely constricted by the salt structures. It has a width of 19.5 km and a length of (at least) 19 km. The upslope limit of MTD 20 coincides with an area of high confinement between diapirs D9 and D10. The uniform width of the majority of the deposit shows a very clear control of minibasin structure on the MTD emplacement. The internal character of MTD 20 is quite heterogeneous, with isolated thickened areas on its western half, but fairly uniform high values recorded along its eastern margin. This is due to localized collapses and the presence of blocks along the eastern lateral scarp (Figure 14.4c). Central eroded slots with well-delimited frontal and lateral ramps are also observed to the south (Figure 14.4C). The presence of MTD 20 at the base of the submarine fan systems agrees with the occurrence of mass-flows within the general model for regressive submarine fans prior to the onset of established turbidite systems (Weimer, 1990). Thus, the occurrence of MTDs at the base of sub-unit 3b may be influenced by salt tectonics and major allocyclic sea-level variations. Other MTDs are observed within the high-amplitude fan system, such as MTD 23. This one originates from a NW source, north of diapir D9, and follows a clear SE-oriented path, possibly exploiting prior channel incisions until is widens and shifts to a south-directed flow (Figure 14.6p). Comparatively to other deposits, the lower width of MTD 23 (up to 9 Km^2) results from increased confinement imposed by salt diapirs and by the overbank deposits bordering the channel system (Figure 14.2b).

Not all deposits are fully contained within the sediment fairway. MTD 24, the topmost one interpreted in Zone 2, covers a very wide area (391 km^2) comparatively to the remaining MTDs in Unit 3. Unlike the majority of the mass flows, which had a source point located to the NW of the basin, the source of MTD 24 is located north of diapirs D10/11 where the continental slope strikes E-W on the flank of the Abrolhos Bank (see Figure 14.1a). A remarkable feature of MTD 24 is that it blankets salt diapirs D10 and D11, revealing a small difference of seafloor topography on its path (Figure 14.4d). Despite the limited flow deviation imposed by salt structures, they still influenced the depositional patterns of MTD 24. Thicker strata showing higher disaggregation occurs either on the upslope flank of the diapirs, or within the main depositional area SSW of these. Post-depositional erosion by the modern Rio Doce turbiditic system has incised into MTDs 23 and 24, as expressed by the gaps within the mass-flow deposits mimicking the path of the erosional channel belt. The modern morphology of the channel system is influenced by the occurrence of MTDs, with the latter establishing preferential capture points for turbiditic flows. The disaggregated nature of the MTD will favor erosion by flows exploiting this sedimentary weakness, leading to channel belts partially controlled by the width of the MTD erosional slot (Qin et al., 2017).

Two examples of MTDs that greatly differ from the generally wide, blanketing deposits described so far are MTDs 21 and 22 (Figure 14.6n,o). These two deposits occur in gaps between salt diapirs and have tortuous paths. Thickness variations in these deposits are controlled by the accommodation space created by the diapirs, with lateral spreading occurring when topographic confinement decreases. This exemplified by the increase in width of MTD 21 on the south flank of diapir D8 (Figure 14.6n). Also common to both MTDs is their SE-directed flow and their origin around salt diapirs, thus consisting of two relatively small Detached MTDs. No clear interpretation can be made regarding any frontal confinement, in part due to entrenchment or erosion by submarine channels.

14.4.3. Zone 3: Distal Compressional Domain

Zone 3 is located further east into the offshore domain of the basin. Salt structures in this domain are markedly different from proximal areas where, instead of isolated diapirs, there are long salt ridges deforming the seafloor (Figure 14.2a and 14.5). MTDs in this domain have been described by Gamboa and Alves (2016), who focused on three Miocene deposits and four others occurring at the seafloor within a salt-confined minibasin. Such short numbers of MTDs cannot possibly be representative of all the styles occurring in Zone 3, but they can provide an

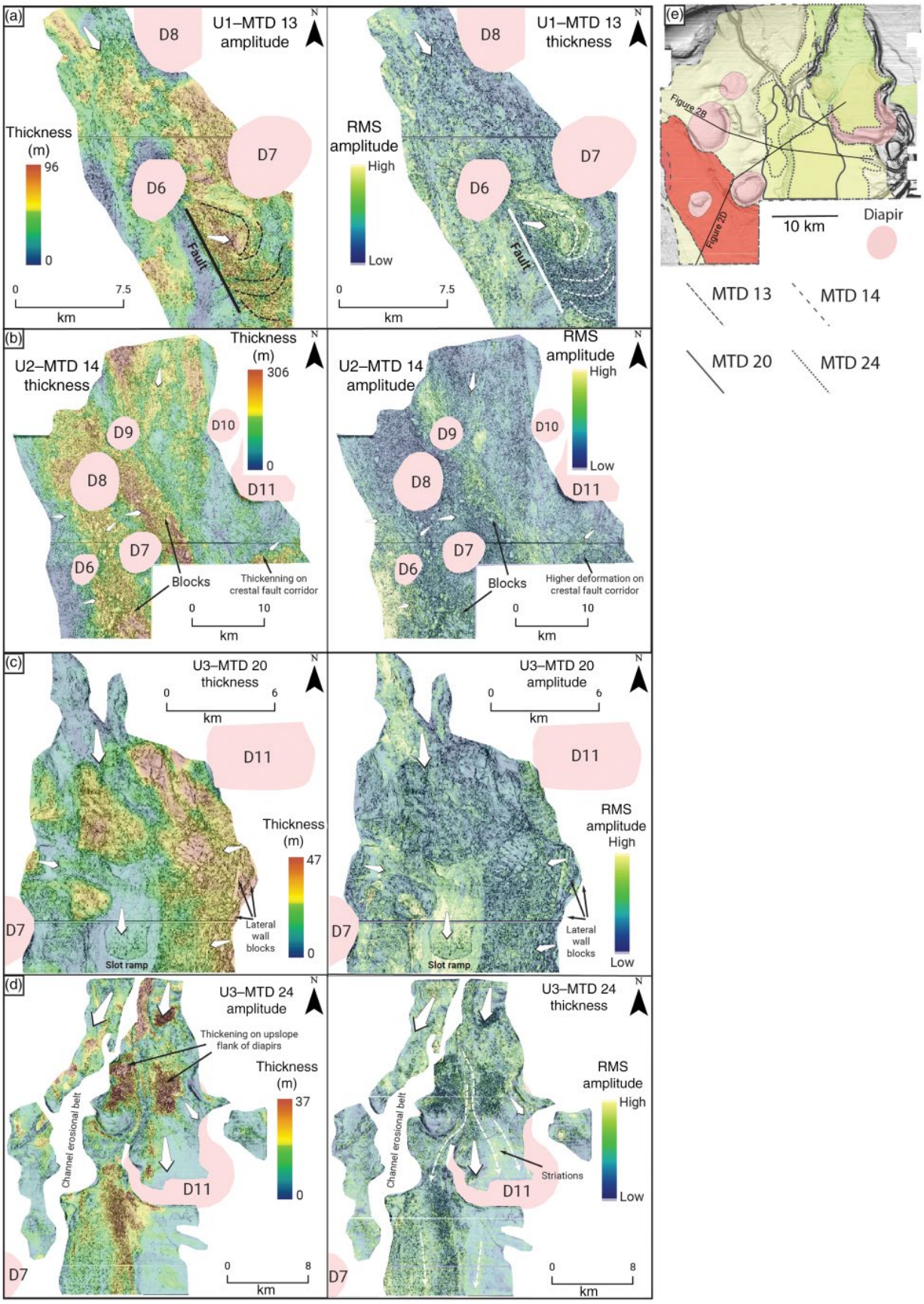


Figure 14.4 (a–d) Attribute maps of four MTDs interpreted in Zone 2. The left-hand panel on each pair shows an attribute blend of thickness (colored) with variance. The right-hand panel shows a blend of RMS amplitude calculated between the top and base of the MTD with variance. High-variance values are shown as dark, mottled patterns on the map. Large arrows indicate directions of flow. (e) Seafloor dip-map overlain by the limits of MTDs shown in this figure.

insight into their size trends. The obvious difference compared to the proximal areas of the ESB is that MTDs in Zone 3 are generally smaller in area and volume, although not necessarily in thickness (Figure 14.7g).

Three buried MTDs are shown within Unit 3, which are generally larger than seafloor MTDs (Figure 14.5). Higher occurrences of MTDs are observed within Unit 2 (Figure 14.5d), similarly to the patterns observed for Zones 1 and 2. Although MTDs in confined minibasins tend to derive from the flanks of salt ridges, MTD25 occurs in an axial position in the minibasin (Figure 14.5a and 14.7c), flowing parallel to its length (for further detail see Gamboa & Alves, 2016). This deposit is 5 km long and 2.8 km wide, covering 13 Km^2. Its stepped basal surface is controlled by underlying crestal faults (Figure 14.5c), which influence the internal character of MTD 25 by forcing its thickening and the development of compressional ridges near horst ramps (Figure 14.5d). MTD 25 followed a SW-directed flow, possibly with variable flow velocities resulting from the interaction with an irregular basal interval. (Figure 14.5d).

MTD 26 is less complex and a typical example of a slope failure flanking a salt structure (Figure 14.5a and 14.6q). It shows a wedge-shaped morphology up of 80 m thick at its toe, pinching out towards the headwall on the flank of the salt ridge. Length and width values of MTD26 are nearly identical, being 2.7 km and 2.5 km respectively, and covering an area of 6.5 km^2. Elongated compressional ridges extend through the full width of MTD 26 at its toe (Figure 14.6q). Sharing a common detachment level with MTD 26 is MTD 27, occurring on the opposite flank of the minibasin (Figure 14.5). MTD 27 is the MTD largest mapped in Zone 3, being 10.7 km wide, almost double its length (5.7 km), and covering 42Km^2. The most striking features are the large slabs in its central area that show no significant internal deformation discernable at seismic scales, thus having an identical character to unremobilized strata above and below the mass-flow (Figure 14.5b,c). The thinnest accumulations occur on the headwall domain, associated with failure episodes along this markedly irregular feature (Gamboa & Alves, 2016). At the toe domain occur numerous ridges formed by elongated pop-up blocks, bounded by opposing dipping faults rooted at the basal interval (Figure 14.5b). MTD 27 is interpreted to result from a slow-moving, east-directed converging flow (or set of flows?), as inferred from the extraordinary degree of internal strata preservation and development of pop-up structures instead of imbricated thrusts at the toe.

At the seafloor of Zone 3 are the smaller MTDs interpreted in the ESB. These occur on the flanks of salt ridge R1, having flow directions perpendicular to the strike of the salt structure. MTD 28 shows a type of failure identical to MTD 27, although much smaller (length and width are 1.4 km and 2.6 km) and covering 2.3 km^2. It is thinner near the scarp, thickening to about 50-60 m in the transitional area, with semi-preserved slabs at the compressional toe areas (Figure 14.6r). More typical emplacement styles are seen in MTDs 29 and 30 (Figure 14.5a and 14.7r,s). Both have linear to slightly arcuate headwalls, with the thinner accumulations adjacent to them and not exceeding 15 to 20 m (Figure 14.6s,t). The deposits thicken in a toe domain marked by compressional ridges and bound by a frontal ramp (Gamboa & Alves, 2016). MTD 29 reaches a maximum of 90 m and MTD 30 of 67 m. Emergent over-running sediment flows extending from the limit of the compressional toe are also observed in both features. In MTD 29 it is about 40 m thick and 1 km wide, extending for 2.4 km. The unconfined portion of MTD 30 is about 1.7 km long and 550 m wide, with a general thickness of 22 m. In both cases the emergent thin portion is about the same length of the bulk of the deposit.

14.5. INFLUENCE OF SALT TECTONICS ON THE EVOLUTION OF THE ESPÍRITO SANTO BASIN MTDs THROUGH SPACE AND TIME

The examples of MTDs presented in this work show a fair variability in size and styles of occurrence within the seismic-stratigraphic unit in which they occur (Figure 14.7). The major limitation of the study is dataset availability, which did not allow the full mapping of the MTDs. A direct consequence is that the larger MTDs are often truncated at length. Thus, only ten MTDs have been mapped to their full extent, effectively leading to partial morphometric data analysis for 70% of the features presented. Interpretation bias must also be taken into account when mapping single MTDs, particularly in Unit 2 where many identical deposits occur side by side. Perhaps MTDs 6 and 7, which merge at a point on their path, are the best examples. Solely based on seismic profiles, it would be tempting to map the whole deformed package as a single entity, thus leading to an overestimated size of the deposit (Figure 14.2d). This issue was overcome by the availability of the 3D seismic data, where seismic attribute maps can corroborate the adequacy of the interpreted MTD limits. Despite the aforementioned limitations, there are relevant observations to be made regarding MTD styles across the basin. The main interpretations on individual MTDs have been made elsewhere (Gamboa et al., 2010, 2011; Omosanya & Alves, 2013a, 2013b, 2014), but all illustrate the common characteristic of a direct or indirect influence of salt tectonics on their evolution.

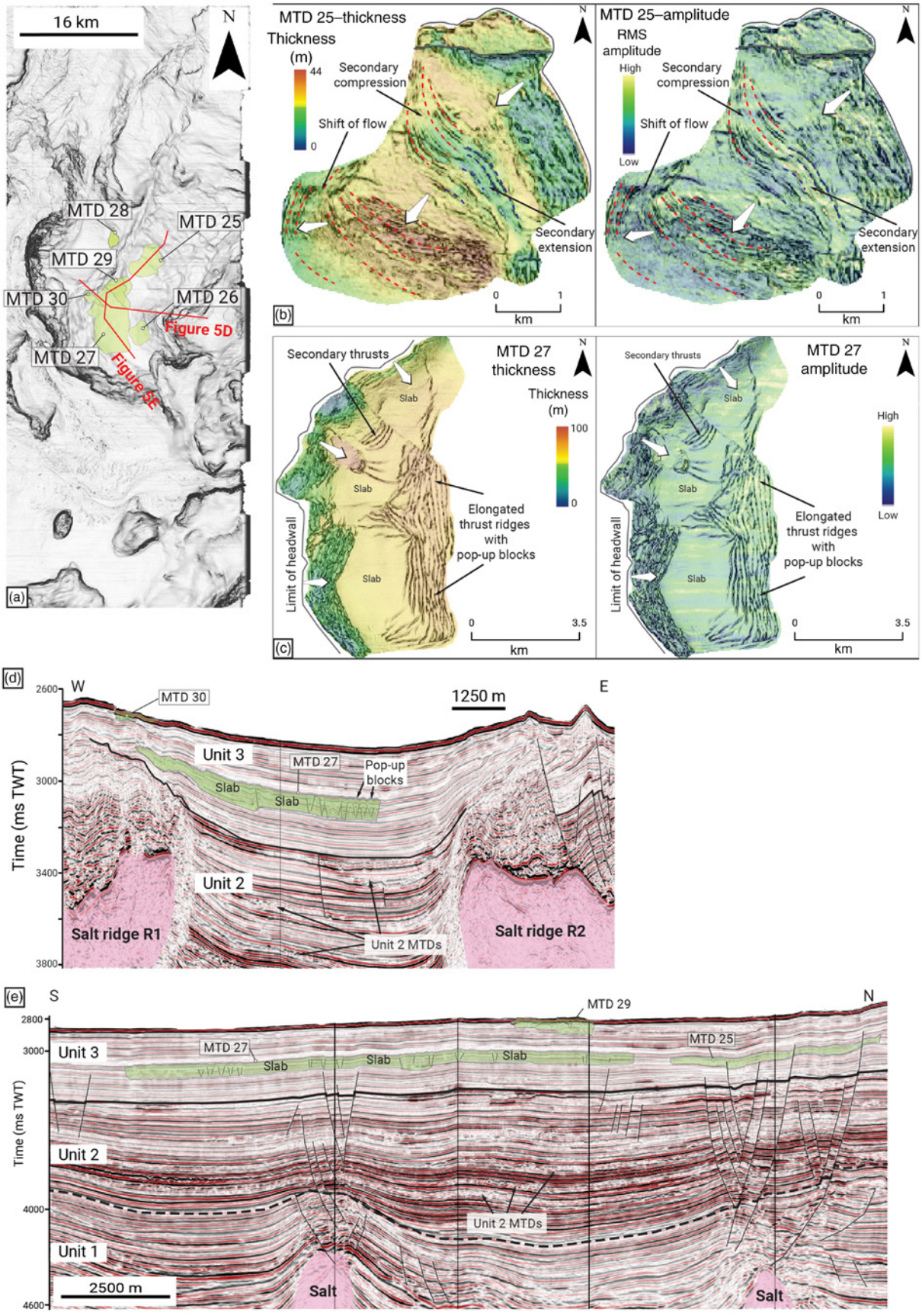


Figure 14.5 (a) Seafloor dip-map of the 3D survey in Zone 3. (b and c) Thickness (left) and RMS amplitude (right) maps of two MTDs interpreted in Zone 3, blended with variance attribute maps. (d and e) Vertical seismic profiles showing the stratigraphic units and deformation features in Zone 3.

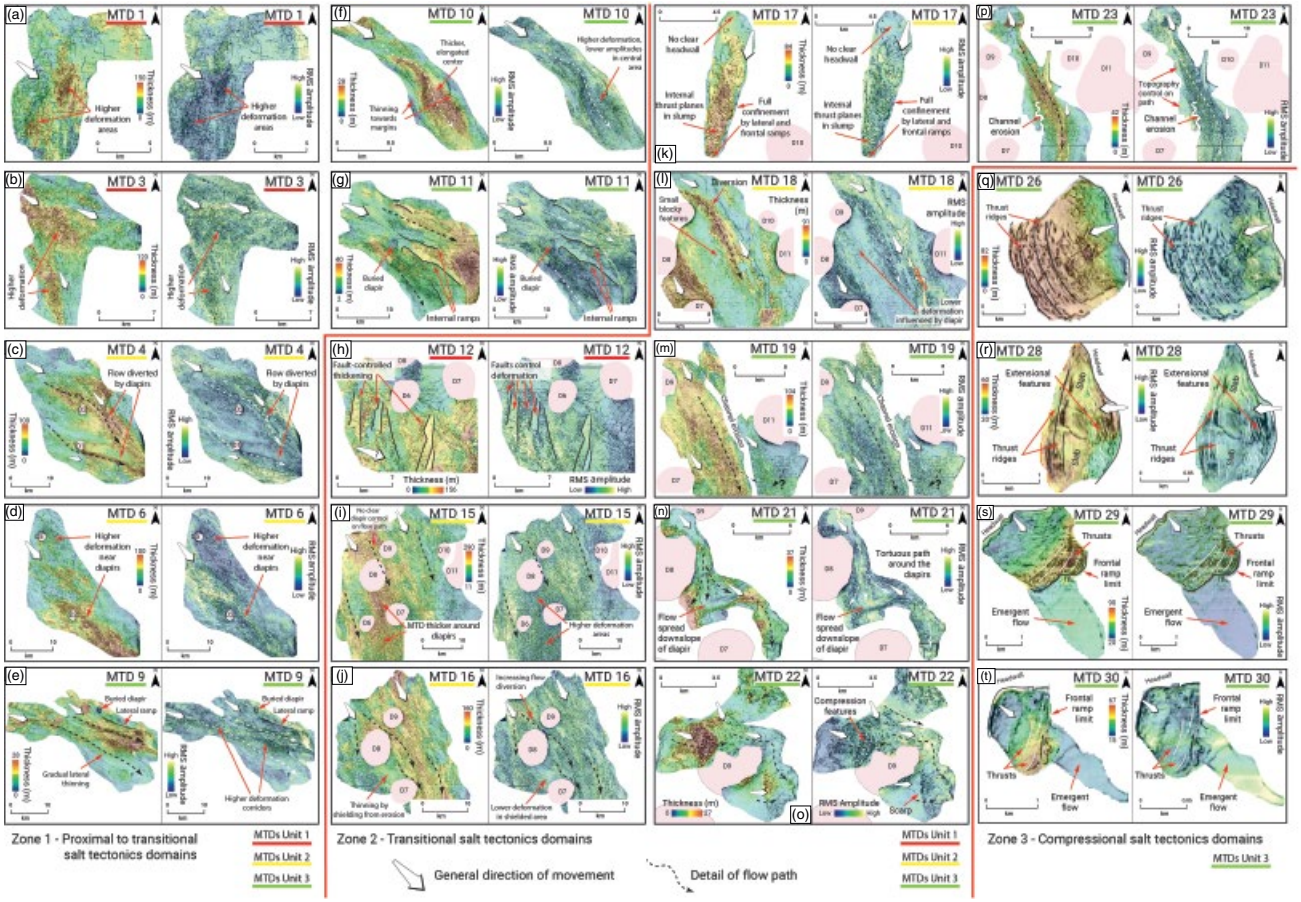
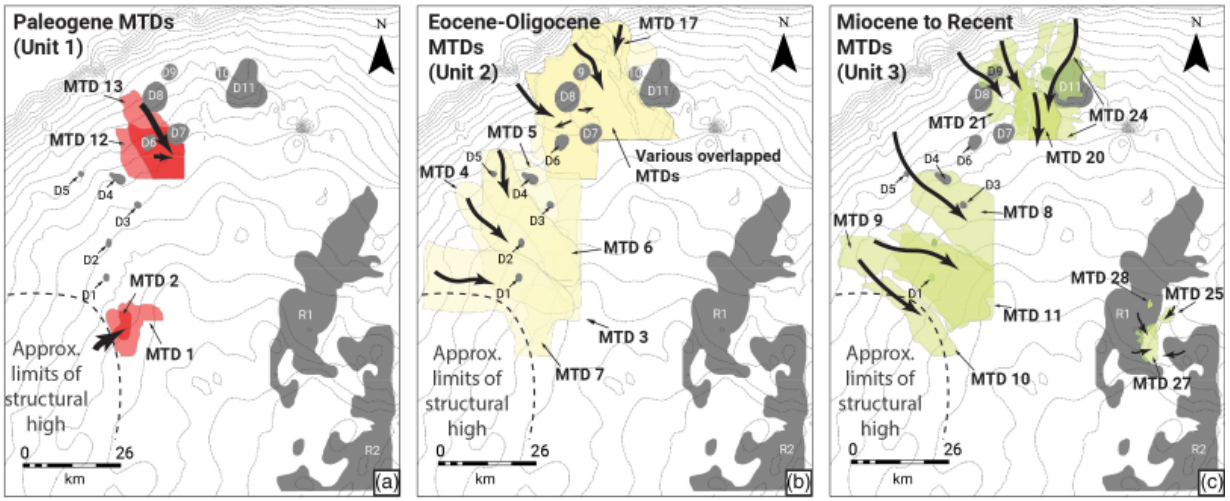
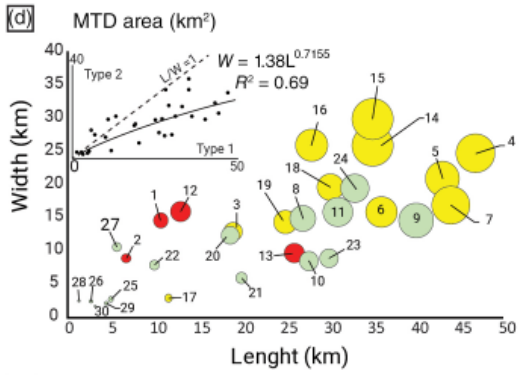
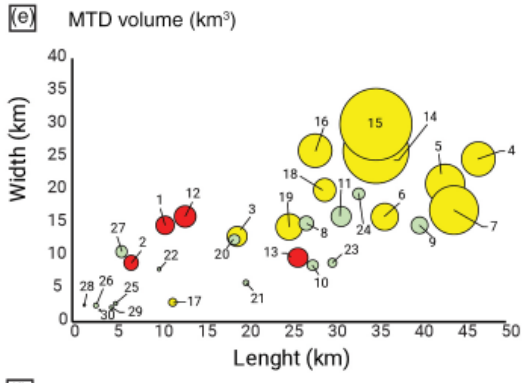
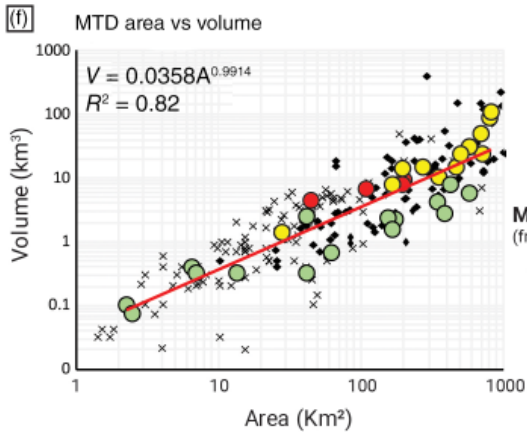


Figure 14.6 Morphological maps of 20 MTDs interpreted in the Espírito Santo Basin, grouped by zone of occurrence. Left-hand panel shows MTD thickness, and right-hand panel shows RMS amplitude, both blended with an intra-MTD variance slice. Large white arrows shows inferred general directions of MTD flow; dashed arrowed lines (black or white) represent interpreted flow paths. Pink subcircular shapes represent salt diapir outlines, identified as Dx. (*See electronic version for color representation of this figure*)









(g)

MTD ID	Zone	Unit	Length (km)	Width (km)	L/W ratio	Area (km²)	Volume (km³)	Max thickn. (m)	Avg thickn. (m)
1	1	1	10.7	14.7	0.7	109.67	7.20	150	65
2	1	1	6.78	9	0.8	44.76	4.78	206	106
3	1	2	19	13	1.5	166.61	8.05	126	48
4	1	2	46.8	24.8	1.9	719.95	24.84	112	34
5	1	2	43	21	2.0	578.75	32.12	148	55
6	1	2	36	16	2.3	474.74	15.53	100	32
7	1	2	44	17	2.6	696.80	51.12	323	73
8	1	3	27	15	1.8	341.08	4.53	61	13
9	1	3	40	14.7	2.7	576.18	6.15	29	10
10	1	3	27.7	8.6	3.2	174.01	2.40	28	13
11	1	3	31	16	1.9	426.61	8.48	40	20
12	2	1	13	16	0.8	199.05	9.83	162	49
13	2	1	26	9.8	2.7	193.85	8.29	135	40
14	2	2	35	26	1.3	819.95	90.05	348	104
15	2	2	35	30	1.2	825.26	110.68	431	131
16	2	2	28	26	1.1	505.37	24.18	165	48
17	2	2	11.6	3	3.9	28.13	1.41	108	49
18	2	2	29	20	1.5	358.11	10.79	136	30
19	2	2	25	14.5	1.7	274.38	14.91	117	54
20	2	3	18.7	12.5	1.5	156.62	2.55	51	16
21	2	3	20	6	3.3	61.94	0.70	38	11
22	2	3	10	8	1.3	41.89	0.34	28	8
23	2	3	30	9	3.3	167.82	1.65	45	10
24	2	3	33	19.5	1.7	391.34	2.95	51	8
25	3	3	5	2.8	1.8	13.36	0.34	43	25
26	3	3	2.7	2.5	1.1	6.46	0.41	82	63
27	3	3	5.7	10.7	0.5	42.04	2.69	100	63
28	3	3	1.35	2.6	0.5	2.29	0.11	62	46
29	3	3	4.5	2.2	2.0	7.09	0.34	90	47
30	3	3	3.2	1.8	1.8	2.50	0.08	65	30
Average	Total		22	13	2	278	15	123	44
	Unit 1		14	12	1	137	8	163	65
	Unit 2		31	20	2	495	35	192	60
	Unit 3		17	9	2	161	2	54	26

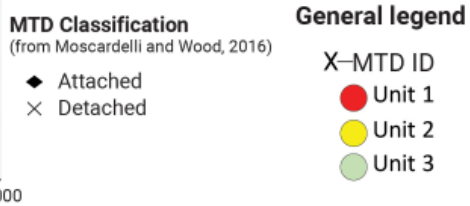


Figure 14.7 (a) Coverage of Paleogene MTDs interpreted in the basin. These have limited areas of occurrence close to structural features. (b) Coverage of early Eocene to Oligocene MTDs. These spread over wide areas along the slope in Zones 1 and 2. No interpreted MTDs in Zone 3 were available for this study. (c) Coverage of Miocene to recent MTDs interpreted in the study area. (d and e) Length vs. width distribution plots, with bubble size representing the area and volume of MTDs, respectively. Insert in (d) shows the general length/width relationships for all the data. (f) Relationship between the area and volume of MTDs analyzed in this study (colored circles), compared with the same parameters of MTDs analyzed by Moscardelli and Wood (2016). Crosses represent detached MTDs and black diamonds represent attached MTDs. *(See electronic version for color representation of this figure.)*

14.5.1. Unit 1 MTDs

The MTDs in Unit 1 are fairly limited in their extent and distribution (Figure 14.7a), occurring in areas adjacent to assumed paleo-structural highs associated with buried salt rafts in Zone 1 (Alves, 2012), and salt-cored anticlines in Zone 2 (Figure 14.2). They occur in areas significantly affected by crestal faults rooted at deeper salt-related features, leading to an origin associated with salt instability and collapse on the flank (or top?) of fractured structural highs. This is supported by the estimated direction of transport towards the ENE in Zone 1, concomitant with a source on the flank of the adjacent structural dome (Figure 14.2e). MTDs in Zone 2 can show SE-directed flows, but this elongation still supports a link to buried salt ridges and crestal fault corridors with NW-SE orientations (Gamboa & Alves, 2015a; Mattos and Alves, 2018). Pre-existing faults at the time of emplacement had a general impact on the thickness, internal deformation, and likely flow dynamics of most MTDs in Unit 1. However, non-mapped MTDs in Unit 1 may have distinct styles, and possibly larger sizes if associated with the large Cretaceous and Paleogene canyons systems (Bruhn and Walker, 1997).

The salt-controlled genesis for the MTDs shown here for Unit 1 fits them on a slope detached classification, with relatively short remobilisation distances, but considerations about their confinement are harder to achieve. The fit into a type 2 MTD classification in Gamboa & Alves (2016) for some of the deposits, initially described for Detached MTDs in distal areas, shows that such morphologies are prone to occur on proximal domains. In this case it would relate to instability events on structural highs during Paleogene or early Eocene times, possibly in a slope setting where the shelf break could be further westward than its modern position.

14.5.2. Unit 2 MTDs

The mid-Eocene to Oligocene Unit 2 includes the most impressive MTDs in the ESB. The deposits often stack on top of each other, especially at the lower levels of the unit in Zone 2, where the thickest MTDs occur (Figure 14.2 and 14.6). It has been well documented that high sediment discharge to the Espírito Santo Basin occurred during mid-Eocene times as a result of uplift and erosion of hinterland mountain ranges and volcanic activity at the Abrolhos Bank. Thus, recurrent slope failure would be expected on the proximal margin during such periods of instability. The major sediment input point in the basin would have been located towards the northwest, confirmed by the generalized SE-directed flow of Unit 2 MTDs (Figure 14.7b). Given the large remobilization distances, often of tens of kilometres, debritic flows probably prevailed. However, complex blocky MTDs found within Unit 2 indicate that such deposits had, at least in part, localized sources and shorter remobilization distances (e.g. MTDs 7 and 14).

Unit 2 MTDs are of particular interest as they can be used as indicators of salt growth in areas affected by diapirs. While accurate ages are not known, a fact supporting this idea is the relationship between the salt structures, MTD thickness and MTD vertical distribution in Unit 2. Thick, uniform accumulations of MTDs at the lower half of Unit 2 are presently pierced by salt diapirs D6-D9, but do not show clear proof of topographic control on their deposition (Figure 14.4b and 14.6i). For this to occur the salt-related bathymetry had to be negligible, possibly due to slope failures along crestal areas, as indicated by MTDs that include unremobilized blocks (Gamboa et al., 2011), or erosion by mass flows (Gamboa et al., 2010). By the time MTDs 16-19 deposited, salt relief was significant, forcing a gradual shift of the depositional locus towards what is now the main sediment fairway. Sediment input here was still predominantly from the northwest, and diapirs created erosional shadow areas at their downslope flanks (Gamboa 2010). MTDs in Zone 1 also record an increasing influence of halokinesis, showing arched paths deflected by diapirs (Figure 14.6c,d) and, in cases, the development of ramps and flats that affect the MTD erosion patterns (Figure 14.3b) (Omosanya and Alves, 2013a). Nevertheless, salt confinement of Unit 2 MTDs in Zone 1 is minor and led to largely unconfined MTDs covering larger areas than their equivalents in Zone 2 (Figure 14.2 and 14.7). The topmost strata in Unit 2 also records one of the most impressive collapses on the margin in MTD7, which includes large in-situ and rafted blocks. Specific features of its volumetrics are detailed elsewhere (e.g., Alves & Cartwright, 2009), but the remnant strata provide a clue about the large volume of sediment that can be evacuated by mass-movements. The MTD's main trigger is associated with the movement of very large normal faults that link to salt rafts in depth and possibly diapir rise during the late Eocene/Oligocene, effectively classifying it as a very large detached MTD.

14.5.3. Unit 3 MTDs

Mass-transport deposits of Miocene to Holocene age exhibit a much stricter control of salt-related topography on their flow paths. A key aspect of Unit 3 MTDs is that they are generally smaller in volume when compared to Unit 2, although not necessarily in area coverage (Figure 14.7g). Two very distinct patterns are observed between the three zones, all linked to the confinement imposed

and input points. In the proximal domains with low expression of salt topography at the seafloor, unconfined MTDs spread over large areas when compared to those domains where diapirs or ridges are present. There is a tendency for MTDs to occur and stack below the 1500 m bathymetric contour (Figure 14.7c), where slope angle also decreases (Figure 14.2d). Taking into account the distance of their accumulation area from the shelf break and association with modern prograding fans, we consider most of these to be detached MTDs associated with instabilities within the slope.

Zones 2 and 3 show clear controls of diapirs and associated fairways on MTD emplacement. Nevertheless, significant differences are still recorded when considering their position relatively to the shelf and sediment input dynamics (Figure 14.7). The most obvious contrasts are clear on MTD size and stacking patterns. MTDs in proximal areas are expectedly larger and in higher number due to the proximity of sediment sources. The MTDs will, however, accumulate within the limited area created by partially isolated fairways and minibasins trapping gravity flows (Fiduk et al., 2004). MTDs are triggered either from increases in flank steepness, originating MTDs with flows perpendicular to the minibasin axis, or subsidence linked to buried salt and associated crestal faults (e.g. MTD 25) or sediment fairways. Although the larger MTDs are triggered or trapped within the fairway, smaller detached MTDs derived from diapir flanks occur as well (e.g. MTDs 21 and 22, Figure 14.6n,o). These have quite tortuous paths controlled by diapir spacing; documenting their accurate width can be problematic as they fan out away from the diapirs. As a note, not all recent MTDs within the salt-controlled areas are constrained by salt structures. Unconfined mass flows also occur, as exemplified by MTD24 (Figure 14.4d). This deposit is sourced from a location immediately north of diapir D11 and covers a great extent of the structures in its path. While diapirs do affect the MTD thickness, they constituted poorly effective barriers, possibly due to a less prominent seafloor relief than they have on the present day.

14.5.4. MTDs in the ESB: Do They Fit Known MTD Classifications?

Classification schemes based on MTD morphometrics have been established with the aim of 'predicting' common MTD characteristics, genesis and remobilization trends based on their size or dimensional ratios (e.g. Clare et al., 2018; Gamboa & Alves, 2016; Moscardelli & Wood, 2016). Overall, the MTDs in the Espírito Santo Basin show clear size contrasts between different units, their relative locations on the slope, and an increase in size towards the distal domains. Large MTDs are up to 50 km in length and 30 km in width in proximal zones, but do not exceed 6km in length in Zone 3. The L/W relationships obtained are consistent for c. 70% of the data samples (Figure 14.7d), but some data points skew the trend to a lower fit. One reason for this is the lack of full 3D seismic coverage for many of the MTDs. More relevant are the type 2 MTDs with length/width ratios <1 as their presence within a geomorphic dataset skews the data into a lower fit. MTDs from Units 2 and 3 with lower flow confinement show the largest areas (up to a maximum of 825 Km^2), often within identical ranges in values for both units (Figure 14.7d). Consequently, lower MTD area values occur in MTDs strongly confined by the salt fairways or derived from the flanks of topographic highs. Importantly, such cross-unit similarities are not observed for MTD volumes (Figure 14.7e). Although there are uncertainties associated with volume calculation, we can undoubtedly say that deposits in Unit 2 have the largest volumes. This is a direct consequence of the generally thicker MTDs in Unit 2, with an average maximum thickness of 192 m when compared to 163 m in Unit 1 and 54 m in Unit 3. Relationships between the MTD area and volume show a well fitted trend with correlation coefficients of 0.82. The relationship between the two parameters may be more adequate for MTD morphometric analyses, not only due to the positive correlations often obtained (Gamboa & Alves, 2016; Moscardelli & Wood, 2016) but also because it decreases the skewing in length-based relationships when type 2 MTDs are present. As MTD volume is directly related to thickness we can also estimate this parameter for features with similar area occurring in different units or slope locations. A second aspect is that the length measurement method used her differs from Moscardelli and Wood (2016) and impacts the L/W ratios, but this is mitigated by using area and volume data if MTDs are adequately mapped.

Figure 14.7f shows our area/volume relationships plotted against MTD data and associated classifications from Moscardelli and Wood (2016). There is generally a good dimensional match between our detached MTDs (triggered by salt tectonics or intra-slope events) and the data domain for this classification. However, there are MTDs in Unit 2 that fall in the attached classification domain, and several others within overlapping values for these classifications. It is also possibile that some of the larger MTDs, appearing to be detached under the current slope configurations, would have been classified as attached at the time of deposition (e.g., MTD 15). For instance, considering that the Mid-Eocene is marked by a wide marine regression (Fiduk et al., 2004), the paleo-shelf and slope could have been located further southeast when the

MTDs were being deposited, but we cannot confirm this detail. Where the current data limits for the detached/attached classification may be problematic is with MTD 14. This has a detached origin (see Gamboa et al., 2011) but its very large dimension plots within the attached field. Instead of just stating any inappropriateness of a specific record-based classification scheme when singular elements seem to disagree, this issue can be tackled by adapting it to new data on MTD morphometrics. Understanding the geological context that led to the slope failure and ultimately controlled the flow and origin of individual MTDs is key to assess the appropriateness of any classification. These natural factors will always over-rule any classification method and probably the best solution is to update them using consistent methodologies while compiling databases for further comparison and analysis (for a further discussion on this the reader is referred to Clare et al., 2018).

Overall, we consider the classification schemes used in this study suitable and applicable. The general trends we obtained for Volume-Area relationships in our study, using 30 samples from the Espírito Santo Basin ($V=0.035A^{0.99}$, $R^2=0.8$), are not drastically different to the detached MTDs sample in Moscardelli and Wood (2016) with 119 samples from various basins and locations ($V=0.026A^{1.1}$, $R^2=0.8$). The classification in Gamboa & Alves (2016) also proved applicable to (currently) proximal areas of slopes in the ESB (MTDs 1 and 2). Considered to preferentially occur as detached features flanking structures, MTDs with L/W ratios <1 in slope locations with similar characteristics similar geneses and internal deformation. What can be limiting is the vague current nomenclature for type 1 and type 2. These do not include any readily distinctive terms, and 'Type X' has been applied for different classifications in MTDs in specific case studies (e.g. Ortiz-Karpf, 2017; Maselli and Kneller, 2018). However, the classification in Gamboa and Alves (2016) is applicable to MTDs observed in the distal domains of the Gulf of Mexico (Madof et al., 2009) and off West Africa (Maia, 2018). The approach of using the ratios between MTD length and width is also better suited, especially when headwalls are absent. Based on the orientation of the MTD longest axis relative to the length orientation, we propose the use of longitudinal MTDs instead of type 1 MTDs (L/W >1) and transverse to replace type 2 MTDs (L/W <2). This terminology is clearer and useful in forthcoming work.

14.6. CONCLUSIONS

The mass-transport deposits in the Espírito Santo Basin exhibit a wide variety of internal complexity and sizes across the slope. The following points summarise our observations:

• Thirty (30) MTDs where interpreted in three distinct areas of the continental slope, each associated with a specific style of salt tectonics. This ranged from an extensional proximal area, a transitional area with circular diapirs, and a compressional distal area with elongated salt ridges.

• MTDs are distributed within three main seismic-stratigraphic units. MTDs in the lower Unit 1 are scarcer and more localized, often associated with paleo-structures. MTDs deposited in Unit 2 are some of the larger examples observed, and this type of deposits can constitute over 60% of the unit's sedimentary accumulations. MTDs in Unit 2 occur over the whole width of the continental slope. MTDs in Unit 3 are widespread, although with smaller dimensions, and show a strong control of existing salt topography on their genesis and flow path.

• Salt tectonics and associated structures play varied roles on MTD genesis and character through time. Unit 1 MTDs commonly interact with crestal faults linked to salt structures, and these also influence the lowermost MTDs in Unit 2. Episodes of salt growth are interpreted to occur towards the late Eocene-Oligocene, indicated by the changes in MTD deposition throughout Unit 2. MTDs in Unit 3 are the most influenced by salt structures, either as triggers or flow controls.

• MTD morphometrics show a clear and expected decrease in their size from proximal to distal domains. However, the stratigraphic units in which MTDs occur also influence these trends. Comparisons of MTD metrics with size-based classification schemes show a good fit to detached MTD classifications for the majority of the examples studied, but some ambiguity may rise for very large detached MTDs, which could be classified as attached. The geological context at the time of deposition is crucial to assess this latter type.

• We proposed a renamed classification based on the orientation of MTD's longest axes in relation to their length. Hence, Longitudinal MTDs comprise elongated deposits with L/W ratios >1, and Transverse MTDs refer to widened deposits with L/W ratios <1.

ACKNOWLEDGEMENTS

D. Gamboa thanks the Sêr Cymru National Research Network for Low Carbon Energy and Environment for financial support, and publishes with the permission of the Executive Director, British Geological Survey. We thank the editors, V. Maselli and an anonymous reviewer for their constructive comments to improve this manuscript.

REFERENCES

Alves, T. M. (2012). Scale-relationships and geometry of normal faults reactivated during gravitational gliding of Albian rafts (Espírito Santo Basin, SE Brazil). *Earth and Planetary Science Letters*, *331–332*(0), 80–96.

Alves, T. M. (2015). Submarine slide blocks and associated soft-sediment deformation in deep-water basins: A review. *Marine and Petroleum Geology*, *67*, 262–285.

Alves, T. M., Cartwright, J., & Davies, R. J. (2009). Faulting of salt-withdrawal basins during early halokinesis: Effects on the Paleogene Rio Doce Canyon system (Espírito Santo Basin, Brazil). *AAPG Bulletin*, *93*(5), 617–652.

Alves, T. M., & Cartwright, J. A. (2009). Volume balance of a submarine landslide in the Espírito Santo Basin, offshore Brazil: Quantifying seafloor erosion, sediment accumulation and depletion. *Earth and Planetary Science Letters*, *288*(3–4), 572–580.

Alves, T. M., & Cartwright, J. A. (2010). The effect of mass-transport deposits on the younger slope morphology, offshore Brazil. *Marine and Petroleum Geology*, *27*(9), 2027–2036.

Barker, P. F., Buffler, R. T., & Gambôa, L. A. (1983). A seismic reflection study of the Rio Grande Rise. In P. F. Barker, R. L. Carlson, & D. A. Hohnson (Eds.), *Initial reports of the Deep Sea Drilling Program* (pp. 953–976). Washington, DC: Government Printing Office.

Baudon, C., & Cartwright, J. (2008). The kinematics of reactivation of normal faults using high resolution throw mapping. *Journal of Structural Geology*, *30*(8), 1072–1084.

Beaubouef, R. T., & Abreu, V. (2010). MTCs of the Brazos-Trinity slope system; thoughts on the sequence stratigraphy of MTCs and their possible roles in shaping hydrocarbon traps. In D. C. Mosher, R. C. Shipp, L. Moscardelli, J. D. Chaytor, C. D. P. Baxter, H. J. Lee, & R. Urgeles (Eds.), *Submarine mass movements and their consequences* (pp. 475–490). Dordrecht, The Netherlands: Springer.

Brown, A. R. (2004). *Interpretation of three-dimensional seismic data, AAPG Memoir* (6th ed., Vol. 42). Tulsa, OK: American Association of Petroleum Geologists.

Bruhn, C. H. L., & Walker, R. G. (1997). Internal architecture and sedimentary evolution of coarse-grained, turbidite channel-levee complexes, early eocene Regência canyon, Espirito Santo Basin, Brazil. *Sedimentology*, *44*(1), 17–46.

Bull, S., Cartwright, J., & Huuse, M. (2009). A review of kinematic indicators from mass-transport complexes using 3D seismic data. *Marine and Petroleum Geology*, *26*(7), 1132–1151.

Clare, M., Chaytor, J., Dabson, O., Gamboa, D., Georgiopoulou, A., Eady, H., et al. (2018). *A consistent global approach for the morphometric characterization of subaqueous landslides, Special Publications* (Vol. 477). London, UK: Geological Society.

Coleman, J. M., & Prior, D. B. (1988). Mass wasting on continental margins. *Annual Review of Earth and Planetary Sciences*, *16*(1), 101–119.

Davison, I. (2007). Geology and tectonics of the South Atlantic Brazilian salt basins. In A. C. Ries, R. W. H. Butler, & R. H. Graham (Eds.), *Deformation of the continental crust: The legacy of Mike Coward, Special Publications* (Vol. 272, pp. 345–359). London, UK: Geological Society.

Davison, I., Alsop, G. I., Evans, N. G., & Safaricz, M. (2000). Overburden deformation patterns and mechanisms of salt diapir penetration in the Central Graben, North Sea. *Marine and Petroleum Geology*, *17*(5), 601–618.

Demercian, S., Szatmari, P., & Cobbold, P. R. (1993). Style and pattern of salt diapirs due to thin-skinned gravitational gliding, Campos and Santos basins, offshore Brazil. *Tectonophysics*, *228*(3–4), 393–433.

Elliott, G. M., Shannon, P. M., Haughton, P. D. W., & Øvrebø, L. K. (2010). The Rockall Bank Mass Flow: Collapse of a moated contourite drift onlapping the eastern flank of Rockall Bank, west of Ireland. *Marine and Petroleum Geology*, *27*(1), 92–107.

Fainstein, R., & Summerhayes, C. P. (1982). Structure and origin of marginal banks off Eastern Brazil. *Marine Geology*, *46*(3–4), 199–215.

Fiduk, J. C., Brush, E. R., Anderson, L. E., Gibbs, P. B., & Rowan, M. G. (2004). Salt deformation, magmatism, and hydrocarbon prospectivity in the Espirito Santo Basin, offshore Brazil. In P. J. Post, D. L. Olson, K. T. Lyons, S. L. Palmes, P. F. Harrison, & N. C. Rosen (Eds.), *Salt-sediment interactions and hydrocarbon prospectivity: Concepts, applications, and case studies for the 21st century. GCSSEPM 24th Annual Research Conference* (pp. 370–392). Tulsa, OK: SEPM.

França, R. L., Del Rey, A. C., Tagliari, C. V., Brandão, J. R., & Fontanelli, P. R. (2007). Bacia de Espírito Santo. *Boletim de Geociencias da Petrobras*, *15*(2), 501–509.

Frey-Martínez, J., Cartwright, J., & James, D. (2006). Frontally confined versus frontally emergent submarine landslides: A 3D seismic characterisation. *Marine and Petroleum Geology*, *23*(5), 585–604.

Gafeira, J., Bulat, J., & Evans, D. (2007). The southern flank of the Storegga Slide: Imaging and geomorphological analysis using 3D Seismic. In V. Lykousis, D. Sakellariou, & J. Locat (Eds.), *Submarine mass movements and their consequences* (pp. 57–66). New York, NY: Springer.

Gamboa, D., Alves, T., & Cartwright, J. (2011). Distribution and characterization of failed (mega) blocks along salt ridges, southeast Brazil: Implications for vertical fluid flow on continental margins. *Journal of Geophysical Research*, *116*(B8), B08103.

Gamboa, D., Alves, T., Cartwright, J., & Terrinha, P. (2010). MTD distribution on a 'passive' continental margin: The Espírito Santo Basin (SE Brazil) during the Palaeogene. *Marine and Petroleum Geology*, *27*(7), 1311–1324.

Gamboa, D., & Alves, T. M. (2015a). Spatial and dimensional relationships of submarine slope architectural elements: A seismic-scale analysis from the Espírito Santo Basin (SE Brazil). *Marine and Petroleum Geology*, *64*, 43–57.

Gamboa, D., & Alves, T. M. (2015b). Three-dimensional fault meshes and multi-layer shear in mass-transport blocks: Implications for fluid flow on continental margins. *Tectonophysics*, *647–648*, 21–32.

Gamboa, D., & Alves, T. M. (2016). Bi-modal deformation styles in confined mass-transport deposits: Examples from a salt minibasin in SE Brazil. *Marine Geology*, *379*, 176–193.

Gamboa, D., Alves, T. M., & Cartwright, J. (2012). A submarine channel confluence classification for topographically confined slopes. *Marine and Petroleum Geology*, *35*(1), 176–189.

GEBCO (2014). GEBCO_2014 Grid, version 20150318. www.gebco.net.

Gee, M. J. R., Gawthorpe, R. L., & Friedmann, S. J. (2006). Triggering and evolution of a giant submarine landslide, offshore angola, revealed by 3D seismic stratigraphy and geomorphology. *Journal of Sedimentary Research*, *76*(1), 9–19.

Giles, K. A., & Lawton, T. F. (2002). Halokinetic sequence stratigraphy adjacent to the El Papalote diapir, northeastern Mexico. *AAPG Bulletin*, *86*(5), 823–840.

Hampton, M. A., Lee, H. J., & Locat, J. (1996). Submarine Landslides. *Review of Geophysics*, *34*(1), 33–59.

Laberg, J. S., & Camerlenghi, A. (2008). The significance of contourites for submarine slope stability. In M. Rebesco & A. Camerlenghi (Eds.), *Contourites* (pp. 537–556). Oxford, UK: Elsevier.

Love, F., Brush, E. R., Fiduk, J. C., Gibbs, P., Brink-Larsen, S., & Farrow, G. (2005). Northern Espírito Santo basin canyon models ancient sand transport. *Offshore*, *65*(3), 74–78.

Madof, A. S., Christie-Blick, N., & Anders, M. H. (2009). Stratigraphic controls on a salt-withdrawal intraslope minibasin, north-central Green Canyon, Gulf of Mexico: Implications for misinterpreting sea level change. *AAPG Bulletin*, *93*(4), 535–561.

Maia, A., 2018. Controls on shallow plumbing systems inferred from the spatial analysis of pockmark arrays (PhD Thesis). Cardiff: Cardiff University.

Maselli, V., & Kneller, B. (2018). Bottom currents, submarine mass failures and halokinesis at the toe of the Sigsbee Escarpment (Gulf of Mexico): Contrasting regimes during lowstand and highstand conditions? *Marine Geology*, *401*, 36–65.

Mattos, N. H., & Alves, T. M. (2018). Corridors of crestal and radial faults linking salt diapirs in the Espírito Santo Basin, SE Brazil. *Tectonophysics*, *728*, 55–74.

Mohriak, W. U. (1995). Salt tectonics structural styles: Contrasts and similarities between the South Atlantic and the Gulf of Mexico. In P. J. Post, D. L. Olson, K. T. Lyons, S. L. Palmes, P. F. Harrison, & N. C. Rosen (Eds.), *Salt-sediment interactions and hydrocarbon prospectivity: Concepts, applications, and case studies for the 21st century. 24th Annual GCSSEPM Foundation Bob F. Perkins Research conference, Houston, Texas* (Vol. 16, pp. 177–191). Tulsa, OK: SEPM.

Mohriak, W. U. (2003). Bacias sedimentares da margem continental Brasileira. In L. A. Bizzi, C. Schobbenhaus, R. M. Vidotti, & J. H. Goncalves (Eds.), *Geologia, Tectonica e Recursos Minerais do Brasil* (pp. 87–165). Brasilia, Brazil: CPRM.

Moreira, J. L. P., & Carminatti, M. (2004). Sistemas deposicionais de talude e de bacia no Eoceno da Bacia de Santos. *Boletim de Geociencias da Petrobras*, *12*(1), 73–87.

Moscardelli, L., & Wood, L. (2016). Morphometry of mass-transport deposits as a predictive tool. *Geological Society of America Bulletin*, *128*(1–2), 47–80.

Mountjoy, J. J., Pecher, I., Henrys, S., Crutchley, G., Barnes, P. M., & Plaza-Faverola, A. (2014). Shallow methane hydrate system controls ongoing, downslope sediment transport in a low-velocity active submarine landslide complex, Hikurangi Margin, New Zealand. *Geochemistry, Geophysics, Geosystems*, *15*(11), 4137–4156.

Nisbet, E. G., & Piper, D. J. (1998). Giant submarine landslides. *Nature*, *392*(6674), 329.

O'Leary, D. (1991). Structure and morphology of submarine slab slides: Clues to origin and behavior. *Marine Georesources & Geotechnology*, *10*(1–2), 53–69.

Omosanya, K. D. O., & Alves, T. M. (2013a). Ramps and flats of mass-transport deposits (MTDs) as markers of seafloor strain on the flanks of rising diapirs (Espírito Santo Basin, SE Brazil). *Marine Geology*, *340*, 82–97.

Omosanya, K. D. O., & Alves, T. M. (2014). Mass-transport deposits controlling fault propagation, reactivation and structural decoupling on continental margins (Espírito Santo Basin, SE Brazil). *Tectonophysics*, *628*, 158–171.

Omosanya, K. O., & Alves, T. M. (2013b). A 3-dimensional seismic method to assess the provenance of Mass-Transport Deposits (MTDs) on salt-rich continental slopes (Espírito Santo Basin, SE Brazil). *Marine and Petroleum Geology*, *44*, 223–239.

Ortiz-Karpf, A., Hodgson, D. M., Jackson, C. A. L., & McCaffrey, W. D. (2017). Influence of seabed morphology and substrate composition on mass-transport flow processes and pathways: Insights from the Magdalena Fan, offshore Colombia. *Journal of Sedimentary Research*, *87*(3), 189–209.

Ortiz-Karpf, A., Hodgson, D. M., Jackson, C. A. L., & McCaffrey, W. D. (2018). Mass-transport complexes as markers of deep-water fold-and-thrust belt evolution: Insights from the southern Magdalena fan, offshore Colombia. *Basin Research*, *30*(S1), 65–88.

Paull, C. K., Buelow, W. J., Ussler, W., III, & Borowski, W. S. (1996). Increased continental-margin slumping frequency during sea-level lowstands above gas hydrate–bearing sediments. *Geology*, *24*(2), 143–146.

Pickering, K. T., & Corregidor, J. (2005). Mass-transport complexes (MTCs) and tectonic control on basin-floor submarine fans, middle Eocene, south Spanish Pyrenees. *Journal of Sedimentary Research*, *75*(5), 761–783.

Posamentier, H., & Martinsen, O. J. (2011). The character and genesis of submarine mass-transport deposits: Insights from outcrop and 3D seismic data. In C. Shipp, P. Weimer, & H. Posamentier (Eds.), *Mass-transport deposits in deepwater settings, SEPM Special Publication* (Vol. 96, pp. 7–38). Tulsa, OK: SEPM.

Qin, Y., Alves, T. M., Constantine, J., & Gamboa, D. (2017). The role of mass wasting in the progressive development of submarine channels (Espírito Santo Basin, Se Brazil). *Journal of Sedimentary Research*, *87*(5), 500–516.

Schreiner, S., de Souza, M. B. F. M., & Migliorelli, J. P. R. (2009). Modelo digital da geomorfologia do fundo oceânico do centro-sul da Bacia do Espírito Santo e norte da Bacia de Campos. *Boletim de Geociencias da Petrobras*, *17*(2), 365–369.

Tripsanas, E. K., Bryant, W. R., & Phaneuf, B. A. (2004). Slope-instability processes caused by salt movements in a complex deep-water environment, Bryant Canyon area, northwest Gulf of Mexico. *AAPG Bulletin*, *88*(6), 801–823.

Ward, N. I., Alves, T. M., & Blenkinsop, T. G. (2018). Submarine sediment routing over a blocky mass-transport deposit in the Espírito Santo Basin, SE Brazil. *Basin Research*, *30*(4), 816–834.

Weimer, P. (1990). Sequence stratigraphy, facies geometries, and depositional history of the Mississippi Fan, Gulf of Mexico. *AAPG Bulletin*, *74*(4), 425–453.

Weimer, P., & Shipp, C. (2004). Mass transport complex: Musing on the past uses and suggestions for future directions. Paper presented at the Offshore Technology Conference, Houston, TX.

15

Submarine Landslides on the Nankai Trough Accretionary Prism (Offshore Central Japan)

Gregory F. Moore[1], Jason K. Lackey[1], Michael Strasser[2], and Mikiya Yamashita[3]

ABSTRACT

The Nankai accretionary prism is a prime example of sedimentation controlled by active subduction tectonics. The largest landslide, located where the Kinan Seamount Chain is subducting, is an ~100 × 100 km composite feature that is cut by many smaller secondary landslides. East of the Kinan collision zone, there are at least four smaller, recent slump scars with surficial mass-transport deposits (MTDs) at the toe of the prism. The outer accretionary prism is cut by >800 landslides that are 3–5 km wide and displace surficial slope sediments as well as several tens of meters of the underlying accreted material. The maximum slide volume on the outer prism is ~115 km^3, but most of the slides are <10 km^3. Many of these landslides are due to disintegration of hanging wall anticlines at the tips of accretionary thrusts, and others are caused by seamounts subducting under the prism. The forearc basin has several young 3–5 km wide landslides that are associated with recent normal faults. There are also several older buried landslides in the forearc basin. Only a few of the prism landslides were likely to have created regional tsunamis, because most evacuate <1 km^3 of material.

15.1. INTRODUCTION

Large-scale landsliding is a common process in actively deforming accretionary prisms (e.g., Hampton et al., 1996). The underlying cause of most of the landslides is active compression that generates uplift along thrust faults, creating steep slopes and unstable hanging wall anticlines (e.g., Lackey et al., 2018a; Strasser et al., 2011; Yamada et al., 2010). The resulting submarine landslides are thus a form of tectonically controlled sedimentation that dominates the outer accretionary prism (e.g., Mannu et al., 2016).

Another major cause of large submarine landslides along the lower slopes of many convergent margins is seamounts that are carried into the trench and under the trench landward slope. The compression and uplift caused by the subducting topography lead to gravitational instability and collapse. Examples are along the Middle America Trench off Costa Rica (von Huene, 2008; von Huene et al. 2000, 2004), the Peru-Chile Trench (von Huene et al., 1989), the Japan Trench (Lallemand & Le Pinchon, 1987), and the Hikurangi margin (Pedley et al., 2010). Analogue and numerical models of seamount collisions with accretionary systems have reproduced the main features of observed upper plate deformation (Dominguez et al., 1998; Lallemand et al., 1994; Ruh, 2016).

Quaternary landslides on the Nankai Trough outer accretionary wedge have occurred at the frontal thrust (Kawamura et al., 2010, 2012; Screaton et al., 2009), in trench slope basins (Kanamatsu et al., 2014; Kimura et al., 2011; Moore et al., 2014; Strasser et al., 2011, 2012), and in the forearc basin (FAB) (Lackey et al., 2018b; Moore & Strasser, 2016). Large landslides on active margin slopes are capable of generating destructive

[1] *Department of Earth Sciences, University of Hawaii, Honolulu, Hawaii, United States*

[2] *Institute of Geology, University of Innsbruck, Innsbruck, Austria*

[3] *Japan Agency for Marine-Earth Science and Technology (JAMSTEC), Yokohama, Japan*

Submarine Landslides: Subaqueous Mass Transport Deposits from Outcrops to Seismic Profiles, Geophysical Monograph 246, First Edition. Edited by Kei Ogata, Andrea Festa, and Gian Andrea Pini.
© 2020 American Geophysical Union. Published 2020 by John Wiley & Sons, Inc.

tsunamis that can devastate nearby coastal communities (e.g., Bardet et al., 2003; Kawamura et al., 2014; Satake, 2012; Tappin, 2010). It is likely that some of the Nankai Trough landslides fall into this category.

In this chapter, we identify recent submarine landslides that occur at multiple scales along the Nankai Trough accretionary prism along the southern margin of Japan, quantify their dimensions, and document their characteristics.

15.2. GEOLOGIC AND TECTONIC SETTING

The Nankai Trough marks the plate boundary between the subducting Philippine Sea Plate (PSP) and the Eurasian Plate (Figure 15.1). The PSP is currently subducting to the northwest at a rate of ~4.1–6.5 cm/yr (Miyazaki & Heki, 2001; Seno et al., 1993), with the convergence direction slightly oblique to the trench. Sediment accretion has been ongoing since at least the Cretaceous (Taira, 2001). Currently, all the trench sediments and at least half of the underlying sedimentary section of the Shikoku Basin (northern PSP) are being accreted, forming a wide accretionary prism (e.g., Aoki et al., 1982; Moore et al., 1990, 2001). Out-of-sequence thrusting along a regional megasplay fault (Moore et al., 2007; Park et al., 2002) has uplifted a broad ridge (Gulick et al., 2010; Moore et al., 2015), behind which several isolated FABs have formed (Okino & Kato, 1995). The only well-dated FAB, the Kumano FAB south of Kii Peninsula, was initiated ~1.95–2.0 Ma on a basement of deformed upper Miocene and older accretionary prism rocks unconformably overlain by lower Pliocene trench slope deposits (Kinoshita et al., 2009). The basin strata are cut by numerous normal faults, many of which offset the seafloor (Gulick et al., 2010; Moore et al., 2009; Park et al., 2002).

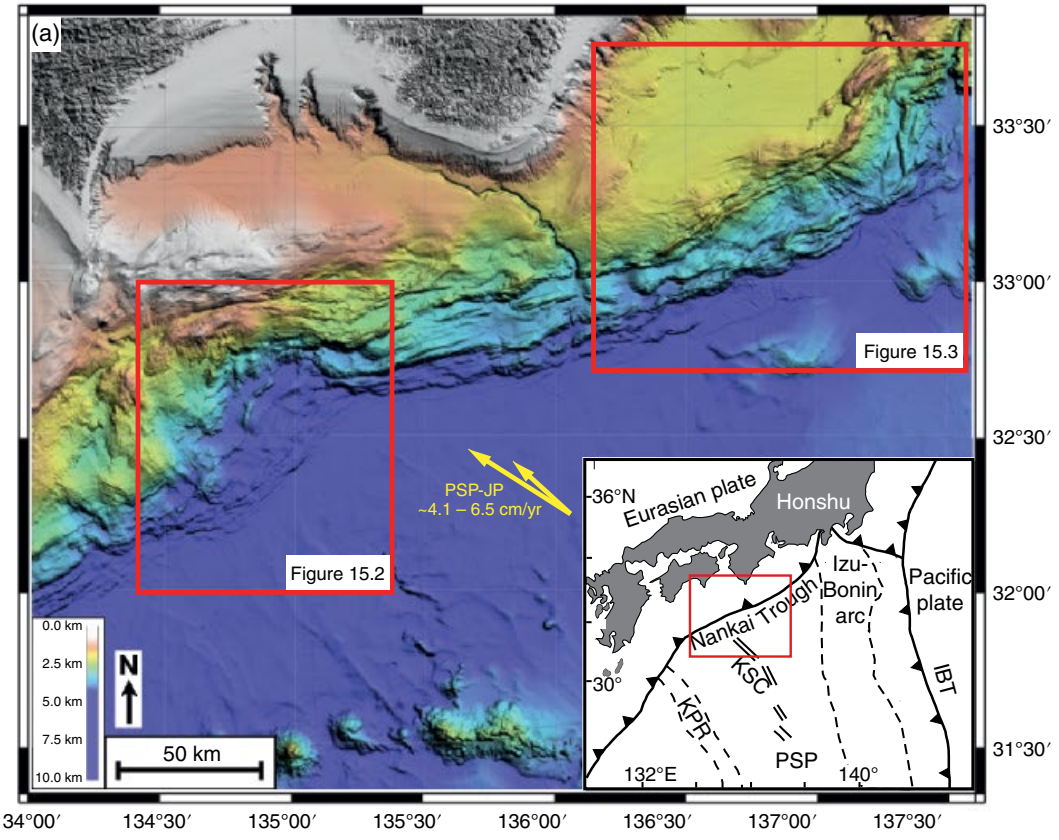
The subducting PSP is characterized by regional and local variations in basement relief, sediment thickness, and sediment type (Ike et al., 2008a, 2008b). The largest region of basement topography is the Kinan Seamount Chain (KSC), which developed contemporaneously with, or just after, cessation of spreading in the Shikoku Basin at ~15 Ma (e.g., Kobayashi et al., 1995; Okino et al., 1994). Subduction of basement highs is known to cause significant deformation in the upper plate (e.g., von Huene, 2008), and subducted seamounts have been imaged under the Nankai forearc region (Kodaira et al., 2000; Park et al., 1999). Yamazaki and Okamura (1989) first proposed that the Tosabae Embayment (Figure 15.1) was formed by collision with a subducting seamount chain.

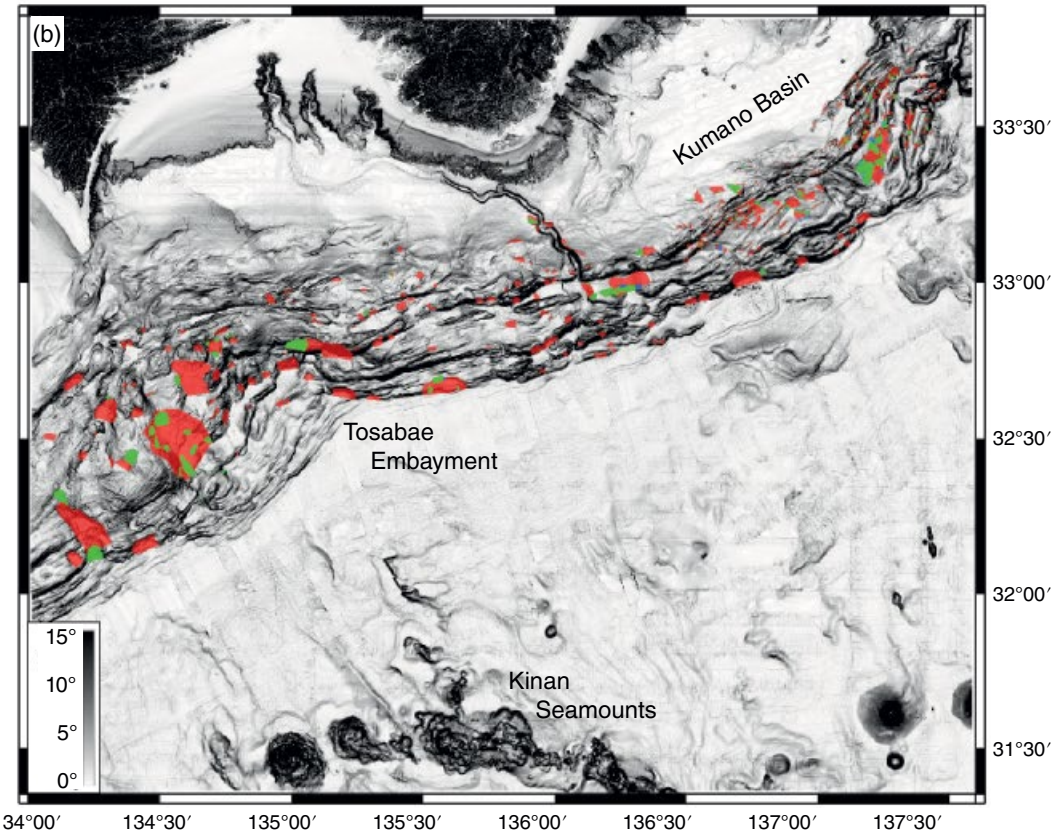
15.3. DATA AND METHODS

We used a regional multibeam echosounder (MBES) bathymetry compilation to identify surficial landslides along the Nankai Trough. The original compilation was made in 2006 from cruises of the Japan Agency for Marine-Earth Science and Technology (JAMSTEC) that used SeaBeam 2112 systems (beam angle of 2.67° × 2.67°) and was gridded at 100 m × 100 m resolution in latitude and longitude using MB-System 5.4 software (Caress & Chayes, 2008). An updated compilation by JAMSTEC used data from more recent cruises in the western part of the area (south of Shikoku Island). We also added higher-resolution MBES data from the Kumano Basin area that were acquired with a 0.5° × 1° Simrad EM122 multibeam system during R/V *Sonne* expedition 251 in October 2016 (Strasser et al., 2017). These newer bathymetric data were gridded in 30 m × 30 m cells. Slope maps were created from the bathymetric data to enhance landslide features.

We used headwall scarps as the primary feature for visual identification of landslides (Lackey et al., 2018a). Scarps are easily resolved in the bathymetry data because they usually have an inverted "U" shape pointing downslope, are tens to hundreds of meters high, and have slopes that generally exceed 10° that are well defined in the slope maps. Each landslide's extent was determined by tracing the "U" shape of the headwall and sidewall scarps and by identifying the toe of the deposit where possible. Tracing was performed manually using polygons in the Global Mapper software package. The color assigned to each landslide polygon on the maps corresponds to their position in the landslide hierarchy (Figures 15.1–15.3): Primary (red, the initial slope failure in a given location), secondary (green, occurs either downslope within the primary landslide's scar or as an upslope event that cuts across the primary landslide scar), or tertiary (blue, any other landslide that cuts across secondary landslides), after Katz et al. (2015). The secondary and tertiary landslides are mostly retrogressive slides with extensional failure that drove successive scarp formation updip (e.g., Sawyer et al., 2009).

Figure 15.1 Regional bathymetry of the Kumano Basin region of the Nankai Trough. (a) Shaded relief map showing locations of detailed maps in Figures 15.2 and 15.3 (red boxes). Yellow arrows, estimated far-field vectors for motion of Philippine Sea Plate (PSP) with respect to Japan (JP; Heki, 2007; Seno et al., 1993). Inset shows regional tectonic setting. Red box shows location of main map. IBT, Izu-Bonin Trench; KSC, Kinan Seamount Chain; PSP, Philippine Sea Plate; KPR, Kyushu-Palau Ridge. (b) Slope map with mapped landslides. Red primary landslides; green secondary landslides; blue, tertiary landslides. Source: Adapted from Heki (2007) and Seno et al. (1993). (*See electronic version for color representation of this figure*)


(a)
Figure 15.3
Figure 15.2
PSP-JP
~4.1 – 6.5 cm/yr
0.0 km
2.5 km
5.0 km
7.5 km
10.0 km
N
50 km
36°N
Eurasian plate
Honshu
Izu-Bonin arc
Pacific plate
Nankai Trough
KSC
KPR
PSP
IBT
30°
132°E
140°
33°30′
33°00′
32°30′
32°00′
31°30′
34°00′
134°30′
135°00′
135°30′
136°00′
136°30′
137°00′
137°30′


(b)
Kumano Basin
Tosabae Embayment
Kinan Seamounts
15°
10°
5°
0°
33°30′
33°00′
32°30′
32°00′
31°30′
34°00′
134°30′
135°00′
135°30′
136°00′
136°30′
137°00′
137°30′

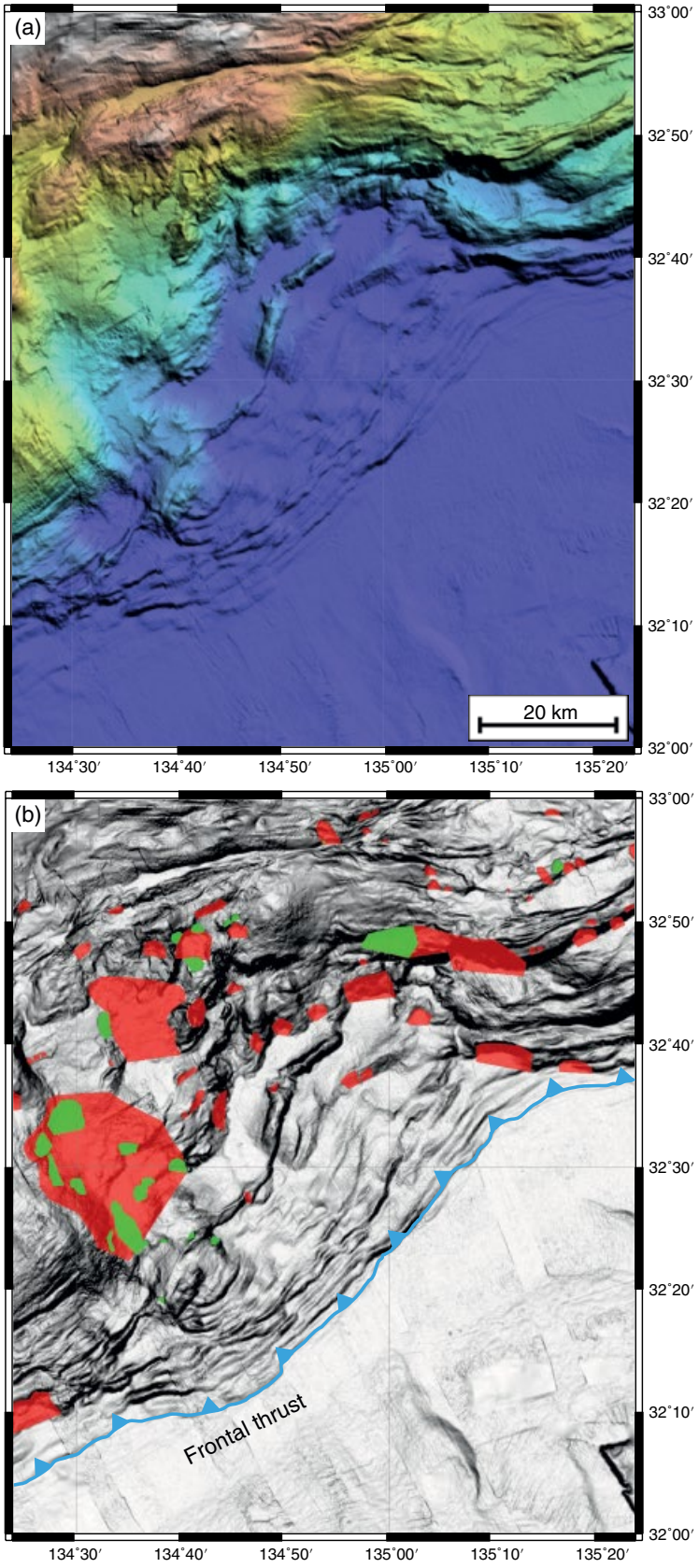


Figure 15.2 Bathymetry of Tosabae Embayment. (a) Shaded relief map. (b) Slope map showing mapped landslides. Red primary landslides; green secondary landslides; blue, tertiary landslides. (*See electronic version for color representation of this figure*)

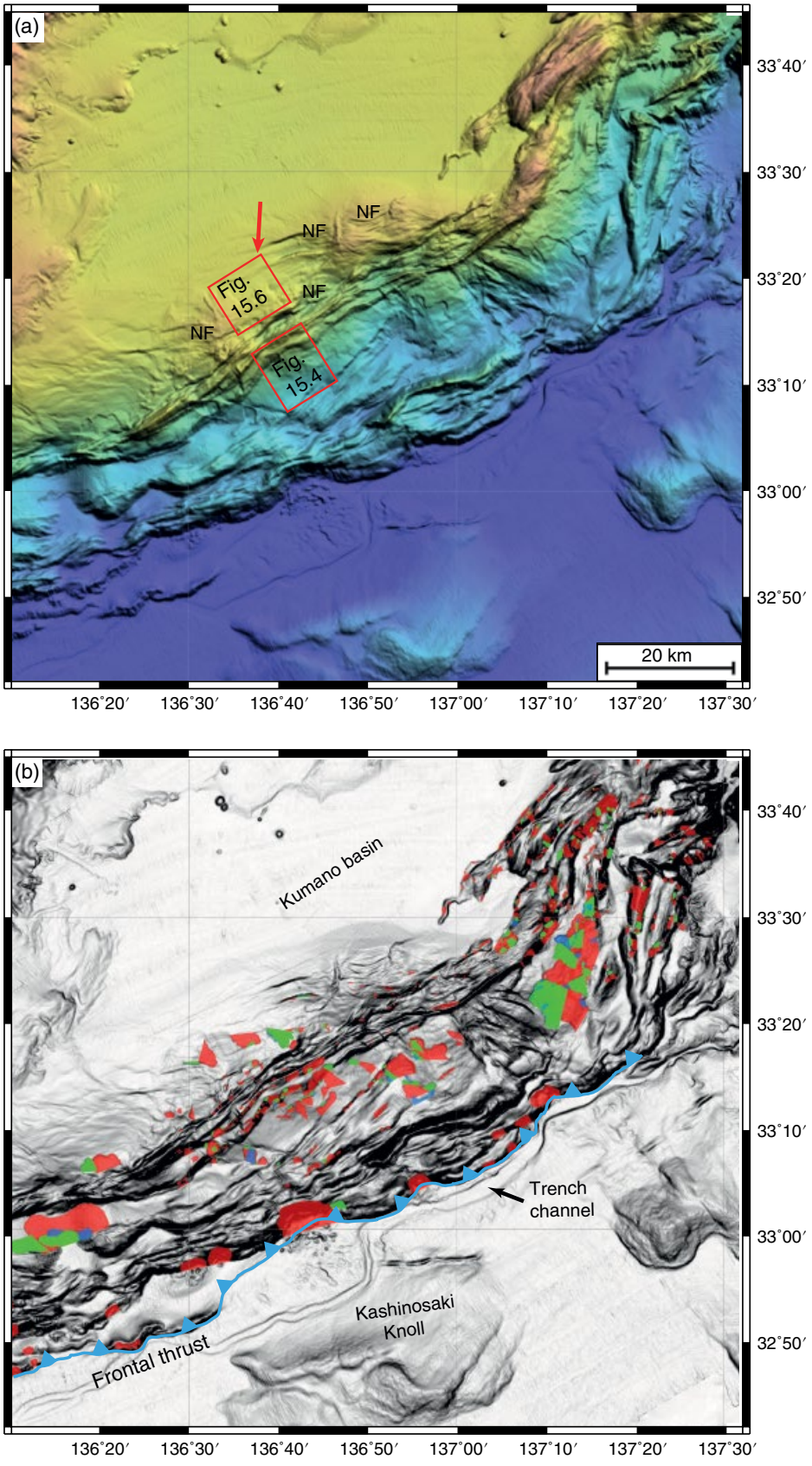


Figure 15.3 Bathymetry of Kumano Basin region. (a) Shaded relief map. Red boxes show locations of diagrams of Figures 15.4a and 15.6; arrow points in viewing direction of Figure 15.6. (b) Slope map showing mapped landslides. Red primary landslides; green secondary landslides; blue, tertiary landslides; NF, normal faults. (*See electronic version for color representation of this figure*)

Table 15.1 Nankai Trough Landslides

	Frontal Thrust	Outer Prism	Forearc Basin
Total number (914)	31	839	44
Primary (593)	25	541	27
Secondary (226)	5	210	11
Tertiary (95)	1	88	6
Deposit			
Yes	14	81	12
No	17	625	29
Area (km^2)			
Total	251	2185	64
Mean	8.1	2.6	1.45
Median	2.8	0.27	0.17
Min	0.4	0.005	0.006
Max	73.8	390.8	9.4
Volume (km^3)			
Total	17.4	229	0.96
Mean	0.56	0.27	0.02
Median	0.07	0.002	0.002
Min	0.003	<0.001	<0.001
Max	7.9	115.2	0.22

The following characteristics were then observed and/or calculated for each individual landslide (Table 15.1):

1. Location as measured by the visual center of the headwall scarp
2. Headwall scarp height and slope angle
3. Area as calculated from the area of the enclosed polygon
4. Hierarchy of each slide

To calculate a landslide's evacuated volume, the Global Mapper software uses the points defined along the perimeter of a given polygon to create a planar surface. This surface serves as the landslide area as well as the top of the calculated volume. Bathymetric data are then used to calculate the base of the volume. ten Brink et al. (2006) used a similar method to measure volumes of carbonate landslides from northern Puerto Rico.

Two- and three-dimensional (2D and 3D) seismic reflection data provide details of several of the landslides' internal structure. A regional 2D seismic data set, collected by JAMSTEC during cruises in 1995–2013, was supplemented by 3D seismic data cubes collected in the Muroto area in 1999 (Moore et al., 1999) and in the Kumano area in 2006 (Moore et al., 2009).

15.4. NANKAI ACCRETIONARY PRISM SUBMARINE LANDSLIDES

To describe the setting of the Nankai landslides, we divide the region into three tectonic provinces: frontal thrust, outer prism, and FAB. Overall, we mapped and characterized 914 surficial landslides, including >700 in the Kumano region (Lackey et al., 2018a) and an additional ~200 along the frontal thrust and on the prism to the southwest of the Kumano region (Table 15.1). The total area of failed slopes encompasses ~2500 km^2 with 10% (250 km^2) occurring along the frontal thrust, 87% (2185 km^2) on the frontal prism, and 3% (64 km^2) in the FABs. The largest single failure is 391 km^2, while the smallest is 0.005 km^2. Primary, secondary, and tertiary landslides account for 65% (593), 25% (226), and 10% (95) of the total landslides, respectively. Landslides displayed either a "simple" or "complex" overall structure (e.g., Katz et al., 2015). Simple landslides (53% (484) of those observed) are single events that result from a single slope failure, whereas complex landslides (47% (430) composed of 88 individual complex structures) result from a hierarchal pattern of multiple temporally sequential (retrogressive) slope failures.

Measurement errors of geomorphic parameters increase with increasing area, volume, and hierarchal complexity of each landslide. Headwall and sidewall scarps typically remain visible and mostly unchanged throughout sediment deposition. The calculated volume, however, can change during sediment deposition as the scar is infilled with new sediment. Additionally, remobilization of the top layers of sediment (tens to hundreds of centimeters) is likely to have occurred many times due to seismic activity (Ashi et al., 2014), thereby redistributing surficial sediment across scarps, altering their surface morphology, and introducing inaccuracies in area and volumetric measurements.

A lack of identifiable landslide deposits resulted in the full area of many landslides being unmeasurable. Only 243 (26.6%) of the landslides had deposits, indicating that the landslides are most often fully disintegrative, therefore necessitating area measurements to be made from the headwall scarp to the furthest observable sidewall scarps. Measurement accuracy is also hampered by fault structures that crosscut slide scars because the fault's interaction with the scar cannot be fully accounted for. This increases the complexity of the scar by geometrically distorting the evacuated volume and area.

A volumetric correction was required for 38 landslides, resulting in a total volume correction of 7.53 km^3 or 5.4%. Evacuated volume corrections for landslides that were part of complex structures were determined by subtracting secondary and/or tertiary volumes from the parent landslide. Because the Global Mapper volume calculation tool includes the volume of both the parent and secondary/tertiary landslides, it is necessary to exclude the volume of any subsequent landslides to accurately represent the volume data.

15.4.1. Prism Toe (Frontal Thrust)

The largest region of submarine landslides on the Nankai prism forms a large reentrant ~100 × 100 km that separates the Muroto and Kumano regions (Figures 15.1 and 15.2). This is where the KSC has been colliding with the Nankai prism (Yamazaki & Okamura, 1989). The embayment is a composite landslide comprising numerous smaller-scale secondary landslides that tend to be retrogressive in character that have occurred during passage of multiple subducting topographic highs. A large seamount with a steep scarp on the overriding prism was imaged by seismic reflection along the west flank of the main embayment (Park et al., 1999).

Four smaller-scale landslide scars occur at the toe of the frontal thrust in the Kumano area (Figure 15.3; Table 15.1). Three of the landslides produce mass-transport deposits (MTDs) that run out onto the floor of the Nankai Trough to distances of 3, 4, and 15 km and contain blocks ranging in size up to 100 m in width and 200 m in height (Kawamura et al., 2012). The trench axial channel was deflected ~12 km to the south by the largest MTD (Figure 15.3; Kawamura et al., 2010). The easternmost scar, surveyed with ROV *Kaiko*, is retrogressively shaped by subsequent small collapses that deposit smaller debris blocks (1–3 m in diameter) on top of the original MTD (Kawamura et al., 2012).

15.4.2. Outer Prism

Across the entire study area, most of the landslides (64%) occur seaward of the outer ridge (Figures 15.2 and 15.3). Diagnostic features of the surficial landslides are observed in bathymetric data (Figures 15.1–15.3; Ikari et al., 2011; Lackey et al., 2018a; Moore et al., 2007). The landslides range in surface area from ~4.7×10^{-3} km^2 to ~86 km^2. The mean area for all landslides is 0.83 km^2, while the median is 0.16 km^2. The large difference between these two values is indicative of a distribution that is positively skewed toward larger area values. Of the 718 landslides, only 94 (13%) were larger than 1 km^2, accounting for 458 km^2 of the 595 km^2 (77%) of failed slope area. Because of the skewed nature of the data, the median is the more accurate representation of the central tendency. The evacuated volume of landslides has a mean of 1.9×10^{-2} km^3 with a median of 9.7×10^{-4} km^3. Here again, the median is the more accurate central tendency representation because of the data exhibiting a skewed distribution. The most and least volumetric evacuations were 3.77 km^3 and 4.0×10^{-6} km^3, respectively, further demonstrating the wide range of landslides in the study area.

Along the Nankai Kumano transect, multiple lines of evidence exist for a range of sediment mass-movement processes seaward of the shallow megasplay fault zone (MSFZ) area and the adjacent trench slope basin. The surficial landslides discussed above are the main agents of sediment delivery to the slope basins. Buried landslides and their deposits in the basins are imaged in 3D reflection seismic data (Figure 15.4; Alves et al., 2014a, 2014b; Kimura et al., 2011; Strasser et al., 2011) and have been recovered from cores drilled by the Integrated Ocean Drilling Program (IODP) (Figure 15.5; Strasser et al., 2012, 2014) documenting a multifarious mass-movement history spanning >1 Ma (Kremer et al., 2017; Strasser et al., 2011, 2012). The largest MTD has a maximum thickness of 182 m and a volume of ~2 km^3 (Strasser et al., 2011). The entire section of this MTD has been completely logged and cored by scientific ocean drilling during IODP expeditions 333 and 338 (Strasser et al., 2012, 2014). Results from sample and data analyses following these expeditions constrain timing and dynamics of large submarine landslide processes in this outer accretionary prism setting and highlight the role of:

1. coarse-grained volcanic ash at the base of the landslide susceptible for liquefaction and accelerated motion during earthquake ground shaking (Sassa et al., 2012);
2. shear localization near the basal sliding plane (Kitamura et al., 2014);
3. initial sediment layering and shear-induced mixing during landslide processes on flow transformation from cohesive slumps to mud flows within short transport distances (Laberg et al., 2016);
4. active anticlinal structure beneath the MTD on the formations of erosional and ramp features during landslide emplacements (thus suggesting that the latter may not be fully reliable as kinematic indicators of the landslide itself (Alves et al., 2014a);
5. local tectonic evolution of the accretionary wedge controlling slope geometry, gradient, and susceptibility to earthquake ground motion and eventually resulting in different flow types and directions of MTD emplacements (Kanamatsu et al., 2014); and
6. the six stacked MTDs occurred over the past ~0.86 Ma (Kremer et al., 2017) which may be the record of previous retrogressive failures.

Interestingly, IODP coring and dating the MTD stratigraphic succession also reveals that the recurrence interval of large MTDs is longer by several orders of magnitude than large earthquakes in the Nankai region.

15.4.3. Forearc Basin

Within the Kumano FAB, both surficial and buried landslides are imaged in our 3D data set (Figure 15.6; Lackey et al., 2018b; Moore & Strasser, 2016). A recent large rotational slump occurs at the seafloor along the NE margin of the 3D survey area (Figure 15.6). The basal sliding surface is developed along a bedding plane

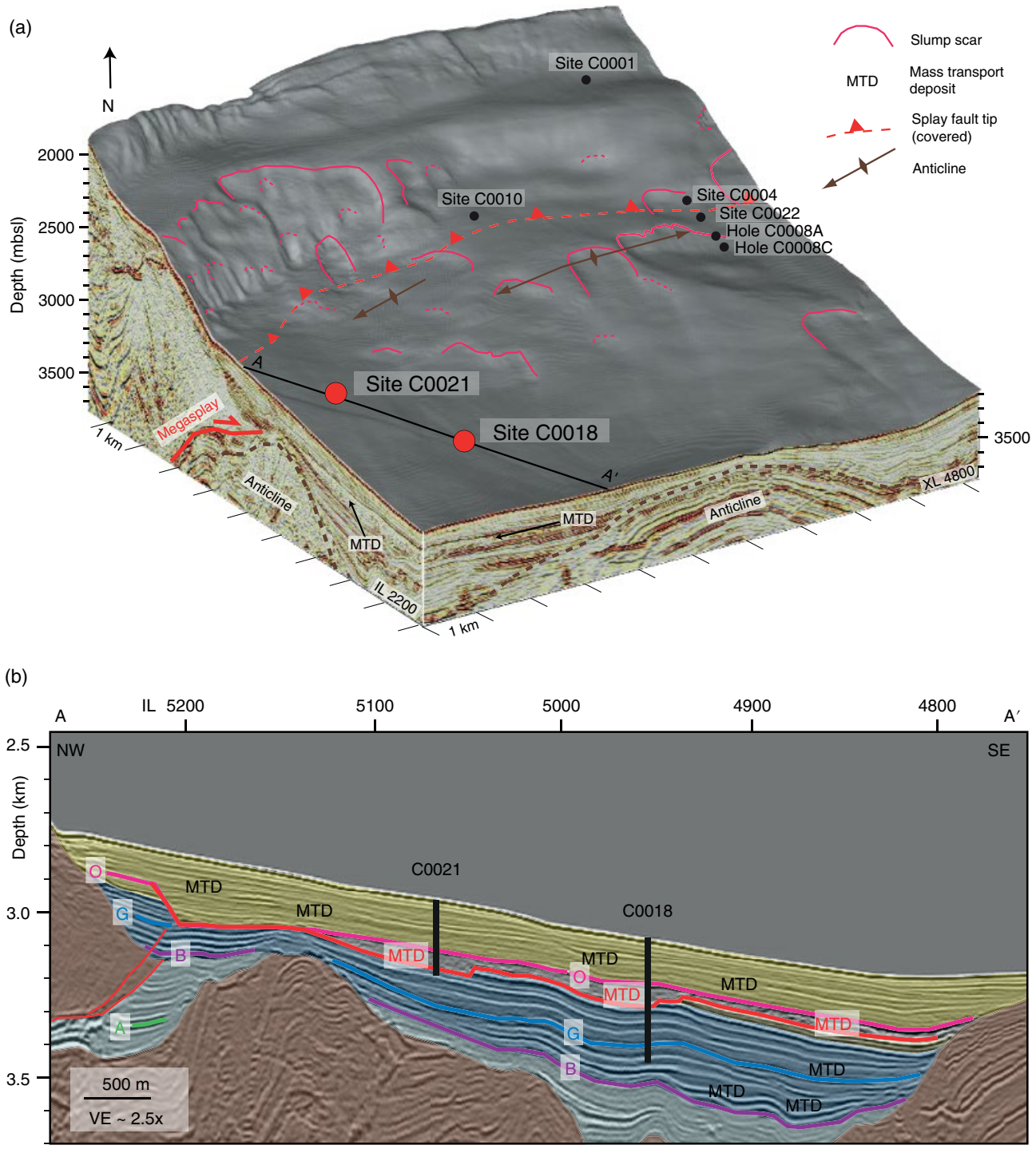


Figure 15.4 (a) Detailed surface morphology and structure of the slope basin at the footwall of the splay fault (Strasser et al., 2011) showing IODP sites that targeted MTDs (red) in relation to other IODP sites (black). Solid black lines, locations of seismic line A–A′ in (b). MTD, mass-transport deposit; IL, in-line; XL, crossline of 3D seismic data (Moore et al., 2009); Source: Figure modified after Moore et al. (2014). (b) Seismic profile of an arbitrary line extracted from the 3D seismic volume (Moore et al., 2009; XL/IL 2177/5273-2400/4751) and its interpretation showing a transect across the slope basin stratigraphic succession intercalated with several MTDs emplaced seaward of the megasplay fault zone area. Location of the line and IODP sites is shown in (a). Horizontal axis indicates crossline numbers. Colors for interpretation and labels of seismic-stratigraphic horizons after Strasser et al., 2011. Source: Modified after Strasser et al. (2011). © 2011 John Wiley and Sons. (*See electronic version for color representation of this figure*)

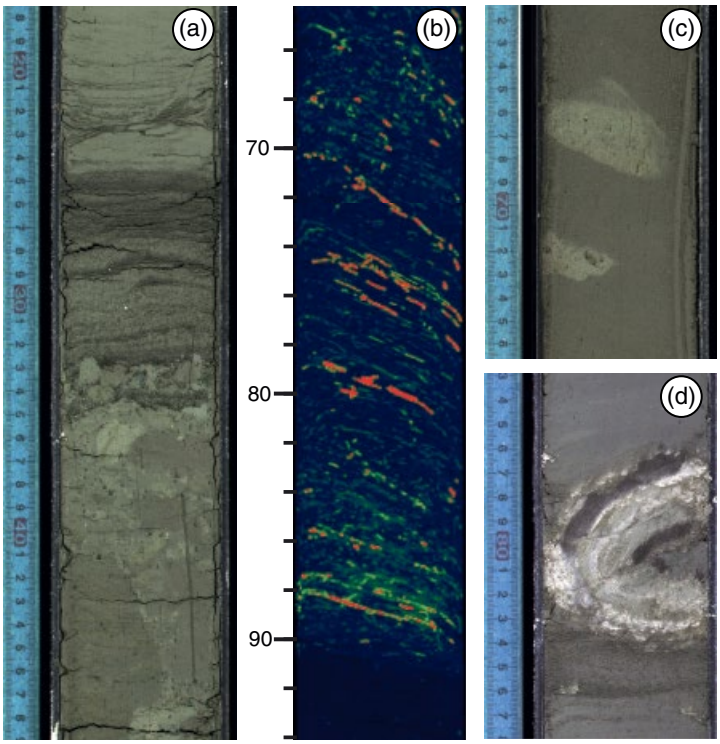


Figure 15.5 Evidence for MTDs as observed in cores and X-CT scans. (a) Visible light image of core C0018A-5H-5, showing turbidite overlying top of MTD 2. (b) Semitransparent rendering of X-CT image C0018A-6H-2, showing organization of pyrite mineralizations as lineations and low-angle planar discontinuities with associated increase in CT values indicating shearing at the base of MTD2. (c) Visible light image of core C0018A-1H-4, showing mud clasts in sandy silty-clay matrix within MTD1. (d) Visible light image of core C0018A-5H-6, showing slump fold within MTD 2. All scales are in centimeter. Source: Modified from Strasser et al. (2012). © 2012 Springer.

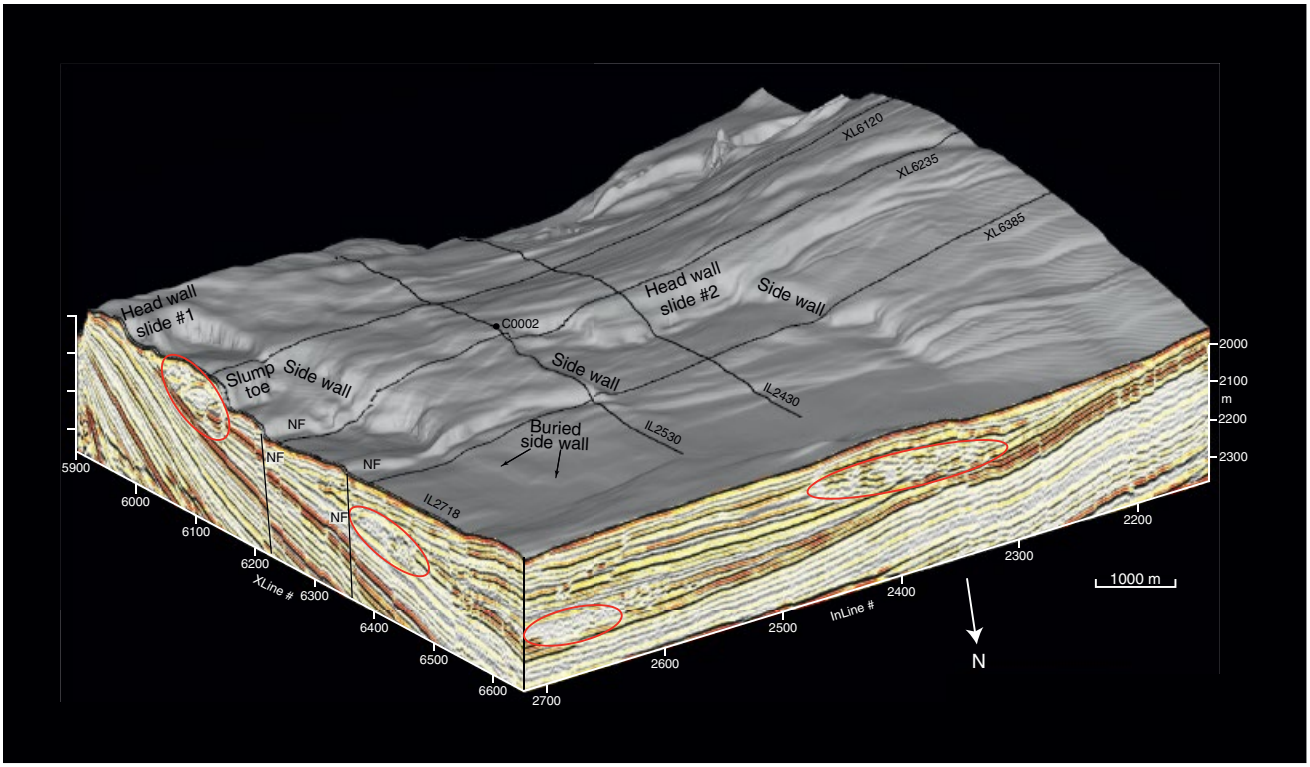


Figure 15.6 Perspective view of 3D seismic volume with surface bathymetry showing prominent slide scars. Major MTDs circled in red. Location shown as red box in Figure 15.3. View is looking to the SSW. Source: Modified after Moore and Strasser (2016). © 2016 Springer. (*See electronic version for color representation of this figure*)

that dips landward ~7°. The slump has a well-developed headwall, SW sidewall, and slump toe.

Several buried MTDs range in area up to ~28 km^2, with volumes up to ~2.8 km^3. They have well-defined basal glide planes, and their internal structure is characterized by coherent blocks with small-offset thrust faults between them. These internal pressure ridges are displayed well in coherency plots (Lackey et al., 2018b; Moore & Strasser, 2016) that show the orientation of the blocks.

There are many more buried MTDs that range from a few meters to a few tens of meters in thickness (Lackey et al., 2018b; Moore & Strasser, 2016). Most are recognized by their chaotic internal reflection character, and several are overlain by thinner MTDs.

15.5. DISCUSSION

Submarine landsliding on the Nankai Trough accretionary prism is responsible for redistributing large amounts of sediment downslope. The greatest number of landslides occurred on the outer accretionary prism. Overall, the Nankai accretionary wedge is in a critical state where the wedge is on the verge of failure everywhere due to slope steepening by the addition of thrust packages at the toe of the prism (e.g., Davis et al., 1983). The slope steepening is a reflection of continued slip along the accretionary thrusts as well as along the large out-of-sequence thrust (megasplay fault) that marks the landward margin of the outer prism. Hanging wall anticlines that are formed above the seaward edges of the thrusts (e.g., Kimura et al., 2011; Strasser et al., 2009) repeatedly become unstable and slump into the adjacent trench slope basin (Strasser et al., 2011) and are associated with the seaward margins of hanging wall anticlines above active thrust faults. The landslides involve not only surficial slope sediments but also the underlying thrust slices. 3D seismic and drilling data demonstrate that this process has been responsible for filling the trench slope basins with deposits that range from 100 m thick MTDs to smaller-scale turbidites.

Subduction of basement topography on the northern PSP, such as the large KSC that has been subducting in the central Nankai region (Figures 15.1 and 15.2), has caused large-scale deformation of the prism with associated landsliding. Collision of the KSC has "bulldozed" a large reentrant into the prism (Tosabae Embayment), generating the largest and most complicated landslide on the inner trench slope. Multiple smaller-scale secondary (retrogressive) landslides have modified the area as seamounts continue to collide.

Smaller-scale subducting basement topography has also generated landslides from the frontal thrust region, a process recognized along many subduction margins (e.g., Dominguez et al., 1998; Ruh, 2016; von Huene et al., 2000). MTDs have accumulated at the bases of these slides, the largest of which has caused the seaward deflection of a large channel in the trench axis (Kawamura et al., 2012). These MTDs are destined to be re-accreted at the frontal thrust and incorporated into the accretionary prism.

Fewer landslides occur in the FAB, and most of those are along the seaward margin adjacent to the active megasplay fault. The topography generated by uptilting at the megasplay provides a landward dipping oversteepened slope that is conducive to landsliding. These landslides involve the youngest strata deposited in the FAB and have produced large coherent MTDs that are well imaged in 3D seismic data.

Although the Nankai region has experienced many great earthquakes, our drilling and seismic data demonstrate that the recurrence interval for large MTD events is on the order of 0.05–0.10 Ma (Moore & Strasser, 2016; Strasser et al., 2011), while the recurrence interval of great earthquakes is much more frequent (~100–200 yr; Ando, 1975). Therefore, although the landslides may ultimately be triggered by earthquake shaking (e.g., Okutsu et al., 2018), the region must be preconditioned to be susceptible to failure during the quakes (Strasser et al., 2012). Potential types of preconditioning include rapid steepening of surface slopes, destabilization of gas hydrates, intersection of fault systems, an extensional stress regime, and lateral transmission of fluid overpressures (e.g., Ikari et al., 2011; Strasser et al., 2011; Urgeles & Camerlenghi, 2013).

At least one FAB landslide occurred along a landward dipping slope of ~5–7°, and other FAB landslides are closely associated with regional normal faults that have 20–30 m of vertical slip, so it is possible that the landslides occurred along the exposed fault scarps in Kumano Basin (Lackey et al., 2018b). Because the ages of large landslides in the Nankai outer prism coincide mostly with interglacial periods, Kremer et al. (2017) suggest that climate forcing might act as a preconditioning factor for slope stability in this active tectonic regime (potentially linked to changes in the bottom water temperatures and gas hydrate stability).

The importance of submarine landslides as a major contributor to tsunami generation has been recognized for many years (e.g., Hampton et al., 1996; Locat & Lee, 2002; Masson et al., 2006; Tappin, 2010; ten Brink et al., 2006, 2016; Vanneste et al., 2014). The potential for tsunami generation exists for fault scar volumes larger than ~10 km^3 (von Huene et al., 2004), but even smaller volume landslides have also been interpreted to be potentially tsunamigenic (Borrero et al., 2001; Fisher et al., 2005). Thus, it is likely that the earliest landslides that generated the Tosabae Embayment should have generated regional tsunamis. We mapped slides with volumes of 115, 33, 11, and 10 km^3 on the Nankai outer prism that also should have generated tsunamis. Landslides with volumes of 4, 6, and 8 km^3 also could have generated tsunamis. All of

these tsunamis could have affected the Japanese islands, but the majority of MTDs along the frontal thrust and outer prism and in Kumano Basin are <1 km^3 in volume, and, therefore, their hazard potential was minimal.

ACKNOWLEDGMENTS

This project was supported by the U.S. National Science Foundation (grant no. OCE-0451790) and the German Ministry of Science and Education (BMBF) through funding (grant 03G0251A) of the R/V *Sonne* cruise SO251 that acquired the new Kumano area bathymetric data. We thank M. Robb for her help in processing and compiling the JAMSTEC regional bathymetry grid and C. Ferreira, who headed the multibeam group during SO251. We thank J. Ruh and an anonymous reviewer for comments that led to a greatly improved manuscript (SOEST contribution no. 10408).

REFERENCES

Alves, T. M., Kurtev, K., Moore, G. F., & Strasser, M. (2014a). Assessing the internal character, reservoir potential, and seal competence of mass-transport deposits using seismic texture: A geophysical and petrophysical approach. *AAPG Bulletin*, *98*(4), 793–824. https://doi.org/10.1306/09121313117

Alves, T. M., Strasser, M., & Moore, G. F. (2014b). Erosional features as indicators of thrust fault activity (Nankai Trough, Japan). *Marine Geology*, *356*, 5–18. https://doi.org/10.1016/j.margeo.2013.07.011

Ando, M. (1975). Source mechanisms and tectonic significance of historical earthquakes along the Nankai Trough, Japan. *Tectonophysics*, *27*, 119–140.

Aoki, Y., Tamano, T., & Kato, S. (1982). Detailed structure of the Nankai Trough from migrated seismic sections. In J. S. Watkins & C. L. Drake (Eds.), *Studies in continental margin geology, American Association of Petroleum Geologists Memoir* (Vol. *34*, pp. 309–322). Tulsa, OK: AAPG.

Ashi, J., Sawada, R., Omura, A., & Ikehara, K. (2014). Accumulation of an earthquake-induced extremely turbid layer in a terminal basin of the Nankai accretionary prism. *Earth, Planets and Space*, *66*, 51.

Bardet, J. P., Okal, E. A., Synolakis, C. E., Davies, H. L., & Imamura, F. (2003). Landslide tsunamis: Recent findings and research directions. *Pure and Applied Geophysics*, *160*(10–11), 1793–1809.

Borrero, J. C., Dolan, J. F., & Synolakis, C. E. (2001). Tsunamis within the Eastern Santa Barbara Channel. *Geophysical Research Letters*, *28*(4), 643–646. https://doi.org/10.1029/2000gl011980

Caress, D.W. & Chayes, D.N. 2008. MB-System: Open source software for the processing and display of swath mapping sonar data, http://www.mbari.org/data/mbsystem/

Davis, D. J., Suppe, J., & Dahlen, F. A. (1983). Mechanics of fold-and-thrust belts and accretionary wedges. *Journal of Geophysical Research*, *88*, 1153–1172.

Dominguez, S., Lallemand, S. E., Malavieille, J., & von Huene, R. (1998). Upper plate deformation associated with seamount subduction. *Tectonophysics*, *293*, 207–224.

Fisher, M. A., Normark, W. R., Greene, H. G., Lee, H. J., & Sliter, R. W. (2005). Geology and tsunamigenic potential of submarine landslides in Santa Barbara Channel, Southern California. *Marine Geology*, *224*(1–4), 1–22. https://doi.org/10.1016/j.margeo.2005.07.012

Gulick, S. P. S., Bangs, N. L. B., Moore, G. F., Ashi, J., Martin, K. M., Sawyer, D. S., et al. (2010). Rapid forearc basin uplift and megasplay fault development from 3D seismic images of Nankai Margin off Kii Peninsula, Japan. *Earth and Planetary Science Letters*, *300*(1–2), 55–62. https://doi.org/10.1016/j.epsl.2010.09.034

Hampton, M. A., Lee, H. J., & Locat, J. (1996). Submarine landslides. *Reviews of Geophysics*, *34*(1), 33–59.

Heki, K. (2007). Secular, transient and seasonal crustal movements in Japan from a dense GPS array: Implications for plate dynamics in convergent boundaries. In T. Dixon & J. C. Moore (Eds.), *The Seismogenic Zone of Subduction Thrust Faults* (pp. 512–539). New York, NY: Columbia University Press.

Ikari, M. J., Strasser, M., Saffer, D. M., & Kopf, A. J. (2011). Submarine landslide potential near the megasplay fault at the Nankai subduction zone. *Earth and Planetary Science Letters*, *312*(3–4), 453–462. https://doi.org/10.1016/j.epsl.2011.10.024

Ike, T., Moore, G. F., Kuramoto, S., Park, J.-O., Kaneda, Y., & Taira, A. (2008a). Tectonics and sedimentation around Kashinosaki Knoll: A subducting basement high in the eastern Nankai Trough. *Island Arc*, *17*(3), 358–375. https://doi.org/10.1111/j.1440-1738.2008.00625.x

Ike, T., Moore, G. F., Kuramoto, S., Park, J.-O., Kaneda, Y., & Taira, A. (2008b). Variations in sediment thickness and type along the northern Philippine Sea Plate at the Nankai Trough. *Island Arc*, *17*(3), 342–357. https://doi.org/10.1111/j.1440-1738.2008.00624.x

Kanamatsu, T., Kawamura, K., Strasser, M., Novak, B., & Kitamura, Y. (2014). Flow dynamics of Nankai Trough submarine landslide inferred from internal deformation using magnetic fabric. *Geochemistry, Geophysics, Geosystems*, *15*(10), 4079–4092. https://doi.org/10.1002/2014gc005409

Katz, O., Reuven, E., & Aharonov, E. (2015). Submarine landslides and fault scarps along the eastern Mediterranean Israeli continental-slope. *Marine Geology*, *369*, 100–115. https://doi.org/10.1016/j.margeo.2015.08.006

Kawamura, K., Kanamatsu, T., Kinoshita, M., Saito, S., Shibata, T., Fujino, K., et al. (2010). Redistribution of sediments by submarine landslides on the eastern Nankai accretionary prism. In D. C. Mosher, L. Moscardelli, R. C. Shipp, J. D. Chaytor, C. D. P. Baxter, H. J. Lee, & R. Urgeles (Eds.), *Submarine mass movements and their consequences IV* (pp. 313–322). Dordrecht, The Netherlands: Springer.

Kawamura, K., Laberg, J. S., & Kanamatsu, T. (2014). Potential tsunamigenic submarine landslides in active margins. *Marine Geology*, *356*, 44–49. https://doi.org/10.1016/j.margeo.2014.03.007

Kawamura, K., Sakaguchi, A., Strasser, M., Anma, R., & Ikeda, H. (2012). Detailed observation of topography and geologic architecture of a submarine landslide scar in a toe of

an accretionary prism. In Y. Yamada, K. Ikehara, R. Urgeles, J. Chator, K. Kawamura, Y. Ogawa, et al. (Eds.), *Submarine mass movements and their consequences* (pp. 301–309). Dordrecht, The Netherlands: Springer.

Kimura, G., Moore, G. F., Strasser, M., Screaton, E., Curewitz, D., Streiff, C., & Tobin, H. (2011). Spatial and temporal evolution of the megasplay fault in the Nankai Trough. *Geochemistry, Geophysics, Geosystems*, *12*. https://doi.org/10.1029/2010gc003335

Kinoshita, M., Tobin, H., Ashi, J., Kimura, G., Lallemant, S., Screaton, E. J., & Exp. 314/315/316 Scientists. (2009). Proc. IODP, 314/315/316. https://doi.org/10.2204/iodp.proc.314315316.2009

Kitamura, Y., Strasser, M., Novak, B., Kanamaru, T., Kawamura, K., & Zhao, X. (2014). Characteristics of magnetic fabrics in mass transport deposits in the Nankai Trough trench slope, Japan. *Advances in Natural and Technological Hazard Research*, *37*, 649–658. https://doi.org/10.1007/978-3-319-00972-8_58

Kobayashi, K., Kasuga, S., & Okino, K. (1995). Shikoku Basin and its margins. In B. Taylor (Ed.), *Back-arc basins* (pp. 381–405). New York, NY: Plenum Press.

Kodaira, S., Kaneda, Y., Takahashi, N., Nakanishi, A., & Miura, S. (2000). Subducted seamount imaged in the rupture zone of the 1946 Nankaido earthquake. *Science*, *289*(5476), 104–106.

Kremer, K., Usman, M. O., Satoguchi, Y., Nagahashi, Y., Vadakkepuliyambatta, S., Panieri, G., & Strasser, M. (2017). Possible climate preconditioning on submarine landslides along a convergent margin, Nankai Trough (NE Pacific). *Progress in Earth and Planetary Science*, *4*(1). https://doi.org/10.1186/s40645-017-0134-9

Laberg, J. S., Strasser, M., Alves, T. M., Gao, S., Kawamura, K., Kopf, A., & Moore, G. F. (2016). Internal deformation of a muddy gravity flow and its interaction with the seafloor (Site C0018 of IODP Expedition 333, Nankai Trough, SE Japan). *Landslides*, *14*, 849–860. https://doi.org/10.1007/s10346-016-0766-7

Lackey, J., Moore, G., & Strasser, M. (2018b). Three-dimensional mapping and kinematic characterization of mass transport deposits along the outer Kumano Basin and Nankai accretionary wedge, southwest Japan. *Progress in Earth and Planetary Science*, *5*(1), 1–19.

Lackey, J. K., Moore, G. F., Strasser, M., Kopf, A., & Ferreira, C. S. (2018a). Spatial and temporal cross-cutting relationships between fault structures and slope failures along the outer Kumano Basin and Nankai accretionary wedge, southwest Japan. *Geological Society of London, Special Publications*, *477*. https://doi.org/10.1144/SP477.10

Lallemand, S., & Le Pinchon, X. (1987). Coulomb wedge model applied to the subduction of seamounts in the Japan Trench. *Geology*, *15*, 1065–1069.

Lallemand, S. E., Schnürle, P., & Malavieille, J. (1994). Coulomb theory applied to accretionary and nonaccretionary wedges: Possible causes for tectonic erosion and/or frontal accretion. *Journal of Geophysical Research. Solid Earth*, *99*(B6), 12033–12055. https://doi.org/10.1029/94jb00124

Locat, J., & Lee, H. J. (2002). Submarine landslides: Advances and challenges. *Canadian Geotechnical Journal*, *39*(1), 193–212. https://doi.org/10.1139/t01-089

Mannu, U., Ueda, K., Willett, S. D., Gerya, T. V., & Strasser, M. (2016). Impact of sedimentation on evolution of accretionary wedges: Insights from high-resolution thermomechanical modeling. *Tectonics*, *35*(12), 2828–2846. https://doi.org/10.1002/2016tc004239

Masson, D. G., Harbitz, C. B., Wynn, R. B., Pedersen, G., & Lovholt, F. (2006). Submarine landslides: Processes, triggers and hazard prediction. *Philosophical Transactions. Series A, Mathematical, Physical, and Engineering Sciences*, *364*(1845), 2009–2039. https://doi.org/10.1098/rsta.2006.1810

Miyazaki, S. I., & Heki, K. (2001). Crustal velocity field of southwest Japan: Subduction and arc-arc collision. *Journal of Geophysical Research, B: Solid Earth*, *106*(3), 4305–4326.

Moore, G. F., Bangs, N. L., Taira, A., Kuramoto, S., Pangborn, E., & Tobin, H. J. (2007). Three-dimensional splay fault geometry and implications for tsunami generation. *Science*, *318*(5853), 1128–1131. https://doi.org/10.1126/science.1147195

Moore, G. F., Boston, B. B., Strasser, M., Underwood, M. B., & Ratliff, R. A. (2015). Evolution of tectono-sedimentary systems in the Kumano Basin, Nankai Trough forearc. *Marine and Petroleum Geology*, *67*, 604–616. https://doi.org/10.1016/j.marpetgeo.2015.05.032

Moore, G. F., Kanagawa, K., Strasser, M., Dugan, B., Maeda, L., Toczko, S., & the IODP Expedition 338 Scientific Party (2014). IODP Expedition 338: NanTroSEIZE Stage 3: NanTroSEIZE plate boundary deep riser 2. *Scientific Drilling*, *17*, 1–12. https://doi.org/10.5194/sd-17-1-2014

Moore, G. F., Park, J. O., Bangs, N. L., Gulick, S. P., Tobin, H. J., Nakamura, Y., et al. (2009). Structural and seismic stratigraphic framework of the NanTroSEIZE Stage 1 transect. *Proc IODP, 314/315/316*, 1-46. https://doi.org/10.2204/iodp.proc.314315316.102.2009

Moore, G. F., Shipley, T. H., Stoffa, P. L., Karig, D. E., Taira, A., Kuramoto, S., et al. (1990). Structure of the Nankai Trough accretionary zone from multichannel seismic-reflection data. *Journal of Geophysical Research-Solid Earth and Planets*, *95*(B6), 8753–8765.

Moore, G. F., & Strasser, M. (2016). Large Mass Transport Deposits in Kumano Basin, Nankai Trough, Japan. In G. E. A. Lamarche (Ed.), *Submarine mass movements and their consequences* (pp. 371–379). New York, NY: Springer.

Moore, G. F., Taira, A., Bangs, N. L., Kuramoto, S., Shipley, T. H., Alex, C. M., et al. (1999). Data Report: Structural Setting of the Leg 190 Muroto Transect. In G. F. Moore, A. Taira, A. Klaus, et al. (Eds.), *Proc. ODP, Init. Repts.* (Vol. 190). College Station, TX: Ocean Drilling Program. http://www-odp.tamu.edu/publications/190_IR/chap_02/chap_02.htm

Moore, G. F., Taira, A., Klaus, A., Becker, L., Boeckel, B., Cragg, B. A., et al. (2001). New insights into deformation and fluid flow processes in the Nankai Trough accretionary prism: Results of Ocean Drilling Program Leg 190. *Geochemistry, Geophysics, Geosystems*, *2*. https://doi.org/10.1029/2001gc000166

Okino, K., & Kato, Y. (1995). Geomorphological study on a clastic accretionary prism: The Nankai Trough. *The Island Arc*, *4*, 182–198.

Okino, K., Shimakawa, Y., & Nagakoa, S. (1994). Evolution of the Shikoku Basin. *Journal of Geomagnetism and Geoelectricity*, *46*, 463–479.

Okutsu, N., Ashi, J., Yamaguchi, A., Irino, T., Ikehara, K., Kanamatsu, T., et al. (2018). Evidence for surface sediment remobilization by earthquakes in the Nankai forearc region from sedimentary records. In *Subaqueous mass movements, Geological Society, London, Special Publications* (Vol. 477). London, UK: Geological Society of London.

Park, J. O., Kaneda, Y., Tsuru, T., Kodaira, S., & Cummins, P. R. (2002). Splay fault branching along the Nankai subduction zone. *Science*, *297*(5584), 1157–1160.

Park, J. O., Kodaira, S., Takahashi, N., Kinoshita, H., Tsuru, T., Kaneda, Y., & Kono, Y. (1999). A subducting seamount beneath the Nankai accretionary prism off Shikoku, southwestern Japan. *Geophysical Research Letters*, *26*(7), 931–934.

Pedley, K. L., Barnes, P. M., Pettinga, J. R., & Lewis, K. B. (2010). Seafloor structural geomorphic evolution of the accretionary frontal wedge in response to seamount subduction, Poverty Indentation, New Zealand. *Marine Geology*, *270*(1–4), 119–138. https://doi.org/10.1016/j.margeo.2009.11.006

Ruh, J. B. (2016). Submarine landslides caused by seamounts entering accretionary wedge systems. *Terra Nova*, *28*(3), 163–170. https://doi.org/10.1111/ter.12204

Sassa, K., He, B., Miyagi, T., Strasser, M., Konagai, K., Ostric, M., et al. (2012). A hypothesis of the Senoumi submarine megaslide in Suruga Bay in Japan: Based on the undrained dynamic-loading ring shear tests and computer simulation. *Landslides*, *9*(4), 439–455. https://doi.org/10.1007/s10346-012-0356-2

Satake, K. (2012). Tsunamis generated by submarine landslides. In Y. Yamada, K. Ikehara, R. Urgeles, J. Chator, K. Kawamura, Y. Ogawa, et al. (Eds.), *Submarine mass movements and their consequences, Advances in Natural and Technological Hazards Research* (Vol. 31, pp. 475–484). Dordrecht, The Netherlands: Springer.

Sawyer, D. E., Flemings, P. B., Dugan, B., & Germaine, J. T. (2009). Retrogressive failures recorded in mass transport deposits in the Ursa Basin, Northern Gulf of Mexico. *Journal of Geophysical Research*, *114*. https://doi.org/10.1029/2008jb006159

Screaton, E., Kimura, G., Curewitz, D., Moore, G., Chester, F., Fabbri, O., et al. (2009). Interactions between deformation and fluids in the frontal thrust region of the NanTroSEIZE transect offshore the Kii Peninsula, Japan: Results from IODP Expedition 316 Sites C0006 and C0007. *Geochemistry, Geophysics, Geosystems*, *10*. https://doi.org/10.1029/2009gc002713

Seno, T., Stein, S., & Gripp, A. E. (1993). A model for the motion of the Philippine Sea plate consistent with NUVEL-1 and geological data. *Journal of Geophysical Research*, *98*, 17941–17948.

Strasser, M., Dugan, B., Kanagawa, K., Moore, G. F., Toczko, S., Maeda, L., & Exp. 338 Scientific Party (2014). *Proceedings of the Integrated Ocean Drilling Program* (Vol. *338*). Yokohama, Japan: Integrated Ocean Drilling Program.

Strasser, M., Henry, P., Kanamatsu, T., Thu, M. K., Moore, G. F., & Exp 338 scientists (2012). Scientific drilling of mass-transport deposits in the Nankai accretionary wedge: First results from IODP Exp 333. In Y. Yamada, K. Ikehara, R. Urgeles, J. Chator, K. Kawamura, Y. Ogawa, et al. (Eds.), *Submarine mass movements and their consequences* (pp. 671–681). New York, NY: Springer.

Strasser, M., Kopf, A., Abegg, F. W., Asada, M., Bachmann, A. K., Cuno, P. et al. (2017). Report and preliminary results of R/V *Sonne* cruise SO251: Extreme events Archived in the Geological Record of Japan's Subduction margins (EAGER-Japan). Berichte, MARUM – Zentrum für Marine Umweltwissenschaften, Fachbereich Geowissenschaften, Universität Bremen.

Strasser, M., Moore, G. F., Kimura, G., Kitamura, Y., Kopf, A. J., Lallemant, S., et al. (2009). Origin and evolution of a splay fault in the Nankai accretionary wedge. *Nature Geoscience*, *2*, 648–652.

Strasser, M., Moore, G. F., Kimura, G., Kopf, A. J., Underwood, M. B., Guo, J., & Screaton, E. J. (2011). Slumping and mass transport deposition in the Nankai fore arc: Evidence from IODP drilling and 3-D reflection seismic data. *Geochemistry, Geophysics, Geosystems*, *12*(Q0AD13). https://doi.org/10.1029/2010gc003431

Taira, A. (2001). Tectonic evolution of the Japanese Island Arc System. *Annual Review of Earth and Planetary Sciences*, *29*, 109–134.

Tappin, D. R. (2010). Mass transport events and their tsunami hazard. In Y. Yamada, K. Ikehara, R. Urgeles, J. Chator, K. Kawamura, Y. Ogawa, et al. (Eds.), *Submarine mass movements and their consequences* (Vol. *28*, pp. 667–684). Dordrecht, The Netherlands: Springer.

ten Brink, U. S., Andrews, B. D., & Miller, N. C. (2016). Seismicity and sedimentation rate effects on submarine slope stability. *Geology*, *44*, 563–566.

ten Brink, U. S., Geist, E. L., & Andrews, B. D. (2006). Size distribution of submarine landslides and its implication to tsunami hazard in Puerto Rico. *Geophysical Research Letters*, *33*(11). https://doi.org/10.1029/2006gl026125

Urgeles, R., & Camerlenghi, A. (2013). Submarine landslides of the Mediterranean Sea: Trigger mechanisms, dynamics, and frequency-magnitude distribution. *Journal of Geophysical Research. Earth Surface*, *118*(4), 2600–2618. https://doi.org/10.1002/2013jf002720

Vanneste, M., Sultan, N., Garziglia, S., Forsberg, C. F., & L'Heureux, J.-S. (2014). Seafloor instabilities and sediment deformation processes: The need for integrated, multi-disciplinary investigations. *Marine Geology*, *352*, 183–214. https://doi.org/10.1016/j.margeo.2014.01.005

von Huene, R. (2008). When seamounts subduct. *Science*, *321*, 1165–1166.

von Huene, R., Bourgois, J., Miller, J., & Pautot, G. (1989). A large tsunamogenic landslide and debris flow along the Peru Trench. *Journal of Geophysical Research*, *94*, 1703–1714.

von Huene, R., Ranero, C. R., & Watts, P. (2004). Tsunamigenic slope failure along the Middle America Trench in two tectonic settings. *Marine Geology*, *203*(3–4), 303–317. https://doi.org/10.1016/s0025-3227(03)00312-8

von Huene, R., Ranero, C. R., Weinrebe, W., & Hinz, K. (2000). Quaternary convergent margin tectonics of Costa Rica, segmentation of the Cocos Plate, and Central America volcanism. *Tectonics*, *19*, 314–334.

Yamada, Y., Yamashita, Y., & Yamamoto, Y. (2010). Submarine landslides at subduction margins: Insights from physical models. *Tectonophysics*, *484*(1–4), 156–167. https://doi.org/10.1016/j.tecto.2009.09.007

Yamazaki, T., & Okamura, Y. (1989). Subducting seamounts and deformation of overriding forearc wedges around Japan. *Tectonophysics*, *160*, 207–229.

16

Seismic Examples of Composite Slope Failures (Offshore North West Shelf, Australia)

Nicola Scarselli[1], Ken McClay[1], and Chris Elders[2]

ABSTRACT

This research presents a seismic geomorphological analysis of slope failures in the Exmouth Plateau, offshore Northwest Shelf of Australia, using high-quality 3D seismic data. Seismic visualization techniques and seismic attribute analysis were employed to investigate the internal architecture of the failures to infer the processes that control their styles of emplacement. The investigation shows the widespread occurrence of slope failures in which sliding and slumping laterally operate and coexist, resulting in composite products. For example, shallow-detaching, second-order slides can originate by the gravitational collapse of the over-thickened leading edge of primary slide features. This mechanism is comparable to degradation processes of thrust-uplifted strata observed along submarine fold belts and in exposed ancient foreland basins. Headscarp retrogression and progressive disaggregation of collapsing earth bodies are commonly observed in subaerial collapse systems. These seem to be common processes able to create composite slide-to-slump and slump-to-slide submarine failures observed in the NW shelf of Australia. The results of this research suggest that caution is necessary when assessing the nature of slope failures when only parts of the systems are accessible for observation.

16.1. INTRODUCTION

16.1.1. Rationale

Processes of slope failure have been classified using a number of schemes (Varnes, 1958; Dott, 1963; Embley & Jacobi, 1977; Nardin et al., 1979; Stow, 1985; Nemec, 1990; Mulder & Cochonat, 1996; Locat & Lee, 2002; McHugh et al., 2002; Lee et al., 2007; Posamentier & Martinsen, 2011). The classical classification scheme is the one based on types of movement (e.g., Varnes, 1958). This scheme classifies slope failure into four main categories: (i) creep, slow strain rate intergranular deformation; (ii) slide, failure along discrete shear surfaces with limited internal deformation; (iii) slump, failure along multiple shear surfaces with significant internal deformation; and (iv) mass flows which can be divided into laminar, non-turbulent flow (i.e., debris flow) and fully turbulent flow (i.e., turbidity current). Recently, criteria for the classification of slope failures have focused on aspects such as form of frontal emplacement of failures (confined vs. frontally emergent; Frey-Martínez et al., 2006) and sourcing region of failures (attached vs. detached; Moscardelli & Wood, 2008).

There is a general consensus that slope failure processes "form a process continuum" (Posamentier & Martinsen, 2011) and "co-occur in the same event" (Moscardelli & Wood, 2008). However, despite a rich literature that describes recent and fossil slope failures (see Shanmugam (2016) and Moscardelli and Wood (2008) for a concise reference list), comparably little effort has been made to understand the coexistence of multiple slope processes in the same failure event (e.g., Mulder & Cochonat, 1996).

[1] *Fault Dynamics Research Group, Department of Earth Sciences, Royal Holloway University of London, Egham, United Kingdom*

[2] *Department of Applied Geology, Curtin University, Perth, Western Australia, Australia*

Submarine Landslides: Subaqueous Mass Transport Deposits from Outcrops to Seismic Profiles, Geophysical Monograph 246, First Edition. Edited by Kei Ogata, Andrea Festa, and Gian Andrea Pini.
© 2020 American Geophysical Union. Published 2020 by John Wiley & Sons, Inc.

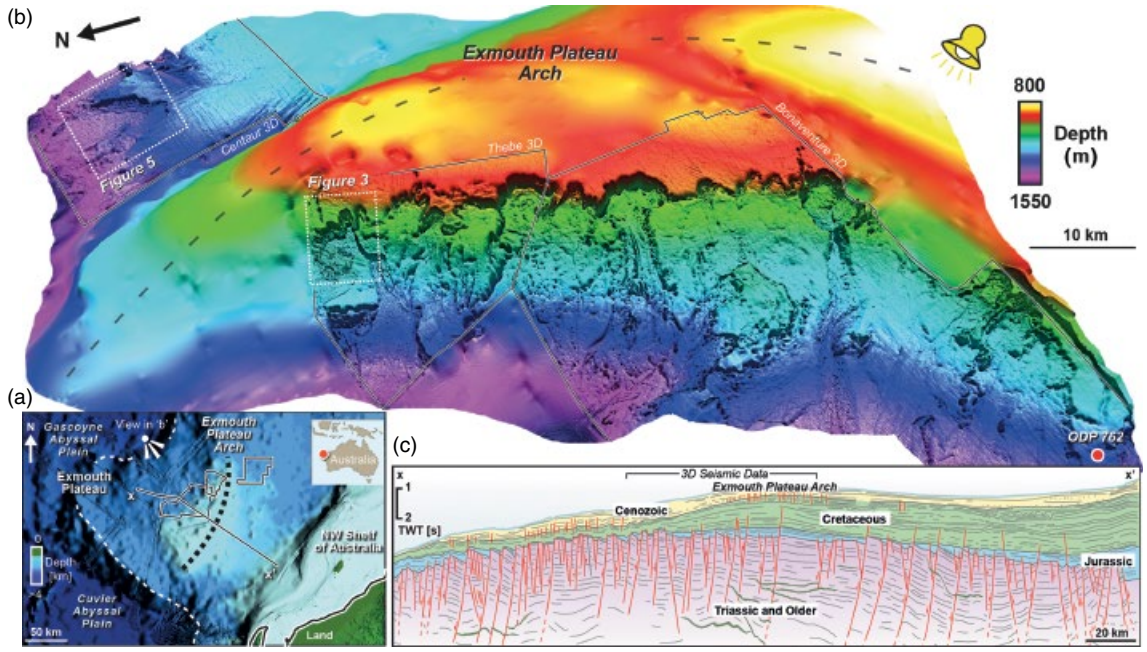


Figure 16.1 (a) Location map of the study area within the Exmouth Plateau in the NW Shelf of Australia. The Exmouth Plateau is formed by stretched continental crust surrounded by the oceanic crust of the Cuvier Abyssal Plain to the south, the Gascoyne Abyssal Plain to the west, and the Argo Abyssal Plain to the north (outside the boundary of this map). The map shows also the location of the 3D seismic surveys analyzed in this research. Source: Bathymetry from Amante and Eakins (2006). (b) Depth structure map of the seabed in the study area. The image shows a series of slope failures that have deeply affected and shaped the bathymetric relief of the Exmouth Plateau Arch. Note that the failures are covered by a series of 3D seismic data sets. Note also the location of ODP well Site 762 in the southern part of the Bonaventure 3D seismic data set. The structure map is from the combined interpretation of 2D and 3D data. (c) Regional geo-seismic section across the study area showing the structural elements and seismic stratigraphic units of the Exmouth Plateau. Section location is shown in "a".

With this research, we use high-quality 3D seismic data from offshore Western Australia (Figure 16.1) to unravel the internal complexity of key slope failures found in the Neogene to recent section of the Exmouth Plateau (Figure 16.2). The examples analyzed occurred near the present-day seabed; therefore the high-frequency content of the shallow seismic enabled resolution of the fine-scale (10–20 m scale; see below) internal structures of these failures, giving exceptional insight into the processes behind their evolution. The work pays particular attention to differentiating multiple slope processes acting in a single event so to contribute to the discussion on how these composite slope failures can generate and evolve. The paper builds on the findings highlighted in Scarselli et al. (2013) where the authors have described composite failures in this part of the Exmouth Plateau.

16.1.2. Regional Outlook

The Exmouth Plateau forms a prominent ~600 km long and ~350 km wide bathymetric relief offshore Northwest Shelf of Australia with water depth ranging between 800 and 4000 m (Figure 16.1a, b). The plateau consists of continental crust that since the Late Devonian underwent multiple phases of rifting as a result of the breakup of Gondwana (AGSO North West Shelf Study Group, 1994; Tindale et al., 1998; Longley et al., 2002; Jitmahantakul & McClay, 2013; Black et al., 2017). These rift events left the stretched continental crust of the Exmouth Plateau surrounded by abyssal plains of oceanic crust, the Cuvier Abyssal Plain to the south, the Gascoyne Abyssal Plain to the west, and the Argo Abyssal Plain to the north (Figure 16.1a). Significant lithospheric stretching occurred at the end of the Triassic and culminated with the opening of the Ceno-Tethys (Metcalfe, 2013). This major extensional event was accompanied by the development of a series of NE-SW trending rift sub-basins that contain Jurassic syn-rift shallow marine and deltaic clastic units (Figure 16.1c). As the plateau subsided to present-day water depths, clastic deposition in the Cretaceous was followed by bathyal carbonate sedimentation that continued throughout the Cenozoic and sealed the underlying rift structures (Figures 16.1c and 16.2a). Since the late Oligocene, the collision of the

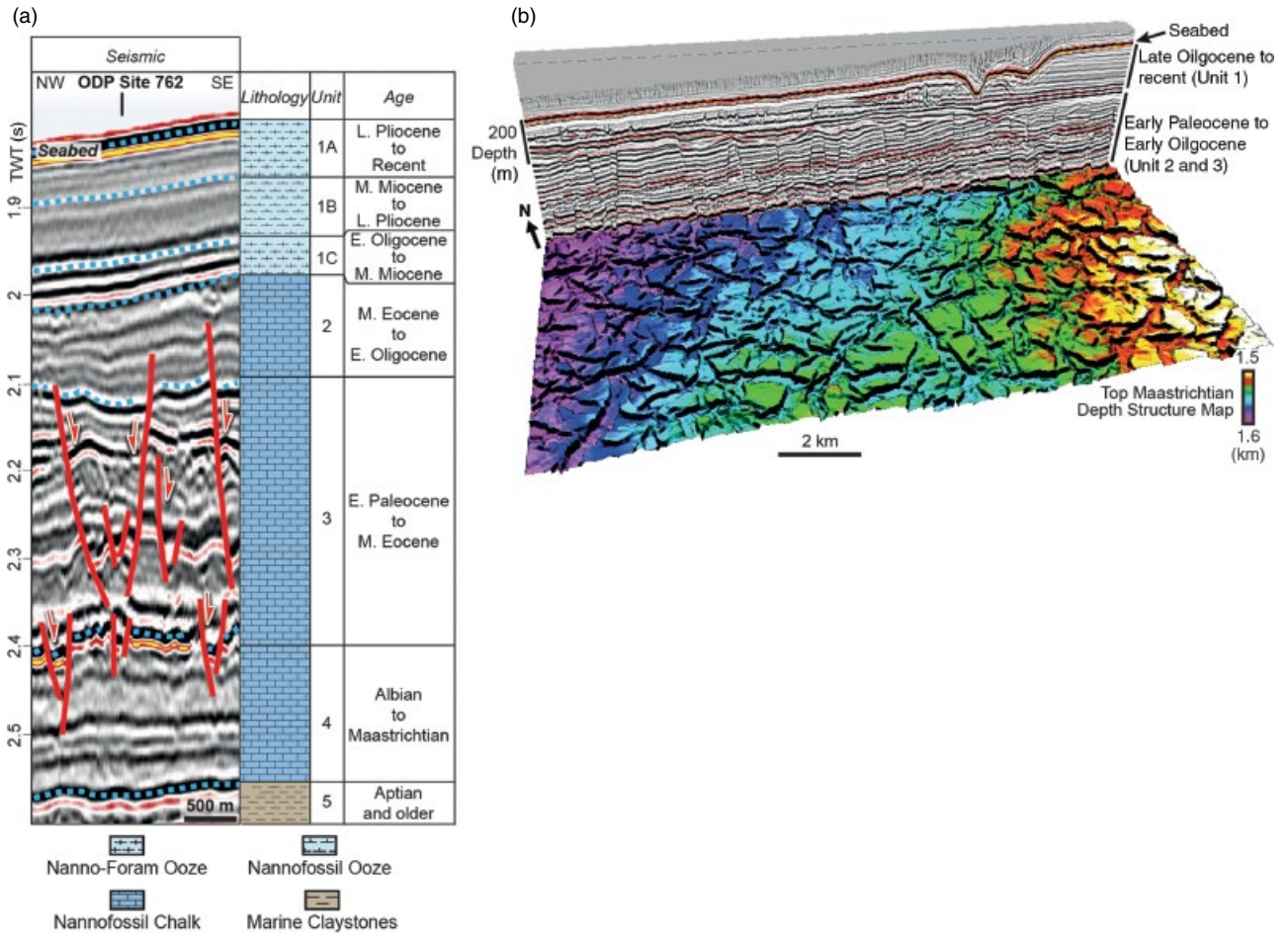


Figure 16.2 (a) Seismic stratigraphy for the Thebe, Bonaventure, and Centaur data sets. Units and ages are those defined for the ODP well Site 762 (Shipboard Scientific Party Report, 1990; Golovchenko et al., 1992). Location of the well is shown in Figure 16.1b. See text for full description of the units. (b) Co-display seismic diagram showing polygonal faults affecting the Paleocene-Oligocene section along the Exmouth Plateau Arch. Note that in places the polygonal faults slightly affect, or terminate immediately below, the late Oligocene to Recent Unit 1. The vertical section and structure map of the Top Maastrichtian surface are from the Bonaventure 3D data set. The units shown in the figure are those defined in the seismic stratigraphic chart in "(a)."

Australian and Eurasian plates caused the inversion of rift faults and the formation of structural highs such as the Exmouth Plateau Arch (Figure 16.1a, b) and other arches along the NW Shelf of Australia - i.e. the Barrow anticline and Giralia and Cape range anticlines (Barber, 1988; Boyd et al., 1992; Keep et al., 1998; Tindale et al., 1998; Hearty et al., 2002; Cathro & Karner, 2006; Whitney et al., 2016).

16.1.3. Stratigraphy

The seismic stratigraphic framework for this study was derived from tying the Ocean Drilling Program (ODP) well at Site 762 with the Bonaventure 3D seismic data (Figure 16.1a, b; Shipboard Scientific Party Report, 1990). Despite the abundance of commercial wells in the study area, the OPD well at Site 762 is the only one that offers information on the near seabed stratigraphy, where the failures here analyzed are found. The failures occurred within the Oligocene to present-day section, classified as Unit 1 in the ODP well (Figure 16.2a).

The basal Unit 1C is typified by a series of high-amplitude, parallel, continuous reflections (Figure 16.2a). This unit rests on top of polygonally faulted reflections with variable amplitude assigned to Units 2 and 3 of early Paleocene to early Oligocene age (Figure 16.2b). In places the polygonal faults slightly affect or terminate immediately below the overlying Unit 1C (Figure 16.2b). The upper part of Unit 1 comprises a series of low-amplitude, parallel, continuous reflections that are divided into Unit 1B, of mid-Miocene to Late Pliocene age, and Unit 1A that extends from the late Pliocene to the seabed. The

package of reflections forming these two sub-units is largely undeformed. The high-amplitude package of the basal Unit 1C and the low-amplitude reflectors of the overlying units 1B and 1A confer a distinct bipartite seismic signature of the whole Unit 1 (Figure 16.2a). This signature at Site 762 is readily recognizable throughout the study area and over the data sets analyzed in this chapter.

From a lithological standpoint, Unit 1 is made of pelagic foraminifera nannofossil ooze with minor clay minerals content (Figure 16.2a; Shipboard Scientific Party Report, 1990). These sediments are poorly consolidated and were deposited at sedimentation rates as slow as 20 m/Ma (Golovchenko et al., 1992). The unit rests above Unit 2 which differs from the overlying sediments in its hardness; in fact Unit 2 is made of white, mainly structureless, nannofossil chalk (Figure 16.2a). The characteristics of the oozes of Unit 1 and the occurrence of numerous minor hiatuses in this section are indicative of eupelagic deposition in a bathyal environment similar to the present-day setting of the Exmouth Plateau Arch, an isolated, distal relief not reached by terrigenous material, affected by periodic erosive bottom currents and where sediments are deposited at very low rates (Shipboard Scientific Party Report, 1990).

16.2. MATERIALS AND METHODS

Three-dimensional Kirchhoff pre-stack time-migrated seismic data sets were used to investigate the near seabed strata of the Exmouth Plateau Arch: Thebe, Bonaventure, and Centaur (Figure 16.1a, b; Table 16.1). The southeastern edge of Thebe data set and the northwestern edge of the Bonaventure data set overlap providing a large coverage of ~5700 m^2 along the NW flank of the arch (Figure 16.1b). The Centaur dataset is located to the east of the Exmouth Plateau Arch and stretches over an area of 2600 m^2. Overall these data sets extend across water depths of 850–1550 m (Figure 16.1b).

The quality of the imaging delivered by the surveys is generally very good as highlighted by sections showing clear imaging of reflections and fault planes throughout, and seismic artifacts such as migration "smiles" are absent (e.g., Figures 16.2 and 16.3).

Table 16.1 details the frequency analysis and estimates of seismic resolution that have been carried out in the near-seafloor section of the data sets where the landslides are found (i.e., Unit 1). As reported by the ODP well at Site 762 (Shipboard Scientific Party Report, 1990) located in the southern part of the Bonaventure data set (Figure 16.1b), the average velocity for this section is ~1700 m/s. Consequently, the vertical and horizontal resolutions for the data sets were estimated to range from 7–10 m to 14–20 m, respectively (Table 16.1).

Time-depth conversion of the data sets was carried to allow measurement and analysis of the seismic data in the depth domain. As the focus of the interpretation was on the shallow section of the data sets, the time-depth conversion was obtained with the construction of a simple "layer-cake" velocity model consisting of two layers divided by the seafloor surface. The top layer comprised the water column; therefore a velocity of 1500 m/s was used for this upper part of the model. The lower layer was limited to a depth of 2.5 s. Information from the ODP well 762 (Shipboard Scientific Party Report, 1990) indicates that an average velocity of 2000 m/s was appropriate for this depth interval. Depth conversion also allowed volumes of failures to be estimated. The volume calculated was that between the top and base surfaces of failures mapped in three dimension in the seismic cube.

Seismic geomorphology techniques were used to analyses slope failures in the study area (e.g., Posamentier et al., 2007; Scarselli et al., 2016). Depth structure maps of the top and basal shear surfaces of the failures were generated. Along these surfaces, root-mean-square (RMS) amplitude and coherency attribute were extracted and integrated with vertical sections (e.g., Figure 16.3). RMS is a standard seismic attribute that highlights changes in amplitude characters. Coherency enhances reflection discontinuities in seismic data. Both attributes are routinely implemented to investigate the internal geometries of slope failures using seismic data (e.g., Gee et al., 2006; Bull et al., 2009; Scarselli et al., 2016). Seismic block diagrams (*sensu* Scarselli et al., 2016) were employed to portray the internal and external characteristics of the failures in order to unravel their overall architecture and propose mechanisms of emplacement (e.g., Figure 16.4).

16.3. OVERVIEW OF SLOPE FAILURES IN THE EXMOUTH PLATEAU ARCH

The seafloor along the Exmouth Plateau Arch has a striking rugose texture which is the result of numerous slope failures (Figure 16.1b). On the NW flank of the arch, a series of contiguous arcuate headscarps are observed at water depths of ~1000 m; these are up to 5 km across, and some display a sharp seafloor expression with slope dips in excess of 25°, indicating recent initiation of slope failure (Figure 16.1b). Down dip of these headscarps, the rugose texture of the seafloor extends beyond the NW edge of the study area, suggesting that the failure complexes extend downslope well below water depths of 1500 m. Similar seafloor characteristics are observed along the SE flank of the arch (Figure 16.1b). Here well-imaged headscarps are observed at water depths of

Table 16.1 Summary Table of the Acquisition Parameters, Dominant Frequency, and Seismic Resolution for the 3D Surveys Located in the Exmouth Plateau

Survey	Water depths (m)	Area (km^2)	Number of inlines, spacing (m)	Number of crosslines, spacing (m)	Sample rate (ms)	Phase	Total record length (s)	Dominant frequency (Hz) near seafloor section	Vertical, horizontal resolution (m) near seafloor section
Thebe	919–1,524	1,428	2,211, 25	4,501, 12.5	4	Zero phase reverse polarity	4.6	60	7, 14
Bonaventure	853–1,558	4,300	6,999, 18.75	12,000, 12.5	4	Zero phase reverse polarity	7.1	40	10, 20
Centaur	978–1,460	2,600	2,940, 18.75	2,878, 25	4	Zero phase reverse polarity	6	40	10, 20

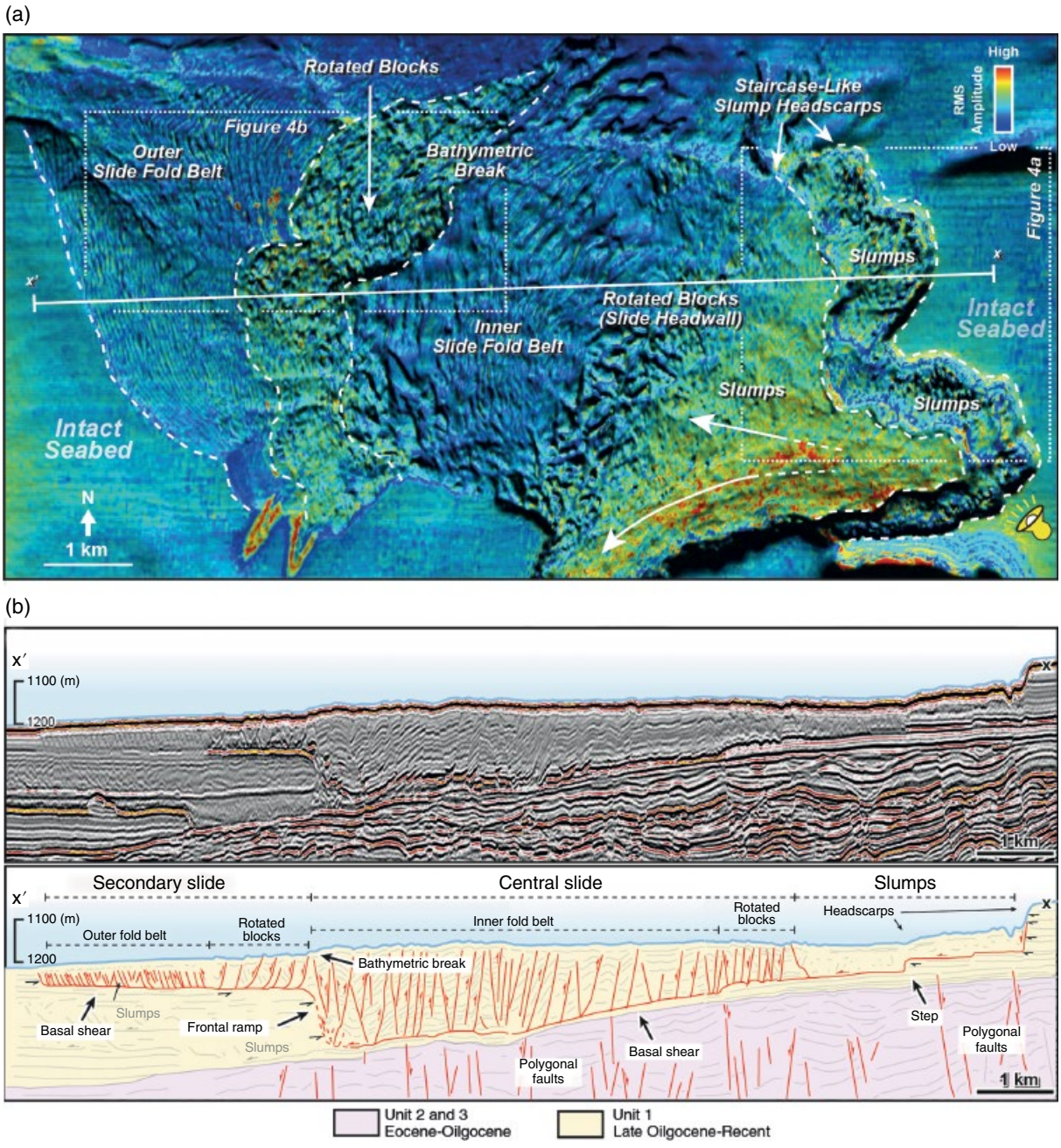


Figure 16.3 (a) Root-mean-square (RMS) amplitude extraction along the seabed horizon of the Thebe 3D data set around the seafloor areas affected by Thebe Complex. (b) Interpreted and uninterpreted seismic section through the Thebe Complex. Section location is shown in "a". The figures show that the proximal part of the Thebe Complex I is infilled by a very disrupted slump-like seismic facies. Also note that the basal shear surface of the complex exhibits here a prominent west facing step which is 20 m high. This feature is interpreted to be the remnant of a slump headscarp. The details of the 3D morphology of the headwall are shown in Figure 16.4a. Note also the occurrence downslope of the slumped mass of a series of rotated fault blocks. These represent the extensional domain of a slide that extends further down dip. Details of the contractional part of the slide are shown in Figure 16.4b.

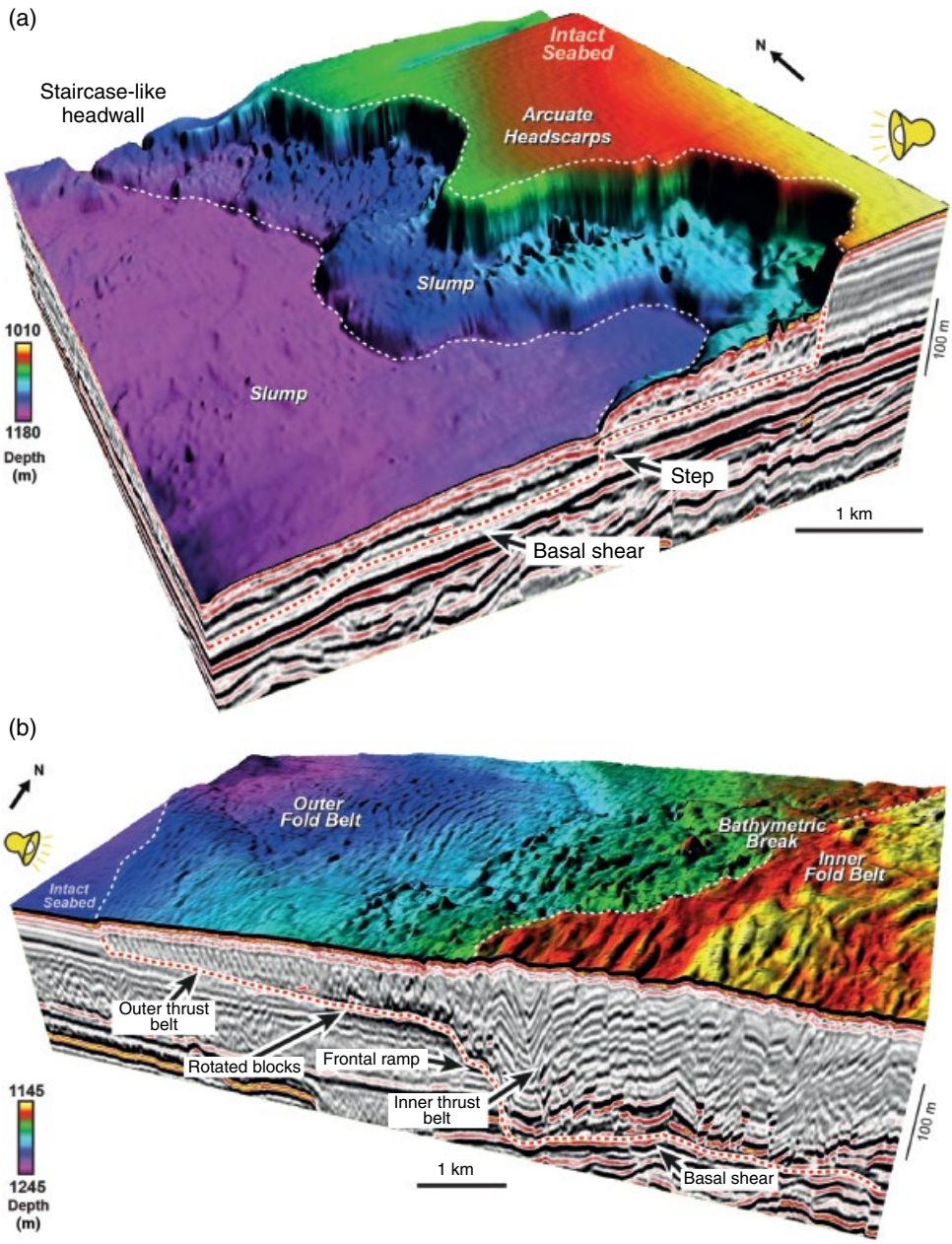


Figure 16.4 (a) Seismic block diagram showing the 3D architecture of the headwall area of the Thebe Complex. The figure illustrates two amalgamated arcuate headscarps infilled with contorted slump deposits that give rise to a rugose pattern to the seafloor. Also note that the bathymetric relief given by the step along the basal shear surface mimics the morphology of the upslope headscarps and imparts an overall staircase morphology to the headwall. This suggests the step represents a relic of a slump headscarp. (b) Seismic block diagram showing the 3D architecture of the toe area of the Thebe Complex. The image illustrates that the inner thrust belt forms at the seabed a prominent fold belt that comprises a series of hundreds of meters wide folds that extend laterally for several kilometers along the extent of the complex. Also note a bathymetric relief that divides the inner fold belts from the blocky seafloor pattern imparted by rotated blocks that occur further down dip. These form the extensional domain of a secondary slide that comprises the outer fold belt observed immediately down dip and cut into the inner fold belt for several hundred meters.

~1200 m, and the failures clearly extend downslope outside the seismic coverage area (Figure 16.1b). The Thebe Complex and the Centaur Complex as shown in Figure 16.1b are described and analyzed in detail in the following sections.

16.4. THEBE COMPLEX

The Thebe Complex occurs along the NW flank of the Exmouth Plateau Arch (Figure 16.1b). The complex is located at the northern edge of the Thebe 3D data set (Figure 16.1b), and it is part of a larger collapse feature formed by multiple segments of failures (Figures 16.1b and 16.3). The complex displays a clear headwall located at a water depth of ~1010 m (Figures 16.1b and 16.3). Main transport direction is to the NW with part of the material evacuated by its collapse being fed a failure that extends downslope to the SW (Figures 16.1b and 16.3). The Thebe Complex extends laterally for at least 8 km and has a runout of 20 km (Figure 16.3a) and thickness that ranges from ~50 m in the headwall area up to 200 m in the toe area (Figure 16.3b). The failure extends over an area of ~100 km^2 with an estimated total volume of ~13 km^3.

The Thebe Complex occurs within the late Oligocene to Recent Unit 1 with its basal shear surface mainly occurring toward the base of this unit (Figure 16.3b). In the headwall area, polygonal faults are clearly observed cutting through Unit 1 and terminating below the basal shear surface of the system (Figure 16.3b). The lack of a seismically resolvable sealing unit above the failure would imply that the system is very recent, and it might be still active at the present day.

16.4.1. Headwall Slumps

The headwall region of the Thebe Complex exhibits two amalgamated ~3 km wide arcuate headscarps with maximum hanging wall offset of ~40 m (Figures 16.3b and 16.4a). The headwall section is characterized by a highly disrupted seismic facies with variable amplitude, and the seafloor relief shows a rugose texture (Figure 16.4a). These observations indicate that slumping was the main slope instability process in this part of the failure (Figure 16.3).

Down dip of the headscarps, the basal shear surface exhibits a prominent 20 m high, west facing step (Figure 16.4a). The step mimics the bathymetric relief of the two main headscarps located further up dip and imparts an overall staircase-like geometry to the whole headwall area (Figures 16.3 and 16.4a). These observations suggest that the step in the basal shear surface may represent the relict of a slump headscarp, and therefore the slump masses in the headwall region of the system were emplaced through multiple collapses. The marked seabed roughness imparted by the slumps up dip of the step may provide further evidence that these proximal deposits collapsed more recently than the slump mass further downslope which exhibits a smoother seabed texture (Figure 16.4a). This evidence implies an unsteady retrogression of the headwall of the Thebe Complex through the collapse of successive slumps.

16.4.2. Central Slide

Down dip, the slump mass passes to a series of hundreds of meter-scale extensional slide blocks (Figure 16.3). The blocks are expressed at the seafloor as a series of elongated extensional ridges up to 1 km in length (Figure 16.3). The blocks are interpreted to form the extensional domain linked to an inner thrust belt of a slide that extends further downslope (Central Slide in Figure 16.3b). Estimates of ~170 m of total extension within the slide blocks and ~200 m of total contraction in the inner thrust belt support this interpretation. These values were calculated simply subtracting bed length along a continuous reflection from the length of the section depicting the domain analyzed.

The inner thrust belt is formed by an imbricate thrust fault system and associated hanging wall fold anticlines (Figures 16.3 and 16.4b). Contractional strain contributed to the significant thickening seen in this part of the complex (Figure 16.4b). Here, in fact, the complex reaches its maximum thickness of ~200 m (Figures 16.3b and 16.4b). Seafloor renderings show that the thrust-related folds are tens of meters to hundreds of meters across and can be traced laterally all along the fold belt (Figure 16.4b).

16.4.3. Secondary Slide

The leading edge of the inner fault belt shows a prominent frontal ramp that abruptly passes down dip into a series of extensional slide blocks and to an outer thrust belt (Figures 16.3 and 16.4b). The blocks are up to ~150 m across and ~50 m high and give rise to a striking blocky seafloor relief (Figure 16.4b). The outer thrust belt comprises an imbricate thrust fault system with spacing between adjacent structures <50 m (Figure 16.4b). The extensional blocks and the outer thrust belt detach at a common shallower stratigraphic level with respect to the rest of the complex (Figures 16.3b and 16.4b). This suggests that the slide blocks and the outer fold belt may represent the extensional and contractional domains of a secondary slide that developed at the front of the inner fold belt (Figures 16.3 and 16.4b). This is supported by the fact that lateral variations in the length of the slope affected by the rotated fault blocks seem to correspond to

comparable length variations of the outer fold belt further down dip (Figure 16.3a).

A clear a break in the bathymetry is observed between the elevated inner thrust belt and the rotated blocks, and its irregular planform indicates that in places, the secondary slide cut up dip into the inner fold belt for several hundred meters (Figures 16.3 and 16.4b). This suggests that the secondary slide is a later feature that may have developed in response of the gravitational collapse of the elevated leading edge of the inner fold belt (Figures 16.3 and 16.4b).

16.5. CENTAUR COMPLEX

16.5.1. Overview

The Centaur Complex is part of a series of failures that affected the SE flank of the Exmouth Plateau Arch (Figures 16.1 and 16.5). The complex is found in the late Oligocene to Recent Unit 1, and as the Thebe Complex, it developed above a basal shear surface located in the lower part of that unit (Figure 16.5). Polygonal faults are commonly observed terminating or being cut below the

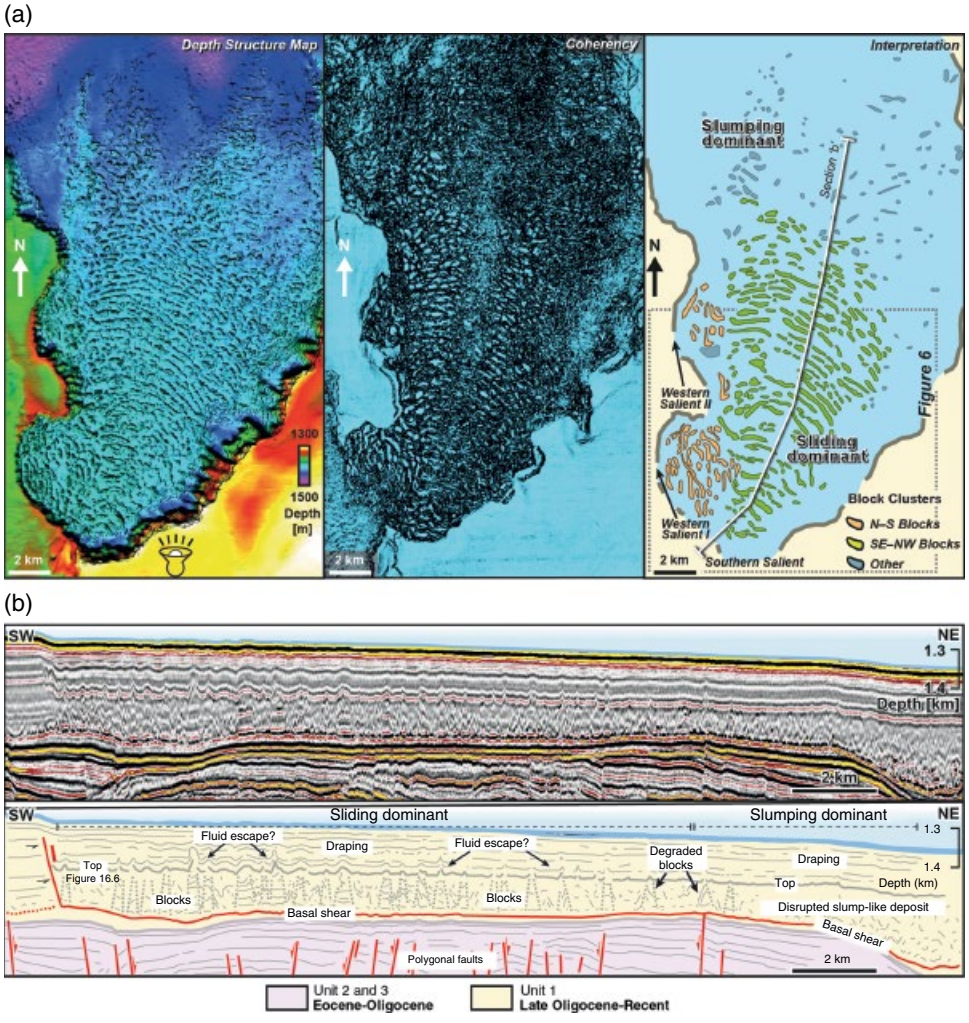


Figure 16.5 (a) From left to right, depth structure map of the top surface of Centaur Complex; coherency extraction of the proportional slice within the Centaur Complex; interpretation of different clusters of blocks observed in the Centaur complex. See text for full discussion of the maps. (b) Interpreted and uninterpreted seismic section through the Centaur Complex. Section location is shown in "a". The section shows that the proximal part of the complex comprises numerous closely spaced, relatively undeformed blocks up to 500 m across. The blocks become sparse downslope and increasingly degraded. It is suggested that this pattern indicates very limited transport and hence degradation of the failure in its up dip segment that progressively increases further downslope, resulting in a fully disrupted slump.

basal shear surface of the failure (Figure 16.5). The Centaur Complex is sealed by a continuous drape section up to 100 m thick (Figure 16.5). The occurrence of this sealing unit of possible late Pliocene age indicates that the complex is not active at the present day.

The Centaur Complex has the headwall located at present-day water depths of ~1200 m (Figure 16.1) and has a thickness of 70 m that increases downslope up to 100 m (Figure 16.5). The measured values for length, area, and volume estimates for this failure are 25 km, 250 km^2, and 21 km^3. These figures are likely to be substantially larger as suggested by the fact that the complex becomes thicker downslope, hence indicating that a large part of the failure extends outside the seismic coverage available (Figures 16.1 and 16.5).

16.5.2. Headwall Salients

The headscarp of the Centaur Complex is a convex upslope ~8 km wide feature with hanging wall offset of 50–80 m (Figure 16.5). The headscarp is formed by three scoop-shaped distinct salient (Figure 16.5). The southern salient is located at the southern end of the headwall. It exhibits an E-W strike direction and a width of ~3 km. The salient cuts up dip (to the south) into the intact slope for ~1 km. The western salient I is a prominent feature located to the west of the southern salient and shows a N-S strike direction. The salient cuts westward into the unfailed slope for ~1.8 km and extends laterally for ~5 km. The western salient II occurs south of the western salient I, and it is divided by this feature by a prominent unfailed promontory that protrudes into the failure. The salient has N-S direction with a width of ~3.5 km, and it cuts to the west for ~1.5 km into the unfailed strata.

16.5.3. Internal Architecture

The Centaur Complex is internally typified by a multitude of blocks, clearly highlighted by coherency extractions, which impart a strong relief on the failure's top surface (Figures 16.5a and 16.6). The blocks typically exhibit a tapered cross-sectional shape with their basal part up to 500 m wide (Figure 16.5b). In places, the apical part of the blocks exhibits a marked cuspate geometry with the top surface of the failure together with the reflections immediately above being clearly breached (Figure 16.5b). This disrupted strata pattern is observed all along the failure and may be related to a mechanism of fluid focusing and escape at the top of the blocks (Figure 16.5b).

In the proximal part of the failure, the blocks are closely spaced, and in places, their basal part is in direct contact (Figure 16.5b). Also, in this part of the complex, the blocks exhibit a limited degree of degradation as indicated by the parallel and largely undeformed nature of their internal strata and by the strong relief that they exhibit at the top surface (Figures 16.5 and 16.6). By contrast, in the distal part of the failure, blocks are increasingly sparser and pass downslope to a very disrupted slump-like deposit

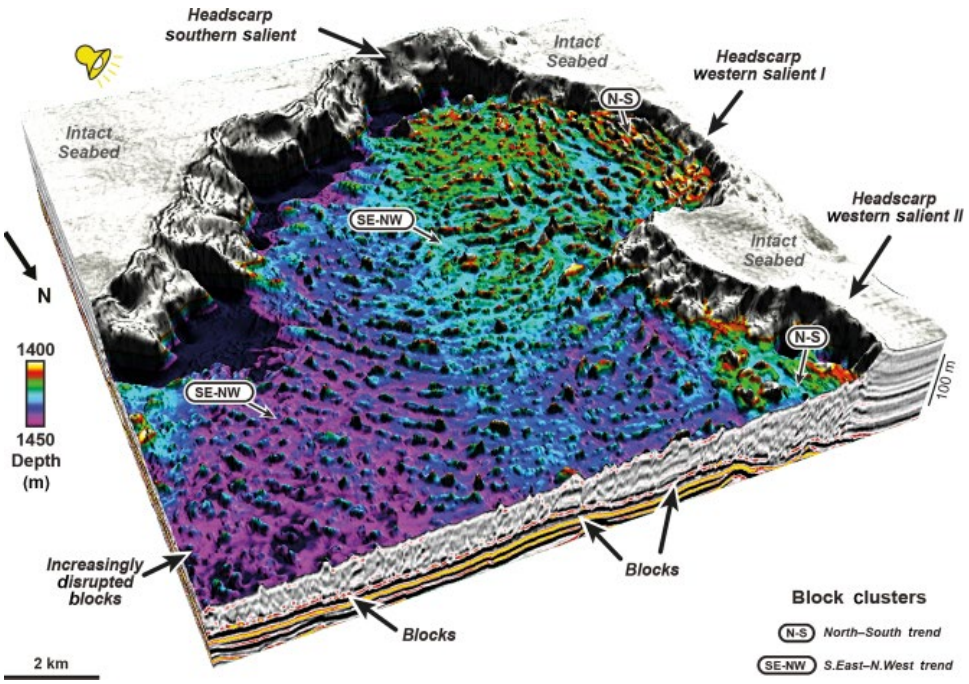


Figure 16.6 Seismic block diagram showing the spatial arrangement of the blocks forming the proximal part of Centaur Complex. See text for full discussion.

(Figure 16.5b). Also, the blocks here are severely degraded as suggested by clear rotation of internal strata and the subtle relief that they impart to the top surface (Figures 16.5 and 16.6). This downslope trend in the internal characters of the complex is clearly indicative of an increment in internal disruption of the failing mass from the proximal to the distal part of the failure. The trend would suggest a transition from a sliding-dominated failure in the upper reach of the system to a slumping-dominated one further down dip (Figure 16.5b).

Analysis of the top surface and coherency extraction of the Centaur Complex have been used to unravel the distribution and the planform morphology of the abundant blocks observed in the proximal part of the failure (Figures 16.5a and 16.6). The blocks here have been found to be elongated with the long axis oriented along two main trends:

1. N-S blocks: These blocks exhibits a marked N-S trending orientation and are found within the western salients I and II. The areal extension of these blocks is clearly constrained by the occurrence to the west of blocks with different orientation.

2. SE-NW blocks: This cluster contains blocks that are arranged in an arcuate fashion and are characterized by an overall southeast-northwest orientation. They are bounded to the west by the N-S trending blocks, and downslope, the cluster transitions into a series of sparse blocks with no preferential orientation, embedded into an increasingly extensive disrupted slump-like facies.

16.6. MECHANISMS FOR GENERATION OF COMPOSITE FAILURES

16.6.1. Collapse of the Frontal Part of Failures

Elevated highs at the front of an early primary failure are likely to be gravitationally unstable and therefore prone to collapse and form secondary failures down dip. This mechanism occurred in the Thebe Complex where the emplacement of the central slides resulted in the structuring of a fold and thrust belt up to 200 thick (Figures 16.3 and 16.4b). The elevated and over-thickened leading edge of the fold belt underwent gravitational collapse which produced a thinner (~50 m) second-order slide that detached at shallower stratigraphic level (Figures 16.3 and 16.4b).

A comparable mechanism of gravitational collapse has been described in the thrust-uplifted Eocene slope deposits of the Ainsa foreland basin, in the Spanish southern Pyrenees (Muñoz et al., 1994). The authors of the study mapped a series of scoop-shaped slump scars up to 20 m wide within the Eocene slope strata. These scars form continuous erosional surfaces laterally traceable for several kilometers. These surfaces together with their infill made of basinal and remobilized platform sediments have been folded and displaced by the advance of the underlying foreland thrust wedge indicating that progressive thickening and uplift of the wedge resulted in the lateral collapse of multiple shallow failures. Similar processes of "fold degradation" have been ascribed to have affected deepwater fold and thrust belts offshore Niger Delta (Heini & Davies, 2006), Baram Delta (Morley, 2009), Orange Basin (Scarselli et al., 2016), and Amazon Fan (Reis et al., 2010).

The overall morphology of the final product of this type of composite failures is similar to "frontally emergent" submarine landslides described by Frey-Martínez et al. (2005) offshore Israel-Eastern Mediterranean. The landslides described there show prominent accumulation of the failing mass above the undisturbed strata at the toe region, immediately down dip of a frontal ramp. Although sharing similarities in final geometries of their products, "frontally emergent" failures are not related to degradation of a primary failure, but rather related to the fact that a failure with high potential energy is able to emerge upward along a frontal ramp and spread at the seabed (Frey-Martínez et al., 2005). Therefore, strictly speaking, "frontally emergent" failures should not be considered composite features. A comparable process of frontal emersion is described by Færseth and Sætersmoen (2008) and Morita et al. (2012) at the leading edge of the Storegga Slide (offshore Norway) and of the Shimokita Peninsula failures (NE Japan), respectively. In these examples, slip at the base of the failure was transferred to a higher stratigraphic level through a frontal ramp. Continued downslope movement of the failing sedimentary body resulted in a prominent fault-bend fold associated to the frontal ramp. Despite similar geometry to the Thebe Complex, the downslope edge of these two failures does not show evidence of frontal degradation, that is, they lack evidence of gravitational collapse of the fault-bend fold by secondary slides. Therefore, also these examples cannot be considered composite failures.

16.6.2. Headscarp Retrogression

This second mechanism is related to different modes in which progressive retrogression might occur at the headscarp of failures. Retrogression develops as headscarp collapse undercuts up dip segments of the slope, which in turn become gravitationally unstable driving further collapses upslope (Mulder & Cochonat, 1996; Bull et al., 2009; Sawyer et al., 2009; Richardson et al., 2011).

In the Thebe Complex, headscarp retrogression occurred as a result of the emplacement of the central slide (Figures 16.3 and 16.4a). The steps observed along the basal shear surface up dip of the slide link increasingly shallow levels of basal slip (Figures 16.3b and 16.4a). This may suggest that failure retrogression affected progressively thinner, and likely less consolidated, slope sections that collapsed as a series of disrupted slumps that now form an amalgamated slump mass upslope of the slide

(Figure 16.3b). In this case, the final product of headwall retrogression is a slump-to-slide composite failure.

In the Centaur Complex, failure retrogression may be suggested by the occurrence of interlocked coherent slide blocks aligned parallel to the headscarp salients in which they are contained and, hence, from which they were evacuated (Figures 16.5a and 16.6). In the case of the Centaur Complex, failure retrogression occurred along a single, flat, and possibly strongly overpressured basal shear that permitted efficient sliding and evacuation of slide blocks. Fluid focusing and escape at the top of the blocks may provide evidence for such basal overpressure (Figure 16.5b). As retrogression occurred, newly created blocks were evacuated from successive, up dip migrating headscarps, whereas early blocks progressively translated down dip (Figure 16.5). Downslope translation of blocks was responsible for their progressive disaggregation into a slump mass. The final product of the failure is a slide-to-slump composite deposit (Figure 16.5b).

This slide-to-slump composite failure can be favorably compared with the Lemieux landslides (Ontario, Canada), a subaerial failure characterized by strong headwall retrogression (Evans & Brooks, 1994). The landslide, which occurred on 27 June 1993, involved ~0.003 km^3 of soil of the east bank of the South Nation River and retrogressed ~700 m into the plain around the river (Evans & Brooks, 1994). The failure affected a section of ~18 m made of basal marine "quick clay" (i.e., sensitive to liquefaction) and an overlying stiffer cap of deltaic sands and silts (Evans & Brooks, 1994). Mobilization of the basal clay initiated the landslip that developed through a series of headwall retrogressions with the evacuation of the stiffer cap in the form of slide blocks which were progressively broken up and disintegrated (Evans & Brooks, 1994). Relatively intact slide blocks up to 100 m long were observed within the headscarp salients of the landslide, whereas the central part of the failure exhibited a heavily deformed slump-like mass, the result of the disintegration of blocks evacuated in the initial phase of collapse.

16.7. TRIGGERING MECHANISMS

16.7.1. Seismic Activity

Earthquakes are thought to be very effective triggers of slope failure because seismic shaking induces shear stress to the sediment column and at the same time creates transitory excess pore pressure in the sediments, which in turn degrades the shear strength of sediments (Hampton et al., 1996; Locat & Lee, 2002; Lee et al., 2007). Along the Exmouth Plateau, recent earthquakes are numerous and have reached magnitude > 5 (Hillis et al., 2008). These have been related to the late Oligocene to present-day Australia-Eurasia collision which has led to reactivation of rift faults and development of inversion structures, such as the Exmouth Plateau Arch and other arches in the surrounding areas (Keep et al., 2007). Therefore slope steeping above inversion structures combined with concurrent induced shear stress and shear strength degradation of slope strata makes the Neogene reactivation of rift faults and associated earthquakes the likely triggers of slope failure in this region (Table 16.2).

Table 16.2 Potential Triggering Factors of Slope Failure in the Exmouth Plateau Arch

		Factors causing submarine slope instability	Exmouth Plateau Arch
Increase of downslope driving stress	*Slope steepening*	Regional tectonics and faulting	Likely relevant. Neogene reactivation of rift structures documented in the area
		Erosion	Likely relevant. Action of bottom currents reported in the region
	Seismic shaking	Earthquakes	Likely relevant. Neogene reactivation of rift structures documented in the area
	Wave loading	Hurricanes Tsunamis Storms	Likely irrelevant. Failures occurred well below wave base
Reduction of sediment strength	*Excess pore fluid pressure*	Dissociation of gas hydrates	Likely irrelevant. Gas hydrates thought to be stable in deep water
		Hydrocarbon generation	Likely irrelevant. Not known source rocks in the Neogene section
		Fluid seepage and migration	Likely relevant. Presence of polygonal faults supports fluid uplift
		Earthquakes	Likely relevant. Neogene reactivation of rift structures documented in the area
		High sedimentation rate	Low sedimentation rate in the Neogene

See text for full discussion.

16.7.2. Wave Loading and Dissociation of Gas Hydrates

Wave loading during tsunamis, storms, and hurricanes and overpressure generation due to dissociation of gas hydrates are considered to be very effective triggering mechanisms of submarine failures. Wave loading is able to induce shear stress at the seafloor in water depths up to 100 m (Henkel, 1970; Bea et al., 1983), and gas hydrates located at water depth <500 m are thought to be unstable under minimal variations of pressure and temperature, leading to their dissociation and resulting in buildup of excess pore fluid pressure within the hosting sediments (Mienert et al., 1998, 2005; Xu & Germanovich, 2006). The range of water depths in which these two triggers are thought to operate (0–500 m) suggests that they may not have played an important role in generating the failure analyzed in this research. In fact, the slope failures observed in the study area occurred at water depth in excess of 1000 m (Figure 16.1; Table 16.2).

16.7.3. Bottom Currents

Bottom currents are able to generate erosion at the seabed and increase the overall steepness of the slope inducing failure (e.g., Sayago-Gil et al., 2010). Also, deposition from steady currents confers good sorting to contourite deposits, which implies higher water content in the sediments and hence their weakness (Laberg & Camerlenghi, 2008). Bottom current activity has been reported to have occurred in the near seabed section along the Exmouth Plateau Arch (Shipboard Scientific Party Report, 1990, Scarselli et al., 2013). Therefore, these currents may have facilitated the initiation of the slope failures observed in the area.

16.7.4. High Sedimentation Rate

High sedimentation rate is thought to hinder effective expulsion of fluids from sediments which can cause onset of overpressures (i.e., disequilibrium compaction overpressures; Swarbrick et al., 2002). For this reason, high sedimentation rate is considered an effective mechanism for the development of weak sedimentary units, prone to collapse.

High sedimentation rate is not likely to be critical for initiation of Neogene slope failures on the Exmouth Plateau Arch because the arch is an isolated bathymetric high ~300 km offshore NW Shelf of Australia and has low sedimentation rates (Golovchenko et al., 1992) and sedimentary characteristics that indicate bathyal environment of deposition (Shipboard Scientific Party Report, 1990).

16.7.5. Fluid Seepage and Migration

Seepage of fluids through sediments can lead to their weakening and failure (Locat & Lee, 2002). Extensive arrays of polygonal faults have been observed underlying the slope failures of the Exmouth Plateau Arch (Figure 16.2). Polygonal fault systems can result from different mechanisms of sediment compaction that typically lead to the release of fluids (Cartwright & Lonergan, 1996; Berndt, 2005; Hustoft et al., 2007). This could suggest that weakening and failure of the slopes along the Exmouth Plateau Arch may have been promoted by fluid migration from the underlying polygonal faults. Similarly, Berndt et al. (2003) have reported the occurrence of polygonally faulted strata beneath the northern sidewall of the Storegga Slide and have proposed that fluid release from the polygonal fault system may have played a role in the collapse of the slide.

16.7.6. Slope Steepening

Gravity exerts a downslope driving stress (gravitational shear stress) as long as the seafloor is not flat (Hampton et al., 1996; Locat & Lee, 2002; Lee et al., 2007). A steep slope is considered a preconditioning factor, whereas the increase of slope steepness is a plausible triggering factor (van Weering et al., 1998; Huhnerbach & Masson, 2004; Masson et al., 2010).

Slope steepening was likely an important factor for the development of slope failure in the Exmouth Plateau. As discussed earlier, in the Exmouth Plateau, the late Oligocene to present-day Australia-Eurasia collision caused inversion of rift faults. Steepening of the slopes around these emerging structures promoted gravitational collapse along their flanks (Table 16.2).

16.8. CONCLUSIONS

The emplacement of the Neogene slope failures observed in the Exmouth Plateau Arch is likely related to a combination of triggering and preconditioning factors. In particular, slope steepening and seismic shaking related to the inversion of rift structures may have provided a very effective triggering mechanism. Fluid seepage from polygonal faults may have played a major role as preconditioning factor causing weakening of the Neogene sedimentary pile.

Detailed 3D seismic analysis of the internal structures of slope collapses has revealed the widespread occurrence of failures in which different processes of failure coexist, resulting in composite products. Two genetic mechanisms are proposed for the generation of these composite failures:

1. Frontal collapse: This mechanism is related to the gravitational collapse of the elevated leading edge of a

primary failure. Elevated highs at the front of a primary failure are likely to be gravitationally unstable and therefore prone to collapse and form secondary failures down dip. This mechanism is comparable to degradation of thrust-uplifted syn- tectonic strata observed along present-day submarine fold belts and subaerially exposed ancient foreland basins. Typical failures generated by this process include shallow-detaching, second-order slides that originate by the gravitational collapse of the leading edge of the primary slide.

2. Headscarp retrogression: This second mechanism is related to progressive retrogression of failures. Initial failure provides evacuated slide blocks, and as retrogression occurs, newly created blocks are produced at the headscarp up dip, whereas early blocks progressively translate down dip and disaggregate into slumps. Typical products of this mechanism are composite slide-slump deposits that compare favorably with similar subaerial failures characterized by a strong component of headwall retrogression (e.g., Lemieux landslides, Canada). Alternatively, retrogression can affect progressively thinner, hence poorly consolidated strata which would result in an amalgamated slump mass upslope of the primary failure.

The occurrence of one or more of these evolutionary paths in composite failures can generate products with a laterally highly variable architecture. This implies that caution is necessary when predicting up dip and down dip facies changes from a single point of observation.

ACKNOWLEDGMENTS

The authors gratefully acknowledge Geoscience Australia for providing the seismic data shown in this study. Resources and equipment for this research were kindly provided by the Fault Dynamics Research Group. Halliburton are thanked for kindly providing Decision Space Desktop seismic interpretation software as a university research grant. The authors are indebted to two anonymous reviewers for their suggestions and comments that greatly improved this contribution.

REFERENCES

AGSO North West Shelf Study Group (1994). Deep reflections on the North West Shelf: Changing perceptions of basin formation. In P. G. Purcell & R. R. Purcell (Eds.), *The sedimentary basins of Western Australia: Proceedings of the Western Australian basins symposium* (pp. 63–76). Perth, WA: PESA, WA Branch.

Amante, C., & Eakins, B. W. (2006). *ETOPO1 1 arc-minute global relief model: Procedures, data sources and analysis*. Boulder, CO: National Geophysical Data Centre, NESDIS, NOAA, US Department of Commerce.

Barber, P. M. (1988). The Exmouth Plateau deep water frontier: A case history. In P. G. Purcell & R. R. Purcell (Eds.), *The North West Shelf, Australia: Proceedings of petroleum exploration society of Australia symposium* (pp. 173–187). Perth, WA: Petroleum Exploration Society of Australia.

Bea, R. G., Sircar, P., & Niedoroda, A. W. (1983). Wave-induced slides in south pass block 70, Mississippi Delta. *Journal of Geotechnical Engineering*, *109*, 619–644.

Berndt, C. (2005). Focused fluid flow in passive continental margins. *Philosophical Transactions of the Royal Society A: Mathematical, Physical and Engineering Sciences*, *363*(1837), 2855–2871.

Berndt, C., Bünz, S., & Mienert, J. (2003). Polygonal fault systems on the mid-Norwegian margin: A long-term source for fluid flow. In P. V. Rensbergen, R. Hillis, A. Maltman, & C. Morley (Eds.), *Origin, processes, and effects of subsurface sediment mobilization on reservoir to regional scale, Special Publications* (Vol. 216, pp. 283–290). London, UK: Geological Society.

Black, M., McCormack, K. D., Elders, C., & Robertson, D. (2017). Extensional fault evolution within the Exmouth Subbasin, North West Shelf, Australia. *Marine and Petroleum Geology*, *85*, 301–315. http://dx.doi.org/10.1016/j.marpetgeo.2017.05.022

Boyd, R., Williamson, P., & Haq, B. U. (1992). Seismic stratigraphy and passive-margin evolution of the Southern Exmouth Plateau. In U. Von Rad & B. U. Haq (Eds.), *Proceedings of the Ocean Drilling Program, Scientific Results* (Vol. 122, pp. 579–603). College Station, TX: Ocean Drilling Program.

Bull, S., Cartwright, J., & Huuse, M. (2009). A subsurface evacuation model for submarine slope failure. *Basin Research*, *21*(4), 433–443.

Cartwright, J. A., & Lonergan, L. (1996). Volumetric contraction during the compaction of mudrocks: A mechanism for the development of regional-scale polygonal fault systems. *Basin Research*, *8*(2), 183–193.

Cathro, D. L., & Karner, G. D. (2006). Cretaceous-Tertiary inversion history of the Dampier Sub-basin, northwest Australia: Insights from quantitative basin modelling. *Marine and Petroleum Geology*, *23*(4), 503–526.

Dott, R. H. (1963). Dynamics of subaqueous gravity depositional processes. *AAPG Bulletin*, *47*, 104–128.

Embley, R. W., & Jacobi, R. D. (1977). Distribution and morphology of large submarine sediment slides and slumps on Atlantic continental margins. *Marine Georesources & Geotechnology*, *2*(1), 205–228.

Evans, S. G., & Brooks, G. R. (1994). An earthflow in sensitive Champlain Sea sediments at Lemieux, Ontario, June 20, 1993, and its impact on the South Nation River. *Canadian Geotechnical Journal*, *31*(3), 384–394.

Færseth, R. B., & Sætersmoen, B. H. (2008). Geometry of a major slump structure in the Storegga slide region offshore western Norway. *Norwegian Journal of Geology*, *88*, 1–11.

Frey-Martínez, J., Cartwright, J., & Hall, B. (2005). 3D seismic interpretation of slump complexes: Examples from the continental margin of Israel. *Basin Research*, *17*, 83–108.

Frey-Martínez, J., Cartwright, J., & James, D. (2006). Frontally confined versus frontally emergent submarine landslides: A 3D seismic characterisation. *Marine and Petroleum Geology*, *23*(5), 585–604.

Gee, M. J. R., Gawthorpe, R. L., & Friedmann, S. J. (2006). Triggering and evolution of a giant submarine landslide, offshore Angola, revealed by 3D seismic stratigraphy and geomorphology. *Journal of Sedimentary Research*, *76*, 9–19.

Golovchenko, X., Borella, P. E., & O'Connell, S. (1992). Sedimentary cycles on the Exmouth Plateau. In U. Von Rad & B. U. HAQ (Eds.), *Proceedings of the Ocean Drilling Program, Scientific Results* (Vol. 122, pp. 279–291). College Station, TX: Ocean Drilling Program.

Hampton, M. A., Lee, H. J., & Locat, J. (1996). Submarine landslides. *Reviews of Geophysics*, *34*(1), 33–59.

Hearty, D. J., Ellis, G. K., & Webster, K. A. (2002). Geological history of the western Barrow Sub-basin: Implications for hydrocarbon entrapment at Woollybutt and surrounding oil and gas fields. In M. Keep & S. J. Moss (Eds.), *The sedimentary basins of Western Australia 3* (pp. 577–598). Perth, WA: Petroleum Exploration Society of Australia.

Heini, P., & Davies, R. J. (2006). Degradation of compressional fold belts: Deep-water Niger Delta. *AAPG Bulletin*, *90*, 753–770.

Henkel, D. J. (1970). The role of waves in causing submarine landslides. *Geotechnique*, *20*(1), 75–80.

Hillis, R. R., Sandiford, M., Reynolds, S. D., & Quigley, M. C. (2008). Present-day stresses, seismicity and Neogene-to-Recent tectonics of Australia's "passive" margins: Intraplate deformation controlled by plate boundary forces. In H. Johnson, A. G. Doree, R. Holdsworth, E. Lundin, & J. D. Ritchie (Eds.), *The nature and origin of compressive margins, Special Publications* (Vol. 306, pp. 71–90). London, UK: Geological Society.

Huhnerbach, V., & Masson, D. G. (2004). Landslides in the North Atlantic and its adjacent seas: An analysis of their morphology, setting and behaviour. *Marine Geology*, *213*(1–4), 343–362.

Hustoft, S., Mienert, J., Bünz, S., & Nouzé, H. (2007). High-resolution 3D-seismic data indicate focused fluid migration pathways above polygonal fault systems of the mid-Norwegian margin. *Marine Geology*, *245*(1), 89–106.

Jitmahantakul, S., & McClay, K. (2013). Late Triassic – Mid-Jurassic to Neogene extensional fault systems in the Exmouth Sub-Basin, Northern Carnarvon Basin, North West Shelf, Western Australia. In M. Keep & S. J. Moss (Eds.), *The sedimentary basins of Western Australia IV: Proceedings of the Petroleum Exploration Society of Australia symposium*. Perth, WA: Petroleum Exploration Society of Australia.

Keep, M., Harrowfield, M., & Crowe, W. (2007). The Neogene tectonic history of the North West Shelf, Australia. *Exploration Geophysics*, *38*(3), 151–174.

Keep, M., Powell, C. M., & Baillie, P. W. (1998). Neogene deformation of the North West Shelf, Australia. In P. G. Purcell & R. R. Purcell (Eds.), *The sedimentary basins of Western Australia 2: Proceedings of the Petroleum Exploration Society of Australia symposium* (pp. 81–91). Perth, WA: Petroleum Exploration Society of Australia.

Laberg, J. S., & Camerlenghi, A. (2008). The significance of contourites for submarine slope stability. *Developments in Sedimentology*, *60*, 537–556.

Lee, H. J., Locat, J., Desgagnes, P., Parsons, J. D., McAdoo, B. G., Orange, D. L., et al. (2007). Submarine mass movements on continental margins. In C. A. Nittrouer, J. A. Austin, M. E. Field, J. H. Kravitz, J. P. M. Syvitski, & P. L. Wiberg (Eds.), *Continental margin sedimentation* (Vol. 28, pp. 213–274). Oxford, UK: Blackwell.

Locat, J., & Lee, H. J. (2002). Submarine landslides: Advances and challenges. *Canadian Geotechnical Journal*, *39*(1), 193–212.

Longley, I. M., Buessenschuett, C., Clydsdale, L., Cubitt, C. J., Davis, R. C., Johnson, M. K., et al. (2002). The North West Shelf of Australia: A woodside perspective. In M. Keep & S. J. Moss (Eds.), *The sedimentary basins of Western Australia 3: Proceedings of the Petroleum Exploration Society of Australia Symposium* (pp. 28–88). Perth, WA: Petroleum Exploration Society of Australia.

Masson, D. G., Wynn, R. B., & Talling, P. J. (2010). Large landslides on passive continental margins: Processes, hypotheses and outstanding questions. In D. C. Mosher, R. C. Shipp, L. Moscardelli, J. D. Chaytor, C. D. P. Baxter, H. J. Lee, & R. Urgeles (Eds.), *Submarine mass movements and their consequences* (Vol. 28, pp. 153–165). Dordrecht, The Netherlands: Springer.

McHugh, C. M. G., Damuth, J. E., & Mountain, G. S. (2002). Cenozoic mass-transport facies and their correlation with relative sea-level change, New Jersey continental margin. *Marine Geology*, *184*(3), 295–334.

Metcalfe, I. (2013). Gondwana dispersion and Asian accretion: Tectonic and palaeogeographic evolution of eastern Tethys. *Journal of Asian Earth Sciences*, *66*, 1–33.

Mienert, J., Posewang, J., & Baumann, M. (1998). Gas hydrates along the northeastern Atlantic margin: Possible hydrate-bound margin instabilities and possible release of methane. In J.-P. Henriet & J. Mienert (Eds.), *Gas hydrates: Relevance to world margin stability and climatic change, Special Publication* (Vol. 137, pp. 275–291). London, UK: Geological Society.

Mienert, J., Vanneste, M., Bunz, S., Andreassen, K., Haflidason, H., & Sejrup, H. P. (2005). Ocean warming and gas hydrate stability on the mid-Norwegian margin at the Storegga Slide. *Marine and Petroleum Geology*, *22*(1), 233–244.

Morita, S., Nakajima, T., & Hanamura, Y. (2012). Possible ground instability factor implied by slumping and dewatering structures in high-methane-flux continental slope. In Y. Yamada, K. Kawamura, K. Ikehara, Y. Ogawa, R. Urgeles, D. Mosher, et al. (Eds.), *Submarine mass movements and their consequences, Advances in Natural and Technological Hazards Research* (Vol. 31, pp. 311–320). Dordrecht, The Netherlands: Springer.

Morley, C. K. (2009). Growth of folds in a deep-water setting. *Geosphere*, *5*, 59–89. http://dx.doi.org/10.1130/GES00186.1

Moscardelli, L., & Wood, L. (2008). New classification system for mass transport complexes in offshore Trinidad. *Basin Research*, *20*(1), 73–98.

Mulder, T., & Cochonat, P. (1996). Classification of offshore mass movements. *Journal of Sedimentary Research*, *66*(1), 43–57.

Muñoz, J. A., McClay, K., & Poblet, J. (1994). Synchronous extension and contraction in frontal thrust sheets of the Spanish Pyrenees. *Geology*, *22*(10), 921–924.

Nardin, T. R., Hein, F. J., Gorsline, D. S., & Edwards, B. D. (1979). A review of mass movement processes, sediment, and

acoustic characteristics and contrasts in slope and base-of-slope systems versus canyon-fan-basin floor systems. *Special Publication: Society of Economic Paleontologists and Mineralogists*, *27*, 61–73.

Nemec, W. (1990). Aspects of sediment movement on steep delta slopes. In A. Colella & D. B. Prior (Eds.), *Coarse-grained deltas, International Association of Sedimentologists Special Publication* (Vol. 10, pp. 29–73). Oxford, UK: Blackwell Scientific.

Posamentier, H. W., Davies, R. J., Cartwright, J. A., & Wood, L. (2007). Seismic geomorphology: An overview. In R. J. Davies, H. W. Posamentier, & L. J. Wood (Eds.), *Seismic geomorphology: Applications to hydrocarbon exploration and production, Special Publications* (Vol. 227, pp. 1–14). London, UK: Geological Society.

Posamentier, H. W., & Martinsen, O. J. (2011). The character and genesis of submarine mass-transport deposits: Insights from outcrop and 3D seismic data. In R. C. Shipp & H. W. Posamentier (Eds.), *Mass-transport deposits in deepwater settings, SEPM Special Publications* (Vol. 96, pp. 7–38). Tulsa, OK: SEPM.

Reis, A. T., Perovano, R., Silva, C. G., Vendeville, B. C., Araujo, E., Gorini, C., & Oliveira, V. (2010). Two-scale gravitational collapse in the Amazon Fan: A coupled system of gravity tectonics and mass-transport processes. *Journal of the Geological Society*,*167*,593e604.http://dx.doi.org/10.1144/0016-76492009-035

Richardson, S. E., Davies, R. J., Allen, M. B., & Grant, S. F. (2011). Structure and evolution of mass transport deposits in the South Caspian Basin, Azerbaijan. *Basin Research*, *23*(6), 702–719.

Sawyer, D. E., Flemings, P. B., Dugan, B., & Germaine, J. T. (2009). Retrogressive failures recorded in mass transport deposits in the Ursa Basin, Northern Gulf of Mexico. *Journal of Geophysical Research*, *114*, B10102.

Sayago-Gil, M., Long, D., Fernandez-Salas, L. M., Hitchen, K., Lopez-Gonzalez, N., Diaz-del- Rio, V., & Duran, M. (2010). Geomorphology of the Talisman Slide (Western slope of Hatton Bank, NE Atlantic Ocean). In D. C. Mosher, R. C. Shipp, L. Moscardelli, J. D. Chaytor, C. D. P. Baxter, H. J. Lee, & R. Urgeles (Eds.), *Submarine mass movements and their consequences* (Vol. 28, pp. 277–288). Dordrecht, The Netherlands: Springer.

Scarselli, N., McClay, K., & Elders, C. (2013). Submarine slide and slump complexes, Exmouth Plateau, NW shelf of Australia. In M. Keep & S. J. Moss (Eds.), *The sedimentary basins of Western Australia IV: Proceedings of the Petroleum Exploration Society of Australia Symposium*. Perth, WA: Petroleum Exploration Society of Australia.

Scarselli, N., McClay, K., & Elders, C. (2016). Seismic geomorphology of cretaceous megaslides offshore Namibia (Orange Basin): Insights into segmentation and degradation of gravity-driven linked systems. *Marine and Petroleum Geology*, *75*, 151–180. https://doi.org/10.1016/j.marpetgeo.2016.03.012

Shanmugam, G. (2016). Submarine fans: A critical retrospective (1950–2015). *Journal of Palaeogeography*, *5*(2), 110–184.

Shipboard Scientific Party Report (1990). Site 762. In B. U. Haq, U. Von Rad, S. O'Conneü, A. Bent, C. D. Blome, P. E. Borella, et al. (Eds.), *Proceedings of the Ocean Drilling Program, initial report* (Vol. 122, pp. 213–288). College Station, TX: College Station University. https://doi.org/10.2973/odp.proc.ir.122.1990

Stow, D. A. V. (1985). Deep-sea clastics: Where are we and where are we going? In P. J. Brenchley & B. P. J. Williams (Eds.), *Sedimentology: Recent developments and applied aspects, Special Publications* (Vol. 18, pp. 67–93). London, UK: Geological Society.

Swarbrick, R. E., Osborne, M. J., & Yardley, G. S. (2002). Comparison of overpressure magnitude resulting from the main generating mechanisms. In A. R. Huffman & G. L. Bowers (Eds.), *Pressure regimes in sedimentary basins and their prediction, AAPG Memoir* (Vol. 76, pp. 1–12). Tulsa, OK: AAPG.

Tindale, K., Newell, N., Keall, J., & Smith, N. (1998). Structural evolution and charge history of the Exmouth Sub-basin, Northern Carnarvon Basin, Western Australia. In P. G. Purcell & R. R. Purcell (Eds.), *The sedimentary basins of Western Australia 2: Proceedings of Petroleum Exploration Society of Australia Symposium* (pp. 447–472). Perth, WA: Petroleum Exploration Society of Australia.

van Weering, T. C. E., Nielsen, T., Kenyon, N. H., Akentieva, K., & Kuijpers, A. H. (1998). Sediments and sedimentation at the NE Faeroe continental margin; contourites and large-scale sliding. *Marine Geology*, *152*(1), 159–176.

Varnes, D. J. (1958). Landslide types and processes. In E. B. Eckel (Ed.), *Landslides and engineering practice, Special Report, National Academy of Science* (Vol. 29, pp. 20–47). Washington, DC: Highway Research Board.

Whitney, B. B., Hengesh, J. V., & Gillam, D. (2016). Styles of neotectonic fault reactivation within a formerly extended continental margin, North West Shelf, Australia. *Tectonophysics*, *686*, 1–18. https://doi.org/10.1016/j.tecto.2016.06.008

Xu, W., & Germanovich, L. N. (2006). Excess pore pressure resulting from methane hydrate dissociation in marine sediments: A theoretical approach. *Journal of Geophysical Research*, *111*, B1.

17

Submarine Landslides Around Volcanic Islands: A Review of What Can Be Learned From the Lesser Antilles Arc

Anne Le Friant[1], Elodie Lebas[2], Morgane Brunet[3], Sara Lafuerza[4], Matt Hornbach[5], Maya Coussens[6], Sebastian Watt[7], Michael Cassidy[8], Peter J. Talling[9], and IODP 340 Expedition Science Party

ABSTRACT

IODP Expedition 340 successfully drilled, for the first time, large and likely tsunamigenic volcanic island arc landslide deposits. These cores provide evidence and tests of previous hypotheses for the composition, origin, and mode of transport of those deposits. Sites in the medial to distal parts of the landslide deposits offshore Montserrat and Martinique recovered seafloor sediment, comprising turbidites and hemipelagic deposits, and lacked the coarse and chaotic subaerial volcanic debris avalanche material. This supports the concepts that (i) the volcanic debris avalanche component of these landslides is restricted to proximal areas and tends to stop at the slope break and (ii) emplacement of volcanic debris avalanches in marine settings can trigger widespread and voluminous failures of preexisting low-gradient seafloor sediment. The most likely mechanism for generating these large-scale seafloor sediment failures appears to be the propagation of a décollement, from proximal areas that are loaded and incised by a volcanic debris avalanche. These results have implications for the magnitude of tsunami generation by volcanic island landslides. Volcanic island landslides composed of mainly seafloor sediment may form smaller magnitude tsunamis than equivalent volumes of subaerial block-rich mass flows rapidly entering water.

17.1. INTRODUCTION

Prodigious submarine landslides offshore volcanic islands have been widely recognized worldwide, such as offshore the Hawaiian Archipelago (Lipman et al., 1988; Moore et al., 1989) and La Réunion (Labazuy, 1996; Le Friant et al., 2011; Oehler et al., 2008) and in the Canary Islands (Holcomb & Searle, 1991; Krastel et al., 2001; Masson et al., 2002, 2006; Urgeles et al., 1997; Watts & Masson, 1995). Individual landslide deposits can contain hundreds to thousands of cubic kilometers of material and can extend over a distance of hundreds of kilometers (Moore et al., 1989). Over the last decades, increasing numbers of marine geophysical surveys, along with modern marine geophysical techniques, have revealed our ability to identify such deposits around volcanic islands, recognizing flank collapses as a common and important process during the evolution of volcanic edifices (Glicken, 1986; Ida & Voight, 1995; McGuire, 1996; Voight, 2000). The landslide deposits, recognized both in oceanic intraplate setting and in subduction zone context, are related to landslides that affected the subaerial and/or submarine parts of the volcanoes and have similar features suggesting that common processes control volcano instability and landslide behavior across all settings. These catastrophic events represent a range of significant volcanic hazards,

[1] *CNRS, Paris Institute of Earth Physics, University of Paris, Paris, France*
[2] *Christian-Albrechts-University of Kiel, Kiel, Germany*
[3] *University of Bremen, Bremen, Germany*
[4] *Sorbonne University, Paris, France*
[5] *SMU Dedman College, Dallas, Texas, United States*
[6] *University of Southampton, Southampton, United Kingdom*
[7] *University of Birmingham, Birmingham, United Kingdom*
[8] *Department of Earth Sciences, University of Oxford, Oxford, United Kingdom*
[9] *Departments of Earth Sciences and Geography, University of Durham, Durham, United Kingdom*

Submarine Landslides: Subaqueous Mass Transport Deposits from Outcrops to Seismic Profiles, Geophysical Monograph 246, First Edition. Edited by Kei Ogata, Andrea Festa, and Gian Andrea Pini.
© 2020 American Geophysical Union. Published 2020 by John Wiley & Sons, Inc.

which also includes the related explosive eruptions (Glicken, 1986; Siebert, 2002) and tsunamis (Lovholt et al., 2008), which can be triggered by relatively small events. Understanding where submarine landslide deposits (SLDs) are coming from and how they were emplaced offshore is crucial, since emplacement dynamics determine the magnitude of the associated tsunamis. The potential magnitude of volcanic landslide generated tsunamis is the subject of an intense debate, mainly due to uncertainties associated with slide physics and dynamics to describe how collapsed material enters the ocean (Cassidy et al., 2014; Hunt et al., 2011; Lovholt et al., 2008; Masson et al., 2006; Mattioli et al., 2007; Slingerland & Voight, 1979; Ward & Day, 2001; Watt et al., 2012a, 2012b, 2014). While some studies indicate that volcanic landslides often generate large (10–100 m high) tsunamis (e.g., Frohlich et al., 2009; Nomanbhoy & Satake, 1995; Ward & Day, 2003), other studies (Gardner, 2010; Hornbach et al., 2015; Moore et al., 1994) suggest that many of these volcanic landslides may deform incrementally, via creep, and therefore represent only a limited tsunami hazard. These mechanisms (creep vs. catastrophic failure) are not mutually exclusive, as both might occur during volcanic flank collapse (e.g., McGuire, 1996). Unfortunately, the very few direct observations of volcanic island landslide processes are limited to small historical events (e.g., Stromboli, Tinti et al., 2006), and we are not able yet to directly monitor submarine landslide processes. Studies on landslide deposit geometry allow some authors to propose conceptual models on the emplacement dynamics of submarine landslides. Bull et al. (2009) presented a review of kinematic indicators from mass-transport complexes, while Frey-Martinez et al. (2006) defined two categories of submarine landslides depending on the existence of an emergent frontal ramp. Watt et al. (2014) focused on volcanic island landslides and provided new constraints and models on the emplacement dynamics for downslope propagation of submarine deformation for different scenarios: (i) erosion and loading of seafloor sediment by volcanic debris avalanche (e.g., Deplus et al., 2001), (ii) loading of seafloor sediment by an overrunning volcanic debris flow (e.g., Watt et al., 2012a, 2012b), (iii) self-loading by downslope propagating seafloor sediment failure (e.g., Watt et al., 2012b), and (iv) décollement propagation from debris avalanche deposit (DAD) loading (e.g., Watt et al., 2012a, 2012b, 2014). However, the impacts of volcanic island landslides are not readily assessed from the final landslide deposits without a good knowledge and understanding of the components that make up the deposits.

Previous ODP Legs in Hawaii (ODP Legs 126 and 200: Garcia, 1993; Garcia & Meyerhoff Hull, 1994; Garcia et al., 2006) and the Canary Islands (ODP Leg 157: Goldstrand, 1998; Schmincke & Sumita, 1998; Schneider et al., 1997) drilled offshore oceanic intraplate volcanic islands, but the drill sites mainly targeted distal turbidite deposits located away from the seismically chaotic landslide deposits recognized in more proximal settings. The first scientific drilling of volcanic arc island landslide deposits was done by IODP Expedition 340 offshore the Lesser Antilles Arc (Figure 17.1). The newly acquired drilled cores and downhole logging data were combined with seismic reflection data acquired during four previous cruises (AGUADOMAR 1999, PI: C. Deplus; CARAVAL 2002, PI: C. Deplus, GWADASEIS 2009, PI: N. Feuillet, and JC45/46, PI: P. Talling; e.g., Deplus et al., 2001; Lebas et al. 2011; Le Friant et al., 2003a; Watt et al., 2012a, 2012b) to reinterpret the composition and emplacement dynamics of the large mass-wasting deposits mapped offshore the volcanic islands of Montserrat and Martinique (Figure 17.1). In this contribution, we discuss the most important outputs of the IODP Expedition 340 concerning (i) the composition of the gigantic chaotic units interpreted as SLDs, (ii) the type of deformation and the mechanisms of the landslide generation and propagation onto the seafloor, (iii) the geohazard potential of such systems, and finally (iv) the implications of our results for other volcanic islands. This contribution is mainly based on a review of earlier published material derived from both the previous seismic and coring campaigns and the IODP Expedition 340 carried out in 2012 (Brunet, 2015; Brunet et al., 2016, 2017; Cassidy et al., 2013, 2014, 2015; Coussens et al., 2016; Fraass et al., 2016; Hornbach et al., 2015; Jutzeler et al., 2014, 2016; Lafuerza et al., 2014; Le Friant et al., 2013, 2015; Palmer et al., 2016; Wall-Palmer et al., 2014; Watt et al., 2012a, 2012b, 2014).

The following terminology is used in this paper: *Landslide* is used as a general term referring to any type of slope failure and resulting mass movement, whether initiated onshore or offshore. The term *debris avalanche* is used for a failure comprising material in a mobile flowage-type landslide from a volcanic edifice (Glicken, 1986; Masson et al., 2002, 2006; Siebert, 2002; Voight et al., 1981, 2002, 2012), and the resulting deposits are referred to as *debris avalanche deposits*. Debris avalanches are distinguished from *slumps*, which are coherent masses of poorly consolidated materials or rocks that move over a relatively short distance downslope, on a concave-up or planar slip surface (e.g., Delcamp et al., 2008). *Debris flows* are water-saturated flows of disaggregated and/or reworked sediment with high sediment concentrations and strong interactions between solid and fluid components (Iverson, 1997). Finally, failures of seafloor sediment located beyond the slope break (i.e., transition between the base of the volcanic edifice and surrounding basin) are referred to as *seafloor sediment failures* (Watt et al., 2012a, 2012b, 2014), and the resulting deposits are referred to as *submarine landslide deposits*.

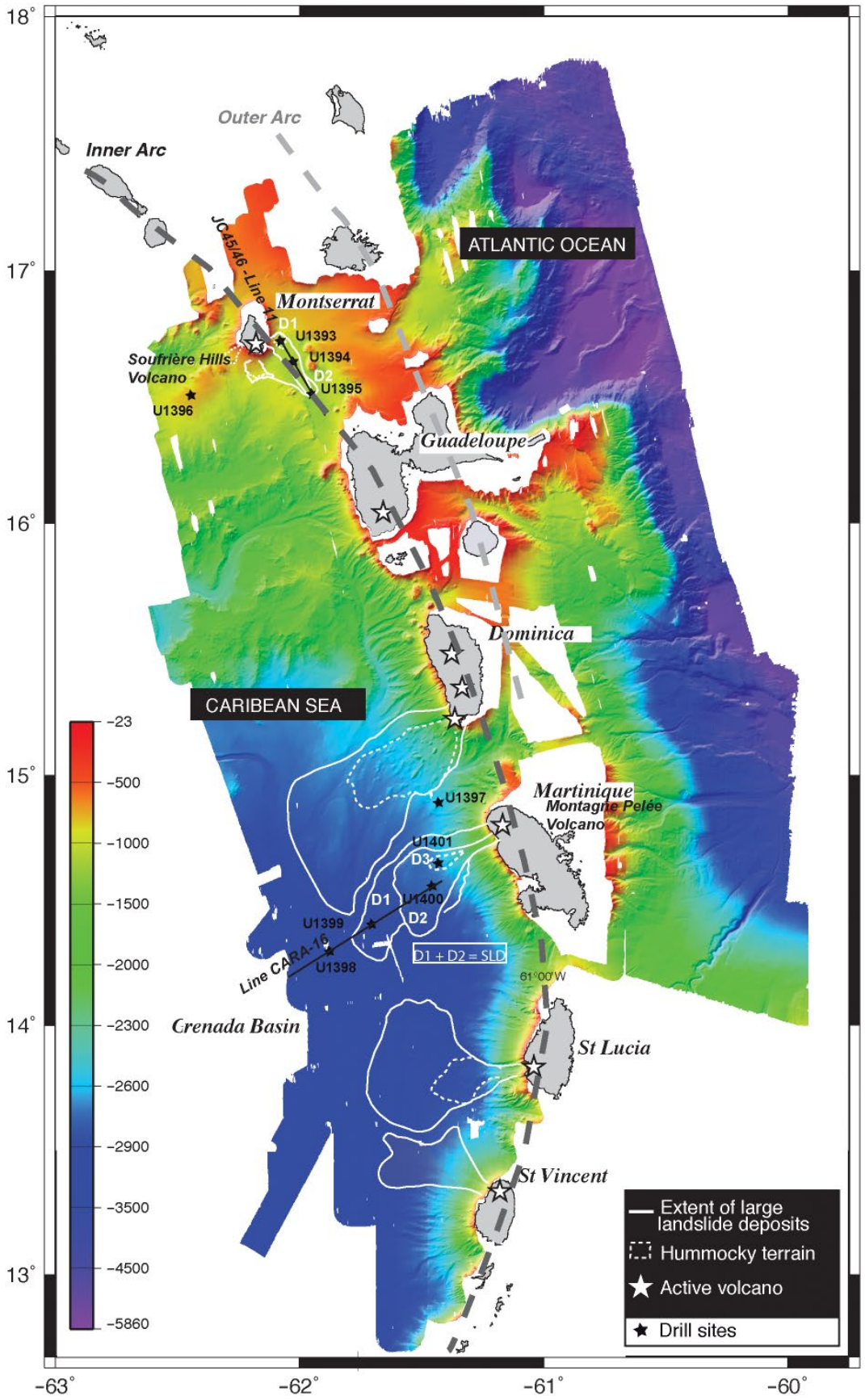


Figure 17.1 The Lesser Antilles Arc from Montserrat to St. Vincent. Extent of the main landslide deposits (chaotic units) on swath bathymetry illuminated from North (AGUADOMAR cruise (1999) and CARAVAL cruise (2002)). Active volcanoes and drilling sites are annotated. Solid lines represent the seismic profiles shown in Figure 17.2. Source: Modified from Le Friant et al. (2015).

17.2. PREVIOUS WORK ON THE LESSER ANTILLES ARC

The Lesser Antilles Arc results from the subduction of the Atlantic oceanic lithosphere beneath the Caribbean Plate (Figure 17.1), at a recent convergent rate of ~2 cm/yr (Feuillet et al., 2002). Compared to other subduction zone volcanic chains, magma productivity in the Lesser Antilles Arc is relatively low and estimated at 3–5 km^3/Ma/km (MacDonald et al., 2000; Sigurdsson et al., 1980; Wadge, 1984). South of Dominica, the volcanic islands are bordered to the west by the 2900 m deep back-arc Grenada Basin (Figure 17.1), which has been a major depocenter for large mass-wasting deposits, volcanogenic turbiditic deposits, pyroclastic flow deposits, and hemipelagic sediment (Boudon et al., 2007; Deplus et al., 2001; Picard et al., 2006; Sigurdsson et al., 1980). Fifty-two individual landslide deposits or flank collapse structures have been identified onshore and offshore on the flanks of the Lesser Antilles Arc volcanoes (Figures 17.1 and 17.2) (e.g., Boudon et al., 1984, 1987, 2007; Cassidy et al., 2014; Crutchley et al., 2013; Deplus et al., 2001; Karstens et al., 2013; Komorowski et al., 2005; Le Friant et al., 2002, 2003a, 2003b, 2004, 2009, 2010; Lebas et al., 2011; Trofimovs et al., 2006, 2010, 2013; Vincent et al., 1989; Watt et al., 2012a, 2012b). Combined analysis of marine geophysical data sets collected along the arc has resulted in a series of hypotheses regarding the composition of the SLDs and their origins and emplacement mechanisms. Deplus et al. (2001) and Le Friant et al. (2002, 2003a, 2003b, 2004) mapped, for the first time, numerous SLDs along the arc and proposed that the landslide deposits correspond to DAD originating from flank collapses affecting the volcanoes onshore. The authors suggested that during the flow, the debris avalanche erodes and mobilizes preexisting seafloor sediment and thus disturbs underlying preexisting sedimentary layers. They proposed that the upper part of the seismically chaotic deposits contains both volcanic debris from the original volcano flank collapse and remobilized preexisting seafloor sediment. In contrast, the lower part would mainly be composed of deformed preexisting seafloor sediment. Lateral transitions from well-bedded seismic reflections to chaotic facies within the landslide units in the seismic data indicate that some landslides internally contain substantial components of seafloor-derived sediment (Figure 17.2). Deplus et al. (2001)

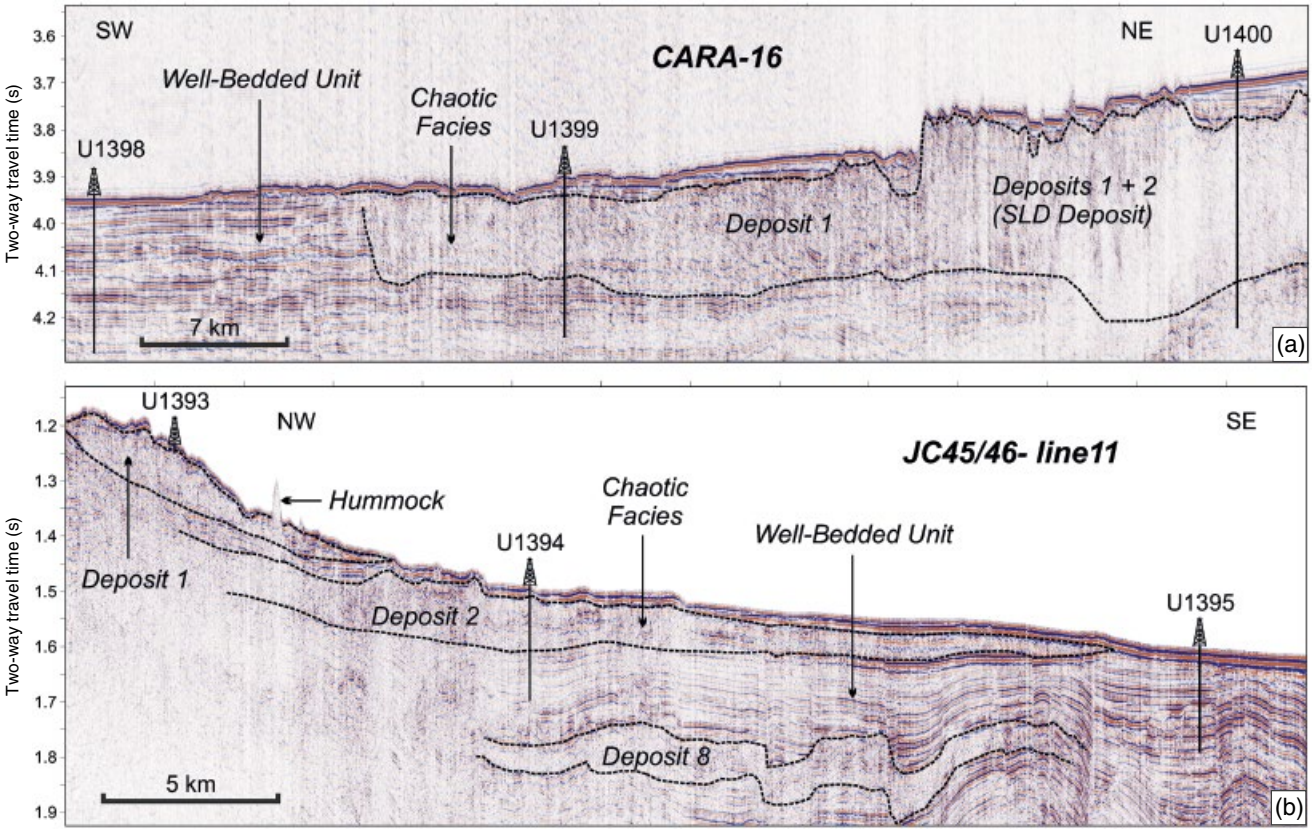


Figure 17.2 Seismic reflection profiles revealing the presence of chaotic deposits offshore (a) Martinique and (b) Montserrat. Location of the profiles is shown on Figure 17.1. Deposits are characterized by chaotic reflectors, which contrast with the well-bedded, subhorizontal sedimentary units. Locations of drilling sites are annotated.

also emphasized that a substantial amount of material derived from the submarine part of the volcanic edifice is commonly involved in the formation of the deposits, as shown by the chutes cutting through the submarine flanks, caused by removal of volcanic debris during avalanches incising the chutes. Le Friant et al. (2004) integrated this information to outline how terrestrial flank collapse scars, submarine chutes, and offshore DADs were linked to the geomorphological evolution of Montserrat. Moreover, Le Friant et al. (2004) and Lebas et al. (2011) also used seismic data to define the extent and volume of the landslide deposits offshore Montserrat. They demonstrated that the volume of seismic chaotic units associated with landslide deposits may be much greater than the volume of the associated subaerial flank collapse scars, thus requiring incorporation of a significant proportion of the volcano's submerged flank or of the adjacent seafloor sediment into the deposits. Truncation of in situ bedded sediment packages was attributed to erosional processes during debris avalanche emplacement. Lebas et al. (2011) also proposed that strong seismic reflectors seen at the base of some of the landslide deposits may result from slide-derived shear zones. Watt et al. (2012a, 2012b, 2014) proposed that the emplacement of volcanic debris avalanches caused erosion and triggered failure of seafloor sediment. Such seafloor sediment failure could be very widespread on low (<1°) gradients and may dominate the total landslide volume. Their working hypothesis is consistent with the concept that rapid emplacement of volcanic edifice material onto the seafloor led to undrained shear loading and failure of underlying seafloor sedimentary layers (Voight & Elsworth, 1997; Voight et al., 2012). Watt et al. (2012a, 2012b) further remarked on the lack of frontal compression and shear breakout (e.g., Frey-Martinez et al., 2006) offshore Montserrat, which suggested that much of the deformed seafloor material they observed did not move over extensive distances. The authors also proposed that some of the landslide deposits may have incorporated large blocks of relatively intact seafloor sediment.

17.3. IODP EXPEDITION 340

The IODP Expedition 340 conducted aboard the R/V *JOIDES Resolution* (March–April 2012) aimed at documenting the eruptive history and edifice collapses in the Lesser Antilles Arc over the last million years (Le Friant et al., 2013). The main objective of Expedition 340 was to understand the timing, emplacement processes, and dynamics of SLDs offshore the Lesser Antilles Arc, with implications for tsunami hazards. Nine sites were drilled offshore Montserrat and Martinique during the IODP Expedition 340 (Figure 17.1), recovering 434 core sections containing 2384 m of seafloor sediment samples (table 1 in Le Friant et al. (2015)). Drilling directly offshore Dominica through the most spectacular DAD was not done, because of the size of the blocks and lessons from previous drilling within blocky deposits offshore Montserrat and Martinique (Le Friant et al., 2013). A wide range of physical properties (thermal conductivity, shear strength, natural gamma ray emissions, P-wave velocities, magnetic susceptibility, and density) have been directly acquired on the cores. Additional information was obtained in situ by downhole logging operations (gamma rays, P-wave velocities, S-wave velocities, magnetic susceptibility, and resistivity; Lafuerza et al., 2014; Le Friant et al., 2013; Manga et al., 2012; Wall-Palmer et al., 2014). The cores contain some of the most sand-rich sequences yet recovered by an IODP expedition, where piston coring disturbances such as basal flow-in and fall-in are the most likely to occur, thus affecting the original texture of the sediment (Jutzeler et al., 2014). Particular attention has been paid to distinguishing disturbed sediment facies from in situ facies. To minimize these coring disturbances and provide better stratigraphic correlations between the sections, a minimum of two holes were drilled at each site (cf., table 1 in Le Friant et al. (2015)).

Sites U1393, U1394, U1399, U1400, and U1401, which will be the focus of the paper, were selected to investigate the landslide deposits and their origins and associated mechanisms of emplacement; sites U1396 and U1397 to study the eruptive history and magmatic evolution of the volcanic centers; and sites U1395 and U1398 to study the differences existing in the sedimentation processes in distal environments between the northern and southern part of the arc (Figures 17.1–17.3; Le Friant et al., 2015; Wall-Palmer et al., 2014). As mentioned above, attempts to drill through the chaotic proximal landslide Deposit 1 offshore Montserrat (U1393) and Deposit 3 offshore Martinique (U1401) were unsuccessful due to the heterogeneous and cohesionless character of the deposits. The only material recovered at these sites consisted of a combination of hemipelagic mud with interbedded tephra layers and/or volcaniclastic turbiditic deposits, overlying (and therefore postdating) the chaotic deposits (Brunet et al., 2016; Le Friant et al., 2013, 2015). A more distal site offshore Montserrat (U1394) intersected a widely dispersed landslide, Deposit 2, identified as a chaotic facies in the seismic reflection data with discontinuous local bedded reflections (Figure 17.2b). The core showed this apparently chaotic deposit to be dominated by a stacked sequence of predominantly thick, massive, and coarse-grained turbiditic deposits, ranging from bioclastic to volcanoclastic in composition. However, it should be noted that core recovery was restricted to the lower half of Deposit 2. No signs of deformation were recognized (Coussens et al., 2016; Le Friant et al., 2015).

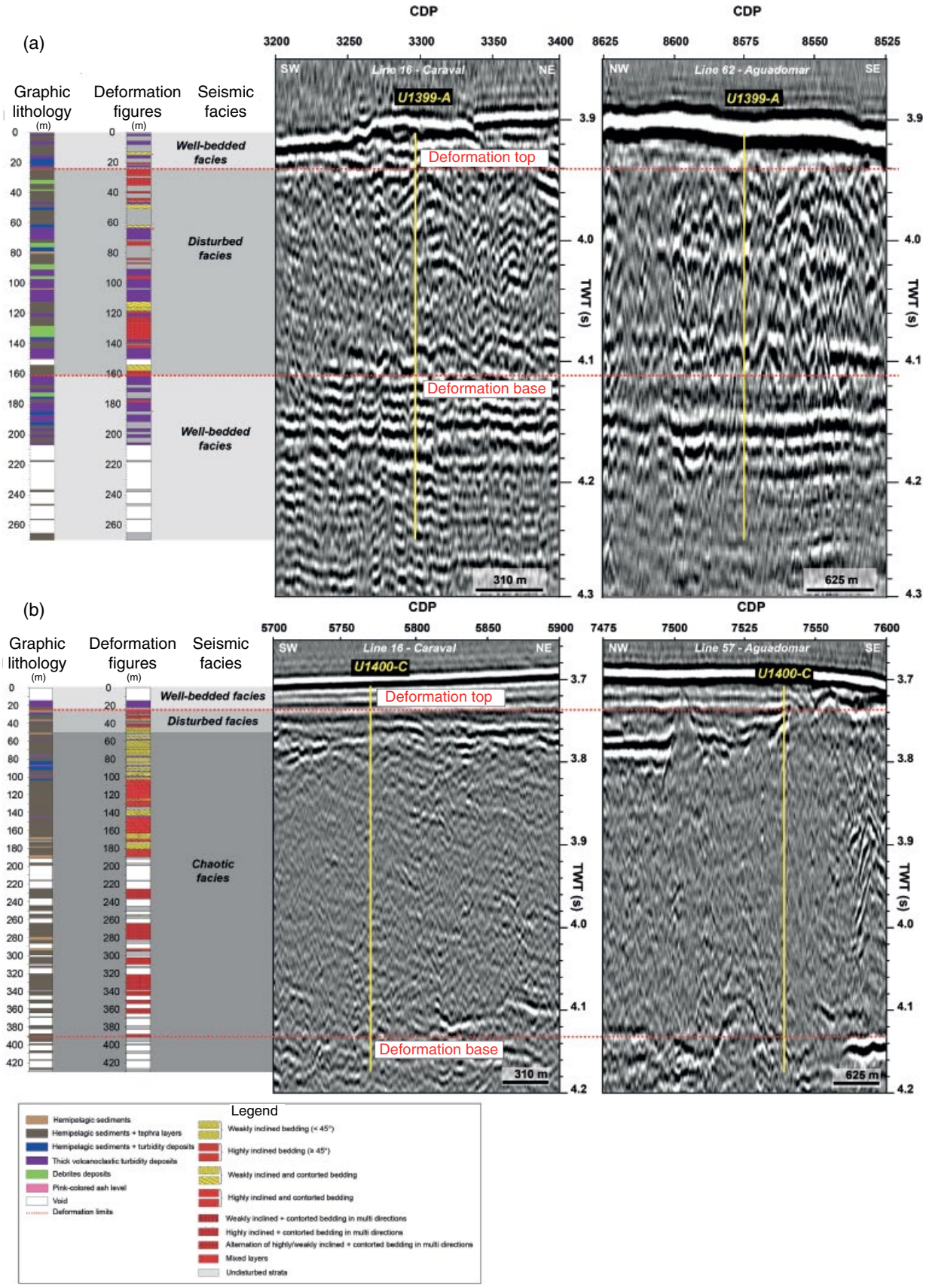


Figure 17.3 Correlation between seismic and drilling data for (a) Hole U1399-A and (b) Hole U1400-C. Deformation on both data sets is well correlated despite their large-resolution differences. Source: Adapted from Brunet et al. (2016).

Sediment retrieved from sites U1399 and U1400 (both offshore Martinique), in the medial and distal parts of widely dispersed landslide deposits (D1 and D2), consisted of deformed seafloor sediment. This sediment was mainly composed of hemipelagic mud, with interbedded tephra layers and volcaniclastic turbiditic deposits (Figures 17.2 and 17.3). Deformed sediment at Site U1400 is characterized by many planar beds inclined in average by 40°, with some dips being as steep as 70°. Interestingly and surprisingly, these widely dispersed landslide deposits D1 and D2 were not unambiguously identified in the cores retrieved in Site 1400, since no difference in composition was observed between the two landslides. Consequently, Brunet et al. (2016) suggested that they belong to the same deposit and referred to it as SLD. Of particular significance is the absence of DADs comprising blocky material from the subaerial volcanic edifice in the cores.

More details about the lithologies encountered in the deposits both offshore Montserrat and Martinique can be found in Brunet et al. (2016), Coussens et al. (2016), Fraass et al. (2016), Jutzeler et al. (2014, 2016), Lafuerza et al. (2014), Le Friant et al. (2015), Palmer et al. (2016), and Wall-Palmer et al. (2014).

17.4. NEW MODEL OF LANDSLIDE GENERATION OFFSHORE THE LESSER ANTILLES ARC

17.4.1. Two Different Instability Processes

Two different types of landslide processes were recognized along the Lesser Antilles Arc: (i) the subaerial instabilities, which correspond to volcanic flank collapses that affected the subaerial part of edifices, generating DAD accumulating offshore, and (ii) the submarine instabilities, which correspond to seafloor sediment failures at the origin of the large SLD identified in the seismic data.

The Deposit 1 offshore Montserrat (Site U1393) and the Deposit 3 offshore Martinique (Site U1401) (Figure 17.1) display very blocky surface morphologies, which were difficult to drill. They are located on the submarine flanks of the volcanic edifices or near the slope break and typically characterized by hummocky topography in the bathymetry (e.g., Deplus et al., 2001; Le Friant et al., 2003a, 2004; Moore et al., 1989; Urgeles et al., 1999). These landslide deposits correspond to debris avalanches associated with volcanic flank collapses as recognized on land (e.g., Mount St. Helens; Glicken, 1986) or offshore (Canary Islands; Urgeles et al., 1999).

The seismically chaotic deposits drilled at sites U1394 (Deposit 2, Montserrat), U1399, and U1400 (SLD, Martinique) reveal, unexpectedly, the absence of volcanic DADs, though the deposits are located in the prolongation of the flank collapse structures (horseshoe shapes) observed on the volcanoes. The chaotic deposits correspond to the second type of instabilities recognized along the arc, that is, submarine landslides. Characteristics of these deposits (i.e., composition, deformation, vertical truncation with adjacent sediments) are consistent with seafloor sediment failure deposits.

A model is proposed to explain how the subaerial volcanic flank collapses are genetically linked to the widespread sediment failures, with respect to the evolution of the volcanoes (Brunet et al., 2016; Le Friant et al., 2015, Watt et al., 2012b).

17.4.2. Décollement Propagation From Debris Avalanche Deposit Loading

Given the spatial relationship between the SLDs, DADs, and collapse scars (subaerial and/or submarine), the new information provided by the IODP Expedition 340 allows us to test the previous hypotheses of emplacement dynamics that have been proposed for these submarine landslides (cf., figure 9 in Le Friant et al. (2015) and Deplus et al. (2001); Watt et al., 2012a, 2012b, 2014). Results of the combined analysis of these data sets (i.e., spatial relationship between the deposits and the collapse structures, composition, type and degree of deformation of the material within the slide units, vertical truncation of the sediments on the seismic reflection profiles, physical properties providing the first insight into the in situ stress state at the décollement and data on pore pressure) suggest that the mechanisms producing the large seafloor sediment failures observed offshore the Lesser Antilles Arc may have been triggered by subaerial and/or submarine flank collapses. We proposed a model of décollement propagation from DAD loading to explain the existence of the large-scale seismically chaotic submarine landslides (Figure 17.4). Previous modeling from Viesca and Rice (2012) suggested that local failure can generate cracks which propagate rapidly over much wider areas than the initial site of failure, similar to thrust fault and décollement mechanics, and snow slab avalanches. Lateral propagation can even occur where the load, in our case a debris avalanche, cannot be dissipated due to the low permeability of the seafloor sediment. This undrained load may generate excess pore fluid pressure and trigger sediment failure in slope and basin areas, which were not originally prone to failure. Our IODP studies provide the first insight into the in situ stress state at the décollement surface (Hornbach et al., 2015; Lafuerza et al., 2014) and indicate both undercompacted and elevated pore fluid pressures in clay-rich layers (e.g., Lafuerza et al., 2014), as well as near-lithostatic pressures in sand-rich turbidites at the décollement (Hornbach et al., 2015). From this, we suggest the sediment at the décollement may be near-critically stressed.

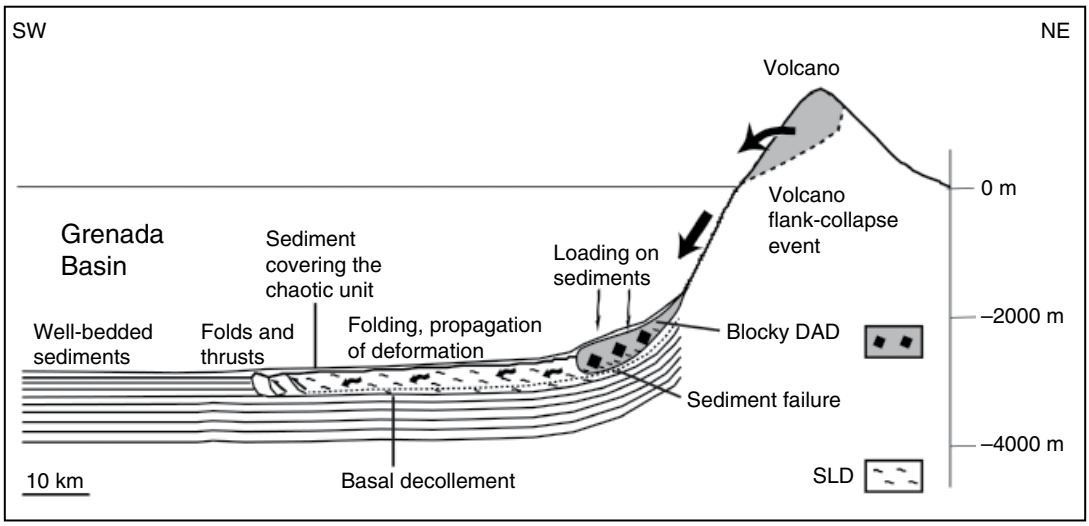


Figure 17.4 Schematic figure of processes which can explain the presence of huge landslide deposits offshore volcanic islands (topographic/bathymetric profile from Martinique). Volcanic flank collapses generate debris avalanches that enter the sea, incise the sediments, and generate failure, propagation, and deformation of marine sediments. Source: From Le Friant et al. (2015).

As a result, one hypothesis is that any small change in pore pressure generated by compaction or minor grain reorganization (due, e.g., to shaking via small earthquakes) might trigger additional failure along the décollement (Hornbach et al., 2015). Current underconsolidated sediment at sites U1400 and U1399 would suggest that these excess pore pressures have not been fully dissipated (Figure 17.6). Lateral loading induced by the debris avalanche, which may have eroded the seafloor, can also promote overpressure. Basal décollement could thus propagate laterally from the emplaced volcanic debris avalanche (Figure 17.4) to produce widespread deformation of the seafloor sediment above the décollement surface.

This model in which the décollement propagates from proximal regions loaded and incised by the emplacement of a volcanic debris avalanche may also explain the large-scale landslide deposits mapped in the southern part of the Lesser Antilles Arc, from Dominica to St. Vincent (Figure 17.1, Deplus et al., 2001). If so, this process may operate at the scale of the entire arc. Whether these failures occur rapidly and catastrophically over a large area or, instead, incrementally over a smaller area is unclear and remains a topic of ongoing lab and numerical research. Ongoing mechanical modeling with BASIN software and consequent sediment deformation and failure with PLAXIS software (e.g., Lopart et al., 2018) have demonstrated overpressure formation by undrained loading. In addition with analogue modeling (Brunet, 2015), these studies represent an important topic of ongoing and future research which will improve the understanding of the décollement propagation in the near future.

17.4.3. Evolution of the Montagne Pelée Volcano Through the Landslide Processes (Martinique)

The volcanic history of Martinique island began at 23 Ma (Germa et al., 2010; Westercamp & Traineau, 1983) and has proceeded through different phases that formed several volcanic centers, including the well-known Montagne Pelée, where three major flank collapses removed much of the western flank (Boudon et al., 2005, 2007; Brunet et al., 2016; Le Friant et al., 2003a, 2003b). The first flank collapse occurred at ~127 ka (Germa et al., 2010, from on-land investigations) leaving behind the first horseshoe-shaped structure on the volcanic flank, with a collapsed volume estimated at 25 km^3 (Le Friant et al., 2003a) (Figure 17.5). The associated debris avalanche entered the sea (DAD1; Figure 17.5), flowed down the submarine flank, and was deposited near the slope break. This first and largest DAD loaded the preexisting seafloor sediment and initiated failure. The resulting submarine landslide propagated along a décollement surface, deforming an in situ succession of alternating hemipelagic sediment and turbiditic deposits. Distributed shearing at multiple levels within the sequence may have acted as potential sliding surfaces within the SLD (1 and 5; Brunet et al., 2016). The SLD translated across the seafloor and stopped in a confined way.

The second flank collapse that affected the Montagne Pelée followed the construction of a new voluminous volcanic edifice inside the scar of the first flank collapse and probably occurred between 45 and 127 ka (Brunet et al., 2016). The collapsed volume has been estimated at about 13 km^3 (Le Friant et al., 2003a) and also generated

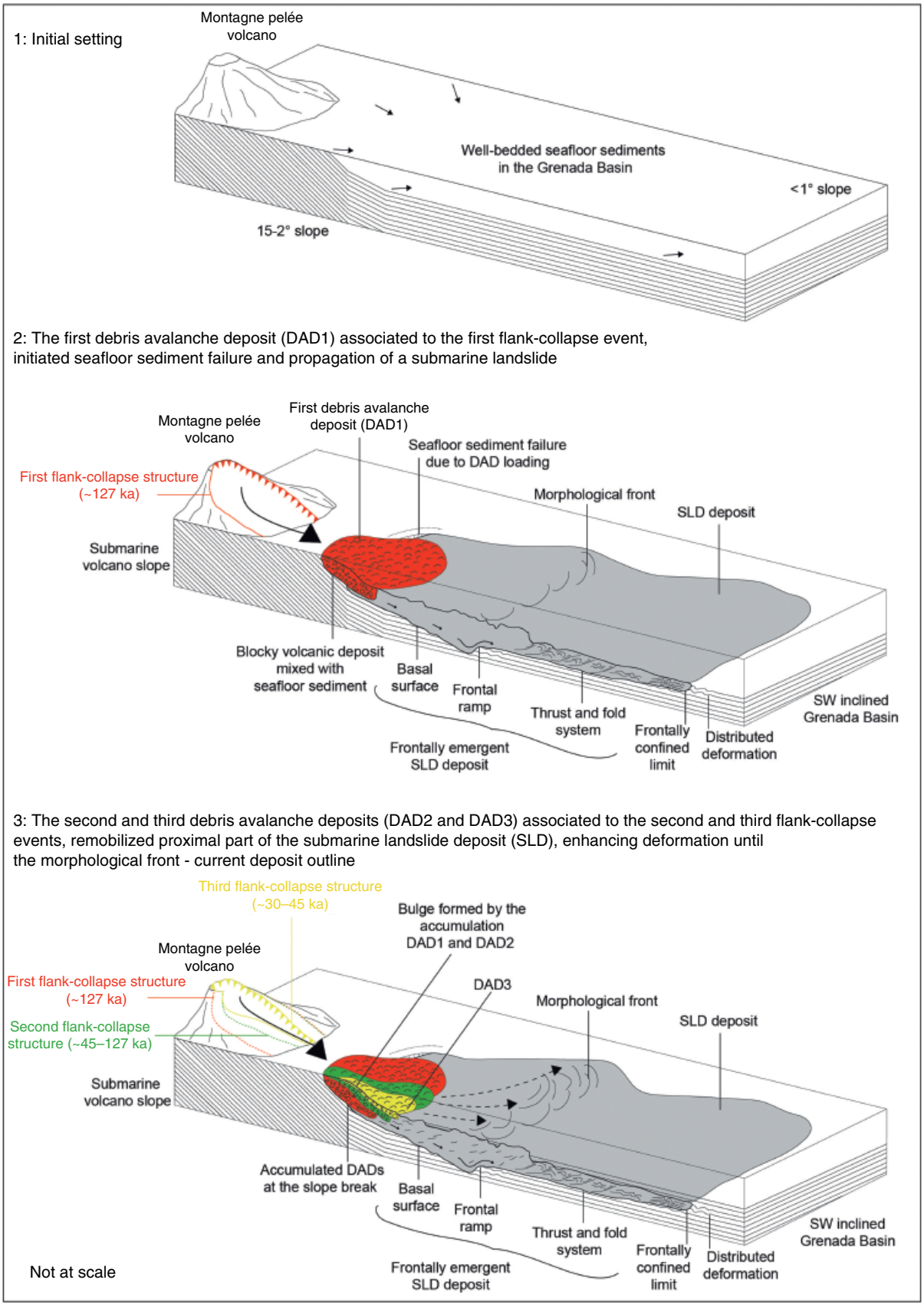


Figure 17.5 Conceptual model of the relation between aerial instability processes (i.e., volcanic flank collapses) and submarine instability processes (i.e., seafloor sediment failures) offshore Martinique. The first debris avalanche deposit (DAD1) weakened and initiated seafloor sediment failure that resulted in a submarine landslide propagation. Successive DADs (DAD2 and DAD3) remobilized unconsolidated surficial sediments within the proximal part of the submarine landslide deposit (SLD). Source: From Brunet et al. (2016).

a debris avalanche (DAD2; Figure 17.5). DAD2 emplaced over DAD1 and may have remobilized unconsolidated surficial sediment within the central part of the SDL deposit, up to the morphological front (Figure 17.5), and be responsible for the southward drifting of the SLD in its southern part.

During a third event, the newly formed cone was destroyed again by a flank collapse forming a smaller horseshoe-shaped structure, whose volume of collapsed material was estimated at 2 km^3 (Brunet et al., 2016; Le Friant et al., 2003a). The age assigned to the related DAD3 (Figure 17.5, which corresponds to D3 offshore Martinique in Figure 17.1), both identified on land and offshore, is still a matter of ongoing discussions and may be dated between 30 and 45 ka based on preliminary measurements of $\delta^{18}O$ samples from the IODP Expedition 340 and previously published ages from terrestrial deposits (table 2 in Le Friant et al. (2015)). As for DAD2, DAD3 (clearly identified on the submarine flank by its hummocky morphology) may have locally remobilized sediments within SLD by exerting an undrained load that supplied the deformation process.

Particularly noteworthy is that the older DAD1 and DAD2 from the conceptual model of Figure 17.5 were not previously identified offshore on Figure 17.1. The seismic data in steeper proximal areas, which represent the submarine flank of the island, are of poor quality and equivocal, although hyperbolic reflections could indicate the presence of some blocks (Figure 17.2a). However, the bathymetric data show a bulge at the base of the volcanic submarine flank, near the slope break, at the same location as DAD3. Thus, Brunet et al. (2016) proposed that this bulge may result from the accumulation of the older DAD1 and DAD2 related to the first and second flank collapses of the Montagne Pelée (Figure 17.5).

17.5. IMPLICATIONS ON THE EMPLACEMENT MECHANISMS OF THE LANDSLIDE DEPOSITS

The new model suggests that the large SLDs recognized offshore the Lesser Antilles Arc result from a décollement propagation of the marine sediment due to the emplacement of DADs on top (Le Friant et al., 2015; Watt et al., 2012b, 2014). In the following section, we investigate the emplacement mechanisms of the two types of landslide deposits encountered in the arc (i.e., flank collapses and seafloor sediment failures) by first using a numerical approach and then by integrating geophysical properties and geotechnical constraints resulting from the IODP Expedition 340. We will use the example and the characteristics of the Martinique deposits to present our results.

17.5.1. Debris Avalanches

Brunet et al. (2016) and Le Friant et al. (2015) recently proposed that flank collapses having affected the Montagne Pelée volcano produced debris avalanches that flowed down the volcanic edifice and the submarine flank to stop around the slope break. This new scenario implies a much shorter runout distance of the debris avalanches than previously suggested (Boudon et al., 2007; Deplus et al., 2001; Le Friant et al. 2003a), and it has consequences for understanding debris avalanche dynamics. To confirm this scenario, numerical simulations have been performed by Brunet et al. (2017) using two complementary depth-averaged thin-layer continuum models, since no complete models were available in the literature at the time of the simulations. The first model used, SHALTOP (Mangeney-Castelnau et al., 2003), describes precisely the topography. It accurately describes dry granular flows over a 3D topography and may be easily extended to describe the submarine avalanche. The second model, HYSEA (Fernandez-Nieto et al., 2008), has the advantage to take into account the interaction with the water column. It describes the subaerial and the submarine parts of the avalanche. These numerical simulations aimed to determine (i) a critical runout distance for the emplacement of the debris avalanches and (ii) the single- or multiphase behavior of the associated flank collapse.

Numerical simulations have shown that the first and largest debris avalanche from the Montagne Pelée (DAD1: 25 km^3) may extend up to 50 km from the coastline, which is not an observation in the IODP data. The simulations have also demonstrated that the runout distance of the debris avalanche does not increase with successive flows of smaller volume (about 5 km^3 each) and stays around 35 km from the coastline. Brunet et al. (2017) noted that the debris avalanche slowed down after losing inertia to accumulate on the slope transition or relatively nearby, at about 35 km from the coastline. These simulations, along with IODP observations showing that the offshore DAD1 could only be found up to 35 km from the coastline, led Brunet et al. (2017) to suggest that the first and largest flank collapse that affected the Montagne Pelée may have occurred in several phases. Therefore, debris avalanche volumes for each phase probably did not exceed 5 km^3, with smaller runout distances than previously thought (Boudon et al., 2007; Deplus et al., 2001; Le Friant et al. 2003a). Complex turbidite stratigraphies correlated with landslide deposits offshore Montserrat suggest that flank collapses may have occurred in multiple stages (e.g., Cassidy et al., 2014). Indeed, analysis of tephra fall and volcaniclastic turbiditic deposits in drill cores at sites U1394 and U1395 revealed three heightened periods of volcanic activity on the island (930–900, 810–760, and 190–120 ka), which coincides with periods of increased

volcano instability and mass-wasting events (Coussens et al., 2016). The youngest period 190–120 ka marks a peak in the volcanic activity of Soufrière Hills. The largest flank collapse having affected the volcano occurred toward the end of this period (~130 ka) and was followed by two younger events occurring during a period of time where the volcanic activity was relatively elevated (Coussens et al., 2016). Multiphase flank collapses have also been described in the Canarian and Hawaiian islands, where they generated distinctive turbidites that comprise multiple fining upward subunits (Garcia & Meyerhoff Hull, 1994; Hunt et al., 2011, 2013; Wynn & Masson, 2003). These observations suggest that flank collapses may occur in multiple stages. Recently, Hunt et al. (2018) related volcano flank failures to volcanic activity (i.e., explosive eruptions) in the Canary Islands and suggested that these multistage events might have been separated by days to weeks.

17.5.2. Seafloor Sediment Failures Triggered by Debris Avalanche Loading

Using core logging and sedimentological and geotechnical data from the IODP Expedition 340, Lafuerza et al. (2014) analyzed the uppermost 200 m of cores at sites U1397, U1398, U1399, and U1400 offshore Martinique. The authors found that shear strength-overburden stress ratios (Su/σ'_v) on most of the hemipelagic sediment tested are lower than 0.17–0.25 (values on normal consolidation conditions; gray shading in Figure 17.6). Contrasting with consolidation tests, the authors demonstrated that low hydraulic conductivity of hemipelagic sediment prevents their consolidation and causes low rates of dewatering in turbidity current deposits and tephra layers, allowing excess pore fluid pressures to persist at depth (Figure 17.6). In all cores, the uppermost 200 m showed clear evidence for excess pore fluid pressures, except at Site U1400 where overpressure only occurred after 180 m downward. Lafuerza et al. (2014) explained this overpressure by a slow escape of pore fluid during the burial of more permeable turbidity current deposits and tephra layers, sandwiched between minimally permeable hemipelagic sediment. Higher overpressures were recognized at sites U1397, U1398, and U1399, where higher abundance of thicker turbiditic deposits and coarser tephra layers were described. Pore pressures at Site U1399 were also investigated by Hornbach et al. (2015) using integration of physical properties, downhole logging measurements from the IODP Expedition 340, and rock physics models (Hornbach & Manga, 2014). The authors indicated that high pore pressures existed throughout much of the entire cores at the same locations and concluded that unusual, elevated pore fluid pressures occurred at present in multiple sand-rich zones within the SLD, specifying that only small changes in the current stress regime may trigger motion. In their work, Hornbach et al. (2015) also discussed the most likely plausible mechanisms responsible for creating excess pore pressures at Site U1399 and concluded that shearing processes resulting from regional strain and grain reorganization during sediment contraction may best explain increasing pore fluid pressures. As also pointed out by Lafuerza et al. (2014), Hornbach et al. (2015) showed that excess pore pressures reside in thicker sand-rich intervals, while intervening mud-rich zones, within and outside the SLD, show very low permeabilities, thus acting as seals. All these observations suggest that highly elevated pore pressures can persist over long time spans within the SLD, long after the initial failure. This implies that deformation within SLD could continue at present or in the near future (Hornbach et al., 2015). The work presented by Hornbach et al. (2015) is coherent with the observations of multiple post-deposition deformation zones within cores U1399-A and U1400-C, suggesting the existence of a series of failure-prone horizons within SLD and not solely a single layer at the base of the deposit (Brunet et al., 2016). These failure-prone horizons may coincide with sand layers, or boundaries between sand and mud layers, which exist in many places inside these drill cores. It is also possible that homogenized muddy sand layers result from previous distributed shearing at multiple levels and that these muddy sand layers act as pressure seals. Ogata et al. (2014) highlighted the fundamental role of shearing-related liquefaction as one of the main factors controlling slide mobility though the "lubrication" of internal and basal friction forces. Thus, these layers may be regarded as multiple décollement surfaces that, when solicited, may act together to promote and enhance deposit mobility and longer runout distances.

17.6. IMPLICATIONS FOR TSUNAMI HAZARDS

Assessing landslide-related tsunami hazards ultimately requires detailed knowledge of slide physical properties, volumes, water depths, speeds, and evolution with time (e.g., Masson et al., 2006; Ward & Day, 2001; Watt et al., 2012a). Unfortunately, in many instances, these basic physical properties are very poorly constrained. By providing direct observations and measurements of slide physical properties (such as stress state, thickness, and sediment type), IODP drilling data ground-truth seismic interpretations, improve our understanding of slide physical properties, and, from this, enhance our understanding of landslide-derived tsunami hazards.

The results derived from the IODP Expedition 340 confirmed that the landslides identified around the Lesser Antilles volcanoes result from two fundamentally different processes: (i) volcanic flank collapses, generating

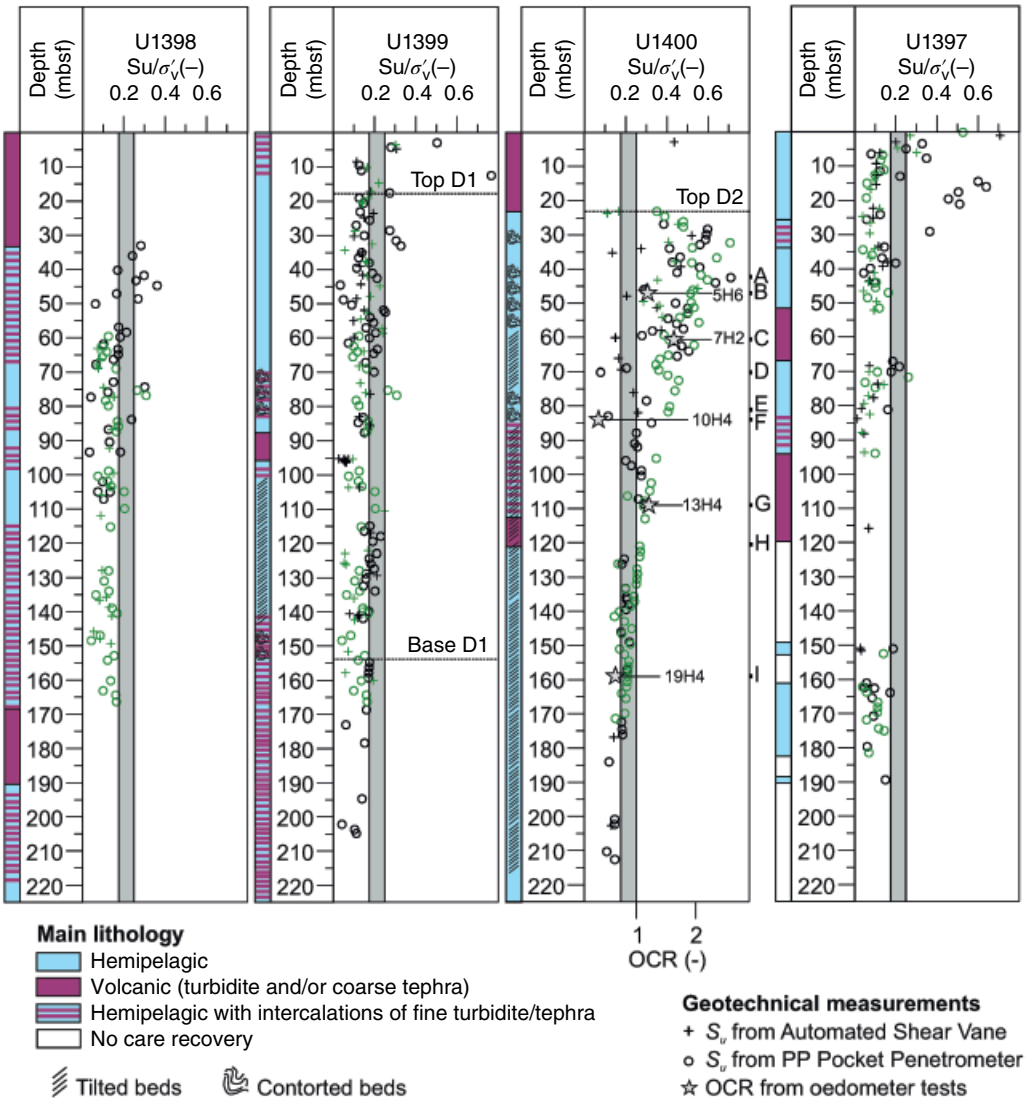


Figure 17.6 Depth distribution of shear strength-overburden stress ratio S_u/σ'_v where S_u corresponds to undrained shear strength and σ'_v to effective vertical stress. Gray shading corresponds to S_u/σ'_v <0.17–0.25 associated with normally consolidated materials. Black and green colors are used to differentiate S_u measurements at holes B (black) and C (green) for each drilling site, except for Site U1397, where hole A is in black and hole C in green. Circles, S_u-handheld penetrometer; crosses, S_u-automated shear vane. Source: From Lafuerza et al. (2014). (*See electronic version for color representation of this figure*)

blocky DADs, and (ii) seafloor sediment failures, generating large and voluminous SLDs. Brunet et al. (2017) suggested through numerical simulations that the largest flank collapse that affected the Montagne Pelée volcano may have occurred in several phases, with individual debris avalanches volumes not exceeding 5 km^3. The multistage character of the volcanic flank collapses is crucial for evaluating the resulting tsunamigenic hazard not only in Martinique but also throughout the Lesser Antilles Arc in general. Both types of landslide may generate a tsunami, but the magnitude of the landslide-derived tsunamis will be different.

Using deposits 1 and 2 offshore Montserrat as examples, Watt et al. (2012a) approximated the tsunami magnitudes that might be expected for the deposits, taking into account different possible triggering, that is, from a failure of (i) the subaerial flank of the volcanic edifice, (ii) the submerged slopes of the volcano, or (iii) deep-water seafloor sediment neighboring the volcano. Watt et al. (2012a) used a series of relationships based on theory or extrapolation of small-scale laboratory experiments previously proposed in the literature and whose assumptions are discussed in detail by the authors. A key point is that tsunami magnitude strongly depends on the

relative landslide and tsunami wave speeds, with tsunami magnitude increasing if the tsunami wave and the submerged landslide travel at comparable speeds. Such a case will typically only occur in shallow water depths (<200 m), implying that seafloor sediment failures occurring in deep water depths tend to produce much smaller tsunami magnitudes (Ward, 2001). Watt et al. (2012a) suggested that a seafloor sediment failure of ~2 km^3 would produce a maximum tsunami amplitude ~100 times smaller than one involving a subaerial or submerged failure of a volcanic flank of comparable volume (see Watt et al. (2012a), more particularly Figure 17.7). Even a seafloor sediment failure with a much larger volume, such as the SLD offshore Martinique (25 km^3), would likely produce a much smaller tsunami magnitude than a failure of the subaerial or submerged parts of the volcanic edifice for a similar volume.

Moreover, the analysis in Watt et al. (2012a) of a seafloor sediment failure related tsunami is based on wave-tank experiments with a sliding block (see Watts et al., 2005). Such a model may not capture the way in which the deformation propagates within the sediment offshore Montserrat and Martinique. It may be that deformation in seafloor sediment failures is slow moving compared to a sliding block and that individual parcels of seafloor sediment move laterally over short distances. If so, such slow velocities and short particle transport distances could further decrease the tsunami magnitude induced by seafloor sediment failures. We have calculated the tsunami wave height versus water depth for the different submarine slide volumes (5, 13, and 25 km^3) and velocities offshore Martinique. We estimate wave heights using the nonlinear shallow-water wave approach (e.g., Jiang & LeBlond, 1992). Although we apply a maximum slide velocity of 50 m/s, turbidity current velocity measurements derived from cable breaks suggest lower values, typically ranging between 5 and 30 m/s (Heezen & Ewing, 1952; Hsu et al., 2008; Krause et al., 1970). Both water depth and slide velocity play an important role in tsunami wave height. The largest wave heights, for a given water depth, typically form when slide velocity approaches the natural shallow-water wave velocity defined by $\sqrt{gd}$, where g is the gravitational acceleration and d is the water depth. Figure 17.7 shows that for an order-of-magnitude change either in the slide velocity or in the water depth, an order-of-magnitude change also occurs in the tsunami

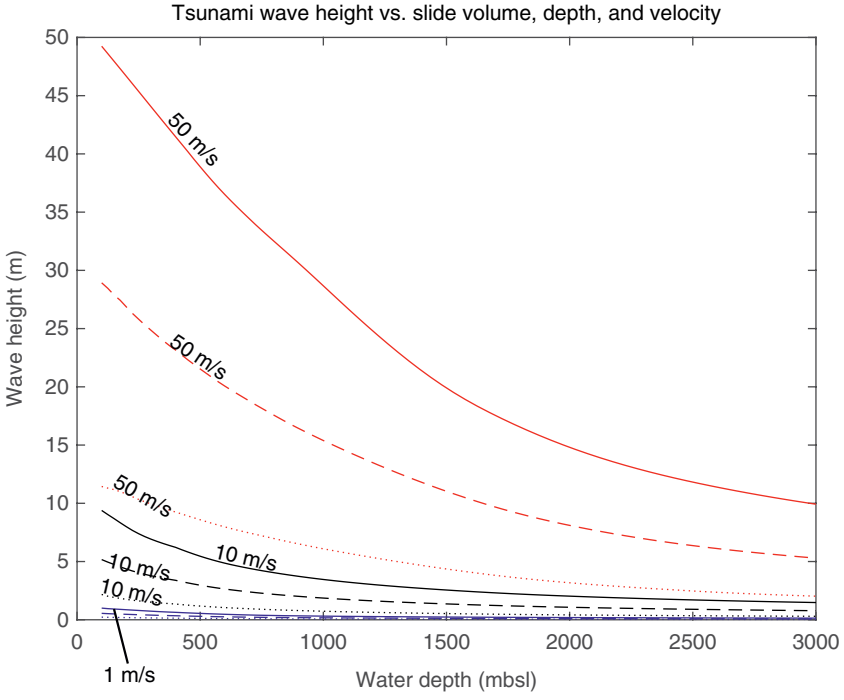


Figure 17.7 Tsunami wave height versus slide velocity and water depth for three different slide volumes discussed in the text (solid lines, 25 km^3; dashed lines, 13 km^3; dotted lines, 5 km^3). We extend the model to a maximum water depth of 3000 m below sea level (mbsl), as this corresponds to the maximum water depth where we observe slide deposits in the Lesser Antilles Arc. Model results show a peak wave height two minutes after slide initiation for three different average slide velocities (red, 50 m/s; black, 10 m/s; blue, 1 m/s). All the calculations assume a constant parabolic slide shape (e.g., Jiang & LeBlond, 1992). (*See electronic version for color representation of this figure*)

wave height, with deeper and slower slides generating smaller tsunami wave heights. This implies that slower-moving slides in deep water offshore the Lesser Antilles may represent a lower tsunamigenic risk. The block of seafloor sediment recovered completely intact at Site U1394 is consistent with relatively slow and limited lateral movement of the landslide. Offshore Martinique, deformation of seafloor sediment appears to occur at different levels within the deposits, which may indicate somewhat more vigorous motion.

A tsunami wave produced by a widespread seafloor sediment failure may thus produce a longer tsunami wavelength than that associated with localized failure of the volcanic edifice. These longer tsunami wavelengths from seafloor sediment failures could increase the runout distance of the tsunami and the regional risk, since longer-wavelength tsunamis can propagate further with less energy loss (Watt et al., 2012a). However, even if the volume of a flank collapse is smaller than the volume of seafloor sediment failures, it may be the most significant in terms of causing tsunami damage on nearby coastlines due to the velocity of the slide associated with the flank collapse, the shallow water depth along the coastline, and the location of the failure near the coast, leading to less warning time.

17.7. COMPARISON WITH SUBMARINE LANDSLIDES AROUND OTHER VOLCANIC ISLANDS

Flank collapses on oceanic island volcanoes have produced some of the largest landslide deposits recognized on Earth. These giant landslides can contain several hundred to several thousands of cubic kilometers of collapsed material (Masson et al., 2002; Moore et al., 1989), exceeding by far the largest known subaerial DAD of Mount Shasta (45 km^3; Crandell, 1989). Criteria for identification of landslide deposits in the submarine area have been developed by several authors in different settings over the last decades. SLDs associated with debris avalanches typically display hummocky terrains on the swath bathymetry, speckled pattern on backscatter images, and a hyperbolic facies on echosounder data (e.g., Deplus et al., 2001; Masson et al., 2002; Moore et al., 1989). On seismic data, these landslide deposits show an acoustically chaotic character with strong energy diffraction, which strongly contrasts with the continuous, subhorizontal, and subparallel reflectors that define underformed, well-stratified sedimentary successions.

The most block-rich volcanic island landslides, such as Nuuanu in Hawaii, are dominated by multiple kilometer-scale blocks corresponding essentially to intact fragments of volcanic edifices that have slid to their site of deposition (Moore & Clague, 2002). The prevalence of angular, intact blocks in some DADs suggests a relative damping of fragmentation in the submarine environment. In the Lesser Antilles Arc, such angular blocky deposits have been observed offshore Dominica (Deplus et al., 2001; Le Friant et al., 2002). Watt et al. (2012a, 2014) suggested that in several instances, seafloor sediment substrate probably fails during the emplacement of volcanic landslides (e.g., Antilles: Deplus et al., 2001; Papua New Guinea: Silver et al., 2009; Aleutians: Montanaro & Beget, 2011) and would remain almost in situ as a deformed package. Furthermore, limited lateral transport distances are implied by the geometry of these seafloor sediment failures, in which the toe of landslide transitions does not emerge above the seafloor (Frey-Martinez et al., 2006; Watt et al., 2014). When the seafloor sediment becomes more extensively disaggregated and no longer confined within the region of initial failure, a debris flow can propagate for hundreds of kilometers from the initial point of failure, as observed for the Canary debris flow induced by the El Golfo debris avalanche (Hunt et al., 2011; Masson et al., 2002).

Drilling through the seismically chaotic deposits offshore the Lesser Antilles volcanoes confirms that chaotic units observed in seismic data do not necessarily represent extensively disaggregated or deformed material that has been transported over long distances from the volcanic edifice (cf., Gafeira et al., 2010) and supports the view that extensive seafloor sediment failures may be relatively commonplace around volcanic islands (Watt et al., 2012a, 2014). The IODP Expedition 340 also provided a valuable opportunity to compare seismic facies with core observations. Such comparison allowed us to understand the amount, style of deformation, and sediment lithologies that produce the different seismic facies. A key issue for such comparison is the substantial differences in resolution of the two types of data, which ranges from millimeters for the sediment cores to tens to hundreds of meters for seismic data (Figure 17.3). For instance, we observed a good correlation between the upper and lower limits of the SLD offshore Martinique identified using seismic profiles and the extent of the deformation within drilled holes (Figures 17.2 and 17.3). The well-bedded seismic facies corresponds to turbidity current deposits and/or debris-flow deposits, or tephra layers interbedded with hemipelagic sediments, which are flat lying and lack deformation in the cores.

New findings from the IODP Expedition 340 thus shed light on the necessity to revisit previous interpretations of large-scale SLDs previously interpreted as resulting from catastrophic large flank collapses of neighboring volcanic islands as these systems are significantly more complex both in space and time than previously believed. Such an approach has recently been taken by Lebas et al. (2018) offshore the volcanic island of La Réunion (Indian Ocean).

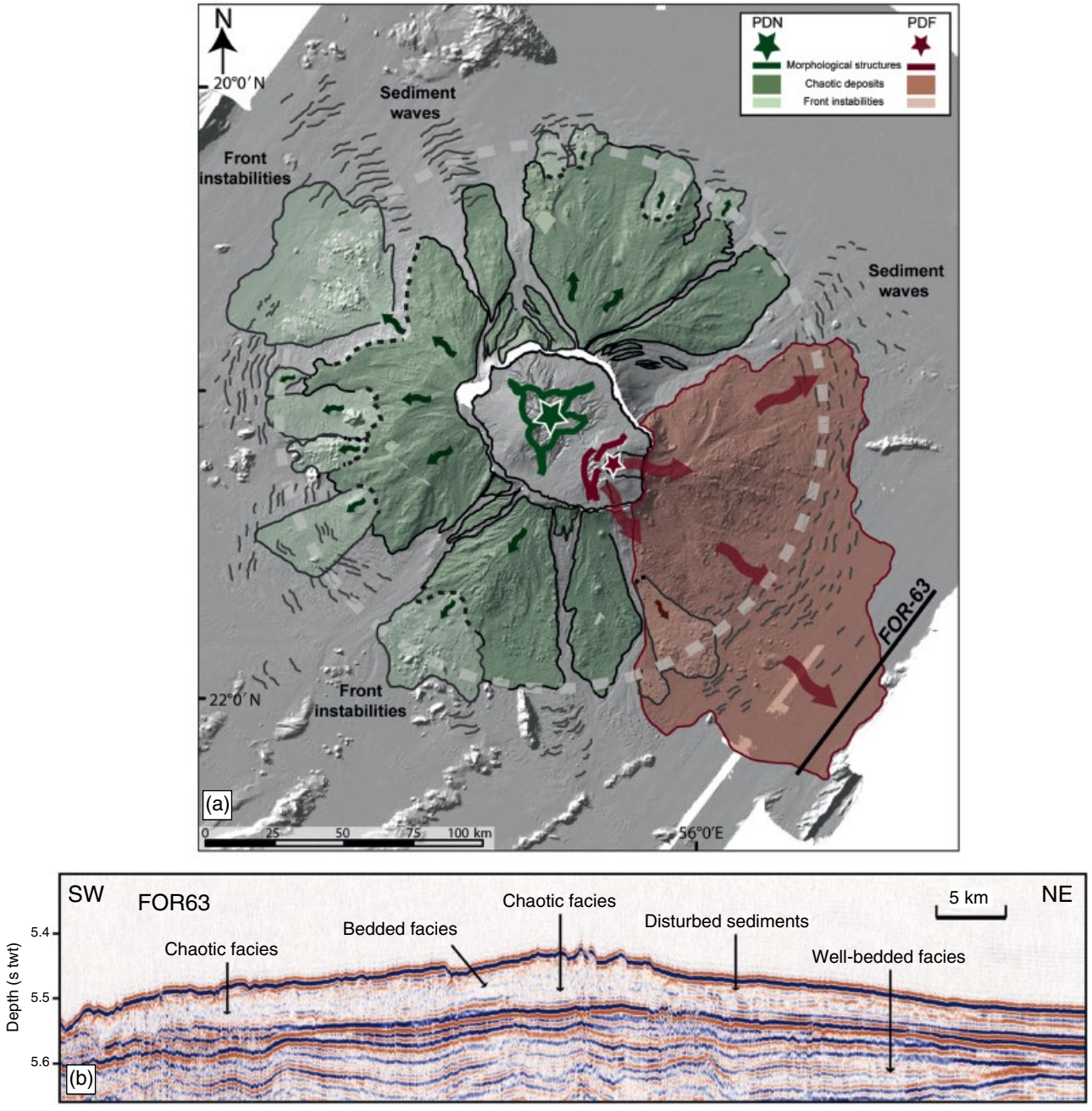


Figure 17.8 (a) Combined bathymetry (FOREVER and ERODER 1 cruises) and topography data of La Réunion volcanic complex illuminated from NW. Dashed thick circle indicates the base of the volcanic complex, with interpretations of mass-wasting processes. The extent of rough and chaotic terrains is mapped in green (Piton des Neiges) and in red (Piton de la Fournaise). Arrows indicates the direction of the instabilities. Secondary front instabilities are mapped in light colors. (b) FOR63 illustrating the seismic signature of the material composing the large submarine landslide deposit (SLD) identified offshore Piton de la Fournaise volcano. Note the long runout of this large SLD, which extends beyond the base of the volcanic complex. Source: Modified from Le Friant et al. (2011) and Lebas et al. (2018). (*See electronic version for color representation of this figure*)

The presence of alternating undisturbed to slightly deformed seismic reflectors and chaotic reflections (Figure 17.8) in the seismically chaotic deposit identified offshore the Piton de la Fournaise volcano led the authors to reinterpret this "chaotic" deposit as widespread, deformed preexisting seafloor sediment. This deposit recorded the emplacement of the Piton de la Fournaise DADs on the submarine flank, where hummocky terrains

were previously observed on the bathymetry (Le Friant et al., 2011; Lénat et al., 1989; Oehler et al., 2004, 2008). Lebas et al. (2018) concluded that such large seismically "chaotic" deposits may be regarded as evidence of former flank collapse events offshore other volcanic islands that might not be identifiable on the volcanic submarine flanks (due to the age or the resolution of the data), but that clearly deformed marine sediment offshore.

ACKNOWLEDGMENTS

We thank the drillers for their relentless efforts to drill through such difficult volcaniclastic material and all R/V *JOIDES Resolution* staff for their collaboration and efficient work on board. We are very grateful to C. Mével who encouraged and helped us to build our drilling proposal. We thank INSU, NERC, ANR-13-BS06-0009, Labex UnivEarthS, FEDER INTERREG Caraibes program, JSPS, and NSF for funding analyses and IPGP for funding postdocs and PhD. We thank the staff of the Montserrat Volcano Observatory and the Martinique and Guadeloupe Volcanological and Seismological Observatory for assistance during the cruise and outreach education activities. Data from the IODP Expedition 340 can be obtained through the expedition's implementing organization USIO (http://iodp.tamu.edu/database) (IPGP contribution 3960).

17.A: IODP 340 EXPEDITION SCIENTISTS

Tatsuya Adachi
Department of Earth and Environmental Science, Yamagata University, Yamagata, Japan

Mohammed Aljahdali
Department of Earth, Ocean and Atmospheric Sciences, Florida State University, Tallahassee, FL, USA

Georges Boudon
Institut de Physique du Globe de Paris, Paris, France

Christoph Breitkreuz
Physical Volcanology and Sedimentology, Institut für Geologie und Paläontologie, Technische Universität Bergakademie Freiberg, Freiberg, Germany

Benoît Caron
Sorbonne Université, ISTEP, Paris, France

Daisuke Endo
Earth Evolution Sciences, University of Tsukuba, Tsukuba, Japan

Andrew J. Fraass
Department of Geosciences, University of Massachusetts, Amherst, MA, USA

Akihiko Fujinawa
Department of Earth Sciences, Ibaraki University, Mito, Japan

Hervé Guyard
Institut de Physique du Globe de Paris, Paris, France

Robert G. Hatfield
College of Oceanic and Atmospheric Sciences, Oregon State University, Corvallis, OR, USA

Osamu Ishizuka
Geological Survey of Japan, AIST, Tokyo, Japan

Martin Jutzeler
Geology Department, University of Otago, Dunedin, New Zealand

Kyoko S. Kataoka
Research Institute for Natural Hazards and Disaster Recovery, Niigata University, Nishi-ku, Japan

Fukashi Maeno
Earthquake Research Institute, University of Tokyo, Bunkyo-ku, Tokyo, Japan

Michael Manga
Department of Earth and Planetary Science, University of California, Berkeley, CA, USA

Michael Martinez-Colon
College of Marine Science, University of South Florida, St. Petersburg, FL, USA

Molly C. McCanta
Department of Geology, Tufts University, Medford, MA, USA

James McManus
College of Earth, Ocean, and Atmospheric Sciences, Oregon State University, Corvallis, OR, USA

Sally Morgan
Borehole Research Group, Department of Geology, University of Leicester, Leicester, UK

Martin R. Palmer
School of Ocean and Earth Science, National Oceanography Centre, University of Southampton, Southampton, UK

Takeshi Saito
International Young Researchers Empowerment Center, Shinshu University, Matsumoto, Japan
Currently at Department of Geology, Faculty of Science, Shinshu University, Matsumoto, Japan

Angela L. Slagle
Borehole Research Group, Lamont-Doherty Earth Observatory of Columbia University, Palisades, NY, USA

Adam Stinton
Montserrat Volcano Observatory, Flemings, Montserrat, West Indies

Nicole A. Stroncik
Integrated Ocean Drilling Program, Texas A&M University, College Station, TX, USA

Konduri S. V. Subramanyam
Geochemistry Division, National Geophysical Research Institute (NGRI), Hyderabad, Telangana, India

Yoshihiko Tamura (Tabata)
Institute for Research on Earth Evolution (IFREE), Japan Agency for Marine-Earth Science and Technology, Yokosuka, Japan

Benoît Villemant
Université P&M Curie, UPMC-CNRS UMR 7193 ISTeP, Paris, France

Deborah Wall-Palmer
School of Earth, Ocean and Environmental Sciences, Plymouth University, Plymouth, UK

Fei Wang
Institute of Geology and Geophysics, Chinese Academy of Sciences, Beijing, People's Republic of China

REFERENCES

Boudon, G., Le Friant, A., Komorowski, J.-C., Deplus, C., & Semet, M. P. (2007). Volcano flank instability in the Lesser Antilles Arc: Diversity of scale, processes, and temporal recurrence. *Journal of Geophysical Research*, *112*, B08205. https://doi.org/10.1029/2006JB004674

Boudon, G., Le Friant, A., Villemant, B., & Viodé, J.-P. (2005). Martinique. In J. M. Lindsay, R. E. A. Robertson, J. B. Shepherd, & S. Ali (Eds.), *Volcanic hazard atlas of the Lesser Antilles* (pp. 65–102). Trinidad and Tobago, West Indies: Seismic Research Unit, The University of the West Indies.

Boudon, G., Semet, M. P., & Vincent, P. M. (1984). Flank failure-directed blast eruption at Soufrière, Guadeloupe, French West Indies: A 3,000-yr-old Mt. St. Helens? *Geology*, *12*, 350–353.

Boudon, G., Semet, M. P., & Vincent, P. M. (1987). Magma and hydrothermally driven sector collapses: The 3100 and 11,500 y. B.P. eruptions of la Grande Découverte volcano, Guadeloupe, French West Indies. *Journal of Volcanology and Geothermal Research*, *33*, 317–323.

Brunet, M. (2015).Caractérisation des processus d'instabilité affectant les îles volcaniques: Application au volcan de la Montagne Pelée à partir de l'exploitation des forages de l'Expédition IODP 340 (PhD thesis). Paris, France: Université Paris.

Brunet, M., Le Friant, A., Boudon, G., Lafuerza, S., Talling, P., Hornbach, M., et al. (2016). Composition, geometry, and emplacement dynamics of a large volcanic island landslide offshore Martinique: From volcano flank-collapse to seafloor sediment failure? *Geochemistry, Geophysics, Geosystems*, *17*(3), 699–724. https://doi.org/10.1002/2015GC006034

Brunet, M., Moretti, L., Le Friant, A., Mangeney, A., & Fernandez Nieto, E. (2017). Numerical simulations of 30–45 ka debris avalanche flow of Montagne Pelee volcano, Martinique: From volcano flank-collapse to submarine emplacement. *Natural Hazards*, *87*(2), 1189–1222.

Bull, S., Cartwright, J., & Huuse, M. (2009). A review of kinematic indicators from mass transport complexes using 3D seismic data. *Marine and Petroleum Geology*, *26*(7), 1132–1151.

Cassidy, M., Trofimovs, J., Palmer, M. R., Talling, P. J., Watt, S. F. L., Moreton, S. G., & Taylor, R. N. (2013). Timing and emplacement dynamics of newly recognised mass flow deposits at ~8–12 ka offshore Soufrière Hills volcano, Montserrat: How submarine stratigraphy can complement subaerial eruption histories. *Journal of Volcanology and Geothermal Research*, *253*, 1–14.

Cassidy, M., Trofimovs, J., Watt, S. F. L., Palmer, M. R., Taylor, R. N., Gernon, T. M., et al. (2014). Multi-stage collapse events in the South Soufrière Hills, Montserrat as recorded in marine sediment cores. *Geological Society, London, Memoirs*, *39*, 383–397.

Cassidy, M., Watt, S. F. L., Talling, P. J., Palmer, M. R., Edmonds, M., Jutzeler, M., et al. (2015). Rapid onset of mafic magmatism facilitated by volcanic edifice collapse. *Geophysical Research Letters*, *42*(12), 4778–4785.

Coussens, M., Wall-Palmer, D., Talling, P., Watt, S., Cassidy, M., Jutzeler, M., et al. (2016). The relationship between eruptive activity, flank collapse and sea-level at volcanic islands: A long-term (>1 Ma) record offshore Montserrat, Lesser Antilles. *Geochemistry, Geophysics, Geosystems*, *17*(7), 2591–2611.

Crandell, D. R. (1989). *Gigantic debris avalanche of Pleistocene age from ancestral Mount Shasta volcano, California, and debris-avalanche hazard zonation, United State Geological Survey Bulletin*. Washington, DC: U.S. Government Printing Office.

Crutchley, G. J., Karstens, J., Berndt, C., Talling, P. J., Watt, S. F. L., Vardy, M. E., et al. (2013). Insights into the emplacement dynamics of volcanic landslides from high-resolution 3D seismic data acquired offshore Montserrat, Lesser Antilles. *Marine Geology*, *335*, 1–15. https://doi.org/10.1016/j.margeo.2012.10.004

Delcamp, A., van Wyk de Vries, B., & James, M. (2008). The influence of edifice slope and substrata on volcano spreading. *Journal of Volcanology and Geothermal Research*, *177*(4), 925–943.

Deplus, C., Le Friant, A., Boudon, G., Komorowski, J.-C., Villemant, B., Harford, C., et al. (2001). Submarine evidence for large-scale debris avalanches in the Lesser Antilles arc. *Earth and Planetary Science Letters*, *192*(2), 145–157.

Fernandez-Nieto, E., Bouchut, F., Bresch, D., Castro-Diaz, M. J., & Mangeney, A. (2008). A new Savage–Hutter type model for submarine avalanches and generated tsunami. *Journal of Computational Physics*, *227*(16), 7720–7754.

Feuillet, N., Manighetti, I., Tapponnier, P., & Jacques, E. (2002). Arc parallel extension and localization of volcanic complexes in Guadeloupe, Lesser Antilles. *Journal of Geophysical Research*, *107*(B12), 2331. https://doi.org/10.1029/2001JB000308

Fraass, A. J., Wall-Palmer, D., Leckie, R. M., Hatfield, R. G., Burns, S. J., Le Friant, A., et al. (2016). A revised Plio-Pleistocene age model and paleoceanography of the north-eastern Caribbean Sea: IODP Site U1396 off Montserrat, Lesser Antilles. *Stratigraphy*, *13*(3), 183–203.

Frey-Martinez, J., Cartwright, J., & James, D. (2006). Frontally confined versus frontally emergent submarine landslides: A 3D seismic characterisation. *Marine and Petroleum Geology*, *23*, 585–604.

Frohlich, C., Hornbach, M. J., Taylor, F. W., Shen, C. C., Moala, A., Morton, A. E., & Kruger, J. (2009). Huge erratic boulders in Tonga deposited by a prehistoric tsunami. *Geology*, *37*(2), 131–134.

Gafeira, J., Long, D., Scrutton, R., & Evans, D. (2010). 3D seismic evidence of internal structure within Tampen Slide deposits on the North Sea Fan: Are chaotic deposits that chaotic? *Journal of the Geological Society*, *167*, 605–616.

Garcia, M. O. (1993). Pliocene-Pleistocene volcanic sands from site 842: Products of giants landslides. In R. H. Wilkens, J. Firth, & J. Bender (Eds.), *Proceedings of the Ocean Drilling Program, Scientific Results* (Vol. 136, pp. 53–63). College Station, TX: Ocean Drilling Program.

Garcia, M. O., & Meyerhoff Hull, D. (1994). Turbidites from giant Hawaiian landslides: Results from Ocean Drilling Program Site 842. *Geology*, *22*, 159–162.

Garcia, M. O., Sherman, S. B., Moore, G. F., Groll, R., Popova-Goll, I., Natland, J. H., & Acton, G. (2006). Frequent landslides from Koolau Volcano: Results from ODP Hole 1223A. *Journal of Volcanology and Geothermal Research*, *151*, 251–268.

Gardner, J. V. (2010). The West Mariana Ridge, western Pacific Ocean: Geomorphology and processes from new multibeam data. *Bulletin*, *122*(9–10), 1378–1388.

Germa, A., Quidelleur, X., Labanieh, S., Lahitte, P., & Chauvel, C. (2010). The eruptive history of Morne Jacob volcano (Martinique Island, French West Indies): Geochronology, geomorphology and geochemistry of the earliest volcanism in the recent Lesser Antilles arc. *Journal of Volcanology and Geothermal Research*, *198*, 297–310.

Glicken, H. (1986). Study of the rockslide avalanche of May 18 1980, Mount St Helens Volcano (PhD thesis, 303 p.). Santa Barbara, CA: University of California.

Goldstrand, P. M. (1998). Provenance and sedimentologic variations of turbidite and slump deposits at sites 955 and 956. In P. P. E. Weaver, H.-U. Schmincke, J. V. Firth, & W. Duffield (Eds.), *Proceedings of the Ocean Drilling Program, Scientific Results* (Vol. 157, pp. 343–360). College Station, TX: Ocean Drilling Program.

Heezen, B. C., & Ewing, M. (1952). Turbidity currents and submarine slumps, and the 1929 Grand Banks earthquake. *American Journal of Science*, *250*(12), 849–873.

Holcomb, R., & Searle, R. (1991). Large landslides from oceanic volcanoes. *Marine Geotechnology*, *10*, 19–32.

Hornbach, M. J., & Manga, M. (2014). The ability of rock physics models to infer marine in situ pore pressure. *Geochemistry, Geophysics, Geosystems*, *15*, 4769–4780. https://doi.org/10.1002/2014GC005442

Hornbach, M. J., Manga, M., Genecov, M., Valdez, R., Miller, P., Saffer, D., et al. (2015). Permeability and pressure measurements in Lesser Antilles submarine slides: Evidence for pressure-driven slow-slip failure. *Journal of Geophysical Research: Solid Earth*, *120*(12), 7986–8011. https://doi.org/10.1002/2015JB012061

Hsu, S. K., Kuo, J., Lo, C. L., Tsai, C. H., Doo, W. B., Ku, C. Y., & Sibuet, J. C. (2008). Turbidity currents, submarine landslides and the 2006 Pingtung Earthquake off SW Taiwan. *Terrestrial, Atmospheric and Oceanic Sciences*, *19*(6), 767–772.

Hunt, J. E., Cassidy, M., & Talling, P. J. (2018). Multi-stage volcanic island flank collapses with coeval explosive caldera-forming eruptions. *Scientific Reports*, *8*(1), 1146. https://doi.org/10.1038/s41598-018-19285-2

Hunt, J. E., Wynn, R. B., Masson, D. G., Talling, P. J., & Teagle, D. A. H. (2011). Sedimentological and geochemical evidence for multistage failure of volcanic landslides: A case study from Icod landslide on north Tenerife, Canary Islands. *Geochemistry, Geophysics, Geosystems*, *12*, 1–36. https://doi.org/10.1029/2011GC003740

Hunt, J. E., Wynn, R. B., Talling, P. J., & Masson, D. G. (2013). Multistage collapse of eight western Canary Island landslides in the last 1.5 Ma: Sedimentological and geochemical evidence from subunits in submarine flow deposits. *Geochemistry, Geophysics, Geosystems*, *14*(7), 2159–2181.

Ida, Y. and Voight, B. (eds.) (1995). Models of magmatic processes and volcanic eruptions. *Journal of Volcanology and Geothermal Research*, *66*(Special Issue), 426 pp.

Iverson, R. M. (1997). The physics of debris flows. *Reviews of Geophysics*, *35*, 245–296.

Jiang, L., & LeBlond, P. H. (1992). The coupling of a submarine slide and the surface waves which it generates. *Journal of Geophysical Research, Oceans*, *97*(C8), 12,731–12,744.

Jutzeler, M., Manga, M., White, J. D. L., Talling, P. J., Proussevitch, A. A., Watt, S. F. L., et al. (2016). Submarine deposits from pumiceous pyroclastic density currents traveling over water: An outstanding example from offshore Montserrat (IODP 340). *GSA Bulletin*, *129*(3–4), 392–414. https://doi.org/10.1130/B31448.1

Jutzeler, M., White, J. D. L., Talling, P. J., McCanta, M., Morgan, S., Le Friant, A., & Ishizuka, O. (2014). Coring disturbances in IODP piston cores with implications for offshore record of volcanic events and the Missoula megafloods, Geochem. *Geochemistry, Geophysics, Geosystems*, *15*. https://doi.org/10.1002/2014GC005447

Karstens, J., Crutchley, G. J., Berndt, C., Talling, P. J., Watt, S. F. L., Trofimovs, J., et al. (2013). Insights into pyroclastic flow emplacement from high-resolution 3D seismic data offshore Montserrat, Lesser Antilles. *Journal of Volcanology and Geothermal Research*, *257*, 1–11.

Komorowski, J. C., Boudon, G., Semet, M., Beauducel, F., Anténor-Habazac, C., Bazin, S., & Hammouya, G. (2005). Guadeloupe. In J. Lindsay, R. Robertson, J. Shepherd, & S. Ali (Eds.), *Volcanic hazard atlas of the Lesser Antilles* (pp. 65–102). Trinidad: University of the West Indies - Seismic Research Unit and IAVCEI.

Krastel, S., Schmincke, H. U., Jacobs, C. L., Rihm, R., Le Bas, T. M., & Alibés, B. (2001). Submarine landslides around the Canary Islands. *Journal of Geophysical Research*, *106*(B3), 3977–3997.

Krause, D. C., White, W. C., PIPER, D. J. W., & Heezen, B. C. (1970). Turbidity currents and cable breaks in the western New Britain Trench. *Geological Society of America Bulletin*, *81*(7), 2153–2160.

Labazuy, P. (1996). Recurrent landslides events on the submarine flank of Piton de la Fournaise volcano (Reunion Island). In W. J. McGuire, A. P. Jones, & J. Neuberg (Eds.), *Volcano instability on the earth and other planets, Geological Society Special Publication* (Vol. 110, pp. 295–306). London, UK: Geological Society.

Lafuerza, S., Le Friant, A., Manga, M., Boudon, G., Villemant, B., Stroncik, N., et al. (2014). Geomechanical characterizations of submarine volcano flank sediments, Martinique, Lesser Antilles Arc. In S. Krastel, J.-H. Behrmann, D. Völker, M. Stipp, C. Berndt, R. Urgeles, et al. (Eds.), *Sumarine mass movements and consequences, Advances in Natural and Technological Hazards Research* (Vol. 2014, pp. 37). Cham, Switzerland: Springer International. https://doi.org/10.1007/978-3-319-00972-8_7

Le Friant, A., Boudon, G., Arnulf, A., & Robertson, R. (2009). Debris avalanche deposits offshore St Vincent (West Indies): Impact of flank-collapse events on the morphological evolution of the island. *Journal of Volcanology and Geothermal Research*, *179*, 1–10.

Le Friant, A., Boudon, G., Deplus, C., & Villemant, B. (2003a). Large scale flank collapse events during the activity of Montagne Pelée, Martinique, Lesser Antilles. *Journal of Geophysical Research*, *108*(B1), 2055.

Le Friant, A., Boudon, G., Komorowski, J.-C., & Deplus, C. (2002). L'île de la Dominique, à l'origine des avalanches de débris les plus volumineuses de l'arc des Petites Antilles. *Comptes Rendus Géoscience*, *334*(4), 235–243.

Le Friant, A., Deplus, C., Boudon, G., Feuillet, N., Trofimovs, J., Komorowski, J.-C., et al. (2010). Eruption of Soufrière Hills (1995–2009) from an offshore perspective: Insights from repeated swath bathymetry surveys. *Geophysical Research Letters*, *37*, L11307. https://doi.org/10.1029/2010GL043580

Le Friant, A., Harford, C., Deplus, C., Boudon, G., Sparks, S., Herd, R., & Komorowski, J.-C. (2004). Geomorphological evolution of Montserrat (West Indies): Importance of flank collapse and erosional processes. *Geological Society London*, *161*, 147–160.

Le Friant, A., Heinrich, P., Deplus, C., & Boudon, G. (2003b). Numerical simulation of the last flank collapse event of Montagne Pelée, Martinique, Lesser Antilles. *Geophysical Research Letters*, *30*(2), 1034.

Le Friant, A., Ishizuka, O., Boudon, G., Palmer, M. R., Talling, P., Villemant, B., et al. (2015). Submarine record of volcanic island construction and collapse in the Lesser Antilles arc: First scientific drilling of submarine volcanic island landslides by IODP Expedition 340. *Geochemistry, Geophysics, Geosystems*, *16*(2), 420–442.

Le Friant, A., Ishizuka, O., Stroncik, N. A., & the Expedition 340 Scientists (2013). *Proceedings of Integrated Ocean Drilling Program (IODP)* (Vol. 340). College Station, TX: Integrated Ocean Drilling Program Management International, Inc. https://doi.org/10.2204/iodp.proc.340.2013

Le Friant, A., Lebas, E., Clément, V., Boudon, G., Deplus, C., de Voogd, B., & Bachèlery, P. (2011). A new model for the evolution of la Réunion volcanic complex from complete geophysical surveys. *Geophysical Research Letters*, *38*. https://doi.org/10.1029/2011GL047489

Lebas, E., Le Friant, A., Boudon, G., Watt, S., Talling, P., Feuillet, N., et al. (2011). Multiple widespread landslides during the long-term evolution of a volcanic island: Insights from high-resolution seismic data, Montserrat Lesser Antilles. *Geochemistry, Geophysics, Geosystems*, *12*, 1. https://doi.org/10.1029/2010GC003451

Lebas, E., Le Friant, A., Deplus, C., & de Voogd, B. (2018). Understanding the evolution of an oceanic intraplate volcano from seismic reflection data: A new model for La Réunion, Indian Ocean. *Journal of Geophysical Research, Solid Earth*, *123*, 1035–1059. https://doi.org/10.1002/2017JB014959

Lénat, J.-F., Vincent, P., & Bachèlery, P. (1989). The offshore continuation of an active basaltic volcano: Piton de la Fournaise (Réunion Island, Indian Ocean); structural and geomorphological interpretation from sea beam mapping. *Journal of Volcanology and Geothermal Research*, *36*, 1–36.

Lipman, P. W., Normark, W. R., Moore, J. G., Wilson, J. B., & Gutmacher, E. (1988). The giant submarine Alika debris slide, Mauna Loa, Hawaii. *Journal of Geophysical Research*, *93*, 4279–4299.

Lopart, J., Lafuerza, S. Le Friant, A., Urgeles, R. (2018). *Hydrogeological evolution as a pre-conditioning factor for slope failure in a back-arc volcanic setting, W off Martinique Island*. Paper presented at 8th International Symposium on Submarine Mass Movements and their consequences (ISSMMTC), 7–9 May 2018, Victoria, British Columbia.

Lovholt, R., Pedersen, G., & Gisler, G. (2008). Oceanic propagation of a potential tsunami from the La Palma island. *Journal of Geophysical Research*, *113*, C09026.

MacDonald, R., Hawkesworth, C. J., & Heath, E. (2000). The Lesser Antilles volcano chain: A study in arc magmatism. *Earth Science Reviews*, *49*, 1–76.

Manga, M., Hornbach, M., Le Friant, A., Ishizuka, O., Stroncik, N., Adachi, T., et al. (2012). Heat flow in the Lesser Antilles island arc and adjacent back arc Grenada basin. *Geochemistry, Geophysics and Geosystems*. https://doi.org/10.1029/2012GC004260

Mangeney-Castelnau, A., Vilotte, J. P., Bristeau, M. O., Perthame, B., Bouchut, F., Simeoni, C., & Yernini, S. (2003). Numerical modeling of avalanches based on Saint-Venant equations using a kinetic scheme. *Journal of Geophysical Research*, *108*(B11), 2527.

Masson, D. G., Harbitz, C. B., Wynn, R. B., Pedersen, G., & Løvholt, F. (2006). Submarine landslides: Processes, triggers and hazard prediction. *Philosophical Transactions of the Royal Society A*, *364*, 2009–2039.

Masson, D. G., Watts, A. B., Gee, M. J. R., Urgeles, R., Mitchell, N. C., Le Bas, T. P., & Canals, M. (2002). Slope failures on the flanks of the western Canary Islands. *Earth-Science Reviews*, *57*, 1–35.

Mattioli, G. S., Voight, B., Linde, A. T., Sacks, I. S., Watts, P., Widiwijayanti, C., et al. (2007). Unique and remarkable dilatometer measurements of pyroclastic flow-generated tsunamis. *Geology*, *35*, 25–28.

McGuire, W. J. (1996). Volcano instability: A review of contemporary themes. In W. J. McGuire, A. P. Jones, & J. Neuberg (Eds.), *Volcano instability on the Earth and other planets, Geological Society Special Publication* (Vol. 110, pp. 1–23). London, UK: Geological Society.

Montanaro, C., & Beget, J. (2011). Volcano collapse along the Aleutian Ridge (western Aleutian Arc). *Natural Hazards and Earth System Sciences*, *11*, 715–730. http://dx.doi.org/10.5194/nhess-11-715-2011

Moore, J. G., & Clague, D. A. (2002). Mapping the Nuuanu and Wailau landslides in Hawaii. In E. Takahashi, P. W. Lipman, M. O. Garcia, J. Naka, & S. Aramaki (Eds.), *Hawaiian volcanoes: Deep underwater perspectives* (pp. 223–244). Washington, DC: *American Geophysical Union*. http://dx.doi.org/10.1029/GM128p0223

Moore, J. G., Clague, D. A., Holcomb, R. T., Lipman, P. W., Normark, W. R., & Torresan, M. E. (1989). Prodigious submarine landslides on the Hawaiian ridge. *Journal of Geophysical Research*, *94*(B12), 17,465–17,484.

Moore, J. G., Normark, W. R., & Holcomb, R. T. (1994). Giant hawaiian landslides. *Annual Review of Earth and Planetary Sciences*, *22*(1), 119–144.

Nomanbhoy, N., & Satake, K. (1995). Generation mechanism of tsunamis from the 1883 Krakatau eruption. *Geophysical Research Letters*, *22*(4), 509–512.

Oehler, J.-F., Labazuy, P., & Lénat, J.-F. (2004). Recurrence of major flank landslides during the last 2-Ma-history of Reunion Island. *Bulletin of Volcanology*, *66*, 585–598.

Oehler, J. F., Lenat, J. F., & Labazuy, P. (2008). Growth and collapse of the Reunion Island volcanoes. *Bulletin of Volcanology*. https://doi.org/10.1007/s00445-007-0163-0

Ogata, K., Mountjoy, J. J., Pini, G. A., Festa, A., & Tinterri, R. (2014). Shear-zone liquefaction in mass transport deposit emplacement: A multi-scale integration of seismic reflection and outcrop data. *Marine Geology*, *356*, 50–64.

Palmer, M., Hatter, S. J., Gernon, T. M., Taylor, R. N., Cassidy, M., Johnson, P., et al. (2016). Discovery of a large 2.4 Ma Plinian eruption of Basse-Terre, Guadeloupe, from the marine sediment record. *Geology*, *44*(2), 123–126. https://doi.org/10.1130/G37193.1

Picard, M., Schneider, J.-L., & Boudon, G. (2006). Contrasting sedimentary processes along a convergent margin: The Lesser Antilles arc system. *Geo-Marine Letters*, *26*(6), 397–410.

Schmincke, H.-U., & Sumita, M. (1998). Volcanic evolution of Gran Canaria reconstructed from apron sediments: Synthesis of vicap project drilling. *Proceeding of the Ocean Drilling Program, Scientific Results*, *157*, 443–469.

Schneider, J.-L., Gérard, M., Schmincke, H.-U., Weaver, P. P. E., Firth, J., Baraza, J., et al. (1997). Du volcan au sediment: La dynamique du talus volcanoclastique sous-marin de Gran Canaria, Canaries (Atlantique oriental, Leg ODP 157). *Comptes Rendus de l'Academie des Sciences Series IIA Earth and Planetary Science*, *324*, 891–898.

Siebert, L. (2002). Landslides resulting from structural failures in volcanoes. In S. G. Evans & J. V. DeGraff (Eds.), *Catastrophic landslides: Effects, occurrence, and mechanisms, Reviews in Engineering Geology* (Vol. XV, pp. 209–235). Boulder, CO: Geological Society of America.

Sigurdsson, H., Sparks, R. S. J., Carey, S., & Huang, T. C. (1980). Volcanogenic sedimentation in the Lesser Antilles Arc. *Journal of Geology*, *88*, 523–540.

Silver, E., Day, S., Ward, S., Hoffmann, G., Llanes, P., Driscoll, N., et al. (2009). Volcano collapse and tsunami generation in the Bismarck Volcanic Arc, Papua New Guinea. *Journal of Volcanology and Geothermal Research*, *186*, 210–222. http://dx.doi.org/10.1016/j.jvolgeores.2009.06.013

Slingerland, R., & Voight, B. (1979). Occurrence and predictive models for slide-generated water waves. In B. Voight (Ed.), *Rockslides and avalanches* (Vol. 2, pp. 317–400). Amsterdam, The Netherlands: Elsevier.

Tinti, S., Pagnini, G., & Zaniboni, F. (2006). The landslides and tsunamis of the 30th of December 2002 in Stromboli analysed through numerical simulations. *Bulletin of Volcanology*, *68*(5), 462–479.

Trofimovs, J., Amy, L., Boudon, G., Deplus, C., Doyle, E., Fournier, N., et al. (2006). What happens when pyroclastic flows enter the ocean? *Geology*, *34*, 549–552.

Trofimovs, J., Fisher, J. K., Macdonald, H. A., Talling, P. J., Sparks, R. S. J., Hart, M. B., et al. (2010). Evidence for carbonate platform failure during rapid sea-level rise; ca 14 000 year old bioclastic flow deposits in the Lesser Antilles. *Sedimentology*, *57*(3), 735–759.

Trofimovs, J., Talling, P. J., Fisher, J. K., Sparks, R. S. J., Watt, S. F. L., Hart, M. B., et al. (2013). Timing, origin and emplacement dynamics of mass flows offshore of SE Montserrat in the last 110 ka: Implications for landslide and tsunami hazards, eruption history, and volcanic island evolution. *Geochemistry, Geophysics, Geosystems*, *14*(2), 385–406. https://doi.org/10.1002/ggge.20052

Urgeles, R., Canals, M., Baraza, J., Alonso, B., & Masson, D. (1997). The most recent megalandslides of the Canary Islands: El Golfo debris avalanche and Canary debris flow, west El Hierro Island. *Journal of Geophysical Research*, *102*(B9), 20,305–20,323.

Urgeles, R., Masson, D. G., Canals, M., Watts, A. B., & Le Bas, T. (1999). Recurrent large-scale landsliding on the west flank of La Palma, Canary Islands. *Journal of Geophysical Research*, *104*(B11), 25,331–25,348.

Viesca, R. C., & Rice, J. R. (2012). Nucleation of slip-weakening rupture instability in landslides by localized increase of pore pressure. *Journal of Geophysical Research*, *117*, B03104.

Vincent, P. M., Bourdier, J.-L., & Boudon, G. (1989). The primitive volcano of Mount Pelée: Its construction and partial destruction by flank collapse. *Journal of Volcanology and Geothermal Research*, *38*, 1–15.

Voight, B. (2000). Structural stability of andesite volcanoes and lava domes. *Philosophical Transactions of the Royal Society of London, Series A*, *358*, 1663–1703.

Voight, B., & Elsworth, D. (1997). Failure of volcano slopes. *Geotechnique*, *47*, 1–31.

Voight, B., Glicken, H., Janda, R. J., & Douglass, P. M. (1981). Catastrophic rockslide avalanche of May 18. In P. W. Lipman & D. R. Mullineaux (Eds.), *The 1980 Eruptions of Mount St. Helens, Washington, Professional Paper US Geological Survey* (Vol. 1250, pp. 347–378). U.S. G.P.O.

Voight, B., Komorowski, J.-C., Norton, G. E., Belousov, A. B., Belousova, M., Boudon, G., et al. (2002). The 26 December (Boxing Day) 1997 sector collapse and debris avalanche at Soufrière Hills Volcano, Montserrat. In T. H. Druitt & B. P. Kokelaar (Eds.), *The eruption of Soufriere Hills Volcano, Montserrat, from 1995 to 1999, Memoirs* (Vol. 21, pp. 363–407). London, UK: Geological Society.

Voight, B., Le Friant, A., Boudon, G., Deplus, C., Komorowski, J. C., Lebas, E., et al. (2012). Undrained sediment loading key to long-runout submarine mass movements: Evidence from the Caribbean Volcanic Arc. In Y. Yamada, K. Kawamura, K. Ikehara, Y. Ogawa, R. Urgeles, D. Mosher, et al. (Eds.), *Submarine mass movements and their consequences, Advances in Natural and Technological Hazards Research* (Vol. 31, pp. 417–428). https://doi.org/10.1007/978-94-007-2162-3-37

Wadge, G. (1984). Comparison of volcanic production rates and subduction rates in the Lesser Antilles and Central America. *Geology*, *12*, 555–558.

Wall-Palmer, D., Coussens, M., Talling, P. J., Jutzeler, M., Cassidy, M., Marchant, I., et al. (2014). Late Pleistocene stratigraphy of IODP U1396 and compiled chronology offshore of south and south west Montserrat, Lesser Antilles. *Geochemistry, Geophysics, Geosystems*, *15*. https://doi.org/10.1002/2014GC005402

Ward, S. N. (2001). Landslide tsunami. *Journal of Geophysical Research*, vol *106*, n°6 p 11,201–11,215.

Ward, S. N., & Day, S. (2003). Ritter Island volcano: Lateral collapse and the tsunami of 1888. *Geophysical Journal International*, *154*(3), 891–902.

Ward, S. N., & Day, S. J. (2001). Cumbre Vieja volcano – Potential collapse and tsunami at La Palma, Canary Islands. *Geophysical Research Letters*, *28*, 3397–3400.

Watt, S. F. L., Talling, P. J., & Hunt, J. E. (2014). New insights into the emplacement dynamics of volcanic-island landslides. *Oceanography*, *27*, 46–57.

Watt, S. F. L., Talling, P. J., Vardy, M. E., Heller, V., Hühnerbach, V., Urlaub, M., et al. (2012a). Combination of volcanic-flank and seafloor sediment failure offshore Montserrat, and their implications for tsunami generation. *Earth and Planetary Science Letters*, *319*(2), 228–240. https://doi.org/10.1016/j.epsl.2011.11.032

Watt, S. F. L., Talling, P. J., Vardy, M. E., Masson, D. G., Henstock, T. J., Huehnerbach, T. A., et al. (2012b). Widespread and progressive seafloor-sediment failure following volcanic debris avalanche emplacement: Landslide dynamics and timing offshore Montserrat, Lesser Antilles. *Marine Geology*, *323*, 69–94. https://doi.org/10.1016/j.margeo.2012.08.002

Watts, A. B., & Masson, D. G. (1995). A giant landslide on the north flank of Tenerife, Canary Islands. *Journal of Geophysical Research*, *100*(B12), 24,487–24,498.

Watts, P., Grilli, S. T., Tappin, D. R., & Fryer, G. J. (2005). Tsunami generation by submarine mass failure. II: Predictive equations and case studies. *Journal of Waterway Port, Coastal, and Ocean Engineering*, *131*, 298–310.

Westercamp, D. and Traineau, H. (1983). Carte géologique au 1/20 000 de la Montagne Pelée, avec notice explicative. Eds Bureau de Recherche Géologiques et Minières. Orléans, France.

Wynn, R. B., & Masson, D. G. (2003). Canary Islands landslides and tsunami generation: Can we use turbidite deposits to interpret landslide processes? In J. Locat & J. Mienert (Eds.), *Submarine mass movements and their consequences* (pp. 325–332). Boston, MA; London, UK: Kluwer Academic.

18

Submarine Landslides in an Upwelling System: Climatically Controlled Preconditioning of the Cap Blanc Slide Complex (Offshore NW Africa)

Morelia Urlaub[1], Sebastian Krastel[2], and Tilmann Schwenk[3]

ABSTRACT

Continental slopes are areas of high primary productivity, in particular where strong winds allow cold, nutrient-laden deep water to upwell. The seafloor in upwelling areas is affected by repeated large submarine landslides, but the special environmental conditions have as yet not been taken into account in the analysis of these landslides. We show evidence for a potential link between environmental conditions and landslide occurrence for the Cap Blanc Slide Complex in the center of the Cap Blanc upwelling zone. Ocean Drilling Program Site 658 was drilled inside the slide complex, and its integration with high-resolution seismic lines reveals that the onset of sliding postdates the onset of glaciations in the Northern Hemisphere. The sediment associated with failure surfaces of all seven slide events comprises of diatom ooze, the conditions for the formation of which are only met at the end of glacials. Preconditioning of the slope in the Cap Blanc Slide Complex is thus climatically controlled. We conclude that the presence of ooze formed under specific environmental conditions is an important factor in preconditioning slopes to fail in the Cap Blanc Slide Complex and potentially also at other continental slopes with high primary productivity.

18.1. INTRODUCTION

Submarine landslides are an important process for global sediment fluxes and can generate damaging tsunamis. For instance, the deposits of the Storegga Slide offshore Norway have a volume of over 3000 km^3 and cover an area larger than Scotland (Haflidason et al., 2004). This same landslide caused a tsunami that heavily affected the entire North Atlantic region 8150 years ago (Bondevik et al., 2005). More recently, a submarine landslide with a volume of approximately 5 km located offshore Papua New Guinea produced a localized tsunami that killed 2200 people in 1999 (Tappin et al., 2008). For sediment budget studies as well as for hazard assessments, it is therefore crucial to understand under which conditions submarine landslides can occur and which factors precondition slopes to fail.

It has been proposed that changes in global climate influence the frequency of submarine landslides at continental slopes. An increase in landslide frequency during sea level rise has been observed during periods of glaciations and/or during glacial to interglacial transitions (Maslin et al., 2004; Owen et al., 2007; Lee, 2009). Several other authors report an increased recurrence interval of submarine landslides from various geographical locations worldwide during sea level lowstand and during sea level rise (Paull et al., 1996; Prins et al., 2000; Piper et al., 2003; Lebreiro et al., 2009; Henrich et al., 2010; Lee et al., 2010; Brothers et al., 2013). At high-latitude margins, contrasting sedimentary patterns imaged in high-resolution seismic

[1] *GEOMAR Helmholtz Centre for Ocean Research Kiel, Kiel, Germany*

[2] *Institute of Geosciences, Christian-Albrechts-University, Kiel, Germany*

[3] *Faculty of Geosciences, MARUM-Center for Marine Environmental Sciences, University of Bremen, Bremen, Germany*

Submarine Landslides: Subaqueous Mass Transport Deposits from Outcrops to Seismic Profiles, Geophysical Monograph 246, First Edition. Edited by Kei Ogata, Andrea Festa, and Gian Andrea Pini.
© 2020 American Geophysical Union. Published 2020 by John Wiley & Sons, Inc.

data reflect environmental conditions at the time of failure, and most landslides appear to have occurred during deglaciations (Bryn et al., 2005, Llopart et al., 2015). However, few submarine landslides have been dated with accuracy. Once realistic error bars are included in frequency analyses, there is no strong correlation between landslide frequency and sea level (Urlaub et al., 2013), or the available landslide dates are too inaccurate to tell (Pope et al., 2015). Moreover, it is important to distinguish between factors that precondition or trigger slope failures. It is possible that a climate-controlled preconditioning factor could significantly reduce the stability of continental slopes so that a climatically independent trigger, such as an earthquake, can initiate the landslide, resulting in temporally random recurrence intervals.

Northwest Africa is highly sensitive to climate perturbations, which is reflected, for example, in repeated occurrences of so-called African human periods in the late Quaternary. Dramatic shifts in hydroclimate caused more humid conditions when the Sahara was a well-vegetated landscape, crosscut by a network of rivers and lakes (de Menocal et al., 2000). Different styles of sediment transport shape the continental slope off Northwest Africa. Some sections of the margin show a large concentration of upper slope canyons but no indication for significant mass wasting, whereas other sections are characterized by large-scale mass wasting with no canyons or gullies (Krastel et al., 2012, 2018). Therefore, this margin is an ideal setting to investigate the effect of changes in global climate, local hinterland climate, and vegetation on the occurrence of submarine landslides.

Previously, Krastel et al. (2006) and Wien et al. (2007) reported on a headwall area located in water depths of 3575 m over 200 km offshore of Cap Blanc based on parasound data. Jacobi and Hayes (1992) first mapped a series of slides originating further upslope at ~2000 m water depth, which is the target area of this study. This is the upper headwall area of the Cap Blanc Slide, which we refer to as Cap Blanc Slide Complex from here on. In this study, we establish a chronological evolution of the Cap Blanc Slide Complex and relate the timing of individual events to local and global climate. We also identify potential preconditioning factors and assess their dependence on climate. We do this for the Cap Blanc Slide Complex offshore Mauritania because Ocean Drilling Program (ODP) Site 658 (20°44′57″N, 18°34′51″W, 2263 m water depth) was drilled in midst of the landslide complex and a substantial net of 2D high-resolution seismic data is available that connects the drill site with the individual failure planes (Figure 18.1b). Landsliding caused a lack of sedimentation continuity at ODP Site 658, with the most prominent hiatus affecting the mid-Pleistocene transition from 1.573 to 0.731 Ma (Ruddiman et al., 1988).

18.1.1. Oceanography and Climate of the Cap Blanc Slide Area

Cap Blanc, also known as Ras Nouadhibou, is a narrow, ~40 km long peninsula shared by Mauritania and Western Sahara. The offshore area marks the southern edge of the Cape Verde Frontal Zone that separates warmer, saltier North Atlantic Central Water flowing south, and cooler, fresher South Atlantic Central Water flowing north. Off Cap Blanc upwelling of cold and nutrient-rich waters from the South Atlantic Central Water and its transport to the open ocean by the Canary and Mauritania currents give rise to one of the most bioproductive ocean environments on Earth (Figure 18.1a). The Cap Blanc upwelling area is one of the four major eastern boundary upwelling ecosystems of the world's oceans (Sicre et al., 2001; Adkins et al., 2006). It hosts intense primary production in the surface water and, consequently, exports large amounts of organic carbon to the seafloor. The upwelling filament extends for 600 km offshore and persists all year with substantial variations on seasonal, interannual, and geological time scales (Cropper et al., 2014). A major agent driving upwelling is the Northeast Trade Wind (NETW) blowing equatorward (Figure 18.1a). The NETW along with the African Easterly Jet transports large amounts of dust from the African hinterland into the area (Stuut et al., 2005). Apart from the aeolian input, terrestrial input is minimal given the absence of major rivers. Sedimentation rates have been below 0.15 m/ka in the Quaternary (Ruddiman et al., 1988).

Inland of Cap Blanc, the phytogeography at present is dominated by desert vegetation to the north and savanna and dry open forest to the south marked by the Sahara-Sahel boundary (Figure 18.1a). This boundary has shifted throughout the past as the whole system is very sensitive to ice sheet instability and changes in ocean circulation. A full-blown Sahara Desert originated in the late Pliocene coupled to the development of major ice sheets on the northern continents and their further expansion during the mid-Pleistocene transition (Vallé et al., 2014). During the Quaternary in the so-called African humid or Green Sahara periods, the Sahara was a well-vegetated landscape, crosscut by a network of rivers and lakes, implying that repeated dramatic shifts in North African hydroclimate occurred (de Menocal et al., 2000).

18.2. METHODS AND DATA

18.2.1. Acoustic Data

Bathymetric and seismic data were collected during RV Meteor expedition M58/1 in 2003 and RV Maria S. Merian expedition MSM11/2 in 2009 (Figure 18.1b).

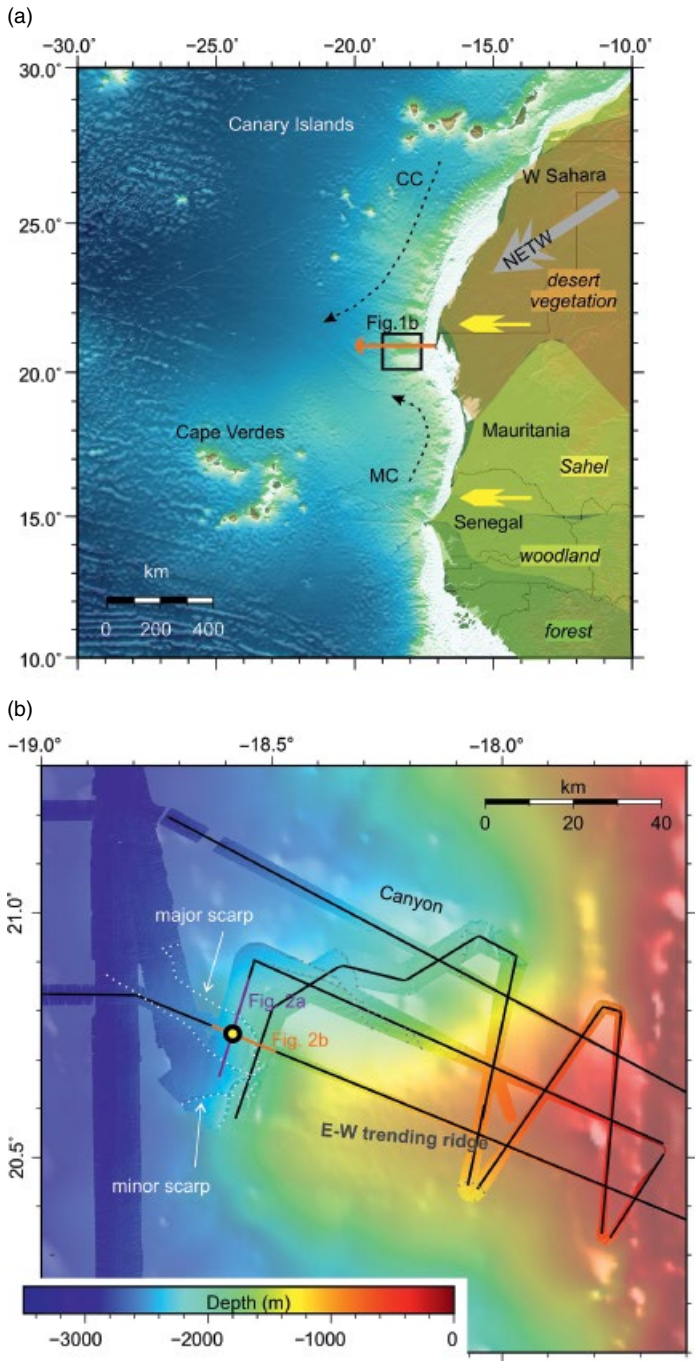


Figure 18.1 (a) Topographic map of Northwest Africa and its continental margin (GEBCO). The study area (black square) lies within the Cap Blanc upwelling filament (orange arrow) and is affected by major dust transport (yellow arrows) induced by the North East Trade Winds (NETW) (Sicre et al., 2001). The oceanographic setting is dominated by the northward flowing warm Mauritania Current (MC) and the cooler Canary Current (CC), which is the main driver of the upwelling system. Modern vegetation belts on the continent are simplified after Kuechler et al. (2018). (b) Combined GEBCO (background) and multibeam bathymetry for the study area offshore Cap Blanc including the net of seismic lines available to this study (black lines). The study area focuses on an east-west trending sedimentary ridge, at the toe of which Ocean Drilling Program (ODP) Site 658 was drilled (yellow dot). Dotted lines delineate landslide scarps identified in the multibeam data. (*See electronic version for color representation of this figure*)

Multibeam bathymetric data were collected with the hull-mounted HYDROSWEEP system by Krupp Atlas Elektronik during M58/1 and the Kongsberg Simrad system EM120 during MSM11/2. Processing was carried out with the open-source software MB-System as well as Fledermaus Pro (QPS) to create a grid with 50 m resolution. The 30 arc-second interval grid provided by the General Bathymetric Chart of the Oceans (GEBCO) is used to fill gaps in multibeam coverage.

High-resolution seismic data were collected during both cruises using a 2 × 1.7 liter GI-gun with a center frequency of 100 Hz (Figure 18.1b). The seismic signals were recorded with a 500 m long analogue streamer hosting 80 channels. Seismic data processing was carried out with VISTA (Schlumberger) and included binning with 5 m size, trace editing, normal moveout correction, and stacking as well as time migration. The data are capable of resolving layers with thickness as low as 5 m. In order to establish a local stratigraphy, we define prominent seismic reflectors and manually trace these all across the network of seismic lines and, in particular, to ODP Site 658 (Ruddiman et al., 1988) using the IHS Kingdom® software.

18.2.2. ODP Site 658 Core Data

Core data were downloaded from the International Ocean Discovery Program (IODP) Janus database. All depths were converted to hole B depth using the updated composite depth by Meckler et al. (2013). The data were not further processed except for density as the calculation of a synthetic seismogram for the core-seismic integration requires continuous and filtered density values. Gamma ray attenuation (GRA) density values are available for ODP cores 658 A, B, and C at an interval of about 0.6 cm including several gaps of up to a few meters. Although core A represents the longest record, the bulk of GRA values (0–165 m) were taken from core B as it contains less and smaller gaps. Problems with GRA density measurements occur where the core liner is not entirely filled with sediment or where there is gas expanding in the sediment. Hence to avoid density values affected by free gas (and thus conditions that are not representative to those below the seafloor), the density data are filtered to eliminate values lower than 1.025 g/cm^3, equal to the density of seawater (a lower value may only occur if gas is present in the pore space). We also apply a high-cut filter for values larger than 2.7 g/cm^3 (representing the density of pure clay or silt particles). The filtering of GRA density led to a reduction of data points from 38,516 to 33,165 values. Filtering also causes gaps in the density data in some locations (e.g., between 97 and 100 mbsf and 209 and 212 mbsf). These data gaps are linearly interpolated to the next density value. Finally, a smoothing of the density record was achieved by the use of a 10 cm running average.

18.2.3. Core-Seismic Integration

We calculate the synthetic seismogram for ODP Site 658 based on densities determined from GRA and a constant p-wave velocity of 1500 m/s, since due to expansion of free gas in the sediment during core recovery, reliable measurements of p-wave velocity are only available for the upper 10 m of the core (Ruddiman et al., 1988). However, velocity values normally scatter around a mean trend, and variations in marine surface sediments do not exceed 5%, whereas density variations are much higher (>20%) within these sediments (Breitzke, 2000). Velocity data are thus less important for the calculation of reflection coefficients in this specific environment.

Reflection coefficients are calculated from the density values and constant velocity (seismic impedance) and convolved with a wavelet, which approximates the seismic signal observed in the field. As a source wavelet, a standard Ricker wavelet (1953) is preferred over a wavelet extracted from seismic traces near the borehole. The synthetic wavelet appears smoother than the recorded one and has proven to be more useful for a visual correlation of measured and synthetic data. The wavelet contains a frequency of 100 Hz corresponding to the dominant frequency of the GI-gun used to acquire the seismic data. For the core-seismic integration, we use the SynPAK module in the IHS Kingdom® software. The synthetic seismogram is shifted, stretched, or squeezed to match the nearby seismic survey traces, and the interval velocities are adapted correspondingly. The software recalculates the synthetic seismogram using the updated velocity-depth profile.

18.3. THE CAP BLANC SLIDE COMPLEX

18.3.1. Seafloor Morphology in the Slide Complex

The continental slope off Western Sahara and Mauritania shows several prominent bulges extending from the shelf toward the continental rise, where they disappear (Figure 18.1a). Our study area is on the largest of the bulges off Cap Blanc that has an elongated ridge-like shape reaching from east to west (Figure 18.1b). The ridge is about 110 km long from the shelf to the continental rise and about 90 km wide. The maximum slope angles of its northern and southern flanks are 2.3° and 2.6°, respectively. Toward the continental rise to the west, that is, the ridge's toe, the slope gradient is slightly higher with 2.8°. Multibeam bathymetry is available for some parts of the ridge's northern flank and its toe (Figure 18.1b). In these data, a canyon is visible in the trough north of the ridge. The southern trough also seems to accommodate a canyon as inferred from the coarser GEBCO bathymetry.

Multibeam coverage is densest at the western, seaward directed toe of the ridge and highlights the partial outline of a large landslide that accommodates a smaller landslide inside its failed area (Figure 18.1b). Hereafter, we refer to "major" slide describing the large slide and "minor" slide to describe the smaller slide inside the bigger failed area. These slides have been described in detail by Urlaub et al. (2018). A prominent scarp, representing the northern sidewall of the major slide, can be traced for 35 km from the northeastern part of the ridge at 1950 m water depth toward the northwest into water depth of 2740 m. The scarp is 90 m high in the eastern part and 30 m at the northwestern end. South of this major scarp, another smaller scarp ("minor scarp" in Figure 18.1b) also extends to the northwest over a length of 40 km, which represents the northern sidewall of the minor landslide that occurred within the scar of the major slide. The scarp height is 50 m in the east and 25 m in the northwest. The headwall area is more complex. Both major and minor slides partly share the same headwall. The headwall of the major slide is 100 m high. The headwall height increases to almost 200 m where the smaller slide has cut into the sediment. The multibeam data also show a short part of the southern sidewall of the minor slide. The southern sidewall of the major slide is not covered.

In addition to the major and minor slides, the multibeam data also show numerous scarps at the northern flank of the east-west trending ridge (Figure 18.1b). Multibeam coverage is not complete, so it is likely that several scars remain hidden. Most scarps offset the seafloor by ~50 m, except for one that is 90 m high. On the southern flank, we observe only one ~40 m high scarp, but this might not be representative due to limited multibeam and seismic data coverage.

The seafloor inside all slide areas is very smooth, indicating translational sliding along a bedding-parallel glide plane and nondeposition. Depressions at the base of all scarps are formed by the interaction of sedimentation and bottom currents (contouritic moats).

18.3.2. Slides at the Ridge Toe

The slope parallel seismic line GeoB09-040 (Figure 18.2a) crosses the sidewalls of both the major (in-line distance of 16 km) and the minor (5 km) slide as well as ODP Site 658 (11 km). Seismic line GeoB03-017 runs downslope and crosses the headwall of the major slide (29.5 km), ODP Site 658 (24.5 km), and line GeoB09-040 (24.5 km; Figure 18.2b). Both seismic lines cross at a vertical angle at the ODP Site. In addition to the scarps at the seafloor, another buried slide scarp is imaged in line GeoB09-040 about 1 km south of the drill site at 10 km in-line distance and 3.24 s TWT. We picked 12 seismic reflectors that cross the borehole and are represented by different colors

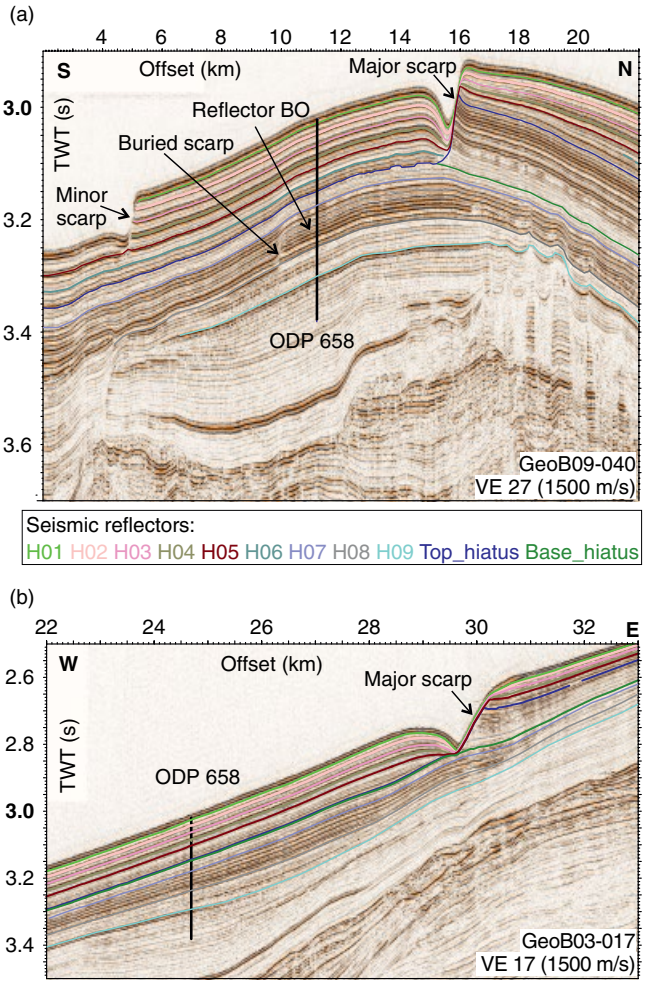


Figure 18.2 (a) Slope parallel seismic line GeoB09-040 and (b) vertically crossing seismic line GeoB03-017 (for locations see Figure 18.1b).

in Figure 18.2a and b. Reflectors H01–H09 are prominent reflectors characterized by their high amplitudes. The reflectors Top_hiatus and Base_hiatus are merged at the drill site but diverge north of the major slide scarp (Figure 18.2a).

Despite prominent landslide scarps at the seafloor, the seismic data do not show evidence for large mass-transport deposits, implying a predominantly erosive behavior of all slides in their source areas. None of the basal glide planes of the imaged slides cut across stratigraphy; hence all slides failed parallel to the bedding. Bottom current activity has shaped the infill next to the scarps, expressed by the presence of typical convex drift bodies ("infill drift") adjacent to local nondeposition at the toe of the scarp (Rebesco et al., 2014). The base of the drift bodies represent the onset of sedimentation after failure and thus aid in the identification of glide planes and the onset of post-failure sedimentation. The failure surface corresponding to the

major scar coincides with the reflector termed Base_hiatus. The slide removed an approximately 100 m thick sediment package, and the first post-slide deposit is represented by the Top_hiatus reflector. The minor scar developed along the high-amplitude reflector H05, and the corresponding slide mobilized about 56 m of sediment. Reflector H02 draped the slide scar after failure. The failure surface of the buried slide corresponds to H08, a reflector that is of normal polarity in the failed section (south of the scarp) and of reversed polarity in the unfailed section. The buried scarp height is 31 m. Reflector BO marks the onset of post-failure sedimentation.

18.3.3. Slides at the Northern Ridge Flank

Figure 18.3a shows a close-up of the northern ridge flank bathymetry. Five scarps are evident at the seafloor termed S1–S5. In order to identify the failure surfaces and the onset of sedimentation after failure, we show extracts of the seismic lines crossing the individual scarps.

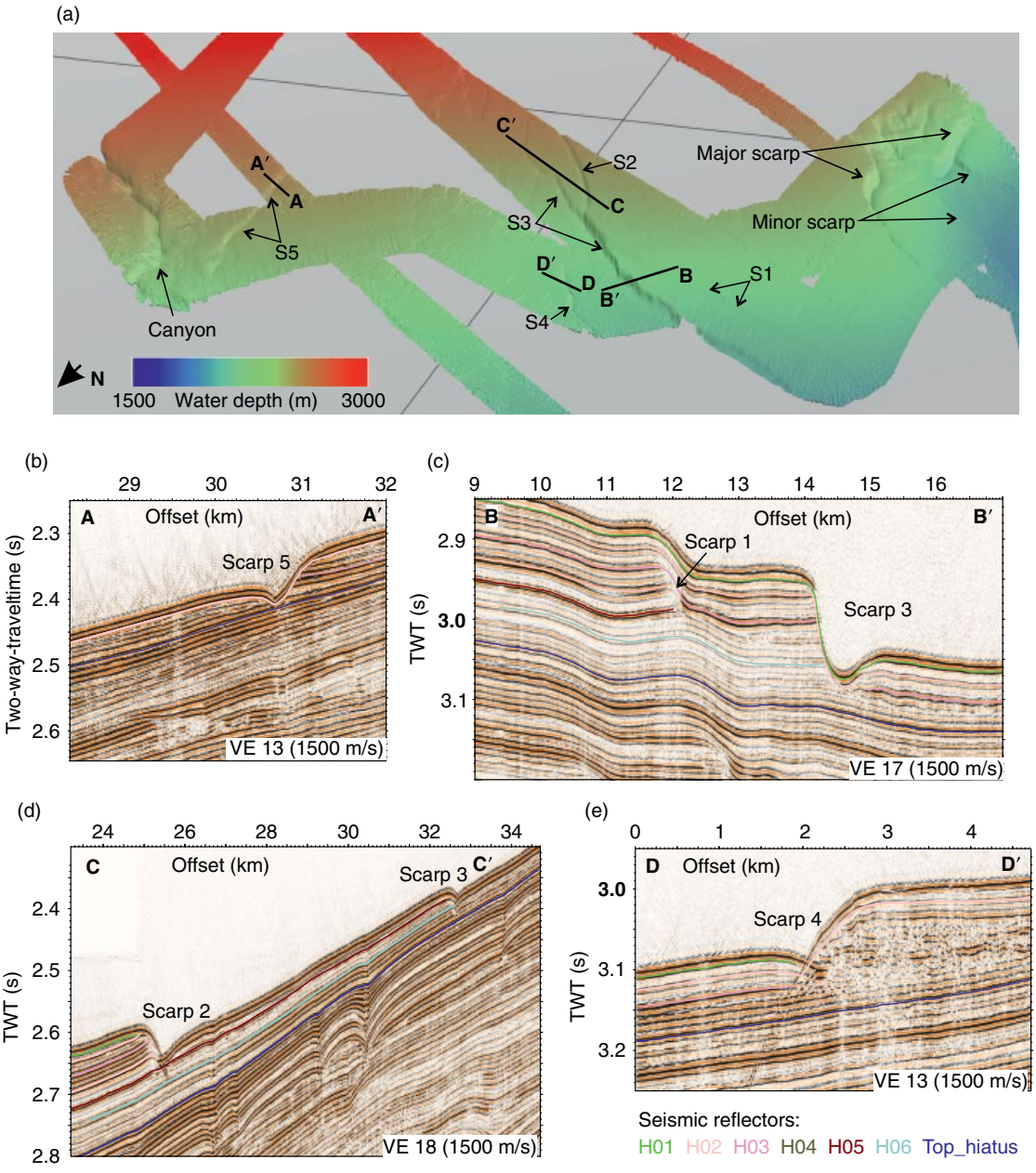


Figure 18.3 (a) Perspective 3D view of the northern ridge flank. Slide scarps at the northern flank are termed S1–S5. (b–e) Close-ups of seismic sections crossing the scarps at the northern flank with seismic reflectors identical to those in Figure 18.2.

Reflectors correspond to those introduced in Figure 18.2. Although visible as a step on the seafloor, scarp 1 (S1) is actually buried by a sediment package containing reflectors H01, H02, and H03 (Figure 18.3c). The slide corresponding to this 50 m high scarp moved along reflector H05. The failure surface of scarp 2 (S2) corresponds to reflector H05 and the slide removed about 55 m of sediment (Figure 18.3d). Reflector H01 marks the onset of post-failure sedimentation. Scarps 3 and 4 are almost parallel and exhibit the same failure surface implying that they belong to the same event (Figure 18.3c, d). The failed sediment moved along a glide plane between reflectors H06 and Top_hiatus. It is not possible to identify the reflector marking the glide plane because the sediment package between H06 and Top_hiatus is much thinner at the borehole than at the slide scarp. The first post-failure deposit is reflector H03. The slide forming scarp 5 at the northern part of the study area moved along the Top_hiatus reflector (Figure 18.3a). The removed sediment package was 50 m thick, and post-failure sedimentation starts with a unit between reflectors H02 and H03. As for S3 and S4, it is difficult to trace this unit to the drill site due to varying sediment thickness and contouritic overprint between the scarp and the drill site. As for the major and minor slides, hardly any debris is evident on the failure surface in the seismic data, implying that all sediment was removed by sliding along bedding-parallel glide planes.

18.4. STRATIGRAPHY OF THE CAP BLANC SLIDE COMPLEX

The age of the sediment draped onto the failure surface provides a minimum estimate of the landslide's age. While the age of the draping deposit will be closer to the landslide's real age, a bracket can be obtained as dating of sediments immediately below the basal glide plane provides a maximum age. Via the net of seismic profiles available in this study (Figure 18.1b), these reflectors can be traced to ODP Site 658, for which a detailed stratigraphy is available (Tiedemann, 1991; Meckler et al., 2013). Reflectors are linked to the appropriate core depth by means of core-seismic integration.

18.4.1. Core-Seismic Integration and Reflector Ages

The calculated synthetic seismogram is compared to seismic traces in the direct vicinity of the borehole (Figure 18.4). Both the synthetic seismogram and the seismic traces show several distinctive reflectors with similar shapes in both records in the upper 100 m. The resulting p-wave velocity in the upper 100 m ranges between 1250 and 1600 m/s after stretching and squeezing of the synthetic seismogram. The values are reasonable for

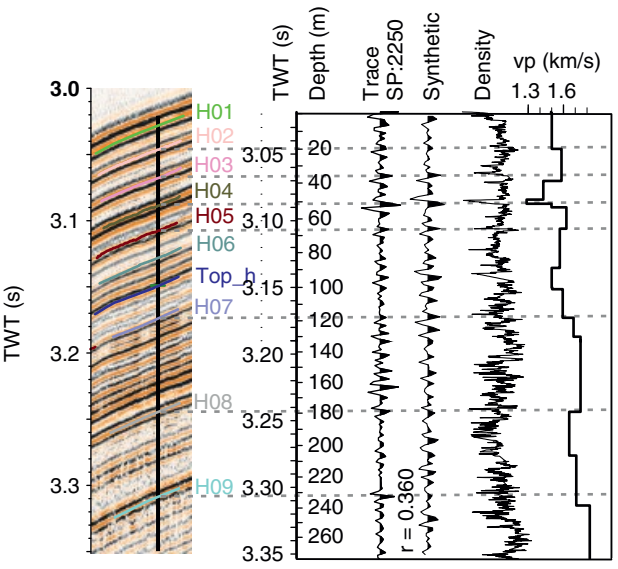


Figure 18.4 Correlation of seismic traces and ODP Site 658 core data. From left to right: seismic section including seismic reflectors, time-depth correlation, seismic trace in the direct vicinity of the borehole (shot point 2250), synthetic seismogram, core density log, and modified p-wave velocity resulting from stretching and squeezing of the synthetic seismogram. The correlation coefficient *r* between the synthetic seismogram and the seismic trace is 0.36.

surface-near marine sediments (Press, 1966). Zones of low velocity correspond to low densities measured on the core. High amplitudes correspond to zones of decreased density. For thicker low-density layers, the polarity of amplitudes is reversed; strong negative amplitudes precede strong positive ones, for example, at 46–51 m core depth (Figure 18.4). In comparably thin zones of low density, for example, at 33–35 m core depth, strong positive amplitudes appear at the bottom of the low-density zones, where density rapidly increases again. These observations imply that the seismic data are capable of resolving layers as thin as 5 m. Correlation is more difficult below 100 m core depth, as a series of strong reflections occurs in the measured data which can hardly be subdivided into single ones, while the synthetic seismogram shows less reflections with larger spacing. The velocity ranges between 1600 and 1800 m/s.

The core-seismic integration established a time-depth relationship, which now allows assigning ages to individual reflectors. Table 18.1 provides the ages for all seismic reflectors and other key horizons extracted from the age model for ODP Site 658 (Tiedemann, 1991; Meckler et al., 2013). The seismic reflectors H01–H06 are evenly spaced in depth and time, with ~15 m of sediment, or ~100 ka, in between individual reflectors. The reflector termed Top_hiatus correlates with a hiatus in the drill core in the time interval between 731 and 1573 kyr. It has

to be noted that a reflector in the seismic data represents an interval of 5 m due to its resolution. In the core, 5 m correspond to 30 kyr on average (Tiedemann, 1991), which represents the age uncertainty.

18.4.2. Landslide Ages and Errors

Dating of submarine landslides usually involves dating of the hemipelagic sediment deposited after failure. This will provide a minimum age of the landslide. The true age, however, differs from that age. This uncertainty can be large if the area is prone to erosion or if sedimentation rates are comparably low (Urlaub et al., 2013), both of which is the case for the Cap Blanc area. Importantly, here we also need to take into account the reflector age uncertainty resulting from the core-seismic integration. As the first factors are difficult to quantify, we use the latter uncertainty of ±30 kyr to represent our landslide age error.

Table 18.1 Core Depths of Seismic Reflectors Traced Across the Net of Seismic Lines (compare Figure 18.4)

Reflector	Hole B Depth (m)	Age (kyr)
H01	8	46
H02	20	165
H03	34	266
H04	51	352
H05	66	457
H06	83	525
H07	118	1800
B0	153	2205
H08	181	2490
H09	233	2960
Top_hiatus	100	731
Base_hiatus	100	1573

The ages are obtained from the age model for ODP Site 658 of Tiedemann (1991) that was updated by Meckler et al. (2013). Given the limited seismic resolution, the ages involve an uncertainty interval of approximately 30 kyr.

Sliding history at the ridge offshore Cap Blanc reaches back at least to the early Quaternary and lasted until 50 kyr (Table 18.2). Due to the limited seismic data coverage, we cannot exclude older and younger slides. Focusing only on those slides that are clearly defined by our seismic data, we identify the following sequence of events: buried slide, major slide, S3/S4/S1, S5, minor slide, S2.

18.5. SEDIMENTOLOGY OF REFLECTORS AND FAILURE PLANES

The core-seismic integration provides information about the nature of the sediments that make up the seismic reflectors and, correspondingly, the failure surfaces observed in the seismic section, including their physical properties. Figure 18.5 shows selected physical, mechanical, and sedimentological properties measured on the ODP Site 658 core. We show vane shear strength, but only consider its relative changes. The data are not indicative for formation shear strength as much of the cored material suffered a high degree of disturbance caused by the expansion of gas. Prominent seismic reflectors are gray shaded with uncertainty of ±2 m. We estimate this uncertainty based on our finding that the seismic data only resolve layers thicker than or equal to 5 m.

The high-amplitude seismic reflectors H01–H09 correlate with zones of low density, high porosity, and high opal content. Tiedemann (1991) reports large concentrations of siliceous microfossils (diatoms) in these zones. Diatoms are of high porosity and low density, and the occurrence of large amounts can explain this observation.

Results from the seismic data analyses show that the failure surfaces of three slides (minor, S1, S2) coincide with reflector H05 in core depth of ~66 m. Within H05, density decreases to values as low as 1.28 g/cm^3 in an interval of 2.5 m. At 66.5 m, porosity reaches 72%. The ratio of Si and Al shows a prominent peak reaching 3.5 between 65 and 67 m. In the same interval, opal makes up

Table 18.2 Morphological Characteristics and Ages Obtained From Tracing of Seismic Reflectors From ODP Site 658 Across the Study Area for All Investigated Slides

Slide ID	Seafloor Offset (m)	Removed Package (m)	Glide Plane Reflector	Onlap Reflector	Min. Age (kyr)	Max. Age (kyr)
Major	100–200	100	Base_hiatus	Top_hiatus	731 ± 30	1573 ± 30
Minor	50	56	H05	H02	149 ± 30	457 ± 30
Buried	—	31	H08	BO	2205 ± 30	2490 ± 30
S1	50	50	H05	H03	247 ± 30	457 ± 30
S2	50	55	H05	H01	50 ± 30	457 ± 30
S3	90	60	H06/Top_hiatus	H03	247 ± 30	525–731
S4	50	70	H06/Top_hiatus	H03	247 ± 30	525–731
S5	50	50	Top_hiatus	H03/H02	247–149 ± 30	731 ± 30

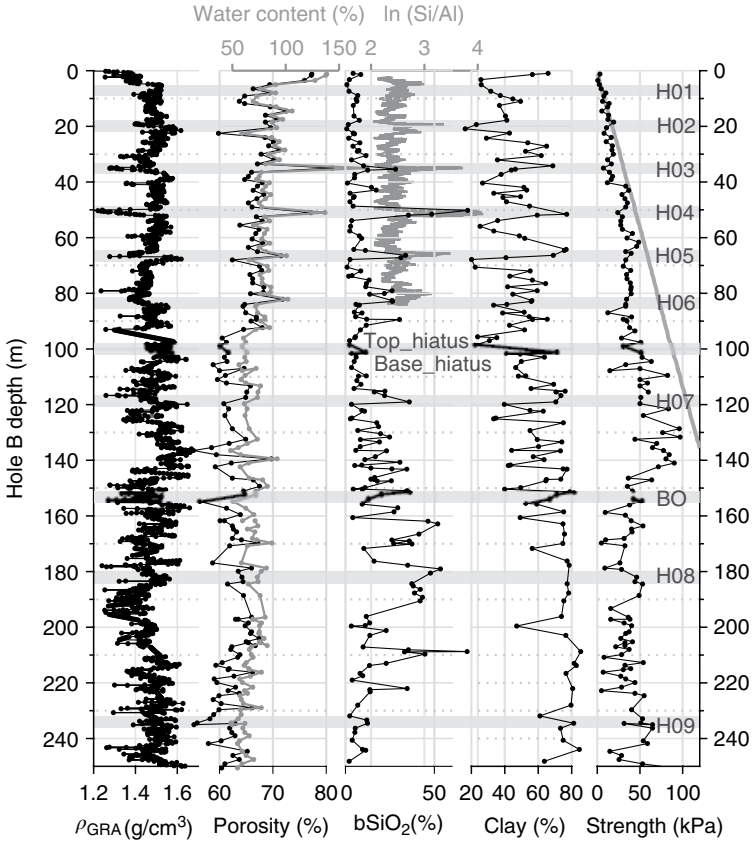


Figure 18.5 Core data from ODP Site 658 from left to right: bulk density, ρ_{GRA} (from gamma ray attenuation measurements, filtered for realistic values); porosity (black) and water content (gray) from moisture and density measurements; biogenic silica equivalent to opal content in the silt fraction, $bSiO_2$ (black), and element log ratio of silica to aluminum, ln(Si/Al) (gray); clay content (<2 μm); tor vane undrained shear strength. For the latter, we also show the lower bound of the normalized undrained shear strength (gray line) corresponding to 0.2*effective overburden pressure (assuming hydrostatic pore pressure and integrating over the sediment column making use of ρ_{GRA}). X-ray fluorescence scanning-derived element log ratio of silica to aluminum counts (ln(Si/Al); Meckler et al., 2013) is a proxy for sediment opal content. Average sample distances are 1.5 m (0–100 m) and 2.5 m (100–200 m). Seismic reflectors used in this study are shaded in gray with an uncertainty of ±2 m owing to the vertical resolution of the seismic data. (*See electronic version for color representation of this figure*)

40% of the sediment. Within the horizon, the clay content decreases sharply from 77% at 64 m depth in the core to 20% at 68 m. The sediment just above the H05 reflector has the highest clay content, and the clay-rich zone extends from 60 to 66 m. The shear strength shows a gradual decrease from 60 m down to 70 m. H05 coincides with a 2.5 m thick diatom ooze layer, which observations on the drill core confirm (Tiedemann, 1991).

The failure surface of the buried slide corresponds to H08 at ~183 m core depth. It coincides with a local density maximum of 1.57 g/cm^3. However, approximately 5 m above, H08 density reaches a minimum with 1.25 g/cm^3. Porosity is 63% but increases to 68% within H08. The opal content at this depth is comparatively low (15%) based on two data points only. We observe a local minimum of 56% in clay content at 181 m coinciding with a minimum in shear strength. H08, however, is embedded in zones of high opal and high clay contents. Most notably, an almost 10 m thick package with opal contents >50% and a clay fraction of 80% covers H08. The interval below H08 (185–190 m) shows an inverse density gradient. In this interval, the opal content is >50%, and clay makes up 80% of the bulk sediment.

We identify the glide plane corresponding to the major slide and scarp S5 as the Top_hiatus and Base_hiatus reflector. A low-density zone covers the Top_hiatus and Base_hiatus reflector, but due to a data gap, the thickness of this low-density zone remains unknown. The porosity is relative uniform with 60% above and below this reflector. In the overlying sediment, a peak in opal content is observed. With 70% clay content, the sediment near the Top_hiatus and Base_hiatus reflector is richer in clay

than the surrounding sediment. The shear strength increases below the reflector.

The failure surface between scarps S3 and S4 locates in between the H06 and Top_hiatus reflectors. Within this interval, two drops in density can be observed in the core at 88 and 94 m. A local peak in opal content (30%) and a zone with high clay content (80%) coincide with the density drop at 88 m. Shear strength is comparatively high in this interval but shows a significant minimum just above at 86 m. However, the core data might not be indicative of the respective failure surface as the sediment package with the glide plane is much thinner near the drill site than it is near the scarps. In addition, tracing the seismic reflector that represents the glide plane involves crossing one slide scarp.

In summary, the failure surfaces of all slides locate either inside or just below layers of increased opal content, called diatom oozes, and are covered by clay-rich sediment. The opal in these layers is of biogenic origin and is caused by high amounts of diatoms in the sediment, which are responsible for the low density and high porosity in the respective layers.

18.6. DISCUSSION

18.6.1. Timing of Landslides in the Cap Blanc Slide Complex

By tracing reflectors that mark the onset of post-slide deposition to ODP Site 658, we are able to establish a chronological order of landslide occurrence in the Cap Blanc Slide Complex. The slide complex formed in at least five stages that are depicted in Figure 18.6. The earliest identified slide is 2205 ± 30 kyr, and the youngest one is 50 ± 30 kyr. The seismic data show evidence for few deeply buried, much older landslides. We do not consider these slides as no age control is available and their sparse distribution and old age suggest that they belong to a different slide complex. Due to the large age uncertainty, a correlation between landslide occurrence and sea level changes is impossible, as all four youngest slides (S2, minor, S1, and S3/S4) may have fallen into periods of sea level lowstands, sea level rise, fall, or highstands. Landslide occurrence seems independent of short-term changes in African climate (African humid periods) in the past 125 kyr (Figure 18.6). The major slide occurred during the mid-Pleistocene transition. This period was characterized by substantial perturbations of the climate system caused by readjustment of the enlarged late Pleistocene ice sheets and weakening of global ocean circulation. However, as only one slide occurred during this period, it remains uncertain whether the major slide was affected by these global environmental changes. The oldest slide in our record, the buried slide, occurred after the onset of Northern Hemisphere glaciations at 2800 kyr. The appearance of large ice sheets caused enhanced global ocean circulation, which in turn results in large increases in upwelling off Northwest Africa. A coincidence between the onset of glaciations and frequent submarine sliding has been observed at the Norwegian continental margin (Hjelstuen et al., 2004). Hence, environmental conditions resulting from the presence of large ice sheets, or probably more importantly the variability of these conditions implied by ice sheet dynamics, could have initiated frequent submarine landsliding in the Cap Blanc Slide Complex.

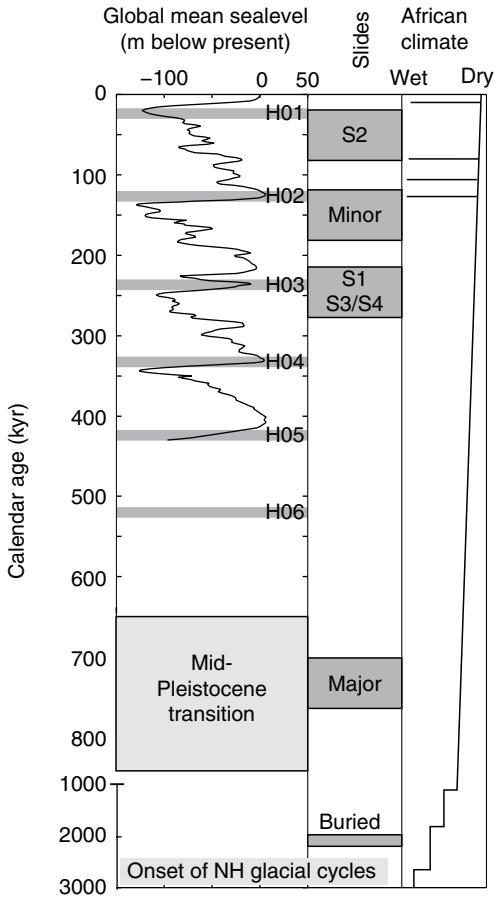


Figure 18.6 Comparison of landslide timing and environmental conditions. From left to right: global mean sea level curve (Waelbroeck et al., 2002) including the age of diatom layers corresponding to reflectors H01–H06 and major global paleoclimatic events, timing of the slides in the upper Cap Blanc Slide area with uncertainty interval of ±30 kyr, and African climate variability expressed by a humidity index (de Menocal, 1995; Larrasoaña et al., 2013).

18.6.2. Preconditioning and Triggers in the Cap Blanc Slide Complex

The failure surfaces of all seven landslide events that we identified as part of the Cap Blanc Slide Complex correlate with diatom ooze layers. In contrast, not all diatom

ooze layers are associated with landslides, but only those covered by clay. The failure process involving diatom ooze covered by clay has been discussed in detail by Urlaub et al. (2018). During burial, the ooze expels pore water that cannot drain through the overlying clay layer. Excess pore water pressure increases, causing the sediment's shearing resistance to increase at a lower rate than the shear stress. When the shear stress exceeds the shearing resistance, the sediment fails. This may happen due to constant loading by newly deposited sediment or by external triggers that locally increase shear stresses or further decrease shearing resistance. Potential triggers acting on a preconditioned slope include earthquakes, local uplift, or toe erosion.

Trigger mechanisms for individual slide events are highly speculative, and their identification is complicated by the large uncertainty regarding their timing. In contrast, the formation of diatom oozes as a potentially important preconditioning factor is well constrained. Diatom oozes are typically found in the southern and tropical oceans as the burial of biogenic opal relies on sufficient supply of silicate and thus high diatom productivity in surface waters. Diatom blooms are also common in upwelling areas along continental margins, where deep, nutrient-rich cold water rises toward the surface. Strong winds and intensified upwelling favors productivity. Such conditions are particularly met during glacials. In the subtropical North Atlantic, a reduction in the formation of silicate poor glacial North Atlantic Intermediate Waters during terminations allowed underlying silicate rich deeper water to increase the silicate supply to the surface ocean, which led to the formation of diatom oozes at ODP Site 658 and other places along the entire Western African continental margin (Meckler et al., 2013). The occurrence of diatom ooze layers observed in our study area is therefore limited to terminations (Figure 18.6). Hence, the intensity of primary productivity, and thus the abundance of diatoms in the sediment, depends on global ocean circulation and climate. Consequently, climate is a controlling factor for preconditioning of slopes along the Western African margin, but not necessarily for the ultimate trigger.

The spatial extent of diatom ooze layers is limited to the location of upwelling cells. Our study area is in the center of one of the world's largest upwelling cell (Figure 18.1a). Nevertheless, due to a lack of multibeam bathymetry data coverage beyond our study area, we cannot say with certainty whether submarine landslide occurrence changes with distance to the center of the upwelling cell.

18.7. CONCLUSIONS

We analyzed the timing and preconditioning mechanisms of the Cap Blanc Slide Complex offshore Mauritania, Northwest Africa, by integrating high-resolution seismic and ODP core data. The onset of sliding within the slide complex appears to be linked to the onset of Northern Hemisphere glacial cycles. Layers of diatom ooze deposited during terminations were involved in all seven failure stages of the slide complex. We therefore propose that the climatically controlled deposition of diatom ooze is an important preconditioning factor that determines the failure potential of the continental slope. The actual timing of failure is independent of climate and more likely related to the thickness of the overburden. As the process of burial of diatom ooze layers is currently ongoing, there is a potential for future landslides to take place in the Cap Blanc Slide Complex. The slide complex has developed in the center of a large and highly productive upwelling system and is thus likely representative for other continental slopes affected by coastal upwelling.

ACKNOWLEDGMENTS

We thank the captains, crews, and scientific participants of RV Meteor cruise M58/1 and RV Maria S. Merian cruise MSM11/1. Sascha Fricke is gratefully acknowledged for processing the seismic data.

REFERENCES

Adkins, J., deMenocal, P., & Eshel, G. (2006). The "African humid period" and the record of marine upwelling from excess 230Th in Ocean Drilling Program Hole 658C. *Paleoceanography*, *21*(4), PA4203.

Bondevik, S., Lovholt, F., Harbitz, C., Mangerud, J., Dawson, A., & Svendsen, J. I. (2005). The Storegga Slide tsunami-comparing field observations with numerical simulations. *Marine and Petroleum Geology*, *22*(1–2), 195–208.

Breitzke, M. (2000). Acoustic and elastic characterization of marine sediments by analysis, modeling, and inversion of ultrasonic P wave transmission seismograms. *Journal of Geophysical Research: Solid Earth*, *105*(B9), 21411–21430.

Brothers, D. S., Luttrell, K. M., & Chaytor, J. D. (2013). Sea-level–induced seismicity and submarine landslide occurrence. *Geology*, *41*(9), 979–982.

Bryn, P., Berg, K., Forsberg, C. F., Solheim, A., & Kvalstad, T. J. (2005). Explaining the Storegga Slide. *Marine and Petroleum Geology*, *22*, 11–19. https://doi.org/10.1016/j.marpetgeo.2004.12.003

Cropper, T. E., Hanna, E., & Bigg, G. R. (2014). Spatial and temporal seasonal trends in coastal upwelling off Northwest Africa, 1981–2012. *Deep Sea Research Part I: Oceanographic Research Papers*, *86*, 94–111.

deMenocal, P., Ortiz, J., Guilderson, T., Adkins, J., Sarnthein, M., Baker, L., & Yarusinsky, M. (2000). Abrupt onset and termination of the African Humid Period: Rapid climate responses to gradual insolation forcing. *Quaternary Science Reviews*, *19*(1), 347–361.

deMenocal, P. B. (1995). Plio-Pleistocene African climate. *Science*, *270*(5233), 53–59.

Haflidason, H., Sejrup, H. P., Nygard, A., Mienert, J., Bryn, P., Lien, R., et al. (2004). The Storegga Slide: Architecture, geometry and slide development. *Marine Geology*, *213*, 201–234.

Henrich, R., Cherubini, Y., & Meggers, H. (2010). Climate and sea level induced turbidite activity in a canyon system offshore the hyperarid Western Sahara (Mauritania): The Timiris Canyon. *Marine Geology*, *275*(1–4), 178–198.

Hjelstuen, B. O., Sejrup, H. P., Haflidason, H., Nygard, A., Berstad, I. M., & Knorr, G. (2004). Late Quaternary seismic stratigraphy and geological development of the south Voring margin, Norwegian Sea. *Quaternary Science Reviews*, *23*, 1847–1865.

Jacobi, R. D., & Hayes, D. E. (1992). Northwest African continental rise: Effects of near-bottom processes inferred from high-resolution seismic data. In C. W. Poag & P. C. Graciansky (Eds.), *Geologic evolution of Atlantic continental rises* (pp. 293–325). New York, NY: Springer.

Krastel, S., Li, W., Urlaub, M., Georgiopoulou, A., Wynn, R.B., Schwenk, T., et al. (2018). Mass wasting along the NW-African continental margin. In Lintern, D., D. C. Mosher, L. G. Moscardelli, P. T. Bobrowsky, C. Campbell, J. D. Chaytor, J. J. Clague, et al. (eds), *Subaqueous mass movements, Special Publications*, *477*. Geological Society, London.

Krastel, S., Wynn, R. B., Georgiopoulou, A., Geersen, J., Henrich, R., Meyer, M., & Schwenk, T. (2012). Large-scale mass wasting on the Northwest African Continental Margin: Some general Implications for mass wasting on passive continental margins. In Y. Yamada, K. Kawamura, K. Ikehara, Y. Ogawa, R. Urgeles, D. Mosher, et al. (Eds.), *Submarine mass movements and their consequences* (pp. 189–199). Dordrecht, The Netherlands: Springer.

Krastel, S., Wynn, R. B., Hanebuth, T. J. J., Henrich, R., Holz, C., Meggers, H., et al. (2006). Mapping of seabed morphology and shallow sediment structure of the Mauritania continental margin, Northwest Africa: Some implications for geohazard potential. *Norwegian Journal of Geology*, *86*(3), 163–176.

Kuechler, R. R., Dupont, L. M., & Schefuß, E. (2018). Hybrid insolation forcing of Pliocene monsoon dynamics in West Africa. *Climate of the Past*, *14*(1), 73–84.

Larrasoaña, J. C., Roberts, A. P., & Rohling, E. J. (2013). Dynamics of green Sahara periods and their role in hominin evolution. *PLoS ONE*, *8*(10), 1–12.

Lebreiro, S. M., Voelker, A. H. L., Vizcaino, A., Abrantes, F. G., Alt-Epping, U., et al. (2009). Sediment instability on the Portuguese continental margin under abrupt glacial climate changes (last 60 kyr). *Quaternary Science Reviews*, *28*, 3211–3223.

Lee, H. J. (2009). Timing and occurrence of large submarine landslides on the Atlantic Ocean Margin. *Marine Geology*, *264*, 53–64.

Lee, S. H., Bahk, J. J., Kim, H. J., Lee, K. E., Jou, H. T., & Suk, B. C. (2010). Changes in the frequency, scale, and failing areas of latest Quaternary (<29.4 cal. ka B.P.) slope failures along the SW Ulleung Basin, East Sea (Japan Sea), inferred from depositional characters of densely dated turbidite successions. *Geo-Marine Letters*, *30*, 133–142.

Llopart, J., Urgeles, R., Camerlenghi, A., Lucchi, R. G., Rebesco, M., & De Mol, B. (2015). Late Quaternary development of the Storfjorden and Kveithola Trough Mouth Fans, northwestern Barents Sea'. *Quaternary Science Reviews*, *129*, 68–84. https://doi.org/10.1016/j.quascirev.2015.10.002

Maslin, M., Owen, M., Day, S., & Long, D. (2004). Linking continental-slope failures and climate change: Testing the clathrate gun hypothesis. *Geology*, *32*, 53–56.

Meckler, A. N., Sigman, D. M., Gibson, K. A., Francois, R., Martinez-Garcia, A., Jaccard, S. L., et al. (2013). Deglacial pulses of deep-ocean silicate into the subtropical North Atlantic Ocean. *Nature*, *495*(7442), 495–498.

Owen, M., Day, S., & Maslin, M. (2007). Late Pleistocene submarine mass movements: occurrence and causes. *Quaternary Science Reviews*, *26*, 958–978.

Paull, C. K., Buelow, W. J., William Ussler, I. I. I., & Borowski, W. S. (1996). Increased continental-margin slumping frequency during sea-level lowstands above gas hydrate-bearing sediments. *Geology*, *24*, 143–136.

Piper, D. J. W., Mosher, D. C., Gauley, B. J., Jenner, K., & Campbell, D. C. (2003). The chronology and recurrence of submarine mass movements on the continental slope off southeastern Canada. In J. Locat, J. Mienert, & L. Boisvert (Eds.), *Submarine mass movements and their consequences* (pp. 299–306). Dordrecht, The Netherlands: Springer.

Pope, E. L., Talling, P. J., Urlaub, M., Hunt, J. E., Clare, M. A., & Challenor, P. (2015). Are large submarine landslides temporally random or do uncertainties in available age constraints make it impossible to tell? *Marine Geology*, *369*, 19–33.

Press, F. (1966), Seismic velocities, In S.P. Clark *Handbook of physical constants* (195–218). New York, NY: The Geological Society of America.

Prins, M. A., Postma, G., & Weltje, G. J. (2000). Controls on terrigenous sediment supply to the Arabian Sea during the late Quaternary: The Makran continental slope. *Marine Geology*, *169*, 351–371.

Rebesco, M., Hernández-Molina, F. J., Rooij, D. V., & Wåhlin, A. (2014). Contourites and associated sediments controlled by deep-water circulation processes: State-of-the-art and future considerations. *Marine Geology*, *352*, 111–154.

Ricker, N. (1953). The form and laws of propagation of seismic wavelets. *Geophysics*, *18*(1), 10.

Ruddiman, W., Sarnthein, M., & Scientists, E. (1988). *Proceedings of the Ocean Drilling Program, Scientific Results, Expedition* (Vol. 108). College Station, TX: Ocean Drilling Program.

Sicre, M.-A., Ternois, Y., Paterne, M., Martinez, P., & Bertrand, P. (2001). Climatic changes in the upwelling region off Cap Blanc, NW Africa, over the last 70 kyear: A multi-biomarker approach. *Organic Geochemistry*, *32*(8), 981–990.

Stuut, J., Zabel, M., Ratmeyer, V., Helmke, P., Schefuß, E., Lavik, G., & Schneider, R. (2005). Provenance of present-day eolian dust collected off NW Africa. *Journal of Geophysical Research D: Atmospheres*, *110*(4), 1–14.

Tappin, D. R., Watts, P., & Grilli, S. T. (2008). The Papua New Guinea tsunami of 17 July 1998: Anatomy of a catastrophic event. *Natural Hazards and Earth System Science*, *8*, 243–266. http://dx.doi.org/10.5194/nhess-8-243-2008

Tiedemann, R. (1991). Acht Millionene Jahre Klimageschichte von Nordwest Afrika und Paläo-Ozeanographie des angrenzenden Atlantik: Hochauflösende Zeitreihen von ODP-Sites 658–661 (PhD thesis). Kiel, Germany: University of Kiel.

Urlaub, M., Geersen, J., Krastel, S., & Schwenk, T. (2018). Diatom ooze: Crucial for the generation of submarine mega-slides? *Geology*, *46*(4), 331.

Urlaub, M., Talling, P. J., & Masson, D. G. (2013). Timing and frequency of large submarine landslides: Implications for understanding triggers and future geohazard. *Quaternary Science Reviews*, *72*, 63–82.

Vallé, F., Dupont, L. M., Leroy, S. A. G., Schefuß, E., & Wefer, G. (2014). Pliocene environmental change in West Africa and the onset of strong NE trade winds (ODP Sites 659 and 658). *Palaeogeography, Palaeoclimatology, Palaeoecology*, *414*, 403–414.

Waelbroeck, C., Labeyrie, L., Michel, E., Duplessy, J. C., McManus, J. F., Lambeck, K., et al. (2002). Sea-level and deep water temperature changes derived from benthic foraminifera isotopic records. *Quaternary Science Reviews*, *21*(1–3), 295–305.

Wien, K., Kölling, M., & Schulz, H. D. (2007). Age models for the Cape Blanc Debris Flow and the Mauritania Slide Complex in the Atlantic Ocean off NW Africa. *Quaternary Science Reviews*, *26*, 2258–2573.

19

Submarine Landslides Along the Mixed Siliciclastic-Carbonate Margin of the Great Barrier Reef (Offshore Australia)

Ángel Puga-Bernabéu[1,2], Jody Michael Webster[2], Robin Jordan Beaman[3], Amanda Thran[4], Javier López-Cabrera[5], Gustavo Hinestrosa[2], and James Daniell[6]

ABSTRACT

Submarine landslides on modern mixed siliciclastic-carbonate margins are poorly understood compared to their counterparts in other settings. We present a synthesis of four representative submarine landslides types along the Great Barrier Reef margin, the largest extant mixed siliciclastic-carbonate province in the world. The investigated examples are 5–31 km in length, extend over 18–528 km^2, and have remobilized an estimated 0.025–32 km^3 of sediments. They display morphological features corresponding to debris avalanches and slides. The estimated timing of two dated landslides is coincident with deglaciations corresponding to the transitions MIS 12–11 and MIS 2–1. Large seismic events were the most likely triggering mechanism for the landslides, where high pore water pressure in examples close to paleo-deltaic systems could also have preconditioned the eventual failure. A potential preconditioning factor, yet to be confirmed, is the geologic control associated with alternating mixed siliciclastic and carbonate sediments in the failed lithologies. The Gloria Knolls Slide is large enough to have significant tsunamigenic potential. Tsunami simulations show that this landslide would produce a sizable tsunami under present-day sea level conditions, with coastal run-up heights of 0.5–2 m. We highlight a reef buffering effect due to broader-scale shelf bathymetry and the complex structure of coral reefs.

19.1. INTRODUCTION

Continuous advances in the resolution and coverage of multibeam bathymetry, 2D/3D seismic, and sub-bottom profiler data have driven the extensive identification and study of large- and medium-scale submarine landslides on the world's continental margins (Canals et al., 2004; Frey-Martínez et al., 2005; Solheim et al., 2005; Twichell et al., 2009; Freire et al., 2014). Submarine landslides are among the most important mechanisms in transferring vast amounts of margin sediments to the deep ocean (Korup, 2012), remobilizing over 10,000 km^3 of material in exceptional cases (Hjelstuen et al., 2007; Iribarren et al., 2007; Calvès et al., 2015). These processes significantly shape continental margins (Winkelmann et al., 2006; Joanne et al., 2010) and create preferential conduits for post-failure sediment routing via sediment gravity flows (Algar et al., 2011; Quin et al., 2017). Socioeconomically, submarine landslides are an important marine hazard, potentially threatening seabed infrastructure and low-lying coastlines due to their tsunamigenic potential with far-reaching effects (Fine et al., 2005; Ioualalen et al., 2010; Tehranirad et al., 2015).

[1] *Department of Stratigraphy and Paleontology, University of Granada, Granada, Spain*

[2] *School of Geosciences, Geocoastal Research Group, University of Sydney, Sydney, New South Wales, Australia*

[3] *College of Science and Engineering, James Cook University, Cairns, Queensland, Australia*

[4] *School of Geosciences, EarthByte Group, University of Sydney, Sydney, New South Wales, Australia*

[5] *Irish Centre for Research in Applied Geosciences, University College Dublin, Dublin, Ireland*

[6] *College of Science and Engineering, James Cook University, Cairns, Queensland, Australia*

Submarine Landslides: Subaqueous Mass Transport Deposits from Outcrops to Seismic Profiles, Geophysical Monograph 246, First Edition. Edited by Kei Ogata, Andrea Festa, and Gian Andrea Pini.
© 2020 American Geophysical Union. Published 2020 by John Wiley & Sons, Inc.

Submarine landslides are ubiquitous seafloor features in different tectonic settings with a variety of sediment sources, such as active and passive margins (Harders et al., 2011; Hill et al., 2017), volcanic islands (Smoot & King, 1993), carbonate platforms (Hine et al., 1992), glaciated margins (Haflidason et al., 2004), fluvial-supplied margins (Lastras et al., 2004), or lacustrine basins (Moernaut & De Batist, 2011). Most of these settings have been included in a recent global morphometric submarine landslide database compiled by Moscardelli and Wood (2016), which is useful for disentangling the relationships between a given landslide's tectonic setting and its causal mechanisms. However, examples of submarine landslides on modern mixed siliciclastic-carbonate margins are virtually lacking despite these margins extending over 1000s kilometers. Examples include the northeastern Brazil margin, New Caledonia, or the Great Barrier Reef (GBR) margin in northeastern Australia. Recent work along the GBR margin has identified several different submarine landslide types and advanced our understanding of slope failures on mixed siliciclastic-carbonate margins (Webster et al., 2016; Puga-Bernabéu et al., 2017).

In this chapter, we present a synthesis of high-resolution multibeam bathymetry and sub-bottom profiler data from four representative examples of submarine landslides in different geomorphic settings along the GBR margin. The selected landslides originated at different depths from the shelf edge to the base of the slope, and their dimensions range from 5 to 31 km in length, extend between 18 and 528 km^2, and have remobilized an estimated 0.025–32 km^3 of sediments. We first describe the main geomorphologic characteristics of the landslides and then discuss the timing of the slope failures, the types of mass movement, and likely preconditioning factors and triggering mechanisms. We additionally assess the tsunamigenic potential of the largest landslide complex in the GBR and its impact on adjacent coasts under present-day sea level conditions. The results presented here will help to fill gaps and advance our understanding of landslide morphometrics in mixed siliciclastic-carbonate margins. These results also help to explain the possible impacts of landslide-tsunami generation on reef-rimmed platform margins.

19.2. REGIONAL SETTING

19.2.1. Depositional History

The passive margin of northeastern Australia is the largest modern mixed siliciclastic-carbonate province in the world, and the iconic GBR is the largest extant coral reef system (Davies et al., 1991a; Hopley et al., 2007). This margin formed during Late Cretaceous rifting and subsequent fragmentation of what is now the Australian continent, where a predominantly extensional tectonic regime persisted until the Paleocene to earliest Eocene (Taylor & Falvey, 1977; Gaina et al., 1999; Hill & Hall, 2002). The sedimentary development of the margin after rifting is divided into five phases (Symonds et al., 1983; Hopley et al., 2007): (i) infilling of rift basins with alluvial and fluvial deposits between 50 and 24 Ma, (ii) onlap phase of sedimentation due to marine transgression and marginal subsidence between 24 and 14 Ma, (iii) progradation of fluvial and deltaic deposits during a falling sea level period between 15 and 5 Ma, (iv) shelf aggradation (>200 m) and progradation of the shelf margin due to high sediment clastic input between about 5 and 0.7 Ma, and (v) onset of the modern GBR on siliciclastic foundations and episodic reef growth linked to late Pleistocene sea level fluctuations (Humblet & Webster, 2017).

At the end of the Eocene, northeastern Australia was located between 29° and 44°S latitude, and since then, the region has moved to its present location between 9° and 24°S (Davies et al., 1989). This northward plate movement, together with the complex subsidence regime (DiCaprio et al., 2010), influenced the long-term platform evolution, especially the large-scale facies distribution due to latitudinal climatic zonation. Bryozoan-rich sediments of temperate zones were progressively replaced first by subtropical coralline algae deposits and then by tropical coral reef systems. At the shorter term, oceanographic changes such as the progressive development of the East Australian Current since the Miocene and sea level fluctuations, which controlled the development of siliciclastic and carbonate platform facies, were the main controlling factors (Davies et al., 1989). The modern GBR comprises eight shallowing upward reef sequences reflecting shelf inundation during each post-glacial sea level rise and highstand, each of them with broadly similar coral associations (Humblet & Webster, 2017).

19.2.2. Modern Physiography and Sediment Distribution

The present morphology of the GBR margin is controlled by the structural style and development history of the initial rift system. Three broad physiographic regions are observed in the study region between 15 and 19°S latitude (Figure 19.1a): (i) the continental shelf that includes the GBR, (ii) the slope and basin environments of the Queensland and Townsville troughs, and (iii) the Queensland Plateau, a deep (~1000 m) isolated carbonate reef platform (Davies et al., 1991a). The northern margin has a narrow (<50 km) reef-rimmed shelf that connects to a steep (8–12°) continental slope, where depths descend to >2000 m in the basin. In the central part of the margin, the shelf is wider (60–70 km), unrimmed with reefs generally situated on the mid to outer shelf, and the moderately steep (4–5°) slope leads to water depths between 1300 and

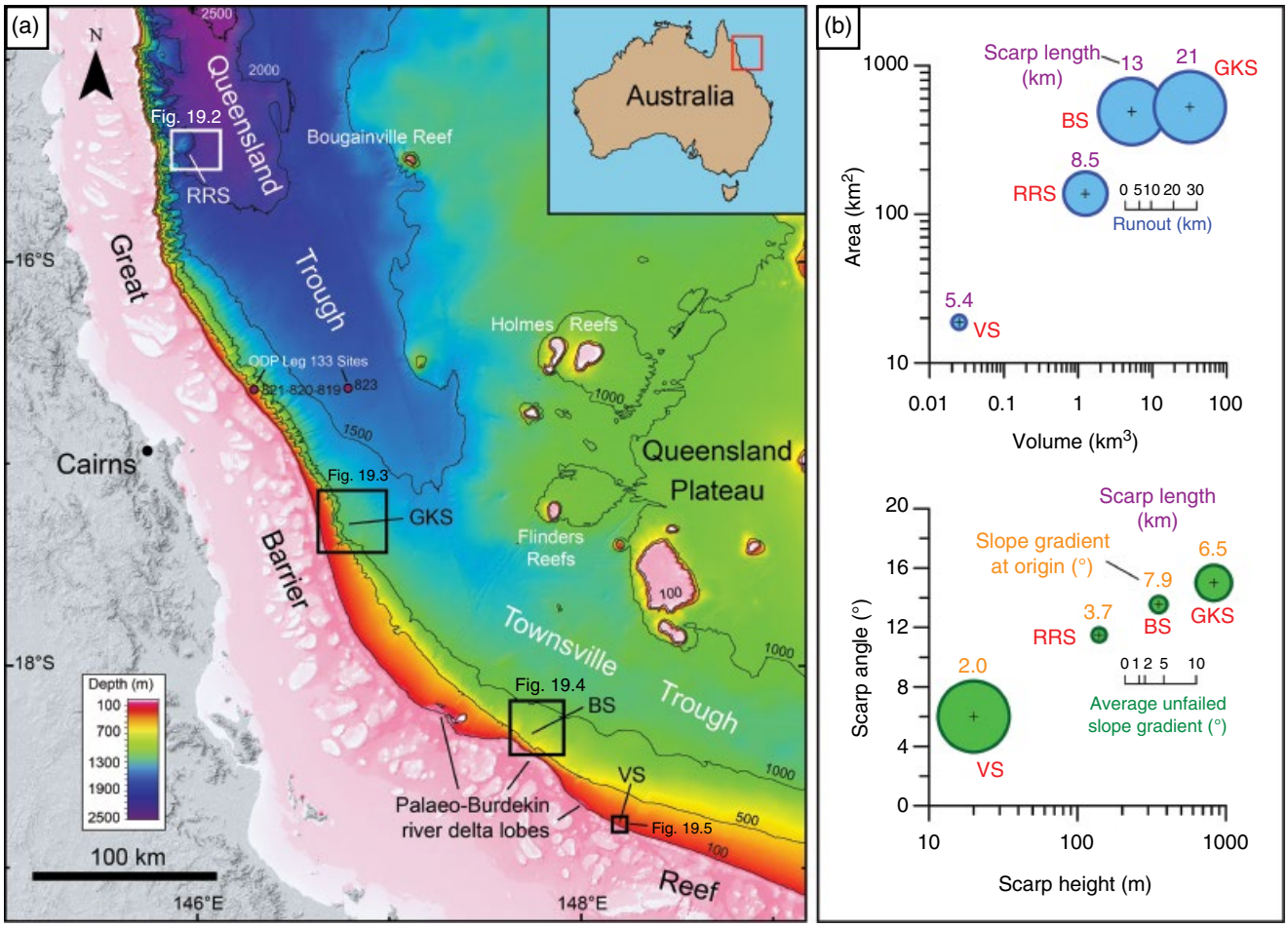


Figure 19.1 (a) Bathymetry (100 m resolution DEM) of the northeastern Australian margin showing the main physiographic regions: the Great Barrier Reef, the Queensland and Townsville troughs, and the Queensland Plateau. Inset shows the location of the study submarine landslides. RRS, Ribbon Reef Slide; GKS, Gloria Knolls Slide; BS, Bowl Slide; VS, Viper Slide. (b) Dimensional and morphometric parameters of the landslides. Note that morphometric parameters are not dependent on landslide dimension.

1800 m. In the southern part, the unrimmed shelf widens up to 125 km and the gently (~2°) dipping slope entering a basin floor between 1000 and 1200 m.

Modern surface sediments on the shelf, slope, and basin comprise both terrigenous siliciclastics and biogenic carbonates with a variable spatial distribution along the margin (Francis et al., 2007; Mathews et al., 2007). On the shelf, carbonate content progressively increases offshore forming shore-parallel facies belts (Harris et al., 1990), although high siliciclastic content is found in some interreef passages and in fluvial paleo-channels (Fielding et al., 2003). On the slope and basin, a more complex facies distribution is observed, which results from cross-shelf sediment transport (e.g., river plumes, tidal currents, cyclones; Francis et al., 2007). Subsurface slope sediments drilled during ODP Leg 133 (sites 819, 820, and 821; Figure 19.1a) record a late Pleistocene 400 m thick succession of mixed hemipelagic-pelagic carbonate- and clay-rich oozes. In the basin, hemipelagic-pelagic sediments are interbedded with mass-transport deposits ranging from the Miocene to the late Holocene in age (Watts et al., 1993; Webster et al., 2012; Puga-Bernabéu et al., 2014).

19.3. METHODS

19.3.1. Data Sets and Analysis

High-resolution multibeam data were collected using a Kongsberg EM300 multibeam echosounder (30 kHz) during the RV *Southern Surveyor* cruises in 2007 and 2008 (Webster et al., 2008; Tilbrook & Matear, 2009). These data and all available bathymetry data were integrated into a 100 m resolution grid for the entire margin (Beaman,

2010) and enhanced by four high-resolution grids (10–30 m resolution) of the landslides (Figure 19.1a). The cleaned ASCII XYZ (longitude, latitude, depth) records were imported into Esri ArcGIS and QPS Fledermaus as digital elevation models (DEMs). Sub-bottom profiles from the outer shelf across the continental slope and into the adjacent Queensland Trough were acquired across two landslides (Viper Slide [VS] and Gloria Knolls Slide [GKS]; Webster et al., 2016; Puga-Bernabéu et al., 2017) using a Kongsberg TOPAS PS 18 seismic system during the RV *Southern Surveyor* cruise in 2007 (Webster et al., 2008). The dimensions of the landslides and additional morphometric parameters were measured and compiled using ArcGIS and QPS Fledermaus. The volume loss of the material removed from the GBR margin due to the case study landslides was calculated by comparing pre-landslide and post-landslide bathymetries, following the approach of Völker (2010).

19.3.2. Tsunami Modeling

To estimate the tsunamigenic potential under present-day conditions of the largest submarine landslide in the GBR margin, the GKS (Puga-Bernabéu et al., 2017), we used GeoWave to simulate initial tsunami generation by the submerged landslide (Watts et al., 2003) and FUNWAVE-TVD (v. 3.0) to simulate tsunami propagation across the shelf. For the first generation phase, the initial waver surface was produced using a series of semi-empirical formulations that relate key dimensions of the landslide scar to a characteristic tsunami amplitude and wavelength (Watts et al., 2005). The resulting free surface is a three-dimensional double Gaussian shape positioned over the slide (Watts et al., 2005). This approach is valid when the landslide length to submergence depth ratio is less than 17, a condition that is satisfied for all the modeled failures (see Section 19.4.5). This initial wavefield was then interpolated onto a 100 m × 100 m grid to simulate tsunami propagation using FUNWAVE-TVD (Shi et al., 2012), a fully nonlinear Boussinesq waver model that incorporates a high-order, adaptive time-stepping TVD solver. For the bathymetric boundary condition, a comprehensive DEM, called the gbr100grid, of the entire northeastern Australian continental margin was used (Beaman, 2010). The gbr100 grid captures critical elements of the shelf's geometry, including the coral reef platforms. A present-day sea level and coastline were assumed; however, tidal oscillations were not considered in this study.

Due to a lack of dense high-resolution nearshore bathymetry data, run-up was estimated using the formulation of Ward and Asphaug (2003):

$$R = A(d)^{4/5} \cdot d^{1/5}$$

where R is the estimated run-up and $A(d)$ is the maximum wave amplitude obtained from virtual tide gauges placed in water depths of $d \sim 20$ m. While based on the conservation of wave energy flux in linear theory, this formula is limited in its ability to capture place-specific impacts of shallow-water bathymetry and onshore topography on the final tsunami inundation extent. We therefore present our results as estimated run-up projections, following Brune et al. (2010).

19.3.2.1. A Note on Bottom Friction

While propagating in shallow water, tsunamis are sensitive to energy attenuation by bottom friction (Dao & Tkalich, 2007), which is caused by high seafloor roughness. On the GBR shelf, coral reefs introduce a high degree of structural complexity, resulting in a high attenuation of wind waves (Ferrario et al., 2014; Gallop et al., 2014; Harris et al., 2018). We have therefore aimed to account for this in the present study. Here, attenuation of wave energy by bottom friction is parameterized using a standard quadratic shear law, where we prescribe a friction factor of CD = 0.1522 to the reef platforms (Nelson, 1996). This dimensionless parameter was empirically derived at a study site within the GBR and falls well within the range of other values determined for coral reef environments (Harris et al., 2018; Rosman & Hench, 2011). A standard value of CD = 0.0025 was prescribed to the surrounding shelf, where a sandy bottom was assumed.

19.4. RESULTS

The high-resolution multibeam bathymetry reveal seafloor instability features as discontinuous breaks in the continental slope and indentations in water depths ranging between 90 and 2500 m. Bathymetry data, together with sub-bottom profile data, have allowed the detailed interpretation of some of these slope instabilities (Webster et al., 2016; Puga-Bernabéu et al., 2017), but most of them remain unexplored. For this chapter, we have selected four representative landslides characterized by the presence of a clearly visible debris field. The study landslides are named from north to south: Ribbon Reef Slide (RRS), Gloria Knolls Slide (Puga-Bernabéu et al., 2017), Bowl Slide (BS), and Viper Slide (Webster et al., 2016) (Figure 19.1a). Their dimensions are highly variable, and their main morphometric parameters are shown in Figure 19.1b.

19.4.1. Ribbon Reef Slide (RRS)

19.4.1.1. Overview

The RRS is located offshore of the Ribbon Reef Canyon (RRC) system (Puga-Bernabéu et al., 2011), a

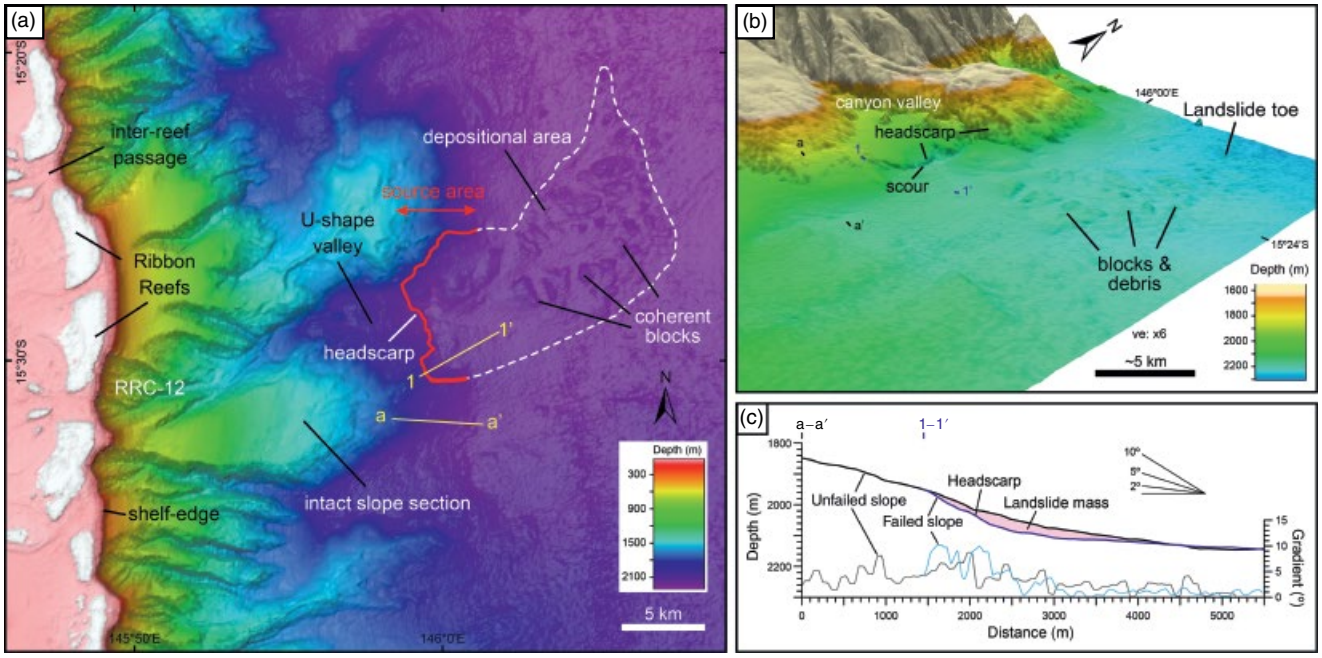


Figure 19.2 (a) Bathymetry (30 m resolution DEM) of the Ribbon Reef Slide (RRS) area showing the seafloor terrains (source and depositional areas) that can be distinguished in this landslide located at the mouth of Ribbon Reef Canyon (RRC) 12 valley. Adjacent seafloor features and locations of depth profiles shown in (c) are also marked. (b) Northwesterly view showing the RRS and adjacent seafloor features. Note the deflection of the failed mass to the north following the axis of the Queensland Trough and the decreasing size of the landslide debris toward the landslide toe. Locations of depth profiles shown in (c) are also indicated. (c) Depth profiles (see Figure 19.2a, b for location) of the reconstructed slope before RRS (black) and present-day slope (blue) and corresponding slope gradients. Pink area indicates the estimated failed slid mass. (*See electronic version for color representation of this figure*)

few kilometers from the mouth of RRC 12, from 145°59′E and 146°8′E longitude and from 15°21′S to 15°31′S latitude (Figures 19.1a and 19.2). Puga-Bernabéu et al. (2011) identified this landslide from the bathymetry but has not yet been described in detail. The RRS excavated a ~25 km^2 area of the lower slope at depths from ~1950 to 2170 m, with slide debris extending across the Queensland Trough to 2260 m depth. The volume of sediment remobilized by this landslide is an estimated ~1.2 km^3.

19.4.1.2. Slope Morphology

The N-S oriented continental margin upslope the RRS is heavily carved by the RRC system (Puga-Bernabéu et al., 2011, 2013b). This canyon system mostly comprises single- or multi-fed shelf-incised canyons. The presence of reef barriers rimming the canyon heads partially obstructs the sediment supply from the shelf to these canyons. The outer shelf is connected to the continental slope by a steep shelf break between about 70 and 100 m, where the gradient increases sharply from ~5° to >20° (Puga-Bernabéu et al., 2011). Depth profiles across the slope exhibit linear to exponential shapes. In the vicinity of the RRS, between 1800 and 2100 m depth, slope gradients have mean values of 3.5° and then change abruptly at the basin floor with gradients of <0.5° (Figure 19.2c).

19.4.1.3. Source Area

The RRS scar is located ~7 km to the east of RRC 12, which is separated by a U-shaped (in cross section) valley up to 7 km wide that opens toward the landslide (Figure 19.2a, b). The RRS scar has a roughly crescent shape that opens to the east, is 8.5 km wide, and indents up to 4 km into the lower slope (Figure 19.2a, b). The headscarp with a total length of ~13 km extends from 1950 to 2170 m depth with mean gradients between 9° and 14° and reaching a maximum height of 140 m (generally 40–55 m). A thickness of 30–45 m for the failed section is estimated from the comparison between the reconstructed adjacent slope and the depth profiles across the landslide (Figure 19.2c). The depth profile across the landslide is steeper than the adjacent unfailed slope (Figures 19.1b and 19.2c). A scour is observed at the foot of the headscarp in the central part of the landslide (Figure 19.2b), which could be formed by sediment gravity flows originated from the upslope canyon. The headscarp might have also been reshaped and eroded by such flows. The seafloor is locally mounded at the headscarp toe, indicating that the source area has not been fully denuded and part of the failed material remained within this area.

19.4.1.4. Depositional Area

The seafloor area immediately downslope of the headscarp is relatively smooth. However, ~5 km further downslope from the headscarp, a lobe-shaped elongate deposit (~90 km^2) with a characteristic hummocky geometry is noticeable in the bathymetry. This deposit is deflected to the north, following the axis of the Queensland Trough (Figure 19.2a, b) before reaching a maximum distance of ~22 km from the headscarp. The mass-wasting deposit is formed by a distinctive cluster of closely spaced (100–600 m apart) coherent blocks of varying sizes (Figure 19.2a). Larger blocks are abundant and oriented nearly perpendicular to the inferred downslope flow direction (Figure 19.2a, b). They have elongated shapes with long axes (1.5–2.5 km) and rounded crests that are elevated 20–50 m above the surrounding seafloor. Smaller blocks have nearly circular perimeters, are 400–700 m in diameter, and rise 10–30 m above the surrounding seafloor. Larger blocks have similar sizes and are located in a similar deepwater setting to the knolls generated by the GKS, which show evidence of a living and fossil cold-water coral community (see Section 19.4.2; Puga-Bernabéu et al., 2017). The mass-wasting blocks of the RRS could be another potential site to investigate the spatial relationship that exists between submarine landslides and the presence of cold-water corals in the deep sea (Savini et al., 2016).

19.4.2. Gloria Knolls Slide (GKS)

19.4.2.1. Overview

The GKS is the largest landslide complex on the continental slope of the central GBR margin (Puga-Bernabéu et al., 2017), situated between about 146°41′E and 147°E longitude and 17°11′S and 17°25′S latitude, at water depths ranging between 250 and 1350 m (Figures 19.1a and 19.3). It forms a ~20 km along-slope and ~8 km across-slope indentation in the margin that remobilized about 32 km^3 of sediment. The thickness of the GKS deposits observed in the sub-bottom profiles ranges between 17 and 37 m in profiles parallel to the scar and between 23 and 31 m profiles perpendicular to the scar (Puga-Bernabéu et al., 2017).

19.4.2.2. Slope Morphology

The continental margin in the GKS area has a general NNW-SSE orientation. The shelf break is located between 90 and 100 m and connects with a gently inclined (<1.5°), 10–12 km wide upper slope shoulder, which is heavily dissected by the GKS. Other smaller slope failures have also modified the slope morphology around the GKS (Puga-Bernabéu et al., 2013a). The reconstructed depth profiles across the continental slope display a sigmoidal shape with an average gradient of 9° and with the steepest values (>9°) between 300 and 1000 m (Figure 19.3c).

19.4.2.3. Source Area

The GKS scar has a bow shape with two well-preserved headscarps at ~250 m (main headscarp) and between 600

and 700 m (secondary headscarp). These headscarps correspond to landslide events 2 (main headscarp) and 1 (secondary headscarp) interpreted by Puga-Bernabéu et al. (2017). The scar has a total length of ~27 km, a length-width ratio (ratio between the straight line joining the headwall extremities and the maximum perpendicular distance of the headwall from this line) of ~3.1, and covers an area of ~174 km^2. Headscarp height spans up to 830 m for main headscarp and up to 400 m in the secondary headscarp. Average slope gradients range from 15° to 17°, which are much steeper than the reconstructed unfailed slope (Figures 19.1b and 19.3c). The failure likely involved deep, more consolidated slope material that was subsequently transported and deposited as coherent blocks (Figure 19.3). The comparison between pre- and post-failure slope cross sections yields thicknesses at the center of mass of the landslide of ~190–330 m for event 1 and 160–290 m for event 2 (Figure 19.3c). No tensional cracks are observed on the upper slope to landward of the main headscarp. The two sidewall scarps of the landslide complex show a WSW-ENE direction (Figure 19.3a), with heights of 355–430 m and steep gradients ranging between 10° and 16° on average. The source area is carved by small gullies <100 m deep, especially in the northern part, while a slope-confined submarine canyon is excavated along the southern sidewall (Figure 19.3a, b).

19.4.2.4. Depositional Area

The bathymetric data reveal significant sediment evacuation from the GKS source area, with a distinct U shape in cross section and deposition of the failed material over the headscarp toe. The depositional area can be divided into a proximal depositional area and a distal depositional area (PDA and DDA, respectively) (Figure 19.3a, d; Puga-Bernabéu et al., 2017). The seafloor is completely smooth and flat (<1°) in the PDA, which ranges from 1050 to 1200 m depth, and displays no signs of depositional features related to the slope failure. This notwithstanding, sub-bottom profiles reveal localized, transparent reflectors at the foot of the headscarp interpreted as small-scale mass-transport deposits (Figure 19.3e). The DDA, extending from 1200 to 1350 m depth, is the main depocenter of the GKS. The seafloor topography in the DDA is irregular and topographically rugged due to the presence of debris blocks and knolls (i.e., large blocks). Over 70 individual smaller debris blocks, 300–500 m wide and 5–15 m high are observed (Figure 19.3e). They are smaller, nearly spherical, and regularly spaced in the northern part of the DDA and larger and elongated in shape in the southern part (Puga-Bernabéu et al., 2017). The knolls form a distinctive cluster extending ~15.3 km^2 over the surrounding seafloor (Figure 19.3d). They are elliptical to elongated in shape and have rounded to ridgelike crests, showing no obvious preferred orientation. The size of the knolls ranges from 700 to 3600 m in length and 44 to 105 m in height and have areas of 0.5–7.9 km^2. All knolls show evidence of moats on their northern sides (Figure 19.3d). A dredge sample from the top of the largest knoll recovered live and abundant fossil biota, which points to a cold-water coral community on these blocks (Puga-Bernabéu et al., 2017). Hemipelagic drapes and sediment gravity flows are interpreted from sub-bottom profiles across and along the DDA (Figure 19.3e; Puga-Bernabéu et al., 2017). Below the sediment drapes, the deposits forming the GKS comprise wedge-shaped bodies, where reflectors are transparent in the PDA and discontinuous/chaotic in the DDA (Figure 19.3e). At the toe of the landslide, discontinuous reflectors display imbricate patterns forming small thrusts (Figure 19.3e).

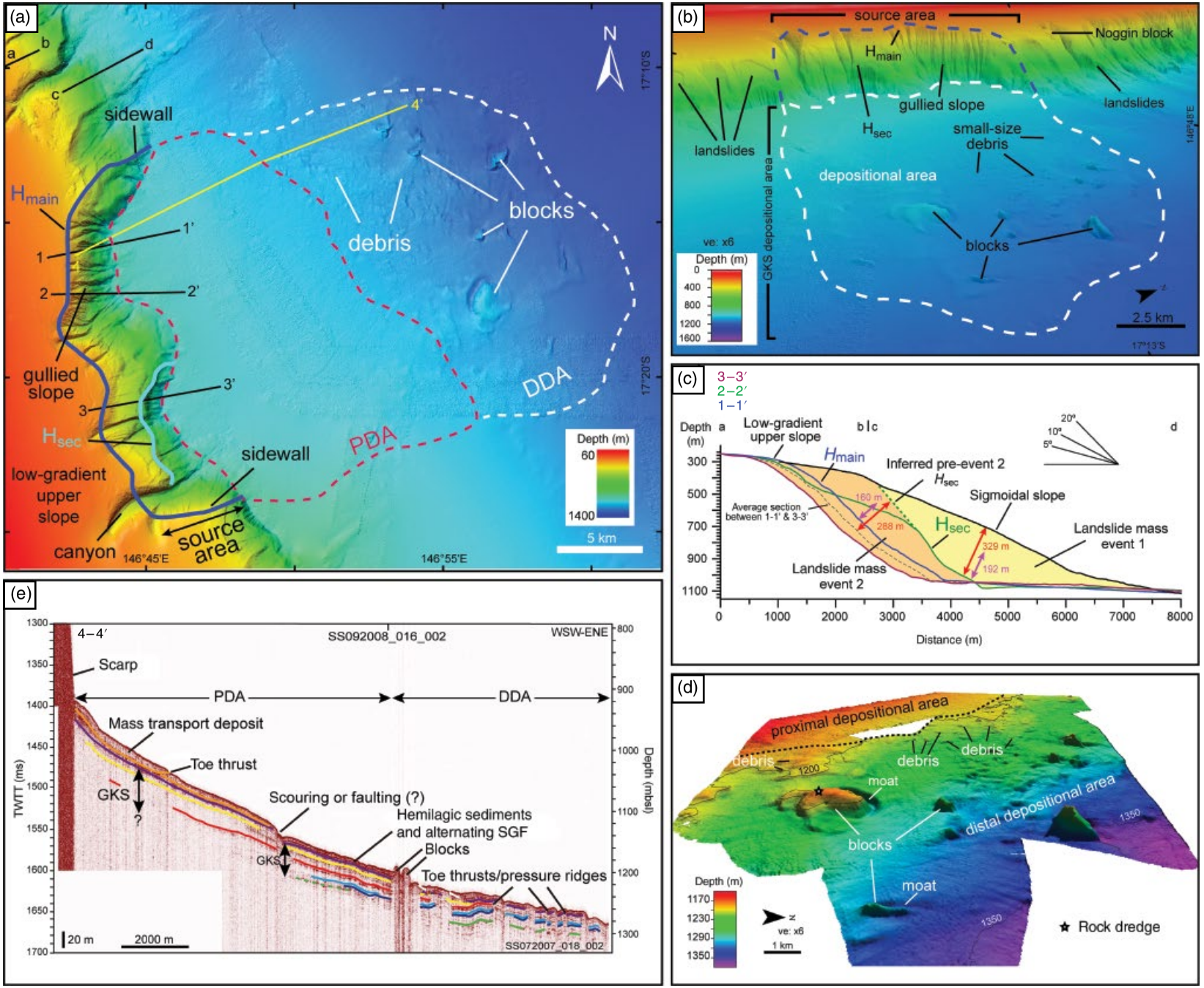
19.4.3. Bowl Slide (BS)

19.4.3.1. Overview

The BS is a landslide complex located between 147°39′E and 147°54′E longitude and between 18°09′S and 18°26′S latitude (Figures 19.1a and 19.4). It extends offshore the paleo-Burdekin river delta (Johnson & Searle, 1984; Harris et al., 1990) from depths of ~105 m to at least 1040 m, as the outer limit is poorly defined on the bathymetry. The BS scar shows a complex morphology with well-exposed headscarps at different depths, suggesting that its overall formation resulted from several (likely three) failure events. The entire complex covers ~492 km^2 of the seafloor with an estimated ~5.3 km^3 of sediment remobilized, being one of the largest submarine landslides in the GBR margin.

19.4.3.2. Slope Morphology

The general NW-SE direction of the shelf edge in the southern sector of the central GBR is significantly deflected by the presence of a large (>60 km along-shelf) bulge that extends ~10 km across shelf to the northeast (Figure 19.1a). This lobe-shaped feature corresponds to the shelf-edge paleo-Burdekin river delta (Symonds et al., 1983), whose modern counterpart has the largest natural sediment yield of any river in northeastern Australia (Belperio, 1983; Waters et al., 2014). The shelf break is located at 110–115 m depth with an average gradient change to the uppermost slope from 5° to >12° (Figure 19.4). Depth profiles across the slope display a linear to exponential shape overall, slightly sigmoidal between 150 and 500 m depth, and gently (<2°) linear toward the base of the slope and basin (Figure 19.4c). The slope adjacent to the BS is disturbed at the lower slope by smaller shallow-seated landslides and by small incipient slope-confined gullies and canyons in the middle slope (Figure 19.4b).


(a)
N
a
b
c
d
sidewall
4
4'
Hmain
1'
1
2
2'
blocks
debris
gullied slope
3'
3
Hsec
DDA
PDA
sidewall
low-gradient upper slope
canyon
source area
Depth (m)
60
1400
5 km
17°10'S
17°20'S
146°45'E
146°55'E
(b)
source area
Noggin block
Hmain
gullied slope
landslides
landslides
Hsec
small-size debris
depositional area
GKS depositional area
blocks
ve: x6
Depth (m)
0
400
800
1200
1600
2.5 km
17°13'S
146°48'E
(c)
3–3′
2–2′
1–1′
Depth (m)
a
Low-gradient upper slope
b
c
d
Hmain
Inferred pre-event 2
Hsec
Sigmoidal slope
Average section between 1-1' & 3-3'
160 m
288 m
Hsec
329 m
192 m
Landslide mass event 1
Landslide mass event 2
300
500
700
900
1100
0
1000
2000
3000
4000
5000
6000
7000
8000
Distance (m)
20°
10°
5°
(d)
proximal depositional area
debris
debris
debris
1200
moat
distal depositional area
1350
blocks
moat
1350
Depth (m)
1170
1230
1290
1350
ve: x6
1 km
Rock dredge
(e)
4–4′
SS092008_016_002
WSW-ENE
Scarp
PDA
DDA
Mass transport deposit
Toe thrust
GKS
?
Scouring or faulting (?)
Hemilagic sediments and alternating SGF
Blocks
GKS
Toe thrusts/pressure ridges
TWTT (ms)
Depth (mbsl)
1300
1350
1400
1450
1500
1550
1600
1650
1700
800
900
1000
1100
1200
1300
20 m
2000 m
SS072007_018_002

19.4.3.3. Source Area

The source area of the BS is located below 105 m depth and extends ~12.9 km along the slope and ~7.8 km across the slope. It shows U-shaped morphology in plan view facing the northeast, and it is formed by three headscarps, here named H1–H3 (Figure 19.4). The headscarp H1 is sinuous and extends from 485 to 750 m depth. It ranges from ~30 m high for the northwestern side to ~170 m for the southeastern side and has an average gradient of ~13°. The sidewalls of H1 open downslope in opposite directions, crosscutting the bathymetric contours of the unfailed slope (Figure 19.4a). The seafloor across the landslide downslope of headscarp H1 is steeper than the adjacent unfailed slope (Figures 19.1b and 19.4c). The headscarp H2 starts between 200 and 230 m and is ~9.5 km long. It has a slightly sinuous morphology formed by three bow-shaped segments with walls up to 75 m high and average gradients of 19°. The southeastern part of H2 has been reshaped by a submarine canyon head, increasing the gradients >25°. At the northwestern side, the H2 headscarp passes laterally to a rectilinear, steep (15–35°) sidewall up to 65 m high, while the southeastern sidewall now belongs to a canyon margin (Figure 19.4a, b). The slope gradient across the landslide between headscarps H2 and H1 is similar (~6.3°) to the adjacent unfailed slope (Figure 19.4c). Further upslope from H2, the headscarp H3 is visible in water depths of ~105–120 m, carving the shelf edge itself and indenting 1–2 km into the shelf for 10 km in distance (Figure 19.4a, b). This headscarp is up to 80 m high and 15–25° but has a gentler relief in the central part (Figure 19.4b). The northwestern sidewall of headscarp H3 runs parallel to that of H2. This sidewall is up to 70 m high and has an average gradient of 15°. On the slope, a 3.5 km^2 area between the headscarp H2 and where H3 indents, the shelf break is covered by randomly distributed blocks 100–200 m wide and 2–10 m high (Figure 19.4b).

19.4.3.4. Depositional Area

The depositional area has a fan shape in plan view and opens toward the northeast from the toe of headscarp H1. This area extends ~25 km across the basin floor and covers a total area of ~440 km^2. The seafloor on this area is uneven, with mean gradients of <1°. Three main depositional terrains are recognized in this area:

1. Cone-shaped debris field, which covers most of the accumulation zone (Figure 19.4a, b). This feature has a mounded shape in cross-sectional profile, with a maximum relief of 70 m over the surrounding seafloor (Figure 19.4c). The seafloor in this area is very irregular and rough, owing to the roughly circular coherent blocks ranging in size from 100 to 600 m in length and 5 to 30 m in height. There is no preferred orientation of these blocks.

2. Low-relief corridor, situated to the west of the debris cone (Figure 19.4a, b). This scour is 3–4 km in width and generally lies <30 m below the debris cone topography (Figure 19.4c). The seafloor is similarly uneven, showing a pattern of topographically elevated blocks that are overall smaller (90–285 m long) than those in the adjacent debris cone.

3. Debris apron accumulated at the foot of headscarp H1 and separated from it by a moat-like scour (Figure 19.4b). The surface of this deposit dips at 1.5–2°

Figure 19.3 (a) Bathymetry (30 m resolution DEM) of the Gloria Knolls Slide (GKS) showing seafloor terrains identified in this landslide. The depositional area is divided into a proximal depositional area (PDA) adjacent to the source area and a distal depositional area (DDA) that include abundant debris and blocks elevated over the surrounding seafloor (Source: From Puga-Bernabéu et al. (2017) with permission of Elsevier). Location of depth profiles shown in (c) and sub-bottom TOPAS profile shown in (e) are also indicated. H_{main}, main headscarp; H_{sec}, secondary headscarp. (b) Westerly view showing the GKS and adjacent seafloor features. Note that large blocks reached further distances than smaller debris. (c) Depth profiles (see Figure 19.3a for location) of the reconstructed slope before RRS (black) and present-day slope (colors). Yellow- and orange-shaded areas indicate the estimated landslide mass during failure events 1 and 2. The thickness of the worst-case (red) and conservative (pink) scenarios for each event used in the tsunami simulation are indicated. (d) Westerly view of the distal depositional area of the GKS showing the distribution of larger knolls and smaller debris blocks on the seafloor. Note the presence of moats at the northern sides of the knolls. White star marks the position of the collected rock dredge on top of the largest knoll (Source: From Puga-Bernabéu et al. (2017) with permission of Elsevier). (e) Sub-bottom TOPAS seismic section across the depositional area of the GKS (see Figure 19.3a for location), with main reflectors marked in colors. The GKS deposits are characterized by weak amplitude, transparent reflectors in the proximal depositional area (PDA), and more discontinuous and chaotic in the distal depositional area (DDA), where toe thrusts/pressure ridges are observed. Note the presence of blocks rising over the surrounding seafloor. A drape of hemipelagic sediment and alternating sediment gravity flow (SGF) deposits (continuous parallel to subparallel high-amplitude reflectors bundled with low-amplitude reflectors) covers the GKS deposit. Vertical scale is based on a sound velocity of 1550/ms (Davies et al., 1991a). (*See electronic version for color representation of this figure*)

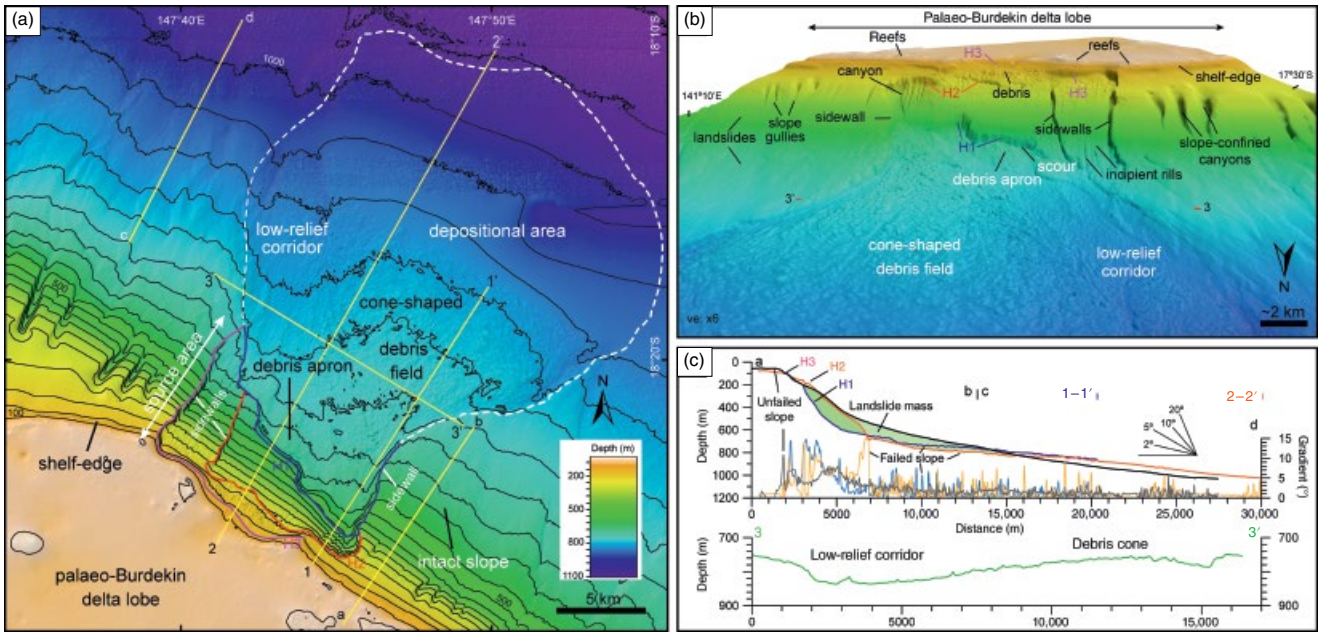


Figure 19.4 (a) Bathymetry (30 m resolution DEM) of the Bowl Slide (BS) area showing the distribution of the source and depositional areas over the seafloor. The source area includes three headscarps (H1–H3). Note that headscarp H3 indents the depositional lobe of the paleo-Burdekin river delta. The depositional area is divided into three terrains: debris apron, cone-shaped debris field, and a low-relief corridor. Location of depth profiles shown in (c) is also indicated. Bathymetric contours in meters. (b) Southerly view showing the BS and adjacent seafloor features. Location of depth profile 3-3′ over the depositional area is also shown. (c) Depth profiles (see Figure 19.4a, b for location) of the reconstructed slope before BS (black) and present-day slope (blue and orange) and corresponding slope gradients (above) and over the depositional area (below). Shaded green areas indicate the estimated failed slide mass of the landslide in at least two different events. (*See electronic version for color representation of this figure*)

and shows nearly circular, small meter-sized blocks. The BS has a minimum runout of 29 km length, measured from the top of headscarp H1. Unfortunately, the definitive outer limit of the depositional area is poorly defined on the compiled bathymetry because of a lack of multibeam coverage.

19.4.4. Viper Slide (VS)

19.4.4.1. Overview

The VS is located ~68 km southeast of the BS and ~22 km southeast of the southernmost lobe of the paleo-Burdekin river delta (Symonds et al., 1983), between 148°10′E and 148°13.5′E longitude and between 18°44.9′S and 18°48.15′S latitude (Figures 19.1a and 19.5). The VS represents a collapse of a 5.4 km long section of the shelf edge, extending ~5 km to seaward from ~100 to 225 m depth on the upper slope (Figure 19.5a). The VS covers a total area of 18.7 km^2 and remobilized a volume of 0.025 km^3 (Webster et al., 2016). The maximum thickness of the VS deposits observed in the sub-bottom profiles is between 21 and 31 m (25 ms TWTT; Webster et al., 2016).

19.4.4.2. Slope Morphology

The NW-SE oriented shelf edge in the region surrounding the VS is characterized by the presence of narrow and discontinuous submerged reef terraces between 80 and 110 m depth (Abbey et al., 2011) (Figure 19.5a). The outer shelf is connected to the upper slope by a steep shelf break at ~110 m, where the gradient increases from ~4° to >10°. Between 140 and 250 m, depth profiles across the slope exhibit gently dipping (~1.2°) linear shapes. No other seafloor features, such as canyons or gullies or slope failures, are observed on the adjacent slope near the VS.

19.4.4.3. Source Area

The VS scar shows a sinuous morphology with a length-width ratio of ~7.5. The VS scar is formed by three arcuate indentations, 1.5–1.8 km long and 400–500 m wide (Figure 19.5a). The headscarp is located in relatively shallow water (~90 and 120 m depth) and has a stepped morphology, where gradients vary between 6° and 13°. Such gradients are similar or slightly gentler than the adjacent unfailed slope (Figure 19.1b). Upslope from the headscarp, a sequence of drowned reefs in depths of <85 m wrap around the headscarp at its northwestern side and the central part (Figure 19.5a). The headscarp has not been fully disintegrated, as two large (~1–1.5 km long) detached ridges are observed close to the headscarp at its northwestern side (Figure 19.5b). These 8–12 m high ridges are ~250 m apart and the closest one to the headscarp is separated by a similar distance. The ridges are slightly rotated toward the headscarp and have rounded crests. At the central and southeastern side scar indentation, a cluster of randomly oriented blocks is observed at the foot of the headscarp (Figure 19.5b). The VS lacks exposed sidewalls.

19.4.4.4. Depositional Area

The depositional area of the VS extends across 4.8 km on the upper slope from 120 to 130 m water depth. This accumulation zone has a triangular shape that narrows in the flow direction toward the northeast (Figure 19.5a, b). This zone exhibits a generally irregular and hummocky seafloor topography and is easily distinguished from the adjacent, smooth upper slope sediments. Five main depositional terrains are recognized in this area based on the seafloor topography, backscatter, and sub-bottom data (Figure 19.5a–c; Webster et al., 2016):

1. Large block debris field. This area spans ~7 km^2 and represents the main depocenter of the VS, with relatively high backscatter (Figure 19.5c). It comprises two depositional slide features: ridges and blocks. The ridges are located at the northwestern half of the depositional area and represent a continuation of the ridges observed in the headscarp area. They are closely spaced (<100 m), spanning from 100 to 500 m long and 4 to 17 m high. The ridges, resembling compressional features, roughly decrease in size in the direction of flow, displaying a transverse nearly radial alignment to the adjacent source area (Figure 19.5a). Two small ridges are also found at the southernmost part of the depositional area between ~145 and 155 m depth (Figure 19.5b). The blocks dominate the southeastern half and distal part of the large block debris field (Figure 19.5a). Blocks are nearly circular to ellipsoidal and their surface is topographically rounded. They are 50–120 m long and rise upon the surrounding seafloor by <10 m. The size of the blocks decreases progressively to the distal part of this terrain.

2. Mixed blocks and sediment area. The uneven seafloor in this area envelopes and is interspersed with the large block debris field (Figure 19.5a, c). Backscatter imagery of this terrain is relatively lower in comparison to the large block debris field, indicating a smoother surface. Blocks in this seafloor terrain are overall smaller (usually <80 m long) compared with those in the debris field, rising just a few meters above the surrounding seafloor. A few outsized (>150 m long) blocks are also observed.

3. Small debris and sediment area. This area is located to the eastern side of the depositional area in transition from the mixed blocks and sediment area (Figure 19.5a, c). This terrain is mounded, shows moderate to low backscatter, and contains only minor small blocks of similar size to those of the mixed blocks and sediment area, which rise <1 m upon the seafloor.

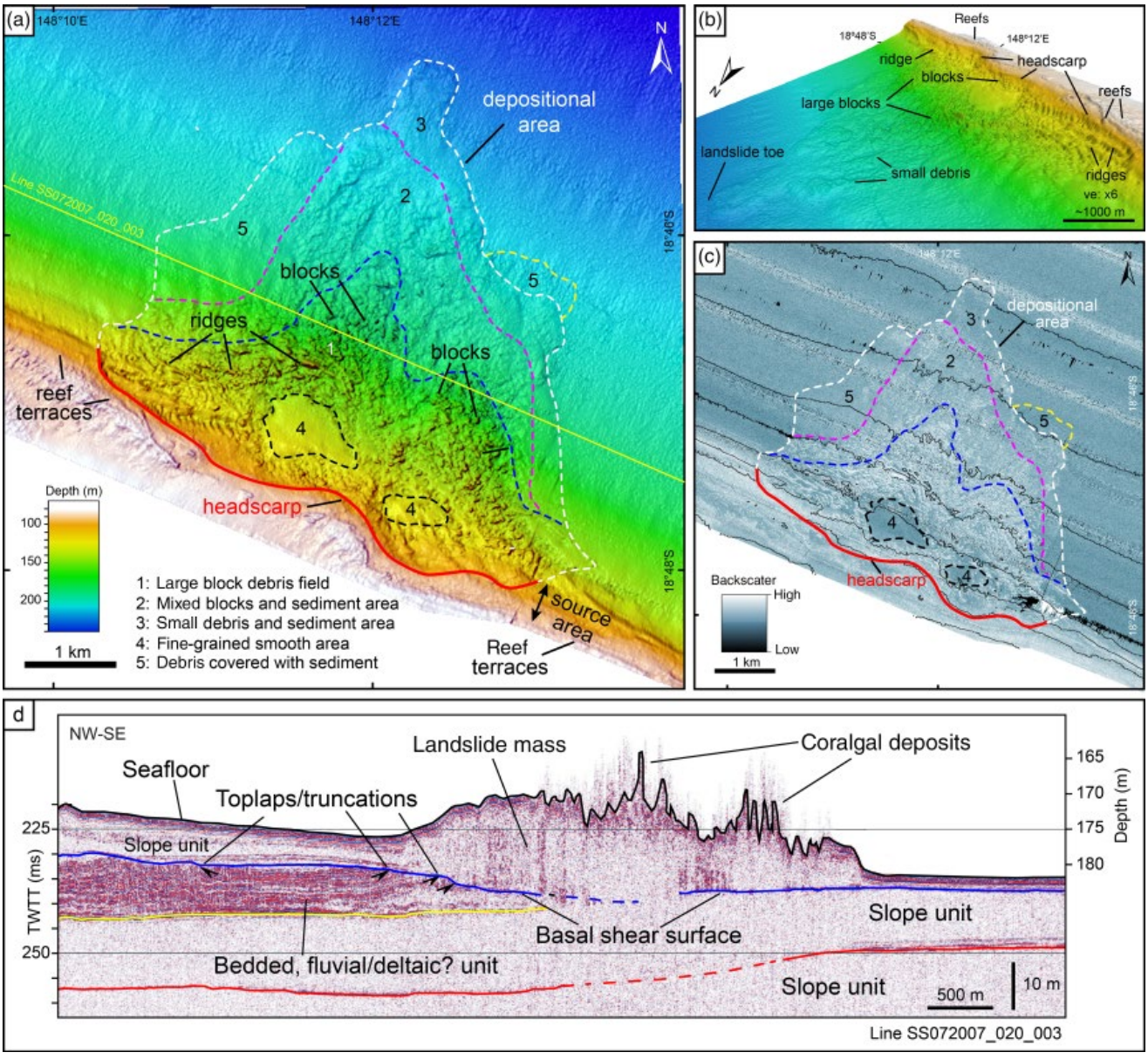


Figure 19.5 (a) Bathymetry (10 m resolution DEM) of the Viper Slide (VS) area showing the distribution of the source and depositional areas of the landslide. The depositional area comprises five seafloor terrains characterized (1–5). Location of sub-bottom TOPAS profile (yellow line) shown in (d) is also indicated. (b) Southwesterly view showing the VS and adjacent seafloor features. Note the presence of ridges parallel to the headscarp and the decreasing size of the blocks and debris downslope. (c) Map showing the interpreted backscatter image gridded at 2 m of the VS area showing the main seafloor terrains (1–5) identified in (a). (d) Interpreted sub-bottom profile (see Figure 19.5a for location) across the central part of the VS depositional area. The basal shear surface is visible within the upper slope units, which crosscuts high-amplitude, subparallel reflectors interpreted as older fluvial-deltaic deposits. The vertical scale bar is estimated by assuming an intermediate p-wave velocity (2100/ms) between the values assigned to outer shelf and upper slope materials in the region (1700–2500/ms; Hinestrosa et al., 2014). The top of the landslide blocks is covered by coralgal deposits (Abbey et al., 2013). Source: From Webster et al. (2016) with permission of Elsevier. (*See electronic version for color representation of this figure*)

4. Fine-grained smooth area. This terrain comprises two regions that cover ~1 km^2 of the depositional area, with the largest and best exposed region situated in the central part, close to the foot of the headscarp and separated by <100 m distance (Figure 19.5a, c). The seafloor in this terrain is smooth and gently dipping (~2.5°) and shows low backscatter, which suggests the presence of fine-grained sediments on the seafloor. This terrain likely represents a remnant of the original slope that remained unaffected during the failure.

5. Debris covered with sediment. This area is located to the western side of the depositional area and in local patches at the eastern side (Figure 19.5a, c). This area is similar to the small debris and sediment area, but the seafloor here is smoother and debris remains are buried below a thin cap of high-amplitude continuous reflectors.

The sub-bottom profiles along the upper slope show that the blocky deposits are characterized by transparent seismic facies (Figure 19.5d). The basal shear surface is clearly visible over the autochthonous slope sediments (Figure 19.5d). This detachment surface is flat and lacks grooves or ramp and flats structures (e.g., Bull et al., 2009). Toward the northwest, the basal surface crosscuts well-bedded deposits characterized by high-amplitude, subparallel reflectors, interpreted to be older fluvial-deltaic deposits that are likely related to the paleo-Burdekin river delta (Webster et al., 2016).

19.4.5. Tsunami Modeling of the Gloria Knolls Slide

The GKS is a landslide complex large enough (32 km^3) to be considered as a potential tsunamigenic landslide (e.g., ten Brink et al., 2006; Iglesias et al., 2012) but resulted from a sequential failure process comprising at least two large events and third smaller event (Puga-Bernabéu et al., 2017). Therefore, we have evaluated the tsunamigenic potential of the first and second events separately. We used depth profiles across the GKS and compared them with the reconstructed pre-failure slope to estimate the thickness of the failed section in each event (Figure 19.3c). We considered two cases for each event: (i) a worst-case scenario that takes into account the maximum thickness of the failed mass and (ii) a conservative scenario that considers a more uniform thickness through the failed section (Figure 19.3c and Table 19.1).

Tsunami simulations imply that a failure of similar scale to the GKS would produce a sizable tsunami wave under present-day sea level conditions and modern coastline (Figure 19.6). Maximum wave height distributions are "dipolar" and reflect characteristic point-source tsunami behaviors such as radial damping, where tsunami amplitude declines proportionally to the increasing distance from the landslide source (Okal & Synolakis, 2003). Estimated run-up distributions generally follow a bell curve shape (Figure 19.6), where areas of the shoreline lying closer to the landslide source tended to experience higher run-ups. Across scenarios, maximum estimated run-ups range from ~0.5 to 2 m, where wave trains arrived at the present-day coast after a roughly 50 minute propagation time from the source. The worst-case scenarios for both events produced the largest wave height distributions and run-ups, while the conservative scenarios produced smaller tsunamis. The largest run-ups were produced by the worst-case GKS Event 2, where estimates regularly surpassed 1.5 m along the affected coastline.

As the tsunami propagated across the shelf and advanced toward the shore, obstruction by reef platforms resulted in typical shallow-water wave behaviors such as reflection, diffraction, focusing, and shoaling. Efficient dissipation via bottom friction occurred as waves surge over shallow, coral-covered platforms. This

Table 19.1 List of Key Parameters for the Initial Generation of the Tsunami Source of the Gloria Knolls Slide

	Event 1 Worst-Case Scenario	Event 1 Conservative Scenario	Event 2 Worst-Case Scenario	Event 2 Conservative Scenario
Latitude	17°19′21.9″S	17°19′21.9″S	17°19′34.2″S	17°19′34.2″S
Longitude	146°45′07.4″E	146°45′07.4″E	146°44′14.2″E	146°44′14.2″E
Length (m)	4,755	4,755	3,947	3,364
Width (m)	19,500	19,500	19,200	19,200
Maximum thickness (m)	329	192	288	160
Initial submergence depth (m)	670	670	420	420
Slope of rupture surface (degrees)	8.9	8.9	9.1	9.1
Orientation of failure (degrees clockwise from north)	73	73	73	73
Length-depth ratio	7.1	7.1	9.4	8.0
Characteristic tsunami amplitude (m)	53.7	30.5	141	29.9
Characteristic tsunami wavelength (km)	17	17	12	12

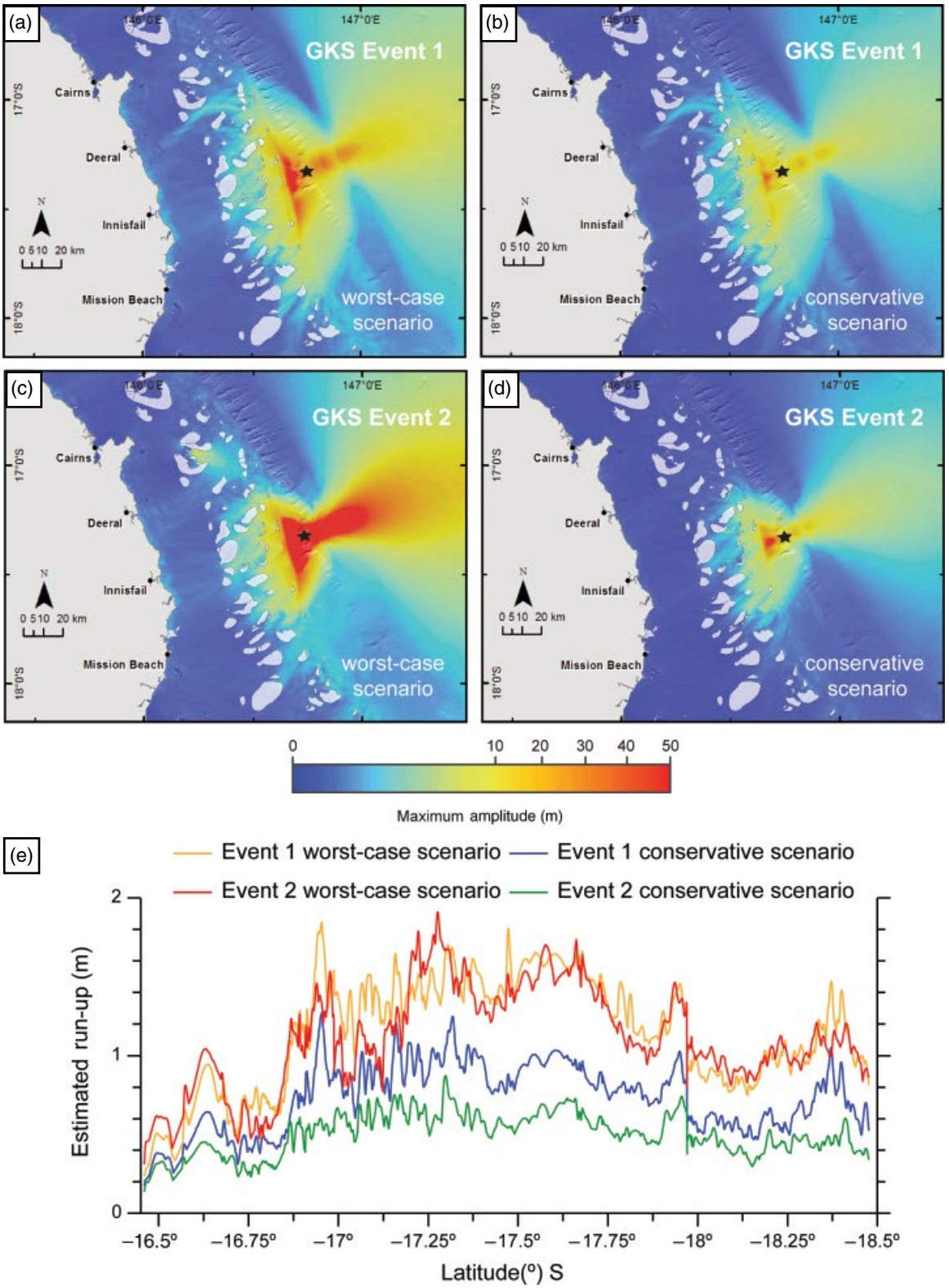


Figure 19.6 (a–d) Maximum wave height distributions of the four GKS scenarios over the duration of the roughly 2 hours tsunami propagation time. Amplitudes are largest toward the landslide source region (indicated by the black star), declining as the tsunami radiates outward from the source. A gamma stretch was applied to the color scale to help accentuate the trajectories of the lower-amplitude wave trains. Reef platforms are shown in white. Also shown beneath wave amplitude distribution is bathymetric hillshade (azimuth = 45°; altitude = 30°). (e) Estimated run-up distributions from the four GKS tsunami scenarios as a function of latitude. (*See electronic version for color representation of this figure*)

effect is apparent in the maximum wave height distributions (Figure 19.6). Overall, the entire reef system appears to impart a significant dampening effect on the tsunami, both at the individual reef scale and at the regional scale.

19.5. DISCUSSION

19.5.1. Timing of the Mass Movements

Understanding the frequency and timing of large submarine landslides is of great importance for geohazard assessment. The past frequency distribution of large submarine landslides has been linked to climate change and atmospheric methane abundance (Haq, 1998; Maslim et al., 2004, 2010). However, many problems are found when age dating submarine landslides (Owen et al., 2007), and such dating uncertainties can obscure the causal relationship between the frequency of the slope failures and the factors that influence them. Among the landslides described here, only the GKS and VS have been dated (Webster et al., 2016; Puga-Bernabéu et al., 2017). Radiocarbon U-Th paired ages on fossil corals on the top of the largest knoll linked to the GKS (Figure 19.3d) provided an age of at least 302 ± 19 ka (Puga-Bernabéu et al., 2017). This age, together with the time estimated to deposit the ~15 m of hemipelagic sediment on top of the knoll, constrains the emplacement of the GKS between 412 and 441 ka. In the VS, age data come from deepwater coralline algae crusts dredged from the top of the large block debris field, which yielded a ^{14}C-AMS age of 14.01 ± 0.4 ka (Abbey et al., 2013). This age, together with the geomorphological relationship among the landslide scars, reef terraces, and buried paleo-channels, constrains the timing of the VS between 14 and 20 ka (Webster et al., 2016). In both the GKS and VS, the estimated timing of the slope failures is coincident with a deglaciation (transitions MIS 12–11 and MIS 2–1, respectively). This suggests a causal link between rapid sea level rise and these submarine landslides on the GBR margin as a consequence of the sudden overburdening of the water column on the slope sediments. Similar causal relationships have been argued for other late Pleistocene landslides in other settings (Owen et al., 2007), although questioned by Urlaub et al. (2013). These authors did not find statistical evidence for a climate or sea level control on the timing of large submarine landslides. However, Smith et al. (2013) asserts that the rapid sea level rise during the early Holocene was probably an important factor in the development of the iconic Storegga Slide. The database used by Urlaub et al. (2013) includes landslides mainly from siliciclastic margins in the Northern Hemisphere, and so slope instability trends could respond differently to sea level changes in different margins. Intriguingly, the highest rates of hemipelagic slope sedimentation over the last 130 ka also occurred during the transgressions (Dunbar et al., 2000; Dunbar & Dickens, 2003; Page & Dickens, 2005). Therefore, on the GBR margin, sediment buildup on the continental slope during sea level transgressions could have contributed to sediment overburdening, which in turn favored slope failures.

19.5.2. Type of Mass Movements

Submarine landslide is a generic term used to refer to processes that lead to mass-transport deposits, which can be further categorized according to different classification schemes (Mulder & Cochonat, 1996; Canals et al., 2004). The landslides presented here display morphological features corresponding to debris avalanches (disaggregated rock fragments resulting from rapid slope failures with energy dissipation by grain contact) and slides (coherent masses of sediments failed from distinctive failure planes surfaces). All the GBR landslides fall within translational landslides according to their Skempton ratio (maximum thickness of the landslide to maximum initial length downslope ratio; Skempton & Hutchinson, 1969), which ranges between ~0.008 for the BS and ~0.054 for the VS. In the case of the GKS and BS, the presence of several headscarps at different depths on the source area is indicative of multiple failure events, although the exact time period between these events is unknown. In contrast, the VS and RRS were presumably the result of single slope failure events.

In the GKS and RRS, the failed sediment slabs were evacuated, transported, and disintegrated downslope, leaving a relatively smooth area close to the foot of the headscarp, and were accumulated much further downslope (Figures 19.2a, b and 19.3a, b; Hogan et al., 2013). In the BS and VS, the collapsed material accumulated immediately downslope from the headscarp toe and formed debris cones, but the debris cones exhibit opposing spreading patterns. In the BS, the relatively confined morphology of the deepwater headscarp H1 enabled the material to spread laterally from the base of the slope (Figure 19.4a, b; e.g., Laberg & Vorren, 2000; Normark et al., 2004), while the unconfined shallow headscarp of the VS allowed the failed material to move along slope while narrowing downslope (inverted triangular shape; Figure 19.5a, b). The ridge and trough morphology oriented parallel to the VS headscarp (Figure 19.5a, b), together with the large length-width ratio of the VS headscarp, are indicative of extension processes that can be interpreted as gravitational spreading (Micallef et al., 2007). Spreading is a type of mass movement identified in the headscarp domain of submarine landslides at a variety of sizes (e.g., Lastras et al., 2006, Micallef et al., 2007, Li et al., 2017). The sediment slab breaks up and undergoes extension along a planar surface, resulting

in a progressive disintegration of blocks downslope (Figure 19.5a). On the upper part of the BS scar, translational sliding might have occurred along the smooth and planar surfaces rooted at different depths and separated by well-exposed headscarps and sidewalls (Figure 19.4a, b; e.g., Li et al., 2017). However, the lack of subsurface data over the BS prevents the identification of plane-parallel stratigraphic surfaces needed to confirm its translational origin.

A decreasing blocky debris size with increasing distance is observed in the RRS and VS (Figures 19.2a, b and 19.5a, b) and less clearly in the BS (Figure 19.4a), but such a trend is not evident in the GKS (Figure 19.3a, b). This different pattern of block distribution is likely related to the interaction between the seawater and the landslide mass during its propagation and emplacement. In the GKS, the formation of pressure ridges or thrusts rising on the frontal part of the landslide (Puga-Bernabéu et al., 2017) could lead to a sudden reduction of landslide velocity (Mazzanti & De Blasio, 2010). This consequent freezing of the slide mass could have prevented the disintegration of the debris into smaller-size blocks. In contrast, more uniform slope gradients such as for the VS, BS, and RRS would favor increasing block disintegration toward the distal part (Alves & Cartwright, 2009). In the case of the VS, the spreading at the headscarp region entails a downslope thinning of the slide mass (Micallef et al., 2007) that is also consistent with the decrease in the size of the blocks in the depositional area (Figure 19.5a, b). Debris avalanches and slides often disintegrate into debris flows (Piper et al., 1999; Talling et al., 2007; Georgiopoulou et al., 2009), but such transformation in the GBR landslides remains unknown as no long sediment cores are available on the failed deposits.

The dynamics of subaqueous landslides is still poorly understood. One of the most used criteria to establish a preliminary evaluation of their mobility is the relationship between the volume and height/length (H/L) (McAdoo et al., 2000; Canals et al., 2004). The mobility of the study landslides in the GBR, shown as a function of the H/L ratio versus volume, is depicted in Figure 19.7. The GBR landslides fit within the boundaries of submarine landslides. GBR landslides fall within a relatively narrow range of H/L ratio between 0.016 and 0.035 (Figure 19.7). This suggests that the mobility of the GBR landslides is relatively independent of their size, and it may be indicative of more consolidated sediments on the slopes, with sediments that exhibit large shear strength. In such conditions, the runout distance is reduced as slope failures would require more energy to disintegrate the sediment pile, which reduces the potential energy that can be transformed in kinetic energy (Moernaut & De Batist, 2011). Comparable sediment remobilization (2–20 km^3) over short distances and involving indurated carbonate sediments has been described in the slopes environments of the Great Bahama Bank (Principaud et al., 2015). The mobility of the GBR landslides is also lower than that observed in the largest submarine landslides (>1000 km^3; e.g., the Storegga Slide, Hinlopen Slide, or South Makassar Strait Slide), but comparable to medium-size landslides (20–30 km^3, e.g., the Gebra Slide and BIG'95 debris flow; Canals et al., 2004). The relationship between headscarp gradient and headscarp height (Figure 19.1b) has been used to infer the sediment strength in open slope landslides (McAdoo et al., 2000) and landslides within submarine canyons (Green & Uken, 2008). Steeper scarps (e.g., GKS, BS; Figure 19.1b) presumably indicate sediment over-consolidation and higher dynamic strengths, in comparison to gentler scarp slopes that indicate normally consolidated and weaker material (e.g., VS; Figure 19.1b). The steeper headscarps of the GBR landslides are consistent with higher H/L (i.e., lower mobility) for the GKS, BS, and VS, which support a relationship among headscarp angle, sediment strength, and mobility of the landslides in the GBR. In the case of the RRS, located at the end of a canyon valley (Figure 19.2), this relationship is not straightforward as the headscarp height and its angle might have been modified by sediment gravity flows crossing the landslide scarp. Future research could focus on obtaining long sediment cores and performing slope stability simulations to gauge the impact of varying carbonate and siliciclastic lithologies on the stability, mobility, and disintegration of the GBR slope sediments.

19.5.3. Possible Preconditioning Factors and Triggers for Slope Instability in the GBR

Seismic activity, gas hydrate dissociation, storm and tsunami waves, high sedimentation rates, and excess pore pressure are considered the main triggers for submarine landslide generation (Canals et al., 2004; Masson et al., 2006). These processes were discussed by Puga-Bernabéu et al. (2017) for the GKS, but it was suggested that an unusually large seismic event (M_w 7.0) was the most likely trigger based on previous slope stability simulations (Puga-Bernabéu et al., 2013a). Gas hydrate dissociation by disturbance of the pressure-temperature regime may influence the static stable sediment conditions on the slope and lead to slope failures by modifying the sediment strength (Sultan et al., 2004). However, no definitive gas hydrates have so far been identified in Australian waters (Geoscience Australia and BREE, 2012); however, contribution by gas hydrates cannot be altogether dismissed and requires further research. Cyclically oscillating high pressure and low pressure on the seafloor sediments generated by large storms and tsunami waves have the potential to generate slope failures (Rogers &

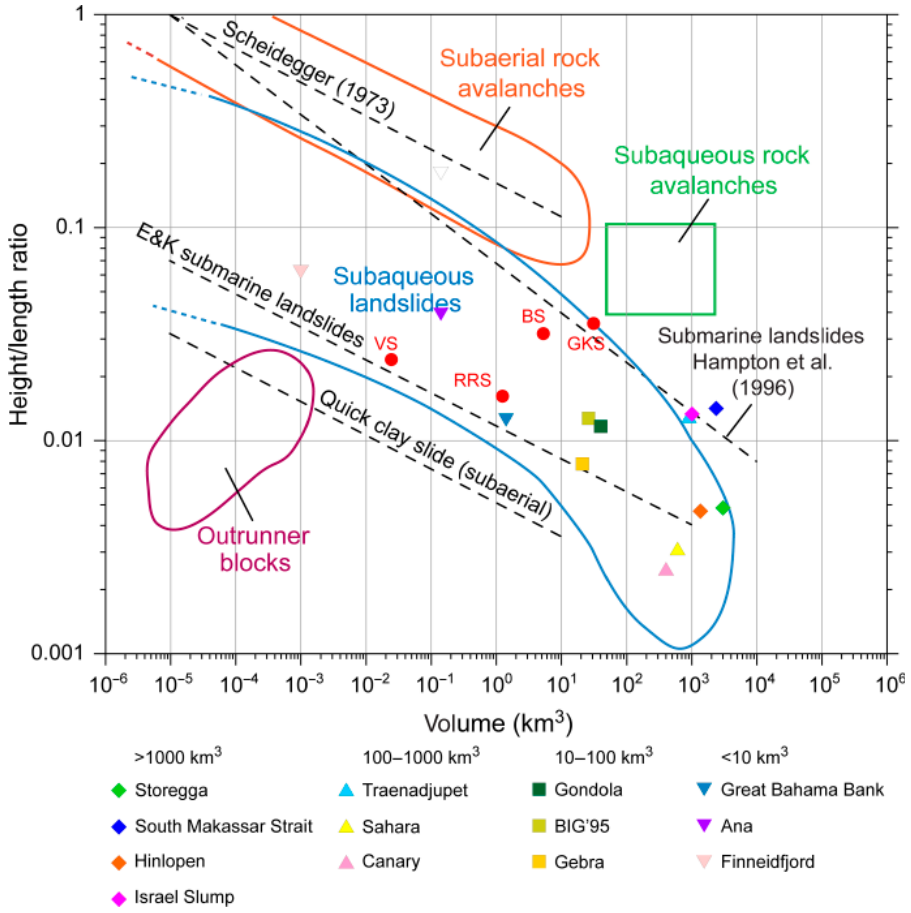


Figure 19.7 Mobility of submarine mass movements as a function of the height-length ratio versus volume of failed mass applied to the study GBR landslides (RRS, Ribbon Reef Slide; GKS, Gloria Knolls Slide; BS, Bowl Slide; VS, Viper Slide) and comparison with other well-known landslides from different tectonic settings and varying sizes (compiled from Canals et al., 2004; Frey Martínez et al., 2005; Vanneste et al., 2006; Georgiopoulou et al. 2010, Armandita et al., 2015; Dalla Valle et al., 2015; Schnyder et al., 2016). Curves from lower bound values for submarine landslides (Edgers & Karlsrud, 1982), subaerial quick clay slides (Edgers & Karlsrud, 1982), average values for subaerial landslides proposed by Scheidegger (1973), and upper bound for submarine landslides from Hampton et al. (1996) are plotted for reference. The colored envelopes are from De Blasio et al. (2006). (*See electronic version for color representation of this figure*)

Goodbred, 2010). The GBR margin is affected periodically by tropical cyclones (Puotinen, 2004), but only the headscarps of the VS and BS lie shallow enough to be affected by direct cyclone pumping, especially during low sea level. Therefore, ocean waves cannot be fully discarded as a triggering mechanism of upper slope failures in the GBR.

High sedimentation rates may trigger slope failures by creating high excess pore pressures in the sediment and/or by oversteepening (Dugan & Sheahan, 2012). Sedimentation rates on the GBR upper slope are relatively low (20–50 cm/ky; Dunbar et al., 2000) and, according to preliminary results from recent numerical simulations, are unlikely to generate overpressures (Urlaub et al., 2015). In the cases of the RRS and GKS, they also lack nearby large fluvial-deltaic systems that could increase such sedimentation rates. In contrast, the headscarp of the BS partially indents one the largest shelf-edge lobes of paleo-Burdekin river delta (Figure 19.4), and the VS is relatively close to the southernmost lobe of this delta, and it is situated next to shelf paleo-channels (Figure 19.5). High pore water pressure resulting from higher sedimentation rates close to this deltaic system, especially within low-permeability fine-grained sediments, could have promoted the generation of the VS and shallowest part of the BS, as found in other landslides linked to shelf-edge deltaic systems (Dalla Valle et al., 2013). In these conditions, a rapid sea level rise could promote transient excess pore pressures (Smith et al., 2013), which could be the case of the VS during the meltwater pulse 1A (Webster et al., 2016). Lateral fluid flow

within the sediments may also produce local excess pore pressure at the base of the slope, favoring slope failure (Dugan & Flemings, 2000), which may have contributed to the triggering of the deepwater GKS and RRS.

Among the preconditioning factors, the presence of weak layers within the sedimentary column is commonly invoked to explain submarine slope failures, but its role is still subject to debate (Locat et al., 2014; Wiemer & Kopf, 2015, 2017). Weak layers can form continuous horizons that may act as the slip plane for single or several slope failures (Lastras et al., 2006; Vardy et al., 2012) and can occur at different stratigraphic levels. The presence of potential weak layers cannot presently be confirmed as long sediment cores from the study landslides are unavailable. Using the only available long sediment cores in the study region, Puga-Bernabéu et al. (2017) showed that detachment surfaces of buried slumps found at Site 819 of ODP Leg 133 (~85 km north of the GKS; Figure 19.1a; Davies et al., 1991b) lie at similar depths to the secondary headscarp of the GKS. These detachment surfaces coincide with the boundary between multimeter-scale cycles of varying lithologies. The authors suggested that the presence of alternating carbonate and siliciclastic lithologies deposited during successive sea level cycles at different sedimentation rates on the mixed GBR margin might have generated weak layers within the sediment package. The secondary headscarp of the GKS and headscarp H1 of BS are at similar water depth (~600 m on average), and there is a similar matching between the VS headscarp and headscarp H1 of BS (~100–120 m). Additionally, headscarps of smaller landslides adjacent to the GKS and upper slope areas prone to failing (e.g., Noggin Block; Puga-Bernabéu et al., 2013a) are also coincident with the headscarp depths of the GKS (Figure 19.3b). In the absence of subsurface data, we cannot confirm the potential role of weak layers for slope failing in the GBR which needs future research, but our data suggest a potential geological control likely related with the depositional evolution of the GBR margin during the late Pleistocene.

19.5.4. Tsunami Capacity of the Gloria Knolls Slide

Given the uncertainties associated with estimating certain landslide parameters, four different GKS failure scenarios were considered (Table 19.1). Under each scenario, results suggest that landslides with similar dimensions and attributes to the GKS would be tsunamigenic (Table 19.1), posing a potential hazard to the northeastern Australian coast.

Results reflect the tsunami generation model's sensitivity to certain landslide parameters, which in turn affect the landslide's hazard potential. Failure depth is a key parameter. Of the two scenarios that produced the largest tsunamis, the Event 2 worst-case scenario containing the smaller landslide triggered the larger tsunami (Figure 19.6), as its failure depth was over 200 m shallower. This notwithstanding, the landslide in the Event 2 conservative scenario produced a significantly smaller tsunami than that of the Event 2 worst-case scenario, despite failing at a similar depth and having similar overall dimensions (Table 19.1). These results show the model's sensitivity to slide thickness, which is consistent with previous findings (Haugen et al., 2005; Løvholt et al., 2005; Brune et al., 2010). Indeed, the two largest tsunamis simulated in this study were produced by slides of comparably large thickness (329 and 288 m). Note that landslide thickness is particularly difficult to constrain and resolve in tsunami generation models, making this factor responsible for model uncertainty. Other parameters, such as slide width, failure orientation, and the gradient of the reconstructed failure surface, are held fairly consistent across scenarios in the present study. However, they are also not without uncertainty, and they would benefit from a more rigorous sensitivity analysis.

Despite the uncertainties inherent in modeling tsunamis of this nature, this work provides a valuable first assessment of the tsunamigenic capacity of the largest landslide on the GBR margin. The generative capacity of the GKS is sufficiently larger than other landslides considered in this region (Power et al., 2015; Webster et al., 2016). This tsunami generation behavior is consistent with that of supercritical landslides (Harbitz et al., 2006), which are favored by relatively shallow failures. Because waves propagate more slowly in shallow water, the initial tsunami remains over the landslide source for a longer duration, allowing for more effective dynamic building of the wave during the landslide's critical initial acceleration period (Watts et al., 2003). For deeper landslides, this effect is less pronounced, as the initial wave departs from the source area before the tsunami sufficiently builds (Harbitz et al., 2006). The shallow failure depth, along with the large thickness and volume (32 km^3) of the sediment mass involved in the GKS, renders it a potentially tsunamigenic landslide for this reason. Consequently, a substantial part of the coast would be impacted, according to our approach. We predict that other large landslides in the GBR region (e.g., BS) would produce tsunamis of similar magnitude under their respective worst-case scenarios. Nevertheless, due to model sensitivity to certain parameters, this hypothesis requires more robust, place-specific testing with ample consideration for the timing, frequency, and magnitude of such events.

In addition to the broader-scale bathymetric reef buffering effect noted by other researchers (Baba et al., 2008; Xing et al., 2015; Webster et al., 2016), we also highlight a finer-scale buffering effect of the structurally complex coral reef communities, which would have impacted the final run-up estimates (Kunkel et al., 2006). This finding

agrees with previous conclusions surrounding the protective benefit of the GBR against tsunamis (Baba et al., 2008; Xing et al., 2015; Webster et al., 2016).

This study feeds into the larger global efforts to understand the tsunami hazards posed by submarine landslides (Harbitz et al., 2014). In the GBR margin, the origins of large boulder deposits within the study area (Nott, 1997) remain unresolved. While storm surges remain a viable proposed mechanism of transport (Kortekaas & Dawson, 2007), the GKS, under present-day sea level conditions, could produce a tsunami of similar scale to the one posited by Nott (1997) in the assessment of boulder transport. However, linking specific deposits to this landslide, while important for model validation, would require a more detailed consideration of failure timing, eustatic sea level, and paleo-shoreline position (Webster et al., 2016). This lies beyond the scope of this study, but it is nonetheless a goal worthy of future investigation.

19.5.4.1. Model Limitations

Our approach is accompanied by a few critical limitations that must be acknowledged and considered by future investigators. Firstly, while the semiempirical formulations used to characterize the tsunami source greatly benefited from rigorous validation from experiments (Watts et al., 2005), the laboratory setup requires a substantial simplification of slide characteristics and their relation to key tsunami parameters. In particular, assumptions and extrapolations are made with regard to landslide rigidity, slope morphology, and failure trajectory downslope. Future work should aim to compare these formulations with different generation models. Of particular note are models that aim to resolve the dynamic displacement of the water column above a modeled slide body (Løvholt et al., 2005, 2018). Secondly, the present study could also benefit from a more rigorous examination of onshore inundation extent, where a nested grid approach would be implemented, as opposed to computing run-up estimates with the aforementioned run-up formula (see Section 19.3.2). Finally, a more detailed investigation of tsunami interaction with GBR reefs is recommended to improve the overall accuracy in estimating final run-ups. Models should ideally be run at spatial resolutions that are capable of resolving intricate tsunami behaviors (≤50 m), though this will come at a computational cost.

19.6. CONCLUSIONS

Our understanding of submarine landslides on mixed siliciclastic-carbonate continental margins is rapidly improving through the investigation of landslides on the GBR margin of northeastern Australia. Based on the most complete bathymetric and sub-bottom profile data sets available for the region, we describe four landslides that morphologically correspond to debris avalanches and translational slides. Gravitational spreading is reported for the first time in a mixed siliciclastic-carbonate margin. The mobility of the GBR landslides seems to be relatively independent of their size, which may be indicative of more consolidated sediments on the slopes. Slopes with uniform gradients favored progressive disintegration of failed material into smaller debris. In contrast, changes in slope favored the formation of pressure ridges at the landslide toe that prevented such size segregation. Dated landslides in the GBR contribute to the debate linking the frequency of major failure events and eustatic sea level changes. The largest (GKS) and the smallest (VS) landslides were triggered during the deglaciations corresponding to the transitions between MIS 12–11 and MIS 2, respectively. The GBR landslides are small (<32 km^3) compared with their counterparts in glaciated margins, but still large enough to generate potentially destructive tsunamis. Tsunami modeling suggests that the generative capacity of the GKS failure events is sufficiently large to generate high-amplitude wave(s) that would reach run-up heights of ~0.5–2 m along GBR coast under present-day sea level conditions and healthy reef growth. We anticipate that the risk of such slope failures is greatly reduced by the capacity of the GBR to dissipate the tsunami wave energy.

ACKNOWLEDGMENTS

We thank the Australian Hydrographic Office and Geoscience Australia for providing much of the source data used in the bathymetry data compilation. APB was supported by the Research Group RNM190 of the Junta de Andalucía (Spain). J.M.W. was supported by a grant from the Australian Research Council (grant DP1094001). A.T. was supported by the University of Sydney DBH Scholarship. The codes used for tsunami modeling, GeoWave and FUNWAVER-TVD, are available for download (http://appliedfluids.com/geowave.html; http://fengyanshi.github.io/build/html/index.html).

REFERENCES

Abbey, E., Webster, J. M., & Beaman, R. J. (2011). Geomorphology of submerged reefs on the shelf edge of the Great Barrier Reef: The influence of oscillating Pleistocene sea levels. *Marine Geology*, *288*(1–4), 61–78. https://doi.org/10.1016/j.margeo.2011.08.006

Abbey, E., Webster, J. M., Braga, J. C., Jacobsen, G. E., Thorogood, G., Thomas, A. L., et al. (2013). Deglacial mesophotic reef demise on the Great Barrier Reef. *Palaeogeography Palaeoclimatology Palaeoecology*, *392*, 473–494. https://doi.org/10.1016/j.palaeo.2013.09.032

Algar, S., Milton, C., Upshall, H., Roestenburg, J., & Crevello, P. (2011). Mass-transport deposits of the deepwater northwestern Borneo margin: Characterization from seismic-reflection, borehole, and core data with implications for hydrocarbon exploration and exploitation. In R. C. Shipp, P. Weimer, & H. W. Posamentier (Eds.), *Mass-transport deposits in deepwater settings, SEPM Special Publication* (Vol. 96, pp. 351–366). https://doi.org/10.2110/sepmsp.096.351

Alves, T. M., & Cartwright, J. A. (2009). Volume balance of a submarine landslide in the Espírito Santo Basin, offshore Brazil: Quantifying seafloor erosion, sediment accumulation and depletion. *Earth and Planetary Science Letters*, *288*(3–4), 572–580. https://doi.org/10.1016/j.epsl.2009.10.020

Armandita, C., Morley, C. K., & Rowell, P. (2015). Origin, structural geometry, and development of a giant coherent slide: The South Makassar Strait mass transport complex. *Geosphere*, *11*(2), 376–403. https://doi.org/10.1130/GES01077.1

Baba, T., Mleczko, R., Burbidge, D., Cummins, P. R., & Thio, H. K. (2008). The effect of the Great Barrier Reef on the propagation of the 2007 Solomon Islands tsunami recorded in northeastern Australia. In P. R. Cummins, K. Sakate, & L. S. L. Kong (Eds.), *Tsunami science four years after the 2004 Indian Ocean tsunami* (pp. 2003–2018). Basel, Switzerland: Birkhäuser. https://doi.org/10.1007/978-3-0346-0057-6_3

Beaman, R. J. (2010). Project 3D-GBR: A high-resolution depth model for the Great Barrier Reef and Coral Sea. *Marine and Tropical Sciences Research Facility* (Project 2.5i.1a Final Report, pp. 13 plus Appendix 1). Cairns, Australia: MTSRF. https://www.deepreef.org/bathymetry/65-3dgbr-bathy.html.

Belperio, A. P. (1983). Terrigenous sedimentation in the central Great Barrier Reef Lagoon: A model from the Burdekin region. *BMR Journal of Australian Geology & Geophysics*, *8*, 179–190. http://www.ga.gov.au/metadata-gateway/metadata/record/81147

Brune, S., Ladage, S., Babeyko, A. Y., Müller, C., Kopp, H., & Sobolev, S. V. (2010). Submarine landslides at the eastern Sunda margin: Observations and tsunami impact assessment. *Natural Hazards*, *54*(2), 547–562. https://doi.org/10.1007/s11069-009-9487-8

Bull, S., Cartwright, J., & Huuse, M. (2009). A review of kinematic indicators from mass transport complexes using 3D seismic data. *Marine and Petroleum Geology*, *26*(7), 1132–1151. https://doi.org/10.1016/j.marpetgeo.2008.09.011

Calvès, G., Huuse, M., Clift, P. D., & Brusset, S. (2015). Giant fossil mass wasting off the coast of West India: The Nataraja submarine slide. *Earth and Planetary Science Letters*, *432*, 265–272. https://doi.org/10.1016/j.epsl.2015.10.022

Canals, M., Lastras, G., Urgeles, R., Casamor, J. L., Mienert, J., Cattaneo, A., et al. (2004). Slope failure dynamics and impacts from seafloor and shallow sub-seafloor geophysical data: Case studies from the COSTA project. *Marine Geology*, *213*(1–4), 9–72. https://doi.org/10.1016/j.margeo.2004.10.001

Dalla Valle, G., Gamberi, F., Foglini, F., & Trincardi, F. (2015). The Gondola Slide: A mass transport complex controlled by margin topography (South-Western Adriatic Margin, Mediterranean Sea). *Marine Geology*, *366*, 97–113. https://doi.org/10.1016/j.margeo.2015.05.001

Dalla Valle, G., Gamberi, F., Rocchini, P., Minisini, D., Errera, A., Baglioni, L., & Trincardi, F. (2013). 3D seismic geomorphology of mass transport complexes in a foredeep basin: Examples from the Pleistocene of the Central Adriatic Basin (Mediterranean Sea). *Sedimentary Geology*, *294*, 127–141. https://doi.org/10.1016/j.sedgeo.2013.05.012

Dao, M. H., & Tkalich, P. (2007). Tsunami propagation modelling? A sensitivity study. *Natural Hazards and Earth System Science*, *7*(6), 741–754. https://doi.org/10.5194/nhess-7-741-2007

Davies, P. J., McKenzie, J. A., Palmer-Julson, A., et al. (1991a). *Proceedings of the ocean drilling program initial reports 133*. College Station, TX: Ocean Drilling Program. https://doi.org/10.2973/odp.proc.ir.133.1991

Davies, P. J., McKenzie, J. A., Palmer-Julson, A., et al. (1991b). *Proceedings of the ocean drilling program initial reports 133, Site 819* (pp. 451–508). College Station, TX: Ocean Drilling Program. https://doi.org/10.2973/odp.proc.ir.133.112.1991

Davies, P. J., Symonds, P. A., Feary, D. A., & Pigram, C. J. (1989). The evolution of the carbonate platforms of northeast Australia. In P. D. Crevello, J. L. Wilson, J. F. Sarg, J. F Read (Eds.), *Controls on carbonate platforms and basin development, SEPM Special Publication* (No. *44*, 233–258). Tulsa, OK: SEPM Society for Sedimentary Geology. https://doi.org/10.2110/pec.89.44.0233

De Blasio, F. V., Elverhøi, A., Engvik, L. E., Issler, D., Gauer, P., & Harbitz, C. (2006). Understanding the high mobility of subaqueous debris flows. *Norwegian Journal of Geology*, *86*, 275–284.

DiCaprio, L., Müller, R. D., & Gurnis, M. (2010). A dynamic process for drowning carbonate reefs on the northeastern Australian margin. *Geology*, *38*, 11–14. https://doi.org/10.1130/G30217.1

Dugan, B., & Flemings, P. B. (2000). Overpressure and fluid flow in the New Jersey continental slope: implications for slope failure and cold seeps. *Science*, *289*, 288–291. https://doi.org/10.1126/science.289.5477.288

Dugan, B., & Sheahan, T. C. (2012). Offshore sediment overpressures of passive margins: Mechanisms, measurement, and models. *Review of Geophysics*, *50*(3), RG3001. https://doi.org/10.1029/2011RG000379

Dunbar, G. B., & Dickens, G. R. (2003). Massive siliciclastic discharge to slopes of the Great Barrier Reef platform during sea level transgression; constraints from sediment cores between 15°S and 16°S latitude and possible explanations. *Sedimentary Geology*, *162*(1–2), 141–158. https://doi.org/10.1016/S0037-0738(03)00216-1

Dunbar, G. B., Dickens, G. R., & Carter, R. M. (2000). Sediment flux across the Great Barrier Reef shelf to the Queensland Trough over the last 300,000 years. *Sedimentary Geology*, *133*(1–2),49–92.https://doi.org/10.1016/S0037-0738(00)00027-0

Edgers, L., & Karlsrud, K. (1982). Soil flows generated by submarine slides: Case studies and consequences. In C. Chryssostomomidis & J. J. Connor (Eds.), *Proceedings of the third international conference on the behavior of offshore structures* (Vol. 2, pp. 425–437). Bristol, PA: Hemisphere Publications.

Ferrario, F., Beck, M. W., Storlazzi, C. D., Micheli, F., Shepard, C. C., & Airoldi, L. (2014). The effectiveness of coral reefs for coastal hazard risk reduction and adaptation. *Nature Communications*, *5*, 3794. https://doi.org/10.1038/ncomms4794

Fielding, C.R., Trueman, J.D., Dickens, G.R., & Page, M. (2003). Anatomy of the buried Burdekin River channel across the Great Barrier Reef shelf: How does a major river operate on a tropical mixed siliciclastic/carbonate margin during sea-level lowstand? *Sedimentary Geology*, *157*, 291–301. https://doi.org/10.1016/S0037-0738(02)00238-5

Fine, I. V., Rabinovich, A. B., Bornhold, B. D., Thomson, R. E., & Kulikov, E. A. (2005). The Grand Banks landslide-generated tsunami of November 18, 1929: Preliminary analysis and numerical modeling. *Marine Geology*, *215*(1–2), 45–57. https://doi.org/10.1016/j.margeo.2004.11.007

Francis, J. M., Dunbar, G. B., Dickens, G. R., Sutherland, I. A., & Droxler, A. W. (2007). Siliciclastic sediment across the North Queensland margin (Australia): A Holocene perspective on reciprocal versus coeval deposition in tropical mixed siliciclastic-carbonate systems. *Journal of Sedimentary Research*, *77*(7), 572–586. https://doi.org/10.2110/jsr.2007.057

Freire, F., Gyllencreutz, R., Jafri, R. U., & Jakobsson, M. (2014). Acoustic evidence of a submarine slide in the deepest part of the Arctic, the Molloy Hole. *Geo-Marine Letters*, *34*(4), 315–325. https://doi.org/10.1007/s00367-014-0371-5

Frey-Martinez, J., Cartwright, J., & Hall, B. (2005). 3D seismic interpretation of slump complexes: Examples from the continental margin of Israel. *Basin Research*, *17*(1), 83–108. https://doi.org/10.1111/j.1365-2117.2005.00255.x

Gaina, C., Müller, R. D., Royer, J., & Symonds, P. (1999). Evolution of the Louisiade triple junction. *Journal of Geophysical Research*, *104*(B6), 12927–12939. https://doi.org/10.1029/1999JB900038

Gallop, S. L., Young, I. R., Ranasinghe, R., Durrant, T. H., & Haigh, I. D. (2014). The large-scale influence of the Great Barrier Reef matrix on wave attenuation. *Coral Reefs*, *33*(4), 1167–1178. https://doi.org/10.1007/s00338-014-1205-7

Georgiopoulou, A., Masson, D. G., Wynn, R. B., & Krastel, S. (2010). Sahara Slide: Age, initiation, and processes of a giant submarine slide. *Geochemistry, Geophysics, Geosystems*, *11*(7), Q07014. https://doi.org/10.1029/2010GC003066

Georgiopoulou, A., Wynn, R. B., Masson, D. G., & Frenz, M. (2009). Linked turbidite–debrite resulting from recent Sahara Slide headwall reactivation. *Marine and Petroleum Geology*, *26*(10), 2021–2031. https://doi.org/10.1016/j.marpetgeo.2009.02.013

Geoscience Australia, BREE (2012). *Australian gas resource assessment 2012* (pp. 1–68). Canberra, Australia: Geoscience Australia. https://industry.gov.au/Office-of-the-Chief-Economist/Publications/Pages/Australian-gas-resource-assessment.aspx

Green, A., & Uken, R. (2008). Submarine landsliding and canyon evolution on the northern KwaZulu-Natal continental shelf, South Africa, SW Indian Ocean. *Marine Geology*, *254*(3–4), 152–170. https://doi.org/10.1016/j.margeo.2008.06.001

Haflidason, H., Sejrup, H. P., Nygard, A., Mienert, J., Bryn, P., Lien, R., et al. (2004). The Storegga Slide: Architecture, geometry and slide development. *Marine Geology*, *213*(1–4), 201–234. https://doi.org/10.1016/j.margeo.2004.10.007

Hampton, M. A., Lee, H. J., & Locat, J. (1996). Submarine landslides. *Review of Geophysics*, *34*(1), 33–59. https://doi.org/10.1029/95RG03287

Haq, B. U. (1998). Natural gas hydrates: Searching the long-term climatic and slope stability records. In J.-P. Henriet & J. Meinert (Eds.), *Gas hydrates: Relevance to world margin stability and climate change, Geological Society, Special Publications* (Vol. 137, pp. 303–318). London: Geological Society.

Harbitz, C. B., Løvholt, F., & Bungum, H. (2014). Submarine landslide tsunamis: How extreme and how likely? *Natural Hazards*, *72*, 1341–1374. https://doi.org/10.1007/s11069-013-0681-3

Harbitz, C. B., Løvholt, F., Pedersen, G., & Masson, D. G. (2006). Mechanisms of tsunami generation by submarine landslides: A short review. *Norwegian Journal of Geology*, *86*, 255–264.

Harders, R., Ranero, C., Weinrebe, W., & Behrmann, J. H. (2011). Submarine slope failures along the convergent continental margin of the Middle America Trench. *Geochemistry, Geophysics, Geosystem*, *12*(6), Q05S32. https://doi.org/10.1029/2010GC003401

Harris, D. L., Rovere, A., Casella, E., Power, H., Canavesio, R., Collin, A., et al. (2018). Coral reef structural complexity provides important coastal protection from waves under rising sea levels. *Science Advances*, *4*(2), eaao4350. https://doi.org/10.1126/sciadv.aao4350

Harris, P. T., Davies, P. J., & Marshall, J. F. (1990). Late Quaternary sedimentation on the Great Barrier Reef continental shelf and slope east of Townsville, Australia. *Marine Geology*, *94*(1–2), 55–77. https://doi.org/10.1016/0025-3227(90)90103-Q

Haugen, K. B., Løvholt, F., & Harbitz, C. B. (2005). Fundamental mechanisms for tsunami generation by submarine mass flows in idealised geometries. In A. Solheim, P. Bryn, K. Berg, & J. Mienert (Eds.), *Ormen Lange: An integrated study for safe field development in the Storegga Submarine area* (pp. 209–217). Amsterdam, The Netherlands: Elsevier. https://doi.org/10.1016/B978-0-08-044694-3.50022-6

Hill, J. C., Brothers, D. S., Craig, B. K., ten Brink, Y. S., Chaytor, J. D., & Flores, C. H. (2017). Geologic controls on submarine slope failure along the central U.S. Atlantic margin: Insights from the Currituck Slide Complex. *Marine Geology*, *385*, 114–130. https://doi.org/10.1016/j.margeo.2016.10.007

Hill, K. C., & Hall, R. (2002). Mesozoic-Cenozoic evolution of Australia's New Guinea margin in a west Pacific context. In R. R. Hillis & R. D. Müller (Eds.), *Special papers: Geological Society of America* (Vol. 372, pp. 265–290). Boulder, CO: Geological Society of America. https://doi.org/10.1130/0-8137-2372-8.265

Hine, A. C., Locker, S. D., Tedesco, L. P., Mullins, H. T., Hallock, P., Belknap, D. F., et al. (1992). Megabreccia shedding from modern, low-relief carbonate platforms, Nicaraguan Rise. *Geological Society of America Bulletin*, *104*(8), 928–943. https://doi.org/10.1130/0016-7606(1992)104<0928:MSFMLR>2.3.CO;2

Hinestrosa, G., Webster, J. M., Beaman, R. J., & Anderson, L. M. (2014). Seismic stratigraphy and development of the shelf-edge reefs of the Great Barrier Reef, Australia. *Marine Geology*, *353*, 1–20. https://doi.org/10.1016/j.margeo.2014.03.016

Hjelstuen, B. O., Eldholm, O., & Faleide, J. I. (2007). Recurrent Pleistocene mega-failures on the SW Barents Sea margin. *Earth and Planetary Science Letters*, *258*(3–4), 605–618. https://doi.org/10.1016/j.epsl.2007.04.025

Hogan, K. A., Dowdeswell, J. A., & Mienert, J. (2013). New insights into slide processes and seafloor geology revealed by side-scan imagery of the massive Hinlopen Slide, Arctic

Ocean margin. *Geo-Marine Letters*, *33*(5), 325–343. https://doi.org/10.1007/s00367-013-0330-6

Hopley, D., Smithers, S. G., & Parnell, K. E. (2007). *The Geomorphology of the Great Barrier Reef: Development, diversity, and change*. Cambridge, MA, Cambridge University Pres. https://doi.org/10.1017/CBO9780511535543

Humblet, M., & Webster, J. M. (2017). Coral community changes in the Great Barrier Reef in response to major environmental changes over glacial-interglacial timescales. *Palaeogeography, Palaeoclimatology, Palaeoecology*, *472*, 216–235. https://doi.org/10.1016/j.palaeo.2017.02.003

Iglesias, O., Lastras, G., Canals, M., Olabarrieta, M., González, M., Aniel-Quiroga, I., et al. (2012). The BIG'95 submarine landslide–generated tsunami: A numerical simulation. *Journal of Geology*, *120*(1), 31–48. https://doi.org/10.1086/662718

Ioualalen, M., Migeon, S., & Sardoux, O. (2010). Landslide tsunami vulnerability in the Ligurian Sea: Case study of the 1979 October 16 Nice international airport submarine landslide and of identified geological mass failures. *Geophysical Journal International*, *181*(2), 724–740. https://doi.org/10.1111/j.1365-246X.2010.04572.x

Iribarren, L., Vergés, J., Camurri, F., Fullea, J., & Fernàndez, M. (2007). The structure of the Atlantic–Mediterranean transition zone from the Alboran Sea to the Horseshoe Abyssal Plain (Iberia–Africa plate boundary). *Marine Geology*, *243*(1–4), 97–119. https://doi.org/10.1016/j.margeo.2007.05.011

Joanne, C., Collot, J.-Y., Lamarche, G., & Migeon, S. (2010). Continental slope reconstruction after a giant mass failure, the example of the Matakaoa Margin, New Zealand. *Marine Geology*, *268*(1–4), 67–84. https://doi.org/10.1016/j.margeo.2009.10.013

Johnson, D. P., & Searle, D. E. (1984). Post-glacial stratigraphy, central Great Barrier Reef, Australia. *Sedimentology*, *31*(3), 335–352. https://doi.org/10.1111/j.1365-3091.1984.tb00863.x

Kortekaas, S., & Dawson, A. G. (2007). Distinguishing tsunami and storm deposits: An example from Martinhal, SW Portugal. *Sedimentary Geology*, *200*(3–4), 208–221. https://doi.org/10.1016/j.sedgeo.2007.01.004

Korup, O. (2012). Earth's portfolio of extreme sediment transport events. *Earth Science Reviews*, *112*(3–4), 115–125. https://doi.org/10.1016/j.earscirev.2012.02.006

Kunkel, C. M., Hallberg, R. W., & Oppenheimer, M. (2006). Coral reefs reduce tsunami impact in model simulations. *Geophysical Research Letters*, *33*(23), L23612. https://doi.org/10.1029/2006GL027892

Laberg, J. S., & Vorren, T. O. (2000). The Traenadjupet Slide, offshore Norway Ð morphology, evacuation and triggering mechanisms. *Marine Geology*, *171*(1–4), 95–114. https://doi.org/10.1016/S0025-3227(00)00112-2

Lastras, G., Canals, M., Amblas, D., Ivanov, M., Dennielou, B., Droz, L., et al. (2006). Eivissa slides, western Mediterranean Sea: Morphology and processes. *Geo-Marine Letters*, *26*, 225–233. https://doi.org/10.1007/s00367-006-0032-4

Lastras, G., Canals, M., Urgeles, R., De Batist, M., Calafat, A. M., & Casamar, J. L. (2004). Characterisation of a recent debris flow deposit on the Ebro margin, Western Mediterranean Sea, after a variety of seismic reflection data. *Marine Geology*, *231*(1–4), 235–255. https://doi.org/10.1016/j.margeo.2004.10.008

Li, W., Alves, T. M., Urlaub, M., Georgiopoulou, A., Klaucke, I., Wynn, R. B., et al. (2017). Morphology, age and sediment dynamics of the upper headwall of the Sahara Slide Complex, Northwest Africa: Evidence for a large Late Holocene failure. *Marine Geology*, *393*, 109–123. https://doi.org/10.1016/j.margeo.2016.11.013

Locat, J., S. Leroueil, A. Locat, & H. J. Lee (2014). Weak layers: Their definition and classification from a geotechnical perspective. In S. Krastel, J.-H. Behrmann, D. Vølker, M. Stipp, C. Berndt, R. Urgeles, et al. (Eds.), *Submarine mass movements and their consequences, Advances in Natural Hazard Research* (Vol. 37, pp. 3–21). Switzerland: Springer International. https://doi.org/10.1007/978-3-319-00972-8 1

Løvholt, F., Harbitz, C. B., & Haugen, K. B. (2005). A parametric study of tsunamis generated by submarine slides in the Ormen Lange/Storegga area off western Norway. In A. Solheim, P. Bryn, K. Berg, & J. Mienert (Eds.), *Ormen Lange: An integrated study for safe field development in the Storegga Submarine area* (pp. 219–231). Amsterdam, The Netherlands: Elsevier. https://doi.org/10.1016/B978-0-08-044694-3.50023-8

Løvholt, F., Schulten, I., Mosher, D., Harbitz, C., & Krastel, S. (2018). Modelling the 1929 Grand Banks slump and landslide tsunami. In D. G. Lintern, D. C. Mosher, L. G. Moscardelli, P. T. Bobrowsky, C. Campbell, J. D. Chaytor, et al. (Eds.), *Subaqueous mass movements and their consequences: Assessing geohazards, environmental implications and economic significance of subaqueous landslides, Geological Society, Special Publications* (Vol. 477). London: Geological Society. https://doi.org/10.1144/SP477.28

Maslim, M., Owen, M., Day, S., & Long, D. (2004). Linking continental-slope failures and climate change: Testing the clathrate gun hypothesis. *Geology*, *32*(1), 53–56. https://doi.org/10.1130/G20114.1

Maslin, M., Owen, M., Betts, R., Day, S., & Dunkley Jones, T. (2010). Gas hydrates: Past and future geohazard? *Philosophical Transactions of the Royal Society A*, *368*(2), 2369–2393. https://doi.org/10.1098/rsta.2010.0065

Masson, D. G., Harbitz, C. B., Wynn, R. B., Pedersen, G., & Lovholt, F. (2006). Submarine landslides: Processes, triggers and hazard prediction. *Philosophical Transactions of the Royal Society A: Physical, Mathematical and Engineering Sciences*, *364*(1845), 2009–2039. https://doi.org/10.1098/rsta.2006.1810

Mathews, E. J., Heap, A. D., & Woods, M. (2007). *Inter-reefal seabed sediments and geomorphology of the Great Barrier Reef, a spatial analysis* (Record 2007/09, pp. 1–140). Canberra, Australia: Geoscience Australia. https://data.gov.au/dataset/inter-reefal-seabed-sediments-and-geomorphology-of-the-great-barrier-reef-a-spatial-analysis

Mazzanti, P., & De Blasio, F. V. (2010). Peculiar morphologies of subaqueous landslide deposits and their relationship to flow dynamics. In D. C. Mosher, R. C. Shipp, L. Moscardelli, J. D. Chaytor, C. D. P. Baxter, J. L. Lee, & R. Urgeles (Eds.), *Submarine mass movements and their consequences, Advances in Natural and Technological Hazards Research* (Vol. 28, pp. 141–151). Switzerland: Springer International. https://doi.org/10.1007/978-90-481-3071-9

McAdoo, B. G., Pratson, L. F., & Orange, D. L. (2000). Submarine landslide geomorphology, US continental slope.

Marine Geology, *169*(1–2), 103–136. https://doi.org/10.1016/S0025-3227(00)00050-5

Micallef, A., Masson, D. G., Berndt, C., & Stow, D. A. V. (2007). Morphology and mechanics of submarine spreading: a case study from the Storegga Slide. *Journal Geophysical Research, Earth Surface*, *112*(F3), F03023. https://doi.org/10.1029/2006JF000739

Moernaut, J., & De Batist, M. (2011). Frontal emplacement and mobility of sublacustrine landslides: Results from morphometric and seismostratigraphic analysis. *Marine Geology*, *285*(1–4),29–45.https://doi.org/10.1016/j.margeo.2011.05.001

Moscardelli, L., & Wood, L. (2016). Morphometry of mass-transport deposits as a predictive tool. *Geological Society of America Bulletin*, *128*(1–2), 47–80. https://doi.org/10.1130/B31221.1

Mulder, T., & Cochonat, P. (1996). Classification of offshore mass movements. *Journal of Sedimentary Research*, *66*(1), 43–57. https://doi.org/10.1306/D42682AC-2B26-11D7-8648000102C1865D

Nelson, R. C. (1996). Hydraulic roughness of coral reef platforms. *Applied Ocean Research*, *18*(5), 265–274. https://doi.org/10.1016/S0141-1187(97)00006-0

Normark, W. R., McGann, M., & Sliter, R. (2004). Age of Palos Verdes submarine debris avalanche, southern California. *Marine Geology*, *203*(3–4), 247–259. https://doi.org/10.1016/S0025-3227(03)00308-6

Nott, J. (1997). Extremely high-energy wave deposits inside the Great Barrier Reef, Australia: Determining the cause—tsunami or tropical cyclone. *Marine Geology*, *141*(1–4), 193–207. https://doi.org/10.1016/S0025-3227(97)00063-7

Okal, E. A., & Synolakis, C. E. (2003). A theoretical comparison of tsunamis from dislocations and landslides. *Pure and Applied Geophysics*, *160*(10–11), 2177–2188. https://doi.org/10.1007/s00024-003-2425-x

Owen, M., Day, S., & Maslin, M. (2007). Late Pleistocene submarine mass movements: Occurrence and causes. *Quaternary Science Reviews*, *26*(7–8), 958–978. https://doi.org/10.1016/j.quascirev.2006.12.011

Page, M. C., & Dickens, G. R. (2005). Sediment fluxes to Marion Plateau (southern Great barrier Reef province) over the last 130 ky: New constraints on "transgressive shedding" off northeastern Australia. *Marine Geology*, *219*(1), 27–45. https://doi.org/10.1016/j.margeo.2005.05.002

Piper, D. J. W., Cochonat, P., & Morrison, M. L. (1999). The sequence of events around the epicentre of the 1929 Grand Banks earthquake: Initiation of debris flows and turbidity current inferred from sidescan sonar. *Sedimentology*, *46*(1), 79–97. https://doi.org/10.1046/j.1365s-3091.1999.00204.x

Power, H. E., Clarke, S. L., Wilson, O., & Hubble, T. T. (2015). Tsunami hazard from submarine landslides: 3D inundation modelling in New South Wales, Australia. Paper presented at Australasian Coasts & Ports Conference 2015: 22nd Australasian Coastal and Ocean Engineering Conference and the 15th Australasian Port and Harbour Conference, Engineers Australia and IPENZ (p. 696).

Principaud, M., Mulder, T., Gillet, H., & Borgomano, J. (2015). Large-scale carbonate submarine mass-wasting along the northwestern slope of the Great Bahama Bank (Bahamas): Morphology, architecture, and mechanisms. *Sedimentary Geology*, *317*, 27–42.

Puga-Bernabéu, Á., Beaman, R. J., Webster, J. M., Thomas, A. L., & Jacobsen, G. (2017). Gloria Knolls Slide: A prominent submarine landslide complex on the Great Barrier Reef margin of north-eastern Australia. *Marine Geology*, *385*, 68–83. https://doi.org/10.1016/j.margeo.2016.12.008

Puga-Bernabéu, Á., Webster, J. M., & Beaman, R. J. (2013a). Potential collapse of the upper slope and tsunami generation on the Great Barrier Reef margin, north-eastern Australia. *Natural Hazards*, *66*(2), 557–575. https://doi.org/10.1007/s11069-012-0502-0

Puga-Bernabéu, Á., Webster, J. M., Beaman, R. J., & Guilbaud, V. (2011). Morphology and controls on the evolution of a mixed carbonate-siliciclastic submarine canyon system, Great Barrier Reef margin, north-eastern Australia. *Marine Geology*, *289*(1–4), 100–116. https://doi.org/10.1016/j.margeo.2011.09.013

Puga-Bernabéu, Á., Webster, J. M., Beaman, R. J., & Guilbaud, V. (2013b). Variation in canyon morphology on the Great Barrier Reef margin, north-eastern Australia: The influence of slope and barrier reefs. *Geomorphology*, *191*, 35–50. https://doi.org/10.1016/j.geomorph.2013.03.001

Puga-Bernabéu, Á., Webster, J. M., Beaman, R. J., Reimer, P. J., & Renema, W. (2014). Filling the gap: A 60 ky record of mixed carbonate-siliciclastic turbidite deposition from the Great Barrier Reef. *Marine and Petroleum Geology*, *50*, 40–50. https://doi.org/10.1016/j.marpetgeo.2013.11.009

Puotinen, M. (2004). Mapping tropical cyclone disturbance of the Great Barrier Reef. *The Globe*, *55*, 31–41. http://ro.uow.edu.au/smhpapers/2025

Quin, Y., Alves, T. M., Constantine, J., & Gamboa, D. (2017). The role of mass wasting in the progressive development of submarine channels (Espírito Santo Basin, SE Brazil). *Journal of Sedimentary Research*, *87*(5), 500–516. https://doi.org/10.2110/jsr.2017.18

Rogers, K. G., & Goodbred, S. L., Jr. (2010). Mass failures associated with the passage of a large tropical cyclone over the Swatch of No Ground submarine canyon (Bay of Bengal). *Geology*, *38*(11), 1051–1054. https://doi.org/10.1130/G31181.1

Rosman, J. H., & Hench, J. L. (2011). A framework for understanding drag parameterizations for coral reefs. *Journal of Geophysical Research: Oceans*, *116*(C8), C08025. https://doi.org/10.1029/2010JC006892

Savini, A., Marchese, F., Verdicchio, G., & Vertino, A. (2016). Submarine slide topography and the distribution of vulnerable marine ecosystems: A case study in the Ionian Sea (Eastern Mediterranean). In G. Lamarche, J. Mountjoy, S. Bull, T. Hubble, S. Krastel, E. Lane, et al. (Eds.), *Submarine mass movements and their consequences, Advances in Natural and Technological Hazards Research* (Vol. 41, pp. 163–170). Switzerland: Springer International.

Scheidegger, A. E. (1973). On the prediction of the reach and velocity of catastrophic landslides. *Rock Mechanics*, *5*(4), 231–236. https://doi.org/10.1007/BF01301796

Schnyder, J. S. D., Eberli, G., Kirby, J. T., Shi, F., Tehranirad, B., Mulder, T., et al. (2016). Tsunamis caused by submarine slope failures along western Great Bahama Bank. *Scientific Reports*, *6*, 35925. https://doi.org/10.1038/srep35925

Shi, F., Kirby, J. T., Harris, J. C., Geiman, J. D., & Grilli, S. T. (2012). A high-order adaptive time-stepping TVD solver for Boussinesq modeling of breaking waves and coastal inundation. *Ocean Modelling*, *43*, 36–51. https://doi.org/10.1016/j.ocemod.2011.12.004

Skempton, A. W., & Hutchinson, J. N. (1969). Stability of natural slopes and embankment foundations. State-of-the-art report. Paper Presented at the 7th International Conference on Soil Mechanics Foundation Engineering, Mexico City, Mexico.

Smith, D. E., Harrison, S., & Jordan, T. (2013). Sea-level rise and submarine mass failures on open continental margins. *Quaternary Science Reviews*, *82*, 93–103. https://doi.org/10.1016/j.quascirev.2013.10.012

Smoot, C., & King, R. W. (1993). Three-dimensional secondary surface geomorphology of submarine landslides on northwest Pacific plate guyots. *Geomorphology*, *6*(2), 151–174. https://doi.org/10.1016/0169-555X(93)90044-3

Solheim, A., Berg, K., Forsberg, C. F., & Bryn, P. (2005). The Storegga Slide complex: Repetitive large scale sliding with similar cause and development. *Marine and Petroleum Geology*, *22*(1–2), 97–107. https://doi.org/10.1016/j.marpetgeo.2004.10.013

Sultan, N., Cochonat, P., Foucher, J.-P., & Mienert, J. (2004). Effect of gas hydrates melting on seafloor slope instability. *Marine Geology*, *213*(1–4), 379–401. https://doi.org/10.1016/j.margeo.2004.10.015

Symonds, P. A., Davies, P. J., & Parisi, A. (1983). Structure and stratigraphy of the central Great Barrier Reef. *BMR Journal of Australian Geology and Geophysics*, *8*, 277–291. https://data.gov.au/dataset/dd16893e-b5d1-4994-bb75-1ab954a0206f

Talling, P. J., Wynn, R. B., Masson, D. G., Frenz, M., Cronin, B. T., Schiebel, R., et al. (2007). Onset of submarine debris flow deposition far from original giant landslide. *Nature*, *450*, 541–544. https://doi.org/10.1038/nature06313

Taylor, L. W. H., & Falvey, D. A. (1977). Queensland Plateau and Coral Sea Basin: Stratigraphy, structure and tectonics. *The APEA Journal*, *17*(1), 13–29. https://doi.org/10.1071/AJ76002

Tehranirad, B., Harris, J. C., Grilli, A. R., Grilli, S. T., Abadie, S., Kirby, J. T., & Shi, F. (2015). Far-field tsunami threat in the north Atlantic basin from large scale flank collapses of the Cumbre Vieja volcano, La Palma. *Pure and Applied Geophysics*, *172*(15), 3589. https://doi.org/10.1007/s00024-015-1135-5

Ten Brink, U. S., Geist, E. L., & Andrews, B. D. (2006). Size and distribution of submarine landslides and its implications to tsunami hazard in Puerto Rico. *Geophysical Research Letters*, *33*(11), L11307. https://doi.org/10.1029/2006GL026125

Tilbrook, B., & Matear, R. (2009). Carbon chemistry of the Great Barrier Reef. In *CSIRO voyage summary SS09/2008* (pp. 1–17). Hobart, Australia: CSIRO Marine National Facility. http://www.cmar.csiro.au/datacentre/process/data_files/cruise_docs/SS200809sum.pdf

Twichell, D. C., Chaytor, J. D., ten Brink, U. S., & Buczkowski, B. (2009). Morphology of late Quaternary submarine landslides along the U.S. Atlantic continental margin. *Marine Geology*, *264*(1–2), 4–15. https://doi.org/10.1016/j.margeo.2009.01.009

Urlaub, M., Talling, P. J., & Masson, D. G. (2013). Timing and frequency of large submarine landslides: Implications for understanding triggers and future geohazard. *Quaternary Science Reviews*, *72*, 63–82. https://doi.org/10.1016/j.quascirev.2013.04.020

Urlaub, M., Talling, P. T., Zervos, A., & Masson, D. (2015). What causes large submarine landslides on low gradient (<2∘) continental slopes with slow (∼ 0.15 m/kyr) sediment accumulation? *Journal of Geophysical Research Solid Earth*, *120*(10), 6722–6739. https://doi.org/10.1002/2015JB012347

Vanneste, M., Mienert, J., & Bünz, S. (2006). The Hinlopen Slide: A giant, submarine slope failure on the north Svalbard margin, Artic Ocean. *Earth and Planetary Science Letters*, *245*(1–2), 373–388. https://doi.org/10.1016/j.epsl.2006.02.045

Vardy, M. E., L'Heureux, J. S., Vanneste, M., Longva, O., Steiner, A., Forsberg, C. F., et al. (2012). Multidisciplinary investigation of a shallow near-shore landslide, Finneidfjord, Norway. *Near Surface Geophysics*, *10*(4), 267–277. https://doi.org/10.3997/1873-2012022

Völker, D. J. (2010). A simple and efficient GIS tool for volume calculations of submarine landslides. *Geo-Marine Letters*, *30*(5), 541–547. https://doi.org/10.1007/s00367-009-0176-0

Ward, S. N., & Asphaug, E. (2003). Asteroid impact tsunami of 2880 March 16. *Geophysical Journal International*, *153*(3), F6–F10. https://doi.org/10.1046/j.1365-246X.2003.01944.x

Waters, D. K., Carroll, C., Ellis, R., Hateley, L., McCloskey, G. L., Packett, R., et al. (2014). Modelling reductions of pollutant loads due to improved management practices in the Great Barrier Reef catchments. In *Whole of GBR* (Technical Report 1). Toowoomba, QLD: Queensland Department of Natural Resources and Mines.

Watts, K. F., Varga, L. L., & Feary, D. A. (1993). Origins, timing, and implications of Miocene to Pleistocene turbidites, debris flows, and slump deposits of the Queensland Trough, northeastern Australia (Site 823). In J. A. McKenzie, P. J. Davies, A. Palmer-Julson, & J. F. Sarg (Eds.), *Proceedings of the ocean drilling program, Scientific Results Ocean Drilling Program* (Vol. 133, pp. 379–445). College Station, TX: Ocean Drilling Program. https://doi.org/10.2973/odp.proc.sr.133.248.1993

Watts, P., Grilli, S. T., Kirby, J. T., Fryer, G. J., & Tappin, D. R. (2003). Landslide tsunami case studies using a Boussinesq model and a fully nonlinear tsunami generation model. *Natural Hazards and Earth System Science*, *3*(5), 391–402. https://doi.org/10.5194/nhess-3-391-2003

Watts, P., Grilli, S. T., Tappin, D. R., & Fryer, G. J. (2005). Tsunami generation by submarine mass failure. II: Predictive equations and case studies. *Journal of Waterway Port Coastal and Ocean Engineering*, *131*(6), 298–310. https://doi.org/10.1061/(ASCE)0733-950X(2005)

Webster, J. M., Beaman, R. J., Puga-Bernabéu, Á., Ludman, D., Renema, W., Wust, R. A. J., et al. (2012). Late Pleistocene history of turbidite sedimentation in a submarine canyon off the northern Great Barrier Reef, Australia. *Palaeogeography, Palaeoclimatology, Palaeoecology*, *331–332*, 75–89. https://doi.org/10.1061/(ASCE)0733-950X(2005)131:6(298)

Webster, J. M., Davies, P. J., Beaman, R. J., Williams, S., & Byrne, M. (2008). Evolution of drowned shelf edge reefs in the GBR; implications for understanding abrupt climate change, coral reef response and modern deep water benthic habitats. In *CSIRO voyage summary SS07/2007* (pp. 1–18).

Hobart, Australia: CSIRO Marine National Facility. http://mnf.csiro.au/~/media/Files/Voyage-plans-and-summaries/Southern-Surveyor/Voyage%20plans-summaries/2007/VOYAGE%20SUMMARY%20SS07-07.ashx

Webster, J. M., George, N. P. J., Beaman, R. J., Hill, J., Puga-Bernabéu, Á., Hinestrosa, G., et al. (2016). Submarine landslides on the Great Barrier Reef shelf edge and upper slope: A mechanism for generating tsunamis on the north-east Australian coast? *Marine Geology*, *371*, 120–129. https://doi.org/10.1016/j.margeo.2015.11.008

Wiemer, G., & Kopf, A. (2015). Altered marine tephra deposits as potential slope failure planes? *Geo-Marine Letters*, *35*(4), 305–314. https://doi.org/10.1007/s00367-015-0408-4

Wiemer, G., & Kopf, A. (2017). Influence of diatom microfossils on sediment shear strength and slope stability. *Geochemistry, Geophysics, Geosystems*, *18*(1), 333–345. https://doi.org/10.1002/2016GC006568

Winkelmann, D., Jokat, W., Niessen, F., Stein, R., & Winkler, A. (2006). Age and extent of the Yermak Slide north of Spitsbergen, Arctic Ocean. *Geochemistry, Geophysics, Geosystems*, *7*(6), Q06007. https://doi.org/10.1029/2005GC001130

Xing, H. L., Ding, R. W., & Yuen, D. A. (2015). Tsunami hazards along the Eastern Australian Coast from potential earthquakes: Results from numerical simulations. *Pure and Applied Geophysics*, *172*(8), 2087–2115. https://doi.org/10.1007/s00024-014-0904-x

20

Submarine Landslides on the Seafloor: Hints on Subaqueous Mass-Transport Processes From the Italian Continental Margins (Adriatic and Tyrrhenian Seas, Offshore Italy)

Fabiano Gamberi, Giacomo Dalla Valle, Federica Foglini, Marzia Rovere, and Fabio Trincardi

ABSTRACT

In the recent years, a large amount of marine geophysical data has been acquired along the Italian continental margins. Geophysics techniques such as multibeam and high-resolution sub-bottom profiles have been particularly useful in the reconstruction of the recent and active processes whose traces are found both at the seafloor and in the upper stratigraphy of slope and basin. In this chapter, we present a review of the available studies on a suite of submarine landslides along two portions of the Italian seas. The study areas are in the southwestern Adriatic Sea and in the southeastern Tyrrhenian Sea. Submarine landslides have been investigated through the analysis of their seafloor morphology and their internal architecture. Our study gives a detailed insight, from a marine geology perspective, on the large variety of internal geometry and features that characterize the deposits associated with submarine landslides. This chapter emphasizes the importance of the fine-scale characterization of the range of elements within the different sectors of mass-transport deposits. The recognition and the comprehension of these elements are crucial for a better definition of the controlling factors that drive the final arrangement of failed sediments.

20.1. INTRODUCTION

Submarine mass-transport processes are among the most important depositional events in the evolution of continental margins worldwide. The morphology, geometry, lithology, degree of internal deformation, and facies of mass-transport deposits (MTDs) are a result of the mechanisms of sediment failure and transport, of the paleo-topography prior to failure, and of the depositional environment. Sediment failures can be discrete episodes that originate mobilized masses which, during their downslope movement, are usually subject to varying mechanisms of transport and deposition. Therefore, complex MTDs with greatly variable geometry and internal structure originate. In addition, in many slope setting, recurring episodes of sediment failures result in the stacking of single MTDs into composite depositional bodies referred to as mass-transport complexes (MTCs) (*sensu* Moscardelli and Wood, 2008).

Kinematic models for sediment failure and landslide movement and emplacement can be reconstructed through the characterization of the internal facies and morphology of MTDs (Lucente and Pini, 2003; Frey-Martinez et al., 2005; Pickering and Corregidor, 2005; Gee et al., 2006; Moscardelli et al., 2007; Lamarche et al., 2008; Tripsanas et al., 2008; Bull et al., 2009). In particular, some attributes of landslide deposits, such as lithology, degree and type of internal deformation, surface morphology, size, volume, and runout, can be used to understand the initiation and the progressive evolution of a sediment failure. Furthermore, the same attributes can be used to discern whether the deformed mass represents the depositional product of an MTD or whether it is an

Institute for Marine Sciences (ISMAR), National Council of Research (CNR), Bologna, Italy

Submarine Landslides: Subaqueous Mass Transport Deposits from Outcrops to Seismic Profiles, Geophysical Monograph 246, First Edition. Edited by Kei Ogata, Andrea Festa, and Gian Andrea Pini.
© 2020 American Geophysical Union. Published 2020 by John Wiley & Sons, Inc.

MTC resulting from multiple stacked MTDs (Moscardelli and Wood, 2008; Gamberi et al., 2011; Dalla Valle et al., 2015; Martorelli et al., 2016).

Submarine landslides can be studied in outcropping successions. However, particularly in the case of large deposits, outcrops usually do not show the complete 3D geometry of landslides and the distribution of their internal facies. In addition, outcrops commonly do not allow the direct observation of the relationships between the headwall, the translational, and the toe domain of large submarine landslides. Traditional exploration seismics furnishes a good characterization of landslide geometry and a direct image of the relationships between the different parts of landslides; it cannot, however, show the finer-scale geometry and the different internal facies of landslides.

The advent of 3D seismics, particularly with the development of the seismic geomorphology techniques, and the progress in marine geophysical data acquisition in the present-day continental margin have recently, at least partially, filled the observational gap between outcrop and traditional seismics studies. The progressive increase in the resolution of multibeam bathymetric acquisition systems and very high resolution sub-bottom technology has greatly improved the resolution of marine geology studies (Tripsanas et al., 2008; Gamberi and Dalla Valle, 2009; Gamberi et al., 2011, 2013; Casalbore et al., 2016, 2018). Concomitantly, our knowledge of the processes connected with seafloor instability and submarine landslide along continental margins has greatly benefited from the integration of the interpretation of geomorphological attributes and shallow-subsurface stratigraphic organization.

During the last two decades, after the first regional multibeam data acquisition (Gamberi et al., 1998), the study of seafloor geomorphology and shallow stratigraphy has greatly advanced also in the Italian seas. Therefore, extensive landslide deposits have been discovered and described along with many portions of the Italian continental margins. In this chapter, we review the results of submarine landslide investigation carried out in some portions of the Italian continental margin by the "Istituto di Scienze Marine" (ISMAR) of the Consiglio Nazionale delle Ricerche (CNR). The aim of our chapter is to present a summary of the characteristics of MTDs found in the southern Adriatic Sea and the southeastern Tyrrhenian Sea (Figure 20.1), with emphasis on their geometry, surface texture, and seismic facies. These attributes have been used to reconstruct possible mechanism of failure, transport, and deposition of the numerous MTDs and MTCs.

20.2. SOUTHWESTERN ADRIATIC SEA

The Adriatic Sea is the foredeep and foreland domain of the Southern Alps, the Apennines, and the Dinarids-Hellenids fold and thrust belts (Ori et al., 1986; Ricci Lucchi, 1986) (Figure 20.1a). The evolution of the Southwestern Adriatic Margin (SWAM) during the Cenozoic consists in the reactivation and inversion of inherited Mesozoic extensional faults (Argnani et al., 1993). In the southern Adriatic region, the main deformation zone, known as the south Gargano system (Colantoni et al., 1990; Tramontana et al., 1995), extends both on land (Ortolani and Pagliuca, 1987) and offshore with the Gondola-Dauno Deformation Belt (Finetti et al., 1987) (Figure 20.1a). During the Quaternary, the SWAM was affected by uplift and deformation (Doglioni et al., 1994). The SWAM is a seismically active area, and during the last 500 kyr, active tectonic deformation was mainly focused along the Gondola-Dauno Fault Zone (GDFZ) and along slope and basin plain anticlines such as the Dauno Anticline (Figure 20.1b) where evidence of recent deformation (up to late Holocene) has been documented by Ridente and Trincardi (2006). The SWAM has a length of about 350 km, from the Gargano Promontory to the Otranto Strait (Figure 20.1a). The continental shelf, about 95 km wide in the northern sector, narrows southward to only 20 km (Figure 20.1a). The depth of the shelf break ranges from 180 to 220 m, whereas the base of the continental slope lies between 1000 m bsl in the north and 850 m bsl in the south (Figure 20.1b). The SWAM appears pervasively dominated by sediment waves and erosional and depositional contouritic features that reflect the activity of bottom currents of thermohaline origin and their interaction with seafloor topography (Trincardi et al., 2007) (Figure 20.1b).

20.2.1. Northern SWAM: Vieste Slide MTC

In the northern sector of the SWAM, a series of exposed and buried MTDs were originally interpreted as a single mass-transport event (named GS by Minisini et al. (2006)), which also included the Gondola Slide further south (Minisini et al., 2006). Successively, Dalla Valle et al. (2014) have divided the GS into two separate bodies: the Gondola Slide and the Vieste Slide (VS); the latter is developed in the northern SWAM. Both the GS and the VS are composed of discrete MTDs; thus, they can be considered as MTCs and are here named GS-MTC and VS-MTC, respectively.

The VS-MTC covers an area of about 300 km^2 and is the product of a series of vertically stacked MTDs linked to failures along a 40 km long sector of the SWAM parallel to the axis of a buried N-S trending tectonic antiform (Figure 20.2a). The VS-MTC consists of two vertically stacked MTDs (V1 and V2) (Figure 20.2a) (Dalla Valle et al., 2014).

The V1-MTD has an E-W extent of 24 km and an N-S longitudinal elongation of 25 km, terminating in the basin plain, and accounts for about 95% of the total volume of

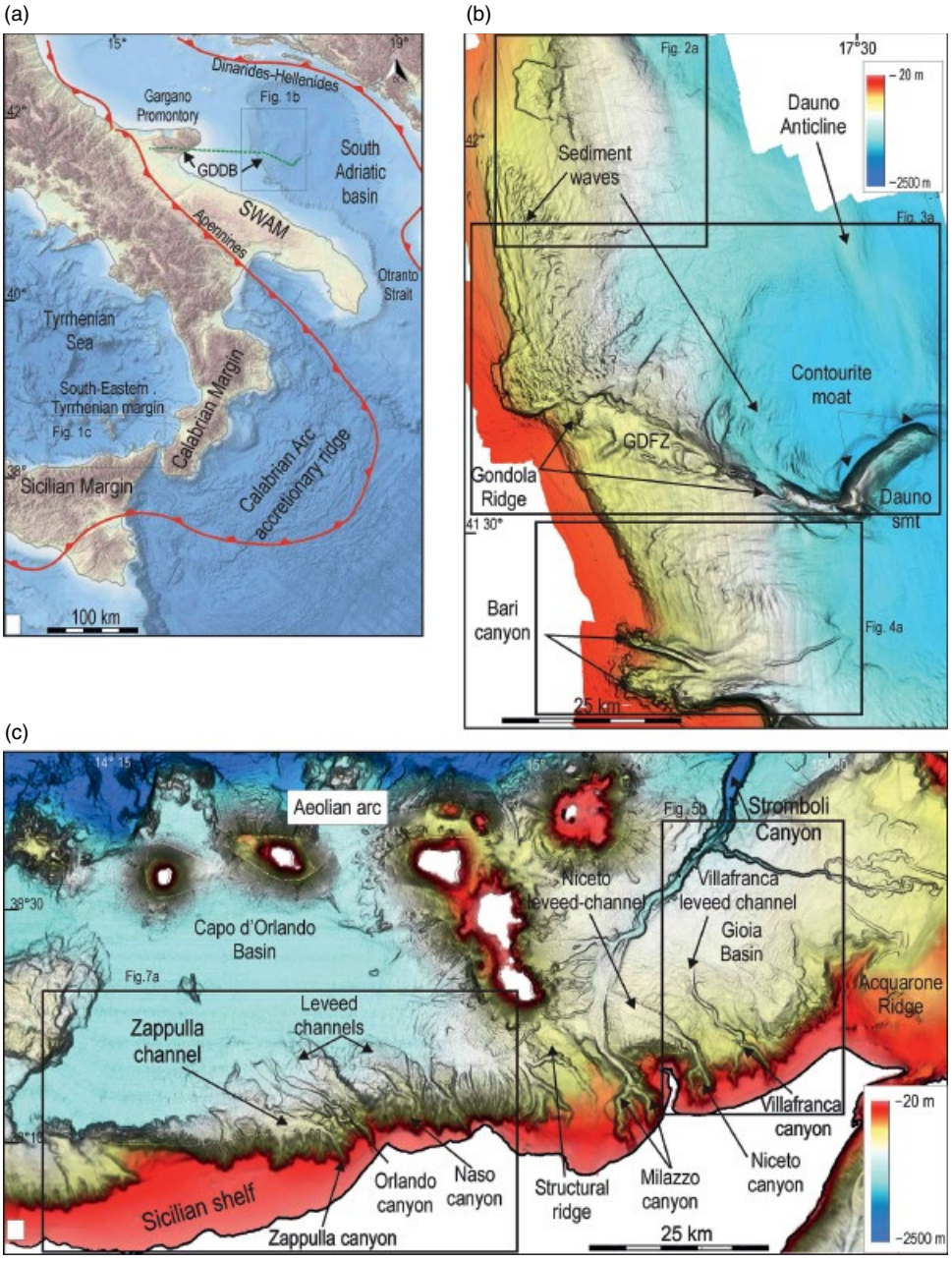


Figure 20.1 (a) Location of the study areas in the Adriatic and Tyrrhenian seas. (b) Shaded relief map, from multibeam bathymetric data, of the southeastern Adriatic Sea. (c) Shaded relief map, from multibeam bathymetric data, of the southeastern Tyrrhenian Sea.

the VS-MTC (Dalla Valle et al., 2016) (Figure 20.2a). Its evacuation headwall area is 30 km long, up to 40 m high, but to the south, it is barely visible (Figure 20.2a) (Dalla Valle et al., 2014). The failed mass is attached to its source area and lies above a detachment surface that is never exposed at the seafloor and corresponds with a bedding plane (Figure 20.2b, c) (Minisini et al., 2006; Dalla Valle et al., 2016). The V1-MTD is made up of 30–40 m of weakly reflective, quasi-transparent chaotic seismic facies, and apart from its proximal region, it is always draped by a 10–20 m thick contourite drift deposit succession (Figure 20.2b, c) (Dalla Valle et al., 2014, 2016).

The V2-MTD consists of several smaller-scale acoustically transparent deposits that are exposed at the seafloor, downslope of a U-shaped headwall composed of an upper and a lower scarp (Figure 20.2a). The two headwall scarps have a relief of 40 m and have partially remobilized the V1-MTD (Dalla Valle et al., 2014). In the accumulation

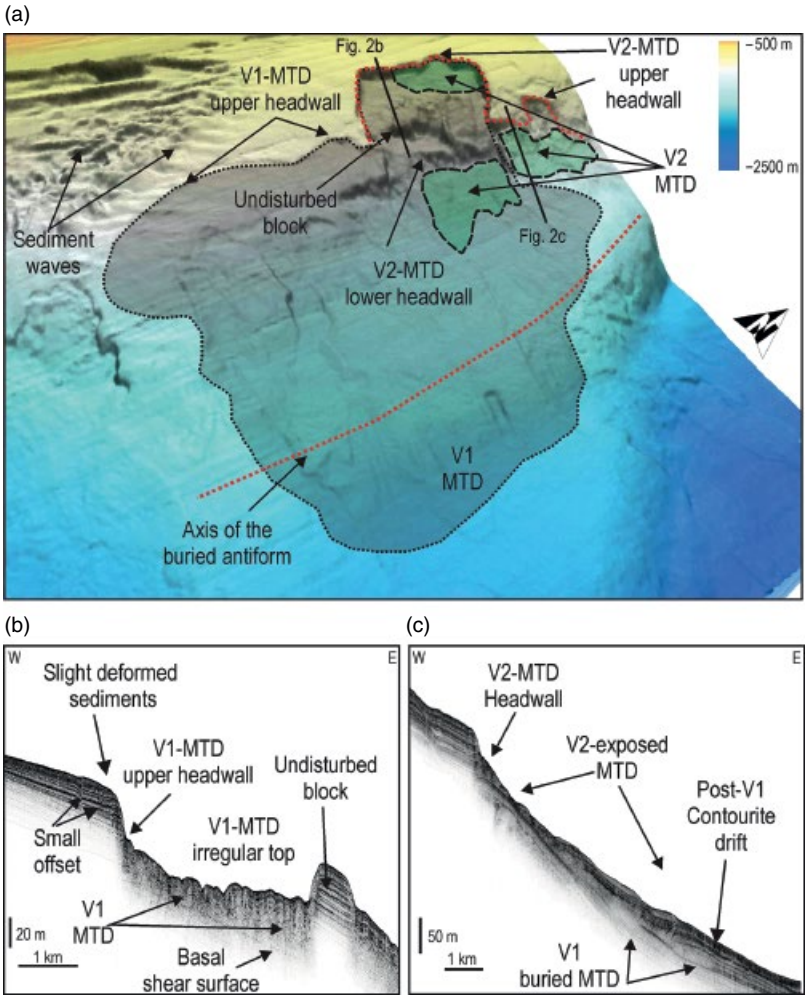


Figure 20.2 (a) 3D shaded relief bathymetry showing the extent of the MTDs, V1 and V2, composing the Vieste Slide. The V1 evacuation region consists of multiple superimposed failure scars that have been reworked by the successive failure of V2. The large V1 failure affects a mid-slope sediment wave field. (b) The V1 MTD comprehends both completely disrupted material and intact failed slab, with preserved internal stratigraphy. (c) V2 MTD is in general outcropping at the seafloor, being younger than V1, which is covered by a thin sedimentary unit, and pointing to a retrogressive style of failure.

zone, the V2-MTD consists of an around 10 m thick and 3.5 km long acoustically transparent deposit exposed at the seafloor and deposited on top of the V1-MTD (Figure 20.2c) (Dalla Valle et al., 2014).

Upslope from the heavily reworked sediment of V1-MTD and V2-MTD, barely deformed sediments made up of faint reflectors accompanied by small vertical offsets possibly indicate more coherent material with very low degree of deformation about to fail; proceeding basinward, the internal character of the failed deposit changes into a transparent facies with irregular base and top, suggesting increased remolding of the sediments through mass flow (Minisini et al., 2006).

At the base of the slope, an old deeply buried MTC (Old-Vieste MTC) was deposited over an area of 290 km^2 (see Minisini et al. (2006) for its location; Dalla Valle et al., 2014). Because older MTDs do not extend upslope from the youngest headwall, Minisini et al. (2006) suggested that VS-MTC failures propagated upslope in a retrogressive fashion. A similar behavior has been documented in many other landslide cases (*among others*, Wilson et al., 2004; Sawyer et al., 2009; Krastel et al., 2012).

20.2.2. Central SWAM: Gondola MTC

The Gondola MTC is composed of three different MTDs: G1-MTD and the minor G2-MTD and G3-MTD (Figure 20.3a) (Dalla Valle et al., 2015). The G1-MTD has a volume of 40 km^3, accounting for almost 90% of the GS-MTC, and extends with an area of about 1050 km^2

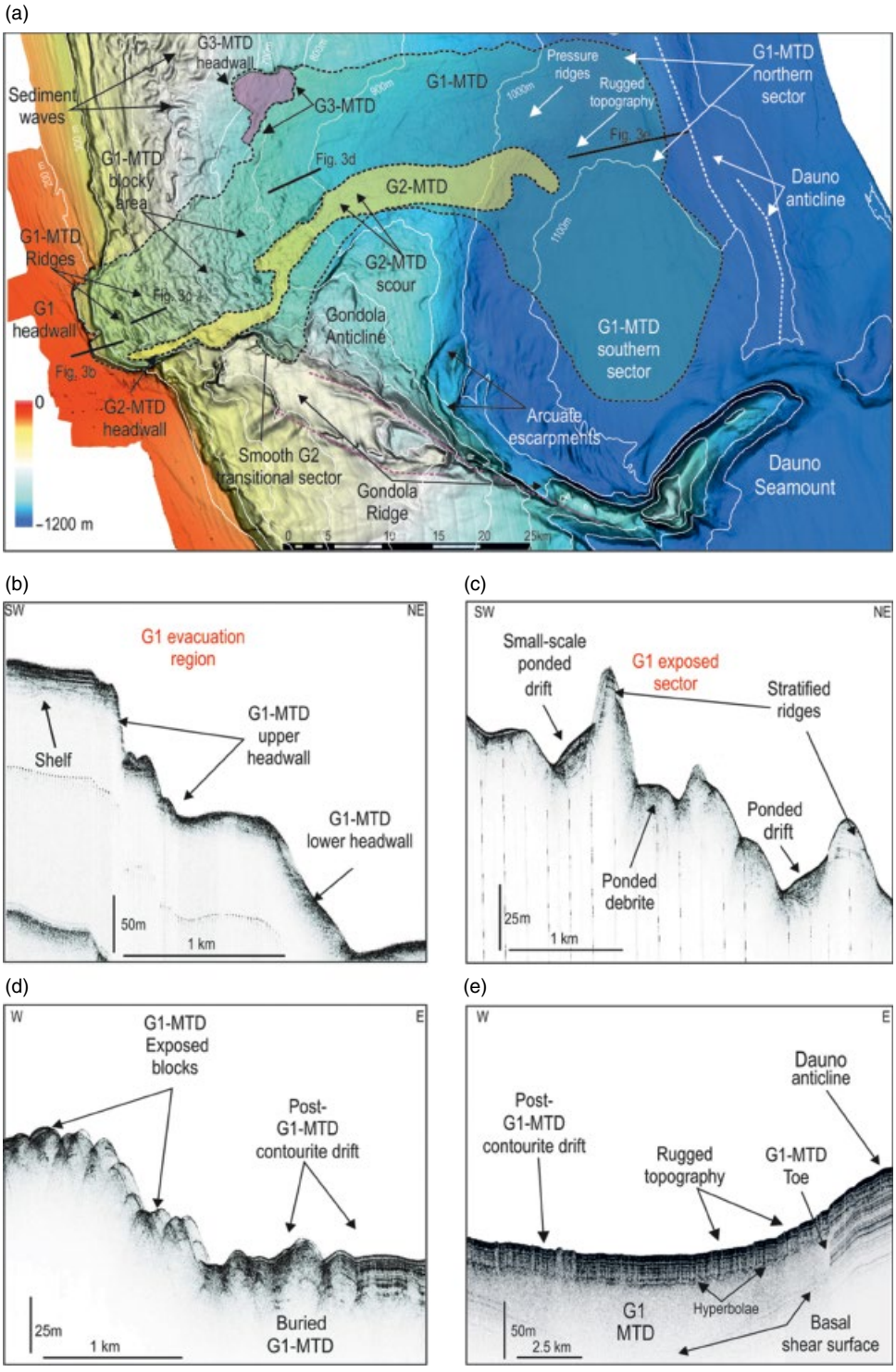


Figure 20.3 (a) Shaded relief bathymetry of the Gondola MTC area. The limits of the MTDs that make up the Gondola MTC, G1-MTD, G2-MTD, and G3-MTD, are indicated. The Gondola-Dauno Fault Zone (GDFZ) is indicated by purple lines; the Dauno Anticline trend is marked with a white dashed white line (Source: Modified from Ridente et al. (2010)). The G1-MTD proximal sector outcrops at the seafloor and has by elongated km-scale ridges followed downslope by blocks. The flat floor of the G2-MTD translational region is also evident. (b) CHIRP sonar profile illustrating the two escarpments of the G1 headwall. (c) In the proximal area of the G1-MTD, ponded debrites result from the degradation of the elongated ridges. Contouritic drifts plastered against the ridges are also present and are the results of the activity of cascading currents (Trincardi et al., 2007). (d) CHIRP sonar profile showing the passage between the exposed Gs1 blocky region and the more relatively smooth distal region of G1-MTD, covered by a thick contouritic drift. (e) CHIRP profile showing the onlap of the G1-MTD against the western flank of the Dauno Anticline in the basin plain; the base of the G1-MTD has a strong erosional character.

over a longitudinal distance of 55 km (Figure 20.3a). In the upper slope, it has a width of around 14 km, being confined southward by the topographic highs of the Gondola Ridge, which belongs to the tectonic lineament of the GDFZ (Figure 20.3a); in the basin plain, G1-MTD reaches a maximum width of 40 km and is deflected southward by the 40 m high relief of the N-S trending Dauno Anticline (Figure 20.3a).

The headwall of the G1-MTD is indented up to 5 km into the outer shelf and is composed of 2 main escarpments with a height of 75 and 120 m that form a 10 km wide U-shaped composite feature dipping up to 25° (Figure 20.3a, b) (Dalla Valle et al., 2015). Mid-Pleistocene outer-shelf progradational sequences are exposed along the headwall escarpment (Ridente and Trincardi, 2006). The G1-MTD southern sidewall is a 200 m high escarpment deeply carved into the outer shelf and partly corresponding with the Gondola Ridge (Figure 20.3a); in contrast, the northern sidewall has a relief of only 100 m in the outer shelf that rapidly further decreases to only 25 m in the upper slope (Figure 20.3a).

In the slope, the proximal accumulation domain of the G1-MTD is exposed at the seafloor down to a depth of about 850 m (Figure 20.3a, c) (Dalla Valle et al., 2015). In its upper part, ridges parallel to the G1-MTD headwall scarp cover an area of about 55 km^2 (Figure 20.3a). They rest above a failure plane, corresponding with a high-amplitude reflector parallel to the regional dip of the slope strata (Dalla Valle et al., 2015). The largest ridges have lengths of 3 km with heights up to 50 m but become gradually shorter and less prominent in relief downslope (Figure 20.3a, c). Usually, they show reduced acoustic penetration and diffraction hyperbolae, but locally their original stratigraphy, consisting of parallel, high-frequency high-amplitude reflectors, is preserved (Figure 20.3c). From a lithological point of view, ridges consist mainly of sandy shelf-margin strata, as Freiwald et al. (2009) have documented through ROV inspections.

Starting from a water depth of 550 m, the ridges are progressively replaced by blocks with subcircular or elliptical planform that occupy an area of 130 km^2 (Figure 20.3a). Blocks commonly have diameters of less than 500 m and are 30 m in height (Figure 20.3d). Acoustically transparent deposits, corresponding with ponded debrites, resulting from block disintegration, are locally developed in the ridge and blocky areas (Figure 20.3c) (Dalla Valle et al., 2014). Both in the ridge and in the block areas, small-scale ponded contourite drifts are part of the sparse post-failure deposition (Figure 20.3c); downcurrent, comet marks are generated by strong bottom current impacting on the irregular seafloor at the top of the MTD (see Verdicchio and Trincardi, 2006; Trincardi et al., 2007).

In water depths greater than 850 m, the G1-MTD accumulation domain is buried by an up to 35 m thick sedimentary cover, and therefore, its upper texture can only be observed in CHIRP profiles (Figure 20.3a, d, e). Close to the G1-MTD northern toe, a rough bathymetry characterizes a 10 km long sector; the rugged topography at the seafloor matches with that shown by discontinuous hyperbolae and pressure ridge development at the top of the underlying G1-MTD (Figure 20.3a, e). Along the Dauno Anticline flank, the base of the G1-MTD is erosive and ramp upsection (Figure 20.3e; see also figure 5a, b in Dalla Valle et al. (2015)). The southern G1-MTD accumulation sector is characterized by a transparent, incoherent seismic facies and has a flat top surface (see figure 5f in Dalla Valle et al. (2015)).

The G2-MTD results from a further collapse of the sediment forming the G1-MTD; it covers an area of around 158 km^2 and has a headwall carved into the larger G1-MTD headwall in proximity of the Gondola Ridge (Figure 20.3a) (Dalla Valle et al., 2014). Its southern sidewall, in fact, runs initially along the Gondola Ridge (Figure 20.3a), but further downslope, both G2-MTD sidewalls have an SW-NE trend and are carved for up to 30 m of into the G1-MTD blocky area (Figure 20.3a). The G2-MTD transitional domain corresponds with a narrow, less than 1.5 km wide, corridor with smooth seafloor, within the G1-MTD blocky region (Figure 20.3a). Some sparse blocks, with an orientation different from those of the G1-MTD, are found along the G2-MTD transitional zone (see figure 6a in Dalla Valle et al. (2015)). From a water depth of 840 m, the seafloor of the G2-MTD transitional domain is incised by a rectilinear erosional scour (G2-MTD scour) that further downslope, where the Gondola Anticline gradually plunges beneath the basin floor and loses its bathymetric expression, bifurcating into a series of erosional grooves, less than 5 m deep (see figure 6a in Dalla Valle et al. (2015)). The G2-MTD accumulation domain, traceable down to a depth of 1070 m, beyond the Gondola Anticline (Figure 20.3a), is characterized by blocks aligned in E-W direction; blocks up to 3 m high are present at the distal toe of the G2-MTD accumulation zone (Dalla Valle et al., 2015). G2-MTD is buried below a approximately 20 m thick sedimentary cover, which is however always thinner than that covering the G1-MTD (Dalla Valle et al., 2015).

The G3-MTD, the youngest MTD of the Gondola MTC, originates from a minor failure affecting sediment waves in the slope (Figure 20.3a) (Dalla Valle et al., 2014). The G3-MTD headwall scarp is U shaped, around 3.5 km wide, and is carved into the G1-MTD with a maximum relief of 75 m (Figure 20.3a) (Dalla Valle et al., 2015). Its northern lateral margin is around 5 km long with a maximum relief of 30 m (Figure 20.3a). The G3-MTD

accumulation zone covers an area of 38 km^2 with a total runout distance of 6 km (Figure 20.3a). Internally, the G3-MTD is characterized by a chaotic seismic facies, with good seismic penetration, suggesting that it is made up of fine-grained sediments likely representing a mud flow (see figure 7 in Dalla Valle et al. (2015)). The G3-MTD presents a very thin, hardly recognizable post-failure sedimentary cover (Dalla Valle et al., 2015).

Further landslide headwalls are observable in the area of the Gondola Anticline. The largest correspond with arcuate, concentric escarpments at the seafloor located in the eastern flank of the Gondola Anticline close to the GDFZ, but their related deposits are not exposed at the seafloor (Figure 20.3a).

20.2.3. Bari Canyon Area MTC

The Bari Canyon MTC spans the SWAM slope between the Gondola Ridge and the Bari Canyon (Figures 20.1b and 20.4a). The Bari Canyon MTC is composed of the stacked B1-MTD and B2-MTD. The MTDs occurred from multiple failures at the expense of upper slope contouritic drifts developed along a 30 km long slope sector within the head of the Bari Canyon System (Figure 20.4a) (Minisini et al., 2006; Dalla Valle et al., 2015). Based on the available data, the B1-MTD headwall region is unclear, although we tentatively suggest that the failure originates just beneath the shelf break, in the upper slope region, as the numerous scars suggest (Figure 20.4a).

Buried failed masses lying on irregular surfaces of preexisting structural reliefs are locally ponded (see figure 11f of Minisini et al. (2006)). The largest deposit, B1-MTD, is made up of fully chaotic, quasi-transparent seismic facies, with a thickness that does not exceed 35 m (Figure 20.4a, b); it reaches the deep basin plain, at 1100 m of depth, with a runout distance that exceeds 50 km (Figure 20.4a). Close to the shelf-break region, the B1-MTD is exposed at the seafloor and is modified by the action of cascading bottom currents (Figure 20.4b, c); further downslope, along with the upper slope, the B1-MTD becomes progressively healed by a post-failure contourite deposit (Dalla Valle et al., 2016). The B1-MTD is partially overlain by the smaller B2-MTD, which develops in the upper slope with a length of about 20 km, widening at the base of slope and assuming a lobate shape (Figure 20.4a).

Recent mass wasting in the southern area occurs along the steep walls of structural highs and, particularly, along the Bari Canyon System, where elongated incisions on the Bari Canyon walls and chaotic deposit cropping out at the seafloor suggest that the canyon is impacted by mass-transport events in recent times (Figure 20.4a) (see Minisini et al., 2006).

20.3. SOUTHEASTERN TYRRHENIAN SEA

The Southeastern Tyrrhenian Margin is part of the Calabrian Arc, an orogenic wedge that was affected by the extensional and transcurrent/transtensional tectonics that led to the opening of the Tyrrhenian back-arc basins (Figure 20.1a) (Patacca and Scandone, 1989). The area is affected by a high rate of regional uplift (Westaway, 1993) and ongoing fault activity as displayed by the seismicity of the area (Pondrelli et al., 2006; Lentini et al., 1996).

The Capo d'Orlando and the Gioia intraslope basins develop in the Southeastern Tyrrhenian Margin (Figure 20.1c). The two basins are separated by a structural ridge that connects the Sicilian margin to the volcanic high of the Aeolian Island arc (Figure 20.1c). The Gioia Basin spans the easternmost part of the Sicilian margin and the southernmost part of the Calabrian Arc margin (Figure 20.1c). It deepens northeastward and is enclosed between the Sicilian margin and Calabrian Arc and the Aeolian Island arc (Figure 20.1a, c). It has a length of about 80 km and a width that increases from 40 to 80 km northeastward; the basin axis is the site of the Stromboli Canyon (Figure 20.1c). In the western part of the basin, the Villafranca, the Milazzo, and the Niceto canyons reach the coastal areas (Gamberi et al., 2014, 2015, 2017). The flanks of the Milazzo and the Niceto canyons were affected by failures of sediment packages as thick as 300 ms (Gamberi and Marani, 2007). The failed material is found both as disrupted bodies along the flanks of the canyon and as a transparent or chaotic valley floor infill of around 170 m in thickness (see figure 5 in Gamberi and Marani (2007)).

In the central part of the basin, the Acquarone Ridge is an elevated area, corresponding with a horst, formed during the extensional tectonics that originated the present-day setting of the margin (Figures 20.1c and 20.5a).

The Capo d'Orlando Basin is located along the central part of the northern Sicilian margin and is about 70 km long and 50 km wide (Figure 20.1c). The continental shelf is in general narrow, attaining a maximum width of 10 km to the west and becoming progressively smaller toward the east, except for the Gulf of Patti (Casalbore et al., 2017) (Figure 20.1c). The shelf break is in general at a depth of about 140 m, even if it reaches a maximum depth of 150 m in the Gulf of Patti (Casalbore et al., 2017). The upper slope of the Capo d'Orlando Basin is characterized by canyons that have their heads at the shelf break but more often very close to the coastline (Figure 20.1c) (Gamberi et al., 2015, 2017). In the lower slope, the canyons connect with leveed channels that have a general southeast-northwest trend (Gamberi and Dalla Valle, 2009). The basin plain is located at an average depth of approximately 1500 m and is the site of lobe deposits formed beyond the channel mouths (Gamberi et al., 2015).

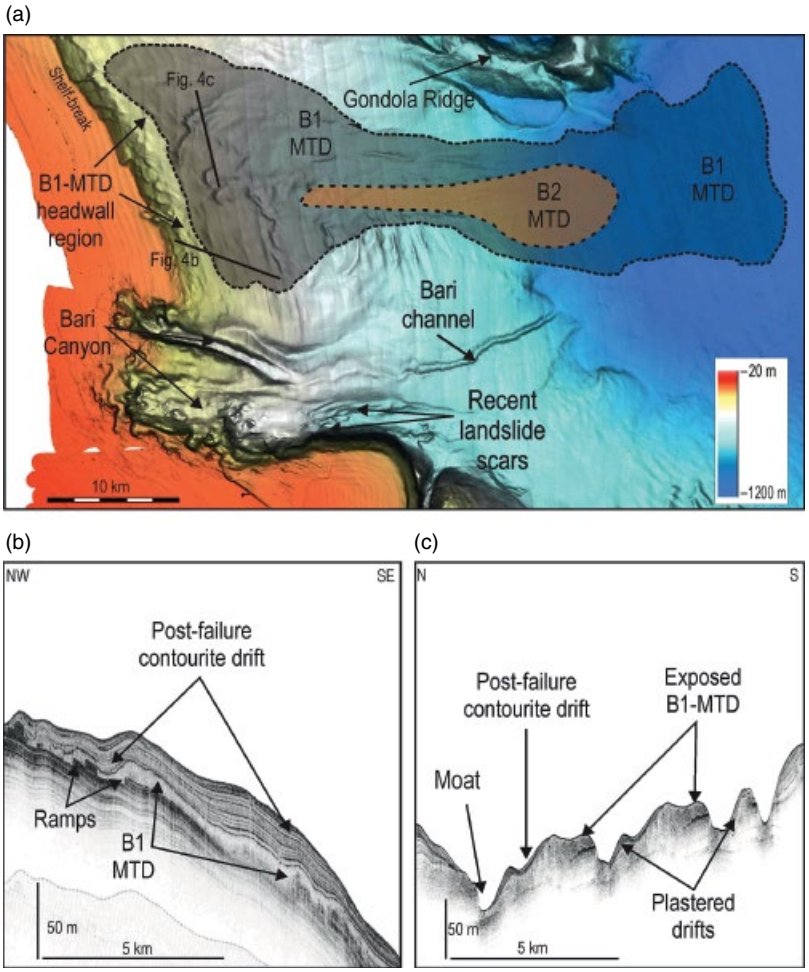


Figure 20.4 (a) Shaded relief bathymetry of the Bari Canyon MTC area. The dashed lines correspond with the areas of B1 and B2, the MTDs of the Bari Canyon MTC. Recent sediment failures, shown by headwall scars that indent the shelf, affect the Bari Canyon. A branch of the Bari Canyon down-cuts the right-hand levee of Bari channel, producing elongated landslide scars at the base of the slope. (b) A post-failure contouritic drift drapes the B1. The basal shear surface of the B1 has ramps at different stratigraphic levels. (c) The upper evacuation region of B1-MTD shows a complex topography and internal stratigraphy due to the strong interaction between bottom current and the topography of the MTD.

20.3.1. Gioia Basin MTC

Downslope from canyons, a leveed-channel system spans the Sicilian margin for a total width of 20 km (Figure 20.1c) (Gamberi and Marani, 2006). Slump scars cause the removal of sediment packages as wide as 1 km from the inner side of the levee of the Milazzo channel (see figure 7 in Gamberi and Marani (2007)). More importantly, numerous MTD scars show that sediment failure is a recurring process in the eastern levee of the Villafranca channel (Figure 20.5a, f) (Gamberi and Rovere, 2011). In the upper part of the Villafranca levee wedge, the headwall scarp of MTD 2 is followed downslope by its completely evacuated basal shear surface (Figure 20.5a, f); a thickness of about 30 m of sediment was involved in MTD 2 (Figure 20.5f). The headwall scarp of MTD 2 joins downslope with that of MTD 1 (Figure 20.5a). The basal shear surface of MTD 1 is covered by a thin slump deposit and corresponds with a stratigraphic level that is 30 m deeper than that corresponding to the MTD 2 basal shear surface (Figure 20.5f).

To the northeast of the channel-levee system, the recent Villafranca mass-transport complex (VMTC) corresponds with a rough seafloor and is the major MTC of the Gioia Basin slope (Figure 20.5a) (Gamberi and Marani, 2006; Gamberi et al., 2011). The VMTC covers a surface of around 225 km^2 with a length of around 25 km, and an average lateral extent of around 9 km (Figure 20.5b), and its maximum thickness reaches 300 m

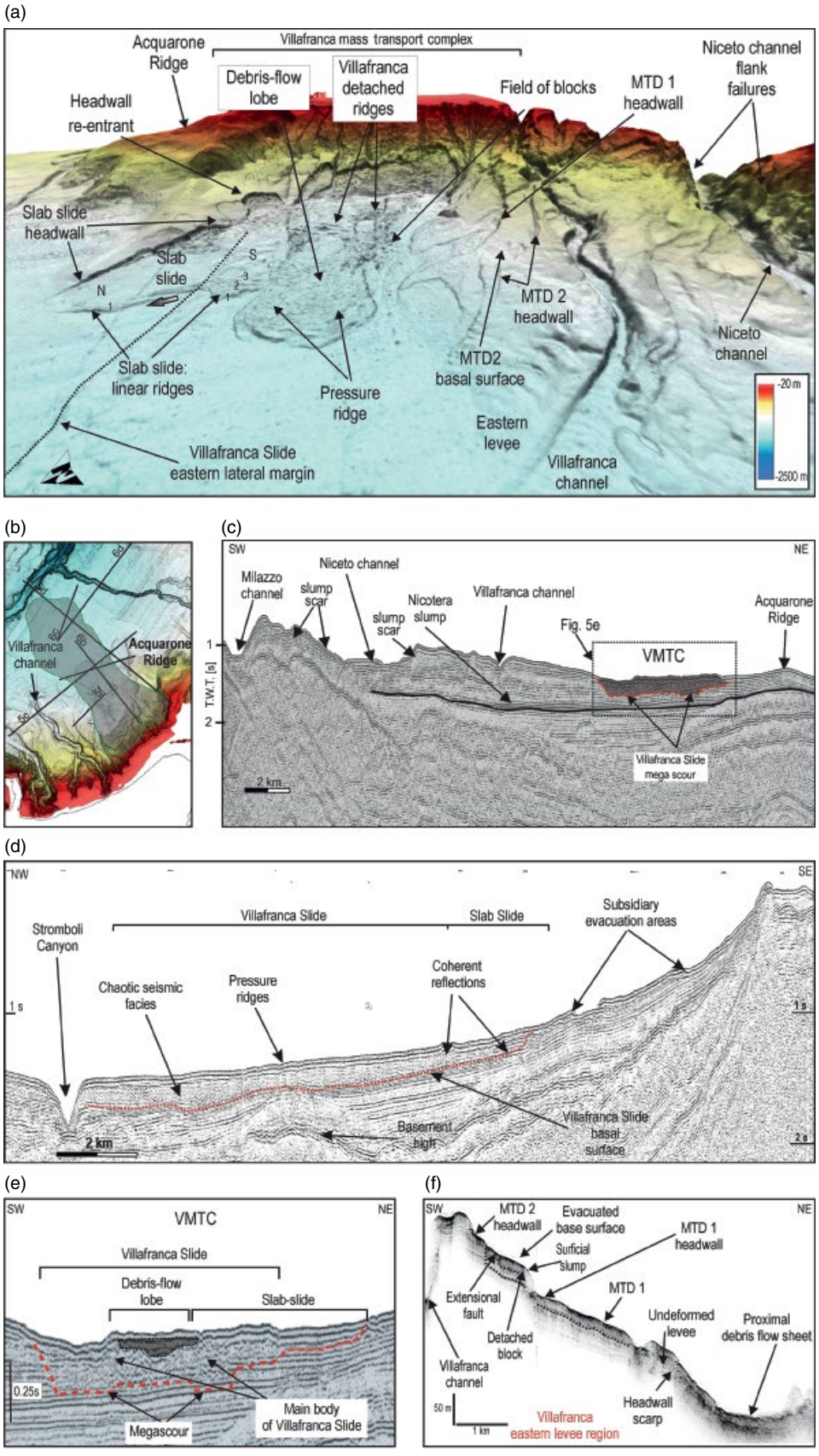
(Figure 20.5d). An evacuated area with multiple headscarps spans more than 8 km of the margin in the slope and the base-of-slope deposits (Figure 20.5a) (Rovere et al., 2014). The scars correspond to the failure surfaces of the Villafranca Slide that eventually led to the 300 m thick chaotic body of the VMTC and occupies the entire basin down to the Stromboli Canyon (Figure 20.5d). The VMTC is composed of the Villafranca Slide, consisting of a debris-flow sheet, a slab slide, and a debris-flow lobe (Figure 20.5a, d, e) (Gamberi et al., 2011).

The large Villafranca Slide, up to about 300 m thick (on average 200 m thick), with an estimated volume of 46 km^3 and an area of 230 km^2 represents the basal thickest portion of the VMTC (Figure 20.5c, d, e). The basal shear surface of the Villafranca Slide lies in general at the same stratigraphic level, but it originates two megascours in the proximal part (Figure 20.5c, e) and has a ramp and flat geometry more distally. Both the lateral margins of the Villafranca Slide cut up stratigraphy from the basal shear plane (Figure 20.5c, e). Whereas the western lateral margin of the Villafranca Slide is not visible in the bathymetry since it is healed by successive deposits, the eastern lateral margin shows up as a relatively continuous SE-NW trending seafloor step (Figure 20.5a). The toe region of the Villafranca Slide is characterized by a frontal ramp along which the displaced mass is buttressed against the undeformed stratigraphic section (Gamberi et al., 2011). The main body of the Villafranca Slide is characterized by chaotic seismic facies and by discrete panels with more coherent reflections (Figure 20.5c, d, e) possibly resulting from relatively intact blocks within a chaotic matrix (Gamberi et al., 2011). The Villafranca Slide is generally covered by younger deposits and was reworked by subsequent failures; thus, the details of its internal makeup and surface texture can be fully appreciated through the bathymetric data and the CHIRP profiles only in a small number of locations. In particular, detached ridges are present in the proximal area of the Villafranca Slide (Figure 20.5a); they are up to 200 m large and 10 m high with the long axis consistently oriented in a NE-SW direction (Figure 20.5a) (Rovere et al., 2014). On the contrary, linear undulations are visible in its distal toe region and its eastern margin (Figures 20.5a and 20.6c) and correspond with folded pop-up blocks showing that a mainly contractional regime affected the distal part of the sliding mass.

The debris-flow sheet corresponds with a homogeneous transparent layer up to 30 m thick, widespread in the distal part of the Gioia Basin; it covers an area of 100 km^2 with a volume of 0.94 km^3 (see "DFS" in figure 4 of Rovere et al. (2014) for its areal extent). It has, in general, a very homogeneous thickness (Gamberi et al., 2011; Rovere et al., 2014) with a gradual basinward tapering (Figure 20.6a, b). However, the thickness of its distal part is largely influenced by the seafloor undulations at the top of the underlying Villafranca Slide, and it pinches out against the relief created in the toe region of the Villafranca Slide (Figure 20.6c). Further upslope, the debris-flow sheet is confined by the western lateral margin of the Villafranca Slide and corresponds with a narrow, downslope elongated area of blocks cropping out at the seafloor eastward from the detached ridges of the Villafranca Slide (Figure 20.5a).

The slab slide consists of a detached mass of sediment showing in general little internal deformation with an area of 32 km^2: it represents the eastern portion of the VMTC (Figure 20.5a) (see "SS" in figure 4 of Rovere et al. (2014) for its areal extent; Gamberi et al., 2011). Its headwall is the site of extensional faults that result in a linear scarp with S-N trend at the base of the Acquarone Ridge (Figures 20.5a and 20.6a). The northern and central sectors of the headwall have a linear trend, while in the southern sector, a circular upslope reentrant is present (Figure 20.5a). A rather flat upper surface and relatively undeformed sediments characterize the northern sector of the slab slide, whereas a rough surface with internal deformation and pop-up blocks is found in its southern part (Figures 20.5a and 20.6a). The northern and southern sectors of the slab slide are separated along a NW-SE trending lineament that corresponds with the eastern lateral margin of the Villafranca Slide (Figure 20.5a). NE-SW linear ridges with remarkable topographic relief mark the frontal area of the slab slide. These linear ridges are formed by downslope translated sediments piled up against the in-place sediments (Figure 20.5a). The number of ridges diminishes from three, in the southern sector of the slab slide, to one in its northern sector; concomitantly, a decrease in the relief of the linear ridges region is observed (Figure 20.5a).

The debris-flow lobe corresponds with a body resting above the proximal part of the Villafranca Slide (Figure 20.5a, e). The area covered by the debris-flow lobe is 38 km^2, and its estimated volume is 1.9 km^3 (Figure 20.5a) (Gamberi et al., 2011; Rovere et al., 2014). The debris-flow lobe front is marked by a steep high-relief downslope convex ridge that lies at a depth of about 1100 m where a decrease in the slope gradient from approximately 4° to 1° occurs (Figures 20.5a and 20.6a, b). The rough surface of the debris-flow lobe and the abundant hyperbolic reflections are due to pressure ridges originated by syn-depositional thrusting of relatively undeformed blocks (Figures 20.5a and 20.6a, b) (Gamberi et al., 2011; Rovere et al., 2014). Downslope, the pressure ridges in the toe region of the debris-flow lobe affect an area where the debris flow has transparent facies pointing to completely homogenized matrix material (Figure 20.6b). Although the lateral margins of the debris-flow lobe are less steep than its head, they form prominent escarpments at the


(a)
Acquarone Ridge
Villafranca mass transport complex
Debris-flow lobe
Villafranca detached ridges
Field of blocks
MTD 1 headwall
Niceto channel flank failures
Headwall re-entrant
Slab slide headwall
Slab slide
Slab slide: linear ridges
Pressure ridge
MTD 2 headwall
MTD2 basal surface
Niceto channel
Eastern levee
Villafranca channel
Villafranca Slide eastern lateral margin
-20 m
-2500 m
(b)
Villafranca channel
Acquarone Ridge
(c)
SW
NE
Milazzo channel
slump scar
Niceto channel
Nicotera slump
slump scar
Villafranca channel
Fig. 5e
Acquarone Ridge
VMTC
T.W.T. [s]
Villafranca Slide mega scour
2 km
(d)
NW
SE
Stromboli Canyon
Villafranca Slide
Slab Slide
Subsidiary evacuation areas
Chaotic seismic facies
Pressure ridges
Coherent reflections
1 s
2 km
Basement high
Villafranca Slide basal surface
(e)
SW
NE
VMTC
Villafranca Slide
Debris-flow lobe
Slab-slide
0.25s
Megascour
Main body of Villafranca Slide
(f)
SW
NE
MTD 2 headwall
Evacuated base surface
MTD 1 headwall
Sufficial slump
MTD 1
Extensional fault
Undeformed levee
Proximal debris flow sheet
Detached block
Villafranca channel
Headwall scarp
50 m
1 km
Villafranca eastern levee region

seafloor (about 20 m; Figure 20.6a). The western margin loses the character of a steep escarpment only over a short reach, where a field of blocks is laterally adjacent to the main body of the debris-flow lobe (Figure 20.5a).

In the relatively deep basin infill, the Nicotera slump (NS) is an almost basin-wide slump, with a transparent or chaotic seismic facies that is consistently buried below a thick section of younger sediments (Figure 20.6d) (Gamberi and Marani, 2006). The NS covers an area of 636 km^2 and its estimated volume is 30 km^3 (see figure 2a of Gamberi et al. (2011) for the NS areal extent). In the Sicilian sector, the NS is sheetlike with a rather homogeneous low thickness (around 50 ms, but sometimes at the limit of seismic resolution) with only a gradual thinning toward the SW onlap against the Capo di Milazzo Ridge (see Gamberi and Marani, 2006). A thickening of the NS occurs in its northern part close to the slope of the Capo Vaticano Ridge where a rough upper surface is possibly due to folds (Figure 20.6d). The source area of the NS is healed by successive deposition, and thus its location is not easily identifiable but can be tentatively followed from the western slope of the Acquarone Ridge, through the Calabrian basin sector, to the Capo Vaticano Terrace (Gamberi and Marani, 2006; Gamberi et al., 2011).

20.3.2. Capo d'Orlando Basin MTC

The main characteristic of the Capo d'Orlando succession is the high degree of sedimentary deformation and mass-wasting processes that affect the channel-levee deposits (Gamberi and Dalla Valle, 2009). Scars with an elongated or amphitheater planform are ubiquitous on the channel flanks and on the levees (Figure 20.7a, b). They are as high as 100 m and correspond with the up-dip boundary of displaced levee blocks with a planform size of about 6 km^2 (Gamberi and Dalla Valle, 2009). The Orlando channel crosses the headwall of a landslide involving a large portion of a preexisting levee wedge (Figure 20.7a, b). The fill of the channels often consists of chaotic seismic units that may represent the product of levee degradation (Figure 20.7b); similar seismic facies also develops on the surface of the levees (Figure 20.7b). In some cases, the levee-wedge failures results in lobe-shaped depositional bodies at the base of slope (Figure 20.7a). In the straight, fault-controlled western flank of the Naso channel, small landslide headwall scarps are present (Figure 20.7a). Downchannel, significantly larger landslide headwall scarps continue to modify the western channel margin (Figure 20.7a). MTDs are abundant on the Naso channel floor, as shown by the widespread blocky side-scan sonar facies and by seafloor sampling (see figure 8b and c in Gamberi et al. (2015)).

The Zappulla canyon has a head that forms a large shelf-edge embayment affected by sediment failure (Figures 20.1c and 20.7a); it connects with the Zappulla channel parallel to the base of slope with a very high backscatter and blocky floor, indicative of MTDs at the seafloor (Figure 20.7a). Distally, the Zappulla channel connects to small debris-flow lobes (8 km long and 5 km wide) with a similar backscatter pattern (Figure 20.7a, c) that are made up of blocks in muddy matrix (Gamberi et al., 2015). Similar MTDs compose also the major part of the sub-bottom succession of the Zappulla fan lobe, as shown by a stack of 4 transparent layers in the last 50 m of the lobe sequence (Figure 20.7d). A fan mainly composed of debris-flow deposits is thus formed and occupies much of the western part of the basin (Figure 20.7a) (Gamberi et al., 2015).

20.4. DISCUSSION

The large variety of the MTDs of the SAM and of the southeastern Tyrrhenian Sea allows advancing some generalities about the processes inherent to submarine mass movements. The observed different surface texture, geometry, and seismic facies can be reconciled with different processes of sediment failure, transport, and deposition.

20.4.1. Detached Ridges

Detached ridges, arranged parallel to the strike of the headwall scarp, rest just downslope from the evacuation area of the G1-MTD (Figure 20.3a, c). They have been interpreted by Dalla Valle et al. (2015) as resulting from

Figure 20.5 The Gioia Basin mass-transport deposits and the Villafranca mass-transport complex. (a) Relief of the Gioia Basin seen from the north. The Villafranca Slide, the largest body of the VMTC, is mostly buried below the successive deposits, that is, the debris-flow sheet, the slab slide, and the debris-flow lobe, that compose the VMTC. (b) Overview of the Villafranca Slide (overplayed) with location of the presented seismic profiles and labelling of the main geomorphic features. (c) The VMTC develops in a destructional portion of the margin to the east of a channel-levee complex. The Villafranca Slide has mainly a transparent seismic facies, but some coherent block shown by preserved reflectors sit within the deformed body. (d) The Villafranca Slide with its transparent facies occupies the whole basin from the base of slope to the axis of the basin in the area of the Stromboli Canyon. (e) Close of the line in (c), showing the megascours in the basal shear surface of the Villafranca Slide. (f) CHIRP profile showing the headwalls of the main landslides that affects the eastern levee wedge of the Villafranca channel. The basal shear surfaces can be either completely evacuated and exposed at the seafloor or covered by slump deposits.

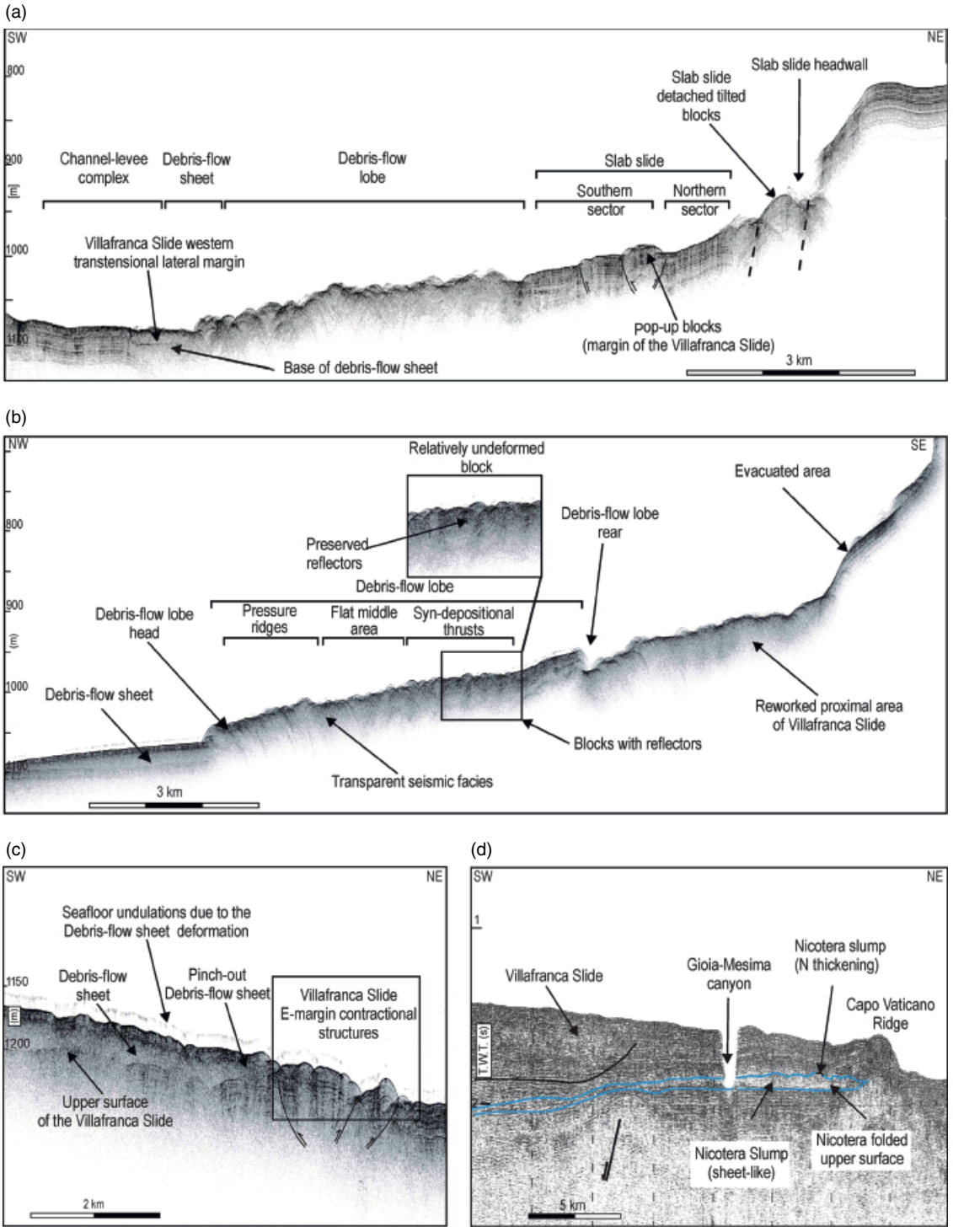


Figure 20.6 Seismic lines showing the mass-transport deposits in the Gioia Basin. (a) Strike line crossing the VMTC: the slab slide, downslope from an extensional headwall, consists of slightly deformed sediment with contractional faults; the debris-flow lobe has a rough surface due to widespread contractional deformation resulting in pressure ridges; the distal part of the debris-flow sheet has a smooth surface and a homogeneous thickness. (b) Dip line crossing the VMTC: the Villafranca Slide crops out only in the proximal part of the MTC; the debris-flow lobe has a proximal part that displays pressure ridges separating blocks with partially preserved stratigraphy and a very steep toe region; the debris-flow sheet thins gradually downslope. (c) CHIRP profile showing the western part of the VMTC: the western lateral ramp of the Villafranca Slide corresponds with a contractional bulge of folded panels with relatively undeformed stratigraphy; the debris-flow sheet pinches out against the relief created by the underlying Villafranca slide. (d) Airgun seismic line showing the northeast closure of the Nicotera slump in the Calabrian margin. Approaching the Capo Vaticano Ridge, the Nicotera slump thickens and has an undulating top surface possibly indicative of contractional deformation.

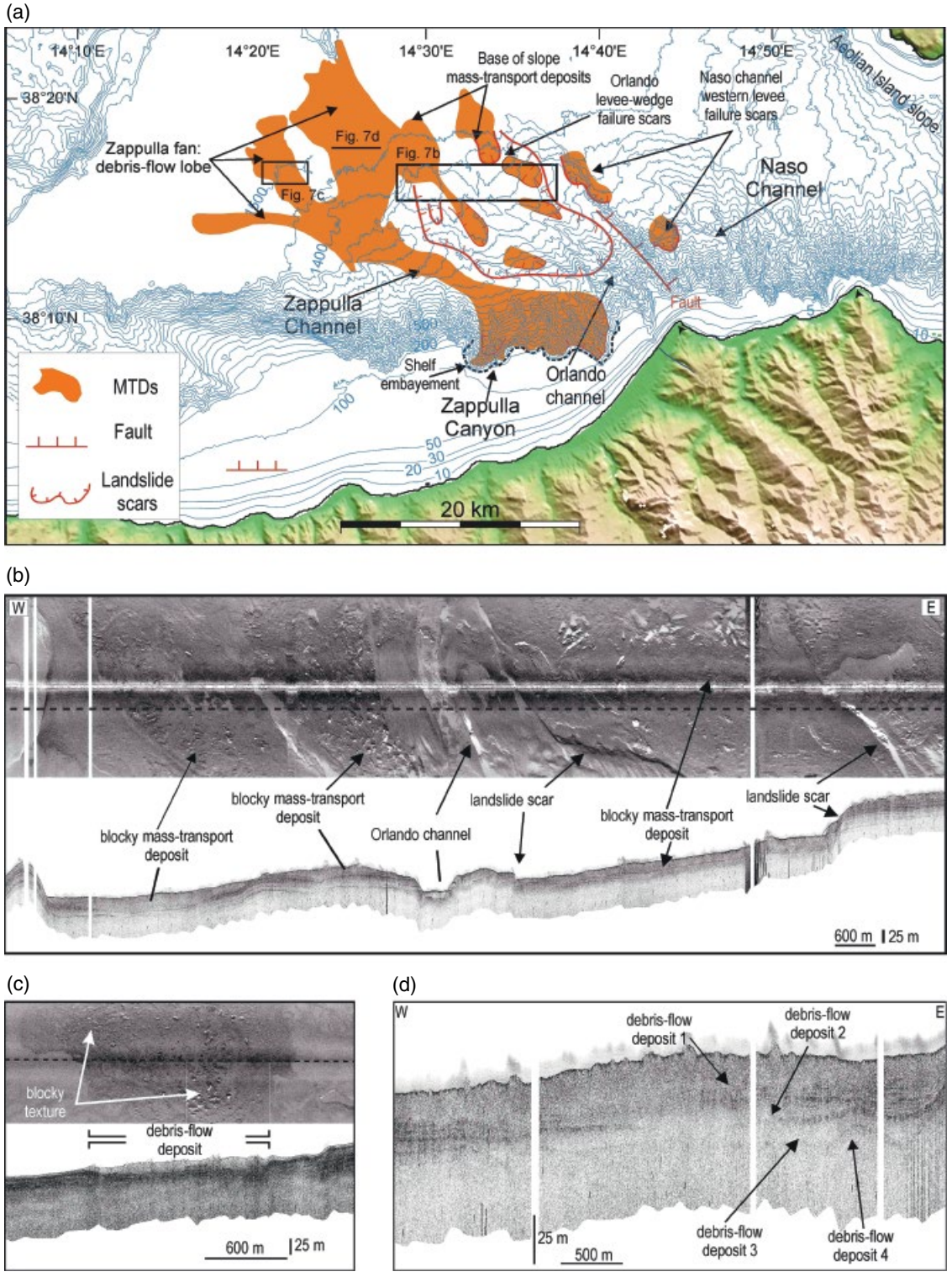


Figure 20.7 The mass-transport deposits of the Capo d'Orlando Basin. (a) Map showing the distribution of the main mass-transport deposits. In the western part of the basin, numerous debris-flow lobes form the Zappulla fan. The Orlando channel-levee wedge is affected by extensive sediment failures and by the deposition of mass-transport deposits. Mass-wasting processes are also widespread in the flanks of the Naso channel. (b) Sub-bottom and Mak deep-tow side-scan sonar images of the mass-transport deposits in the Orlando channel levee. The failed masses accumulate at the base of headwalls, in general with amphitheater shape, and consist of blocks. (c) Sub-bottom and Mak deep-tow side-scan sonar images of one of the debris-flow lobe that compose the Zappulla fan. The lobe has mainly a blocky texture, although also smoother areas are visible. (d) Sub-bottom profile showing the stacking of the debris-flow lobes that compose the Zappulla fan.

tensional stress, affecting mid-Pleistocene outer-shelf lithified sequences (Ridente and Trincardi, 2002) and causing their failure and rupture into elongated kilometer-scale ridges. The ridges are displaced along a basal shear surface parallel to the regional dip of slope strata (Dalla Valle et al., 2015). Those located progressively downslope are shorter and less defined having experienced higher translation and a higher degree of deformation (Figure 20.3a).

Large coherent detached ridges are also present in the proximal part of the Villafranca Slide (Gamberi et al., 2011). Here they only occupy two small distinct areas close the main headwall of the slide (Figure 20.5a). The Villafranca Slide has been abundantly reworked (Figure 20.6b) and buried by successive MTDs, making it possible that its area with ridges was originally larger (Figure 20.5f). In the G1-MTD and in the Villafranca Slide, the ridges have a common location, proximal within the failed masses and very close to their headwalls. In both cases, the landslides moved downslope translating above basal shear surfaces that follow a stratigraphic horizon. Moreover, both landslides cut deeply into the preexisting seafloor, exposing old, presumably indurated sequences. These observations appear to substantiate that ridges form when failures cut thick succession affecting relatively stiff sediments. After the failure, the ridges move downslope, experiencing a very little amount of downslope displacement. A similar behavior has been deduced from observations made along some of the major submarine landslide worldwide, as the Storegga Slide (Haflidason et al., 2004; Micallef et al., 2009) and the Trænadjupet Slide (Laberg et al., 2002), in addition to fossil, exhumated landslide examples (Macdonald et al., 1993; Dakin et al., 2013).

20.4.2. Blocks

A widespread area with a blocky surface texture characterizes the G1-MTD, downslope from the ridges (Figure 20.3a, d); the blocks diminish in size and frequency downslope. These observations have led Dalla Valle et al. (2015) to interpret the blocks as the result of the progressive disruption and disintegration of downslope translating ridges. The blocks that make up part of the G1-MTD were successively remobilized during the movement of G2-MTD. Blocks were transported further downslope and suffered a reorientation that allow their distinction from those that have not been affected by later movement (see figure 6a of Dalla Valle et al. (2015)). This observation shows that block orientation can be a good indicator of composite bodies that have suffered from discrete, repeated phases of movement (Joanne et al., 2013; Alves, 2015).

In the VMTC, blocks also flank a portion of the western margin of the debris-flow lobe that is by far less steep than the adjacent areas (Figures 20.5a and 20.6a). They have been interpreted as blocks fallen from the western lateral margin of the debris-flow lobe (Gamberi et al., 2011). Detached slide blocks, in fact, can be created when a tension crack penetrates to the base of the debris flow, and the segregated part typically tends to slide downslope over a thin layer of water (Marr et al., 2001).

Moreover, a blocky seafloor characterizes only the proximal part of the 30 m thick debris-flow sheet, where blocks appear to outline a channelized feature within the otherwise flat surface of the distal debris-flow sheet (Gamberi et al., 2011). Therefore, it can be assumed that blocks are an exclusive feature of the channelized part of the debris-flow sheet. Here they are related to the dynamics of the proximal part the subaqueous flow that had presumably a more viscous behavior than the dilute flow further downslope where the deposit has a flat top surface and lacks blocks (Dakin et al., 2013).

A blocky texture is always the major component of the debris-flow lobe of the Capo d'Orlando fan (Figure 20.7c). Here, however, blocks are found both in the channelized proximal part of the deposits and in their distal lobate portion (Figure 20.7b, c). It can, therefore, be advanced that in the latter case, the debris flows had mainly a viscous behavior and did not evolve into a dilute flow. This different kind of behavior is also be substantiated by the smaller areal extent of the debris-flow lobe of the Zappulla fan than the widespread distribution of the debris-flow sheet. Blocks are also the main component of the MTDs in the levee wedge of the Capo d'Orlando Basin (Figure 20.7a). Here they can represent a small part of the failed material that was otherwise mostly involved into a dilute flow and evacuated the basal shear surface.

20.4.3. Contractional Features

The Villafranca Slide has a steep frontal ramp, and thrust-related folds in its toe region provide the evidence that it is characterized by a highly compressed frontal region (Gamberi et al., 2011). The Villafranca Slide represents an example of a frontally confined landslide, as classified by Frey-Martínez et al. (2006). The northern accumulation sector of the G1-MTD has also a steep frontal ramp along which the moving mass was buttressed against the adjacent undeformed sediment (Figure 20.3e) (Dalla Valle et al., 2015). Close to its frontally confined toe, the G1-MTD shows a thickening, which is accompanied by pressure ridges, a strongly erosional base, and a positive bathymetric expression (Figure 20.4e). Both the Villafranca Slide and the G1-MTD are very thick deposits (up to 300 m) and thus confirm that, as suggested by Frey-Martínez et al. (2006) through a simple mechanical explanation, a large thickness of MTDs hampers the possibility

for landslides to ramp upward and leads to widespread contractional deformation.

Contractional structures shown by linear ridges mark also the frontal area of the slab slide where the detached slab slide is in contact with the adjacent in-place undisturbed sediments (Figure 20.5a) (Gamberi et al., 2011; Rovere et al., 2014). Also, the slab slide is, therefore, a frontally confined landslide, but differently from the Villafranca Slide and the G1-MTD, it is relatively thin. In this case, the contractional structures at the front of the failed mass have been interpreted as resulting from the low gradient of the seafloor that caused the mass to suffer only of a very small amount of movement with contractional deformation concentrated at the front (Gamberi et al., 2011).

The debris-flow lobe of the VMTC has a proximal confined part and a distal lobate unconfined part that spreads freely above the paleo-seafloor (Gamberi et al., 2011). Pressure ridges development, due to syn-depositional thrusting, shows that contractional deformation affected its proximal confined part and its distal region (Gamberi et al., 2011). The widespread occurrence of pressure ridges and the very steep, high-relief toe of the debris-flow lobe are in accordance with relatively high-viscosity flow (Bunz et al., 2005).

Contractional structures also develop along the eastern margin of the Villafranca Slide (Figure 20.6c) and form a positive relief at the seafloor (Figure 20.5a). This setting has been explained by Gamberi et al. (2011) as the proof of a slightly oblique movement of the Villafranca Slide, capable of generating transpressional deformation and accumulation of material along its eastern margin.

20.4.4. Barely Deformed Bodies

The slab slide, one of the MTDs that compose the VMTC in the Gioia Basin, is mostly made up of a succession with almost intact internal stratigraphy (Figure 20.6a) showing that it is a body that has suffered a very low degree of internal deformation. These observations have been reconciled with an interpretation that sees the slab slide as having originated through a simple clockwise rotation of a sediment pile originally located along the base of the Acquarone Ridge (Gamberi et al., 2011). Scarcely deformed bodies downslope from extensional features are also found in the western levee of the Villafranca channel (Figure 20.5f) (Gamberi and Rovere, 2011) as well as in the area upslope from the headwall escarpments of the Vieste MTC (Minisini et al., 2006; Dalla Valle et al., 2016). In both areas, a retrogressive character of failures is evident. Therefore, the slight deformed detached bodies, like those found in the headwall region of V1-MTD, can be the precursors of an incipient failure that eventually would result in the complete evacuation of the material (Figure 20.2b). Also, the slab slide could be the initial stage of a more evolved failure that could originate a completely translated mass. Gamberi et al. (2011) have suggested that this evolutionary scenario could be invoked to explain the formation of the debris-flow lobe that happened at the expenses of part of the slab slide.

20.4.5. Matrix-Rich Debris Flows

The G1-MTD distal accumulation domain, with its transparent seismic facies, high acoustic-signal penetration, and a very flat upper surface, can be indicative of a landslide body that mostly consists of a homogeneous mass, presumably corresponding with a matrix with fine-grained lithologies (Gee et al., 1999; Bowles et al., 2003; Dalla Valle et al., 2015). These observations, therefore, are suggestive of a dilute debris flow that could spread over much of the basin floor.

Also part of the debris-flow sheet of the VMTC has characters very similar to G1-MTD, as it is characterized by a transparent seismic facies, a flat upper surface, relatively high-signal penetration, and large areal extent (Figure 20.6a, b). Its nature is therefore similar to matrix-rich debris flow, a hypothesis which is also substantiated by its source area being located in the slope and thus presumably consisting of fine-grained, mostly muddy deposits. Alternatively, it can be hypothesized that the debris-flow sheet was produced by a flow which changed properties while flowing under the control of processes like hydroplaning or shear wetting (see *as examples* Gee et al., 1999; Lastras et al., 2004; De Blasio et al., 2005).

The NS always exhibits transparent seismic facies and a very large areal extent spanning almost the whole Gioia Basin (Figure 20.6d) (Gamberi and Marani, 2006). Also, in this case, therefore, the Nicotera failed body has been interpreted as consisting of completely disrupted and homogenized sediments. See Elverhoi et al. (1997).

20.5. CONCLUSIONS

MTDs are widespread in the southwestern Adriatic and in the southeastern Tyrrhenian margins. Barely deformed, detached successions are found upslope from landslide headwalls and can represent precursors to eventual sediment collapses. Ridges develop close to the headwall regions when the collapse affects old indurated successions; they undergo further disintegration during translation and transform into blocks downslope. Blocks also form on channelized debris flows and as the main component of debris-flow lobes that can be predominant in basin infill stratigraphy and originate a debris-flow lobe fan. Contractional features are located at the toe of frontally confined landslides or in slumps halted

by seafloor topography. Contractional features can also form along lateral margins of landslides when the sliding mass has an oblique movement. More dilute debris flows result in deposits with large areal extent and homogeneous texture likely consisting of fine-grained muddy material. In general, our study indicates that subaqueous mass-transport processes proceed through various mechanisms of failure, transport, and deposition to attain very different geometries that also reflect different rheology of the failed masses. The resultant type of MTD depends on the degree of disruption and disintegration of moving failed masses: as deformation intensity increases, it is possible to obtain a range of deposits ranging from slightly deformed detached sequences to ridges and blocks and to completely disaggregated masses mainly consisting of matrix. Lithology of the failed masses and source area and topography of the seafloor are also important factors that control the type of MTD. More broadly, our study highlights that marine geology studies can result in the definition of useful analogues for the reconstruction of continental margin evolution where subaqueous mass-transport processes are a prominent component. They can contribute to filling the gap between seismic and outcrop observations, furnishing important inputs to the characterization of submarine landslide processes.

ACKNOWLEDGMENTS

We would like to thank all our colleagues who, over a very long stretch of time, have contributed in various ways to the many different phases of the research that has led to the characterization of the geology of the Adriatic and Tyrrhenian Sea margins. In addition, our thanks goes to Claudia Romagnoli and Daniele Casalbore who carefully revised an early version of our manuscript, thus improving its quality. Finally, we are grateful to Key Ogata and Andrea Pini for their editorial advice. This chapter is contribution of ISMAR (Istituto di Scienze Marine) Bologna.

REFERENCES

Alves, T. M. (2015). Submarine slide blocks and associated soft-sediment deformation in deep-water basins: A review. *Marine and Petroleum Geology*, *67*, 262–285.

Argnani, A., Favali, P., Frugoni, F., Gasperini, M., Ligi, M., Marani, M., Mattietti, G., & Mele, G. (1993). Foreland deformational pattern in the southern Adriatic sea. *Annali di Geofisica*, *36*, 229–247.

Bowles, F. A., Fass, R. W., Vogt, P. R., Sawyer, W. B., & Stephens, K. (2003). Sediment properties, flow characteristics, and depositional environment of submarine mudflows, Bear Island Fan. *Marine Geology*, *197*, 63–74.

Bull, S., Cartwright, J., & Huuse, M. (2009). A review of kinematic indicators from mass transport complexes using 3D seismic data. *Marine and Petroleum Geology*, *26*, 1132–1151.

Bünz, S., Mienert, J., Bryn, P., & Berg, K. (2005). Fluid flow impact on slope failure from three dimensional seismic data: A case study in the Storegga Slide. *Basin Research*, *17*, 109–122.

Casalbore, D., Bosman, A., Chiocci, F. L., Ingrassia, M., Macelloni, L., Sposato, A., & Martorelli, E. (2016). New insights on failure and post-failure dynamics of submarine landslides on the intra-slope Palmarola Ridge (Central Tyrrhenian Sea). In G. Lamarche, J. Mountjoy, S. Bull, T. Hubble, S. Krastel, E. Lane, et al. (Eds.), *Submarine mass movements and their consequences: 7th international symposium, Advances in Natural and Technological Hazards Research* (Vol. 41, pp. 93–101). Dordrecht, The Netherlands: Springer.

Casalbore, D., Martorelli, E., Bosman, A., Morelli, E., & Chiocci, F. L. (2018). Failure dynamics of landslide scars on the lower continental slope of the Tyrrhenian Calabrian margin: Insights from an integrated morpho-bathymetric and seismic analysis. *The Geological Society, London, Special Publications*, *477*. https://doi.org/10.1144/SP477.16

Casalbore, D., Ridente, D., Bosman, A., & Chiocci, F. L. (2017). Depositional and erosional bedforms in Late Pleistocene Holocene pro-delta deposits of the Gulf of Patti (Southern Tyrrhenian Margin, Italy). *Marine Geology*, *385*, 216–227.

Colantoni, P., Tramontana, M., & Tedeschi, R. (1990). Contributo alla conoscenza dell'avampaese apulo: struttura del Golfo di Manfredonia (Adriatico meridionale). *Giornale di Geologia*, *52*, 19–32.

Dakin, N., Pickering, K. T., Mohrig, D., & Bayliss, N. J. (2013). Channel-like features created by erosive submarine debris flows: Field evidence from the Middle Eocene Ainsa Basin, Spanish Pyrenees. *Marine and Petroleum Geology*, *41*, 62–71.

Dalla Valle, G., Campiani, E., Foglini, F., Gamberi, F., Maselli, V., Pellegrini, C., & Trincardi, F. (2016). *Morphology of late Quaternary mass-transport complexes along the South-Western Adriatic Margin*. Paper presented at Proceedings of the 12th International Symposium on Landslides, Napoli, Italy, 12–19 June 2016.

Dalla Valle, G., Campiani, E., Foglini, F., Gamberi, F., & Trincardi, F. (2014). Mass transport complexes from contourite and shelf-edge deposits along the South-western Adriatic margin (Italy). In S. Krastel, J. H. Behrmann, D. Völker, M. Stipp, C. Berndt, R. Urgeles, et al. (Eds.), *Submarine mass movements and their consequences, Advances in Natural and Technological Hazards Research* (Vol. 37, pp. 447–457). Dordrecht, The Netherlands: Springer.

Dalla Valle, G., Gamberi, F., Foglini, F., & Trincardi, F. (2015). The Gondola Slide: A mass transport complex controlled by margin topography (South-Western Adriatic Margin, Mediterranean Sea). *Marine Geology*, *366*, 97–113.

De Blasio, F. V., Elverhøi, A., Issler, D., Harbitz, C. B., Bryn, P., & Lien, R. (2005). On the dynamics of subaqueous clay rich gravity mass flow: The giant Storegga slide, Norway. *Marine and Petroleum Geology*, *22*, 179–186.

Doglioni, C., Mongelli, F., & Pieri, P. (1994). The Puglia uplift (SE-Italy): An anomaly in the foreland of the Apenninic

subduction due to buckling of a thick continental lithosphere. *Tectonics*, *13*, 1309–1321.

Elverhoi, A., Norem, H., Andersen, E. S., Dowdeswell, J. A., Fossen, I., Haflidason, H., et al. (1997). On the origin and flow behaviour of submarine slides on deep-sea fans along the Norwegian-Barents Sea continental margin. *Geo-Marine Letters*, *17*, 119–125.

Finetti, I., Bricchi, G., Del Ben, A., Pipan, A., & Xuan, Z. (1987). Geophysical study of the Adria plate. *Membro Societa Geologica Italiana*, *40*, 335–344.

Freiwald, A., Beuck, L., Rüggeberg, A., Taviani, M., & Hebbeln, D. R/V Meteor Cruise M70-1 participants(2009). The white coral community in the central Mediterranean Sea revealed by ROV surveys. *Oceanography*, *22*, 58–74. http://dx.doi.org/10.5670/oceanog.2009.06

Frey-Martínez, J., Cartwright, J., & James, D. (2006). Frontally-confined versus frontally emergent submarine landslides: A 3D seismic characterization. *Marine and Petroleum Geology*, *23*, 585–604.

Frey-Martinez, J., Cartwright, J. A., & Hall, B. (2005). 3D seismic interpretation of slump complexes: Examples from the continental margin of Israel. *Basin Research*, *17*, 83–108.

Gamberi, F., Breda, A., & Mellere, D. (2017). Depositional canyon heads at the edge of narrow and tectonically steepened continental shelves: Comparing geomorphic elements, processes and facies in modern and outcrop examples. *Marine and Petroleum Geology*, *87*, 157–170.

Gamberi, F., & Dalla Valle, G. (2009). The impact of margin-shaping processes on the architecture of the Sardinian and Sicilian margin submarine depositional systems within the Tyrrhenian sea. In B. Kneller, O. J. Martinsen, & B. McCaffrey (Eds.), *External controls on deep-water depositional systems, SEPM Special Publication* (Vol. 92, pp. 207–219). Tulsa, OK: SEPM.

Gamberi, F., & Marani, M. P. (2006). Hinterland geology and continental margin growth: The case of the Gioia Basin (southeastern Tyrrhenian Sea). *Geological Society, London, Special Publications*, *262*, 349–363.

Gamberi, F., & Marani, M. P. (2007). Downstream evolution of the Stromboli Slope Valley (southeastern Tyrrhenian Sea). *Marine Geology*, *243*, 180–199.

Gamberi, F., & Rovere, M. (2011). Architecture of a modern transient slope fan (Villafranca fan, Gioia basin–Southeastern Tyrrhenian Sea). *Sedimentary Geology*, *236*, 211–225.

Gamberi, F., Rovere, M., Dykstra, M., Kane, I. A., & Kneller, B. C. (2013). Integrating modern seafloor and outcrop data in the analysis of slope channel architecture and fill. *Marine and Petroleum Geology*, *41*, 83–103.

Gamberi, F., Rovere, M., & Marani, M. P. (2011). Mass-transport complex evolution in a tectonically active margin (Gioia Basin, Southeastern Tyrrhenian Sea). *Marine Geology*, *279*, 98–110.

Gamberi, F., Rovere, M., Marani, M. P., & Dykstra, M. (2015). Modern submarine canyon feeder-system and deep-sea fan growth in a tectonically active margin (northern Sicily). *Geosphere*, *11*, 307–319.

Gamberi, F., Rovere, M., Mercorella, A., Leidi, E., & Dalla Valle, G. (2014). Geomorphology of the NE Sicily continental shelf controlled by tidal currents, canyon head incision and river-derived sediments. *Geomorphology*, *217*, 106–121.

Gamberi, F., Savelli, C., Marani, M. P., Ligi, M., Bortoluzzi, G., Landuzzi, V., et al. (1998). Contesto morfo-tettonico e depositi idrotermali di solfuri ed ossidi di ferro in una porzione sommersa dell'arco eoliano (in base ad indagini ad alta definizione). *Italian Journal of Geoscience*, *117*, 55–71.

Gee, M. J. R., Gawthorpe, R. L., & Friedmann, S. J. (2006). Triggering and evolution of a giant landslide, offshore Angola revealed by 3D seismic stratigraphy and geomorphology. *Journal of Sedimentary Research*, *76*, 9–19.

Gee, M. J. R., Masson, D. G., Watts, A. B., & Allen, P. A. (1999). The Saharan debris flow: An insight into the mechanics of long runout submarine debris flows. *Sedimentology*, *46*, 317–335.

Haflidason, H., Sejrup, H. P., Nygård, A., Bryn, P., Lien, R., Forsberg, C. F., et al. (2004). The Storegga Slide: Architecture, geometry and slide-development. *Marine Geology*, *231*, 201–234.

Joanne, C., Lamarche, G., & Collot, J.-Y. (2013). Dynamics of giant mass-transport in deep submarine environments: The Matakaoa Debris Flow, New Zealand. *Basin Research*, *25*, 1–18.

Krastel, S., Wynn, R. B., Georgiopoulou, A., Geersen, J., Henrich, R., Meyer, M., & Schwenk, T. (2012). Large-scale mass wasting on the Northwest African Continental Margin: Some general implications for mass wasting on passive continental margins. In Y. Yamada, K. Kawamura, K. Ikehara, Y. Ogawa, R. Urgeles, D. Mosher, et al. (Eds.), *Submarine mass movements and their consequences, Advances in Natural and Technological Hazards Research 31* (pp. 189–192). The Netherlands: Springer.

Laberg, J., Vorren, T., Miener, J., Bryn, P., & Lien, R. (2002). The Trænadjupet Slide: A large slope failure affecting the continental margin of Norway 4000 years ago. *Geo-Marine Letters*, *22*, 19–24.

Lamarche, G., Joanne, C., & Collot, Y. J. (2008). Successive, large mass-transport deposits in the south Kermadec forearc basin, New Zealand: The Matakaoa Submarine Instability Complex. *Geochemistry, Geophysics, Geosystems*, *9*, 1–30.

Lastras, G., Canals, M., Urgeles, R., Hughes-Clarke, J. E., & Acosta, J. (2004). Shallow slides and pockmark swarms in the Eivissa Channel, western Mediterranean Sea. *Sedimentology*, *51*, 837–850.

Lentini, F., Carbone, S., Catalano, S., & Grasso, M. (1996). Elementi per la ricostruzione del quadro strutturale della Sicilia orientale. *Membro Societa Geologica Italiana*, *51*, 179–195.

Lucente, C. C., & Pini, G. (2003). Anatomy and emplacement mechanism of a large submarine slide within a Miocene foredeep in the Northern Apennines, Italy: A field perspective. *American Journal of Science*, *303*, 565–602.

Macdonald, D. I. M., Moncrieff, A. C. M., & Butterworth, P. J. (1993). Giant slide deposits from a Mesozoic fore-arc basin, Alexander Island, Antarctica. *Geology*, *21*, 1047–1050.

Marr, J. G., Harff, P. A., Shanmugam, G., & Parker, G. (2001). Experiments on subaqueous sandy gravity flows: The role of clay and water content in flow dynamics and depositional

structures. *Geological Society of America Bulletin*, *113*, 1377–1386.

Martorelli, E., Bosman, A., Casalbore, D., & Falcini, F. (2016). Interaction of down-slope and along-slope processes off Capo Vaticano (southern Tyrrhenian Sea, Italy), with particular reference to contourite-related landslides. *Marine Geology*, *378*, 43–55.

Micallef, A., Masson, D. G., Berndt, C., & Stow, D. A. V. (2009). Development and mass movement processes of the north-eastern Storegga Slide. *Quaternary Science Reviews*, *28*, 433–448.

Minisini, D., Trincardi, F., & Asioli, A. (2006). Evidence of slope instability in the South-Western Adriatic margin. *Natural Hazards and Earth System Sciences*, *6*, 1–20.

Moscardelli, L., & Wood, L. J. (2008). New classification system for mass transport complexes in offshore Trinidad. *Basin Research*, *20*, 73–98.

Moscardelli, L., Wood, L. J., & Mann, P. (2007). Mass-transport complexes and associated processes in the offshore area of Trinidad and Venezuela. *American Association of Petroleum Geologists Bulletin*, *90*, 1059–1088.

Ori, G. G., Roveri, M., & Vannoni, F. (1986). Plio-Pleistocene sedimentation in the Apenninic-Adriatic foredeep (Central Adriatic sea, Italy). In P. A. Allen & P. Homewood (Eds.), *Foreland basins, International Association of Sedimentologists, IAS Special Publications* (Vol. 8, pp. 183–198). Oxford: Wiley-Blackwell.

Ortolani, F., & Pagliuca, S. (1987). Tettonica transpressiva nel Gargano e rapporti con le catene Appenninica e Dinarica. *Membro Societa Geologica Italiana*, *38*, 205–224.

Patacca, E., & Scandone, P. (1989). Post Tortonian mountain building in the Apennines. The role of the passive sinking of a relic lithospheric slab. In A. Boriani, M. Bonafede, G. B. Piccardo, & G. B. Vai (Eds.), *The Lithosphere in Italy, Advances in earth science research. Accademia Nazionale dei Lincei* (Vol. 80, pp. 157–176). Roma: Accad. Nazionale dei Lincei.

Pickering, K. T., & Corregidor, J. (2005). Mass-transport complexes (MTCS) and tectonic control on basin-floor submarine fans, Middle Eocene, south Spanish Pyrenees. *Journal of Sedimentary Research*, *75*, 761–783.

Pondrelli, S., Salimbeni, S., Ekström, G., Morelli, A., Gasperini, P., & Vannucci, G. (2006). The Italian CMT dataset from 1977 to the present. *Physics of the Earth and Planetary Interiors*, *159*(3–4), 286–303.

Ricci Lucchi, F. (1986). The Oligocene to recent foreland basins of the Northern Apennines. In P. A. Allen & P. Homewood (Eds.), *Foreland basins, International Association of Sedimentologists, IAS Special Publications* (Vol. 8, pp. 105–139). Oxford: Wiley-Blackwell.

Ridente, D., Di Bucci, D., Fracassi, U., & Trincardi, F. (2010). *Assessing seismogenic potential of offshore Faults in seismic hazard perspective (SW Adriatic Margin, Italy)*. Paper presented at Proceedings of ESF-FWFL-FUI Conference "Submarine Paleoseismology: The Offshore Search of Large Holocene Earthquakes", Obergurgl, Austria, 11–16 September.

Ridente, D., & Trincardi, F. (2002). Eustatic and tectonic control on deposition and lateral variability of Quaternary regressive sequences in the Adriatic Basin (Italy). *Marine Geology*, *184*, 273–293.

Ridente, D., & Trincardi, F. (2006). Active foreland deformation evidenced by shallow folds and faults affecting late Quaternary shelf-slope deposits (Adriatic Sea, Italy). *Basin Research.*, *18*, 171–188.

Rovere, M., Gamberi, F., Mercorella, A., & Leidi, E. (2014). Geomorphometry of a submarine mass-transport complex and relationships with active faults in a rapidly uplifting margin (Gioia Basin, NE Sicily margin). *Marine Geology*, *356*, 31–43.

Sawyer, D. E., Flemings, P. B., Dugan, B., & Germaine, J. T. (2009). Retrogressive failures recorded in mass transport deposits in the Ursa Basin, Northern Gulf of Mexico. *Journal of Geophysical Research*, *114*, B10102.

Tramontana, M., Morelli, D., & Colantoni, P. (1995). Tettonica plioquaternaria del sistema sud-garganico (settore orientale) nel quadro evolutivo dell'Adriatico centro meridionale. *Studi Geologici Camerti*, *2*, 467–473.

Trincardi, F., Foglini, F., Verdicchio, G., Asioli, A., Correggiari, A., Minisini, D., et al. (2007). The impact of cascading currents on the Bari Canyon System, SW-Adriatic Margin (Central Mediterranean). *Marine Geology*, *246*, 208–230.

Tripsanas, E., Piper, D. J. W., & Cambpell, D. C. (2008). Evolution and depositional structure of earthquake-induced mass movements and gravity flows: Southwest Orphan Basin, Labrador Sea. *Marine and Petroleum Geology*, *25*, 645–662.

Verdicchio, G., & Trincardi, F. (2006). Short-distance variability in slope bed-forms along the southwestern Adriatic margin (central Mediterranean). *Marine Geology*, *234*, 271–292.

Westaway, R. (1993). Quaternary uplift of Southern Italy. *Journal of Geophysical Research*, *98*, 21741–21772.

Wilson, C. K., Long, D., & Bulat, J. (2004). The morphology, setting and processes of the Afen Slide. *Marine Geology*, *213*, 149–167.

INDEX

Note: f denotes figures and t denotes tables

Age dating, 189–90
Ammoudhares Formation, 73
Anisotropy of magnetic susceptibility (AMS), 142
Aquitanian-Burdigalian, 29
Autoacephalation, 8

Back-arc oceanic crust, 118
Backthrusts, 144, 145f
Bari Canyon MTC, 345
Basal breccias, 165, 167
Basal glide plane, 79, 82, 84f, 91, 256, 303, 305
Basal interaction, 91, 96, 102, 127
Basal shear surface (BSS), 91–92
Bedding, 5, 48, 51, 58, 60, 63f, 78f, 97f, 99, 102, 110, 113, 121, 124, 141, 158f, 159, 161, 164f, 173, 253, 303, 305, 341
Bed disarticulation, 161
Bioclasts, 60, 63f, 166
Blocky-flow facies, 38
Boso Peninsula, 58
Boulder conglomerates
  block and debris-flow deposits, 77–78
Bowl Slide (BS), 319–23
Breccia-conglomerates, 77
Bulldozing processes, 155, 156, 166, 168

Calciclastic Flysch, 157–65
Cap Blanc Slide
  acoustic data, 300–2
  climate, 300
  core-seismic integration, 302, 305–6
  failure planes, 306–8
  landslide ages and errors, 306
  oceanography, 300
  ODP Site 658 core data, 302
  reflectors, 306–8
  slide complex, 304–5
    preconditioning and triggers, 308–9
    ridge toe, 303–4
    seafloor morphology, 302–3
Capo d'Orlando Basin MTC, 349
Capping calcarenite-marl, 159
Carbonate blocks, 73, 75, 77, 79, 85
Carbonate megabreccias, 14, 77, 85
Carbonate platform margins, 10
Carboniferous, Cerro Bola NW Argentina
  block generation, 101–2
  geological setting, 92–93
  MTD I, 94–96
  MTD II, 96–98
  MTD III, 98–99
  seafloor interaction, 99–101
Casaglia-Monte della Colonna
  displaced intrabasinal sediments, 130–31
  geological setting, 118–20
  internal deformation domains, 128–30
  North verging slope deposits, 124–27
  physiography and internal structures, 121–27
  Santerno sector, North verging basin plain deposits, 127
  shear zone, 127–28
  southwest to northeast directed basin plain deposits
    Casaglia sector, 121–24
    Marradi sector, 124
  southwest verging basin plain deposits, 127
  translation mechanism, 130–31
Centaur Complex
  headwall salients, 270
  internal architecture, 270–71
Cervarola Sandstones Formation (CSF)
  facies analysis of, 32
  stratigraphy of, 32
Cervarola Sandstones succession
  megabeds, 34–38
  Pievepelago Formation, 32–34
  Sestola-Vidiciatico Formation, 32–34
  slumps, 34
  stratigraphic boundary, 39
Chaotic complexes, 29, 31
Chaotic deposits, 6, 34, 212, 280, 281, 283, 290–92, 345
Clastic elements, 49–50
Clast/matrix relationships, 50–51
Climate changes, 189, 327
Climate control, 190, 300
Close range photogrammetry, 118
Co-genetic debris flow, 121, 124
Colombine layers, 120
Colored melange, 45, 53
Compressional ridges, 236, 240
Concretions, 96, 173
Continental crust, 262

Submarine Landslides: Subaqueous Mass Transport Deposits from Outcrops to Seismic Profiles, Geophysical Monograph 246, First Edition. Edited by Kei Ogata, Andrea Festa, and Gian Andrea Pini.

© 2020 American Geophysical Union. Published 2020 by John Wiley & Sons, Inc.

Continental margin architecture, 185
Coseismic slip, 141
Counter-verging basin plain, 130, 131
Crater lakes, 202, 209
Critical taper model, 147, 151

Dammed lakes, 202
Dead Sea basin
  contractional structures, 146–47, 151
  external geometry
    critical taper model, 147
    dislocation models, 147–50
    frontally confined/emergent models, 147
    thrust ramps, 150
  internal evolution of MTDS
    general structural sequences, 142, 150
    thrust sequences, 142–46
  regional patterns, 141–42, 150
  regional setting, 139–41
  reworking triggered by multiple seismic events, 146, 150–51
Dead Sea Fault, 139, 140, 146
Debris avalanche deposit (DAD) loading, 278, 286–87
  décollement propagation from, 283–84
  seafloor sediment failures triggered by, 287
Debris avalanches, 278
Debris flow, 5, 6, 8, 10–12, 14, 38, 40, 50, 53, 58, 85, 105, 112, 121, 124, 155, 157, 163, 165–69, 179, 186, 187f, 191, 202, 261, 278, 290, 328, 353, 354
Debris-flow deposits, 77–78, 85, 163, 165, 290, 349
Debris-flow formation, 11
Debris-flow lobe, 347, 349, 352, 353, 358f
Debris-flow sheet, 347, 349f, 350f, 352, 353
Deepwater submarine canyons, 193
Deformation style, 94, 128, 129f, 130, 228
Degree of lithification, 17
Delta collapses, 202, 212–14, 215f, 220
Detached ridges, 323, 347, 349–52
Discrete shear zone, 14, 127
Dislocation models, 147–50
Disrupted blocks, 77
Distal compressional domains, 240
Duplex-style compression, 161

Epi-nappe olistostromes/sedimentary melanges, 12
Espirito Santo Basin (ESB), SE Brazil, 75–77
  data and methods, 231
  geological settings of, 228–31
  influence of salt tectonics, 240–43
  mass-transport deposits character
    distal compressional domains, 240
    proximal to transitional domains, 231–38
    transitional domains, 238–39
Eurasian plate, 48, 248, 263
Exmouth Plateau Arch, 262f, 263–69, 272t, 273
Exotic blocks, 6, 14, 45, 50, 53, 101, 102
Extrabasinal “chaotic” units, 32–34

Fault-dominated sandstone, 113
Flank collapses, 277, 278, 280, 281, 283, 284, 285f, 286–88, 290, 292
Flattening structures, 130
Flow perturbation models, 142
Fluid migration, 50, 211, 212f, 219, 273
Fluvial lakes, 202
Foredeep basin
  Cervarola Sandstones Formation (CSF)
    facies analysis of, 32
    stratigraphy of, 32
  geological setting, 29
    geometrical relationships and previous interpretations, 29–31
    tectonic remarks, 31–32
  MTDs within Cervarola Sandstones succession
    megabeds, 34–38
    Pievepelago Formation, 32–34
    Sestola-Vidiciatico Formation, 32–34
    slumps, 34
Frontal collapse, 273–74
Frontally confined/emergent models, 13, 85, 147
Frontal tectonic erosion, 11
Frontal thrust, 15, 209, 247, 252, 253, 256, 257

Gamma ray attenuation (GRA) density, 302, 307f
Gargano system, 340
Gas charging, 185, 188
General Bathymetric Chart of the Oceans (GEBCO), 302
Geohazards, 86, 327
  potential and tsunamis, 190–93
Geotectonics
  high-resolution stratigraphic framework, 58–60
  Kazusa Group on Boso Peninsula, 58
  of mass-transport deposits, 59f
Gioia Basin MTC, 346–49
Glacigenic lakes, 202, 212, 217, 219
Gloria Knolls Slide (GKS), 318–19
  preconditioning factors, 328–30
  and triggers for slope instability, 328–30
  tsunami capacity, 330–31
  tsunami modeling, 325–27
Gondola Slide
  MTC, 342–45
  SWAM, 340
Gravitational collapse, 73, 77, 85, 227, 269, 271, 273, 274
Great Barrier Reef margin
  bottom friction, 316
  Bowl Slide (BS), 319–23
  data sets and analysis, 315–16
  Gloria Knolls Slide (GKS), 318–19
    preconditioning factors, 328–30
    and triggers for slope instability, 328–30
    tsunami capacity, 330–31
    tsunami modeling, 325–27
  mass movements
    timing of, 327
    types of, 327–28
  regional setting
    depositional history, 314
    modern physiography, 314–15
    sediment distribution, 314–15

Ribbon Reef Slide (RRS), 316–18
tsunami modeling, 316
Viper Slide (VS), 323–25
Groundwater charging, 185
Guandacol Formation, 92, 107, 108

Headscarp retrogression, 271–72, 274
Heterolithic mudstone, 113
High resolution multibeam systems, 193
High-resolution photographs, 161
High sedimentation rate, 46, 58, 179, 188f, 190, 328, 329
Neogene and Quaternary sedimentary, 172
Northwest Shelf of Australia, 273
Holomictite, 110, 111f, 115
Homogeneous vertical stratigraphy, 13
Hydroplaning, 8, 17, 83, 110, 112, 115, 185, 353
HYSEA, 286

Ierapetra Basin, SE Crete, 75
Imbricate-dominated sandstones, 113
Imbricated thrusts, 162, 163, 166, 240
Infill drift, 303
Integrated Ocean Drilling Program (IODP), 253
Interbedded sandstone and mudstone, 173
Intercalated MTDs
Lake Calafquén, 219
Lake Como, 217–19
Lake Fagnano, 219
sedimentology of Calciclastic Flysch, 157–65
Skilak Lake, 217
Internal deformation, 8, 58, 64, 93, 98, 117, 118, 124, 128–32, 158, 159, 161, 162, 165, 186, 187f, 228, 236, 240, 241, 243, 261, 339, 347, 353
Internal thrusts, 161
International Ocean Discovery Program (IODP) Janus database, 302
Intrabasinal slumps, 40
Intra-nappe olistostromes/sedimentary melanges, 12
IODP Expedition 340, 278, 281–83, 286, 287, 290

Japan Agency for Marine-Earth Science and Technology (JAMSTEC), 248

Kalamavka Formation, 75, 76f, 77, 78f, 81, 82
Karstic lakes, 202
Katsuura Formation, 60
Kinan Seamount Chain (KSC), 248
Kiwada Formations, 58, 60
Kumano Basin region, 248, 251f, 256

Lacustrine MTDs
delta collapses, 212–14
lateral slope landslides, 209–11
margin collapses, 211–12
rockfalls, 215–17
Lake Calafquén, 219
Lake Como, 217–19
Lake Fagnano, 219
Landslide ages/errors, 306
La Peña Canyon, Argentina
depositional model, 113–15
local setting, 108
MTD1, 108
MTD2, 108
MTD3, 109–10
MTD4, 110
MTD5, 110–13
MTD6, 113
regional setting, 106–8
Lateral slope landslides, 202, 209–11, 217
Lesser Antilles Arc, 280–81
instability processes, 283
Montagne Pelée volcano through landslide processes, 284–86
Lisan Formation, 140–42, 143f, 145f, 146, 147, 148f, 151

Major slide, 303, 306–8
Makran olistostrome
approximate volume, 51–52
characteristics, 48f
covered area, 51–52
geological setting, 45–48
geometry and internal structure
clastic elements, 49–50
clast/matrix relationships, 50–51
matrix features, 49
host sedimentary succession, 51
updated interpretations, 52–53
Makrilia Formation, 75, 76f, 78, 80f, 81, 82
Males Formation, 75, 77, 81
Mappable sedimentary deposits, 5
Margin collapses, 202, 211–12
Mass-flow transformation
dimensions, 167
facies model, 165–67
geological setting, 156–57
sedimentology of Calciclastic Flysch
MTD1, 157–59
MTD2, 157–59
MTD3, 159–61
MTD4, 161–63
MTD5, 163–65
MTD6, 163–65
source area, 168
triggering mechanism, 167–68
Mass-transport complexes (MTCs), 3, 186
Mass-transport deposits (MTDs), 27, 73
Carboniferous, at Cerro Bola NW Argentina
MTD I, 94–96
MTD II, 96–98
MTD III, 98–99
within Cervarola Sandstones succession
megabeds, 34–38
Pievepelago Formation, 32–34
Sestola-Vidiciatico Formation, 32–34
slumps, 34
mechanical characteristics, 58
mixing process, 115
outcrops, 62f, 63f

Mass-transport deposits (MTDs) (*cont'd*)
progressive slumping within, 115
three-dimensional (3D), 3
two-dimensional (2D), 3
type 1, 76f, 77
in Kazusa group, 60
type 2, 81
in Kazusa group, 60–64
type 3, 77
in Kazusa group, 64–65
type 4, 80f
type 5, 80f, 81
Mass-wasting processes, 167, 168
Megabeds, 4f, 14, 28f, 32, 34–40, 96, 120
Megabreccias, 10, 12, 14, 77, 85
Megasplay fault zone (MSFZ), 253
Megaturbidites, 4f, 35, 38, 40, 202, 213, 215, 217–20
Melange formation, 5, 6, 13
Mesoscopic ductile faults, 128
Meteorite-impact lakes, 202, 211
Minab-Zendan fault zone, 51
Mineoka ophiolite complex, 58
Minor slide, 303, 305, 306
Mithi Formation, 75
Miura peninsulas, 58
Modino Pievepelago, 31
Modino succession, 28f, 29, 31
Mollusks, 60
Montagne Pelée volcano
through landslide processes, 284–86
MTD1
Calciclastic Flysch and intercalated, 157–59
Carboniferous, at Cerro Bola NW Argentina, 94–96
La Peña Canyon, 108
MTD2
Calciclastic Flysch and intercalated, 157–59
Carboniferous, at Cerro Bola NW Argentina, 96–98
La Peña Canyon, 108
MTD3
Calciclastic Flysch and intercalated, 159–61
Carboniferous, at Cerro Bola NW Argentina, 98–99
intensity of deformation, 160
La Peña Canyon, 109–10
photomosaic of, 160f, 162f
MTD4
Calciclastic Flysch and intercalated, 161–63
La Peña Canyon, 110
MTD5
Calciclastic Flysch and intercalated, 163–65
La Peña Canyon, 110–13
MTD6
Calciclastic Flysch and intercalated, 163–65
La Peña Canyon, 113
MTD8, 64
MTD10, 64
MTD N78, 172, 177–79
Mud-dominated deposits, 13
Muddy debris flow, 8, 65
Muddy matrix, 46, 48f, 50, 51, 53, 82, 108, 113, 118, 215, 349
Multibeam bathymetry, 209, 210f, 211, 301f, 302, 309, 313, 314, 316
Multibeam echosounder, 248, 315
Multi-cell flow model, 147, 149f, 150

Nankai Trough accretionary prism
data and methods, 248–52
geologic setting, 248
landslides, 252
submarine landslides
forearc basin, 253–56
outer prism, 253
prism toe, 253
tectonic setting, 248
Nicotera slump (NS), 349
North Taranaki, New Zealand
geologic setting of, 172–73
Rapanui Stream, 173–75
seismic example, 177–78
Tongaporutu Beach, 175–77
Northwest Shelf of Australia
Centaur Complex
headwall salients, 270
internal architecture, 270–71
composite failures mechanisms
collapse of frontal part failures, 271
headscarp retrogression, 271–72
materials and methods, 264
rationale, 261–62
regional outlook, 262–63
seismic stratigraphic, 263–64
slope failures, 264–68
Thebe Complex
central slide, 268
headwall slumps, 268
secondary slide, 268–69
triggering mechanisms
bottom currents, 273
fluid seepage and migration, 273
high sedimentation rate, 273
seismic activity, 272
slope steepening, 273
wave loading and dissociation of gas hydrates, 273
Nummulites tests, 162, 163

Ocean bottom seismometers (OBS), 193
Oceancontinent transition (OCT) zones, 10
Ocean Drilling Program (ODP), 263, 264
Offshore infrastructure
age dating, 189–90
characteristics and peculiarities, 183–85
climate control and interplay, 190
distribution and classification, 185–87
geohazard potential and tsunamis, 190–93
long-term monitoring, 193–94
preconditioning factors, 187–89
triggers factors, 187–89

Ohara Formations, 58, 60
Olistostromes, 3
  geographical distribution of, 4f, 10–12
  historical outline, 5–6
  as markers of geologic events, 15–16
  "size" and "preservation"
    slide-flow transformation, 13–14
    slide volume, 14
    tectonic reworking, 14–15
  submarine landslide
    integrated approach, 6
    processes and products, 6–10
Outcrop data, 5, 73, 81, 91, 92
Out-of-plane movement, 147, 151
Oversteepening, 11, 72, 82, 185, 187, 213, 227, 329
Overstep thrust sequences, 144f, 145f, 146, 150

Particle interlocking, 189
Passive continental margins, 227
Patquia Formation, 92, 108
Pebbly mudstones, 48, 50, 53, 113, 114f
Philippine Sea Plate, 58, 248
Photomosaic, of MTD-3, 160f, 162f
Pievepelago Formation, 29, 31–34, 38
Piezometers, 193
Piggyback thrust sequences, 142, 143f–145f, 146, 150
Pleistocene Kazusa Group
  geotectonic
    high-resolution stratigraphic framework, 58–60
    Kazusa Group on Boso Peninsula, 58
  MTDs in
    type I, 60
    type II, 60–64
    type III, 64–65
Pop-up block, 113, 240, 347
Post-depositional erosion, 239
Precursory olistostromes, 5, 6, 12, 38
Proximal to transitional domains, 231–38

Quaternary landslides, 247

Radiocarbon dating, 190
Rapanui Stream, 173–75, 179
Rapid sedimentation, 185, 187, 188, 190
Rhodoliths tests, 162, 163
Ribbon Reef Slide (RRS), 316–18
Ricker wavelet, 302
Rockfall deposits, 202, 215–17
Rolled-up sandstone blocks, 60
Rounded gravel clasts, 60

Salt diapirs, 77
Salt-rich continental margins, 227
Salt tectonic domains, 228, 229f, 230f, 231, 239–43
Sand distribution, 115
Sand-dominated deposits, 13
Sandstone
  and mudstone blocks, 173
  and siltstone blocks, 96
SeaBeam 2112 systems, 248
Seafloor instability, 189, 316, 340
Seafloor sediment failures, 278, 281, 283, 285f, 286–90
Seafloor topography, 85, 239, 319, 323, 340, 354
Second-order dislocation/flow cells, 147
Sedimentary cap, 145f, 146, 150
Sedimentary mélange, 3
  geographical distribution of, 4f, 10–12
  historical outline, 5–6
  as markers of geologic events, 15–16
  "size" and "preservation"
    slide-flow transformation, 13–14
    slide volume, 14
    tectonic reworking, 14–15
  submarine landslide
    integrated approach, 6
    processes and products, 6–10
Sedimentary olistostrome, 38
Sediment cores, 190, 209, 213, 215f, 217f, 290, 328, 330
Sediment failures, 40, 53, 187f, 278, 281, 283f, 285f, 286–90, 339, 346, 349, 351f
Sediment fluxes, 57, 202, 299
Seepage of fluids, 273
Seismic
  activity, 272
  amplitudes, 230
  data, 73
  example, 177–78
  geomorphology techniques, 264, 340
  loading, 185
  profiles, 57–58
Sestola-Vidiciatico Formation, 31–34, 38–40
SHALTOP, 286
Shear failure, 58, 91
Shear strength, 185, 187–89, 272, 281, 287, 288f, 306–8, 328
Shear stress, 40, 101, 102, 159, 161–63, 165–68, 187, 272, 273, 309
Single-cell dislocation model, 149f, 150
Skilak Lake, 217
Slide-flow transformation, 13–14
Slide-to-slump composite failure, 272
Slope destabilization, 186
Slope failures, 131, 184f, 185–91, 193
  in Exmouth Plateau Arch, 272
  Northwest Shelf of Australia, 264–68
Slope instability, 11, 17, 73, 82, 85, 190, 193, 211, 227, 268, 272t, 316, 327–30
Slope/shelf attachment, 231
Slope steepening, 256, 272t, 273
Slope stratigraphy, 147, 185, 188
Slump fold orientation, 141
Slump-related structures, 160
Soft-sediment deformation, 98
Southeastern Tyrrhenian Margin
  barely deformed bodies, 353
  blocks, 352
  Capo d'Orlando Basin MTC, 349
  contractional features, 352–53
  detached ridges, 349–52

Southeastern Tyrrhenian Margin (*cont'd*)
  Gioia Basin MTC, 346–49
  matrix-rich debris flows, 353
Southwestern Adriatic Margin (SWAM)
  Bari Canyon MTC, 345
  Gondola MTC, 342–45
  Vieste Slide MTC, 340–42
SS 477 outcrop, 123, 127
Storm wave loading, 185
Stratal disruption, 6, 11, 118, 121, 123, 124, 128, 130
Strike-slip basin, 107
Structural geology, 6, 8, 17
Subaerial instabilities, 283
Submarine instabilities, 283, 285f
Submarine landslide deposits (SLDs), 3–17, 183, 285f, 291f
Submarine mass flow, 49, 51–53, 155, 239
Submarine slide block, 72, 73, 85
Surging/slackening flow, 150, 151
Synchronous thrusting, 142, 144, 150
Synclines, 31, 51, 53, 120, 127, 158–60
Syn-rift strata, 71
Syn-tectonic deformation, 82

Tectonic
  and depositional processes, 5
  reworking, 14–15
Tectonic events, 15–16, 27
Tectonic lakes, 202, 211
Tectonic movements, 83, 187, 211. *See also* Oversteepening
Tectonic unit, 31
Tectonism markers, in marine extensional basins
  data set and methods, 73
  geological setting
    Espirito Santo Basin (ESB), SE Brazil, 75–77
    Ierapetra Basin, SE Crete, 75
  tectonic activity
    kinematic indicators of syn-tectonic deformation, 82
    slumping and folding of oversteepened slopes, 81–82
    thickening and deepening of marine facies, 81
  types of syn-tectonic mass-transport deposits
    blocks and debris-flow deposits (boulder conglomerates), 77–78
    carbonate blocks and breccia-conglomerates, 77
    carbonate megabreccias, 77
    chaotic volumes of turbidites, chalk, and evaporites, 78–79
    disrupted blocks, 77
    steep debris on foot of large fault scarps, 79–81
Tephra marker beds, 60, 64
Thebe Complex
  central slide, 268
  headwall slumps, 268
  secondary slide, 268–69
Thinned continental margins, 10
3D surveys
  in Exmouth Plateau, 264–68
  seismic, 236
Thrust, internal, 161
Thrust ramps, 150, 151
Thrust sequences
  overstep, 144f, 145f, 146, 150
  piggyback, 142, 143f–145f, 146, 150
Tide cyclic loading, 185, 188
Tiltmeters, 193
Tongaporutu Beach, 173t, 175–77
Tosabae Embayment, 248, 250f, 256
Transitional domains, 238–39
Tsunamis
  capacity of GKS, 330–31
  geohazard potential and, 190–93
  hazards, 287–90
  modeling of GKS, 325–27
  wave heights, 289
Tupe Formation, 92, 108
Turbiditic foredeep deposits, 29
Turbidity currents, 32, 34, 38, 40, 115, 120, 155, 157, 159, 161, 165–68, 184, 185, 187f, 191, 193, 202, 209, 218, 261, 287, 289, 290

Unconfined-type MTD, 178

Vieste Slide (VS)
  MTC, 340–42
  SWAM, 340
Villafranca mass-transport complex (VMTC), 346–47
Viper Slide (VS), 323–25
Visco-plastic submarine mass flow, 51
Volcanic islands
  debris avalanche loading, 286–87
    décollement propagation from, 283–84
    seafloor sediment failures triggered by, 287
  IODP Expedition 340, 281–83
  landslide deposits mechanisms of, 286–87
  Lesser Antilles Arc, 280–81, 290–92
    instability processes, 283
    Montagne Pelée volcano, 284–86
  magnitude of volcanic landslide, 278 (*See also* Tsunamis)
  tsunami hazards, 287–90
Volcanism, 107, 172, 227
Volcano instability, 277, 287

Wave loading/dissociation, 273
Wilson cycle, 10, 11, 15